efzn

Energie-Forschungszentrum
Niedersachsen

Final Report of Geothermal Energy and High-Performance Drilling Collaborative Research Program (gebo)

Schriftenreihe des Energie-Forschungszentrums Niedersachsen (EFZN)

Band 30-1

Das EFZN ist eine wissenschaftliche Einrichtung der

TU Clausthal

in Kooperation mit den Universitäten

Technische Universität Braunschweig

GEORG-AUGUST-UNIVERSITÄT GÖTTINGEN

Leibniz Universität Hannover

CARL VON OSSIETZKY universität OLDENBURG

Final Report

of

Geothermal Energy and High-Performance Drilling Collaborative Research Program (gebo)

Niedersachsen

Partners:

Technische Universität Braunschweig (TUBS)

Technische Universität Clausthal (TUC)

Gottfried Wilhelm Leibniz Universität Hannover (LUH)

Georg-August-Universität Göttingen (UGOE)

Leibniz-Institut für Angewandte Geophysik (LIAG)

Bundesanstalt für Geowissenschaften und Rohstoffe (BGR)

Energie-Forschungszentrum Niedersachsen (EFZN)

Speaker:
Kurt M. Reinicke;
Georg-Peter Ostermeyer

Goslar, July 2015

Contents

1   Executive Summary

The federal state of Niedersachsen (Lower Saxony) pursues the ambitious goal to maximize the use of its geothermal potential for the supply of thermal heat and electrical power. The political requirement for the generation of electrical base load power was 5 MW_{el} net per geothermal power plant or more.

To achieve this objective economically requires a supply of thermal fluids to a geothermal power plant at high rates and high temperatures, and at minimized capital expenditure and operating costs. To provide the high temperatures, deep wells are necessary under typical geological conditions in Niedersachsen. To achieve the necessary high rates at the depths considered, fracture systems must be developed to allow an efficient heat exchange and to reduce the inflow resistance into the well. The fracture systems may be either naturally present or artificially created. Also, high rate fluid supply requires wells of large diameter for low outflow resistance out of the well. The construction of the subsurface systems demands materials and electronic components which operate reliably under the deep hot, hard rock conditions. The systems must be sustainable, a challenge in view of the corrosivity and scaling tendency of the high salinity formations brines, encountered at sub salt levels in Northern Germany. Total costs of geothermal projects are dominated by the costs for the construction of wells and geological heat exchangers. Well costs for deep natural gas wells in Niedersachsen average approx. 2.5 Million Euro per 1.000 m, which is too high to achieve satisfactory economics for geothermal application. Well cost analysis shows that a significant cost reduction is only possible by a novel approach to the construction concept of deep wells.

To meet all these challenges requires a multi-disciplinary approach focusing first of all on the issues that have the largest impact, i.e. the safe construction of wells under "hot-hard rock" conditions and the development of sub-surface heat exchangers at significantly reduced costs and risks. To this end the „Niedersächsisches Ministerium für Wissenschaft und Kultur" (MWK) has initiated a research collaboration program "Geothermal Energy and High Performance Drilling" (gebo). The collaborative program, co-financed by Baker Hughes, is a 5-year effort funded with approx. 12 Million Euro. The program, coordinated by the "Energie-Forschungszentrum Niedersachsen" (EFZN), combined the traditional strengths of the participating Niedersachsen based universities and research institutions in geosciences, drilling technology, materials science and technical systems. More than 40 gebo financed scientists and engineers collaborated to evaluate existing and develop new concepts, materials and components. The program was carried out in close coordination with the participating industry. gebo university based research excels with a high-risk, "high-end" approach, that will typically

not be covered by typical industry development activities. Although all projects were directed towards improving the economics of geothermal energy recovery from petrothermal systems, significant gebo "spin-off" effects are expected to benefit a broader industrial sector, in particular from the materials and systems technology research.

The objective was pursued in 32 projects organized in four focus areas: Geosystems, Drilling Technology, Materials, and Technical Systems. The accountability for achieving the overall objective rested with a Steering Committee, make up of a speaker, the focus area coordinators and representatives of the participating industry. Steering Committee and MWK were advised by the gebo Advisory Board, comprising members from the international research community, industry, geothermal operators and the banking sector.

The opening event for the program was in May 2009. While first projects resumed their work as early as February 2009, staffing for some projects took as long as mid 2010. Reasons were administrative restrictions and difficulties in finding the required skills. In the meantime precautions have been taken to ensure a timely successful completion of all projects by 2014. Altogether, progress of the gebo program was in line with the plan documented with the formal application document as of June 2009.

Main achievements to date were as follows:

Coordination and General Overview: Communication and steering efforts to establish a common knowledge basis for the parties from very different disciplines and the alignment of their contributions towards the goal set was recognized as a major challenge. To this end Steering Committee, Advisory Board and monthly "Jour Fixe" meetings were successfully carried out. In particular the latter proved very effective in aligning the individual efforts and to share knowledge.

Early emphasis has been put on networking with international organizations (Geoforschungszentrum Potsdam; Marinnovation, Frankreich; University Stavanger, International Research Organization Stavanger; Texas A&M University; US Department of Energy) which has provided and will provide valuable input.

Progress achieved was documented in more than 150 publications of which more than 35 have appeared in referenced in traceable journals and conference proceedings and 9 patent applications up to end December 2014. Progress achieved in the 4 focus areas is summarized below.

To ensure fit-for-purpose contributions a sample petrothermal system was defined, consistent with the political requirements, and a construction concept to develop the system is proposed. Some of the key requirements are a true vertical depth (TVD) of 6.000 m, a fluid production of 100 l/s, and a bottom hole flowing temperature of 200 °C.

The well bore construction concept assumes conventional or casing drilling down to approx. 1.000 m followed by conventional or coiled tubing drilling of a constant diameter well of size 10 3/4 in. to the target depth. The lower section is assumed to be cased with a folded pipe to be expanded to a diameter of 8 5/8 to 9 in. once setting depth is reached.

Focus Area Geosystem: For the success of a geothermal project, the hydraulic properties and temperature of the geothermal reservoir are crucial. New methodologies in seismics, geoelectrics and reservoir geology are currently being tested at locations where structures of interest are found at or near the surface before applying them to target depth. Tools were developed (Benchmark models and experimental techniques) that help in the evaluation and interpretation of acquired data. Special emphasis was placed on the investigation of rock properties, on the development of early reservoir assessment even during drilling, and on the interaction between the drilling apparatus and the reservoir formation. The propagation of fractures and the behavior of fluid and heat transport within the regional stress field were investigated using different approaches (field studies, seismic monitoring, multi-parameter modeling). Geologic structural models have been created for simulation of the local stress field and hydromechanical processes. Furthermore, a comprehensive dataset of hydrogeochemical environments was collected allowing characterization and hydrogeochemical modeling of the reservoir.

Focus Area Drilling Technology: Project work addressed features and processes related to drilling and the construction of geothermal wells under hot-hard rock conditions. Particular emphasis was placed on differences in processes (borehole hydraulics, borehole stability, rock destruction, cuttings transport, drill string dynamics, etc.), procedures (pipe handling, drilling process) and reservoir simulation (heat recovery) of geothermal relative to standard oil and gas well construction caused by the hot-hard rock environment and the selected construction concept. In order to drive geothermal plant economics, the current well construction concept was focused on a mono-diameter well design. Efforts were also directed towards integrating the different process models with a view to develop a concept for a drilling simulator that is able to support well planning and execution. Several novel geothermal one and two well designs were defined for evaluation of viability, energy recovery, and costs.

Focus Area Materials: The fatigue resistance and life cycle of modern drilling technologies are restricted by the severe environmental conditions. The mechanical loads caused by drilling in increased depths and through hard formations, as well as high ambient temperatures in wells are very critical. Moreover, the strains caused by ambient pressures and corrosive media are of great importance. New materials, material coatings, tools and systems are required. Therefore, the following efforts are being made: For a proper design of drilling systems the strains must be characterized realistically; high strength, heat resistant and corrosion resistant materials and coatings as well as material-adapted processing techniques and novel composite designs must be developed. The achieved objectives were a test environment for stress analysis, realistic synthetic load spectra and first life time calculations. Furthermore, functional coatings and welding techniques were being developed as well as geometries of folded tubulars which were also expanded in simulations.

Focus Area Technical System: Electronics in downhole tools (Measurement While Drilling "MWD") use large scale integrated electronic circuits for control and measurement tasks, but such electronic components are not commercially available for the expected ambient temperatures at present. Therefore, one contribution for the gebo project was to investigate the possibilities for a realization of MWD-electronics on the basis of "Silicon on Insulator" (SOI) technology and to identify the best-suited processor architecture designs. With active cooled circuit boards it is possible to protect these components against high temperatures. A high-temperature resistant die attach was developed for electronic devices and sensors to be used for data logging during extreme conditions. For the navigation of the drilling assembly and for the determination of the ambient formation characteristics, various sensors for operation temperatures up to 250 °C were developed and tested. The feasibility of a complete new antenna design for a Ground Penetrating Radar inside the BHA was investigated, so the drill process could be optimized thanks to the detection of boundary layers ("frac zones") within the hard-rock geothermal pay zone.

2 General Information

2.1 Organizational overview

2.1.1 Management structure
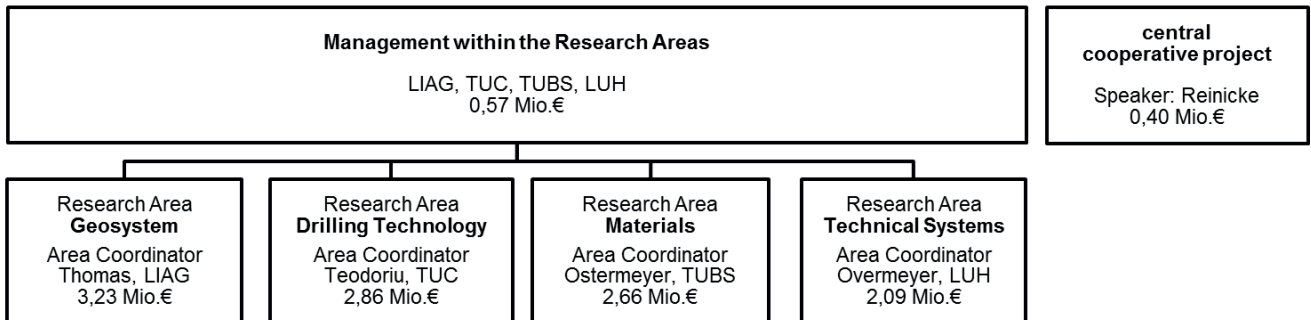
Figure 1: Organisation of the Collaborative Research Program gebo

Baker Huges Contacts were:

- Geosystem   Dr. Anne Bartetzko
- Drilling Technology   Dipl.-Ing. Jörg Lehr
- Materials   Dr.-Ing. Hendrik John
- Technical System   Dr.-Ing. Thomas Kruspe
- Steering Committee   Dr.-Ing. Joachim Oppelt

2.1.2 Summary table of the technical projects

No.	project title	responsible
	Geosystem, Dr. Thomas, LIAG	
G1	Detection of Fault Zones Using Seismic Methods	LIAG: Thomas / Buness
G2	Detection of Fault Zones Using Electric and Electromagnetic Methods	LIAG: Grinat / Günther
G3	Heterogeneous Rock Properties, Drilling Efficiency and Fracture Propagation	UGOE: Philipp
G4	Characterisation of Enhanced Geothermal Reservoirs by Diagnostic Methods	BGR: Wegler
G5	Hydromechanics of Geothermal Reservoirs	LIAG: Schellschmidt / Schulz
G6	Hydraulic, Heat and Tracer Tests at Wellbore and Reservoir Scale	UGOE: Sauter
G7	Modelling of Coupled Thermo-hydro-mechanical Processes in Georeservoirs	UGOE: Sauter
G8	Electrical Impedance Tomography for the Characterisation of Geothermal Systems	TUBS: Hördt
G9	Hydrogeochemical Processes in Geothermal Systems	TUC: van Berk

5

Drilling Technology, Dr. Teodoriu, TUC

B1	Cost effective drilling methods for „hot-hard-rock" conditions	TUC: Teodoriu
B2	Drilling Simulator	TUC: Teodoriu
B3	Automation of the drilling process by application of a flexible drill string	LUH: Overmeyer, Denkena
B4	Geo parameters from well logging and their utilization	TUC: Hou, LIAG: Wonik
B5	Assurance of efficient drill cuttings transport	TUC: Brenner, Reinicke
B6	Computer simulation of fluid dynamics	TUBS: Krafczyk
B7	Drill string dynamics and modeling	TUBS: Ostermeyer
B8	Monitoring and control of drill string loads	TUC: Teodoriu
B9	Innovative drilling concepts for geothermal energy exploitation	TUC: Teodoriu, TUBS: Ostermeyer

Materials, Prof. Ostermeyer, TUBS

W1	Life cycle of Coated High-Performance Materials	TUBS: Rösler
W3	Materials and Surfaces for Extreme Demands	TUBS: Klages
W4	Coatings with High Electrical Conductivity and Abrasion Resistance	LUH: Bach
W5	Materials, Welding and Machining Technology for Deep Drilling	LUH: Bach (IW), Denkena (IFW)
W6	Desing of Folded Tubulars for Casing Applications	LUH: Bach (IW), Denkena (IFW)
W7	Design of Fatigue Resistant Mechanical Components for Drill String Applications	TUBS: Ostermeyer TUC: Esderts
W8	Technical Systems Reliability of Downhole Components	TUC: Esderts, Beck

Technical System, Prof. Overmeyer, LUH

T1	High Temperature Electronics	LUH: Blume, Barke
T2	Joining and Packaging Techniques for High Temperature Electronics	TUBS: Waag, Peiner
T3	Packaging of Electronic Components for High Temperature Applications (substrate and heat dissipation)	LUH: Overmeyer
T4	Thermal Management	TUBS: Schilling, Ludwig
T5	High Temperature Sensors	LUH: Reithmeier. Rissing
T6	Fluxgate Sensors for 250 °C	TUBS: Schilling, Ludwig
T7	Intelligent Sensor-based Drilling Tools	LUH: Overmeyer

Management of Projects and Collaborative Research Program

GS, BS WS, TS	Management within the research areas	Speaker of research areas
Z	central cooperative project	TUC: Reinicke, EFZN: Mattioli

2.1.3 List of all gebo project managers

name, first name, academical title	Institute	project no.
Bach, Friedrich-Wilhelm, Prof. Dr.-Ing.	LUH, Institut für Werkstoffkunde	W4, W5, W6
Beck, Hans-Peter, Prof. Dr.-Ing.	TUC, Institut für Elektrische Energietechnik	W8
van Berk, Wolfgang, Prof. Dr.	TUC, Institut für Endlagerforschung	G9
Brenner, Gunther, Prof. Dr.-Ing.	TUC, Institut für Technische Mechanik	B5
Blume, Holger, Prof. Dr. Ing.	LUH Elektrotechnik, Institut für Mikroelektronische Systeme (IMS)	T1
Denkena, Berend, Prof. Dr.-Ing.	LUH Maschinenbau, Institut für Fertigungstechnik und Werkzeugmaschinen (IFW)	B3, W5, W6
Esderts, Alfons, Prof. Dr.-Ing.	TUC, Institut für Maschinelle Anlagentechnik und Betriebsfestigkeit	W7, W8
Grinat, Michael, Dipl.-Geophys.	LIAG, S2, Geoelektrik und Elektromagnetik	G2
Hördt, Andreas, Prof. Dr.	TUBS, Institut für Geophysik und Extraterrestrische Physik	G8
Hou, Michael Zhengmeng, apl. Prof. Dr.-Ing. habil.	TUC, Institut für Erdöl- und Erdgastechnik	B4
Klages, Claus-Peter, Prof. Dr.	TUBS, Institut für Oberflächentechnik	W3
Krafczyk, Manfred, Prof. Dr.-Ing. habil.	TUBS, Institut für rechnergestützte Modellierung im Bauwesen	B6
Ludwig, Frank, Dr. AOR	TUBS Institut für Elektrische Messtechnik und Grundlagen der Elektrotechnik	T4, T6
Ostermeyer, Georg-Peter, Prof. Dr.-Ing. habil.	TUBS, Institut für Dynamik und Schwingungen	B7, B9, W7, **WS**
Overmeyer, Ludger, Prof. Dr.-Ing.	LUH Maschinenbau, Institut für Transport- und Automatisierungstechnik (ITA)	B3, T3, T7, **TS**
Peiner, Erwin, Dr. rer. nat...	TUBS, Institut für Halbleitertechnik	T2
Philipp, Sonja, JProf. Dr.	UGOE, Geowissenschaftliches Zentrum, Abteilung Strukturgeologie und Geodynamik	G3
Reinicke, Kurt M., Prof. Dr.	TUC, Institut für Erdöl- und Erdgastechnik	B5, **gebo-speaker**
Reithmeier, Eduard, Prof. Dr.-Ing.	LUH Maschinenbau, Institut für Mess- und Regelungstechnik (IMR)	T5
Rissing, Lutz, Prof. Dr.-Ing.	LUH Maschinenbau, Institut für Mikroproduktionstechnik (IMPT)	T5
Rösler, Joachim, Prof. Dr.	TUBS, Institut für Werkstoffe	W1
Sauter, Martin, Prof. Dr.	UGOE, Geowissenschaftliches Zentrum, Abteilung Angewandte Geologie	G6, G7
Schellschmidt, Rüdiger, Dipl. Geophys.	LIAG, S4, Geothermik und Informationssysteme	G5
Schilling, Meinhard, Prof. Dr. rer. nat.	TUBS, Institut für Elektrische Messtechnik und Grundlagen der Elektrotechnik	T4, T6
Schulz, Rüdiger, Dr.	LIAG, S4, Geothermik und Informationssysteme	G5
Teodoriu, Catalin, Dr. Dr.-Ing.	TUC, Institut für Erdöl- und Erdgastechnik	B1, B2, B8, B9, **BS**

Thomas, Rüdiger, Dr. rer. nat.	LIAG, Ltg., Forschungsschwerpunkt Geothermische Energie	G1, **GS**
Waag, Andreas, Prof. Dr. rer. nat. habil.	TUBS, Institut für Halbleitertechnik	T2
Wegler, Ulrich, Dr. rer. nat.	BGR, B4.3, CTBT, seismologisches Zentralobservatorium	G4
Wonik, Thomas, Dr.	LIAG, S5 - Petrophysics and Borehole Geophysics	B4

2.1.4 Participating public facilities as well as expressions of interest from industrial and other partners

The gebo Collaborative Research Program comprised scientists and technicians of different research institutions and universities who were working in 33 projects. The individual projects were assigned to one of the 4 main research fields or focus areas. They were described in more detail in one the "Main Field" pages.

The gebo Collaborative Research Program started its activities in 2009 with 7 project partners participating:

- Federal Institute for Geosciences and Natural Resources, Hanover
- Energie-Forschungszentrum Niedersachsen, Goslar
- Leibniz Institute for Applied Geophysics, Hanover
- Gottfried Wilhelm Leibniz University, Hanover
- Technische Universität Carlo-Wilhelmina zu Braunschweig
- Clausthal University of Technology, Clausthal-Zellerfeld
- Georg-August University Göttingen, Göttingen

Baker Hughes, as an industry partner, participated by providing its experience as well as financial funds.

2.2 Scope and Objectives Overview

2.2.1 Introduction

"The federal state Niedersachsen (Niedersachsen) pursues the ambitious goal to make comprehessive use of its geothermal potential for the production of thermal heat and electric power". This was the statement of the Niedersachsen Minister for Science and Culture, Mr Lutz Stratmann on the occasion of the startup event of the new Collaborative Research Program "Geothermal Energy and High Performance Drilling, gebo" on May 20, 2009.

Despite relatively moderate temperatures in the geological subsurface, the preconditions in Niedersachsen are good, for this state to achieve its goals: It possesses a considerable geothermal potential. The knowledge of the geological subsurface, resulting from more than 20.000 oil and natural gas wells, and 2D and 3D seismic, is good. In addition, the scientific and industrial infrastructure for exploration and development of the geological subsurface is excellent. The development of deep geothermal energy is, however, connected with high costs and risks. They result in particular from the expensive and time-consuming construction of the necessary deep boreholes and required geological heat exchangers.

The goal of the gebo Collaborative Research Program was to carry out research and survey new concepts to improve the economic efficiency of geothermal energy recovery from deep geological formations. With its focus on innovative aspects of drilling and of subsurface heat exchanger development, the association addresses those aspects of geothermal power projects for which both costs and risks are the highest (ca. 70% of the total investment). The gebo Collaborative Research Program united the traditional strengths of the participating universities of the federal state of Niedersachsen and (independent) research institutions in geosciences, drilling technology, materials science and technical systems. In the association, more than 100 scientists and engineers collaborated to develop and evaluate new concepts, materials and components.

The project was carried out in close coordination with participating industry. The gebo Collaborative Research Program focused on broad-scale, partly extremely high-risk problems in the "High-End" area of research; at the same time, the participating industry was carrying out applied systems developments. From the work, directed towards improving the economics of geothermal energy recovery from petrothermal systems, significant gebo "spin-off" effects were expected to the industrial sector, in particular from the materials and systems technology research.

2.2.2 Background and genesis of the joint project

The comprehensive use of deep geothermal energy is to make a significant contribution to climate protection and a secure energy supply in the future. This is the conclusion of a report on geothermal energy enacted by the federal cabinet on May 13, 2009. By 2020 approx. 280 MW are to be installed to generate electrical power from geothermal energy. Assuming a capacity of 5 MW_{el} per power station, more than 50 stations must be built to achieve the objective. On the basis of two wells per station, more than 100 wells with sustainable high production capacities need to be constructed within the next 10 years. After 2020 an acceleration in the growth of the installed power production is expected with up to 850 MW installed capacity by 2030.

Niedersachsen's preconditions for a usage of geothermal power from the deep subsurface are good: the geothermal potential is available, the knowledge concerning deep geological subsurface is profound, and the infrastructure for its exploration and development is nowhere better in Germany.

The geological conditions in Niedersachsen are challenging, however. The wells in Niedersachsen have neither the high production rates for thermal water as in the Molasse Basin (South Germany) nor do they have the high temperatures in the shallow sub-surface, as in the Oberrheintalgraben. In Niedersachsen wells must be drilled down to 6.000 m in order to reach a temperature level of 200 °C up to 250 °C, which is required for an efficient generation of electrical power. In addition, Niedersachsen brines are of high salinity, expected to lead to corrosion and scaling problems in the primary cycle of the thermal system. Hence, the resulting technological challenges for an efficient development of the huge potential are reflected by the goals of the gebo research association.

2.2.3 Current State of Research

There are 3 different systems for the recovery of geothermal energy:

- Hydro-thermal systems: utilization of the energy which is contained in the water of the deep subsurface
- Petro-thermal systems: utilization of the energy, which is contained in the rock of the deep subsurface (Hot-Dry-Rock (HDR), Hot-Wet-Rock (HWR), Hot-Fractured-Rock (HFR), Enhanced Geothermal System (EGS))
- Deep heat probe (borehole heat exchanger): uses wells up to 3.000 m deep in which a heat transfer liquid circulates in a closed system for heat production.

With the exception of wells in areas affected by volcanic activities, all three systems require deep boreholes. To achieve high production rates of hydro-thermal or petro-thermal systems,

wells are drilled to connect to naturally existing fracture systems in the subsurface or fracture systems are generated in hydraulic treatments after the well has been drilled. To generate electrical power, only petro-thermal systems are relevant and to a certain degree hydro-thermal systems, if conditions are favourable.

The currently available technology for the construction of deep wells is adapted for the needs of the oil and natural gas industry. Oil and natural gas wells are constructed to provide a safe connection between a reservoir in the subsurface and the surface installations for the duration of the exploitation. This is also valid for geothermal wells, especially for hydro-thermal wells with final depths of 3.000 – 4.000 m. For petro-thermal systems, aiming at recovering the heat stored in "dry and hard" rock, well requirements are quite different from those in typical oil and natural gas wells:

- the average temperature is higher
- the target is not a relatively soft reservoir rock but hard rock, for example, volcanic rocks
- thermal operations require sustainable heat exchangers with large contact areas, either naturally existing or artificially created
- minimization of the hydraulic resistance in the wells during production and injection requires large cross sectional areas for flow
- the average depth is larger.

All these less favourable conditions require new solutions. At the same time, the system costs must be decreased: approximate cost in the oil and natural gas industry for 5.000 m wells are ca. 2,5 – 3,0 million Euros per 1.000 m. Well costs this high, are not economically efficient for deep geothermal systems. The main goal of the gebo Collaborative Research Program was therefore to make solid contributions to

- decrease the cost of drilling
- improve drilling technologies for hard and hot rock drilling
- improve the chance of success for achieving economic rates

2.2.4 Objectives of the joint project (goals)

The overriding objective of the gebo collaborative research program was making essential contributions for a safe construction of wells under the "hot-hard-rock" conditions existing in Niedersachsen and their further development to a geothermal system with sustainable geological heat exchangers.

This goal should be achieved by the investigation of highly innovative technology approaches as modelues of an overall concept for a novel construction of deep geothermal wells in hard rock

- in interdisciplinary cooperation of engineers and scientists
- in cooperation between industry and University, researchers and users.

Targets were to

- develop new technologies allowing a proper recording and characterization of the geological subsurface
- assure high well productivities by sustainable geological heat exchangers
- identify and explore ideas and concepts to decrease well construction costs, dominating the initial investment for geothermal power plants
- make critical contributions to the realization of a reliable operation of the modern drilling technology in a hot-hard rock environment with temperaures up to >200°C
- improve hard-rock drilling by developing new materials and tools
- make contributions to manage technical risks caused by high temperatures/production rates, cyclic loading, high salinity brines, etc.

2.2.5 Presentation of the research program

2.2.5.1 Research Area Geosystem

Various geophysical and geological techniques were being employed for the exploration of geothermal reservoirs. Combined seismic, geoelectrical and geological investigations were carried out at the Leinetalgraben north of Göttingen. This allowed for a complex investigation of a north German setting for a geothermal reservoir, characterised by the presence of fault zones. Using hydraulic and transport investigations, fluid flow and heat transport parameters (hydraulic conductivities, specific area, effective porosity, reservoir shape, geomechanic properties) did be quantified. Particular emphasis was also being placed on the assessment of the chemical composition of the highly saline brines and its effect on the formation of borehole skins. Finally, numerical models shall be developed investigating the effect of thermo-hydro-mechanical process coupling as well as for the prediction of the long-term development of the geothermal reservoir.

The following results were expected:

- exploration strategy for fault systems
- knowledge of reservoir characteristics for the optimum choice of the drilling technology
- determination and evaluation of relevant parameters by means of hydraulic, tracer and heat tests
- recommendations concerning reservoir behaviour in long-term simulation for efficient energy production.

Coordinator: Dr. Rüdiger Thomas
Baker Hughes Contact: Dr. Anne Bartetzko

Projects

The research area "Geosystem" consists of four categories, which work on nine projects. The four categories are: exploration, exploitation (development) and characterization of geothermal reservoir, as well as modelling of geothermal energy reservoirs.

The cooperation between the different geoscientific projects was strengthened by an interdisciplinary work package called "benchmark models". In this work package, a set of representative models was generated which describes geological structures relevant for geothermal exploration in Niedersachsen. The models were the basis for numerical simulation of different physical processes carried out by several geoscientific projects. All Geosystem projects contribute to the work package "benchmark models", which was coordinated within G8,

with their knowledge either on geology, or on the physical parameters that were required to characterise the different geologic formations and the borehole. The intense discussion on the models had considerably increased the mutual understanding among the different disciplines.

Finally, the resulting set of models did be transferred to the other gebo research areas as well as the geoscientific public as representative geothermal reservoir models for the North German basin.
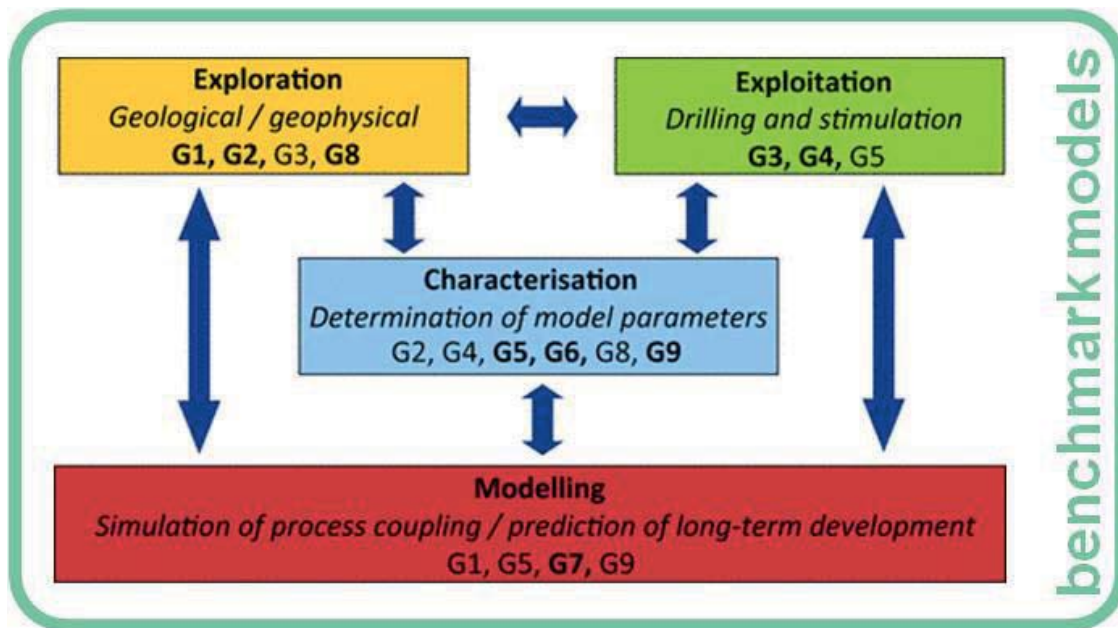

Figure 2: Networking inside the research area Geosystem

G1: Detection of Fault Zones Using Seismic Methods
Dr. Rüdiger Thomas, Leibniz Institute for Applied Geophysics (LIAG)

G2: Detection of Fault Zones Using Electric and Electromagnetic Methods
Dipl.-Geophys. Michael Grinat, Leibniz Institute for Applied Geophysics (LIAG)

G3: Heterogeneous Rock Properties, Drilling Efficiency and Fracture Propagation
JProf. Dr. Sonja Philipp, Geoscience Centre, University of Göttingen, Department of Structural Geology and Geodynamics

G4: Characterisation of Enhanced Geothermal Reservoirs by Diagnostic Methods
Dr. Ulrich Wegler, Federal Institute for Geosciences and Natural Resources (BGR)

G5: Hydromechanics of Geothermal Reservoirs
Dipl.-Geophys. Rüdiger Schellschmidt, Leibniz Institute for Applied Geophysics (LIAG)

G6: Hydraulic, Heat and Tracer Tests at Wellbore and Reservoir Scale
Prof. Dr. Martin Sauter, Geoscience Centre, University of Göttingen, Department of Applied Geology

G7: Modelling of coupled Thermo-Hydro-Mechanical Processes in Georeservoirs
Prof. Dr. Martin Sauter, Geoscience Centre, University of Göttingen, Department of Applied Geology

G8: Electrical Impedance Tomography for the Characterisation of Geothermal Systems
Prof. Dr. Andreas Hördt, Institute for Geophysics and Extraterrestrial Physics, TU Braunschweig

G9: Hydrogeochemical Processes in Geothermal Systems
Prof. Dr. Wolfgang van Berk, Institute for Radioactive and Hazardous Waste Management, Clausthal University of Technology

2.2.5.2   Research Area Drilling Technology

A widespread utilization of geothermal energy requires cost-effective deep drilling. The objective of the research area "Drilling Technology" was to make contributions towards a novel method of constructing deep geothermal wells in hot hard rock formations by exploring highly innovative technology concepts.

Overriding objective was the safe construction of deep wells of high mechanical integrity under hot-hard rock conditions at significantly lower costs. This objective was to be achieved by:

- new drilling technologies to allow utilization of smaller and less complex rigs and facilities
- new technologies to permit drilling with smaller initial well diameters and hence, lower consumption of drilling fluid, pipe steel and cement
- new drilling processes to increase the rate of penetration and the productive drilling time
- new technologies for increased system reliability
- improved drilling and well integrity under high pressures and temperatures

Coordinator:	Dr. Catalin Teodoriu
Baker Hughes Contact:	Dipl.-Ing. Jörg Lehr
	Dipl.-Ing. Carsten Freyer
	Dipl.-Ing. Thomas Dahl
	Dipl.-Ing. Roland May
	Dr.-Ing. Hanno Reckmann
	Dr.-Ing. Dmitriy Dashevsky
	Dr. Anne Bartetzko

Projects

The main research field, "Drilling Technology", consists of 9 projects which deal with the specific problems of drillings for geothermal power utilization as well as with the solution of the costs problem in their combination. The projects were divided into 4 areas:
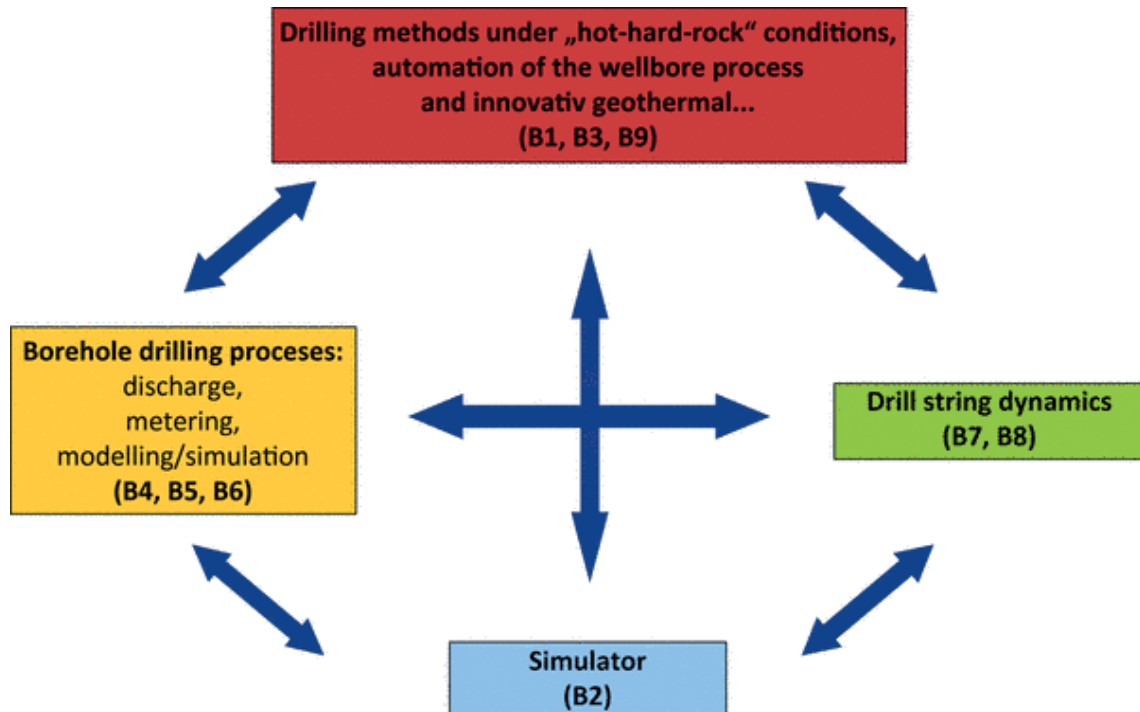

Figure 3: Networking inside the Research Area Drilling Technology

B1: Cost effective drilling methods for „hot-hard-rock" conditions
Dr. Catalin Teodoriu, Institute of Petroleum Engineering, Clausthal University of Technology

B2: Drilling Simulator
Dr. Catalin Teodoriu, Institute of Petroleum Engineering, Clausthal University of Technology

B3: Automation of the drilling process by application of a flexible drill string
Prof. Dr. Ludger Overmeyer, Institute of Transport and Automation Technology,
Prof. Dr. Berend Denkena, Institute of Production Engineering and Machine Tools, Leibniz University Hannover

B4: Geo parameters from well logging and their utilization
Prof. Dr. Michael Zhengmeng Hou, Institute of Petroleum Engineering,
Clausthal University of Technology and Energie-Forschungszentrum Niedersachsen
Dr. Thomas Wonik, Leibniz Institute for Applied Geophysics (LIAG)

B5: Efficient cuttings transport
Prof. Dr. Gunther Brenner, Institute for Applied Mechanics, Clausthal University of Technology
Prof. Dr. Kurt M. Reinicke, Institute of Petroleum Engineering

B6: Computer simulation of fluid dynamics
Prof. Dr. Manfred Krafczyk, Institute for Computational Modeling in Civil Engineering, TU Braunschweig

B7: *Drill string dynamics and modeling*
Prof. Dr. Georg-Peter Ostermeyer, Institute of Dynamics and Vibrations, TU Braunschweig

B8: Monitoring and control of drill string loads
Dr. Catalin Teodoriu, Institute of Petroleum Engineering, Clausthal University of Technology

B9: Innovative drilling concepts for geothermal energy exploitation
Prof. Dr. Georg-Peter Ostermeyer, Institute of Dynamics and Vibrations, TU Braunschweig
Dr. Catalin Teodoriu, Institute of Petroleum Engineering, Clausthal University of Technology

2.2.5.3   Research Area Materials

The fatigue resistance and reliability of modern drilling technologies are restricted by the severe environmental conditions. The mechanical load caused by drilling in increased depths and through hard formations, as well as high surrounding temperatures in wells is very critical. Moreover, the strains caused by ambient pressures and corrosive media are of great importance. New materials, material coatings, tools and systems are required. For increased fatigue resistance and reliability of modern drilling technologies the following efforts were being made:

- The strains had be characterized realistically. This was important for a proper design of drilling systems
- High strength, heat resistant and corrosion resistant materials and coatings had be developed
- Material-adapted processing techniques and novel composite designs had be developed.
- Novel tubular for future casing techniques had be developed
- Due to the investigation of the system component's reliability, maintenance, availability and its consequence to the overall system the drilling system's reliability had be improved.

In order to realize these aims inside the research area "Materials" on the one hand a compact networking between load specification, new material systems and novel processing and design methods was arranged (figure 5). On the other hand the networking between the further research fields together with the belonging interfaces ensured the integration into the overall research project. Thus, new drilling systems and components could be designed under operating conditions.
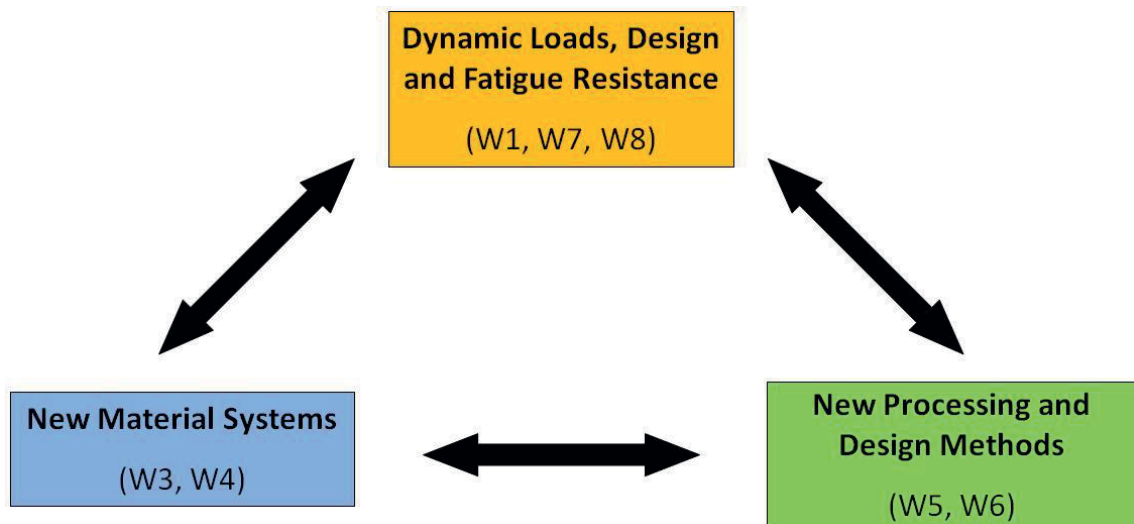
Figure 4: Networking inside the Research Area Materials

The results which were supposed to be achieved within the framework of these research fields could be used additionally in the area of geothermal subsurface constructions. Therefore, negative impacts, by means of the downhole environmental conditions, could be considered for geothermal downhole applications as well as for the development of high strength, heat resistant and corrosion resistant materials and coatings within the framework of the research area "materials". New processing methods and designs for drilling and casing technologies generate know-how that was able to provide the development of geothermal downhole applications in future.

Coordinator: Prof. Dr. Georg-Peter Ostermeyer
Baker Hughes Contact: Dr.-Ing. Hendrik John
                          M.Sc. John Stevens

Projects:

W1: Life cycle of Coated High-Performance Materials
Prof. Dr. Joachim Rösler, Institute of Materials Science, TU Braunschweig

W2: Computation of Folded Tubular and Coated High-Performance Materials
The project is deleted at the very beginning without replacement (see remarks).

W3: Materials and Surfaces for Extreme Demands
Prof. Dr. Claus-Peter Klages, Institute for Surface Technology, TU Braunschweig

W4: Coatings with High Electrical Conductivity and Abrasion Resistance
Prof. Dr. Friedrich-Wilhelm Bach, Institute of Materials Science, Leibniz University Hannover

W5: Materials, Welding and Machining Technology for Deep Drilling
Prof. Dr. Friedrich-Wilhelm Bach, Institute of Materials Science,
Prof. Dr. Berend Denkena, Institute of Production Engineering and Machine Tools, Leibniz University Hannover

W6: Desing of Folded Tubulars for Casing Applications
Prof. Dr. Friedrich-Wilhelm Bach, Institute of Materials Science,
Prof. Dr. Berend Denkena, Institute of Production Engineering and Machine Tools, Leibniz University Hannover

W7: Design of Fatigue Resistant Mechanical Components for Drill String Applications
Prof. Dr. Alfons Esderts, Institute for Plant Engineering and Fatigue Analysis, Clausthal University of Technology
Prof. Dr. Georg-Peter Ostermeyer, Institute of Dynamics and Vibrations, TU Braunschweig

W8: Technical Systems Reliability of Downhole Components
Prof. Dr. Alfons Esderts, Institute of Plant Engineering and Fatigue Analysis,
Prof. Dr. Hans-Peter Beck, Institute for Electrical Power Engineering, Clausthal University of Technology

Remarks:

As written in the additional gebo-proposal the financial resources of the cancelled project W2 were shifted to project W1 in order to additionally consider corrosion in their measurements. The substantial scientific questions of project W2 were shifted to project W7 that had integrated the computation of folded tubular by using complex non-linear FE-tools. Therefore, the funding was provided by the IDS using its own basic resources. This funding ends to gebo's first period.

2.2.5.4   Research Area Technical Systems

Modern drilling systems are equipped with electronic modules for electric power supply, communication and sensor technologies. The severe environmental conditions, especially high pressures and temperatures, make heavy demands the electronic components have cope with. The main point of the contributions is a thorough increase of the drilling systems technical reliability for geothermal energy use.

It is necessary then:

- to develop new electronic and sensor technologies which are suitable for severe environmental conditions
- their energy supply must be guaranteed
- that opportunities of the determination of the position and measure data transmission must be improved

In addition to these three main points, work on the reliability problem is necessary due to extreme mechanical loads (owing to drilling processes in larger depths and geologically hard formations). The three components: high level of technical and operational reliability, low accident risk must be guaranteed due to systematic studies of availability and trustworthiness of peculiar components and parts, as well as their cooperative work.

The research area "Technical Systems" surveyed the way well-known technical solutions function under new conditions, like new dimensions and new system environment.

Coordinator:	Prof. Dr. Ludger Overmeyer
Baker Hughes Contact:	Dr.-Ing. Dr.-Ing. Thomas Kruspe
	Dr. Sascha Schwarze
	Dr. Sebastian Jung

Projects

For development of necessary high temperature electronics the research area "Technical Systems" was working on 7 projects, which could be divided into 4 sub-areas: chip design, heat dissipation, sensor technologies and geo radar.
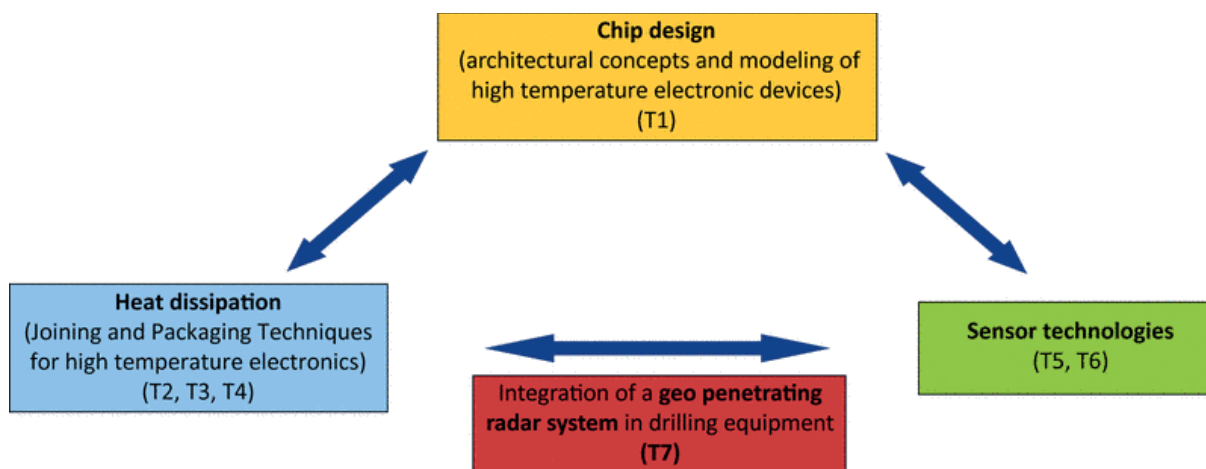

Figure 5: Networking inside the Research Area Technical Systems

T1: High Temperature Electronics
Prof. Dr. Holger Blume, Institute of Microelectronic Systems, Leibniz University Hannover

T2: Joining and Packaging Techniques for High Temperature Electronics
Prof. Dr. Andreas Waag, Institute of Semiconductor Technology, TU Braunschweig

T3: Packaging of Electronic Components for High Temperature Applications (substrate and heat dissipation)
Prof. Dr. Ludger Overmeyer, Institute of Transport and Automation Technology, Leibniz University Hannover

T4: Thermal Management
Prof. Dr. Meinhard Schilling, Institute of Electrical Measurement Science and Fundamental Electrical Engineering, TU Braunschweig

T5: High Temperature Sensors
Prof. Dr. Eduard Reithmeier, Institute of Measurement and Automatic Control,
Prof. Dr. Lutz Rissing, Institute of Microproductiontechnics, Leibniz University Hannover

T6: Fluxgate Sensors for 250 °C
Prof. Dr. Meinhard Schilling, Institute of Electrical Measurement Science and Fundamental Electrical Engineering, TU Braunschweig

T7: Intelligent Sensor-based Drilling Tools
Prof. Dr. Ludger Overmeyer, Institute of Transport and Automation Technology, Leibniz University Hannover

2.3   Integration of the Collaborative Research Program in Niedersachsen

The developments described were to be pursued in a holistic approach with many disciplines and parties contributing to achieve one common goal. Cooperating parties were BGR and LIAG, the NTH universities LUH, TUBS, TUC, and university UGOE and the Niedersachsen-based drilling and service industry.

Baker Hughes in Celle, as a substantial supporter of the research program, was also involved in the definition of the tasks. It was expected that in addition to Baker Hughes further companies would network with gebo and potentially join the program.

2.4   Organization Details

The gebo Collaborative Research Program employed scientists and technical staff of different research institutes and universities of Niedersachsen (Niedersachsen). For a successful realization of the research projects the coordination with regard to content and time was essential. This was the task of the **speaker** of the collaborative research program, Prof. Dr. Kurt M. Reinicke (until November 2013) and later on Prof. Dr. Georg-Peter Ostermeyer (former the vice-speaker).

The four **research area coordinators** were:

- Dr. Rüdiger Thomas: research area "Geosystem"
- Dr. Catalin Teodoriu: research area "Drilling Technology"
- Prof. Dr. Georg-Peter Ostermeyer: research area "Materials"
- Prof. Dr. Ludger Overmeyer: research area "Technical Systems"

The cooperation of the four research areas and participating industry was assured by a **steering committee** consisting of the research area coordinators and there representatives, the speakers of the association and representatives of the participating industry.
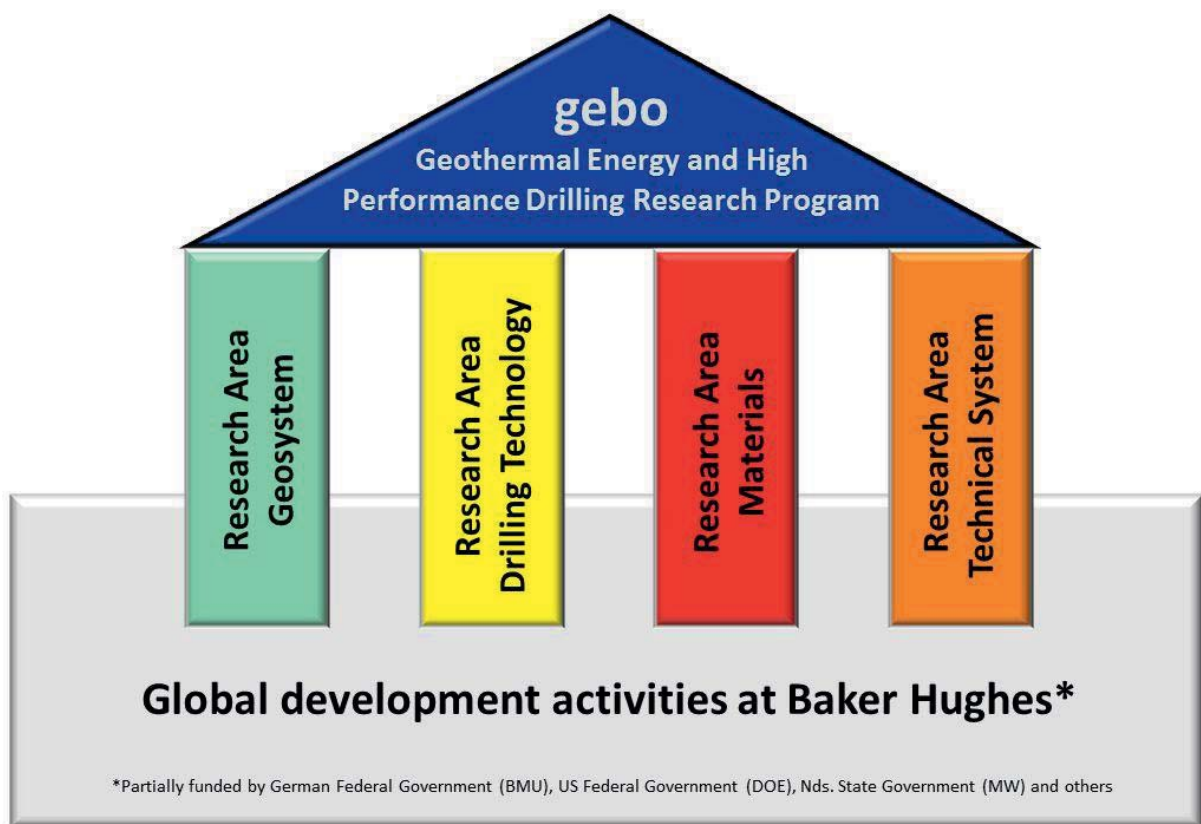

Figure 6: Organisation of the Collaborative Research Program gebo

The steering committee was supported by an **advisory board** which deals with scientific, financial and energy policy goals. Speakers and steering committee were supported by an **administrative office** at the Energie-Forschungszentrum Niedersachsen in Goslar.

Steering Committee

The steering committee guarantees the compliance with the economical and scientific objectives. It decides questions of fundamental importance and is as well responsible for the cooperation of the gebo Collaborative Research Program and other geothermal research initiatives.

The steering committee is headed by the **speaker** of the Collaborative Research Program gebo, **Prof. Dr. Kurt M. Reinicke** (until the November 2013) and later on **Prof. Dr. Georg-Peter Ostermeyer** (former the vice-speaker).

Members of the steering committee were:

- Dr. Joachim Oppelt (Baker Hughes)
- Prof. Dr. Georg-Peter Ostermeyer (research area Materials)
- Prof. Dr. Ludger Overmeyer (research area Technical Systems)
- Dr. Catalin Teodoriu (research area Drilling Technology)
- Dr. Rüdiger Thomas (research area Geosystem)

and:

- Dr. Barbara Hahne (representative research area Geosystem)
- M.Sc. Amjad Moussa (representative research area Drilling Technology)
- Prof. Dr. Martin Sauter (representative research area Geosystem)
- Dr. Frank Schiefer (representative research area Materials)
- Dr. Andreas Stock (representative research area Technical Systems)
- Dipl.-Ing. Frank Mattioli (gebo-office)

Advisory Board

The advisory board advised the steering committee and the Ministry for Science and Culture of Niedersachsen (MWK) concerning compliance with scientific, economic, and energy policy objectives, taking particular account of Niedersachsen's planned expansion in geothermal energy exploitation. Members **of the advisory board** were:

- Dipl. Ing. Friedhelm Makohl, Baker Hughes (**chairman 2009/2010**)
  Dipl. Ing. Johannes Witte, Baker Hughes (**chairman 2011/2014**)
- Prof. Per Arne Bjørkum,
  Dekan of the Faculty of Science and Technology, University of Stavanger
- Prof. Dr.-Ing. Elmar Breitbach, European Center of Adaptive Systems (ECAS) e.V.
- Dr. Jörg Buddenberg, CEO of EWE ERNEUERBARE ENERGIEN GmbH

- Dr. Peter Burri, President at Swiss Association of Energy Geoscientists (SASEG)
- Dipl. Ing. Burkhard Grundmeier, Wirtschaftsverband Erdöl- und Erdgasgewinnung e.V.
- Prof. Dr.-Ing. Rolf Hellinger, Head of Technology Field Power & Energy Technologies, Siemens AG,
- Dr. Erwin Knapek, Geothermal Energy Project Unterhaching
- Prof. Dr. Thomas Kohl,
  Karlsruher Institut für Technologie (KIT), EnBW-Stiftungslehrstuhl für Tiefe Geothermie
- Präsident Lothar Lohff,
  Geschäftstelle Geothermie, Landesamt für Bergbau, Energie und Geologie (LBEG)
- Dr. Thomas Neuber, EWE Aktiengesellschaft
- Prof. Dr. Michael Sinapius, Landesinitiative Nano- und Materialinnovationen
- Ltd. BergD Klaus Söntgerath,
  Geschäftstelle Geothermie, Landesamt für Bergbau, Energie und Geologie (LBEG)
- Dr. Christian Urbanke, Siemens AG
- Andreas Ufer, KfW IPEX-Bank GmbH

gebo office

The gebo office at the Energie-Forschungszentrum Niedersachsen (EFZN) in Goslar was headed by Dipl.-Ing. Frank Mattioli, gebo-office (EFZN)

The focus area "Geosystem"

Barbara Hahne & Rüdiger Thomas*

Leibniz Institute for Applied Geophysics, Stilleweg 2, 30655 Hannover, Germany

*Corresponding Author: Ruediger.Thomas@liag-hannover.de

1. Introduction

In Germany, successful deep geothermal projects are mainly situated in Southern Germany in the Bavarian Molasse Basin, furthermore in the Upper Rhine Graben and, to a minor extent, in the North German Basin (Figure 1). Mostly these are hydrothermal projects with the aim of heat production. In a few cases, they are also constructed for the generation of electricity.
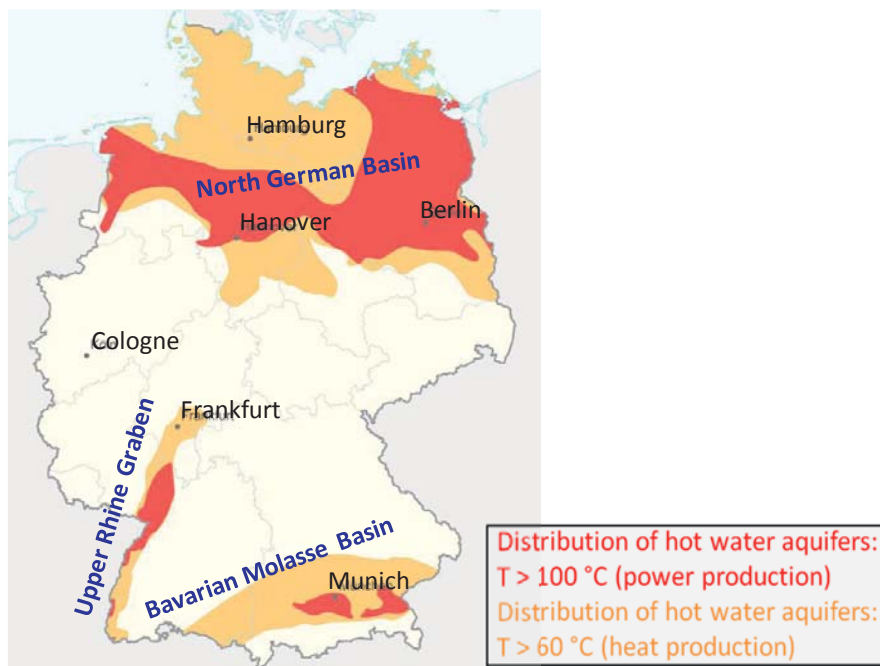

Figure 1: Overview of areas in Germany (aquifers) that are potentially usable for deep hydrothermal projects (after Schulz et al., 2007). Moderate temperature gradients of roughly 30 K/km in Germany implicate a large depth of hydrothermal reservoirs, if they are indented to be used for direct heat extraction or electrical power generation. In the later case temperatures of more than 100 °C are needed, which results in a minimum depth of about 3 km.

For the success of a geothermal project, the hydraulic properties and temperature of the geothermal reservoir are crucial. The geology of the federal state of Lower Saxony is dominated by the North West German Basin where temperature gradients are moderate. Some areas of the basin show a slightly increased geothermal gradient compared to the average of 30 K/km. Therefore, temperatures sufficiently high for production of electrical energy (120 °C and higher) are expected at depth levels of 4000 m and deeper. However, in most areas the porosity of the sedimentary and crystalline rocks is not sufficient for hydrothermal projects, so that natural fracture zones have to be used or the rocks must be hydraulically stimulated. Furthermore, formation fluids in the North German Basin are highly mineralised and can therefore cause compositional and structural alteration of well case materials. Precipitating minerals can even lead to clogging of wells and damage pumping equipment.

In the focus area "Geosystem" of the collaborative research association gebo, the focus of research lay on the geothermal reservoir itself. A special aspect was the geothermal potential of fault zones which can show increased permeabilities compared to undisturbed regions. By means of a combination of different geoscientific methods, physical and geological processes in geothermal systems were to be investigated, as well as their prospecting and production rate. The main parameters are transmissivity (measure of the penetrability/permeability) and temperature, as well as distribution and geometry of natural fault-zones and artificially produced fractures. Modeling allowed making predictions concerning thermo-hydraulic, hydro–geochemical and mechanical rock characteristics in direct drilling environment, as well as statements concerning long-term behaviour of expanded subsurface heat exchangers.

Particular aims of the focus area Geosystem were

(1) the optimization of geothermal exploration strategies, especially of fault zones, with seismic and geoelectrical methods

(2) quantification of mechanical rock properties and the hydromechanical infrastructure of fault zones to better adapt the drilling strategy for deep geothermal wells to the geological situation in different North German settings

(3) determination and evaluation of relevant parameters by means of hydraulic, tracer and heat tests

(4) recommendations concerning reservoir behavior in long-term simulation for efficient energy production

(5) characterization of the natural and the technically influenced hydrogeochemical environments in deep aquifers of the North German Basin (useable for geothermal

energy production), identification of the controlling hydrogeochemical processes within these environments.

(6) prediction of scaling and corrosion effects according to the composition of geothermal waters, their temperature and pressure gradients

The focus area consisted of nine subprojects which contributed to the research fields of geophysical exploration, drilling and stimulation, characterization and modeling of the reservoir (Figure 2). Thus, the projects offered different approaches leading to an improvement of geothermal exploration and exploitation as well as to a better understanding of the processes within geothermal reservoirs.
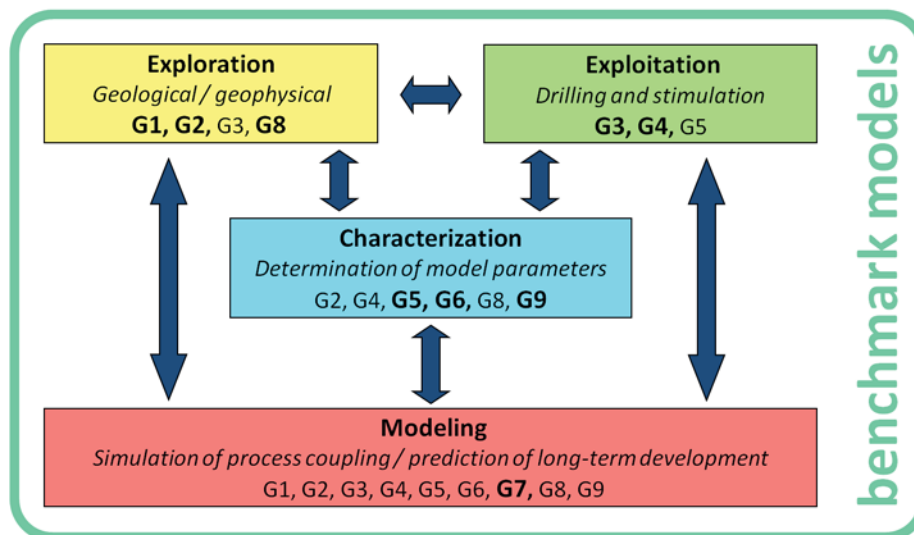

Figure 2: Four research fields of the focus area Geosystem. They are all interconnected. The subprojects G1…G9 are assigned to one of the research fields (number printed bold) but usually also cover one or more aspects of other research fields too (number printed normal). A collective work package called "benchmark models" served for modeling of different aspects on common models (see description below).

The nine subprojects were carried out in collaboration of the Leibniz Institute for Applied Geophysics in Hannover, the University of Göttingen (Department of Applied Geology, Department of Structural Geology and Geodynamics), the Institute for Geophysics and Extraterrestrial Physics of the TU Braunschweig, the Institute for Radioactive and Hazardous Waste Management of the TU Clausthal as well as the Federal Institute for Geosciences and Natural Resources (BGR). Furthermore, it benefited from the close collaboration with our contact person of the industry partner Baker Hughes, Celle.

2. Overview on the subprojects

The nine subprojects of the focus area "Geosystem" were:

G1: Detection of Fault Zones Using Seismic Methods

G2: Detection of Fault Zones Using Electric and Electromagnetic Methods

G3: Heterogeneous Rock Properties: Outcrop Studies, Laboratory Analyses and Models

G4: Characterization of Enhanced Geothermal Reservoirs by Diagnostic Methods

G5: Hydromechanics of Geothermal Reservoirs

G6: Hydraulic, Heat and Tracer Tests at Wellbore and Reservoir Scale

G7: Modeling of coupled Thermo-Hydro-Mechanical Processes in Georeservoirs

G8: Electrical Impedance Tomography for the Characterization of Geothermal Systems

G9: Hydrogeochemical Processes in Geothermal Systems

The basis for all projects is detailed knowledge about rock physical parameters of typical North German rocks and about fracture infrastructure. Therefore, comprehensive investigations of these parameters were carried out in subproject **G3** and communicated between the subprojects. Apart from comprehensive field studies on fault zones and layering, laboratory analyses of rock samples of the North German Basin were carried out within the frame of G3 that give an overview on petrophysical and mechanical rock properties and regression functions for estimating parameters for reservoirs at depth (see final report of G3). In the research field of *exploration*, various geophysical and geological techniques were tested for the exploration of geothermal reservoirs. Combined seismic and geoelectrical investigations were carried out at the Leinetal Graben, a graben system in the southernmost part of the North German Basin in Lower Saxony (subprojects **G1**, **G2**, and **G8**, with input from G3). The structure was chosen because it is a fault structure cropping out at the surface and comprises typical rocks of the North German Basin. The measurements allow a complex investigation of a north German setting for a geothermal reservoir, characterised by the presence of fault zones. From the insights gained at these near-surface structures it may be possible to transfer the exploration strategy to fault structures at target depth.

In this environment, subproject **G1** investigated SH-wave seismic investigations as a supplement to P-wave seismic surveys and their potential to give additional hints on the presence of fluids in the subsurface. Results show, that while the P-wave seismic survey clearly images the reflectors interpreted as fault zone, in the SH-waves it is difficult to resolve the structure. Modeling was carried out to explain this behavior (see final report G1).

Fault systems are typically indicated by relatively low electrical resistivity values when conductive minerals and/or brines within fractures are present. In subproject **G2**, very large-scale Direct Current (DC) measurements and transient electromagnetics were applied at the Leinetal Graben system for obtaining greater investigation depths. The electric and

electromagnetic methods supplement the seismic method (subproject G1). The resulting resistivity image shows clear correlations to the fault segments and layers. The fault structure could be investigated up to depths of about 1 km, which shows that fault location and dip can principally be imaged by this method. Another aspect of G2 was modeling of North German magnetotelluric data in order to investigate the influence of local conditions (i.e. overlying sediments, electrical conductivities) on the detectability of a deep-seated geothermal target layer. Thus, 1D and 2D models of the subsurface were designed that investigated potential features within the basin structure. Furthermore, maps of the North German Basin were created which combine available data important for the localization of potential geothermal target layers (see final report of G2).

Subproject **G8** investigated whether the method of electrical impedance tomography (also called spectral induced polarization, SIP) may be applicable for geothermal exploration, because the complex conductivity of sediments may be related to hydraulic conductivity. Field investigations in the Leinetal Graben showed that electrical anisotropy of the subsurface should not be neglected during interpretation of the obtained data, because an anisotropic model may be more consistent with geological information than a conventional isotropic inversion model. In a second part of G8, a theoretical model is developed which describes the processes at the pore scale which lead to complex conductivity behavior. Finally, laboratory investigations on rock samples were carried out in order to investigate the effect of the induced polarization at the pore scale itself and its dependence on temperature (see final report of G8).

The research field of *exploitation* contained mainly subprojects G3 (described above) and **G4**. Within the scope of G4 the monitoring of micro-seismic events and ambient seismic noise is investigated and extended in terms of exploring geometries and positions of hydraulically induced fractures and fracture systems (exact identification of the location of the geothermal reservoir). Thus, a new technique was developed that allows for estimation of the seismic attenuation of the reservoir. This can provide additional information for the geomechanical model of the reservoir and be helpful for understanding the structural changes of the geothermal reservoir after hydraulic stimulation (see final report of G4).

In the research field of *characterization* of geothermal reservoirs, subproject **G5** investigated the behavior of the stress field under specific North German conditions (e.g. in the vicinity of salt layers, diapirs and fault zones) as well as the manifold parameters which affect fracture propagation during and after stimulation of the reservoir. One aspect of the subproject was numerical modeling of fracture propagation during stimulation for diverse scenarios such as multiple layers with varying properties. The pressure needed to run continuous heat/power production depends on the hydromechanical interaction of the fracture with the surrounding

rock. Modeling results for different cases varying e.g. in elastic properties, fracture toughness and initial situations of pre-existing fractures are given in the final report of G5.

As another aspect of *characterization*, the quantification of fluid flow and heat transport parameters was aimed at by subproject **G6.** Tracer techniques are relatively new in the deep geothermal field in Germany. The focus of this project was on the design and dimensioning of tracer tests of single-well and inter-well type, aimed at (1) early reservoir characterization at 'new-wellbore' testing stages, (2) evaluating the performance of fracturing/stimulation treatments and (3) reservoir monitoring during long-term operation. Main questions were the determinability of important transport parameters and of their changes with time, the predictability of thermal breakthrough from early inter-well tracer test signals, and the contribution of tracer tests to assessing not only the thermal, but also the hydrogeomechanical and hydrogeochemical lifetime of a geothermal reservoir. Thus, e.g. the use of artificial tracers as a tool for matrix and fracture characterization is demonstrated (see final report of G6).

Particular emphasis was furthermore placed on the assessment of the chemical composition of the highly saline brines and their effects on the formation of borehole skins (subproject **G9**), because the efficiency of geothermal energy production from deep aquifers or hot dry rocks strongly depends on the natural hydrogeochemical characteristics of the reservoir (fluid-rock interaction) and the alteration of geothermal water induced by the interaction within the technical systems. A comprehensive inventory of mineral contents of formation fluids of North German rock formations was established and served as a basis for high pressure/high temperature hydrogeochemical thermodynamic modeling of processes induced within the reservoir as well as with the technical equipment of geothermal power plants. With the "gebo"-database, chemical water compositions and scalings can be successfully predicted (see final report of G9).

Although numerical modeling was to some extent an element of all subprojects, subproject **G7** was associated fully to the research field of *modeling*. It dealt with the prediction of reservoir performance following stimulation and operation, which relies to a major extent on the modeling of groundwater flow, heat transport and the mechanical response of the reservoir to variable stresses. Numerical models were developed investigating the effect of thermo-hydro-mechanical process coupling as well as for the prediction of the long-term development of the geothermal reservoir. The classical doublet situation as well as matrix-fracture-interaction and a complex geological benchmark model were examined (see final report of G7).

The projects are interconnected in terms of providing e.g. structural information from seismic measurements as constraint for inversion of geoelectrical data, geochemical information that influence tracer propagation, or co-operation concerning fracture and deformation modeling.

Thus, the projects offer diverse approaches that lead to an optimization of the exploration and exploitation of deep geothermal reservoirs as well as a better understanding of the complex processes within the reservoir itself.

3. The common work package "Benchmark models"

For many of the subprojects of the focus area "Geosystem", numerical simulation was an essential tool. Numerical simulation always requires a model, and the proper design of a model may constitute a significant amount of the work. The model must be reasonably simplified to be tractable with numerical codes, but still include sufficient detail to catch the key features. Different modellers working in similar areas carry out their own research and define their own models, which might lead to situations where results are difficult to compare or to merge just because different models were used.

Therefore, within the gebo research association and especially within the focus area "Geosystem", we defined a set of seven geological "benchmark" models to facilitate the model definition for the different disciplines. They consist of geometrical and physical parameters and serve as a reference set that may be used by different researchers to ensure that results are comparable and refer to the same model. At the same time, the models are suited to describe the main geological features in Lower Saxony that are relevant for deep geothermal exploration.

The models were defined using different sources, such as the Geothermal atlas of Europe (Hurtig et al., 1992), the so-called TAB survey (TAB, 2003), and the NIBIS® Mapserver (soil information system of the Federal State of Lower Saxony, www.lbeg.niedersachsen.de), the Southern Permian Basin Atlas (Doornenbal & Stevenson, 2010) as well as own field surveys, sampling and laboratory studies carried out within the research project. Each model consists of a geometry defining different zones, and physical parameters, such as density, E-modulus, and electrical conductivity. The data set is neither complete, nor do we consider it to be perfect in any sense. The benefit lies in the fact that it may serve as a common starting point for other researchers and may save others a significant amount of extra work. Figure 3 gives an overview on the models as geological profiles, as well as the criteria that led to their selection.

In the research area "Geosystem" the models were used for simulation of expected geophysical data (see final report of G2) and stress field behaviour (see final report of G3), the simulation of fluid flow patterns for different matrix and fracture geometries (see final report of G7), or the simulation of the temperature during the exploitation phase (see final report of G6). The models were furthermore used in the research area "Drilling techniques" for calculating expected drilling costs.
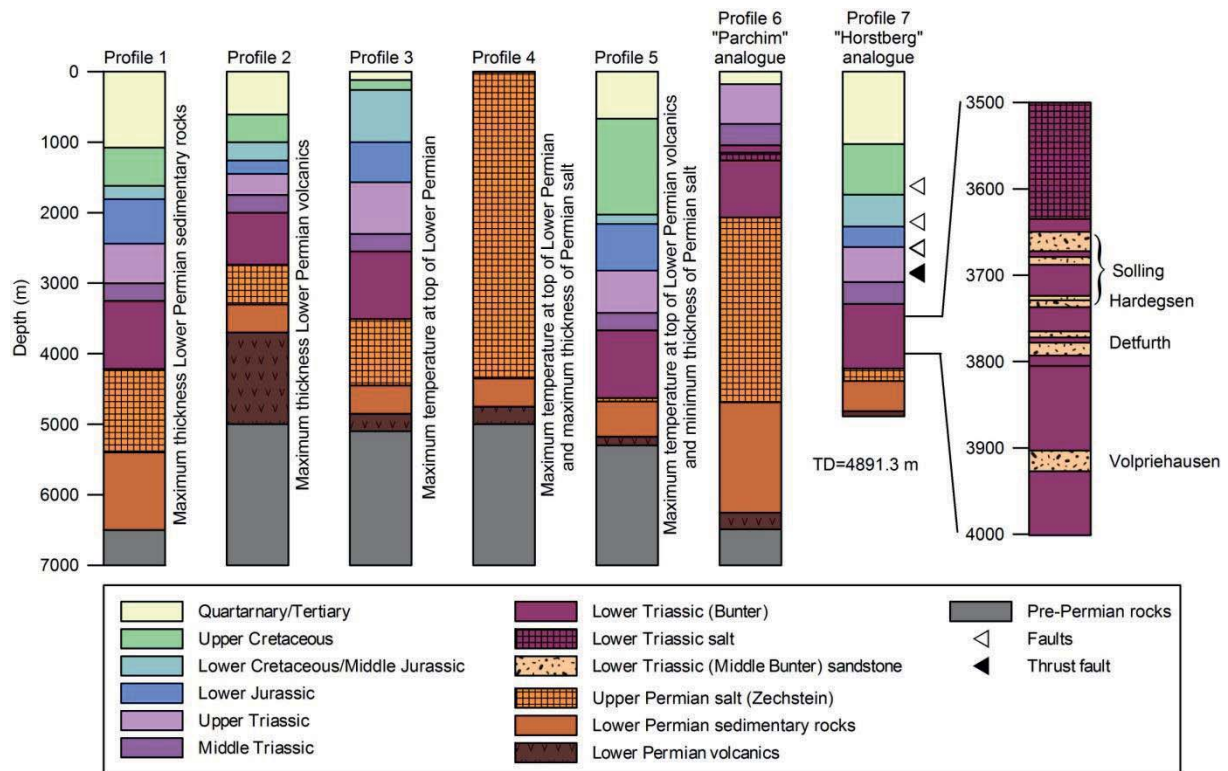
Figure 3: The profiles used for modeling in the work package "benchmark models". All profiles are located in the federal state of Niedersachsen except profile 6 (Mecklenburg-Vorpommern). Profiles 1 to 5 are based on geological maps, profiles 6 and 7 are based on existing wells.

As a general result, our benchmark models represent very different scenarios and thus demonstrate that the geology of North Germany, although dominated by sedimentary basins, is far from simple. Therefore, finding the optimum drilling location for a geothermal project in North Germany is absolutely not straightforward.

Our examples show that such models maybe useful for quite different types of numerical simulation, ranging from the evaluation of drilling technologies over the simulation of the thermal history of a reservoir, the simulation of thermal drawdown and hydrogeochemistry to the assessment of geophysical methods. However, all scientists used only a small subset of the parameters included in the benchmark models or a subset of a model, or even required modifications or extensions. Still, we believe it is useful to refer to a common set of models not only for practical reasons (time can be saved), but also because interdisciplinary research that is essential for geothermal exploration, requires a common understanding of the models that should be used.

4. Outlook

During the mid-term evaluation of the gebo project in 2011, the reviewers recommended a „medium- to long-term research strategy", as well as the writing of research proposals for follow-up projects. Therefore, the members of the gebo focus area „Geosystem" developed a concept for a new research association dealing with the geothermal exploration and characterization of the Lower Carboniferous of the North German Basin. Within several subprojects of different geoscientific fields (geology, geophysics, geochemistry, modeling) we plan to continue our collaboration and investigate a new potential target area for geothermal energy extraction.

5. Collective publications resulting from the focus area "Geosystem"

Hahne, B., Thomas, R., and team gebo-Geosystem (2014): Deep Geothermal Energy for Lower Saxony (North Germany) - Combined Investigations of Geothermal Reservoir Characteristics, *Energy Procedia, Vol. 59*, p. 198-204. *doi: 10.1016/j.egypro.2014.10.367*

Hahne, B., Thomas, R., and team gebo-Geosystem (2014): Deep Geothermal Energy for Lower Saxony (North Germany) - Combined Investigations of Geothermal Reservoir Characteristics, *Geophysical Research Abstracts, Vol. 16*, EGU2014-5346, General Assembly European Geosciences Union (EGU) (Vienna, Austria 2014).

Hahne, B., Thomas, R., gebo-Geosystem working group (2012): Combined geophysical, geochemical and geological investigations of geothermal reservoir characteristics in Lower Saxony, Germany, *Geophysical Research Abstracts, Vol. 14*, EGU2012-4225, General Assembly European Geosciences Union (EGU) (Vienna, Austria 2012).

Hahne, B., Thomas, R., and team gebo-Geosystem (2011): Combined geoscientific investigations of geothermal reservoir characteristics in Lower Saxony, Germany, *Geophysical Research Abstracts, Vol. 13*, EGU2011-10054, General Assembly European Geosciences Union (EGU) (Vienna, Austria 2011).

6. References

Doornenbal, J.C. & Stevenson, A.G. 2010. Petroleum Geological Atlas of the Southern Permian Basin Area (SPBA). EAGE Publications b.v. (Houten).

Hurtig, E.Cermak, V., Cermak, V.Haenel, R., Haenel, R., & Zui, V. (Eds.). 1992. Geothermal atlas of Europe. Haack, Gotha, Germany.

TAB (Büro für Technikfolgen-Abschätzung beim Deutschen Bundestag, authors: Paschen, H., Oertel, D., Grünwald, R.) 2003. Möglichkeiten geothermischer Stromerzeugung in Deutschland, TAB Arbeitsbericht Nr. 84, Berlin, Germany.

G1: Detection of Fault Zones Using Seismic Methods

Britta Wawerzinek[1], Patrick Musmann[1,2], Hermann Buness[1] & Rüdiger Thomas[1]

[1] Leibniz Institute for Applied Geophysics, Stilleweg 2, 30655 Hannover, Germany

[2] now at: Federal Institute of Geosciences and Natural Resources, Stilleweg 2, 30655 Hannover, Germany

*Corresponding Author: Britta.Wawerzinek@liag-hannover.de

Abstract

Deep fault zones have a high potential for geothermal energy extraction, but their usability depends on complex factors (e.g., structure, lithology and tectonics). Therefore a detailed fault zone exploration as well as a deeper understanding of the factors' interaction is needed. In the framework of gebo project G1 we tested the application of reflection seismic P- and SH-wave measurements to analyze and characterize fault zones. For this purpose we explored a fault system which is located at the eastern margin of the Leinetal Graben in Lower Saxony, Germany. Several reflection seismic surveys (P- and SH-wave) were conducted perpendicular and parallel to the graben structure. By using a combined analysis of P- and SH-waves a high-resolution image of the complex graben and its fault system was revealed: It comprises both steeply-dipping and shallowly-dipping normal faults, and includes a rollover structure. The structural image indicates independent tectonic development of the uppermost (<500 m) and deeper (>500 m) depth levels; with Upper Permian (Zechstein) salt as a decoupling horizon. One of the shallowly west-dipping normal faults, which is traceable from the surface down to 500 m depth, shows different reflection characteristics of P- and SH-waves: The fault zone is visible as a strong P-wave reflector whereas only discontinuous SH-wave reflections are observed. We conducted a petrophysical analysis to further investigate this fault zone by deriving elastic properties and seismic modeling. The elastic properties (v_P, v_S, ρ) show a good correlation with the geological interpretation and are in correspondence to literature values. However, no significant changes in elastic properties are observed at the fault zone itself. The elastic properties of the model and the fault zone were checked by seismic modeling. The field data are better reproduced if the fault zone is modeled as an extended layer instead of an interface. This project showed that a combined analysis of P- and SH-waves is useful for fault zone exploration, but further research on this area is strongly needed.

1. Introduction

Deep fault zones have a high potential for geothermal energy extraction since their permeability is often expected to be enhanced compared to the surrounding rocks. However, their usability depends on very complex lithological and tectonic factors underlining the need for fault zone exploration. We tested the application of seismic P- and SH-waves to analyze and characterize fault zones.

In this study, we explored the fault system of the eastern border of the Leinetal Graben which is located in Northeim, district Sudheim, in Lower Saxony, Germany. This location was chosen after a comprehensive assortment of possible areas. The fault system intersects Triassic units which are considered to be of interest for geothermal energy extraction in the North German Basin. The shallow location permits high-resolution investigations which are supported by borehole information (Grupe, 1909, 1923) as well as geological mapping of fault zones (Reyer, 2008).

The Leinetal Graben (Fig. 1) is an N-S-trending asymmetric graben, approximately 60 km long and 10 km wide. It is located at the southern margin of the North German Basin. Triassic units of Middle Triassic und Lower Triassic crop out on the flanks of the Leinetal Graben. Upper Triassic and Lower Jurassic as well as secondary Middle Triassic strata are exposed inside the graben (Tanner et al., 2010a).

Graben formation started presumably between Lower Jurassic and Upper Cretaceous. It continued during Tertiary and lasted until Pliocene (Tanner et al., 2010b). Over time the stress regime changed, besides extensional also compressional and transpressional features have been recognized, e.g. by Reyer (2008). An inversion occurred presumably during Late Cretaceous – Early Tertiary, while inversion tectonic of the North German Basin took place as well (Tanner et al., 2010b).

Salt tectonics characterizes the Leinetal Graben (Jordan, 1986), leading to complex deformations of overlaying Mesozoic and Cenozoic strata. Upper Permian (Zechstein) salt diapirs and salt intrusions into Mesozoic saliniferous formation strata are common.

Further details of the geological and tectonic setting of the Leinetal Graben can be found in Leiss et al. (2012), Tanner et al. (2010a) and Wunderlich (1955). From these data and outcrops the structural settings as well as the geophysical rock properties are relatively well known.

2. Reflection seismic surveys and data processing

2.1 Reflection seismic surveys

We designed the P-wave survey to image subsurface strata and fault pattern from the near-surface domain at high resolution down to the base Upper Permian, expected above 2 km depth. In total, 3 P-wave reflection seismic profiles with a length of 1.8 (P-2, P-3) and 3.2 km (P-1) were acquired across the main fault confining the Leinetal Graben on the eastern side (Fig. 1).
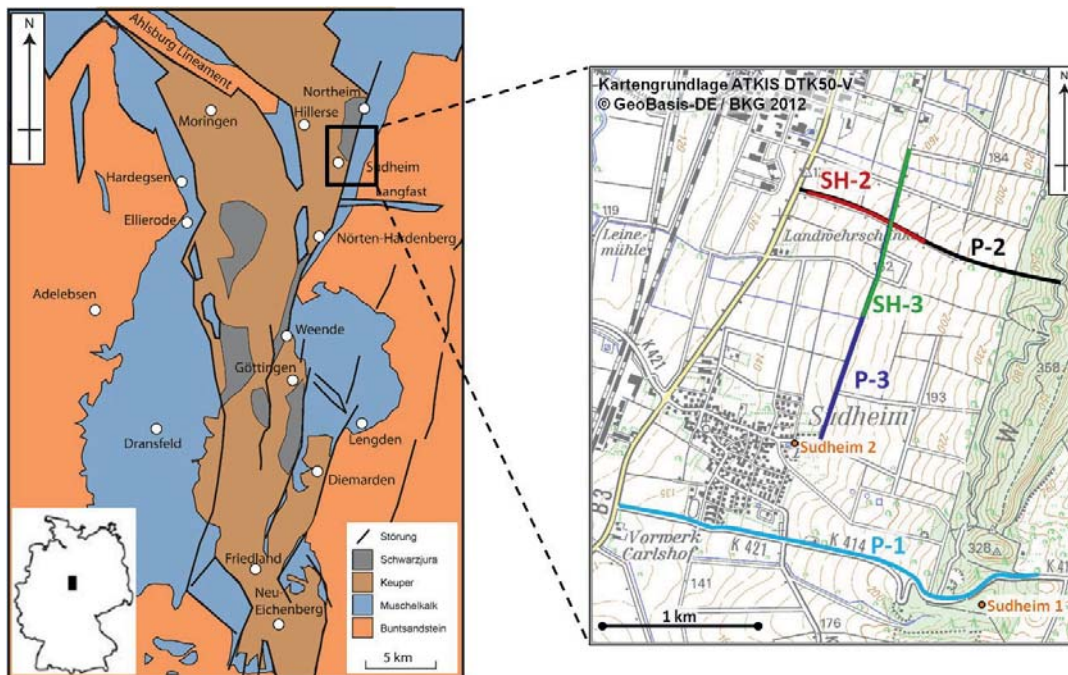

Figure 1: *Left: Geological map of the Leinetal Graben (modified after Tanner et al., 2010a). A black square marks the study area. Right: Location map of the seismic reflection profiles using P-waves (P-1, P-2 and P-3) and SH-waves (SH-2 and SH-3). Sudheim 1 and 2 are well locations (c.f. Grupe, 1909).*

The small hydraulic vibrator (MHV4-P) used in this survey as seismic source was developed at Leibniz Institute for Applied Geophysics (LIAG) and is specifically designed for high-resolution, near-surface measurements. The vibrator can generate frequencies between 16 and 500 Hz using a peak force of approx. 27 kN (Buness, 2007). We used a linear source up-sweep of 16 s duration, ranging from 20 Hz up to 160 Hz and 180 Hz, for profiles P-2 and P-1 as well as P-3, respectively (Tab. 1). These values are a compromise between desired penetration depth, resolution, signal-to-noise ratio and the available resources. As measurements were exposed to high anthropogenic noise, 4-6 sweeps were shot at each source point to improve signal-to-noise ratio. The close receiver spacing of 5 m resulted in a sufficient coverage of the near-surface domain, as well as in a small CMP bin size of only 2.5 m. In order to save acquisition time, shot distance was set to twice this value. Using 360

channels, a high fold of 90 and an active spread length of 1.8 km were achieved. However, actual fold and maximum offset depend on the field geometry and acquisition progress in practice.

The S-wave survey was done only after a first reconnaissance using P-waves, since the S-wave seismic profiling is much slower. This is due to the much shorter wavelength requiring a denser wavefield sampling. We used LIAG's small hydraulic shear-wave vibrator (MHV4-S) for generating seismic SH-waves. After intensive testing we decided to use relatively low frequencies of 10 – 60 Hz, since the desired target depth was up to 500 m. The source spacing was 4 m and 2 sweeps were shot at each source point. At the receiver side, we employed two of our 120 m long landstreamer units (Krawczyk et al., 2013), towed one after each other, giving a total length of 240 m with receiver spacing of 1 m. Since the offset to the first geophone was up to 40 m, a maximum offset of 280 m resulted on profile SH-2, whereas the maximum offset on profile SH-3 was 240 m. After checking the seismic inventory of the P-wave lines, we decided to carry out the S-wave measurements on a part of profile P-2. Thereafter a second profile followed along a part of profile P-3, crossing the first one perpendicular, in order to confirm the results.

Detailed acquisition parameters of P- and SH-wave surveys are summarized in Table 1.

Acquisition parameters	P-1	P-2	P-3	SH-2	SH-3
Sweep frequency in Hz	20 – 180	20 – 160	20 – 180	10 – 60	10 – 60
Sweep duration in s	16	16	16	32	32
Source spacing in m	10	10	10	4	4
Receiver spacing in m	5	5	5	1	1
CMP spacing in m	2.5	2.5	2.5	0.5	0.5
Max. offset in m	1600	1775	1840	280	240
Profile length in m	3200	1800	1830	720	1040
Mean CMP coverage	90-fold	90-fold	90-fold	30-fold	30-fold

Table 1: *Acquisition parameters of the seismic reflection surveys (Fig. 1).*

2.2 Seismic processing

We used the ProMAX^{TM} software package (Landmark Graphics Corporation) for reflection seismic processing. The basic processing sequence consists of normal and dip move-out stacking with subsequent time migration and depth conversion (Yilmaz, 2001; Sheriff & Geldart, 1995). The processing sequence applied in this study (Tab. 2) has been proven to be adequate for high-resolution fault imaging at other survey sites (e.g., Musmann & Buness, 2010).

Processing was carried out using both normalized and true amplitudes, the first one for an optimized structural imaging, the second one for comparison with results of seismic

modeling. Basically, the same processing sequence was applied to all profiles, minor changes are due to different ambient noise levels of the profiles. However, P- and SH-wave data processing varied due to different acquisition parameters and frequency ranges. An offset limit of 450 m was set for profile P-2 to enable reliable amplitude analyses.

	Seismic processing	P-1	P-2	P-3	SH-2	SH-3
1.	Geometry and quality control	✓	✓	✓	✓	✓
2.	Static corrections	RS	RS	RS	RS	RS
3.	Amplitude normalization	AGC	AGC	AGC	AGC	AGC
		TAR	TAR	TAR	TAR	TAR
4.	Spectral balancing	SD	SW_t	SW_t	SS_f	SS_f
5.	Disturbance wave suppression	SM, BM	SM*	ABA	TM	TM
		BB	BB	BB	FK	FK
6.	Velocity analysis	IVA, TOMO	IVA, TOMO	IVA, HVA	IVA	IVA
7.	Dynamic correction (NMO, DMO)	✓	✓	✓	✓	✓
8.	CMP Stack	✓	✓	✓	✓	✓
9.	Migration (FD time migration)	✓	✓	✓	–	–
10.	Time-to-depth conversion	✓	✓	✓	✓	✓

Table 2: *Main processing steps of the seismic P- and SH-wave data, processing steps*

colored in gray are omitted for some analyses.

Abbreviations: RS – refraction statics, AGC – automatic gain control,

TAR – spherical divergence correction, SD – zero phase spiking deconvolution,

SW_t – time-domain spectral whitening, SS_f – frequency-domain spectral shaping,

SM – surgical mute, BM – bottom mute, SM* - surgical mute around air blast,

ABA – air blast attenuation, TM – top mute, BB – band-pass filter

(20/25 – 140/160 Hz), FK – velocity dip filter ($|v| \geq 500$ m/s),

IVA – interactive velocity analysis using semblance analysis,

TOMO – first break tomography, HVA – horizon velocity analysis,

NMO – normal moveout correction, DMO – dip moveout correction.

Refraction statics for individual source and receiver stations were derived from first-break arrivals to compensate the influence of the weathering layer. Large velocity fluctuations of the refractor used give indications of fault outcrops, presumably due to the increased heterogeneity accompanying this zone.

To improve time resolution, we whitened frequency spectra within the excited sweep range. Frequency limits for subsequent band-pass filtering are a reasonable compromise between a high resolution in the near-surface domain and reflections from deeper targets not obscured by noise.

Velocity models were derived by both reflection and refraction processing – no additional velocity information (e.g., VSP) was available. The semblance analysis of reflection events

leads to a stacking velocity model that covers the entire section (Fig. 2a). It was complemented by a refraction tomography of first-breaks, using the Ra2dTomo software (Günther, 2011). It shows a more detailed velocity distribution and correlates better with the structural image of the P-wave seismic data (0-500 m depth) than the velocity model derived by reflected waves (Fig. 2a). However, reflected waves are required to determine the velocity structure of the deeper parts (>500 m depth). Both models were averaged and the resulting model was used for the dynamic corrections. Dip move-out correction was incorporated into the processing flow as steeply-dipping reflections and conflicting dips were observed in the data.
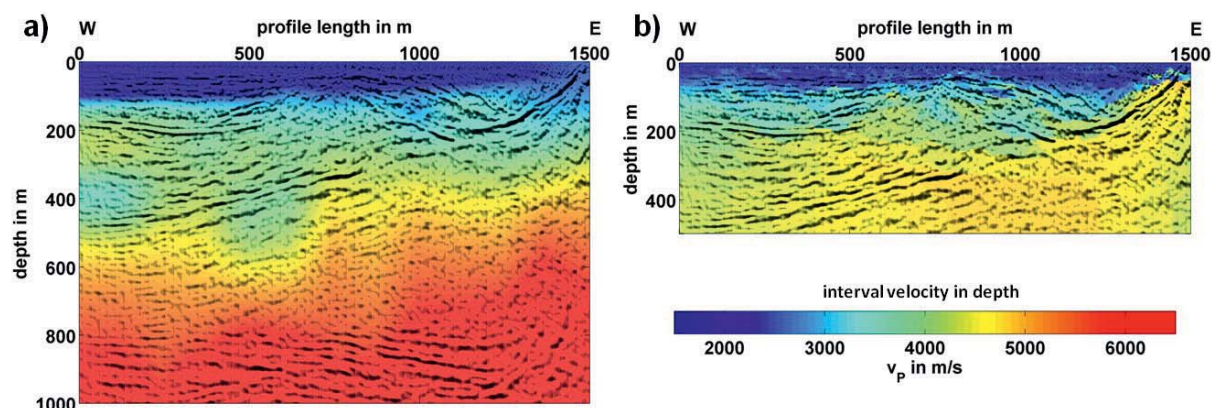
Figure 2: Interval velocities in depth of profile P-2 derived using (a) P-to-P reflected and (b) P-to-P refracted waves overlaid by migrated P-wave seismic data (Musmann et al., 2012).

The post-stack migration used a time-migration algorithm, and depth conversion was finally carried out by a single average velocity function that resulted in much less undulating horizons.

3. Reflection seismic results

3.1 Seismic P-wave sections and interpretation

Figures 3-5 show the migrated and interpreted P-wave depth sections as well as the corresponding geological models. Profiles P-1 and P-2 intersect the graben structure perpendicular whereas profile P-3 runs parallel to the graben structure and connects P-2 and wellbore Sudheim 2 (Fig. 1). The interpretation shown in the figures comprises the information from all P- and SH-wave profiles. Stratigraphic units are interpreted including borehole Sudheim 1 and Sudheim 2 (Grupe, 1909).

Profile P-1 (Fig. 3) shows steeply-dipping normal faults which delimit the graben towards the east and expand into the Upper Permian (z), furthermore, shallowly-dipping normal faults are

visible. Outside of the graben Lower Triassic units (Upper to Lower Bunter; so, sm and su) crop out whereas inside the graben Middle (m) and Upper Triassic (k) as well as Lower Jurassic (j) are expected. The top of Upper Permian structures (Zechstein salt, z) dips gently towards west. In contrast, the top of the mixture of Lower Triassic (so) and Upper Permian salt (z) dips towards east.
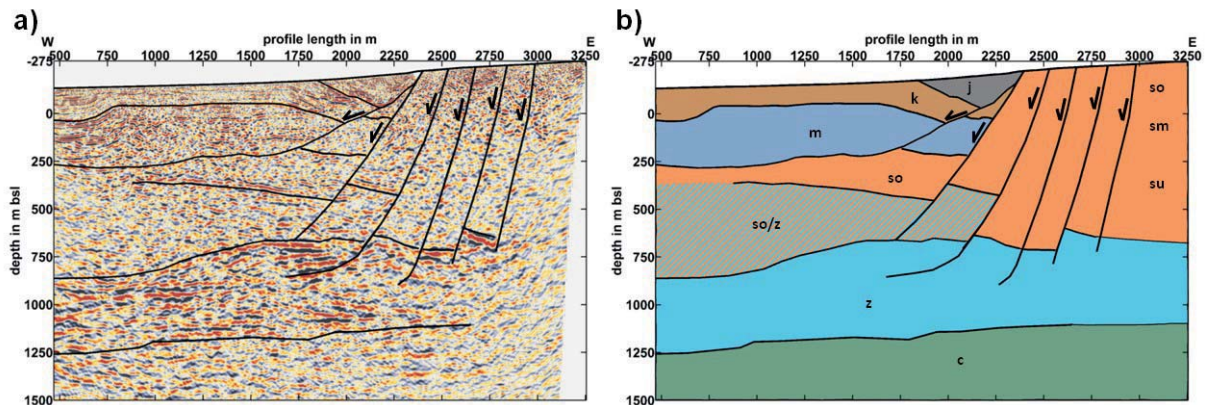

Figure 3: *(a) Migrated P-wave depth section of profile P-1 and (b) corresponding geological model. Abbreviations see Fig. 6.*

Profile P-2 (Fig. 4), which is located north of Sudheim (Fig. 1) shows in principle a similar graben margin structure: The upper part (0-500 m depth below ground level (bgl)) comprises Jurassic and Triassic units and is mainly characterized by shallowly west-dipping normal faults which cause the formation of a rollover structure. Upper Permian structures below 700 m depth bgl again dip slightly towards west. A strong shallowly west-dipping reflector is traceable from surface down to 500 m depth bgl and is interpreted as normal fault.
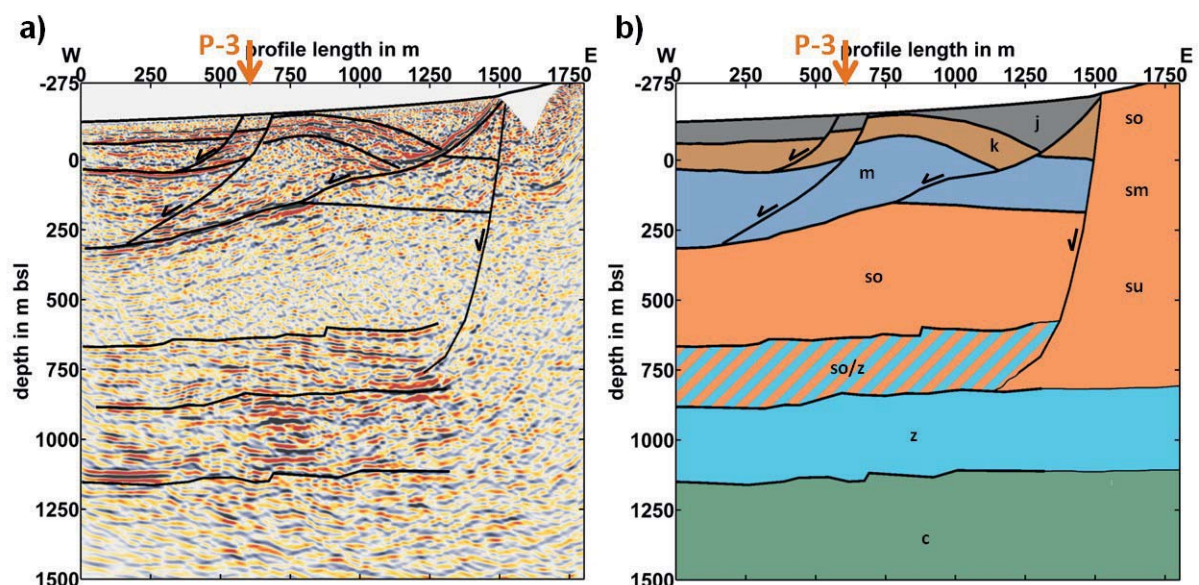
Figure 4: *(a) Migrated P-wave depth section of profile P-2 and (b) corresponding geological model. Arrow marks the intersection of P-3, abbreviations see Fig. 6.*

43

Profile P-3 (Fig. 5) images the same strongly disturbed structure in the shallow part (0-400 m depth bgl) as it is seen on profile P-1 and P-2. In the center of profile P-3 an apparent horst structure is visible, which may be either real or an artifact due to a 3D effect along a graben parallel fault. Beneath 650 m depth bgl a north-dipping reflector is visible. Taking into account the geological information of well Sudheim 2 (Grupe, 1909) this reflector is interpreted as Upper Permian structures within the Lower Triassic, which means that due to salt tectonics (halokinesis) Upper Permian salt propagated into Upper Bunter.
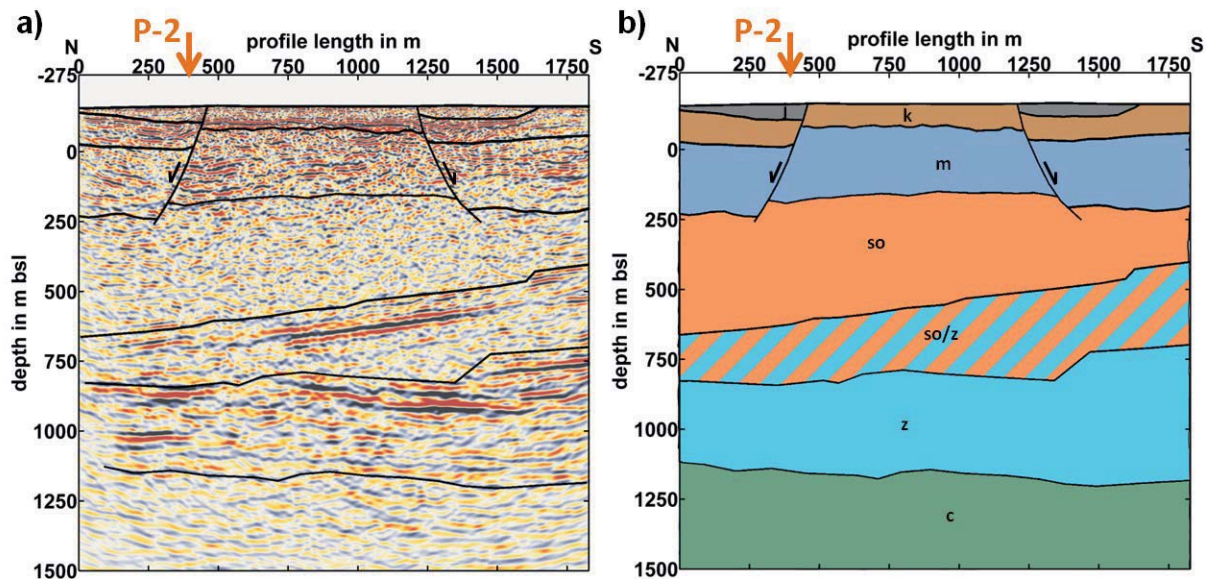
Figure 5: *(a) Migrated P-wave depth section of profile P-3 and (b) corresponding geological model. Arrow marks the intersection of P-2, abbreviations see Fig. 6.*

The seismic P-wave data reveal a high-resolution image of the complex graben structure (Fig. 6) which indicates an independent tectonic development of the shallow and deep depth levels with Upper Permian (Zechstein) salt as decoupling layer (Tanner et al., 2015). The graben system comprises both steeply- and shallowly-dipping normal faults. One of these shallowly west-dipping normal faults is traceable from the surface down to 500 m depth bgl. This normal fault was selected for further SH-wave analysis because it is visible as a strong P-wave reflector.

In addition, the structural image of the Leinetal Graben revealed from reflection seismic P- and SH-wave measurements was used as a priori information for constraints in the inversion of electric and electromagnetic data (c.f. project G2).
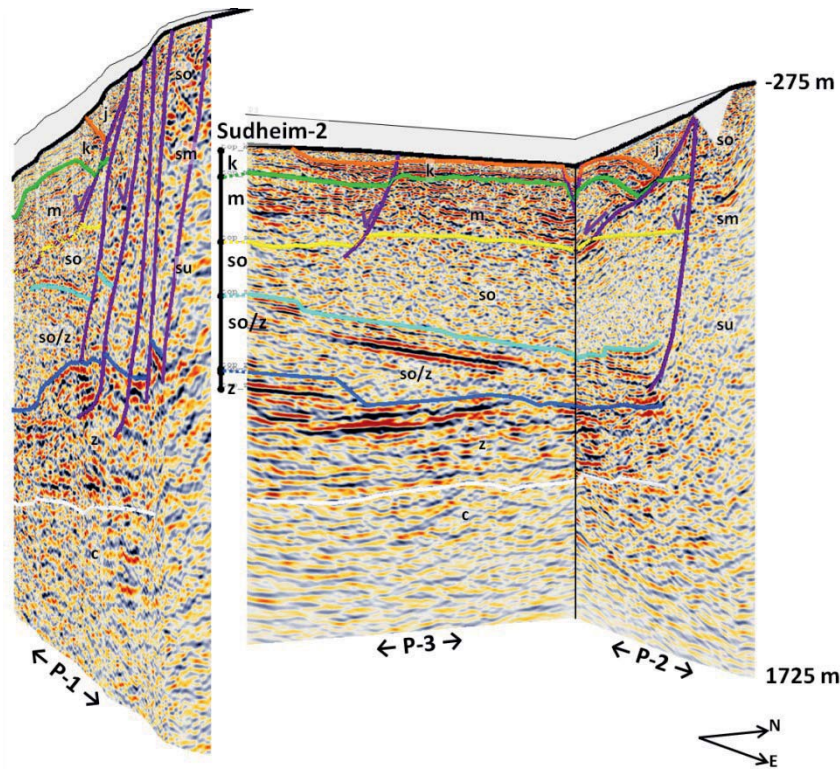
Figure 6: *Fence section of the interpreted P-wave seismics with vertical exaggeration of approx. factor 2. Abbreviations: j – Lower Jurassic, k – Upper Triassic, m – Middle Triassic, s – Lower Triassic (so – Upper Bunter, sm – Middle Bunter, su – Lower Bunter), z – Upper Permian, so/z – mixture of so and z, c – Carboniferous. Well Sudheim-2 c.f. Grupe (1909).*

3.2 Seismic SH-wave sections and seismic interpretation

Complementary to seismic P-wave measurements, seismic SH-wave measurements were conducted along parts of the P-wave profiles which run parallel and perpendicular to the fault system. For a detailed description of acquisition parameters and seismic data processing see Tables 1 and 2. The interpreted SH-wave depth sections are shown in Figure 7. Both sections correlate in general with the geological interpretation obtained from P-wave seismics and were used to complement the structural image derived from P-wave sections. In the deeper part (below 300 m depth bgl) the transition from Middle (m) to Lower Triassic (so) units is poorly imaged on SH-2 (Fig. 7a) as well as SH-3 (Fig. 7b). At least non continuous reflection elements on SH-2 are presumably related to the transition from Middle to Lower Triassic units. In contrast, the upper part of the depth section of profile SH-3 is imaged with a very high resolution.

45
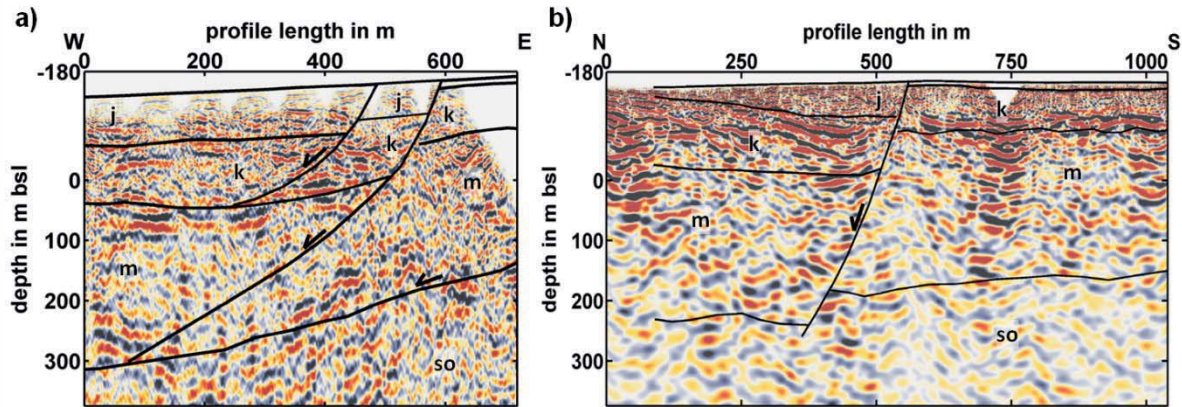
Figure 7: *Interpreted depth section of profiles (a) SH-2 (unmigrated) and (b) SH-3. Interpretation is compiled taking into account P- and SH-wave seismics.*

3.3 Comparison of seismic P- and SH-wave measurements

SH-wave seismic measurements were conducted along parts of the P-wave measurements; hence their reflection characteristics may be compared (see Figs. 8-9). P- and SH-wave data on profile 2 show a good correlation in the shallow part (0-300 m depth bgl, Fig. 8), whereas the structural image differs beneath 300 m depth bgl: The seismic P-wave depth section is dominated by a strong P-wave reflector interpreted as fault zone. In the corresponding SH-wave depth section this reflector is imaged weakly with only discontinuous reflections. The P- and SH-wave measurements on profile 3 (Fig. 9) display a similar picture. In the near-surface domain (0-200 m depth bgl), the structural images of P-3 and SH-3 correlate well. Beneath 200 m depth bgl P-3 shows strong, continuous reflectors whereas SH-3 shows weak and discontinuous reflections.
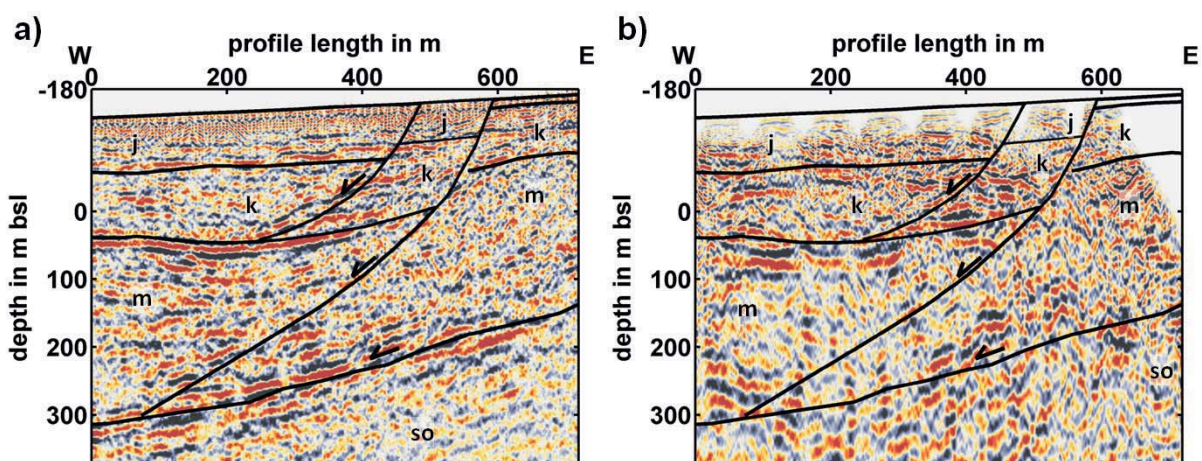
Figure 8: *Comparison of profiles (a) P-2 and (b) SH-2. Both are unmigrated, abbreviations see Fig. 6.*
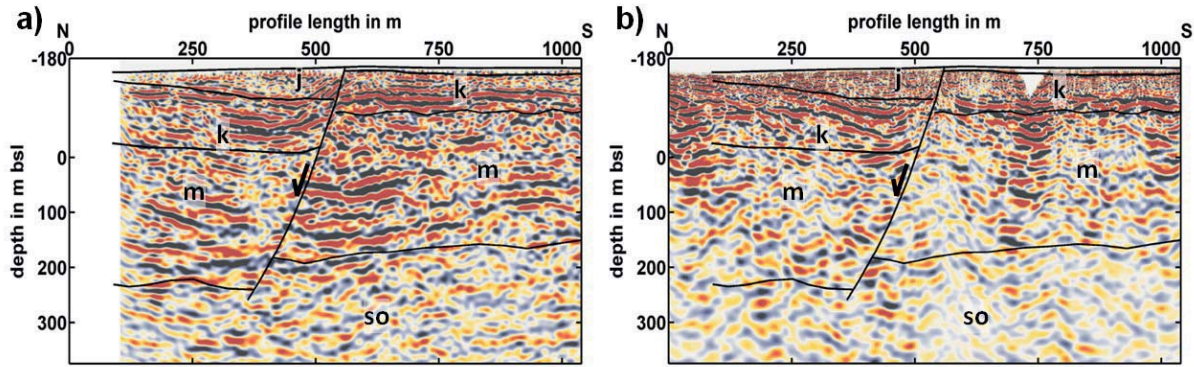
Figure 9: *Comparison of profiles (a) P-3 and (b) SH-3. Abbreviations see Fig. 6.*

This phenomenon of different reflection characteristics of seismic P- and SH-wave data (Figs. 8-9) might be caused by lithological or structural effects, or a combination of both. Also fluids can be taken into account. Furthermore, 3D effects depending on acquisition parameters cannot be excluded.

3.4 Analysis of reflection coefficients and reflection angles

The geological interpretation obtained from seismic data of profile 2 was converted into a simplified 2D model. Averaged elastic properties (v_P, v_S and ρ) were assigned to each particular lithological unit. By using raytracing software NORSAR-2D and taking into account the applied acquisition parameters of P- and SH-wave measurements (Tab. 1), we computed incidence angles of P-to-P (i_P) and SH-to-SH (i_S) reflections that occurred at the top of the fault zone (Fig. 10). Over the whole offset range of 200 m, SH-to-SH reflection angles are lower than 25° (Fig. 11a) whereas P-to-P reflection angles are distributed from 0° to almost 85° (Fig. 11b) over an offset range of 1500 m. The range of P-to-P reflection angles decreases to 0°-67° if only P-wave data with offsets less than 450 m (see Sec. 2.2) are considered. The vast majority of P-to-P reflection angles is lower than 55°. Taking into account seismic interval velocities v_P and v_S the critical P-to-P (i_{cP}) and SH-to-SH (i_{cS}) reflection angles were computed (Aki & Richards, 2002):

$$\sin(i_{cS}) = \frac{v_{S1}}{v_{S2}} \qquad \sin(i_{cP}) = \frac{v_{P1}}{v_{P2}}$$

Calculated SH-to-SH reflection angles (Fig. 11a) are much lower than the critical reflection angle of i_{cS} = 58.5°. In case of P-to-P reflections the critical angle i_{cP} is 62.3°, and with few exceptions the P-to-P reflection angles of the offset range 0-450 m are lower than i_{cP}.
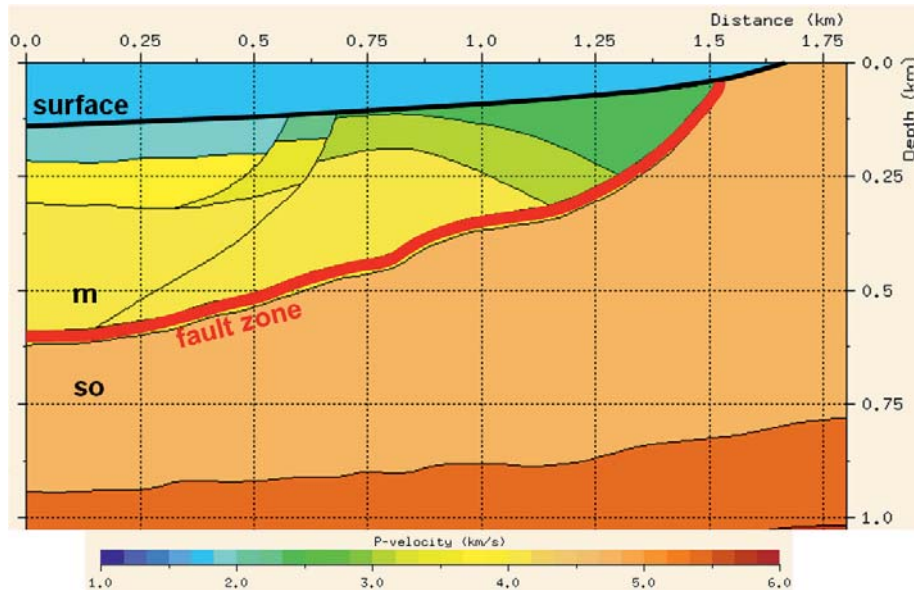
Figure 10: *Simplified NORSAR-2D model of profile 2 to compute the reflection angles of P-to-P and SH-to-SH reflections that occurred at the top of the fault zone (red).*
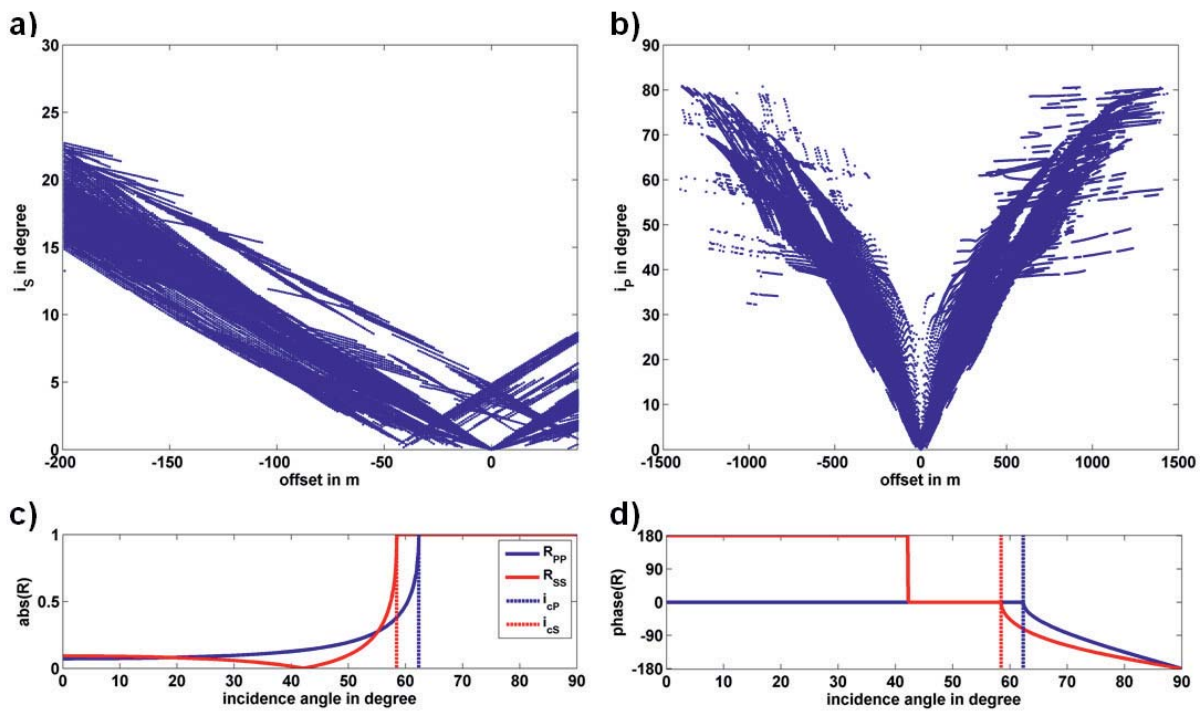

Figure 11: *Modeled reflection angles of (a) SH-to-SH and (b) P-to-P reflections at the fault zone using raytracing software NORSAR-2D. (c) Reflection coefficients and (d) phases of P-to-P (R_{PP}, blue) and SH-to-SH (R_{SS}, red) reflections at the fault zone. Elastic properties used for the calculations: v_{P1} = 4140 m/s, v_{S1} = 1500 m/s, ρ_1 = 2.4 g/cm³; v_{P2} = 4675 m/s, v_{S2} = 1760 m/s, ρ_2 = 2.46 g/cm³. v_P and v_S derived from seismic data, ρ is taken from Tanner et al. (2010b).*

In order to estimate the effect of different acquisition parameters for P-to-P and SH-to-SH amplitudes, Zoeppritz equations are used to calculate the corresponding reflection coefficients R_{SS} and R_{PP} (e.g. Aki & Richards, 2002).

$$R_{SS} = \frac{\rho_1 v_{S1} \cos(i_{S1}) - \rho_2 v_{S2} \cos(i_{S2})}{\rho_1 v_{S1} \cos(i_{S1}) + \rho_2 v_{S2} \cos(i_{S2})} \qquad R_{PP} = \frac{\rho_2 v_{P2} \cos(i_{P1}) - \rho_1 v_{P1} \cos(i_{P2})}{\rho_2 v_{P2} \cos(i_{P1}) + \rho_1 v_{P2} \cos(i_{P2})}$$

$$\sin(i_{S2}) = \sin(i_{S1}) \frac{v_{S2}}{v_{S1}} \qquad \sin(i_{P2}) = \sin(i_{P1}) \frac{v_{P2}}{v_{P1}}$$

where R_{SS} and R_{PP} are the SH-to-SH and P-to-P reflection coefficients, ρ_1 and ρ_2 are the densities of layer 1 and 2; v_{S1} and v_{S2} are the shear wave velocities of layer 1 and 2; v_{P1} and v_{P2} are the P-wave velocities of layer 1 and 2; i_{S1} and i_{P1} are the reflection angles of SH- and P-waves; i_{S2} and i_{P2} are the refraction angles of SH- and P-waves. In this case layer 1 corresponds to Middle Triassic units (m) and layer 2 corresponds to the fault zone.

The reflection coefficient R_{PP} (blue line in Fig. 11c) shows a gradual increase of R_{PP} with increasing incidence angle of the P-wave, until at and above the critical angle i_{cP} total reflection ($R_{PP} = 1$) is observed. The phase remains stable up to the critical angle. In contrast, R_{SS} decreases up to an incident angle at approximately 42°, where it approaches zero and a 180° jump in phase occurs. At higher angles amplitudes increase, until the critical angle i_{cS} is reached. For incidence angles higher than i_{cS} total reflection occurs ($R_{SS} = 1$).

Realistic acquisition parameters lead to similar R_{SS} and R_{PP} below 30°. Due to larger offsets and thus larger P-wave incidence angles (>30°), P-to-P reflections at the top of the fault zone tend to have larger amplitudes than SH-to-SH reflections. Nevertheless, assuming that the assigned elastic properties of the model are realistic, the fault zone should be imaged in seismic SH-wave data.

4. Derivation of elastic properties

We estimated elastic parameters (Fig. 12, e.g. v_P, v_S, v_P/v_S, ρ, μ and κ) by using seismic P- and SH-wave data. First of all, interval velocities v_P and v_S were derived from stacking velocities, v_P/v_S was directly calculated as quotient of v_P and v_S. The density ρ was estimated by applying the empirical formula of Gardner et al. (1974):

$$\rho = \alpha v_P^{\beta} \qquad \text{where } \alpha = 1.741 \text{ and } \beta = 0.25.$$

Since the seismic velocities are described by density ρ, shear modulus μ and bulk modulus κ (Sheriff & Geldart, 1995) it is possible to derive shear and bulk modulus from seismic interval velocities:

$$v_S = \sqrt{\frac{\mu}{\rho}} \qquad \rightarrow \qquad \mu = v_S^2 \rho$$

$$v_P = \sqrt{\frac{\kappa + \frac{4}{3}\mu}{\rho}} \qquad \rightarrow \qquad \kappa = v_P^2 \rho - \frac{4}{3}\mu$$

The calculation of the elastic properties is based on the seismic interval velocities. In contrast to the small uncertainties of P-wave velocities, which were due to larger acquisition offsets and the application of first break tomography, the uncertainties of S-wave velocity beneath approx. 300 m depth are very large and have to be taken into account in the interpretation.
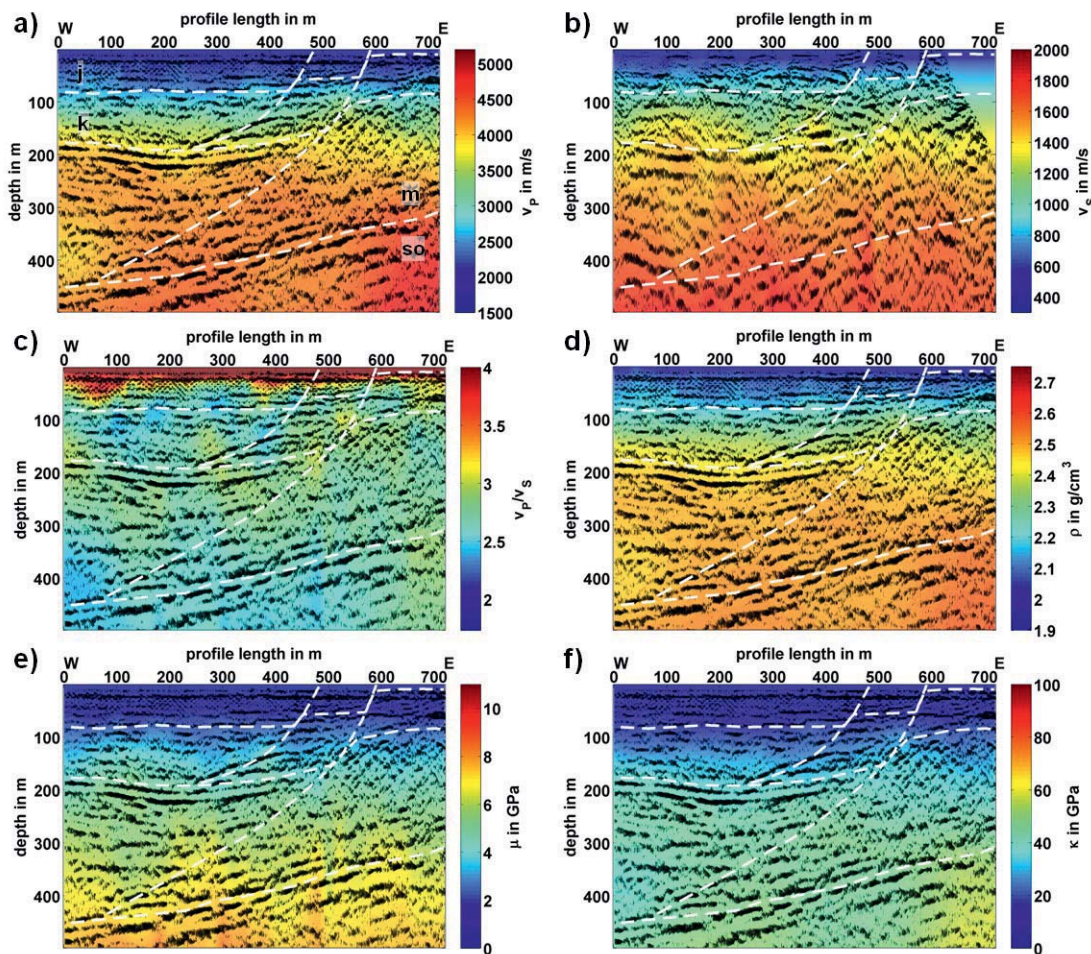
Figure 12: *P-wave (a,c-f) and S-wave (b) unmigrated amplitudes of profile 2 overlain with elastic properties: (a) P-wave velocity v_P, (b) S-wave velocity v_S, (c) v_P/v_S ratio, (d) density ρ, (e) shear modulus μ and (f) bulk modulus κ. White dashed lines show the structural interpretation, abbreviations (j, k, m, so) see Fig. 6.*

Figure 12 shows the derived elastic parameters v_P, v_S, ρ, v_P/v_S, μ and κ, P- and SH-wave seismics as well as the seismic interpretation (white dashed lines for profile 2). Both interval velocities v_P (Fig. 12a) and v_S (Fig. 12b) change at the interpreted lithological interfaces (e.g. transition from j to k at 150 to 200 m depth). The detailed v_P distribution shows only a velocity

increase at the fault zone due to the lithological transition from Middle (m) to Lower Triassic (so) units, but no significant changes within the fault zone itself.

If the rocks at the fault zone are more brittle and sheared than the surrounding host rock an increase in v_P/v_S ratio is expected. In the near-surface area high v_P/v_S ratios have been identified (e.g., Pugin et al., 2013) due to unconsolidated rocks and very low v_S velocities (Erickson et al. 1968). In our data we observe very high v_P/v_S ratios (above 3) and strong lateral changes possibly due to shallow faults in the shallow subsurface (0-100 m depth). The v_P/v_S ratio (Fig. 12c) decreases strongly with increasing depth.

The density ρ (Fig. 12d) is very low above 100 m depth due to unconsolidated rocks and sediments, but increases sharply beneath. The density values are in the range of literature values (Tanner et al., 2010b). Since ρ (Fig. 12d) is directly dependent on v_P (Fig. 12a) no fault-related changes are visible for this parameter as well.

The distribution of the estimated shear modulus (Fig. 12e) and bulk modulus (Fig. 12f) are very similar to the distribution of v_S and v_P (Fig. 12a,b).

By analyzing seismic P- and SH-wave data it is possible to derive v_P, v_S and therewith connected elastic properties v_P/v_S, ρ, μ and κ. All elastic properties (Fig. 12) show changes due to lithological changes but no fault-related changes. This might be caused by the smooth velocity distribution of v_S, uncertainties in the velocity determination or the low resolution of the seismic velocities below 300 m. However, this study pointed out a combined analysis of P- and SH-waves leads to the derivation of additional elastic properties.

5. Seismic Modeling

Seismic modeling was performed to check the expected derived properties of the fault zone by comparing field and synthetic data. A strongly simplified 2D model of profile P-2 was created and average elastic properties were assigned to each block and unit. v_P and v_S were derived from seismic data, ρ was taken from Tanner et al. (2010b) and constant quality factors for S-wave modeling ($Q_S = 20$) and P-wave modeling ($Q_P = 50$) were used (Fig. 13a). Modeling (Tab. 3) was done using raytracing software NORSAR-2D as well as FD modeling software SOFI-2D (Seismic mOdeling with FInite differences; Bohlen, 2002).

The fault zone was modeled as interface (Fig. 13a) and as layer (Fig. 13b) with variations of its elastic parameters. Table 4 lists the exemplary input properties of the fault zone.
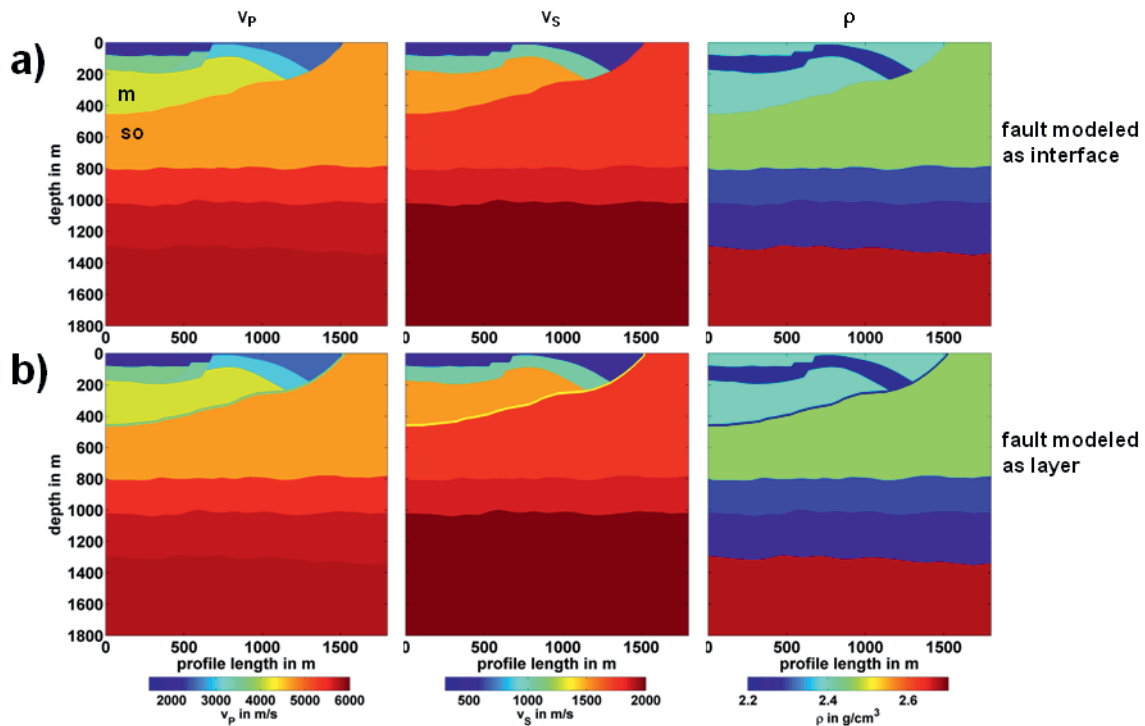
Figure 13: *Input models for seismic modeling: v_P (left), v_S (center) and ρ (right). The fault at the transition from Middle (m) to Lower Triassic (so) units is modeled (a) as interface and (b) as layer (fault properties see Tab. 4).*

The raytracing method used a normal incidence point raytracer to simulate post-stack (zero-offset) unmigrated data. Only rays departing at normal incidence from the selected horizons are calculated. In our modeling, we considered only primary reflections from all model boundaries. In principle, also multiples and diffractions can be modeled by specifying the corresponding wavecode. Amplitudes of P-waves at normal incidence tend to be slightly lower compared to amplitudes resulting from a stack including larger incidence angles (comp. Fig. 11c).

modeling acquisition	NORSAR-2D	SOFI-2D
P-wave seismic		P-SV version, damping edges
source mode	plane waves	
receiver spacing	5 m	1 m
central frequency	80 Hz	80 Hz
SH-wave seismic		SH-version, damping edges
source mode	plane waves	
receiver spacing	1 m	1 m
central frequency	30 Hz	33 Hz

Table 3: *Seismic modeling acquisition parameters.*

Finite difference (FD) modeling includes inherently all parts of the wavefield including multiples and diffractions. However, resulting synthetic data look still different from field data,

52

since the real world complexity cannot be achieved in a simplified model and no noise was added to the modeled data. FD modeling was done using the plane wave approach with sources positioned at the surface. The model borders, including the surface, were set to be absorbing ones.

Fault zone modeling	v_P in m/s	v_S in m/s	ρ in g/cm³
Fault as interface:	**Transition from m-to-so**		
m - Middle Triassic	4140	1500	2.40
so - Lower Triassic (Upper Bunter)	4675	1760	2.46
Fault as layer:	**Layer between m and so**		
Layer I (13 m wide, 10 % reduction)	3726	1350	2.16
Layer II (13 m wide, 5 % reduction)	3933	1425	2.28
Layer III (13 m wide, 3 % reduction)	4016	1455	2.328

Table 4: *Input properties of the fault zone used for seismic modeling.*

Finally, synthetic and field data have to be compared. Because the determination of absolute amplitude values of the field data is very difficult regarding the complexity of data acquisition and processing, it is much easier and more reliable to consider only relative amplitudes. This is done be choosing a suitable reference horizon, well visible on both P- and S-wave seismic data. We chose the lithological boundary between Upper Triassic to Middle Triassic units and determined the averaged absolute amplitude of this reflector and the fault zone reflector (red arrows in Fig. 14), calculated their amplitude ratio and compared the amplitude ratios of field and synthetic data. For comparing amplitude ratios the field data had to be reprocessed without amplitude normalization (AGC), but with spherical spreading correction. No Q-compensation was applied. Figure 14 (left column) shows the P- and SH-wave field data and their corresponding amplitude ratio. The amplitude ratio of P-seismics is 1.5 which means the amplitude of the upper reflector is 1.5-times larger than the amplitude of the deeper reflector. Since the deeper reflector in SH-seismics is only discontinuously visible, the estimated amplitude ratio of 1.1 gives only the lower limit of the amplitude ratio.

Figure 14 images the comparison of field data (left) and synthetic data using NORSAR-2D (center) and SOFI-2D (right) by modeling the fault zone as interface (transition between Middle to Lower Triassic units, Tab. 4). The seismic image obtained by seismic modeling using NORSAR-2D (center) and SOFI-2D (right) differ clearly because the later one additionally includes diffracted and multiple waves.
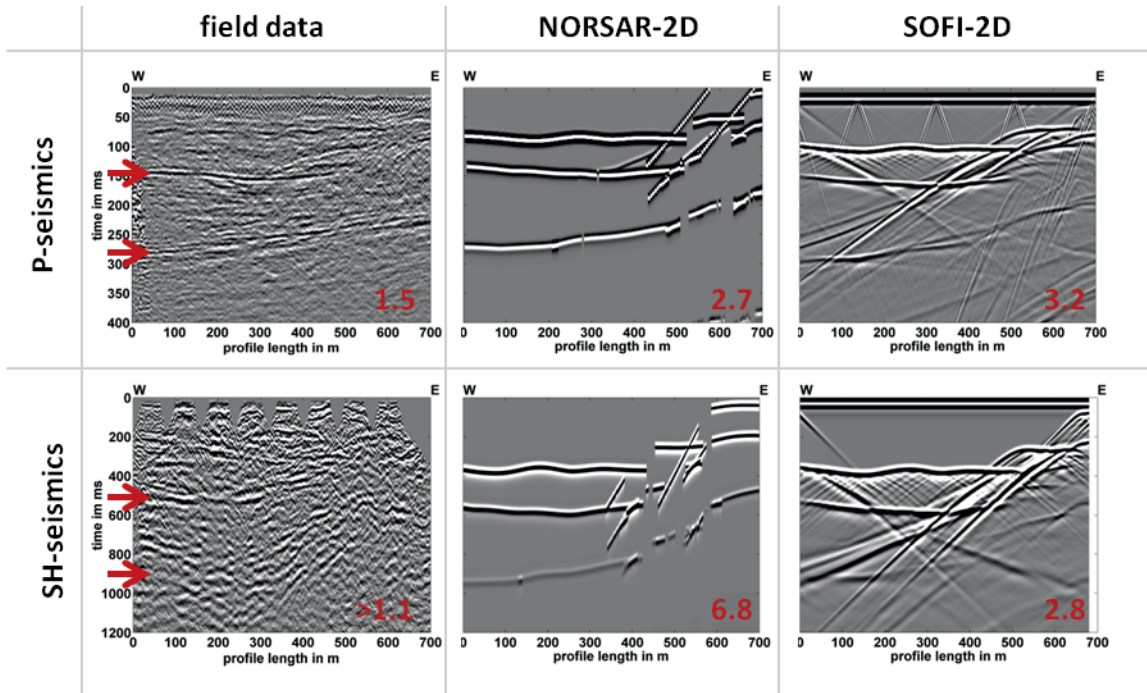
Figure 14: *Seismic fault zone modeling I. Comparison of field data (left) and synthetic data using raytracing software NORSAR-2D (center) and FD-software SOFI-2D (right). Red arrows mark the position of the reflectors used for the determination of amplitude ratios (red number in the right bottom corner).*
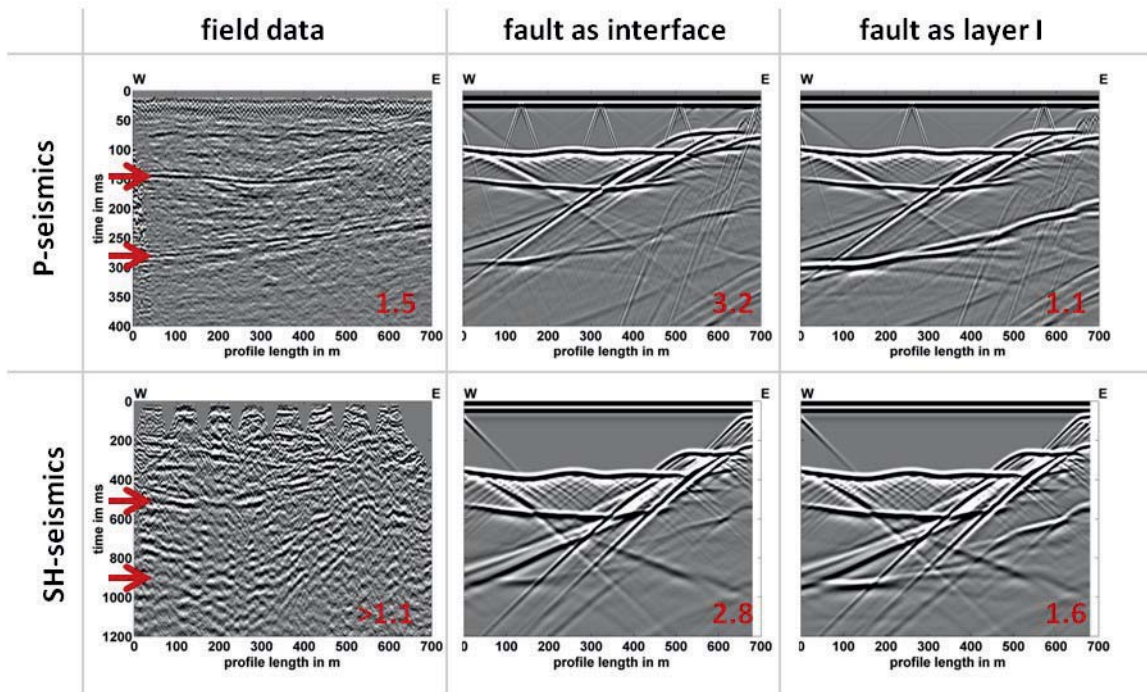

Figure 15: *Seismic fault zone modeling II using FD-software SOFI-2D (Bohlen, 2002). The fault is modeled as interface (center) and as layer (right; 13 m wide and 10 % elastic property reduction). Red arrows mark the position of the reflectors used for the determination of amplitude ratios (red number in the right bottom corner).*

This difference affects the synthetic SH-wave section (bottom row) obviously more than the synthetic P-wave section (top row). This contributes to the large difference of the amplitude ratios of synthetic SH-wave seismics between both modeling methods. In contrast, the amplitude ratios of synthetic P-wave seismics vary only to a minor degree (top row). The absolute maximum amplitude of the reflectors were determined in time gates and if diffracted waves arrived within the time gate sampling a later reflection, they might contribute to the amplitude. However, synthetic P-wave amplitude ratios are higher than the field data, which means that the amplitudes of the modeled fault zone are too small.

In the second step, seismic modeling is done using SOFI-2D software (Bohlen, 2002) to account for diffracted waves, which of course are present in the field data, but obscured by noise. The fault zone is modeled as layer between Middle Triassic and Lower Triassic (Upper Bunter) units. To achieve a possible tuning effect, i.e. a constructive interference of reflections from the top and bottom of a layer (Sheriff & Geldart, 1995), the width of the layer (fault zone) is set to 13 m, corresponding to a quarter of the wavelength inside the fault zone.
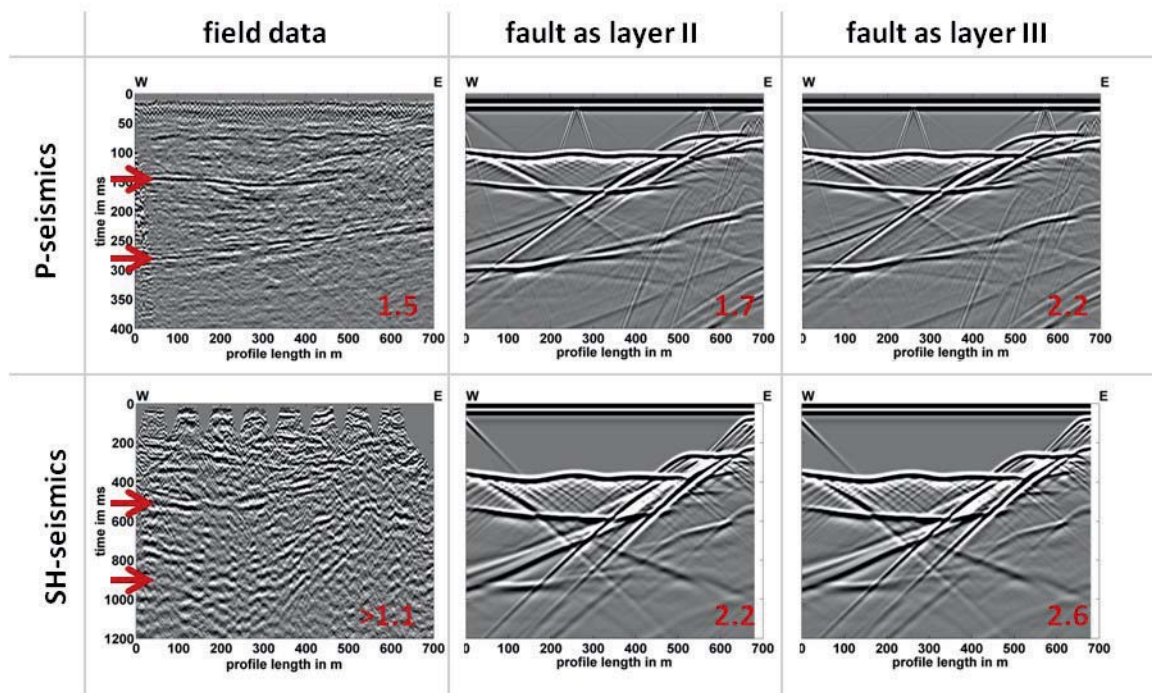
Figure 16: *Seismic fault zone modeling III using FD-software SOFI-2D (Bohlen, 2002). The fault is modeled as layer (13 m wide) with different elastic properties: 5 % (center) and 3 % (right) elastic property reduction. Red arrows mark the position of the reflectors used for the determination of amplitude ratios (red number in the right bottom corner).*

Values of the elastic properties of the layer are decreased relative to elastic properties of the Middle Triassic unit (Tab. 4). The comparison of fault zone modeling as interface (center)

55

and layer (right, model layer I) is shown in Figure 15. The elastic parameters (v_P, v_S, and ρ) of the fault zone are decreased by 10 % relative to the averaged elastic properties of Middle Triassic (Tab. 4). By inserting the fault zone as layer I the amplitude value of the second reflector increases, leading to smaller amplitude ratios of the synthetic data (right). However, the amplitude ratio of synthetic P-wave seismics (right) is too low compared to the field data (left). The synthetic SH-wave seismics (right) has a higher amplitude ratio than the field data. Since the amplitude ratio of the field data is the lower limit, the fault zone model layer I is not in contradiction to the field data (left).

To better adjust the synthetic P-wave seismics further modification were applied to the layer models (layer II, layer III; Fig. 16). By decreasing the reduction of the elastic properties from 10 % to 5 % or 3 % the amplitude ratios increase.

Seismic modeling shows that the field and synthetic data match better if the fault zone is modeled as a layer and not as an interface. The adjustment of synthetic P-wave seismics to field data is best if the fault zone is modeled as a layer using model layer II (Tab. 4). In contrast to that, the synthetic SH-wave data is best adapted using fault zone model layer I (Tab. 4). In order to characterize the fault zone it appears that seismic modeling is an auxiliary tool to check the elastic properties which are assigned to the fault zone in the model.

6. Conclusions

A high-resolution image of the complex structure of the eastern Leinetal Graben margin is revealed by P-wave reflection seismics: It comprises both steeply-dipping and shallowly-dipping normal faults, which cause a rollover structure. In addition structures due to salt tectonics are observed. The structural image indicates independent tectonic development of the uppermost (<500 m) and deeper (>500 m) depth levels. Reflection seismic SH-wave measurements complement the structural image of the fault system especially in the near-surface area. The combined analysis of P- and SH-wave seismics enabled the identification of areas with different P- and SH-wave reflection characteristics. For example, one of the shallowly west-dipping fault zones is clearly traceable by P-wave data from the surface down to 500 m depth, but only discontinuous SH-wave reflections are observed.

P- and SH-wave measurements enabled the determination of seismic velocities v_P and v_S and the derivation of further elastic parameters e.g. v_P/v_S and ρ. The elastic parameters correlate well with the geological interpretation and are in correspondence to literature values. However, no significant changes in elastic properties are observed at the fault zone itself, probably due to a too low resolution of the derived seismic velocities. The assigned

elastic properties of the model and the fault zone were investigated by seismic modeling. The field data are better reproduced if the fault zone is modeled as an extended layer instead of an interface and if the elastic parameters are decreased about 5% relative to the confining upper layer.

The result of this project also pointed out that fault zone exploration still suffers from unsolved problems in S-wave processing and interpretation, that result in low resolution and high uncertainties of v_S. Thus, to fully exploit the methods applied in this study, the reliability of SH-wave data has to be improved. Another technique to investigate to the elastic parameters in fault zones could be the inclusion of P-to-S converted waves. The investigation of the near-surface area may be realized by SH-wave analysis, whereas deeper targets and horizons may be analyzed using P-to-S converted waves.

The combined analysis of P- and SH-wave seismics improves the structural image of the subsurface and leads to new insights, which are based on different reflection characteristics of P- and SH-waves. The combined analysis of P- and SH-waves permitted the derivation of further elastic properties e.g. v_P/v_S and ρ. Seismic modeling is a valuable tool to validate elastic parameters in fault zones. This project showed that a combined analysis of P- and S-waves is useful for fault zone exploration, but further research on this area is strongly needed.

7. Acknowledgements

8. Publications resulting from the project

Tanner, D.C., Musmann, P., Wawerzinek, B., Buness, H., Krawczyk, C.M. & Thomas, R. (2015). Salt tectonics of the eastern border of the Leinetal Graben, Lower Saxony, Germany, as deduced from seismic reflection data. *Interpretation*, under revision.

Günther, T., Schaumann, G., Musmann, P. & Grinat, M. (2011). Imaging of a fault zone by large-scale dc resistivity experiment and seismic structural information. EAGE Near Surface, 12.-14.09.2011, Leicester/UK.

Musmann, P., Thomas, R. & Buness, H. (2011). Seismische Erkundung von geologischen Störungszonen am Beispiel des Leinetalgrabens: Erste Ergebnisse. Annual Meeting of the Deutsche Geophysikalische Gesellschaft, 21.-24.02.2011, Köln.

Musmann, P., Schaumann, G., Günther, T., Kenkel, J., Hördt, A., Grinat, M., Buness., H. & Thomas, R. (2011). Combined geophysical investigations of fault zones as potential reservoirs for geothermal exploitation. Celle Drilling, 12.-13.09.2011, Celle.

Musmann, P., Günther, T., Buness, H. & Thomas, R. (2012). Reflexions- und refraktions-seismische Bestimmung der P-Wellen-Geschwindigkeitsverteilung eines Störungs-systems. Annual Meeting of the Deutsche Geophysikalische Gesellschaft, 05.-08.03.2012, Hamburg.

Musmann, P., Polom, U., Buness, H. & Thomas, R. (2012). Reflection seismic survey across a fault zone in the Leinetal Graben, Germany, using P- and SH-waves. *Geophysical Research Abstracts* 14, EGU2012-4201, EGU General Assembly, 22.-27.04.2012, Vienna/Austria.

Wawerzinek, B., Musmann, P., Polom, U., Buness, H. & Thomas, R. (2013). Vergleich von P- und SH-Wellenmessungen an einem Störungssystem im Leinetalgraben. Annual Meeting of the Deutsche Geophysikalische Gesellschaft, 04.-07.03.2013, Leipzig.

Wawerzinek, B., Musmann, P., Polom, U., Buness, H. & Thomas, R. (2013). Erkundung eines Störungssystems mittels P- und S-Wellen am Beispiel des Leinetalgrabens. Der Geothermiekongress, 12.-14.11.2013, Essen.

Wawerzinek, B., Buness, H., Musmann, P., Polom, U. & Thomas, R. (2014). Charakterisierung einer Störungszone mittels P- und S-Wellenseismik. Annual Meeting of the Deutsche Geophysikalische Gesellschaft, 10.-13.03.2013, Karlsruhe.

Wawerzinek, B., Buness, H., Polom, U., Tanner, D.C. & Thomas, R. (2014). Fault zone characterization using P- and S-waves. *Geophysical Research Abstracts* 16, EGU2014-13682, EGU General Assembly, 27.04.-02.05.2014, Vienna/Austria.

Wawerzinek, B., Buness, H., Tanner, D.C., Polom, U. & Thomas, R. (2014). Analyse einer Störungszone im Leinetalgraben mittels P- und S-Wellenseismik. Der Geothermie-kongress, 11.-13.11.2014, Essen.

Wawerzinek, B., Buness, H., Musmann, P., Tanner, D.C., Krawczyk, C.M. & Thomas, R. (2015). Seismische P- und S-Wellenmessungen zur Untersuchung einer Störungszone im geothermischen Kontext. Annual Meeting of the Deutsche Geophysikalische Gesellschaft, 23.-26.03.2015, Hannover.

Wawerzinek, B., Buness, H., Musmann, P., Tanner, D.C., Krawczyk, C.M. & Thomas, R. (2015). Fault zone exploration in a geothermal context using P- and S-wave measurements. EGU General Assembly, 12.-17.04.2015, Vienna/Austria.

9. References

Aki, K. & Richards, P.G. (2002). Quantitative seismology (2nd edition). University Science Books.

Bohlen, T. (2002). Parallel 3-D viscoelastic finite difference seismic modelling. *Computers & Geosciences* 28(8), 887-899. doi:10.1016/S0098-3004(02)00006-7.

Buness, H. (2007). Improving the processing of vibroseis data for very shallow high-resolution measurements. *Near Surface Geophysics* 5(3), 173-182. doi:10.3997/1873-0604.2006029.

Erickson, E.L., Miller, D.E. & Waters, K.H. (1968). Shear wave recording using continuous signal methods part II – later experimentation. *Geophysics* 33(2), 240-254. doi:10.190/1.1439925.

Gardner, G.H.F., Gardner, L.W. & Gregory, A.R. (1974). Formation velocity and density – The diagnostic basics for stratigraphic traps. *Geophysics* 39(6), 770-780. doi:10.1190/1.1440465.

Grupe, O. (1909). Über die Zechsteinformation und ihr Salzlager im Untergrunde des hannoverschen Eichsfeldes und angrenzenden Leinegebietes nach neueren Bohrergebnissen. *Zeitschrift für praktische Geologie* 17, 185-205.

Grupe, O. (1923). Zur Entstehung des Göttinger Leinetalgrabens. *Jahrbuch der Preußischen Geologischen Landesanstalt* 42, 595-620.

Günther, T. (2011). Ra2dTomo Software, http://www.resistivity.net/, last access, 11/28/2014.

Jordan, H. (1986). Halotektonik am Leinetalgraben nördlich Göttingen. *Geologisches Jahrbuch* A 92, 3-66.

Krawczyk, C.M., Polom, U. & Beilecke, T. (2013). Shear-wave reflection seismics as a valuable tool for near-surface urban applications. *The Leading Edge* 32(3), 256-263. doi:10.1190/tle32030256.1.

Leiss, B., Tanner, D.C., Vollbrecht, A. & Arp, G. (2012). Neue Untersuchungen zur Geologie der Leinetalgrabenstruktur. Universitätsverlag Göttingen.

Musmann, P. & Buness, H. (2010). High-resolution seismic imaging of near-surface fault structures within the Upper Rhine Graben, Germany. In: Miller, R.D., Bradford, J.H., Holliger, K. (eds.). Advances in near-surface seismology and ground-penetrating radar. *SEG Geophysical Developments Series* 15, chap. 17, 281-296. doi:10.1190/1.9781560802259.ch17.

Musmann, P., Polom, U., Buness, H. & Thomas, R. (2012). Reflection seismic survey across a fault zone in the Leinetal Graben, Germany, using P- and SH-waves. *Geophysical Research Abstracts* 14, EGU2012-4201, EGU general assembly 2012, Vienna/Austria.

Pugin, A.J.-M., Brewer, K., Cartwright, T., Pullan, S.E., Didier, P., Crow, H. & Hunter, J.A. (2013). Near surface S-wave seismic reflections profiling – new approaches and insights. *First Break* 31, 49-60. doi:10.3997/1365-2397.2013005.

Reyer, D. (2008). Geologische Kartierung im Bereich der östlichen Grabenrandstörung des Leinetalgrabens südlich von Sudheim, 1 : 10 000, Georg-August-Universität Göttingen.

Sheriff, R.E. & Geldart, L.P. (1995). Exploration seismology. Cambridge University Press.

Tanner, D.C., Leiss, B. & Vollbrecht, A. (2010a). The role of strike-slip tectonics in the Leinetal Graben, Lower Saxony. *Zeitschrift der Deutschen Gesellschaft für Geowissenschaften* 161(4), 396-377. doi:10.1127/1860-1804/2010/0161-0369.

Tanner, D.C., Albero, F., Leiss, B. & The Göttingen Geothermal Group (2010b). Modelling the Geothermal Potential of the Eastern Border of the Leinetal Graben, Lower Saxony. *Zeitschrift für geologische Wissenschaften* 38(1), 61-68.

Tanner, D.C., Musmann, P., Wawerzinek, B., Buness, H., Krawczyk, C.M. & Thomas, R. (2015). Salt tectonics of the eastern border of the Leinetal Graben, Lower Saxony, Germany, as deduced from seismic reflection data. *Interpretation*, under revision.

Wunderlich, H.G. (1955). Jüngste Tektonik im Gebiet des Leinetalgrabens. *Geologische Rundschau* 43(1), 78-93.

Yilmaz, Ö. (2001). Seismic data analysis: Processing, inversion, and interpretation of seismic data. *SEG Investigations in Geophysics Series* 10.

60

G2: Detection of Fault Zones Using Electric and Electromagnetic Methods

Gerlinde Schaumann, Michael Grinat* & Thomas Günther

Leibniz Institute for Applied Geophysics, Stilleweg 2, 30655 Hannover, Germany

*Corresponding Author: Michael.Grinat@liag-hannover.de

Abstract

Electric and electromagnetic methods were investigated concerning their ability to image geological fault zones at depths of interest for geothermal applications. Additionally a compilation of maps with important information for geothermal exploration was undertaken to figure out already known geological features of the North German Basin.

Initially a shallow fault system in the *Leinetal Graben* was investigated by using DC resistivity and Transient Electromagnetics with bigger survey setups and stronger transmitters. The fault could be delineated well by changes in resistivity. Structural information from a seismic survey supported the interpretation and the combined results of the three applied methods were able to show the trace of the fault with depth down to several hundred metres. For depths of about 3 to 7 km, numerical calculations were carried out using magnetotelluric data.

The benefit of combining all the information supports the evaluation of a survey design by determining areas of interest where exploration can be carried out.

1. Introduction

Electric and electromagnetic methods investigate changes of the electrical conductivity (resp. resistivity, i.e. 1/conductivity) in the ground. This parameter is interpreted to represent different subsurface properties. Electromagnetic methods are successfully applied to detect zones bearing electric conductive fluids, provided that the porosity of a rock is adequate, and can therefore be used to determine changes in the underground properties. The hydrogeochemical composition of the fluid essentially influences its electrical conductivity and therefore this parameter is very sensitive to detect brines (SPICHAK & MANZELLA 2009). In high-enthalpy regions like Iceland brines at depth and low resistive clay caps are common and therefore electric methods are highly preferred for geothermal exploration. In low-enthalpy regions, for instance in the North German Basin, fault zones are possible pathways for fluids at depth. They can be targets to explore with electromagnetic methods. A high mineralisation of the formation water can be found in most of the deeper aquifers of the North German Basin (BOZAU et al. 2015). BUJAKOWSKI et al. (2010) present an exploration methodology for low-enthalpy systems in sedimentary formations at a geothermal test site in central Poland to identify formations with high fracture permeability and the presumed flow path of geothermal brines in the subsurface.

In the project G2 electric and electromagnetic prospection methods are investigated concerning their ability to image geological fault zones in depths of interest for geothermal applications. For large-scale geologic structures with depths up to a few km, resistivity is a valuable key parameter in water-dominated reservoirs. Electric and electromagnetic methods were jointly operated at a selected shallow fault system at the study area *Leinetal Graben,* where a known fault crops out at the surface; they were interpreted together with seismic data. At a later stage of the project the study was extended to deeper structures. The aim was to investigate the detectability of fault zones from the surface till depths of interest for geothermal exploitation (about 3 to 7 km in the North German Basin). Hence numerical and practical investigations were carried out with emphasis on the comparison of the possibilities and limitations of the methods used.

At the *Leinetal Graben* it was possible to image the fault zone using very large-scale DC resistivity and Transient Electromagnetic (TEM) measurements, combined with structural information from seismic surveys. The results of Magnetotelluric (MT) measurements from the North German Basin were basis for 1D and 2D modelling under consideration of data from drillings and typical geological features.

For an overview of available data, e.g. the position of present temperature anomalies as well as the location of salt domes, the traces of already known faults and many other features

63

relevant for geothermal exploration, a collection and compilation was undertaken to identify areas of interest under the geothermal point of view. Maps were compiled which allow a blending or the combination of several features for the North German Basin. This is the initial step before exploring in the field starts and contributes to evaluate a procedure for investigating potential zones of interest. On this basis a field survey can be designed which considers the advantages and limitations as well as the compliments of the methods used.

2.   Near surface exploration of a fault zone in the Leinetal Graben

Large scale DC resistivity and Transient electromagnetics were operated at a shallow selected fault system in the *Leinetal Graben* together with the seismic exploration method to prove their performance. This study area was chosen because a fault zone is cropping out at the eastern slope. The electric and electromagnetic methods supplement the seismic method applied in project G1 by imaging the underground structure with their ability to provide information about the resistivity, which is directly associated to the mineralization of groundwater or hydrothermal fluids in the subsurface, if present. LEISS et al. (2011) and TANNER et al. (2010) give an overview of the local geology.

Several field surveys using the DC resistivity method and the Transient Electromagnetic method (TEM) were carried out perpendicular to the strike of the fault. In the scope of the surveys the field performance was adapted to yield greater exploration depths. The setup of both methods was enlarged and stronger transmitters were used. In the following a short summary of these measurements and the results for profile no. 2 is given. The surveys were carried out in the area between Northeim and Sudheim (fig. 2.2).

In general the enlargement of the survey setups and the stronger transmitters enabled greater investigation depths for both methods and contributed to delineate the trace of the fault down to several hundred meters.

2.1 Technical developments used in the project

A high current source for Geoelectrics

For large-scale 2D and 3D investigations high sensitive amplifiers for the potential dipoles and a high current source for the injection dipoles are necessary. The current source used for the measurements in the *Leinetal Graben* is an electronically driven transverter, which enables to generate user-defined signals as direct current or alternating current up to frequencies of 100 Hz. The constant current can be up to 50 A with 40 kW. The transverter is

64

driven by a control card in real-time and supplied by a 100 kVA AC generator. The generated signal and the number of periods for an injection interval are defined and facilitate determining the signals at the potential dipoles. The controller program was developed by the institute. An application is introduced by RONCZKA et al. (2014). The DC resistivity measurements on profile 2 in the *Leinetal Graben* were performed with this equipment.

Large scale Transient Electromagnetics

The standard equipment for the instrument terraTEM, owned by LIAG, was extended to enable higher transmitter moments which are necessary for deeper exploration. By operating a high current transmitter and applying an adapted survey design with a larger layout in the field, it is possible to detect deeper structures and also to improve the resolution of the resistivity distribution in the ground. A field test was performed at the Horstberg site in the area west of Uelzen. By help of an adapted survey layout, information about the resistivity distribution down to more than 600 m could be determined. Three soundings at the same site but with different loop sizes (squares with side length of 50 m, 200 m and 300 m) are compared. The results are shown in figure 2.1. The decay curves gained with bigger transmitter loops yield clearly more information at later times (resp. greater depth) than measurements with smaller loops before they are disturbed by the local noise level. The resulting investigation depth deduced from the 1D modelling is increased compared to depths reached with smaller loop sizes. On the other hand, bigger loops are often not able to resolve near surface layers, which are much better determined by help of smaller transmitter loops. In the presented example the investigation depth is enhanced by help of the stronger transmitter moment. A 1D inversion of the data yields a resistivity of about 100 Ωm for a near surface layer down to ca. 50 m (best determined with data from smaller loop setups). For depths of more than 200 m, the resistivity is distinctly decreasing to approximately 1 Ωm (best determined by application of a bigger survey setup). A more detailed description is given in the milestone 1 report (SCHAUMANN et al. 2011).

An experiment with a very large loop for transmitting the signal into the ground was performed at the *Leinetal Graben*. A square transmitter loop of side length 1000 m was layed out in the field. Data were gained with various receiver positions. This big setup enabled a larger investigation depth, but the high signal to noise ratio in the area did not allow a distinct deeper interpretation compared to other sites with smaller Tx loops of 400 m side length.
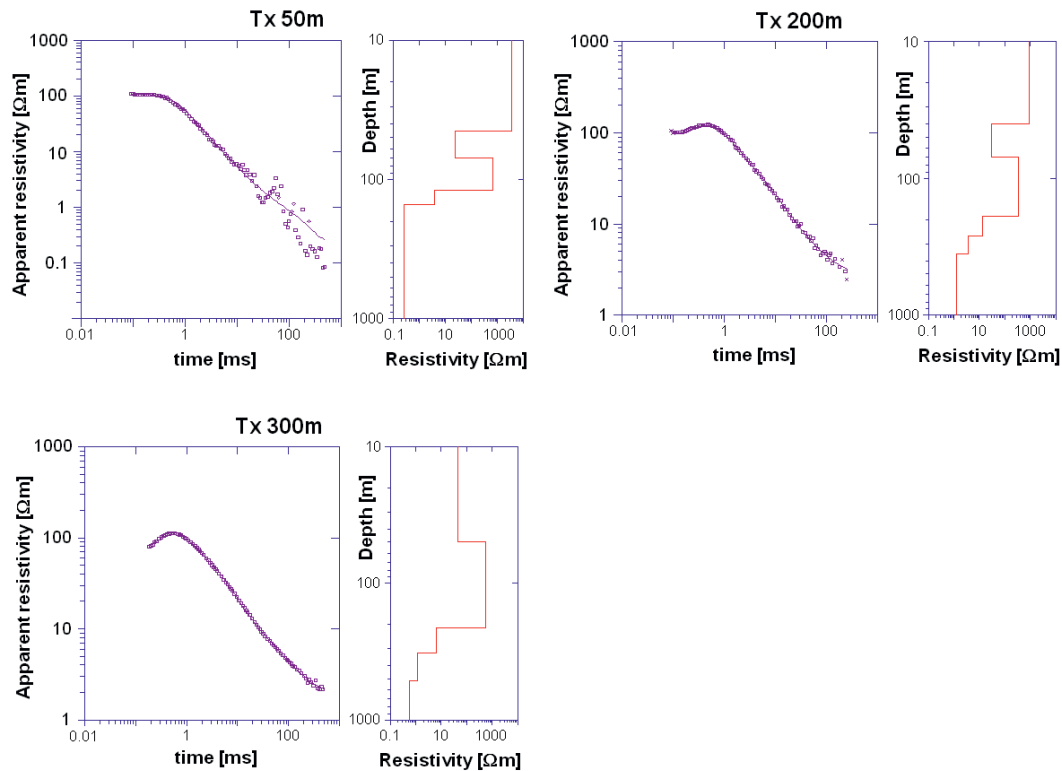
Fig. 2.1: *Comparison of apparent resistivity curves (left) gained with different transmitter loop sizes (Tx) at the same site at Horstberg and resulting 1D models (right).*

First application of Magnetotellurics

The Magnetotelluric (MT) method is established at the institute to enable further exploration for deep geothermal targets. A broadband registration which allows an investigation from a few hundred meters to several kilometers depth is possible with the installed frequency range of the equipment. The remote reference technique for reducing anthropogenic noise in highly industrial or densely populated areas can be used. A single sounding was already performed in the *Northeimer Stadtwald*. Furthermore a combination with the already installed methods at the institute is requested and reasonable.
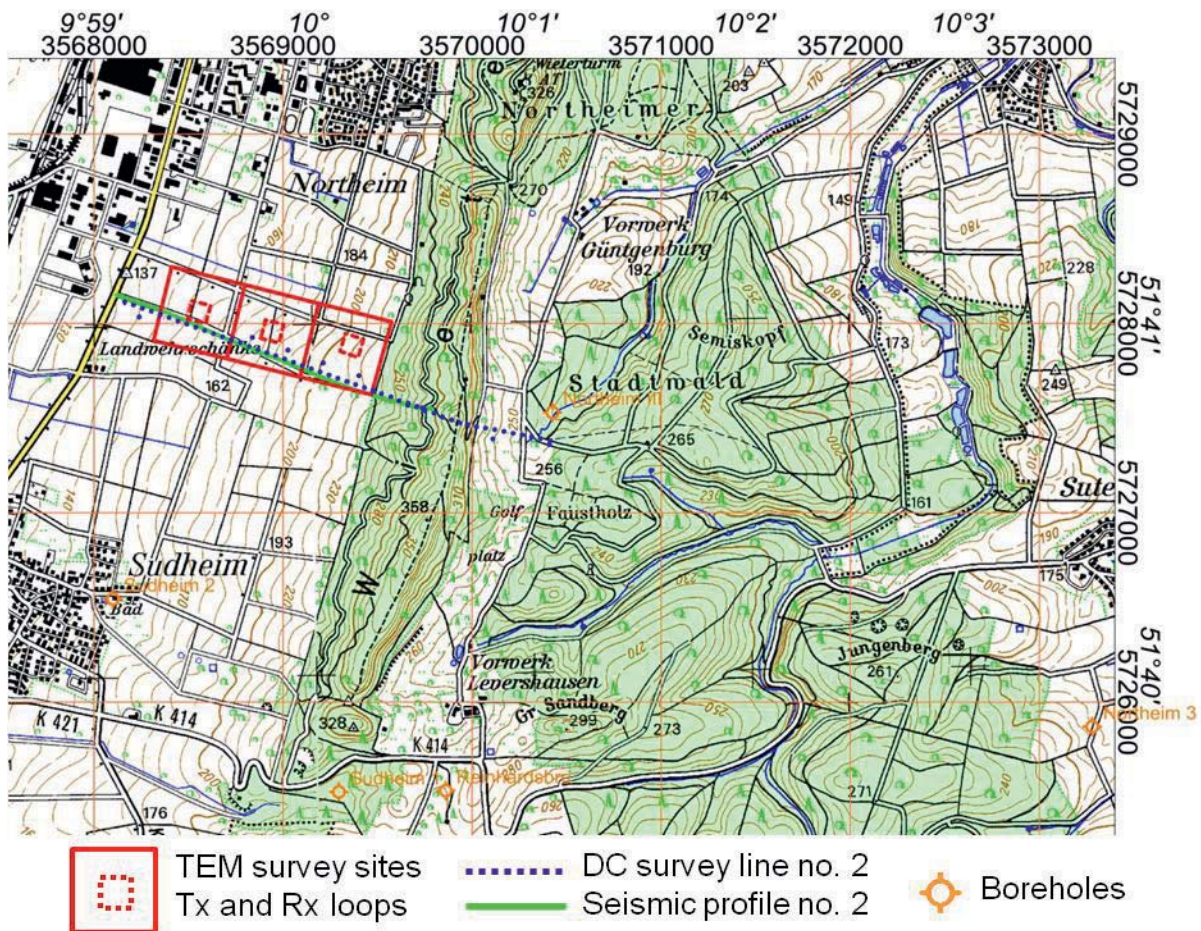
Fig. 2.2: *DC resistivity and seismic survey lines and TEM sites with a Tx coil side length of 400 m in the study area ´Leinetal Graben´ between Northeim and Sudheim.*

2.2 Surveys in the Leinetal Graben

DC resistivity in the eastern Leinetal Graben area south of Northeim

The DC resistivity survey line no. 2 was situated about 1 km south of Northeim and coincides with the seismic profile no. 2 (see project G1). Non-standard large-scale measurements in a dipole-dipole configuration (50 m potential electrode spacing, 200 m current dipoles) energized by a high current source (up to 40 A) were applied. A strong transmitter and continuous registration of potential differences were used to acquire apparent resistivities on the profile of more than 2 km length. The time series were processed to obtain about several hundred apparent resistivities. An inversion without a-priori information already revealed clearly the trace of the fault line but showed a smoothed resistivity distribution (GÜNTHER et al. 2011).

TEM in the eastern Leinetal Graben area south of Northeim

TEM soundings with a strong transmitter delivering up to 50 A and high transmitter moments caused by a square transmitter coil (Tx) with side lengths of 400 m and 1000 m (not shown here) were carried out close to profile no. 2, see fig. 2.2. The receiver coil (Rx) was placed in the centre of the loop. The instrument used was the terraTEM from Monex GeoScope with the transmitter terraTX-50. The soundings were 1D inverted with the software WinGLink (SCHAUMANN et al. 2012a, 2014c). The large scale setup improved the data quality, but the strong noise level in the study area allowed only a sparse extension of the investigation depth to approximately 900 m, but below depths of about 800 m the interpretation is unconfident because of unsufficient data quality. Fig. 2.3 shows the TEM interpretation results of the sites measured with the 400 m transmitter loops (without a-priori information), plotted on the DC resistivity as vertical columns; additionally the seismic reflectors (see project G1) are superposed. The change from lower resistivities to higher resistivities in greater depths in the DC section correlates with the interpreted trace of the fault from the seismic interpretation already without using any constraints. Some thin low resistive layers from the TEM interpretation also correlate with seismic reflectors. At depths where the fault is assumed distinct changes in resistivity can be seen. Whilst DC resistivity measurements hamper the delineation of thin low resistive layers, TEM is an appropriate method to supplement this disadvantage. The depths of the seismic reflectors can be used to inspect equivalent cases of interpretation.

Joint interpretation with Seismics

Seismic data from a reflection survey are able to improve the resistivity image by adding structural information to the inversion problem (GÜNTHER & RÜCKER 2006, 2009). This high-resolution structural information is associated to lithologic changes and therefore decreases the non-uniqueness of the inverse problem. The most prominent reflectors of the processed seismic reflection profile no. 2 were inserted as lines in the mesh generation and serve as allowed resistivity boundaries. So the seismic structural information was used as a constraint for the geometry at the 2D interpretation of the DC resistivity, which was performed with the inversion algorithm BERT (GÜNTHER & RÜCKER 2006). It uses triangle meshes as anisotropic smoothness constraints, which subdivide the surface. Topography was measured using GPS and defines the upper boundary of the modelling domain. The lower boundary and penetration depth was estimated from 1D sensitivity analysis to be at 800 m below surface. GÜNTHER et al. (2011) presented this large-scale resistivity experiment to image the fault system down to a depth of a few hundred metres. The trace of the fault is revealed by a change to higher resistivities in greater depths. So the adding of this structural information improved the interpretation (fig. 2.3). A more detailed geological interpretation can be found at the G1 report.
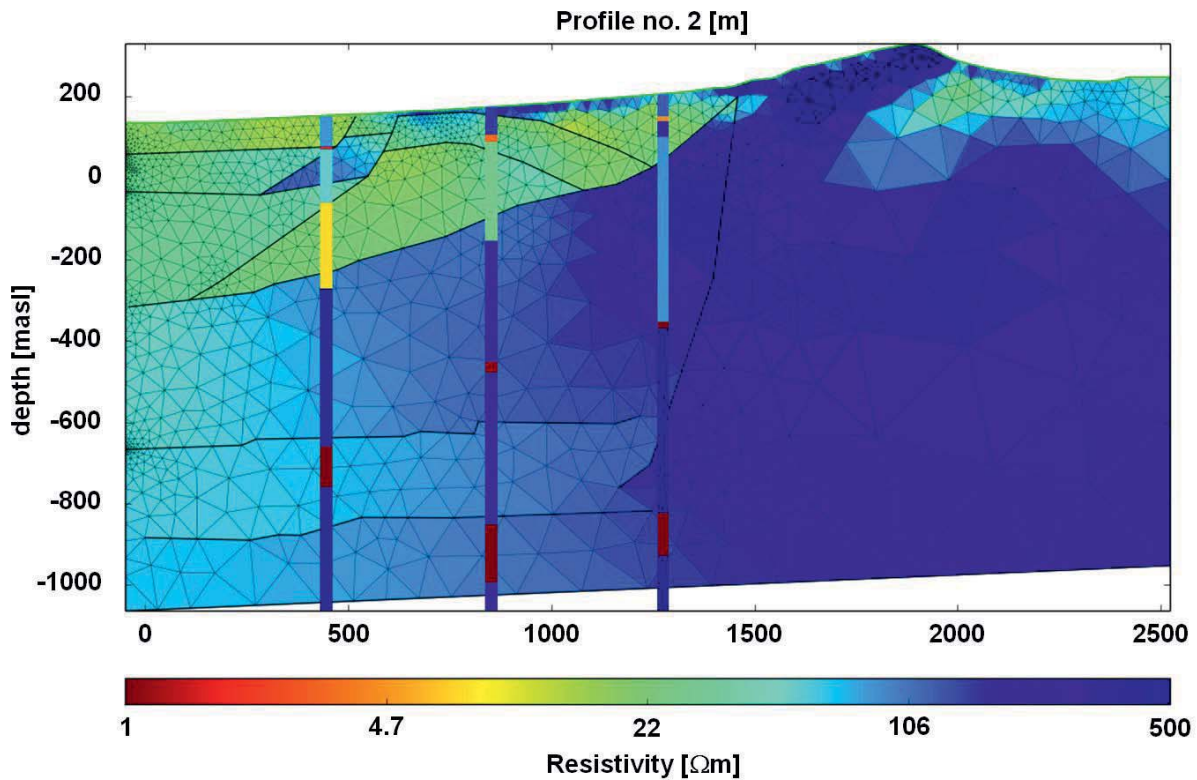
Fig. 2.3: *DC resistivity of profile no. 2 (with constraints), seismic reflectors (black lines) and 1D TEM interpretation results (vertical columns, no constraints).*

3. Investigation of deeper structures in the North German Basin

Deeper structures of interest for geothermal application in Northern Germany were investigated from the electromagnetic point of view. Besides the sampling of information from boreholes, resistivities were collected by collocating already measured magnetotelluric data. Survey lines were plotted on maps with different geological background information.

3.1 Collection of resistivity values

Resistivities from boreholes

KNÖDEL et al. (1978) supplied resistivities as a significant parameter for formations from Tertiary to Devonian, based on calculations from electric logs of measurements in deep boreholes situated in the North German Basin (Appendix, Table 1). They also estimated porosities at a particular depth under consideration of temperature, pressure and an estimated value for a salt concentration for several resistivity values. From the drilling Velpke-Asse Devon 1 resistivity values were estimated by approximation of equivalent resistivities based on dual-laterolog measurements in the borehole (KELCH & PAULUS 1980). Here an approximated resistivity of several hundreds of Ωm was gained for the Lower Permian Rotliegend volcanics. Among the few available data, electric logs from the Groß

Buchholz GT-1 drilling site in Hannover (Genesys drilling) were investigated. Table 2 (see Appendix) shows the resistivities that were determined. Unfortunately, the log starts not until a depth of 3000 m. The exclamation mark at a few formations indicates that the depth determined by the drilling and the corresponding depth where resistivity changes occur fit very well.

From the vicinity of the survey profiles in the *Leinetal Graben* around Northeim and Sudheim, several resistivities were gained from local boreholes not deeper than 1300 m. Elaborated tables are given in SCHAUMANN et al. (2011). The interpretation of DC resistivity and TEM data from this area, presented in chapter 2, is based on them.

Temperature, porosity and salinity influence the bulk resistivity of a lithology. Therefore one can find different values at other areas and depths. Because of the few available, very selective data, no broadly based parameter collection could be performed. In particular no area-wide data basis could be obtained. It is therefore reasonable to compile the data needed from available sources in each individual case.

Collection of available Magnetotelluric data

For investigations of the subsurface structure to depths of many kilometers the Magnetotelluric (MT) method can be applied. By relating natural variations of magnetic and electric field components at different frequencies information about the distribution of electrical conductivities can be gained. By help of sounding curves of apparent resistivities a rough estimation about the resistivity distribution in the subsurface is yielded, depending on the frequency range considered. An inversion enables a quantitative interpretation of the data by adapting a model to the data until they are explained under given conditions. The sounding frequency and the conductivity structure of the Earth influence the penetration depth (SIMPSON & BAHR 2005). Field variations registered at longer periods resp. lower frequencies give information from deeper structures. The accurate determination of the electrical conductivity structure in a certain depth depends also on the electrical properties and thicknesses of the rocks above. Besides that data quality is of important influence. In general low resistive layers complicate the detection of deeper structures. For an ideal 2D case, electric and magnetic fields are mutually orthogonal and the basic equations, which describe the field variations, can be described by two modes, the E-polarisation (TE mode, electric fields parallel to strike) and the B-polarisation (TM mode, magnetic fields parallel to strike) (SIMPSON & BAHR 2005).

The map in fig. 3.1 shows available Magnetotelluric data after a collection from accessible sources during the run of the project. It will enable more insight about deeper structures,

when this data pool is reconditioned and screened for areas of geothermal interest. This collection can be a basis for new surveys and may complement own measurements, which can then be adapted with an adequate survey design (location of sites, frequency range, etc.).

Profile B which runs from the area of Magdeburg to the island of Rügen is indicated in the map. It was already interpreted by HOFFMANN et al. (1998, 2008) and JÖDICKE et al. (2001). Many MT measurements performed in the area of Northern Germany were operated with frequency ranges which do not allow to interprete the upper 5 km of the North German Basin in more detail. Therefore a common interpretation is that the basin is mainly low resistive in the order of 1 Ωm for most parts.
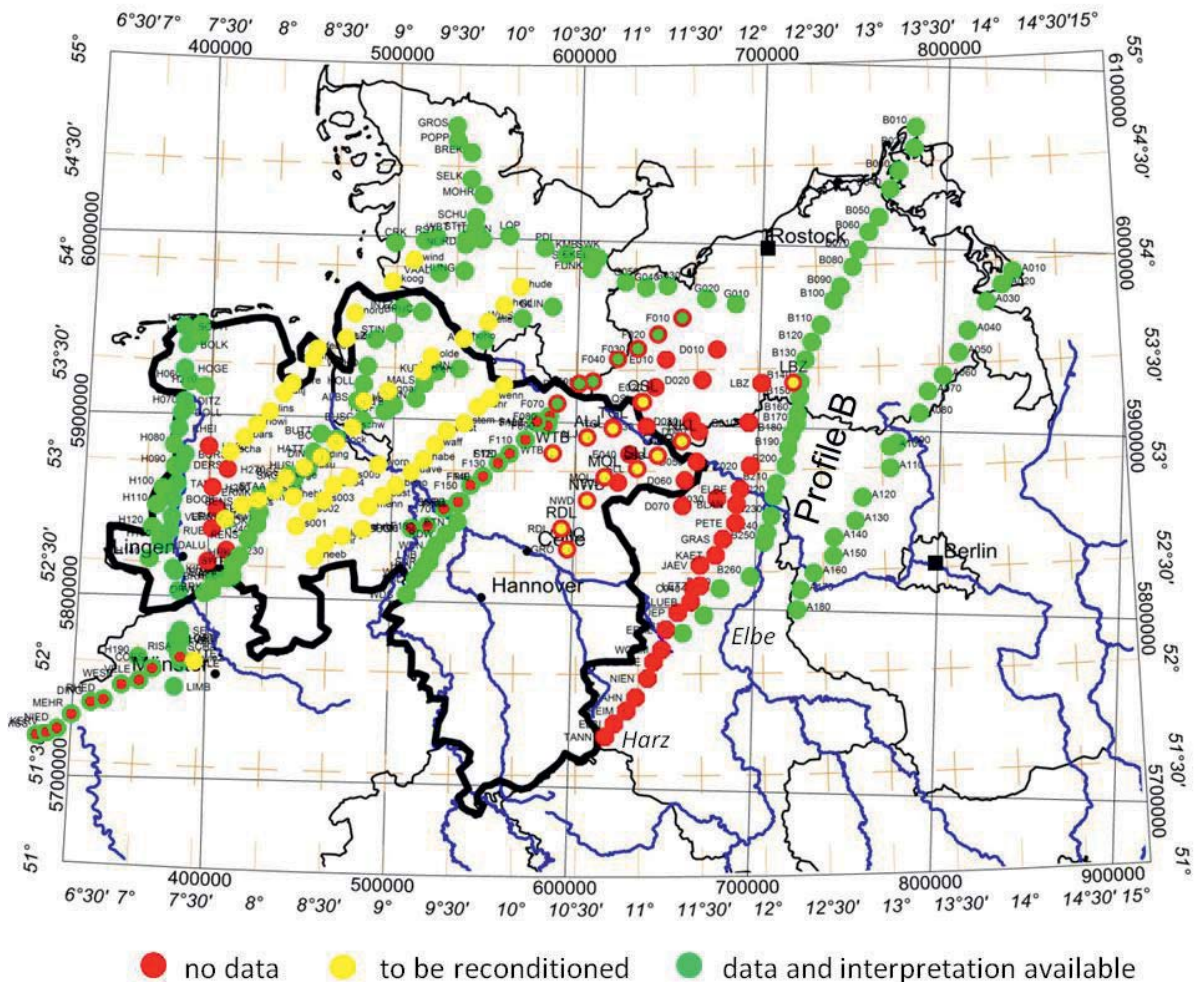
Fig. 3.1: *Availability of MT data of Northern Germany (March 2014). Symbols with mixed colors indicate if data (core of the circle) and/or interpretation (frame of the circle) are available. Profile B runs from the area of Magdeburg to the island of Rügen.*

3.2 Compilation of maps for the North German Basin

The issue of investigating deep faults in the North German Basin led to an extensive inquiry of data available for depths up to 6 km and more because the target depth in the gebo research project ´drilling technology´ was 6 km. A general introduction of the geology of the North German Basin is given by ZIEGLER (1990) and WALTER (2007). Among the broad range of electromagnetic methods the favoured source for identifying the distribution of electrical conductivities at that depth are magnetotelluric investigations. Later on, some investigations are based on data from MT profile B which crosses the eastern part of the North German Basin. In Northern Germany magnetotellurics may also be favoured over seismic standard explorations because the latter can be hampered by the widely spread Zechstein base, which covers deeper exploration targets (DOHR 1989).

Because many geological data are already available for Northern Germany, a collection and compilation was undertaken to identify areas of interest under the geothermal point of view. The distribution of MT sites, already measured in the nineties and the noughties, is of great interest. Maps were compiled which allow the combination of several features for the North German Basin. The position of present temperature anomalies as well as the location of salt domes, the strike of already known faults and many other features are relevant for geothermal exploration. The combination of different facts is therefore needed as a contribution to face the question of substance and challenges in deep geothermal exploration. As a base for the required information the ´Geotektonischer Atlas´ (KOCKEL 1998, BALDSCHUHN et al. 2001), the distribution of salt structures (REINHOLD et al. 2008) and data from the Southern Permian Basin Atlas (SPBA) from DOORNENBAL & STEVENSON (2010), which is based on the former, were collected and blended. Additional information was used from the Geothermal Information System for Germany (GeotIS) which is installed at LIAG; furthermore data of geological 3D models of the deeper subsurface of Lower Saxony (GTA3D), prepared by LBEG as Gocad files, were used. For selected areas 3D views were created with these Gocad files for depths down to the Zechstein base which show the traces of faults and different geological horizons in more detail. These models are based on data of the ´Geotektonischer Atlas von Nordwestdeutschland und dem Deutschen Nordsee-Sektor´ (BALDSCHUHN et al. 2001). A main task was the presentation of the different data in a common coordinate system.

Prepermian faults and faults in the Rotliegend or Zechstein formations can be traced as well as the locations of salt structures, the traces of temperature isolines for several depths and heat flux density (after AGEMAR et al. 2012). Maps of geophysical parameters, e.g. anomalies of the total Earth´s magnetic field (GABRIEL et al. 2010), Bouguer anomalies (SKIBA et al. 2010), depths, thicknesses and distribution of geological formations, drilling sites sorted by

depth (Source: GeotIS) and prominent geological structures, the traces of survey lines, etc. can be combined depending on the issue of interest.

A few selected examples of the compiled maps and sections are shown in figs. 3.2 to 3.10. The shape of the federal state of Lower Saxony is outlined black. Fig. 3.2 shows the depth of the base of the Upper Rotliegend Clastics in combination with temperature isolines and the traces of prepermian and Rotliegend faults. Fig. 3.3 shows the Zechstein thickness and salt structures. In fig. 3.4 the delineation of the basin's lateral extension at certain depths of selected sediments is shown for depths of more than 5000 m, here the Base to the Upper Rotliegend Clastics in the area of the Southern Permian Basin and adjacencies.
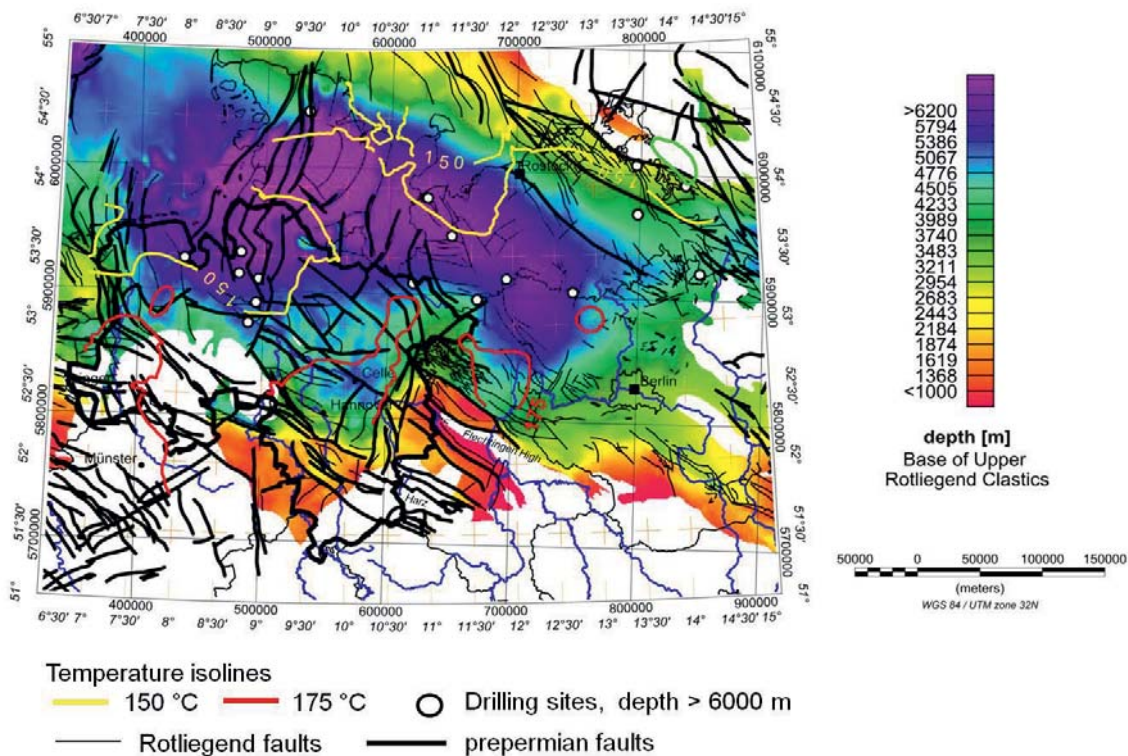
Fig. 3.2: Depth to the base of the Upper Rotliegend Clastics in Northern Germany, combined with temperature isolines, drilling sites and the map traces of selected faults.
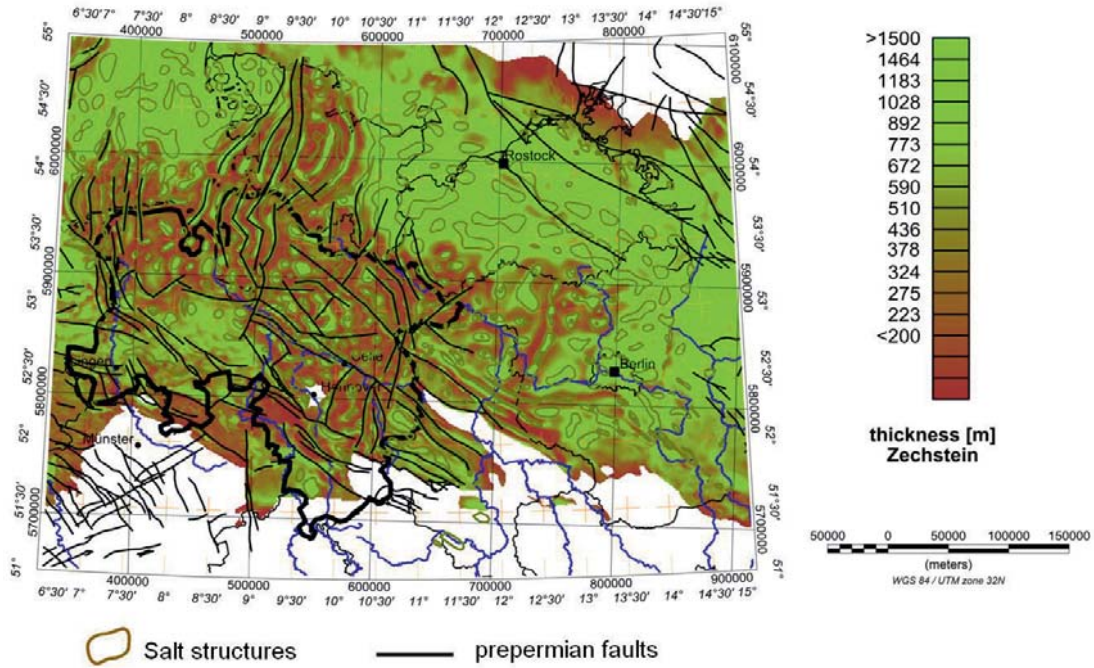
Fig. 3.3: *Thickness of Zechstein in Northern Germany, combined with salt structures and the map traces of selected prepermian faults.*
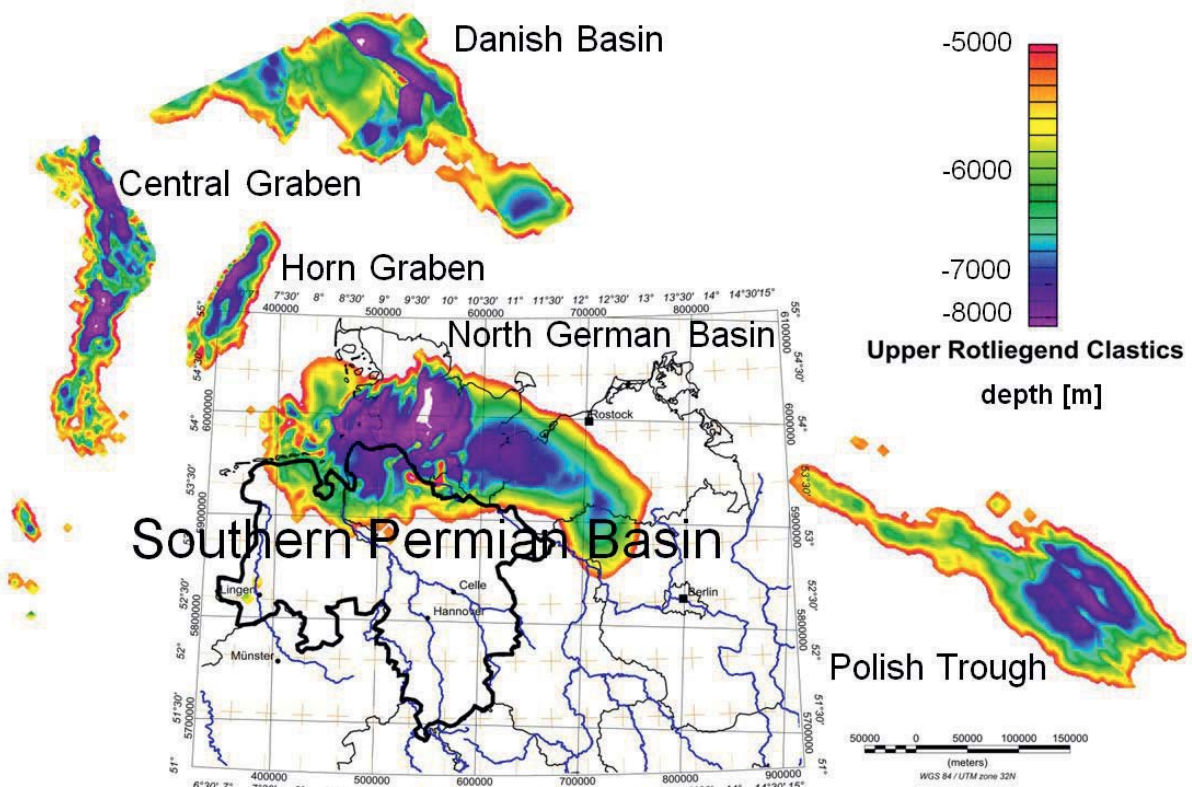
Fig. 3.4: *Occurrence of the Upper Rotliegend Clastics in the area of the Southern Permian Basin and adjacencies at depths of more than 5000 m.*

Mesozoic layers were interpreted to be low resistive in the eastern part of the North German Basin by JÖDICKE et al. (2001), see chap. 4.2. Because of this interpretation, all the thicknesses of single Mesozoic layers were summed up (data provided by DOORNENBAL & STEVENSON 2010) and a map was created which shows the distribution of Mesozoic sediment thicknesses in Northern Germany (fig. 3.5). This map reveals possible areas with smaller coverage of the Lower Permian Rotliegend sediments by supposed low resistive Mesozoic layers. Particularly at the basin's rim and close to the salt domes the coverage is reduced. At most parts within the central eastern basin the thickness of Mesozoic layers adds up to about 4000 m or more. This plays an important role for investigating deeper structures with MT. The map trace of the MT profile B which crosses the whole eastern basin is also shown in fig. 3.5. A more detailed elaboration is given by SCHAUMANN & GRINAT (2014a).
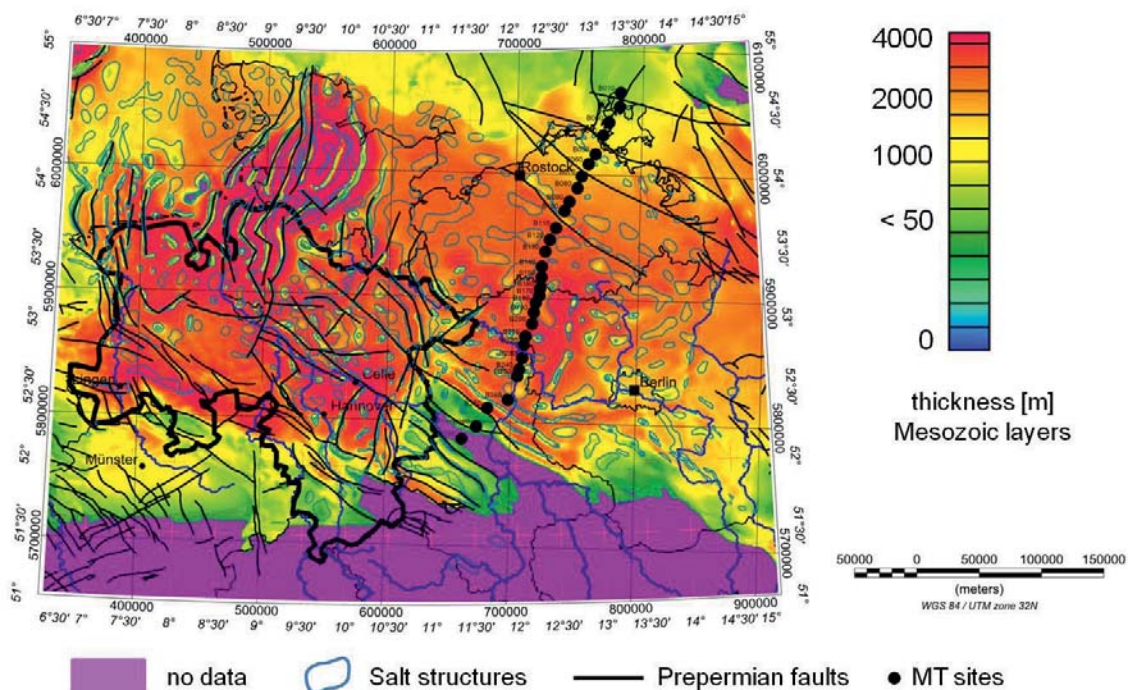
Fig. 3.5: *Thicknesses of Mesozoic layers in Northern Germany and map trace of MT profile B, combined with salt structures and the map trace of prepermian faults.*

Several 3D views are shown in figs. 3.6, 3.7 and 3.8. In fig. 3.6 a 3D voxel for the temperature distribution in a cube of about 50 km x 50 km x 5 km in the area of Celle is combined with the Zechstein base and Zechstein and Buntsandstein faults at the salt dome Wathlingen-Hänigsen. Fig. 3.7 shows the same cube together with Bouguer anomalies and salt structures.

75
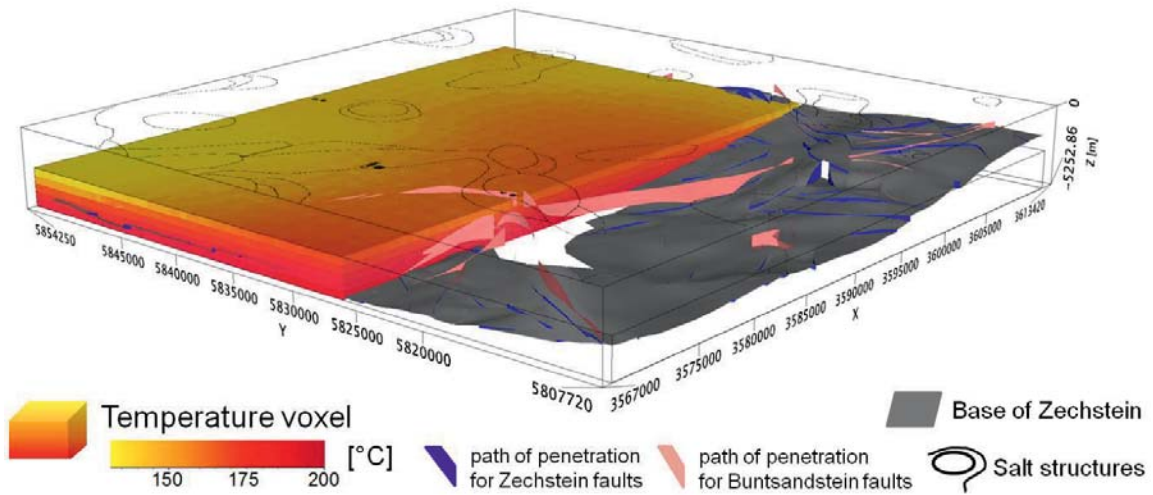
Fig. 3.6: *3D voxel for the temperature distribution in a cube of approximately 50 km x 50 km x 5 km in the area of Celle showing the Zechstein base and Buntsandstein faults at the salt dome Wathlingen-Hänigsen.*
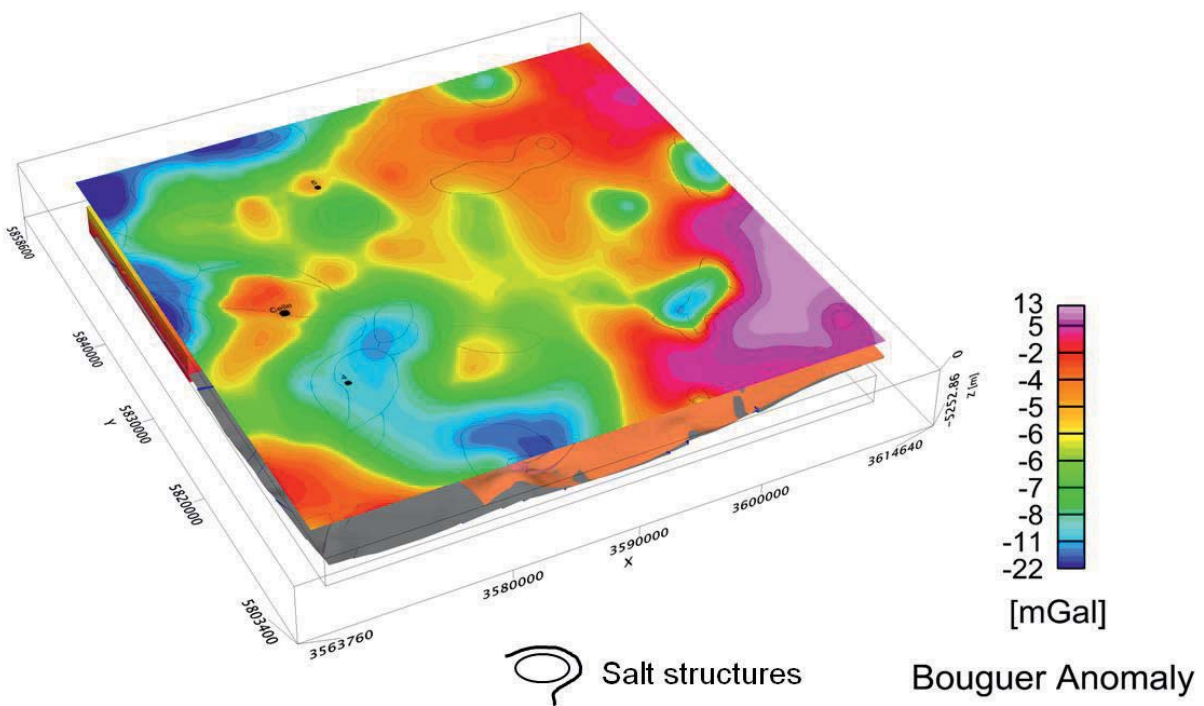

Fig. 3.7: *Bouguer anomalies as cover of the same cube (see fig. 3.6), no. 4 marks the Wathlingen-Hänigsen salt dome.*

The trace of MT profile L-L´ from Wiedensahl (WDS) to Büchten (BTN), crossing the Rehburg Graben, the salt dome Husum and the Steinhuder Meer lineament, is also shown in a 3D view together with the base of geological horizons (fig. 3.8). A plot of the Zechstein thickness in this area is given in fig. 3.9.
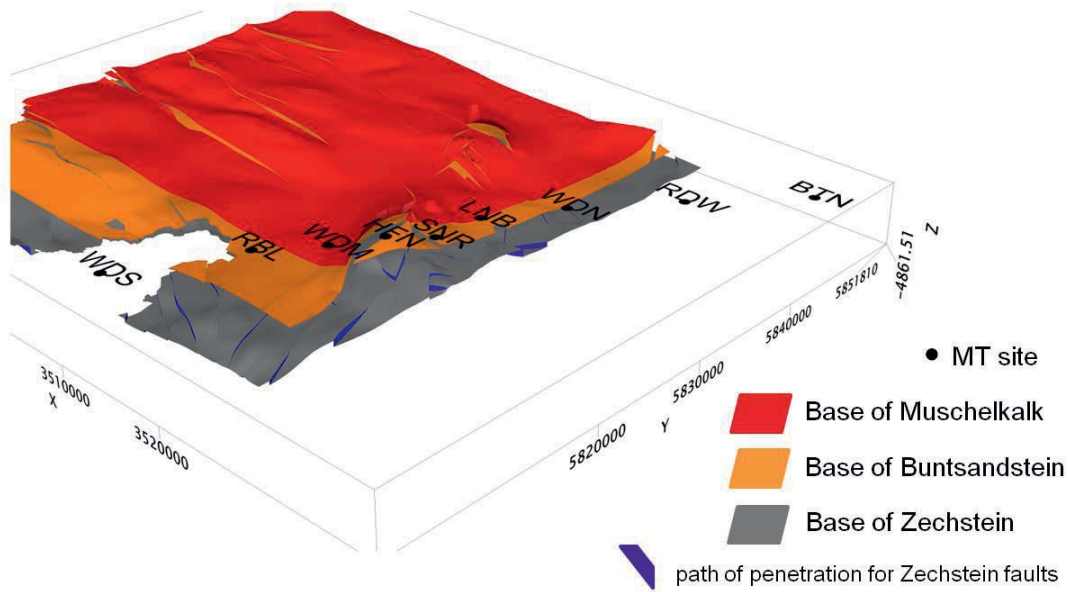
Fig. 3.8: *Base of geological horizons at MT profile L-L´, crossing the Rehburg Graben and the salt dome Husum, see also the following fig. 3.9.*
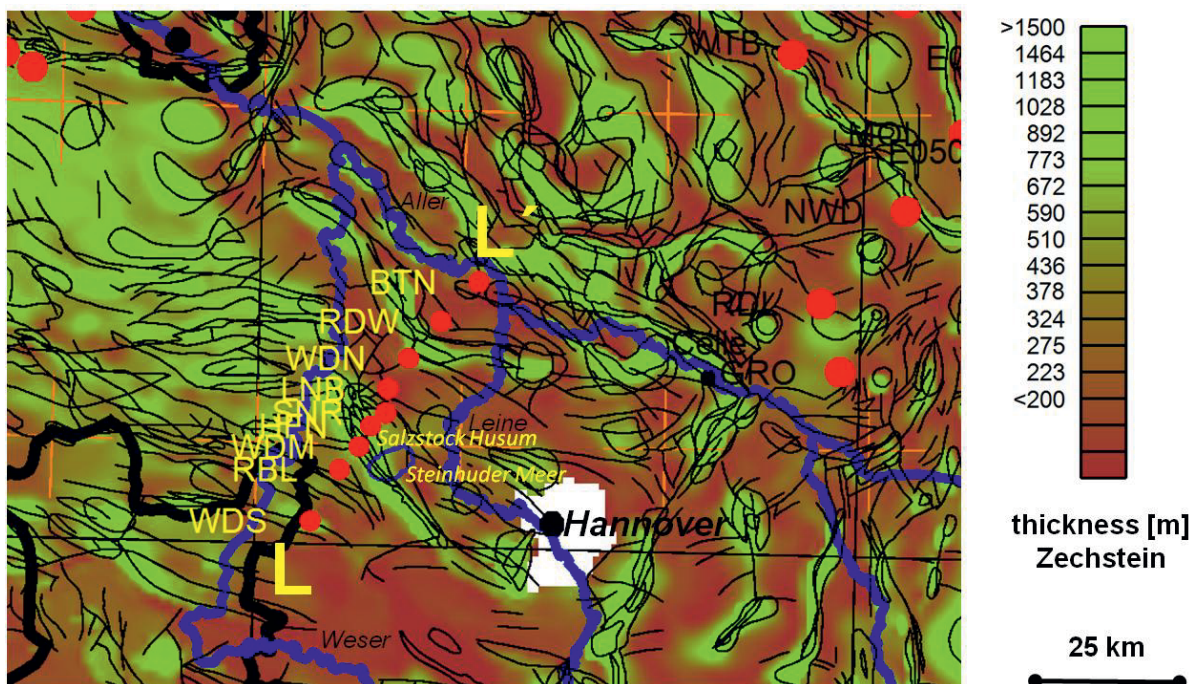
Fig. 3.9: *Zechstein thickness with MT sites of profile L-L´ (red dots with characters), crossing the salt dome Husum close to the Steinhuder Meer.*

Fig. 3.10 shows the depth of selected geological layers and the temperature at 5000 m depth in the course of profile B. It runs from the area south of Magdeburg to the island of Rügen (see also fig. 3.1).
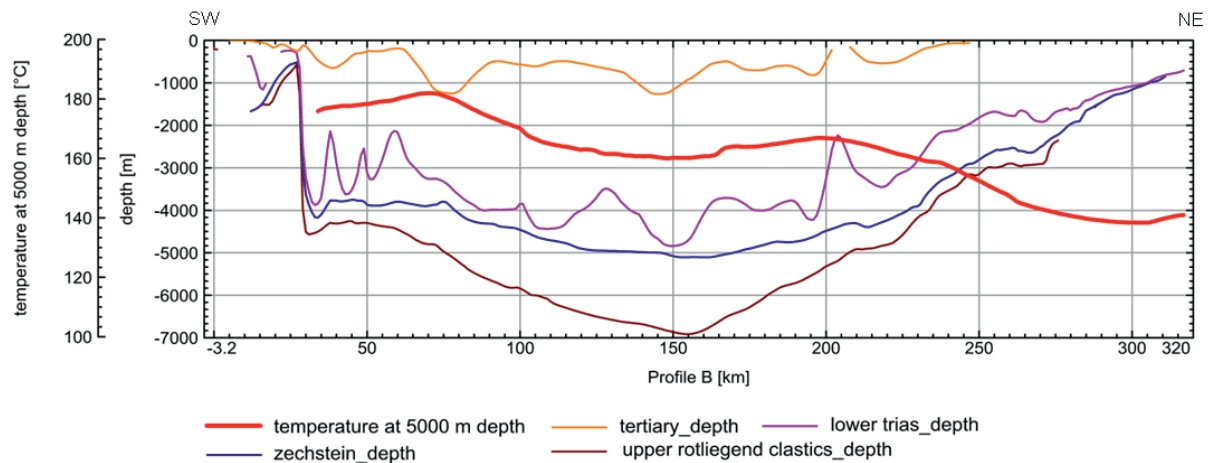

Fig. 3.10: *Depth of selected geological layers (Tertiary, Lower Triassic, Zechstein, Upper Rotliegend Clastics) along profile B and temperature at 5000 m depth.*

4. Modelling

4.1 1D modelling based on Transient Electromagnetic data

The influence of the transmitter coil size and resulting transmitter moment at TEM measurements is demonstrated for the detection of low resistive layers at different depths. Besides that the resistivity of the overburden is important for the detection of deeper targets. The detection of a layer of interest depends mainly on the strength of the transmitter moment. It is the product of the coil area and the current flowing in the cable. If noise is high as it is common in industrial or otherwise anthropogenic influenced areas, a transmitter moment as high as possible under the instrumental conditions is desired. A few cases are presented here.

1D forward modelling for different survey designs

A low resistive layer with a resistivity of 5 Ωm and a thickness of 10 m is placed in 350 m and in 600 m depth. The resistivity of the overburden is assumed to be higher than 20 Ωm. Fig. 4.1 shows synthetic transients for a square transmitter coil with a side length of 200 m for the given models. Fig. 4.2 shows the same models but for a transmitter coil side length of 1000 m. All synthetic transients were generated using a 1D forward modelling for the inloop configuration (after WEIDELT 1984), i.e. for a given model decay curves resp. transients were

computed. The last time window of the transient is marked at 475 ms; this corresponds to the time series of the terraTEM instrument applied in the field. A typical time for the big Tx loop case, which separates the early time and the late time stage is about 135 µs (fig. 4.2).
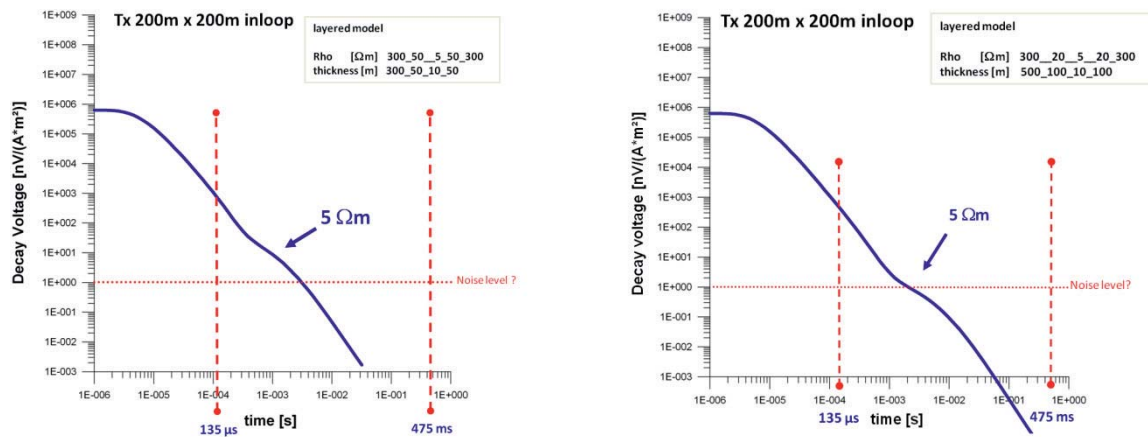

Fig. 4.1: *Synthetic transients for a transmitter coil with 200 m side length for the given models. A low resistive layer (5 Ωm) with a thickness of 10 m is placed in 350 m and 600 m depth.*
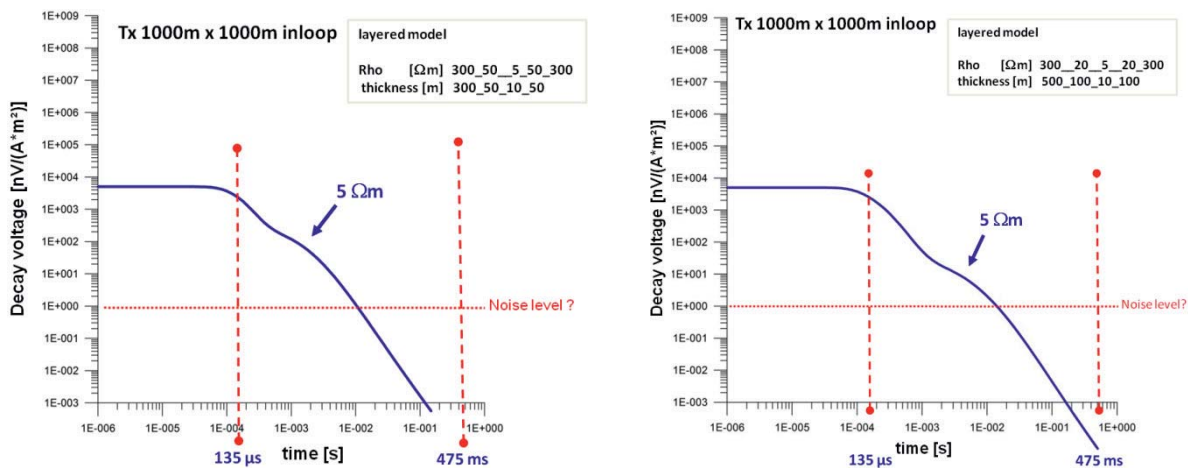

Fig. 4.2: *Synthetic transients for a transmitter coil with 1000 m side length for the given models. A low resistive layer (5 Ωm) with a thickness of 10 m is placed in 350 m and 600 m depth.*

In the presented example the transmitter coil area was enhanced from 40 000 m² to 1 000 000 m². The low resistive layer at 600 m depth can only be detected with an enhanced

loop size. Unfortunately, transients measured with bigger transmitter loops cannot be used for investigating smaller depth as it can easily be seen comparing figs. 4.1 and 4.2. The transient for the bigger loop size is influenced by the so called ´early time´ behaviour for decay times earlier than 135 µs in this example, which does not allow the transient to decay. The bigger the loop size the more this restriction is important. Therefore it is necessary to perform a field survey with several loop sizes if an investigation over the whole range beginning from the surface to greater depth is aspired. For the interpretation the results from both survey designs can then be combined (SCHAUMANN et al. 2012a, SCHAUMANN & GRINAT 2014c).

Whilst only synthetic cases are considered here, examples for transients measured with different transmitter moments in the field are given in chap. 2.1.

1D inversion for synthetic data from 3-layer cases

For several cases in reference to the results from the surveys in the *Leinetal Graben* a 1D modelling was performed to investigate the detectability of a target layer at depth. An elaborated description is given by SCHAUMANN et al. (2012a, 2012b).

Synthetic transients were computed for the introduced models. Afterwards an inversion process was performed for three predefined RMS fitting degrees, which should represent the interpretation at different data quality (fig. 4.3 to 4.6). Figs. 4.3 to 4.5 show the influence of the thickness of the second layer and the influence of the uppermost layer´s resistivity on its detectability. Thicknesses of several decameters can be determined when a low fitting error is assumed. The lower the fitting error, the better is the determination of the second layer. If the contrast of the first and the second layer is not sufficient, the second layer cannot be identified. At a thickness of 10 m, the layer cannot be found anymore; the result is a 2-layer case (fig. 4.4). Only a higher contrast to the first layer's resistivity and a small fitting error allow the approximately determination of the second layer (fig. 4.4). When reducing the resistivities of the uppermost layer it is evident that it is more complicated to identify the 3-layer model (fig. 4.5).

The starting model has an important influence on the detection of the layer's succession. If the inversion process starts with the adequate number of layers and resistivities in the proper range, it is more likely to find the correct layering. To guess the best starting model, information can be added from other surveys such as DC resistivity and seismic surveys or from drillings. In fig. 4.6 the thin second layer cannot be detected until the starting model is adequate. A two layer case already explains the data and does not motivate to add more layers to the model unless additional information is known.
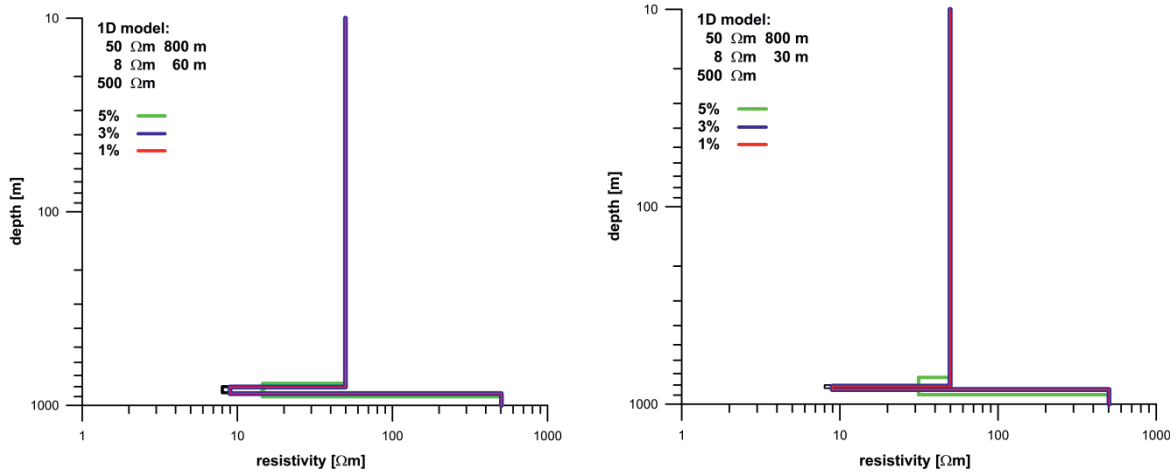
Fig. 4.3: *Inversion result for three different fitting errors, second layer with 60 m and 30 m thickness.*
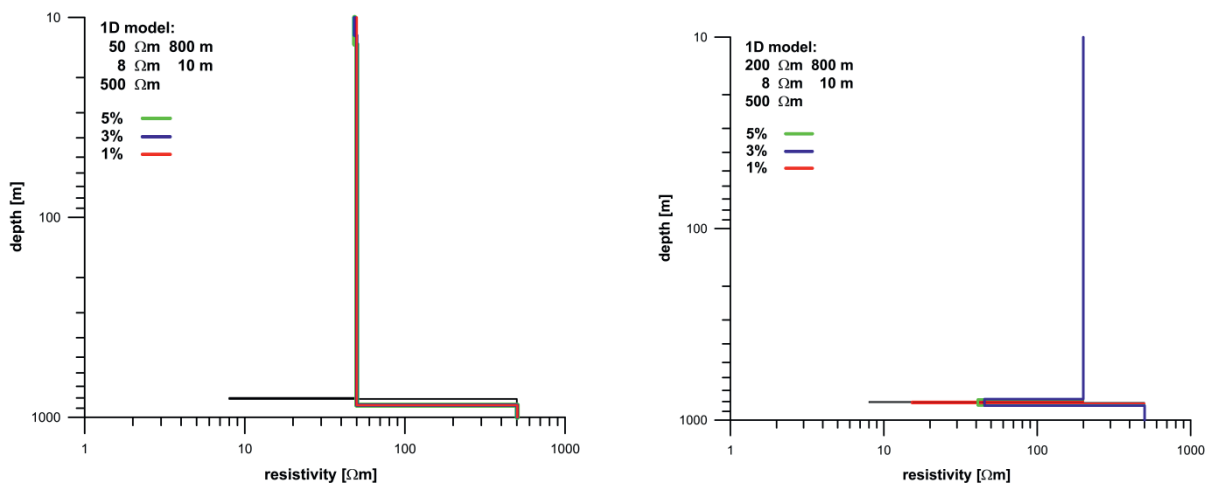

Fig. 4.4: *Inversion result for three different fitting errors, second layer with a thickness of 10 m and different resistivities of the uppermost layer (50 Ωm resp. 200 Ωm).*
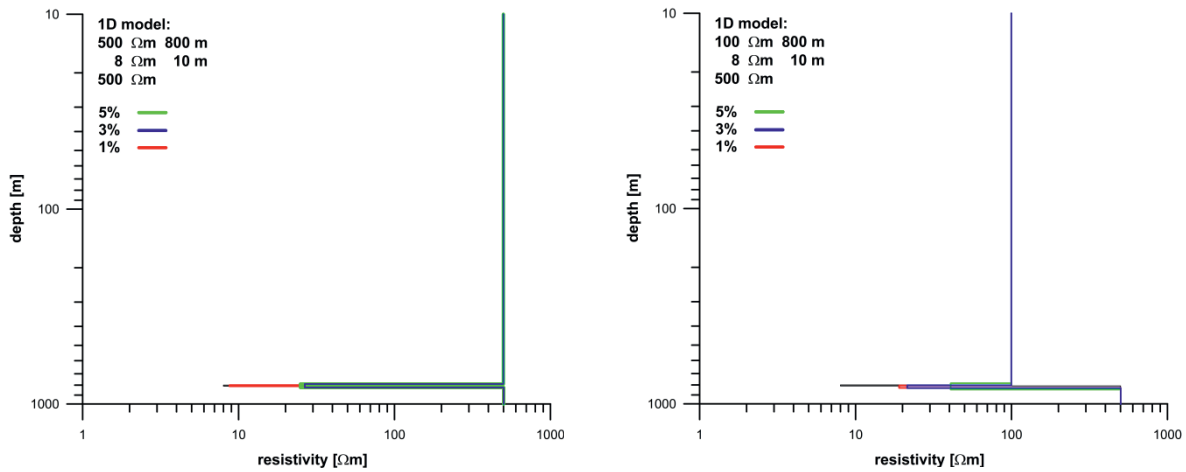
Fig. 4.5: *Inversion result for three different fitting errors, different resistivities of the first layer (500 Ωm resp. 100 Ωm).*
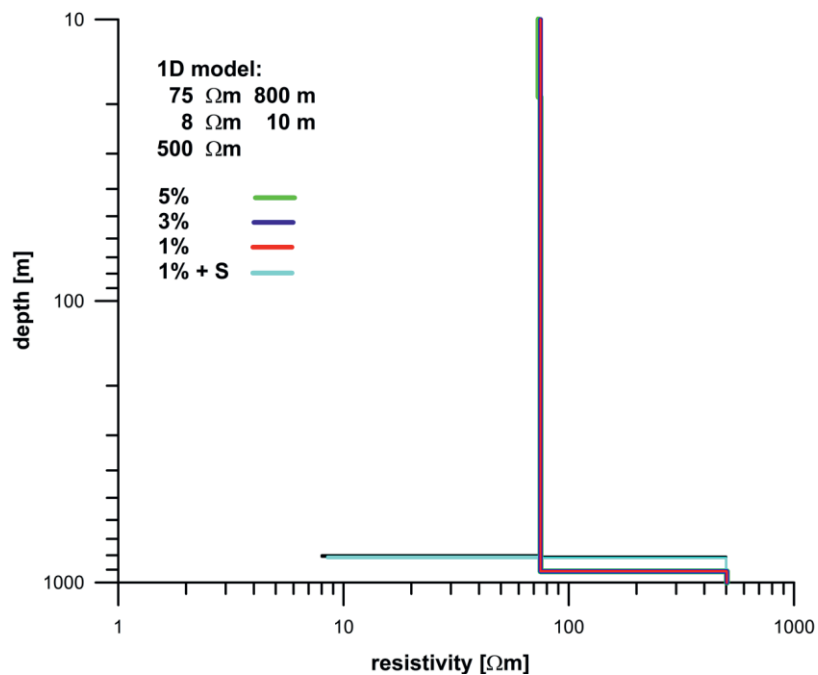

Fig. 4.6: *Inversion result for three different fitting errors and with additional information (cyan step model).*

1D inversion for synthetic data from 5-layer cases

5-layer cases are more complex and allow more variances. Because of the large amount of possible combinations of resistivities and thicknesses in the 1D model, only models similar to the results from the *Leinetal Graben* surveys were investigated. Expected depths for the target layer are based on geological background information. Thus a supposed fault with low resistivity is to be detected at about 800 m depth and allocated with different thicknesses,

covered by another low resistive layer at 550 m depth. The prospected layer thickness can be expected to be in the range from 10 m to 60 m (Tanner, pers. comm.). The RMS fitting error is set to 1 %.

Fig. 4.7 shows that a thin low resistive layer at a depth of 800 m cannot be detected. Only the low resistive layer above with a thickness of 60 m is determined. In fig. 4.8 the thickness of the upper low resistive layer is reduced to 10 m. In this case the deeper target layer can be detected. But already a 3-layer case interprets the data sufficiently and an adequate starting model is needed for identifying the inherent 5-layer case. If the deeper low resistive layer is more bulky, e.g. 60 m, it can be detected (fig. 4.9).
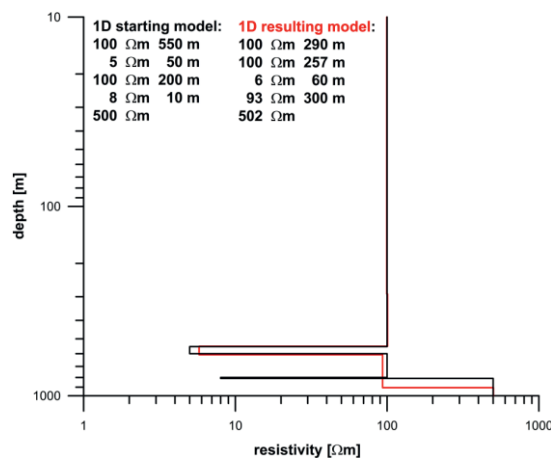

Fig. 4.7: *Result after inversion: the low resistive layer with a thickness of 10 m is not detected.*
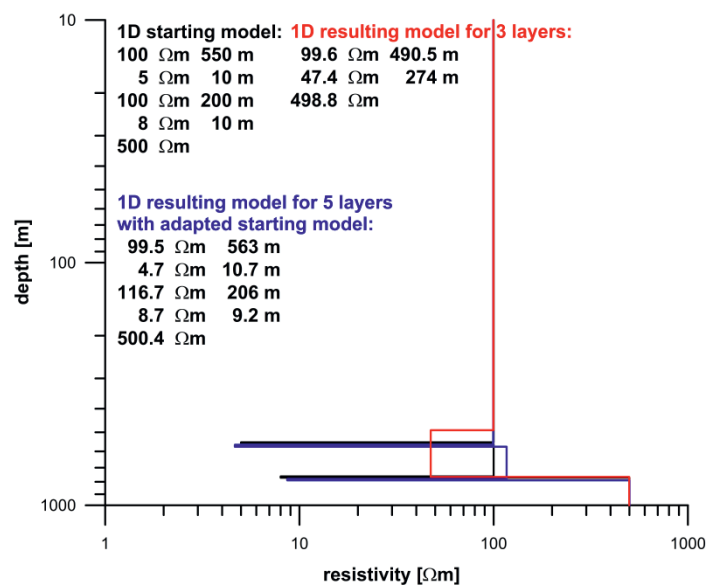

Fig. 4.8: *Results after inversion: the second layer's thickness was reduced from 50 m to 10 m, cf. fig. 4.7.*
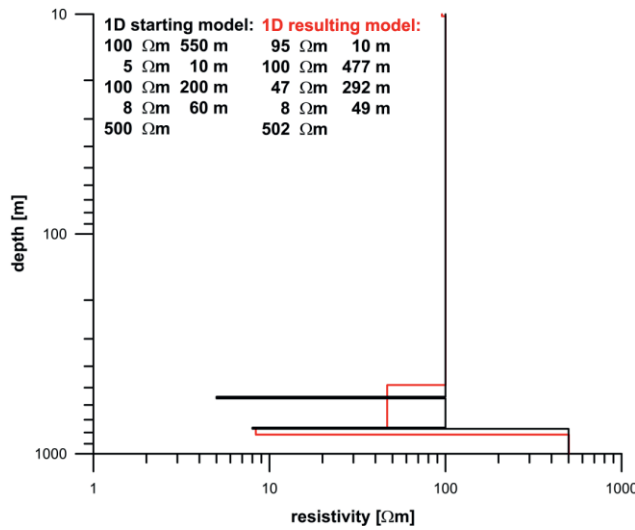
83

Fig. 4.9: *Result after inversion with a deeper low resistive layer, which is more bulky.*

For another study the resistivity of the target layer is further reduced to 2 Ωm and the thickness of an overlain higher resistive layer is increased. The interpretation is possible with a 3-layer case. Hints for the right number of layers can be determined using the Occam inversion. Here the problem of equivalent models, which explain the data under the same fitting error, is important (fig. 4.10). Another example showing the problem of equivalent models is demonstrated by help of apparent resistivity curves in figs. 4.11 and 4.12. The latter shows also a suite of these equivalent models for the 5-layer case.
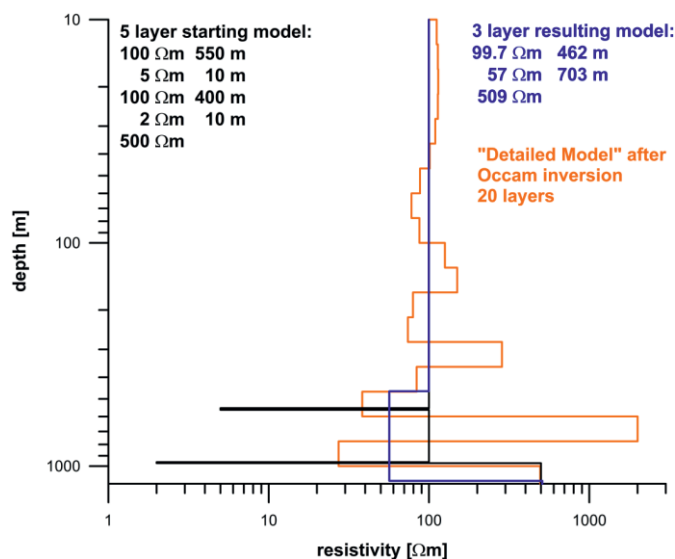

Fig. 4.10: *Results after block inversion (blue step model) and Occam inversion (orange step model). The interpretation is already possible with a 3-layer case, the inherent 5-layer case is indicated by the layers sequence obtained by the Occam inversion.*
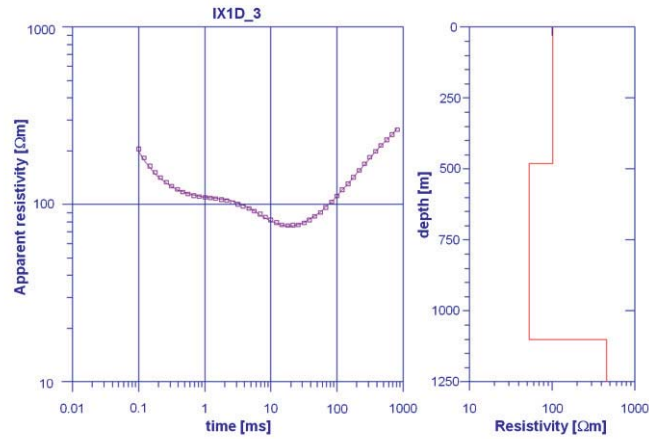
Fig. 4.11: *Synthetic apparent resistivity curve for the 5-layer case interpreted with a 3-layer model, see also fig. 4.12.*
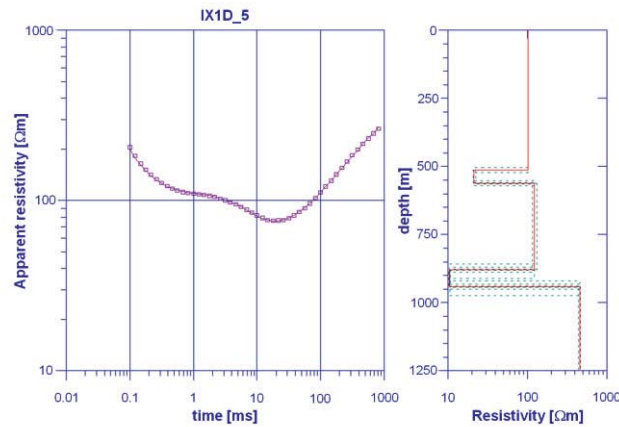

Fig. 4.12: *Synthetic apparent resistivity curve for the 5-layer case interpreted with a 5-layer model. Dashed green lines show equivalent models.*

When the thickness of the target layer is increased to 60 m, it is possible to detect this layer with an adequate starting model, which can be derived from the Occam inversion (fig. 4.13).
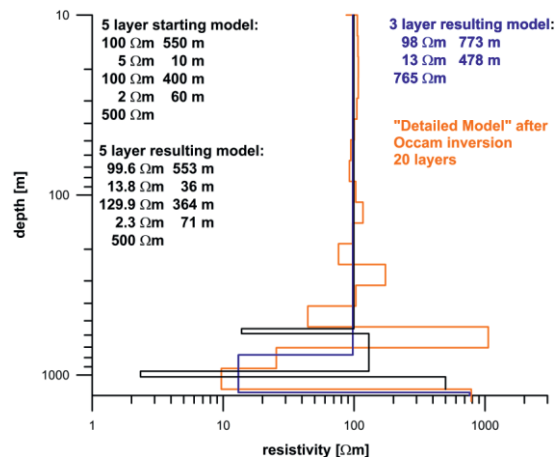

Fig. 4.13: *Result after inversion for 3 layers, 5 layers and Occam inversion.*

These selected modelling results already show important rules for detecting a target layer, here a supposed low resistive geological horizon at a certain depth. Data quality is important and substantial when small variations in the measured sounding curves have to be detected. If the target layer is too small, it cannot be detected without additional information. Also the problem of equivalent models is important. Additional knowledge about the survey area is also needed. Models with fewer layers can often already interpret the data sufficiently. Therefore it is of great importance to sample further information about the survey area and to include also results from other methods into the interpretation, especially when the target is small and covered by thick low resistive overburdens.

4.2 1D and 2D modelling based on Magnetotelluric data

1D forward modelling

The following modelling attends the question of detecting electrical conductive objects such as saline fluids in depth by investigating the influences of overlying layers and the electrical conductivity of the target itself. These 1D models are regarded only as a first approach. It is assumed that a fluid can be found in the target layer making it low resistive. In the example presented here layers' depths and succession are taken approximately from the Parchim drilling 1/68 (FRANKE et al. 1988), the resistivities are mainly from the 2D modelling of MT data from profile B by HOFFMANN et al. (1998, 2008) and JÖDICKE et al. (2001), who supposed the Mesozoic layers to be low resistive. Approximated values were also taken from the drilling Velpke-Asse (KELCH & PAULUS 1980). Several resistivities of the target that are caused by different porosities and fluid properties were supposed. The thickness of the target layer is assumed to be 300 m at a depth from 5900 m to 6200 m. The target should represent a section of the Lower Permian Rotliegend sediments. Several hundreds of Ωm were assumed for the Lower Permian Rotliegend volcanics. The Upper Permian Zechstein was attributed with a high resistivity of 5000 Ωm.

The modelling considers three variations of the thicknesses and resistivities of the overlain Mesozoic layers:

1. Case 1: Thickness of 1800 m, resistivity of 1 Ωm (salt dome present)
2. Case 2: Thickness of 4500 m, resistivity of 1 Ωm (in respect to a 2D MT result for the central part of the eastern basin, without salt dome)
3. Case 3: Thickness of 1800 m, resistivity of 1000 Ωm (salt dome present).

Four different resistivities of the target layer (50 Ωm as the assumed resistivity for the Rotliegend sediments; 8 Ωm, 2 Ωm and 0.1 Ωm under influence of salinity and porosity) were investigated because most fluids sampled at greater depth in the North German Basin are highly mineralized. Synthetic MT sounding curves for the frequency range from 1000 Hz (period: 0.001 s) to 1/1000 Hz (period: 1000 s) were created for the described cases by a 1D forward modelling. These presumed data were 1D inverted assuming no data error.

The results for the target layer´s resistivities of 2 Ωm and 0.1 Ωm combined with the three different overburdens in respect to the three cases are shown in fig. 4.14. As expected from the experience with electromagnetic methods, case 2 is the most demanding case. Here the thick Mesozoic sediments with a low resistivity make it very difficult to detect the target layer, especially when it is characterized by higher resistivity values. The lower the resistivity of the target the better is the determination of its depth and resistivity, even if covering sediments are low resistive.

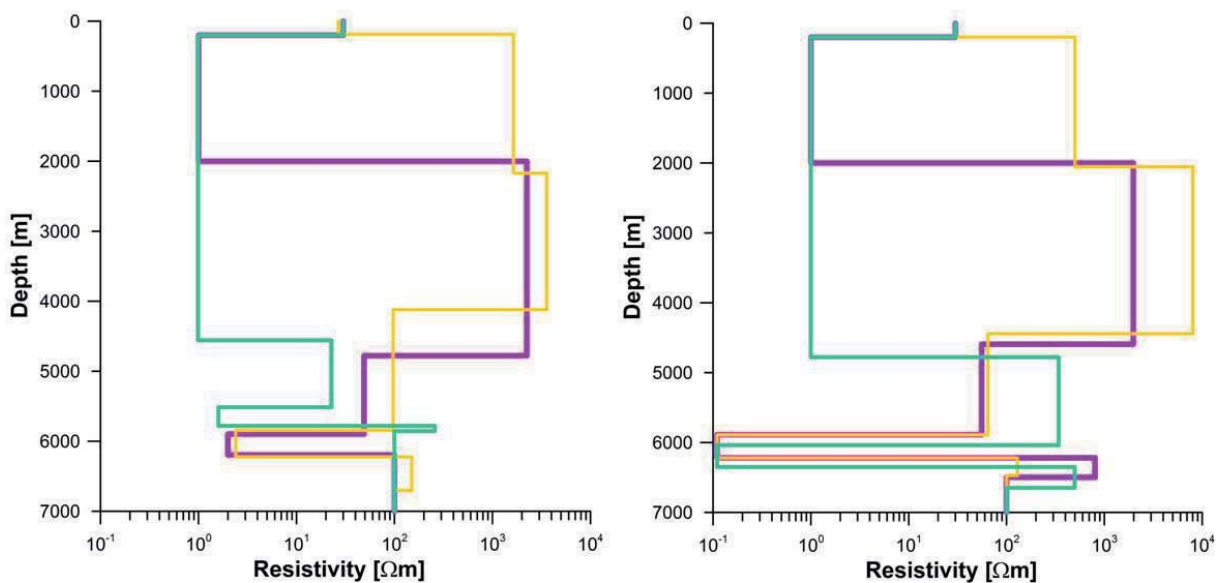**Fig. 4.14:** *Target layer at the depth of about 6000 m with a resistivity of 2 Ωm (left) and 0.1 Ωm (right) in dependence of the overburden for the three cases (case 1: violet, case 2: green and case 3: yellow).*

A more elaborated demonstration is given by SCHAUMANN & GRINAT (2014a, 2014b).

2D forward modelling

The 2D models for the forward calculations were adapted to approximated structures in the North German Basin and a simplified scheme of the basin and the resistivities was designed (fig. 4.15). It is based on the former 2D interpretation of profile B by JÖDICKE et al. (2001) and HOFFMANN et al. (2008). Then resistivities of the basin´s Mesozoic sediments as well as of a fault as target object and its lateral extend were varied. The supposed fault was placed at a depth from 4200 m to 6200 m. A slope is simulated by displacing the two mesh cells, which represent the fault, from each other by row and column. Apparent resistivity curves were calculated for several sites at certain distances from the fault, which correspond to the position of survey sites from profile B. Some selected results are shown in figs. 4.16 to 4.19. Phases are not shown here.

In fig. 4.20 the apparent resistivity curves for the closest site (3.2 km resp. 3.7 km distance to the fault, depending on its extent) are shown. It can easily be seen that the resistivity of the supposed fault predominantly influences the shape of the sounding curves.
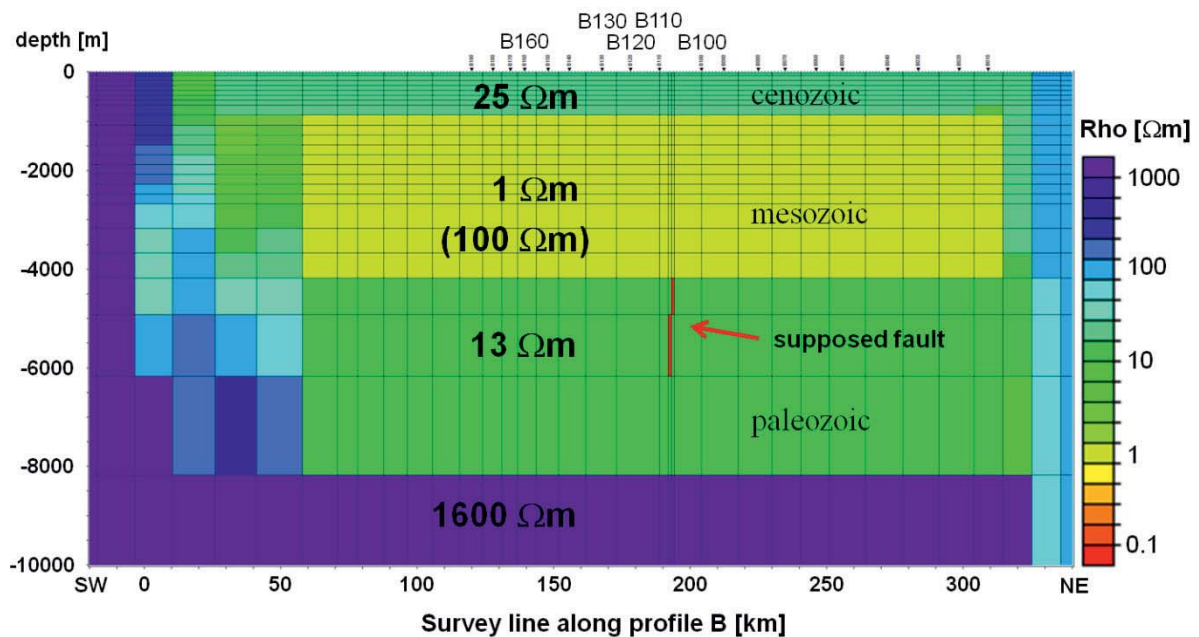

Fig. 4.15: *Rough 2D model of the North German Basin based on MT data from profile B. The Mesozoic sediments were allocated with a resistivity value of 1 Ωm resp. 100 Ωm, the fault with a width of 750 m resp. 1.2 km was allocated with resistivities of 0.1 Ωm and 0.01 Ωm.*

88

Fig. 4.16: *Apparent resistivity curves for several sites of a 2D model with 1 Ωm for the Mesozoic sediments of the North German Basin down to 4.2 km depth and a 1.2 km wide fault with a resistivity of 0.1 Ωm.*

Fig. 4.17: *Apparent resistivity curves for several sites of a 2D model with 1 Ωm for the Mesozoic sediments of the North German Basin down to 4.2 km depth and a 750 m wide fault with a resistivity of 0.1 Ωm.*

Fig. 4.18: *Apparent resistivity curves for several sites of a 2D model with 1 Ωm for the Mesozoic sediments of the North German Basin down to 4.2 km depth and a 750 m wide fault with a resistivity of 0.01 Ωm.*
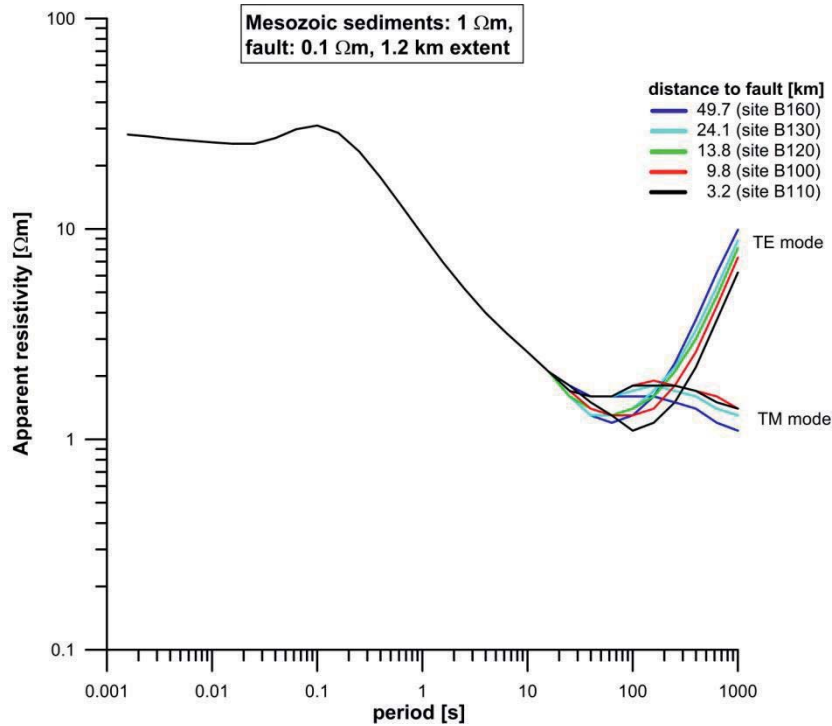

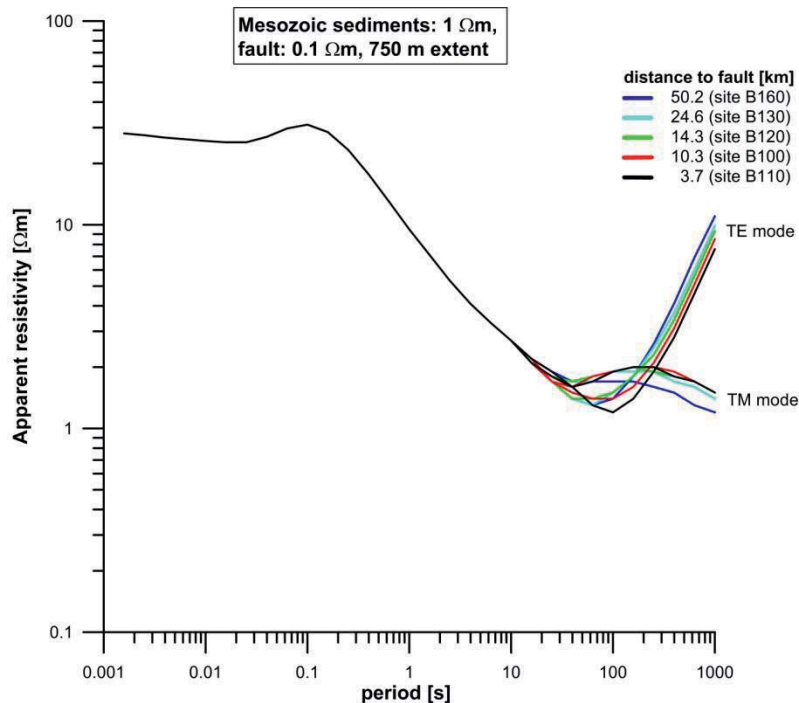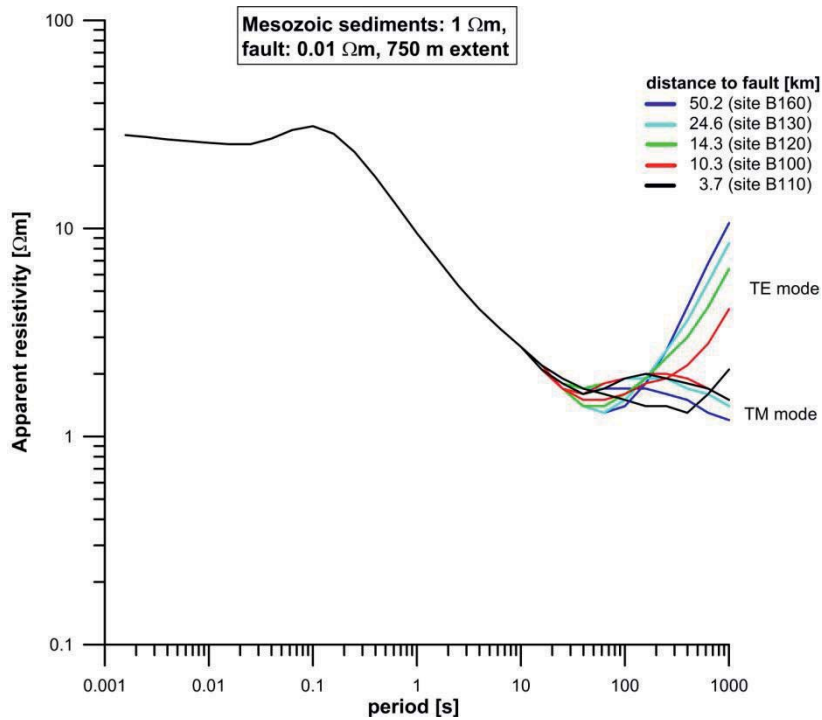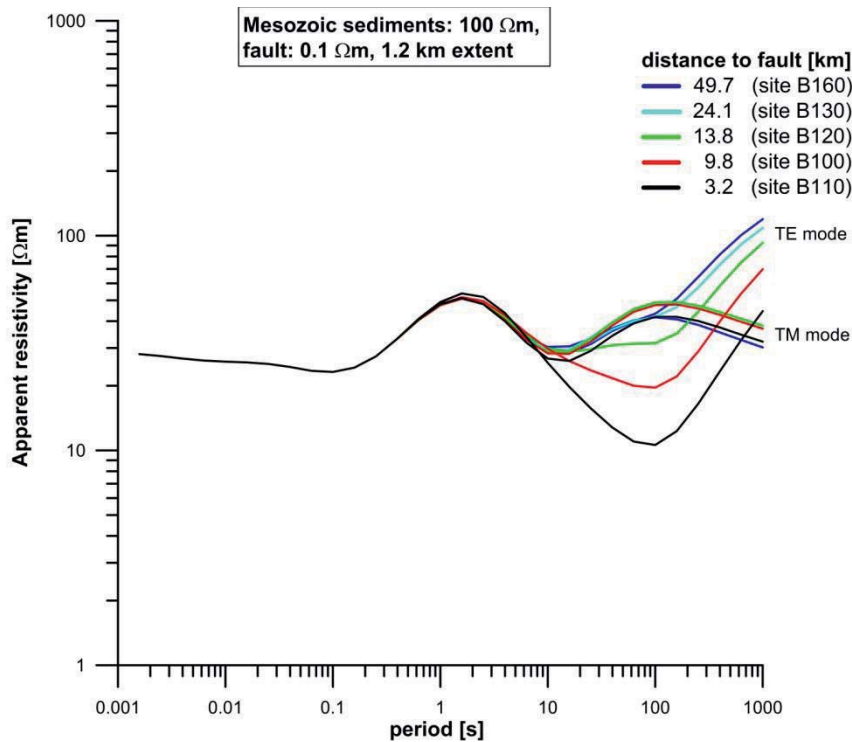**Fig. 4.19:** *Apparent resistivity curves for several sites of a 2D model with 100 Ωm for the Mesozoic sediments of the North German Basin down to 4.2 km depth and a 1.2 km wide fault with a resistivity of 0.1 Ωm.*
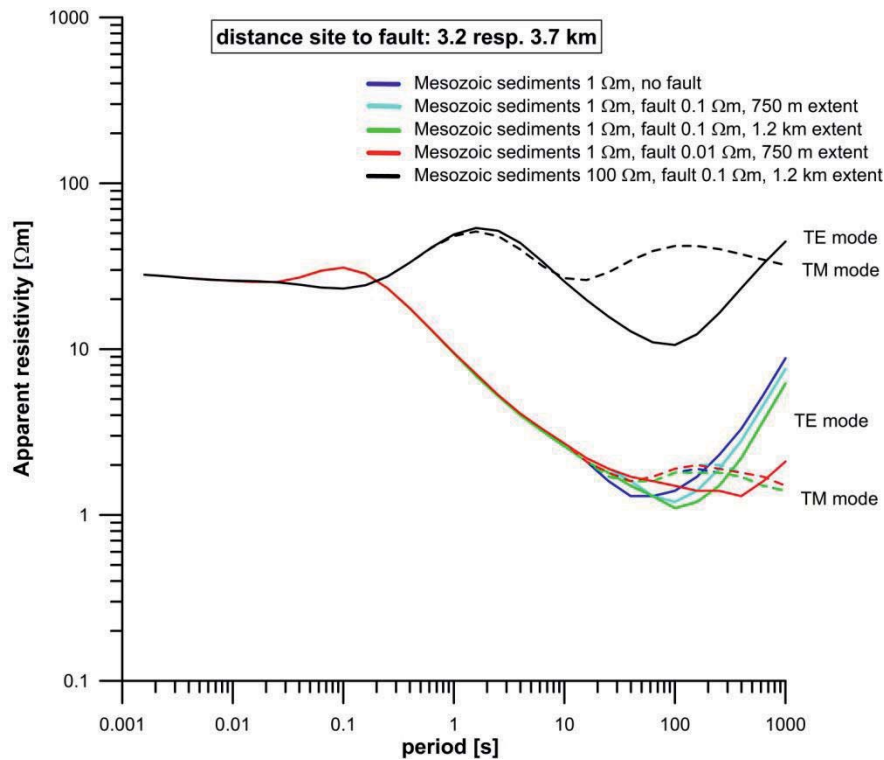
Fig. 4.20: *Apparent resistivity curves for the closest site with 1 Ωm and 100 Ωm for the Mesozoic sediments of the North German Basin, fault widths of 750 m and 1.2 km and resistivities of 0.1 Ωm and 0.01 Ωm.*

5. Conclusions

In the *Leinetal Graben* practical investigations for delineating the trace of a fault with depth were carried out using DC resistivity and TEM, which are present methods at LIAG. An increase of the exploration depth was undertaken by bigger survey setups and stronger transmitters for both. The results of the DC resistivity revealed clearly the trace of the fault in the *Leinetal Graben*. Additionally, structural information from reflection seismic measurements can contribute to improve the image, but the resistivity contrast between the segments, which are divided by the fault, is big enough to delineate the fault in a 2D interpretation. TEM results help to figure out layers of low resistivity which cannot be resolved well by DC resistivity measurements and give hints for zones of higher mineralization in the subsurface. The seismic reflectors help to overcome the problem of equivalent models. Together these three methods enable the exploration of shallow fault systems to depth of approximately 1000 m. To figure out the trace of a fault already from the surface is essential for planning the trajectory of a well.

Another aim was to investigate the detectability of fault zones till depth of interest for geothermal exploitation (about 3 to 7 km in the North German Basin). Hence numerical investigations were carried out with special emphasis on the magnetotelluric method. They were used to analyze the detectability of faults under various conditions. The resistivity contrast is of great importance, also the distance of survey sites from the target. A survey with narrowed sites close to the target as well as recording times long enough for interpreting deeper structures is suitable for identifying also faults at depth. The local geological features are important to enable electromagnetic measurements and therefore a survey area has to be chosen well.

An exploration from the surface to depths of several kilometers cannot be performed by a single method alone with sufficient accuracy. A combination of several geophysical methods is essential for delineating features in the subsurface. Not before a general overview of the results from several methods is provided, an intensified survey with a single method should be carried out. This is the initial step before exploring in the field starts and contributes to evaluate a procedure for investigating potential zones of interest. On this basis a field survey can be designed which considers the advantages and limitations as well as the compliments of the methods used.

6. Acknowledgements

7. Publications resulting from the project

Günther, T., Schaumann, G., Musmann, P. & Grinat, M. (2011). Imaging of a fault zone by a large-scale dc resistivity experiment and seismic structural information. – Ext. Abstr., Near Surface 2011, Sept. 12-14, 2011; Leicester, UK.

Schaumann, G. & Grinat, M. (2014). Electrical conductivities as an indication for potential geothermal target layers within the North German Basin in respect to local geological conditions. – Submitted to Z. dt. Ges. Geowiss.; Stuttgart.

Schaumann, G. & Grinat, M. (2014). Delineation of potential target layers for geothermal application within the North German Basin by investigations on electrical conductivities. – Submitted to Geothermics.

Schaumann, G., Günther, T., Grinat, M. & Meyer, R. (2012). Tiefe Erkundung des Leinetal-Störungssystems mit geoelektrischen und elektromagnetischen Messungen. – Protokoll über das 24. Schmucker-Weidelt-Kolloquium für Elektromagnetische Tiefenforschung in Neustadt an der Weinstraße vom September 2011 (Herausgegeben von Ralph-Uwe Börner und Katrin Schwalenberg), ISSN 0946-7467.

8. References

Agemar, T., Schellschmidt, R. & Schulz, R. (2012). Subsurface temperature distribution in Germany. – Geothermics 44, 65-77.

Baldschuhn, R., Binot, F., Fleig, S. & Kockel, F. (2001). Geotektonischer Atlas von Nordwest-Deutschland und dem deutschen Nordsee-Sektor. – Geologisches Jahrbuch A 153; Hannover.

Bozau, E., Sattler, C.-D. & van Berk, W. (2015). Hydrogeochemical classification of deep formation waters. Applied Geochemistry 52, 23-30.

Bujakowski, W., Barbacki, A., Czerwinska, B., Pajak, L., Pussak, M., Stefaniuk, M. & Trzesniowski, Z. (2010). Integrated seismic and magnetotelluric exploration of the Skierniewice, Poland, geothermal test site. – Geothermics 39, 78–93; doi:10.1016/j.geothermics.2010.01.003.

Dohr, G. (1989). Ergebnisse geophysikalischer Arbeiten zur Untersuchung des tieferen Untergrundes in Norddeutschland. – Nds. Akad. Geowiss. Veröfftl. 2, 4-47; Hannover.

Doornenbal, J.C. & Stevenson, A.G. (2010). Petroleum Geological Atlas of the Southern Permian Basin Area (SPBA). – EAGE Publications b.v.; Houten.

Franke, D., Kahlert, E., Meissner, B. & Weyer, D. (1988). Das Präperm der übertiefen Forschungsbohrung Parchim 1/68. – Wissenschaftlich-Technischer Informationsdienst des Zentralen Geologischen Instituts 29, 1-47; Berlin.

Franke, D. (2014). Regionale Geologie von Ostdeutschland – Ein Wörterbuch. – Website www.regionalgeologie-ost.de.

Gabriel, G., Vogel, D., Scheibe, R., Wonik, T., Pucher, R., Krawczyk, C. & Lindner, H., (2010). Anomalien des erdmagnetischen Totalfeldes der Bundesrepublik Deutschland, 1:1.000.000. – GeoCenter Scientific Cartography; Stuttgart.

Giolito, C., Ruggieri, G., Manzella, A. & Gianelli, G. (2008). Resistivity reduction in the vapour-dominated field of Travale (Italy). – 70th EAGE Conference & Exhibition, 9-12 June 2008; Rome, Italy.

Günther, T. & Rücker, C. (2006). A general approach for introducing information into inversion and examples from dc resistivity inversion. Ext. Abstract, EAGE Near Surface Geophysics, 04.-06.09.2006, Helsinki.

Günther, T. & Rücker, C. (2009). BERT – user tutorial.

Günther, T., Schaumann, G., Musmann, P. & Grinat, M. (2011). Imaging of a fault zone by a large-scale dc resistivity experiment and seismic structural information. – Ext. Abstr., Near Surface 2011, Sept. 12-14, 2011; Leicester, UK.

Hoffmann, N., Hengesbach, L., Friedrichs, B. & Brink, H.-J. (2008). The contribution of magnetotellurics to an improved understanding of the geological evolution of the North German Basin – review and new results. – Z. dt. Ges. Geowiss. 159/4, 591-606; Stuttgart.

Hoffmann, N., Jödicke, H., Fluche, B., Jording, A. & Müller, W. (1998). Modellvorstellungen zur Verbreitung potentieller präwestfalischer Erdgas-Muttergesteine in Norddeutschland – Ergebnisse neuer magnetotellurischer Messungen. – Z. angew. Geol. 44/3, 140-158.

Jödicke, H., Hoffmann, N. & Müller, W. (2001). Magnetotellurik und Erdmagnetische Tiefensondierung entlang des DEKORP-Profils 9601, Teilabschnitt Bad Wilsnack – Hasselfelde. – Abschlussbericht DFG-Forschungsvorhaben II C 5, Jo 188/2-1; Münster, Berlin, Hannover.

Kelch, H.-J. & Paulus, B. (1980). Die Tiefbohrung Velpke-Asse Devon 1. – Geologisches Jahrbuch A57; Hannover.

Knödel, K., Losecke, W. & Müller, W. (1978). Detailauswertung magnetotellurischer Vermessungen tiefer Stockwerke in Norddeutschland für Rückschlüsse auf mögliche erdölgeologisch interessante Strukturen. – BMFT-Projekt ET 3214, Bundesanstalt für Geowissenschaften und Rohstoffe; Archiv-Nr. 79922; Hannover.

Kockel, F. (1998). Geotektonischer Atlas von Nordwest-Deutschland 1:300.000. Teil 18: Die paläographische und strukturelle Entwicklung Nordwestdeutschlands, Band 1. – Bundesanstalt für Geowissenschaften und Rohstoffe; Hannover.

Leiss, B., Tanner, D., Vollbrecht, A. & Arp, G. (2011). Neue Untersuchungen zur Geologie der Leinetalgrabenstruktur, Bausteine zur Erkundung des geothermischen Potentials der Region Göttingen. – Universitätsverlag Göttingen.

Losecke, W. (1972). Bericht über die Ortung von Salzstöcken mit der Magnetotellurik. – Bundesanstalt für Geowissenschaften und Rohstoffe; Archiv-Nr. 7548; Hannover.

Muñoz, G., Bauer, K., Moeck, I., Schulze, A. & Ritter, O. (2010). Exploring the Groß Schönebeck (Germany) geothermal site using a statistical joint interpretation of magnetotelluric and seismic tomography models. – Geothermics 39, 35-45; doi:10.1016/j.geothermics.2009.12.004.

Reinhold, K., Krull, P. & Kockel, F. (2008). Salzstrukturen Norddeutschlands, Geologische Karte 1:500.000. – Bundesanstalt für Geowissenschaften und Rohstoffe; Berlin, Hannover.

Reyer, D. (2008). Geologische Kartierung im Bereich der östlichen Grabenrandstörung des Leinetalgrabens südlich von Sudheim. – Unveröffentlichte Diplomkartierung, Georg-August-Universität Göttingen.

Ronczka, M., Günther, T. & Oppermann, F. (2014). Monitoring inland salt-water intrusion with long-electrode ERT. – In: Wiederhold, H., Michaelsen, J., Hinsby, K., Nommensen, B. (Eds.): SWIM 2014, 23rd Salt Water Intrusion Meeting, 195-198; ISBN 978-3-00-046061-6.

Schaumann, G., Grinat, M. & Günther, T. (2011). Geosystem Project G2: Detection of Fault Zones Using Electric and Electromagnetic Methods, Report to Work Package 1: Electrical properties of rocks as basis for benchmark models (Milestone 1). – LIAG; Hannover.

Schaumann, G., Günther, T., Grinat, M. & Meyer, R. (2012a). Tiefe Erkundung des Leinetal-Störungssystems mit geoelektrischen und elektromagnetischen Messungen. – Börner, R.-U. & Schwalenberg, K. (Hrsg.): Protokoll über das 24. Schmucker-Weidelt-Kolloquium für Elektromagnetische Tiefenforschung in Neustadt an der Weinstraße vom September 2011, ISSN 0946-7467.

Schaumann, G., Günther, T. & Grinat, M. (2012b). Geosystem-Projekt G2: Elektrische und elektromagnetische Erkundung geologischer Störungszonen, – Bericht zum Arbeitspaket 2: Erste Simulationsmodelle (Meilenstein 2). – LIAG; Hannover.

Schaumann, G. & Grinat, M. (2014a). Electrical conductivities as an indication for potential geothermal target layers within the North German Basin in respect to local geological conditions. – Submitted to Z. dt. Ges. Geowiss., Stuttgart.

Schaumann, G. & Grinat, M. (2014b). Delineation of potential target layers for geothermal application within the North German Basin by investigations on electrical conductivities. – Submitted to Geothermics.

Schaumann, G. & Grinat, M. (2014c). Geosystem-Projekt G2: Elektrische und elektromagnetische Erkundung geologischer Störungszonen. – Bericht zum Arbeitspaket 3: Messkonzept, Messungen (Meilenstein 3). – LIAG; Hannover.

Simpson, F. & Bahr, K. (2005). Practical magnetotellurics. – Cambridge University Press; Cambridge, UK.

Skiba, P., Gabriel, G., Scheibe, R. & Seidemann, O. (2010). Schwerekarte der Bundesrepublik Deutschland 1:1.000.000, Bouguer – Anomalien. – GeoCenter Scientific Cartography; Stuttgart.

Spichak, V. & Manzella, A. (2009). Electromagnetic sounding of geothermal zones. – Journal of Applied Geophysics 68, 459-478.

Tanner, D., Albero, F., Leiss, B. & The GGG (GeothermieGruppeGöttingen) (2010). Modelling the Geothermal Potential of the Eastern Border of the Leinetal Graben, Lower Saxony. – Z. geol. Wiss. 38 (1) 2010, 61-68; Berlin.

Walter, R. (2007). Geologie von Mitteleuropa. – 7th Edition, Schweizerbart'sche Verlagsbuchhandlung; Stuttgart, Germany.

Weidelt, P. (1984). Bericht über Inversion transient-elektromagnetischer Messungen über geschichtetem Untergrund. – Bundesanstalt für Geowissenschaften und Rohstoffe; Archiv-Nr. 96720; Hannover.

Ziegler, P.A. (1990). Geological Atlas of Western and Central Europe. – Shell International Petroleum Company; Den Haag, Netherlands.

Web links:
http://www.geotis.de/, http://nibis.lbeg.de/cardomap3

9. Appendix to Project G2

9.1 Abbreviations

LIAG: Leibniz Institute for Applied Geophysics

LBEG: Landesamt für Bergbau, Energie und Geologie

DEKORP: Deutsches Kontinentales Reflexionsseismisches Programm

MT: Magnetotelluric

TEM: Transient Electromagnetic

SPBA: Southern Permian Basin Atlas

GeotIS: Geothermal Information System for Germany (LIAG, Hannover)

9.2 Parameter values from deep boreholes in the North German Basin

Formation	Approximated resistivity from borehole logs [Ωm]
Tertiary	0.8 - 1.2
Cretaceous	0.5 - 8.0
Jurassic	0.8 - 23
Triassic	0.7 - 150
Zechstein	10 - 10 000
Rotliegend	2.7 - 4 000
Carboniferous	3.7 - 100
Devonian	70 - 130

Table 1: Approximated resistivity by KNÖDEL et al. (1978) from boreholes in Northern Germany.

Electrical resistivity [Ωm]	Log depth [m]	Formation	Depth of drilling [m]	Total vertical depth below topography [m]
			3030.00	3028.00
2000.00		Basisanhydrit		
	3045.00		3045.00	3043.00
100.00		Unterer Muschelkalk !		
	3055.00			
10.00				
	3065.00			
100.00				
	3160.00		3162.00	3160.00
		Oberer Buntsandstein !		
10.00				
	3215.00		3215.00	3212.00
		Rotbraune Gruppe !		
4.00				
	3240			
8				
	3260		3270	3266
2000		Roet-Salinar Zwischenmittel		
	3275			
10				
	3295			
50				
	3310			
2000				
	3325			
20				
	3330			
2000				
	3355			
20				
	3360			
2000				
	3440		3440	3424
10		Mittlerer Buntsandstein !		
	3530		3527	3504
20		Detfurth Folge !		
	3785			
			3840	3774
		Ton		

Table 2: Electrical resistivities from a borehole log at the drill site Groß Buchholz GT-1.
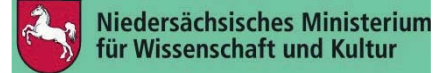
Projekt G3:

Heterogenitäten mechanischer Gesteinsparameter und ihr Einfluss auf die Bohreffizienz und die Bruchausbreitung in der Umgebung von Bohrungen

Abschlussbericht

Projektleitung: Prof. Dr. Sonja L. Philipp, Geowissenschaftliches Zentrum der Georg-August-Universität Göttingen, Abteilung Strukturgeologie und Geodynamik

Projektbearbeiterin: Dr. Dorothea Reyer

Projektlaufzeit: 01.05.2009 – 31.12.2014

G3: Heterogeneous rock properties: outcrop studies, laboratory analyses and models

Sonja L. Philipp* & Dorothea Reyer[1]

Geoscience Centre, University of Göttingen, Department of Structural Geology and
Geodynamics, Goldschmidtstr. 3, D-37077 Göttingen, Germany

*Corresponding Author: Sonja.Philipp@geo.uni-goettingen.de

[1] now at: State Authority of Mining, Energy and Geology – Zentrum für TiefenGeothermie,
Celle, Germany

Abstract

Heter ogeneities of rock mechanical properties (in particular due to layering and fault zone structure) affect drilling efficiency and success of geothermal projects in sedimentary basins such as the North German Basin (NGB). Here we show how high resolution data from outcrop analogues can be used to improve predictions of both fault structure and rock mechanical conditions at greater depths. We analysed 77 outcrop-scale (mostly normal) fault zones in detail and found evident differences between carbonate and clastic rocks. Mainly in carbonate rocks clear fault damage zones with increased fracture densities occur that may enhance permeability in fluid reservoirs. Physical (P-wave velocities, porosity, and bulk and grain density) and mechanical parameters (Uniaxial compressive strength (UCS), Young's modulus, destruction work and indirect tensile strength; each perpendicular and parallel to layering) were determined for 35 outcrop samples taken from quarries and 14 equivalent core samples (same stratigraphic age and comparable sedimentary facies based on thin section petrographic analyses). Regression analyses of UCS with all physical and mechanical parameters allow prediction of in situ rock properties from outcrop analogue samples. Triaxial test sequences on a subgroup of the samples show that it is possible to apply Mohr-Coulomb failure criteria for clastic and volcanic rocks, but less so for carbonates, when porosity and texture of outcrop equivalents and core samples are comparable.

Presented analytical models accentuate the effects of heterogeneities such as fractures on fluid flow and in situ rock properties. Numerical modelling with BEASY (Boundary Element Method) focussed on stress fields and fracture propagation in layered rocks, highlighting the effects of contrasts in Young's modulus between layers. Using the gebo benchmark-model 'Horstberg' and COMSOL Multiphysics (Finite Element Method) the current local stress field for a typical locality in the North German Basin was modelled, indicating considerable effects of layering and fault zone structure. Hence, both outcrop studies combined with laboratory analyses and models improve geothermal exploration and drilling.

1. Introduction

Advancing highly efficient and effective production of geothermal energy with low geological and technical risks relies on profound information about the subsurface (Stober and Bucher, 2014). One major task in geothermal exploration therefore is to find reservoirs with either a high natural hydraulic permeability, or those which can be stimulated hydraulically to generate new flow paths. In addition it is essential to define the best target and well path to exploit a reservoir economically (Huenges, 2010).

Another important task is to prevent wellbore instabilities in order to lower drilling time and total costs (e.g., Zeynali, 2012, Li et al., 2012). To achieve this, substantiated estimations of the mechanical properties of reservoir rocks and overlying strata are needed prior to drilling (Zhang, 2005). Thereby optimal mud weight and wellbore design can be determined to avoid borehole breakouts, washouts, or tensile fracturing which may lead to wellbore collapse (Abdideh and Fathabadi, 2013). This means as much as possible is needed to know about the geologic situation, the lithology, and physical and mechanical rock properties to be expected.

All rocks are to some extent heterogeneous (Fig. 1). There is a primary heterogeneity and anisotropy due to differences in mineral content, grain sizes etc. Secondary heterogeneity is due to changes in the rock related to compaction, diagenesis or tectonic forces subsequent to the layer formation. Mechanical heterogeneity occurs mainly because all host rocks contain pores – or fractures and faults, and contacts – or show variations in texture. The heterogeneities occur at different scales, from crystals, grains and pores to cooling joints, contacts between layers, and large fractures and faults.
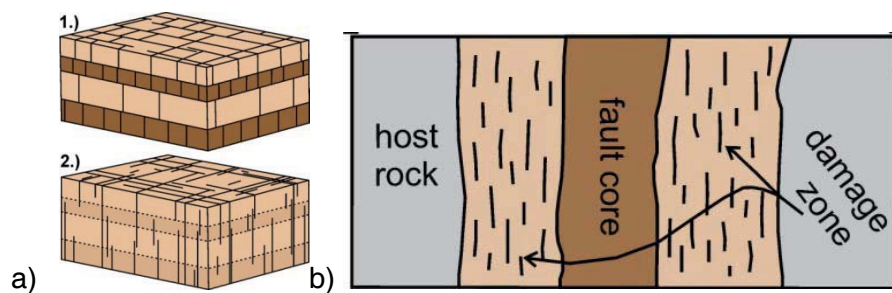
Figure 1: Common heterogeneities in geothermal reservoirs. a) Layering. 1.) Contrasting rock mechanical properties of the layers strongly affect fracture propagation, so that most fractures are confined to individual layers (are 'stratabound'). By contrast, in 2.) layering does not affect fracture growth ('non-stratabound' fractures; Odling et al., 1999). b) Typical fault zone structure with a fault core around the main slip plane surrounded by a strongly fractured damage zone (based on Caine et al., 1996).

The North German Basin (NGB) is, as is typical for sedimentary basins, composed of various rock types with different physical and mechanical properties. These heterogeneous rock properties may result in mechanical layering, i.e., mechanical rock properties change between layers (Philipp et al., 2013), which is a universal feature of many heterogeneous rock masses (Fig. 1a). Layered reservoirs are well known in petroleum engineering (Aguilera, 2000) and also occur in geothermal reservoirs. Mechanical layering commonly affects fracture propagation, that is, many fractures are restricted to single layers (Philipp et al., 2013), referred to as 'stratabound' fractures (Odling et al., 1999). For 'non-stratabound' fractures, in contrast, layering does not affect fracture growth (Odling et al., 1999).

The second important heterogeneity in a (geothermal) reservoir is due to fault zones (Philipp, 2007; Fig. 1b). The simplest description of a fault zone structure considers two major mechanical units, namely a fault core and a damage zone (cf. Caine et al., 1996; Faulkner et al., 2010). The fault core is a narrow zone, formed through repeated slip on the principal fault plane (Faulkner et al., 2010). Commonly it is brecciated, has a very low stiffness, rather deforms in a plastic manner (Gudmundsson, 2011), whereas cemented fault rocks may have high stiffnesses (Agosta et al., 2007). Permeability is low when the fault is not active (slipping, Gudmundsson, 2000). The damage zone surrounds the fault core and is a wider zone mechanically affected by slip. It is characterised by a high fracture density (defined as number of fractures per metre along a line; Hudson and Harrison, 1997) with still discernible former host rock fabric (Caine et al., 1996; Faulkner et al., 2010) and commonly higher permeability (Gudmundsson, 2011). This two-hydromechanical-units structure may be difficult to apply to all rock lithologies because different deformation mechanisms may be of importance in different rocks. For example, in porous rocks deformation bands may form (e.g., Aydin, 1978; Antonellini et al., 1994; Johansen et al., 2005), whereas in carbonate rocks there may be stylolites due to dissolution processes (Tondi et al., 2006). In this study, however, the simple damage-zone/fault-core model for fault description is convenient since the focus is on the fluid transport potential of fault zones, mainly through open fractures. Fault zone structure, i.e. widths of fault core and damage zone, and fault-related permeability strongly depend on fault zone type (normal, reverse or strike-slip faults), lithology, displacement and orientation within the recent stress field (Aydin, 1978; Caine et al., 1996; Faulkner et al., 2010, 2011; Gudmundsson, 2011).

For successful exploration of geothermal reservoirs (i.e., in particular to obtain high flow rates), as well as to minimise the risk in terms of borehole stability while drilling in the NGB, it is important to predict the geology of the subsurface in terms of fractures affected by layering and the fracture distribution within fault zones in detail. Information on the subsurface, however, is limited to geophysical exploration methods and existing wellbores. In prospective depths of more than 3000 m the resolution of established geophysical methods, such as

seismic and geoelectric operations, is too low to analyse mechanical layering, fault zone structure and associated fracture systems in detail. Wellbores, in contrast, provide high resolution information, but for one small location only and we do not get information on lateral heterogeneities.

Project G3 aimed at providing data and information on fault structure and mechanical rock properties based on outcrop analogue studies in typical rocks of the NGB. Particular emphasis was given on the analysis of differences in layering and fault zone structure in various lithostratigraphic units (sedimentary and volcanic rocks) from Permian to Cretaceous. Main connections were with projects G7, G8 and B4, whereas data were made available also for G1, G2, G5, and G9.

Field studies were supplemented by laboratory analyses of petrophysical (mainly rock mechanical) properties and petrographic analyses of thin sections. Parameters measured included uniaxial compressive strength, failure and friction criteria, tensile strength, Young's modulus, destruction work, P-wave velocity, density, and porosity, both on outcrop samples and drill cores. Rock strengths were obtained with both uniaxial and triaxial testing. With this data, a database of rock properties valid for the NGB was compiled (gebo, unpublished; parts in Hahne et al., in prep.). Developed regression functions build the basis for the estimation of specific parameters of interest (Section 4). Further, data are useful as input for analytical numerical modelling of geo- and hydromechanical behaviour of rocks.

In this report we first give a brief overview on the field studies and samples taken (Section 2), then summarise three published papers (Sections 3-5) and finally present previously unpublished analytical and numerical models (Sections 6-7).

Figure 2: Location and lithology of all studied outcrops and wellbores at the southwestern margins of the North German Basin (cf. Table 1); (from Reyer and Philipp, 2014).

*Table 1: List of all outcrops and samples. Detailed field studies (including fault zone structure) were performed in those formatted in **bold**, outcrops in which samples were taken are formatted in italics. Samples used for triaxial testing are marked with an asterisk*. Sst.: Sandstone, TVD: Total vertical depth.*

Outcrop	Sample ID	Lithology	System	Local Name	Location (R, H)
Höver	KrCa	Chalk marl		Kreidemergel	3561295, 5801360
Goslar Sudmerberg	GoSa	Sandstone		Sudmerberg-F.	3601395, 5754100
Eberholzen		Limestone		Turon-Kalk	3557065, 5768455
Irmenseul		Limestone		Turon	3563510, 5761055
Hoppenstedt	HoT	Marl		Rotpläner	3614250, 5764290
Brüggen	BrCe	Limestone		Cenoman-Kalk	3555425, 5767345
Ostlutter	OLH	Sandstone		Hils-Sst.	3588880, 5762390
Gildehaus	GiUK	Sandstone	**Cretaceous**	Gildehaus-Sst.	3370880, 5798215
Bad Bentheim	FrUK	Sandstone		Bentheimer-Sst.	3375950, 5798135
Obernkirchen	OK*	Sandstone		Wealden-Sst.	3512950, 5791580
Drillhole 1: Eulenflucht 1 (EF1)	EF1WS*	Sandstone		Wealden-Sst.	3527450, 5783260 TVD: 35 m
Drillhole 2: Groß Buchholz (Gt1)	Gt1WS1*	Sandstone		Wealden-Sst.	3556309, 5808333 TVD: 1221 m
Gt1	Gt1WS2	Sandstone		Wealden-Sst.	TVD: 1211 m
Thüste	ThüJ	Limestone		Serpulit	3545150, 5765705
Varrigsen	GVa*	Limestone		Gigas Schichten	3558025, 5755240
EF1	EF1GS*	Limestone		Gigas Schichten	TVD: 210 m
Dannhausen	OKDa*	Limestone		Oberer Kimmeridge	3576820, 5748510
EF1	EF1OK*	Limestone		Oberer Kimmeridge	TVD: 243 m
Marienhagen		Limestone		Korallenoolith	3547340, 5766700
Salzhemmendorf	ShJk*	Limestone	**Jurassic**	Korallenoolith	3541455, 5769995
EF1	EF1UKK*	Limestone		Korallenoolith	TVD: 282 m
EF1	EF1KO*	Limestone		Korallenoolith	TVD: 286 m
Dielmissen	HSDi, HSDi2	Limestones		Heersumer Schichten	3542985, 5761300
EF1	EF1HS	Limestone		Heersumer Schichten	TVD: 325 m
Wolfsburg-Neuhaus	AlWo	Sandstone		Aalen-Sst.	3626705, 5809755
Velpke	koVe*	Sandstone		Rhät-Sst.	3630335, 5810610
Querenhorst	koQ*	Sandstone		Rhät-Sst.	3635425, 5802500
Weende	kuWe	Siltstone		Lettenkohlen-Sst.	3565795, 5715650
Diemarden		Limestone		Ceratitenkalk (mo2)	3566305, 5704260
Evessen		Limestone		Trochitenkalk (mo1)	3617845, 5786375
Hessenbühl		Limestone		Trochitenkalk (mo1)	3505140, 5705550
Emmenhausen	EM*	Limestone	**Triassic**	mo1+Wellenkalk	3557935, 5716250
Hardgesen	H	Limestone		Schaumkalk (mu)	3558030, 5725220
Elvese	EL 1*, 2*, 3	Limestone		Gelbkalk+Wellenkalk	3567815, 5726650
Ossenfeld		Limestone		Wellenkalk (mu)	3555225, 5711735
Papenberg		Limestone		Wellenkalk (mu)	3566650, 5723480
Petersberg		Limestone		Wellenkalk (mu)	3508880, 5698940
Sudheim		Limestone		Wellenkalk (mu)	3569067, 5725650
Borlinghausen		Limestone		Unterer Muschelkalk	3503530, 5716717
Watenstedt	soWa	Shale-Gypsum		Röt 1	3626895, 5774505

Table 1 continued.

Outcrop	Sample ID	Lithology	System	Local Name	Location (R, H)
Steinberg		Sandstone		Solling-Folge	3500675, 5708355
Wrexen		Sandstone		Hardegsen-Folge	3499958, 5708750
Hardegsen	smHN*	Sandstone		Hardegsen-Folge	3556880, 5725000
Erbbegräbnis		Sandstone		Detfurth-Folge	3500200, 5709950
Gt1	Gt1DU1*	Sandstone		Detfurth-Folge	TVD: 3535.8 m
Gt1	Gt1DU2*	Sandstone		Detfurth-Folge	TVD 3534.3 m
Gt1	Gt1DU3*	Sandstone		Detfurth-Folge	TVD: 3534.7 m
Gt1	Gt1DW	Siltstone	**Triassic**	Detfurth-Folge	TVD: 3537.2 m
Bad Salzdetfurth	smD*	Sandstone		Detfurth-Folge	3569655, 5771150
Hammerbachtal		Sandstone		Detfurth-Folge	3500200, 5709955
Gelliehausen	smVG*, smVG2	Sandstones		Volpriehausen-Folge	3574130, 5705475
Gt1	Gt1VS1*	Sandstone		Volpriehausen-Folge	TVD: 3655.5 m
Gt1	Gt1VS2*	Sandstone		Volpriehausen-Folge	TVD: 3657.8 m
Bilshausen	BiSu*	Sandstone		Bernburg-Folge	3583215, 5722735
Heeseberg	suHe*	Rogenstein		Rogenstein	3627660, 5773810
Seesen		Sandstone		Rotliegend-Sst.	3582945, 5753280
Bebertal (Flechtingen)	BeRo*, BeRoK	Sandstones	**Permian**	Rotliegend-Sst.	3657440, 5792315
Dönstedt (Flechtingen)	DöRo*	Andesite		Rotliegend-Vulkanit	3658375, 5794210
Flechtingen	FL2, FL6*	Rhyolites		Rotliegend-Vulkanit	3650940, 5799975
Marsberg		Siltstone		Oberkarbon	3489506, 5703830
Via Regia		Siltstone	**Carboniferous**	Arnsberg-Schichten (Oberkarbon)	3489690, 5703745

2. Field and laboratory data, samples

The sedimentary succession in the NGB comprises mainly carbonate and clastic rocks with some intercalated evaporites and volcanic rocks from Late Carboniferous to Quaternary (Betz et al., 1987; Walter, 2007). At the southern and western basin margins, sedimentary and volcanic rocks that occur at geothermally relevant depths in the centre and north crop out (Baldschuhn, 1996).

Composition and texture of all samples were determined by analysis of one thin section per sample with a transmitted light microscope (Zeiss Axioplan 2; Fig. 3). The mineralogical composition of all sandstone samples was analysed quantitatively counting 500 grains per thin section with a half-automated point counter (Petrolog lite). Here we present a QFL-plot (McBride, 1963) considering only quartz, feldspar and lithoclasts (Fig. 4) of the sandstone samples. For detailed petrography see Reyer and Philipp (subm.) and Reyer (2013).
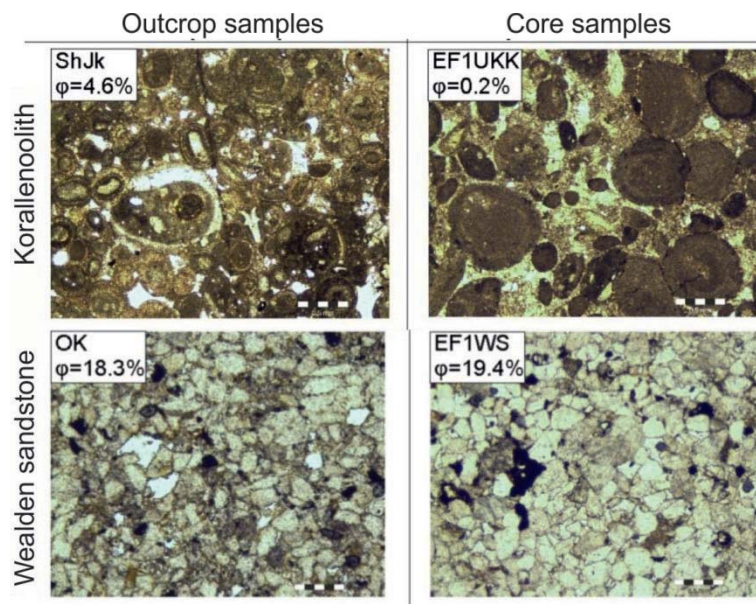
Figure *3: Two examples of outcrop samples (left) and equivalent core samples (right).* The *upper thin section micrographs show the Jurassic Korallenoolith sample ShJk from the outcrop in Salzhemmendorf and its equivalent EF1UKK from the Eulenflucht 1 well (Table 1), the lower ones the Wealden sandstone sample OK from Obernkirchen and its equivalent EF1WS from the Eulenflucht 1 well (Table 1). Scale bars of 0.5 mm and porosities φ are displayed (modified from Reyer and Philipp, subm.).*

In total, 46 outcrops (Fig. 2; Table 1), exposing stratigraphic units of Upper Carboniferous to Upper Cretaceous, including quarries, road cuts, etc., were investigated. In 22 of these outcrops we performed detailed structural geological field studies focusing on fracture system parameters and fault zone structure (Section 3). In freshly exposed, unfaulted and undamaged parts of 29 outcrops representative oriented samples were taken (Fig. 2; Table 1) to measure physical and mechanical properties of the rocks (Section 4). Additionally, failure and friction criteria are determined for 18 of these samples (Table 1; Section 5). In addition 14 samples from two wellbores were taken (Fig. 2, Table 1; Sections 4 and 5). We aimed at finding equivalent core and outcrop samples, meaning that the outcrop sample is of the same stratigraphic age and of comparable sedimentary facies, composition, texture and porosity as the associated core sample (Fig. 3). Using water-cooled diamond hollow drills, saws and grinder cylindrical specimens were prepared both parallel and perpendicular to the sedimentary layering (for details see Reyer and Philipp, 2014; subm., and Reyer, 2013).
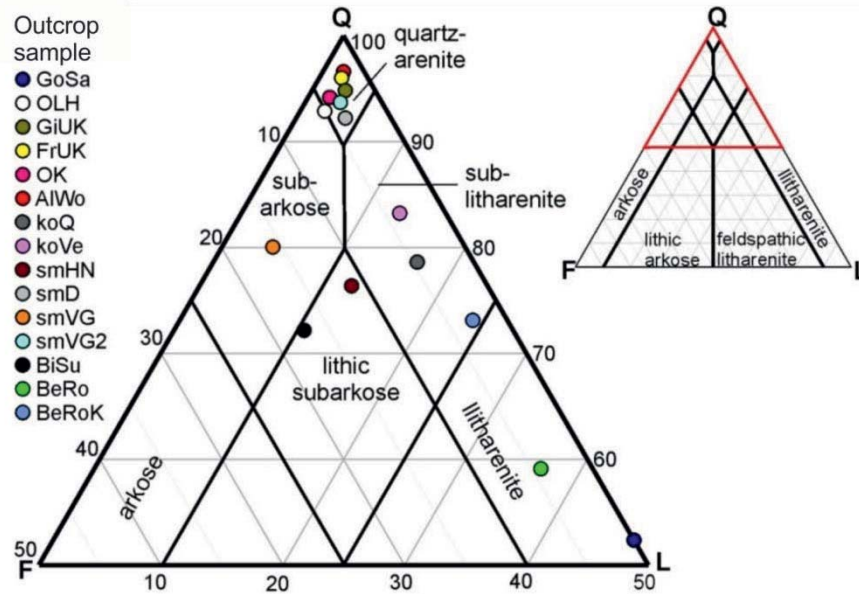
Figure 4: Classification of all sandstone samples from outcrops (see key) according to the QFL (quartz-feldspar-lithoclasts) classification plot by McBride (1963); determined with point-counting with 500 counts each (n = 15) (modified from Reyer, 2013).

3. Fracture systems in normal fault zones

With the aim of gaining new insights on fracture orientation, density, aperture and length of 77 fault zones in the NGB, we performed structural analysis of 26 selected outcrop analogues (Table 1). The studied outcrops expose sedimentary rocks of comparable stratigraphy, lithology and facies to those found at depth. Results for 58 normal fault zones in 22 outcrop analogues were presented in Reyer and Philipp (2012) and are here summarised briefly.

Scanline surveys were performed perpendicular to the major slip surface. Each scan line was placed at the structural position of maximum exposed displacement. Structural elements associated with normal faults, including extension fractures, shear fractures, deformation bands and fault cores, were recorded and characterised in detail. For every fracture its orientation (strike direction and dip angle), aperture and length are measured. Relative to the bed thickness fracture termination is analysed, distinguishing 'stratabound' and 'non-stratabound' fractures (cf. Section 1). Profile lengths were adapted to the total fault zone width to obtain fracture data for both damage zones and undisturbed host rocks.

For each fault zone damage-zone width was determined as to where the fracture density increases abruptly and significantly in the outcrop compared with the host rock. Fracture orientations, densities, apertures and lengths, as well as fault zone structural indices, were then analysed separately for fault damage zones and host rocks.

105

The mean structural indices F_m [-] of the normal fault zones were determined as the ratio of damage zone width DZ [m] and total fault-zone width FZ [m] according to (Caine et al.; 1996):

$$F_m = \frac{DZ}{FZ}$$

(1)

By their nature structural indices can obtain values from 0 to 1, where the minimum would apply for a fault zone with practically no damage zone, and the maximum for a fault zone without a fault core, respectively. Thus higher structural indices typically indicate higher fault zone permeabilities.

Our field data show that, in most cases, the majority of the fault-related fractures strike sub-parallel to the fault plane; fractures in the damage zones, however, may differ significantly in orientation from that in the host rocks. Data also show that the aperture of fault-related fractures is much larger than aperture of background fractures. Whereas the maximum aperture is similar for both units, the percentage of fractures with large apertures is much higher in the damage zones than in the host rocks. The percentage of non-stratabound fractures is higher in fault damage zones than in host rocks.
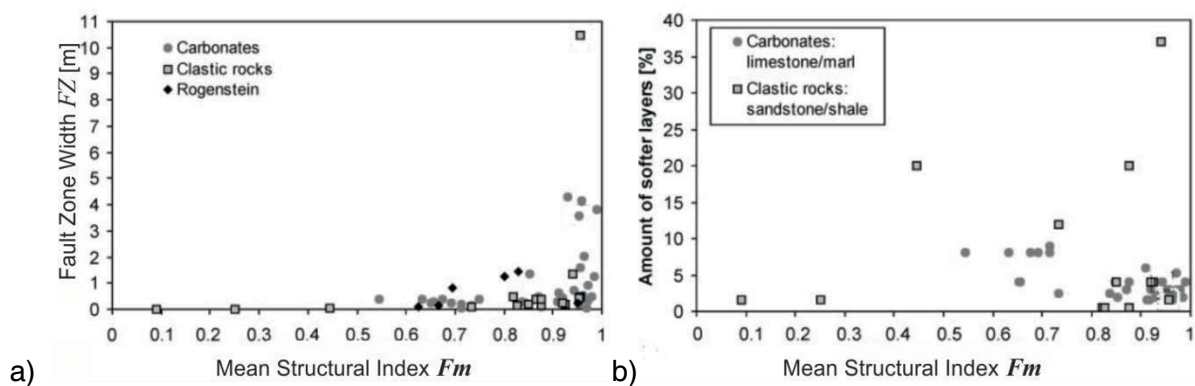

Figure 5: a) Mean structural index F_m (eq. (1); Caine et al., 1996) vs. fault zone width FZ (n = 58) separately for carbonate rocks (circles), clastic rocks (squares) and Rogenstein (diamonds); b) Mean structural index F_m vs. amount of relatively soft layers. This plot includes only normal fault zones in stratigraphic units with mechanical layering (n = 50). Fault zones with non-normal components are marked by rectangles (modified from Reyer and Philipp, 2012).

There are pronounced differences between carbonate and clastic rocks. Normal fault zones in clastic rocks show smaller total fault-zone widths than those in carbonate rocks (Fig. 5a). Further, the structural indices of normal fault zones in clastic rocks are comparatively low because of their thin damage zones. In carbonate rocks we found presence of clear damage zones, characterised by higher fracture densities than in the host rocks. The structural indices indicate that normal fault zones in carbonate rocks are more damage-zone dominated than those in clastic rocks, that is, their structural indices have higher values.

Clastic-rock normal fault zones with large structural indices are characterised by the presence of deformation bands. For the Rogenstein, as a carbonate rock with clastic texture (Usdowski, 1962), normal fault zones show intermediate values (Fig. 5a). For carbonate rocks with strong mechanical layering of limestones and marls, there is an inverse correlation of structural indices and the amount of soft marl layers (Fig. 5b). Presented data lead to the conclusion that there is a higher positive effect of normal fault zones on permeability increase in carbonate rocks compared with that in clastic rocks. For details see Reyer and Philipp (2012).

4. Empirical relations of rock properties of outcrop and core samples

There are several relevant rock mechanical and other physical parameters with importance given to different stages of geothermal drilling and exploitation. For geomechanical modelling, the uniaxial compressive strength (UCS) is the most important mechanical input parameter (Nabaei and Shahbazi, 2012; Vogt et al., 2012). The static Young's modulus, E_S, is a measure of rock stiffness and interesting in terms of predictions of fracture propagation (Jaeger et al., 2007; Gudmundsson, 2011). The indirect tensile strength, T_0, gives information about the rock's resistance to tensile fractures. These parameters are of interest in terms of dimensioning of hydraulic fracturing operations, wellbore stability and drilling mud selection (e.g. Zoback, 2007). The destruction work, W, is one parameter providing information on the amount of energy needed to destroy the rock while drilling. It is known to correlate with the drilling efficiency which is a term used to describe the effects of a number of geological and machine parameters on the drilling velocity (Thuro, 1997). Therefore, it is desirable to make reasonable assumptions about these parameters for drilling through the rock units.

Some parameters may be obtained from well logs of existing adjacent boreholes. For example, physical properties such as density, ρ [kg m^{-3}] and P- and S-wave velocities, v_p and v_s [m s^{-1}], respectively, are parameters that can be measured directly in wellbores; the porosity, φ [%], is derivable from such well logs (Edlmann et al., 1998). The dynamic Young's modulus is derived from velocity and density logs (Zoback, 2007; Rider and Kennedy, 2011), whereas E_S must be acquired in the laboratory with a uniaxial compression test (ISRM, 2007). In the same test, UCS is obtained.

To build geomechanical models before drilling, necessary for the calculation of optimum mud weights to avoid wellbore instabilities, or to validate these models while- and after-drilling empirical relations between UCS parameters which are either knowable before drilling or determinable with logging-while-drilling tools are useful (Reyer et al., 2014). There already exist several software approaches for building and updating geomechanical models (Settari

and Walters, 2001; geomechanics software, e.g. GMI, www.baker-hughes.com). Generally, however, such geomechanical modelling software uses empirical relationships that were developed for hydrocarbon reservoirs in other geological settings. This study (Reyer and Philipp, 2014) is, to our knowledge, the first attempt to review and adapt existing models and provide relationships valid for geothermal reservoirs of the NGB.

The above mentioned parameters were measured on 35 outcrop samples from quarries (both parallel and perpendicular to sedimentary layering to consider anisotropy) and 14 core samples from two wellbores with the same stratigraphic units, comparable lithologies and facies. That is, typical sedimentary and volcanic rocks of the North German Basin (NGB) were analysed; equivalent samples from outcrops and depth were compared to explore mechanical property changes due to uplift and alteration. We performed standard measurements according to ISRM (2007); for details on laboratory measurements see Reyer and Philipp (2014) and Reyer (2013).

With regression analyses (linear- and non-linear) empirical relations were developed to predict UCS values from all other parameters. In the first step all samples together were taken into account. The second step comprised a separate analysis for sandstone and carbonate samples. In each case, regressions were made both for outcrop samples only and for all samples including core samples to examine if results from core samples plot in the same range of values as outcrop samples. Calculation of coefficients of determination, between UCS and the described parameters, to evaluate the statistical significance of the developed regression functions, 90% confidence and prediction bands were added. A confidence band covers the area in which the true curve of the empirical relation plots with a prescribed probability, in this case 90%. It consequently represents the uncertainty of the true position of the curve. A prediction band, in contrast, encloses the area which contains with a prescribed probability single results of future measurements of samples from the same data set. It can therefore be used for analysing the quality of predicted values of future measurements (Wooldridge, 2009).

Regression functions for UCS with the other mechanical properties E_S, W, and T_0, show high statistical significance. Core samples plot within 90% prediction bands from outcrop samples, indicating that the equations are applicable for rocks from greater depths.

There is a wider scatter for the regression functions for UCS with other physical properties (φ, ρ and v_p) indicating that the statistical significance is low. The developed equations yield distinct under- and over-predictions of UCS values. Although prediction of UCS from these parameters therefore is less precise, properties of core samples plot within the scatter of outcrop samples and lie within the 90% prediction bands. That is, the regression functions work well for at least estimating core sample properties with comparatively small deviation.
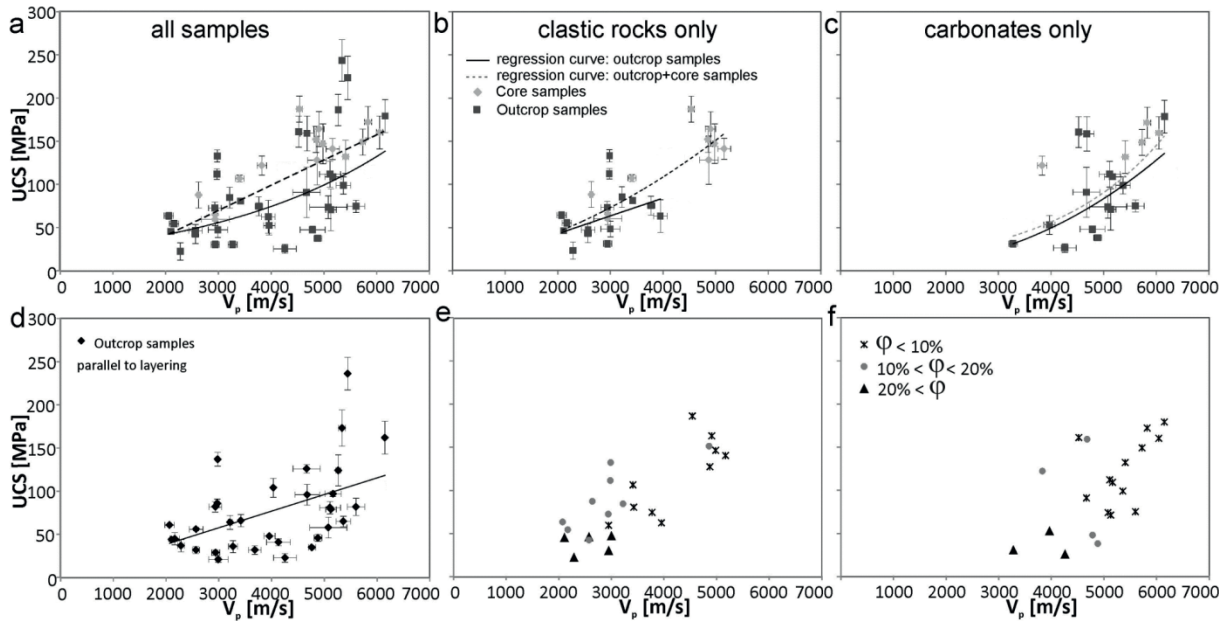
Figure 6: v_p versus UCS for specimens taken perpendicular to layering for outcrop and core samples separately for a) all samples (n = 49), b) only clastic rock samples (n = 24) and c) only carbonate samples (n = 20); d) v_p versus UCS for all specimens taken parallel to layering in outcrops (n = 33); regression curves shown for both outcrop and core samples and outcrop samples only (see regression functions in equations (2) and (3). Error bars indicate standard deviations of all measurements of each sample. e, f) v_p versus UCS for low, medium and high-porosity samples of clastic rocks (e) and carbonates (f) (modified from Reyer and Philipp, 2014).

As an example we here present scatter plots and regression functions for UCS versus v_p, because many studies show that UCS correlates positively with v_p and travel time, respectively (Freyburg, 1972; Sharma and Singh, 2008). v_p is one parameter determined easily with borehole acoustic logs (e.g., Rider and Kennedy, 2011) and it may be relevant for the geomechanical model validation and logging-while-drilling.

UCS- v_p data show a wide scatter for all samples (Fig. 6a). The coefficients of determination are rather poor for both outcrop samples only and core samples included (Reyer and Philipp, 2014). However, there are only small differences between best fit curves for outcrop samples only and core samples included. Especially for carbonates the regression curve differs only slightly when core samples are included. There are conspicuous interdependencies between UCS, v_p and φ for both clastic rocks and carbonates. High porosity clastic and carbonate rocks have lowest UCS and v_p values, and low porosity samples have highest values (Fig. 6e, f). For further details and all equations of regression functions see Reyer and Philipp (2014).

5. Failure and friction criteria based on samples from outcrop analogues for core property prediction

Knowledge of rock failure and friction criteria helps to avoid wellbore stability problems. Hence this study (Reyer and Philipp, subm.) aimed at predicting failure and friction criteria of potential geothermal reservoir rocks and overburden rocks.

At best, criteria are derived from core samples. In particular, from the younger rock units above, that have to be drilled through to reach the reservoir, core samples are in most cases even unavailable. In these rock units, however, many cases of wellbore instabilities occur (McLean and Addis, 1990; Zeynali, 2012). Because drill core material is rare, in most cases it is not viable to perform complete triaxial test series with core samples to determine their failure criteria. Equivalent samples from outcrop analogues of these units, in contrast, are easy and cheap to provide.

We therefore analysed if Mohr-Coulomb failure and friction criteria for drill cores and conditions at larger depths may be predictable utilising equivalent samples from outcrop analogues. For this purpose we took six samples from drill cores of different stratigraphic units from two wellbores in the western NGB: Groß Buchholz 1 (Gt1; e.g., Schäfer et al, 2012) and Eulenflucht 1 (EF1; Fig. 2). We then looked for equivalent samples from outcrop analogues for all core samples. Here, 'equivalent' means that the outcrop sample is of the same stratigraphic age and of comparable sedimentary facies and composition as the associated core sample. Such equivalent outcrop samples were taken in quarry parts as freshly exposed as possible to minimise changes of mechanical properties as a consequence of exposure. Equivalence of core and outcrop samples was evaluated using thin section analyses with focus on texture, cementation, grain size, porosity, and mineralogical composition. For the stratigraphic units to be drilled through to reach potential geothermal reservoirs not represented in drill cores, we included outcrop samples to obtain a comprehensive rock mechanical data base for the NGB. In total 18 samples were analysed (Table 1).

Conventional triaxial tests were performed, utilizing a pressure vessel using oil as the confining medium. For each outcrop sample a total of five cylindrical specimens were measured. Due to limited core material it was only possible to measure one to two specimens per core sample. Specimens had diameters of 30 mm and lengths of 60 to 65 mm (details in Reyer and Philipp, subm.). Confining pressures were chosen with respect to the maximum depths in which the different rock units occur. For example, maximum depth of Wealden sandstone (Lower Cretaceous) in Lower Saxony is 2500-3000 m (NIBIS Kartenserver, 2012). In the NGB this depth corresponds to a minimum principal stress of 60 MPa (Röckel and Lempp, 2003). The set of triaxial measurements of Wealden sandstone sample (OK) is consequently performed with confining pressures of 10, 20, 30, 50 and 60

MPa (cf. Reyer and Philipp, subm.). For stratigraphic units occurring at greater depths, appropriate higher confining pressures are chosen.

Linear failure and friction criteria were derived from linear regressions of maximum ($\Delta\sigma_{max}$ [Pa]) and residual stress differences ($\Delta\sigma_{res}$ [Pa]) and confining pressure p_c [Pa].

Mohr-Coulomb failure criterion, expressed in normal and shear stresses, is:

$$\tau_f = \mu_i \, \sigma_n \tag{2a}$$

with:
$$\tau = \frac{\Delta\sigma_{max}}{2\sin(2\beta)} \tag{2b}$$

$$\sigma_n = p_c + \frac{\Delta\sigma_{max}}{2(1+\cos(2\beta))} \tag{2c}$$

where τ_f [Pa] is the cohesive strength and μ_i [-] is the coefficient of internal friction. Shear (τ)[Pa] and normal stresses (σ_n) [Pa] are calculated taking into account the dip angle β, that is equal to the angle between fault normal and maximum principal stress σ_1, of observed induced shear fractures.

Friction criterion is calculated with friction cohesion (τ_0) and coefficient of friction (μ_{fric}) from residual shear (τ_{res}) and normal stresses ($\sigma_{n\,res}$):

$$\tau_{res} = \tau_0 + \mu_{fric} \, \sigma_{n\,res} \tag{3a}$$

with:
$$\tau_{res} = \frac{\Delta\sigma_{res}}{2\sin(2\beta)} \tag{3b}$$

$$\sigma_{n\,res} = p_c + \frac{\Delta\sigma_{res}}{2(1+\cos(2\beta))} \tag{3c}$$

Criteria for outcrop samples were obtained separately and the resulting 90 % confidence and prediction bands compared with core sample results. If there is a good equivalence regarding texture and porosity, it is concluded that obtained failure criteria are applicable for core property prediction. Grain size and mineralogical composition are of minor importance for the addressed question. Friction data are in good accordance with Byerlee friction; no considerable differences of friction between core and outcrop samples were detected.

Linearized Mohr-Coulomb failure and friction criteria were calculated from triaxial test sequences for all outcrop samples. Additionally, linear regression analyses are performed adding 90 % confidence and prediction bands (cf. Section 4) of determined failure and friction criteria. The criteria determined for outcrop samples were then applied to equivalent core samples to calculate shear stresses (τ) and residual shear stress (τ_{res}) values for core samples. These calculated values of τ and τ_{res} are then compared with the directly measured values. That is, failure and friction criteria of outcrop samples are used to calculate and predict, respectively, resulting shear stresses.

In Figure 7, shear stresses are plotted as functions of normal stresses for two examples of outcrop-core sample couples (cf. thin section micrographs in Fig. 3). For sandstone samples (e.g., OK) failure criteria are less precise than those of carbonate and volcanic rock samples which is reflected in wider confidence bands (Fig. 7a). Core sample values tend to plot

slightly above the Mohr-Coulomb failure line. That is, core samples can stand slightly higher axial stresses before failure. Sample Gt1WS is the only clastic rock sample with suboptimal comparability to its equivalent outcrop sample.
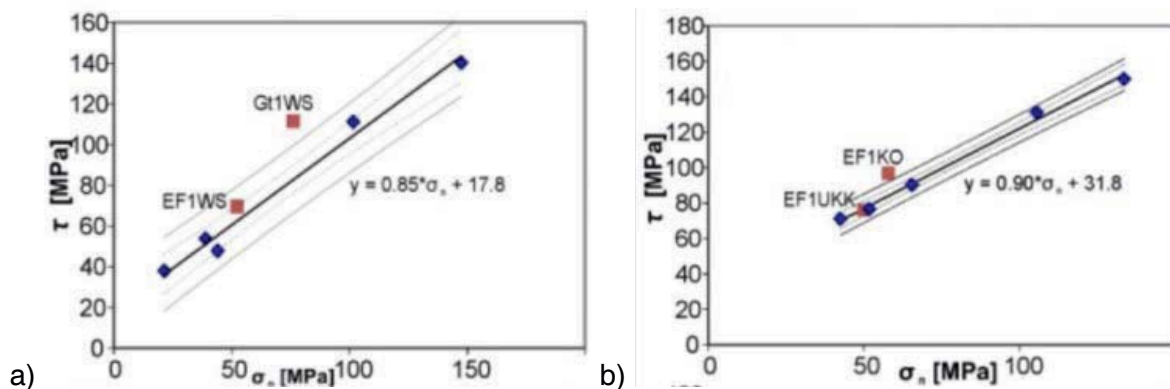

Figure 7: Shear stress τ and normal stress σ_n of selected samples from depth (red squares) and equivalent outcrop samples (blue diamonds) with Mohr-Coulomb failure criteria calculated from equivalent outcrop sample results with equation (3). a) Wealden-Sandstone samples OK, Gt1WS, and EF1WS. b) Korallenoolith samples ShJK, EF1KO, EF1UKK (modified from Reyer and Philipp, subm.)

We also present examples of comparisons of static Young's modulus E_S measurements for different confining pressures p_c (Fig. 8). The uniaxial E_S (i.e., where p_c = 0) of sample OK plots below the extrapolated triaxial test results (Fig. 8a). For the carbonate samples presented in Figure 8b, however, comparable results of uniaxial E_S and those derived from triaxial tests were obtained. That means there have to be mechanisms controlling how strong an absent confinement affects the elastic behaviour. Microfracture catalogue has a strong effect on the strain at low axial loads (e.g., Jaeger et al., 2007). Steeper stress-strain curves are obtained because applying certain confining pressure on the specimen already closes most of the respective microfractures. Consequently, in rock samples where high amounts of microfractures are present, measured uniaxial Young's moduli are expected to give lower values than deduced ones from triaxial test series (more detail in Reyer and Philipp, subm.) Applicability of outcrop sample failure and friction criteria for wellbore stability analyses is concluded when equivalence of chosen outcrop samples, regarding textural similarity, especially grain interlocking and cementation of sandstone samples, and porosity is ensured. Still we recommend re-checking the conclusions drawn from this study with further comparative analyses of core samples with equivalent outcrop samples.
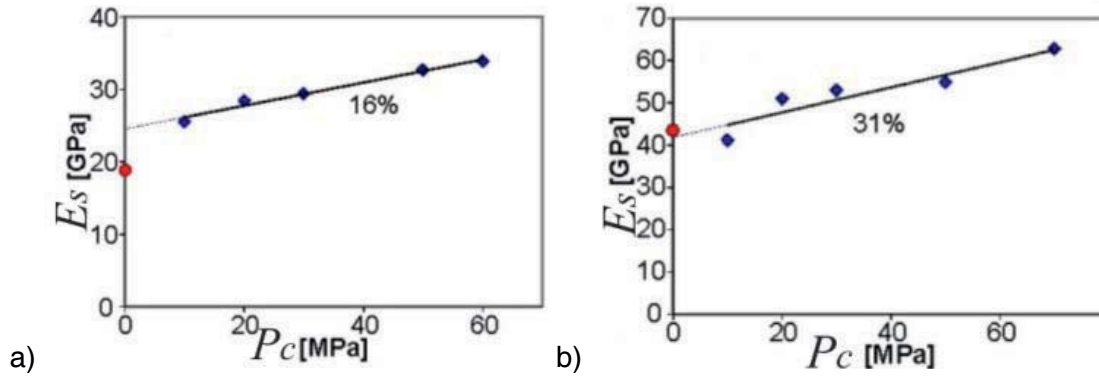
Figure 8: Effect of increasing confining pressure p_c on Young's modulus E_S for exemplified sandstone (a; OK) and carbonate (b; ShJk) samples (cf. Fig. 3). E_S values determined from uniaxial compressive strength test (red circles;) and the percentage increase of E_S with confining pressure are given.

6. Analytical models

6.1 Fluid flow in fracture systems

For the economic use of a geothermal reservoir, high fluid flow rates are essential. Few open fractures with larger apertures may enhance fluid flow, because the flow rate depends on the cube of the fracture aperture (cubic law; de Marsily, 1986).

In G3 we aimed at investigating which fracture orientations of fractures enhance the permeability of a fracture system. Therefore we calculate the hydraulic conductivity k_f [m s^{-1}] (as an equivalent of permeability in case of water, relevant for the fluid flow rate) for sets of parallel and open fractures to show using an extension of the cubic law after Bear (1993):

$$k_f = \frac{\rho_f \cdot g}{12\mu \cdot L}\left(\sum_{i=1}^{m} b^3\right) \qquad (4)$$

where ρ_f is the fluid density [kg m^{-3}], g the acceleration due to gravity [m s^{-2}], μ the dynamic viscosity [Pa s], L the profile length [m] and b the fracture aperture [m]. Since we use fracture data of surface measurements in outcrop analogues for the calculations, for geothermal reservoirs we would have to consider that fracture apertures and densities would be reduced with increasing depth (Lee and Farmer, 1993). Therefore, we aim at highlighting fracture orientations with enhanced permeabilities, but do not provide absolute values.

Here we show as an example the calculations based on the fracture measurements for the outcrop Steinberg in the Egge-System (Fig. 2, Table 1), where sandstones of the Solling-Folge of the Middle Buntsandstein are exposed. For each 20°-orientation class a value for k_f was calculated with equation 4 and plotted logarithmically in a diagram similar to a classical rose diagram (e.g., Fossen, 2010) of fracture orientations (Fig. 9), where for each orientation class (e.g., 0-20°), the number of fractures is plotted similar to a histogram. Most

fractures trend N-S (Fig. 9a), but the widest fractures occur in E-W direction, parallel to one of the faults (Fig. 9b). This leads to high permeability and flow rates in this direction. Note that in this example, although the fracture system is strongly anisotropic (Fig. 9a), the fluid flow distribution is almost isotropic (Fig. 9d). However, this is not always the case (Meier et al., in press), and could also occur vice versa.
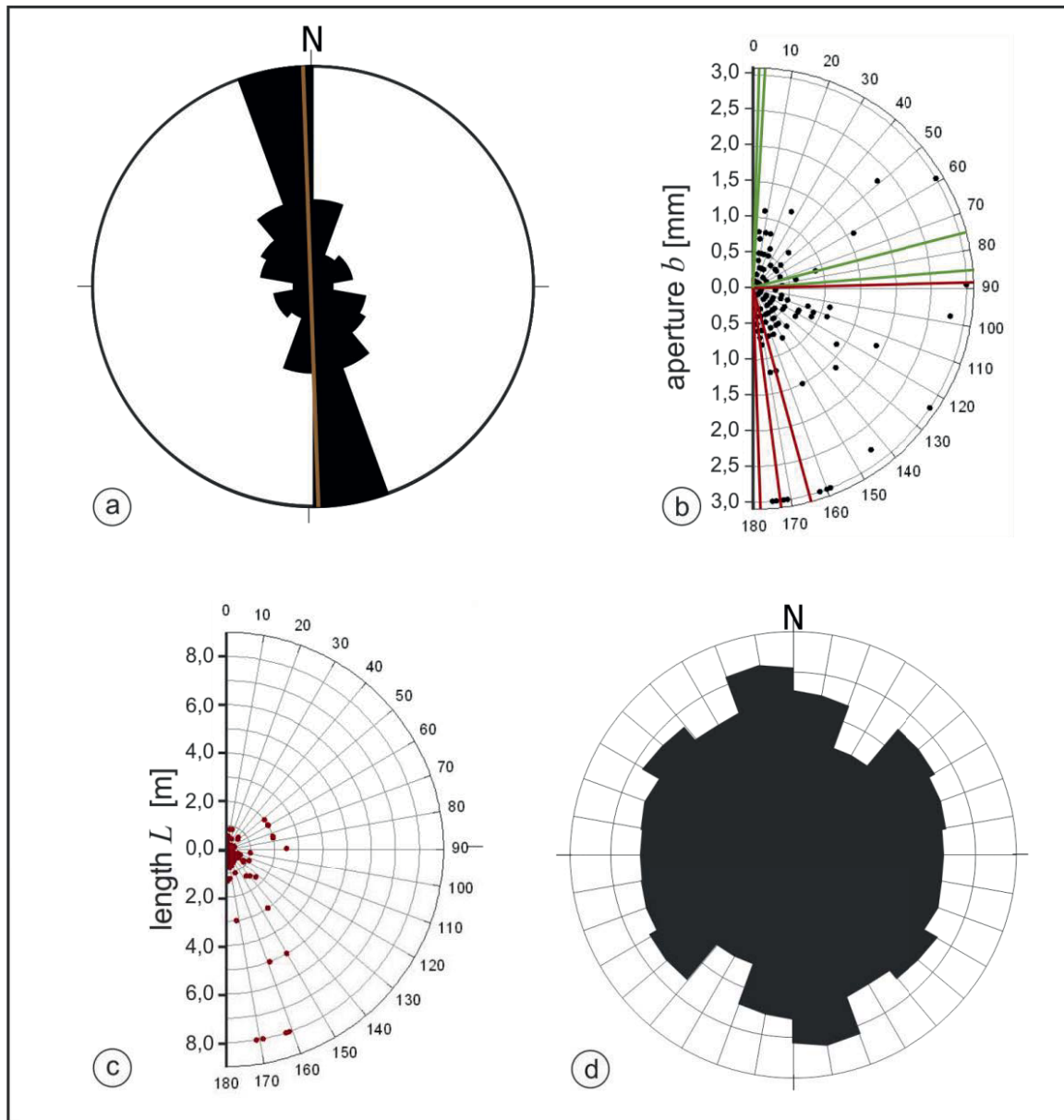

Figure 9: a) Rose diagram of the fracture orientations in outcrop Steinberg (Middle Buntsandstein, Egge-System), 20° classes, n = 134; b) apertures vs. fracture orientation (strike); red lines: fault zone strike; c) fracture lengths vs. fracture strike; d) calculated hydraulic conductivity k_f using eq. (4); (modified from Bauer, 2010).

6.2 Stiffness distribution in fault zones

Rock stiffness (e.g, E_s) is interesting in terms of predictions of fracture propagation and commonly correlates well with UCS (Section 4). Therefore it is noteworthy to estimate stiffnesses of *in situ* rock masses.

Fractures reduce the stiffnesses of *in situ* rock masses, whereas rock samples measured in the laboratory are nearly free of fractures. Hence, *in situ* static Young's moduli tend to be lower than those measured in the laboratory of intact samples of the same rock types (E_i [Pa]; Heuze, 1980). *In situ* effective Young's modulus, E_e, (the Young's modulus affected by fracturing, [Pa]) and fracture spacing (the distance between parallel fracture planes or the inverse of fracture density defined in Section 1) commonly show a strong correlation (Walsh, 1965; Priest, 1993). This is important in particular in fault zones, where in the fault damage zone, the fracture spacing commonly decreases towards the fault core, meaning that E_e decreases proportionally. To obtain an estimate on how much E_e differs from E_i we use the analytical model by Priest (1993):

$$E_e = \sigma_n \frac{L}{\Delta L} = \left(\frac{1}{E_i} + \frac{1}{\bar{s}k_n} \right) \tag{5}$$

where σ_n [Pa] is the stress normal to the fracture planes, L [m] is the original length of the profile, ΔL [m] is the change in length, $\bar{s}$ [m] is the average fracture spacing, and k_n [Pa] is the fracture stiffness. For k_n 20 % of UCS values is a reasonable approximation for macrofractures at near-surface conditions based on experiments and theoretical considerations by Priest (1993).
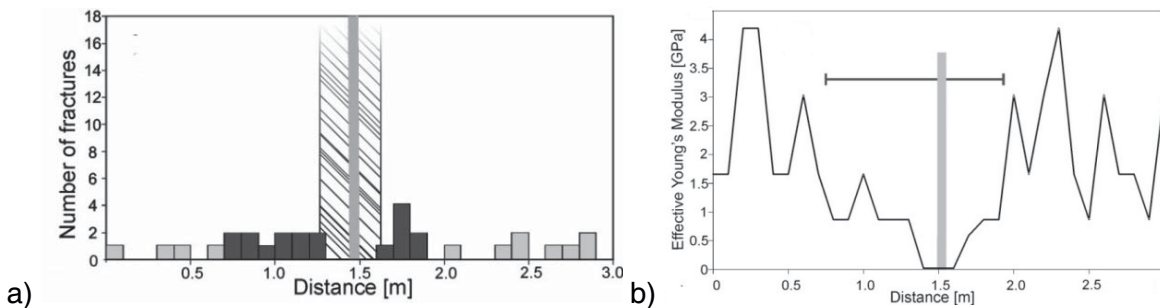

a)   b)

Figure 10 a) Number of fractures in 10 cm intervals perpendicular to normal fault planes for Lower Cretaceous Wealden-sandstone in Obernkirchen (Fig. 2, Table 1; cf. Fig. 3a). The grey line represents the fault plane location, the dark grey bars show the damage zone width and the striped rectangle defines a region with strong brecciation, so that not every fracture could be detected. b) Distribution of effective Young's moduli E_e perpendicular to the normal fault plane (grey line) for the outcrop in a) based on equation 5 and field data (modified from Reyer and Philipp, 2012).

115

In the following we present as an example calculations of the effective Young's modulus distribution in the normal fault zone in Obernkirchen, exposed in Lower Cretaceous Wealden-sandstone (Fig. 10; cf. Reyer and Philipp, 2012). Young's modulus and UCS of the intact rock sample OK (Table 1) are E_i = 18 GPa, and UCS = 91 MPa, respectively. The number of fractures (from which the fracture spacing can easily be found) was counted for 10 cm-intervals along a scanline across the fault zone (Fig. 10a). We use the parameters E_i and UCS from the laboratory measurements, together with the field measurements of fracture spacing to calculate the E_e distribution of the *in situ* rock masses within the fault zone perpendicular to the fault plane using equation (5).

Results show that there is a clear decrease of E_e in the damage zone compared with the host rock (Fig. 10b). Similar results were obtained for many other investigated normal fault zones (Reyer and Philipp, 2012). Because of their high fracture densities, the decrease of E_e is more pronounced for carbonate rocks than for clastic rocks (Reyer and Philipp, 2012). We conclude that normal fault zones in carbonate rocks have more profound effects on enhancing permeability in fluid reservoirs than those in clastic rocks. The results are of great importance for modelling the hydromechanical behaviour of normal fault zones in subsurface fluid reservoirs.

6.3 Rock toughness

In reservoirs drilling efficiency depends in particular on brittle or ductile rock behavior. This can be described in terms of the mechanical parameter G_c, [N m^{-1}] commonly referred to as 'material toughness' of the rock (Gudmundsson, 2011), or simply 'rock toughness'. G_c also is the critical strain energy release rate, a measure for the energy absorbed per unit area and equivalent to the resistance of the rock against fracture propagation (Gudmundsson, 2011) or drilling/tunneling, then referred to as 'destruction work' (Thuro, 1997). It mainly depends on layering, stiffness, fracture systems, rock ductility, pore pressure and temperature (Ashby and Jones, 2005).

To obtain G_c for a rock sample, its connection to the elastic strain energy per unit volume U_0 [kJ m^{-3}] can be used (Gudmundsson, 2011):

$$G_C = U_0 \pi a \qquad (6)$$

where a [m] is the radius of the propagating fracture. U_0 is found as the area below the stress-strain-curve in compression tests (Thuro, 1997).

To show which different values of rock toughness can be expected for the rocks to be drilled through in the North German Basin we here present two examples: 1) Schaumkalk (sample H) and 2) Wellenkalk (sample EL2; see Appendix; cf. Reyer and Philipp, 2014); in both cases

tested perpendicular to bedding. Schaumkalk is an oolithic limestone with rather isotropic properties and no distinct layering inside the dm- to m-thick beds. By contrast, Wellenkalk typically shows strong layering in the cm-scale of micritic limestone and marly layers. For the Schaumkalk sample H we obtain an elastic strain energy per unit volume of 122 kJm^{-3}, for the Wellenkalk EL2, by contrast, U_0 is 546 kJm^{-3}. To estimate the rock toughness G_c, with equation (6) a fracture radius has to be assumed. Since we here are interested in the relative differences only, we assume a fracture length of 1 mm, i.e., the fracture radius is 0.5 mm. Equation (6) results in rock toughnesses of 192 Nm^{-1} for the Schaumkalk sample H, and 857 Nm^{-1} for the Wellenkalk sample EL2, respectively. This clearly shows that the strong layering of the Wellenkalk leads to much higher elastic strain energy and therefore rock toughness than the rather homogeneous Schaumkalk.

7. Numerical models

In G3 we have also run numerical models for the analysis and prediction of stress fields and fracture propagation. These are also helpful for the understanding of fault- and fracture-related permeability in fluid reservoirs and thus widely used (e.g., Zhang and Sanderson, 1996; Rawling et al., 2001; Brenner, 2003; Gudmundsson, 2011; Philipp et al., 2013).

In this section we present two examples of numerical models of special situations. Since most rocks behave as linear elastic up to 1-3 % strain at low temperature and pressure (Paterson 1978), that is, in the upper crust, we define all linear elastic materials. For linear elastic materials stress varies linearly with strain (Hooke's law) and the ratio of stress to strain is Young's modulus ('stiffness'). The second elastic constant to be defined (Hudson and Harrison, 1997) is Poisson's ratio, which is a measure of the absolute ratio of strain (change in size) in perpendicular directions.

7.1 Fracture propagation in layered and fractured rock

We used BEASY Fracture Wizard (www.beasy.com; Boundary Element Method) for dynamic modelling of fracture propagation based on real layered and fractured rock geometries. The analysis is based on the incremental linear discretization of the propagation path of a hybrid fracture ('mixed-mode crack'), in which for each increment the software calculates stress intensity factors with J-integrals for each fracture mode (K_I, K_{II}, K_{III}). The effective stress intensity factor K_{eff} according to the sum of squares-method is then:

$$K_{eff} = \sqrt{K_I^2 + K_{II}^2 + K_{III}^2} \tag{7}$$

and the fracture propagation path is calculated automatically perpendicular to the local direction of the minimum principal compressive stress σ_3.
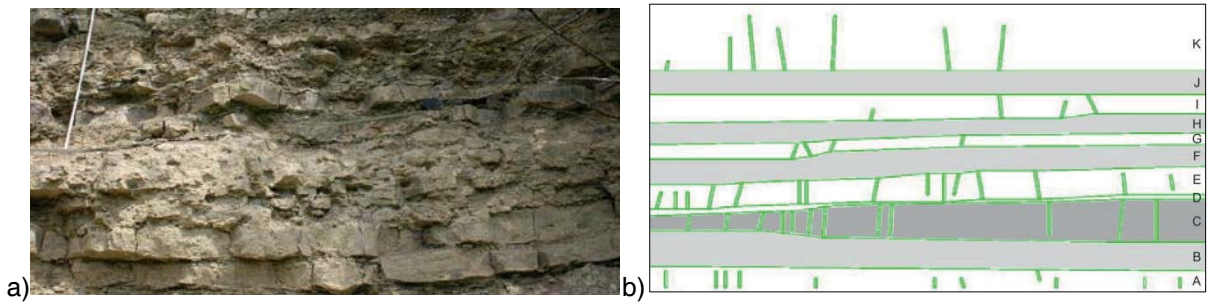
117

Figure 11: a) Part of an outcrop in Ceratitenkalk (Upper Muschelkalk) near Göttingen (Diemarden). b) 2D-model geometry based on layering in (a); limestone (white), marly limstone (light grey), marl (grey). Green: pre-existing fractures (modified from Parchwitz, 2010).

Figure 11 shows an outcrop (a) and the related model geometry (b). Exposed is layered and fractured Ceratitenkalk (Triassic). The rock mechanical properties were defined estimating in situ Young's moduli according to the results of laboratory measurements as 30 GPa for limestone, 25 GPa for marly limestone and 15 GPa for marl. The model is loaded to a fictive remote tension of -3 MPa.
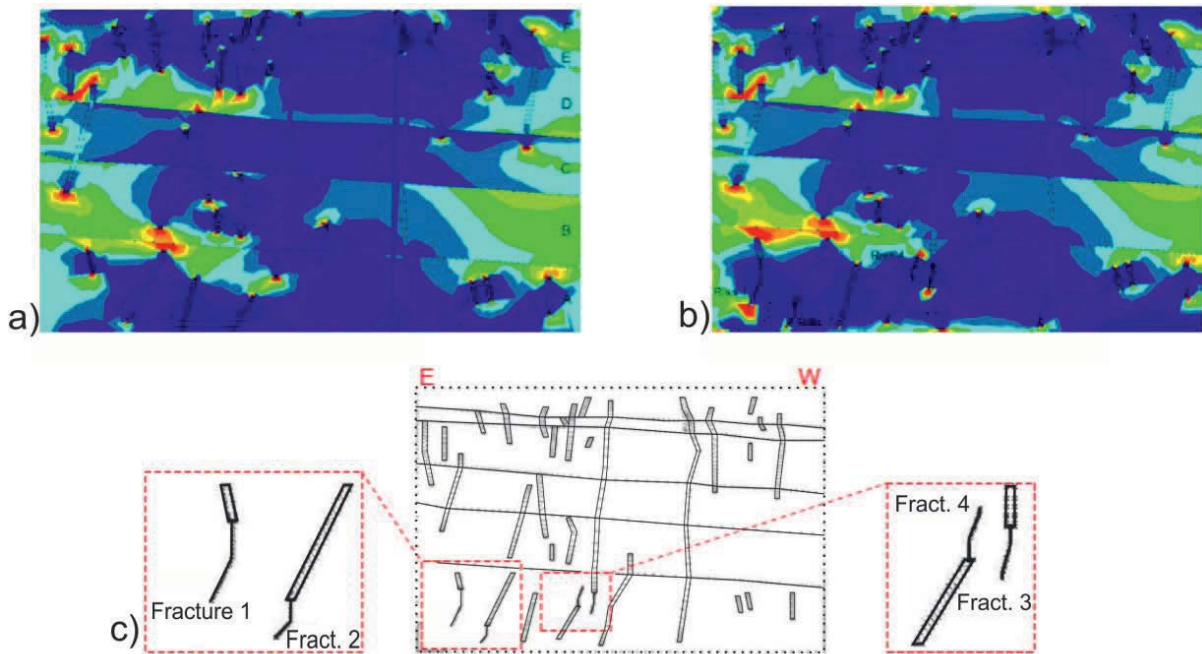
Figure 12: a) Resulting minimum principal compressive (maximum principal tensile stress) for the model in Fig. 11b for remote tensile stress of -3 MPa. b) model in a) after fracture propagation. c) fracture propagation paths (modified from Parchwitz, 2010).

The model in Figure 12a shows the resulting tensile stress (σ_3). Stress shadows build up next to the fractures, but stress concentrations occur at fracture tips, in particular within the stiff limestone layers. In the next step, the four fractures with highest stress concentrations were allowed to propagate, resulting in the model in Figure 12b. The model results show that fracture propagation starts in mixed-mode in most cases. In the following fracture propagation continues rather in mode I (tension or opening mode), the fractures develop more and more into pure tension fractures. Fractures propagating towards each other may affect each other's propagation direction (cf. fractures 3 and 4).

The rock mechanical properties clearly affect fracturing. In the stiffer limestone layers, more fractures occur. Many fractures terminate at contacts to softer marl layers, they are stratabound (cf. Section 1). Thus, marl layers acted as stress barriers, so that mechanical layering corresponds to lithological layering. For details of these models see Parchwitz (2010). For other field examples of stratabound fractures and models of fracture propagation in layered rocks see, for example, Philipp et al. (2013).

7.2 'Horstberg benchmark'

In the following we model the current local stress field of the 'Horstberg benchmark' (cf. Hahne et al., in prep.). This model, also used, for example, in G7, represents a typical fault zone in the NGB simplified from a seismic section and information from the borehole Horstberg Z1 near Celle. Here the focus is on local stress field variations within the various layers and inside the fault zone, based on realistic definitions of the boundary conditions, i.e., the regional stress field and model constraints.

The model geometry is shown in Figure 13; we used COMSOL Multiphysics standard quadratic finite elements on tetrahedra with mesh refinement inside the fault zone. Young's moduli and Poisson's ratios of all layers were defined as given in the gebo-database (Hahne et al., in prep.). Inside the fault zone, the Young's moduli are given as follows: the fault core has a constant Young's modulus of 2 GPa in all the layers, simulating fault breccia, the damage zone Young's moduli are half of those of the host rocks indicating higher fracture densities (cf. Section 6.2). The fault plane itself in this first model run is not slipping, that is, no failure or friction criteria were defined.

The focus of this static model is on local stress field variations within the various layers and inside the fault zone, based on realistic definitions of the boundary conditions. The model is constrained at the base (i.e., zero displacement is defined; grey plane in Fig. 13); free movement is allowed at the top only. Along the outer vertical surfaces, remote horizontal stresses form the loading and are defined as follows.

The vertical stress component σ_V is always zero at the surface (where the depth z = 0) and increases with depth because of the weight of the rocks (overburden). The rock densities listed in the gebo-database (Hahne et al., in prep.) result in a maximum σ_V of 117.3 MPa at 5000 m depth, the other values are plotted in Figure 13.

According to the World Stress Map (Heidbach et al., 2008), in the North German Basin the maximum horizontal stress component, σ_H, is, on average, oriented NW-SE in sub-salinar (i.e., below Upper Permian Zechstein evaporites) measurements. Although supra-salinar (i.e., above Zechstein evaporites) measurements show strongly varying orientations (e.g., Schäfer et al., 2012) the sub-salinar orientation is rather stable, explainable by a plate-tectonic compressional direction resulting from Atlantic ridge push and Alpine compression, and is therefore assumed to represent the mean remote orientation of σ_H (Fig. 13).
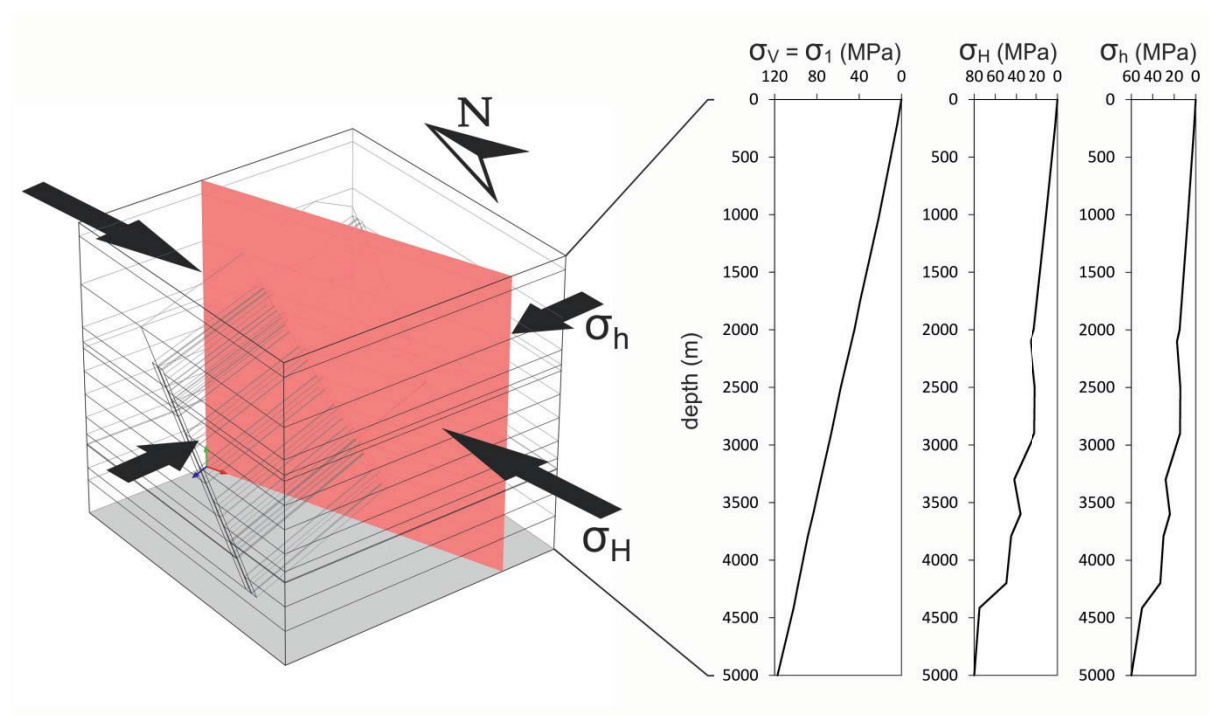
Figure 13: Model geometry of 'Horstberg benchmark' with defined remote stress field. Indicated in pink is the sectional area shown in the results (Fig. 14). The thick black arrows point out the orientations of σ_H and σ_h. Their magnitudes, as well as those of σ_V, are plotted to the right.

Similar to Moeck et al. (2008) at Groß Schönebeck near Berlin we here assume a normal faulting regime where the vertical stress component is equal to the maximum principal compressive stress, i.e., $\sigma_V = \sigma_1$. Considering the Poisson effect (e.g., Gudmundsson, 2011) only, the minimum horizontal stress component, σ_h, can then be calculated as:

$$\sigma_h = \frac{\nu\, \sigma_V}{1 - \nu} \qquad\qquad (8)$$

where ν is Poisson's ratio. Because in Muschelkalk and Zechstein ν is rather high (0.27 and 0.33, respectively; Hahne et al., in prep.), relatively high values for σ_h are obtained (see plot in Fig. 13). In addition, pore fluid pressure should be taken into account in a sedimentary basin. The only reliable estimate of σ_h at Horstberg, however, results from the fracture pressure of 33 MPa (at wellhead) for the hydraulic fracturing of the Buntsandstein at 3800 m depth (www.genesys.de). Substracting an average *in situ* tensile strength of 3 MPa (cf. Haimson and Rummel, 1982) and some pressure loss in the wellbore from this value, σ_h must be around 29-30 MPa at this depth.

In some models, σ_H, is equal to σ_h (e.g., Meneses Rioseco et al., 2013). These models, however, do not explain the occurrence of borehole breakouts or tensile fractures, that are common in Horstberg and Groß-Buchholz, Hanover (Schäfer et al., 2012), and are only possible if $\sigma_H > \sigma_h$ (e.g., Zoback et al., 2003; Zoback, 2007). For a depth of 4100 m inside the Rotliegend at Groß Schönebeck Moeck et al. (2008) use the frictional equilibrium method by Peska and Zoback (1995) to estimate σ_H as being at least 1.5 σ_h. We use this relationship for a rough estimate of σ_H down to the Zechstein (Fig. 13). For the Lower Permian Rotliegend (i.e., sub-salinar) we assume somewhat higher pore pressures, resulting in a smaller difference of σ_H and σ_h (Fig. 13).
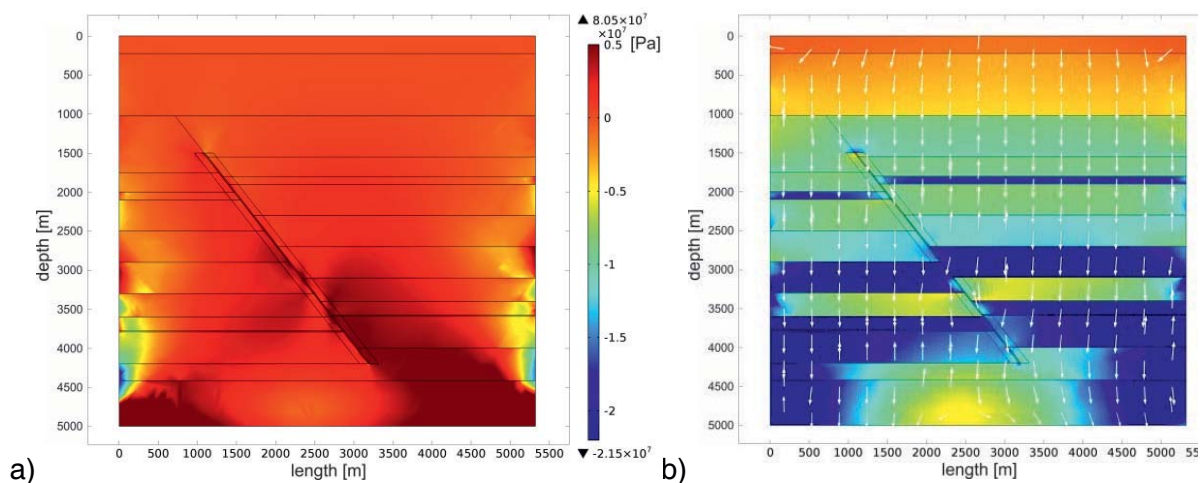
Figure 14: Magnitude (according to the colour scale to the right) of the minimum principal compressive stress (σ_3) (a) and magnitude (accorvding to the same colour scale) and direction (stress trajectories shown as white arrows) of the maximum principal compressive stress (σ_1) (b) along the sectional area across the fault plane indicated in Figure 13.

First results are shown in Figure 14. Both the minimum principal compressive stress, σ_3, (Fig. 14a) and maximum principal compressive stress, σ_1 (Fig. 14b) show varying stresses between the layers related to the varying Young's moduli (high stresses at the model boundaries are artefacts due to model constraints). A closer look at the fault zone reveals

that, although no slip at fault plane is possible, the low Young's moduli within the damage zone and fault core have considerable effects on the stress field. Lowest relative tensile stresses (σ_3) and compressive stresses (σ_1) occur at some points within the fault core. Stress trajectories of σ_1 in the surrounding host rock (white arrows in Fig. 14b) point out that some rotation of the stress field takes place (i.e., the principal stresses are oriented in different directions), although no ductile salt is present. Since σ_1 shows the direction in which extension fractures, such as hydraulic fractures, propagate (e.g., Gudmundsson, 2011), such models can be used to predict the outcome of hydraulic fracture treatments.

Ongoing work is on further development of the present model. For example, slip along at the fault plane defined with Mohr-Coulomb criterion, as well as anisotropic Young's moduli are included. Some results will be discussed in Hahne et al. (in prep.).

8. Conclusions

Heterogeneous rock properties in terms of layering and fault structure are common phenomena, typical in sedimentary basins such as the North German Basin (NGB), and affect many issues at different stages of geothermal project development.

Project G3 contributed to current geothermal exploration and exploitation concepts for the NGB with emphasis on fault zone utilization, and prediction of geomechanical conditions for drilling and stimulation modelling from data collected in outcrop analogues. Structural geological field studies in 47 different outcrops (sedimentary and volcanic) and rock analyses of 35 outcrop and 14 core samples from two wellbores reveal following main conclusions:

1. Fault damage zones are identified as promising geothermal reservoirs. Independent of lithology, most fault-related fractures have orientations similar to the fault strike and enlarged fracture aperture, length, and connectivity. However, mechanical layering of the rock mass directly controls the amount of stratabound fractures and therefore fracture connectivity. Normal fault zones in carbonate rocks are more damage-zone dominated than those in clastic rocks. Hence there is a higher positive effect of normal fault zones on permeability increase in carbonate rocks compared with that in clastic rocks.

2. Values of compressive strength (uniaxial and triaxial), failure and friction criteria, tensile strength, Young's modulus, destruction work, P-wave velocity, density, and porosity, were obtained both on outcrop samples and drill cores. Selection of appropriate outcrop samples, supposed to be equivalent to respective core samples, was ensured by respecting stratigraphic age, lithology, and facies with special emphasis on similar grain sizes, compositions, and porosities. Database can be used as input parameters for analytical and numerical modelling.

3. Linear and non-linear regression analyses were performed separately for carbonate and clastic rocks. The comparison of core sample properties with results of outcrop samples was performed by using statistical methods such as residual analyses, 90 % confidence and prediction bands of empirical relations and failure and friction criteria developed for outcrop samples. Regression functions of UCS with other parameters, in particular those with other rock mechanical properties and P-wave velocity, show high statistical significance. That is, it is possible to use outcrop samples of the rocks that have to be drilled through to provide good assumptions on rock mechanical properties at varying depths. Predictions of geomechanical conditions at future geothermal project sites may be improved.

4. Analytical and numerical models give insight to hydraulic and mechanical processes in geothermal reservoirs. For example, stress concentrates in particular within stiff (high-Young's modulus) layers and outside fault zones.

9. Acknowledgements

10. Publications resulting from the project

10.1   Peer-reviewed articles in scientific journals

Reyer, D., Bauer, J.F., & Philipp, S.L. (2012). Fracture Systems in Normal Fault Zones Crosscutting Sedimentary Rocks, Northwest German Basin, *Journal of Structural Geology, 45*, 38-51. doi:10.1016/j.jsg.2012.06.002.

Reyer, D. & Philipp, S.L., (2014). Empirical relations of rock properties of quarry and core samples from the Northwest German Basin for geothermal drilling. *Geothermal Energy Science 2: 21-37.* www.geoth-energ-sci.net/2/21/2014/

Reyer, D. & Philipp, S.L. *(submitted)* Applicability of failure and friction criteria based on outcrop analogue samples on wellbore stability prediction. *International Journal of Rock Mechanics and Mining Sciences.*

10.2   Accessible (extended) Abstracts

Philipp, S.L. & Reyer, D. (2010). Mechanical rock properties, fracture propagation and permeability development in deep geothermal reservoirs. *Geophysical Research Abstracts,* 12, EGU2010-11145.

Philipp, S.L., Reyer, D. & Bauer, J.F. (2010). Abschätzung effektiver Elastizitätsmoduli von Sedimentgesteinen in Störungszonen im Norddeutschen Becken. In: Hoppe, A., Röhling, H.-G., Schüth, C. (Hrsg.): GeoDarmstadt 2010 – Geowissenschaften sichern Zukunft. *Schriftenreihe der Deutschen Gesellschaft für Geowissenschaften,* 68, 434.

Philipp, S.L., Reyer, D., Afsar, F., Meier, S., Bauer, J.F. & Parchwitz, S. (2011). Extension fractures and fault zone structure in layered carbonate rocks. *Geophysical Research Abstracts*, 13, EGU2011-2475.

Philipp,. S.L., Reyer, D. & Bauer, J.F. (2011). Estimation of effective Young's moduli of sedimentary rocks in fault zones. *Geophysical Research Abstracts,* 13, EGU2011-2486.

Philipp, S.L., Lim, P.Y., Parchwitz, S. & Reyer, D. (2011). Numerical models of extension fracture propagation in mechanically layered rocks. *Geophysical Research Abstracts,* 13, EGU2011-2481.

Philipp, S.L., Reyer, D., Meier, S., Bauer, J.F., Afşar, F. & Reinecker, J. (2014). Fault zones and associated fracture systems in palaeogeothermal fields and geothermal reservoirs. In: GeoFrankfurt2014, Dynamik des Systems Erde / Earth System Dynamics, *Schriftenreihe der Deutschen Gesellschaft für Geowissenschaften*, 85; ISBN 978-3-510-49234-3

Philipp, S.L., Reyer, D., Meier, S., Bauer, J.F., Afşar, F. (2014). Internal structure of fault zones in geothermal reservoirs: Examples from palaeogeothermal fields and potential host rocks. *Geophysical Research Abstracts*, 16, EGU2014-1203.

Reyer, D. & Philipp, S.L. (2010). Architecture of small-scale fault zones in the context of the Leinetalgraben Fault System. *Geophysical Research Abstracts*, 12, EGU2010-7995.

Reyer, D. & Philipp, S.L. (2012). Realitätsnahe numerische Modelle zur Stimulation von potenziellen geothermischen Reservoiren im Nordwestdeutschen Becken. In: Geothermische Vereinigung (Hrsg.): *Der Geothermiekongress 2012*; Kongressband CD-Rom. 6 p.

Reyer, D &, Philipp, S.L. (2012). Bruchausbreitung und Stimulation von Sedimentgesteinen im Nordwestdeutschen Becken. In: Kümpel, H.-J., Röhling, H.-G., Steinbach, V. (eds.) GeoHannover 2012: GeoRohstoffe für das 21. Jahrhundert. Hannover, *Schriftenreihe der Deutschen Gesellschaft für Geowissenschaften*, 80. ISBN 978-3-510-49228-2.

Reyer, D., Philipp, S.L. (2012). Heterogeneities of mechanical properties in potential geothermal reservoir rocks of the North German Basin. *Geophysical Research Abstracts*, 14, EGU2012-346.

Reyer, D. & Philipp, S.L. (2013). Applicability of failure criteria and empirical relations of mechanical rock properties from outcrop analogue samples for wellbore stability analyses. AGU Fall Meeting, San Francisco 9-13 December, MR13A-2222.

Reyer, D. & Philipp, S.L. (2013). Applicability of failure criteria and empirical relations of mechanical rock properties from outcrop analogue samples for wellbore stability analyses. In: Philipp, S.L., Acocella, V. (eds.): *Rock Fractures in Geological Processes*, Universitätsdrucke Göttingen, ISBN 978-3-86395-141-2, 70 p., Universitätsverlag Göttingen. 45-48.

Reyer, D. & Philipp, S.L., (2014). Pre-drilling calculation of geomechanical parameters for safe geothermal wells based on outcrop analogue samples. *Geophysical Research Abstracts*, 16, EGU2014-1514.

Reyer, D., Bauer, J.F. & Philipp, S.L. (2009). Infrastruktur und Permeabilität von Störungszonen im Unteren Muschelkalk auf der westlichen Grabenschulter des Leinetalgrabens. In: Geothermische Vereinigung (Hrsg.): *Der Geothermiekongress 2009*. ISBN 978-3-932570-64-3, TF08_Reyer, 10 p.

Reyer, D., Bauer, J.F. & Philipp, S.L. (2010). Structural geological field studies in outcrop analogues of potential fault-related geothermal reservoirs. *Geotectonic Research* 96/01, Special Issue TSK 13 Abstracts.

Reyer, D., Bauer, J.F. & Philipp, S.L. (2010). Architektur und Permeabilität von Störungszonen in Sedimentgesteinen des Norddeutschen Beckens. In:

Geothermische Vereinigung (Hrsg.): *Der Geothermiekongress 2010,* Kongressband CD-Rom. ISBN 978-3-932570-65-0, F1.3_Reyer et al., 9. p.

Reyer, D., Lünsdorf, N.K., Sieck, P. & Philipp, S.L. (2011). Heterogenitäten bohrungsrelevanter Gesteinseigenschaften im Norddeutschen Becken: Geländestudien und Laboranalysen. In: Geothermische Vereinigung (Hrsg.): *Der Geothermiekongress 2011,* Kongressband CD-Rom. 9 p.

Reyer, D., Lünsdorf, N.K., Sieck, P. & Philipp, S.L. (2011). Heterogenities of Rock Properties Relevant to Drilling in the North German Basin. CelleDrilling 2011. The Way Ahead. 12.-13. September, Celle.

Reyer, D., Bauer, J.F. & Philipp, S.L. (2011). Influence of fault zones on fracture systems in sedimentary geothermal reservoir rocks in the North German Basin. – *Geophysical Research Abstracts*, 13, EGU2011-6230.

Reyer, D., Bauer, J.F. & Philipp, S.L. (2011). Fault zone architecture and fracture systems in sedimentary rocks of the North German Basin. *Geophysical Research Abstracts,* 13, EGU2011-6403.

Reyer, D., Vogt, E. & Philipp, S.L. (2014). Empirical relations of geomechanical parameters for while-drilling calculation of uniaxial compressive strengths. CelleDrilling 2014. The Way Ahead - Drilling Modeling, Simulation and Automation. 15.-16. September, Celle.

10.3   Theses

Bauer, J.F. (2010). Infrastruktur und Entwicklung ausgewählter Störungszonen im südlichen Norddeutschen Becken. MSc Thesis, University of Göttingen.

Lim, P.Y. (2011). Stress fields and fracture propagation in geothermal reservoir rocks of the North German Basin. MSc Thesis, University of Göttingen.

Parchwitz, S. (2010). Ein numerischer Ansatz zur Charakterisierung faziesabhängiger Bruchsysteme zur Bestimmung des geothermischen Potentials (Oberer Muschelkalk, Nordost-Deutschland). MSc Thesis, University of Göttingen.

Reyer, D. (2013). Outcrop Analogue Studies of Rocks from the Northwest German Basin for Geothermal Exploration and Exploitation: Fault Zone Structure, Heterogeneous Rock Properties, and Application to Reservoir Conditions. Dissertation, University of Göttingen, 108 p., http://hdl.handle.net/11858/00-1735-0000-0023-98FA-1.

Wong, L.W. (2010). Fluid Transport in Fractured Porous Media – Application to Geothermal Reservoirs in the North German Basin. MSc Thesis, University of Göttingen.

11. References

Abdideh, M. & Fathabadi, M.R. (2013). Analysis of stress field and determination of safe mud window in borehole drilling (case study: SW Iran). *Journal of Petroleum Exploration and Production Technology*. doi: 10.1007/s13202-013-0053-2.

Aguilera, R. (2000). Well test analysis of multi-layered naturally fractured reservoirs. *Journal of Canadian Petroleum Technology,* 39, 31-37.

Agosta, F., Prasad, M. &Aydin, A., (2007). Physical properties of carbonate fault rocks, fucino basin (Central Italy): implications for fault seal in platform carbonates. *Geofluids*, 7, 19-32.

Antonellini, M., Aydin, A. & Pollard, D.D. (1994). Microstructure of deformation bands in porous sandstones at Arches National Park, Utah. *Journal of Structural Geology,* 16, 941-959.

Ashby, M.F. & Jones, D.R.H. (2005). *Engineering Materials 1: An Introduction to Properties, Applicatons and Design.* Elsevier, New York.

Aydin, A. (1978). Small faults formed as deformation bands in sandstone. *Pure and Applied Geophysics, 116*, 913-930.

Baldschuhn, R., Frisch, U. & Kockel, F. (1996). *Geotektonischer Atlas von Nordwest-Deutschland, 1:300.000.* Bundesanstalt für Geowissenschaften und Rohstoffe, Hannover.

Bear, J. (1993). Modelling flow and contaminant transport in fractured rocks. – In: Bear, R.J., Tsang, C.F. & de Marsily (eds): *Flow and Contaminant Transport in Fractured Rocks*, Academic Press, 1-37, New York.

Betz, D., Führer, F., Greiner, G. & Plein, E. (1987). Evolution of the Lower Saxony Basin. *Tectonophysics*, 137, 127-170.

Brenner, S.L. (2003). *Field Studies and Models of Hydrofractures in Heterogeneous Reservoirs*. Dissertation, University of Bergen, Norway.

Caine, J.S., Evans, J.P. & Forster, C.B. (1996). Fault zone architecture and permeability structure. *Geology,* 24, 1025-1028.

de Marsily, G. (1986). *Quantitative Hydrogeology*. Academic Press, New York.

Edlmann, K., Somerville, J.M., Smart, B.G.D., Hamilton, S.A. & Crawford, B.R. (1998). Predicting rock mechanical properties from wireline porosities, SPE/ISRM Eurock 47344.

Faulkner, D.R., Jackson, C.A.L., Lunn, R.J., Schlische, R.W., Shipton, Z.K., Wibberley, C.A.J. & Withjack, M.O. (2010). A review of recent developments concerning the structure, mechanics and fluid flow properties of fault zones. *Journal of Structural Geology,* 32, 1557-1575.

Faulkner, D.R., Mitchell, T.M., Jensen, E. & Cembrano, J. (2011). Scaling of fault damage zones with displacement and the implications for fault growth processes. *Journal of Geophysical Research,* 116, B05403, doi:10.1029/2010JB007788.

Fossen, H. (2010). *Structural Geology*. Cambridge University Press, New York.

Freyburg, E. (1972). Der Untere und Mittlere Buntsandstein SW-Thüringen in seinen gesteins-technischen Eigenschaften. *Berichte der Deutschen Gesellschaft für Geologische Wissenschaften,* 17, 911-919.

Gudmundsson, A. (2000). Active fault zones and groundwater flow. *Geophysical Research Letters,* 27, 2993-2996.

Gudmundsson, A. (2011). *Rock Fractures in Geological Processes*. Cambridge University Press, New York.

Haimson, B.C. & Rummel, F. (1982). Hydrofracturing stress measurements in the Iceland research drilling project drill hole at Reydarfjordur, Iceland. *Journal of Geophysical Research*, 87, 6631-6649.

Hahne, B., Hördt, A., Bartetzko, A., Bozau, E., Ghergut, I., Grinat, M., Holzbecher, E., Paz Carvajal, C.A., Perozo Baptista, N.R., Philipp S.L., Räuschel, H., Reyer, D., Schaumann, G., van Berk, W., Thomas, R. (in prep.). A common set of benchmark models and their use for multi-disciplinary investigations of deep geothermal reservoirs in the North German Basin.

Heidbach, O., Tingay, M., Barth, A., Reinecker, J., Kurfeß, D., & Müller, B. (2008). The World Stress Map database release 2008. doi:10.1594/GFZ.WSM.Rel2008.

Heuze, F. (1980). Scale effects in the determination of rock mass strength and deformability. *Rock Mechanics and Rock Engineering*, 12, 167-192.

Hudson, J.A. & Harrison, J.P. (1997). *Engineering Rock Mechanics: an Introduction to the Principles.* Pergamon, Oxford.

Huenges, E. (ed.). (2011). Geothermal Energy Systems: Exploration, Development, and Utilization, Wiley, Weinheim.

ISRM (2007). The Complete ISRM Suggested Methods for Rock Characterization, Testing and Monitoring: 1974-2006. Suggested Methods Prepared by the Commission on Testing Methods,

International Society for Rock Mechanics, R. Ulusay & J. A. Hudson (eds.), Compilation Arranged by the ISRM Turkish National Group, Ankara, Turkey.

Jaeger, J.C., Cook, N.G.W. & Zimmerman, R.W. (2007). *Fundamentals of Rock Mechanics.* 4th edn. Blackwell Publishing, Malden.

Johansen, T.E.S., Fossen, H. & Kluge, R. (2005). The impact of syn-faulting porosity reduction on damage zone architecture in porous sandstone: an outcrop example from the Moab Fault, Utah. *Journal of Structural Geology,* 27, 1469-1485.

Lee, C.H. & Farmer, I.W. (1993). *Fluid Flow in Discontinuous Rocks.* Chapman and Hall, London.

Li, S., George, J. & Purdy, C. (2012). Pore-pressure and wellbore-stability prediction to increase drilling efficiency. *Journal of Petroleum Technology,* 64, 99-101.

McBride, E.F. (1963). A classification of common sandstones. *Journal of Sedimentary Petrology,* 33, 664-669.

McLean, M.R., Addis, M.A. (1990). Wellbore stability: The effect of strength criteria on mud weight recommendations. SPE 20405-MS, SPE Annual Technical Conference and Exhibition, New Orleans, USA.

Meier, S., Bauer, J.F. & Philipp, S.L. (2015). Fault zone characteristics, fracture systems and permeability implications of Middle Triassic Muschelkalk in Southwest Germany. *Journal of Structural Geology 70, 170-189.* doi: 10.1016/j.jsg.2014.12.005

Meneses Rioseco, E., Löhken, J., Schellschmidt, R., Tischner, T. (2013). 3-D geomechanical modelling of the stress field in the North German Basin: Case study Genesys-borehole GT1 in Hanover Groß-Buchholz. *Proceedings, Thirty-Eighth Workshop on Geothermal Reservoir Engineering* Stanford University, Stanford, California, February 11-13, 2013, SGP-TR-198.

Moeck, I., Schandelmeier, H. and Holl, H.-G. (2008). The stress regime in a Rotliegend reservoir of the Northeast German Basin. *International Journal of Earth Sciences (Geologische Rundschau).* doi 10.1007/s00531-008-0316-1.

Nabaei, M. & Shahbazi, K. (2012). A new approach for predrilling the unconfined rock compressive strength prediction. *Petroleum Science and Technology*, 30, 350-359.

NIBIS Kartenserver (2012). Bohrungen und Profilbohrungen. LBEG, Hannover.

Odling, N.E., Gillespie, P., Bourgine, B., Castaing, C., Chiles, J.P., Christensen, N.P., Fillion, E., Genter, A., Olsen, C., Thrane, L., Trice, R., Aarseth, E., Walsh, J.J. & Watterson, J. (1999). Variations in fracture system geometry and their implications for fluid flow in fractured hydrocarbon reservoirs. *Petroleum Geoscience,* 5, 373-384.

Paterson, M.S. (1978). Experimental Rock Deformation: The Brittle Field. Springer, Berlin.

Peska, P., Zoback, M.D. (1995). Compressive and tensile failure of inclined well bores and determination of in situ stress and rockstrength. *Journal of Geophysical Research*, 100(B7), 12,791–12,811.

Philipp, S.L. (2007). Bedeutung von Störungszonen und Bruchsystemen für die Permeabilität: Vergleich natürlicher Paläoreservoire mit stimulierten geothermischen Reservoiren. In: Geothermiekongress 2007, Bochum, Conference Proceedings, pp. 224-230.

Philipp, S.L., Afşar, F. & Gudmundsson, A. (2013). Effects of mechanical layering on hydrofracture emplacement and fluid transport in reservoirs. *Frontiers in Earth Science,* 1, 1-19. doi: 10.3389/feart.2013.00004.

Priest, S.D. (1993). *Discontinuity Analysis for Rock Engineering.* Chapman and Hall, London.

Rawling, G.C., Goodwin, L.B. & Wilson, J.L. (2001). Internal architecture, permeability structure, and hydrologic significance of contrasting fault-zone types. *Geology*, 29, 43-46.

Rider, M. & Kennedy, M. (2011). *The Geological Interpretation of Well Logs.* Rider-French Consulting.

Röckel, T. & Lempp, C. (2003). Der Spannungszustand im Norddeutschen Becken. *Erdöl Erdgas Kohle*, 119, 73-80.

Schäfer, F., Hesshaus, A., Hunze, S., Jatho, R., Luppold, F.W., Orilski, J., Pletsch, T., Röhling, H.G., Tischner, T. & Wonik, T. (2012). Summarized report of geothermal well Groß Buchholz Gt1. *Erdöl Erdgas Kohle* 128, 20-26.

Settari, A. & Walters, D.A. (2001). Advances in coupled geomechanical and reservoir modeling with applications to reservoir compaction. SPE 74142, 335-342.

Sharma, P.K. & Singh, T.N. (2008). A correlation between P-wave velocity, impact strength index, slake durability index and uniaxial compressive strength. *Bulletin of Engineering Geology and Environment*, 67, 17-22.

Stober, I. & Bucher, K. (2014). *Geothermie*, 2nd edn. Springer.

Thuro, K. (1997). Drillability prediction: geological influences in hard rock drill and blast tunneling. *Geologische Rundscha,* 86, 426-438.

Tondi, E., Antonellini, M., Aydin, A., Marchegiani, L. & Cello, G. (2006). The role of deformation bands, stylolites and sheared stylolites in fault development in carbonate grainstones of Majella Mountain, Italy. *Journal of Structural Geology*, 28, 376-391.

Usdowski, H.E. (1962). Die Entstehung der kalkoolithischen Fazies des norddeutschen Unteren Buntsandsteins. *Beiträge zur Mineralogie und Petrographie,* 8, 141-179.

Vogt, E., Reyer, D., Schulze, K. C., Bartetzko, A., & Wonik, T. (2012). Modeling of geomechanical parameters required for safe drilling of geothermal wells in the North German Basin, Celle Drilling, Celle, Germany.

Walter, R. (2007). *Geologie von Mitteleuropa.* 7th edn. Schweizerbarth, Stuttgart.

Walsh, J.B. (1965). The effect of cracks on the uniaxial elastic compression of rocks. *Journal of Geophysical Research*, 70, 399-411.

Wooldridge, J.M. (2009). *Introductory Econometrics: A Modern Approach.* 4th ed. Mason: South-Western, Cengage Learning; 2009.

Zeynali, M.E. (2012). Mechanical and physico-chemical aspects of wellbore stability during drilling operations. *Journal of Petroleum Science and Engineering,* 82-83, 120-124.

Zhang, L. (2005). Engineering Properties of Rocks. *Geoengineering Book Series 4*, Elsevier, London.

Zhang, X. & Sanderson, D.J. (1996). Numerical modelling of the effects of fault slip on fluid flow around extensional faults. *Journal of Structural Geology*, 18, 109-119.

Zoback, M.D. (2007). Reservoir Geomechanics. Cambridge University Press, New York.

Zoback, M.D., Barton, C.A., Brudy, M., Castillo, D.A., Finkbeiner, T., Grollimund, B.R., Moos, D.B., Peska, P., Ward, C.D. and Wiprut, D.J. (2003). Determination of stress orientation and magnitude in deep wells. *International Journal of Rock Mechanics and Mining Sciences*, 40, 1049–1076.

G4: Diagnostic methods for the characterization of stimulated geothermal reservoirs

Daniel Fielitz[1]*, Margarete Vasterling, Ulrich Wegler

Federal Institute for Geosciences and Natural Resources, Stilleweg 2, 30655 Hannover,

Germany

Abstract

Hydraulically induced microseismicity and ambient seismic noise are used to study elastic and anelastic properties of enhanced geothermal systems (EGS) in the high-frequency range (1 - 72 Hz). Seismogram envelope inversion and passive image interferometry are considered regarding their potential for the field of reservoir characterization.

Firstly, seismogram envelopes of induced microearthquakes are jointly inverted for structural parameters of the propagation medium (intrinsic absorption and heterogeneity), source parameters and site amplification factors. Modeling of synthetic envelopes is based on radiative transfer theory (RTT). To speed up inversion, an analytical solution of the radiative transfer equation for a 3D isotropic scattering medium is implemented. In order to compensate for the actual anisotropic earth, a smoothing algorithm is applied to introduce envelope broadening and peak delay. Full S-wave envelopes are inverted in 12 overlapping frequency bands with center frequencies between 1.5 and 72 Hz in order to reveal the frequency-dependence of the inversion parameters. From the inversion, we infer average values of the scattering and the intrinsic quality factors Q_s and Q_i, in particular for the rarely probed frequency range between 30 - 70 Hz. From further analysis of the inverted source energy spectrum we infer estimates of seismic moment, corner frequency and magnitude of the induced earthquake. Finally, evaluated site amplification factors reflect local geology of the near-recording site superimposed by source radiation characteristics.

Secondly, passive image interferometry is considered to monitor seismic velocity changes associated with fluid injection into the geothermal reservoir based on continuous records of ambient seismic noise. Synthetic Green's functions are calculated from cross-correlations of noise recordings at various station pairs. By using surface and near-surface borehole stations distinct changes in seismic velocity associated with particular injection periods or the occurrence of larger induced events ($M_w = 1.0$) could not be identified. Possible reasons for the failure of PII are in the case of KTB the insufficient monitoring period before and after the stimulation and in case of GeneSys the difficult noise conditions due to the location in an urban environment. Furthermore, anticipated velocity changes due to fluid injection in a deep geothermal reservoir might be too small to be registered with a surface monitoring network.

---

[1] Corresponding Author: daniel.fielitz@bgr.de

1. Introduction

The goal of the collaborative research program "Geothermal Energy and High Performance Drilling – gebo" is to carry out research and survey new concepts allowing an improved economic efficiency of geothermal energy generation from deep geological formations. With its focus on innovative aspects of the development and characterization of enhanced geothermal systems (EGS) the primary goal of the project G4 *Diagnostic Methods for the Characterization of Enhanced Geothermal Reservoirs* was to evaluate the potential of existing, seismological techniques regarding their application to the field of geothermal reservoir characterization. Generally, developing an EGS hydraulic stimulation is employed to generate pathways that enable fluid circulation within the geothermal reservoir. The injection of fluids can induce or trigger earthquakes due to several possible mechanisms, e.g. pore pressure increase or volume change. Such induced seismicity related to operating geothermal fields or EGS, respectively, has been reported worldwide. Seismic monitoring, using local networks, accounts for a surveillance analysis, since the observation of a large number of small events allows for estimating the probability for the occurrence of larger events. Furthermore, studies on induced seismicity have collectively shown that data, obtained from microseismic monitoring, has the ability to provide highly detailed information about the reservoir that no other method can provide (House and Flores, 2002).

Surveying new concepts within the research project G4 is motivated by the fact that high-frequency seismograms (>1 Hz) contain information on the type of seismic source, the near-recording site and traversed medium, summarized as source, site, and path effect. The path effect combines the influences of elastic and anelastic properties of the propagation medium on the seismic wavefield along the source-receiver path. Within the scope of project G4 the monitoring of hydraulically induced microseismic events has been investigated in terms of its potential to quantify seismic attenuation, in particular the individual contributions of scattering and intrinsic attenuation, in the considered geothermal reservoir. Attenuation properties might be used to complement other physical measurements for characterizing rock properties. Different sensitivity of attenuation to attributes, such as lithology, fluid saturation, permeability or porosity, makes the estimation of attenuation highly valuable for various disciplines, e.g. mining or geothermal exploration. In addition, physical relations quantifying seismic attenuation are needed for seismic hazard analysis to correctly predict the distance decay of ground motions. Besides the analysis of induced seismicity, the monitoring of ambient seismic noise before, during and after the injection of fluids might be used to evaluate changes in the elastic properties of the reservoir, in particular the temporal variation

132

of the seismic velocity, and thus enable us to possibly predict the temporal development of the geothermal reservoir.

The report is organized as follows. In Section 2 the hydraulic stimulation experiments and data obtained at the German Continental Deep Drilling (KTB) site and at the GeneSys Hannover site are introduced. Based on the type of considered data and the applied seismological technique the work in G4 is separated into two main research sections:

(A) Attenuation & Heterogeneity:

Inversion of seismogram envelopes

Hydraulically induced seismicity

(B) Temporal variation:

Passive image interferometry

Ambient seismic noise

In section 3 the work and results related to the research focus (A) are presented. The methodology of envelope inversion, including data preparation issues, the modelling of synthetic envelopes and the considered inversion scheme, are described in Section 3a-c. Results for inverted attenuation parameters, source strength, and site amplification factors are presented in Section 3d-f.

The procedure of passive image interferometry used to evaluate the temporal variation of the seismic velocity, including the general methodology and data preparation issues is introduced in Section 4a and 4b. Results for the KTB and the GeneSys site are presented separately in Section 4c and 4d. Finally, the overall results of the project G4 and individual findings of the two different research areas are summarized and discussed in Section 5.

2. Data from hydraulic stimulation

The present report deals with the application of seismological techniques to data from geothermal regions, and in particular from operating enhanced geothermal systems (EGS). Generally, hydraulic stimulation can induce or trigger seismicity due to several possible mechanisms, such as pore pressure increase or volume change. Seismicity related to operating geothermal fields and EGS has been reported worldwide, e.g. The Geysers (USA), Cooper Basin (Australia) or Soultz-sous-Forêts (France). Majer *et al.* (2007) review the different mechanisms that have been hypothesized to explain induced seismicity and several case studies.

The overall objective of the project G4 was the application of diagnostic, seismological methods to data recorded in typical geologies of Lower Saxony. As qualified microseismic data sets acquired in Lower Saxony were not available during the first phase of gebo, seismological methods were tested with a passive, microseismic data set from a hydraulic fracturing treatment in crystalline rocks, in particular from the German Continental Deep

Drilling site (KTB). We treat the KTB site as an analogy for an EGS since fundamental enhancements associated with an EGS were completed at the time of the considered hydraulic experiment. These enhancements come from 1) deep drilling so that sufficiently high temperatures are reached; 2) creating enough permeability via hydraulic stimulation so that fluid can be flushed at significant rates through the hot-dry rock (Jeanloz and Stone, 2013). In the second phase of the project, it was planned to analyze a microseismic data set acquired in Lower Saxony, in particular from the GeneSys (*Generated Geothermal System*) site in Hannover.

2.1 KTB

The KTB area is situated in the Southeastern part of Germany (Figure 1a). Emmermann and Lauterjung (1997) give an overview of the KTB project. This large-scale interdisciplinary project aimed to achieve a better understanding of the structure and evolution of the continental crust in central Europe. For this purpose, two boreholes, 200 m apart, have been drilled, which reach to depths of about 4000 m for the pilot hole (*Vorbohrung* or VB) and 9000 m for the main hole (*Hauptbohrung* or HB). The deep drilling was accompanied by a large suite of borehole logs measuring physical and chemical properties. After completing drilling and logging activities, the two boreholes were used as deep crustal laboratories for *in situ* scientific and technical investigations including several fluid injection experiments. In 1994, a first, short-term (48 hours) fluid injection experiment was conducted in order to study fluid transport processes and crustal stress at the KTB (Zoback and Harjes 1997), named hereafter KTB1994. This initial experiment was followed by a long-term (60 days) experiment in 2000 (Baisch et al. 2002), named hereafter KTB2000, trying to enable fluid migration away from the injection interval. Another period of injection experiments started in 2002 addressing the special, hydraulic features of fault systems (Shapiro et al. 2006). The present study focuses on data recorded with a temporary seismic network installed during the KTB2000 experiment. Over a period from August to November 2000, a total of 4000 m³ of fresh water was injected at a flow rate of 0.5 - 1.2 l/s directly into the well head of HB. Due to some unrecognized leakages in the borehole casing, seismicity occurred at distinct depth levels at approx. 3-km, 5-km and 9-km depths. Three-component data recorded with a 37-station surface network surrounding the main borehole (Figure 1a) were processed. All surface stations were equipped with Mark L4-3c seismometers recording continuously at 200 Hz sampling rate on a PDAS-100 data logger. In addition to the surface network, seismicity was recorded by a borehole tool within the VB. However, in practice, surface networks monitoring microseismic activity have established as standard add-on feature in conjunction with geothermal installations, whereas deep borehole data are only rarely available. Thus, we restrict the present analysis to the processing of data recorded with the surface network.
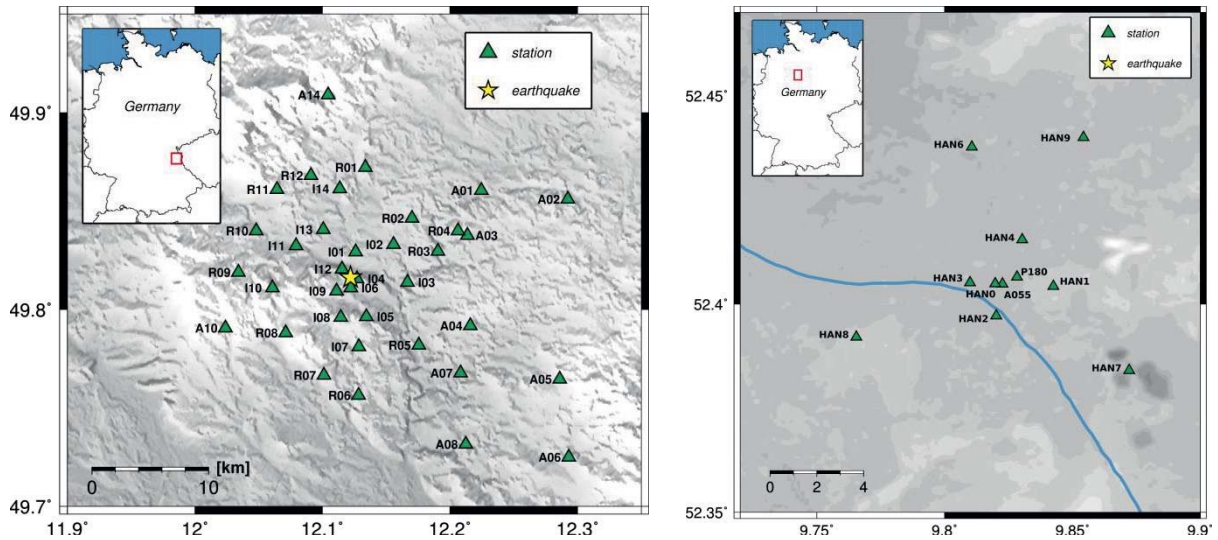
Figure 1: *Local seismic network: (a) at the KTB drilling site (Southern Germany), and (b) at the GeneSys Hannover site (North German Basin). Note that the location of the induced earthquake in (a) denotes also the location of HB.*

A total of 261 events could be identified on more than four stations on the surface (Baisch et al. 2002). In order to ensure sufficient station coverage, only the four strongest, induced events, occurring within a period from 01 October to 16 October, having maximum magnitude $M_w = 1.0$ are considered (see Fig. 2 as an example of these events). For simplicity reasons, all earthquakes are assumed to be horizontally centered at the position of the main borehole. This assumption is confirmed by the fact that Bohnhoff et al. (2004) specified the maximum offsets with respect to HB of all induced events to be below 500 m. Focal depth and moment magnitude M_w of considered microseismic events, as provided by Kueperkoch (2003), are listed in Table 1.

Table 1: *List of considered microearthquakes induced during the KTB2000 experiment. Focal depths and moment magnitudes M_w are provided by Kueperkoch (2003). M_w was estimated after Hanks and Kanamori (1979).*

N°	Date	Time	Depth [km]	M_w
e016.275	2000/10/01	03:41:30.7	5.4	0.9
e027.275	2000/10/01	05:00:25.9	5.3	0.9
e103.275	2000/10/01	15:46:35.8	9.0	0.9
e048.290	2000/10/16	04:20:49.4	5.3	1.0

2.2 GeneSys

The GeneSys project was initiated as a demonstration project at the GEOZENTRUM Hannover in cooperation of the BGR, LIAG and LBEG. It was intended to investigate concepts that allow the usage of the widely spread low permeable sediments in the North German Basin for geothermal energy extraction and finally to supply heat for the complex buildings of the GEOZENTRUM Hannover (Orzol et al. 2005). For this reason a single borehole was drilled down to a depth of 4 km. In May 2011, during a massive hydraulic stimulation treatment a total of 20,000 m^3 of fresh water was injected at a depth of 3,700 m. The injection rate was as high as 90 l/s with a maximum downhole pressure of 470 bar (Bischoff et al. 2012). As the geothermal test site is located in an urban area, the injection was paused during night time for noise protection. For monitoring purposes a local network (Fig. 1b) was installed consisting of 12 stations in two circles around the deep drilling hole. At the outer circle, with a radius of 4 km, four 1 Hz LE-3D-lite seismometers were installed at the surface. The inner circle, having a radius of 1 km from the borehole, consists of four borehole stations with 4.5 Hz geophones being installed at depths of approx. 100 m. In the center, very close to the injection hole, two more borehole stations (100 m and 180 m) and two surface stations were installed. All data were recorded at a sampling rate of 250 Hz taking into account the high-frequency energy radiation of shallow induced earthquakes. Despite the dense network, having a detection level of M = 0.5 (Bischoff et al. 2012), no seismic events from the reservoir could be registered. Thus, standard seismological analyses cannot be used to get information on the reservoir's orientation, extend, or temporal development.

3. Envelope inversion

Envelope inversion pursues a stochastic, time-frequency approach to quantify the source, site and path effect based on a physical model of the energy propagation of seismic S-waves in a random medium with statistically distributed heterogeneities. The inversion is based on fitting a theoretical curve to the observed energy density E_{obs} in a particular frequency band of the recorded microseismic data. This approach is advantageous as it takes into account the portions of intrinsic and scattering attenuation, together making up the path effect, separately. In application to real data, the squared velocity seismogram envelopes (MS envelope), which are linearly proportional to the energy density of the seismic wave, are considered. Modelling of synthetic envelopes is based on radiative transfer theory (RTT). In subsections 3.1 to 3.3, the key elements of the proposed inversion methodology are described. Subsequently, the results, obtained for the evaluation of the path effect (3.4), the source (3.5) and site effect (3.6), are presented separately.

3.1 Data preparation

The microseismic records (Fig. 2) go through a filterbank to separate the data into appropriate frequency bands. The filterbank is designed with 50 percent overlap in order to map the frequency dependence of the inversion parameters more reliably. From the bandpassed velocity seismograms $\dot{u}(t,r)$ the observed energy density (Fig. 2) is obtained using:

$$E_{obs}(f,t,r) = \rho_0 \frac{\dot{u}^2(f,t,r) + \mathcal{H}^2\big(\dot{u}(f,t,r)\big)}{2} \qquad (1)$$

The Hilbert transform H is used to generate smooth envelopes, more appropriate for comparison with synthetic curves. The envelope is windowed from the *S*-wave onset to the observable end of the coda, defined by the signal-to-noise ratio (SNR). SNR is calculated relative to the presignal noise-level (2s before the *P*-wave onset). To accommodate the particular characteristics of microseismic data, envelope sections are selected according to the following criteria:

- Maximum SNR (ballistic peak) ≥ 16,
- Minimum SNR (coda end) ≥ 6,
- Window length (l_w) of invertible envelope sections ≥ 10 s,
- Noise level at individual stations is less than 2 times the mean noise level, calculated as network mean (per frequency band / per event).

3.2 Envelope modelling

The synthetic energy density E_{syn} at time *t* and distance *r* from the source is parameterized as follows:

$$E_{syn}(f,t,r) = 4W(f)R_i(f)G(f,t,r)e^{-b(f)\cdot t} \qquad (2)$$

where $W(f)$ is a source term corresponding to the total radiated energy in a particular frequency band and $R_i(f)$ the site amplification factor at the *i*th station.
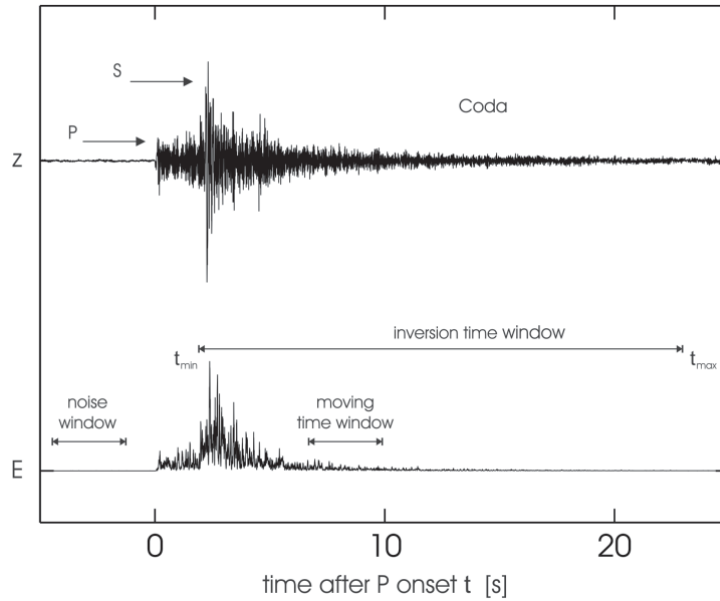
Figure 2: Top panel: unfiltered raw waveform example (z-component) of a fluid-induced microseismic event. Bottom panel: associated seismogram envelope in the [32 – 64] Hz frequency band (centered at $f_c = 48\ Hz$) with different (active) time windows used in the inversion.

The term $G(f,t,r)$ represents the effective energy density Green's function and governs the complex redistribution of the radiated energy due to multiple scattering. The inherent parameter that controls the scattering strength is the transport scattering coefficient $g^*(f)$. The intrinsic attenuation is accounted for by an exponential decay term with the absorption parameter $b(f)$. The forward modeling routine, which is basically the correct prediction of the Green's function $G(f,t,r)$, is significantly speed up by implementing an analytical approximation for $G(f,t,r)$. Paasschens (1997) provided an approximate solution by interpolating between the exact solution in 2D and 4D yielding:

$$G(t,\mathbf{r}) \simeq \frac{e^{-v_0 g_0 t}}{4\pi v_0 r^2}\delta(t - r/v_0) + \frac{(1 - r^2/(v_0^2 t^2))^{1/8}}{(4\pi v_0 t/(3g_0))^{3/2}}$$
$$\times\ e^{-v_0 g_0 t} K\left(v_0 g_0 t\left[1 - \frac{r^2}{v_0^2 t^2}\right]^{3/4}\right)H(v_0 t - r) \tag{3}$$

where $K(x) \simeq e^x\sqrt{1 + 2.026/x}$, and H is the step function. It is a good approximation to the exact solution provided by Zeng et al. (1991). The relative error is around 2 ~ 3 %. By using the transient part of the seismogram (direct wave), we cannot ignore anisotropic scattering effects. We use a smoothing algorithm to introduce moderate envelope broadening and peak delay of the maximum amplitude, which are usually observed related to the actual amount of anisotropy. This approach is valid for a simple model, assuming isotropic sources and isotropic scattering of S-waves in a half-space. Due to conversion scattering S-waves rapidly

become dominant in the later part of the seismogram, the so-called seismic coda, only the prediction of *S*-wave attenuation is possible using this simple approach.

3.3 Inversion scheme

The inversion is divided into two sections, the actual least-square inversion and the quantification of the site amplification factors. Firstly, the scattering coefficient $g^*(f)$ and the absorption parameter $b(f)$ as well as the source term $W(f)$ are determined without considering the site effect; implicitly assuming R_i to be one. This primary inversion combines a 1D grid search for $g^*(f_c)$ and a linear inversion for $b(f_c)$ and $W(f_c)$ with f_c being the center frequency of the evaluated frequency band. For a particular value of g^*, Green's functions are computed for all preselected stations and then smoothed. In the next step, we substitute E_{obs} for E_{syn} in eq. (2) and partly linearize the inversion problem by taking its logarithm:

$$\ln\left(\frac{E_{obs}(f_c,t,r_i)}{G(f_c,t,r_i)}\right) = \ln\left(4W(f_c)\right) - b(f_c)t \tag{4}$$

The corresponding values for the absorption parameter $b(f_c)$ and the source term $W(f_c)$ are obtained from a simple least-square method. Practically, the estimation is done by fitting a linear curve to the left hand side of eq. (4) as function of time (Fig. 3b). The problem is solved for a variety of g^* (but all stations simultaneously), and g^* is found by a 1D grid search (Fig. 3c) that minimizes the logarithmic misfit:

$$\epsilon = \sum_{i=1}^{N} \sum_{j=start_i}^{end_i} \left[\log\left(\frac{E_{obs}(f_c,t_j,r_i)}{E_{syn}(f_c,t_j,r_i)}\right)\right] \tag{5}$$
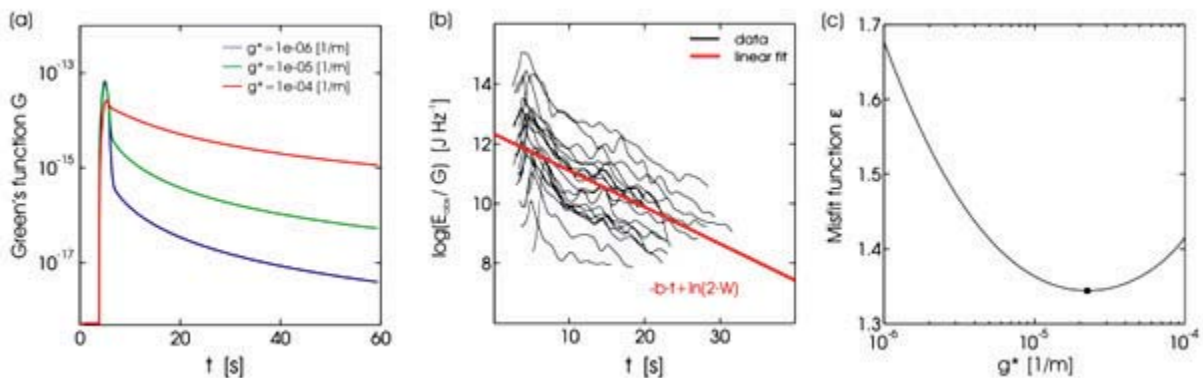
Figure 3: *Inversion strategy: (a) Modeling of a suite of synthetic Green's functions for a probed range of g^*, (b) Linear fit to estimate $W(f)$ and $b(f)$ according to eq. (4), (c) Misfit function ϵ versus g^*.*

With the corresponding parameters of the best-fitting model (g^*, b, W), obtained in the primary inversion, an evaluation of the site response relative to the network mean $(R_i = 1)$ becomes possible. Site amplification factor at the ith station R_i is calculated as the logarithmic average of the difference between the observed and synthetic envelopes in a frequency band with f_c:

$$\ln\left(R_i(f_c)\right) = \frac{1}{N_j} \sum_{j=start_i}^{end_i} \ln\left(\frac{E_{obs}\left(f_c, r_i, t_j\right)}{E_{syn}\left(f_c, r_i, t_j\right)}\right) \tag{6}$$

where N_j is the number of samples in the considered time window. Generally, site amplification factors help to improve the level of fitting between synthetic and observed envelopes (Fig. 4). Any remaining differences are attributed to the simple modeling approach.
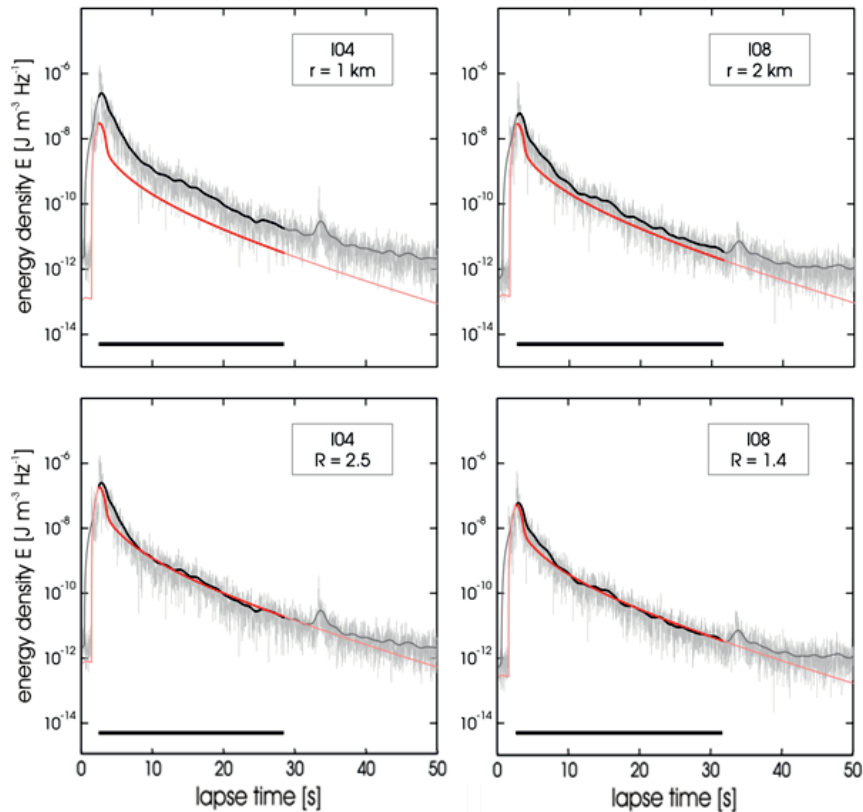
Figure 4: *Model fit for the induced event e013.275 in the 32 – 64 Hz (f_c = 48 Hz) frequency band. Grey curves: observed envelopes; black curves: smoothed envelopes; red curves: synthetic envelopes; black bars (at the bottom of each plot): inversion time window. Top Panel: without consideration of site effect; Lower Panel: site corrected.*

Finally, considering R_i, the estimation of b and W in the primary inversion becomes more plausible (Fig. 5).
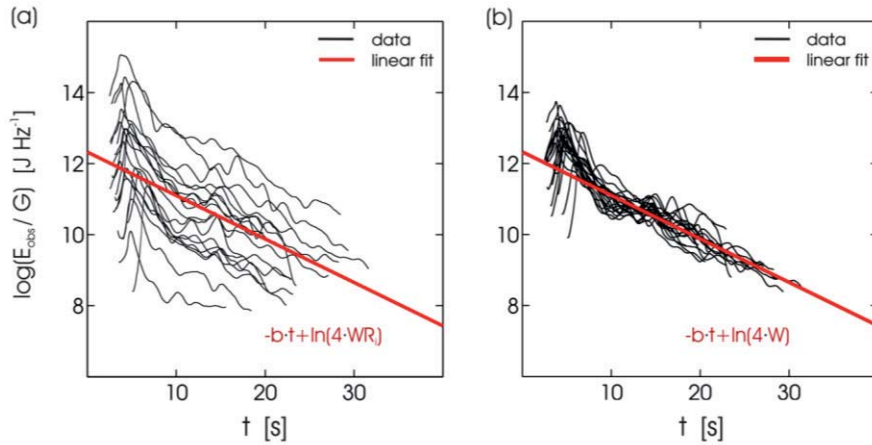
Figure 5: *Linear fitting (according to eq. 4) to obtain appropriate values for b and W: (a) without and (b) with consideration of site response R_i.*

3.4 Attenuation parameters

Assuming a homogeneous half-space model and spatial averaging, our attenuation estimates represent bulk quantities averaged over the probed subsurface. The area of investigation is roughly confined by the focal depth and the dimensions of the receiver network. Therefore, lateral variations and/or depth dependency in the structural parameters are implicitly neglected. It is known that low-energy events are high-frequency sources. Furthermore, monitoring of induced seismicity is commonly accomplished by a local seismic network. Due to the short epicentral distances of the receivers (< 20 km), most of the radiated energy remains in the higher frequency bands. As a consequence of these facts, inversion only provides robust and reliable results for the higher frequency bands ($f_c \geq 6\,\mathrm{Hz}$).

From the inversion, we infer average values of the transport scattering coefficient $\mathbf{g}^*$ and the intrinsic absorption parameter b as well as corresponding quality factors Q_s^{-1} and Q_i^{-1}. Figs 6a and 6b show $\mathbf{g}^*$ and Q_i^{-1} as a function of frequency f. Small grey dots indicate results from evaluation of individual events. Black squares with error bars denote the logarithmic average of the four individual measurements together with their 1σ-confidence limit (σ–standard deviation). The overall scatter of individual results is due to the uncertainties of the measurements. The larger scatter towards the low-frequency limit is most likely to be caused by the decreasing length of l_w, as well as by a smaller number of selected stations. To compare intrinsic and scattering attenuation in the KTB region the corresponding quality factors are calculated according to:

$$Q_i^{-1} = \frac{b}{2\pi f} \tag{7}$$

$$Q_s^{-1} = \frac{g^* v_0}{2\pi f} \tag{8}$$

$$Q_t^{-1} = Q_i^{-1} + Q_s^{-1} \tag{9}$$

Within the evaluated high-frequency range we observe a frequency dependence of the attenuation parameters. Assuming a power-law form of $y = y_0 \cdot f^n$ to fit the attenuation values in a least square sense, and giving each data point its proper amount of influence (inverse of σ^2) over the parameter estimates, we find:

$$g^* = 7 \times 10^{-4} \cdot \left(\frac{f}{\text{Hz}}\right)^{0.7} \, [\text{km}^{-1}] \tag{10}$$

$$b = 4 \times 10^{-2} \cdot \left(\frac{f}{\text{Hz}}\right)^{0.3} \, [\text{s}^{-1}] \tag{11}$$

$$Q_i^{-1} = 6 \times 10^{-3} \cdot \left(\frac{f}{\text{Hz}}\right)^{-0.7} \tag{12}$$

$$Q_s^{-1} = 4 \times 10^{-4} \cdot \left(\frac{f}{\text{Hz}}\right)^{-0.3} \tag{13}$$

Intrinsic absorption is the dominant cause of attenuation in the evaluated frequency range from 6–72 Hz. The intrinsic quality factor is at least one magnitude smaller than the corresponding one for the scattering attenuation (Fig. 6c), while both approach similar values towards the high-frequency limit. Our results feature low-to-moderate scattering and moderate-to-high intrinsic attenuation as compared to estimates from different regions worldwide (Table A1 and A2). Due to the analogy between high-enthalpy geothermal regions and volcanic areas, our results are compared to attenuation estimates from studying the volcanoes Mt. Fuji (Japan) by Chung et al. (2009), Etna (Italy) by del Pezzo et al. (1995) and Kilauea (Hawaii, USA) by Mayeda et al. (1992) as well as the Wakayama earthquake swarm (Japan) by Matsunami and Nakamura (2004) . Generally, volcanic regions are characterized by a large amount of scattering attenuation. The Q_s^{-1}-values exceed all other estimates by at least one order of magnitude. This supports the view that an EGS tends to be characterized by crystalline rocks with a low ratio of natural cracks. In contrast, volcanic areas are known to be composed of very heterogeneous materials. The KTB estimates fit best to results obtained from moderately tectonically active regions, for example from the Friuli region (northern Italy, Bianco et al. 2005). For the intrinsic attenuation (see Table A2), there is no clear distinction between results from volcanic and non-volcanic regions. Nevertheless, the Q_i^{-1}-estimates for the KTB are among the highest reported values worldwide. Moreover, the apparent attenuation (Q_t^{-1}) might be compared to values independently estimated with the spectral ratio technique (Fig. 6d). Jia (1996) provided frequency-dependent attenuation estimates using borehole data of the KTB1994 experiment. Unlike the present study, time windows of 0.1 s lengths were considered solely including the transient part of the S-wave.

Furthermore, the frequency range of the borehole tool was limited to an interval between 30 Hz and 200 Hz. Although different techniques, disparate parts of the *S*-wave seismogram, and varying source-receiver distances (borehole or surface) are used, almost identical attenuation models are derived from both KTB1994 and KTB2000 experimental data with mean deviations in the order of 3 – 5 %.
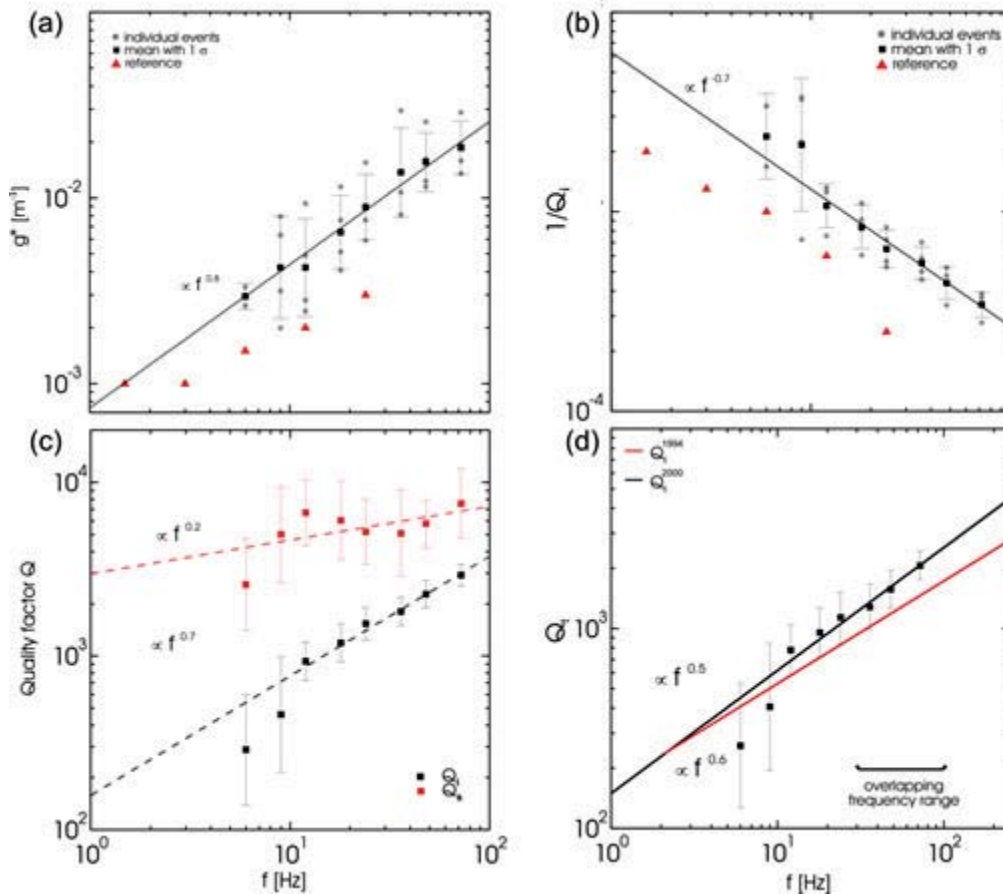

Figure 6: *Results for (a) the scattering coefficient g*, (b) the absorption parameter b, (c) the corresponding quality factor of intrinsic and scattering attenuation Q_i^{-1}, Q_s^{-1}, and the quality factor for the total attenuation Q_t^{-1}. Grey dots: results from evaluation of individual events; black squares with error bars: logarithmic mean with 1sig-confidence limit. Solid lines indicate power-law fits. Q_t^{2000} and $\mathbf{Q}_t^{1994}$ denote the total attenuation obtained from evaluation of data from the KTB2000 and KTB1994 experiment, provided by Jia (1996).*

Finally, from the frequency dependence of the transport scattering coefficient g^*, based on approximations for different types of random media provided by Przybilla et al. (2009), it can be inferred that a von Karman-type of random medium with a Hurst exponent of $\kappa = 0.11$ is a good model for representing the fractured subsurface at the KTB. The fractal distribution of scatterers agrees well with results derived from independent analysis of acoustic logs (Holliger 1996).

3.5 Source parameters

By measuring the source energy at various frequencies we obtain the source energy spectrum $W(\omega)$ of radiated S-waves. In order to further evaluate the energy spectrum $W(\omega)$ in terms of source parameters, such as seismic moment M_0 and corner frequency f_0, we assume the particle motion to be caused by a double couple and an observation in the far field. By integrating the energy-flux density given by Sato and Fehler (1998, eq. 6.1) for S-waves over the surface of a sphere and time, we get a theoretical expression for the S-wave source energy spectrum:

$$W(\omega) = \frac{\omega^4 |M(\omega)|^2}{10\pi\rho_0 v_0{}^5} \qquad (14)$$

where v_0, ρ_0 and $M(\omega)$ denote the mean S-wave velocity, mean density and the Fourier transform of the seismic moment time function, respectively. Moreover, the S-wave energy in a frequency band of width Δf and central frequency f_c is $W(2\pi f_c) \cdot \Delta f$. Thus, our inverted source energy spectrum $W(\omega)$ has to be normalized by the corresponding Δf before further analysis. From eq. (14) we obtain the source displacement spectrum $\omega|M(\omega)|$, which is the general basis for an objective estimation of source parameters. Seismic source theory predicts that the source displacement spectrum is flat at low frequencies and decays in inverse proportion to some power of frequency beyond a corner frequency (Masuda and Suzuzki, 1982). The considered functional form which characterizes the above spectral features is:

$$\omega|M^{th}(\omega)| = \frac{M_o}{1 + \left(f/f_0\right)^2} \qquad (15)$$

As aforementioned the principal inversion did not yield reliable results for the lower frequency bands. Thus, a correct prediction of the low-frequency plateau, corresponding to seismic moment M_0, is difficult based on the original source energy spectrum. We propose a second inversion for the source energy $W(\omega)$, only, using the estimated power-law fits for the transport scattering coefficient g^* and the absorption parameter b (eq. 10–11). Reformulation of eq. (2) yields:

$$W_k(f_c) = \frac{1}{N_j} \sum_{j=start_i}^{end_i} \frac{E_{obs}(t, r_k, f_c)}{4 \cdot \Delta f \cdot G(t, r_k, g^*(f_c))} e^{b(f_c) \cdot t} \qquad (16)$$

144

$start_i$ and end_i correspond to the indices of the bounds of the inversion time window at the kth station, whereas N_j denotes the number of samples. The final value of the source energy spectrum in the corresponding frequency band $W(f_c)$ is obtained by averaging over all considered stations.

To invert the obtained source displacement spectra for appropriate values of seismic moment M_0 and corner frequency f_0, we use a 2D grid search procedure. f_0 is probed in the frequency range between 1 Hz and 100 Hz; whereas M_0 is varied in the range from 10^{-10} Nm to 10^{-12} Nm. For each parameter combination a corresponding theoretical spectrum $\omega \left| M^{th}(\omega) \right|$ is calculated according to eq. (15). Then, the misfit between theoretical and observed spectra is computed in a least-square sense, similar to eq. (5). The final source model for a particular event is the one with the smallest misfit value. We introduce a high-frequency weighting in order to give the frequency band of the original source energy spectrum a stronger amount of influence.

Fig. 7 shows observed and theoretical source displacement spectra $\omega |M(\omega)|$. Open red squares indicate the values related to the original source energy spectrum $W(f)$, whereas black squares denote the re-inverted spectrum based on eq. (16). The solid red curve shows the best-fitting theoretical spectrum $\omega \left| M^{th}(\omega) \right|$. We see that due to the re-calculation the obtained spectra are smoother and thus more appropriate for comparison with theoretical spectra.
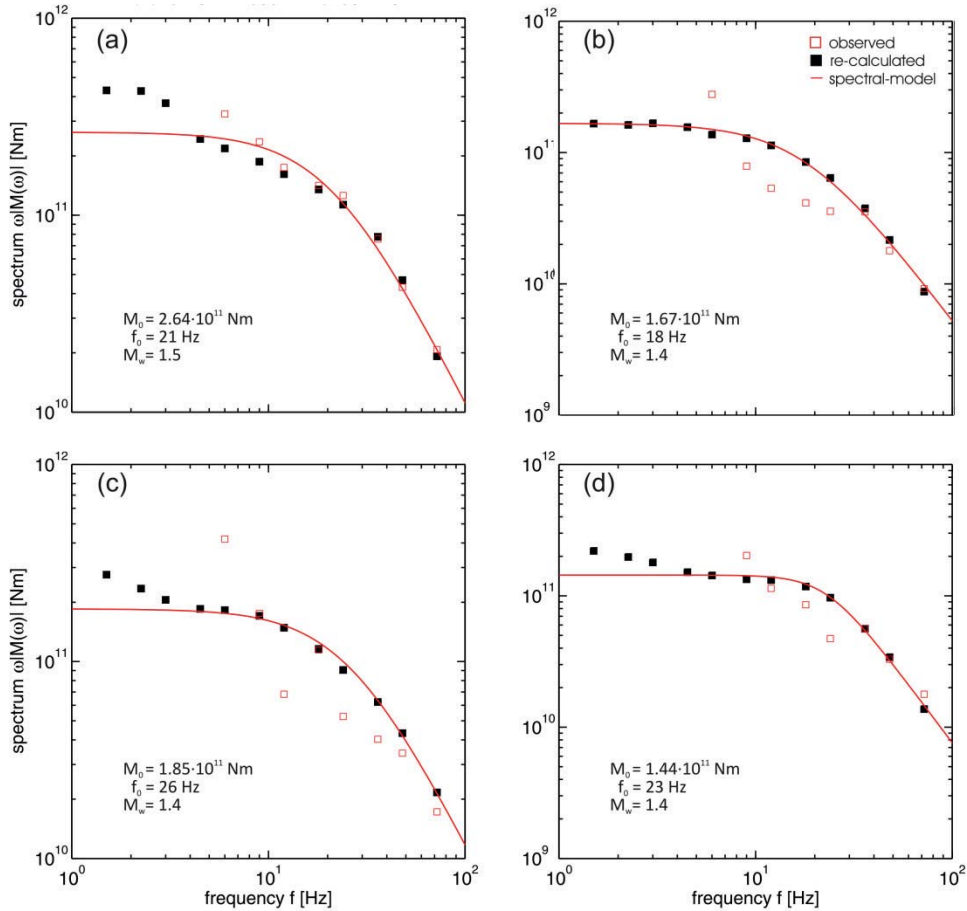
Figure 7: *Source model fits of the induced events: (a) e027.275, (b) e027.275, (c) e103.275 and (d) e048.290. Numerals indicate the inverted source parameters of the individual events.*

3.6 Site amplification factors

All events, recorded at a given site, are evaluated by computing logarithmic averages and corresponding error bars (1σ-level). From estimated site amplification factors for the energy density distribution (R_i) appropriate measures for velocity amplitudes (R_i^v) are obtained by taking the square root. These values are related to local geology. Referring to Sens-Schönfelder and Wegler (2006) crystalline sites for example are related to amplifications below 1, whereas stations on sediments exhibit values above 2. Sites on sedimentary rocks occupy an intermediate range around 1. Amplification values for velocity amplitudes range between 0.4 and 5.4. By analyzing the results for the site response, stations can be grouped into two main clusters. Fig. 8 shows site factors R_i^v as a function of frequency f for stations I14 and A04, representing the two clusters. Black Dots with error bars indicate the mean with uncertainty at 1σ level.
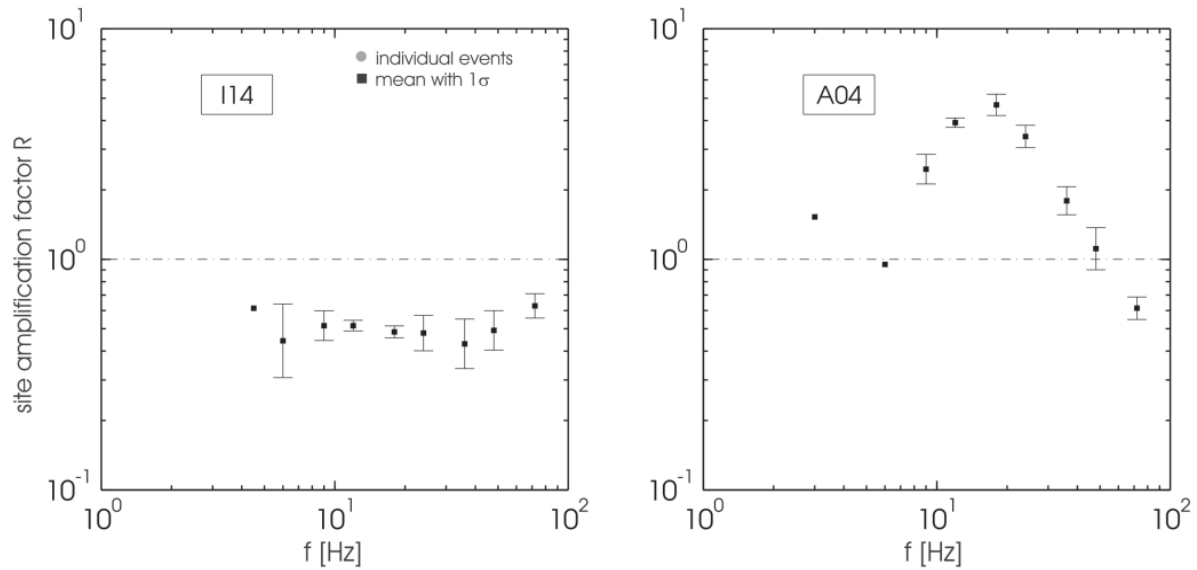
Figure 8: *Site response for stations I14 and A04, representing the two types of frequency dependence. Black squares with error bars: logarithmic average of individual event evaluation with 1σ-confidence limit.*

For station I14, R_i^v shows no significant frequency dependence with a mean value of 0.5. This is in good agreement with the interpretation of Sens-Schönfelder and Wegler (2006). Stations north of the KTB boreholes are mainly situated on crystalline rocks, in particular granite and granodiorite (Fig. 9c). In contrast, the site response for station A04 is clearly a function of frequency. Such a frequency response typically correlates with a weathering layer having low velocity and varying thickness.

However, although *S*-waves have a less pronounced radiation pattern than P-waves (Sato and Fehler 1998, p. 150) the radiation characteristics of the source may have an impact on the prediction of the site amplification factors. The non-isotropic source radiation, for example a double-couple (Fig. 9b), is mapped to some extent in the site response values (Fig. 9a). Thus, a more precise prediction of site amplification values has to be accompanied by a plausible quantification of the radiation pattern.

To check the reliability of our estimates for the site responses, independent inversion techniques, for example reference site methods (Kato et al. 1995), or coda-normalization methods (Takemoto et al. 2012) would have to be considered. Moreover, in a microzonation study using synthetic and seismological data from central Italy, Parolai et al. (2000) demonstrated that the generalized inversion technique (GIT) is capable of revealing absolute values of the site response. Their approach showed that their results are highly consistent with site response estimated with reference methods.
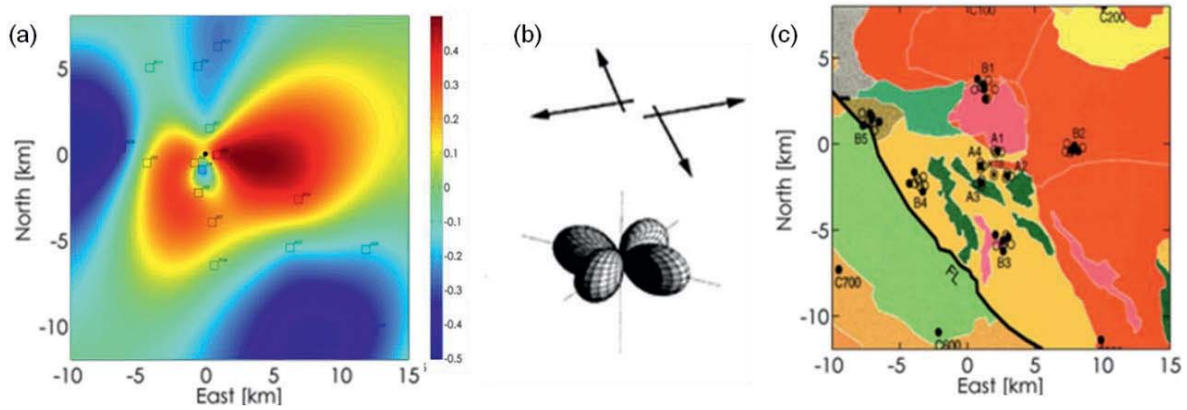
Figure 9: *Site amplification and radiation pattern: (a) 2D graphical representation of R_i^v for the 32 – 64 Hz frequency band of event e016.275, (b) typical double-couple source radiation pattern, (c) local geology at the KTB site (Zoback and Harjes, 1997).*

4. Passive Image Interferometry

4.1 Method

Maeda et al. (2010) demonstrated that Passive Image Interferometry (PII, Sens-Schönfelder and Wegler 2006; Wegler and Sens-Schönfelder 2007) can be used to monitor velocity changes associated with natural fluid migration into a geothermal site. We assume that the opening of fractures by hydraulic stimulation changes the seismic velocity at the geothermal reservoir (Figure 10). A change in the seismic velocity will result in a time-shift of the coda wave, which can be analyzed by Coda Wave Interferometry (Snieder et al. 2002). Using PII the ambient seismic noise is deployed as seismic source and the Green's Function between two stations is calculated from the cross correlation of seismic noise at these stations. The coda of the Green's Function is used as input for Coda Wave Interferometry.

The newly opened fractures reduce the average seismic velocity resulting in a time shift between the trace before and after the stimulation (red and blue lines in Figure 10 and Figure 11), which increases with time. The direct wave (green in Figure 10 and Figure 11) is almost identical before and after the stimulation, whereas the difference is more pronounced in the coda (yellow in Figure 11).
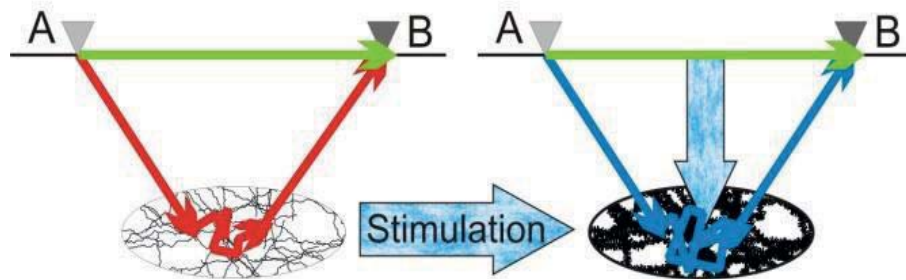
Figure 10: *Schematic figure of the changing seismic reservoir properties due to the stimulation. Red line: before stimulation; blue line: after stimulation; green line: direct wave.*
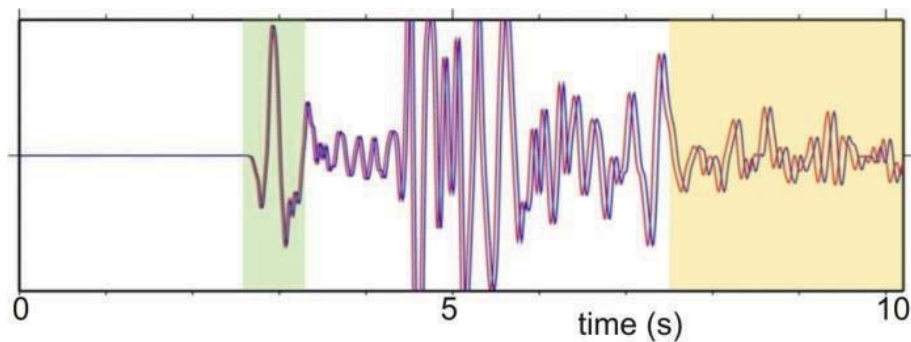
Figure 11: *Variation of the Green's Function as a result of changed subsurface parameters (red: before the stimulation, blue: after the stimulation). The sections of the direct and coda wave are marked in green and yellow, respectively.*

The first processing step is the calculation of one Green's Function (GF) per day from cross correlation of ambient seismic noise recorded at a pair of stations. Different lag times as well as different frequency bands are considered. In a second step a reference GF for each station pair is constructed by averaging all daily GFs. This reference GF is stretched with a set of time-changes resulting in a set of reference GFs, each representing a different time- and thus velocity change. For every day the daily GF is correlated to this set of reference traces with the maximum correlation coefficient giving the respective velocity change.

4.2 Data preparation

Different frequency bands with a high-frequency limit of 20 Hz are tested. Figure 12 shows the synthetic Green's function and the corresponding velocity change for the station pair A01 - R05 away from the reservoir. For the two lower frequency bands the GF shows a distinct phase at a lag time of 4 s, whereas the GFs become more diffusive towards higher frequencies. In contrast, the associated velocity changes dv/v feature strong and rapid variations for the lower frequency bands, and almost constant values for the higher frequency bands. The maximum value of the correlation coefficient R (color code of dv/v in Figure 12) tends to decrease with increasing frequency. The occurrence of the larger

induced events (dashed lines) causes a significant drop of R in the lower frequency bands [0.4 – 10] Hz and [1 – 20] Hz. Hence, the frequency band [0.4 – 10] Hz is used for further analysis due to the fact that the continuous phase is clear, velocity changes are stable, and the drop of the correlation coefficient is clearly visible.
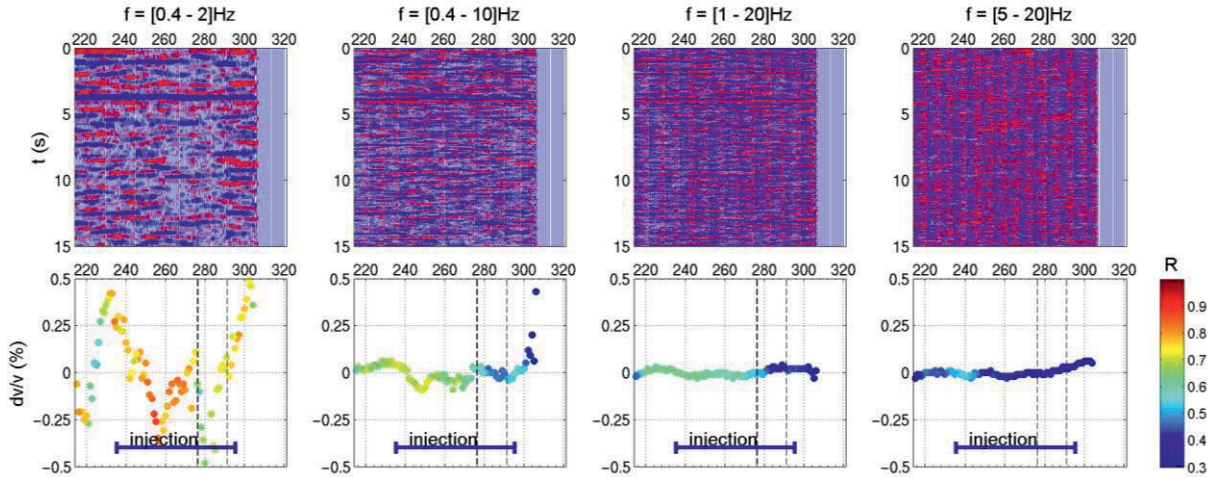
Figure 12: *Comparison of GF (upper panel) and velocity change (lower panel) for different frequency bands, exemplarily shown for the station pair A01 – R05. The daily GFs are averaged over 10 days. The dark dashed line indicates the occurrence of events e016.275 – e103.275 (day of year - doy 275); whereas the light dashed line denotes event e048.290 (doy 290). The injection period is marked by a blue horizontal line at the bottom of each subplot (lower panel).*

Different time windows for averaging the daily Green's function are tested. Without averaging no clear phases are visible in the GF (left panel of Figure 13) and corresponding velocity changes are very unsteady. Average Green's function are calculated according to:

$$GF_n = \text{mean}(GF)_{n-d/2}^{n+d/2} \tag{17}$$

When averaging is accomplished by using periods of 4 or 10 days ($d_{mean} = 4$, $d_{mean} = 10$), a continuous phase appears in the calculated GF at a lag time of about 3 s (Figure 14). Generally, averaging of daily GFs stabilizes the velocity changes. Moreover, by using longer averaging intervals a decrease of the correlation coefficient R with increasing doy becomes fully apparent. This drop is accompanied by the occurrence of the series of induced events with $\mathbf{M_w} \cong \mathbf{1.0}$ between doy 275 – 290. For the further analysis, averaging over 10 days will be considered.
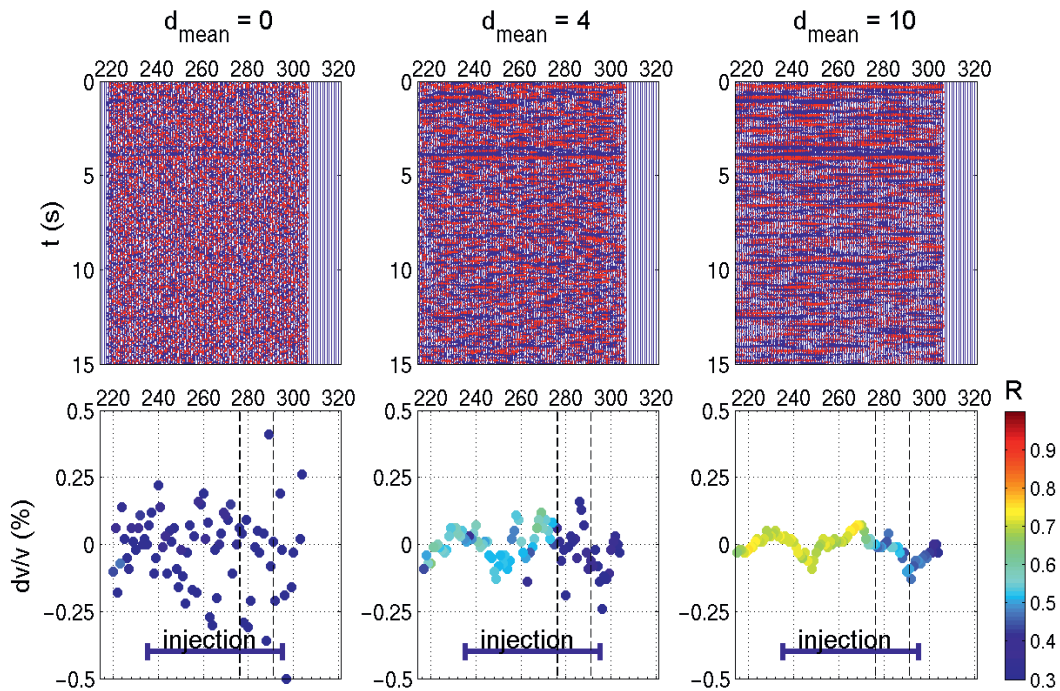
Figure 13: *Comparison of GF (upper panel) and velocity change (lower panel) using different window lengths, exemplarily shown for the station pair A01 – R05. The frequency band is [0.4 – 20] Hz and the lag time window is [0 – 15] s. Dashed lines indicate the time of the four largest mircoseismic events (see Table 1), at doy 275 and 290. The injection period is marked as a blue bar at the bottom of the subfigures in the lower panel.*

4.3 KTB Results

For the KTB1994 experiment a change in seismic velocity has been observed by Bokelmann and Harjes (2000) by applying shear wave splitting to seismic borehole data. We analyze data from the KTB2000 experiment to adjust and test PII for a small, local network with a maximum distance between station pairs of approx. 21 km and high frequency noise. The dataset contained 107 days of continuous data covering the 60 days of stimulation and 20 days before and after the stimulation.

In Figure 14 the averaged GFs for all station pairs are plotted as a function of distance between paired stations. Positive and negative lag times represent the causal and the noncausal part of the GF, respectively (corresponding to a seismic wave travelling from station 1 to station 2 and a second wave traveling in reverse direction). The point in time of the absolute maximum of each trace is marked where the color indicates the distance to the lines of best fit indicating the onset of the direct waves (red and blue line in Figure 14). A lag time window ranging from 3 to 7 s (after the *S*-wave onset) is selected for further analysis (shaded dark grey in Figure 14).
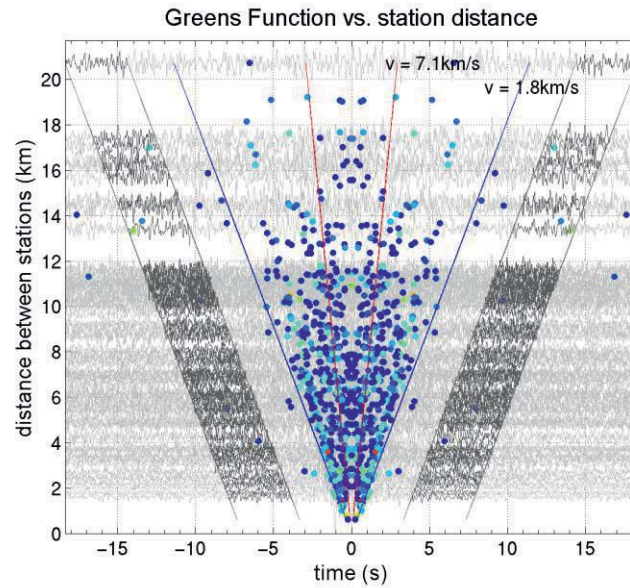
Figure 14: *Averaged GF for each station pair in a frequency band [0.4 - 10] Hz with lag time and station distance. Selected lag time window [3–7] s is shaded in dark grey. Coloured dots indicate t(|max(GF)|) coded according to the distance from best fit lines (red: v = 7.1 km/s, blue: v = 1,8km/s).*

The GFs for a station pair away from the reservoir (A01 – R05, left panel) and one pair across the reservoir (I03 – I10, right panel) are given in Figure 15. Both show a continuous phase at a lag time of about +/-6 s. A clear phase offset, which would indicate a distinct chance in seismic velocity, is not visible.
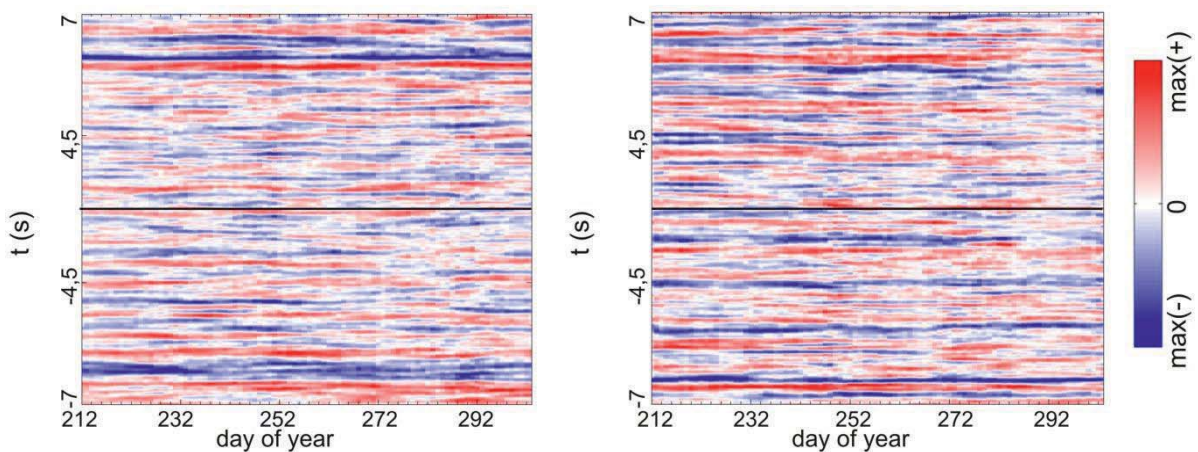
Figure 15: *GF for one station pair away from the reservoir (A01– R05, left panel) and one pair crossing the reservoir (I03–I10, right panel) using a frequency band of [0,4 - 10] Hz and a lag time window of [3 - 7] s after the direct wave. GFs are averaged over 10 days.*

152
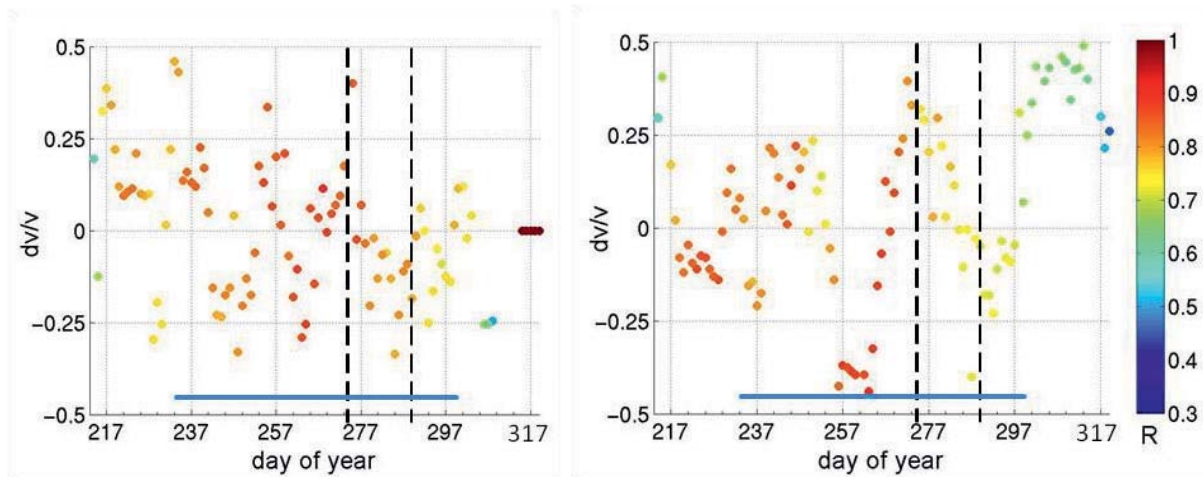
Figure 16: *Velocity changes for frequency band [0,4 - 10] Hz and lag time window [3 - 7] s. Left panel: station pair A01 – R05 (away from the reservoir); Right panel: station pair I03 – I10 (crossing the reservoir). GFs are averaged over 10 days. Dashed lines indicate series of larger events (two at doy 275). The blue bar marks the injection period.*

Figure 16 shows two examples of calculated velocity changes. The injection period (blue bar) and the occurrence of the series of larger events (dashed lines) are marked. The velocity changes are fluctuating, and no systematic trend is visible. Additionally, the station pairs away and across the reservoir do not reveal any significant difference. However, a decrease of the correlation coefficient seems to correlate with the occurrence of larger events.

An overview of the calculated correlation coefficients R is given in Fig. 17 for station pairs away from the reservoir (left panel) and station pairs crossing the reservoir (right panel), separately. The stimulation period is shaded in light blue. Recording period of almost all stations lasted only until the end of the stimulation. We follow the approach to fill gaps in the daily GF with the reference GF, which results in a correlation coefficient of 1. The data quality of some stations diminished during the stimulation experiment, which led to a significant decrease of the correlation coefficient (gray lines). Systematic changes related to the beginning of the injection period or to the occurrence of larger induced events could not be identified.
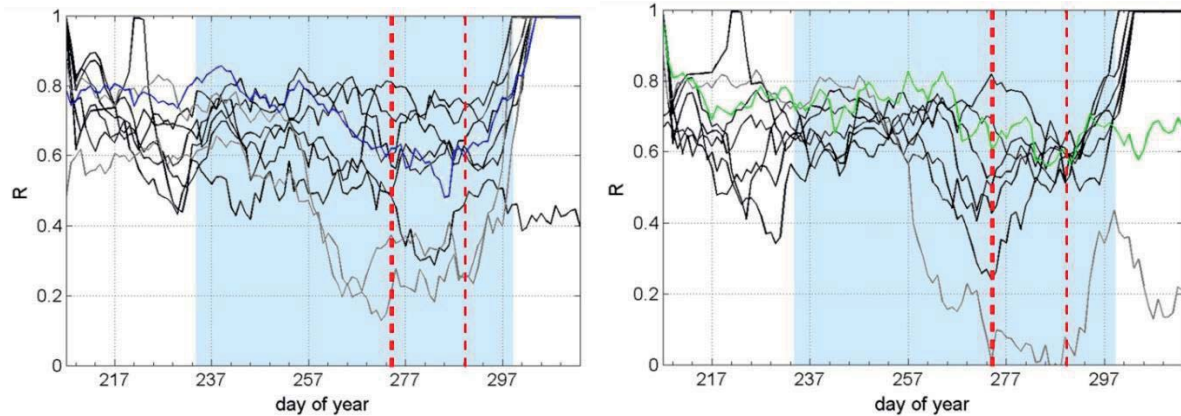
Figure 17: *Correlation coefficient of one day GFs and averaged GFs using the frequency band [0.4 - 10] Hz and lag time window of [3 - 7] s. Left panel: station pairs away from the reservoir (blue: A01 – R05); Right panel: station pairs crossing the reservoir (green: I03 – I10). Gray lines indicate station pairs with R03, featuring systematic problems. Stimulation period is shaded in light blue. Series of larger events is marked by dashed red lines.*

4.4 GeneSys Results

The algorithms developed for the KTB data are applied to records of ambient seismic noise acquired within the GeneSys project in Hannover. Continuous data for the entire year 2011 are analyzed in order to consider sufficiently long periods before and after the stimulation. This strategy enables us to construct a more reliable reference GF. During the stimulation period noisy injection pumps were installed in the center of monitoring network and run at daytime. Thus, only data from nighttime are considered for this study. Figure 18 exemplarily shows averaged GFs for the GeneSys data set, as in Fig. 14 for the KTB data set.

The GFs for an exemplary station pair away from the reservoir (HAN1 – HAN4, left panel) and a station pair across the reservoir (HAN2 – HAN4, right panel) are compared in Fig. 19. The station pair HAN1 – HAN2 features no distinct continuous phases. For the station pair HAN2 – HAN4 (crossing the reservoir), a continuous phase at a lag time of approx. 7.5 s is visible. However, no clear phase offset is apparent that would indicate a distinct change in seismic velocity.

Figure 20 shows two examples of calculated velocity changes. The velocity changes are fluctuating, in particular during the first days. For the station pair away from the reservoir (left panel) no systematic trend is visible. The station pair crossing the reservoir (right panel) features a significant drop between doy 165 and doy 185.
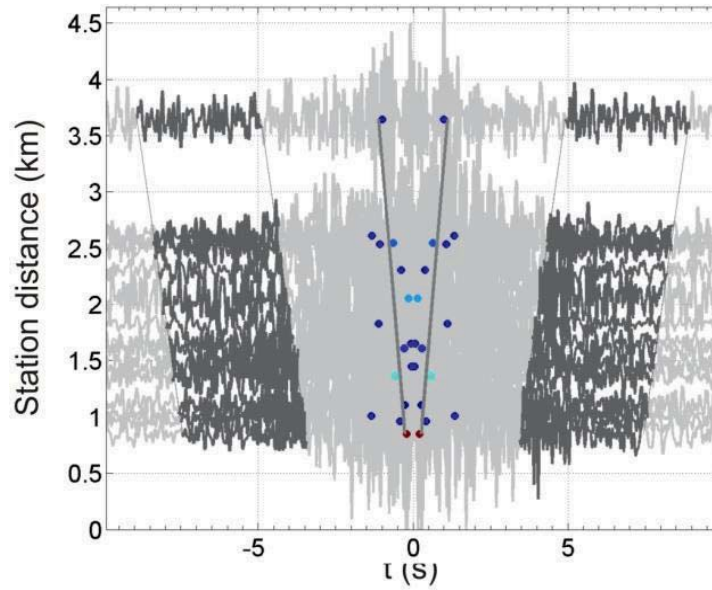
Figure 18: *Averaged GF for every station pair at a frequency band of [1 - 10] Hz, plotted over the station distance; dark grey: selected time ([3 - 7] s after the direct wave); dots: t(|max(GF)|), color coded according to the distance from the lines of best fit (red: $v_P = 7$ km/s, blue: $v_S = 2,4$ km/s).*
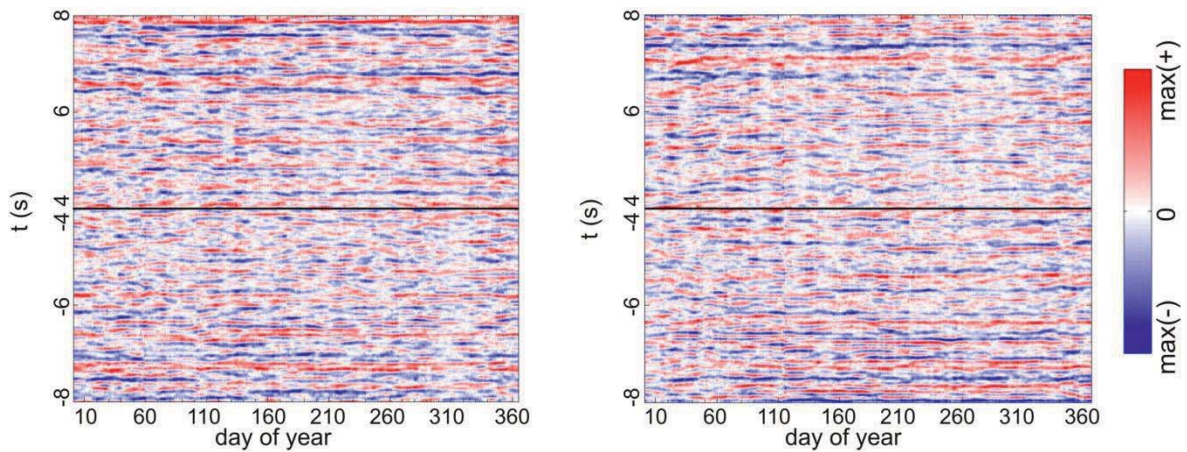

Figure 19: *GF for one station pair away from the reservoir (HAN1 – HAN2, left panel) and one pair crossing the reservoir (HAN2 – HAN4, right panel) using a frequency band of [1 - 10] Hz and a lag time window of [3 - 7] s. GFs are averaged over 10 days.*
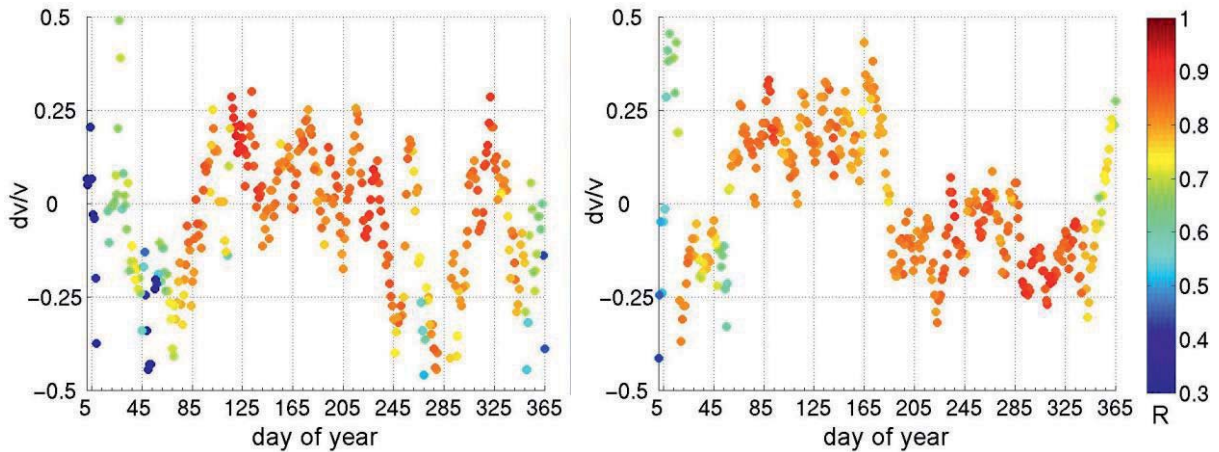
Figure 20: *Velocity changes for frequency band [1 - 10] Hz and lag time window of [3 - 7] s. Left panel: station pair HAN1 – HAN4 (away from the reservoir); Right panel: station pair HAN2 – HAN4 (crossing the reservoir). Velocity changes dv/v are color coded by the correlation coefficient. GFs are averaged over 10 days.*

The correlation coefficients of all station pairs are depicted in Fig. 21. The stimulation period is shaded in light blue. The station HAN3 featured a very poor data quality, which caused significantly lower correlation coefficients (gray lines) for pairs including HAN3. Systematic changes of the correlation coefficient related to the injection period are not evident. For station pairs crossing the reservoir, a decrease of R is observed (similar to the KTB data set). All station pairs exhibit a significant drop of the correlation coefficient around doy 45, even though no activities, related to the operation of the borehole, were reported.
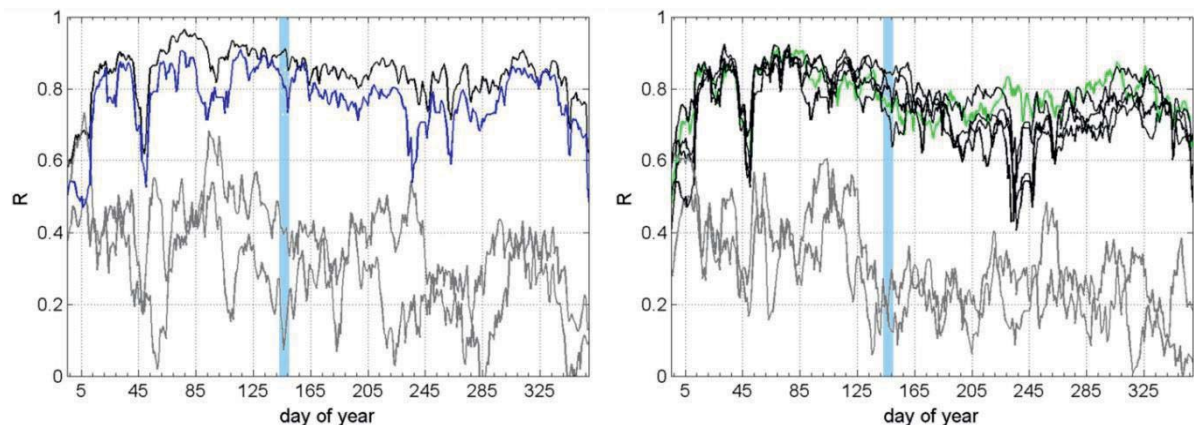
Figure 21: *Correlation coefficient of the one day GFs and averaged GFs for frequency band of [1 - 10] Hz and lag time window of [3 - 7] s. Left panel: station pairs away from the reservoir (blue: HAN1 – HAN4); Right panel: station pairs crossing the reservoir (green: HAN2 – HAN4). Gray lines indicate station pairs with HAN3, which constantly show systematic problems. Stimulation period is shaded in light blue.*

5. Conclusions

Firstly, we demonstrated that records of hydraulically induced microearthquakes can be used to study attenuation properties in upper-crustal formations containing the geothermal reservoir, source characteristics and site amplification factors of the local monitoring network. The shape and amplitude of *S*-wave envelopes, calculated from passive recordings of in induced microearthquakes in an EGS, are related to the structural properties of the propagation medium (heterogeneity, absorption). To accommodate the fact that low-energy and short-duration signals, recorded at short source-receiver distances, are considered, estimation of the source strength and the site amplification are directly included in the inversion. In addition, specifically designed inversion constraints on the selection of appropriate envelopes are introduced.

Overall, the envelope inversion is an adaptation of a general procedure from seismology to microseismic data that includes original elements: (1) specifically designed inversion criteria adapted to particularities of microseismic data and (2) full *S*-wave envelope inversion using fast forward modelling procedure. We see an appreciable advantage in that no *a priori* information or reference data (data normalization) are needed. Moreover, both types of attenuation, which affect the total attenuation differently, are estimated separately through incorporation of time-frequency analysis in the inversion process. Besides the estimation of the attenuation parameters, the source energy spectrum and frequency-dependent site amplification factors are simultaneously obtained during the inversion.

Secondly, presuming that the fractures, created from hydraulic stimulation cause a change in the seismic velocity, Passive Image Interferometry is applied to two data sets to analyze these velocity changes from ambient seismic noise recordings. The first data set is from the KTB2000 experiment where microseismicity was monitored with an extensive seismic network of surface stations. A systematic change of the seismic velocity or the correlation coefficient with the beginning of the injection or with the seismic events could not be observed. Probably the time series of records from 20 days before and after the stimulation was too short to get a sufficient reference Green's function. Additionally, data from the stimulation within the GeneSys project was analyzed, where the network was working for a few years. One year of data recorded at five borehole stations was analyzed. Station pairs away from the reservoir and pairs crossing the reservoir are compared; however it is almost impossible to recognize a difference. Station pairs including stations with data quality problems show significantly lower correlation coefficients for both data sets.

Finally, the idea of applying seismological techniques to data from hydraulic stimulation experiments are originated by the fact that attenuation parameters are sensitive to attributes, such as lithology fluid saturation, permeability or porosity . Thus, attenuation properties might be used to complement existing techniques for characterizing rock properties. On the other

hand, changes in seismic velocity might be related to changes in porosity or pore pressure. In order to quantify the elastic and anelastic properties in the actual geological formation, representing the geothermal reservoir, complex subsurface models are needed. Sensitivity analysis based on deterministic earth structures, like a depth-dependent velocity and/or scattering coefficient (e.g. Margerin et al. 1998; Lacombe et al. 2003), will help to clarify if small variations of reservoir properties in a confined subsurface volume produce variations in energy density or seismic velocity detectable with a local monitoring system and inversion approaches based on stochastic seismology.

6. Acknowledgements

7. Publications resulting from the project

Journal articles:

Fielitz, D. & Wegler, U., 2014, Intrinsic and scattering attenuation as derived from fluid induced microseismicity at the German Continental Deep Drilling site. Submitted to Geophys. J. Int.

Conference paper:

Fielitz, D. & Wegler, U., 2014. Time-frequency seismogram analysis of induced seismicity and its perceived value for reservoir characterization. in *Proceeding of Celle Drilling 2014: The Way Ahead – Drilling Modeling, Simulation and Automation*, Celle, Germany, http://www.celle-drilling.com/2014/upload/files/.

Fielitz, D. & Wegler, U., 2013. Upper-crustal scattering parameters as derived from induced micro-seismicity and acoustic log data (solicited), Geophysical Research Abstracts, Vol. 16, EGU2013-10706-2, General Assembly European Geosciences Union 2013, Vienna, Austria, http://meetingorganizer.copernicus.org/EGU2013/EGU2013-10706-2.pdf.

Fielitz, D. & Wegler, U., 2012. Radiative transfer theory for estimation of scattering and intrinsic attenuation within the geothermal reservoir at the KTB deep drilling site. in: *Noise and diffuse wavefields* (eds. Schmidt, A., Sens-Schönfelder, C., Hadziioannou, C., Wegler, U. & Niederleitinger, E.), Mitteilungen der DGG, Sonderband IV/2012, p. 34-35, ISSN 0947-1944.

Fielitz, D. & Wegler, U., 2012. Statistical analysis of sonic log data from the German Continental Deep Drilling (KTB) project for the estimation of scattering attenuation, in: *Noise and diffuse wavefields* (eds. Schmidt, A., Sens-Schönfelder, C., Hadziioannou, C., Wegler, U. & Niederleitinger, E.), Mitteilungen der DGG, Sonderband IV/2012, p. 32-33, ISSN 0947-1944.

Fielitz, D. & Wegler, U., 2011. Estimation of scattering and intrinsic seismic attenuation parameters with radiative transfer theory: Application to fluid-induced seismicity at the KTB Deep Drilling Hole, Germany, Abstract S41C – 2205 presented at *2011 AGU Fall Meeting*, San Francisco, CA, USA.

Fielitz, D. & Wegler, U., 2011. Scattering and intrinsic attenuation in the Earth's crust at the German Continental Deep Drilling (KTB) site from envelope inversion of hydraulically induced earthquakes, in: *Proceedings of Workshop on Recent developments in seismic wave scattering and heterogeneities in the Earth,* Tohoku University, Sendai, Japan, http://www.zisin.gp.tohoku.ac.jp/scat2011/2011scatWS11-abstract.pdf.

Fielitz, D. & Wegler, U., 2011. Inversion von Seismogrammeinhüllenden zur Charak-terisierung geothermischer Reservoire (im Rahmen des gebo – Forschungsverbundes), Abstract SO P15 presented at *2011 Annual Meeting of Deutsche Geophysikalische Gesellschaft (DGG)*, Cologne, Germany, http://www.geomet.uni-koeln.de/fileadmin/DGG2011/abstract_volume_2011-02-04.pdf.

Vasterling, M. & Wegler, U., 2013. Zeitliche Änderung der seismischen Geschwindigkeit bei Stimulation eines geothermischen Reservoirs, Abstract SO-2.003 presented at *2013 Annual Meeting of Deutsche Geophysikalische Gesellschaft (DGG)*, Leipzig, Germany, http://www.ufz.de/export/data/425/46632_DGG_2013_Tagungsprogramm.pdf

Vasterling, M. & Wegler, U., 2012. Seismic noise – A tool for geothermal reservoir characterization?, in: *Noise and diffuse wavefields* (eds. Schmidt, A., Sens-Schönfelder, C., Hadziioannou, C., Wegler, U. & Niederleitinger, E.), Mitteilungen der DGG, Sonderband IV/2012, p. 91-92, ISSN 0947-1944.

Vasterling, M. & Wegler, U., 2012. Zeitliche Änderung der seismischen Geschwindigkeit bei Stimulation eines geothermischen Reservoirs, Abstract SO-2.003 presented at *2012 Annual Meeting of Deutsche Geophysikalische Gesellschaft (DGG)*, Hamburg, Germany, https://www.geophysics.zmaw.de/fileadmin/documents/DGG/Tagungsband_web.pdf

Patents:

Fielitz, D. & Wegler, U. Verfahren und eine Vorrichtung zur Bestimmung einer seismischen Dämpfung basierend auf einem mikroseismischen Ereignis. 4189-14 BGR008 (angemeldet beim DPMA 2.7.2014).

8. References

Baisch, S., Bohnhoff, M., Ceranna, L., Tu, Y., & Harjes, H. P., 2002. Probing the crust to 9 km depth: Fluid injection experiments and induced seismicity at the KTB superdeep drilling hole, Bull. seism. Soc. Am., **92**, 2369–2380.

Bianco, F., Del Pezzo, E., Malagnini, L., Di Luccio, F., & Akinci, A., 2005. Separation of depth-dependent intrinsic and scattering seismic attenuation in the northeastern sector of the Italian Peninsula, Geophys. J. Int., **161**, 130–142, doi: 10.1111/j.1365-246X.2005.02555.x.

Bischoff, M., Keyser, M., Plenefisch, T., Wegler, U., Wetzig, E., Ceranna, L. & Bönnemann, C., 2012. Microseismic survey at the geothermal site GeneSys in Hannover, Germany, Geophysical Reserach Abstracts, Vol. **14**, EGU2012-12050, General Assembly European Geosciences Union 2012, Vienna, Austria.

Bohnhoff, M., Baisch, S., & Harjes, H. P., 2004. Fault mechanisms of induced seismicity at the superdeep German Continental Deep Drilling Program (KTB) borehole and their relation to fault structure and stress field, J. Geophys. Res., **109**(B2), B02309, doi:10.1029/2003JB002528.

Bokelmann, G. and Harjes, H.-P., 2000, Evidence for Temporal Variation of Seismic Velocity within the Upper Continental Crust. J. Geophys. Res., **105**, 23879-23894.

Chung, T. W., Lees, J. M., Yoshimoto, K., Fujita, E., & Ukawa, M., 2009. Intrinsic and scattering attenuation of the Mt Fuji region, Japan, Geophys. J Int., **177**, 1.366–1.382.

Del Pezzo, E., Ibanez, J., Morales, J., Akinci, A., & Maresca, R., 1995. Measurements of intrinsic and scattering seismic attenuation in the crust, Bull. seism. Soc. Am., **85**(5), 1.373–1.380.

Emmermann, R. & Lauterjung, J., 1997. The German Continental Deep Drilling Program KTB: Overview and major results, J. Geophys. Res., **102**(B8), 18.179–18.201.

Hanks, T. C. & Kanamori, H., 1979. A moment magnitude scale, J. Geophys. Res., **84**(B5), 23482350, doi:10.1029/JB084iB05p02348.

Holliger, K., 1996. Upper-crustal seismic velocity heterogeneity as derived from a variety of P-wave sonic logs, Geophys. J. Int., **125**, 813–829.

House, L.S. and Flores, R., 2002. Seismological studies of a fluid injection in sedimentary rocks, East Texas, Pure and Applied Geophysics, **159**, 371–401.

Jeanloz, R. & Stone, H., 2013. Enhanced Geothermal Systems, Tech. Rep. JSR-13-320, JASON - The MITRE Corporation, McLean, Virginia, sponsored by US DOE.

Jia, Y., 1996. Bestimmung der scheinbaren Dämpfung seismischer Wellen in der europäischen Lithosphäre, Ph.D. thesis, Ruhr Universität Bochum, Germany, (in German).

Kato, K., Aki, K., & Takemura, M., 1995. Site amplifications from coda waves: Validation and application to S-wave site response, Bull. seism. Soc. Am., **85**(2), 467–477.

Kueperkoch, L., 2003. Source parameters from fluid-injection-induced microearthquakes at the KTB, Master's thesis, Ruhr Universität Bochum, Germany.

Lacombe, C., Campillo, M., Paul, A. & Margerin, L., 2003. Separation of intrinsic absorption and scattering attenuation from Lg coda decay in central France using acoustic radiative transfer theory, Geophys. J. Int., **154**(2), 417–425.

Maeda, T., K. Obara, and Y. Yukutake, 2010. Seismic Velocity Decrease and Recovery Related to Earthquake Swarms in a Geothermal Area. Earth Planets Space, **62**(9), 685-691.

Majer, E. L., Baria, R., Stark, M., Oates, S., Bommer, J., Smith, B., & Asanuma, H., 2007. Induced seismicity associated with Enhanced Geothermal Systems, Geothermics, **36**, 185–222, doi:10.1016/j.geothermics.2007.03.003.

Margerin, L., Campillo, M., & Van Tiggelen, B. A., 1998. Radiative transfer and diffusion of waves in a layered medium: new insight into coda Q, Geophys. J. Int., **134**, 596–612.

Masuda, T. & Suzuki, Z., 1982. Objective estimation of source parameters and local Q values by simultaneous inversion method, Phys. Earth Planet. Inter., **30**, 197–208.

Matsunami, K. & Nakamura, M., 2004. Seismic attenuation in a nonvolcanic swarm region beneath Wakayama, southwest Japan, J. geophys. Res., **109**(B09302), doi:10.1029/2003JB002758.

Mayeda, K., Koyanagi, S., Hoshiba, M., Aki, K., & Zeng, Y., 1992. A comparative study of scattering, intrinsic, and coda Q^{-1} for Hawaii, Long Valley Caldera, and central California between 1.5 and 15.0 Hz, J. Geophys. Res., **97**(B5), 6.643–6.659.

Orzol, J., Jung, R., Jatho, R., Tischner, T., Kehrer, P., 2005. The GeneSys-Project: Extraction of geothermal heat from tight sandstones. In: *Proceedings World Geothermal Congress*, Antalya, Turkey.

Paasschens, J. C. J., 1997. Solution of the time-dependent Boltzmann equation, Phys. Rev. E, **56**(1), 1.135–1.141, doi:10.1103/PhysRevLett.93.254301.

Padhy, S., Wegler, U., & Korn, M., 2007. Seismogram envelope inversion using a multiple isotropic scattering model: application to aftershocks of the 2001, Bhuj earthquake, Bull. seism. Soc. Am., **97**(1B), 222–233, doi:10.1785/0120060035.

Parolai, S., Bindi, D., & Augliera, P., 2000. Application of the generalized inversion technique (GIT) to a microzonation study: Numerical simulations and comparison with different site-estimation techniques, Bull. seism. Soc. Am., **90**(2), 286–297, doi: 10.1785/0119990041.

Przybilla, J., Wegler, U., & Korn, M., 2009. Estimation of crustal scattering parameters with elastic radiative transfer theory, Geophys. J. Int., **178**(2), 1.105–1.111, doi:10.1111/j.1365-246X.2009.04204.x.

Sato, H. & Fehler, M. C., 1998. Seismic Wave Propagation and Scattering in the Heterogeneous Earth, Springer-Verlag, New York.

Snieder, R., Grêt, A., Douma, H., Scales. J., 2002. Coda wave interferometry for estimating nonlinear behavior in seismic velocity, Science, **295** (22 March 2002), 2253-2255.

Sens-Schönfelder, C. & Wegler, U., 2006. Radiative transfer theory for estimation of the seismic moment, Geophys. J. Int., **167**, 1363–1372, doi: 10.1111/j.1365-246X.2006.03139.x.

Shapiro, S. A., Kummerow, C., Dinske, C., Ash, G., Rothert, E., Erzinger, J., Kümpel, H. J., & Kind, R., 2006. Fluid induced seismicity guided by a continental fault: Injection experiment of 2004/2005 at the German Continental Deep Drilling site KTB, Geophys. Res. Lett., **33**, L01309, doi: 10.1029/2005GL024659.

Takemoto, T., Furumura, T., Saito, T., Maeda, T., & Noguchi, S., 2012. Spatial- and frequency-dependent properties of site amplification factors in Japan derived by the coda normalization method, Bull. seism. Soc. Am., **102**(4), 1.462–1.476.

Wegler, U., Sens-Schönfelder, C. (2007): Fault zone monitoring with passive image interferometry. Geophys. J. Inter., **168**(3), p. 1029-1033.

Wessel, P. & Smith, H. F., 1995. New version of the Generic Mapping Tools released, Eos Trans. AGU, **76**, 329.

Zeng, Y., Su, F., & Aki, K., 1991. Scattering wave energy propagation in a random isotropic scattering medium: 1. Theory, J. Geophys. Res., **96**(B1), 607–619.

Zoback, M. & Harjes, H. P., 1997. Injection induced earthquakes and the crustal stress at 9 km depth at the KTB deep drilling site, J. Geophys. Res., **102**(B8), 18.477–18.491.

Appendix A Comparison with attenuation estimates worldwide

Table A1: Comparison of scattering attenuation $Q_s^{-1}(\times 10^{-3})$ for different regions in the high-frequency range (6 – 72 Hz)

Reference	Region	6 Hz	9 Hz	12 Hz	16[a]/18[b] Hz	24 Hz	32[a]/36[b] Hz	48 Hz	72 Hz
	volcanic areas								
Del Pezzo et al. (1995)	Etna (Italy)	6.17	-	4.18	3.31[b]	-	-	-	-
Chung et al. (2009)	Mt. Fuji (Japan)	0.84	-	0.14	-	0.09	-	-	-
Mayeda et al. (1992)	Hawaii (USA)	1.85	0.58	0.31	0.16[a]	-	-	-	-
M. & N. (2004)[2]	Wakayama swarm (Japan)	9.88	-	4.85	3.2[a]	2.4	1.6[a]	1.0	-
	non-volcanic areas								
Bianco et al. (2005)		0.37	0.25	0.19	0.14[a]	-	-	-	-
Padhy et al. (2007)		1.22	0.83	0.63	0.43[b]	0.33	-	-	-
Mayeda et al. (1992)		1.81	1.35	0.85	0.51[a]	-	-	-	-
S. & W. (2006)[3]		0.14	-	0.09	-	0.07	-	-	-
this study		0.27	0.2	0.17	0.18[b]	0.21	0.21[b]	0.18	0.14

[2] Matsunami & Nakamura (2004)
[3] Sens-Schönfelder & Wegler (2006)

162

Table A2: Comparison of intrinsic attenuation $Q_i^{-1}(\times 10^{-3})$ for different regions in the high-frequency range (6 – 72 Hz)

Reference	Region	6 Hz	9 Hz	12 Hz	16[a]/18[b] Hz	24 Hz	32[a]/36[b] Hz	48 Hz	72 Hz
volcanic areas									
Del Pezzo et al. (1995)	Etna (Italy)	7.72	-	4.18	2.92[b]	-	-	-	-
Chung et al. (2009)	Mt. Fuji (Japan)	2.14	-	0.84	-	0.44	-	-	-
Mayeda et al. (1992)	Hawaii (USA)	2.61	1.75	1.1	0.65[a]	-	-	-	-
M. & N. (2004)	Wakayama swarm (Japan)	12.7	-	6.15	4.5[a]	3.8	3.1[a]	2.3	-
non-volcanic areas									
Bianco et al. (2005)		0.95	0.64	0.47	0.35[a]	-	-	-	-
Padhy et al. (2007)		0.98	0.73	0.6	0.44[b]	0.36	-	-	-
Mayeda et al. (1992)		2.96	2.4	1.72	1.25[a]	-	-	-	-
S. & W. (2006)		1.0	-	0.6	-	0.25	-	-	-
this study		2.4	2.17	1.07	0.84[b]	0.65	0.55[b]	0.44	0.34

G5: Hydromechanical behavior of geothermal reservoirs

Ernesto Meneses Rioseco[1], Jörn Löhken[2] & Rüdiger Schellschmidt[1]

[1]Leibniz Institute for Applied Geophysics, Stilleweg 2, 30655 Hannover, Germany

[2]DYNAenergetics GmbH & Co. KG, Kaiserstr. 3, 53840, Troisdorf, Nordrhein-Westfalen

Germany

[1]Corresponding Author: Ernesto.MenesesRioseco@liag-hannover.de

Abstract

The exploitation of geothermal energy has gained considerable momentum in the last decades. Understanding the complex hydro-mechanical response of geothermal reservoirs is crucial for every geothermal exploitation project. Among the geothermal projects intended to evaluate the geothermal capabilities in northern Germany, the project "Hydro-mechanical response of geothermal reservoirs in the stress field caused by complex geological structures" is a subproject of the interdisciplinary research association "Geothermal energy and high-performance drilling techniques (Geothermie und Hochleistungsbohrtechnik "gebo") in Lower Saxony. One of the major aims of this subproject is to improve and refine the knowledge and understanding of the hydro-mechanical behavior of geothermal reservoirs during and post- drilling and –stimulation. Due to the wealth in data collected in the GeneSys-Borehole GT1 geothermal demonstration site in Groß-Buchholz Hannover, and the complex geological structures surrounding it, which makes it a representative area for the North German Basin, this region has been chosen as the study area. Using numerical modeling, we focus in this final report on three fundamental issues: (I) the present-day stress field reigning in the reservoir, caused by complex geological structures typical of the North German Basin (NGB), (II) the possible surface deformation that hydraulic stimulation may trigger, and (III) parameters controlling fluid-driven fracture path and geometry in layered reservoirs as well as the hydro-mechanical interaction between conglomerates of pre-existing natural joints and newly hydraulically induced fractures.

Employing COMSOL Multiphysics as finite-element code, 3-D present-day geo-mechanical modeling of the stress field in a complex lithologically layered region containing salt domes, were conducted. Geological/geophysical constraints for the numerical modeling comprise the real composition, thickness and structure of sediments provided by the geotectonic atlas of Northwest Germany and valuable measurements on density and seismic velocities carried out within the context of the GeneSys project. Modeling results of the stress field are overall consistent with measurements of the stress field obtained from borehole breakout and tensile

fractures analyses. Especially the observed rotations of the minimum horizontal stress component over depth are reproduced remarkably well in the deeper depths of the modeling domain. Numerical simulation results for the magnitude of the horizontal components of the stress field seem to be lower than the values suggested by an initial mini-frac test in the study area. This may indicate that additional far-field stresses may be important when it comes to understanding the current *in-situ* stress field in the area under investigation. In addition, model results reveal that depending on the rheological properties and rheological model adopted for salt, the resulting stress field in the area of interest exhibits strikingly different patterns. In particular, the combination of far-field stresses and the different assumed rheological properties and model for salt seems to be critically important for the analysis of the stress field in the study area.

As far as surface deformation as a result of hydraulic stimulation is concerned, field measurements were performed in the framework of the GeneSys frac experiment. Using GPS and differential SAR-interferometry techniques it was possible to monitor any surface vertical displacement throughout the entire GeneSys frac experiment. The processing and analyses of the data gathered in these field measurements show no significant surface deformation as a result of hydraulic stimulation in the area under investigation. These field measurements were accompanied with numerical simulation of possible volume deformation resulting from the injection of considerable amounts of water into a typical modeling domain. Model results demonstrate that no significant volume deformation is caused by the injection of the amount of water and the operating infection rates used in the frac experiment in the GeneSys project.

Finally, hydro-mechanical processes are at the heart of geothermal reservoirs. In particular, the fracture trajectory and geometry in a complex layered reservoir is affected by a myriad of factors such as different mechanical and hydraulic material properties, different stress patterns in the respective layers, material heterogeneities, interaction with pre-existing joints, and others. These controlling factors can be effectively examined using numerical modeling. We utilize FRACOD as 2-D boundary element code to numerically examine a series of models involving relevant scenarios. Several numerical simulations with similar layer sequences to the ones encountered at targeted depths in the NGB were carried out. In doing so, a wide range of possible scenarios was tested. Modeling results suggest that the difference in elastic parameters such as Young's modulus and Poisson's ratio between the involved sedimentary layers has limited impact on the characteristics of fracture path. The differences in these elastic properties do not result in fracture containment or arrest but rather in the alteration of fracture aperture. This is in line with previous field and laboratory observations. Differences in mechanical properties like fracture toughness in mode I and II and their ratio at material contacts turn out to have a considerable impact on the fracture

path and mode of deformation. Model simulations show that with specific but measured values in laboratory of fracture toughness in both modes of deformation, the fracture path may significantly deviates from its original orientation, and switch modes of deformation while crossing material interfaces. Model results concerning the hydro-mechanical interaction of conglomerates of pre-existing joints with newly hydraulically induced fractures demonstrate important hydro-mechanical features of this interaction. Pre-existing joints experience significant deformation and changes in their hydraulic properties in advance of meeting the hydraulically generated fractures. Furthermore, when these latter bump into the pre-existing joints, they do not proceed with their propagation, but rather the pre-existing fractures are reactivated and become the main hydraulic conduits. Model results clearly show the tendency of the pre-existing joints to propagate in the direction of maximum shear when meeting the hydraulically generated fractures.

1. Introduction

Hydro-mechanical processes involved in geothermal reservoir engineering have captured the interest of numerous scientists and reservoir engineers in the last decades. Irrespective of additional thermal and chemical couplings related to this subject, their dynamic interplay alone is highly complex and has been intriguing for many geoscientists addressing hydraulic fracturing in natural and engineered geosystems. The complexity of hydro-mechanical interaction implicated in geothermal systems cannot be experimentally fully studied in laboratories or directly observed in nature. Hence, the need of numerical modeling capable of handling the dynamics of the hydro-mechanical interaction at reservoir scale is of paramount importance.

Remarkable efforts have been made to advance the knowledge and understanding of hydro-mechanical numerical modeling in hydrocarbon and geothermal reservoirs in the last decades (e.g. Adachi et al. 2007, McClure & Horne 2013, McClure 2014 a, b, and references therein). Among numerous projects operating worldwide, the project "Hydro-mechanical response of geothermal reservoirs in the stress field generated by complex geological structures" is a subproject of the interdisciplinary research association "Geothermal energy and high-performance drilling techniques" (Geothermie und Hochleistungsbohrtechnik "gebo") in Lower Saxony, Germany (e.g. Reinicke et al. 2010, http://www.gebo-nds.de/en/). The aim of this subproject is to improve the understanding of the hydro-mechanical behavior of geothermal reservoirs during and post- drilling and -stimulation in regions typical of the North German Basin.

Because of the ample hydraulic and mechanical data collected in the project GeneSys (see e.g. www.genesys-hannover.de) the region surrounding the drilling demonstration site GeneSys-Borehole GT1 in Hanover Groß-Buchholz has been chosen as the study area (Fig.

1). Data gathered in the GeneSys project has provided reliable geological and geophysical constraints used in the numerical modeling part of this work.
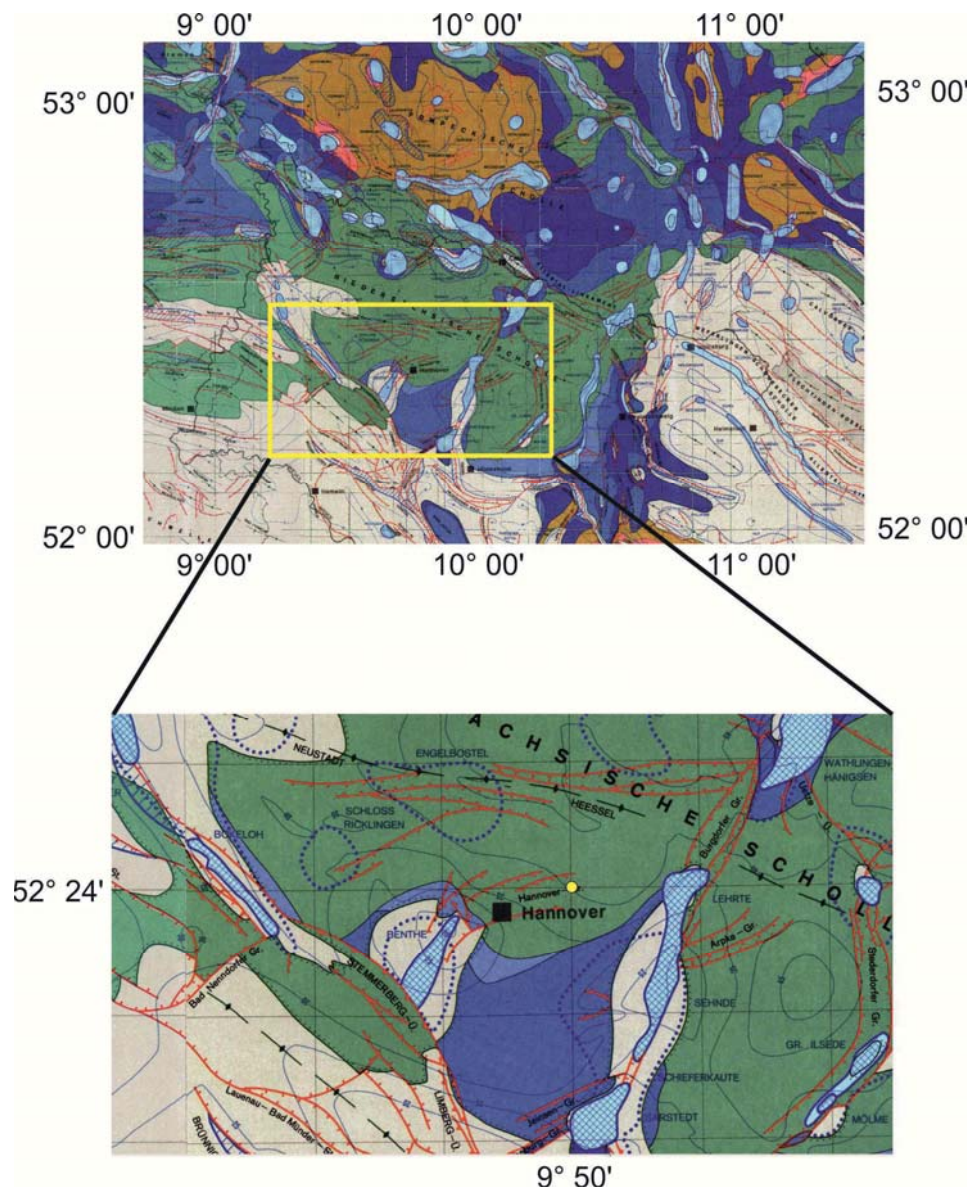
Figure 1: *Map showing the North German Basin with numerous salt structures inherent of this area. This map has been drawn using the geotectonic atlas of NW Germany (Baldschuhn et al., 2001). Yellow circle denotes the demonstration site GeneSys-Borehole GT1 in Hanover Groß-Buchholz. Salt domains are depicted in light blue. Note the two relatively large salt diapirs Lehrte and Benthe in the neighboring area of the demonstration site.*

The GeneSys project of the Federal Institute for Geosciences and Natural Resources (BGR) basically comprises the arrangement of single-well concepts as well as the implementation of water-frac techniques to tight sedimentary rocks, see Fig. 2. Hence, similar geological

scenarios to the identified sediment sequences at the targeted depth were adopted in the present study to address key questions raised within the framework of the GeneSys project.

Pumping water at high pressure into tight sediments requires examining several issues. One of these issues is linked to the present-day state of the in-situ stress field, which determines how the stimulation, exploitation, and in particular the drilling path concept should be designed. Another issue relates to possible surface deformation that significant quantities of fluid pumped into the Earth might cause. At the heart of all these aspects is the hydro-mechanical behavior of geothermal reservoirs. How is the interaction between hydraulics and mechanics in such a complex geothermal system? What controls and how the initiation and propagation of existing and hydraulically induced fractures? How do these fractures interact with each other? What controlling factors dominate the major fluid conduits? All these aspects are going to be addressed in the next sections of this final report.

The present-day stress field in the North German Basin is particularly complicated by the diverse salt structures such as salt domes and salt layers naturally occurring in this area. An introductory overview of the key issues concerning the current general state of the stress field in the upper most part of the crust in the North German Basin is presented in section 2.1.
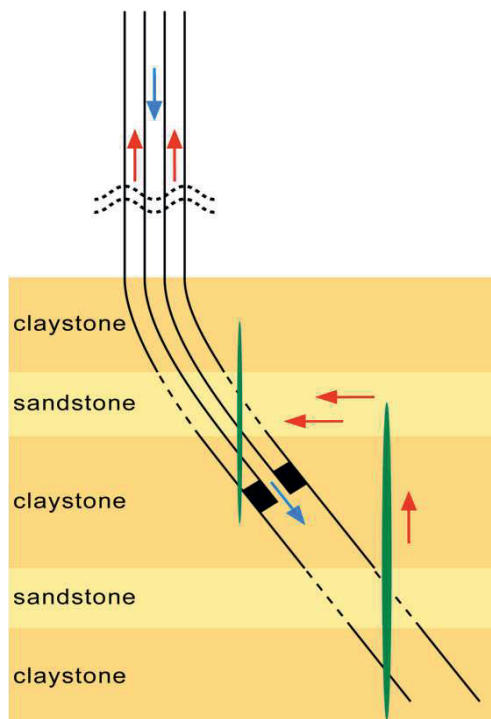
Figure 2: *Schematic representation of the drilling, injection as well as extraction concept drawn and implemented in the context of the GeneSys Groß-Buchholz GT1 geothermal drilling project. Note the large vertical hydrofractures (vertical green elliptical features) planned as part of the production concept. These vertical or subvertical hydraulic fractures connect different sediment layers.*

Hydraulic fractures are generally considered to be extensional fractures and therefore their predominant pathways are controlled by the orientation of the principal horizontal stress components. Well planning includes, thus, a previous thorough geological/geophysical examination and modeling of the current state of the stress field, especially close to complex geological structures, in conjunction with an adequate selection of the drilling path. In general, having profound insight in the operating stresses is crucial when it comes to understanding the tectonics of a region. In particular, present-day *in situ* stresses have a major influence on the short- and long-term spatiotemporal evolution of hydraulically stimulated geothermal reservoirs. We summarize the modeling results of our 3-D present-day geo-mechanical model of the stress field in the study area in chapter 2. A more detailed description of this work can be read in Meneses et al. 2013 a.
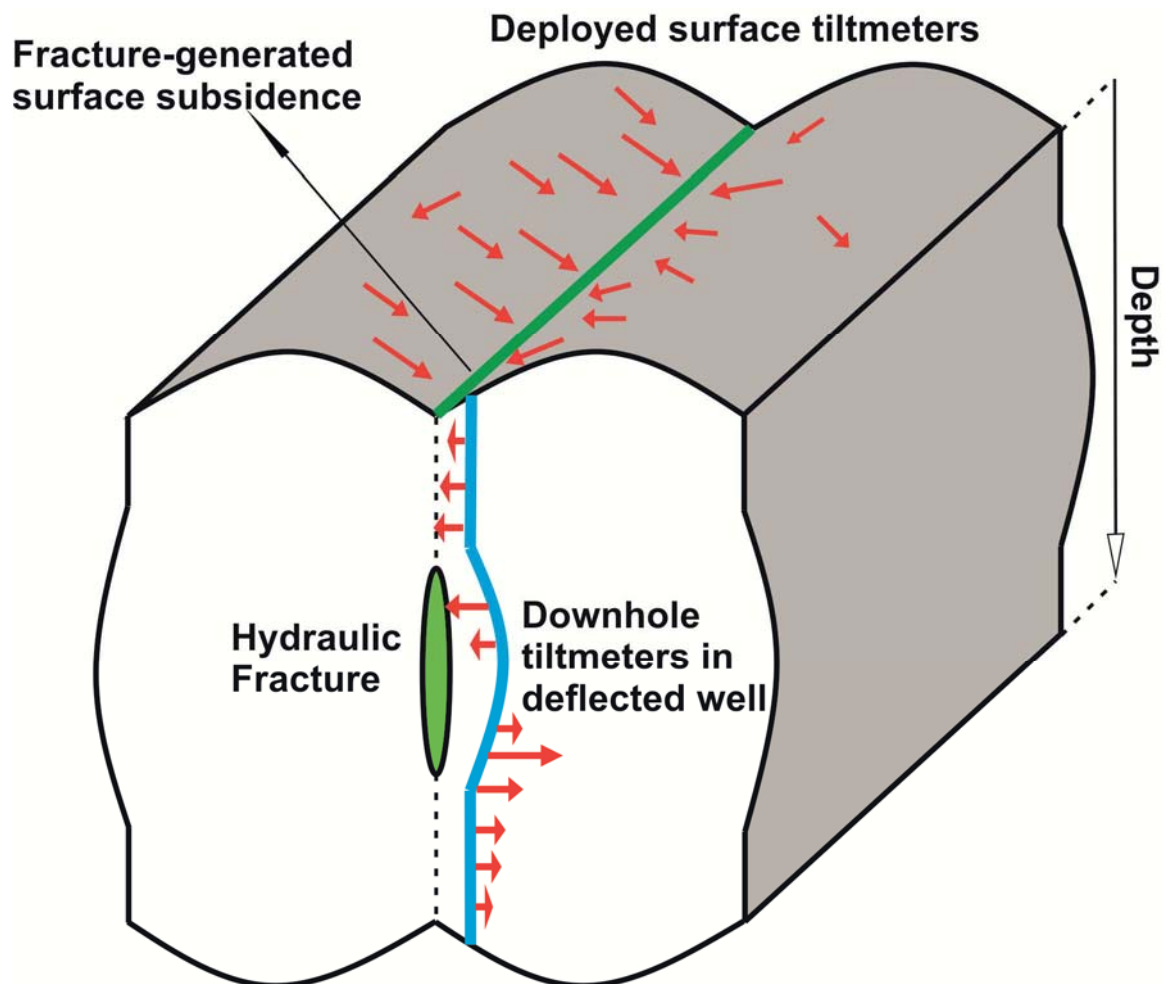
Figure 3: *Schematic representation of the method of tiltmeter fracture mapping (modified after Pinnacle Technologies Inc. 2007). Two-dimensional tiltmeter array (randomly deployed red arrows) and one-dimensional downhole tiltmeter array (light blue line with red arrows) are generally deployed to detect rock mass deformation. Note that*

this schematic representation is a cartoon of the general situation. In the present study, no downhole tiltmeter was employed, and fracture geometry and orientation may differ from the one displayed. See Schön 2011 for detailed information about tiltmeter exact coordinates and positioning strategy.

The gebo project aims at reducing the costs of deep geothermal wells in order to make geothermal energy production in Lower Saxony more economically attractive. One part of the necessary steps to cost-effectively obtain geothermal energy from the deep underground comprises hydrofracing operations and the consequences of its implementation in terms of upper-crustal deformation. This was also one of the main objectives of the gebo project G5 and the measurements and numerical modeling carried out in this study is described in the chapters 3 and 4 of this report. In particular, possible, presumably small hydrofracing-induced surface deformation is of special academic and public interest. Similar kinds of investigations have been previously conducted in hydraulic fracture experiments (e.g. Saleh et al. 2003 and Chen 2008, and references therein) as well as other prominent continental deep drilling projects involving hydraulic stimulation (e.g. Jahr et al. 2006, and references therein).

As mentioned earlier, the question related to possible shallow crustal deformation caused by hydraulic stimulation in the North German Basin is addressed in this study by means of field measurements and numerical modeling. One of the motivations for monitoring and measuring the deformation of the earth's surface is linked to possibly describing the propagation of shallow hydro-fractures (see Fig. 3). The collected field data is then subsequently processed and interpreted, leading to constraining the damage zone. This data analysis is generally accompanied by numerical modeling to better understand the controlling factors related to the deformation source.

The field measurements mainly involve two techniques: (1) GPS and (2) Satellite differential SAR-Interferometry. SAR stands for Synthetic Aperture Radar. The field measurements were conducted in the framework of the GeneSys hydraulic fracturing experiments. The numerical modeling task consists of assessing possible surface deformations resulting from volume deformation simulations related to hydrofracing operations under similar mechanical and hydraulic conditions as those encountered in GeneSys-GT1 borehole.

Chapter 5 of this final report is devoted to sum up the main modeling results of the complex hydro-mechanical behavior of layered, low-porosity, and fractured geothermal reservoirs typical of the North German Basin. In particular, several factors controlling the fracture path and geometry while crossing different material interfaces are systematically studied, since this is envisaged as an important part of cyclic injection and exploitation concepts in the GeneSys project. We specifically focus on the influence of elastic parameters, mechanical fracture parameters on the fracture propagation. Finally, the hydro-mechanical interaction

171

between conglomerates of pre-existing natural joints and hydraulically induced fractures are investigated using numerical simulation since this scenario corresponds to future target depths (e.g. vulcanite formation) for geothermal exploitation in the NGB. A more detailed description of the modeling results can be found in Meneses et al. 2013 b.

2. 3-D geomechanical modeling of the stress field in the North German basin?

This part of the study is focused on the numerical simulation of the stress field triggered by complex geological structures that occur in the North German Basin. As representative for the North German Basin the region surrounding the GeneSys-Borohole GT1 geothermal demonstration site in Hannover Groß-Buchholz has been chosen. The GeneSys GT1 drilling project has provided comprehensive and detailed data for the numerical modeling. In the fallowing sections, the most prominent features of the present-day stress field in the North German Basin, the model setup, as well as the main findings concerning the numerical simulation are presented. Special attention is paid to the rheological properties of salt and their consequences to the current stress field in the region. An extensive description of the modeling results of this study can be found in Meneses et al. 2013 a.

2.1 What do we know about the stress field in the upper most part of the crust in the North German basin?

The North German Basin classifies as a common passive-rifting sedimentary basin (e.g. Kockel 2002, and references therein). An around 10 kilometer thick Permian-to-Cenozoic sediment cover defines locally this basin that is regarded as being basically the result of thermal subsidence (cooling) after a previous event of mantle plume activity (e.g. Kockel 2002, Ziegler 1990, and references therein). The evolution of the North German Basin is especially characterized by intensive salt tectonics, in particular diapirism. These salt displacements have resulted in the formation of conglomerates of salt structures such as salt ridges, salt pillows, and salt domes. Due to its mechanically decoupling character, Zechstein salt is largely recognized as critical when it comes to evaluate the stress field in the North German Basin (e.g. Röckel & Lempp 2003). In general, the rheological properties of Zechstein evaporites, and especially its inherent isotropic state of stress, manifest themselves in different stress patterns for the suprasalinar (Triassic and younger depositions), the salinar (Zechstein), and the subsalinar (lower-Permian and older depositions including crystalline) successions. Whereas the maximum horizontal stress component in the suprasalinar sequences exhibits a rather uneven, scattering pattern (so-called fan-like pattern), the stress components in the salinar veneer show an isotropic state without any preferential orientation. In contrast to both previously mentioned patterns of the stress field, in the subsalinar successions the maximum horizontal stress component exhibits

a vigorous N-S orientation in the middle of the NGB, with minor departures of this overall trend in the western and eastern part of the basin (e.g. Röckel & Lempp 2003).

As far as the magnitude of the principal stresses is concerned, it is well known that in a passive sedimentary basin the horizontal stresses are primarily determined by the gravitational load. In particular, the magnitude of the vertical stress is given by the overburden weight, and the magnitude of the maximum and minimum horizontal stress components are almost equal and are given by a fraction of the magnitude of the vertical stress component. This is broadly acknowledged as being the overall present-day state of the stress field in the North German Basin. However, the overall picture of the stress field may be locally disturbed by the occurrence of abundant salt domes and other considerable salt-bearing sediment layers (e.g. Heidbach et al. 2007, and references therein). Extensive, valuable information about the present-day stress state can be read in a variety of important reports of the World Stress Map (Heidbach et al. 2009).

Altogether it can be conclusively said that locally the stress field in the uppermost part of the crust in the NGB is largely heterogeneous. This is one of the main motivations for carefully studying the local stress field in the North German Basin at relatively shallow depths (above Upper Permian).

2.2 The rheological behavior of salt and its impact on the regional stress field

Salt is a typical constituent of sedimentary basins. Among its most prominent material properties are the following: It is mechanically comparably weak. It has a relatively low density which makes it gravitationally unstable. Its high heat conductivity makes it function as heat conduits, so-called "chimney effect" among other sediments. It is highly incompressible and impermeable. Due to the mobility of salt and the previously mentioned properties, it causes large domains of deformation (e.g. Fossen 2010). When it comes to the rheological behavior of salt, several approaches have been adopted in the last decades depending on the type of salt as well as on the temperature and pressure conditions applied. Due of the ability of salt to flow its rheological behavior should not only be described by linear elasticity. Salt deformation is controlled also by creep mechanisms and these may significantly influence the stress field in adjacent sediments to salt diapirs and salt layers. In general, the most striking effect of salt units embedded in sediments on the stress state results from the fact that salt cannot withstand any differential stress and as a consequence creeps when any deviatoric stress is exerted (e.g. Fredrich et al., 2003, 2007; van der Zee et al., 2011, and references therein). The inability of salt to accommodate deviatoric stresses makes the constitutive laws governing its rheological behavior as well as the mechanical boundary conditions at the contact interfaces with surrounding sediments especially difficult. This is an issue that has been discussed at length in the published literature. In particular, this latter rheological property results in a reorientation of the stress field at the material contact

between salt and the surrounding non-salt material. This again is caused by the isotropic state of stress that commonly reigns within salt geological structures. For this requirement to be fulfilled, the stress field in the neighborhood of the material contact between salt complexes and adjacent sediment material is significantly altered from its otherwise general far-field pattern. This makes the stress field in the vicinity of such material interfaces extremely complex. The rheological behavior of salt is extensively studied in numerous laboratory experiments and successfully modeled by a great deal of authors (e.g. Fredrich et al., 2003, 2007; van der Zee et al., 2011). Due to the extent of this work, aims of research and the selected study area, however, a stationary approach as a starting point has been taken, capturing the basic properties of salt-bearing sediments.

2.3 Model setup

The geological setting for the modeling domain, which encompasses the region of Groß-Buchholz Hanover, was designed using data from the geotectonic atlas of Northwest Germany (Baldschuhn et al., 2001). Data is missing, however, in some regions, especially in municipal areas of Hannover. For the modeling, the depths corresponding to those domains were computed utilizing a cubic interpolation function. This is based on the fact that also the geological maps used for the construction of the geological setting in the study area originated essentially from the interpolation of point and line data on areas, where rather less mathematical interpolation methods than geological assumptions and considerations were adopted. Therefore, the data amassed in the geotectonic atlas of Northwest Germany capture rather an estimate picture where only locally reliable data is available. The geological model is certainly the best available model but certainly not everywhere accurate. That is the reason why the geological stratification of the area under investigation was enhanced and complemented with more recent and accurate data provided by the borehole demonstration site GeneSys in Groß-Buchholz Hanover.

Fig. 4 shows each sedimentary layer taken into consideration. The outcropping of the upper layer on the model surface is a special feature of the model. Another prominent feature of the model relates to lower sequences going partly though upper layers in the vicinity of the salt domes, as expected from the mechanism of salt diapirism. In particular, the from-south-to-north-going depression of the geological horizons between the salt domes, which intensifies in the northeast direction, is probably propelled by salt tectonics as well.
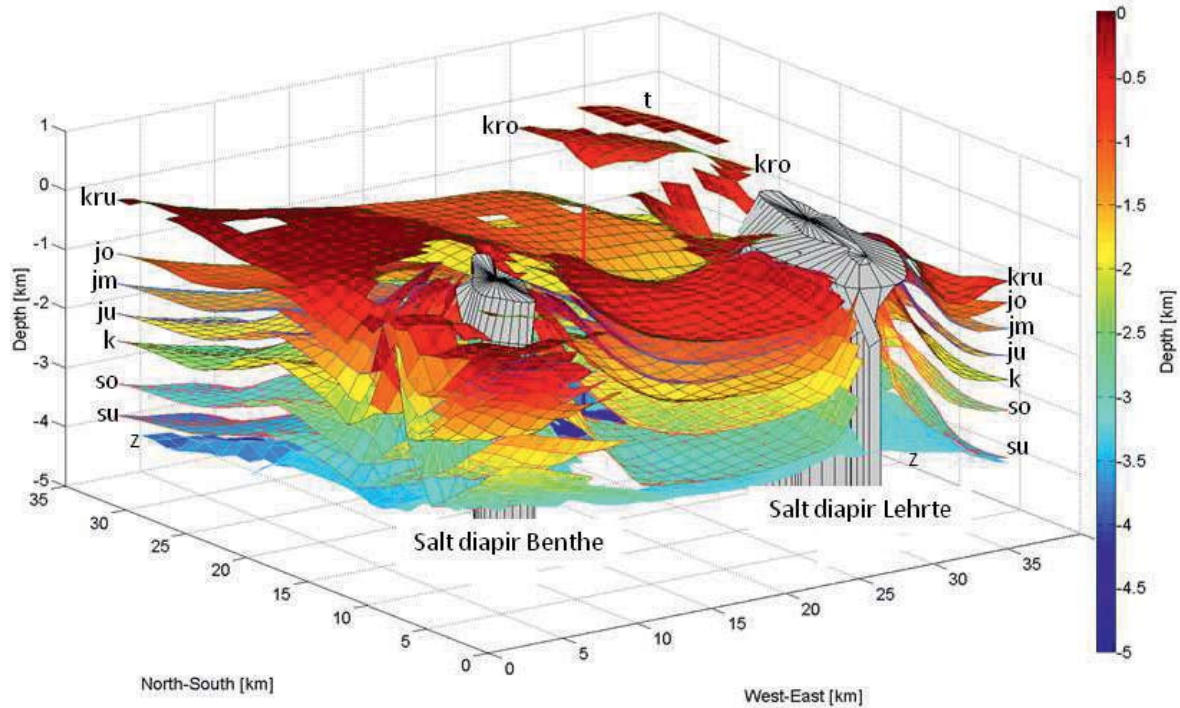
Figure 4: *Geological arrangement of the region surrounding the demonstration site Groß-Buchholz Hannover. Salt diapirs (depicted in gray) pinch out of the neighboring sedimrntary veneers resulting in arching and buckling of the sedimentary sequences. The notation employed follows: t=Tertiary/Tertiär, kro=Upper Cretaceous/Oberkreide, kru=Marine Lower Cretaceous/Marine Unterkreide, jo=Upper Jurassic/Malm, jm=Middle Jurassic/Dogger, ju=Lower Jurassic/Lias, k=Upper Triassic/Keuper, so=Upper Bunter/Röt, su=Lower Bunter/Unterer Buntsandstein, z=Upper Permian/Zechstein. Each plane corresponds to the base of the layer.*

The lateral extents of the salt diapirs are given for each layer in the geotectonic atlas. In some cases, however, these cannot be sharply distinguished from fault zones or by salt diapirism disturbed horizons. A more detailed description of the model setup can be read in Meneses et al. 2013 a.

Since the rheological model assumed so far in this study is elastic or more precise poroelastic, the starting point is gathering the required elastic parameters of all involved lithological layers. Elastic parameters were computed from real seismic velocity and density measurements conducted in the borehole test well Groß-Buchholz GT1. The measured compression wave velocity (V_p), the shear wave velocity (V_s), and the density (ρ) deliver the Young's modulus (E) and the Poisson's ratio (v) for each lithological sequence through the following equations:

$$E = \rho \cdot V_s^2 \left[\frac{3V_p^2 - 4V_s^2}{V_p^2 - V_s^2} \right] \quad \text{and} \quad v = \frac{0.5\left(V_p/V_s\right)^2 - 1}{\left(V_p/V_s\right)^2 - 1}$$

Averaged material and rheological parameters that are considered representative for each compositional layer can be read in table Tab. 1. It should be mentioned that the values listed in Tab. 1 for Upper and Lower Permian were adopted from Zimmer 2001 and Trautwein 2005, respectively.

The adopted 3-D geological structure and composition for the numerical modeling is displayed in Fig. 5. A model cube with lateral extents and height 31,5 km x 30 km x 5 km consists of eleven differently lithologically composed sediment sequences. In addition, the salt domes Benthe and Lehrte are embedded in the model block. It should be mentioned that these two salt domes are included in the model block with their complex geometry. This block is exposed to gravitational loading and its elastic and/or poroelastic response is examined in terms of the resulting stress field. In addition, the lower boundary of the model block remains fixed during the entire modeling time. The upper boundary of the model, however, can move vertically. Laterally, no compression or extension of the model is allowed. Only vertical displacement of the lateral outermost edges of the model block is permitted.
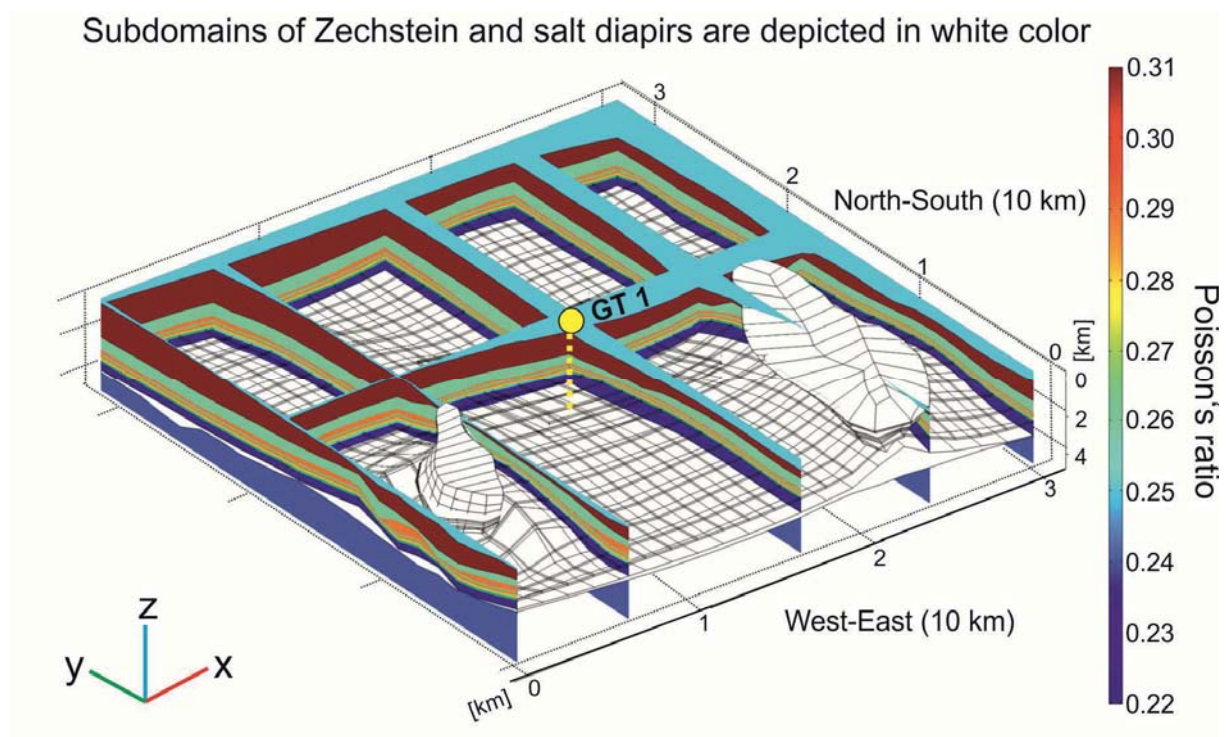
Figure 5: *Geological model used for the modeling setup (input data) in COMSOL-Multiphysics. The modeling domain dimensions are 31,5 km x 30 km x 5 km. Yellow circle and dashed yelow line depict the drilling site GeneSys GT1 at Groß-Buchholz Hannover. Salt material is displyed in white color. The Poisson's ratio*

assigned to salt material in this case is 0.28.Different colors represent different sedimentary layers.

For the final numerical simulation, the isolines of every single material layer in the geotectonic atlas were given a 1500 m x 1500 m grid and next read by the software COMSOL Multiphysics. This software is an all-purpose, powerful finite-element numerical tool especially applicable to handling the solution of geo-mechanical problems with complex geometries. The resolution of the grid (discretization of the space) is heavily dependent on this latter aspect. Certainly, a finer discretization would lead to a better resolution of small-scale geometrical features, however making computational calculations much more expensive. In particular, when having small-scale complex geometrical features, as it is the case in the immediate neighborhood of the salt domes, additional mesh refinements are unsuccessful. Especially sharp angles and cross-sections at the material interfaces with the salt domes complicate the creation of a finite-element mesh.

Compositional layers	Depth (m)	Density (kg/m^3)	Young's modulus (Gpa)	Poisson's ratio (-)
Younger covering layers to Lower Cretaceous	To 1187	2450	25	0.25
Lower Jurassic	2380	2666	25	0.31
Upper Triassic	2850	2724	49	0.26
Middle Triassic	3160	2755	65	0.29
Upper Bunter	3331	2670	52	0.27
Lower Bunter	3982	2710	59	0.22
Upper Permian	4032	2171	35	0.28
Lower Permian	5000	2650	45	0.24
Middle Triassic halite	2948-3038	2202	38	0.26
Upper Bunter halite	3331-3430	2071	34	0.25

Table 1: *Material and rheological parameters for each lithological layer that is used for the 3-D geomechanical modeling.*

2.4 Modeling results

As aforementioned, the general stress field in the Northwest German Basin has been extensively studied in diverse works (e.g. Fleckenstein et al. 2003, Kockel 2002, Röckel & Lempp 2003, and references therein). It is broadly acknowledged that the stress field in the North German Basin above the Upper Permian layer is generally heterogeneous and controlled by the influence of regional/local geological structures, whereas beneath the Upper Permian formation the stress field shows a uniformly favored North-South fan-shaped orientation. That is the reason why it is of paramount importance to study locally the stress

field at uppermost depths (above Upper Permian) of the crust in the North German Basin since it is locally heavily affected by neighboring geological structures such as salt domes and faults. Diverse log measurements were performed in the demonstration site GeneSys GT1 borehole in Hannover Groß-Buchholz. These measurements were made along a vertical cross-section starting from a depth of approximately 1000 m going downward, so that data in the uppermost 1000 m was not recorded. The implementation of a six-arm caliper tool together with the use of acoustic and electric methods (UBI, FMI) made possible the documentation and further refinement of borehole breakouts and tensile fractures detected at the borehole wall.

These data enabled the generation of a vertical profile of the stress field for the region of Hannover (e.g. Tingay et al. 2008). Fig. 6 displays the result of the analyses (T. Röckel, 2010, personal communication) for the minimum horizontal stress component. According to findings obtained by Röckel & Lempp 2003, the vertical stress component was assumed as the largest one. As shown in Fig. 6 (right), in the depth interval between 1000 m and 2600 m the minimum horizontal component rotates from 80° in the north direction to 170°. This reveals a reorientation of the minimum horizontal stress component from East-West to North-South. At a depth of around 3500 m, the direction of the minimum horizontal stress component changes again to 120°. One can conclusively say that the orientation of the minimum horizontal stress component exhibits an overall "swirl-pattern" over depth.

The changes in the orientation of the minimum horizontal stress component over depth significantly complicate the scheme and design of the drilling path, particularly its bending and deviation, which is instrumental for an economical and efficient geothermal energy extraction using deep-circulation or multi-fracture schemes. When needed, the deflection of the drilling path has to be performed in the direction of the minimum horizontal stress component. This way it can be avoided that the drilling trajectory coincide with the plane of the fracture growth, which is in the plane of the maximum horizontal stress component.

In this study the entire numerical computations of the stress field were conducted with the finite-element code COMSOL Multiphysics. Taking into account different assumptions such as the absence of far-field stresses, negligible pore pressure, and some specific choice of boundary conditions explained in the previous section, it is possible to explicitly express the minimum horizontal stress component (σ_h) in terms of the vertical stress component (σ_V) for a horizontally parallel layering of geological formations:

$$\sigma_h = \frac{\nu}{1-\nu}\sigma_V$$

This is a broadly acknowledged relation between the minimum horizontal stress and the vertical stress components for a passive sedimentary basin (e.g. Zang & Stephansson 2010). Under the assumption and simplification of a linear elastic response according to Hook's law as the prevailing behavior of such a domain for the time-scale considered, the horizontal

tectonic stresses generated by the gravitational load are given in general by the Young's modulus and Poisson's ratio of the respective lithological sequence (e.g. Ranalli 1995, Turcotte & Schubert 2002, Karato 2008, and references therein).

As the focus of the first numerical simulations lies on the orientation of the stress field, the pore pressure is ignored. The pore pressure has a direct effect on the magnitude of the principal stress components but not on their respective directions. Therefore, only the elastic response of the model at hand is addressed at this point of the modeling. Additional analyses intended to compare model values with values obtained from a mini-frac test of the minimum horizontal stress component don consider a hydrostatic state of pore pressure.

First model results concerning magnitude and direction of the stress field are shown in Fig. 6. The minimum and intermediate principal stress components overlap almost fully (Fig. 6, left). The slight difference is around 2-5%. Moreover, the minimum principal stress component is also computed according to the equation presented previously, it being almost in exact agreement with the values resulting from the numerical simulation. This suggests that no significant disturbance to the magnitude of the principal stresses is triggered by the complex geological structures present in the modeling domain. Nevertheless, as far as the orientation of the minimum horizontal stress component is concerned, it is obvious from Fig. 6 (right) that the complex topology of the compositional layers has a significant impact on it.
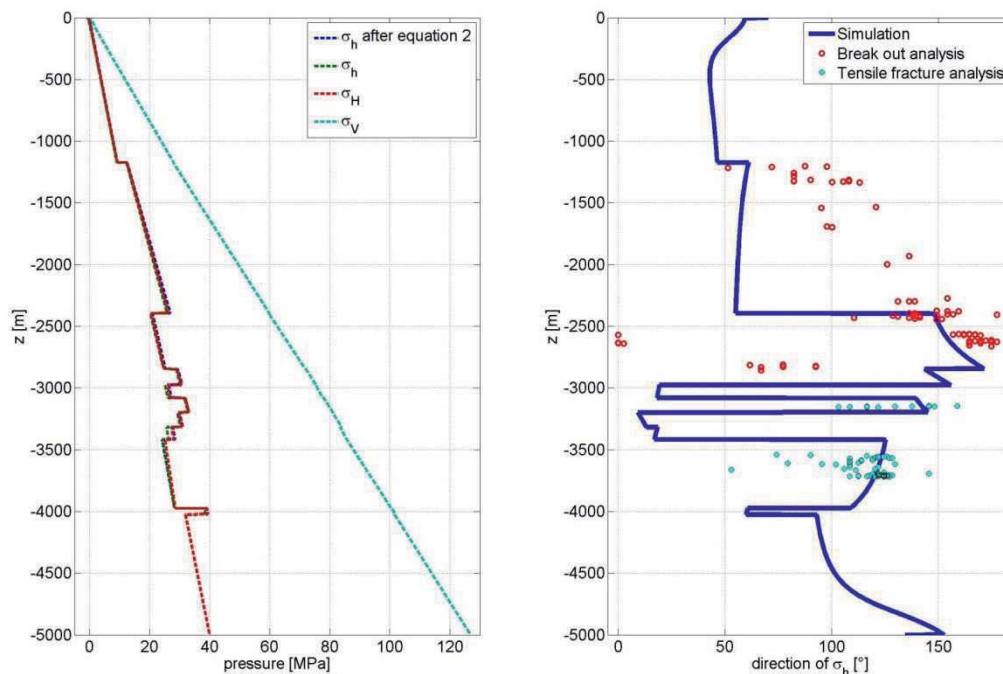
Figure 6: *Modeling results for the magnitude of the principal stress components (left) and σ_h calculated according to equation 2 as well as the direction of the minimum horizontal stress component (right). The direction of the minimum horizontal stress*

component obtained from breakout analyses and tensile fractures conducted at the drilling site Groß-Buchholz GT1 is displayed with circles of different colors.

Fig. 6 (right) displays both the modeling results of the direction of the minimum principal stress component and the data gathered from the measurements recorded at the borehole GeneSys GT1 Groß-Buchholz. With the exception of the vertical segment between 1200 m and 2400 m, the model direction of the minimum principal stress component is fully consistent with the *in situ* measurements. Model results match quite well the considerable rotation of the minimum horizontal stress component from 180° to in the Upper Triassic to 120° in the Lower Triassic. In a similar way, model results are in good agreement with the change in the direction of the minimum principal stress component within Triassic.

Diverse efforts were made to possibly resolve the mismatch between model results and *in situ* measurements of the direction of the minimum horizontal stress component in the vertical section encompassing the layers overlying Middle and Lower Jurassic. Among the attempts taken, the most prominent were the following: (I) a refinement of the troubled vertical section, adding new compositional layers such as Wealden, (II) the density of the layers involved was varied over a wide range of admissible values. None of these efforts led to a reproduction of the measured direction of the minimum horizontal stress component in the uppermost vertical section.

Alternatively, the combination of different rheological properties of predominantly salt-bearing geological structures and the influence of far-field stresses can be held to account for such direction of the minimum horizontal stress in the aforementioned upper part of the modeling domain.

As a proxy for the different rheological behaviors of salt, mainly two broadly acknowledged approaches were taken, according to Fleckenstein et al. 2003 and Thiercelin & Roegiers 2000. Whereas Fleckenstein et al. 2003 reduce the Young's modulus of salt making it weaker, Thiercelin & Roegiers 2000 simulate the expected lithostatic stress state for salt all the principal stress components by assuming a Poisson's ratio value of 0.5 and letting intact the Young's modulus. According to the "weak" and "lithostatic" approaches mentioned before, the elastic parameters of the three most prominent salt complexes (Upper Permian salt layer, and Benthe and Lehrte salt domes) were consistently varied. The goal at this point of modeling is to discriminate the impact that each salt structure and its rheological deformation mode may have on the local/regional stress field. Model results are displayed in Fig. 7 and Fig. 8.
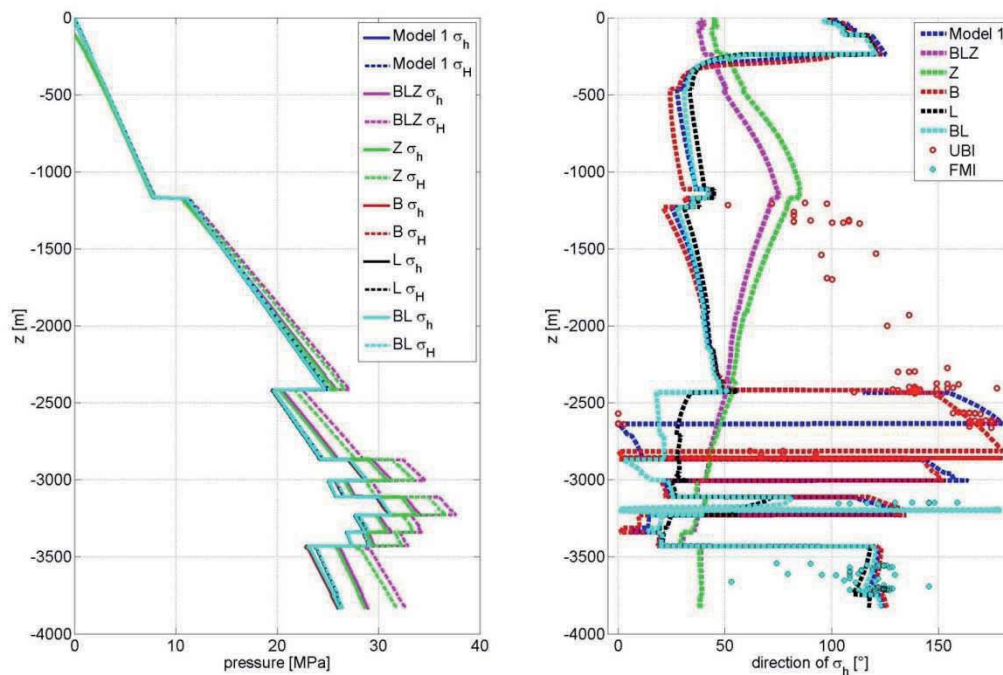
Figure 7: *Modeling results considering rheologically "weak" salt. On the left hand side, the*
magnitude of the principal stress components for different scenarios is displayed.
On the right hand side, the direction of the minimum horizontal stress component is
shown for several cases considered. Additional values obtained from breakout and
tensile fracture analyses conducted at the drilling site Groß-Buchholz GT1 are
included. The notation employed (see legend upper right) reveals which salt
modeling domain is given rheologically "weak" properties. B: Benthe salt dome
only, L: Lehrte salt dome only, Z: Zechstein layer only, BL: Benthe and Lehrte salt
domes, BLZ: Zechstein layer together with Lehrte and Benthe salt domes. Model 1
corresponds to the unaffected initial model where the rheological properties of salt
have not been changed.

For both rheological approaches used, model results suggest that the direction of the
minimum horizontal stress component is greater affected by the salt dome Lehrte than by the
salt dome Benthe. When the latter is in a rheologically "weak" or a "lithostatic" state, at a
depth of about 3400 m an overall uniform northeast-southwest orientation of the minimum
horizontal stress component is attained, which rotates then again 90° in Lower Triassic.

Similar results are obtained when varying the rheological parameters of the salt layer
contained in the Upper Permian formation. In this case, however, important departures from
the observed direction of the minimum horizontal stress component occur. The
aforementioned rotation of the minimum horizontal stress component by 90° occurs only
when this salt layer is assumed in "lithostatic" state. In contrast, when the salt layer is given

rheologically "weak" properties, no such rotation of the minimum horizontal stress component occurs and its direction remains almost unchanged over the entire considered depth.
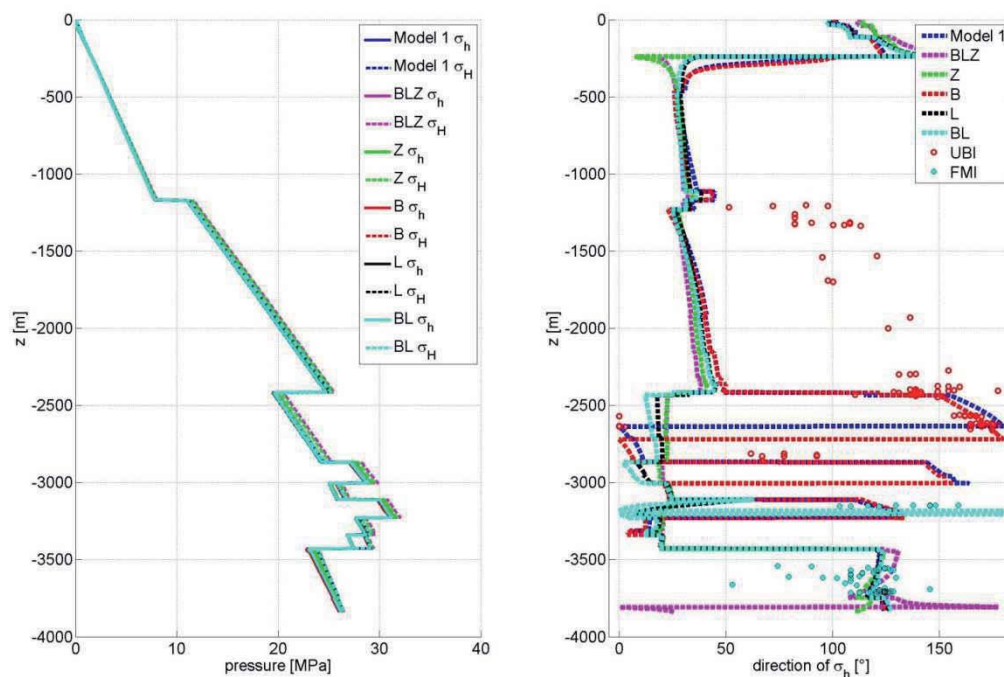
Figure 8: *Modeling results concerning the "lithostatic" salt approach. On the left hand side, the magnitude of the principal stress components for diverse scenarios are shown. On the right hand side, the direction of the minimum horizontal stress component are displayed for different cases. Additional values obtained from breakout and tensile fracture analyses conducted at the drilling site Groß-Buchholz GT1 are included. The notation utilized (see legend upper right) reveals which salt modeling domain was given rheologically so-called "lithostatic" properties. Further details regarding notation used can be read in the previous figure.*

The most reliable mini-frac test performed at the GeneSys-borehole GT1 revealed a 50-bar-higher value of the magnitude of the minimum horizontal stress component than the value obtained from the numerical simulation, where the assumed pore pressure and Biot coefficient play a relatively minor role. As shown previously, the discrepancy between the measured and the model magnitude of the minimum horizontal stress component can be resolved assuming for example "weak" rheological properties for salt material, however comprising important information about the direction of the minimum horizontal stress in the upper part of the model. Therefore, other effects on the local stress field picture such as those triggered by far-field stresses are addressed in the following.
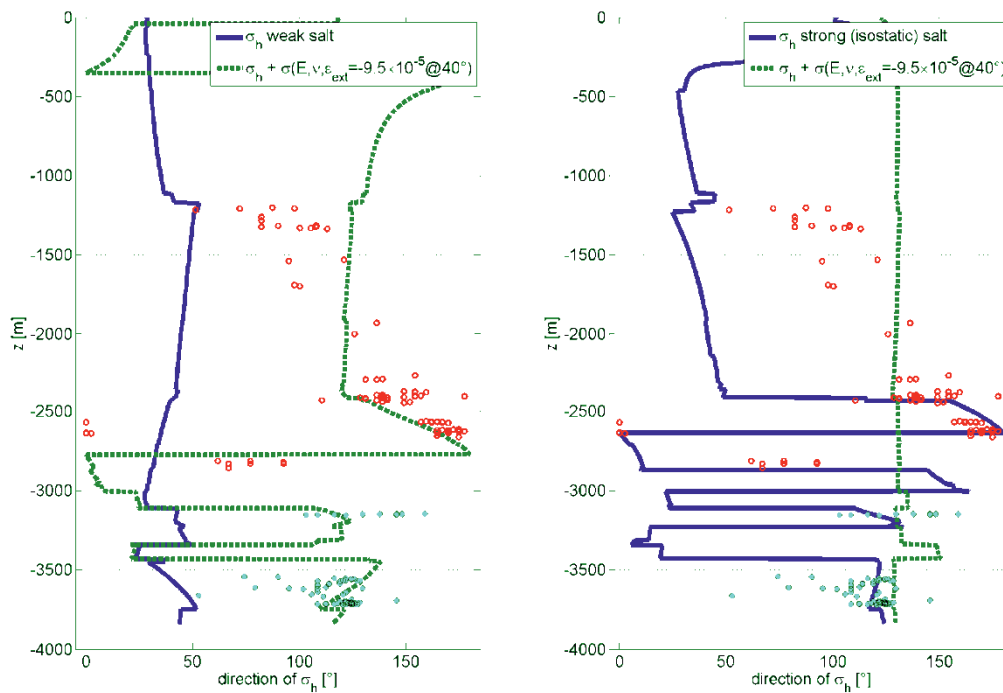
Figure 9: *Modeling results with respect to the direction of the minimum horizontal stress component (solid blue line and dashed green line). Measured values from breakout and tensile fracture analyses are displayed with cicles of different colors (see the previous two graphs for further details). On the left hand side, the direction of the minimum horizontal stress component is shown for the case that includes the effect of the rheologically "weak" salt. In addition, the direction of the minimum horizontal stress component is displayed for the case when an external compression to the modeling domain is exerted (dashed green line). On the right hand side, analogous to the right graph, the corresponding curves and results are shown, however, in this scenario a rheologically "strong" salt material with a Poisson's ratio of 0.27 has been assumed.*

According to regional tectonics and recent studies on the regional stress field in the area under investigation, a compressional strain of around 0.01% at 40° in the north direction is exerted, resulting in a superpositional stress to the local stress field. Model results are shown in Fig. 9. Employing linear elasticity for the respective sediment sequence, this compressional strain translates into additional stresses, which depending on the adopted rheological properties for salt are accommodated as deformation in the entire modeling domain.

In a similar way to the previous rheological assumptions, two cases were chosen where the occurring salt structures were assigned "weak" rheological properties and a "lithostatic" stress state. Fig. 9 (left) illustrates model results corresponding to the case where all salt

183

conglomerates considered in the model are given a smaller value of Young's modulus, called in this study "weak" salt. In this particular scenario, modeling results demonstrate that with the addition of carefully selected far-field stresses (i.e. external deformation by compression), the direction of the minimum horizontal stress component obtained from numerical simulations is consistent with the measured direction at the GeneSys-borohole GT1 Groß-Buchholz Hannover. Furthermore, in this model case the increase in the magnitude of the model minimum horizontal stress component equalizes the required 50 bar. Fig. 9 (right) shows modeling results for the scenario where the salt conglomerates occurring in the model are assigned a lower value of Poisson's ratio to simulate rather stronger rheological properties of salt, what is called in this study "strong" salt. In this specific scenario, the whole modeling block behaves rigidly as a non-deformable block and the stress field is homogeneously oriented. The external forces applied to the modeling block control the stress field within the block, adopting over the entire depth considered a uniform orientation in the direction of around 130°. All otherwise observed changes in the direction of the minimum horizontal stress component over depth are no longer reproducible since they are suppressed by the imposed far-field stresses.

3. Field measurements of rock deformation caused by hydrofacing

Hydraulic fracturing basically involves breaking the rock mass and displacing the fracture walls to create a fracture aperture. As previously mentioned, hydraulic fracture geometry can be derived from fracture-induced upper-crustal deformation. This is the essence of tiltmeter fracture mapping (e.g. report by Pinnacle Technologies Inc. 2007). An array of tiltmeters deployed on the surface and/or arranged downhole measures the upper-crustal deformation distributed in the key deformable domain. There exists extensive literature describing the main measuring techniques used in data acquisition by means of these tiltmeters (e.g. Pinnacle Technologies Inc. 2007, Cong 2007, Crosseto et al. 2009, 2010; and references therein). As shown in Fig. 3, monitoring and measuring the surface deformation field with a two-dimensional arrangement of tiltmeters complements the deformation field obtained by a one-dimensional arrangement downhole in a deviated wellbore. The latter arrangement, however, was not implemented in this study.

Surface tiltmeter mapping consists of measuring the tilt at several points about the hydraulically generated fracture domain. It follows as part of the study solving the geophysical inverse problem to assess the fracture dimensions that correspond to such measured deformation field. This is based on the principles that the generated surface deformation field is fundamentally a function of fracture parameters such as fracture azimuth, total fracture length and width, dip, and depth to fracture center. Reservoir mechanical properties as well as *in situ* stress field apparently have a negligible influence on the induced deformation field. The major drawback of surface tilt mapping, however, is that it is not

possible to obtain detailed information about individual fracture characteristics at depths greater than the induced fracture dimensions.

The Institute of Geodesy (IfE, Institut für Erdmessung) as well as the Institute of Photogrammetry and GeoInformation (IPI, Institut für Photogrammetrie und GeoInformation) of the Leibniz University of Hannover were commissioned to conduct the field measurements. Two major reports followed these field measurements (I) Monitoring of selected points using GPS in the context of the GeneSys frac experiment (Schön 2011) and (II) Area-measured monitoring using differential SAR-interferometry in the context of the GeneSys Frac experiment (Sörgel & Schunert 2011). The main findings of the field measurements and the resulting data analysis covered in these two reports are briefly presented below.

3.1 Monitoring of selected points using GPS

To monitor and possibly detect any surface deformation related to hydrofracing operations conducted within the GeneSys project framework, up to five individual stations were installed in the surroundings of the GeneSys-GT1 borehole. These five stations enabled precise and accurate GNSS (Global Navigation Satellite System) measurements. The measuring time period comprises altogether around three weeks, one week before stimulation, one week during hydraulic pumping, and one week after the injection. In doing so, the pre-injection surface position and the possible surface deformation during and after stimulation procedures can be determined.

Numerous high-quality, geodetic GNSS receivers equipped with modern and leading-edge receiving aerial form part of the vast equipment inventory owned by the Institute of Geodesy of the Leibniz University of Hannover. The stations placed in the neighborhood of the GeneSys-GT1 borehole were provided with consistent and uniform equipment and consequently an excellent homogeneity and accuracy of the measured coordinates can be expected.

The first report by Schön 2011, using the GPS technique, describes how high-quality coordinate time series were successfully computed with 6h resolution during the time period of three weeks. The variance or more precise the error bar is on the order of +/- 2 mm for the horizontal position and individually up to +/- 5 mm for the vertical location. By means of day-averaged or week-averaged values it was possible to substantially reduce the variation. Local individual artifacts such as the movement of door post by the station HAN4 (nomenclature assigned to the deployed stations, so-called "stations-ID", see Schön 2011) were identified. Linear displacements over the entire time period were negligible. Similarly, a strain analysis over the state of the network during and after the stimulation operation exhibits no significant displacements.

3.2 Area-measured monitoring using differential SAR-interferometry

Similarly and with the purpose of complementing the previously mentioned GPS measurements, the Institute of Photogrammetry and GeoInformation conducted a two-dimensional areal processing of data by means of differential SAR-Interferometry from satellite images. The differential SAR-Interferometry procedure consists basically of recording and registering detectable surface displacements. High-quality radar images, which were generated by the Synthetic Aperture Radar technique, were analyzed.

In addition to the field measurements using GPS, Sörgel and Schunert 2011 employed differential SAR-Interferometry to obtain area-covered field data. According to their report, analysis of the data obtained by SAR-Interferometry shows no ground displacement caused by the frac experiment conducted in GeneSys-GT1. This confirms the results of the GPS measurements by Schön 2011. Possible reasons for this result may be negligible underground deformation caused by the hydraulic stimulation or/and the relatively short time period during which the frac experiment was conducted. The first effect might have combined with atmospheric effects and/or might have been affected by noise (although the coherence at least at the building was high) to result in no surface horizontal or vertical displacement.

4.   Numerical modeling of rock deformation caused by hydrofracing

Numerical modeling of rock mass deformation caused by hydrofracing is also part of the task of the gebo project G5 concerning hazard assessment of massive hydraulic stimulation in geothermal reservoirs. In particular, special attention is paid to surface deformation since this may have a direct impact on neighboring communities.

Using COMSOL-Multiphysics, a variety of models were tested with different rock elastic properties typical of the North German Basin. Similarly, fluid volumes and injection rates comparable to those injected in GeneSys-GT1 frac experiment were used. None of the modeling results reveals any significant surface deformation that can be detected by any tiltmeter array displaced on the surface. With the mechanical properties similar to those encountered in the GeneSys-GT1 borehole, the hydraulic characteristics found in the surroundings of the GeneSys-GT1 geothermal demonstration site, and fluid volumes pumped into the rock mass (used in the GeneSys frac experiment) at around 3700 m depth, model results show amplitudes of surface vertical displacement around 0.025 millimeters. As an example, Fig. 10 shows an initial model with simplified characteristics. A homogeneous block of around 15 km lateral dimensions and 10 km depth was considered for the model setup. A Young modulus of 20 GPa, Poisson's ratio of 0.25, and a density of around 2850 kg/m^3 were assumed for this model. A fracture at 3700 m depth with half length 1000 m as well as 100 m height, and a constant fracture width of 1 cm were adopted for the modeling.
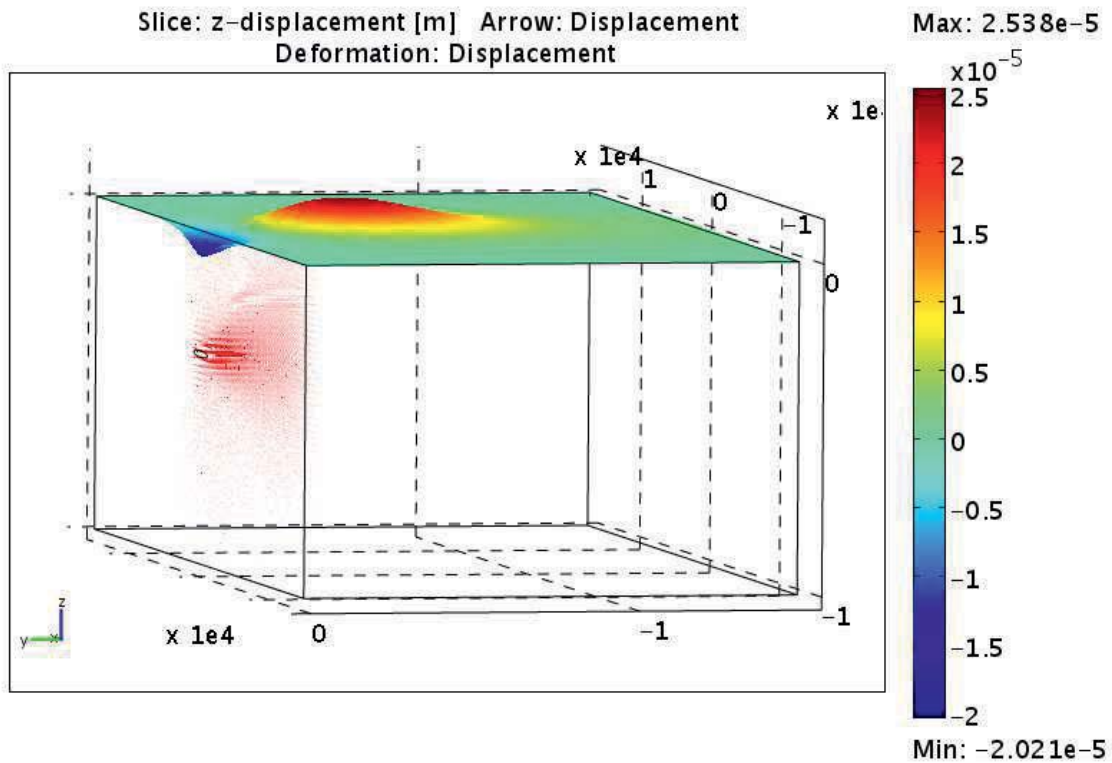
Figure 10: *Model results of rock mass deformation as a result of hydraulic stimulation using COMSOL Multiphysics. The simplified model is a homogeneous block of 15 km lateral span and 10 km depth. Note surface vertical displacement on the order of 0.025 mm. The color table shows surface vertical displacement in meter. Model dimensions are also given in meter.*

Another considered scenario that still needs more systematic investigation involves a more complex lithological stratification than the case previously shown. This model, however, contains a more realistic sediment layering, typical of the North German Basin. The model domain comprises a block of 5 km x 5 km x 5 km. The rock mass deformation and specifically the surface deformation of such a domain during and after hydraulic stimulation is the focus of interest at this stage of the modeling. In this model poro-elastic considerations are taken into account. Analogous to the previous case, a single fracture at 3700 m depth was hydraulically induced. Fig. 11 displays a horizontal cross-section at 3700 m depth of deformation caused by fluid pressure within the fracture. Fig. 12 shows the surface deformation modeling result after three days of constant injection rate of 80 l/s. Surface deformation in this case is on the order of few millimeters. However, the deformation pattern at the surface is difficult to reconcile with what is expected to result from such a scenario (see Fig. 3). Therefore, this result must be reconsidered as more systematic numerical modeling is required for such a complex scenario.
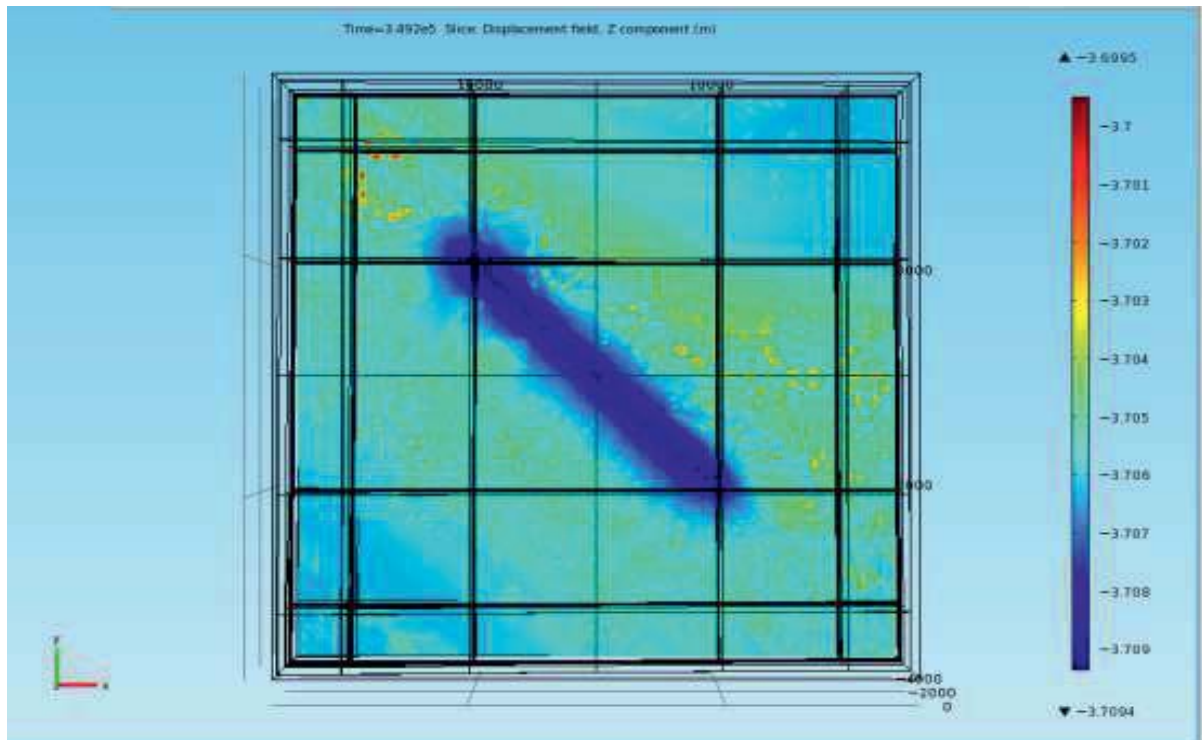
Figure 11: *Model results of cross-sectional rock deformation at 3700 m depth and after three days of constant infection rate of 80 l/s as a result of fluid pressure within the fracture using COMSOL Multiphysics. Note that the minus signs at the color table relate to extensional deformation. The color table shows the vertical deformation in meter. Model dimensions are also given in meter.*

188
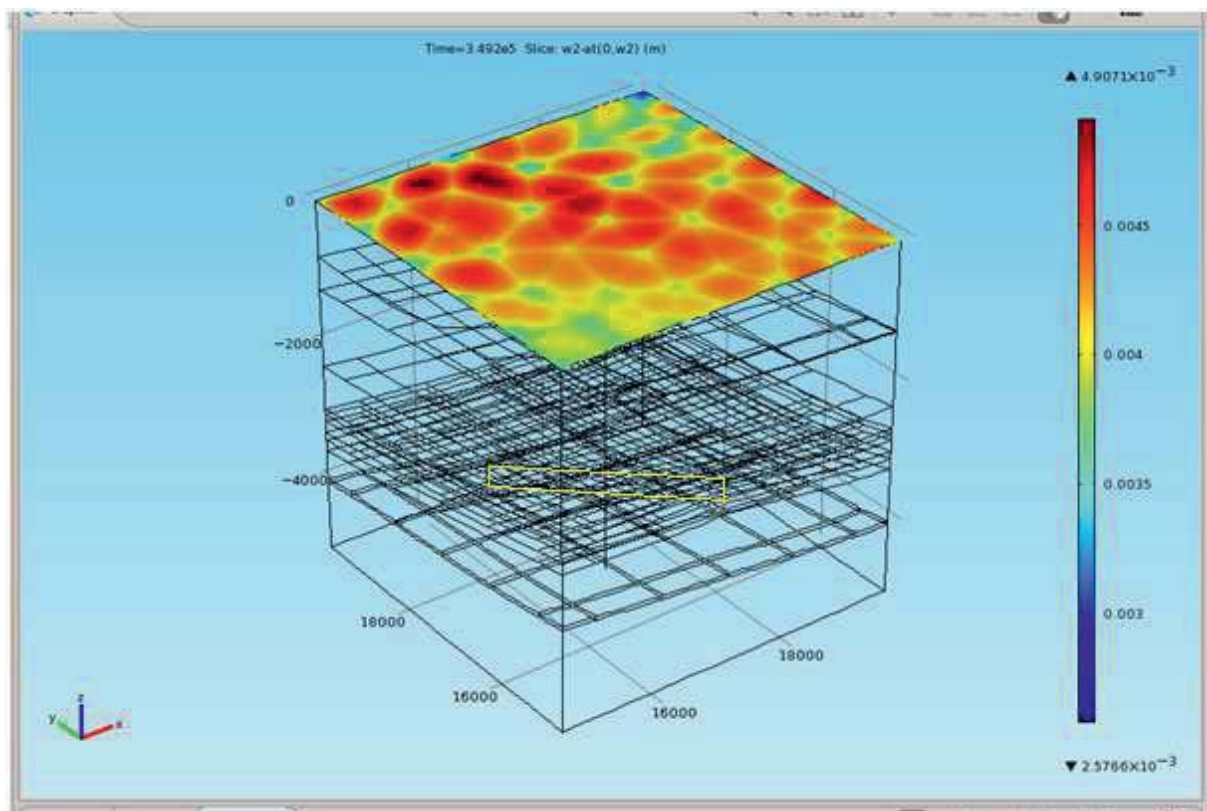
Figure 12: *Model results concerning surface deformation of a more complex lithologically layered model after three days of constant injection rate of 80 l/s using COMSOL Multiphysics. Note surface vertical displacement on the order of few millimeters. The color table shows surface vertical displacement in meters. Model dimensions are also given in meter. Note the outlined (in yellow) fracture most severely affected area.*

5. Hydro-mechanical behavior of fracture deformation

Adressing the question related to fluid-driven fracture path and geometry is essential for every geothermal study dealing with EGS in low-permeable rock formations. Important questions posed within the framework of the GeneSys project involve the fracture trajectory, the fracture dimensions, fracture hydro-mechanical interaction with the surrounding rock matrix and pre-existing joints, as well as factors controlling them. Regardless of the intricate and multifold hydro-mechanical dynamic coupling that to a large extent controls fracture initiation and growth, several other factors directly influence the fracture trajectory and geometry. In the following sections some of these controlling factors are addressed using numerical modeling. A detailed description of this study can be read in Meneses at al. 2013 b. This work was conducted in collaboration with the subproject G3 "Heterogeneous Rock Properties, Drilling Efficiency and Fracture Propagation", which provided valuable data on material parameters as well as important geological guidance.

5.1 Model setup

Due to the ample mechanical and hydraulic data gathered within the GeneSys geothermal project, comparable reservoir layering and material properties to the ones found at targeted depths were assumed. This, in turn, is intended to possibly answer questions posed within the GeneSys framework associated with fracture path and fracture geometry under comparable loading and hydraulic conditions. Additional valuable data on the mechanical properties of rock has been taken from Reyer and Phillip (2014) and Backers and Stephansson (2012). The considered scenarios of different lithologically stratified layering are shown in Fig. 13, 14, and 15.

The *in situ* stresses applied at the model boundaries of the reservoir region have been adopted from previous geo-mechanical modeling (Meneses Rioseco et al. 2013 a) as well as from results of a minifrac test conducted in the framework of the GeneSys project. Additionally, important data on the regional/local stress field published by Röckel and Lempp (2003) was taken into consideration. The loading conditions and the material properties are varied over a wide range to possibly cover a large number of sandstone, claystone, halite, and siltstone formations. Fluid pressure is kept constant over the entire simulation time for all models examined in the present work.
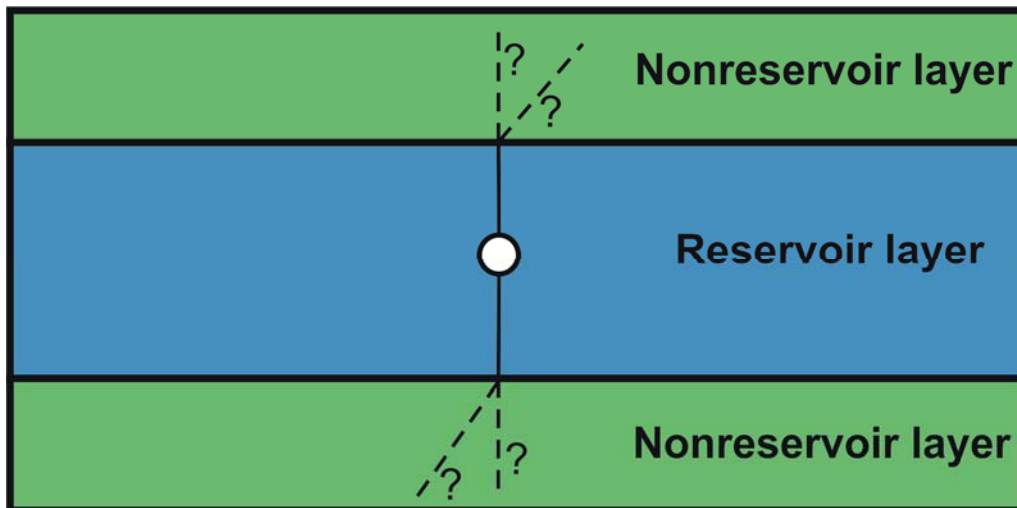
Figure 13: *2-D Model setup of a stratified reservoir with vertical symmetry. The white circle in the middle shows an injection hole from which hydraulically induced fractures (solid black lines) propagate. Dashed black lines indicate possible trajectories of through-going fractures. A particular typical scenario of the North German Basin consists of a sandstone layer sandwitched between overlying and underlying claystone layers.*
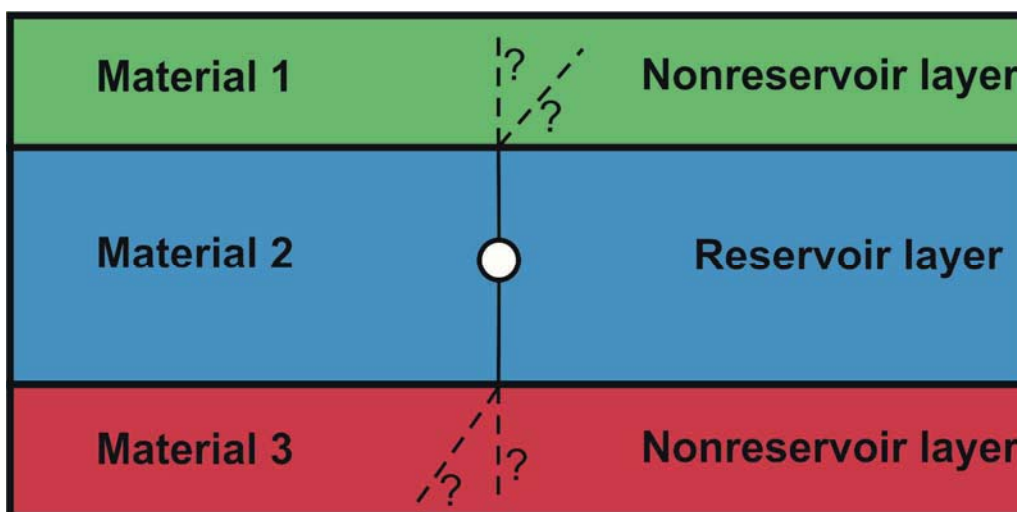
Figure 14: *Analogous to the previous picture, Fig., this scenario is related to a three-layered case of vertically asymmetric distribution of sedimentary veneer. A typical three-layered sequence of sediment encountered at targeted depths in the North German Basin constitutes halite, sandstone and claystone or siltstone formations alternated with the two preceeding sediments. For further detais see the caption of Fig. 13.*
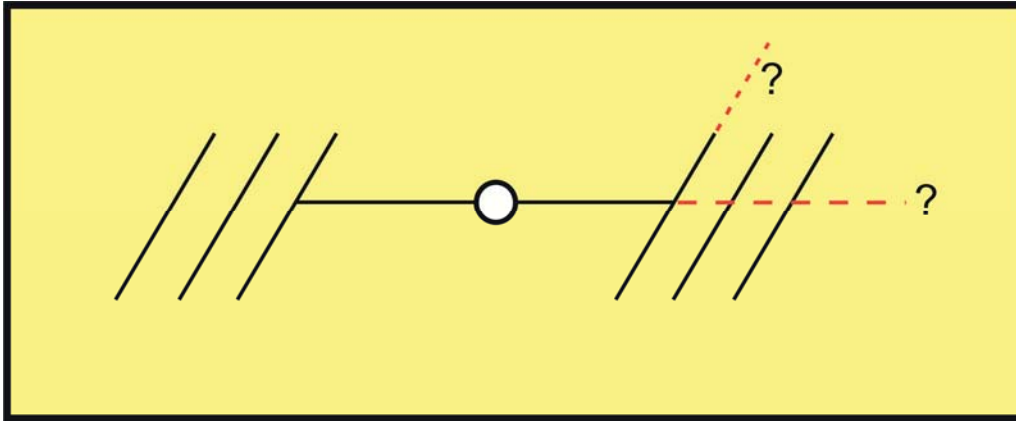
Figure 15: *Model setup considering the interaction of a hydraulically induced fracture with a conglomerate of pre-existing joints. This scenario is also relevant to deeper geothermal reservoirs in the North German Basinsuch as vulcanite. Inclined black solid lines represent pre-existing joints. Dashed red lines denote possible fracture propagations after the hydraulically generated fracture hits the pre-existing joints. Further picture details can be read in previous figures, e.g. Fig. 13.*

5.2 Numerical technique and underlying physics

The numerical code employed for the simulation of hydro-mechanical coupling mechanics involved in geothermal reservoirs is FRACOD (e.g. Shen et al. 2013). This code is a two-dimensional boundary-element tool specifically designed to capture the essential features of the fully coupled hydro-mechanical response of a rock matrix under mechanical and hydraulic loading. It is a fracture initiation and propagation code that utilizes the Displacement Discontinuity Method (DDM). In particular, FRACOD is adequate for modeling fracture initiation and fracture growth, as well as fracture hydro-mechanical interaction with matrix and pre-existing joints in elastic and isotropic media (e.g. Shen and Stephansson 1992, 1993a, b, Shen 1994, 1995, Shen et al. 1995, 2002, 2004, 2013). Mohr Coulomb failure criterion is employed to model fracture initiation. Fracture growth is modeled using a so-called modified G-criterion proposed by Shen and Stephansson 1993 a, b. One of the main capabilities of FRACOD is that fracture deformation is reproducible in tensional and shear mode, an aspect that few current codes can dynamically model. Porous flows is mimicked by means of Darcy's law. The fluid flow in damaged fractured zones is simulated with the help of the assume channel flow, which is described by the cubic law.

5.3 Modeling results

Numerous scenarios were modeled with different vertical lithologies at the targeted depths envisaged in the GeneSys project or in general encountered layering at geothermal reservoir relevant depths typical of the North German Basin. The possible fracture path and its geometry were examined based on modeling results obtained with laboratories values as

191

well as core and log measurements of elastic, mechanical and hydraulic parameters. Essentially, Young's modulus and Poisson's ratio were used as elastic parameters. The major mechanical parameter employed is fracture toughness in mode of deformation I and II. As for hydraulic parameters, the hydraulic conductivity of the rock matrix and its porosity as well as the initial values of fracture permeability were used.

Especially factors controlling fracture path through material interfaces between different sedimentary veneers were studied. A specific scenario of a conglomerate of pre-existing joints oriented with a certain angle with respect to the *in situ* stress field is included to mimic the case of deeper reservoirs such as vulcanite, where a dense population of cracks is expected. The hydro-mechanical interaction between the hydraulically generated fractures and the conglomerate of pre-existing joints is of particular interest at this stage of the work. Due to the extent of this final report, only the most conspicuous resulting cases are discussed.
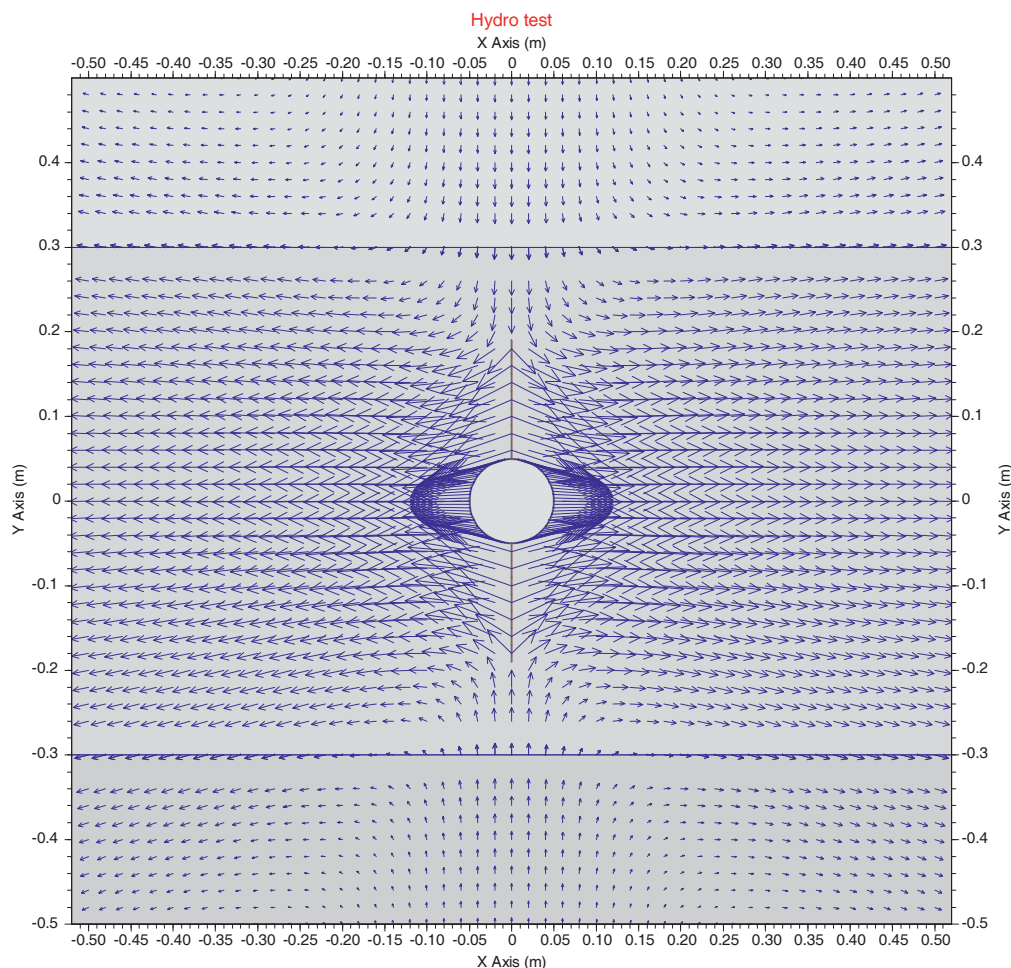
Figure 16: *Modeling results of fracture-induced displacement field around an injection hole and hydraulically generated fractures in an initial stage of modeling. The maximum displacement at this state of development corresponds to 1.756 x 10^{-4} m. Bleue arrows denote the displacement field. Solid red lines depict the hydrofractures filled with water. The white circle shows the injection hole. Horizontal blue lines mark*

material interfaces separating different sediment materials. Note advancing hydrofractures towards material interfaces.

Diverse scenarios consisting of a sandstone layer intercalated with claystone layers as well as several combinations of vertically asymmetric three-layered reservoirs of halite, sandstone, claystone and siltstone were considered. In addition, the elastic parameters of the previously mentioned sediment formations were varied over a wide range to appraise the influence of the variation of such modeling parameters on fracture arrest, fracture containment, fracture deflection, and fracture deformation in general.
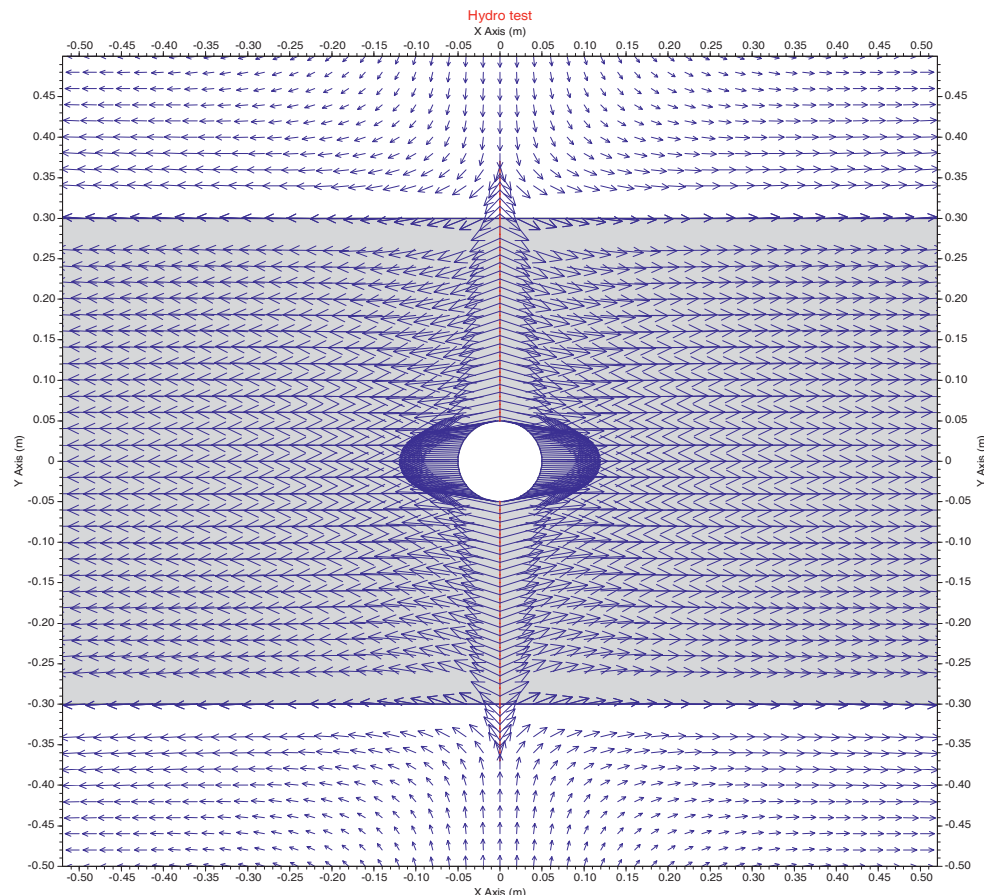
Figure 17: Modeling results of a displacement field generated by hydraulically induced fractures in an advanced stage of modeling.Different background colors (white and gray) indicate different sediment formations. Note the through-going fractures at the material interfaces. Further details of the picture can be read in the previous picture, Fig. 16.

Model results reveal that varying the Young's modulus and the Poisson's ratio over a broad range of values does not significantly contribute to fracture arrest. According to modeling results, fracture containment, whereby fractures going through material interfaces undergo damping and their apertures decrease, may be a result of varying these elastic parameters. This has already been observed in laboratories and *in situ* experiments (e.g. Fisher and Warpinski 2012, Teufel and Clarck 1984, Warpinski et al. 1982). However, these modeling

results contradict previous numerical modeling works (Jung and Sperber 2009) in regards to the intersection of hydraulic fractures through geological formations of similar kinds. Furthermore, these modeling results substantiate and confirm the concepts adopted in the GeneSys project of creating hydraulically induced fractures crossing material interfaces and connecting hydraulically different sedimentary sequences are feasible. So far, based on the current modeling results, contrast in elastic properties of the different sediment materials does not seem to arrest or deflect or switch the mode of deformation of fractures at the material interfaces (see Fig. 16 and 17). Nevertheless, this requires to be taken carefully since some assumptions and simplification are made in this modeling that otherwise may have severe implications in the results. For instance, it is broadly accepted from field and laboratory observations that interfaces themselves play a significant role in fracture path. Under certain circumstances, most probable at shallow depths, the boundedness of the interfaces may be weak enough for the hydrofractures to continue their path along the material contacts, when hitting the last ones. This phenomenon is known in the published literature as T-shaped fracture (see Gudmundsson 2011, and references therein). At significant depths, as it is the case for the targeted depths in the GeneSys project or any depth envisaged for high geothermal energy production in the North German Basin, such effect can hardly be expected.

194
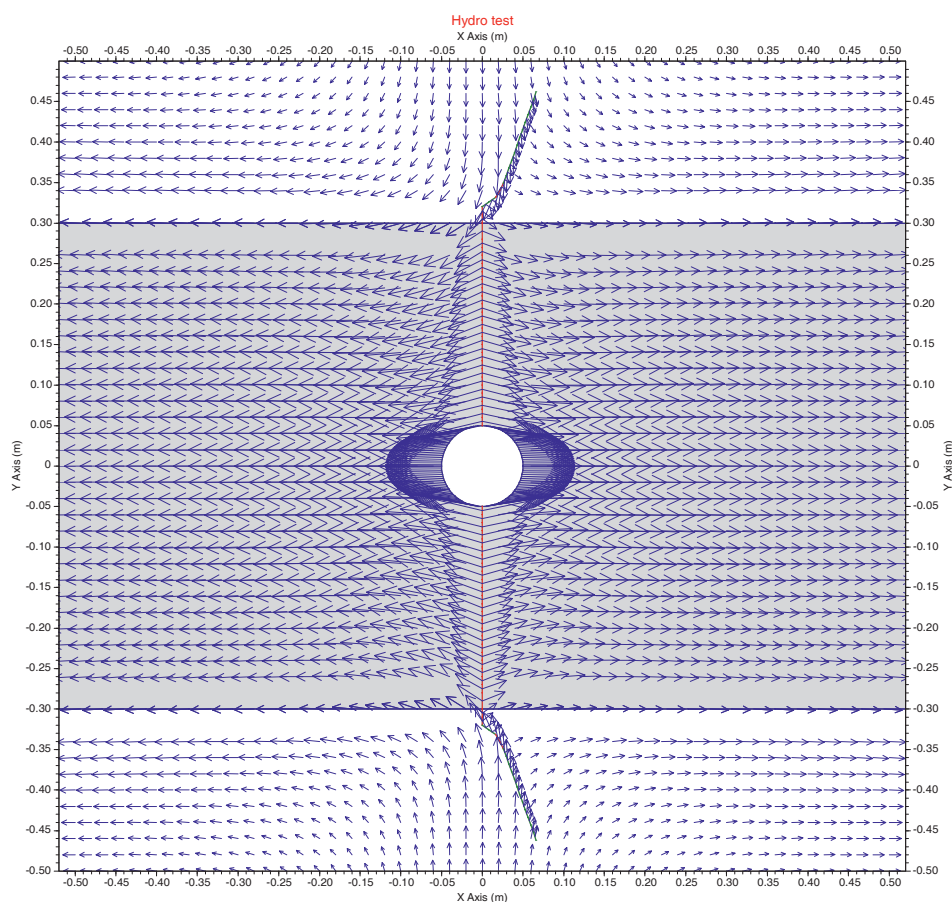
Figure 18: *Modeling results of a displacement field generated by hydraulically induced fractures that go through material interfaces and kink immediately after crossing the material interfaces. Note the switch of demormation mode from open water-filled tensional fractures (red line) to closed and shear demoation fractures (red lines, although difficult to see in the picture due to overlying features).Further details in the picture can be read in previous pictures such as Fig. 16 and 17.*
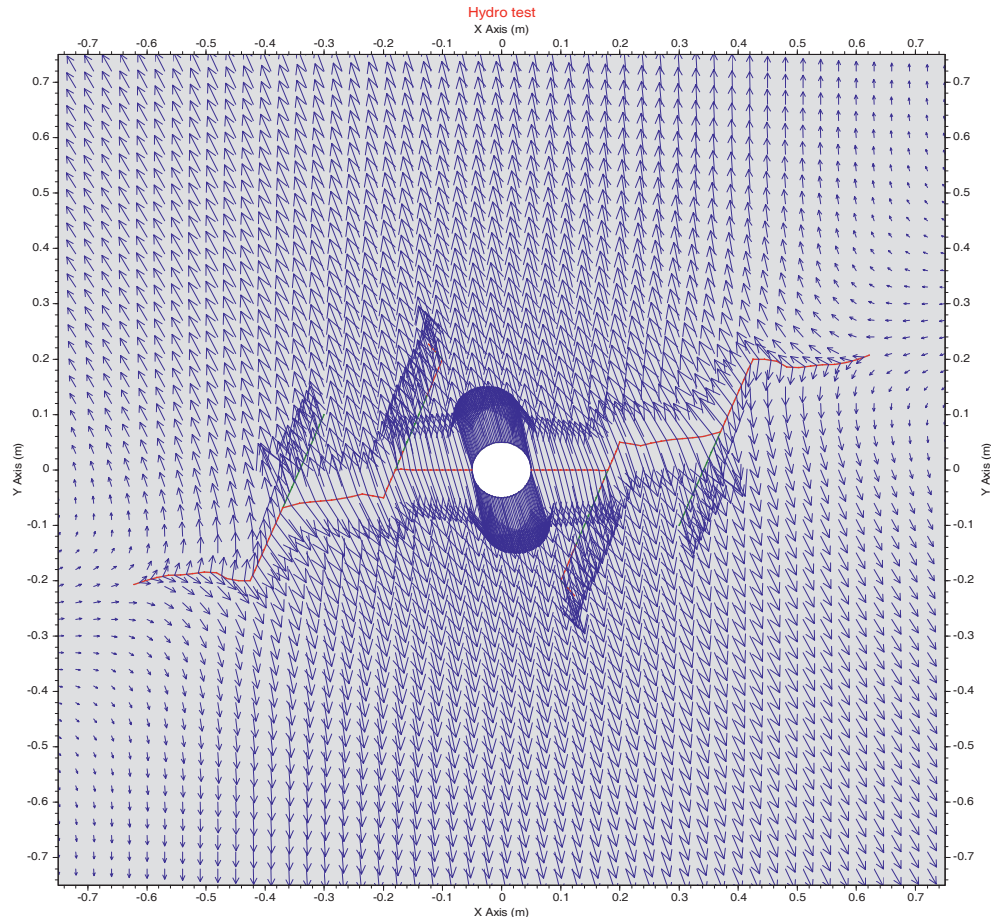
Figure 19: *Modeling results of a displacemnt field generated by the hydro-mechanical interaction of hydraulically induced fractures with pre-existing joints at an advanced stage of modeling.Note the reactivation and further propagation of pre-existing fractures initially closed. The hydraulically induced fractures propagate until they hit the pre-existing joints which reactivate and further propagate, becoming and overtaking the main hydraulic conduits.Further datails of the picture can be read in Fig. 16.*

Another important issue concerning hydro-mechanical interaction is the fracture aperture. Model results show that depending on the contrast in the elastic properties of the different material sequences involved the fracture aperture may vary. Scenarios involving stiffer materials seem to exhibit more squeezing of the fractures. This means that the fracture conductivity is slightly reduced. This, in turn, may have considerable effects on the

spatiotemporal evolution of the different flow regimes of hydraulic fractures (e.g. linear, bilinear and radial) in the shut-in phases of hydraulic stimulation (Wessling et al. 2008).

The fracture path seems to be considerably influenced by mechanical material properties such as fracture toughness. In particular, the ratio of fracture toughness in mode I and mode II of deformation of the corresponding sedimentary material in a lithologically stratified reservoir plays a key role. The fracture geometry and path as well as its hydraulic properties at the material interfaces and while penetrating the next sedimentary material seem to be severely affected by the ratio of fracture toughness in mode I and II of deformation. Generally, laboratory data on fracture toughness in mode I and II of deformation is very scarce. For the present study, values of fracture toughness in mode I and II of deformation were first acquired from laboratory data on specimens typical of the study area and later varied over a relatively wide range.

Especially for a range of values of fracture toughness in mode I and in mode II of deformation close to one another, the fracture propagation orientation deviates from its initial direction when traversing material interfaces (see Fig. 18). Moreover, the fracture mode of deformation switches from a water-filled extensional mode to a shear-dominated mode. This, in turn, implies that the hydraulic properties of the through-going fracture considerable change. The hydraulic conductivity of the section of the fracture that has crossed the material interfaces has significantly decreased.

Due to the fact that dissimilar kinds of cracks/fractures occur in different orientations with respect to the *in situ* or far-field stresses that most likely persist at the time of fracturing (e.g. Mutlu and Pollard 2008, and references therein), diverse scenarios were setup to simulate the hydro-mechanical interaction between a conglomerate of pre-existing fractures and a water-driven fracture. As mentioned previously, these study cases are of relevance for deeper formations (e.g. vulcanite), envisioned for future geothermal projects in the investigation area that also requires hydraulic stimulation.

Doing an inventory and adequately classifying fracture types and their mechanical and hydraulic properties is an essential component for evaluating and assessing the orientation of fracture populations as an entire entity. This, in turn, is vital when it comes to envisaging proper drilling trajectories and designing reservoir models.

Four pre-existing natural cracks are initially placed within the reservoir with an arbitrarily chosen orientation with respect to the *in situ* stress field (see starting point model setup in Fig. 15). What happens is, as the hydraulically generated fractures progress in time, the pre-existing fracture walls already slide past each other as a consequence of the advancing "pressure wave" ahead of the hydraulic fracture tips. Some parts of the pre-existing joints, close to the approaching hydro-fracture tips, undergo water-filled extension deformation. Already at this stage of the modeling, and in particular, of the advancing hydraulically

196

induced fractures, it is clear that different cracks/fractures or joints are characterized by different hydraulic properties. Although this modeling findings have been obtained for cases where only one sedimentary material containing the fractures has been considered, special kinds of fractures/joints may be solely generated in specific rock types or in particular geologic settings.

Fig. 19 shows the hydro-mechanical fracture interaction between conglomerates of four pre-existing fractures and a newly hydraulically induced fracture at an advanced stage of the modeling. At the onset of pressurization, the hydro-fractures propagate in the direction of one of the exerted boundary stresses. This seems to be a common behavior already discussed in previous similar modeling (e.g. Shen et al. 2013). When bumping into the pre-existing fractures, the hydraulically induced fractures cease their progress. The fluid pressure and the constantly changing stress field reactivate the pre-existing fractures and make them overtake the further propagation. The newly generated fractures tend to coalescence with the neighboring pre-existing fractures. Moreover, the newly generated fractures created at the pre-existing joints propagate in the direction of maximum shear applied to the whole host rock. Therefore, the pre-existing cracks/joints show a controlling character on the hydro-mechanical properties of the rock matrix. This correlates with previous modeling conducted by Shen et al. 2013.

Although not shown here, modeling results give also valuable insights into the hydraulic properties and in particular the spatiotemporal evolution of the fracture conductivity. Initially, at an early phase of modeling, the hydraulically induced fractures have much greater hydraulic conductivity than the pre-existing joints. As the hydraulically induced fractures progress and hit the pre-existing joints, different parts of the latter hydraulically activate and exhibit considerable conductivity. Specifically the newly generated fractures that originate from the pre-existing crack tips take up a significant portion of the hydraulic conductivity of the fracture network, becoming in this way the hydraulic dominant conduits. These modeling results are extensively described in Meneses Rioseco 2013 b.

Certainly, there are other important mechanisms that may considerably contribute to fracture arrest and fracture containment. One of these mechanisms is the so-called stress barrier. Concerning this topic, ample literature can be found (e.g. Naceur et al. 1990, Gudmundsson 2011, and references therein). Stress barriers, in other words, significant stress differences between adjacent material layers are considered to be a major factor controlling fracture arrest and containment. This issue, however, is not addressed in this work.

6. Concluding remarks

The North German Basin is particularly distinguished by the occurrence of ample salt complexes. This makes the present-day regional stress field considerably heterogeneous. The region comprising the drilling demonstration site GeneSys GT1 has been chosen as the

study area mainly because of two reasons: (I) abundant data collected and (II) two neighboring salt domes, which make this area a representative section of the North German Basin. As far as the present-day stress field in this area is concerned, a series of scenarios has been setup to numerically assess the factors controlling it. In doing so, several model cases were considered varying the parameter space. The combination of integrated, reliable data provided by the GeneSys project and valuable data acquired from laboratory measurements of specimens from the study area was instrumental to constraint the model and validate model results. Despite assuming a fairly simplified rheological model for salt material, the model stress field in the region surrounding the demonstration site GeneSys GT1 in Groß-Buchholz Hannover seems to agree favorably well with measurements performed in this place. The orientation of the stress field in the neighborhood of the salt diapirs and salt-bearing layers turn out to be especially sensitive to both the rheological properties and the rheological type of deformation assumed for salt. In particular, model results show that the superposition of specific rheological properties of salt together with tectonic far-field stresses and the interplay between them is critical when it comes to understanding the present-day state of the stress field in the study area. A more realistic and comprehensive modeling of the rheological behavior of salt would include a temperature-dependent creep mechanism. Apart from been numerically challenging, this latter aspect in turn, would require to significantly expand both the lateral boundaries of the model, which would unfortunately include new salt structures, and also the thickness of the model (going to much deeper depths of the crust/lithosphere), which is not aim of the project.

An important aspect related to hydraulic stimulation is the possible surface deformation that may be caused by it. In the context of the GeneSys frac experiment, field measurements intended to record any surface vertical displacement were performed. Using both GPS and differential SAR-interferometry techniques it was possible to focus on selected local points as well as area-covered domains. The extensive processing and analyses of the data recorded in these field measurements reveal conclusively that no significant surface deformation occurs as a result of hydraulic stimulation in the study area. Numerical simulation of several scenarios, set up with similar rock properties to those encountered in the GeneSys-borehole GT1 in Groß-Buchholz in Hannover and amount of fluid pumped into the study area, are consistent with the field measurements conducted in the are under investigation. Model results demonstrate that the volume deformation caused by the amount of water injected with similar injection rates to those applied in the frac experiment in the GeneSys project are negligible.

Another focus of this study lies in the investigation of the hydro-mechanical response of fluid driven fractures under typical mechanical and hydraulic loading conditions. Using numerical modeling, fracture geometry and path controlling model parameters such as Young's

modulus and Poisson's ratio as well as fracture toughness in mode I and II were varied over a tolerable range of region-specific, laboratory values. Several scenarios with similar lithological composition and layering to those encountered at targeted depths in the North German Basin were considered. Typical sediment sequences of the Middle Bunter were setup for the numerical modeling. Moreover, model cases involving the hydro-mechanical interaction between conglomerates of pre-existing joints and newly hydraulically created fractures were addressed to possibly conclude on future targets of hydraulic stimulation in deeper formations such as vulcanite.

Modeling results reveal that in scenarios involving sandstone sequences intercalated between overlying and underlying layers of claystone, siltstone and halite, elastic properties such as Young's modulus and Poisson's ratio do not seem to contribute to fracture arrest at material contacts. Since in the GeneSys project hydro-fractures connecting different layers are envisaged, elastic properties of material do not represent an obstacle to the realization of such cyclic exploitation procedures. However, hydro-fractures apertures may undergo some reduction while crossing material interfaces due to the difference in elastic properties of the different sediment materials. This is in line with previous laboratory and field observations. Another important controlling factor for fracture geometry and path is the fracture toughness in mode I and II of deformation and their ratio. Simulation results show that considerable differences in this material property between adjacent material sequences may cause hydro-fractures to significantly deflect from its original and prevailing path while traversing material interfaces. In addition, the fracture mode of deformation may switch from a tensional to a shear mode. This is consistent with the obtained fracture aperture reduction while propagating through different material contacts in lithologically layered reservoirs. This has considerable implications for the dynamic, fully-coupled hydro-mechanical behavioral analysis of hydro-fractures.

Model results of the hydro-mechanical interaction between conglomerates of pre-existing joints and newly generated hydraulic fractures suggest that some combination of shear displacement and opening tensional mode of deformation in naturally pre-existing cracks occurs, in advance of running into the progressing hydraulically generated fractures. This corroborates previous modeling and analytical considerations that state that as pressure in the matrix increases, the effective principal stresses applied on the pre-existing joints are reduced, facilitating shear displacement along the natural crack walls. Besides, numerical simulations reveal that when the newly water-driven fractures run bump into the pre-existing cracks, they do not continue their original path trend. Pre-existing joints undergo substantial mechanical and hydraulic alterations, propagating at their tips in the direction of the maximum shear stress. As for the newly generated hydraulic fractures, their paths are heavily influenced by the pre-existing conglomerates of joints. While initially growing in the

direction of the minimum principal stress, they are arrested at the meeting point with the pre-existing joints, and the latter overtake the further propagation. The complex of pre-existing joints undergoes major hydraulic changes. Whereas the newly created hydraulic fractures exhibit relatively high values of hydraulic conductivity over the whole simulation time, only some sections of the natural pre-existing joints interchangeably open and act as important fluid conduits, showing significant fracture aperture.

7. Acknowledgements

8. Publications resulting from the project

Meneses Rioseco, E., Löhken, J., Schellschmidt, R. & Tischner, T. (2013). 3-D Geo-mechanical modeling of the stress field in the North German Basin: Case study GeneSys-Borehole GT1 in Hanover Groß-Buchholz, *Proceedings of the Thirty-Eighth Workshop on Geothermal Reservoir Engineering Stanford University,* Stanford, California, February 11-13, 2013, SGP-TR-198.

Meneses Rioseco, E., Reyer, D. & Schellschmidt, R. (2013). Understanding and predicting coupled hydro-mechanical fracture propagation, *Proceedings of the European Geothermal Congress,* Pisa, Italy, June 3-7, 2013.

9. References

Adachi, J., Siebrits, E., Peirce, A., and Desroches, J. (2007). Computer simulation of hydraulic fractures. *International Journal of Rock Mechanics & Mining Sciences*, 44, 739 – 757, doi:10.1016/j.ijrmms.2006.11.006.

Backers, T. and Stephansson, O. (2012). ISRM suggested method for the determination of mode II fracture toughness, *Rock Mechanics and Rock engineering*, 45, 1011-1012.

Baldschuhn, R., Binot, F., Fleig, S. and Kockel, F. (2001). Geotektonischer Atlas on Nordwestdeutschland und dem deutschen Nordsee-Sektor. *Geologisches Jahrbuch*, A 153, Stuttgart (Schweizerbar).

Chen, H.-Ch. (2008). Pump induced tilt and pore pressure variations at Fuhrberg, north of Hanover and their modeling in layered half space. *Ph.D thesis, Faculty of Natural Science*, Gottfried Wilhelm Leibniz Universität Hannover.

Cong, X. Y. (2007). Untersuchung von durch unterirdische Kernexplosionen verursachten Bodenabsenkungen mittels differentieller SAR-Interferometrie. *Diplomarbeit im Studiengang Geodäsie und Geoinformatik, Leibniz Universität Hannover*.

Crosetto, M., Monserrat, O., Jungner, A., Crippa, B. (2009). Persistent Scatterer Interferometry: Potential and limits. - *ISPRS Hannover Workshop 2009*: High-Resolution Earth Imaging for Geospatial Information; ISPRS Archives – Volume XXXVIII-1-4-7/W5: 6 p.

Crosetto, M., Monserrat, O., Iglesias, R., Crippa, B. (2010). Persistent scatterer interferometry: Potential, limits and initial C- and X-band comparison. *Photogrammetric Engineering and Remote Sensing*. 76, N. 9, pp. 1061-1069.

Fisher, K. and Warpinski, N. (2012). Hydraulic-fracture-height growth: Real data, *Proceedings of the SPE Annual Technical Conference and Exhibition 2012*, Denver, Stanford, USA, SPE 145949.

Fleckenstein, P., Reuschke, G., Müller, B. and Connolly, P. (2003). Predicting stress re-orientations associated with major geological structures in sedimentary sequences. *Report to the DGMK-Research Program 593-5* "Tight Gas Reservoirs".

Fossen, H. (2010). Structural Geology, *1st edition, University Press*, New York.

Fredrich, J. T., Coblentz, D., Fossum, A. F. and Thorne, B. J. (2003). Stress perturbations adjacent to salt bodies in the deep-water Gulf of Mexico. *Society of Petroleum Engineers/Annual Technical Conference and Exhibition Drilling Conference*, Denver, Colorado, SPE Paper 84554, 14 p.

Fredrich, J. T., Engler, B. P., Smith, J. A., Onyia, E. C. and Tolman, D. N. (2007). Predrill estimation of subsalt fracture gradient: Analysis of the spa prospect to validate nonlinear finite element stress analyses. Society of Petroleum Engineers/*International Association of Drilling Contractors Drilling Conference*, Amsterdam, Netherlands, SPE Paper 105763, 8 p.

Gudmundsson, A. (2011). Rock Fractures in Geological Processes, *Cambridge University Press*, Cambridge.

Heidbach, O., Reinecker, J., Tingay, M., Müller, B., Sperner, B., Fuchs, K. and Wenzel, F. (2007). Plate boundary forces are not enough: Second- and third-order stress patterns highlighted in the World Stress Map database. *Tectonics*, 26, TC6014, doi:10.1029/2007TC002133.

Heidbach, O., Tingay, M., Barth, A., Reinecker, J., Kurfeß, D. and Müller, B. (2009). The World Stress Map based on the database release 2008, equatorial scale 1:46,000,000. *Commission for the Geological Map of the World*, Paris, doi:10.1594/GFZ.WSM. Map2009, 2009.

Jahr, T., Letz, H., Jentzsch, G. (2006). Monitoring fluid induced deformation of the earth's crust: A large scale experiment at the KTB location/Germany. *Journal of Geodynamics*, 41, pp. 190-197.

Jung, R. and Sperber, A. (2009). Erschließung der Vulkanite des Norddeutschen Beckens mit Multiriss-Systemen, *Geothermiekongress 2009*, Bochum, Deutschland, 17.-19. November (2009).

Karato, S. (2008). Deformation of Earth Materials. *1st Edition. Cambridge University Press*, New York.

Kockel, F. (2002). Rifting processes in NW-Germany and the German North Sea Sector. *Netherlands Journal of Geosciences/Geologie en Mijnbouw*, 81~(2), 149-158.

Meneses Rioseco, E., Löhken, J., Schellschmidt, R. & Tischner, T. (2013) a. 3-D Geo-mechanical modeling of the stress field in the North German Basin: Case study GeneSys-Borehole GT1 in Hanover Groß-Buchholz, *Proceedings of the Thirty-Eighth Workshop on Geothermal Reservoir Engineering Stanford University,* Stanford, California, February 11-13, 2013, SGP-TR-198.

Meneses Rioseco, E., Reyer, D. & Schellschmidt, R. (2013) b. Understanding and predicting coupled hydro-mechanical fracture propagation, *Proceedings of the European Geothermal Congress,* Pisa, Italy, June 3-7, 2013.

McClure, M. W., and R. N. Horne (2013). Discrete Fracture Network Modeling of Hydraulic Stimulation: Coupling Flow and Geomechanics. *SpringerBriefs in Earth Sciences, Springer International Publishing*, Heidelberg, Germany, doi: 10.1007/978-3-319-00383-2.

McClure, M. W. (2014) a. Diagnostic fracture injection tests with complex fracture networks. *The Leading Edge*, 33(5), 546-548, doi: 10.1190/tle33050546.1.

McClure, M. W. (2014) b. The potential effect of network complexity on recovery of injected fluid following hydraulic fracturing. *SPE 168991, paper presented at the SPE Unconventional Resources Conference* - USA, The Woodlands, TX.

Mutlu, O. and Pollard, D. D. (2008). On the patterns of wing cracks along an outcrop scale flaw: A numerical modelling approach using complementarity, *J. Geophys. Res.*, 113, B06403.

Naceur, K. B., SPE, Touboul, E. and Schlumberger, D. (1990). Mechanisms controlling fracture-height growth in layered media, *SPE Production Engineering*, *Society of Petroleum Engineers*, May, 1990.

Pinnacle Technologies, Inc. (2007). Surface tiltmeter fracture mapping results for the Klatt No. 31-14H. Final report for Marathon Oil Company. Project No. MARA-1677, Report date: November 14.

Ranalli, G. (1995). Rheology of the Earth. *2nd Edition. Chapman & Hall*, London.

Reinicke, K. M., Oppelt, J., Ostermeyer, G. P., Overmeyer, L., Teodoriu, C. and Thomas, R. (2010). Enhanced Technology Transfer for Geothermal Exploitation through a New Research Concept: The Geothermal Energy and High-Performance Drilling Research Program: gebo. In: *SPE Annual Technical Conference and Exhibition*, 19-22 September 2010; Florence, Italy.

Reyer, D. and Philipp, S. (2014). Empirical relations of rock properties of outcrops and core samples from the Northwest German Basin for geothermal drilling, *Geothermal Energy Science*, doi:10.5194/gtes-2-21-2014.

Röckel, Th. And Lempp, Chr. (2003). Der Spannungszustand im Norddeutschen Becken, *Erdöl Erdgas Kohle 119*, Helft 2.

Saleh, B., Sadoun, B., Blum, P. A. (2003). Measurements of surface deformation associated with hydrofracture. *Proceedings 11th FIG Symposium on Deformation Measurements*, Santorini, Greece.

Schön, S. (2011). Monitoring ausgewählter Punkte mittels GPS im Rahmen des GeneSys Frac-Experiments. Abschlussbericht, Leibniz Universität Hannover, Institut für Erdmessung.

Shen, B. and Stephansson, O. (1992). Deformation and propagation of finite joints in rock masses, In: Myer et al. (eds), *Fractured and Jointed Rock Masses*, pp. 303-309.

Shen, B. and Stephansson, O. (1993) a. Modification of the G-criterion of crack propagation in compression. International, *Journal of Engineering Fracture Mechanics*, 47(2)**,** 177-189.

Shen, B. and Stephansson, O. (1993) b. Numerical analysis of Mode I and Mode II propagation of rock fractures, *International Journal of Rock Mechanics and Mining Sciences & Geomechanics*, 30(7)**,** 861-867.

Shen B. (1994). Mechanics of fractures and intervening bridges in hard rock, *Bergmekanikdag 1994*, pp. 213-231.

Shen, B., Stephansson, O., Einstein, H. H. and Ghahreman, B. (1995). Coalescence of fractures under shear stresses in experiments, *Journal of Geophysical Research*, 100(B4)**,** 5975-5990.

Shen, B. (1995). The mechanism of fracture coalescence in compression - experimental study and numerical simulation, *International Journal of Engineering Fracture Mechanics*, 51(1)**,** 73-85.

Shen, B., Stephansson, O. and Rinne, M. (2002). Simulation of borehole breakouts using FRACOD2D, *In: Oil & Gas Science and Technology - Revue de l'IFP, special issue for International Workshop of Geomechanics in Reservoir Simulation*, 5 to 7 December 2001, IFP. Rueil-Malmaison, France, 57(5): 579-590.

Shen, B., Stephansson, O., Rinne, M., Lee, H. S., Jing, L. and Roshoff, K. (2004). A fracture propagation code and its applications to nuclear waste disposal, *International Journal of Rock Mechanics & Mining Sciences*, 41, No.3., pp. 448–449, and Paper 2B 02 — SINOROCK2004 Symposium.

Shen, B., Stephansson, O. and Rinne, M. (2013). Modelling fractured rocks. A fracture mechanics approach using FRACOD, in print, Springer, Heidelberg, New York.

Sörgel, U. & Schunert, A. (2011). Flächenhaftes Monitoring mittels differentieller SAR-Interferometrie im Rahmen des GeneSys Frac-Experiments. Abschlussbericht, Leibniz Universität Hannover, Institut für Photogrammmetrie und GeoInformation.

Teufel, L. W. and Clark, J. A. (1984). Hydraulic fracture propagation in layered rock: Experiment studies of fracture containment, *Society of Petroleum Engineers Journal*.

Thiercelin, M.C. and Roegiers, J.~C. (2000). Formation characterization: rock mechanics. *In: M.J. Economides and K.G. Nolte*, Editors, Reservoir Stimulation, Wiley and Sons Ltd., United Kingdom.

Tingay, M., Reinecker, J. and Müller, B. (2008). Borehole breakout and drilling-induced fracture analysis from image logs. http//www.world-stress-map.org.

Trautwein, U. (2005). Poroelastische Verformung und petrophysikalische Eigenschaften von Rotliegend Sandstein. *Dissertation, TU Berlin*,
ULR:http://opus.kobv.de/tuberlin/volltexte/2005/1151/,(2005).

Turcotte, D.~L. and Schubert, G. (2002). Geodynamics. *2nd Edition. Cambridge University Press*, Cambridge.

van der Zee, W., Ozan, C., Brudy, M. and Holland, M. (2011). 3D Geomechanical Modeling of Complex Salt Structures. *SIMULIA Custom.mer Conference*.

Warpinski, N. R., Schmidt, R. A. and Northrop, D. A. (1982). In-Situ Stresses: The predominant influence on hydraulic fracture containment, *Journal of Petroleum Technology*.

Wessling, S., Junker, R., Rutqvist, J., Silin, D.: Sulzbacher, H., Tischner, T. and Tsang, Ch. (2008). Pressure analysis of the hydromechanical fracture behaviour in stimulated tight sedimentary geothermal reservoirs, *Geothermics*, doi:10.1016/j.geothermics.2008.10.003.

Zang, A. and Stephansson, O. (2010). Stress Field of the Earth's Crust. *1st edition. Springer Verlag*.

Ziegler, P. A. (1990). Geological Atlas of Western and Central Europe. *Shell Internationale Petroleum*, Maatschappij/Amsterdam, Elsevier, The Hague. 239 pp.

Zimmer, U. (2001). Quantitative Untersuchung zur Mikrorissigkeit aus akustischen Gesteinseigenschaften am Beispiel von Steinsalz und Anhydrit. *Dissertation, TU Berlin*, ULR: http://opus.kobv.de/tuberlin/volltexte/2001/145/.

G6: Hydraulic, thermal and tracer tests at wellbore and reservoir scale

Julia Ghergut* and Martin Sauter

Applied Geology Group, University of Göttingen, Goldschmidtstr. 3, 37077 Göttingen

*Corresponding author: iulia.ghergut geo.uni-goettingen.de

Abstract

To set up a geothermal reservoir (in the N-German Basin), it does not suffice to drill down to depths where hot fluids are encountered in either sufficiently-permeable formations ('deep aquifers') or in tight layers that are suitable for hydraulic fracturing ('petrothermal'). One must also ensure that such 'reservoirs' can be operated sustainably – for at least three decades, as a rule. Reservoir lifetime cannot be predicted from mere temperature and permeability measurements. The main parameters determining the thermal lifetime of a geothermal reservoir – fluid residence times, heat exchange areas – cannot be captured by geophysical methods or by hydraulic tests. Such parameters can, in principle, be measured by means of tracer tests, conducted in inter-well and/or single-well configurations; however, this is not a trivial task. This report analyzes, extends, revises, and proposes some new tracer techniques for georeservoir characterization, monitoring, and engineering (applicable during specific stages of reservoir development and operation, addressing distinct space and time scales), with a special focus on matching tracer species selection to georeservoir typology, and on improving parameter sensitivity (disambiguation) in single-well tests. The 'gebo *benchmark models*' developed by 'gebo' project partners within 'Focus Area *Geosystem*' provided the backbone of all conceptual models used for simulating and analyzing flow and transport processes. Two field sites in the N-German Basin (Horstberg, and Gr. Schönebeck) are given special consideration, owing to the unique lessons they taught the geothermal community worldwide.

Abbreviations:

EGS: enhanced geothermal system

FC: frac circulation (option tested at the Horstberg site)

IW: inter-well

MRT: mean residence time

PP: 'push-then-pull' (injection-then-withdrawal)

RTD: residence time distribution

SW: single-well

TT: tracer test

1.   Introduction

Tracer methods are indispensable for measuring transport-related properties of subsurface flow systems. In the context of geothermal reservoir development, characterization, monitoring, and engineering, tracer methods are indispensable to determining a number of parameters controlling reservoir productivity and lifetime, like: inter-well connectivity, fluid residence time distribution, heat exchange area, and fluid-rock interface parameters steering corrosion/scaling processes (fig. 1).

Hydraulic and geophysical methods cannot measure the transport-effective values of such parameters, because the signals they detect correlate neither with fluid motion, nor with material fluxes through (fluid-rock, or fluid-fluid) phase interfaces. Typically, pressure signals obtained in hydraulic tests do not enable to distinguish between geological formations with (fig. 2) equal permeability, but different transport-effective porosity, nor between formations with equal permeability, equal transport-effective porosity, but different fluid-rock interface area. The ability to measure this latter parameter is crucial to lifetime predictability for geothermal, gas storage (including CCS), waste disposal, or hydrocarbon reservoirs (especially in advanced depletion stages).

Whereas the use of inter-well tracer tests (IW TT) for assessing inter-well connectivity and fluid residence times is relatively well-established, the use of single-well tracer tests (SW TT) is relatively new in the geothermal realm. Single-well 'push-then-pull' (SWPP) tracer methods appear as attractive for a number of reasons: less uncertainty of design and dimensioning, and lower tracer quantities required, than for IW tests; stronger tracer signals, enabling easier and cheaper metering, and shorter metering duration required, reaching higher tracer mass recovery, than in IW tests; last not least: no need for a second well! However, SW tracer signal inversion faces a major issue (Tomich et al. 1973, Schroth et al. 2001, Ghergut et al. 2013b): the PP design weakens the correlation between tracer residence time distribution (RTD) and fluid transport parameters, inducing insensitivity or ambiguity of tracer signal inversion against precisely those georeservoir parameters that are supposed to be the target of TT par excellence: pore velocity, transport-effective porosity, fracture aperture and spacing or density (where applicable), fluid/solid or fluid/fluid phase interface density. This is why SWPP techniques, and ideas on improving their parameter sensitivity are been paid special attention in this report.

Any TT will involve the injection, with simultaneous or subsequent extraction (or at least sampling) of fluids into / from the reservoir. Since during any such operation flow-rate and pressure gauging is never omitted, hydraulic information (H) will automatically accompany any TT. Moreover, it is a basic endeavor to integrate TT into 'normal' reservoir operation, or into 'standard' hydraulic testing programs, as smoothly as possible. All these aspects are expressed by 'HTT' in the name of this project.
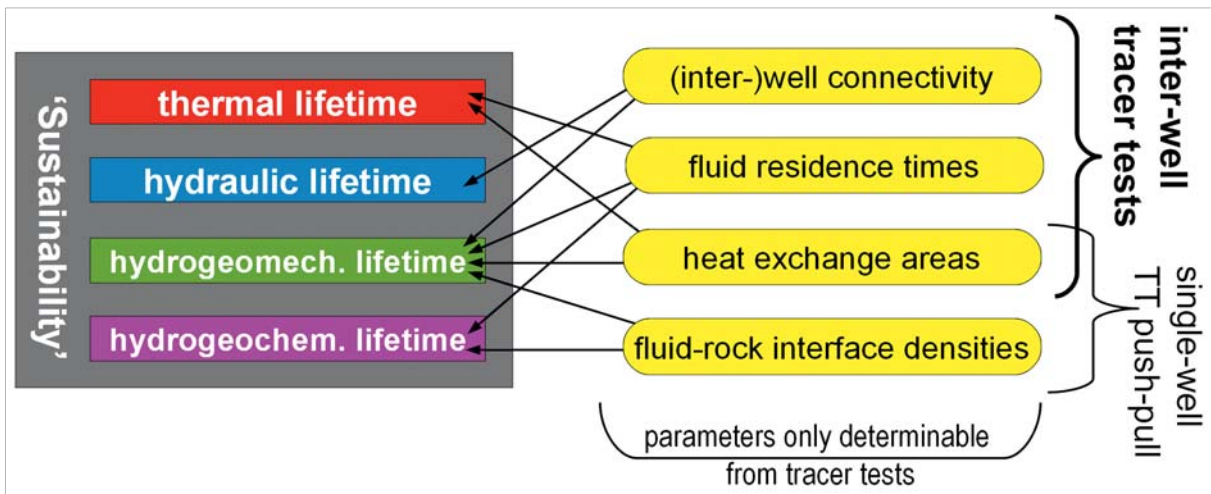
Figure 1: *Main target parameters of tracer tests in geothermal reservoirs.*
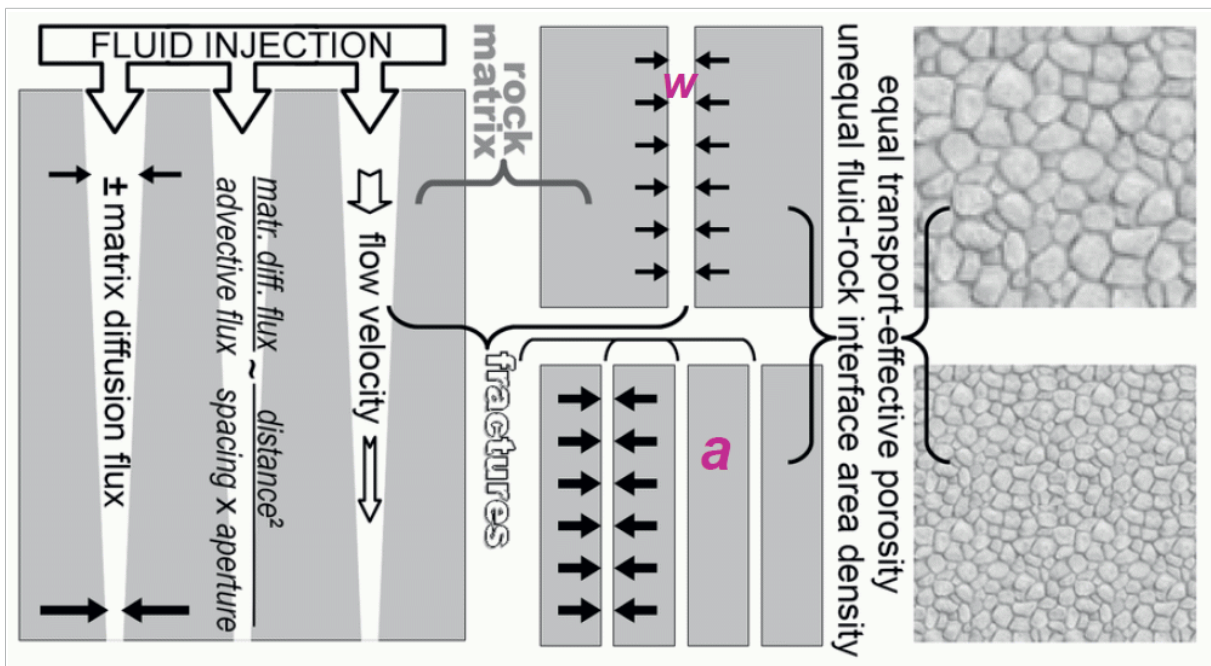
Figure 2: *Symbolic representation of fluid-rock interface-area density in fractured/porous media, and of its possible change induced by coupled THM processes. In a homogeneous parallel-fracture system, characterized by a constant fracture aperture w and a constant fracture spacing a, under spiked fluid injection at rate Q, the relative importance of matrix diffusion against advective-diffusive fluxes at distance r from the tracer injection point varies like $r^2 / (Q \times a \times w)$ at early times, and like $r^2 / (Q \times w^2)$, independently on w, at late times.*

2.   Tracer-based prediction of thermal lifetime

Thermal-lifetime prediction is a major endeavor of IW TT conducted in geothermal reservoirs. Early TT signals (detectable within the first few years of operation) are expected to correlate with late-time production temperature drop (so-called 'thermal breakthrough', supposed to not occur before some decades of operation) of a geothermal reservoir. Whenever a geothermal reservoir can be described as a 'single-fracture' system, its thermal lifetime will, ideally, be determined by two parameters, whose inversion from conservative-TT signals is straightforward and non-ambiguous (provided that the TT, and their interpretation, are performed in accordance to the rules of the art). However, as soon as just 'few' more fractures come into play, this clear-cut correlation is broken. A given geothermal reservoir can simultaneously exhibit (fig. 3) a single-fracture behavior, in terms of heat transport, and a multiple-fracture behavior, in terms of solute tracer transport (or vice-versa), whose effective values of fracture aperture, spacing, and porosity are essentially uncorrelated between heat and solute tracers. Solute transport parameters derived from conservative-tracer tests will no longer characterize the heat transport processes (and thus temperature evolutions) taking place in the same reservoir. Parameters determining its thermal lifetime will remain 'invisible' to conservative tracers in IW TT. We demonstrated this issue at the example of a five-fracture system (fig. 3, r.-h.s.), representing a geothermal reservoir, with well-doublet placement inducing fluid flow and heat transport 'obliquely' to the fractures. Thermal drawdown in this system is found to strongly depend on fracture aperture, whereas conservative-solute tracer signals from inter-well tests in the same system do not show a clear-cut correlation with fractures' aperture. Only by using 'thermosensitive' substances as tracers (assuming their thermal degradation to be governed by Arrhenius' law), a reliable correlation between (early) tracer signals and (later) thermal breakthrough can be re-established. A more detailed analysis of this 'oblique-fracture' paradigm, alongside with further examples can be found in Ghergut et al. (2011, 2012, 2013d). Thus, thermosensitive tracers appear as indispensable for predicting thermal breakthrough, in such geothermal reservoirs whose hydrogeological 'personality' is defined by a finite set of fractures (of in-/finite extension), with flow occurring both across and along the fractures. In terms of the 'gebo *benchmark-model*' typology investigated by Hördt et al. (2011), Hahne and Thomas (2014), such systems combine flow and transport patterns of the 'petrothermal' type and of the so-called 'deep-aquifer' type: across the fractures, heat is traveling faster than conservative-solute tracers; along the fractures, conservative-solute tracers experience much less retardation by transverse exchange (matrix diffusion), than heat; fluid (and tracer) flow is not limited to the fractures; flow within the matrix yields an essential contribution to prolonging the fluid (and tracer) residence time, and thereby increasing the reservoir's thermal lifetime.
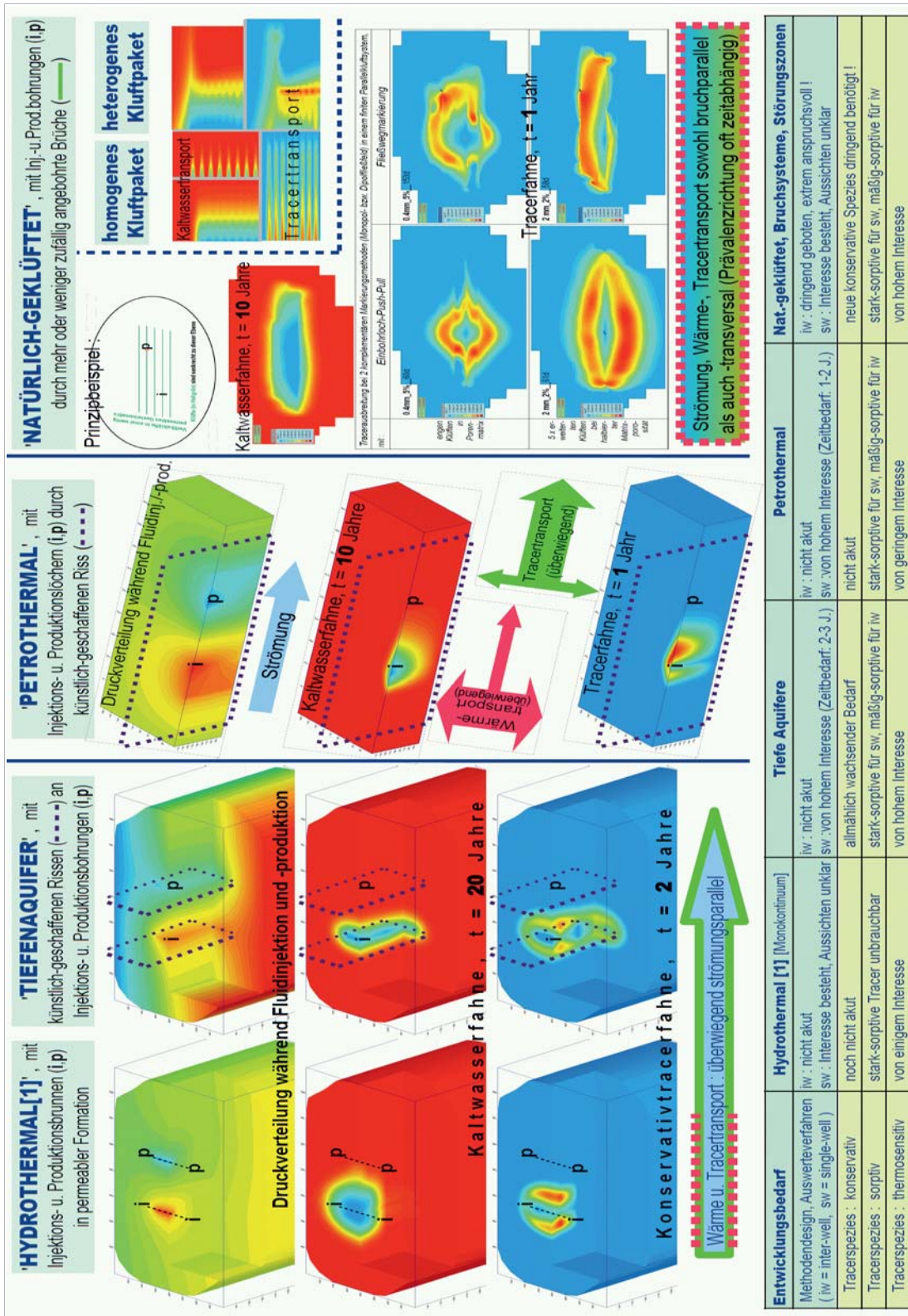
Figure 3: Matching tracer species selection to geothermal reservoir typology.

Thermal lifetime thus results from flow 'splitting' between fractures and matrix (depending on their relative hydraulic transmissivity), alongside with the opposite effects of fracture aperture

as an advection-related parameter (fluid travel time increases with increasing fracture aperture), and advection-unrelated parameter (the fracture-matrix exchange rate increases with decreasing fracture aperture, the latter accelerating transport both across and along the fracture, cf. also fig. 2). In conservative-solute tracer signals, these fracture aperture effects on tracer transport are masked by the very long residence time associated with the matrix flow component. Thermosensitive tracers appear as able to magnify the 'visibility' of fracture aperture effects against matrix flow effects. Furthermore, they are expected to perform this with a finer spatial resolution than the usual large-scale geophysical methods.

Non-conservative tracers, in particular sorptive or thermosensitive compounds (Nottebohm et al. 2010, 2012), can be used to overcome certain (though not all) 'gaps' or 'disparities' between heat and tracer transport. However, significant differences exist, regarding tracer functionality within them, between the distinct types of (liquid-only) geothermal systems: 'hydrothermal' systems, or 'hot natural aquifers', with predominant, or equivalent, 'porous-medium' character, 'aquifer'-based EGS, 'petrothermal'-type EGS, natural porous-fractured systems (fig. 3, l.-h.s.).

In hydrothermal systems, the geologic formation's permeability, times its thickness over which the geothermal wells are screened, is sufficient for ensuring a viable geothermal reservoir – with long enough thermal lifetime, whose correlation with fluid residence time is roughly linear, the relative retardation of the cooling front against the tracer front keeping constant in time. Also, the naturally-given permeability is large enough to prevent excessive pressure buildup/drawdown from developing at injection/ production wells, in spite of the strong hydraulic gradients around the wells. The latter is not the case in 'aquifer'-based EGS: here, artificial fractures are needed in order to prevent such hydraulic gradients from occurring, as well as to increase the effective cross section for heat transport; whereas the correlation between thermal and tracer fronts remains linear, like for hydrothermal systems. In contrast, in 'petrothermal'-type EGS, the geologic formation's permeability is 'bad' enough over a large-enough depth interval, to enable large-scale artificial fracturing; thus created, large-area artificial fractures can be crossed by injection/production wells in sufficient distance from each other, to provide for a viable geothermal reservoir. The correlation between thermal and tracer fronts is no longer linear, but becomes dominated by a MRT-quadratic term. Natural porous-fractured systems (fig. 3, r.-h.s.) can combine various features from all of the above; modeling flow and transport in such systems proves to be quite a demanding endeavor. Heat transport occurs prevailingly along the flow direction, in hydrothermal systems and 'aquifer'-based EGS; it is dominated by transverse exchange across matrix and fracture, in 'petrothermal'-type EGS; whereas for natural porous-fractured systems, the prevailing direction(s) of heat transport cannot be told a priori! Conservative

tracers remain indispensable to characterizing any of these reservoir types, but their RTD correlates differently with thermal lifetime. The more pronounced the 'petrothermal' character, the more the MRT-quadratic term will prevail within the expression of thermal lifetime. It thus turns out that thermo-sensitive tracers are (roughly speaking) less useful in 'petrothermal'-type, than in 'aquifer'-based EGS; whereas sorptive tracers prove more useful in 'petrothermal'-type, than in 'aquifer'-based EGS. This can also be understood from the contrasting roles played by artificial fractures in 'aquifer'-based, versus 'petrothermal'-type EGS, with regard to flow and transport of heat and solutes (including tracers).

3.   SWPP signal sensitivity to fracture aperture and spacing values

We examined the sensitivity of SWPP tracer test signals towards the transport-effective fracture aperture w (for a single- or a parallel-fracture reservoir), as well as towards fracture spacing a (in a parallel-fracture reservoir), as defined by fig. 2, more details being given in (Ghergut et. al 2013c). To be noted, the actual reason for focusing on fracture aperture and fracture spacing is not their geometrical (formal) equivalence with heat exchange areas, but (i) their great diagnostic value during reservoir evaluation and development (also being dealt with by, or being of interest to gebo projects G1, G3, B4, G4, G5, G8, B1, B2); and (ii) their relevance not only to the thermal lifetime, but also to the hydraulic, hydrogeomechanical and hydrogeochemical lifetime (fig. 1) of a geothermal reservoir (also being addressed within project G7, and also being of interest to project G9).

SWPP is best suited for measuring heat exchange areas in 'multi-frac' systems like those proposed by Jung (2013); SWPP is rather inadequate for measuring heat exchange areas in such geothermal systems like those created at Horstberg, Groß Buchholz, Groß Schönebeck in the N-German Basin, or the typical hydrothermal reservoirs in the Eastern Upper Rhine Rift Valley. In the function of a diagnostic and characterization tool, the value of SWPP remains undiminished for any geothermal system in the N-German Basin.

From numerical simulations (Ghergut et al. 2013c), we identified 4 characteristic parameter sensitivity regimes: (i) early-time regime: tracer signals are sensitive to fracture aperture, but insensitive to fracture spacing; sensitivity to fracture aperture first increases, then decreases with T_{push} / T (thus there will be an 'optimum' in terms of T_{push} / T, at early pull times); (ii) mid-time regime: tracer signals are sensitive to fracture spacing, but insensitive to fracture aperture; sensitivity to fracture spacing increases with T_{push} / T ; (iii) late-time regime: with increasing pull duration, tracer signals become increasingly insensitive to fracture spacing, while regaining sensitivity to fracture aperture; (iv) 'very late'-time regime: sensitivity towards fracture aperture becomes independent on T_{push} / T . The non-monotonicity against T_{push} / T seen at early pull times occurs because the effects of matrix diffusion decrease in magnitude

with decreasing T_{push}, while the relative sensitivity to fracture aperture increases with decreasing T_{push}. Generally, SWPP signals are insensitive to fracture porosity (this follows directly from the transport equations); a discussion on porosity effects on SWPP signals in the presence of radial heterogeneity was outlined in Ghergut et al. (2011).

4. Demonstrating the feasibility of a SW-based (hybrid) EGS

The former gas exploration well Horstberg-Z1 was the first in the N-German Sedimentary Basin to be used for testing innovative SW, water-based, proppant-free techniques for creating access to, and heat extraction from deep-seated sedimentary layers (Jung et al. 2005). Target formations included tight ('impermeable') layers (from which petrothermal heat could be extracted only via artificially-induced large fractures), and moderately-permeable (~0.1 mD) layers, the latter being of interest not primarily as a 'hydrothermal' resource, but for their possible 'bridge' function within genuine EGS designs of special geometry. Besides other options tested ('huff-puff', 'large-scale circulation' involving a natural fault zone presumed to become accessible by various wellbore/reservoir treatments), maybe the most interesting, and promising option (Orzol et al. 2005) was that of a so-called 'frac circulation' (FC, fig. 4).
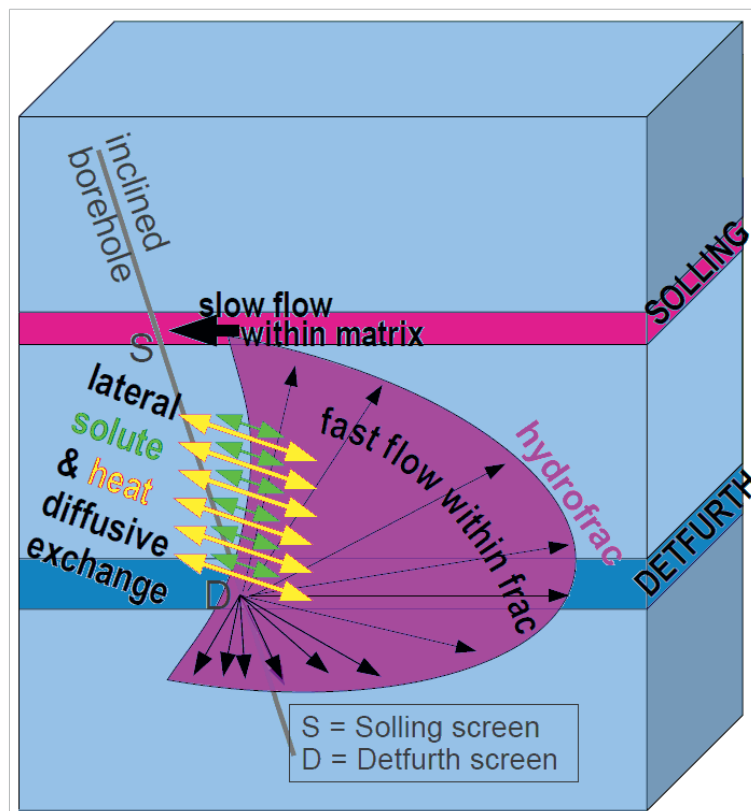
Figure 4: Geothermal heat extraction by a single deviated well: the FC option tested at Horstberg, put in a nutshell, from the viewpoint of fluid transport.

It relied on first creating a large-area frac, primarily by means of massive water injection into a 4-km deep, lowly-permeable layer (Detfurth sandstone). This 'water frac' was supposed, and confirmed by pressure data interpretation (Wessling et al. 2009, Tischner et al. 2010) to propagate into adjacent tight claystone-sandstone layers (Detfurth, Volpriehausen, Hardegsen), more or less vertically, and become arrested, upwards, within a significantly more permeable layer (Solling sandstone). A special wellbore completion provides for 'two wells in one hole': the inner tube is completed with a screen in the frac initiation layer, the wellbore annulus being completed with a screen in the arresting layer. This enables production and injection of fluids, sequentially or simultaneously, using only one hole (sufficient thermal insulation between upwards/downwards circulating fluids, and hydraulic uncoupling by robust downhole packers provided). This FC experiment was accompanied by an artificial TT (Behrens et al. 2006, Ghergut et al. 2013a), involving the injection of a multi-tracer slug at the frac initiation well-screen, and sampling the fluids produced at the outflow well-screen.
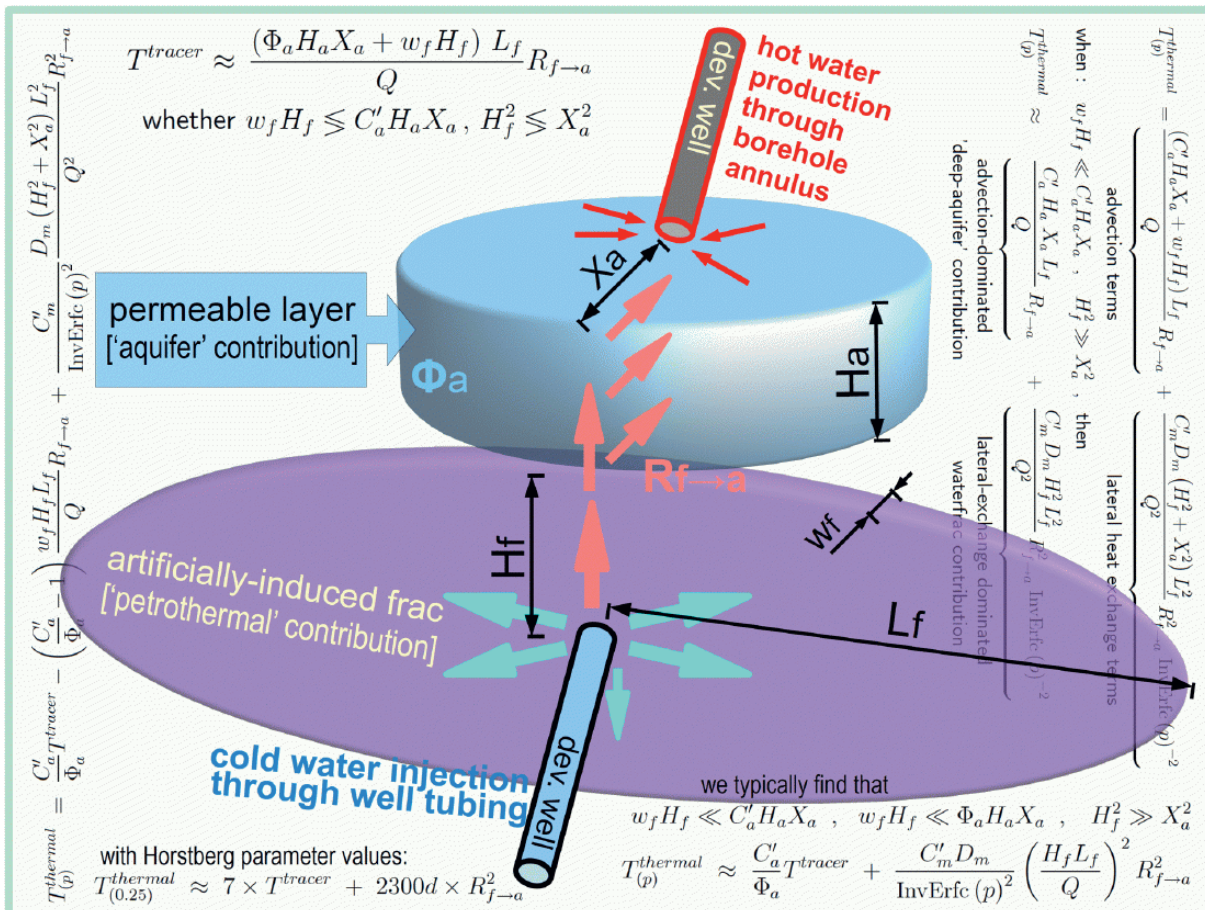
Figure 5: *The FC option for SW-based heat extraction, as tested at Horstberg: identifying the main contributions to thermal lifetime, and their correlation with tracer arrival times (semi-analytical approach).*

Unlike in the SWPP at Gr. Schönebeck (discussed in the next section), the primary aims of the Horstberg SWPP were to ascertain a reservoir-based fluid connectivity between the injection and production well-screens, and to enable predicting the thermal lifetime of the endeavored heat extraction scheme, in the absence of temperature data from the injection and outflow well-screens (downhole temperature metering being technically not feasible at this particular borehole). Relying on a detailed stratigraphical model of the Horstberg site, numerical simulations (Ghergut et al. 2013a) of outflow temperature evolutions during FC nicely revealed the petrothermal component and the 'aquifer' contribution to thermal lifetime (fig. 5), which may also be regarded as the 'HDR' and 'EGS' contributions within a SW-based, 'hybrid EGS'. On the other hand, a semi-analytical approach, not necessitating detailed permeability data but just the involved layers' thickness and their rough classification as 'permeable'/'impermeable', provides closed-form approximations for these two lifetime contributions in terms of two main (unknown) parameters: fluid residence times, and the flow focus angle R from the vertical, large-area frac to the upper, frac-arresting 'aquifer' layer (cf. fig. 5), these two parameters being measurable only by means of an artificial TT conducted during a steady-state FC. With stratigraphy patterns typically targeted for such SW-based 'hybrid EGS' in the N-German Sedimentary Basin, one can expect fluid residence times to be in the order of 10 days, and R values below 50% (the tracer data available from the Horstberg TT, incomplete because of premature FC interruption for cost reasons, yield a mean advective travel time of at least 2 days, and a flow focus angle R of about 20%). An opposite relation between frac and 'aquifer' contributions can thus be expected for tracer travel time versus thermal lifetime: (i) fluid and tracer spend up to two magnitude orders longer time within the 'aquifer', than within the frac (this being the main reason why frac aperture and length cannot be 'inverted' from the measured tracer arrival times); (ii) the cooling front moves advectively up to three magnitude orders slower in the 'aquifer', than in the frac; (iii) in contrast, cooling retardation by transverse-diffusive exchange is about two magnitude orders stronger within frac, than within 'aquifer', this transverse-diffusive retardation being the primary reason why the overall thermal lifetime finally results to be frac-dominated (with one magnitude order higher contribution from frac, than from 'aquifer'), whilst tracer travel times can always be expected to be 'aquifer'-dominated. In Jung's terms (2013), thermal behavior is more HDR-like, while tracer transport is more EGS-like.

Thus, while the multiple-frac EGS at Gr. Schönebeck (cf. next section) was supposed to develop a so-called 'deep aquifer' (Hördt et al. 2011, Hahne et al. 2014), the single-frac 'hybrid EGS' developed at Horstberg is of essentially petrothermal kind, its 'aquifer' component being only ancillary. The well doublet at Gr. Schönebeck relies primarily on fluid flow and advection-dominated heat transport through the 'aquifer', both being largely

perpendicular to the (multiple) fractures. By contrast, the SW heat extraction scheme at Horstberg relies primarily on fluid flow along a single artificially-induced frac, with diffusion-dominated heat transfer perpendicular to the latter; here, a relatively small segment of a 'deep aquifer' is needed just for ensuring reservoir-based well-screen connectivity at the given SW (reservoir-based means: outside the well, and not by some accidental hydraulic shortcut within wellbore/-casing).

Interestingly, similarly to SWPP signals from multiple-frac injection-flowback/production (cf. next section), but for fully different reasons, tracer signals from FC-SWPP are largely insensitive to most frac-related hydrogeologic parameters (frac aperture, frac area, matrix porosity of adjacent claystone), however they strongly depend on the porosity and path length within the frac-arresting outflow layer.

The SW-FC-based design of this 'hybrid EGS' can in principle be repeated wherever in the N-German Basin tight layers of some hundred meters height are found beneath moderately-transmissive (~10 mD x meter, 'aquifer') layers. Wellbore deviation within the frac-target layer should be kept to a minimum, because pressure loss within the 'aquifer' layer becomes prohibitive beyond few meters of 'aquifer' path length, whereas the latter's contribution to thermal lifetime remains of minor importance. A major advantage of the SW-FC scheme, involving only monotonous operation with smooth pressure changes (once the frac was created) and slow (mid-term) cooling, consists in avoiding the cyclic thermo-mechanical loads on wellbore casing and surrounding rock, that would inevitably occur in the 'huff-puff' or large-scale circulation schemes.

There is, however, one persisting issue with tracer signal interpretation for the Horstberg experiment: missing tracer *signal tailings* prevents disambiguation between 'heterogeneous advection' (strongly divergent flow-field) within the large-scale frac (extending beyond Detfurth to Volpriehausen formations), and multiple-scale (multi-porosity, 'intra-particle') diffusion within a limited segment of the Solling sandstone, both of which may theoretically produce similar effects (long-lasting tailings) on measured tracer signals. We may, nevertheless, assume the latter process to prevail, given the marked peak difference between the measured signals of tritiated water and the naphthalenesulfonic tracer. This, again, substantiates the importance of properly-designed laboratory experiments for *metering tracer diffusion coefficients* under representative ionic strength values (in-situ hydration radii of both tracer molecules being likely limited by brine over-saturation).

5.   The issue of SW inflow profiling in multiple-frac backflow and production

Inflow profiling is of elementary importance with any fluid-based reservoir (not only EGS) involving lengthy well screens, and/or production from multiple zones, layers, natural or

artificial fractures. Even with uniform EGS designs intended to rely on a number of 'identical' artificial fractures, the same fracturing protocol being applied repeatedly within the same geological formation, the resulting fractures may differ in size (height, length, aperture), owing to local heterogeneities in hydrogeological/geomechanical parameters and fields. This may have a major impact on how a prescribed total flow rate distributes between multiple fractures under a given head difference, or, in turn, on drawdown levels necessary to maintain the desired value of total flow rate. This latter aspect is illustrated in fig. 6, for both inter-well and single-well production schemes resembling Jung's multi-frac concept (Jung 2013), assuming one or two lengthy horizontal well screens within a hydrogeological setting similar to the deeper part of the Gr. Schönebeck reservoir in the NE-German Basin.
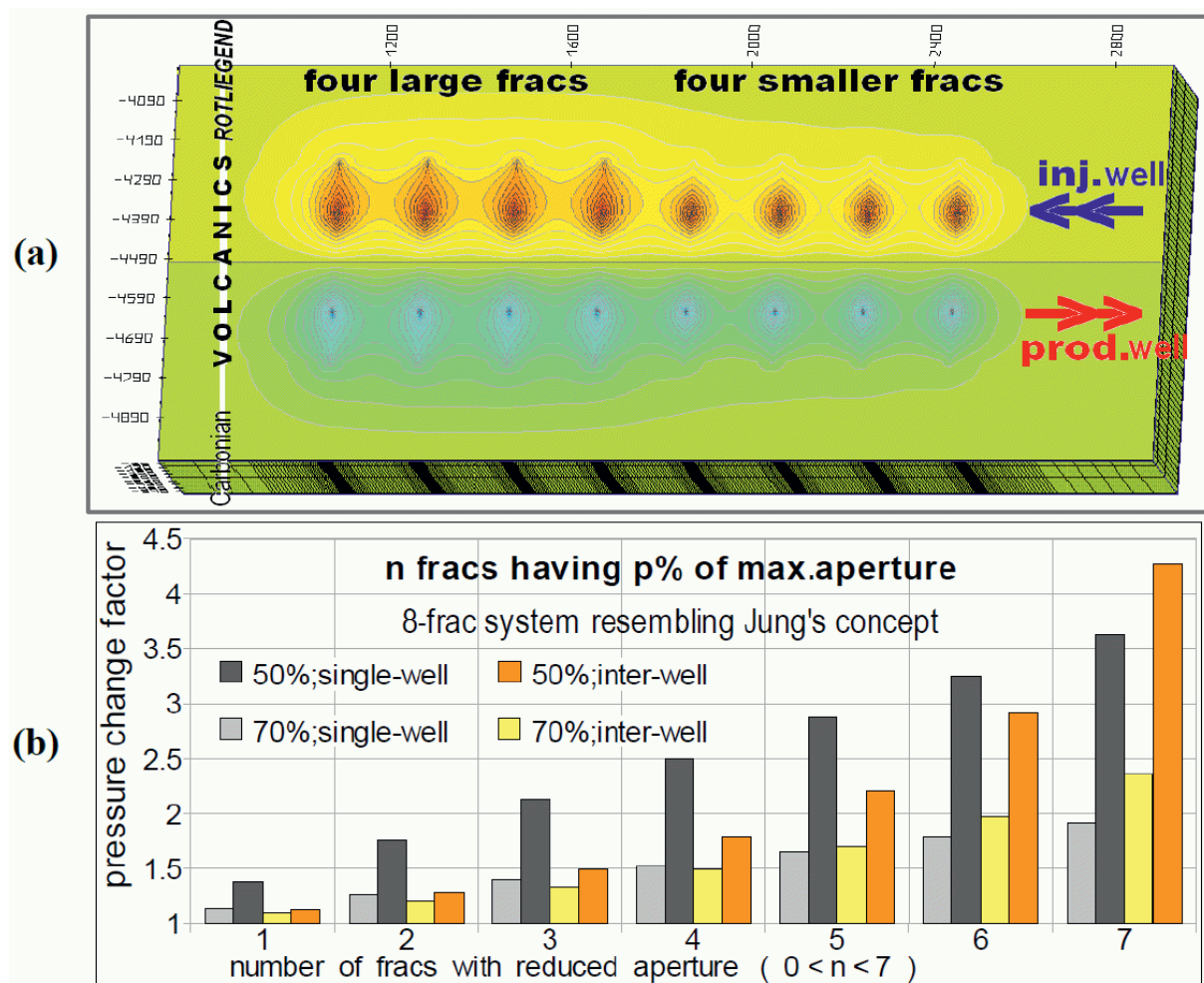
Figure 6: In multi-frac settings *(a)*, a critical issue is: what if some of the artificially-induced fracs have lower transmissivity than expected by fracturing protocols? the diagram *(b)* gives the answer in terms of pressure buildup and drawdown necessary to maintain the same total flow rate, when a number n of fracs have only p % of the maximum-expected aperture (well-doublet vs. 'huff-puff' schemes).

To be noted, Jung deems his multi-frac concept a 'HDR' one, as opposed to 'EGS' concepts; however, as the SW-based metering of reservoir parameters is concerned, we face similar issues in both reservoir types: pressure signals from mere hydraulic tests might indeed indicate the presence of 'less-contributing' fracs (cf. fig. 6b), but they do not enable a frac-resolved inflow profiling; and SWTT, whether in single or multiple fractures, always face the 'flow-field reversal' issue (with consequences discussed by Ghergut et al. 2013b), irrespective of whether the main component of reservoir flow is along (HDR), or across (EGS) the fractures. In the sequel, we re-examine a series of TT conducted at Gr. Schönebeck in conjunction with fracturing operations, to illustrate the SW use of artificial tracers for a frac-resolved discharge metering, and substantiate the need for both conservative and non-conservative tracers in order to render inflow profiling more robust.

5.1. SWPP sensitivity to frac parameters and local discharge values: numerical simulations

Targeting volcanic rocks (Lower Rotliegend) and siliciclastics (Upper Rotliegend) in the Lower Permian by means of several screening intervals between 3.8 and 4.3 km depth, the well doublet at Gr. Schönebeck was supposed to develop an EGS of the so-called 'deep aquifer' type (Hördt et al. 2011, Hahne et al. 2014, Blöcher et al. 2010), relying on several artificial fractures with different geometric and hydromechanical characteristics (Zimmermann et al. 2011, Blöcher et al. 2010) at each well. At the intended-production well (GS-4), one large-area hydrofrac was created in the low-permeability volcanic rocks, and two gel-proppant fracs in selected sandstone layers (fig. 7).

During treatment, each frac received a different species of a conservative solute tracer. During subsequent backflow and production, each frac can contribute a certain (possibly variable) amount to the measured total discharge. Since these individual-frac amounts cannot be measured directly, it was endeavored to 'invert' them from tracer signals as detectable in the total discharge. Therefore, we first need to examine how these tracer signals depend on local discharge values and local hydrogeologic parameters (matrix porosity, permeability distribution; frac transmissivity, thickness, effective area and aperture), and to what extent hydrogeological uncertainty will impede the 'inversion' of local discharge values.

To this end, we first explore hydrogeologic parameter sensitivities on a simplified flow and tracer transport model, assuming Darcian flow within the matrix, Hagen-Poiseuille flow within the water frac, and either D or H-P flow within the gel-proppant fracs; tracer signal simulations (using Feflow 5.4, details to be found in Ghergut et al. 2014b) on this model show that:
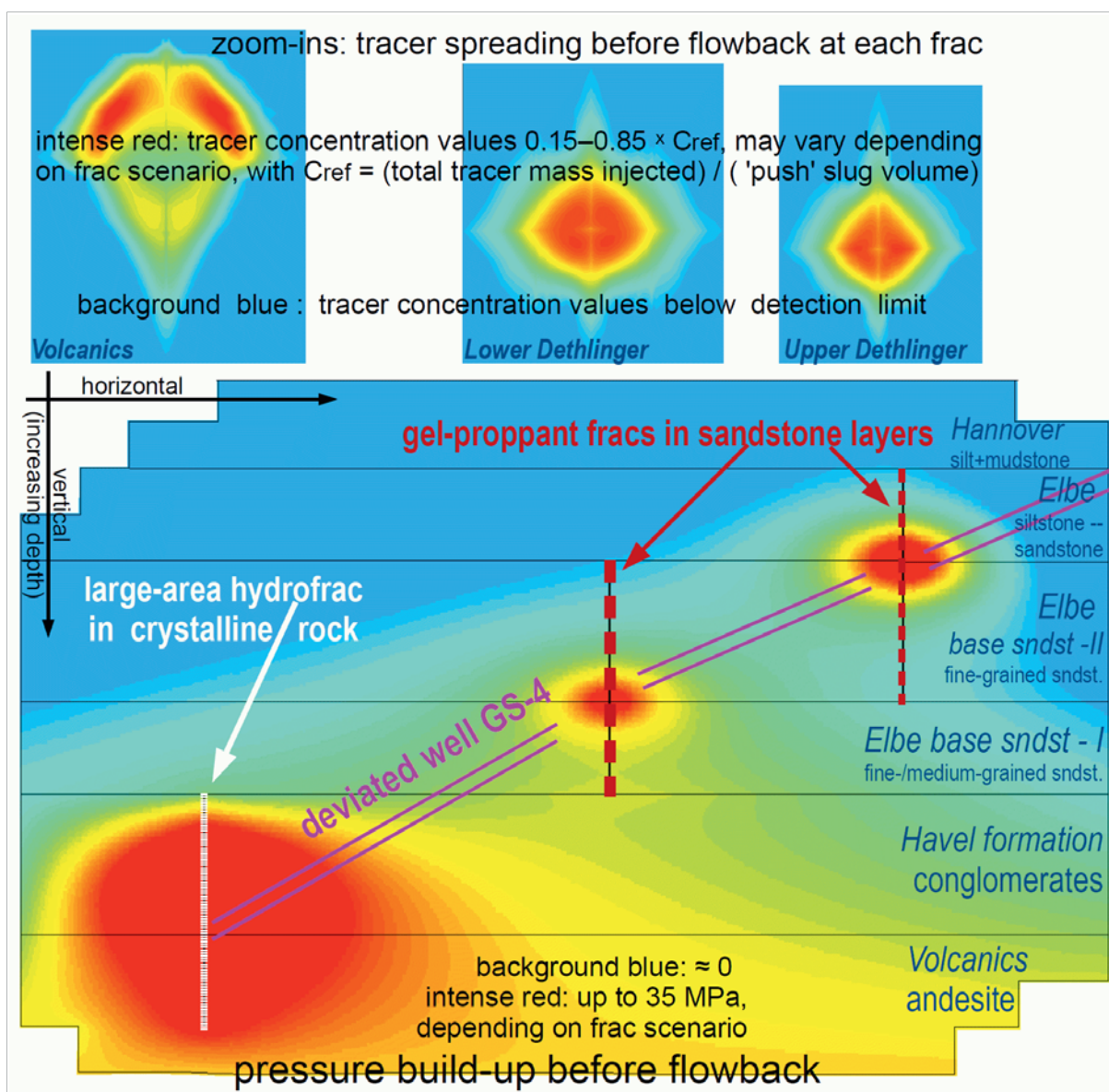
Figure 7: *Schematic representation of a composite, three- frac system, as created at the well GS-4 at the Gr. Schönebeck site in the NE-German Basin.*

(1)   late-time tracer signals (tailings) are almost independent on matrix porosity, permeability distribution, frac area (length), thickness and effective aperture, while being highly sensitive to local discharge values; 'late' means a backflow or production volume at least fivefold the injected chaser volume;

(2a)   early-time tracer signals (concentration 'peak' intervals) may exhibit slight 'acceleration' and 'damping' with increasing matrix porosity or increasing frac aperture (a seemingly paradoxical behavior, which is not really surprising for single-well 'push-then-backflow' tests, actually owing to flow-field dispersion), and

(2b) a non-monotonous response to varying frac area, being almost insensitive to frac area as long as the linear-flow regime prevails against the radial-flow regime (effects of the latter only becoming visible at very low frac areas);

(2c) the effects of these various factors on early-time tracer signals are not unambiguously discernible from each other, and this ambiguity would persist even if frac-resolved (in-situ) discharge metering were feasible.

For each of the three fracs (k = 1,2,3), a 'site-related type-curve' set $C_k(q,t)$ (tracer concentrations as a function of time, parametrized by discharge values q) can be generated by numerical simulations, as applicable to this particular (site-specific) EGS design. Since every frac received a different tracer, tracer signals measured within the overall backflow will differ from individual-frac type-curves by mere dilution (trivial 'superposition'). Type-curve dilution by factor Q_k/Q_{total} can be compared to measured tracer concentrations in the total discharge, $c_k(t_i)$, (i = 1, ... , no. of tracer samplings). From a formal point of view, the unknown discharge values Q_k can be determined as the solution of a linear optimization task subject to the constraint $Q_1 + Q_2 + Q_3 = Q_{total}$ (the latter being a measured value). It is recommendable to perform 'optimization' manually, rather than by resorting to automated solutions provided by some linear programming software. The first items to inspect are the late-time height and slope of measured tracer signal 'tailings': their height yields a first approximation to dilution factors, and thus a first estimate for Q_k, while late-time consistency of observed tailing slopes can be taken as indicative of the applicability of model presuppositions. To be noted, dilution factors associated with individual fracs can vary with time, since a steady-state discharge pattern might not be reached simultaneously at all fracs, this being a further reason why early-time tracer signals should generally be regarded as unsuited for frac discharge 'inversion'. Prolonging signal observation time is recommendable, and this would reduce uncertainty especially for the less-contributing units. The apparent hydrogeologic-parameter insensitivity of tracer signals measurable at the 'single' ('PP') well does not imply that tracer spreading patterns within fractures and reservoir were themselves hydrogeology-independent. Actually, tracer spreading does indeed depend, even at late times (when 'tailings' are recorded at the well), moreover the later the stronger, on all relevant hydrogeologic parameters: fracture area (length), fracture aperture, and matrix porosity (to a lesser extent). Rather, it is the very design of such tracer tests ('push-then-pull') that produces the observed insensitivity.

5.2. *Mono-dispersive continuum: sensitivity to local discharge values and dispersion*

Inspired by the analytical approach used by Schroth et al. 2001 in the realm of contaminant hydrology, we additionally propose semi-analytical approximations ('type curve' families) to

be compared to measured SWPP signals. Being free of site-specific details, the type-curve approach can be extended to a wider class of non-/planar frac structures, and it can be used to derive some recommendations for SWTT design and parameter inversion workflow. The adequacy of a site-independent type-curve approach for multiple-frac inflow profiling is substantiated by previous section's main finding, namely: mid-late SWPP signals (early 'tailings') are almost independent on all hydrogeologic parameters, while being highly sensitive to local discharge values. In line with this finding, the semi-analytical approximation assumes the transport medium can be described in terms of just one parameter, measuring its heterogeneity at tracer 'push' scale (Peclet number Pe, in its second meaning detailed by Ghergut et al. 2013b), nonetheless preserving flow-field geometry (radial/bilinear). Resulting type-curve families are shown in fig. 8, their use for (Pe and) discharge inversion being explained in the next section.
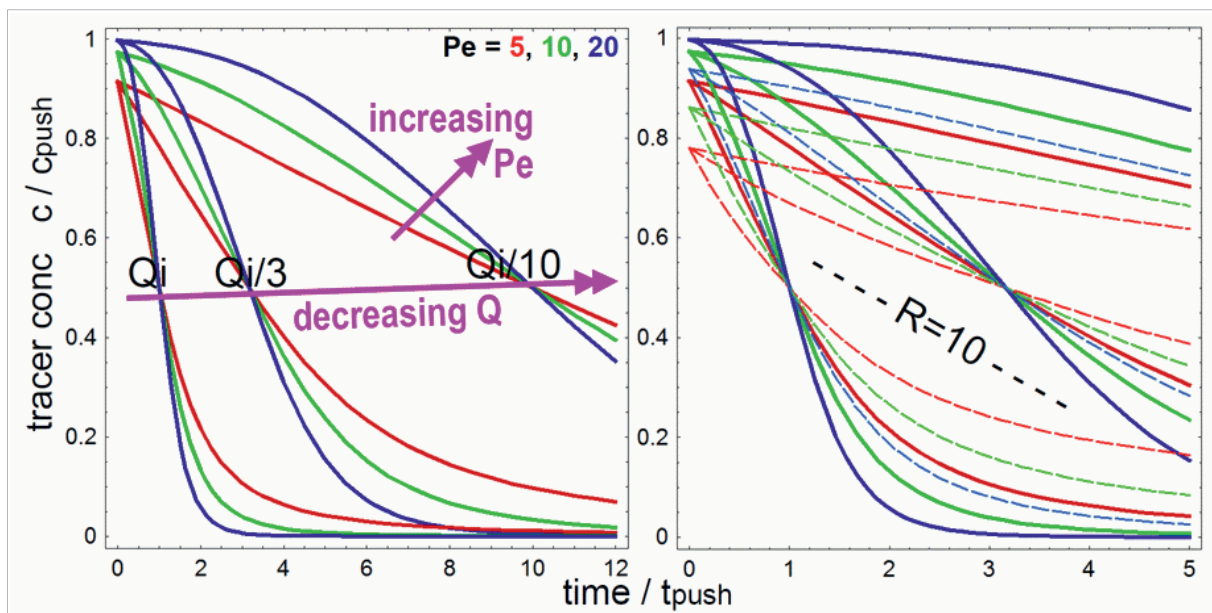
Figure 8: *Main elements and steps of SWPP signal inversion workflow suggested for inflow profiling: type-curve families showing the effects of increasing discharge Q and increasing dispersion (decreasing Pe) on tracer signal shares; contrast between Pe sensitivity of early and late signals; additional signals of equilibrium-sorptive tracers (with retardation factors in the range R>~10) enable disambiguating Pe values in early signals.*

5.3 Recommendations on multiple-frac SWTT design, and parameter inversion workflow

During treatment, at least one conservative tracer species (different for each frac) should be injected, preferably as a uniform spike over the last 1/6 of the treatment slug. During single-frac (k) backflow ('B'), discharge QB[k] being known, tracer signals measured at frac k should be compared to the type-curve family of fig. 8 (l.-h.s.) selected by the known QB[k] value, in order to determine the value of Pe[k]. Later on, during overall multiple-frac production ('P'), the measured signal of tracer k, multiplied by its assumed dilution factor (ratio of total

discharge QP to frac-specific contribution QP[k]), should be compared to the type-curve family of fig. 8 (r.-h.s.) selected in accordance to the previously determined Pe[k] value. Dilution factors shall be varied (subject to the constraint that the sum of all QP[k] always yield the known QP) until a satisfactory match is achieved for all fracs simultaneously. The execution of this task can be automated using linear-programming software; a problem with this approach, however, is that Pe sensitivity is poorer at early times (fig. 8, l.-h.s.), whereas reliable knowledge of Pe values obviously gains in importance at later stages (fig. 8, r.-h.s.). As a workaround, we suggest to additionally use equilibrium-sorptive tracers (with retardation factors in the range R >~10). This helps disambiguate Peclet number values in early signals, as can be seen in fig. 8 (r.-h.s.), and thus to better constrain inflow profiling from late signals.

6. Non-/planar frac structures, seen by dual tracers during SW backflow/production

Relying on a mono-dispersive continuum approach and being else free of site-specific details, the tracer-based discharge inversion tool presented in section 3 can also be applied with non-planar frac or stimulated rock volume structures, as encountered in both conventional 'hydrothermal' reservoirs (Hördt et al. 2011, Reich 2012, Schumacher and Schulz 2013, Hahne et al. 2014), and in un-/conventional EGS and multi-frac systems (Reich 2012, Jung 2013, Brough 2013). Further, it can be extended with dually sorptive and/or reactive tracer species (Tomich et al. 1973, Ghergut et al. 2013b, Ghergut et al. 2014) to enable the determination of some reservoir-specific hydrogeologic parameters, of special interest being parameters that come into very existence as a result of the treatment (e. g., aperture, porosity, spacing of new fractures or fissures, as outlined in fig. 9). In the geothermal realm, its application is independent of whether artificial fracturing is being envisaged or not; it may be applied with a number of (packer-separated) perforated intervals in wellbores targeting native rock layers (possibly subject to stimulation) or fault zones being regarded as a promising 'alternative' (Hördt et al. 2011, Hahne et al. 2014) to petrothermal systems. In the context of early (prospective) new-field development and assessment, this tool helps avoiding misinvestment in sophisticated, wellbore completion-integrated devices for inflow profiling (like those proposed by Brough 2013), especially for unconventional resources when the target formation's productivity is yet uncertain.

To be noted, the mono-dispersive continuum approach to SW signal inversion still faces the 'flow-field reversal' issue (Tomich et al. 1973, Schroth et al. 2001, with specific consequences for geothermal reservoir characterization discussed by Ghergut et al. 2013b); this basically pertains to the impossibility of determining porosity and dispersion independently from each other, when using only conservative tracers.
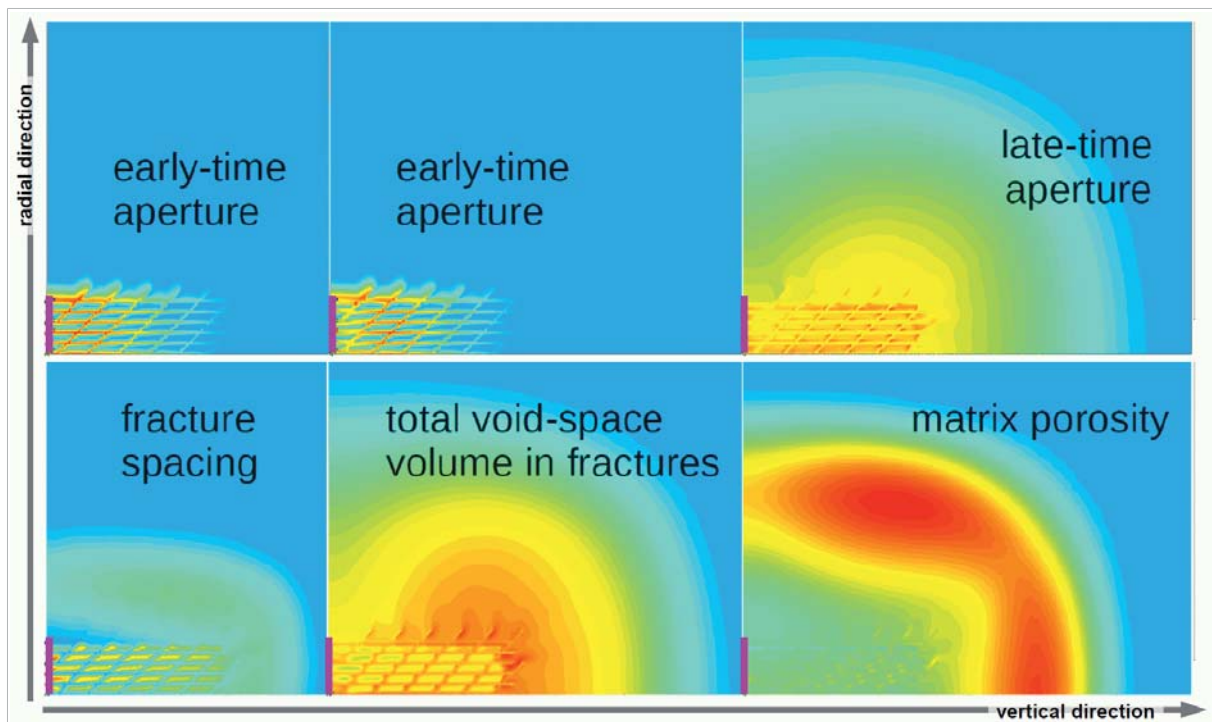
Figure 9: Synopsis on SW use of artificial tracers to interrogate fluid transport parameters in non-planar frac structures: typical patterns (vertical-radial snapshots) of tracer spreading during various flowback/production stages, enabling to determine certain matrix and fracture or fissure network parameters, as indicated. Fluid and tracer injection-retrieval occurs over a horizontal well-screen segment (shown in light magenta at the left of each snapshot), at which stimulation/fracturing was initiated prior to or along with injecting artificial tracers.

As a workaround, the dual-partitioning/reactive tracer approach proposed by Tomich et al. 1973 for measuring residual-oil saturation in mature fields (i. e., dealing with multi-phase flow in general, and one immobile phase in particular) can be extended to the case of single-phase (liquid-only) geothermal reservoirs, using dually-sorptive/reactive tracers, as described by Ghergut et al. 2014, to enable disambiguation of the main flow (advective) parameters: porosity, and dispersion (or Pe).

Further, fig. 9 also refers to geosystem settings and/or parameter sensitivity regimes that obviously *do not fit into the mono-dispersive continuum approach*, two very common examples being, during early- and mid-time stages of tracer transport: fissure/fracture networks (even uniform ones and of infinite extension), and gel-proppant fractures (of finite extension). For the former case, a number of 4 contrasting sensitivity regimes w. r. to fracture aperture w and fracture spacing a (or density $1/a$) have been identified by numerical simulations of conservative tracer signals allowing for tracer diffusion coefficients to span 1½ orders of magnitude (Ghergut et al. 2013c), but a parameter (w, a) inversion protocol has not been implemented as yet. For the latter, Karmakar et al. (2015, submitted)

220

conducts numerical simulations (assuming a simplified set-up of frac operations, largely resembling the EGS design of Gr. Schönebeck), and analyzes the sensitivity of early- and mid-time signals, w. r. to frac parameters, of contrasting-diffusive and of variously-sorptive tracer signals (considering both proppant-coating and matrix sorption processes), and derives recommendations for the design of future intra-fracturing multi-tracer tests. It appears that physico-chemical research and development into (and synthesis of novel) *sorptive* tracer species suitable for application during EGS creation is very much worth pursuing (as had also been anticipated by Rose 2012a); whereby a number of hydrogeochemical aspects (Bozau and Van Berk 2013, Bozau et al. 2015), as well as drawbacks and advantages of temperature-dependent sorption (Ghergut et al. 2013b) would need to be considered.

7. Concluding remarks

To set up a geothermal reservoir (in the N-German Basin), it does not suffice to drill down to depths where hot fluids are encountered in either permeable formations ('hydrothermal', 'hot deep aquifers') or in impermeable layers which can easily be fractured ('petrothermal', EGS). One must also ensure that such 'reservoirs' can be operated sustainably – for at least three decades, as a rule. Reservoir lifetime cannot be predicted from mere temperature and permeability measurements. Two main parameters determining the thermal lifetime of a geothermal reservoir – fluid residence times, and heat exchange areas – cannot be measured in hydraulic or geophysical tests. They can, at least in principle, be measured by means of tracer tests, conducted in inter-well (IW) and/or single-well (SW) configurations; however, this is not a trivial task; no universally-valid recipe exists for deriving lifetime-controlling reservoir parameters from tracer signals measured in IW or SW tests. This issue was given a closer look in **section 2**. Further, a closer look at the 'heat exchange area' notion revealed at least two meanings: in reservoirs dominated by a single fracture or fault, the heat exchange area density (area per mobile-fluid volume) is given by the reciprocal ($2/w$) of transport-effective aperture (to be recalled, 'transport-effective apertures' may differ from 'hydraulic apertures' as well as from 'geomechanical apertures', as was analyzed in a landmark paper by Tsang 1992); in reservoirs consisting of a large number of approximately parallel fractures, the heat exchange area density (area per bulk reservoir volume) is given by the reciprocal ($1/a$) of fracture spacing. This motivated the present study to also examine (**section 3**) the sensitivity of SWPP tracer test signals towards the transport-effective fracture aperture (for a single- or a parallel-fracture reservoir), as well as towards fracture spacing (in a parallel-fracture reservoir). Finally (**sections 4 – 6**), we evaluated the SW use of artificial tracers in conjunction with EGS-related fracturing or stimulation, either chemical-based or plain-hydraulic, with or without proppants, in sedimentary and crystalline formations in the N-

German Basin, with both short-term (intra- and post-treatment) SW tests, and for long-term production monitoring. As an outcome of conservative-tracer signal analysis, we derived a tool for quantifying individual frac contributions to multiple-frac discharge, whose major advantage consists in its independence from hydrogeological a priori knowledge. In early (prospective) new-field development and assessment, this tool helps avoiding misinvestment in wellbore completion-integrated devices for inflow profiling, especially with unconventional resources when the target formation's productivity is yet uncertain. This SW conservative-tracer tool can be extended with dually sorptive and/or reactive tracer pairs to enable the determination of reservoir-specific hydrogeologic parameters, of special interest being parameters that come into very existence as a result of the treatment (aperture, porosity, spacing of new fractures or fissures). In (Ghergut et al. 2014a), we proposed a method for further disambiguating the most 'recalcitrant' parameter pair in SWPP tests (porosity vs. dispersion), relying on dual-partitioning/reactive tracer pairs to restore the correlation between porosity and tracer residence times.

8. Outlook

Retrospectively, two 'simple' lessons can be derived from a twelve-year experience using artificial tracers in various IW and SW field tests in Germany, that were aimed at deep-georeservoir characterization and/or short- to mid-term process monitoring during reservoir operation: if those tests have been successful to a certain extent, it was mainly owing to ascertainedly conservative tracer transport behavior; if those tests have been of limited success, it was because of lack of reactive tracer species with well-defined, and reasonable properties (reasonable means: sensitive to 'something', but not to 'everything' that may 'happen' within the target georeservoir). If the artificial-tracer based quantification of georeservoir hydrogeology and of induced (short- to mid-term) transport processes therein is to become a task for some future geothermal projects, they will need to effectively address this dilemma. Further, if EGS, and especially the petrothermal type shall be on the agenda, then SW tests will be 'unavoidable'. Finally, if the most is to be made out of a SW test, then using tailored reactive tracer pairs is a must-do: not just reactive, not just retarded, but: conservative alongside with reactive, and with contrasting retardation behavior between product and reactant.

9. Acknowledgments

decommissioning is gratefully acknowledged, as well), Jens Orzol, Torsten Tischner, Günter Zimmermann, and their field teams employed by GGA Hannover, BGR Hannover, and GFZ Potsdam. Field tests at these sites were conducted with financial support from the German BMU (Federal Ministry for the Environment, Nature Conservation, and Nuclear Safety) and BMWi (Federal Ministry for Economic Affairs and Energy). The modeling work described in this report was conducted within 'gebo' ("*Geothermie und Hochleistungsbohren*"), funded by the German state MWK (Lower-Saxonian Ministry for Science and Culture) jointly with Baker Hughes (Celle). We are grateful to all 'gebo' colleagues for sustained cooperation – to name just a few: Anne Bartetzko (BH) who kindly reviewed extensive parts of the manuscript, Barbara Hahne who coordinated the geoscientific projects within 'gebo', Frank Mattioli who organized the 'gebo' meetings, Jörg Lehr (BH), Georg-Peter Ostermeyer and Sonja Philipp who rendered them unforgettable.

10.   Publications resulting from the project

Ghergut J, Behrens H, Sauter M (2014[a]) Using tracer reactivity to overcome some dilemmata of single-well tracer test inversion. *European Oil & Gas Magazine*, **40**(1), 30-32.

Ghergut I, Behrens H, Sauter M (2014[b]) Tracer-based resolution of individual frac discharge in single-well multiple-frac backflow: sensitivity study. *Energy Procedia*, **59**, 235-242.

Behrens H, Ghergut J, Bensabat J, Niemi A, Sauter M (2014) Merging single- and inter-well tracer tests into one forced-gradient dipole test, at the Heletz site within the MUSTANG project. *Energy Procedia*, **59**, 249-255.

Ghergut J, Behrens H, Sauter M (2014[c]) Short-term fluid, heat, and solute transport in deep georeservoirs likely to become EGS: some challenges to ICDP hydrogeologists who might like using artificial tracers. *Stanford Geothermal Program Technical Reports*, SGP-TR-**202**, 177-182.

Ghergut J, Behrens H, Sauter M (2013[a]) Geothermal Art in the N-German Sedimentary Basin: Grafting EGS with Aquifers. *Geothermal Research Council Transactions*, **37**, 949-956. [with 'best lecture' award]

Ghergut J, Behrens H, Sauter M (2013[b]) Can Peclet numbers depend on tracer species? going beyond SW test insensitivity to advection or equilibrium exchange. *Stanford Geothermal Program Technical Reports*, SGP-TR-**198**, 326-335.

Ghergut J, Behrens H, Sauter M (2013[c]) Single-well tracer push-pull test sensitivity to fracture aperture and spacing. *Stanford Geothermal Program Technical Reports*, SGP-TR-**198**, 295-308.

Ghergut J, Behrens H, Sauter M (2013[d]) Tracer-based prediction of thermal reservoir lifetime: scope, limitations, and what reactive tracers can tell. *Stanford Geothermal Program Technical Reports*, SGP-TR-**198**, 309-315.

Ghergut J, Behrens H, Sauter M (2013[e]) CCS site characterization by single-well and inter-well tracer tests. *Stanford Geothermal Program Technical Reports*, SGP-TR-**198**, 316-325.

Behrens H, Ghergut I, Sauter M (2010) Tracer properties, and tracer test results, part 3: Modification to Shook's flow-storage diagram method. *Stanford Geothermal Program Technical Reports*, SGP-TR-**188** (4pp).

Ghergut I, Behrens H, Sauter M (2010) Tracer properties, and tracer test results (from geothermal reservoir testing), part 2. *Stanford Geothermal Program Technical Reports*, SGP-TR-**188** (7pp).

- - - - submitted (under peer review) - - - -

Ghergut I, Behrens H, Sauter M: Planar and non-planar frac structures, seen by conservative and reactive tracers during single-well injection-flowback and production (submitted to *Geothermics* on Jan. 30, 2015; currently under peer review)

- - - - extended abstracts: - - - -

Ghergut I, Sauter M (2014) Inter-well and single-well tracer test interpretation techniques (invited lecture). Extended abstract + slides, Proceedings *SPE Workshop on Tracer Technology for Improved Reservoir Management*, Dubai.

Ghergut I, Behrens H, Sauter M (2014) Tracer-based sensing of frac-by-frac inflow in single-well multiple-frac backflow and production. Extended abstract + slides, Proceedings *Celle Drilling 2014*.

- - - - in German language: - - - -

Ghergut I, Behrens H, Sauter M (2011) Wünschelrute, Steine klopfen – und dann? *Ingenieurspiegel*, **4**, 63-64.

Ghergut I, Behrens H, Sauter M (2012) Mit Beiden sieht man besser – Gedanken zur Geothermalreservoircharakterisierung mittels konservativer und reaktiver Tracer. *Ingenieurspiegel*, **4**, 71-73.

Ghergut I, Sauter M (2014) Geothermische Reservoirerschließung und -entwicklung: tracertestbegleitete Erfahrungen aus dem Norddeutschen Becken (invited). Proceedings *DNN-Workshop Erschließung und Entwicklung von konventionellen und geothermischen Reservoiren* (*Drilling Network Niedersachsen*), Celle.

Ghergut I, Sauter M (2014) Tracergestützte Charakterisierung tiefer Geothermiereservoire (invited). Proceedings *7. Norddeutsche Geothermietagung*, Hannover.

- - - - Tagungsbeiträge (full-length, with ISBN): - - - -

Ghergut I, Behrens H, Sauter M (2013) Zur tracergestützten Charakterisierung klüftig-poröser Reservoire: CHOICE (Entscheidungshilfe zur Georeservoirerkundung der 'Ersten Stunde' mit konkurrierenden Einbohrlochverfahren bei beschränktem Fluidumsatz). Tagungsband "*Der Geothermiekongress 2013*" (Nov 12-14, in Essen), Hrsg: GtV-BVG, Berlin (7pp), ISBN: 978-3-932570-68-1.

Ghergut I, Behrens H, Sauter M (2012) Einbohrlochtracertestsensitivität gegenüber Riss- und Gesteinsparametern: Lektion Horstberg. Tagungsband "*Der Geothermiekongress 2012*" (Nov 13-16, in Karlsruhe), Hrsg: GtV-BVG, Berlin (13pp), ISBN: 978-3-932570-67-4.

Ghergut I, Behrens H, Nottebohm M, Licha T, Schaffer M, Maier F, Ptak T, Sauter M (2011) Zeit-/temperaturabhängige Dualtracerbildung in-situ oder Sorption „überlisten" die Push-Pull-Test-Insensitivität gegenüber Austauschprozessen im Gleichgewicht. Tagungsband "*Der Geothermiekongress 2011*" (Nov 15-17, in Bochum), Hrsg: GtV-BVG, Berlin (9pp), ISBN: 978-3-932570-66-7.

Ghergut I, Behrens H, Karmakar S, Maier F, Sauter M (2011) Sensitivität von Tracer-Push-Pull-Tests gegenüber Kluftöffnungsweiten und -dichte in Parallelkluftsystemen. Tagungsband "*Der Geothermiekongress 2011*" (Nov 15-17, in Bochum), Hrsg: GtV-BVG, Berlin (11pp), ISBN: 978-3-932570-66-7.

Ghergut I, Behrens H, Sauter M (2009) Der Tracer kann sich irren. Tagungsband "*Der Geothermiekongress 2009*" (Nov 17-19, in Bochum), Hrsg: GtV-BVG, Geeste (10pp), ISBN: 978-3-932570-64-3.

11.   References

Behrens H, Ghergut I, Licha T, Lodemann M, Orzol J, Sauter M (2006) Reactive behaviour of uranine (fluorescein) in a deep geothermal reservoir tracer test. *Geophysical Research Abstracts*, **8**, 10448.

Blöcher MG, Zimmermann G, Moeck I, Brandt W, Hassanzadegan A, Magri F (2010) 3D numerical modeling of hydrothermal processes during the lifetime of a deep geothermal reservoir. *Geofluids*, **10**, 406-421.

Bozau E, Van Berk W (2013) Hydrogeochemical Modeling of Deep Formation Water Applied to Geothermal Energy Production. *Procedia Earth and Planetary Science*, **7**, 97-100.

Bozau E, Häußler S, Van Berk W (2015) Hydrogeochemical modelling of corrosion effects and barite scaling in deep geothermal wells of the North German Basin using PHREEQC and PHAST. *Geothermics*, **53**, 540-547.

Brough B (2013) Intelligent tracers quantify inflow characteristics in multi-zone horizontal wells. *World Oil Mag*, **234**(10), 1.

Hahne B, Thomas R, team gebo-Geosystem (2014) Deep Geothermal Energy for Lower Saxony (North Germany) – Combined Investigations of Geothermal Reservoir Characteristics. *Energy Procedia*, **59**, 198-204.

Hördt A, Beilecke T, et al (2011) Models of Geothermal Reservoirs as a Basis for Interdisciplinary Cooperation. *American Geophysical Union, Fall Meeting 2011*, abstract #H21E-1178.

Jung R, Orzol J, Jatho R, Kehrer P, Tischner T (2005) Extraction of Geothermal Heat From Tight Sediments. *Procs 30th Workshop on Geothermal Reservoir Engineering*, Stanford University, CA; SGP-TR-**176**.

Jung R (2013) EGS – Goodbye or Back to the Future. Chapter 5 in *Effective and Sustainable Hydraulic Fracturing*, pp 95-121, InTech (http://dx.doi.org/10.5772/56458)

Karmakar S, Ghergut J, Sauter M (2015) Early time tracer signal based parametric study for fracture characterization in an EGS developed in deep crystalline and sedimentary formations, manuscript submitted to *Geothermics* (currently under peer-review).

Nottebohm M, Licha T, Ghergut I, Nödler K, Sauter M (2010) Development of Thermosensitive Tracers for Push-Pull Experiments in Geothermal Reservoir Characterization. *Proceedings, World Geothermal Congress 2010* (25-29 April, Bali, Indonesia).

Nottebohm M, Licha T, Sauter M (2012) Tracer design for tracking thermal fronts in geothermal reservoirs. *Geothermics*, **43**, 37-44.

Orzol J, Jung R, Jatho R, Tischner T, Kehrer P (2005) The GeneSys Project: Extraction of Geothermal Heat From Tight Sediments. *Procs World Geothermal Congress 2005*, Antalya, Turkey.

Reich M (2012) *Hunting Underground – A high-tech search for oil, gas and geothermal energy*. add-books, 160pp.

Rose P, Riasetto D, Siy J, Bartl M, Reimus P, Mella M, Leecaster K, Petty S (2011) Quantum Dots as Tracers in Geothermal and EGS Reservoirs. *Proceedings, 36th Workshop on Geothermal Reservoir Engineering*, Stanford University, Stanford, CA, SGP-TR-**191**.

Rose P, Leecaster K, Clausen S, Sanjuan R, Ames M, Reimus P, Williams M, Vermeul V, Benoit D (2012a) A Tracer Test at the Soda Lake, Nevada Geothermal Field Using a Sorbing Tracer. *Proceedings, 37th Workshop on Geothermal Reservoir Engineering*, Stanford University, Stanford, CA, SGP-TR-**194**.

Rose P (2012b) Injection-backflow technique for measuring fracture surface area adjacent to a wellbore. US Patent no 8162049 B2.

Schroth MH, Istok JD, Haggerty R (2001) In-situ evaluation of solute retardation using single-well push-pull tests. *Adv Water Resour*, **24**(1), 105-117.

Schumacher S, Schulz R (2013) Effectiveness of acidizing geothermal wells in the South German Molasse Basin. *Geoth Energ Sci*, **1**, 1-11.

Tischner T, Evers H, Hauswirth H, Jatho R, Kosinowski M, Sulzbacher H (2010) New Concepts for Extracting Geothermal Energy From One Well: The GeneSys Project. *Procs World Geothermal Congress 2010*, Bali, Indonesia.

Tomich JF, Dalton RL Jr, Deans HA, Shallenberger LK (1973) Single-Well Tracer Method to Measure Residual Oil Saturation. *J of Petrol Technol / Transact*, **255**, 211-218.

Tsang Y W (1992) Usage of "Equivalent Apertures" for Rock Fractures as Derived From Hydraulic and Tracer Tests. *Water Resources Research*, **28**(5), 1451-1455.

US Department of Energy (2007) The Future of Geothermal Energy – Impact of Enhanced Geothermal Systems (EGS) on the United States in the 21st Century. Idaho National Laboratory Report, INL/EXT-06-11746, 372pp. (http://www1.eere.energy.gov/geothermal/pdfs/future_geo_energy.pdf)

US Department of Energy (2008) An Evaluation of Enhanced Geothermal Systems Technology. MIT Report, 37pp. (http://www1.eere.energy.gov/geothermal/pdfs/evaluation_egs_tech_2008.pdf)

Wessling S, Junker R, Rutqvist J, Silin D, Sulzbacher H, Tischner T, Tsang C-F (2009) Pressure Analysis of the Hydromechanical Fracture Behaviour in Stimulated Tight Sedimentary Geothermal Reservoirs. *Geothermics*, **38**, 211-226.

Zimmermann G, Blöcher G, Reinicke A, Brandt W (2011) Rock specific hydraulic fracturing and matrix acidizing to enhance a geothermal system – Concepts and field results. *Tectonophysics*, **503**, 146-154.

G7: Modeling of Coupled Thermo-Hydraulic Processes and Influence of Mechanical Parameters at the Borehole-Georeservoir Interface

Ekkehard Holzbecher

Georg-August Universität Göttingen, Goldschmidtstr. 3, 37077 Göttingen, Germany

*E-Mail: eholzbe@gwdg.de

Abstract

Reported here are an overview and selected findings, obtained by research within the project G7 of gebo (Geothermal Energy and High Performance Drilling Research Program). The report highlights the importance of coupled modelling, taking into account thermal, hydraulic and mechanical processes (THM). Coupled models were applied for various problem settings concerning reservoir characterization and operation of a geothermal facility.

1. Introduction

Prediction of reservoir performance following stimulation and operation relies to a major extent on the modeling of groundwater flow, heat transport and the mechanical response of the reservoir to variable stresses. Following the general schedule of the development of a geothermal reservoir, i.e. the stimulation, reservoir characterization and the operation, modeling is an essential tool in the planning and designing a geothermal facility. Models are capable of predicting the short term as well as the long-term performance, e.g. the prediction of thermal breakthrough.

The performance of models depends strongly on the accuracy of the parameters involved. It is typical for geological systems that they are heterogeneous, that parameters are imprecisely known and vary spatially or even temporarily. Despite of these difficulties, the use of characterization methods, that may include inverse modeling, are without alternative. However, the conditions for their applicability have to be explored and taken into account.

The interaction between the fluid conducting fractures and the rock matrix with the stored heat, the evaluation of hydraulic and transport characterization tests, the optimization of the well configuration, and the simulation of the long-term performance of the reservoir are typical modeling tasks. In the first phase essential components for the planning of a future geothermal project were developed. This includes: a) a configuration tool for geothermal wells, b) fracture-matrix-models for the investigation of the relative importance of the individual sub-domains and their investigation using sensitivity analyses, c) a pore-scale model for the development of upscaling procedures in natural geothermal reservoirs (usually only small scale core samples are available for characterization), d) development of

tools for reservoir characterization (thermal response tests and push-pull experiments, see project gebo-G6).

In geothermal reservoirs, exploration as well as exploitation of a geothermal reservoir is however highly influenced by the effects of coupled processes, in particular hydro-thermal, hydro-mechanical, as well as hydro-thermo-mechanical processes (THM). The latter implies for example that the circulation of cold fluid in a reservoir induces a mechanical reduction in the porous matrix and therefore influences the hydraulic parameters, which in turn affects heat flow. There is another coupling due to the fact that fluid parameters, density and viscosity are temperature dependent. Knowledge of theses processes as well as their prediction is essential for the successful and economical performance of a reservoir. The investigation of the importance of coupled processes as well as the development of the respective tools was the focus in the second phase of the project.

The tasks performed during the project can be divided in two groups: one concerning reservoir characterization, the other concerning the operation of a geothermal facility. Both are relevant tasks already in the planning phase. The results of the characterization experiments are required in models on the operation of a facility. Various constellations and options concerning the operation are the basis for decisions concerning the operational design of geothermal pumping and injection. Within the work on the project several sub-tasks have been examined:

- Geothermal Operation - Development and Simulation of Well Configuration Tools
- Geothermal Operation – Importance of Fracture-Matrix Interaction
- Geothermal Operation - Benchmark Models
- Geothermal Operation - Simulation of a Well Doublet
- Geothermal Operation – Regional Models for Geothermal Production
- Reservoir Characterization - Thermal Response Test (TRT)
- Reservoir Characterization - Push-Pull Experiments
- Reservoir Characterization – Microscale Models
- Reservoir Characterization – Parameter Upscaling with Microscale Models
- Reservoir Operation and Characterization - Models for Fracture-Matrix Heat Transfer

In the following we give a short summary on the work and results of the tasks. Few selected topics are treated in more details.

All modeling work reported was performed using COMSOL Multiphysics and MATLAB®.

2. Geothermal Operation

Concerning operation all tasks are based on or extended from a generic simple situation of a geothermal production facility, which is sketched in Figure 1. Within the deep sub-surface a production and an injection leg both reach a permeable fracture. During operation a hydraulic circulation is initiated that combines production and injection hydraulically. Injected cooler fluid will push hot water towards the production leg, from where it flows towards the earth surface for final

utilization above ground. In the figure a single borehole constellation is visualized. In general multiple borehole set-ups are feasible, but it has to be taken into account that for the deep sub-surface every extra borehole is a financial burden, at least.

A finally set up geothermal plant is usually more complex than shown in the sketch. There may be several boreholes, there may be several production and injection legs, and there may be several fractures. Fractures may not be straight, as in the sketch, its thickness may change spatially and temporally. In reality the fracture plane will be bounded by an irregular geometry. While the technical features are known, the geological circumstances are usually vague, even after performing characterization tests. However the generic situation, as described, and constellations derived from it, can give some clues concerning the design and operation of a geothermal facility.
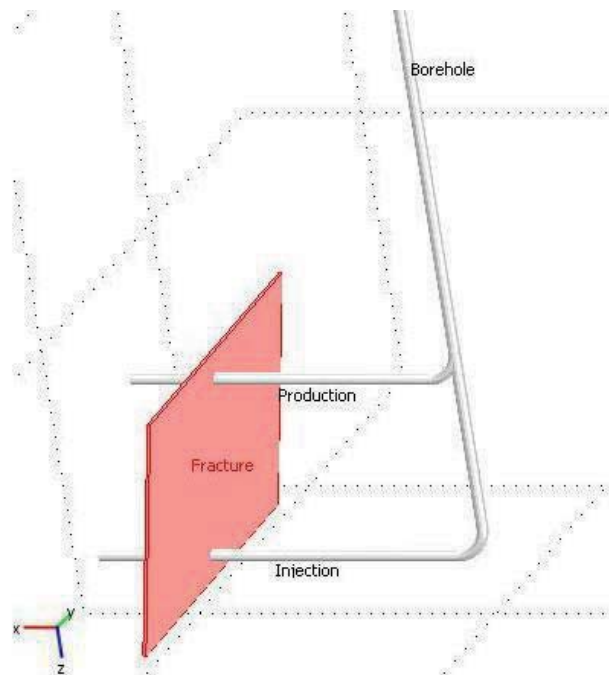
Figure 1: Sketch for simplest injection/production scheme of a geothermal facility using a single borehole ('Einbohrlochkonzept', see for example: Teodoriu 2010).

2.1. Development of a Wells Design Tool

Within a fracture or a permeable layer in the deep subsurface, the flow regime, induced by injection and pumping, can be described by classical methods of potential flow. A program for the design of doublets and doublet systems was developed in MATLAB®. It is based on analytical solutions for 2D flow in porous media. An arbitrary number of doublets can be considered. Baseflow, if present, is assumed to be of constant size and direction in the entire plane. Amount and direction of baseflow are input values, which are set by the user of the software tool.

The program is equipped with output options for potential contours, streamlines and velocities, represented by arrow fields. New developed was the visualization of limit streamlines, which show the

229

margins of catchment zones. The program comes with a graphical user interface (see Figure 2), and can thus also be used by non-specialists (see publications Holzbecher & Sauter 2009, 2010a, 2010b).
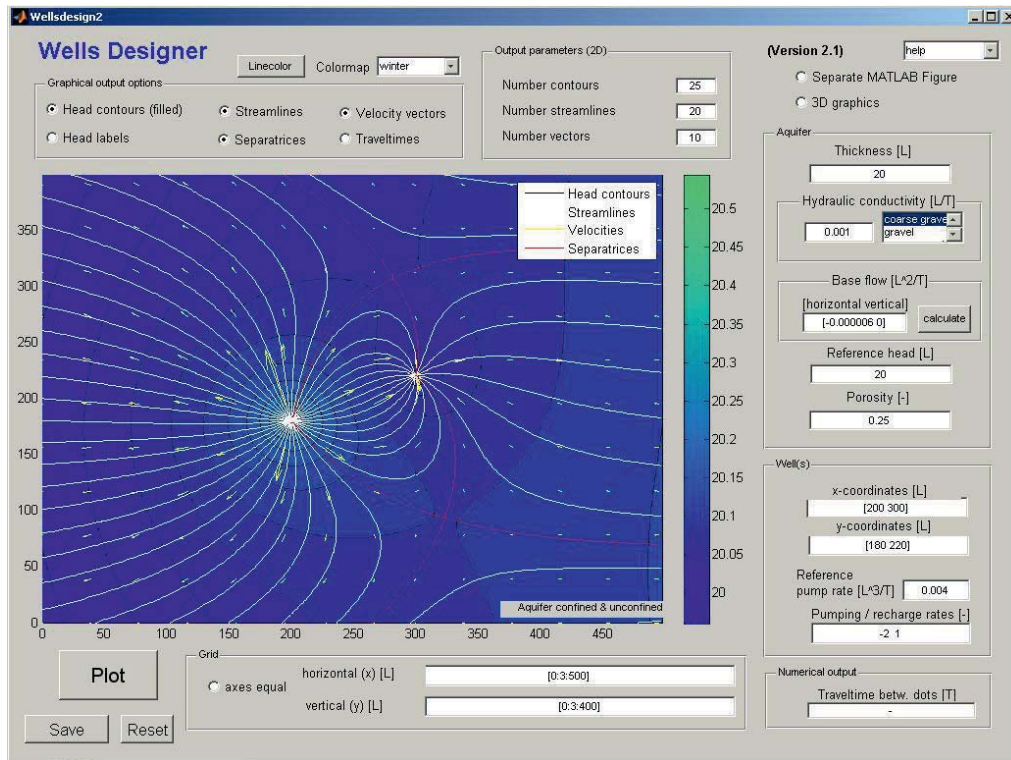
Figure 2: Graphical user interface for designing injection/production well constellations.
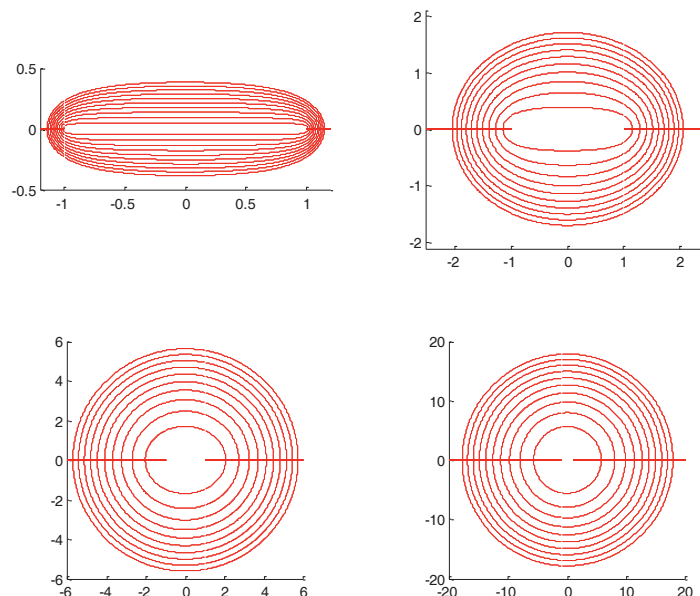
Figure 3: Area of influence for a doublet in constant baseflow field, in dependence of pumping rate; upper left: Q=0.1(0.1)0.9, upper right: Q=1(1)9, lower left: Q=10(10)100, lower right: $Q=10^2(10^2)10^3$

230

Using multiple runs of the algorithm for the single doublet in the presence of baseflow, we examined the area of the doublet catchment. Baseflow is directed parallel to the main axis of the doublet. For low pumping rates the area influenced by the doublet is of nearly elliptical shape, which changes to nearly circular shape for high pumping. This is visualized in Figure 3. Note the different scales in the sub-figures. Well positions are $x=\pm 1$ on the abscissa in all cases.

In order to obtain a scale independent result variables are transformed into dimensionless form. The dimensionless pumping rate is given by $Q=Q_{well}/(Q_0 d)$ with pumping rate Q_{well} [m^3/s], baseflow Q_0 [m^2/s] and distance between the wells d [m]. Unit area is d^2. We computed the size of the doublet area automatically utilizing the limit streamlines, calculated numerically, which led to the relation between pumping rate and doublet area, shown in Figure 4.
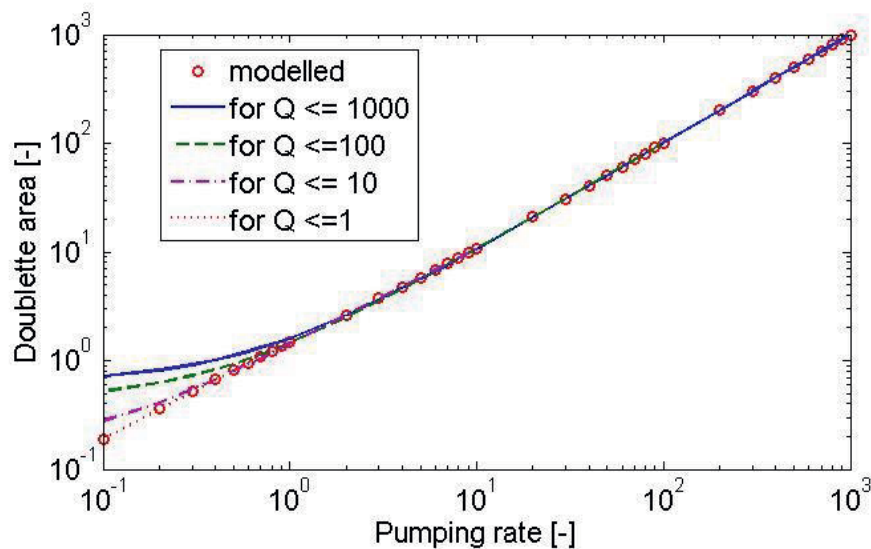
Figure 4: Relation between pumping rate and doublet area (both dimensionless, see text).

Obviously the doublet area increases with pumping rate. For high and intermediate pumping rates there is a linear relationship. For low pumping (dimensionless pumping rates below 1) only a deviation from the linear regime can be observed. This is emphasized in the figure by depicting polynomials, obtained as best fits for different sets of pumping rates. If we use the entire set of pumping rates (dimensionless, from 0.1 to 1000) we obtain better overall fit (blue curve), but higher deviation from the modeled low pumping results.

2.2 Hydraulic Fracture-Matrix Interaction

The interactions between a permeable formation and the adjacent low permeable matrix are important for the withdrawal of heat from a geothermal reservoir. As a first approach into the topic two idealized simple situations in 2D were studied by numerical modeling.

In order to reduce the number of parameters for the sensitivity analysis, the system was transformed into non-dimensional form. For the fracture we investigated two different conceptual approaches. In the full-dimensional approach the fracture is modeled in 2D. This requires a very fine finite element

231

mesh in the vicinity of the fracture, in order to capture the details of the flow across the fracture-matrix interface. In order to circumvent this problem, in the lower-dimensional approach the fracture is treated alternatively as 1D, i.e. a line element.

An extensive sensitivity study was performed, in which the permeability ratio for example was altered up to 8 orders of magnitude. The results of this study were published in a master thesis (Wong 2010) supervised jointly with project gebo G3. In particular the deviations from undisturbed flow, due to the existence of the fracture, were examined. Clear criteria were obtained concerning the parameter ranges, in which the system transforms from a matrix-dominated to a fracture-dominated flow regime.

In the reference model we will treat the doublet system, in which two legs of a geothermal facility are connected to (and by) a single fracture (see sketch in Figure 1).

Results were published by Holzbecher *et al*. (2010). An example is given in Figure 5, in which a fracture of elliptical shape connects two horizontal permeable layers. Depicted are fracture boundaries (black), flow-net (streamlines and iso-potentials, white), potential (color) and the velocity field (arrows). Arrow size is chosen according to absolute value of velocity. Clearly the focussing of streamlines in the fracture and the high permeable outflow layer at the bottom of the model region can be recognized.
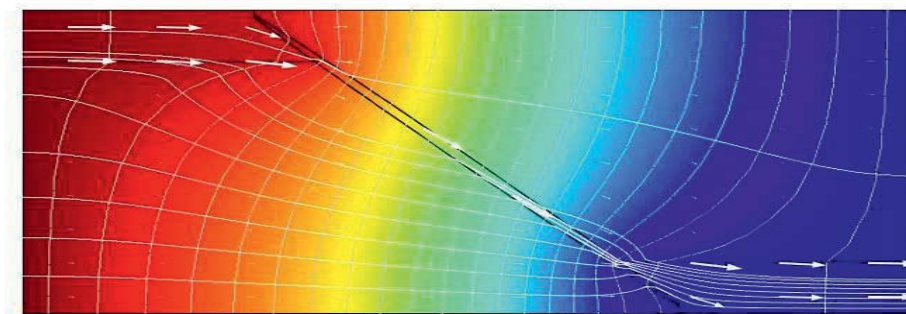
Figure 5: Potential colorplot, streamlines and velocity field for set-up 2 with elliptic fracture and two permeable layers.

It turned out that the lower-dimensional approach has less advantages than could be expected initially. The full-dimensional approach is easier to implement and delivers streamlines through the fracture, without requiring extended execution time.

2.3 Simulation of Bounded Fractures

As an extension of the studies described in 2.1 we examined fractures with prescribed limited extension. The potential approach used above was based on the assumption that the extension of the fracture is much bigger than the region influenced by the injection/production facility. Thus there is only marginal error if the fracture is taken as infinitely extended. However, in practice that is not necessarily fulfilled. In particular, if fractures are result of stimulation procedures, they may extend only locally around the stimulation point.

In cooperation with gebo project gebo B9 several such situations were examined by modeling. We applied the common finite element method (using COMSOL Multiphysics), while in B9 the approach of cellular automata is utilized.
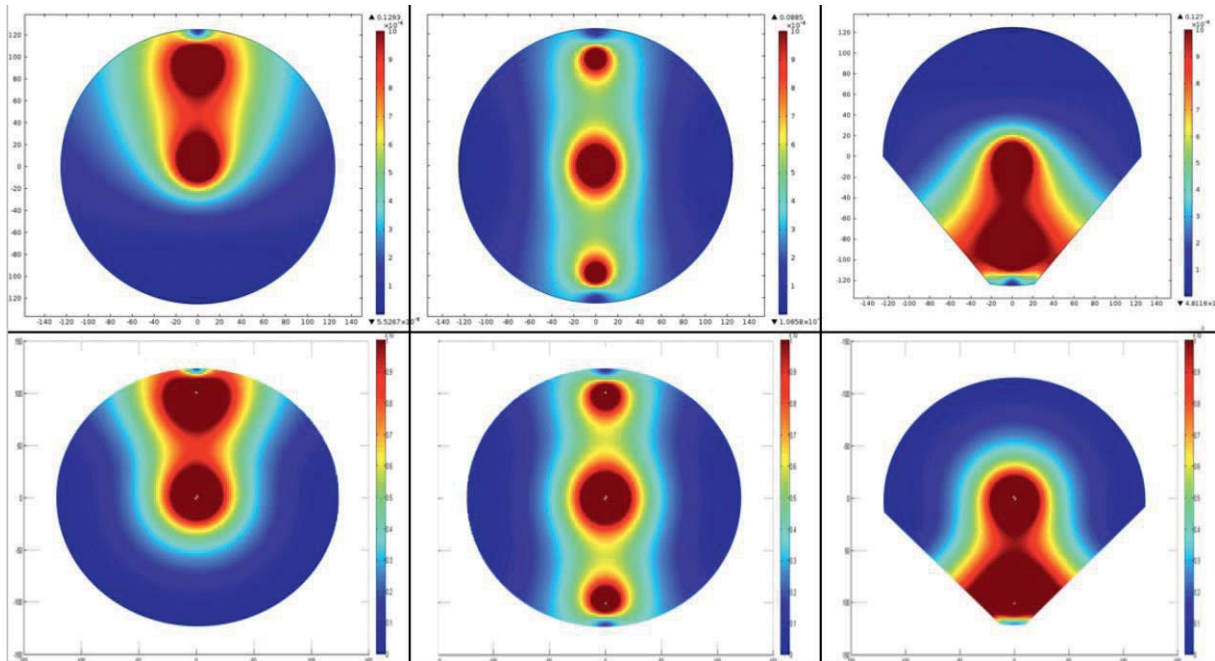
Figure 6: Flow from injection-production schemes in locally extended fractures; three examples for different fracture geometries and well locations; color plots show absolute value of velocity; upper row: finite element method, lower row: cellular automata (Ostermeyer & Srisupattarawanit 2012).

In Figure 6 we show several three examples. The sub-figures center and left deal with fractures of circular extension. The injection is performed in the center. In the left sub-figures the production point is near to the upper boundary, while in the center sub-figures there are two production locations, near the top and bottom of the boundary. The color plots, representing the absolute values of velocity clearly reveal increased flow (red) at both, injection and production positions. The sub-figures on the right show different fracture geometry with injection at the center and production near to the lower boundary.

Comparison of the sub-figures in upper and lower row shows marginal differences between the two different numerical approaches. It can be concluded that for type of problems (flow only) both methods, finite elements and cellular automata, perform very well. For more complex situations, especially when complex coupling have to be considered, extended comparison studies are surely necessary.

2.4 Doublet Simulation - Parameter Dependencies

As another extension of the previous work on injection/production systems, a systematic study was performed involving the density and viscosity dependencies in a coupled heat and fluid flow model for a single doublet. It was the aim to examine the relevance of the couplings for the operation period of the doublet, i.e. until the thermal breakthrough appears.

Groundwater flow modelling is based on the principle of mass conservation (1) and on Darcy's Law (2) generalized for the consideration of variable density effects:

$$S\frac{\partial p}{\partial t} + \nabla \cdot \left(\mathbf{q} \right) = Q \qquad \frac{\partial_v}{\partial t} \qquad (1)$$

$$\mathbf{q} = \frac{k}{} \nabla (p \quad gz) \qquad (2)$$

In the numerical models these equations are solved for hydraulic pressure p as dependent variable. Other variables and parameters are: Darcy velocity vector $\mathbf{q}$, fluid density ρ, permeability k, fluid dynamic viscosity μ, acceleration due to gravity g, Biot constant α, storage parameter S, fluid source/sink-term Q, and volumetric strain ε_v. Volumetric strain only has relevance if geomechanical processes are considered. Otherwise the last term in equation (1) can be omitted.

The thermal regime in the entire model is determined by solving the corresponding convective heat transport equation

$$\left(C \right)\frac{\partial T}{\partial t} + \nabla \cdot \left(\left(C \right)_f T\mathbf{q} \right) = \nabla \cdot k_T \nabla T \qquad (3)$$

which is a differential equation for temperature T as dependent variable. Other variables are: specific heat capacity of fluid $(\rho C)_f$ and of fluid-solid system (ρC), and thermal conductivity k_T. Hydraulics and geothermics are coupled, i.e. equation (3) has to be solved simultaneously with equations (1) and (2). The hydraulics affects heat transport via the velocity $\mathbf{q}$, while on the other hand temperature affects hydraulics via the temperature dependent fluid properties viscosity and density (e.g. Holzbecher, 1998).

Density and viscosity dependencies are neglected in most modeling studies. That is mainly done for the simple reason that flow and transport modelling steps can be separated. As flow becomes independent from the temperature distribution, if dependencies are neglected, it can be simulated in a first step, while the heat transport can then be solved in a second step. In order to check, if that simplified procedure is justified, a model was set up, in which the parameter dependencies are considered as shown in equations equations (1) and (2).

For a typical parameter set-up a model was set up for a doublet within baseflow. The permeable model region has a constant thickness and extends in horizontal direction. Both injection and production wells are ideal, i.e. screened through the entire permeable layer. The porous medium is homogeneous and isotropic. In the model we assume a difference of 70°K between the hot reservoir temperature and

the cold injection temperature. Using COMSOL Multiphysics we consider groundwater flow and heat transport in a 3D model. The 3D approach becomes necessary, as the vertical coordinate explicitly appears in the buoyancy term, the last term in equations (2).
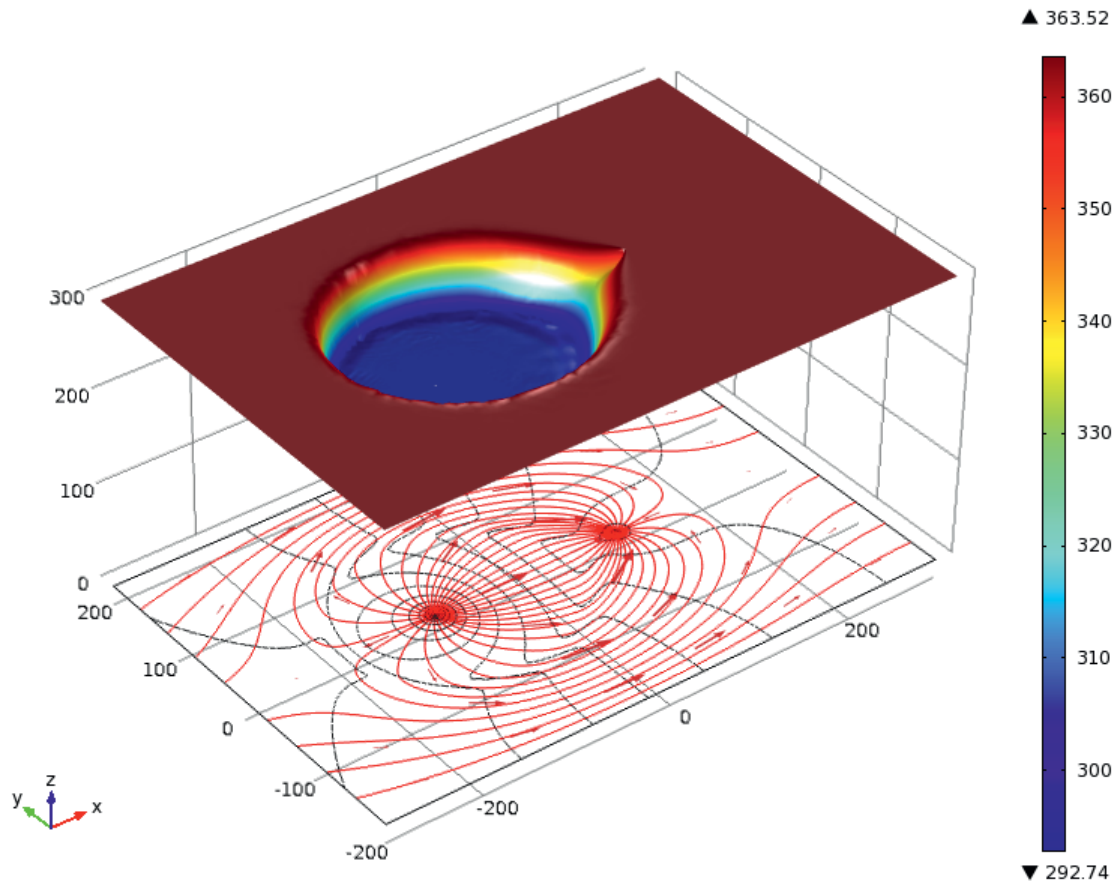
Figure 7: Flow pattern and temperature distribution for a doublet; simulated using COMSOL Multiphysics.

Figure 7 shows the results of the model. In the lower part the velocity field in the horizontal center plane through the model region is depicted, in form of flowpaths and an arrow field, representing the velocity vectors. In the upper part of the figure the temperature in the same plane is visualized, at a time instant, when the coldwater front starts to approach the production well. Red color represents hot, blue cold fluid.

Obviously the flow field shows no significant differences compared to the flow pattern for the classical 2D doublet constellation. There is no circulation due to buoyancy effects, induced by density differences. The temperature field thus shows steep gradients at the cold water front, while in the remaining part of the model region the temperature is nearly constant at high temperature before the front and cold temperature behind the front.

As relevant result we conclude that for typical geological settings as found in the deep sub-surface of the North-German basin, density and viscosity effects are negligible. Thus under usual circumstances

it is justified for modelers to use a simplified approach in which flow is de-coupled from heat transport.

2.5 The 'Horstberg' Benchmark Model

The set-up of a benchmark with typical conditions of geothermal production in the North-German lowlands was the starting point for extensive modelling studies with focus on various coupling features. The reference model roughly orients itself on the aims, formulated in gebo concerning the production from HDR-reservoirs (Teodoriu 2010) – pumping rate 0.1 m^3/s, reservoir temperature 200°C, depth 5000m: in the agreed model set-up the production horizon is located a bit higher and the corresponding temperature is a bit lower.

The model offers the option to simulate hydraulic, geothermal and mechanical states during operation of the geothermal facility in dependence of relevant parameters, as pumping rate, regional flow field, hydraulic conductivities, mechanical parameters (Young modulus, Poisson ratio), coupling parameter (Biot coefficient), fault type, and boundary conditions, etc.

The so called 'Horstberg' benchmark model, developed by the gebo-geosystem projects, was basis and reference for several studies, concerning water flow, heat transport and structural mechanics. The geological features, i.e. layers and fault, of the benchmark model (see *Figure 8*) were set-up in close co-operation with project G5, applying the finite element software COMSOL Multiphysics.
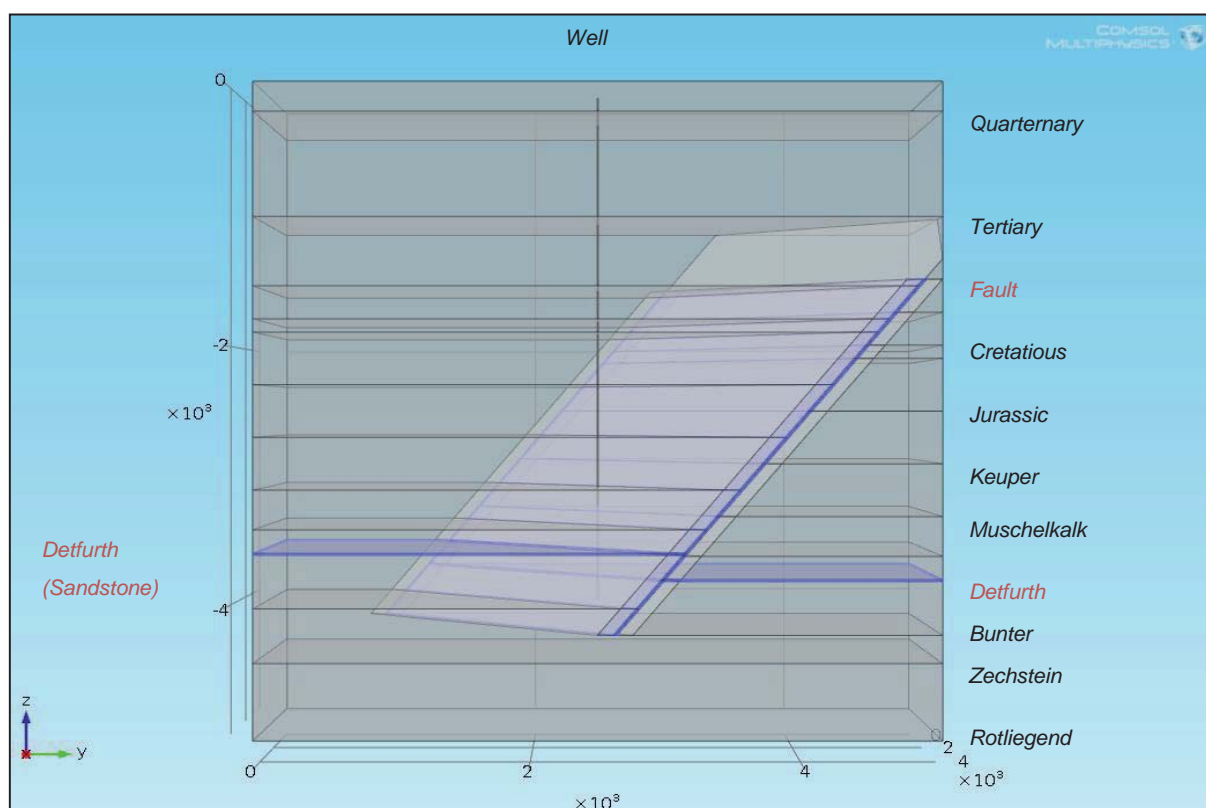
Figure 8: Geological features of the 'Horstberg' benchmark

The model is set up for a typical single borehole scenario. It is assumed that the borehole is screened and thus in contact with the porous sub-surface, where it pierces through the permeable subsurface strata. In the simulations we presumed pumping of hot water at the connection with the inner core of the fault, which was assumed to be permeable. Cold water is injected where the borehole pierces the Detfurth layer. Thus the injection position lies below the pumping position. In the simulations we assumed constant pumping rates.

The coupled heat and flow regime during operation of the geothermal facility was simulated to examine the temperature changes due to the operation of the geothermal plant. The initial condition is a layered temperature profile following the geothermal gradient. Concerning heat transport the boundary conditions are: geothermal gradient at groundwater inflow, fixed temperature at top and base (Dirichlet type), fixed injection temperature (varied from 20°C up to 70°C), and usual outflow conditions at all outlets. The temperature at the pumping locations is thus an output of the simulation.

With one pumping horizon and one injection horizon a doublet-type flow field is induced in a single borehole (compare also for near-surface hydraulics: Hand *et al*. 2012, Jin *et al*., 2014).
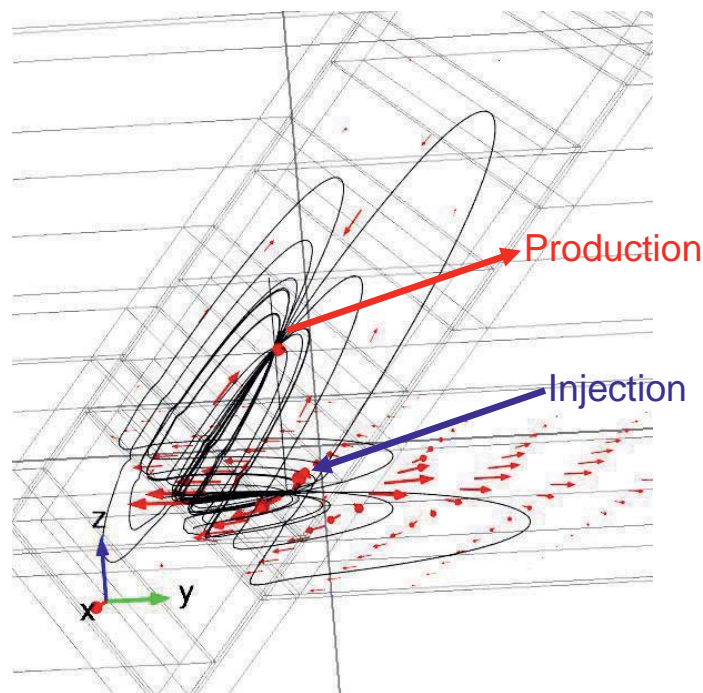
Figure 9: Flow pattern of the Horstberg benchmark, zoomed in to circulating flow between injection and production points; streamlines in black, arrow field representing flow velocities in red.

Due to the complex geological conditions the induced flow pattern differs clearly from the simple circulation in a conventional two-well doublet in a purely layered system (see Figure 9). As the ratio of conductivities between permeable and impermeable parts of the aquifer is high (up to several 1000, see below), the flow follows mainly the permeable strata: the injected water flows dominantly in the deep aquifer towards the aquifer-fault interface, where it changes its direction into the fault towards

the withdrawal position. Similar to classical doublet pattern the flow is highest along the shortest connection with the described features and with distance from that connection slows down significantly. Oberdorfer *et al*. (2012) provide more details.

With the numerical simulation the temperature changes due to the operation of the geothermal facility are calculated. In Figure 10 we show the temperatures after 50 years of perpetual operation of the power plat. Following the flow regime described above, a cold water wedge gradually moves from the injection screen, first mainly horizontal within the aquifer, then following the fault upwards towards the production positions. However, the temperature field changes above and below the production position. Here the colder water wedge shows still temperatures above 360°K, when arriving the production screen. On the opposite (upper) side of the production screen we also observe a cold water wedge, moving through the fault downward (see zoom in Figure 10). In that way the colder water in the upper geological layers is connected to the production site and contributes to the cooling of the pumped fluid. Moreover, using the model we could examine the influence of the pumping rate on the lifetime of the facility, depending on various operation parameters. Temperature breakthrough curves as function of pumping rates are presented by Oberdorfer *et al.* (2012).
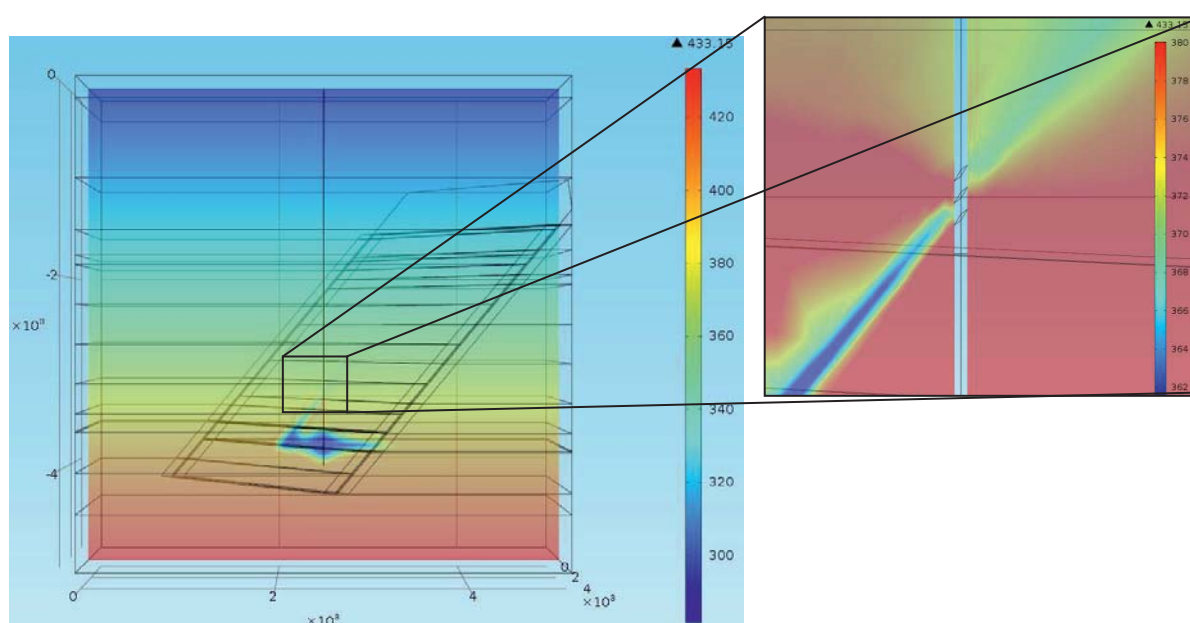
Figure 10: Temperature [°K] distribution after 50 years of perpetual operation of a geothermal power plant.

The benchmark model was examined further with focus on various production scenarios. Relevant parameters studied were the injection/pumping rates, the temperature of the formation, and the base flow – strength and direction.

In order to study deformations due to mechanical or thermal stress, for example with respect to borehole stability, a set of geomechanical equations has to be considered in addition to equations (1)-(3):

$$-\nabla \cdot \boldsymbol{\sigma} = \mathbf{F}_V \tag{4}$$

$$\boldsymbol{\sigma} - \boldsymbol{\sigma}_0 = \mathbf{C} : (\boldsymbol{\varepsilon} - \boldsymbol{\varepsilon}_0) - \alpha p \mathbf{I} \tag{5}$$

$$\boldsymbol{\varepsilon} = \tfrac{1}{2}\left((\nabla \mathbf{u})^T + \nabla \mathbf{u} \right) \tag{6}$$

which is a system of differential equations for which the elements of the deformation vector $\mathbf{u}$ are dependent variables. Further variables are: stress tensor $\boldsymbol{\sigma}$, volume force vector $\mathbf{F}_V$, strain tensor $\boldsymbol{\varepsilon}$ and stiffness tensor $\mathbf{C}$. Concerning the stress-strain ratio we assume linear elastic conditions and use the Young modulus and Poisson ratio for its description (see for example: Wang 2000). The coupling with the hydraulics is given through the pore pressure p in the last term in equation (5) that is quantified by the Biot constant α introduced above. For high Biot constants there is a strong coupling, for low α there is a weak coupling.

Boundary conditions corresponding to mechanics are: fixed constraint at the base, free or roller conditions at outer vertical surfaces, and free movement at the top. Using the mechanical model without coupling we first examined the effects of the fault on the stress field in the model region. Then the model was extended for the production phase in order to explore the hydraulic-mechanical coupling.
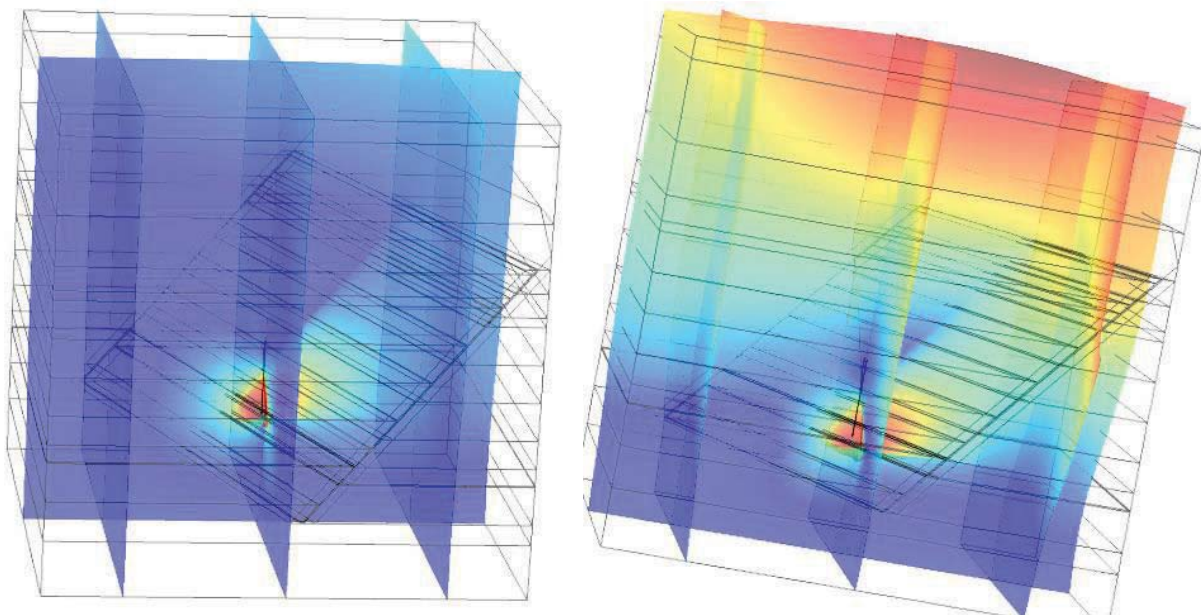
Figure 11: Displacement in [m] in the 3D model: red=high displacement, blue= low displacement; for permeability contrasts of 100 (left, max. deformation = 1.8 mm) and 1600 (right, max. deformation = 3.7 mm) and Biot constant α=0.9; visual representation of the deformation is exaggerated by a factor of 10^5

Concerning the geomechanical coupling first model runs were performed with neglect of temperature and thermal stress. For a basic understanding of the system behaviour the steady state was examined in dependence of base rock permeability. Figure 11 shows the size of displacement on selected slices through the cube for two different scenarios. In one scenario the base rock is by a factor 100 lower permeable than the conductive Detfurth layer, in the other by a factor of 1600. Maximum displacement in these scenarios is slightly below 2 mm in the first case and slightly below 4 mm in the second. In both cases a local maximum of the deformation appears in the middle of the model region along the borehole. This was expected because pressure gradients are highest in that region, due to the operation of the geothermal facility. However the deformation both figures differ significantly concerning the geomechanics in the upper part of the model region.

To examine that situation in more detail, we performed a parametric sweep on the permeability ratio between the permeable aquifer and the fault core on one hand and the surrounding base-rock on the other hand:

$$= k_{perm} / k_{base} \tag{7}$$

We varied κ from small values below 10 up to almost 4000. Within the parameter sweep the permeability of the aquifers was kept at a constant value of $k_{perm} = 10^{-12}$ m^2 and flanks of the fault are assumed to be of intermediate conductivity $k_{medium} = k_{perm} / \sqrt{}$.
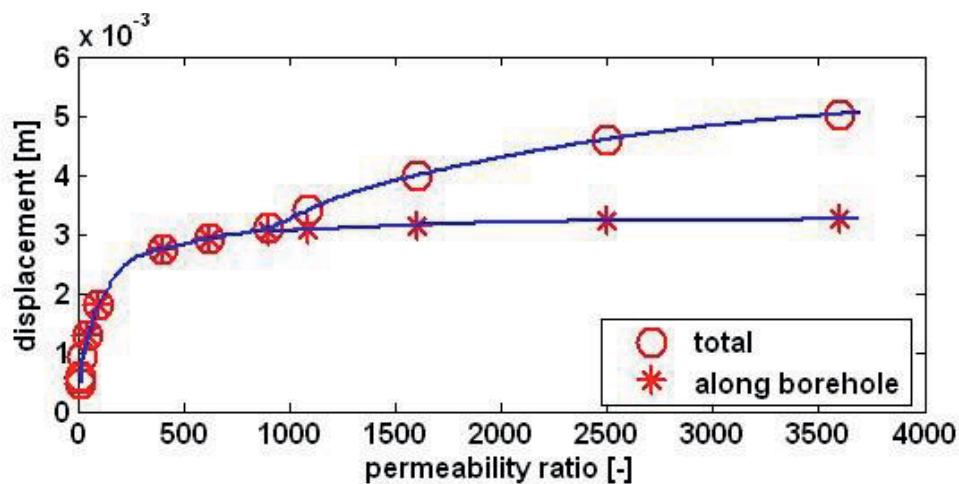
Figure 12: Maximum displacement in the model and maximum displacement along the borehole, as function of permeability contrast (varying from 3 to 3600); for Biot constant α=0.9

Figure 12 shows total displacements as function of the permeability contrast, for the entire model region and along the borehole surface. For small permeability contrasts the displacement is growing strongly with κ. For > 300 the deformation at the borehole approaches a steady state, and for > 1000 there is almost no change of deformation along the borehole. For small permeability ratios both curves coincide, i.e. total displacement is highest at the borehole. For higher κ the displacement is

highest at the ground surface above to the upper fault location. For higher permeability contrasts the setting around the fault is obviously so stiff that stresses migrate along the fault, and become most pronounced at the top of the model.

One may conclude that in highly permeable faults the pore pressure, changed as effect of the pumping regime, is of high influence on the stress regime and the deformation in the fault and even in the overlying layers.

In further studies we focused on borehole stability, examining the deformations along the borehole. Especially between injection and pumping positions the biggest changes can be expected, where there are highest pressure gradients. Holzbecher & Oberdorfer (2014) present the outcome of the THM model, shown in Figure 13. Here total deformation between the two mentioned positions (near 0 for injection, near 550 for production) is depicted as function of distance (along the borehole) and time, changing with time after start of operation. The deformation shows elastic behaviour: it increases with time until approximately 7 years ($2.3 \cdot 10^8$ s), and relaxes then gradually to a near steady state.
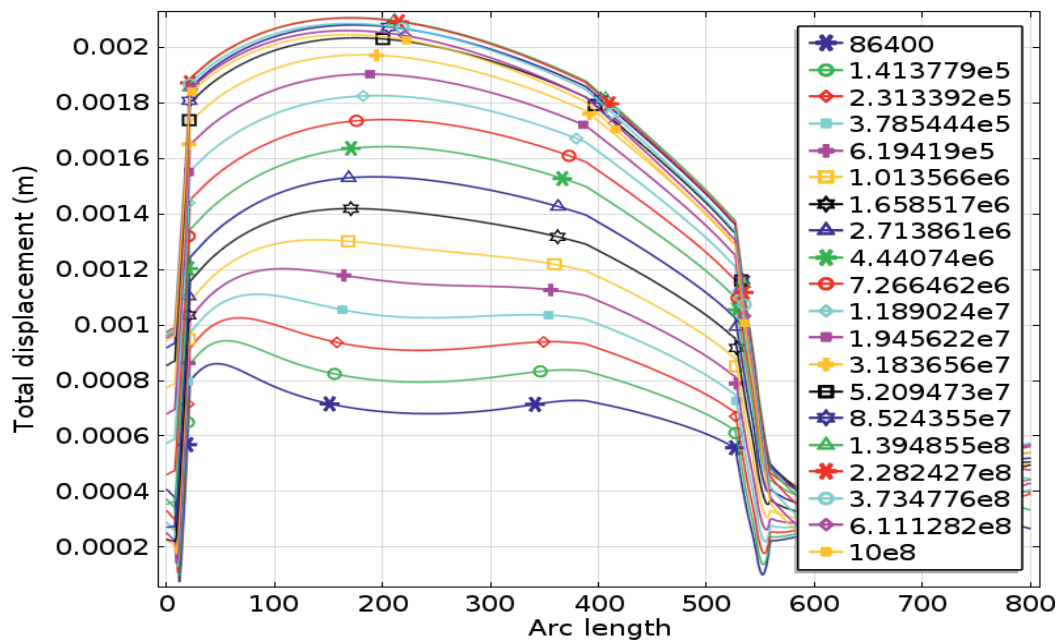
Figure 13: Total displacement along the borehole, as function of depth (x-axis in [m]) and of time (legend for time [s]).

Using the coupled poroelastic model, Holzbecher (2013) depicts displacements along the borehole as function of the Biot-coefficient. All simulations show that maximum deformations along the borehole can be expected below the scale of cm - a scale that should not be critical for borehole stability.

3. Reservoir Characterization

The accuracy of models for the prediction of the performance of geothermal facilities relies very much on input parameters. As the layout of the technical system is known, the concerned parameters are known within a relatively narrow range of uncertainty. The geological parameters however, are only vaguely known and can possibly be determined by reservoir characterization tests. It is a characteristic feature of tests that they are performed on length and time-scales that are much smaller than the scale of interest for the facility operation. Thus, as common in many geological applications, the scale issue is of high importance also here. Tracer tests are utilized to identify characteristic parameters for mass transport. As in geothermics the main interest lies in heat transport, there has to be an analogy between both transport types, in order to transfer the findings from experiment to the final operation. In order to tackle that problem we performed numerical studies with coupled flow and transport models with varying length and time scales, starting from the micro-scale upwards.

In addition classical methods in reservoir characterization, thermal response tests and push-pull experiments, were examined numerically. In contrast to classical evaluations of such tests, based on analytical solutions, numerical models for parameter identification are much more flexible. Analytical solutions can be obtained for selected constellations and conditions only. If these are not fulfilled the application of the evaluation technique may lead to erratic results, and can thus not be applied. Numerical methods offer the chance to adjust the model according to non-ideal conditions usually met in the field.

3.1 Microscale Models

If for the characterization of geothermal reservoirs tracers (of general type, one may also think of reactive tracers), are applied, the techniques are based on the similarity and comparability of heat flow on one side and mass flow on the other side. On the microscale both processes show substantial differences. Heat transport is taking place in the pore space and the porous material, while mass transport is taking place in the pore space only. In order to investigate the differences between heat and mass flow we performed numerical studies with a microscale model. Microscale modeling has become feasible recently due to the fast development of powerful computer hardware and software. On clusters and in high performance computing it is currently performed even for large 3D objects.

We studied heat- and mass transport in relatively simple 2D models. In a first step flow was calculated in the pore-space (micro-model) of a thin section (see Figure 14). This was done using COMSOL Multiphysics sovling the Navier-Stokes equations for laminar flow. In a second step mass and heat flow were simulated on the base of the flow model. Dispersion does not have to be considered in the micro-scale, as it results implicitly from the structure of the pore space.
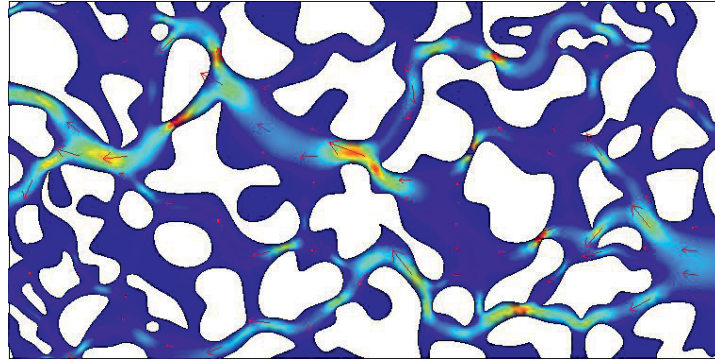
Figure 14: Flow field in a thin cell, simulated using COMSOL Multiphysics, colors represent velocity magnitude (blue = zero, red = high); length extension of the cell: 0.8 mm.

Modeling results show significant differences in heat- and mass transport. At the microscale it is crucial that the heat diffusion coefficient is 3 orders of magnitude higher than the mass diffusion coefficient. For usual low hydraulic gradients at the micro scale heat transport is thus much faster than mass transport. In contrast, for macrodispersion, which becomes relevant at larger scales, it is usually assumed that heat transport is retarded in relation to an ideal tracer. This shows that the scale, at which heat and mass transport appear, is quite relevant. We discuss this point a bit further concerning upscaling methods in section 3.4.

3.2 Thermal Response Test (TRT)

During the performance of a TRT water of higher or lower temperature compared to the reservoir temperature is circulated in a borehole heat exchanger in order to determine reservoir thermal conductivity as well as borehole resistance parameters. It is assumed that the porous medium is homogeneous and that there are no deviations in the direction parallel to the borehole. The simple evaluation formulae are derived under the assumption of no ambient flow, i.e. no convective heat flux and does not take into account measurements at other locations in the vicinity of the borehole. Moreover it is assumed that the heat flux increases from zero to a constant value.

In the project some models have been set up that are valid under less restrictive conditions. For example the situation can be handled in which the heat flux is constant from the start of the test, which is closer to the real practice. With models, as they are set up using MATLAB and COMSOL Multiphysics it is possible to take temperature measurements outside the borehole into account.

3.3 Push-Pull Experiments

In push-pull experiments water of different temperature and/or different chemical characteristic is injected into the reservoir (push phase), followed by a shut-in and a pumping phase (pull phase). These experiments are used in order to determine thermal properties of the reservoir (Pruess & Doughty 2010). For the evaluation of push-pull tests there are no standardized evaluation formulae. Simple evaluation techniques can be derived under simplifying assumptions, and are valid for few parameters

only and consider measurements in the borehole only. Models allow a more general approach for the evaluation of push-pull tests by inverse modelling. Using COMSOL Multiphysics in cooperation with project G6 a model for the evaluation of a push-pull test was developed. The model is based on a 1D representation for the fracture, coupled with a 2D representation for the matrix (Maier *et al*., 2011).

As an example output of the sensitivity analysis made, we here show our result concerning dispersivity. We choose the dispersion lengths α_l in a range from 0.001m to 0.5 m, which correspond to experimental scale up to 10 m (Wheatcraft 1988). In Figure 15 the strong dependence of the breakthrough curves on the dispersivity is clearly visible. While for small dispersivities the breakthrough curves are steep like with slight deviations due to the ambient flow field. For a high dispersivity the breakthrough curve changes to a pure decaying characteristic. This could lead to an ambiguous result which must be considered for further analysis (see below).
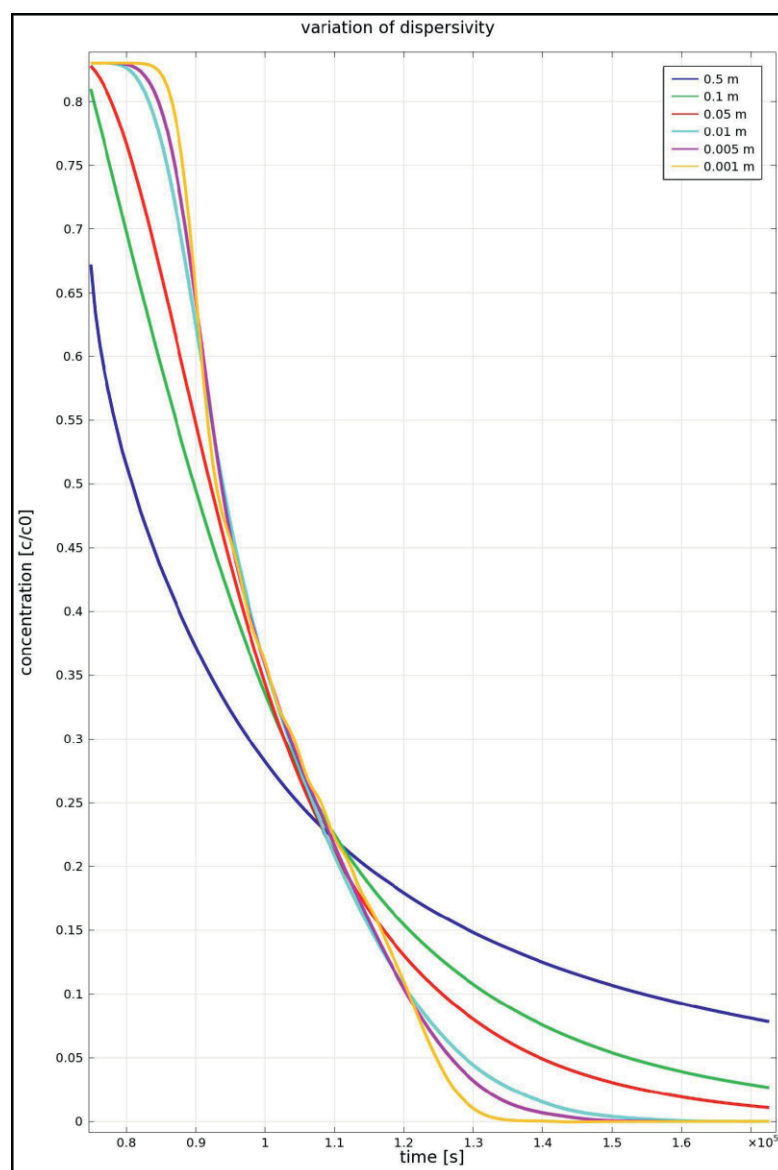
Figure 15: Dependence of breakthrough curves in a push-pull experiment on dispersivities.

In order to interpret breakthrough curves from a push-pull experiment a parametric study over a wide range of ambient groundwater velocities was conducted. Mostly the target of the push-pull experiment is to determine the unknown ambient velocity. Three main types of situations have been identified:

1. When the tracer, due to a very low ambient groundwater velocity, remains more or less located around the well, we have s-shaped breakthrough curve (Figure 16 upper left picture).

2. When the tracer is between the well and the stagnation point the breakthrough curve shows an increase of the concentration with a more or less long tailing since some amount remains in the slow flowing region around the stagnation point (Figure 16 upper right picture).

3. The third case is the zero line when most of the tracer has traveled beyond the stagnation point. In that case the interpretation of the experiment allows only an estimation of the minimum ambient groundwater velocity.
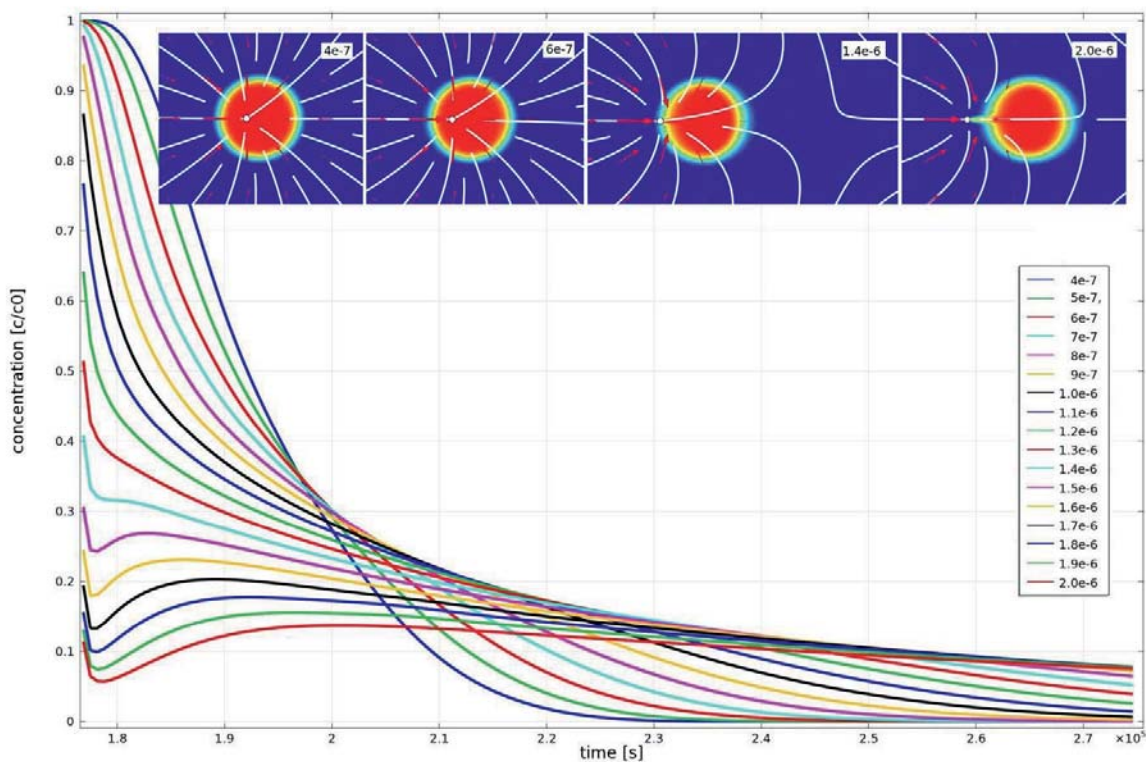
Figure 16: Flow pattern and tracer distribution at the begin of pumping phase (top) and breakthrough curves in a push-pull experiment (bottom) in dependence of flow velocity [m/s]

For the interpretation of the breakthrough curves we have to take care of the ambiguity due to the dispersion effect as shown in Figure 15 a high dispersivity could effect a rather high decay-like decrease of the injected tracer pulse. In that case the type 1 breakthrough curve changes to a declining curve which looks similar to the transition from type 1 to type 2 (Figure 16). Type 2 and 3 as well as the transition between these cases is not affected by dispersion changes in terms of curve shape, but it turns out that for high dispersivities the curves flatten out.

3.4 Parameter Upscaling – Extension of Numerical Modeling on the Microscale

The micro-scale models (see section 3.1) were extended to larger scales. For that purpose artificial porous media, consisting of randomly non-intersecting spheres were created and then treated by the described model approach including free fluid flow coupled (one way) with heat or mass transport. The representative porous medium sample of was created using MATLAB. After importing the structure, the modeling was performed using COMSOL Multiphysics. The spatial size of the model regions was varied over two orders of magnitude from 1 mm to 1 dm. Smaller length scales were not relevant here, as the relation between heat transport on one side and mass transport on the other is the same as in the mm-scale. For length scales larger than 1 dm there were convergence difficulties with the Navier-Stokes solvers, probably due to the larger scale of the pores; due to the construction that with increase of scale also the size of the creating spheres was increased.

Typical results are shown in Figure 17. On the left we see fast heat transport at the small scale. The gradient is mainly equal in flow direction, from right to left; i.e. isotherms are nearly vertical in the shown figure. On the left we show mass transport at the large scale, after a much longer travel time. The front is very irregular, following the fast advection regime. Some flowpaths are shown in white. Further examples were published by Holzbecher & Oehlmann (2012).
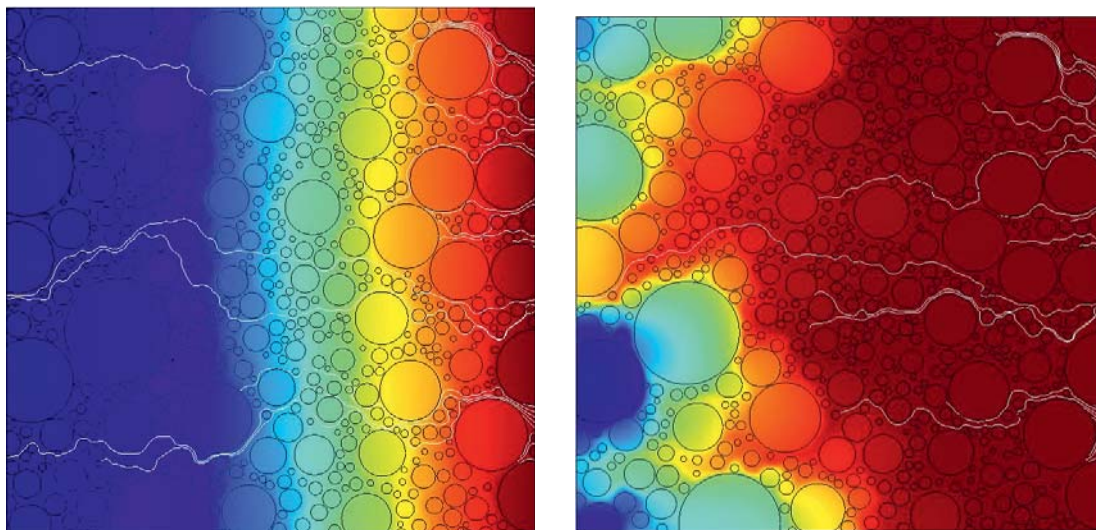
Figure 17 left: Temperature distribution for heat transport at length L=0.001 m; snapshot at t=1 s; right: Concentration distribution for mass transport at length L=0.1 m; snapshot at t=500 s.

The aim of the studies was to obtain a better understanding concerning the transition between the micro-scale phenomenon of 'accelerated' heat transport to retarded heat transport (in comparison to an ideal tracer) on the macro-scale (Shook 2001, Ferguson 2006). Such an understanding is important, when tracers are to be applied for the characterization of geothermal heat production. Tracer

experiments are always performed at a much smaller scale, and they concern mass transport, while with respect to geothermal production the aim is to predict heat transport.

Using analytical solutions for travel-time one can compare arrival times due to pure diffusion for mass and for heat transport: the two lines ('thermal' and 'solute') increase with a distance representing four orders of magnitude. For typical values of groundwater velocity (10^{-6} and 10^{-5} m/s) two arrival times are compared in Figure 18. In addition, for the two velocities the arrival time according to advection are shown; low velocity in blue and higher velocity in green.
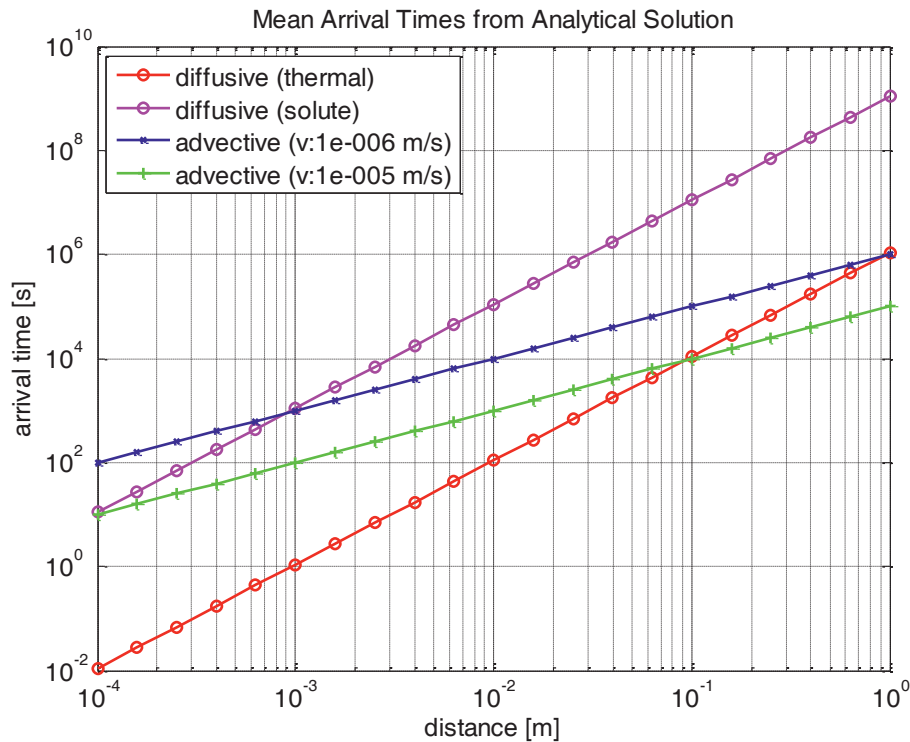
Figure 18: Arrival time comparison for diffusive (thermal and solute) and advective (two velocities) transport.

At the microscale at the left side of the graph, thermal diffusion is the fastest process, with arrival time of t=0.01 s for a distance of 0.1 mm. The corresponding arrival time due to molecular diffusion is 10 s (for the calculations here we used a Lewis number Le=1000). If a velocity of 10^{-5} m/s is prescribed, the traveltime due to advection is also 10 s at that scale. Thus for this velocity and length scale diffusion and advection are of equal relevance. For a smaller velocity the system is diffusion dominated as the diffusion arrival time is shorter.

The relations between the different processes change with the distance, as the arrival time curves for diffusion and advection increase with different slope. Thermal diffusion and advection with the higher velocity become equally relevant at 1 dm. For the lower velocity the equality of advection and solute diffusion is reached for 1 mm and of advection and thermal diffusion for 1 m.

These results can not directly be transferred to the microscale simulations, as parameters are not exactly the same in the analytical derivations and in the numerical simulations. One difference is that

in the latter two different thermal diffusivities have to be considered. However the graphs in Figure 18 give some clues for the understanding of the simulations.

The performed simulations show that the relation between heat transport on one side and mass transport on the other side depends on the length scale in question. When tracer-tests are applied for the characterization of the thermal behavior of a reservoir, the scale should thus be taken into account.

3.5 Fracture-Matrix Heat Transfer

The heat transfer between fracture and matrix is a crucial part of a geothermal heat production. Not only the exchange area and heat transfer coefficient are important. In the simple approaches the heat transfer in the matrix parallel to the matrix is neglected, for example in the widely used Lauwerier analytical approach (Lauwerier 1955, Vinsome & Westerveld 1980, Pruess & Doughty 2010). Using COMSOL Multiphysics we compared several approaches concerning the solutions of fracture-matrix transfer. In all of these the heat transfer in the matrix parallel to the fracture was considered. In a reference model we coupled a lower dimensional approach for the fracture with a full dimensional for the matrix.
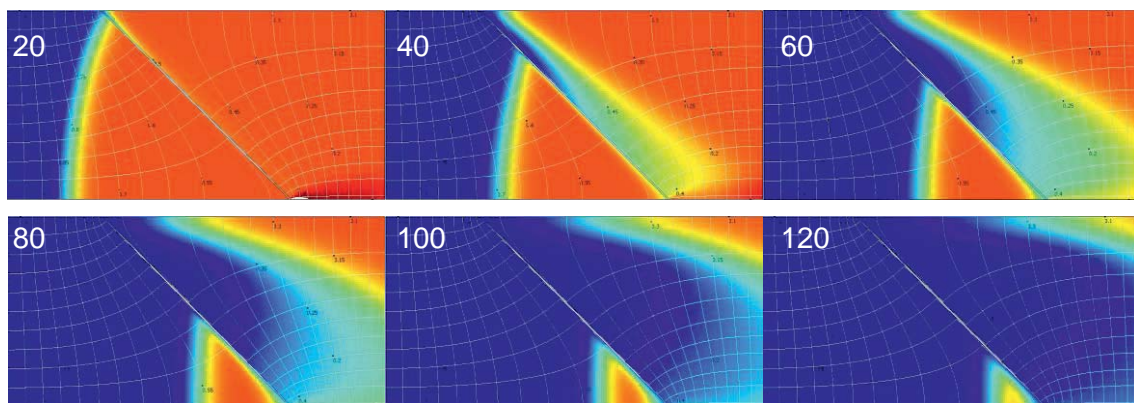
Figure 19: Within a fracture-matrix system: hot water replacing hot water from the left; number in upper left corner indicates dimensionless time.

Figure 19 shows the passage of a cold front through a matrix-fracture system. The hydraulics of such a system was already treated section 2.2. The resulting flow-net is shown by white lines. The temperature field at six different time instants is depicted in the sub-figures. The numbers in the upper left corners indicate time (dimensionless). It becomes quite obvious that the regular front, approaching from the left changes to a more complex shape during passage. The cold water progresses fastest within the fracture and behind the fracture along the lower edge of the model region. Near the upper edge hot water resides for a long time. In an extended system, of which the modeled situation would be a small part, this would lead to an extended tailing in the breakthrough curves. Another observation is that a small plume with elevated temperature remains in the lower part upstream of the fracture. This still resides until long after the front has passed.

4. Conclusions

The importance of coupled TH modeling for geothermal heat production from deep reservoirs or fault zones was highlighted for several problem settings. We examined the classical doublet situation, matrix-fracture interaction and a complex benchmark set-up. The latter, called 'Horstberg' was set-up in close cooperation with the other geo-projects with gebo. Moreover the most relevant scale problem was tackled by numerical methods.

THM was explored for the 'Horstberg' set-up. It turned out that the complex geometry of the benchmark led to several convergence problems for a fully coupled simulation. The process interactions between thermal, hydraulic and mechanical processes have to be studied on simple model settings first (that must not necessarily concern the deep sub-surface). An example for such model development is given by Holzbecher (2014).

5. Acknowledgements

6. Publications Resulting from Project gebo G7

Holzbecher, E. & Räuschel, H. (2014). Heat Transfer in Borehole Heat Exchangers from Laminar to Turbulent Conditions, *Europ. COMSOL Conf.*, Cambridge, https://www.comsol.de/conference2014/europe/file/id/18865/file/22267_holzbecher_paper.pdf

Holzbecher, E. & Oberdorfer, P. (2014). Rock Deformation due to Geothermal Heat Production – a Modelling Study, *Europ. Oil & Gas Magazine*, 40(1), 25-26.

Oberdorfer, P, Holzbecher, E., Hu, R., Ptak, T. & Sauter, M. (2013). A Five Spot Well Cluster for Hydraulic and Thermal Tomography, *38th Workshop on Geothermal Reservoir Engineering*, Stanford, http://www.geothermal-energy.org/pdf/IGAstandard/SGW/2013/Oberdorfer1.pdf

Holzbecher, E., (2013). Poroelasticity Benchmarking for FEM on Analytical Solutions, *Europ. COMSOL Conf.*, Rotterdam, http://www.comsol.de/paper/poroelasticity-benchmarking-for-fem-on-analytical-solutions-15336

Holzbecher, E. (2013). Coupled Hydro-Mechanical Modelling of Deep Geothermal Heat Production, *5th Biot Conference on Poromechanics*, Vienna, Proceedings.

Holzbecher, E. & Oehlmann, S. (2012). Comparison of Heat and Mass Transport at the Micro-Scale, *Europ. COMSOL Conf.*, Milan, http://www.comsol.de/paper/comparison-of-heat-and-mass-transport-at-the-micro-scale-13067

Oberdorfer, P., Holzbecher, E. & Sauter, M. (2012). Modelling Hydraulic and Thermal Responses in a Benchmark for Deep Geothermal Heat Production, *EGU General Assembly*, Vienna.

Oberdorfer, P., Hu, R. Rahman, MA., Holzbecher, E., Sauter, M. & Pärisch, P. (2012). Coupled Heat Transfer in Borehole Heat Exchangers and Long Time Predictions of Solar Rechargeable Geothermal Systems, *Europ. COMSOL Conf.*, Milan, http://www.comsol.de/paper/coupling-heat-transfer-in-heat-pipe-arrays-with-subsurface-porous-media-flow-for-13383

Holzbecher, E., Oberdorfer, P., Maier, F., Jin, Y. & Sauter, M. (2011). Simulation of Deep Geothermal Heat Production, *Europ. COMSOL Conf.*, Stuttgart, http://www.comsol.de/paper/simulation-of-deep-geothermal-heat-production-11119

Maier, F., Hebig, K., Jin, Y. & Holzbecher, E. (2011). Ability of Single-Well Injection-Withdrawal Experiments to Estimate Ground Water Velocity, *Europ. COMSOL Conf.*, Stuttgart, http://www.comsol.de/paper/ability-of-single-well-injection-withdrawal-experiments-to-estimate-ground-water-11086

Oberdorfer, P., Maier, F. & Holzbecher E. (2011). Comparison of Borehole Heat Exchangers (BHEs): State of the Art vs. Novel Design Approaches, *Europ. COMSOL Conf.*, Stuttgart, http://www.comsol.jp/paper/comparison-of-borehole-heat-exchangers-bhes-state-of-the-art-vs-novel-design-app-11095

Holzbecher, E. (2010). Computation and Visualization of Well Catchments, in: J. Wittmann, D.K. Maretis (eds), *Simulation in den Umwelt- und Geowissenschaften*, Osnabrück, 55-62.

Holzbecher, E. & Sauter, M. (2010). The Wells-simulator: Analytical Solutions for Groundwater Flow using Modified Streamfunction Contouring, *Geoenvironmental Engineering and Geotechnics*, ASCE Geotech. Spec. Publ. No. 204, 194-201, Shanghai, China.

Holzbecher, E. & Sauter, M. (2010). The Doublet System Simulator, *World Geothermal Conference,* Bali (Indonesia), Proceedings.

Holzbecher, E., Litz, M.-S. & Wong, L. (2010). Modelling Flow through Fractures in Porous Media, *Europ. COMSOL Conf.*, Paris,

http://www.comsol.com/paper/download/103587/holzbecher_paper.pdf

Holzbecher, E. & Sauter, M. (2009). The Wells-Designer – MATLAB GUI, in: J. Wittmann, M. Flechsig (eds), *Simulation in den Umwelt- und Geowissenschaften*, Potsdam, 33-41.

7.   References

Lauwerier, H.A. (1955). The Transport of Heat in an Oil Layer Caused by the Injection of Hot Fluid, *Appl. Sci. Res*. A5, 145-150.

Ferguson, G. (2006). Potential Use of Particle Tracking in the Analysis of Low-temperature Geothermal Developments, *Geothermics* 35, 44-58.

Hand, J., Sauter, M., Jin, Y. & Holzbecher, E. (2013). Pumping and Injecting from a Single Borehole, *COMSOL News*.

Holzbecher, E. (1998). *Modeling Density-Driven Flow in Porous Media*, Springer Publ., Heidelberg.

Holzbecher, E. (2014). Energy Pile Simulation – an Application of THM-modeling, *COMSOL Conf.*, Cambridge,http://www.comsol.com/conference2014/europe/file/id/18134/file/21035_holzbecher_paper.pdf

Jin, Y., Holzbecher, E. & Sauter M. (2014). A Novel Modeling Approach using Arbitrary Lagrangian-Eulerian (ALE) Method for the Flow Simulation in Unconfined Aquifers, *Computers & Geosciences* 62, 88-94.

Ostermeyer, G.P. & Srisupattarawanit T. (2012). On Multi-Scale of Heat and Flow Modeling for Simulation of Geothermal Reservoirs, *Celle Drilling*, Proceedings.

Pruess, K. & Doughty, C. (2010). Thermal Single-well Injection-Withdrawal Tracer Tests for Determinining Fracture-Matrix Heat Transfer Area, *35th Workshop on Geothermal Res. Eng.*, Stanford, https://pangea.stanford.edu/ERE/pdf/IGAstandard/SGW/2010/pruess.pdf

Shook, G.M. (2001) Predicting Thermal Breakthrough in Heterogeneous Media from Tracer Tests, *Geothermics* 30, 573-589.

Teodoriu C., Bohrtechnik, gebo-Jour Fixe presentation, 13.8.2010

Vinsome, P.K.W. & Westerveld, J. (1980). A Simple Method for Predicting Cap and Base Rock Heat Losses in Thermal Reservoir Simulators, *J. Canadian Pet. Tech*. 19(3), 87-90.

Wheatcraft S. W. & Scott W. T. (1988). An Explanation of Scale-Dependent Dispersivity in Heterogeneous Aquifers Using Concepts of Fractal Geometry, *Water Resources Research*, 24, 566-578.

Wang H.F. (2000). *Theory of Linear Poroelasticity*, Princeton Univ. Press, Princeton.

Wong, L. (2010). Fluid Transport in Fractured Porous Media – Application to Geothermal Reservoirs in North German Basin, Georg-August Univ. Göttingen, Master thesis.

G8: Electrical impedance tomography for the investigation of geothermal reservoirs

Andreas Hördt*, Katharina Bairlein, Matthias Bücker & Johannes Kenkel

Institute of Geophysics and Extraterrestrial Physics, TU Braunschweig, Mendelssohnstr. 3,

38106 Braunschweig, Germany

*Corresponding Author: a.hoerdt@tu-braunschweig.de

Abstract

Electrical impedance tomography (EIT) may potentially be useful for the exploration of geothermal reservoirs, because the complex conductivity of sediments may be related to hydraulic conductivity. Here, we study three aspects of EIT that are particular for geothermal exploration. In the first section, we investigate the possible impact of electrical anisotropy on EIT interpretation. Electrical anisotropy may be caused in the vicinity of large fault zones, which may constitute geothermal reservoirs due to their potentially enhanced hydraulic conductivity. In the second section, we develop a theoretical model to describe the processes at the pore scale causing the complex conductivity behavior. We include pore radii and parameters decribing the electrical double layer, in particular temperature, into the model. In the third section, we carry out laboratory measurements on sandstone and limestone samples to study the temperature dependence of the measured spectra. We describe several features that are common for all samples and discuss differences, in particular related to the pore structure. We also show that our theoretical model qualitatively predicts several feaures observed with measured data.

1. Introduction

Electrical impedance tomography (EIT) is a method that determines the complex conductivity of the subsurface. In recent years, a lot of research has been devoted to the relationship of complex conductivity to hydraulic parameters, such as hydraulic conductivity or cation exchange capacity. All aspects were investigated, ranging from theory (e.g. Revil and Florsch, 2010) over laboratory investigations (Börner and Weller, 1996) to field applications (Hördt et al., 2009). The focus was on application in near-surface groundwater studies, where temperature is fairly constant, or expected temperature variations are small. Therefore the results are mainly valid for a temperature range around 290 K.

Hydraulic parameters are also important for geothermal exploration, and therefore it is natural to use EIT for the exploration of geothermal reservoirs. However, several aspects that are relevant for geothermal exploration were not yet studied extensively in the literature.

Here, we focus on three aspects to advance the state of the art in exploration of geothermal reservoirs with electrical impedance tomography. First, we study the impact of electrical anisotropy on the interpretation of impedance tomography data taken in the field. This is important, because fault zones are a potential geothermal reservoir, as they may provide considerable hydraulic conducticvity necessary to permit sifficient fluid flow. At the same time, due to the particular stress conditions, a fault zone can be expected to cause considerable anisotropy in its vicinity. Second, we develop a theoretical model to simulate the causes of the complex elecftrical behavior at the pore scale. We extend an existing approach based on a one-dimensional pore system to a 2-D model with cylindrical pores, one aim being to include temperature as a parameter. Finally, we study the temperature dependence of impedance spectra in the laboratory, and compare the results with our theoretical model.

2. Electrical impedance tomography

Electrical impedance tomography, in geophysics also referred to as "spectral induced polarization (SIP)" is a method that determines the spatial distribution of complex conductivity, of the subsurface. The principle setup consists of a 4-point electrode configuration, identical to the more common and well known DC resistivity method: An alternating current is injected into the ground through two electrodes, and the potential difference is measured between two other electrodes. The ratio between current and voltage is measured and used to determine the complex resistivity ρ or its inverse, conductivity σ, which may be expressed through its magnitude $|\sigma|$ and phase shift φ, or by its real and imaginary part σ' and σ'':

$$\sigma = \frac{1}{\rho} = |\sigma| e^{-i\varphi} = \sigma' + i \cdot \sigma'' \tag{1}$$

The complex nature of conductivity in sediments arises from the interaction of the mineral surface with the fluid in the pore space, resulting in electrical properties similar to those of a capacitor. Therefore, the pase shift is typicall very small or zero at zero and infinite frequencies, but non-zero in an intermediate frequency range. Figure 1 schematically sketches the typical behaviour of complex conductivity magnitude and phase shift. Two principal types are distinguished which can both be observed with real data. The top row shows a spectrum with distinct phase peak and small transition zone in the conductivity

magnitude, the bottom row a type with constant phase shift over a broad frequency range and broad transition in the magnitude.
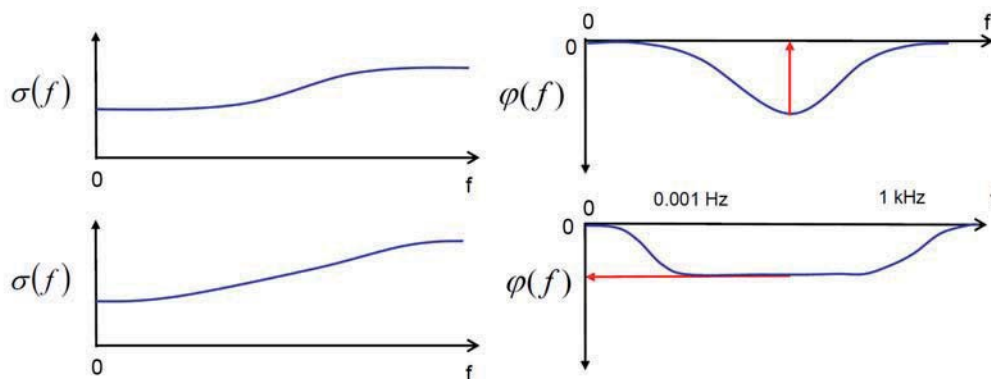
Figure 1: *Schematic types of complex conductivity spectra. Left: Conductivity magnitude.Right: Conductivity phase spectra. Top row: Spectrum with distinct phase peak. Bottom row: Spectrum with constant phase shift over wide frequency range, and corresponding linear increase of conductivity. The red arrows indicate the values that are typically used to estimate hydraulic conductivities.*

The capacitor-like behaviour of conductivity is closely related to the structure of the pore space. Therefore, attempts have been made to estimate hydraulic conductivity from the SIP spectra. The corresponding equations are usually empirical, using either the magnitude of the phase shift (e.g. Börner and Weller, 1996, Hördt et al., 2009) or the peak frequency or a relaxation time derived from it (e.g. Kemna et al., 2005), as indicated in figure 1. The fact that two relatively different concepts are being applied to determine the same parameter, indicates that the physics generating the phase shift at the pore scale is not yet fully understood.

3. Anisotrop y inversion

The spatial distribution of complex conductivity is normally determined with so-called 2-D inversion, i.e. the subsurface is discretised in the direction along a measured profile, and a vertical direction, and a conductivity structure is determined such that the model explains the measured data (e.g. Hördt et al., 2009). Normally, conductivity is assumed to be isotropic, i.e. independent of the direction in which the current flows. However, this assumption may not always be fulfilled, in particular in the vicinity of major fault zones, which are of interest for geothermal exploration, because they may provide large-scale fluid circulation paths. It has been shown earlier for DC resistivity measurements that ignoring anisotropy may lead to a misinterpretation (Nguyen et al., 2007). Therefore, before testing the idea of using SIP to

estimate hydraulic conductivity of fault zones, the possible impact of anisotropy should be well understood.

3.1 Mixing laws

Anisotropy may be caused basically by two mechanisms. The first is called micro-anisotropy and corresponds to an actual anisotropy at the scale of pores or minerals. The second is called macro-anisotropy and is caused by a layering of media with different properties. If the single layers are too thin to be resolved by the method that is applied, the sequence of layers will appear as one package with anisotropic properties. This is sketched in figure 2 for a package consisting of two media with two different complex resistivies.
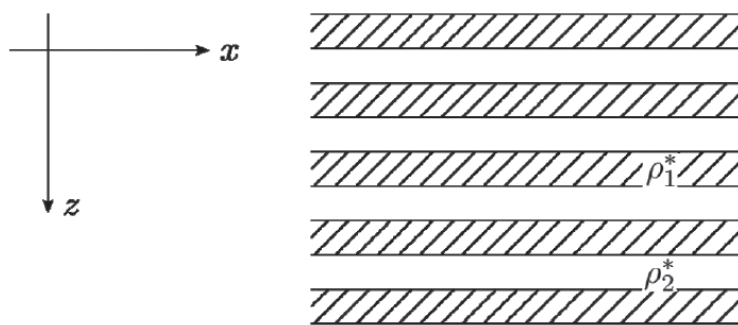
Figure 2: *Sketch of sequence of thin layers with two different complex resistivities ρ_1^* and ρ_2^*.*

The bulk anisotropic properties of such a layer package, in this case complex resistivities in the direction parallel to the layering (x-direction) and perpendicular (z- direction) can be calculated using the known rules for parallel and serial electrical circuits. This had been done before for DC resistivities, corresponding to the real part at zero frequency of SIP measurements. Here, we expanded the theory to complex resistivities, with the particular aim to understand the behaviour of phase shift in the anisotropic case.

For a layer package consisting of two media of the same volume, we find the following equations for the effective complex resistivities in perpendicular direction (Kenkel et al., 2012):

$$\rho_z = |\rho_z| e^{i\varphi_z} \tag{2}$$

with

$$|\rho_z| = \frac{1}{2}\left(|\rho_1| + |\rho_2|\right) \tag{2a}$$

and

$$|\varphi_z| = \frac{|\rho_1|\varphi_1 + |\rho_2|\varphi_2}{|\rho_1| + |\rho_2|} \ .$$ (2b)

And for the parallel direction we obtain:

$$\rho_x = |\rho_x| e^{i\varphi_x}$$ (3)

with

$$|\rho_x| = 2\left(\frac{1}{|\rho_1|} + \frac{1}{|\rho_2|} \right)^{-1}$$ (3a)

and

$$\varphi_x = \left(\frac{1}{|\rho_1|} + \frac{1}{|\rho_2|} \right)^{-1} \left(\frac{\varphi_1}{|\rho_1|} + \frac{\varphi_2}{|\rho_2|} \right)$$ (3b)

Two important simple implications may be taken from eqs. (2) and (3). The first is that the resistivity magnitudes behave like in the DC case, i.e. they are independent of phase shift. Equations (2a) and (3a) are identical to the corresonding DC resistivity equations, applying serial and parallel resistor rules. This independence of phase shift in the magnitude mixing rules is a new result that could not necessarily be intuitively expected. The second important implication is that the phase shift can only be anisotropic if the magnitudes are also anisotropic. This can be seen from eqs. (2b) and (3b): they yield identical phase shifts in x- and z-direction if the resistivity magnitudes of the two media are the same. In other words: There is no phase shift anisotropy without magnitude anisotropy, another important and not necessarily expected result.

3.2 Field application

In order to study the possible impact of anisotropy on the interpretation of field data, we implemented complex conductivity into an anisotropic finite-element forward modelling code (Kenkel et al., 2012). We then used the anisotropic models to fit field data measured over a known fault zone in Germany, and compared the results with those of conventional isotropic inversion. Figure 3 shows the location of the SIP profile. We used 38 electrodes at 6m distance, with a dipole-dipole configuration, resulting in a profile length of 222 m. The data were recorded with the SIP256 unit by Radic research, the key features of which are remote units at each electrode and an optical cable for data transfer to reduce noise through capacitive coupling effects.
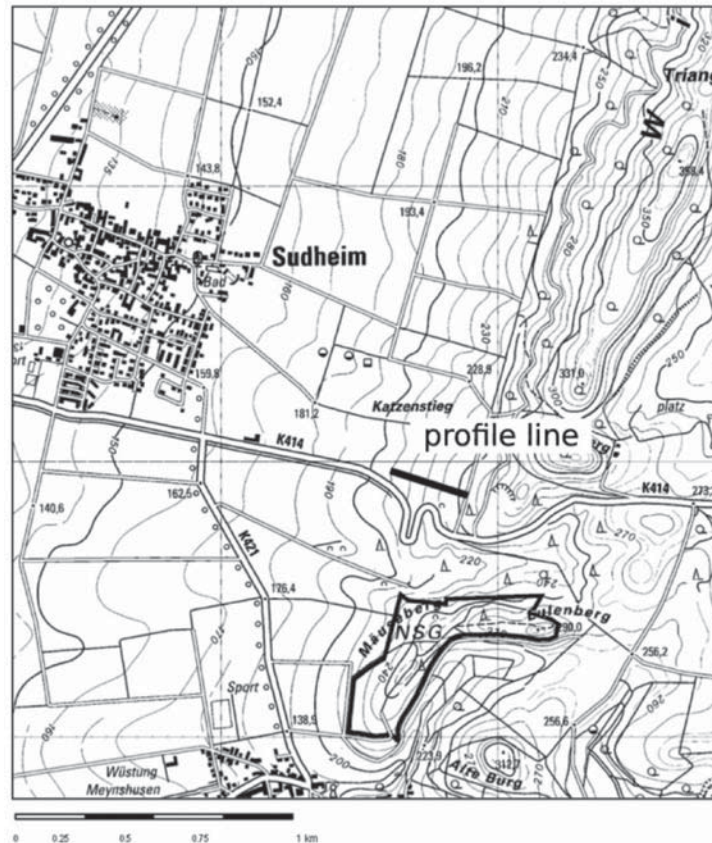
Figure 3: *Location of the SIP-profile close to Sudheim in lower Saxony (from Kenkel et al., 2012).*

Figure 4 shows the result of the conventional isotropic 2-D inversion. There are some correlated features, and some strucures dipping towards the east are visible, that might correspond to the known fault system of the Leinetalgraben, but overall the image is rather heterogeneous. The heterogeneity might be caused by artefacts resulting from ignoring anisotropy (Nguyen et al.2007).

Since anisotropic inversion is not yet available, we constructed an anisotropic model using a priori information from the known geology, and a trial-and-error forward modelling procedure. The subsurface was divided into several blocks with variable geometry taken from geology, and the boundaries and complex resistivities were varied manually, until a satisfactory fit between measured and calculated data was obtained. The resulting model is shown in figure 5 for the phase shift, because the anisotropic phase shifts are new compared to earlier work. The model consist of three sections, the phase shift for the two horizontal directions being illustrated in the top panels, the one in vertical direction in the bottom panel. A considerable anisotropy is required to fit the data. For example, the large block towards the East of the profile (x=0), has a phase shift of 2 mrad in the y- and z-direction, and 7 mrad in the x-direction. Overall, the model is more consistent, includes less artefacts and is geologically more plausible compared to the isotropic inversion result.

E   W
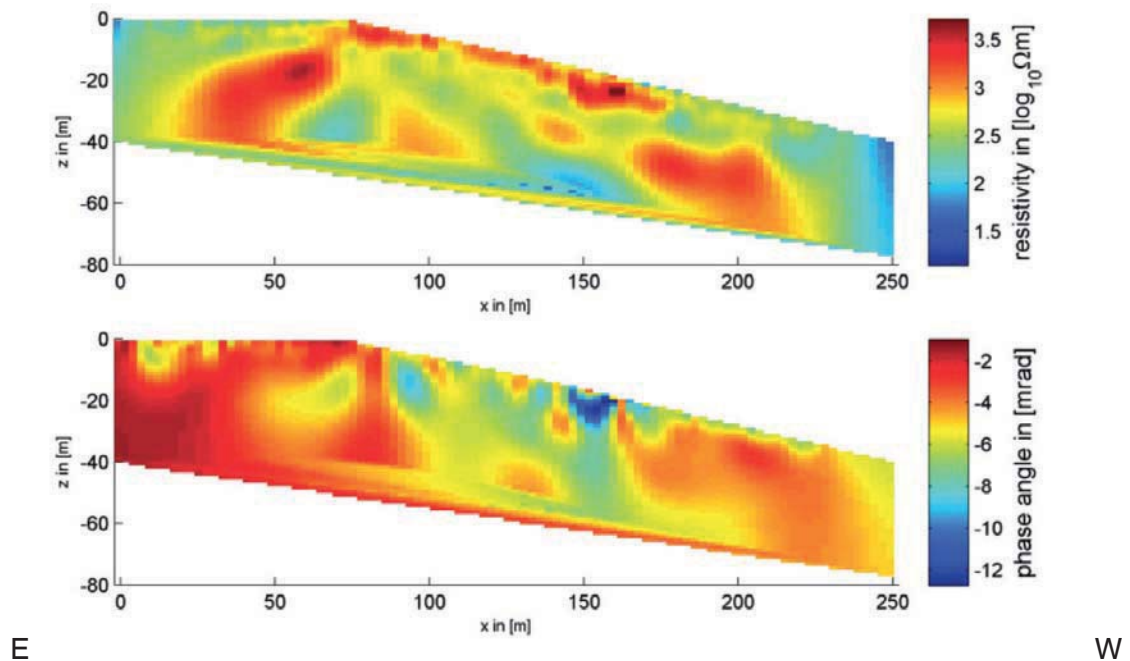
Figure 4: *Result of 2-D inversion of the SIP data recorded at the profile location shown in figure 2 (from Kenkel et al., 2012). The frequency is 1.25 Hz, Top: resistivity magnitude model. Bottom: phase angle model.*
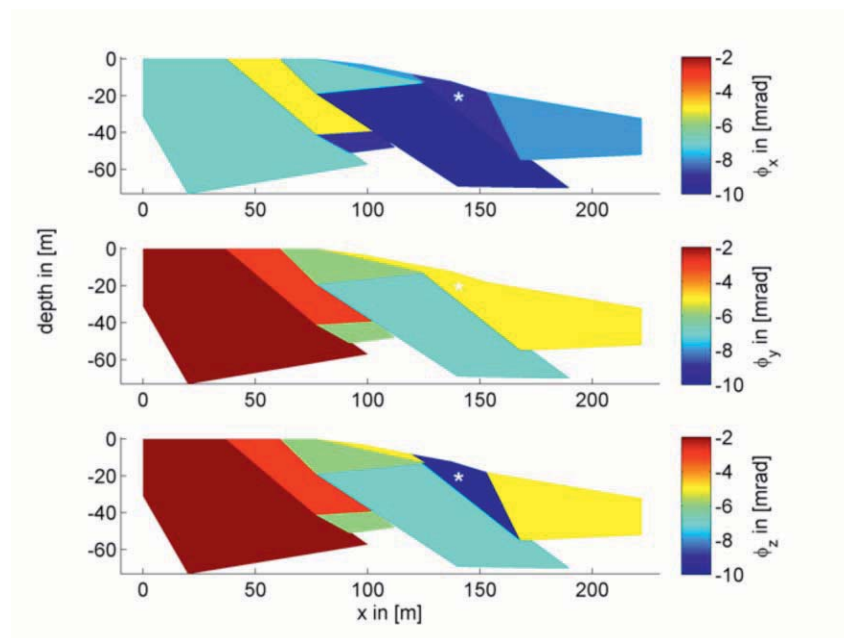
Figure 5: *Phase model cross section view in all three principal axes. The asterisk (*) denotes the block whose isotropic or anisotropic phase angle is compared to the field data (top panel of figure 6) (from Kenkel et al., 2012).*

259

In order to assess the validity of the models, the calculated data are compared with the measured data in figure 6. The top panel is a pseudo section representation of the measured data. The bottom section was calculated for the model shown in figure 5. The calculated data do not reproduce all details included in the measured data, but the overall structure is the same and considering that the model was obtained with a trial-and error procedure, the fit can be considered excellent. In order to illustrate the impact of anisotropy, an alternative model was calculated, where one block, indicated with a white asterisk in figure 5, is isotropic. The resulting pseudo section is shown in the middle panel of figure 6. The difference to the anisotropic model is apparent between 150m and 200m, where the isotropic model does not reproduce the strucure of the measured data very well. The conclusion is that anisotropy is indeed important and is worthwhile being considered during the interpretation of field data.
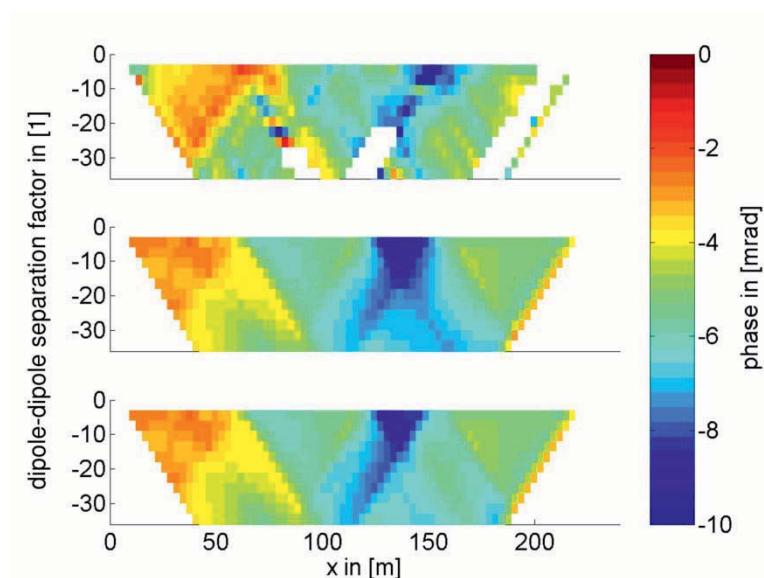
Figure 6: *Pseudo sections of the measured phase angles at 1.25 Hz at the Sudheim field site (top) and modeled pseudo sections (middle and bottom). The middle section is simulated with one block of the model explicitly isotropic, while the bottom image is simulated best-fit model with anisotropic phase angles in that specific block (from Kenkel et al., 2012).*

4. Theoretical   model

As mentioned in chapter 2, the processes causing the capacitor-like behaviour of the subsurface are not yet fully understood, and there is no fully accepted theoretical model. However, a theoretical understanding of the relationship between pore space geometry and electrical impedance is important if one wants to estimate hydraulic conductivity. Therefore,

we study in detail an existing one-dimensional model and expand it to two dimensions, which is necessary to include paramaters such as pore radius and temperature.

4.1 The one-dimensional model

The model we use was suggested by Marshall and Madden (1959). The key element is the electrical double layer (EDL) that builds up at the surface of a mineral grain. The surface is usually negatively charged, causing a surplus of cations, and an anion deficit in the fluid filling the pore space. The cation surplus decays away with distance from the mineral surface. If pores become very narrow, the zones with cation surplus may become significant and even dominate the entire pore. As a result, those narrow pores act as a membrane because the current through is carried only by the cations. In the larger pores, the double layer is insignificant and the current is carried equally be both types of ions. This situation is illustrated in figure 7 (top panel). If an alternating current is injected through such a pore system, the current flow will depend on frequency, because it is hindered by concentration gradients, the buildup of which is associated with a time scale.

Marshall and Madden (1959) set up a differential equation system for the current density and solved it to obtain a complex, frequency-dependent impedance. They described the different current transport by using different mobilities for anions and cations, as sketched in figure 7, bottom panel. Bücker and Hördt (2013a), study some properties of the 1-D model and show that different regimes of pore geometries exist, where either the wide or the narrow pore may dominate the relxation process.
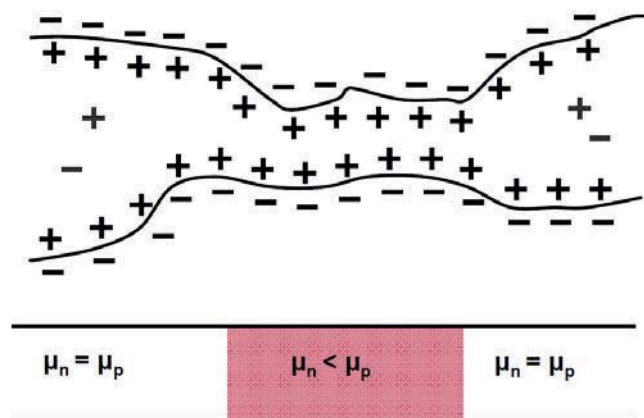
Figure 7: Top panel: Schematic sketch of ion distribution in a sequence of wide and narrow pores. In the wide pores, the current is mainly carried by the free electrolyte, in the narrow pores, it is mainly carried by the cations attached to the negatively charged mineral surface. Bottom panel: One-dimensional model of the situation in the top panel, where the membrane effect is described by a reduced anion mobility.

4.2 Extension to a 2-D model

In reality, the different current transport by cations and anions is caused by different ion densities rather than mobilities. More precisely, the ion density integrated over the radius of the pore, multiplied with mobility, is the characteristic value. This consideration led us to extend the original model to a pseudo 2-D model, where the pore system is described by a sequence of cylindrical pores with different length and radii rather than different mobilities (Figure 8).
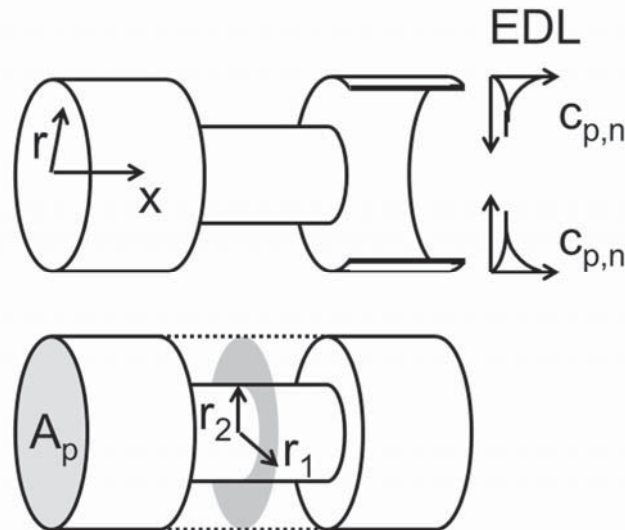
Figure 8: *Schematic sketch of our model consisting of a sequence of wide and narrow pores (from Bücker and Hördt, 2013b). Top: Definition of the coordinate system, and schematic behavior of anomalous cation and anion concentration within the electrical double layer (EDL). Bottom: Definition of the radii r_1 and r_2 of wide and narrow pore, respectively, and definition of the pore section Ap to normalise the current.*

Based on this geometry, we can use the solution developed by Marshall and Madden (1959). The difference is that we replace ion mobility μ in their original formulation by the following expression:

$$\mu \rightarrow \frac{\mu}{c_0 \pi R^2} \int_0^R c(r) 2\pi r dr \qquad (4)$$

Here, c_0 denotes the equilibrium ion concentration in the free electrolyte, R is the radius of the pore, $c(r)$ is ion concentration vs. distance from the center of the pore. The current densities of both pores are then normalised with the section of the wider pore, as indicated in figure 8.

Our extended theory includes an approximation, because we have to assume that the functions describing ion density in radial and horizontal direction are independent of each

other. Bücker and Hördt (2013b), have shown by comparison with numerical simulations that the approximation works reasonably well.

The advantage compared to the existing 1-D model is that the postulation of different mobilities is no longer necessary. Pore radii enter explicitly into the model, as well as parameters defining the electrical double layer, such as the Zeta-potential and temperature. Properties characterising the first ion layer attached to the mineral surface, the so-called Stern layer, are also included through a partition factor that defines the ratio of charge transport by the Stern layer and the diffusive layer. Further details on this as well as the entire model and the corresponding derivations can be found in Bücker and Hördt (2013b).

As an example, a theoretical impedance calculated with our model is shown in figure 9. The impedance magnitude is given in Ωm^2 because it relates to a 1-D system and has to be divided by a pore section to transfer it to finite pore size. The impedance shows the typical behaviour with a distinct phase maximum and a transition of the magnitude in the same range. The phase peak is sharper than what is normally observed with measured data, because the pore system consists only of two pore sizes. To obtain broader spectra, the model has to be extended to more complex systems, which will be subject of future work. Further below, we will show that the present model is able to explain several features in the temperature dependence of measured data.
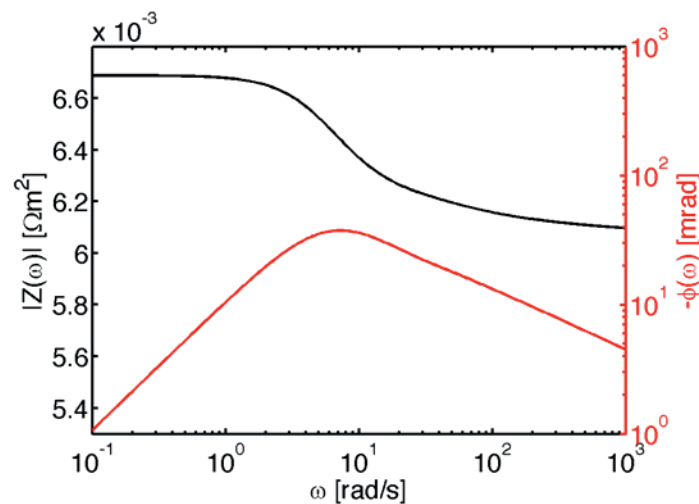
Figure 9: *Magnitude and phase shift of complex impedance vs. frequency, calculated with our extended model of membrane polarisation. The model consists of a sequence of two types of pores, with radii 3µm and 0.06 µm, and lengths 50 µm and 0.05 µm, respectively. The conductivity of the free electrolyte is 0.02 S/m, the temperature is 291 K, and ion mobility of all ions is $5 \cdot 10^{-8}$ $m^2/V/s$. The Zeta potential is -0.75 mV and the partition factor was set to 0.*

5. Temperature dependence of complex electrical impedance

5.1 Laboratory measurements

In order to study the temperature dependence of SIP spectra experimentally, we carried out measurements on a number of sandstone and limestone samples. We used a four-point measuring cell with non-polarizing electrodes (Figure 10, left panel). Cylindrical samples of 5 cm length and 2.5 cm diameter (Figure 10, right panel) were oven dried, filled with sodium chloride solution and brought into the space between the two potential electrodes, controlling the temperature in a climate chamber with an accuracy of 0.1 K. The impedance spectra were measured with a VMP3 impedance analyzer by Princeton Appied Research.
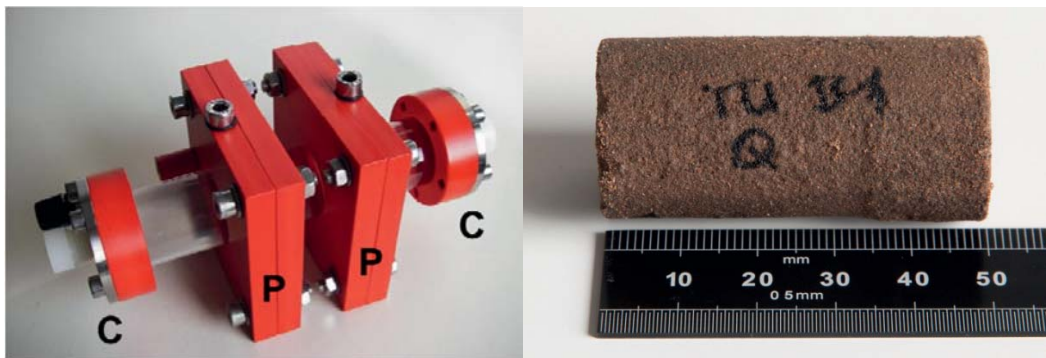
Figure 10: *Left: sample holder used to measure complex impedance spectra with a 4-point electrode configuration. The C and P indicate the current and potential electrodes. The actual sample is in the cylindrical space between the potential electrodes. Right: Example of a cylindrical sandstone sample (TUB1-Q).*

Figure 11 shows an example of measured impedance spectra vs. frequency. The left panel shows that the impedance magnitude decreases with increasing temperature. This behaviour is expected and can be attributed mainly to the increase in ion mobility with increasing temperature. The right panel shows that the spectral shape of the phase shift is only weakly dependent on temperature. The same applies to the maximum phase shift: it remains more or less constant. The strongest impact of temperature can be observed in the spectral position of the phase peak: the curves are shifted towards higher frequencies with increasing temperature, indicating that the peak frequency increases and corresponding time scales decrease.
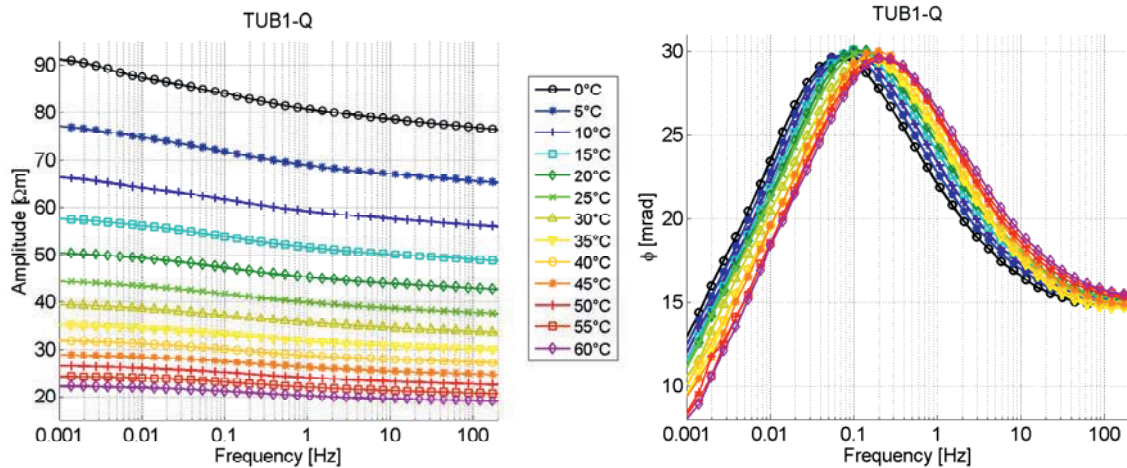
Figure 11: *Example of measured impedance spectra of sample TUB1-Q for different temperatures. Left: Magnitude of the impedance vs. frequency. Right: Phase shift v. frequency.*

The results of two sandstone samples and one limestone sample will be discussed in more detail. Images of the samples are shown in figure 12. The limestone sample (P3) is from an outcrop of the Late Jurassic Neuburger Bankkalk Formation (e.g. Hofmann et al., 2014). The porosity, calculated from the dry and saturated weight and the sample volume, is 0.24. The Bunter sandstone sample (P8) originates from an outcrop in the eastern Thuringian Basin and has a porosity of 0.11. Sample TU-B1 is a sandstone sample of the Stuttgart formation, taken from a drilling core from Ketzin, Germany (e.g. Fleury et al., 2013). The porosity is 0.28. The limestone sample P3 (right) has a considerably finer poree structure compared to the two sandstone samples, which will have a clear impact on the impedance spectra.
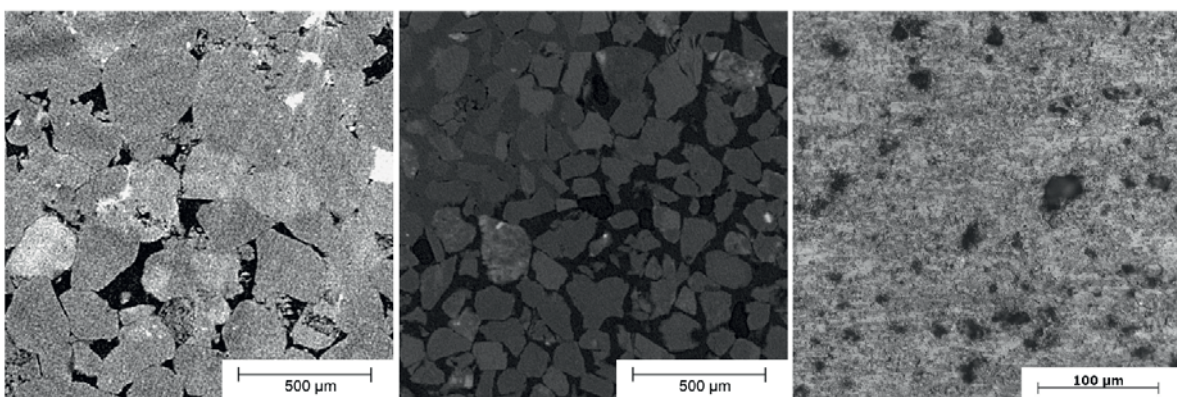
Figure 12: *Images of the three samples for which impedance spectra were shown in figure 12. The sequence is the same, P8, TU B1 and P3 (from left to right). The two left images are computed tomography scans, the right is a microscope image.*

5.2 Results

In the following , we focus on the phase spectra, because they include all the essential information on frequency dependence. The phase spectra of the three samples discussed here were colour coded and displayed vs. frequency and temperature in figure 13. In all three images, the red zones (large phase shift) have a positive slope, meaning that the peak frequency increases with temperature. This behaviour was already observed for sample TUB1 in figure 11, and seems to be a general feature. We also note that the phase shift maximum occurs at much higher frequencies (above 100 Hz) for the limestone sample compared to the two sandstone samples. In fact, the phase maximum is probably out of the measurement range, which cannot be extended due to distortions from inductive and capacitive coupling. However, it seems reasonable to assume that the maximum would occur in the range between 100 and 1000 Hz.

Another detail is in the temperature dependence of the phase shift maximum. For sample P8, the maximum decreases with increasing temperature. For sample TUB1 (middle panel), the maximum is fairly independent of temperature, as we already observed in figure 11. We conclude that this behaviour apparently cannot easily be generalized.
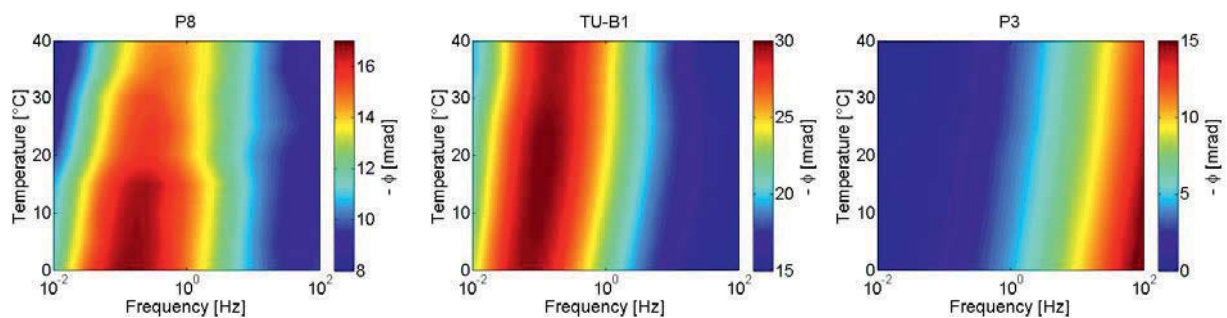
Figure 13: *Phase shift of the impedance, colour coded vs. temperature and frequency, for three different samples.The two lefdt images correspond to sandstone samples (P8 and TU B1), the right spectrum corresponds to a limestone sample (P3). Note that the colur scale is different for all three samples.*

We carried out a model study with our theoretical model described in chapter (4) to find out whether the basic features of the measured spectra can be reproduced. Although the theoretical model only consists of two types of pores and is considerably simpler than the actual pore space, we hypothesize that the underlying differential equations properly describe the physical processes and thus should be able to predict the behaviour of measured data at least qualitatively.

Figure 14 shows two images that were obtained from our theoretical model study. The chosen parameters are identical for the two panels, except the parameters describing

geometry, i.e. pore lengths and pore radii. First, we observe that the peak frequency increases with temperature in both cases, which is qualitatively consistent with the measured data. Also the quantitative behaviour is similar: the temperature dependence of frequency may be described by a power law, with similar exponents for measured and calculated data (Bairlein et al., 2014).
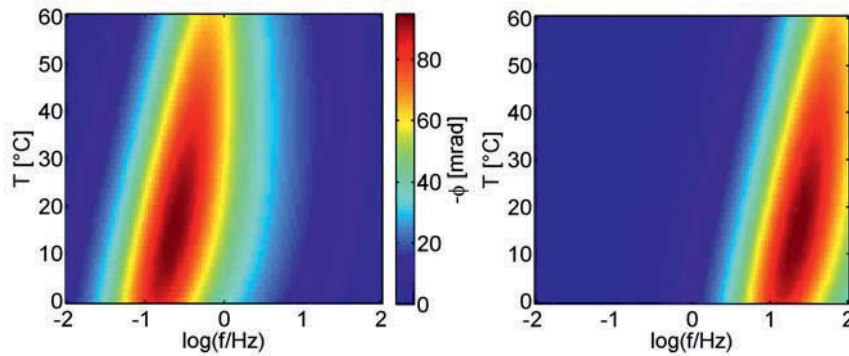
Figure 14: Phase shift of the complex impedance, colour coded vs. temperature and frequency. The spectra were calculated with the theoretical model described in chapter 4. The following parameters were used in the theoretical model: The ionic strength is 1 mol/m³, and ion mobility of all ions is $5 \cdot 10^{-8}$ m²/V/s. The Zeta potential is -0.75 mV and the partition factor was set to 0. The pore radii are 3µm and 0.06 µm, respectively. The difference between the two panels is in the pore lengths, which are 50 µm and 0.05 µm, for the left panel, and 5 µm and 0.005 µm for the right panel.

The second important observation is that the peak frequency strongly depends on geometrical parameters, mainly the pore lengths. In the right panel, the peak frequency is significantly larger compared to the left panel, corresponding to much smaller pore lengths. This is also consistent with the measured data, where the peak frequency and the entire zone of large phase shifts moves towards higher frequencies for the fine-structured limestone with small-scale pore structure (Figure 13, right panel). Finally, we observe a variation of the phase shift maximum with temperature, i.e. there exists a temperature that produces a maximum phase shift, also consistent with the measured data within the range that could be measured.

6. Conclusions

We have investigated several aspects related to the possible application of electrical impedance tomography to the exploration of geothermal reservoirs. First, we have theoretically derived new mixing laws that permit calculation of anisotropic conductivity magnitudes and phase shifts for layered sequences composed of two different media. One fundamental result is that the phase shift of the impedance can only display anisotropic

267

behaviour if the magnitude is also anisotropic. We also discuss inversion results of measured data recorded over a known fault zone. We show that an anisotropic model may be more consistent with geological information compared to the conventional isotropic 2-D inversion result.

We have developed a theoretical model to calculate complex electrical impedances for a system consisting of two cylindrical pores. Our model is based on an earlier development that solved the corresponding differential equations describing the motion of ions in the pore space under an external electric field for a 1-D pore system. One advantage of our extension over the previous model, where the complex behaviour was postulated to be caused by varying ion mobilities, is that we can now include pore radii explicitly as free parameters. This opens up new possibilities to derive relationships between electrical impedance and hydraulic parameters. Another benefit of our new model is that we can include parameters describing the properties of the electrical double layer, and in particular temperature.

The theoretical model reproduces several features of measured spectra, obtained from laboratory experiments with sandstone and limestone samples, indicating that at least part of the physics at the pore scale is correctly described. In particular, the increase of peak frequency with temperature, and the decrease of peak frequency with increasing spatial scale of the pore space is consistent between measured and modeled data. With respect to obtaining measurable phase shifts at large temperatures relevant for geothermal exploration, we can conclude that increasing temperature can, but does not necessarily always decrease phase shift. So far, the behaviour seems to depend on the particular rock type and can not easily be generalized.

7. Acknow ledgements

8. Publications resulting from the project

8.1 Publications in refereed journals

Bücker, M., & Hördt, A. (2013a). Long and short narrow pore models for membrane polarization. *Geophysics, 78*, E299-E314.

Bücker, M., and Hördt, A. (2013b). Analytical modelling of membrane polarization with explicit parameterization of pore radii and the electrical double layer. *Geoph. J. Int.,* doi: 10.1093/gji/ggt136.

Bairlein, K., Bücker, M., Hördt, A., Hinze, B. & Nordsiek, S. (2014). Temperature depencence of spectral induced polarization – a comparison of theory and experiments, *in preparation.*

Kenkel, J., Hördt, A. & Kemna, A. (2012). 2D modelling of induced polarisation data with anisotropic resistivities. Near-surface Geophysics, 6, 533-544.

8.2 Patents

Bücker, M., Hördt, A. & Fulda, C. (2012). Pore parameters and hydraulic parameters from electric impedance spectra. *Patent appl. No. 61532908.*

8.3 Others

Bairlein, K., Hördt, A., Bücker, M. & Nordsiek, S. (2014). Experimental and theoretical studies of the temperature dependence of spectral induced polarization (SIP) based on a membrane polarization model. *3rd international workshop on induced polarization*, 6-9 April 2015, Oleron, France.

Bairlein, K., Bücker, M., Hördt, A. & Nordsiek, S. (2014). Messungen der Temperaturabhängigkeit der spektralen Induzierten Polarisation (SIP) zur charakterisierung der Polarisationsmechanismen in Gesteinen. *Jahrestagung der Deutschen Geophysikalischen Gesellschaft,* Karlsruhe.

Bairlein, K., Bücker, M., Hördt, A. & Nordsiek, S. (2014). Experimental and theoretical studies of the temperature dependence of spectral induced polarization (SIP) based on a membrane polarization model. *SAGEEP,* Boston, USA.

Bairlein, K., Bücker, M., Hördt, A. & Nordsiek, S. (2014). Experimental and theoretical studies of the temperature dependence of spectral induced polarization (SIP) based on a membrane polarization model. *Near-Surface Geoscience,* Bochum*.*

Bairlein, K. & Hördt, A. (2013). Messungen der Spektralen Induzierten Polarisation (SIP) zur Erforschung der Polarisationsmechanismen in Gesteinen. *Jahrestagung der Deutschen Geophysikalischen Gesellschaft,* Leipzig.

Bücker, M. & Hördt, A. (2012). Simulation von induzierter Polarisation auf der porenskala mit expliziter Parametrisierung der Porenradien, *Jahrestagung der Deutschen Geophysikalischen Gesellschaft,* Hamburg.

Bücker, M. & Hördt, A. (2012). Die Abhängigkeit der Relaxationszeit von Porenlänger bei der spektralen induzierten Polarisation, *Jahrestagung der Deutschen Geophysikalischen Gesellschaft,* Hamburg.

Bücker, M. & Hördt, A. (2011). On the dependence of relaxation times on pore lenths in the membrane polarisation model, *2nd international workshop on induced polarisation,* Denver, Colorado.

Bücker, M. & Hördt, A. (2011). On the contribution of membrane polarization to induced polarization. AGU Fall meeting, San Francisco.

Hördt, A., Beilecke, T., Gehrgut, I., Holzbecher E., Löhken, I., Löhken, J., Philipp, S., Sauter, M., Reyer, D. & Thomas, R. (2011). Modelle geothermischer Reservoire als Grundlage für die interdisziplinäre Zusammenarbeit. DGG-Tagung, 2011.

Kenkel, J. (2010). 2-D SIP-Modellierung mit anisotropen Widerständen. Diplomarbeit, TU Braunschweig.

Kenkel, J., Hördt, A. & Kemna, A. (2010). 2-D SIP Modellierung mit anisotropen Widerständen, Kolloquimsband 23. Schmucker-Weidelt Kolloqium „Elektromagnetische Tiefenforschung", 77-87.

9. References

Börner, F.D., Schopper J.R. & Weller, A. (1996). Evaluation of transport and storage properties in the soil and groundwater zone from induced polarization measurements*. Geophys. Prosp. 44*, 583-601.

Fleury, M., Gautier, S., Gland, n., Boulin, P., Norden, B. & Schmidt-Hattenberger, C. (2013). Advanced and integrated petrophysical characterization for CO2 storage: Appication to the Ketzin site. *Oil and gas science technology*, Rev. *IFP Energies novelles* 68(3):557-576.

Hördt, A., Blaschek, R., Binot, F., Druiventak, A., Kemna, A., Kreye, P. & Zisser, N. (2009). Case Histories of Hydraulic Conductivity Estimation with Induced Polarisation at the Field scale. *Near-Surface Geophysics, 7*, 529-545.

Hofmann, H., Blöcher, G., Börsing, N., Maronde, N., Pastrik, N. & Zimmermann, G. (2014). Potential for enhanced geothermal systems in low permeability limestone-simulation strategies for the western malm karst (Bavaria). *Geothermics*, 51:351-367.

Kemna, A., Münch, H.M., Titov, K., Zimmermann, E. & Vereecken, H. (2005). Relation of SIP relaxation time of sands to salinity, grain size and hydraulic conductivity. *11th Eur. Mtg. Env. Eng. Geophys., Exp. Abst.*

Marshall, D. J. & Madden T. R. (1959). Induced polarization: A study of its causes. *Geophysics,* 24, 780-816.

Nguyen, F., Garambois, S., Chardon, d., Hermite, D., Bellier, O., & Jongmans, D. (2007). Subsurface electrical imaging of anisotropic formation affected by a slow active reverse fault, Provence, France. *J. Appl. Geoph.* 62, 338-353.

Revil, A. & Florsch, N. (2010). Determination of permeability from spectral induced polarization in granular media, *Geophys. J. Int.*, 181, 1480-1498.

G9: Hydrogeochemical processes in geothermal systems

Elke Bozau* & Wolfgang van Berk

TU Clausthal, Hydrogeologie, Leibnizstraße 10, 38678 Clausthal-Zellerfeld, Germany

*Corresponding Author: elke.bozau@tu-clausthal.de

Abstract

The natural and the technically influenced hydrogeochemical environments in deep aquifers and petrothermal systems of the North German Basin (useable for geothermal energy production) are characterized and the controlling hydrogeochemical processes within these environments are identified on the basis of hydrogeochemical thermodynamic modeling using the codes PHREEQC, PHAST and the newly developed thermodynamic database named "gebo"-database. The main scientific results were presented at ten scientific conferences and are published in several international scientific journals.

The following highlights of the investigations can be specified:

- Main characteristics of the formation water compositions in the North German Basin according to the stratigraphical units are identified.

- Chemical data of formation water of Europe, Russia and America lead to the conclusion that albitization is the main process responsible for the enrichment of calcium in formation waters.

- The "gebo"-database for modeling hydrogeochemical processes in deep reservoirs of the North German Basin was developed and successfully tested for five geothermal wells of the North German Basin. Chemical water compositions and scalings could be retraced by modeling.

- A first three dimensional model approach using the code PHAST is performed to model barite scaling after surface water injection to a geothermal reservoir.

1. Introduction

Depending on its chemical composition, formation water can cause both chemical and structural alteration of well casing materials.

Formation water in deep sedimentary basins can be classified according to depth, temperature, and salinity (e.g., Graf et al., 1966; Kharaka & Hanor, 2007). Most of the deep formation waters contain dissolved solids in excess of sea water. The hydrogeochemical development of formation water has been discussed for a long time. It is widely accepted that deep aquifers are

influenced by the meteoric cycle and geochemical processes within the crust (Hebig et al., 2012). Similar hydrogeochemical signatures are found in deep formation waters of all continents and can be explained by general geochemical processes within the deep reservoirs (Land, 1995). Hydrogeochemical modeling is a helpful tool for reproducing and predicting natural hydrogeochemical and technically induced processes (e.g., corrosion, scale formation, outgassing) that occur in deep aquifers, oil fields, CO_2 sequestration systems, and geothermal energy production systems (e.g., Yuan and Todd, 1991; Yuan et al., 1994; Thomas, 1994; van Berk et al., 2009; Hellevang et al., 2011).

Hydrogeochemical modeling with the codes PHREEQC (Parkhurst and Appelo, 1999) and PHAST (Parkhurst et al., 2010) is used to evaluate chemical processes affecting the operation of deep wells. Both codes consider a complex web of chemical reactions based on thermodynamic equilibrium conditions and both allow the implementation of Pitzer parameters to model the ion interactions of highly mineralized waters. The aim of the modeling is the identification of parameters that indicate special changes within the geothermal reservoir and any alteration of well casing materials, as well as to test chemical substances that could prevent scaling.

2. Research work and results

Main results of project G9 "Hydrogeochemical processes in geothermal systems" are summarised according to the six work packages.

WP 1:   *Characterization of hydrogeochemical environments in geothermal reservoirs of the North German Basin*

Published hydrogeochemical data of formation waters were collected from the literature. Additionally, the LIAG (Leibniz Institut für Angewandte Geophysik) provided unpublished hydrogeochemical data of about 220 formation waters from different geological formations of the North German Basin taken from the database "GeotIS" (Schulz and GeotIS-Team, 2009). The results are summarised within an internal report, a publication with the title "Hydrogeochemical classification of deep formation waters" (Applied Geochemistry: in review), and were used to create the generic models within WP3. A short evaluation of the collected data and a prognosis of the water quality for the "gebo"-well is given in Figure 1. Compared to other regions (e.g., South Germany), the deep aquifers of the North German Basin are characterized by high salinities. Their pH values are mostly lower than 6. Therefore, these deep formations waters are highly corrosive.

Generally, the salinity of deep formation water in the North German Basin is rising with depth and temperature (Figure 1). Injected water of petrothermal systems can reach much higher

salinities resulting from the solubility of halite at reservoir temperatures. The water composition of the "gebo"-well could follow this trends and display a TDS (Total Dissolved Solids) value of about 280 g/L. But it could also reach a content of TDS up to 400 g/L in the case of halite saturation (worst case). If carboniferous formations are reached within the "gebo"-well, the TDS content could be lower according to the results from the oil field "Schneeren".
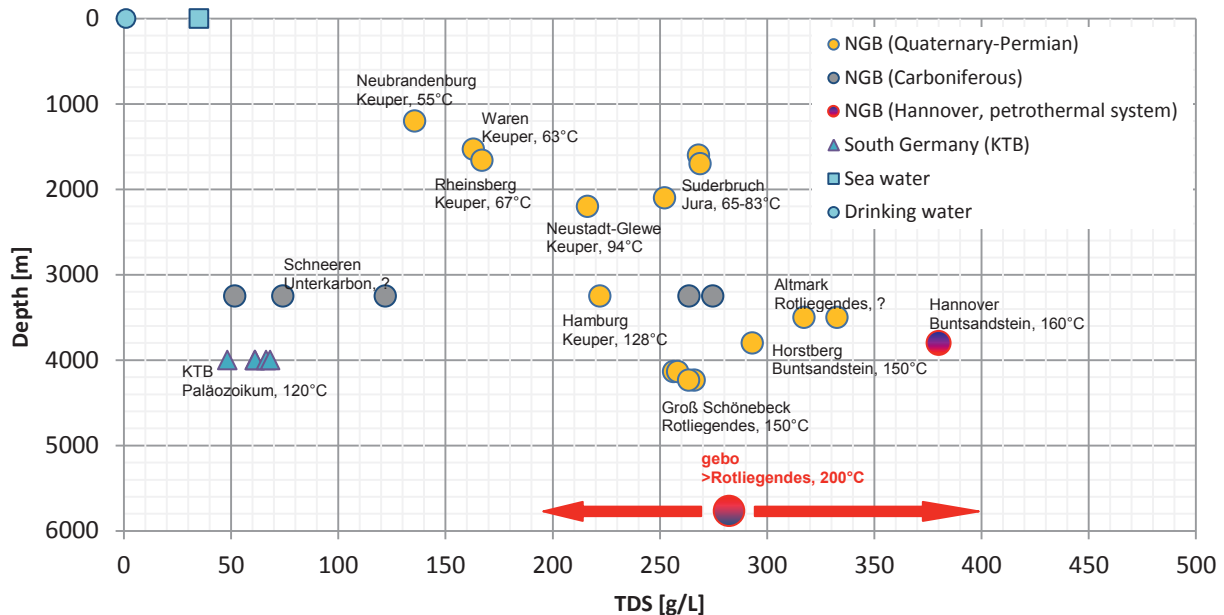
Figure 1: Chemical composition of formation waters (TDS vs. formation depth) in the North German Basin (Quaternary - Carboniferous layers) compared to drinking water, sea water and water from the well "KTB" as well as a prediction of the water quality of the "gebo"-well (red arrows, explanation see text).

Furthermore, the data of the North German Basin are compared to deep formation waters from other regions (Europe, Russia, North America). The aqueous Na^+ and Cl^- concentrations of deep formation water displayed in Figure 2 indicate similar trends in the datasets of all investigated regions. Deep formation waters of different geological units from all over the world can be divided in two main categories: Na-Cl and Na-Ca-Cl waters. More than 95 % of the investigated formation waters have TDS contents up to 250 g/L. Na-Cl waters mainly display TDS contents lower than 250 g/L. At TDS contents of about 250 g/L Na-Ca-Cl waters are dominant in most of the investigated areas. The major anion of deep formation water is chloride. The main processes leading to the composition of formation waters are salt dissolution and an enrichment of calcium by albitization or dolomitization. Considering the investigated data, magnesium and chloride dominated formation waters as prerequisite for dolomitization are rare. According to the preferential occurrence of sodium and chloride dominated formation water, the calcium enrichment by albitization is supposed to exceed an enrichment of calcium caused by

273

dolomitization. Compared to sedimentary basins, higher degrees of albitization are found in the old continents (e.g., Siberian and Canadian Shield).
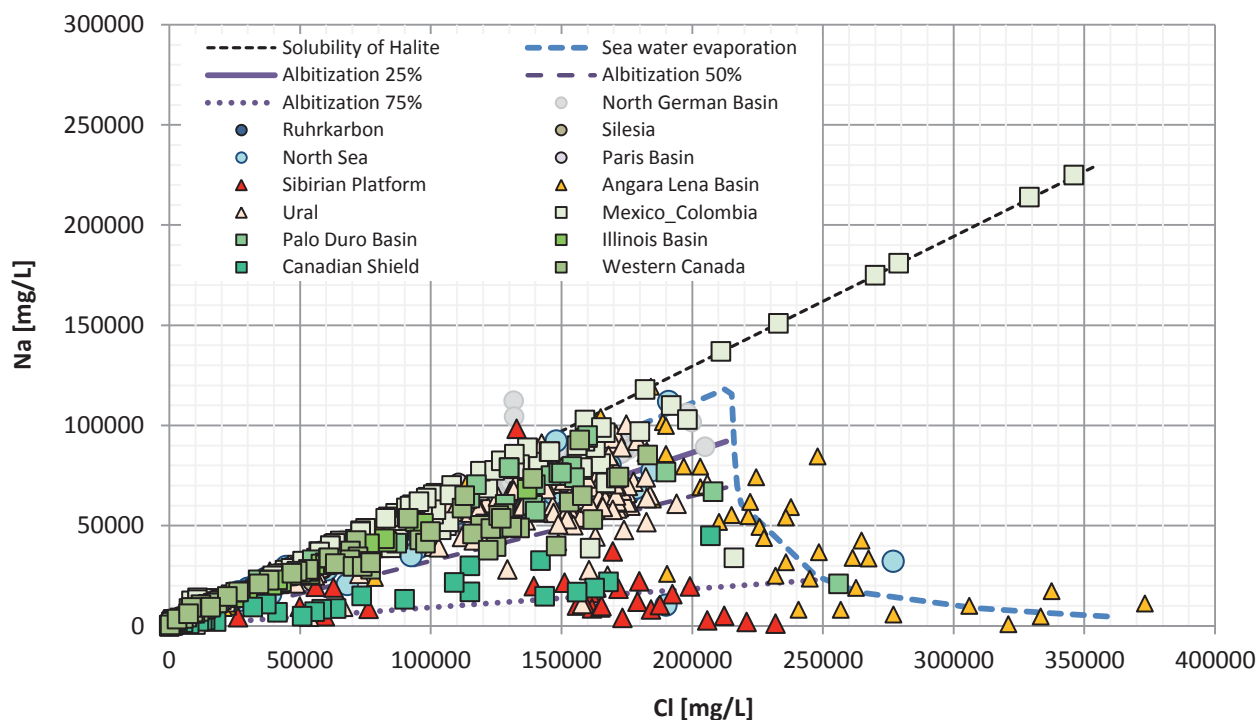
Figure 2: Hydrogeochemical characteristics of deep formation waters from Europe, North America, and Russia. Main possible geochemical processes are indicated: halite solubility, albitisation (exchange of 2 m Na by 1 m Ca at different amounts in %) and sea water evaporation (modeled with PHREEQC and "pitzer.dat").

Typical scalings resulting from the geothermal use of the formation waters in the North German Basin are barite in combination with strontium sulfate, calcite, sulfides and hydroxides of iron and lead, and zinc sulfides. Furthermore, scaling minerals can contain natural radioactive isotopes (e.g., ^{226}Ra, ^{210}Pb) and must be treated as toxic waste causing health hazard and disposal costs. In summary, all these precipitates are one of the most important problems hindering continuous and cost effective geothermal energy production in the North German Basin.

To investigate the potential of carboniferous rock units for geothermal energy production, mine water and atmospheric precipitation samples of the Harz Mountains were investigated, and mine water data of the area "Ruhrgebiet" were collected and evaluated. These data were mainly used for a research proposal (see Section 3). The precipitation samples were analysed for major ions, trace elements and strontium isotopes at the department "Angewandte Geologie" of the University Göttingen. The analytical results, e.g. the isotope ratio ^{87}Sr/^{86}Sr (Abdou et al., 2011), allow for the identification of recent groundwater recharge within geothermal reservoirs.

WP 2: Hydrogeochemical modeling with the "gebo"-database

The modeling of hydrogeochemical processes in saline waters and brines is quite a challenge. The main prerequisite for the modeling is a suitable thermodynamic database. Such a database was developed for the PHREEQC computer code by the extension of the PHREEQC database "pitzer.dat". The extended database (called after the project "gebo"-database) includes additional solution master species of Fe, Fe(+2), Fe(+3), S(-2), N, N(+5), N(+3), N(0), N(-3), C(-4), Si, Zn, Pb, and Al. According to these solution master species, associated solution species, solid phases, and gases, as well as temperature adaptations of the appropriate mass action law constants and Pitzer parameters for the calculation of activity coefficients in aqueous solutions of high ionic strength are implemented. In contrast to the conventional "pitzer.dat" database, its extended version allows for calculating several additional hydrogeochemical equilibrium reactions that are crucial for the compositional development within brines and saline waters. The "gebo"-database is published in the journal "Grundwasser" (Bozau, 2013) and was used for the PHREEQC models within WP3, WP4, and WP5.

After publication the "gebo"-database was further extended by the element uranium by insertions of U species and phases of the database "wateq4f.dat". Figure 3 shows modeled solublities of the phase schoepite at different pH values compared with the experimental data (personal communication V. Neck, INE).
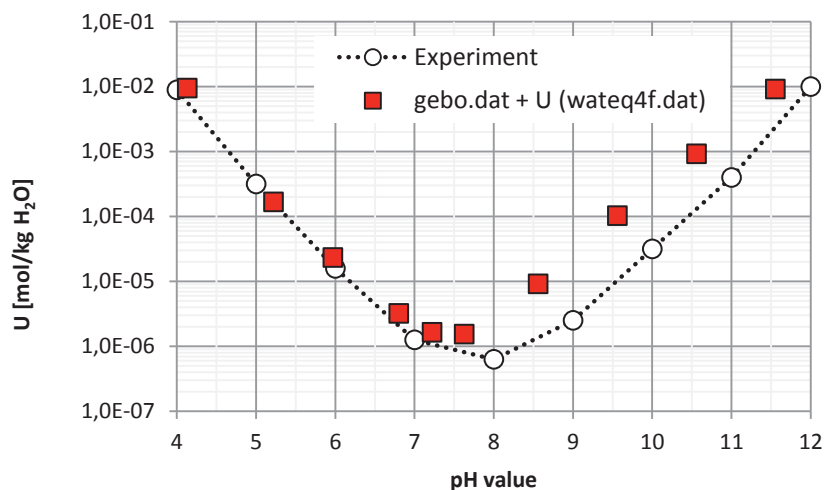
Figure 3: pH dependent solubility of schoepite in 0.03 molal NaCl at 25°C (experimental and modeled data)

The "gebo"-database was transformed to be used within the code PHAST that combines three dimensional groundwater flow, transport and PHREEQC's hydrogeochemical modeling capacities.

WP 3:   Generic modeling of typical hydrogeochemical environments in geothermal reservoirs of the North German Basin

Generic models for groundwaters with TDS values higher than 100 g/L for five geothermally used wells (Bozau & van Berk, 2013) and a petrothermal system (Bozau & van Berk, 2012) in the North German Basin were developed based on conceptual models (Table 1). These models are also used for the further modeling calculation within WP5. Hereby it was shown that it is possible to reproduce and retrace main processes in the geothermal reservoir (salt leaching, albitization, reaction with decomposition products of organic substances).

```
#----------------pure water at formation temperature (Initial Solution)
SOLUTION 1
-pH          7.0 charge
-temp        160.0
#----------------pure water equilibrates with available mineral assemblage
EQUILIBRIUM_PHASES 1
Halite       0.0 10.0
Sylvite      0.0  0.5
Bischofite   0.0 0.05
Anhydrite    0.0 10.0
Barite       0.0 10.0
Celestite    0.0 10.0
Calcite      0.0 10.0
Quartz       0.0 10.0
Albite       0.0 10.0
Anorthite    0.0  2.0
Galena       0.0 10.0
Sphalerite   0.0 10.0
Pyrite       0.0 10.0
Hematite     0.0 10.0
SAVE solution 2
SAVE equilibrium_phases 2
END
#-------brine resulting from equilibration among pure water and available mineral assemblage
reacts with gaseous components derived from organic-inorganic interactions and thermal gas
release
USE solution 2
Use equilibrium_phases 2
REACTION 2
CH4          0.25
CO2          0.50
N2           0.25
0.05 moles
#----------------------multi component gas may form at saturation
GAS_PHASE 2
-fixed_pressure
-pressure    500.0
-temperature 160.0
CH4(g)       0.0
CO2(g)       0.0
N2(g)        0.0
SAVE solution 3
END
```

Figure 4: PHREEQC input file for modeling the chemical composition of an injected surface water when thermodynamic equilibrium with the mineral phases of the geothermal reservoir and the decomposition products of organic material is reached. According to temperature and pressure conditions of the reservoir, gas formation is allowed.

These models and their input files (e.g., Figure 4 for a petrothermal system) can be adapted to the actual conditions of the respective geothermal plant in different geothermal reservoirs (e.g., by considering the ion concentration of the initial water for salt dissolution and feldspar transformation, temperature and pressure concentrations of the geothermal reservoir, and sampling conditions at the well head).

Table 1: Conceptual model steps according to hydrogeochemical processes and technically induced processes within a geothermal system

Model step	
Geothermal reservoir	Pure water at reservoir temperature
	Salt dissolution ($NaCl \leftrightarrow Na^+ + Cl^-$)
	Albitisation ($CaAl_2Si_2O_8$/Anorthite + 2 Na^+/Brine + 4 SiO_2 (Quartz) $\leftrightarrow$ 2$NaAlSi_3O_8$ /Albite + Ca^{2+}/Brine)
	Degradation of organic material
Technically induced processes	Fe corrosion of the well casing ($Fe(0) \leftrightarrow Fe^{2+} + 2 e^-$)
	Reaction of the formation water and cement
	Temperature and pressure changes
	Contact to atmosphere

WP 4: Modeling of triggered hydrogeochemical signals

Based at the developed generic models (WP3) and the collected data, triggered hydrogeochemical signals and interactions of the formation water with the drilling fluids (mainly mixing processes) and well case materials (e.g., dissolution of cement minerals, corrosion of the iron tube) of the well are modeled. The considered processes are listed in Table 1. Table 2 shows the change of hydrogeochemical parameters within the formation water (e.g., Ba, Fe, Mg) induced by the reaction with well case materials and sampling effects at surface conditions at the well head for the geothermal well "Groß Schönebeck".

First modeling tests showed that the three dimensional distribution of scalings can be visualized using the code PHAST. To demonstrate the capabilities of three-dimensional transport modeling with the code PHAST, the "gebo" database and a simple spatial approach of a confined deep aquifer (area: 2000 m * 2000 m, depth: 500 m) are used. The permeability of the model area is defined by a hydraulic conductivity of 10^{-7} m s^{-1}. The water flow is enforced by injection and pumping water via wells with constant pumping rates. The model scenario presented in Figure 5 consists of one injection and two extraction wells with an elevation of the well screens from the bottom to the top of the aquifer. Corresponding to the well "Groß Schönebeck", the formation water consists of Na^+ (1.7 mol kgH_2O^{-1}), Ca^{2+} (1.4 mol kgH_2O^{-1}), Cl^- (5.0 mol kgH_2O^{-1}) and Ba^{2+} (0.5 mmol kgH_2O^{-1}). A water consisting of 0.005 mol Ca^{2+} and SO_4^{2-} is injected with a constant rate of 0.5 m^3 per second to the aquifer (injection well). The two extraction wells work with the same pumping rate of 0.25 m^3 s^{-1}. Temperature differences are not considered in the model. The spatial distribution of precipitated barium sulfate which will reduce the permeability of the aquifer after 1, 5 and 10 years of water injection is shown in Figure 5. The circle of precipitating barium sulfate around the injection well is increasing with time. The three-dimensional models can be used to choose injection and extraction rates which reduce permeability losses due to precipitating minerals. For more realistic modeling results of deep geothermal wells, the

temperature dependence and the geometry of fractures should be included in the three-dimensional model.

Until now, these are the two main problems for using PHAST to model the hydrogeochemical processes in deep formation water, because within the code PHAST groundwater flow is calculated by Darcy's law and fractures must be inserted by the input of a special medium. Furthermore, it is not possible to consider temperature changes for the groundwater flow.
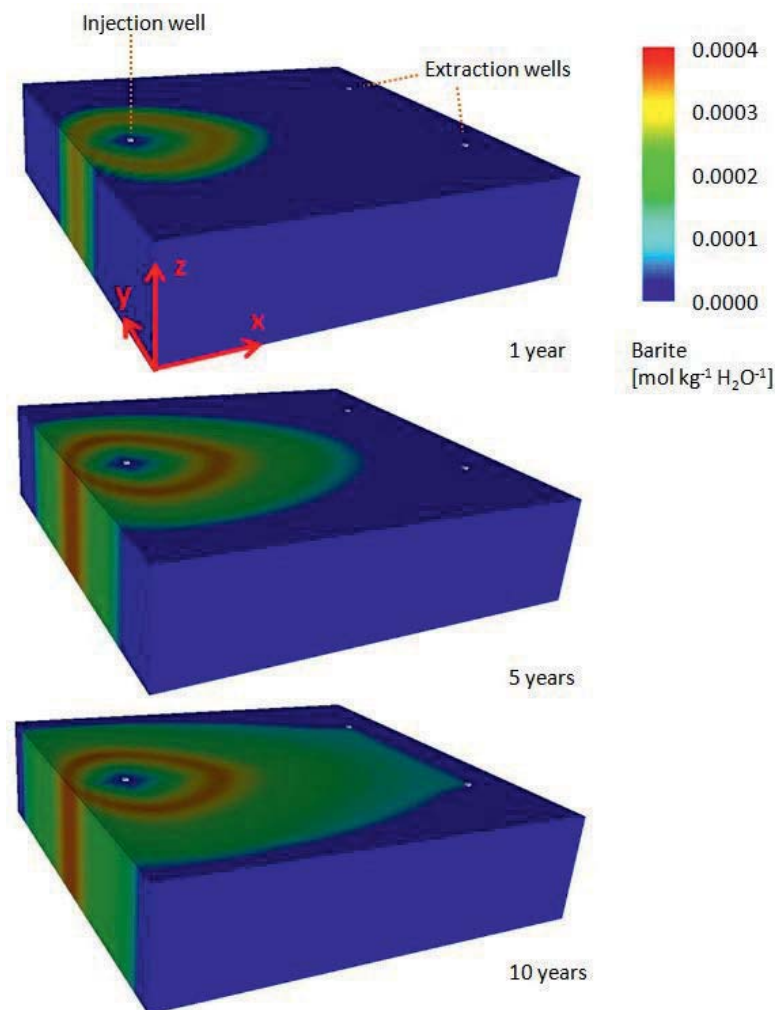
Figure 5: Distribution of barium sulfate scalings in mol kgH_2O^{-1} around one injection well (pumping rate: 0.5 m^3 s^{-1}) and two extraction wells (pumping rate: 0.25 m^3 s^{-1}) after 1, 5 and after 10 years

A precipitated mass of barium sulfate of 0.004 mol kgH_2O^{-1} ($BaSO_4$: molar mass 233 g mol^{-1}; density 4.5 g cm^{-3}) corresponds to a precipitated volume of 0.2 cm^3 $BaSO_4$ kgH_2O^{-1}.

Maybe the further development of the code PHAST and better hydrogeological data of deep reservoirs will allow for a more realistic modeling of hydrogeochemical problems in geothermal plants soon.

Table 2: Modeling of technical induced changes within the water chemistry of the geothermal well "Groß Schönebeck"

[1]concentration, [2]observed

Groß Schönebeck	Measured data and observations	Modeling results — Formation water	Technically induced processes				
Solution mmol L⁻¹	Seibt (2004)[1]	Equilibrium among reservoir mineral phase assemblage, irreversible reaction with gases (reservoir conditions)	Fe(0) corrosion at well casing (reservoir conditions)	Mixture of well casing water with formation water (reservoir conditions)	Mixture of well casing water and formation water in contact with cement (reservoir conditions)	Formation water influenced by corrosion and scaling (25°C and 1 bar)	Formation water sampled in equilibrium with the atmosphere (25°C and 1 bar)
	mmol L⁻¹	mmol kgH₂O⁻¹	mmol kgH₂O⁻¹	mmol kgH₂O⁻¹	mmol kgH₂O⁻¹	mmol kgH₂O⁻¹	mmol kgH₂O⁻¹
pH	5.7	5.6	8.3	5.7	8.8	5.4	2.4
Na^+	1670	1737	1738	1737	1736	1737	1737
K^+	74	74	74	74	74	74	74
Ca^{2+}	1350	1403	1404	1402	1444	1402	1402
Mg^{2+}	18	20	15	20	2.4	20	20
Ba^{2+}	0.25	0.63	0.63	0.59	0.63	0.33	0.33
Sr^{2+}	22	15	15	15	15	15	15
$SiO_2(aq)$	1.3	1.2	1.2	1.1	1.2	1.2	1.2
Cl^-	4713	4707	4710	4707	4706	4707	4707
SO_4^{2-}	1.5	0.9	traces	0.5	0.5	0.2	0.2
HS^-	n.a.	0.008	traces	traces	traces	5 E-08	0
HCO_3^-	0.31	1.7	0.02	0.9	0.02	0.72	0.008
NH_4^+	4.2	0.27	8.1	0.07	0.01	0.05	0
Fe	2.0	0.0007	4.2	0.8	1.0	0.78	0.78
Pb	0.87	0.6	0.5	0.6	0.006	0.6	0.6
Zn	1.1	10	10	10	9.7	10	10
Gases							
Total gas volume	ca. 15 %	-	-	-	-	0.17 L kgH₂O⁻¹	-
$N_2(g)$	83 Vol.%	-	-	-	-	6.8 mmol (ca. 97 %)	-
$CO_2(g)$	1.7 Vol.%	-	-	-	-	0.18 mmol (ca. 3 %)	-
$CH_4(g)$	14 Vol.%	-	-	-	-	traces	-
Scalings	Holl et al. (2003)[2]		mmol kgH₂O⁻¹	mmol kgH₂O⁻¹	mmol kgH₂O⁻¹	mmol kgH₂O⁻¹	
BaSrSO₄ (solid solution)	x	-	-	0.08 BaSO₄ 0.04 + SrSO₄ 0.04	traces	0.28 BaSO₄ 0.26 + SrSO₄ 0.02	-
Calcite	x	-	0.03	0.8	1.69	-	-
Brucite		-	4.9	-	17.4	-	-
Fe sulfides		-	0.9	0.2	-	0.003	-
Fe carbonates		-	9	-	-	-	-
Fe hydroxides	x	-	-	-	-	-	-
Pb elemental		-	-	-	-	-	-
Pb hydroxides	x	-	0.6	-	0.6	-	-
Pb sulfide		-	-	-	-	-	-
Zn sulfide		-	-	-	0.4	-	-

279

WP 5: Modeling of hydrogeochemical processes induced by technical processes

Two main geothermal reservoir types (deep aquifer and hot dry rock) for the production of geothermal energy were considered and modeled:

- Scenario 1 "Deep aquifer"

Generic, hydrogeochemical models were developed for five geothermally used deep wells and research drillings of the Northern German Basin (Neubrandenburg, Neustadt-Glewe, Hamburg, Horstberg, Groß Schönebeck), respectively. Hereby it was shown that it is possible to reproduce and retrace the hydrogeochemical processes in the geothermal reservoir (e.g., salt leaching, albitization, reactions with degradation products of organic substances), in technical systems (e.g., corrosion, mineral scaling) and during sampling at surface conditions (e.g., gas release).

- Scenario 2 "Hot dry rock" (petrothermal system)

A worst case scenario presuming maximum salt dissolution (reaching thermodynamic equilibrium) and a mixture of injected water with residual fluids in the geothermal reservoir was used for the modeling of petrothermal systems. The amount of precipitating minerals at the well head was estimated. The introduced model can be adapted to the actual conditions of the respective geothermal plant (e.g., by considering the ion concentration in the injected water, temperature and pressure concentrations of the geothermal reservoir, and sampling conditions). Furthermore it is discussed, that the solubility of halite which is strongly rising with temperature can increase the TDS of an injected water up to more than 400 g/L within the geothermal reservoir.
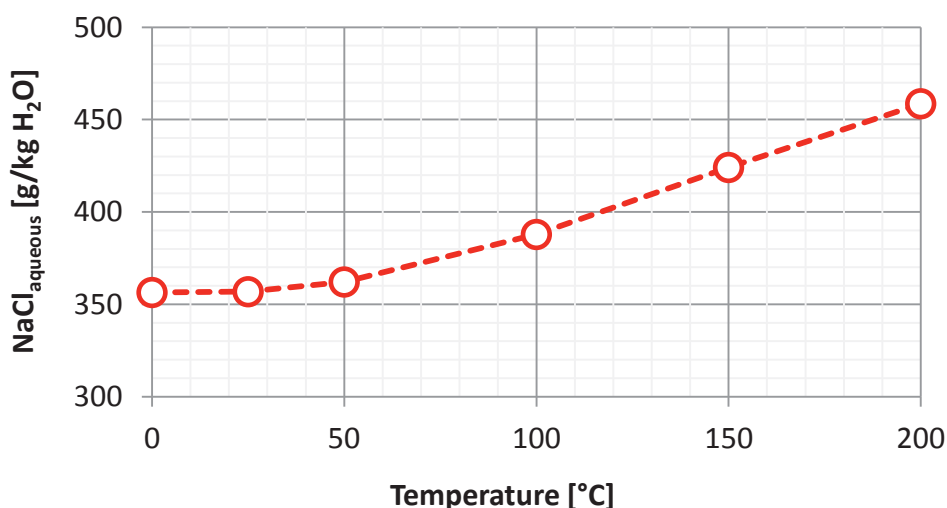
Figure 6: Temperature dependent solubility of halite ($NaCl_{solid}$) modeled with PHREEQC (database: pitzer.dat). A water cooling from 200 to 50°C leads to the precipitation of about 100 g NaCl/kg water.

The modeling results are presented in two journals (Bozau & van Berk, AMS online 2012; Bozau & van Berk, Procedia Earth and Planetary Science 2013) and at four conferences in 2012.

WP 6: Hydrogeochemical modeling of in-reservoir conditions affecting tracer behaviour

There are no experiences with hydrogeochemical tracers used at environmental conditions (200°C and > 500 bar) as foreseen for the "gebo" drilling site. Evaluating the chemical data of formation waters no classical and natural tracers (e.g., Cl^-, REE) to indicate relevant processes in deep geothermal reservoirs of the North German Basin have been found. Furthermore, the high salt concentration of the formation waters and the chemical changes due to temperature and pressure decrease of formation water samples cause severe analytical problems. False or unsure analytical data could lead to wrong interpretations of the tracer behaviour.

Modeling the geochemical behaviour of tracers (e.g., the fluorescent dye Tinopal) with the code PHREEQC is possible as shown in the paper by Licha et al. (2013) published in the Journal of Hydrology. However, important thermodynamic data of the possible tracers (e.g., Pitzer parameters, equilibrium constants of precipitating Mg- and Ca-salts) to extend the modeling for highly mineralized waters and brines are missing. An assessment of tracer stability at high temperatures and pressures must be also performed. Therefore, we favor the development of nonreactive, thermosensitive and sorption tracers as already done and suggested by the proposals of the working group at the university Göttingen (project "Reaktherm", personal communication T. Licha, Uni Göttingen).

3. Further works of the department "Hydrogeology" related to the project G9

Based on the working results of the project G9 the lecture "Hydrogeology for geothermal engineering" is planned and will be given within the Master of Science program in Geothermal Engineering (starting winter semester 2014) at the Institute of Petroleum Engineering (TU Clausthal). The special hydrogeological lectures and exercises will enable the students to improve geothermal energy production in deep or surface reservoirs. Furthermore, basic hydrogeological skills (including modeling of groundwater flow and basic hydrogeochemical reactions) are provided. Focus is also given on the management, ecological tasks and the environmental protection of aquifers and surface waters.

The "gebo" database is documented. It can be used for PHREEQC and PHAST models and will be provided to other scientists. A special workshop with the title "Möglichkeiten und Grenzen der hydrogeochemischen Modellierung hydrothermaler und geothermischer

Prozesse mit PHREEQC" was prepared and already given for students of the University Halle (Angewandte Geowissenschaften).

Both, the hydrogeochemical data and the "gebo" database, will be presented within the lectures of the department Hydrogeology. Students are encouraged to use these data in their works. We hope that there will be the possibility to complete the hydrogeochemical data.

Two research proposals resulted from the work:

- Hydrogeochemische Modellierung zur Optimierung des „mud logging" beim Abteufen von Geothermie-Bohrungen im Norddeutschen Becken (vorbereitet für die „gebo"-Strategiegruppe),
- Hydrogeochemische Charakterisierung paläozoischer Geothermie-Reservoire Norddeutschlands unter besonderer Berücksichtigung hydrogeochemisch induzierter Porositätsänderungen in Reservoiren des Unterkarbons (Einzelprojekt 6 für den BMU-Antrag unter Leitung des LIAG).

The second proposal with the title „Hydrogeochemische Charakterisierung paläozoischer Geothermie-Reservoire Norddeutschlands unter besonderer Berücksichtigung hydrogeochemisch induzierter Porositätsänderungen in Reservoiren des Unterkarbons" is managed by the LIAG and will be submitted again.

4. Conclusions

The application of hydrogeochemical modeling for a better geothermal reservoir management will rise in the next years. Based on the knowledge of the composition of deep formation waters and the hydrogeochemical processes within deep reservoirs, hydrogeochemical modeling can be used to deepen understanding of natural and technically induced processes in deep wells and their surroundings. Every model must be carefully evaluated, however. To improve the quality of hydrogeochemical modeling, thermodynamic data must be completed and more experimental work to test modeling results should be performed. Even considering the limitations of the model approach (e.g., not considering kinetics of redox reactions and scale mineral precipitation), the modeled results generally fit the measured concentrations in the sampled formation water, the residual sampled gas amount and contents, as well as the observed types of scalings. Looking at the several single model steps, the complex web of interdependent reactions responsible for the dominant hydrogeochemical processes that evolve throughout the geothermal system at high ionic strength and high temperature conditions is elucidated. Furthermore, chemical parameters that indicate specific reactions within well casing materials can be identified and used within the monitoring of the well. Cement corrosion of the well casing will lead to

decreasing magnesium and lead concentrations combined with rising pH values. The effect of iron corrosion may be very different depending on the redox conditions and the concentrations of dissolved sulfides, carbon dioxide and oxygen. Iron corrosion can be identified by significantly lowering sulfate concentrations combined with increasing iron concentrations and changing pH values of the pumped water.

5. Acknowledgements

The presented data are the result of the research association "gebo" (Geothermal energy and high performance drilling research) financed by the Ministry of Science and Culture of the Federal State "Niedersachsen" and the industry partner Baker Hughes (Celle, Germany). We also thank Steffen Häußler, Carl-Diedrich Sattler, David Parkhurst and the colleagues of "gebo" for many helpful discussions and contributions. The GeotIS-Team of the LIAG (Hannover) is thanked for providing hydrogeochemical data of the North German Basin. Anna Bogush and Leo Fuhrmann helped in the data collection.

6. Publications resulting from the project

Patent:
Bartetzko, A., Lehr, J., Sarmiento Klapper, H., Davidson, M., Bozau, E., 2012. Methods and systems for monitoring well integrity and increasing the lifetime of a well in a subterranean formation (submitted to TU Clausthal and Baker Hughes).

Scientific publications:
Bozau, E., van Berk, W., 2010. Hydrogeochemische Prozesse im geothermischen System: SiO_2(aq)-Konzentrationen im Löslichkeitsgleichgewicht mit Quarz, DMG, Münster 2010.

Bozau, E., van Berk, W., 2011. Modeling of hydrogeochemical processes in groundwaters of the North German Basin (NGB), Goldschmidt Conference, Prague 2011.

Bozau, E., van Berk, W., 2011. Hydrogeochemical modeling as planning tool for drilling deep aquifers, Celle Drilling 2011.

Bozau, E., van Berk, W., 2012. Generic models of deep formation water calculated with PHREEQC using the "gebo"-database, EGU General Assembly, Wien 2012.

Bozau, E., van Berk, W., 2012. Der "gebo"-Pitzer-Datensatz zur hydrogeochemischen Modellierung von geothermisch genutzten Formationswässern des Norddeutschen Beckens, FH DGG, Dresden 2012.

Bozau, E., van Berk, W., 2012. Die Modellierung hydrogeochemischer Prozesse bei der geothermischen Nutzung von Formationswässern, Schriftenreihe der Deutschen Geologischen Gesellschaft 80, 195 (GeoHannover2012).

Bozau, E., van Berk, W., 2012. Hydrogeochemische Prozesse in geothermisch genutzten Tiefengrundwässern des Norddeutschen Beckens, 5. Norddeutsche Geothermie-Tagung, Hannover 2012.

Bozau, E., van Berk, W., 2012. Geothermische Nutzung tiefer Gesteinsreservoire („Hot dry rock"-Systeme): Ist eine Prognose der chemischen Wasserzusammensetzung möglich? AMS online 4, 8-13 (www.advanced-mining.com).

Bozau, E., 2013. Prozessmodellierung hochsalinarer Wässer mit einem erweiterten PHREEQC-Datensatz. Grundwasser 18, 93-98.

Licha, T., Niedbala, A., Bozau, E., Geyer, T., 2013. An assessment of selected properties of the fluorescent tracer, Tinopal CBS-X related to conservative behavior, and suggested improvements. Journal of Hydrology 484, 38-44.

Bozau, E., van Berk, W., 2013. Hydrogeochemical modeling of deep formation water applied to geothermal energy production. Procedia Earth and Planetary Science 7, 97-100.

Bozau, E., van Berk, W., 2014. Thermal springs hydrogeochemically compared to deep formation water, EGU Generally Assembly, Wien 2014.

Bozau, E., Häußler, S., van Berk, W., 2014. Interaction of well case materials, drilling mud, production fluids and deep formation water, Celle Drilling 2014.

Bozau, E., Häußler, S., van Berk, W., 2015. Hydrogeochemical modelling of corrosion effects and barite scaling in deep geothermal wells of the North German Basin using PHREEQC and PHAST. Geothermics 53, 540-547.

Bozau, E., Sattler, C.-D., van Berk, W., 2015. Hydrogeochemical classification of deep formation waters. Applied Geochemistry 52, 23-30.

Internal reports:

TU Clausthal, Institut für Endlagerforschung, Hydrogeologie, 2010. 1. Zwischenbericht des Teilprojektes G 9 /AP1 im Forschungsverbund Geothermie und Hochleistungstechnik (Interne Plattform „gebo").

TU Clausthal, Institut für Endlagerforschung, Hydrogeologie, 2011. 2. Zwischenbericht des Teilprojektes G 9/AP2 im Forschungsverbund Geothermie und Hochleistungstechnik (Interne Plattform „gebo").

TU Clausthal, Institut für Endlagerforschung, Hydrogeologie, 2012. Meilensteinbericht G9, AP1 – AP3 (Interne Plattform „gebo").

7. References

Abdou, M., Carnegie, A., Mathews, S.G., McCarthy, K., O'Keefe, M., Raghuraman, B., Wei, W., Xian, C., 2011. Finding value in formation water. Oilfield Review 23 (Spring 2011) 24-35.

Graf, D.L., 1982. Chemical osmosis, reverse chemical osmosis, and the origin of subsurface brines. GCA 46, 1431-1448.

Hebig, K.H., Ito, N., Scheytt, T., Marui, A., 2012. Review: Deep groundwater research with focus on Germany. Hydrogeology Journal 20, 227-243.

Hellevang, H., Declercq, J., Aagaard P., 2011. Why is dawsonite absent in CO2 charged reservoirs? Oil & Gas Science and Technology - Reviews 66, 119-135.

Holl, H.-G., Hurter, S., Saadat, A., Köhler, S., Wolfgramm, M., Zimmermann, G., Trautwein, U., Winter, H., Legarth, B., Huenges, E., 2003. First hand experience in a second hand borehole: hydraulic experiments and scaling in the geothermal well Groß Schönebeck after reopening. Int. Geothermal Conference, Reykjavik, Sept. 2003.

Kharaka, Y.K., Hanor, J.S., 2007. Deep fluids in continents: I. Sedimentary Basins. Treatise on Geochemistry 5, 1-48.

Parkhurst, D.L., Appelo, C.A.J., 1999. User's guide to PHREEQC (Version 2) -- a computer program for speciation, batch-reaction, one dimensional transport, and inverse geochemical calculations. US Geological Survey, Water Resources Investigations Report 99-4259.

Parkhurst, D. L., Kipp, K.L., Charlton, S. R., 2010. PHAST Version 2 - A program for simulating groundwater flow, solute transport, and multicomponent geochemical reactions. - U.S. Geological Survey, Denver, Colorado.

Schulz, R., GeotIS-Team, 2009. Der Endbricht zum Projekt „Aufbau eines geothermischen Informationssystems für Deutschland". http://www.geotis.de/homepage/Ergebnisse/ GeotIS_Endbericht.pdf

Seibt, A., 2004. Die Zusammensetzung des Reservoir-Fluids. In: Huenges, E., Winter, H., Experimente zu Produktivitätssteigerung in der Geothermie-Forschungsbohrung Groß Schönebeck 3/90. STR04/16, GFZ, Potsdam, 25-27.

Thomas, L.G., 1994. Hydrogeochemische Untersuchungen an Ölfeldwässern aus NW-Deutschland und dem Oberrheingraben und ihre Modellierung unter dem Aspekt der Entwicklung eines Expertensystems für Fluid-Rock-Interactions (XPS FROCKI). Berliner Geowissenschaftliche Abhandlungen 165, 1-165.

van Berk, W., Schulz, H.-M., Fu, Y., 2009. Hydrogeochemical modeling of CO_2 equilibria and mass transfer induced by organic-inorganic interactions in siliciclastic petroleum reservoirs. Geofluids 9, 253-262.

Yuan, M.D., Todd, A.C., 1991. Prediction of sulfate scaling tendency in oilfield operations. SPE Production Engineering 6, 63-72.

Yuan, M.D., Todd A.C., Sorbie, K.S., 1994. Sulfate scale precipitation arising from seawater injection: a prediction study. Mar. Petrol. Geol. 11, 24-30.

Further references used in the final report (data points in Figure 1 and 2) are given in the corresponding scientific publication in Applied Geochemistry.

Schriftenreihe des Energie-Forschungszentrums Niedersachsen (EFZN)

Band 30-2

Das EFZN ist eine wissenschaftliche
Einrichtung der

TU Clausthal

in Kooperation mit den Universitäten

Technische
Universität
Braunschweig

GEORG-AUGUST-UNIVERSITÄT
GÖTTINGEN

Leibniz
Universität
Hannover

CARL
VON
OSSIETZKY
universität OLDENBURG

Final Report

of

Geothermal Energy and High-Performance Drilling Collaborative Research Program (gebo)

Niedersachsen

Partners:

Technische Universität Braunschweig (TUBS)

Technische Universität Clausthal (TUC)

Gottfried Wilhelm Leibniz Universität Hannover (LUH)

Georg-August-Universität Göttingen (UGOE)

Leibniz-Institut für Angewandte Geophysik (LIAG)

Bundesanstalt für Geowissenschaften und Rohstoffe (BGR)

Energie-Forschungszentrum Niedersachsen (EFZN)

Speaker:
Kurt M. Reinicke;
Georg-Peter Ostermeyer

Goslar, July 2015

Contents

B1: Cost effective drilling methods for „Hot-Hard-Rock" conditions

1 Project Overview

Project Nr.	Title	Subject of research	Project leader, institution, location
B1	Cost effective drilling methods for „Hot-Hard-Rock conditions"	Petroleum Eng. (Drilling)	Dr. Dr-Ing. Catalin Teodoriu, TUC (ITE)

Participating institutes and institutions of the universities and external institutions:

- Institut für Erdöl- und Erdgastechnik (Technische Universität Clausthal)
- Baker Hughes Contact: Dr. Jörg Lehr

List of participating scientists and engineers:

Name	Subject area	University institute or non-university institution	Position is financed by gebo funds (indicate by X)
Dr. Dr.-Ing. Catalin Teodoriu	Petroleum Eng. (Drilling)	ITE, TU Clausthal	
Dipl.-Ing. Carlos Paz	Petroleum Eng. (Drilling)	ITE, TU Clausthal	X
M.Sc. Nelson Perozo	Petroleum Eng. (Drilling)	ITE, TU Clausthal	X

2 Research Program

2.1 Summary

The economic utilization of deep geothermal energy requires first of all the cost-effective drilling of sustainable high rate wells connecting to hot-hard-rock. One possibility to cut down drilling and completion costs is the development of new well construction solutions.

The first project objective is to present the state of the art in drilling technology through a systematic survey of relevant drilling methods, and their technical and economic evaluation, depending on the applications. The second objective is to identify and evaluate new concepts that will cut the drilling costs by up to 50%. In this context coiled tubing (CT) and expanded tubular well construction techniques will be analyzed and compared with conventional techniques. The conventional rotary drilling technique is considered as the reference situation for all cost calculations.

The considerations are guided by the idea to construct wells allowing a production of 5 MW electrical power.

2.2 Relationship of the project to the overall research context and networking with other projects

A significant reduction in well construction costs is only possible if new economically applicable well construction methods are developed. To this end, a joint effort of all parties

287

involved in the association is necessary. Fit-for-purpose contributions from materials, technical systems, and to a lesser extent from geosciences require a common understanding of the type of well to be constructed, the way it is constructed, the loads expected during the construction and possible stimulation needs to achieve the necessary productivity. A principle task of project B1 is to provide this information and communicate it within the association. In addition investigations will be carried out to test aspects of the well construction method proposed in this project.

Input from other projects:

- Automation of the drilling process (B3)
- Hydraulic model for the drilling fluid. (B5)
- Materials projects (W)

Output to other projects:

- Sample well, construction method and loads during construction (all projects)
- Strength and fatigue behavior of CT, expandables and the folding pipes. (W)
- Boundary conditions for cutting transport (B5/B6)
- Boundary conditions for drill string loads. (B7/B8)

Additionally, the project B1 offered in 2009 two dedicated courses on drilling engineering in order to bring all gebo partners from other projects to the same understanding level of the drilling technology.

2.3   Work packages carried out according to (original) plan and results

WP1: Drilling cost analysis/drivers

Drilling cost drivers were identified on the basis of a comprehensive cost analysis for several wells drilled in Germany as well as worldwide. The results of this study showed that in order to cut drilling costs by 18% one must reduce drilling rig costs, drilling time and trip time by approx. 50%, respectively. Further cost reduction can be achieved only if *well construction, rig concept and drilling method are newly defined.* Table 1 shows how the time spent on the different drilling operations is divided. Due to its rather low percentage (26%) of the total well time, an improvement of the well drilling time will be not enough to achieve the 50% of cutting costs which is as target of the gebo project.

Cutting drilling costs can be achieved by improving the actual drilling methods and technologies or by developing new drilling methods (especially on rock destruction), new well construction solutions, new drilling equipment (especially drilling rigs) or a combination of all. However, the results of the studies performed in this work package showed that when drilling depth increases, significant savings can be achieved only by the well construction, since casing and cementing account for more than 50% of the well costs.

Drilling Operations	Time Spent in %
Drilling	26
Tripping	20
Cementing	15
Measurements	12
Other Works	8
Drilling Fluid related Work	6
BOP related Work	4
Top Drive	4
Repairs	2
Fishing Operations	1
Costruction and Dismantling	1

Table 1: Percentage of the productive time [1]

Work package WP1 was concluded with a final report presenting the cost drivers and cost reduction options. Two other reports on well construction and coiled tubing have been also completed within this work package as well as two sessions on drilling technology.

WP2: Market overview and state of the art

The detailed analysis of the costs involved in the realization of geothermal projects shows the need for technologies that allow the decrease of tripping and drilling time as a possible means to drilling costs reduction. One of the tasks in B1 is the investigation of possibilities to cut down drilling and completion costs by applying alternative well construction solutions and the implementation of nonconventional drilling techniques and technologies.

A full overview of the world wide geothermal well construction methodologies was performed. The overview shows that most of the actual geothermal wells follow the "state of the art" in oil and gas well construction. It is worthy of note that the final diameter for more than 70% of the investigated projects was only 7". All geothermal wells were drilled using conventional telescopic design. On average, geothermal well construction costs were significantly higher costs than average oil and gas wells.

From the analysis it was concluded that the most significant cost reductions can be achieved by reducing the average well diameter, as well as by reducing the tripping time. Several concepts were taken into consideration: lean well concept, slim-hole concept, "ultra-lean" well concept, and monobore. In conclusion the *MONOBORE concept* with an 8½" production casing to a depth around 6000 m was chosen as the means to reduce drilling, tubular and completion costs while maintaining acceptable the pressure losses within the gebo initiative.

A "monobore well" is a well of uniform diameter for the production casing from the reservoir to the surface and where the primary design criterion is the well-productivity rate. Monobore

wells are cased section-by-section as for standard well construction, but the new casing sections are expanded once setting depth has been reached to assume the diameter of the casing through which they have been entered into the wells. Within this concept, all intermediate size casing strings are eliminated. Realization of this downsizing (while still achieving the same size of production casing), will result in significant savings in wellhead equipment, mud, casing steel, cement, drill bit costs and rig costs; in addition, the number of specialist completion services can be reduced, resulting in additional savings for well construction costs and logistics. The reduction in well diameter implies a reduction in energy requirement for rock destruction, expected to result in higher rates of penetration. Overall a monobore concept is expected to lead to significant cost reductions if the technology can be safely applied.

In the context of the research addressed in the WP2 *Market overview and state of the art*, a comparative analysis of the profitability of a geothermal project in the five locations in North Germany showed in the Figure 1 was performed. This study stems from the notion that geothermal power plants should be able to supply 5MW electrical power.
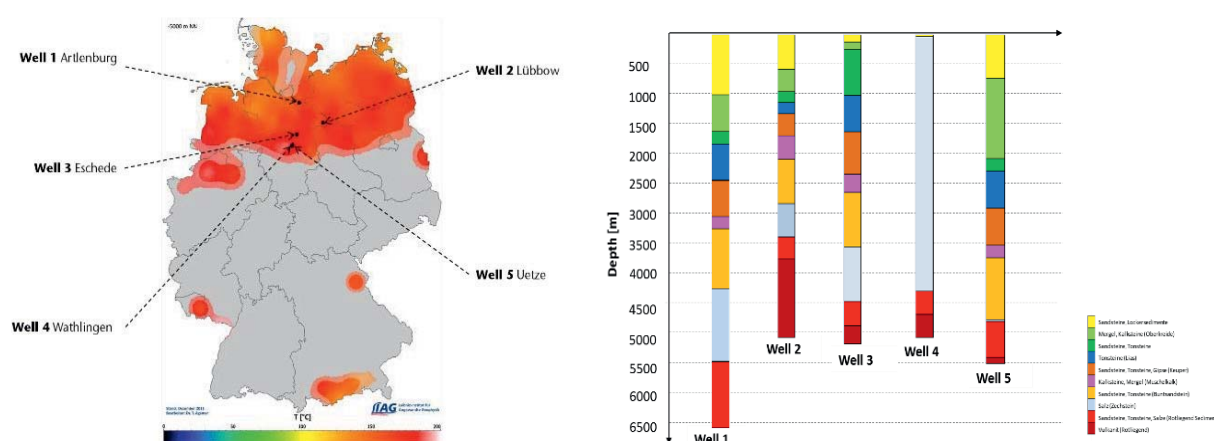
Figure 1. Location and stratigraphy of the posible GEBO well locations

From the geological knowledge of the subsurface at these location was determined the sweet spot where the geothermal resource deliver the required flow rate and temperature for the generation of electricity. The formation layer that presents the most favorable conditions for the exploitation of the geothermal resource is the Rotliegend volcanics due to its favorable thermal and mechanical properties for hydraulic stimulation. Additionally, the study of the stratigraphy of the locations reveals the possibility to improve the overall efficiency of the geothermal projects through an exploitation at low cost of the tight gas resource present in the Upper Rotliegend sandstone section.

An estimation of the reserves in the reservoirs in each location was performed using a probabilistic approach and simulations. These simulations are intended to determine the heat in place and volumetric extent of the reservoir, to forecast the temperature depletions during

production periods and to describe the heat transport inside the reservoir. All these parameters are required to identify hot and gas bearing sweet spots among the proposed wells and to make management commitment towards implementation of the projects.

The assessment of the reservoirs at each location are summarized in Table 1. All the design characteristics of the subsurface heat exchanger used for the construction of the simulation models of the wells in order to guarantee the production of 5MWe for at least 20 years are described therein. The basic well concept design comprises a pair of horizontal injection and production wells located parallel to each other in the vulcanite layer with the producer well above the injection well, oriented along the direction of the minimum horizontal stress and interconnected through the transverse and perpendicular to the wellbore oriented fractures created after a hydraulic stimulation of the production zone.

Table 1. Characterization of the Drilling Targets

Well	1	2	3	4	5
Target Depth Injection Well [m]	6000	4900	5000	4900	5250
Target Depth Production Well [m]	5900	4400	4900	4800	5150
Horizonta Distance Between Wells [m]	500	0	500	500	500
Length Horizontal Well Section [m]	>1300	1120	>1330	>1330	>1330
Fracture Distance [m]	>20	16	>20	>20	>20
Estimated Stored Heat [kJ]	70	70	70	70	70
Estimated Power Capacity [MWe]	3.1E+13	5.2E+14	3.9E+14	3.8E+14	3E+14
Certainty to Produce 5 MWe [%]	0	83	56.2	52.6	21.6

In the table 1 can be observed that due to the reduced effective drainage volume there is no certainty for the generation of 5 MW electricity from well 1 but in contrast, well 2 provides the highest certainty in fact due to the large thickness of the reservoir of up to 1500 m where 16 fractures suffices to produce the required electricity over the lifetime of the project. Wells 3, 4 and 5 need up to 20 fractures for this purpose. The design of the subsurface heat exchanger for the wells 2 to 5 guarantees a temperature production above the cut-off temperature through an effective combination of number and distance between fractures. In addition to the exploitation of the geothermal resource, the use of a multi-fractured sidetrack for the production of around 211 billion SM^3 from the Rotliegend sediments gives an opportunity of increase the earnings from the operation during the 20 years lifetime of the projects. Investigations undertaken within B1 to identify the necessary combination of reservoir temperatures, fluid production rates and well depths resulted in a sample well 6.000 m deep, with a bottom hole temperature from approximately 200 °C, producing at a fluid rate from circa 100-150 l/s.

Figure 1 shows the main well geometry and the designated well sections according to what is proposed as the gebo well design. The main geometrical parameters are also listed. The well will have an equivalent casing of $8^{5/8}$", but contrary to the classical well design, the ID of the well will be kept constant. The ID diameter should be 8" in order to allow the drilling of the next section.

Figure 1: Schematic view of the GEBO well construction
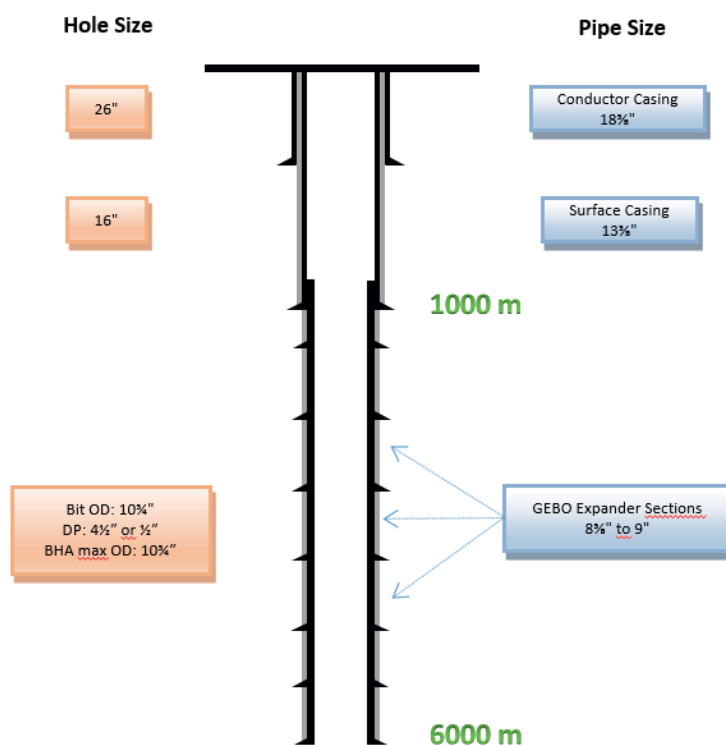
For the gebo well design, a well concept is proposed where the first section of the well (surface casing) is drilled with conventional or preferably casing drilling technology. A conductor casing is firstly rammed according to the existing legislation. Depending on the local geological conditions a $13^{3/8}$" casing is set at a depth of approx. 1000 m. The large size of the casing is required to accommodate the pump used for the circulation process. The further well is constructed as monobore well using expandable metallic pipes (folding technology). The process is sequential and will be performed as follows: well section is drilled using conventional drill string setup or alternative methods (up to 500 m open hole sections), drill string is retrieved, and the expandable pipes are run in the hole with a working string (e.g. coiled tubing or drill pipes).

Figure 2 shows a schematic of the drill string setup for the gebo drilling phase and figure 3 shows the setup of the gebo liner running sequence. The drilling process for one section is based on state-of-the-art drilling engineering and consists of the following steps:

- Run the BHA and drill string to begin drilling a well section

- Add one drill pipe every 10 m in case of a super single drilling rig or 30 m for a conventional drilling rig (triples)

- Trip out the drill string and BHA when the 500 m are drilled or drilling problems occur.

- Run the casing (gebo technology) using welded segments of about 10 m each for the 500 m length and the working string. (Figure 3). The gebo folded casing has a maximum OD of 7"

- Expand the gebo liner. The maximum expansion will generate a casing with an OD of $8^{5/8}$" to 9"

- POOH the working string.

- Cement the section.

- Start drilling the next section.
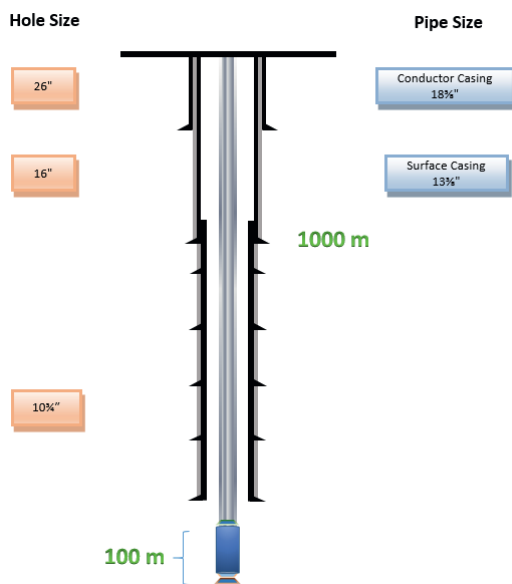
Figure 2: Drill string design for the gebo concept
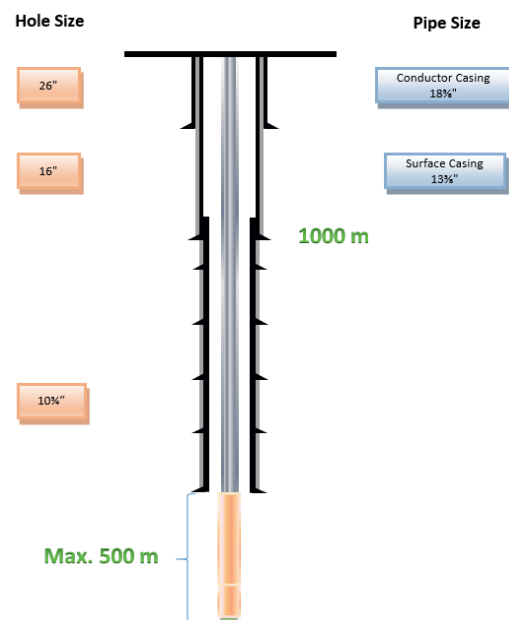
Figure 3: Casing running string design for the gebo concept

The reviewers of the interim report have recommended an extensive study of the economics aspects of the monobore. The main subjects of this study are presented in the following pages. Appendix A and B contain the detailed calculation of the projects and are disclosed for consulting.

In order to estimate the profitability of a geothermal project in these locations is essential in first place to determine the total drilling time needed for the drilling activities on each well, including the drilling time needed to perforate each section of the wellbore, the trip time needed to move the drill string in and out of the hole, the connection time for joining all elements in the string and an appraisal of the non-productive time caused by wellbore integrity issues, lost circulation, formation pressure problems and poor drilling control.[2]

293

The distribution depicted in the Figure 4 reveals, that the injector on well 2 takes longer to be drilled, for being the well with the largest thickness in the vulcanite and the time for drilling the well 4 can be significantly reduced by the higher rate of penetration and lower non-productive time expected from a thick layer of Upper Permian salt. In addition, a monobore design of the wells does not reveal a substantial optimization of the total drilling time since the achievable reduction on drilling time is overshadowed by an increase of the non-productive time involved in the operations of tripping, expansion and cementing of each section of the expandable tubulars used[3].
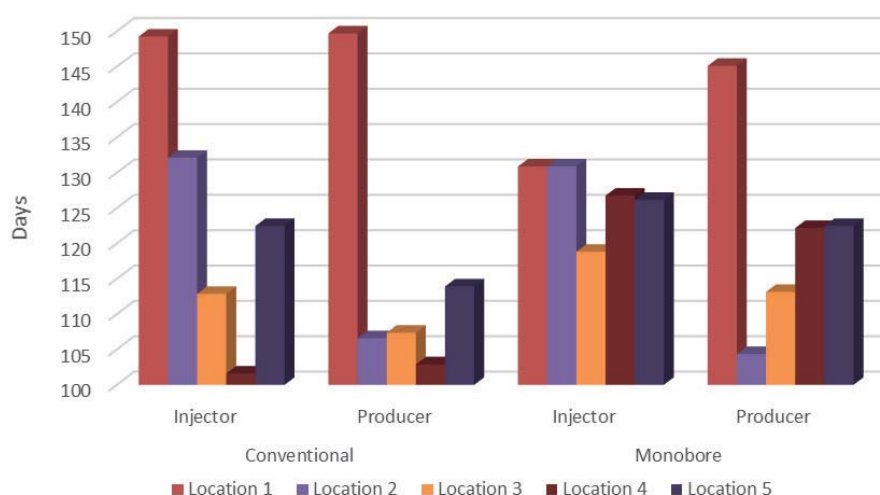
Figure 4. Total Drilling Time in days per Well

In second place and to determine any improvement in the viability of a geothermal project using alternative construction methods two concepts (open hole and cased hole) were considered for the cost analysis performed in each location. The open hole completion offers a high injectivity and productivity of the well but the cased hole completion minimizes the problems related to wellbore stability and sand control with the corresponding benefits in the production performance and completion efficiency.

Table 2. Costs per Well Pair

	Conventional Design Costs (1000€)					Monobore Design Costs (1000€)				
	1	2	3	4	5	1	2	3	4	5
Open Hole	41,753	34,972	33,725	31,973	35,807	33,836	30,116	30,166	31,244	32,397
Cased Hole	42,675	36,250	35,391	33,365	37,199	36,635	32,635	33,265	34,044	34,113

In Table 2 are presented the drilling capital expenditures associated with the different wells in the locations 1 to 5. The cost per well pair totalizes the group of fixed and variable costs

involved in the drilling operations and allows the comparison of the profitability for the geothermal exploitation among the profiles investigated. The analysis of the profitability was made using a profitability index based on the capital and operational expenditures, cash flow, revenue, depreciations, provisions, royalties, taxes, inflation, discount and escalator rates [2][4][5][6][7].
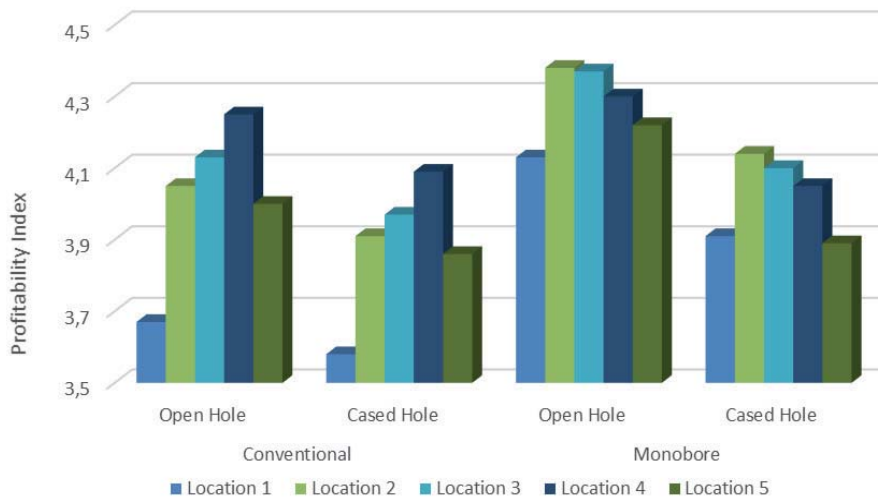
Figure 5. Profitability per Location and Completion Type

Figure 5 shows the profitability index of each project. An index over 1 represents a project that can earn profit. For this study the location 2 is the most suitable for the geothermal activity if a monobore design with open hole completion is implemented. However, technical limitations in availability of casing grades capable of withstanding the pressure in the last sections of the borehole, makes that the election of investment turns to the conventional completion. In this case the location 4 with a conventional design and open hole completion should be the alternative to be selected to accomplish the exploration and exploitation of the geothermal resource based on the state of the art of the drilling technology. The analysis of the profitability of investment in well 1 is based on the type of completion and does not consider the uncertainty of the electricity production from this well described in the Table 1.

Conclusions and Recommendations from WP2:
- For immediate applications, conventional drill string setup is considered the best solution for drilling the wells. As an alternative solution requiring long term investigations, special coiled tubing string and welding technology may be used. When coiled tubing technology is used for the drilling phase the following advantages can be assessed: speed up the drilling process, providing a safe and efficient live well intervention, a rapid mobilization and rig-up, the ability to circulate while running in

and pulling out of hole (RIH/POOH), and a reduction of the trip time, resulting in a significantly cost reduction.

- However further investigation must be performed to find out if such technology is suitable for drilling large diameter holes. Due to the actual limitations in material properties and on site welding capabilities, the alternative drill string is not considered viable by the end of gebo project. Using a conventional drill string will increase the chances to apply the lessons learned in gebo B1 in a short period of time. However coiled tubing technology remains the option to drill the lateral horizontal wells in the reservoir, which will be investigated in the next years through extensive experiments.

- Cementing techniques, which will not be considered in the gebo research program, represent a key factor that require further attention, once well construction concepts are fully determined and calculated. Alternative solutions to well cementing are therefore considered at a theoretical level only. These alternative techniques are: swelling packers, alternative cementing systems.

- Coiled tubing drilling is a good choice to drill the horizontal laterals which are required to develop the geothermal reservoir, when smaller diameters are required. The use of coiled tubing can significantly save tripping time and therefore costs. Project B9 is working on several concepts for reservoir development. The lessons learned will be used to define coiled tubing loads when drilling the lateral horizontal wells.

WP 3 and WP 4: Investigation of materials, processes and strength behaviour for coiled tubing and expanded tubular / process and material selection

The first step for the WP3 and WP4 consists of calculation and design of the testing facility for coiled tubing and expanded tubulars, where pipes of up to 6" external diameter can be tested. Figure 6 shows the final design of the corresponding facility, which has been completed in December 2010.

The testing facility has three hydraulic cylinders. The bending cylinder will simulate the straightening and bending of the coiled tubing from/into the reel and the RIH and POOH events. The torsion cylinder can simulate the vibrations the pipe has due to friction with the well´s internal walls as well as the bit torque, and the axial force cylinder will provide the effect of the WOB (Weight on Bit). In this facility, internal pressure can be applied on the sample if further investigations are needed. Further investigations can be performed in the existing ITE testing center, especially collapse test of the folded pipe.
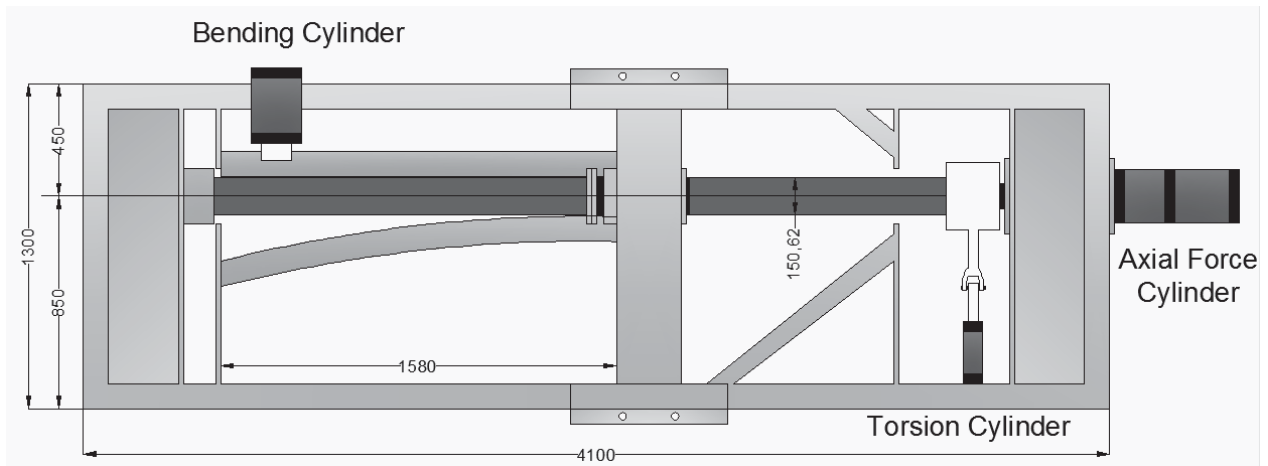
Figure 6: Testing facility for coiled tubing expandable tubulars

As specified in the work plan, the results of the tests of coiled tubing and expanded tubular designed for the gebo project (W projects) are expected to be available by the end of year 2011. The WP 3 and 4 are then only half way completed: the theoretical work has been accomplished. In this new facility coiled tubing and expandable tubular of up to 6" of diameter can be tested. Not only for the case of gebo but also for other applications, the need of larger coiled tubing sizes has increased, being pushed closer to the coiled tubing performance limits in order to satisfy many of the market demands. For this reason and to avoid coiled tubing failures in the field it is important that these limits are understood. With all collected diametral growth data during constant pressure fatigue tests, parameters related with the plasticity of the coiled tubing can be identified, which will help to predict the mechanical response (elongation, diametral growth and wall thinning) of a tubing segment subject to bending, straightening, pressure and axial load.

Coiled tubing has circular shape as it is manufactured, but overtime and due to bending multiple times over the spool and the gooseneck it becomes oval. The ovality of the coiled tubing is very important while considering the mechanical properties because it changes and affects certain mechanical parameters of the coiled tubing, changing the diameter; this deformation affects the wall thickness of the coiled tubing and thus reduces the collapse pressure (Kahn, 2009). Without experimental investigations it is impossible to have a good prediction of these changes, especially for new materials and manufacturing technologies.

A criterion must be chosen as the limiting criteria for determining the pressures and different force limits, in other words the yield envelope for a pipe with specific mechanical properties. This yield limit must be based on the combination of the stresses that causes the tube material to begin to yield. The Von Mises criterion is well accepted in the industry because it is relatively simple to calculate and it agrees well with test data. After subjecting the pipes to this dynamic test, where the plastic deformation has been performed, pipe collapse test will be performed to check how the previous deformations have affected pipe collapse strength.

297

Collapse tests will be performed in the frame RP2 of the ITE (TU Clausthal). When the tests results are available design measures can be identified to increase the life of the pipes by identifying the fatigue conditions and geometric changes they have suffered. In the case of the expanded tubulars it will be studied whether is better to make the expansion process either mechanically or hydraulically.

M 3 and M 4: Results from material tests and "full-scale tests" will be presented as part of a separate PhD Thesis.

A report showing all the results of the full scale tests performed to coiled tubings and expanded tubulars will be presented. The results of these tests will help to decide the proper material to be used as well as the appropriate geometry of the drilling pipes (coiled tubing and expanded tubulars) for the gebo project. The material and the geometry of the pipe depend on each other since all the information to be gathered from these tests is unique. It is believed, however, that the documentation may serve as data for other geothermal or deep drilling projects, especially when tubular integrity poses a challenging problem.

WP4 - Process and Material selection: Geothermal fluids contain dissolved CO_2, H_2S, NH_3 and chloride ions that can cause corrosion of metallic materials. Safe utilization of geothermal systems depends importantly on materials selection. Precautions during the design step, and conscious material selection, have an important role to minimize the effects of corrosion. Optimum cost and safety are factors influencing material selection. For coiled tubing and expanded tubulars ductile metals will be used, which will be plastically deformed to fulfill their function, i.e. low carbon steels. Because of their low expense and convenience, low carbon steels seem to be a sensible material; on the other hand, safe usage of this material depends on the applications in the system.

In the case of gebo, as a geothermal system, probable corrosion models should be put forward by analyzing the system before the design and material selection procedure. The corrosion model should be developed under wellhead and wellbore conditions and should include corrosion chemistry and the effect of the fluid flow rate on erosion corrosion. Hence, suitable material selection and corrosion control for the design would be obtained.

2.4 Conclusions

The economic utilization of deep geothermal energy requires first of all the cost-effective drilling of sustainable high rate wells connecting to hot-hard-rock. One possibility to cut down drilling and completion costs is the development of monobore.

The first project presented the state of the art in drilling technology through a systematic survey of relevant drilling methods, and their technical and economic evaluation, depending on the applications.

The second objective is to identify and evaluate new concepts that will cut the drilling costs by up to 50%, and we show that monobore well construction can help to save up to 50% nof well costs assuming that an intensive project monitoring and real time surveillance exist.

The reviewers of the interim report have recommended an extensive study of the economics aspects of the monobore, which has been performed in the second phase of the project.

The considerations are guided by the idea to construct wells allowing a production of 5 MW electrical power.

2.5 Project Plan

Work packages and milestones	2009	2010	2011	2012	2013	2014
WP1: Drilling cost analysis / Drivers	▬					
WP2: Market Overview, State of the art		▬				
WP3: Materials, processes and strength tests for Coiled Tubing und Expanded Tubular		▬▬▬▬				
WP4: Process and material selection		▬▬▬▬				

Grey, original plan, Blue, actual or current plan, respectively

The project started few months late because we could not get the qualified personal on time.

The first milestone has been completed, the second will be reached in 2011.

3   Delineation of the project from other funded projects

No projects are currently being performed at the moment in ITE, which has any connection to geothermal systems.

4   References

[1] Paulus, M. Kostentreiber von 4. – 5.000m Bohrungen, Institut für Erdöl- und Erdgastechnik, TU Clausthal, 2007

[2] Polsky, Y.; Capuano, L.; Finger, J.; Huh M.; Knudsen, S.; Mansure, A. C.; Swanson, R. (2008). Enhanced Geothermal Systems (EGS) Well Construction Technology Evaluation Report. Albuquerque: Sandia National Laboratories.

[3] Badrack, J., Howie, W., & Hillis, D. (2005). Solid Expandable Technologie Testing and Application. Houstn: NACE International.

[4] Carson, C. C., & Mansure, A. (1982). The Impact of Common Completion and Workover Activities on the Effective Costs of Geothermal Wells. Louisiana: Society of Petroleum Engineers.

[5] Rodolfo, G., Edgardo, A., Alfredo, B., Daniel, C., José, G., SPE, . . . Adrián Alfonso, W. (2001). Optimizing Development Costs by Applying a Monobore Well Design. Buenos Aires: SPE.

[6] Loberg, T., Arild, O., Merlo, A., D&apos, & Alesio, P. (2008). The How's and Why's of Probabilistic Well Cost Estimation . Jakarta: Society of Petroleum Engineers.

[7] Lentsch, D., & Achim, S. (2013). Risk Assessment for Geothermal Wells - A Probabilistic Approach to Time and Cost Estimation. GRC Transactions, 37.

[8] Kahn, A.A. Coiled tubing methods, applications and loads. Institut für Erdöl- und Erdgastechnik, TU Clausthal, 2009

5   Publications, reports and presentations of Project

[1] Teodoriu, C., Cheuffa, C., A Comprehensive Review of Past and Present Drilling Methods with Application to Deep Geothermal Environment, PROCEEDINGS, Thirty-Sixth Workshop on Geothermal Reservoir Engineering, Stanford University, Stanford, California, January 31 - February 2, 2011

[2] Zwischenbericht: Bohrlochkonstruktion, Beispielbohrung, Bohrstrang und Futterrohr, Institut für Erdöl- und Erdgastechnik, TU Clausthal, 2010

[3] Zwischenbericht: Einführung in der Geothermiebohrung: Bohrungsverlauf, Kostenverteilung und Kostenverlauf, Institut für Erdöl- und Erdgastechnik, TU Clausthal, 2010

[4] Teodoriu, C., Einführung in die Bohrtechnik, Vortrag 2009

6   Annex

[A] Economic Drilling of Deep Geothermal Wells (Geothermal Energy & Gas Recovery Project), Group Project 2013 - Gebo I, Institute of Petroleum Engineering, Clausthal University of Technology.

[B] Economic Drilling of Deep Geothermal Wells Group Project 2013 – Gebo II, Institute of Petroleum Engineering, Clausthal University of Technology.

[C] Test results from the full-scale Test.

B2: Drilling Simulator

1 Overview of the project

Projectnr.	Project Title	Subject of research	Project Leader, institution
B2	„Drilling Simulator" for well planning and drilling execution	Oil/Gas technology (ITE) – drilling engineering	Dr. Dr.-Ing. Catalin Teodoriu, TUC (ITE)

Participating institutes and institutions of the universities and external institutions:

- Institute of Petroleum Engineering (ITE), Clausthal University of Technology

List of all participating scientists:

Name	Subject area	Institution or non-university institution	Financing with funds provided for the application?? (X)
Dr. Dr.-Ing. habil. Catalin Teodoriu	Oil/Gas technology	ITE	
M.Sc. Zhenhua Dai	Oil/Gas technology	ITE	X

2 Research Program

2.1 Summary and content classification of the project in the overall project and networking

The aim of this project is the conceptual design and the prototypical development of a software platform as a framework for the optimization wrapper of a drilling simulator. The platform supports and integrates existing and newly developed modules with the purpose of describing the drilling process in all its dependencies. The simulator will be cross-linked with advanced 3D visualization technology.

In the first instance, the simulator is a pre-drill facility allowing the virtual drilling of a well, enabling the identification of drilling problems and options of resolution in an attempt to develop an optimized drilling plan. In addition, the simulator is intended to support the execution process of constructing a well by simulating the conditions in the well in real time providing a better basis for the decisions of the tool pusher.

2.2 Relationship of the project to the overall research context and networking with other projects

An important aspect of the gebo-project is to optimize well construction by use of artificial intelligence to simulate the well construction process in all its dependencies. The networking of the project arises from the necessary input for the project (well trajectory and geometry, geology, process models, and process parameters from gebo-projects) and its output.

Networking is particularly strong with the G and all B projects. The G projects will provide information on the geology and hydrogeology as well as parameters describing the thermal, hydraulic, mechanical and chemical (THMC) properties and conditions of the subsurface. The B-projects provide models and parameters necessary to model rock destruction, wellbore hydraulics, wellbore stability, drill string vibrations, torque and drag, and cuttings transport. Projects B1 and B9 provide the drilling technology and gebo concepts.

The information provided by B1 and B9 together with all other information to initialize a simulation, e.g. geological information provided by the G-projects, will be stored in the archives of the simulator database. B4 will use input like pore pressure gradient (PPG) and frac pressure gradient (FPG) from the database for the mud density calculation. B7 and B8 retrieve material properties from the database to describe and simulate the drillstring vibration. Furthermore, B5 and B6 focus on mud hydraulics and cuttings transport phenomena and consider the interaction with drillstring for dampening effects, which is also to be realized through the drilling simulator. It will also include information from G and W projects.

2.3 *Work packages executed relative to (original) plan and results achieved*

The purpose of the simulator is to allow an improved well planning by simulating the drilling of a well before the well is drilled, and a controlled execution of well construction. The objectives are to be achieved by avoiding drilling problems and non-productive times and by accomplishing an optimum rate of penetration given the geology at the location where the well is drilled. To simulate the well construction, it is necessary to integrate models describing the subsurface and the sub-processes of well construction and their interactions. Issues needing description are the geology and the THMC conditions of the subsurface, rock destruction, wellbore hydraulics, wellbore stability, drill string vibrations, torque and drag, cuttings transport, and well trajectory and geometry.

2.3.1 Reprentative drilling simulators

B2 aims to develop a prototype drilling simulator to serve as optimization wrapper for the process of well construction. For reference purposes, the information available for drilling simulators in the public domain worldwide was identified and analyzed. The evaluation of the identified simulators was carried out against the background of the functionality sought in the B2 simulator, i.e. the ability to model processes such as multiphase flow (cuttings transport), rock destruction (ROP) etc., real-time data transmission, hardware in loop (HiL), open platform, 3D visualization and real-time human machine interface. The representative simulators analyzed with main feature are listed in Table 1. The most simulators for the complete drilling process are commercial (eLAD, DrillScene, DrillTronics from IRIS [5] and eDrilling from Sintef [6]) in comparison with planned drilling simulator Celle (DSC) [8].

	Models	RT data	HiL	Open platform	Visualization	RT HMI
eLAD	☺	☺☺	☹	☺	☺☺	☺
DrillScene	☺	☺	☹	☹	☺	☹
DrillTronics	☺	☺☺☺	☹	☹	☺	☺
eDrilling	☺☺	☺	☹ or ☺	☺	☺☺	☹
DSC	☺☺	☺☺	☺	☺☺	☺☺☺	☺☺

Table 1: Evaluation of representative drilling simulators

Due to the missing drillstring vibration model, the IRIS software tool kits are less complete than the other two simulators. DrillTronics controls the drilling process with continuously updated mathematical process models at rig. Therefore it gets full points by real time data transmission in both directions. eLAD and DSC are development environments, which are able to generate virtual realtime data based on the simulated drilling operation. DrillScene and eDrilling only monitor and diagnose ongoing drilling operations in control center. Due to the data transmission only in one direction both software get the lowest grade in the context of real time data and HMI. HiL is one highlight of DSC, which can switch between software mode and hardware mode. Open platform shows the key feature of a academic drilling simulator. Extern simulation models can be integrated and perform simulation together. Because of the communication via WITSML server, eDrilling and eLAD are also able to offer the exchange of data. By comparison Drill-Scene and DrillTronics cannot integrate extern models. DSC is based on the commercial drilling simulator Drillsim600, which can visualize both surface and downhole conditions. eLAD and eDrilling can only visualize either surface or downhole scenarios, while DrillScene and DrillTronics don't focus on the visualization feature.

2.3.2 Seven tier conceptual model

The drilling simulator is intended to be an automated software system to support the process of well construction throughout the whole process from planning to execution and identification of lessons learned. For better structure the drilling simulator is divided into seven tiers: (1) base, (2) process, (3) database, (4) modeling, (5) logic, (6) visualization and (7) human-machine-interface (HMI). Each tier represents a particular aspect of the software system and is based on lower tiers. The general content of the seven tiers can be taken from Figure 1.

1.   Knowledge Base tier

Base tier is the lowest layer of the drilling simulator and all the other tiers are based on it. This tier consists of all theoretical and practical knowledge needed to build the other tiers above for a drilling simulator. This category has the following six main subcategories:

- Drilling technology

  This subcategory refers to the application of technology for creating boreholes in the earth. Based on it, the drilling procedures will be designed and implemented; the com-

plex drilling system is subdivided into interdisciplinary component areas of (at least) formation, rig, wellbore, fluid and string, which lead into the creation of drilling simulator.
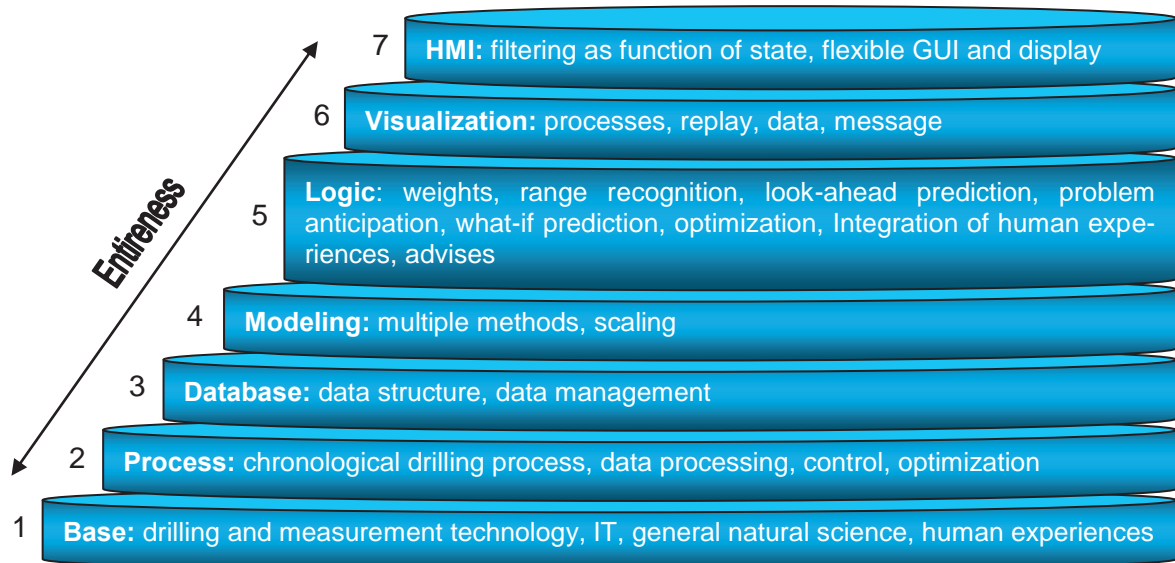
Figure 1: Seven tier concept of the gebo drilling simulator

- Measurement technology

  The measurement technology is used to determine the parameters in the ongoing drilling process. Since the drilling situations are described through measuring parameters, and moreover calibrations of all simulation models are based on the real time data, a great deal of effort must be taken to make measurements as accurate as possible, which is essential in drilling fields.

- Information technology

  Information Technology (abbr. IT) can be seen as another cornerstone of the simulator because huge amount of data from different sources like measurement and modelling will be distributed and stored during the whole planning, drilling and post processes.

- General natural science and mathematics

  The general natural science refers to physics, chemistry and so on, which is understood as obeying rules or laws of natural origin. With the general natural science and mathematics, models to describe different part of drilling process will be distinguished.

- Human experience

  The drilling people's personal experience, which is gathered through the praxis over the years, is also considered as a foundation of the drilling simulator. It helps to interpret the ongoing situations and find solutions for drilling problems.

- Knowledge database

  Finally, all the knowledge, information and data involved with the complete drilling process will be stored in a knowledge database. This database can be seen as the start point, from where a drilling process or drilling simulator can be initialized. It's also the destination, because all the plans developed, data gathered and experiences learned through particular drilling operations are to be accumulated here.

2. Process tier

The second tier is known as process tier, which is based on the base tier and supposed to design underlying workflows for different purposes. Firstly the chronological drilling processes are to be designed here. These processes distinguish the three phases "planning", "execution", and "post-processing" according to time sequence. In the planning phase, the process known as "Drill Well on Paper" (abbr. DWOP) is carried out, to determine the base plan. For this, the process of well construction is divided into several sub processes like mud and casing design, which are accomplished step by step separately. In the phase of execution, the actual drilling process will be fulfilled, which can be also described by means of stepwise and parallel workflow like casing, cementing, tripping and measurement. Post-processing is used to summarize the completed drilling process. The process, how to learn from the executed drilling procedure, will be specified here.

Secondly the data processing is to be developed. The underlying infrastructure for complex data flow from sensors to models to visualization will be designed here. This makes it possible to utilize drilling data in a more efficient and intelligent way for supervision of the drilling conditions by means of real time simulations, automatic diagnosis and decision support.

The workflows for control and optimization are also to be defined here.

3. Database tier

The database tier is used to technically realize the organization, storage, and retrieval of large amounts of data, which are traced back to the underlying process tier. It differs from the knowledge database and deals with the information and data, which are specified through a particular drilling operation. The data structure and data management system are two major considerations in this tier. In the drilling process, each parameter can have many attributes through measurement, calibration, modeling etc. The data structure attends to describe parameter with all its dependencies and enable an efficient way to store and manipulate it. The data management system realizes the data transfer and storage.

4. Modeling tier

In the modeling tier, different sub models, which are defined as a part of the whole drilling simulator in the base layer, interactively designed in the process tier and connected through the

database tier, will be implemented with mathematic and physic equations. The core task within this layer is modeling with appropriate method according to the different concrete situations. In addition an appropriate scaling will be determined, taking into account both the discretization for accuracy of the solution and the required calculation time. For example, the drillstring can be simply described as an ideal mass-spring-damper system with analytical method or as a discretized body with more complicated finite element method (FEM) to study its vibration. It depends on the concrete situation, to choose which method. Furthermore, the balance between the discretization like the fineness of grid in FEM and the calculation time is to be determined.

5.   Logic tier

This tier realizes the truly advanced or intelligent functions of a drilling simulator, in order to optimize the drilling process in all phases. In the planning phase, an optimized drilling plan is based on the weights between ROP, HSE and cost. In the phase of execution, this layer supports the following functions:

- Range recognition: Values of parameters will be checked. If they are against the allowed range, a warning will be sent to the GUI.

- Trend recognition: The general direction in which the observed data trend to move, will be estimated.

- Look-ahead prediction: Look-ahead prediction attempts to predict variable values based on information in the current situation. An example application is the pore pressure prediction ahead of bit by using a look-ahead vertical seismic profile (abbr. VSP) and thereby to reduce the drilling risk.

- Problem anticipation: This function deals with the methodology aiming the diagnosis and anticipation of drilling problems before they occur. The idea is to consider the wellbore, the reservoir vicinity and the drillstring as an integrated domain to be inspected.

- What-if prediction: What-if prediction studies of how model output varies with changes in input. These models aim at characterizing the process being investigated with the purpose of moving the process from a given or ongoing state to a desired goal state

- Interpretation support: The ability of applications to steer the user to a result or conclusion.

- Advises: This refers to the recommendation about what might be done to address a problem, make a decision, or manage a drilling situation.

The logic to learn from the executed drilling procedure will be designed here. Furthermore, experiences from drilling people are to be integrated in this layer, to assist the planning process and interpret the ongoing situations as well.

6.   Visualization tier

The major consideration of this tier is to present information and data by creating charts, diagrams and animations. The information includes workflows like the design steps, the drilling processes like tripping and cementing and so on. Drilling data from different sources (modeling, measurement etc.) will be plotted technically friendly. Message is to be displayed in the form of alarm, interpretation, advises and so on. In addition, the replay function will be also achieved in this tier.

7.   Human-Machine-Interface tier

This is the topmost level of the application. The tier of human-machine-interface is pulled out from the visualization tier and, as its own layer, it focuses on the two-way interaction between user and drilling simulator. In this tier, a graphic user interface will be designed and can be adapted according to user's requirements. In addition, a flexible visualization in form of number, curve or dial with different viewing functionalities like zoom, move will also be realized. Another major consideration is to filter data & information as function of status. This means, the critic aspect of drilling process will be automatic presented to the user. The seven tiers model builds not only the conceptual background of drilling simulator but also gives the guide to develop application, which will be illustrated by the modeling of ECD later.

2.3.3 Software framework

In comparison to conceptual model, the software framework offers concrete tools to build up applications, manage data etc.

2.3.3.1 Components

The main components are compilers, libraries, database and integration interface. As agreed with gebo partners, the programming work will be carried out within the Microsoft platform. Microsoft.Net is used to write libraries, while the database will be built up with Microsoft SQL. In addition, MATLAB is also supported in the software framework to perform mathematical modeling.

Based on Microsoft.Net, the libraries represent collections of resources, to develop software. Library can be traced back to the reuse of programs, which don't need to be rewritten over and over again. Furthermore, the program can be modularized through the disassemble into several libraries. Each library offers certain services. An application is generated through own modeling and reference several libraries to build the framework of program.

To run the simulator, a large amount of data is required, which is cross linked with each other. Therefore it is preferred that all input and output variables will be preserved and managed in database. Furthermore, use of database can avoid the data redundancy, limited access etc. Integration interface is used to connect the sub models to perform calculations, which models different aspects of drilling. In addition, the interface aims to provide the required input, so that

the integrated sub model can be run. According to the needed parameter a logic sequence of required sub models together with data transfer is generated.

2.3.3.2 Realization of software framework

Static and dynamic linked libraries are considered as two primary library types. The static library will be totally fused in the application after compilation, while the dynamic library is only loosely linked. In order to keep the modularity of software, the framework is decided to be built up in dynamic linked libraries.
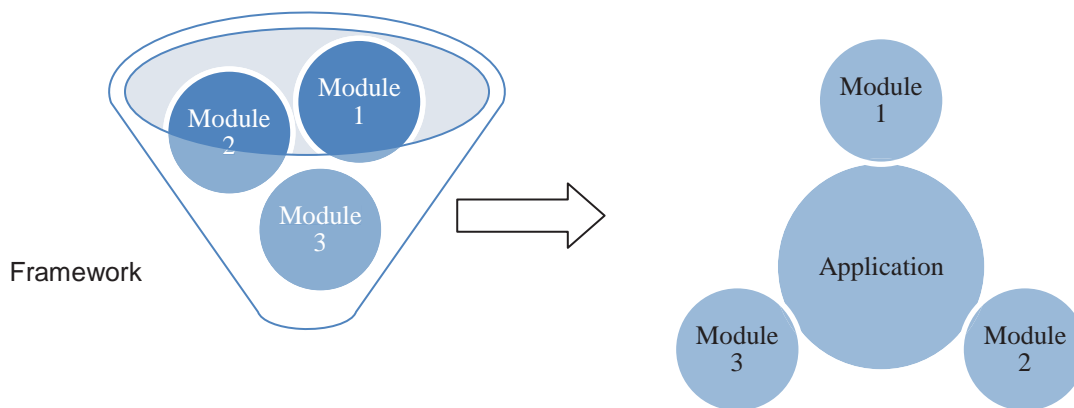
Figure 2: Maintenance of modularity from framework to application

2.3.3.3 Realization of database

A data model is designed for database. Data are divided into standard data, case specific planning data, and real time drilling data. The standard data will be contained in the "library" of the data base. Typical library entries are standard formation and fluid data, casing and liner data, and bit and mud properties. The data are to be entered in the parameter input section. The user can easily add information to the library to define new items. The library will also incorporate default values for the most important property data. The case specific data are for example, the site specific geological (possibly supplied by a geologic model) and geophysical (seismic) information and THMC conditions, the well trajectory, the well geometry, the casing scheme and planned operational conditions.

The real time drilling data encompass the actual operational conditions measured at the surface like hook load, pump rate, torque/turn information, pressure, rate of penetration etc., conditions characterizing the subsurface state, e.g. the bottom hole position and direction of the bottom hole ass embly (BHA), and vibrations (if possible) from MWD, and petrophysical information from LWD. The database shows the globally hierarchical and locally relational structure, see figure 3.
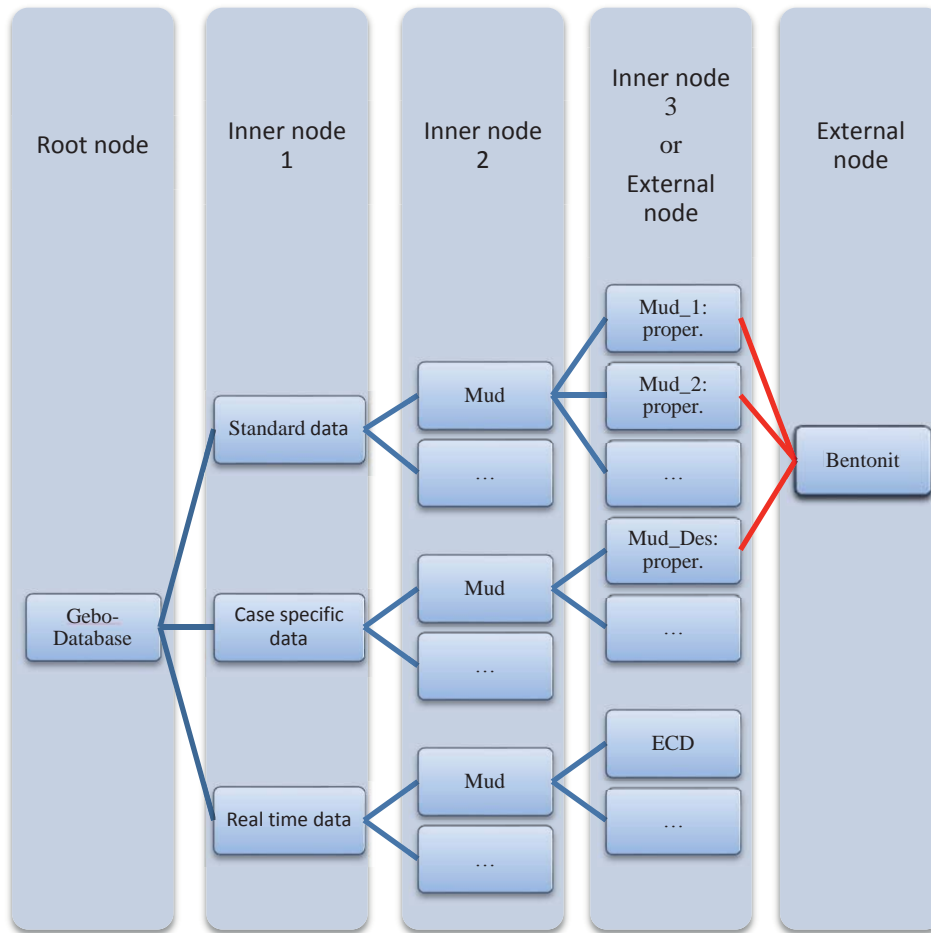
Figure 3: Mud related data in database

Global data is classified into three types. In the figure 3, the hierarchical relationships are expressed by blue line. It is comparable with a family structure, by which father can have many children but each child has only one father.

Locally or more precisely in the end of the hierarchy, the data shows a relational structure, which is represented in figure 3 with red line. Several drilling mud can have the same component like bentonite. In hierarchic structure this same bentonite is saved several time. This leads to data redundancy and huge work to update the same data. Therefore the "bentonite data input" will only be saved once and referenced in all relevant mud types. The relationship of red line cannot be considered as hierarchical, since logically a child cannot have two father at the same time. So this is called relational structure, which focuses on avoiding the data redundancy.

2.3.3.4 Realization of integration interface

Since the integration interface aims to connect simulation models and perform calculations, only data is inputted and after calculation outputted. Thus the first choice is to use database to connect the models. GUI builds a protocol about the data transfer and required models in a sequence. Then it starts the calculation from the base models, which no pre-calculation from other

models requires. The result output from one sub model will trigger the following models and when all needed parameters are available, the integrated model can be run (Figure 4).
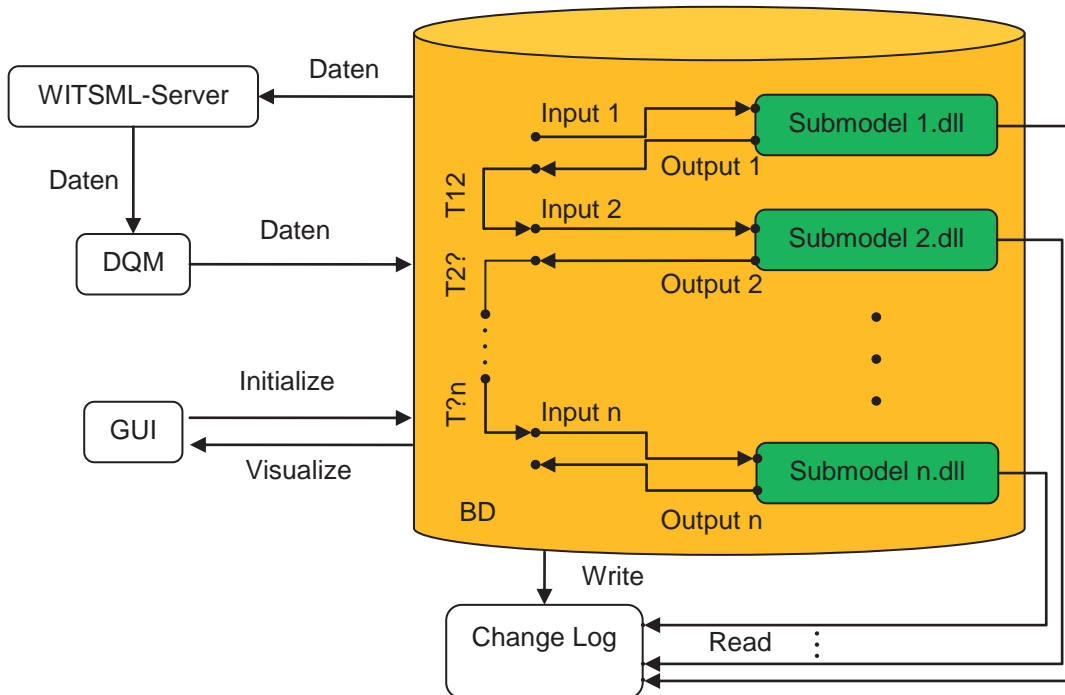
Figure 4: Integration with database

However this idea is proved to be unrealistic after test, because Microsoft.SQL doesn't support the model call with input. This means the input is not sent by the database but read by the sub model (Figure 5). This requires, that the developer of submodel creates a clear structure of database. In addition, any change in database will lead to time-consuming to adjust all submodels.
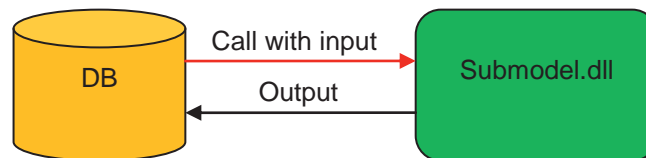
SQL doesn't support the ideal datatransfer
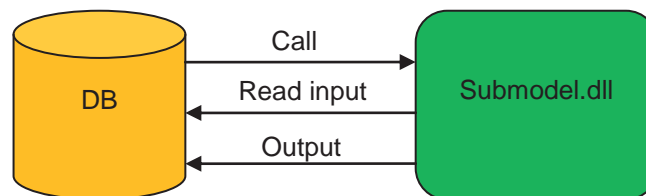
SQL supported datatransfer doesn't work

Figure 5: Dataflow between database and submodel

Because of the disadvantage of the connection through database, the integration interface was built using .Net framework. It represents just a program, which is separated from database, to manage the data transfer. This program will locate the input parameter in database and call the sub model together with the input.

2.3.3.5 Features of framework

- Modularity: the framework is subdivided the system into smaller parts called modules, that can be independently created and then used in different configurations. The modules are reusable and can be recombined according to the requirement to support concrete implementation.
- Extensibility: the software framework will be developed in a most adaptable and extensible form, because with new knowledge new requirements appear regularly.
- Open platform: the open platform focuses on the easy integration of foreign models. The required input generates a protocol about the required models with corresponding data transfer.
- Safety: source code of the infrastructure should be protected. The available functions are protected both timely and locally with license.
- Easy troubleshooting or update: the correction and update of single module should be easy, so that all relevant applications are not complied newly.

2.3.3.6 Main components of framework

The Unit Environment

As one of the foundation module, the unit environment is constructed at the very beginning. Unit environment is different from unit system, by which all units can be generated from so called base units like mass, length, time etc. In oil and gas industry, the unit is not unique for a certain quantity and set rather according to the order of magnitude. For example, both the wellbore diameter and depth belong to the quantity length. In SI system they are both expressed in meter, while in oil and gas industry the diameter is in inch and depth in foot. Therefore the unit environment here is constructed according to the different physical parameter. For each parameter a certain unit is set.

The unit environment is built in form of a server, where all the unit information together with the conversion factor are saved. This means, the unit of certain parameter cannot defined by user himself but obtained by the name of parameter and the defined unit environment. In addition, the information of unit environment will not be saved in the data. All save or calculation operation is performed after the unit conversion into SI system. This excludes the effect from different unit environment on the calculation equations. Therefore all the formals can be expressed uniquely in SI system.
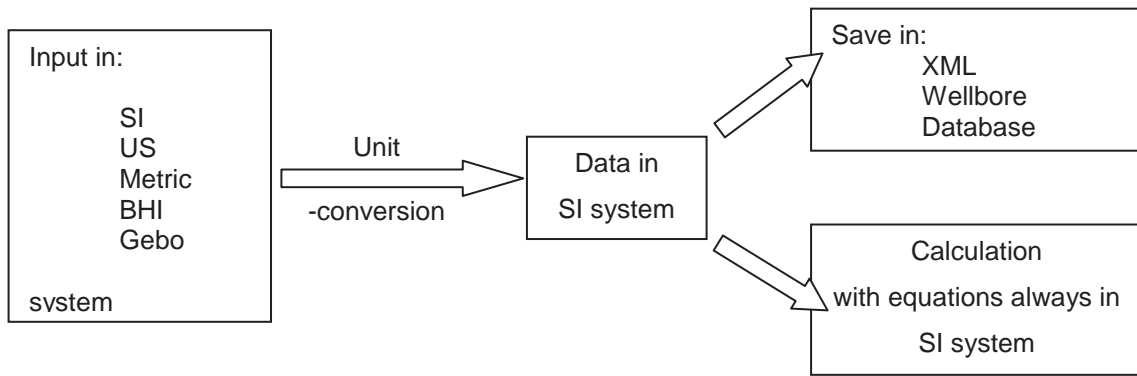
Figure 6: First unit conversion then calculation and saving

Input with multi-possibilities

In the framework many possibilities are available to input the parameter. The most direct method is input through keyboard and graphic user interface like tables, text box etc. In addition, .XML and .Wellbore data represent a good possibility to perform separate data input. One drilling aspect like lithology is save as .XML and then it can be imported into the whole drilling definitions, which is expressed with data suffix .Wellbore. Finally the data can be organized through database.
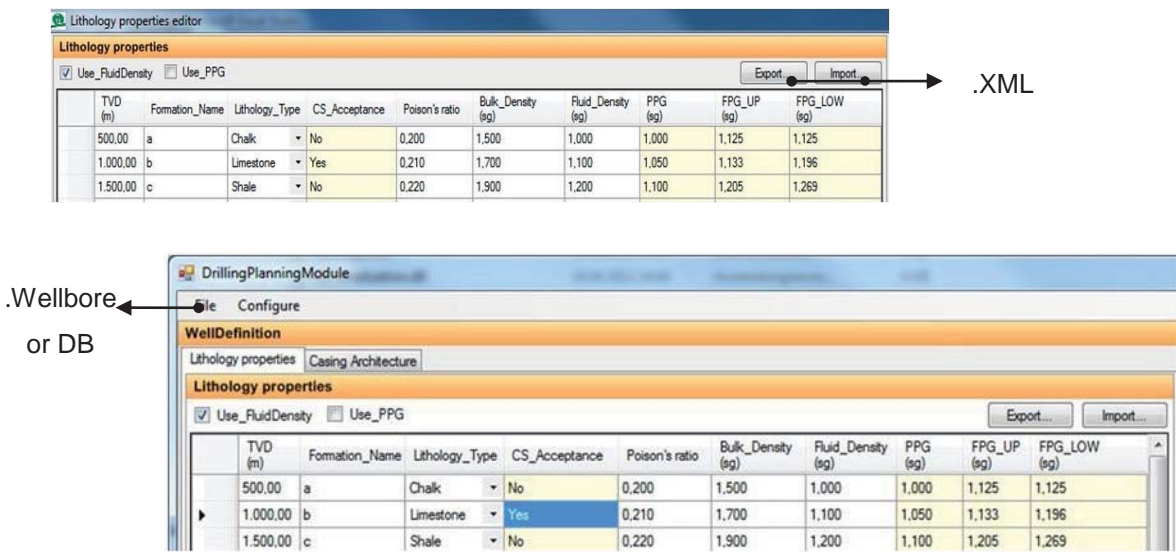
Figure 7: Tab in single and embedded application

Extensible data structure

The data structure here refers to the data organization in .Wellbore document. Hereby the wellbore data is divided into several aspects, like lithology, casing etc. The definition of each aspects is performed separately and after that they will be merged together.
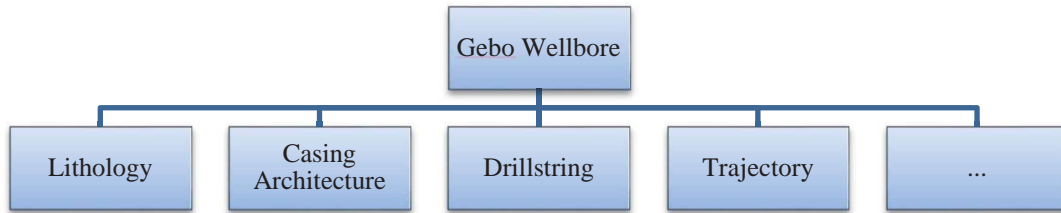
Figure 8: Hierarchical data structure

This structure enables a good extensibility, since you can add new component to each aspect and after the compilation the change will work immediately. The drillstring design shows a typical example, by which new elements can be added continuosly.
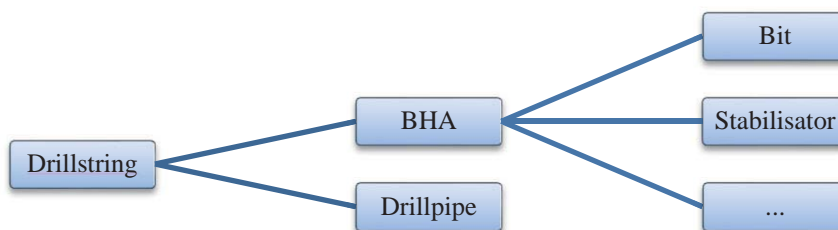
Figure 9: Hierarchical structure of drillstring

Modular tabs and visualization blocks

Tab control is marked by it good flexibility, because any extra tab can be added or deleted at every time. In addition each tab can be constructed individually and then merged together. The definition of tab is exactly the same as data structure. As the figure 7 shows, the modularly designed tab can be used alone or together, while actually the same element is referenced.

In order to achieve the independence of framework, the visualization blocks are set up directly within framework. The visualization blocks can be generally divided into two groups, namely universal and drilling special. Curve, bar and cake chart belong to the universal visualization, which can be used for general purpose. By comparison, wellbore schema and drillstring construction are visualized for special drilling purposes. All visualization blocks are modularly constructed. This means, the blocks can be used as much as possible, without repeating codes.

3D wellbore trajectory stands between universal and special visualization, which uses universal method for drilling purpose.

Communication between tabs

Different drilling aspects are actually cross linked. For example, the casing setting depth is determined by mud window, which is traced back to the lithology tab. Therefore, in addition to the separated defined tabs the communication between them should be built up. The idea behind it is, after the de-selection of a tab, the tab data will be immediately updated and saved in .Wellbore document. Any tab can access the actual data, when it is selected. Then each tab can access all updated data from .Wellbore, while it can only edit its own aspect.
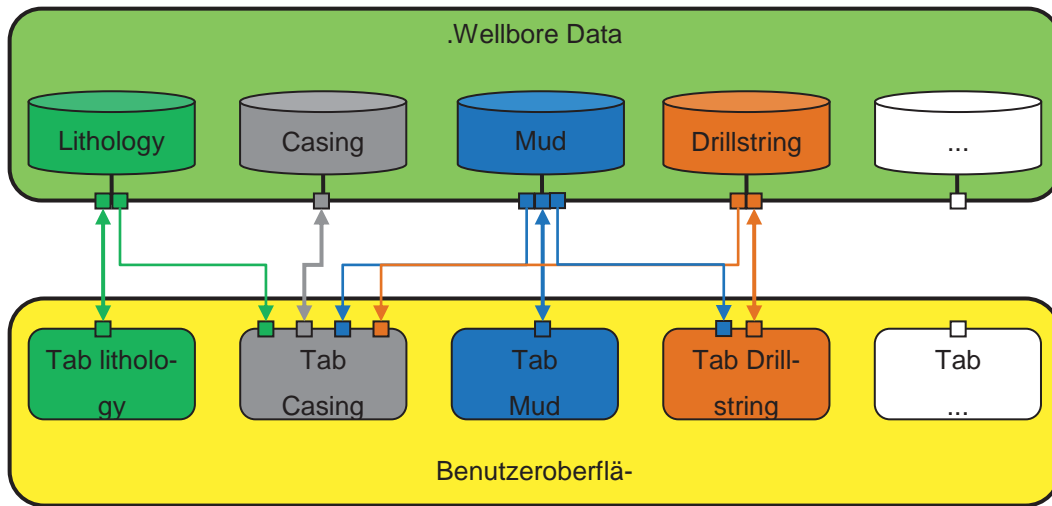
Figure 10: Dataflow between tabs

Extensible tab

Just as same as the data structure, the tab construction should also consider its extensibility, since new elements can be added continuously. The drillstring tab in figure 11 represents a perfectly extensible example. As the figure shows, the tab consists of three parts, namely the main table (left above), the description panel (right above) and modular visualization at the bottom.
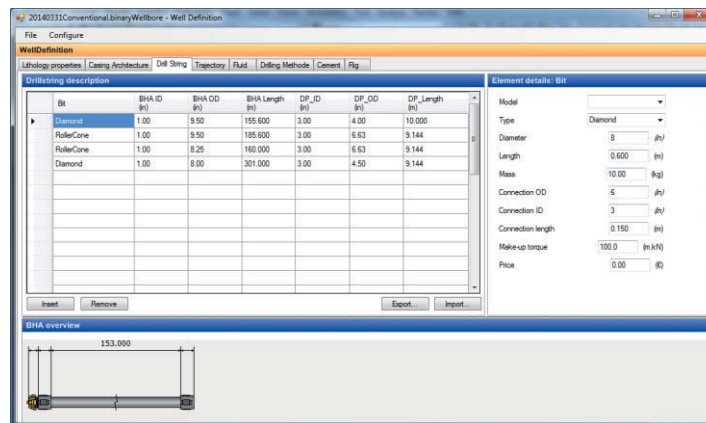
Figure 11: Tab of drillstring

In main table, each row represents a drillstring, which is expressed by bit, BHA and drillpipe. The main table is mainly used to shows the geometry of drillstring, therefore all cells expect BHA OD and BHA ID can not be edited directly in main table. The component is edited in description panel near the main table and the active cell in main table decides the content in description panel (figure 12).

Cell area for bit   Cell area for BHA   Cell area for drillpipe
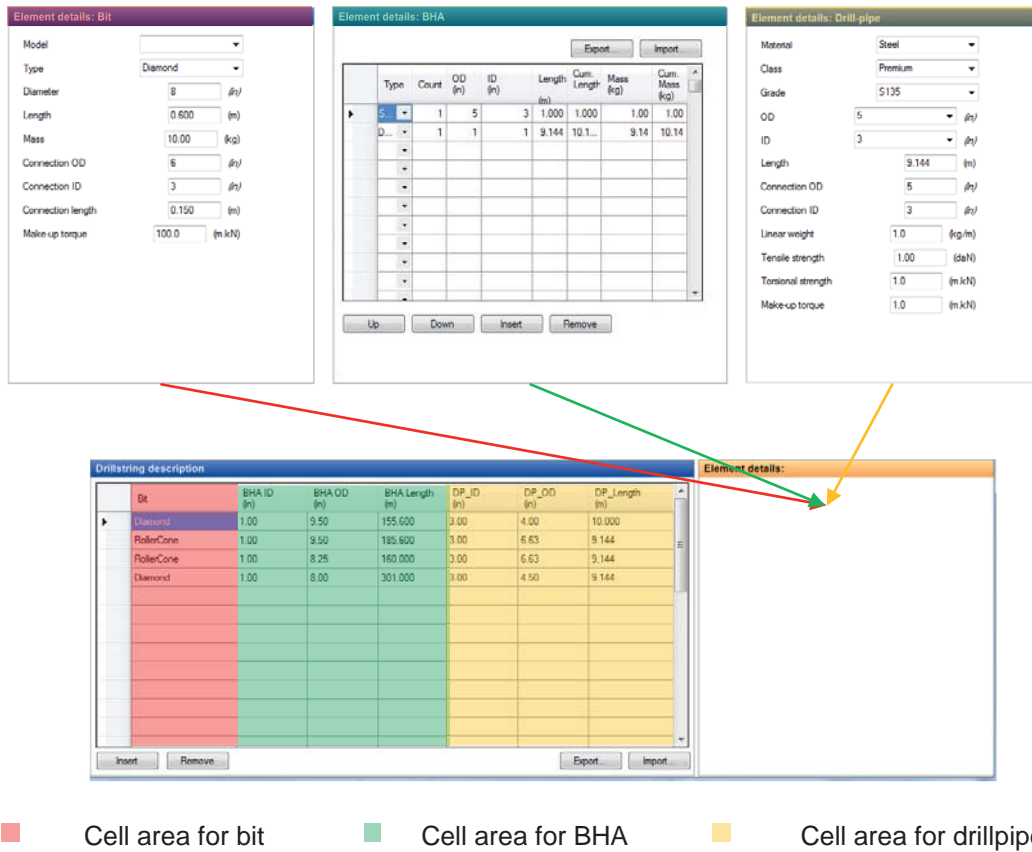
Figure 12: Activation and content of area "Element details"

Furthermore in order to achieve the extensibility of BHA components, the BHA is constructed in form of a table. The corresponding definition form is generated through the choice of element in the table. Therefore on one hand it is possible to define a BHA with unlimited number of elements. On the other hand, the extra BHA component can be defined and added easily through the table.
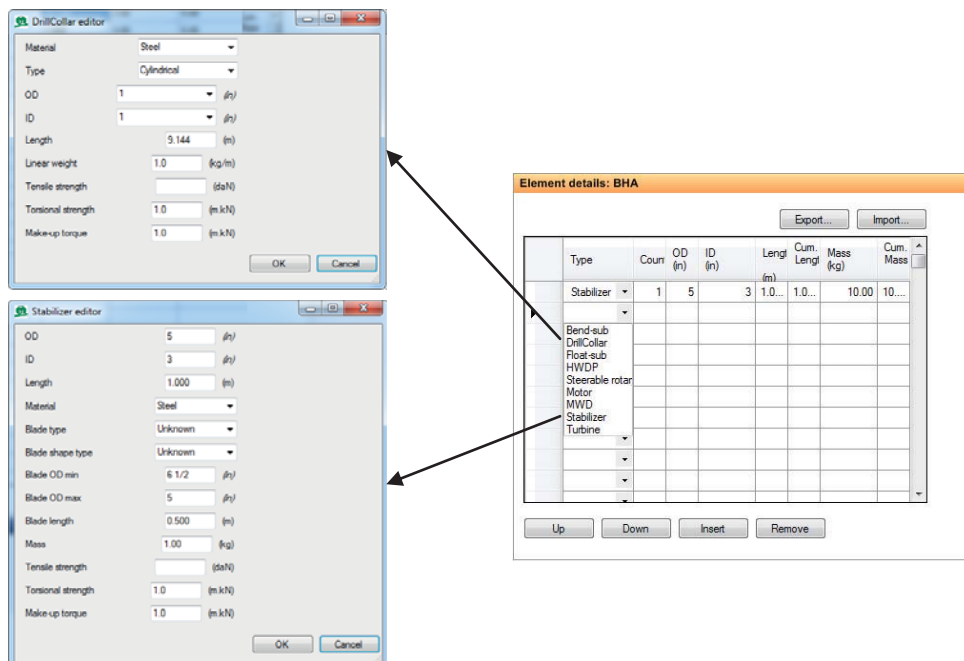
Figure 13: BHA table and input forms

315

2.3.4 Drill a Well on Paper

The initial thrust is the development of a (offline) drilling simulator to support the planning process of well construction. During this phase, a process known as "Drill Well on Paper" (DWOP) is carried out today, to determine the base plan. For this, the process of well construction is divided into several sub processes, which are addressed separately. In the first instance the drilling simulator is meant to support this DWOP process. For this purpose existing and newly developed modules from G and B-projects will be linked and used to prognose parameters and model drilling sub-processes in the planning phase.

In order to illustrate the power of the conceptual 7-tier-model as soul und practical software framework as body, DWOP is to be modeled, so that the wellbore construction is optimized by the casing setting depth under consideration of equivalent circulating density.

2.3.4.1 Problem description

Compare to the conventional wellbore construction with the lean construction in figure 14 shows a totally small casing profile. Small wellbore requires less material like casing, cement, mud and smaller rig. It can be drilled faster and reduce the time dependant drill cost.
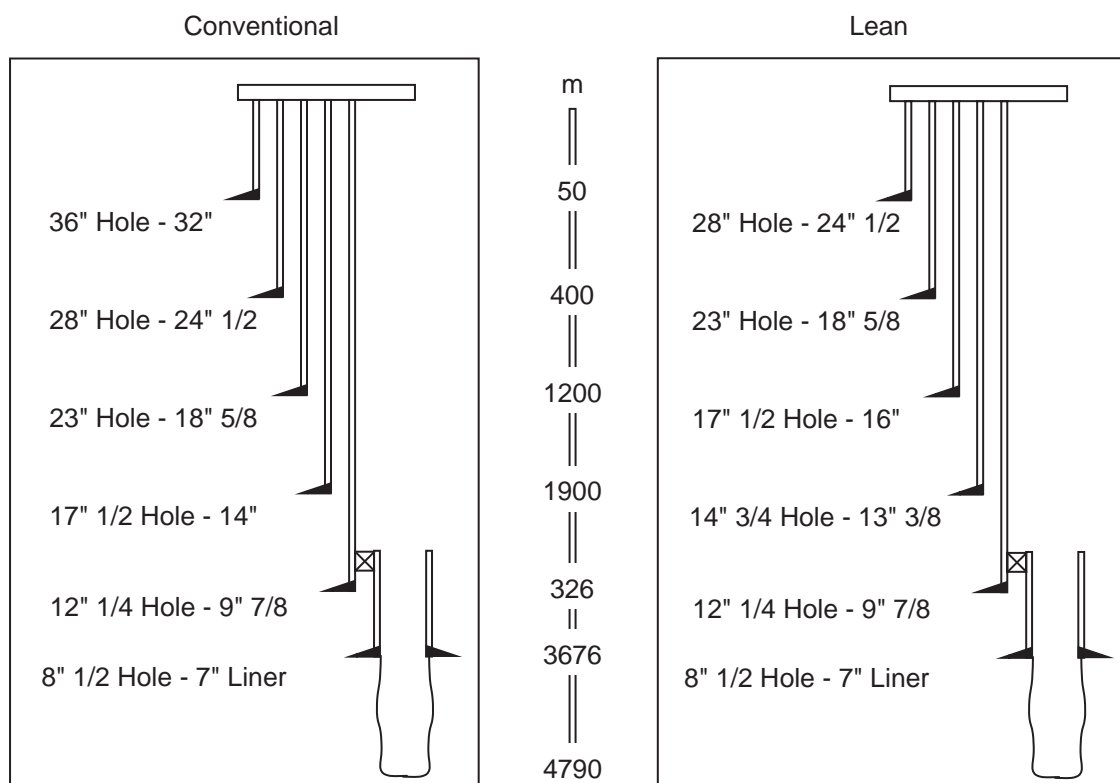
Figure 14: Conventional against lean well construction

However the lean wellbore construction also brings disadvantages due to the narrow annulus between the drillstring, open hole and casing. The annulus between drillstring and open leads to the frictional loss during circulation. This extra component increases the bottom hole pressure,

which can weak the kick margin or fracture the open hole. The annulus between casing and open hole increases also the bottom hole pressure during cementing and can also lead to fracture.
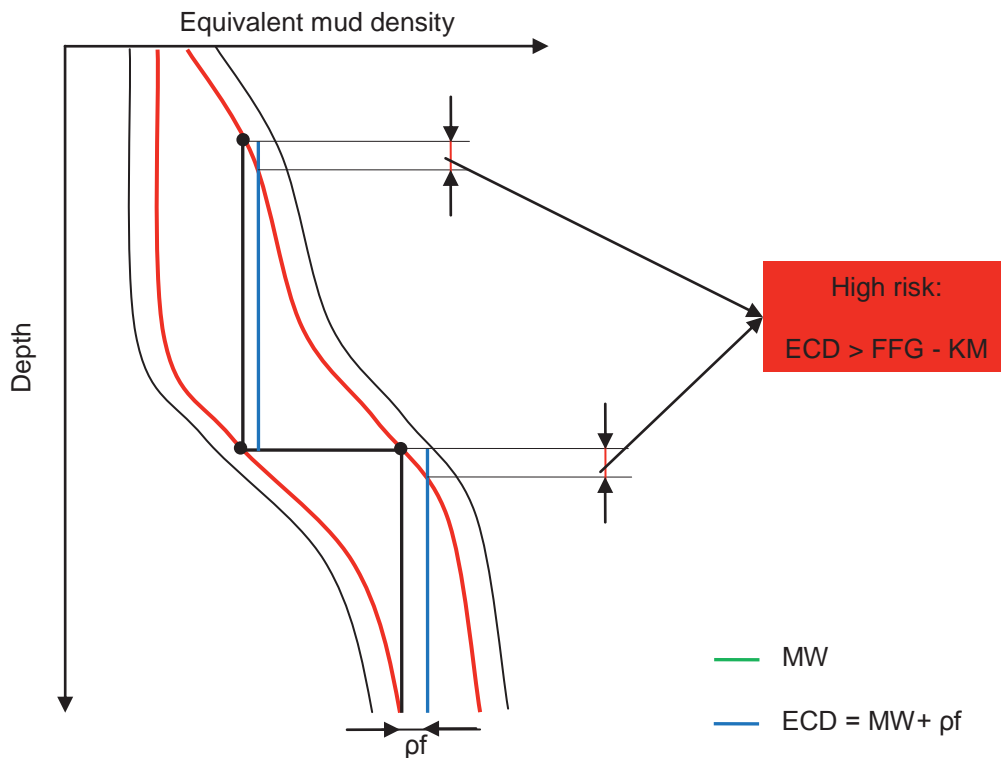
Figure 15: Mud window with ECD

2.3.4.2 Optimization with 7 tier model

Knowledgebase tier

The following part of this paper will describe, how the conceptual architecture is implemented in the planning module to determine the casing setting depth under consideration of mud equivalent circulating density.

All the research backgrounds including the importance of study, available methods with detailed steps and scientific reasons and so on, belong to the base tier, which can be seen as the start point of the development.

Casing serves several important functions in drilling and completing a well, such as consolidation of the hole already drilled and provide primary pressure control together with the BOP. Casing-program process includes the selection of casing seat depth, casing sizes and detailed design calculations that will enable the well to be drilled and operated safely throughout its whole life. In the well planning process, the selection of casing setting depth states a very important task. Many aspects, such as the mechanical and chemical properties of seat formation, directional well profiles etc. have to be considered in this selection.

Elements like pore pressure, geomechanics and well control are involved in the selection of the casing setting depth. The criterions can be summarized into two main scenarios, namely the wellbore stability constraints and integrity of casing itself. However, no matter which criteria is used to determine the casing setting depth, the other one will be applied to verify the result. Aadnoy 2012 describes the different methods in detail, which would not be repeated here. In this paper the determination of casing setting depth will be investigated with emphasis on the mud window and wellbore stability constraints. Therefore the casing integrity doesn't belong to the issues considered here and can be met through selection of different casing grades.

Wellbore stability constraints is generally based on consideration of the pore-pressure gradients and fracture-pressure gradients of the formations to be penetrated. The pore-pressure indicates the pressure of the pore fluid, which is usually water or gas. If the downhole pressure due to mud density is lower than the pore-pressure, the pore fluid will flow into the wellbore and leads to a kick. In the contrary, when the borehole pressure is increased to exceed the formation fracture pressure, the wellbore wall will eventually fail. Mud losses may occur through the resulting fracture. As shown in figure 16, the pore -pressure-gradient and fracture -gradient data are expressed as equivalent densities and plotted against depth. Figure 17 is also called mud window.

In addition, the mud densities are chosen to provide an acceptable trip margin above the anticipated formation pore pressures to allow for reductions in effective mud weight caused by upward pipe movement during tripping operations. At the same time, a kick margin is subtracted from the fracture-gradient line to obtain a design fracture-gradient line. If no kick margin is provided, it is impossible to absorb a kick at the casing-setting depth without causing formation fracture and a possible underground blowout. A commonly used trip margin or kick margin is 0,5 lbm/gal.
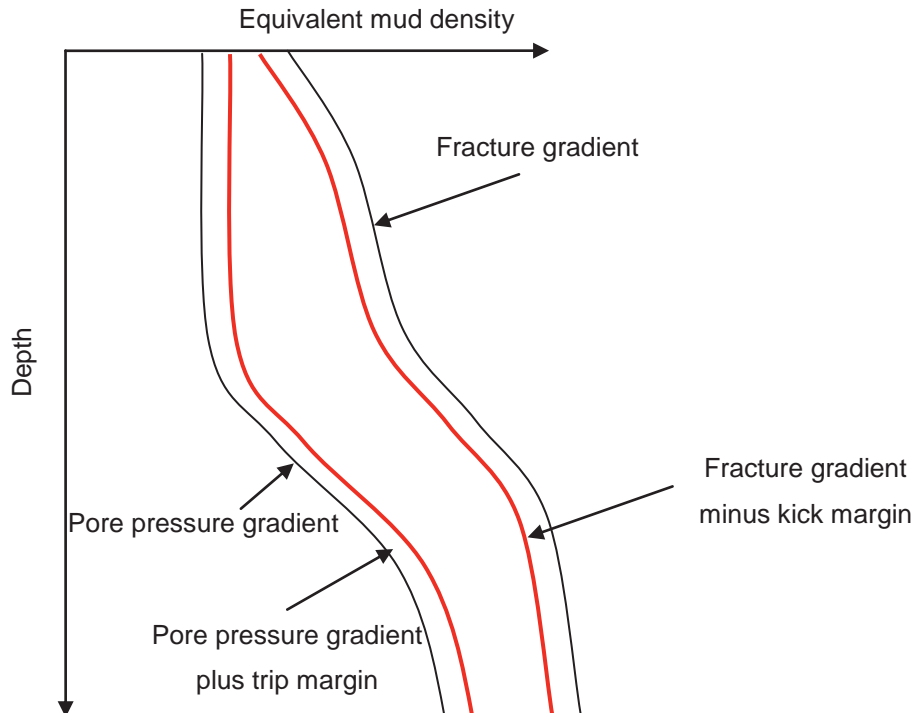
Figure 16: Projected formation pressures and fracture gradients and the safety margins [2]

In order to reach the target depth, the drilling-fluid density shown at point a is chosen. It represents the minimal fluid density to prevent the flow of formation fluid into the well and at the same time requires also the minimal energy to circulate it through the drillstring and wellbore. However, a protective intermediate casing must be set at least to the depth of point b, where the fracture gradient is equal to the mud density needed to drill to point a, if this fluid density is to be utilized without exceeding the fracture gradient of the weakest formation exposed within the open borehole. Similarly, to drill to point b and to set another intermediate casing, the drilling fluid density shown at point c will be needed with the same reason as point a and will require, that surface casing to be set at least to the depth at point d. The process is repeated until the surface is reached [3]
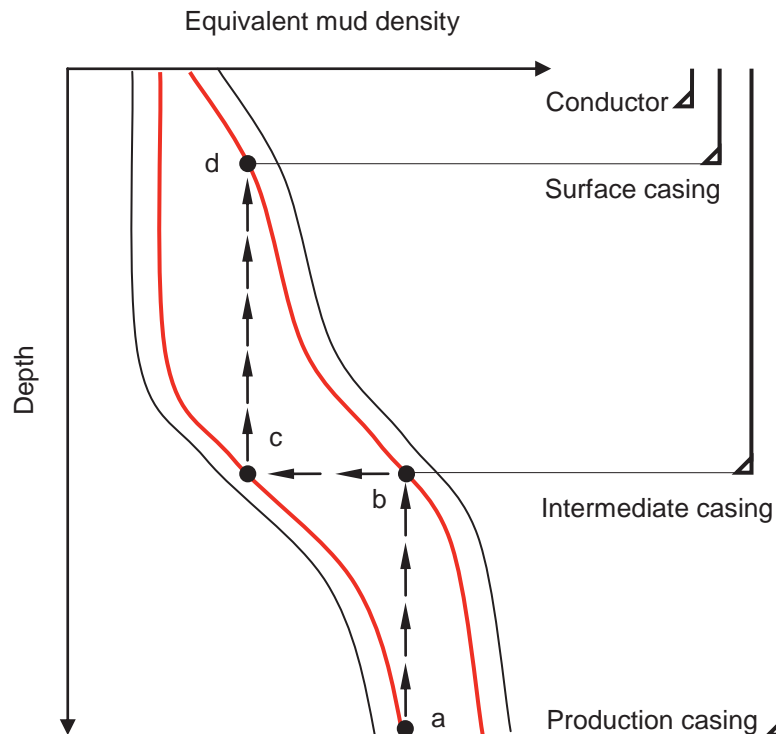
Figure 17: Determination of casing setting depth using bottom-to-top method [3]

As described above, the whole process to determine the casing setting depth is based on the principle, that the downhole pressure should be located within the safe area of the mud window or the area between both curves in figure 18. However, only the hydrostatic part of the fluid pressure or in other words the pressure in fluids at rest is considered so far. When the drilling fluid is circulating through the drillstring, the borehole pressure at the bottom of the annulus will be greater than the hydrostatic pressure of the mud. This extra pressure can be traced back to the frictional pressure loss required to pump the fluid up the annulus. This frictional pressure must be added to the hydrostatic from the mud column to get a true representation of the pressure acting against the formation at the bottom of the well. An equivalent circulating density (ECD) can then be calculated from the sum of the hydrostatic and frictional pressure divided by the true vertical depth of the well. The ECD for a system can be calculated from:

$$\rho_{ecd} = \frac{\Delta P_{friction}}{0.052 \cdot TVD} + \rho_M , ppg$$

Process tier

The frictional pressure loss depends on one hand on the rheological features of the mud type, which is pumped down into the wellbore and on the other hand on the cross sectional area of flow. If the effect of temperature on the mud properties is neglected temporarily, the frictional pressure loss will increase by a narrower cross section. This point represents a main factor, which is used to determine the calculation situation in the following step.

The frictional pressure loss increases the bottom hole pressure and weakens the function of kick margin to withstand a possible blowout. In order to improve the well planning, prevent wellbore-stability problems and reduce borehole drilling trouble time in the oil and gas industry, a new casing shoe setting depth method will be developed.

Based on the theoretical background described in the base tier above, process tier is supposed to design underlying workflows for the calculation with necessary parameters.

The focus of the new model is to improve the bottom-to-top method. Thus the classical bottom-to-top method will be performed at first to select the number of casing strings and their respective setting depth. In addition the geometrical combinations through the annulus between the borehole and drillstring should be also determined, with which die combinations of flow cross sectional areas are defined.

The size of casing strings and corresponding openhole diameter are controlled by the necessary inner diameter of the production string and the number of intermediate casing strings required to reach the depth objective. Selection of casing sizes that permit the use of commonly used bits is advantageous because the bit manufacturers make readily available a much larger variety of bit types and features in these common sizes. The common hole and casing sizes used to drill wells can be read from the figure of Greenip 1978.
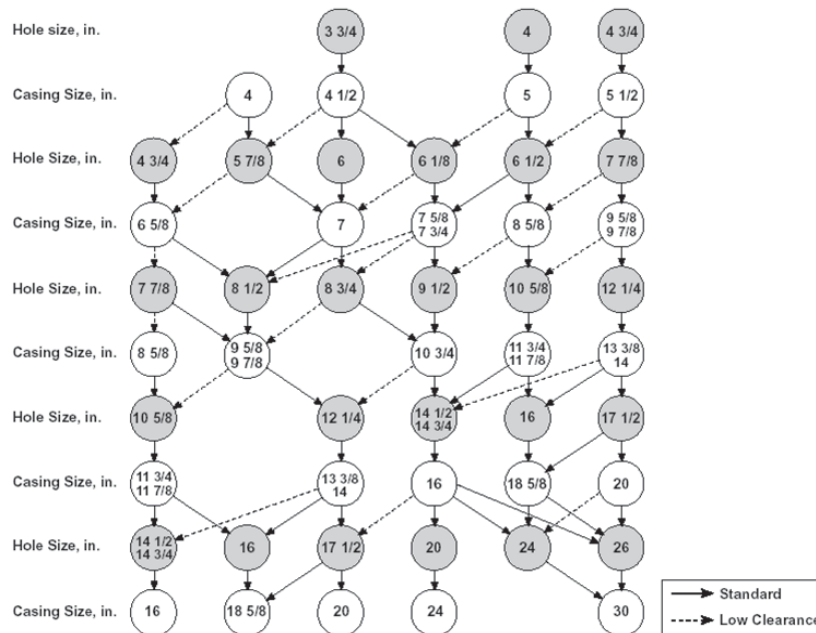
Figure 18: Casing hole size [4]

The underground part of drillstring consists typically of drillpipes connected with tool joints, bottomhole assembly (BHA) and bits. The process of drillstring design will not be described here. But according to the geometrical feature of drillstring, it will be simplified to BHA and drillpipes. Among the geometrical parameters, only the outer diameters of both elements and length of BHA will be considered hereby, since they build the outside profile of drillstring.

In addition, the ECD in respective openhole section will be investigated, while for the cased section the corresponding burst casing strength is valid.

Since a point in the openhole experiences the whole drilling operation of the section, the key of the calculation is to find the critical point, at which the frictional pressure loss through the annulus is the greatest. This is determined by the relative position of drillstring, which forms the annular space together with the fixed casing and openhole schema above the calculated point. Normally, this geometry goes through three combinations during the entire relevant drilling process, namely firstly drilled, BHA passing and BHA passed. According to the detailed analysis, which is based on the factor, that narrower cross section leads to higher pressure loss, the greatest annular friction pressure loss or the maximal value of ECD for a certain depth happens, when the corresponding point is just drilled. At that time, the thick-walled BHA is located totally above the point, which leads to the narrowest annular situation between drill string and wellbore above the investigated point.

The calculation is performed also according to the classical bottom-to-top method and shown schematically in figure 19. Because of the consideration of downhole ECD, the planned mud-density increases and this leads to the new determination of the casing shoe depth, which is normally deeper than the original one.

In summary the new calculation procedure consists of the following steps:

- Determine the number of casing strings with their respective setting depths and mud weight through the classical bottom-to-top method without frictional pressure loss.

- Select the casing sizes, hole sizes [4], corresponding drillstring geometry and mud properties.

- Again, start from the current last mud density to calculate the ECD at the openhole section in situation when it is just drilled and determine the casing shoe setting depth based on the ECD.

- Get the new mud density with the new casing depth and calculate the corresponding ECD with the following casing shoe depth until the surface.

- Check the formation competency to support the casing shoe.

- Adjust the final setting depth based on formation information. This can be done with some degree of contingency plus minus 50 to 100m.
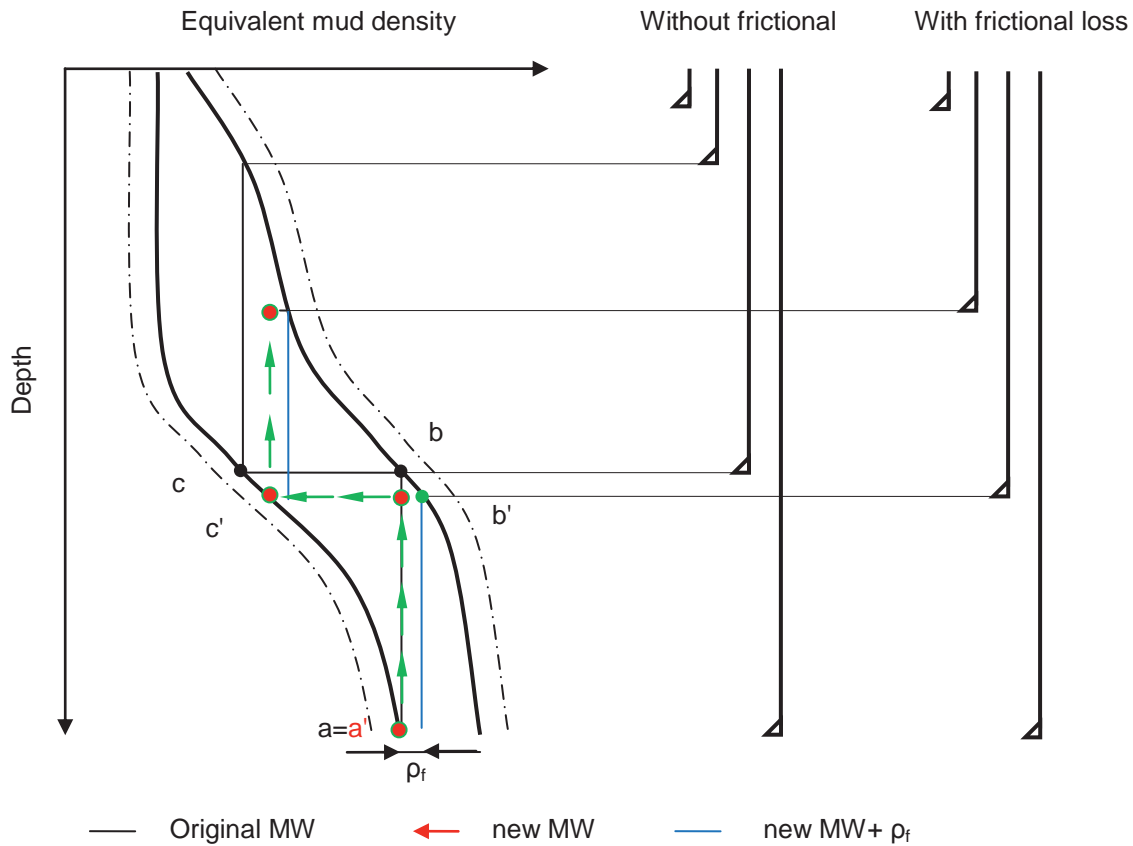
Figure 19: Determination of casing setting depth under consideration of downhole ECD

Data tier

After the calculation procedure is determined in the process tier, the necessary parameters for the data management in the data tier can be also summarized. They are:

- Lithological data: pore pressure gradient, fracture pressure gradient, formation information, kick margin and trip margin
- Telescopic wellbore and casing data: number of casings and open hole sections with corresponding inner diameter (ID) and depth
- Drillstring geometry: length and outer diameter (OD) of drill pipe and BHA
- Rheological data: density, rheometer data and so on for the mud used to drilled each section
- All cost aspects including casing, cement, mud, rig etc.

Furthermore, the data structure should also be considered here. For example, the pore pressure gradient and fracture pressure gradient could have many attributes from the prognosis in the planning phase and from the real time measurement in the drilling execution, which will be seen as a base for the development of logic tier.

Modeling tier

Now the actual calculation of ECD with emphasis on frictional pressure loss will be performed by means of mathematic and physic equations in the modeling tier. In the computation, only the

effects of viscous forces is commonly considered, since extremely large viscous forces must be overcome to move drilling fluid through the long slender annulus. It is a measure of a fluid's ability to resist external influences attempting to change its form. A mathematical description of viscous forces present in a fluid is called rheological model and the general models are Newtonian model, the Bingham plastic model, the power-law model and so on. Backgrounds of different rheological models will not described here. According to the speech with Mr. Aaragall of B5, the mud in this project will modeled with power-law model and cement with herschel-bulkley model.

Logic tier

The logic tier focuses in optimization of wellbore construction based on safety and drilling cost. It is clear in figure , that the consideration of equivalent circulating density leads to not only deeper casing but also heavier mud. This requires larger rig and more powerful pump, so that the drilling cost will be increased. The adjust of casing parameter is not avoidable but the design can be optimized.

The optimization can be performed with following steps:

- The optimization starts with the base scenario, by which all cost aspects should be defined including time independent cost like mud, cement, casing and time dependent cost like rig. Here the total casing number and diameter of production casing is assumed to be constant.
- Then all possible wellbore construction including conventional and lean profiles will be automatically determined according to figure18.
- In third step, the user has the possibility, to add extra casing to the constructions, by which the casing number is not enough and then all ID of casings are defined manually.
- The depths of casing shoes and mud weight are adjusted according to the ECD and mud window.
- Then the hydraulic and mechanic verification of cement and mechanic verification [1] of casing are performed.
- Based on the adjusted wellbore construction the drilling time can be calculated with trip model from B3
- With drilling time and wellbore construction all drilling costs can be determined
- The design, which passes all verification and shows the lowest drilling cost, is the optimal wellbore construction.

Visualization tier

In the visualization tier, the mud window for casing design and construction of drillstring are to be plotted technically friendly.

324

HMI tier

Finally, a graphic user interface is designed to enable the data input.

2.3.5 Open platform

Open platform or easy integration is one of the key objectives in project B2. After comparison, the integration interface is decided to be constructed with C# in .NET. Hereby not only the submodel should be integrated easily and safely but also a protocol about the required models, which are supposed to prepare for the input, is generated.

The submodel is preferred to be delivered in form of .dll, which offers the modeling service and at the same time keeps the code safely. The required information is defined through the following form.

Figure 20: Form to define model input

To show the protocol, the relationship in figure 21 is tested.
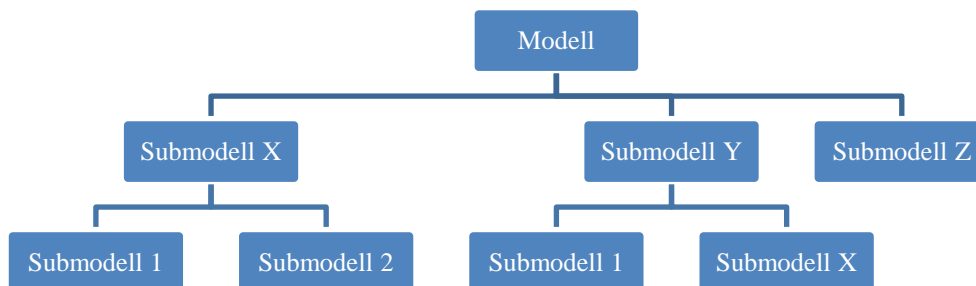
Figure 21: Relationships between models for example

The result shown in figure 22 illustrates the required models and the corresponding data transmition. And the calculation is also successful with assumed data.
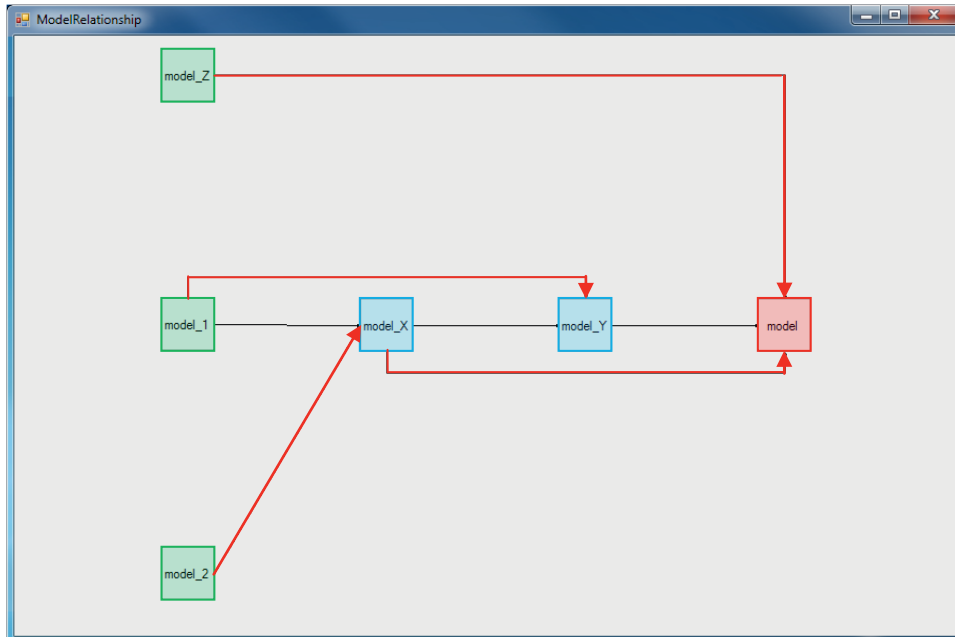
Figure 22: Model schema to integrate

2.3.5.1 Online data acquisition

The software framework is extended towards online platform with Wellsite Information Transfer Standard Markup Language (abbr. WITSML) data acquisition. First of all the WITSML log data is acquired in this framework.
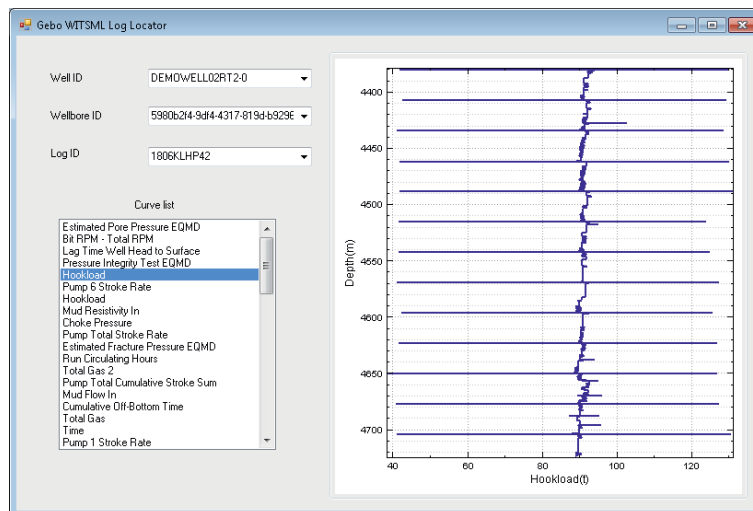
Figure 23: WITSML-Log-Locator

2.3.6 Improvement through fusion

The fusion or rewritten of individual program in framework shows a process of modularization and improvement.

Matrix tool is a program generated by a master thesis at ITE and aims to qualify the different drilling methods and technologies according to the geological situations. The idea behind it is innovative. However its structure does not merge with the simulator concept. For all casing

types, it is constructed repeatedly, the unit is not unique and due to the missing data structure it is impossible to work together with other. After the fusion, the program is according to the corresponding functions modularized. For all casing types there is only one GUI, which is customized according to the specific casing type. Unit environment is added and now the unit is no more defined but generated from the server. With the data structure the program can work either alone or together with other aspects.
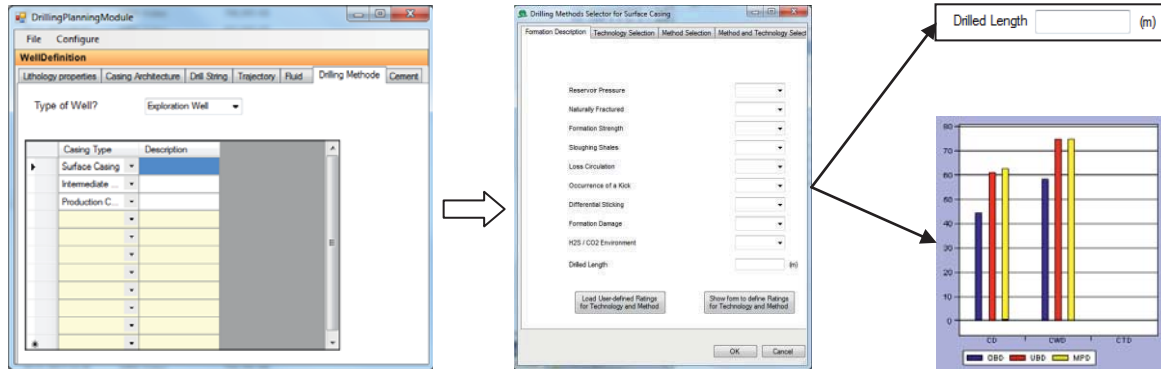
Figure 24: Modularized GUI of matrixtool

1.1.2.3.7   Simulation

2.3.7.1 Monobore construction [7]

First of all the monobore construction module allow to generate the casing schema and mud weight. Since the drilling process of monobore has not been normalized, the drilling time estimation is not included.
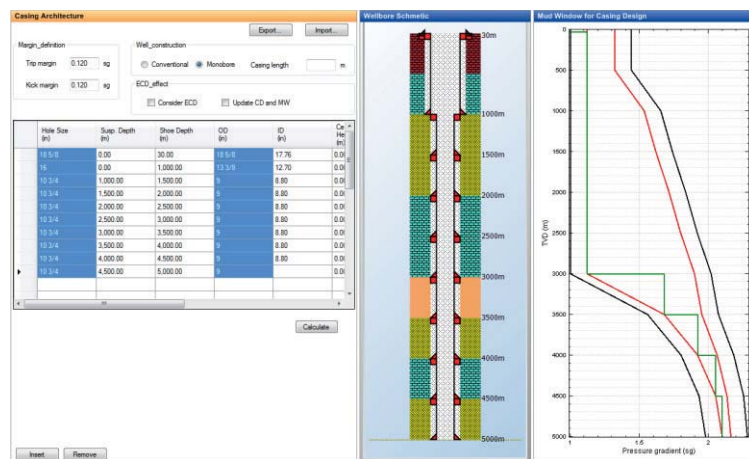
Figure 25: Mud window for monobore construction

2.3.7.2 ECD process

The ECD development along the open hole shows two typical shape, namely the increasing-decreasing and mono increasing tendency. This can be traced back to the combination of flow area and flow regime.
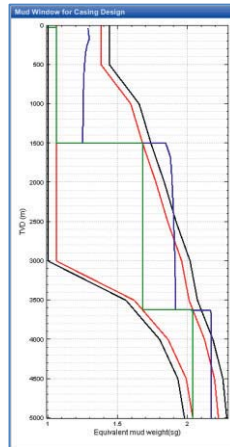
Figure 26: Modeled ECD processes

2.3.7.3 Case study

The first case study focuses on a continues mud window with narrow area at the bottom. The result shows that under consideration of ECD not only the casing will be set deeper but also the mud should be heavier. This will increase the drilling cost but matches the philosophy, that for more safety more money should be invested.
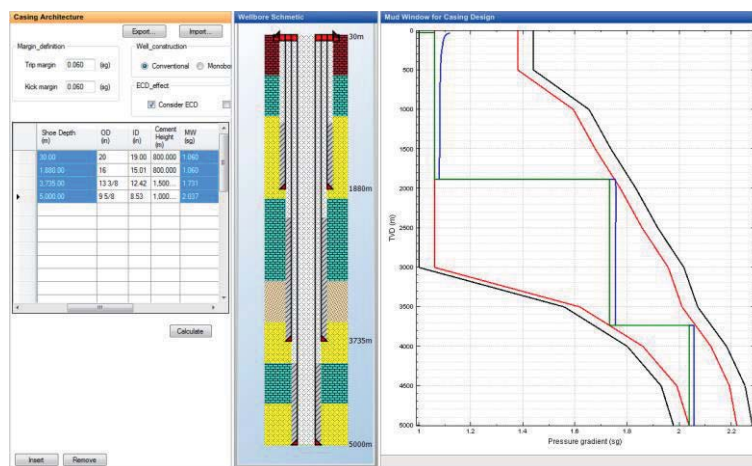
Figure 27: CSD and MW with ECD

The second case studies the situation with abnormal zone, by which the casing setting depth is not determined with relationship between PPG and FPG. In this case, the only way to decrease the ECD is to enlarge the flow area through a new casing hole construction.
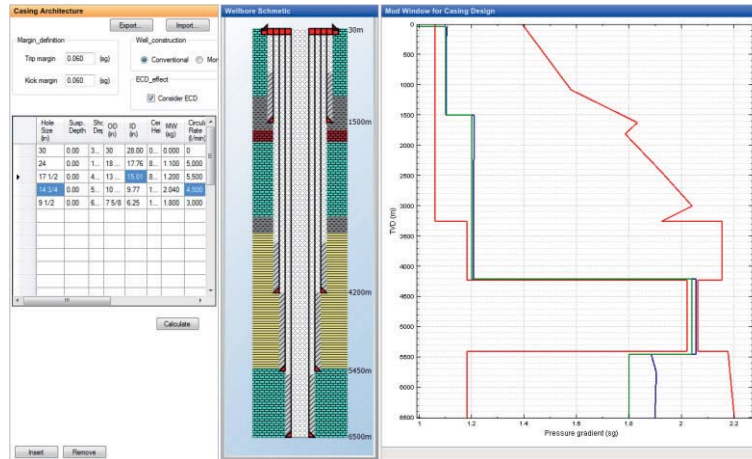
Figure 28: Mud window for a overpressure zone

2.3.7.4 Optimization

In this work the optimization of three wellbore constructions will be studied, namely the standard construction, lean construction from at bottom and lean construction at top.

The simulation results for first two cases are shown in table 2. Due to the ECD the casing should be set to the deeper formation to avoid formation fracking. Especially the first intermediate casing is 150m deeper. By comparison the change of mud weight is not high.

Furthermore, the hydraulic verification for cementing fails by lean construction at bottom. Adjust of wellbore schema can be only performed by enlarging the open hole in the final section, otherwise it will require another wellbore construction, but it is not qualified for the verification, because the ECD at casing shoe depends on the annulus between two casings. Therefore, the lean construction is hydraulically adjusted by cementing and verified by mud, see figure 31.

This leads to an extra casing and the casing schema is shown in table 3. Only so the hydraulic verification by cementing will pass.

Standard construction					Lean construction at bottom				
Hole (in)	Csg. OD (in)	Depth (m)	MW (sg)	CR (L/min)	Hole (in)	Csg. OD (in)	Depth (m)	MW (sg)	CR (L/min)
35	35	30	0	0	30	30	30	0	0
30	24 1/2	800	1,06	23000	24	18 5/8	800	1,06	16800
23	18 5/8	1775	1,06	12000	17 1/2	16	1925	1,06	5500
17 1/2	13 3/8	3715	1,73	6100	14 1/2	11 3/4	3765	1,75	4000
12 1/4	9 5/8	5000	2,04	2200	10 5/8	9 5/8	5000	2,04	1350

Table 2: Wellbore construction for standard and lean profile

Casing	Cement	Weight (s.g.)	Height (m)	Rate (l/min)
SC	C1	1,3	800	1000
IC 1	C1	1,3	800	1000
IC 2	C2	1,8	1500	400
PC	C3	2,1	1000	300
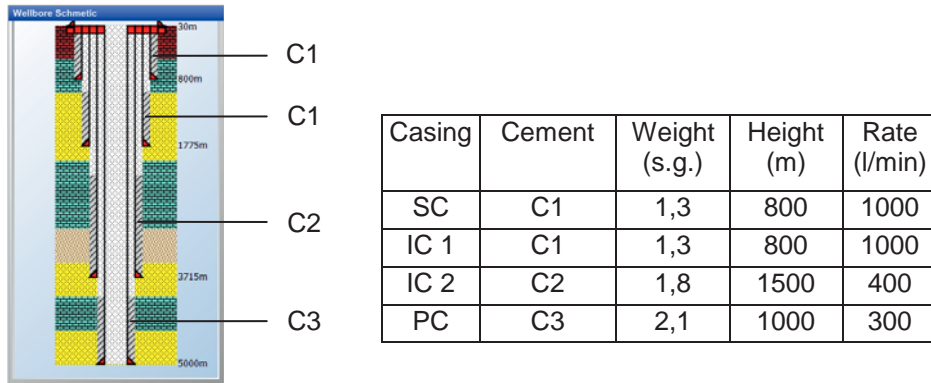
Figure 29: Cement data
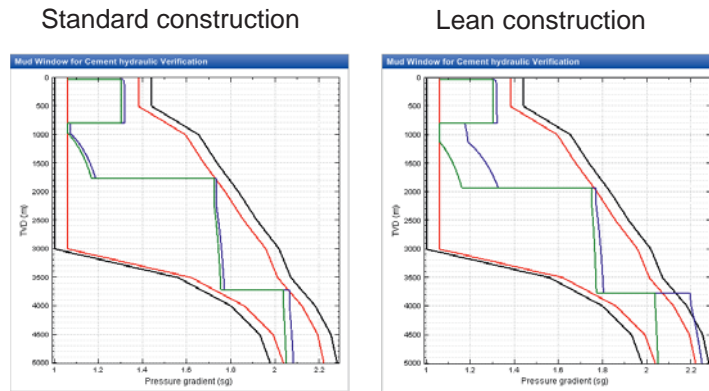
Figure 30: Hydraulic verification of cementing
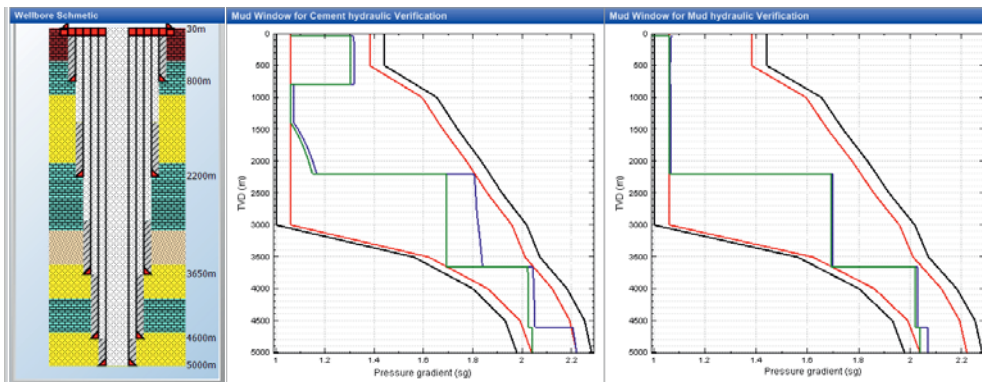
Figure 31: Adjust of wellbore construction with ECD model in cementing

Modified lean construction						
Hole (in)	Csg. OD (in)	Depth (m)	MW (sg)	CW (s.g.)	CH (m)	CR (l/min)
35	35	30	0	0	0	0
30	24 1/2	800	1,06	1,3	800	1000
23	18 5/8	2200	1,06	1,3	800	1000
17 1/2	16	3650	1,69	1,7	800	1000
14 1/2	11 3/4	4600	2,02	2,03	1500	400
11	9 5/8	5000	2,04	2,05	1000	300

Table 3: Modified lean construction

The cost aspects are calculated for both cases. Due to the extra casing, the lean construction at bottom costs in contrast 29% more than the standard construction, see table 4. By comparison the lean construction at top starts with standard casing clearance at bottom and then switch to low clearance. Although both lean construcẗons have two low clearances, the position of low clearance determines the success of construction.

Casing	Time (Tag)		Casing weight (Ton)		Mud volume (m³)		Cement volume (m³)	
	standard	lean	standard	lean	standard	lean	standard	lean
SC (L80)	2.1	2.1	166	166	1834	1834	185	185
IC (L80)	5.4	7.6	231	286	1936	2391	111	111
IC (L150)	25.8	21.3	398	407	2339	2306	145	30
IC (L140)	✕	22.7	✕	360	✕	2096	✕	90
PC (L140)	20.2	7.9	427	427	1539	1195	44	18
Sum	53.5	61.6	1222	1646	7648	9822	485	434
		+15.3%		+34.7%		+28.4%		-10.5%
							Total drilling cost (M€)	
							standard	lean
							10.3	13,3
								+29%

Table 4: Cost aspects between standard and lean constructions

Standard construction					Lean construction in upper sections				
Hole (in)	Csg. OD (in)	Depth (m)	MW (sg)	CR (L/min)	Hole (in)	Csg. OD (in)	Depth (m)	MW (sg)	CR (L/min)
35	35	30	0	0	30	30	30	0	0
30	24 1/2	800	1.06	23000	24	18 5/8	800	1.06	17000
23	18 5/8	1775	1.06	12000	17 1/2	16	1795	1.06	5500
17 1/2	13 3/8	3715	1.73	6100	14 3/4	13 3/8	3715	1.73	4000
12 1/4	9 5/8	5000	2.04	2200	12 1/4	9 5/8	5000	2.04	2200

Table 5: Wellbore construction for standard and lean profile in upper sections

The hydraulic verification of lean construction at top also fails, see figure 32. However it happens at the second intermediate casing and furthermore it passes at same section. After the deepening the casing shoe by about 300m, the hydraulic verification successes (figure 33). According to the cost calculation for this case, the lean construction is proved to be more economic.

Lean construction

Cement	Weight (s.g.)	Height (m)	Rate (l/min)
C1	1,3	800	1000
C1	1,3	800	1000
C2	1,75	1500	400
C3	2,1	1000	300
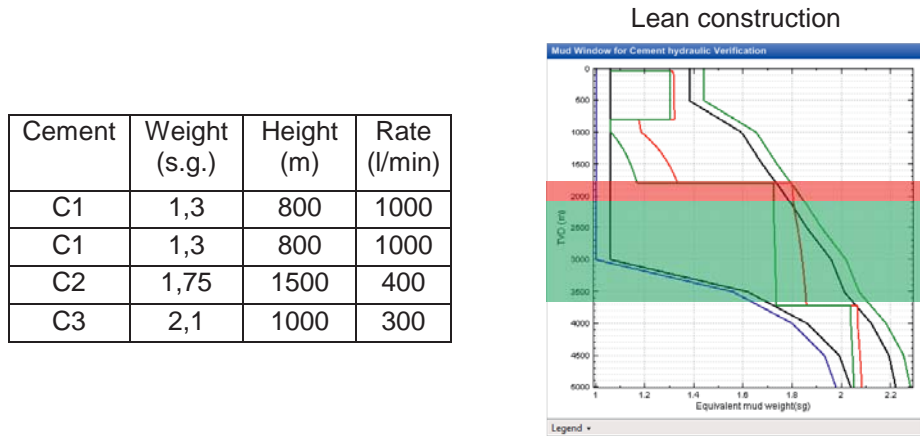
Figure 32: Hydraulic verification of lean profile in upper sections
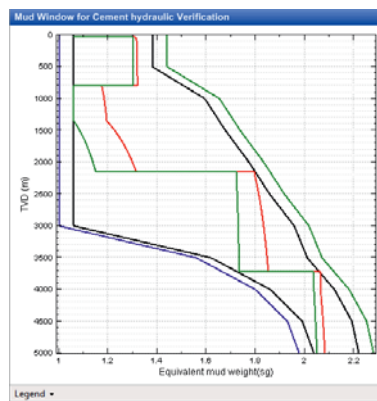
Figure 33: Hydraulic verification of lean profile in upper sections after modification

Casing	Time (Tag)		Casing weight (Ton)		Mud volume (m^3)		Cement volume (m^3)	
	standard	lean	standard	lean	standard	lean	standard	lean
SC (L80)	2.1	2.0	166	102	1834	1183	185	144
IC (L80)	5.4	5.2	231	243	1936	1350	111	30
IC (L150)	25.8	15.6	398	398	2339	1686	145	44
PC (L140)	20.2	20.2	427	427	1539	1539	44	44
Sum	53.5	43	1222	1170	7648	5758	485	262
		-19.6%		-4%		-24.7%		-46%
							Total drilling cost (M€)	
							standard	lean
							10,3	8.8
								-14,5%

Table 6: Cost aspects between standard and lean construction in upper sections

2.4 Conclusions

At the beginning of this project the available drilling simulators nowadays are summarized with emphasis of the features in corresponding aspects.

A conceptual and software framework was developed, which structures all the scientific knowledge of drilling simulator and at the same time supports concrete implementation with software modules.

Architecturally complex drilling systems can be subdivided into tiers of knowledge base, process, database, modeling, logic, visualization and human machine interface. Each tier represents a particular aspect of the drilling simulator and interacts with others. A representation of the complete drilling process can be achieved.

The developed software framework shows to be a very friendly and powerful environment to implement models, to perform simulation after integration, to visualize the results and to manage data. It is modularly designed and presents a good extensibility with a standardized process.

With the support from powerful conceptual and software frameworks developed herein, the Drill a Well on Paper is optimized in terms of the lean wellbore construction under consideration of equivalent circulating density of mud and cement. The drilling costs are also calculated. Furthermore a module to real time data acquisition from a Wellsite Information Transfer Standard Markup Language server is realized.

In the future the prototypical software framework and databank will be extended. In addition more models from gebo projects should be integrated, in order to show the capability of the framework and to achieve a better description of drilling processes.

3 Demarcation from other funded projects

At this time no other project similar with B2 are ongoing at the institute

References

[1]   Aadnoy, B.S., Kaarstad E., Belayneh M. (2012): Multiple Criteria Casing Seat Selection Method, SPE 150931, IADC/SPE Drilling Conference and Exhibition held in San Diego, California, USA, 6-8 March 2012

[2]   Adams, N. (1980): Well Control Problems and Solutions, Petroleum Publishing Company, Tulsa, Oklahoma

[3]   Adam T. Bourgoyne Jr., Keith K. Millheim, Martin E. Chenevert, F.S. Young Jr. (1986): Applied Drilling Engineering, Society of Petroleum Engineers, Richardson, TX USA

[4]   Greenip, J.F. Jr. (1978): Designing and Running Pipe, Oil and Gas J. (9, 16, and 30 October and 13 and 27 November)

[5]   Jan-Einar Gravadal: "Drilling related activities at IRIS", Presentation, Celle, Germany, 01 October 2010

[6]   Rolv Rommetveit: "Drilling a Challenging HPHT Well Utilizing an Advanced ECD Management System with Decision Support and Real Time Simulations", IADC/SPE Drilling Conference and Exhibition, New Orleans, U.S.A., 2-4 February 2010, SPE 128648

[7]   Teodoriu, C., Lehr, J., Grimmer, H. (2012): A New Method for Casing Shoe Depth Calculation with Application to Monobore Well Construction, DGMK/ÖGEW-Frühjahrstagung, Celle, 19-20 April 2012

[8]   Teodoriu, C. Drilling Simulator in Celle: , Celle Drilling, 2013, September 2013

Abschlussbericht im gebo-Teilprojekt

B3: Automatisierung des Bohrprozesses durch den Einsatz eines flexiblen Bohrstrangs

B3: Automation of the drilling process by the application of a flexible drill rod

Inhaltsverzeichnis

1 Einleitung und Motivation

Im Schwerpunkt Bohrtechnik des Forschungsverbundes „Geothermie und Hochleistungsbohrtechnik" (gebo) werden Methoden untersucht, die zu einer Senkung der Bohrkosten führen. Ein zentraler Ansatz ist dabei die Herstellung einer Mono-Durchmesser-Bohrung mithilfe von kleeblattförmig gefalteten Futterrohren. In Abbildung 1-1 ist der schematische Aufbau einer Mono-Durchmesser-Bohrung sowie der Querschnitt dieses gefalteten Futterrohrs dargestellt.
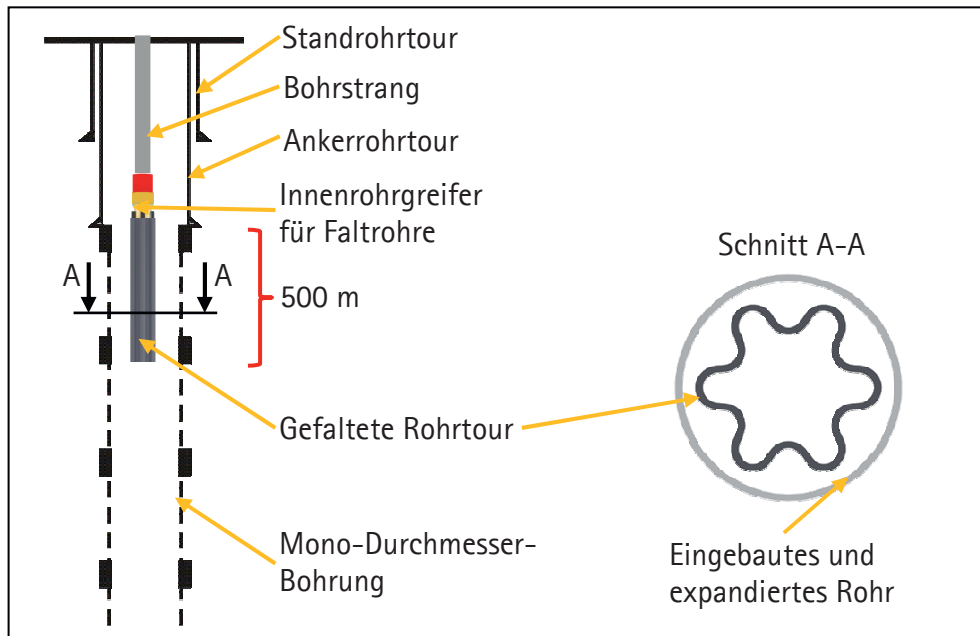
Abbildung 1.1: Das gebo–Konzept und die verwendete Faltrohrgeometrie.

Nach dem Einbau der Stand- und der Ankerrohrtour werden Rohrtouren aus gefalteten Futterrohren mit einem speziellen Innenrohrgreifer an die gewünschte Untertageposition befördert und dort auf einen zylindrischen Querschnitt expandiert. Die maximale Länge einer Rohrtour wurde im gebo-Forschungsverbund auf 500 m festgelegt. Um das vollständige Expansionspotenzial dieser Rohrstrukturen nutzen zu können, ist der Einsatz eines hochfesten und hochduktilen Stahls (Duplex-Stahl 1.4462 mit einer Streckgrenze von $R_{p0,2} = 450$ N/mm²) mit einem Verformungspotenzial von über 30 % notwendig [VBH1].

Im Rahmen des Teilprojekts B3 wurden Konzepte zur Handhabung und Verbindung gefalteter Futterrohre zu einer Rohrtour und zum anschließenden Einbringen der Rohrtour in die Bohrung erstellt und untersucht. Bestehende Systeme an Tiefbohranlagen sind jedoch ausschließlich auf Rohre mit zylindrischem Querschnitt ausgelegt, wodurch sich ein Entwicklungsbedarf vor allem im Bereich der Greif- und Verbindungseinheiten ergab. Zusätzlich wurde der Materialfluss für die gefalteten Futterrohre untersucht. Hierbei war auf eine zeitliche Optimierung des Materialflusses zu achten. Um die Einflussfaktoren auf die Zeitanteile im Rahmen des Materialflusses analysieren und bewerten zu können, wurde ein Berechnungsmodell entwickelt, welches den zeitlichen Ablauf von Tiefbohrung mit zuvor definierten Tiefbohranlagen detailliert nachbildet.

2 Handhabung und Verbindung von gefalteten Rohren

An konventionellen Tiefbohranlagen werden sowohl die Bohrstrangkomponenten als auch die Futterrohre in etwa 9 m langen Segmenten angeliefert, gelagert und mithilfe eines Handhabungssystems zur Arbeitsplattform transportiert. Dort werden die Segmente mit dem Bohrstrang bzw. der Rohrtour über eine Gewindeverbindung verbunden.

Die Handhabung und Verbindung von Rohren mit komplexen, nicht zylindrischen Querschnitten wird durch die derzeit verwendeten Systeme an den Bohranlagen jedoch nicht unterstützt. Daher sind Anpassungen erforderlich, die sowohl die Lager- und Handhabungseinrichtungen als auch die Verbindungstechnik modifizieren.

2.1 Handhabung der gefalteten Rohre

Die Handhabung der gefalteten Rohrsegmente beginnt mit dem Vereinzeln aus einem Lager oder Magazin. Um einen sicheren Handhabungsprozess und damit auch einen sicheren Verbindungsprozess zu garantieren, muss die Lage des Rohrsegments jederzeit bekannt sein. Daher ist zunächst ein Magazin für Faltrohre zu entwickeln, welches einen sicheren Transport und die Bereitstellung der Faltrohre ohne die Gefahr einer unvorhergesehenen Lageänderung gewährleistet. Die Abbildung 2.1 zeigt das im Rahmen des gebo-Teilprojekts B3 entworfene modulare Faltrohrmagazin.
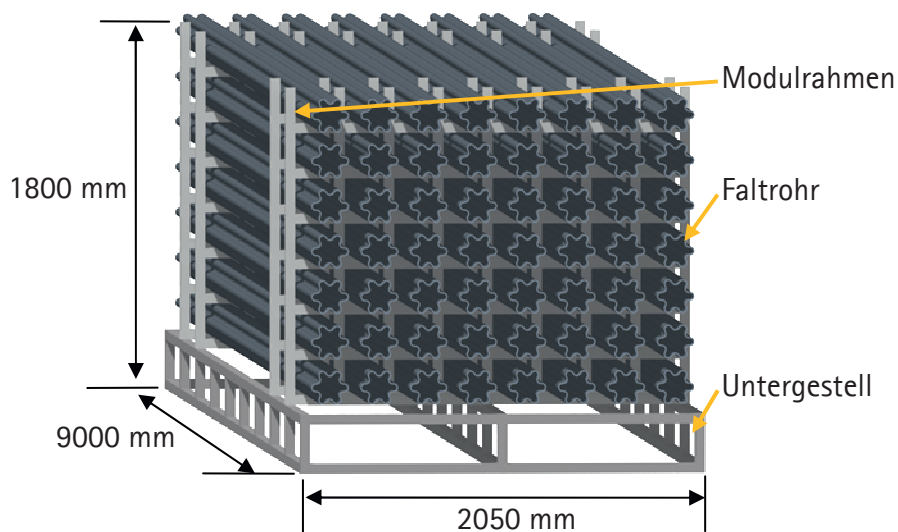
Abbildung 2.1: Modulares Magazin für gefaltete Futterrohrsegmente

Das Magazin besteht aus mehreren Modulrahmen, die über ein Stecksystem miteinander und mit dem Untergestell verbunden sind. Das Untergestell hat eine Grundfläche von 2050x9000 mm und erlaubt eine Handhabung durch gängige Fördermittel, wie z. B. Gabel- und Containerstapler oder Reach Stacker. Die Modulrahmen lassen sich nach dem Baukastenprinzip auf das Untergestell stecken. Dadurch entstehen Lagerplätze, in denen Faltrohrsegmente in einer definierten Orientierung eingelagert werden können. Ein Verdrehen der Faltrohrsegmente ist in diesen Lagerplätzen nicht möglich. Je nach Anzahl der Modulrahmen lässt sich die Kapazität des

Magazins erhöhen. In der oben dargestellten Form besitzt das Magazin eine Höhe von 1,8 m und kann Faltrohrsegmente mit einer Gesamtlänge von etwa 504 m aufnehmen. Die Montage einer zusätzlichen Bodenplatte an die Stirnseite des Untergestells erlaubt ein Aufstellen des Magazins, wodurch der Einsatz sowohl als Horizontallager als auch als Vertikallager möglich ist.

Für den Transport zwischen Lager und Arbeitsplattform sind angepasste Greifeinrichtungen notwendig. Zur Entnahme der Faltrohre aus dem Magazin und zum Transport ist eine Greifeinheit für die gefaltete Außenkontur entwickelt worden. Diese ist auf der folgenden Abbildung dargestellt.
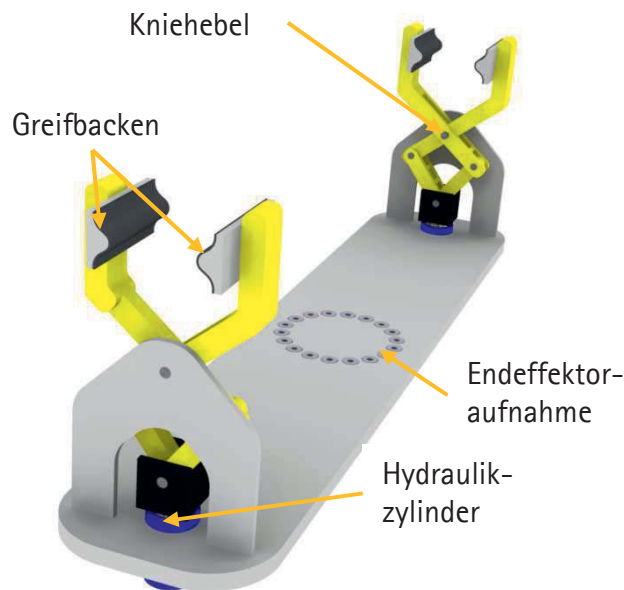
Abbildung 2.2: Greifeinheit für die Außenkontur der gefalteten Rohre

Die Greifeinheit besteht aus zwei Greifern, die mithilfe von Hydraulikzylindern betätigt werden. Die Bewegung des Hydraulikzylinders für die notwendige Greifkraft wird über Kniehebel auf die Greifbacken übertragen. Aufgrund dieses Prinzips ist eine flache Bauweise der Greifer und somit ein Vereinzeln der gefalteten Rohre aus dem Magazin möglich. Die Greifbacken der Greifer weisen eine Negativform der gefalteten Rohrkontur auf, um eine sichere Handhabung der Faltrohrsegmente zu gewährleisten.

Die Prozesse auf der Arbeitsplattform erfordern, sowohl für die Zuführung in einen Verbindungsautomaten als auch zum Einfahren der Rohrtour in die Bohrung, eine Manipulation der Faltrohrsegmente in vertikaler Ausrichtung. Für diese Handhabungsart werden an konventionellen Tiefbohranlagen Elevatoren und Casing Running Tools eingesetzt. Da diese Komponenten jedoch auf zylindrische Rohrquerschnitte ausgelegt sind, ist die Entwicklung eines angepassten Innenrohrgreifers unumgänglich. Der entwickelte Greifer ist in Abbildung 2.3 dargestellt.
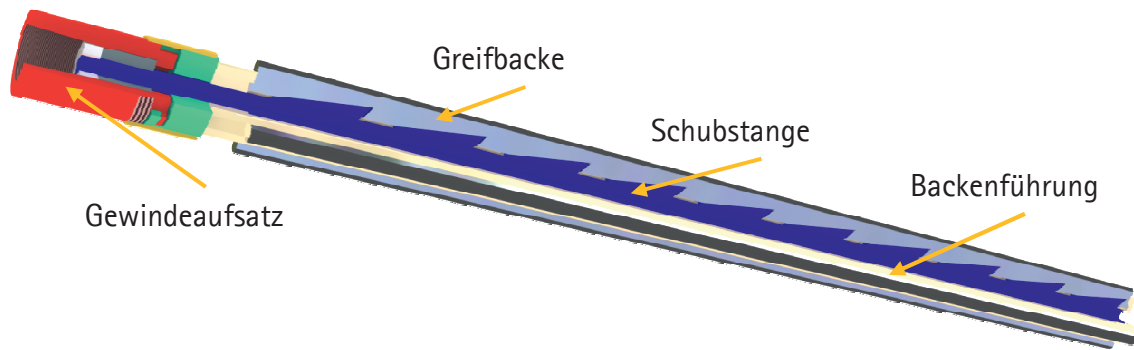
Abbildung 2.3: Schnittansicht des Innenrohrgreifers für gefaltete Rohrkonturen

Der Greifer funktioniert nach dem Spreizkegelprinzip. Ist der Greifmechanismus aktiviert, werden die Greifbacken durch die Bewegung der Schubstange und der darauf befindlichen Keile zu einer radialen Bewegung gezwungen. Der Winkel der Keilflächen ist so gewählt worden, dass der Greifer automatisch die benötigte Kraft zum Halten der Faltrohrtour bereitstellt. Mit dem Innenrohrgreifer ist es möglich, eine Faltrohrtour mit einem Nenndurchmesser von $8^{5}/_{8}$ in und einer Länge von 500 m zu halten und in das Bohrloch abzulassen, ohne dass plastische Verformungen an den Komponenten des Greifers oder den Faltrohren auftreten. Eine ausführliche Beschreibung dieser Untersuchungen ist im 3. Meilensteinbericht dargestellt. [Bär13c]

2.2 Verbindung von gefalteten Rohrsegmenten

Die Verbindung der gefalteten Futterrohrsegmente ist nicht wie bei konventionellen Ölfeldrohren über Gewindeverbindungen realisierbar. Im Rahmen des gebo-Teilprojekts W5 wird daher ein Schweißverfahren mit magnetisch bewegtem Lichtbogen (MBL, engl. Magnetically Impelled Arc Butt, MIAB) als alternative Verbindungsmethode untersucht. Dieses Verfahren ist schematisch in Abbildung 2.4 dargestellt.
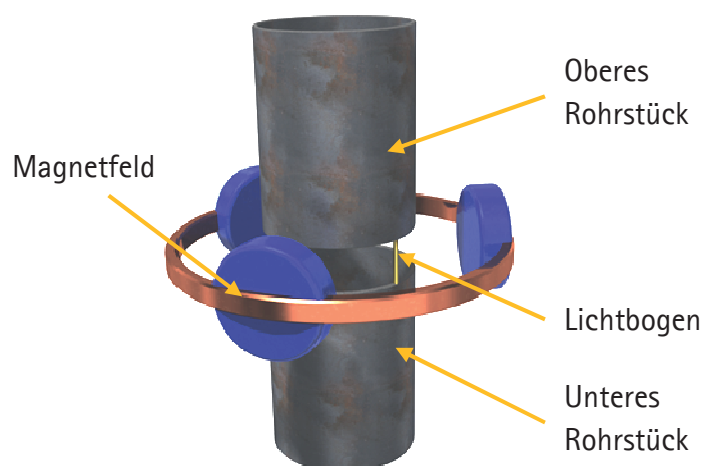
Abbildung 2.4: Schematische Darstellung des MIAB–Schweißverfahrens

Bei diesem Schweißverfahren wird ein Lichtbogen zwischen den Stirnflächen zwei einander gegenüber positionierter Rohre gezündet. Dieser Lichtbogen wird mithilfe der Lorentzkraft, die über ein Magnetfeld erzeugt wird, zwischen den Stirnflächen der Rohre rotiert. Der umlaufende Lichtbogen erhitzt die Stirnflächen der Rohre, bis diese aufgeschmolzen sind. Durch ein Zusammenpressen der Rohre werden diese gefügt.

Aus Gründen des Explosionsschutzes sowie zur Sicherstellung einer gleichbleibenden Schweißnahtgüte hat der Schweißprozess unter Schutzgas zu erfolgen. Um eine Schutzgasatmosphäre im Bereich der Fügestelle zu gewährleisten, ist eine Abdichtung vor allem der Rohrinnenkontur der gefalteten Rohre von großer Bedeutung. Im Rahmen dieses Projekts wurde deshalb ein Dichtwerkzeug für die Innenkontur der gefalteten Rohre entwickelt.

2.3 Entwicklung eines multifunktionalen Innenrohrwerkzeugs

Um die Handhabungszeiten der gefalteten Rohre gering zu halten, wird die Integration eines Dichtwerkzeugs innerhalb des Innengreifers aus Abbildung 2.3 angestrebt. Somit lässt sich ein Werkzeugwechsel zwischen Schweiß- und Absenkvorgang vermeiden und eine erhebliche Zeitersparnis realisieren. Ein erstes Konzept für die Umsetzung eines derartigen multifunktionalen Innenrohrwerkzeugs ist in Abbildung 2.5 dargestellt.
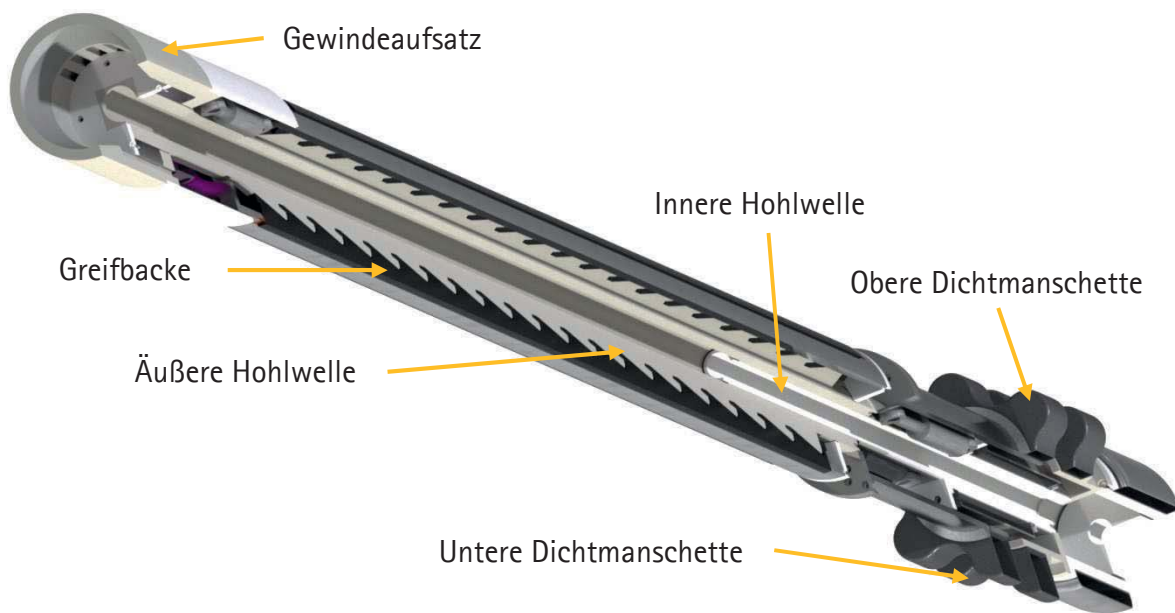
Abbildung 2.5: Schnittansicht des multifunktionalen Innenrohrwerkzeugs

Analog zum Innenrohrgreifsystem aus Abbildung 2.3 wird der Greifmechanismus über eine Schubstange betätigt, die die Greifbacken über Keile bewegt. Allerdings ist die Schubstange bei diesem Werkzeug als Hohlwelle ausgeführt, um eine Versorgung der Dichtmanschetten im unteren Bereich des Werkzeugs mit Druckluft zu ermöglichen. In der äußeren Hohlwelle läuft eine innere Hohlwelle, die an ihrem unteren Ende einen Wellenabsatz besitzt. Auf diesem Wellenabsatz wird die untere Dichtmanschette montiert. Die obere Dichtmanschette befindet sich auf einem Wellenabsatz des oberen Gehäuses. Eine axiale Gleitlagerung der inneren Hohlwelle in der äußeren Hohlwelle erlaubt eine Variation des Dichtmanschettenabstands sowie eine Kompensation der Bewegungen während des Schweißprozesses. Dieses Konzept, jedoch zur Abdichtung zylindrischer Rohre, ist zusammen mit der Firma Baker Hughes in den Schutzrechten [HVB13] und [HVB13a] patentiert worden.

3 Konzepte zur Handhabung gefalteter Futterrohre an Tiefbohranlagen

Eine hohe Reduzierung der Kosten für die Herstellung der Tiefbohrung wird erzielt, wenn die Tiefbohranlage mit maximaler Effizienz arbeitet. Dafür ist eine zeitlich optimierte Handhabung der gefalteten Futterrohre erforderlich. Im Folgenden werden die im Rahmen dieses Teilprojekts untersuchten Handhabungskonzepte näher erläutert.

3.1 Konventionelle Handhabungskonzepte

Die Handhabung von Rohrsegmenten ist aus der konventionellen Tiefbohrtechnik bereits hinreichend bekannt und kann auf diverse Arten erfolgen. Generell wird dabei zwischen Catwalk-Systemen und Greifarm-Systemen unterschieden. Um gefaltete Rohre nach diesen Methoden zu manipulieren, sind lediglich die herkömmlichen Systemkomponenten der Handhabungseinrichtungen durch die in Kapitel 2 beschriebenen Komponenten zu ersetzen. Die schematische Anordnung der Komponenten für diese Handhabungsarten ist in Abbildung 3.1 dargestellt.
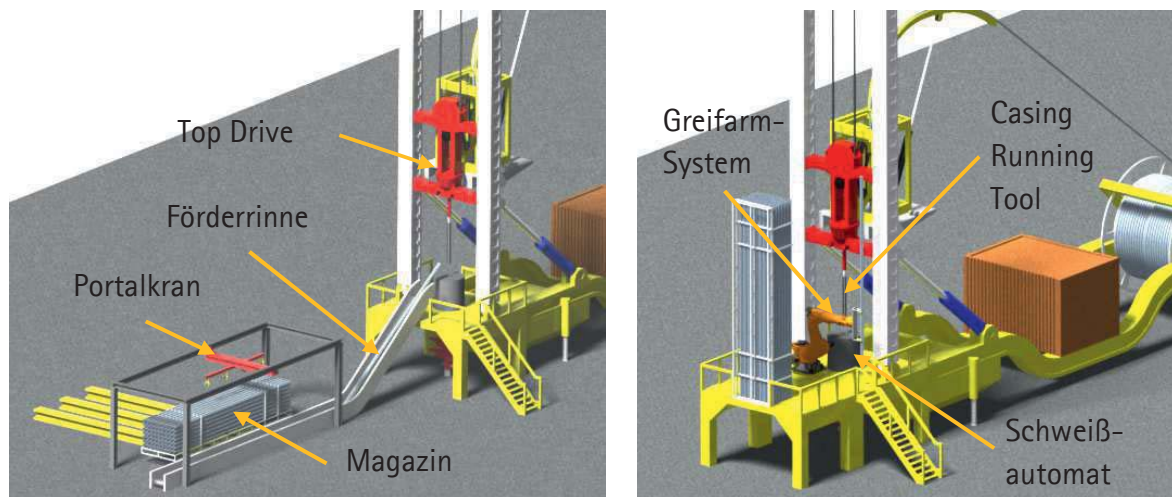
Abbildung 3.1: Konventionelle Handhabungskonzepte für gefaltete Futterrohrsegmente

Bei dem Catwalk-System werden die gefalteten Rohrsegmente mithilfe eines Portalkrans aus dem horizontal positionierten Magazin entnommen und über eine Förderrinne, dem Catwalk, zur Arbeitsplattform transportiert. Dort erfolgt die Übergabe an das am Top Drive befestigte Innenrohrwerkzeug, welches das gefaltete Rohrsegment greift und dem Schweißautomaten zuführt.

Verwendet die Tiefbohranlage ein Greifarm-System, ist dieses System auf bzw. an der Arbeitsplattform montiert. Die Rohrsegmente werden dabei meist in einem vertikalen Lagersystem vorgehalten, dort direkt vom Greifarm-System entnommen und dem Schweißautomaten zugeführt. Detaillierte Beschreibungen zu den Handhabungsprozessen finden sich im 1. Meilensteinbericht dieses Teilprojekts [Bär12].

Zur Steigerung der Produktivität wird das Bohrgestänge an einer Tiefbohranlage mit Greifarm-System zu Zügen á drei Segmente vorverschraubt und diese Züge in einem vertikalen Lager deponiert. Die Abbildung 3.2 zeigt einen möglichen Aufbau dieses Szenarios.
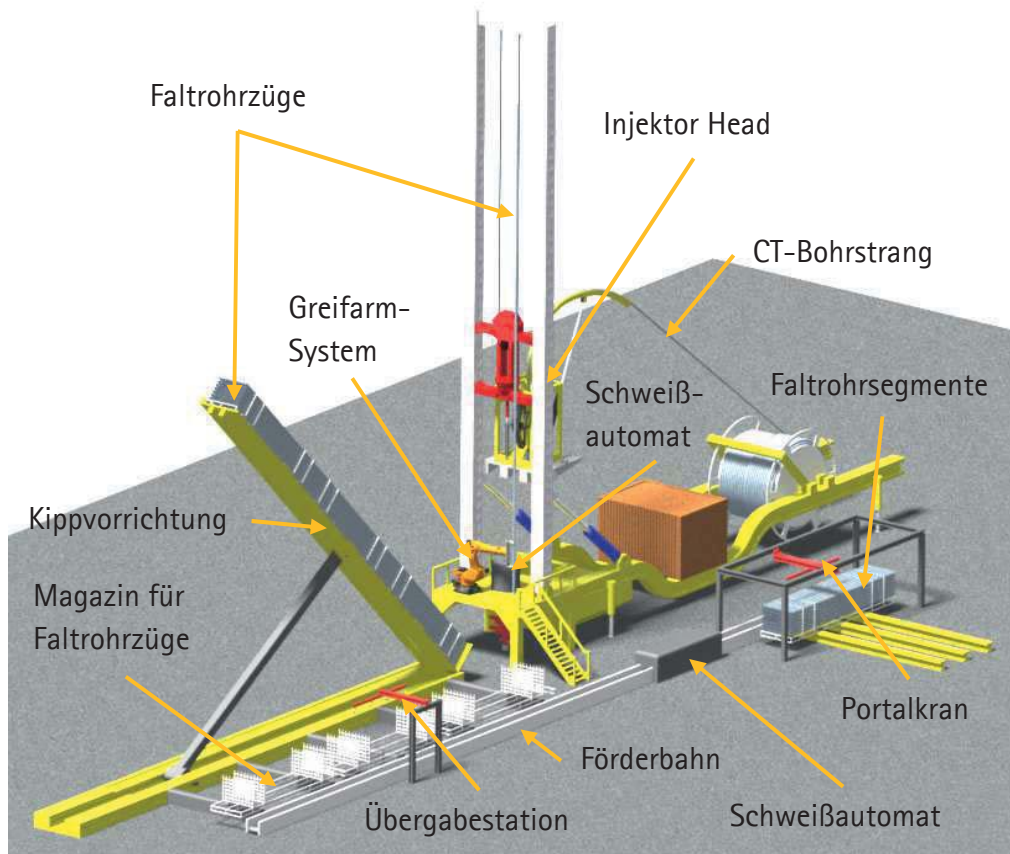
Abbildung 3.2: Konventionelles Handhabungskonzept für gefaltete Futterrohrzüge

Die Handhabung bei diesem Konzept erfolgt analog zu dem Konzept des Greifarm-Systems für Rohrsegmente. Jedoch ist zur Herstellung der Rohrzüge eine vorgelagerte Produktionsstraße erforderlich, in der die Herstellung der Rohrzüge durch die Verbindung der Rohrsegmente vorgenommen wird. Hierbei werden die Rohrsegmente aus einem horizontalen Lager mit einem Portalkran entnommen. Über eine Förderbahn werden die Rohre einem horizontalen Schweißautomaten zugeführt und dort zu Rohrzügen verbunden. Die Züge werden anschließend in einem Magazin, analog zu dem modularen Magazin aus Abbildung 2.1, eingelagert. Eine Kippvorrichtung, bestehend aus einem starren Untergestell und einem kippbaren Tisch, überführt das Magazin schließlich in eine vertikale Lage.

3.2 Innovative Handhabungskonzepte

Die Handhabung und Verbindung von Rohrsegmenten und –zügen an Tiefbohranlagen ist sehr zeitaufwändig. Für den Bohrstrang wurde daher das Coiled Tubing-Verfahren entwickelt. Bei diesem Verfahren wird ein auf einer Trommel aufgewickeltes Rohr mit einer Länge von mehreren hundert Metern als Bohrstrang verwendet [CTE05]. Aufgrund der hohen Spannungen in den Rohren infolge der plastischen Verformungen während des Verfahrens sind für dieses Verfahren bislang lediglich Rohre bis zu einem Außendurchmesser von 5 in verfügbar. Ein Ansatz, um die Höhe der Spannungen und die Anzahl der plastischen Verformungen zu reduzieren, ist die Verwendung größerer Trommeldurchmesser, wie z. B. bei KEIJSER ET AL. diskutiert [KKK00]. NOBILEAU stellt zudem einen Ansatz vor, welches den Einsatz des Coiled Tubing-Verfahrens für gefaltete Futterrohre theoretisch ermöglicht, vgl. [Nob98]. Bislang ist jedoch noch kein Nachweis der

343

Machbarkeit eines Coiled Tubing-Verfahrens mit gefalteten Futterrohren erfolgt. Daher handelt es sich bei dem nachfolgend aufgeführten Handhabungskonzept um eine rein theoretische Betrachtung, die sich lediglich mit einem möglichen Prozessablauf befasst. Dieser Ansatz dient daher als Idealfall bei den Untersuchungen der zeitlichen Einsparpotenziale. Der schematische Aufbau einer Bohranlage für diesen Fall ist in Abbildung 3.3 dargestellt.
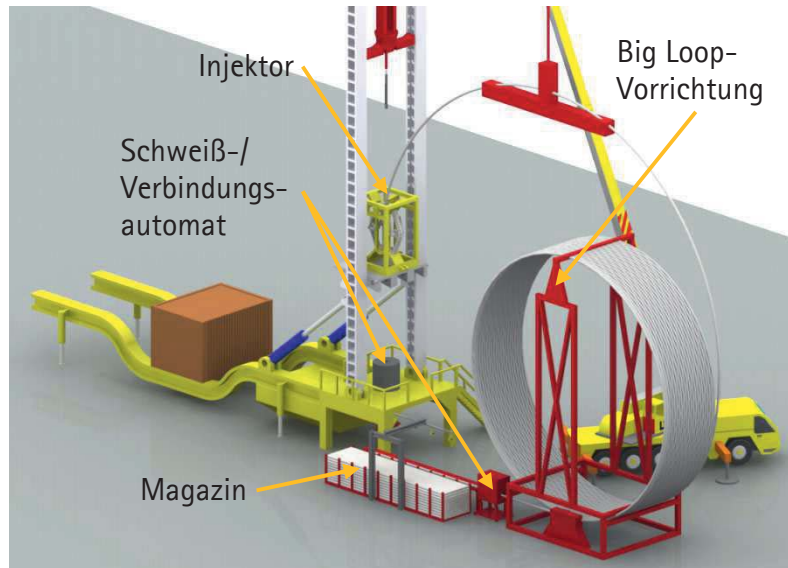
Abbildung 3.3: Handhabung gewickelter und gefalteter Futterrohre

Die Handhabung der gefalteten Futterrohrsegmente erfolgt analog zu der Handhabung an der Produktionsstraße in Abbildung 3.2. Jedoch werden hierbei die entstehenden Züge nicht in ein Magazin eingelagert, sondern als Endlosrohr mithilfe einer Biegemaschine in Schlaufen als Big Loop gewickelt und in einer entsprechenden Vorrichtung eingehängt. Sobald die geforderte Rohrtourlänge in der Vorrichtung zur Verfügung steht, kann die Rohrtour wie bei dem konventionellen Coiled Tubing-Verfahren über einen Injektor in das Bohrloch abgelassen werden.

4 Optimierung der Handhabung des Bohrstrangs

Die Verringerung der Bohrlochdurchmesser infolge der Ausführung der Bohrlochkonstruktion als Mono-Durchmesser-Bohrung eröffnet die Möglichkeit, das Coiled Tubing-Verfahren als Handhabungsverfahren des Bohrstrangs einzusetzen. Zwei wesentliche Vorteile dieses Verfahrens gegenüber dem konventionellen Drehbohrverfahren sind die erhöhte Bohrgeschwindigkeit sowie die Reduzierung der Anzahl der Handhabungs- und Verbindungsprozesse. Die erhöhte Bohrgeschwindigkeit resultiert aus Effekten, die bei Bohroperationen mit geringerem Spülungsdruck (underbalanced drilling) auftreten, die Reduzierung der Handhabungs- und Verbindungsprozesse wird durch die wesentlich größeren Länge des gewickelten Bohrstrangs erreicht.

Aufgrund von Restriktionen bezüglich Größe und Gewicht des Transportguts auf öffentlichen Straßen, dürfen lediglich Bohrstränge mit einer Länge von einigen hundert Metern transportiert werden. Zur Optimierung der Abläufe an Tiefbohranlagen werden daher die zeitlichen Einsparungen untersucht, die durch die Herstellung eines gewickelten Bohrstrangs mit einer Länge, die mindestens der Endteufe der geplanten Tiefbohrung entspricht, zu erreichen sind. Die Abbildung 4.1 zeigt die entsprechende Anordnung der Komponenten für ein derartiges Vorhaben.
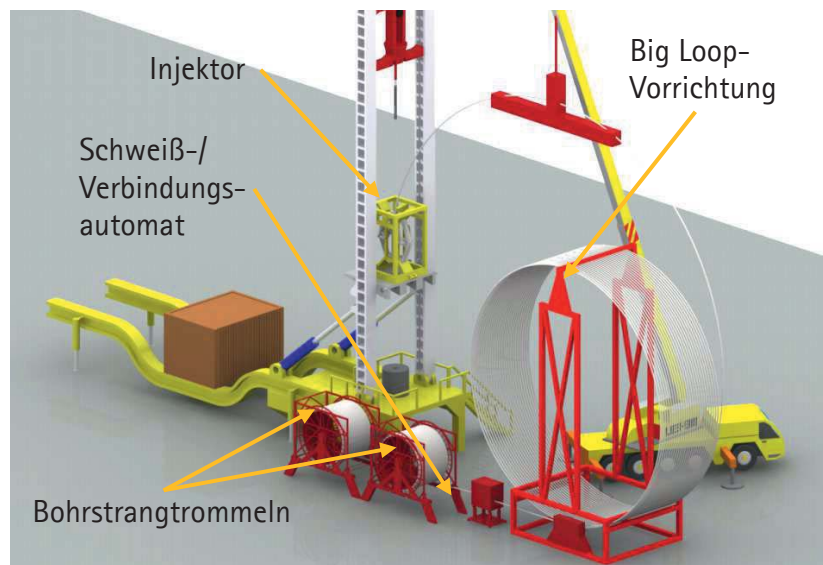
Abbildung 4.1: Herstellungsprozess eines langen Bohrstrangs zur Eliminierung der Handhabungs- und Verbindungsprozesse.

Der größte kommerziell verfügbare Außendurchmesser von Coiled Tubing-Bohrsträngen beträgt 4,5 in. Die Transportrestriktionen erlauben hierbei lediglich den Transport von Trommeln mit Bohrstranglängen von etwa 800 m. Zur Herstellung eines Bohrstrangs mit einer Länge von mehr als 6000 m sind somit 8 Trommeln anzuliefern und deren Bohrstränge miteinander zu verbinden. Dazu wird der Bohrstrangabschnitt der ersten Trommel mithilfe einer Biegemaschine in großen Schlaufen in eine Big Loop-Vorrichtung gewickelt und das Ende in einem Verbindungsautomaten positioniert [KKK00]. Die leere Trommel wird anschließend gegen eine volle Trommel gewechselt und der Anfang des Bohrstrangabschnitts der zweiten Trommel ebenfalls dem Verbindungsautomaten zugeführt. Für die Verbindung ist der Einsatz eines wickelbaren Konnektors oder einer Schweißverbindung möglich.

5 Konzeptbewertung mit dem Berechnungsmodell

Für die in Kapitel 3 und 4 erläuterten Optimierungsansätze sind nun die theoretischen zeitlichen Einsparungen zu ermitteln. Dazu werden die entsprechenden zeitlichen Verläufe dieser Ansätze mit dem Verlauf einer konventionellen Tiefbohranlage bei der Herstellung von Tiefbohrungen verglichen. Die Abbildung der zeitlichen Verläufe erfolgt anhand eines speziell entwickelten Berechnungsmodells.

Im Rahmen dieses Kapitels werden zunächst die Entwicklung sowie der Aufbau und die Funktionsweise dieses Berechnungsmodells näher erläutert. Abschließend erfolgt die Bewertung der Optimierungsansätze hinsichtlich ihrer Effektivität anhand der Berechnungsergebnisse.

5.1 Entwicklung des Berechnungsmodells

Eine detaillierte Darstellung des zeitlichen Verlaufs einer Tiefbohrung erfordert eine genaue Kenntnis der für diesen Verlauf relevanten Prozesse an Tiefbohranlagen. Aus diesem Grund wurde eine umfangreiche Prozessanalyse durchgeführt und die Abläufe in Form von Flussdiagrammen nach DIN 66001 dargestellt. Die Abbildung 5.1 zeigt das Flussdiagramm für den allgemeinen Ablauf zur Herstellung einer Tiefbohrung mit einer Tiefbohranlage.
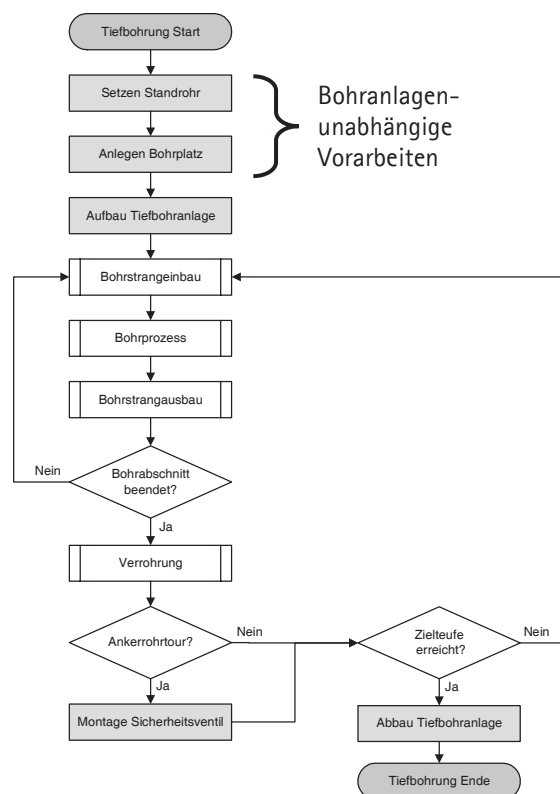
Abbildung 5.1: Ablauf der Bohrungserstellung beim Drehbohrverfahren

Wie in der Abbildung 5.1 zu erkennen ist, beginnt die Bohrung, sobald der Bohrplatz angelegt, die Standrohrtour gesetzt und die Bohranlage aufgebaut ist, mit dem Bohrstrangeinbau. Liegt der Meißel am Bohrstrangende auf der Bohrlochsohle auf, wird der Bohrprozess gestartet. Hierbei wird der Bohrstrang sukzessive verlängert, bis der Meißel verschlissen oder das Ende eines

Bohrabschnitts erreicht ist. Der Bohrstrang wird dann aus der Bohrung ausgebaut. Ist das Ende eines Bohrabschnitts erreicht, wird das Bohrloch verrohrt, um einen Kollaps der Bohrung zu verhindern. Dieser zyklische Prozessablauf wird wiederholt, bis die Zielteufe erreicht und die Bohranlage abgebaut werden kann. Danach ist die Tiefbohrung beendet.

In diesem Flussdiagramm sind Prozesse durch weiße Rechtecke mit doppelten vertikalen Linien und Entscheidungen bzw. Abfragen durch weiße Rauten gekennzeichnet. Einzelne Arbeitsschritte, denen direkte Zeitwerte zugeordnet werden, sind durch grau hinterlegte Rechtecke dargestellt. Für die detaillierte Beschreibung des zeitlichen Ablaufs ist es notwendig, sämtliche Prozesse in die einzelnen Arbeitsschritte zu zerlegen, um eine vollständige mathematische Beschreibung der Abläufe an Tiefbohranlagen zu ermöglichen. Eine programmiertechnische Umsetzung dieser mathematischen Beschreibung liefert dann das Berechnungsmodell. Die detaillierte Zerlegung der Prozesse und Ableitung der mathematischen Gleichungen wird im 2. Meilensteinbericht ausführlich beschrieben, vgl. [Bär13].

5.2 Aufbau und Funktionsweise des Berechnungsmodells

Das Berechnungsmodell besteht aus einer Datenbank und einem Berechnungsmodul. Die Datenbank setzt sich aus mehreren Tabellen einer Excel-Datei zusammen. In diesen Tabellen werden die zur Berechnung benötigten Zeitwerte der bohranlagenspezifischen Arbeitsschritte, die Geometriedaten der Bohrlochkonstruktionen sowie die Lithographie des Untergrundes hinterlegt. Die Datenbank wird über eine eigene Benutzeroberfläche verwaltet. Die Abbildung 5.2 zeigt die Startseite dieser Benutzeroberfläche.

Abbildung 5.2: Formular zur Verwaltung der Bohranlagentabelle

Auf dieser Startseite der Benutzeroberfläche sind die wichtigsten allgemeinen Daten der Bohranlage aufgeführt. Ebenfalls besteht dort die Möglichkeit, ein Bild der Bohranlage mit dem entsprechenden Datensatz zu verknüpfen und anzeigen zu lassen. Über die Karteikarten im oberen Bereich werden die weiteren Formularseiten aufgerufen. Bei einem Start der Benutzeroberfläche wird der erste Bohranlagendatensatz angezeigt. Über ein Dropdown-Menü sind die weiteren Datensätze auswählbar. Auf allen Formularseiten besteht die Möglichkeit, die Daten manuell zu ändern. Über die Schaltflächen „Übernehmen", „Neuen Datensatz erzeugen" und

„Anlage löschen" können Änderungen gespeichert, neue Datensätze erzeugt oder bestehende Datensätze gelöscht werden. Die Schaltfläche „BLK öffnen" öffnet eine Formularseite zur Verwaltung der Daten der Bohrlochkonstruktionen. Über „Matlab öffnen" wird die Software Matlab, sofern vorhanden, geöffnet und das Berechnungsmodul gestartet.

Das Berechnungsmodell ist die programmiertechnische Umsetzung der in Kapitel 5.1 beschriebenen Prozessabläufe in der Softwareumgebung Matlab. Wird das Berechnungsmodul gestartet, sind über eine Eingabeaufforderung die Kombinationen aus Bohranlage und Bohrlochkonstruktion anzugeben, die nachfolgend berechnet werden sollen. Aus der Datenbankdatei werden dann alle relevanten Daten eingeladen und die Berechnung des zeitlichen Verlaufs durchgeführt. In Abbildung 5.3 ist das Vorgehen der Berechnung exemplarisch in Form eines Zeit-Teufe-Diagramms dargestellt.
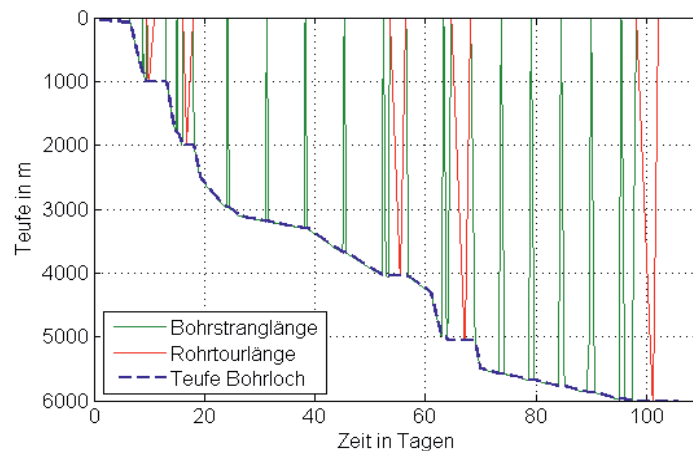
Abbildung 5.3: Grafisches Schema des Ablaufs der Berechnung des Bohrfortschritts

Bei dem Berechnungsmodell handelt es sich um eine strukturierte, zustandsorientierte Programmierung. Die Berechnung orientiert sich dabei an den Längen des Bohrstrangs und des Futterrohrs in der Bohrung. Der zeitliche Verlauf der Längenänderung des Bohrstrangs wird durch die grüne Kurve dargestellt. Dieser Verlauf gibt die Zeiten an, in denen der Bohrstrang während des Einbauvorgangs und der Bohroperationen verlängert wird sowie die Zeiten zur Verkürzung des Bohrstrangs während des Ausbaus. Die rote Kurve beschreibt die Längenänderung der Rohrtour über die Zeit. Darin enthalten sind die Zeiten zum Herstellen der Rohrtour, das Zementieren und, für den Fall, dass eine verlorene Rohrtour eingebaut wird, die Ein- und Ausbauzeit des Bohrstrangs. Werden expandierbare Futterrohre eingebaut, fließt die Expansionszeit ebenfalls an dieser Stelle in die Berechnung mit ein. Sobald die Verrohrung eingebaut ist, wird die Länge der Rohrtour wieder auf den Wert 0 zurückgesetzt. Die Darstellung der Teufe der Bohrung über die kombinierten Zeiten der beiden Längenänderungen ergibt das bekannte Zeit-Teufe-Diagramm (blaue, gestrichelte Kurve).

Zur weiteren Auswertung wird die Gesamtzeit in Einzelzeiten zerlegt. Die Aufteilung erfolgt in die Kategorien Bohren, Nachsetzen, Bohrstrangeinbau, Bohrstrangausbau, Verrohren, Expansion und Zementierung. Die Darstellung der Gesamtzeiten sämtlicher Kombinationen aufgeteilt in die o. g. Zeitanteile erfolgt in Form von Balkendiagrammen.

5.3   Diskussion der Berechnungsergebnisse

Die Berechnungen der zeitlichen Verläufe werden zunächst für konventionelle Bohrlochkonstruktionen mit konventionellen Tiefbohranlagen durchgeführt. Die Ergebnisse dieser Berechnungen dienen zum einen zur Analyse der Effizienz der unterschiedlichen Handhabungs- und Verbindungssysteme, zum anderen als Grundlage zur Bewertung der zeitlichen Einsparpotenziale der in Kapitel 3 und 4 beschriebenen Optimierungsansätze.

Dieses Vorgehen erfordert drei fiktive Tiefbohranlagenarten sowie drei Bohrlochkonstruktionen, deren Datensätze in die Datenbank einzufügen sind. Die Abbildung 5.4 zeigt drei reale Tiefbohranlagen, die als Grundlage für die fiktiven Tiefbohranlagen herangezogen werden.
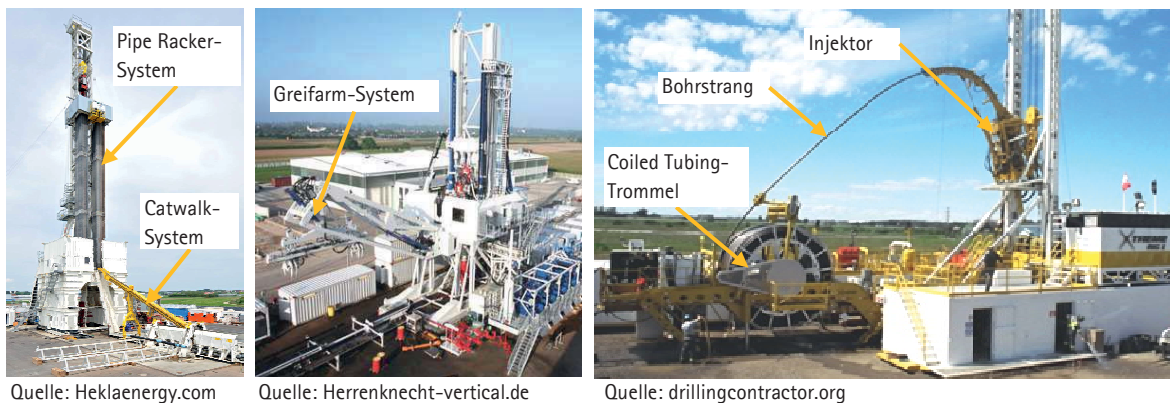
Abbildung 5.4: Reale Bohranlagen als Grundlage der fiktiven Referenzbohranlagen.

An der fiktiven Bohranlage 1 (FB 1) werden Rohrsegmente aus einem horizontalen Rohrlager vereinzelt, über ein Catwalk-System zur Arbeitsplattform transportiert und dort vom Top Drive übernommen. Zusätzlich bietet diese Bohranlage die Möglichkeit, vorverschraubte Rohrzüge (á 3 Rohrsegmente von je 9 m) in einem vertikalen Rohrlager direkt auf der Arbeitsplattform zwischenzulagern. Die Handhabung erfolgt hierbei mit einem Greifarm-System. Die fiktive Bohranlage 2 (FB 2) besitzt ein Schwenkarm-System für die Handhabung von Rohrzügen (á 2 Rohrsegmente von je 9 m). Die Rohrzüge werden hierbei aus einem horizontalen Lager vereinzelt und einer Vorrichtung zugeführt, von der aus die Greifelemente des Schwenkarm-Systems den Rohrzug aufnehmen können. Anschließend erfolgen der Transport zur Arbeitsplattform und die Übergabe an den Top Drive. Bei der letzten fiktiven Bohranlage 3 (FB 3) handelt es sich um eine Coiled Tubing-Bohranlage. An dieser Bohranlage werden Trommeln mit gewickelten Bohrsträngen mit etwa 800 m Länge verwendet. Die zur Berechnung erforderlichen Eingangsparameter dieser Tiefbohranlagen sind Aufzeichnungen von Feldstudien der TU Clausthal sowie den Datenblättern der Bohranlagen und der Fachliteratur entnommen.

Neben den Tiefbohranlagen bzw. deren Komponenten zur Handhabung der Rohre ist auch die zu bohrende Bohrlochkonstruktion für den zeitlichen Verlauf der Tiefbohrung entscheidend. Um den Einfluss unterschiedlicher Bohrlochkonstruktionen auf den zeitlichen Verlauf der Tiefbohrung detailliert zu untersuchen, sind die grundlegenden Konstruktionsvarianten aus Abbildung 5.5 in das Modell integriert worden.
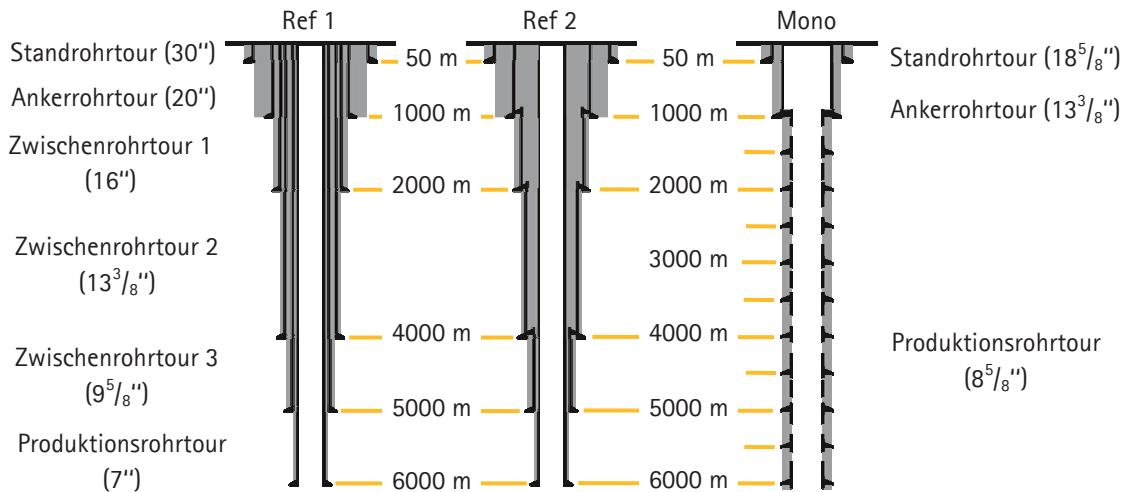
Abbildung 5.5: Konstruktionsvarianten für die Tiefbohrung des Berechnungsmodells

Zur geothermischen Stromerzeugung sind eine hohe Förderrate und damit auch ein relativ großer Durchmesser der Produktionsrohrtour notwendig. Der minimale Durchmesser der Produktionsrohrtour wurde daher vom gebo-Forschungsverbund auf 7 in festgelegt. Die Referenzbohrungen Ref 1 und Ref 2 sind zwei mögliche konventionelle Bohrlochkonstruktionen für Tiefbohrungen mit einem derartigen Durchmesser der Produktionstour. Der Unterschied dieser Bohrlochkonstruktionen liegt lediglich in der Ausführung der Zwischenrohrtouren. In der Bohrung Ref 1 sind sämtliche Rohrtouren als komplette Rohrtouren ausgeführt, in der Bohrung Ref 2 werden für die Zwischenrohrtouren verlorene Rohrtouren (Liner) verwendet. Die Bohrlochkonstruktion Mono ist hingegen eine Mono-Durchmesser-Bohrung. Nach der Ankerrohrtour werden hierbei expandierbare gefaltete Rohrtouren verbaut. Die Bohrung Mono weist zudem einen optimierten Durchmesser der Produktionsrohrtour von $8^5/_8$ in auf.

Die Kombination der konventionellen Tiefbohranlagen und Tiefbohrungen ergibt zunächst sechs logische Tiefbohroperationen, deren zeitliche Verläufe zu untersuchen sind. In Abbildung 5.6 sind die Berechnungsergebnisse dieser Kombinationen als normierte Zeitanteile in Form von Balkendiagrammen dargestellt. Das linke Diagramm zeigt die nichtproduktiven Zeiten, das rechte Diagramm die normierten Gesamtzeiten der Bohroperationen. Die Normierung der Zeiten bezieht sich hierbei auf die erste Kombination (FB 1, Catwalk, Ref 1).
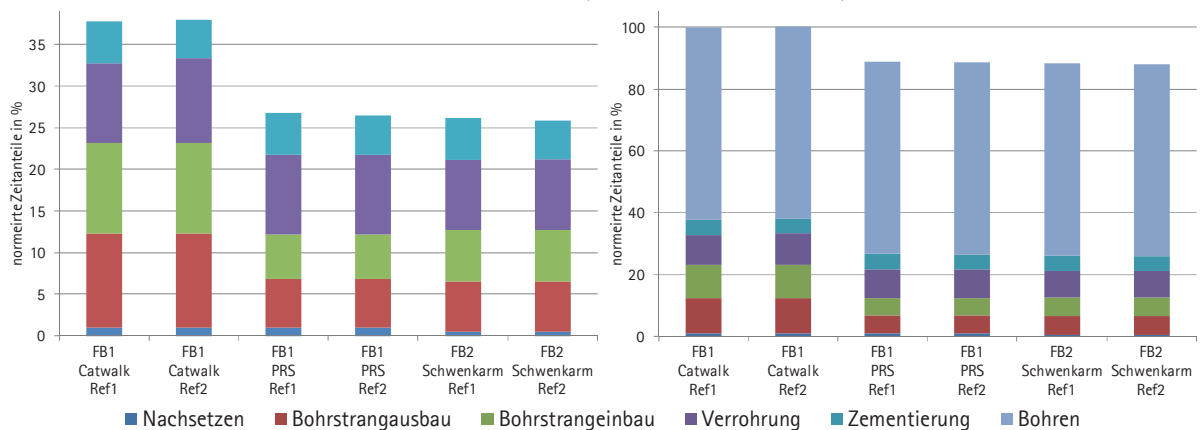
Abbildung 5.6: Vergleich der zeitlichen Bohrverläufe bei der Herstellung konventioneller Tiefbohrungen mit unterschiedlichen Tiefbohranlagen. Links: Balkendiagramm der nichtproduktiven Zeiten. Rechts: Balkendiagramm der Gesamtzeiten.

Wie die Diagramme zeigen, ist es möglich, die Herstellungszeit durch den Einsatz eines Vertikal-lagersystems auf der Arbeitsplattform als Zwischenlager um etwa 11 % zu reduzieren, vgl. FB 1. Die Gründe für diese Zeiteinsparungen sind die verkürzten Transportwege bei den Ein- und Auslagerprozessen der Rohrsegmente sowie die Reduzierung der Anzahl der Handhabungs- und Verbindungsvorgänge durch die Verwendung von vorverbundenen Rohrzügen. Obwohl das Schwenkarm-System lediglich Rohrzüge mit 2 Rohrsegmenten transportiert, arbeitet dieses System geringfügig effizienter als das Vertikallagersystem. Die Einsparung liegt bei etwa 11,6 % im Vergleich zur Tiefbohranlage mit dem Catwalk-System. Der Grund dafür ist, dass zum Aus-tausch des Bohrstrangs sämtliche Rohrzüge bei der Bohranlage FB 1 mithilfe des zeitaufwändi-gen Catwalk-Systems von der Arbeitsplattform entfernt werden müssen. Auch die Futterrohre werden hierbei in einzelnen Rohrsegmenten mit dem Catwalk-System bewegt, wohingegen das Schwenkarm-System in der Lage ist, die Futterrohre ebenfalls als Rohrzüge á 2 Segmente zu transportieren.

Weiterhin ist, außer bei der Handhabung der Rohre mit dem Catwalk-System, ein geringer zeitlicher Vorteil von etwa 0,3 % bei der Herstellung der Bohrung Ref 2 zu erkennen. Dieser Vorteil resultiert aus den zeitlichen Einsparungen bei der Zementierung der verlorenen Rohrtou-ren. Bei dem Catwalk-System wird dieser Vorteil jedoch durch den zeitlichen Zusatzaufwand, der sich aus der Summe der Ein- und Ausbauzeiten der Bohrstrangsegmente gegenüber dem Futterrohreinbau ergibt, eliminiert, vgl. Ref 1 und Ref 2. Eine Mono-Durchmesser-Bohrung, wie sie vom Forschungsverbund gebo angestrebt wird, vgl. Abbildung 5.5, führt nicht zwangsweise zu einer zeitlichen Einsparung. Die Abbildung 5.7 zeigt dazu die Ergebnisse der Berechnung des zeitlichen Verlaufs an der Tiefbohranlage FB 2 bei der Herstellung dieser Mono-Durchmesser-Bohrung im Vergleich zu den Bohrlochkonstruktionen Ref 1 und Ref 2. Zudem ist der zeitliche Verlauf zur Herstellung der Mono-Durchmesser-Bohrung mithilfe der Coiled Tubing-Bohranlage FB 3 dargestellt.
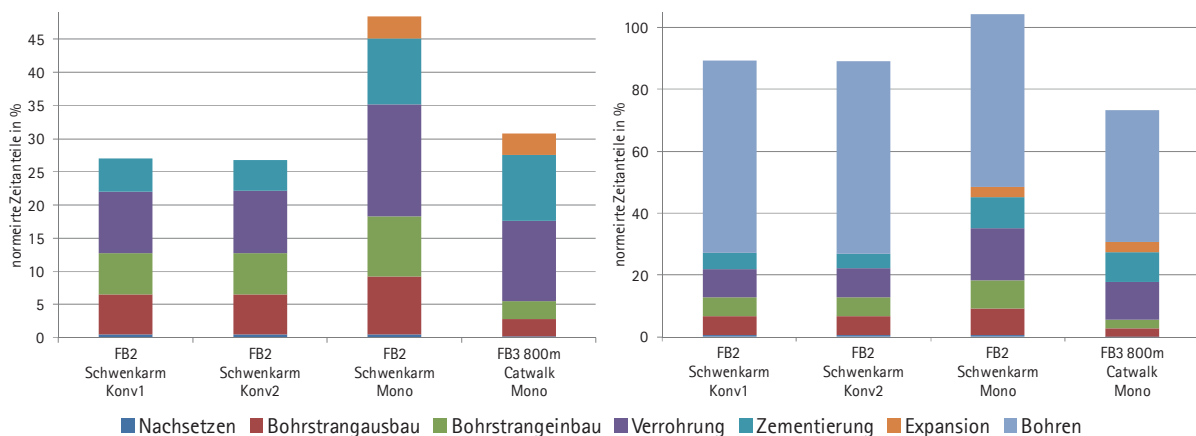
Abbildung 5.7: Vergleich der zeitlichen Bohrverläufe bei unterschiedlichen Bohrlochkonstruktionen. Links: Balkendiagramm der nichtproduktiven Zeiten. Rechts: Balkendiagramm der Gesamtzeiten.

Wie in dieser Abbildung zu sehen ist, ist der Zeitaufwand im Bereich der nichtproduktiven Pro-zesse bei der Herstellung einer Mono-Durchmesser-Bohrung (Mono) weitaus größer als der Aufwand für die konventionellen Tiefbohrungen Ref 1 und Ref 2, da die gefalteten Rohrtouren unter Tage expandiert werden müssen. Weiterhin wird die Mono-Durchmesser-Bohrung in

351

wesentlich kleinere Bohrabschnitte unterteilt, sodass die Anzahl der Verrohrungen sowie Ein- und Ausbauprozesse des Bohrstrangs deutlich häufiger auftreten. An der Tiefbohranlagen FB 2 ergibt sich durch die Mono-Durchmesser-Bohrung ein Zuwachs von ca. 15 %. Auch durch die Verwendung einer Coiled Tubing-Bohranlage (FB 3), deren Handhabungsprozesse aufgrund des langen, gewickelten Bohrstrangs deutlich kürzer ausfallen und weniger häufig auftreten als an konventionellen Tiefbohranlagen, kann dieser Zusatzaufwand nicht vollständig kompensiert werden. Allerdings kann bei einer Coiled Tubing-Bohranlage die Bohrgeschwindigkeit, infolge der Verwendung von Spülungen mit geringerer Dichte (underbalanced drilling), um den Faktor 1,5 bis 2 erhöht werden. Somit sind zeitliche Einsparungen von etwa 26,5 % bei einer Mono-Durchmesser-Bohrung gegenüber der Tiefbohroperation (FB 1, Catwalk, Ref 1) erreichbar.

In Kapitel 3 und 4 dieses Berichts wurden bereits Optimierungsansätze vorgestellt, die zu weiteren Zeiteinsparungen bei der Herstellung einer Mono-Durchmesser-Bohrung führen sollen. Die Ergebnisse der Untersuchungen dieser Optimierungsansätze sind in Abbildung 5.8 aufgeführt.
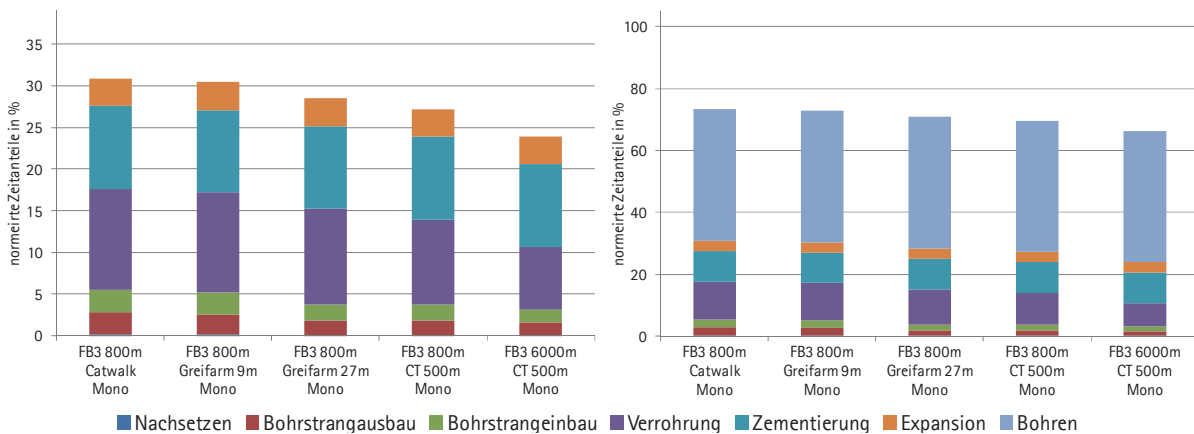
Abbildung 5.8: Vergleich der zeitlichen Bohrverläufe von Mono-Durchmesser-Bohrungen mit unterschiedlichen Optimierungsansätzen. Links: Balkendiagramm der nichtproduktiven Zeiten. Rechts: Balkendiagramm der Gesamtzeiten.

Die ersten drei Balken der Diagramme in Abbildung 5.8 zeigen die Prozesszeiten der Coiled Tubing-Bohranlage FB 3, bei der ein Bohrstrang verwendet wird, der aus gewickelten Bohrstrangsegmenten zu je 800 m Länge besteht. Der Transport der gefalteten Futterrohre geschieht hierbei über konventionelle Handhabungssysteme, wie dem Catwalk- bzw. dem Greifarm-System, vgl. Kapitel 3.1. Die Diagramme zeigen zeitliche Einsparungen durch die Verwendung des Greifarm-Systems zur Handhabung der gefalteten Futterrohre, da bei diesem System geringere Zeiten für die Handhabung der Rohrsegmente im Vergleich zum Catwalk-System anfallen. Durch die Verwendung vorverbundener Rohrzüge, sowohl für die gefalteten Futterrohre als auch für die Komponenten der Bohrgarnitur, lässt sich die Effizienz der Bohroperation weiter verbessern. Der Einsatz gewickelter Futterrohre, wie in Kapitel 3.2 beschrieben, führt zu einer weiteren Zeitersparnis im Bereich der Verrohrung, vgl. FB 3 800 m, CT 500 m, Mono. Der verwendete Bohrstrang mit der Länge von 800 m erfordert jedoch diverse Handhabungs- und Verbindungsprozesse, um den Bohrstrang für die Bohr- und Verrohrungsprozesse in tieferen Bohrabschnitten zu verlängern. Um diese Zeitanteile zu eliminieren, wird ein Bohrstrang mit einer Länge von über 6000 m eingesetzt, vgl. Kapitel 4. Die Zeit für die Bohroperation erreicht somit einen Minimalwert. Die prozentuale Einsparung gegenüber der Ausgangsbohroperation (FB 1, Catwalk, Ref 1) entspricht etwa 34 %.

6 Zusammenfassung

Im Rahmen dieses Teilprojekts wurden Komponenten und Verfahren entwickelt und untersucht, die zu einer effizienten Realisierung einer Mono-Durchmesser-Bohrung beitragen sollen. Ein besonderes Augenmerk lag dabei auf der Integration der gefalteten Futterrohre in den Material-fluss von Tiefbohranlagen. Neben den entsprechenden Komponenten zur Manipulation sind daher ganzheitliche Ansätze für die Prozessabläufe zur Handhabung und Verbindung von gefalteten Futterrohren entstanden.

Zur Bewertung der Effizienz dieser Prozesse, ist ein Berechnungsmodell entwickelt worden, welches die Abbildung und Gegenüberstellung der zeitlichen Verläufe von Bohroperationen ermöglicht. Das Berechnungsmodell stellt eine mathematische Beschreibung der Prozesse an konventionellen Tiefbohranlagen sowie der Prozesse an Coiled Tubing-Bohranlagen dar. Somit lassen sich sämtliche Bohroperationen von konventionellen Tiefbohranlagen und Coiled Tubing-Bohranlagen sowie die in diesem Teilprojekt entwickelten Optimierungsansätze mit diesem Modell abbilden.

Die Ergebnisse des Berechnungsmodells zeigen, dass die Herstellung einer Mono-Durchmesser-Bohrung nicht zwangsläufig zu einer Zeitersparnis und damit zu einer effizienteren Tiefbohrung im Vergleich zu einer konventionellen Tiefbohrung führt. Die Gründe dafür sind vor allem der zusätzliche Aufwand im Bereich der Verrohrung durch die größere Anzahl der Bohrabschnitte sowie die zusätzliche Zeit zur Expansion der gefalteten Futterrohre. Eine Zeitersparnis bei der Mono-Durchmesser-Bohrung wird durch den Einsatz einer Coiled Tubing-Bohranlage mit der Technik des underbalanced drilling erreicht. Die, infolge dieser Technik, erhöhte Bohrgeschwin-digkeit sowie der geringere Zeitaufwand zur Handhabung und Verbindung von Rohrsegmenten an Coiled Tubing-Bohranlagen kompensieren den zusätzlichen Aufwand für die Verrohrung der Mono-Durchmesser-Bohrung. Die im Rahmen dieses Teilprojekt vorgestellten Optimierungsan-sätze zur Handhabung der gefalteten Futterrohre führen zu weiteren zeitlichen Einsparungen. Im Idealfall ist somit eine Zeitersparnis von etwa 34 % gegenüber einer konventionellen Tief-bohroperation möglich.

Literatur

[Bär12]   BÄR, F.: Bericht zum 1. Meilenstein im gebo-Teilprojekt B3: Automatisierung des Bohrprozesses durch den Einsatz eines flexiblen Bohrstrangs. gebo-interne Veröffentlichung, Hannover, 2012.

[Bär12a]   BÄR, FLORIAN: A Cost-Efficient Monobore Well Construction for Deep Geothermal Resources, Präsentation, Wien, 2012

[Bär13]   BÄR, F.: Bericht zum 2. Meilenstein im gebo-Teilprojekt B3: Automatisierung des Bohrprozesses durch den Einsatz eines flexiblen Bohrstrangs. gebo-interne Veröffentlichung, Hannover, 2013.

[Bär13a]   BÄR, F.; TEODORIU, C., OVERMEYER, L.: Ansätze zur Ermittlung und Reduktion nicht-produktiver Zeiten an Tiefbohranlagen, Logistics Journal: Proceedings, 2013

[Bär13b]   BÄR, F.; TEODORIU, C.: Einfluss der Trip-Zeiten auf die Gesamtkosten von Tiefbohrungen mit einer monoboren Bohrlochkonstruktion, Präsentation, Freiberg, 2013

[Bär13c]   BÄR, F.: Bericht zum 3. Meilenstein im gebo-Teilprojekt B3: Automatisierung des Bohrprozesses durch den Einsatz eines flexiblen Bohrstrangs. gebo-interne Veröffentlichung, Hannover, 2013.

[CTE05]   CTES, L. P.: Coiled Tubing Manual. Rev. 72005-A. Conroe, Texas, USA, 2005. http://ctes.nov.com/documentation/manuals/ctmanual/default.aspx

[BVH11]   BÄR, F.; VARAHRAM, A.; HASSEL, T.; BACH, FR.-W.; OVERMEYER, L.: Cost-efficient Monobore Well Construction for Geothermal Energy, 16th Annual International Conference on Industrial Engineering Theory, Applications & Practice. Stuttgart: IJIE (International Journal of Industrial Engineering), 2011.

[HVB13]   HASSEL, T; VARAHRAM, A; BENEDICT, D. ET AL.: Enhanced Magnetically Impelled Arc Butt Welding (MIAB) Technology, Schutzrecht WO 2013/055598 A1

[HVB13a]   HASSEL, T; VARAHRAM, A; BAER, F. ET AL.: Arc Guiding, Gripping and Sealing Device for a Magnetically Impelled Butt Welding Rig, Schutzrecht WO 2013/055600 A1

[KKK00]   KEIJSER M. P., KOSTER E, KOCH K. ET AL: Big Loop: On-Site Welded Continuous Pipe, Society of Petroleum Engineers, 2000

[Nob98]   NOBILEAU, P. C.: Method for casing a wellbore. Schutzrecht US 005794702A. 1998

Abschlussbericht zum GeBo-Teilprojekt:

355

B3: Automatisierung des Bohrprozesses durch den Einsatz eines flexiblen Bohrstrangs

B3: Automation of the drilling process by the application of a flexible drill rod

Dipl.-Ing. Dominik Brouwer

Institut für Fertigungstechnik und Werkzeugmaschinen

Inhaltsverzeichnis

1   Einleitung

Am 13. Mai 2009 hat das Bundeskabinett in der Pressemitteilung [BMU09] den Beschluss bekannt gegeben, dass bis zum Jahr 2020 in Deutschland eine Leistung von etwa 280 Megawatt tiefer Geothermie erzeugt werden soll. Wird von einer elektrischen Leistung von P_{elektr} = 5 MW pro Kraftwerk ausgegangen, müssen 55 Kraftwerke aufgebaut werden. Da zur effektiven Gewinnung elektrischer Energie aus tiefer Geothermie eine Bohrungsdoublette notwendig ist, müssen somit 110 fündige Bohrungen mit nachhaltig hoher Ergiebigkeit in den nächsten 10 Jahren erstellt werden. Bis 2030 soll sogar eine installierte elektrische Leistung von 850 Megawatt aus der tiefen Geothermie bereitgestellt werden.

Zur Gewinnung von geothermischer Energie müssen Bohrungen abgeteuft werden. Wie die Studie des Bundesministeriums für Umwelt [BMU07] zeigt, sind die Kosten für die Bohrungsherstellung mit rund 70 % der Gesamtinvestition mit Abstand der größte Kostenfaktor bei der Errichtung einer Anlage zur Gewinnung tiefer geothermischer Energie, vgl. Abbildung 1. Um die Wirtschaftlichkeit der geothermischen Energiegewinnung in Niedersachsen zu steigern, ist daher eine signifikante Reduktion der Bohrkosten notwendig.
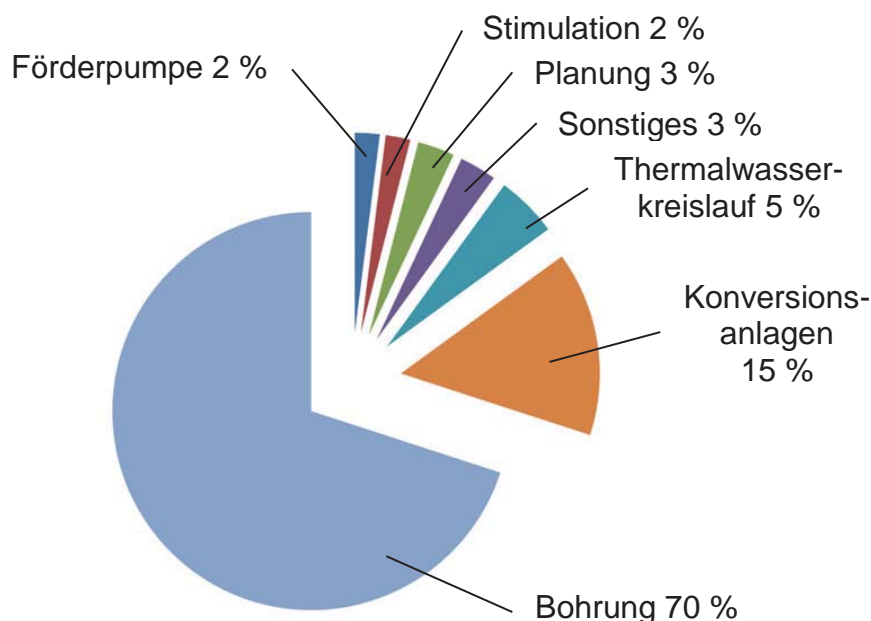
Abbildung 1: Kostenanteile bei der Errichtung einer Anlage zur Gewinnung tiefer geothermischer Energie nach [BMU07]

Der Forschungsverbund „Geothermie und Hochleistungsbohrtechnik", kurz gebo, hat sich zur Aufgabe gemacht, die Kosten für Bohrungen zur Gewinnung geothermischer Energie zu senken, um somit den Einsatz dieser regenerativen Energiequelle voranzutreiben. In diesem Teilprojekt werden die Abläufe und Prozesse an einer Bohranlage analysiert. Auf Basis die-

ser Analyse werden Ansätze für eine Verbesserung der Wirtschaftlichkeit geothermischer Tiefbohrungen herausgearbeitet.

Um einen erfolgversprechenden Ansatz für eine signifikante Senkung der Bohrkosten handelt es sich bei der Herstellung eines monobaren Bohrlochs, also einem Bohrloch mit einem konstanten Durchmesser von der Oberfläche bis zum Zielhorizont. Um dies zu realisieren, werden flexible Rohrstrukturen verwendet, die untertage mit Hilfe einer entsprechenden Vorrichtung expandiert werden sollen. Die Entwicklung von Automatisierungskonzepten zum Verrohren von Tiefbohrungen mit Hilfe dieser expandierenden Rohre ist Aufgabenbereich dieses Teilprojekts.

2   Aufbau einer Tiefbohranlage

Zur Herstellung von Tiefbohrungen wird aktuell hautsächlich das Rotary Drilling verwendet. Der Aufbau einer konventionellen Rotary Drilling Anlage wird nachfolgend beschrieben.

2.1   Aufbau einer Rotary Drilling Tiefbohranlage

Soll eine Tiefbohrung hergestellt werden, muss diese zunächst vorbereitet werden. Dazu gehören geologische Untersuchungen des Untergrundes und darauf basierend die Bestimmung des Bohrplatzes. Ist der Bohrplatz ausgewählt, wird an der Bohrstelle ein so genanntes Standrohr gesetzt. Dieses Standrohr wird von einer Spezialtiefbaufirma in die obersten Erdschichten gerammt und hat eine Länge von 5 bis 20 m sowie einen Durchmesser von etwa 0,5 m. Es dient dazu, ein stabiles Loch bis unter die grundwasserführenden Schichten zu erhalten. An der Stelle, an der der Bohrturm später stehen wird, wird ein stabiles Betonfundament gegossen. Anschließend wird der Bohrplatz großflächig mit Beton und Asphalt versiegelt. Auf diesem Bohrplatz wird dann eine Bohranlage errichtet.

Abbildung 2 zeigt den Aufbau einer Rotary-Bohranlage mit den dazugehörigen Komponenten. Unterhalb der Arbeitsplattform ist der Blowout-Preventer (10) angebracht. Diese Einrichtung muss laut Gesetz bei jeder Tiefbohrung installiert werden [REI09]. Sie verhindert, dass durch Kicks verursachte Druckanstiege in der Bohrung zum explosionsartigen Austreten von Fluiden aus der Bohrung führen. Es handelt sich dabei um ein Ventil, welches sich innerhalb kürzester Zeit verschließen lässt. Um dem Überdruck in der Bohrung standzuhalten wird der Blowout-Preventer mit dem Fundament der Ankerrohrtour verbunden. Die Ankerrohrtour ist der oberste Futterrohrabschnitt einer Bohrung, der fest im Untergrund einzementiert ist [REI09], [REI04]. Das Setzen des Standrohres, das Versiegeln des Bohrplatzes sowie das

Setzen der Ankerrohrtour und die Installation des Blowout Preventers ist gesetzlich vorge-schrieben und muss an allen Bohranlagen vorgenommen werden.
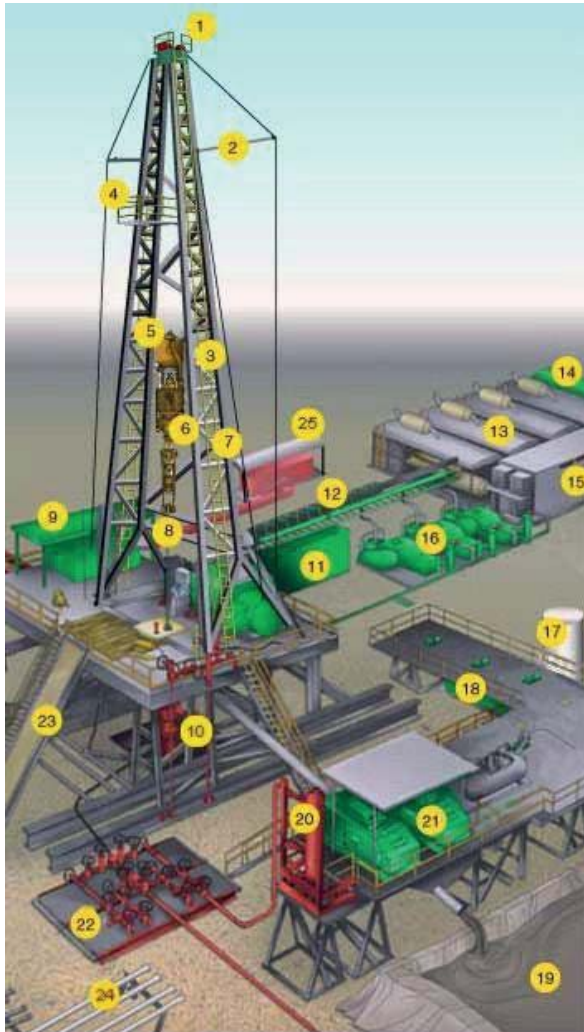
1	oberer Rollenblock des Flaschenzugs
2	Ausleger mit Seil für den Seilzug
3	Drahtseil am Flaschenzug (Drilling line)
4	Fingerbühne
5	unterer Rollenblock des Flaschenzugs
6	Top Drive
7	Mast
8	Bohrstrang
9	Doghouse
10	Blowout Preventer
11	Wassertank
12	Kabelträger
13	Generatoren
14	Treibstofftanks
15	Schalthaus
16	Spülungspumpen
17	Tank für Bulk Mud Komponenten
18	Absetztanks
19	Absetzbecken
20	Spülung-Gas-Separator
21	Schüttelsieb
22	Mehrfachdrossel
23	Rohrrampe
24	horizontales Rohrlager
25	hydraulische Speichereinheit

Abbildung 2: Aufbau einer Onshore-Bohranlage [OSH09]

Abbildung 2 zeigt, ist der Bohrturm einer Rotary Anlage lediglich ein Kran mit einem Fla-schenzug. Die Komponenten mit den Bezeichnungen 1, 2, 3 und 5 stellen die einzelnen

359

Elemente des Flaschenzugs dar. An dem unteren Rollenblock (5) des Flaschenzugs ist ein Haken befestigt, der den gesamten Bohrstrang hält. Über die Geschwindigkeit des unteren Rollenblocks des Flaschenzugs wird die Zuführung des Bohrstrangs (8) geregelt.

Beim Rotary Drilling wird der Bohrstrang durch einen übertägigen Antrieb in Rotation versetzt. Rotary-Anlagen können nach der Art des Antriebs kategorisiert werden. Die Rotation des Bohrstrangs wird dabei entweder über einen Drehtisch am Boden des Bohrturms oder durch einen Top-Drive (6) am oberen Ende des Bohrstrangs eingeleitet. Eine detaillierte Ansicht dieser Antriebssysteme ist in Abbildung 3 dargestellt.
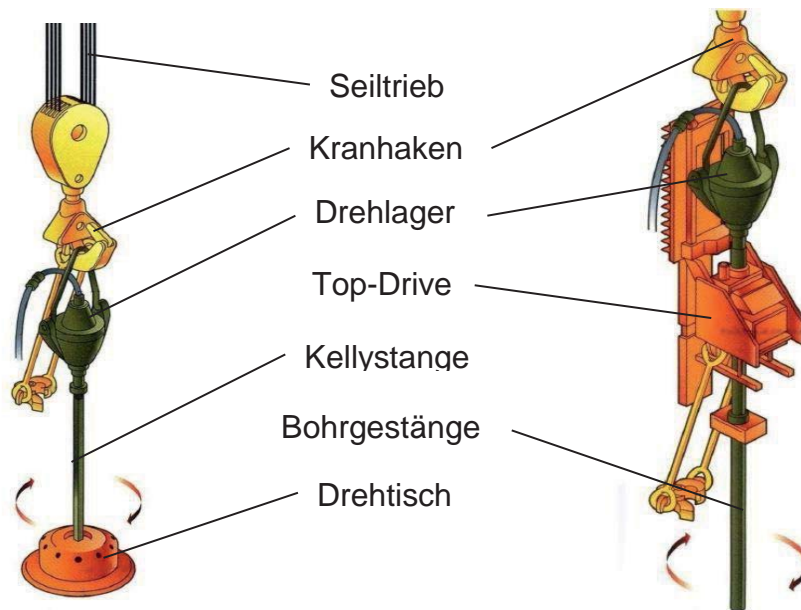
Abbildung 3: Rotary-Bohranlage und Antriebssysteme [TEO09]

Bei Anlagen die mit Hilfe eines Drehtisches arbeiten, hängt ein Drehlager an einem Kranhaken. In diesem Drehlager sitzt eine Kellystange, die einen quadratischen Querschnitt aufweist und formschlüssig vom Drehtisch in Rotation versetzt wird. Der Bohrstrang ist ebenfalls formschlüssig mit der Kellystange verbunden. An Anlagen die das Bohrgestänge über einen Top-Drive antreiben, wird das Bohrgestänge unmittelbar unterhalb des Drehlagers in Rotation versetzt. Es wird keine Kellystange zur Übertragung des Drehmoments benötigt.

Laut Reich [REI09], [REI04] besteht der Bohrstrang beim Rotary-Drilling aus mehreren Komponenten. Um einen Bohrfortschritt zu erzielen wird ein Meißel benötigt. Die Meißelauswahl wird nach der Art des zu bohrenden Materials getroffen. Rollenmeißel werden zumeist in weichen Materialschichten verwendet, da bei dieser Meißelart geringere Anschaffungskosten anfallen. Treten laut der zuvor angestellten geologischen Untersuchung hauptsächlich harte Gesteinsformationen auf, finden Diamantmeißel Anwendung, da diese eine höhere Lebensdauer aufweisen. Direkt über den Meißel befindet sich die Bohrgarnitur. Die Bohrgar-

nitur ist das Gehirn des Bohrwerkzeugs, da sich dort die gesamte Sensorik befindet. Über der Bohrgarnitur ist das Bohrgestänge angeordnet. Nach [DYK99] und [REI09] sind drei Arten von Rohren zu unterscheiden, die von der Bohrgarnitur bis zum Bohrhakenverbaut werden:

- Schwerstangen (Drill Collars)
- Übergangsstangen (Heavy Weight Drill Pipes)
- Bohrgestänge (Drill Pipes)

Oberhalb der Bohrgarnitur sind die Schwerstangen angebracht. Sie sind sehr stabil und dickwandig. Durch die Gewichtskraft der Schwerstangen wird der Anpressdruck des Meißels auf die Bohrlochsohle hergestellt. Zwischen den Schwerstangen und dem Bohrgestänge werden Heavy Weight Drill Pipes verwendet, um einen Übergang zu von den Schwerstangen zu dem Bohrgestänge mit geringerem Durchmesser zu schaffen. Den längsten Teil des Bohrstrangs stellt das Bohrgestänge mit kleinem Durchmesser dar, um das Gewicht des Bohrstrangs gering zu halten.

Das Bohrgestänge besteht aus 9 m bis 10 m langen Rohrsegmenten, die an ihren Enden über konische Gewinde verfügen. Über diese Gewinde werden die Bohrstangen miteinander verschraubt. Während ein neues Rohrsegment an das Gestänge angesetzt wird, muss der Bohrvorgang angehalten werden. Um diese Bohrpausen kurz zu halten, werden während des Bohrprozesses drei dieser Segmente zu Zügen von 27 m bis 30 m Länge vorverschraubt. Diese Züge werden dann in einem Magazin (24) bereitgestellt. Somit muss der Bohrprozess nur alle 27 m bis 30 m angehalten werden, um einen neuen Zug an das Bohrgestänge anzusetzen. Sobald ein Zug abgebohrt ist wird der nächste Zug über die Rohrrampe (23) auf den Bohrturm gefördert. Der abgebohrte Zug wird mittels einer keilförmigen Buchse in Höhe der Arbeitsbühne festgeklemmt. Der neue Zug wird dann durch einen Arbeiter auf der Fingerbühne (4) in den Haken eingehängt und kann nun mit dem abgebohrten Zug verschraubt werden. Die Stromversorgung der Bohranlage findet mit Hilfe von Generatoren (13) statt. Der Treibstoff für diese Generatoren wird in großen Treibstofftanks (14) gelagert.

2.2 Bohrlochauskleidung

Zur Bohrungsherstellung ist eine Bohrlochauskleidung, das Casing, notwendig. Diese Auskleidung schützt das Bohrloch gegen Einstürze und ungewolltes Eintreten von Fluiden aus dem umliegenden Erdreich in die Bohrung sowie einem Verlust der Bohrspülung durch poröse Gesteinsschichten. Laut REICH [REI09] ist das Einsetzen des Casings in das Bohrloch bislang jedoch sehr zeitaufwendig, da hierzu ein hohes Maß an manueller Arbeit erforderlich ist. Zudem bewegt sich das Bohrpersonal dabei im Gefahrenbereich der Bohranlage.

Wie in Kapitel 2.1 bereits beschrieben, muss zunächst ein Standrohr gesetzt werden. Dieses Standrohr wird etwa 5 bis 20 Meter in den Boden gerammt und geräumt. Es verhindert ein Einfallen des Loches durch eindringendes Grundwasser. Anschließend werden die lockeren oberen Erdschichten durchbohrt, bis man auf tragfähige Gesteinsschichten stößt. Dort wird die Ankerrohrtour in das Bohrloch eingesetzt und fest im Untergrund einzementiert. Anschließend wird der Blowout-Preventer auf die Ankerrohrtour aufgesetzt.

Nachdem die Bohrung gesichert ist, wird mit den eigentlichen Bohrarbeiten durch die verschiedenen Gesteinsschichten begonnen. Laut REICH [REI09] stellen einige dieser Gesteinsschichten, z.B. Salz, Ton oder poröse Schichten, Problemzonen dar. Um Probleme und den damit einhergehenden Zeitverlust zu minimieren, wird das Bohrloch in bestimmten Abständen von innen mit einer Auskleidung, dem Casing oder Futterrohr, versehen. Dies geschieht bevor die Bohrspülung aus der Bohrung entfernt wird. Die Rohrabschnitte die eingesetzt werden, um o.g. Effekte zu verhindern, heißen technische Rohrtouren [REI09]. Der Rohrabschnitt, welcher nach Beendigung der Bohrung eingesetzt wird, heißt Produktionsrohrtour.
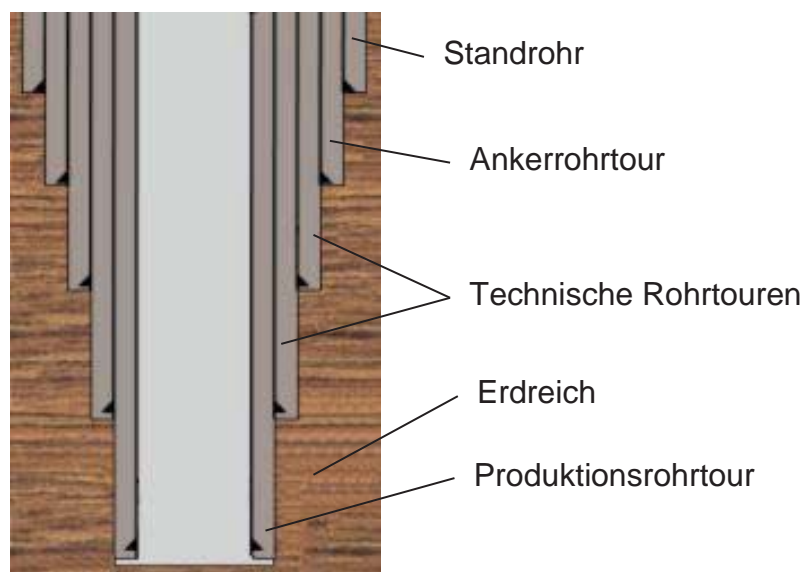
Abbildung 4: Schematischer Aufbau einer konventionellen Verrohrung einer Tiefenbohrung

Die technischen Rohrtouren werden zur Zeit mit zylindrischen Rohren bewerkstelligt, welche je nach gewünschter Länge aus mehreren 9 m bis 10 m langen Segmenten zusammengeschraubt werden [REI09]. Abbildung 4 zeigt den Aufbau einer konventionellen Verrohrung nach dem Long-String Prinzip. Dieses bedeutet, dass alle Casingabschnitte von der (temporären) Bohrlochsohle bis zur Erdoberfläche herausgeführt werden. Der Bohrlochdurchmesser wird somit stufenweise verringert. Besonders im oberen Bereich der Bohrung, muss daher

ein großes Volumen an Gestein abgetragen werden, obwohl dieses nicht zu Förderzwecken dient.

Um Kosten im Bereich der Bohrlochauskleidung zu senken, wurden Liner Hanger Systeme entwickelt. Bei diesem System werden die Liner im unteren Bereich des bestehenden Casings mit Hilfe komplexer Klemmsysteme fixiert und gegen die Umgebung abgedichtet [MOT06]. Somit muss nicht jede neue Rohrtour durch die gesamte bestehende Verrohrung reichen. Die Produktionsrohrtour kann anschließend bei Bedarf als Long-String eingesetzt werden [SCH10].
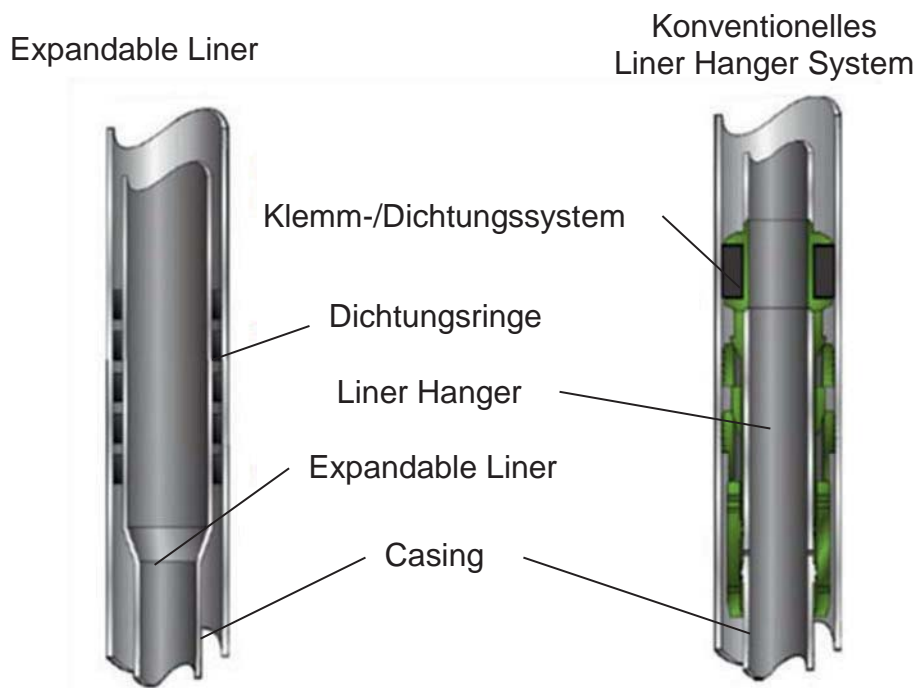
Abbildung 5: Vergleich Liner Hanger und Expandable Liner [WRA09]

Eine Weiterentwicklung der konventionellen Liner Hanger sind die Expandable Liner. Dabei handelt es sich ebenfalls um zylindrische Liner, die in der Bohrung aufgeweitet und mit dem bereits bestehenden Casing verklemmt werden. Dadurch lässt sich der Verrohrungsvorgang wesentlich einfacher vollziehen, als bei konventionellen Liner Hanger Systemen. Die Abdichtung der Abschnitte im Überlappungsbereich wird mit Hilfe von Dichtungsringen realisiert. Die Dichtungsringe werden zuvor am unteren Ende des bereits zementierten Casingabschnitts angebracht[MOT06]. Sowohl Long-String als auch die vorgestellten Liner Systeme führen zur teleskopartigen Ausprägung der Bohrung. An den Expandable Linern ist jedoch gezeigt worden, dass das untertägige Aufweiten von Rohren möglich ist. Durch den Einsatz von Expandable Monobore Linern ist eine Möglichkeit entwickelt worden, die Liner nicht nur im Überlappungsbereich sondern auf ihrer vollen Länge aufzuweiten [Bak07]. Durch diese Technik kann Rohrmaterial und Bohrzement eingespart werden. Zudem ist die notwendige

Verringerung des Bohrdurchmessers nach jedem Liner dadurch geringer geworden. Trotz aller Bemühungen besteht bislang noch keine Möglichkeit ein auf seiner vollen Länge mono-bares Bohrloch herzustellen.

3   Verbesserung der Wirtschaftlichkeit der Bohrlochherstellung

Ein wichtiger Ansatz zur Verbesserung der Wirtschaftlichkeit einer Geothermieanlage ist die Schaffung eines effizienten und ökonomischen Gesamtsystems mittels automatisierter Bohrungsherstellung und der Bohrungsauskleidung durch expandierbare Rohrstrukturen. Um eine Steigerung der Wirtschaftlichkeit zu erreichen, muss der Automatisierungsgrad der Bohranlage und des Bohrprozesses gesteigert werden. Es werden Konzepte zur automatisierten Bohrungsherstellung erarbeitet. Dazu werden verschiedene im Stand der Technik gängige Verfahren zum Tiefbohren mit neuen Konzepten zur Bohrlochauskleidungsherstellung kombiniert.

Diese Konzepte konzentrieren sich auf das Handling und den möglichst zeiteffizienten Einbau der expandierbaren Bohrlochauskleidungen sowie die Eliminierung des Verschraubungsvorgangs von Casings. Die Automatisierungskonzepte werden für die im Rahmen des gebo-Teilprojekts W5 konzipierten Bohrlochauskleidungen aus entfaltbaren Rohren realisiert. Der bisherige Einbauprozess wird mit einem umsatzorientierten Funktionsmodell dargestellt. Dem gegenübergestellt wird das Funktionsmodell des wirtschaftlich idealen Prozesses. Anhand der Modelle werden die Automatisierungskonzepte, die im Rahmen des ersten Arbeitspakets des gebo-Teilprojekts B3 entwickelt wurden, dargestellt und beschrieben. Anschließend erfolgt die Bewertung der Konzepte anhand der VDI-Richtlinie 2225. Schließlich werden die ausgewählten Konzepte zur automatisierten Bohrlochauskleidungsherstellung mit gängigen Bohrverfahren zur Schaffung eines Gesamtkonzepts kombiniert. Die Bewertung der Lösungskombinationen wird mit der binären Bewertung von Lösungsvarianten vorgenommen.

3.1   Handhabungs- und Automatisierungskonzepte

In diesem Abschnitt werden die entwickelten grundlegenden Konzepte für einen neuen wirtschaftlichen, automatisierten Bohrlochauskleidungsprozess vorgestellt. Die Abbildung 6 zeigt umsatzorientierte Funktionsmodelle des Bohrlochverkleidungsausbaus. Die Funktionen des Prozesses wurden für die Ideenbildung abstrakt formuliert. Links wird die derzeitige Umsetzung des Bohrlochverkleidungseinbaus mit der Hauptfunktion „Casing ablassen" und den Nebenfunktionen dargestellt. Der rechte Teil der Abbildung zeigt das Zeit- und Kostenoptimum. Dieses theoretische Optimum entsteht durch Eliminierung aller Nebenfunktionen und die Konzentration auf die wertschöpfende Hauptfunktion.

Um die Wirtschaftlichkeit der Geothermieanlage zu steigern, werden durch Variation des Funktionsmodells und dem Suchen nach verbesserten Nebenfunktionen Lösungen gesucht, die sich dem Ideal nähern. Wie in der Abbildung zu sehen ist, wird das Optimum erreicht,

wenn die Nebenfunktionen entfernt werden und das Grundmaterial direkt aus dem Speicher in das Bohrloch ohne Unterbrechungen abgelassen wird. Die Länge des Grundmaterials liegt je nach Beschaffenheit des zu verrohrenden Abschnitts bei dreihundert Metern bis zu einem Kilometer. Kann diese theoretisch ideale Länge nicht erreicht werden, müssen dem Ideal Nebenaufgaben zum Zuführen, Fügen und Handhaben des Materials während des Einbaus hinzugefügt werden. Tabelle 1, am Ende dieses Abschnitts, enthält die Übersicht über prinzipielle Lösungen mit Bewertungen, die im Rahmen des Projekts erarbeitet wurden. Diese werden einzeln in dem folgenden Abschnitt näher betrachtet.
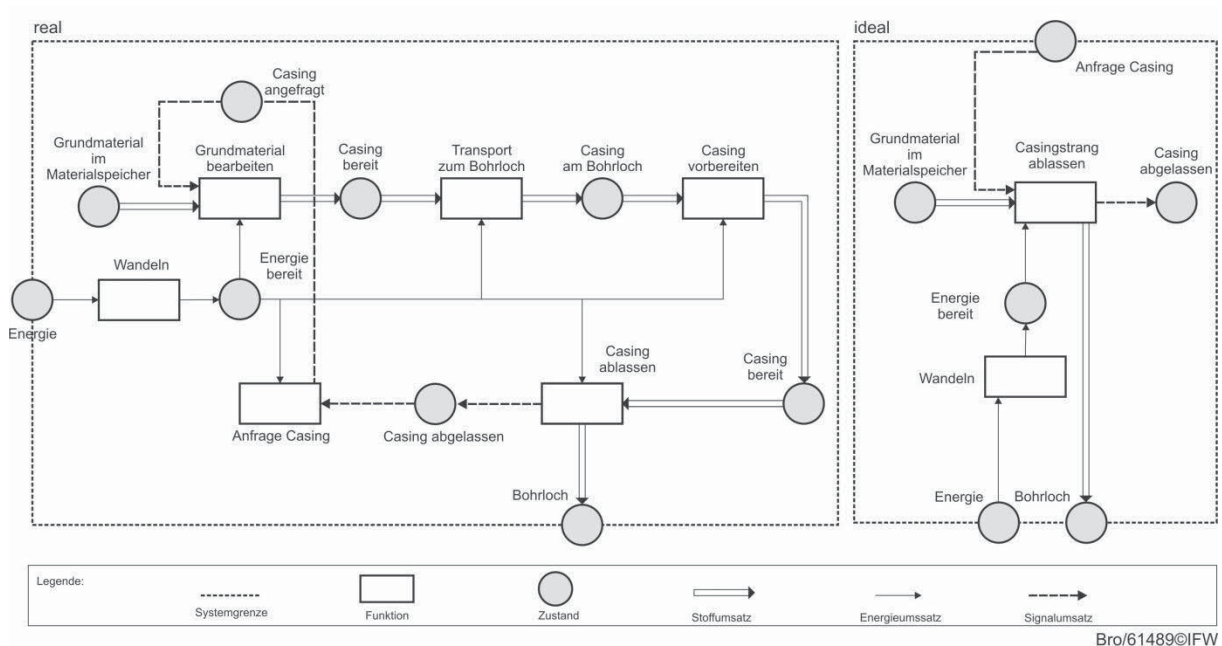
Abbildung 6: Umsatzorientiere Funktionsmodelle Bohrlochauskleidungseinbau

Abbildung 7 zeigt vereinfachte Funktionsskizzen zu den Lösungsmöglichkeiten I a und I b. Für die Lösungsmöglichkeit I a wird in eine Tiefbohranlage eine Maschine zur Verbindung der einzelnen Segmente in Standardlänge direkt über dem Bohrloch mit den sich im Bohrloch befindlichen Casings integriert. Die Segmente werden mit einem Zuführungsmechanismus von einem Magazin zum Bohrloch transportiert und dort gefügt. Der Verschraubungsautomat der ursprünglichen Anlage wird durch die Maschine zum Fügen der Segmente substituiert. Bei Lösungsmöglichkeit 1b werden statt einzelner Segmente vormontierte Züge aus mehreren Segmenten verwendet. Die Vorteile bei dieser Anordnung sind die verhältnismäßig geringe Anpassung der bestehenden Anlage. Der Zeitgewinn von Lösungsmöglichkeit I a, der gegenüber dem Stand der Technik als gering eingeschätzt wird, wird durch die Vormontage mehrere Segmente mittels Lösungsmöglichkeit I b gesteigert.

Die Vormontage von Segmenten zu Zügen findet mit dem dafür vorgesehenen Fügeautomaten statt. Eine Transporteinrichtung, wie beispielsweise ein Portalkran, übernimmt die Zufüh-

rung. Die montierten Züge werden anschließend mit dem Zuführungsmechanismus zum Bohrloch transportiert und dort mit den sich im Bohrloch befindlichen Segmenten gefügt. Die Vormontage der Züge findet immer dann statt, wenn im Arbeitsablauf keine Bohrlochauskleidung gefordert ist. Der Vorteil bei dieser Anordnung gegenüber der Lösungsalternative I a ist der dadurch entstehende größere Zeitvorteil. Die Nachteile sind die notwendige Vergrößerung des Bohrturms aufgrund der deutlich längeren Segmente, das aufwändigere Handling aufgrund der gesteigerten Masse des Zugs und durch die gesteigerte Länge des Faltrohres. Ferner ist eine zweite Maschine zum Vormontieren der Segmente und eine weitere Transporteinrichtung nötig.
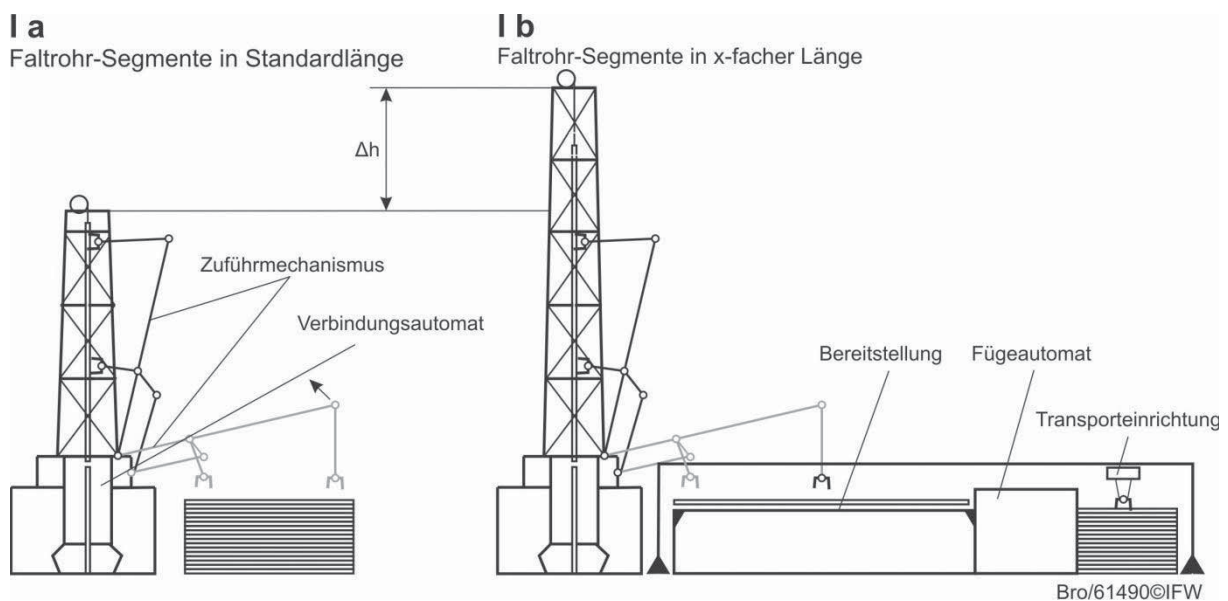
Abbildung 7: Schematische Darstellung der Lösungsalternative I a und I b

Abbildung 8 zeigt die Lösungsalternativen II und III. Bei der Lösungsmöglichkeit II werden vormontierte Faltrohr-Teleskope in einem Magazin vorgehalten. Bei Bedarf wird ein Teleskop mit dem Zuführmechanismus automatisch zur Fügeposition über dem Bohrloch transportiert.

367
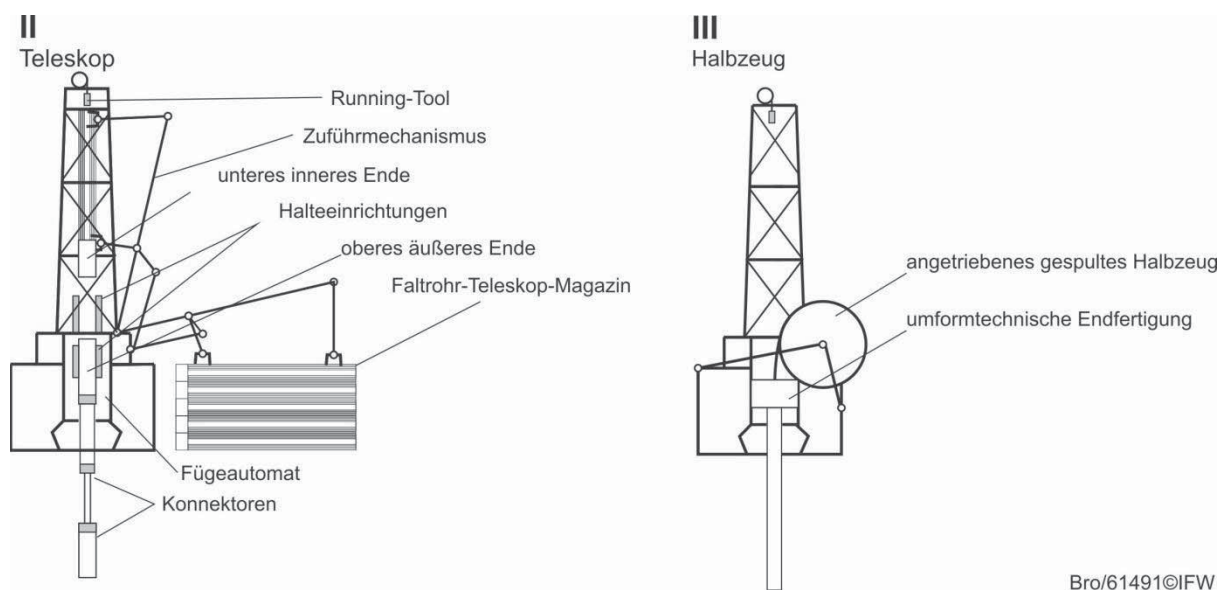
Abbildung 8: Schematische Darstellung der Lösungsalternativen II und III

Das Teleskop ist derart ausgeführt, dass das untere innere Ende mit dem oberen äußeren Ende mit einem Adapter oder einer Fügetechnik gefügt wird. Die einzelnen Teleskopteile werden mit Konnektoren verbunden. Das sich im Bohrloch befindliche Teleskopende und das innere Teleskopende des neu zugeführten werden positioniert und mittels zwei Halteeinrichtungen gehalten. Danach wird der innere Teil des Teleskops direkt über dem Bohrloch mit dem äußeren Teil des Teleskops des neu zugeführten Casing mit dem Fügeautomaten gefügt. Während des Fügens wird das Werkzeug zum Ablassen des Casings ("Running-Tool") mit dem Flaschenzug des Bohrturms heruntergelassen und positioniert. Das „Running-Tool" wird aktiviert und hält das Casing. Die Haltevorrichtungen werden deaktiviert und das gesamte Casing wird mit dem Werkzeug am Seil abgelassen. Anschließend beginnt der Prozess erneut. Nachteile bei dieser Lösungsmöglichkeit sind die aufwändige Bauweise und Vormontage sowie die durch den Bohrlochdurchmesser begrenzten „Lagen" des Teleskops, die die Maximallänge eines Teleskopes eingrenzen.

Die Lösungsmöglichkeit III behandelt die umformtechnische Endfertigung des Faltrohres, erst in Bohrlochnähe aus einem gespulten und rohrförmigen Halbzeug durch z.B. Ziehen oder Drücken durch eine Matrix. Das Volumen des Halbzeuges entspricht dem der fertigen Auskleidung. Unter der Annahme, dass sich das Halbzeug so schnell endfertigen lässt, wie es abgelassen werden kann, liegen die Vorteile dieser Lösungsmöglichkeit in den folgenden Punkten: Es ist kein Fügen von Segmenten nötig, die Länge des herzustellenden Casings ist unbegrenzt und flexibel regelbar und der Einbauprozess wird nicht durch Fügevorgänge unterbrochen. Das in Abbildung 6 beschriebene Ideal wird erreicht. Die Hauptnachteile sind die schwierige Umsetzung der schnellen Umformung und die voraussichtlich sehr hohen Kosten für die Fertigungstechnik.

In Abbildung 9 werden die Lösungsmöglichkeiten IV und V dargestellt. Die Lösungsmöglichkeit IV stellt in einem Magazin zu „Paketen" plastisch senkrecht zur Achsrichtung zusammengefaltete Segmente dar. Die Knickstellen werden im Vorfeld als Festkörpergelenke gefertigt. Das erste Segment wird bei Bedarf mittels eines translatorisch bewegbaren Schlittens zum Bohrloch transportiert und dem Antrieb zugeführt. Der Antrieb ist als Injector-Head ausgeführt. Das über den Schlitten angelieferte Segment wird bei gleichzeitigem Zurückbiegen der nächsten Gelenke in einer ununterbrochenen Bewegung in das Bohrloch hinabgelassen. Zur Steuerung der Bewegung wird das Paket im Magazin linear nachgeführt. Bei Bedarf wird das nächste Paket stoffschlüssig oder mittels Konnektor gefügt. Der Vorteil bei dieser Anordnung ist die geringe Anzahl der Fügevorgänge zwischen den Paketen. Ferner ist ein Fügeautomat über dem Bohrloch nicht notwendig. Nachteilig sind das technische Risiko in der Umsetzbarkeit sowie die nötige Kalibrierung der Festkörpergelenke bei dem Entfalten im Bohrloch sowie die hohen Materialbelastungen und Kräfte durch die plastischen Verformungen. In der Lösungsmöglichkeit V werden die Knickstellen der plastischen Verformung der Variante IV durch elastische Konnektoren ersetzt.
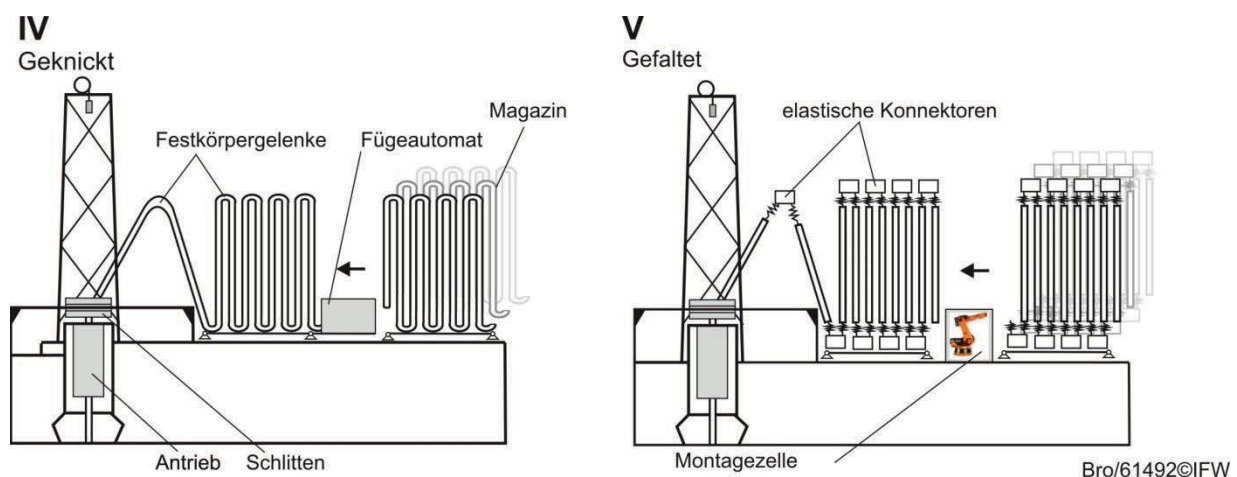
Abbildung 9: Schematische Darstellung der Lösungsalternativen IV und V

Der Nachteil der hohen Materialbelastungen des Casings und der Kräfte von Lösungsmöglichkeit IV werden eliminiert. Der Nachteil dieses Lösungsansatzes besteht hingegen in der aufwendigen Entwicklungsarbeit und der der technischen Machbarkeit der Konnektoren (Zugbelastung, Verhalten bei Entfaltung, Zementierung und Dichtigkeit usw.). Diese Variante bietet hingegen den Vorteil eines quasi endlosen Casings durch automatisiertes Montieren neuer Elemente mit Konnektoren in der Montagezelle aber ohne stoffschlüssiges Fügen und ohne Unterbrechungen. Thermische Belastungen und Gefügeänderungen entfallen. Der Einsatz von Robotern ist denkbar. Auch die direkte Montage der Konnektoren im Prozess ohne Lagerhaltung kann in Betracht gezogen werden.
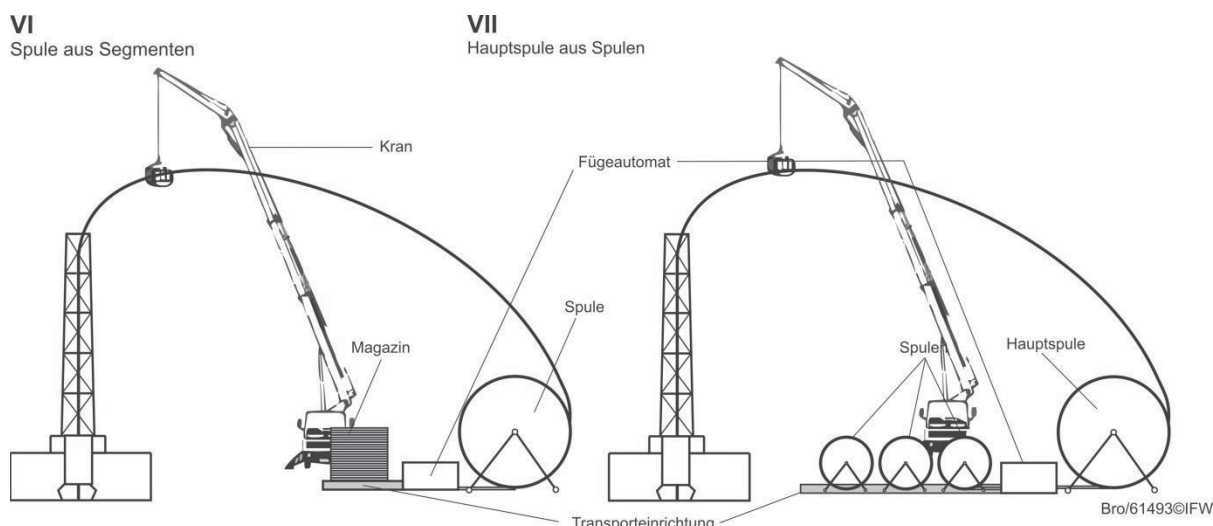
Abbildung 10: Schematische Darstellung der Lösungsalternativen VI und VII

Die Abbildung 10 zeigt Skizzen zu den Lösungsmöglichkeiten VI und VII. Ziel dieser Lösungsmöglichkeiten ist es, durch große Spulen dem Ideal aus Abbildung 6 möglichst nahe zu kommen. Mit der Transporteinrichtung wird bei beiden Alternativen Faltrohrcasing automatisch einem Automaten zugeführt. Der Automat fügt das zugeführte Casing in Lösungsmöglichkeit VI a und VII a stoffschlüssig, bei Alternative VI b VII b mittels Konnektoren an den Faltrohrstrang. Der Faltrohrstrang ist somit vor dem Ablassen komplett auf einer Spule aufgewickelt um schnellstes Auskleiden zu ermöglichen. Um die Strukturbelastungen zu minimieren wird der Durchmesser der Hauptspule so ausgeführt, dass bei dem Aufspulen nur elastische Verformungen auftreten. Zur Minimierung der Prozesszeit werden der Durchmesser und die Breite der Spule derart ausgeführt, dass das Ablassen des Casings ununterbrochen ohne Fügevorgänge erfolgt. Die Zuführung zum Bohrloch erfolgt mittels eines Krans. Der Antrieb zum Ablassen wird mit einem Injector-Head realisiert.

In Lösungsmöglichkeit VI erfolgt die Fertigung der Hauptspule aus Segmenten die in einem Magazin bevorratet werden und mittels der Transporteinrichtung dem Fügeautomaten zugeführt werden. In der Lösungsalternative VII wird der Faltrohrstrang aus Spulen geringeren Durchmessers gefertigt. Der Durchmesser dieser Spulen ist so ausgeführt, dass der Transport und die Anlieferung mittels LKW an den Bohrplatz erfolgen können. Die Spulen werden nacheinander auf die Hauptspule aufgespult. Dazu wird das jeweilige Ende der Spule mit dem Anfang der neuen Spule verbunden. Die Zuführung der neuen Spule erfolgt mit Einkuppeln des Spulenanfangs an den Stetigförderer der Transporteinrichtung. Ein Nachteil der Möglichkeiten VI und VII sind die großen Abmessungen und die hohe Masse der komplettierten Spule. Des Weiteren ist grundsätzliche Spulbarkeit der Faltrohrstrukturen anzuzweifeln. Vorteile der Lösungsalternativen VI und VII sind die Möglichkeit des unterbrechungsfreien Ablassens des Casings und der Fertigung des gesamten Strangs während der Nebenzeiten.

Es sind keine Fügevorrichtungen über dem Bohrloch nötig. Die große Entfernung der Füge-vorrichtung vom Bohrloch ist bei der Nutzung von Schweißverfahren vorteilhaft. Möglichkeit VII hat gegenüber Möglichkeit VI den Vorteil, dass sehr viel weniger Fügevorgänge aufgrund der sehr viel größeren Länge der Spulen gegenüber Segmenten nötig sind.
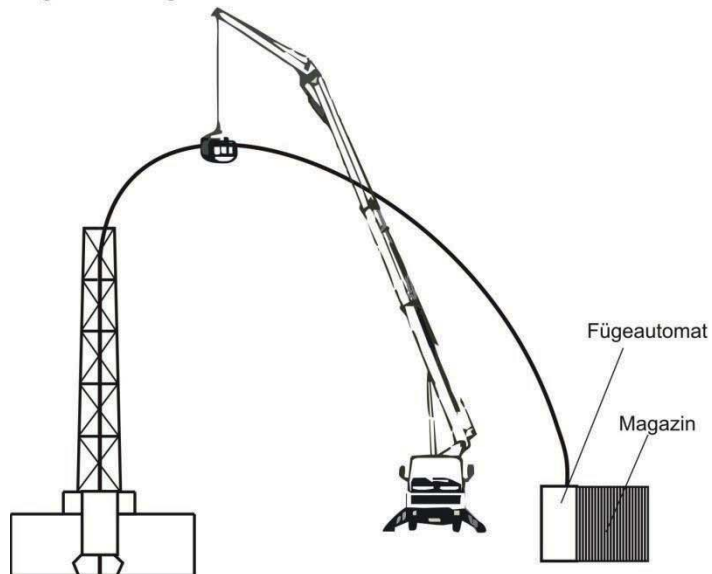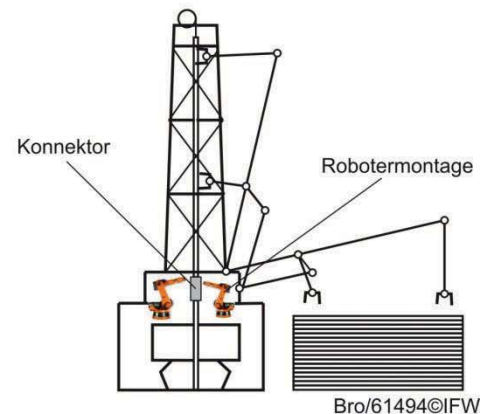
Abbildung 11: Schematische Darstellung der Lösungsalternativen VIII und IX

Nr.	Alternative	Wirkprinzip	Produktivität	Entwicklungsaufwand	Machbarkeit	Kosten	Gesamt
I a	Faltrohr-Segmente in Standardlänge	Stoffschlüssiges Fügen von Segmenten	◔	◑	◑	◑	◑
I b	Faltrohr-Segmente in x-facher Länge (Faltrohr-Zug)	Stoffschlüssiges Fügen einzelner vormontierter Segmente	◑	◑	◑	◔	◑
II	Teleskop	Ausfahren eines Segment-Teleskopes	◔	○	◔	○	○
III	Halbzeug	Umformen eines endlosen Rohres aus rohrförmigem Halbzeug	●	◑	○	◔	○
IV	Geknickt	Plastisches Zusammenfalten eines langen Faltrohres	◕	◔	○	○	◔
V	Gefaltet	Falten von gelenkig verbundenen Segmenten	◕	◑	◔	◔	◑
VI a, b	Spule endlos aus Segmenten a: Stoffschluss b: Konnektoren	Abrollen eines Endlosrohres von einer Rolle	◕	◔	◔	◔	◔
VII a, b	Spule endlos aus Spulen a: Stoffschluss b: Konnektoren	Abrollen eines Endlosrohres von einer Rolle	●	◔	◔	◔	◑
VIII	Bogen aus Segmenten	Bogen aus Segmenten	◑	◑	○	◔	◔
IX	Vorrichtungs- oder Robotermontage von Konnektoren oder automatisiertes Schweißen	Vorrichtungs- oder Robotermontage von Segmenten mit Konnektoren oder Verschweißen	◑	◑	◑	◕	◑

Legende, Richtlinie 2225					
Unbefriedigend	Gerade noch tragbar	Ausreichend	Gut	Sehr gut	
○	◔	⊖	◑	●	

Tabelle 1: Prinzipielle Lösungsmöglichkeiten zum automatisierten Casingeinbau

Die Abbildung 11 zeigt die Lösungsalternativen VIII und IX. Bei der Lösungsmöglichkeit VIII wird ein Bogen aus Segmenten während des Bohrens gefertigt und bereitgestellt. Wird die Auskleidung des Bohrlochs erforderlich, wird der Bogen unter ständiger Verlängerung mittels Nutzung des Fügeautomaten in das Bohrloch hinabgelassen. Der Vorteil dieser Anordnung besteht in der großen Entfernung des Fügeautomaten zur kritischen Explosionsschutzzone. Des Weiteren wird nur ein Fügeautomat benötigt. Nachteilig sind die schwierige Handhabung des großen Bogens und der im Vergleich zu anderen Varianten geringe Zeitvorteil. Die Faltrohrstrukturen werden in Möglichkeit IX mit entfaltbaren Konnektoren über dem Bohrloch gefügt oder geschweißt. Die Montage der Konnektoren bzw. das Schweißen erfolgt automatisch durch Roboter mittels einer Presseinrichtung mit dessen Hilfe der Kraftschluss zwischen Konnektoren und den Rohrenden hergestellt wird oder einer automatischen Schweißanlage. Vorteilhaft an dieser Möglichkeit ist die geringe notwendige Anpassung bestehender Anlagentechnik. Nachteilig sind der gegenüber dem Stand der Technik voraussichtlich geringe Zeitvorteil und die Notwendigkeit der Neuentwicklung der Verbindungstechnik. Die Tabelle 1 zeigt die Übersicht der vorgestellten Konzepte und deren Bewertung anhand der VDI 2225 anhand der Kriterien Produktivität, Entwicklungsaufwand, Machbarkeit und Kosten. Exemplarisch sind in der Abbildung 12 zwei Prinzipentwürfe dargestellt. Die Mockups zeigen die Konzepte Ib und VI.
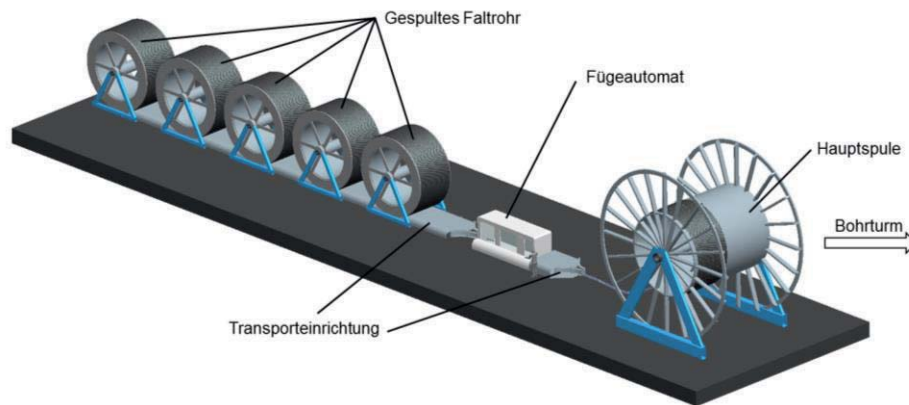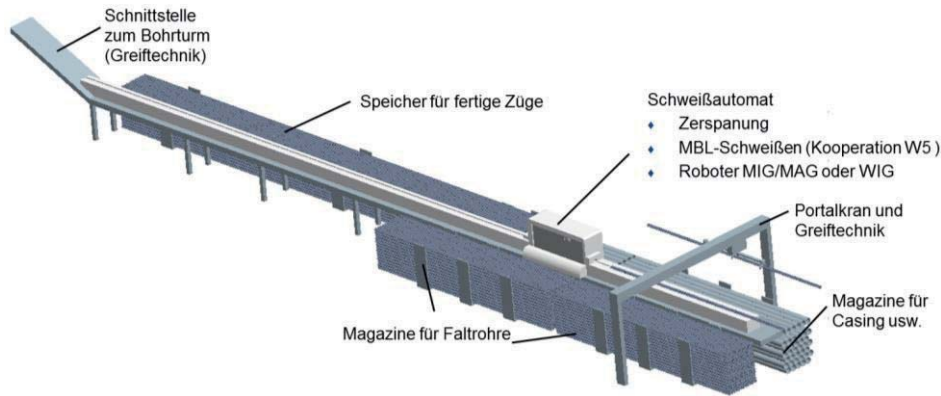
Abbildung 12: Prinzipentwürfe der Konzepte I a und VI

3.2 Bohranlagenkonzept

Zur Erstellung eines ganzheitlichen Bohranlagenkonzepts wurde mit den fünf ausgewählten Bohrlochauskleidungsautomatisierungskonzepten und verschiedenen Bohrtechniken eine Morphologie erstellt. Die Matrix der Kombinationen zeigt Tabelle 2. Es sei angemerkt, dass als Bohrverfahren das Casing Drilling mit Faltrohren bis zum Mai 2010 definiert war, jedoch wegen der als schlecht eingeschätzten Machbarkeit des Experten Herrn Nobilliou vom leitenden Bohrtechnikprojekt verworfen wurde [GEB10]. Die bis Dato zu diesem Bohrverfahren entworfenen Automatisierungsverfahren sind auf andere Bohrverfahren nicht anwendbar und werden aus diesem Grunde an dieser Stelle nicht dargestellt.

		Bohrlochauskleidung				
		I a	I b	V	VII	IX
	Coiled-Tubing	1	2	3	4	5
	Rotary-Drilling	6	7	8	9	10
Bohrverfahren	**Rotary-Drilling und Coiled-Tubing**	**11**	**12**	**13**	**14**	**15**
	~~Casing-Drilling mit Faltrohren~~	~~16~~	~~17~~	~~18~~	~~19~~	~~20~~

Tabelle 2: Variantenbildung zum Bohranlagenkonzept

Des Weiteren wurde durch die Bohrtechnik Experten des Teilprojekts B1 festgestellt, dass die hohen Anforderungen an das Bohrverfahren nur vom hybriden Bohren mit Coiled-Tubing und Rotary Drilling erfüllt werden [TEO10]. Entsprechend beschränkt sich die Auswahl für die weiteren Betrachtungen auf die Varianten 11-15 (vgl. Tabelle 2). Die sonstigen im Rahmen dieses Projekts betrachteten Varianten werden an dieser Stelle nicht weiter dargestellt. Die Gegenüberstellung der entstehenden Varianten und deren Bewertung werden als binäre Bewertung von Lösungsvarianten mittels Dominanzmatrizen ausgeführt. Zur Darstellung der Ergebnisse dient Tabelle 3. Die dargestellte Dominanzmatrix stellt eine Grobeinschätzung dar. Sie wird dann angewendet, wenn die objektiven Eigenschaften nur unzuverlässig ange-geben, eingeschätzt oder nur mit unverhältnismäßig großem Aufwand objektiv ermittelt wer-den können [PAH04].

	Variante				
	11	**12**	**13**	**14**	**15**
11		0	0	0	1
12	1		1	1	1
13	1	0		1	1
14	1	0	0		1
15	0	0	0	0	
Summe	**3**	**0**	**1**	**2**	**4**
Rang	**2**	**5**	**4**	**3**	**1**

(Zeilenbeschriftung links: „.. ist besser im Vergleich zu Variante …")

Tabelle 3: Bewertung der Bohranlagenkonzepte

Die höchste Bewertung erzielt die Variante 15. Die Vorteile der Variante gegenüber den Alternativen sind die einfache Automatisierbarkeit mittels Robotern und die geringe notwendige Anpassung der Bohranlage. Außerdem ist eine Platzersparnis und das leichtere Handling gegenüber den Varianten 11 und 14 zu nennen. Das Handling der Rohre in Standardlänge ist voraussichtlich leichter zu realisieren. Ferner ist es denkbar mit Robotern die Montage der Handelsüblichen Coiled-Tubing Konnektoren während des Bohrens mit Coiled-Tubing zu realisieren (mit Unterstützung einer Pressvorrichtung). Vorbereitende Maßnahmen beim Rotary-Bohren wie beispielsweise das Schmieren der Gewinde der Drillpipe sowie deren Reinigung und Zentrierung kann mittels der Roboter erfolgen. Nachteilig ist der Entwicklungsaufwand der speziellen Faltrohr-Konnektoren. Das automatische Schweißen hingegen ist besonders interessant da es zukunftsnah umgesetzt werden kann. Den zweiten Rang belegt Variante 11. Vorteile sind hier ebenfalls das leichtere Handling der Rohre in Standardlänge, die Platzersparnis gegenüber den Varianten 12 und 14 und die vergleichsweise geringere notwendige Anpassung der bisherigen Anlagentechnik. Nachteilig gegenüber Variante 15 ist der geringere Automatisierungsgrad aufgrund der zum Fügen notwendigen Maschine/Vorrichtung, die bei Bedarf jedoch problemlos hinzugefügt werden kann. Nachteilig sind die Schwierigkeit der Umsetzung der Schweißtechnik direkt im explosionsgefährlichen Bereich über dem Bohrloch und die sehr hohen Anforderungen an das Schweißverfahren. Rang drei belegt die Variante 14 aufgrund der Möglichkeit des unterbrechungslosen Ablassens des Casings. Ferner werden keine Vorrichtungen zum Fügen im explosionsgefährlichen Bereich über dem Bohrloch benötigt. Negativ sind die durch den Wickelradius voraussichtlich sehr hohen Radien der Spulen sowie die hohen Massen der Spulen.

3.3 Fazit

Im vorangegangenen Abschnitt wurden verschiedene Lösungsvarianten für neue Bohranlagenkonzepte erarbeitet und bewertet. Die am besten bewertete ist die Variante 15. Interessant ist insbesondere das automatisierte Schweißen von Bohrlochauskleidungen. Vorteilhaft kann vor allem das im TP W5 erforsche MIAB-Schweißverfahren verwendet werden. Im folgenden Abschnitt werden technische Herausforderungen herausgearbeitet, die bei der Verwendung des MIAB-Verfahrens auf Bohranlagen berücksichtigt werden müssen. Anschließend werden Lösungen erarbeitet, realisiert und untersucht.

4 Problemstellung und Lösungsansatz

Für das Verschweißen von Bohrlochauskleidungen (Casing) mit dem MIAB-Verfahren ist eine sehr hohe geometrische Genauigkeit der Rohrstirnflächen (axialer Fehler < 0,1 mm) notwendig, damit der Lichtbogen gezündet werden kann und stabil rotiert. Die Spannsituation auf Bohranlagen erlaubt jedoch kein genaues Einspannen der Werkstücke vor dem Prozess. Es ist daher notwendig, eine genaue, definierte Lage der Werkstücke vor dem Schweißprozess herzustellen. Die Problemstellung und der Lösungsansatz wird schematisch in Abbildung 13 illustriert (Fehllagen und geometrische Abweichungen werden stark übertrieben dargestellt). Für die Ausrichtung der beiden zu schweißenden Komponenten sind zwei wesentliche Schritte durchzuführen. Als erstes sind die Positionen beider Komponenten im Raum zu bestimmen.
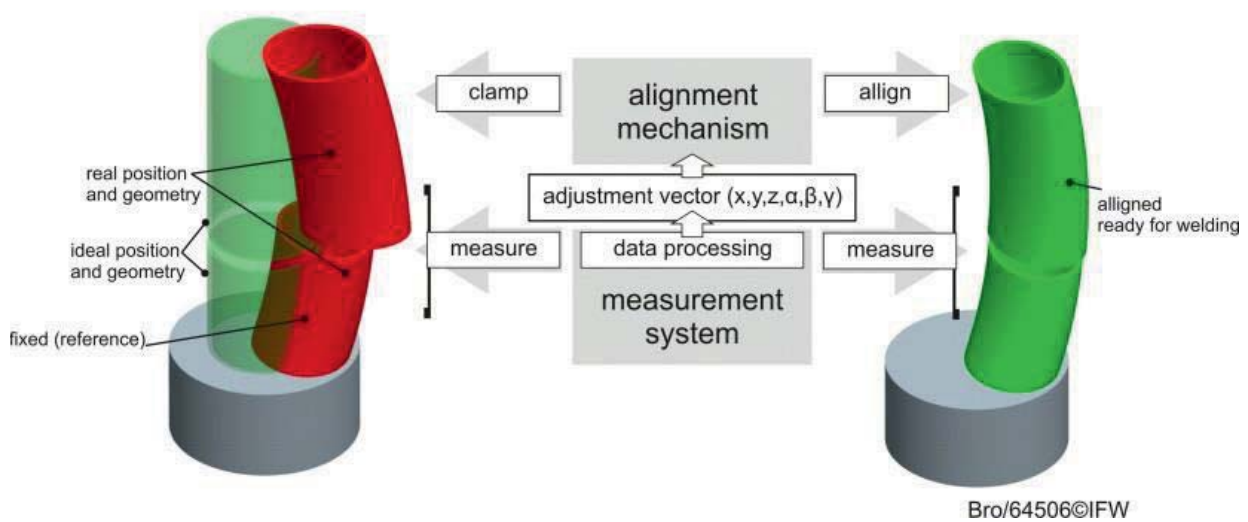
Abbildung 13: Problemstellung und Lösungsansatz

Zu diesem Zweck muss ein entsprechendes Messsystem entwickelt werden. Im zweiten Schritt muss, basierend auf den bestimmten Positionen, ein Korrekturvektor berechnet werden, der das neu gelieferte (obere) Casing hochpräzise relativ zum unteren, festgespannten Casing, ausrichtet. Für die Ausrichtung wird ein Berechnungsverfahren entwickelt. In den folgenden Abschnitten werden das Messsystem und das Berechnungsverfahren realisiert.

5 Messsystem

Die Oberfläche von zylindrischen Werkstücken messtechnisch in drei Dimensionen zu erfassen, ist eine Aufgabe bei der sich besonders eine Messanordnung anbietet, die einen zylinderförmigen Arbeitsraum aufspannt. Diese Anordnung wurde in einem Vorversuch umgesetzt und erfolgreich getestet. Die Abbildung 14 zeigt den Versuchsaufbau, bei dem ein 3-D

gedrucktes Faltrohr um die Drehachse eines Mikro-Rundtisches rotiert. Gleichzeitig wird die Oberfläche radial von außen durch einen Laser-Lichtschnitt-Triangulations-Sensor abgetastet.
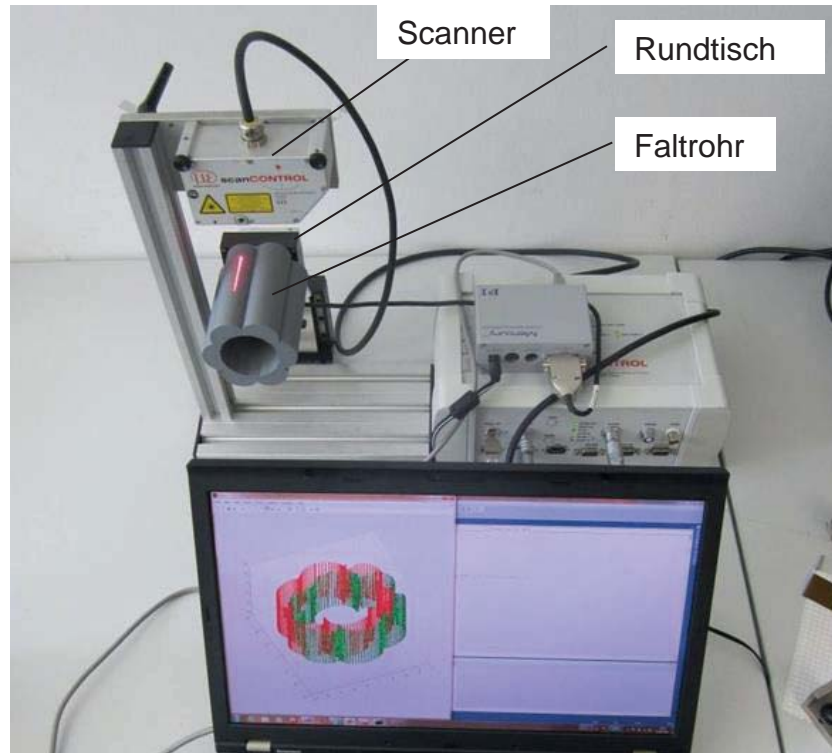
Abbildung 14: Vorversuch zum Messsystem

Da es in den späteren Anwendungsbereichen unmöglich ist, die Werkstücke zu rotieren, ist es sinnvoll schon im Versuchsstadium eine Bauweise umzusetzen, bei der die Messbewegung sensorseitig ausgeführt wird. Es wird zwar das gleiche Messverfahren zugrunde gelegt wie im Vorversuch, die Messobjekte sollen allerdings, wie in der Realität, fest im Arbeitsraum liegen. Der 2D Laserlichtschnittsensor wird daher auf einer Kreisbahn bewegt und misst in radialer Richtung die Objektoberflächen. Mit der in der Abbildung 15 dargestellten Anordnung ist somit neben der Drehachse keine weitere Bewegungsachse erforderlich. Im Folgenden werden das Messsystem und das Verfahren zur Datenverarbeitung umgesetzt.

Kreisbahn des Sensors

Werkstücke

Lichtvorhang

Sensor

Verstellachse zur Anpassung des Messbereichs
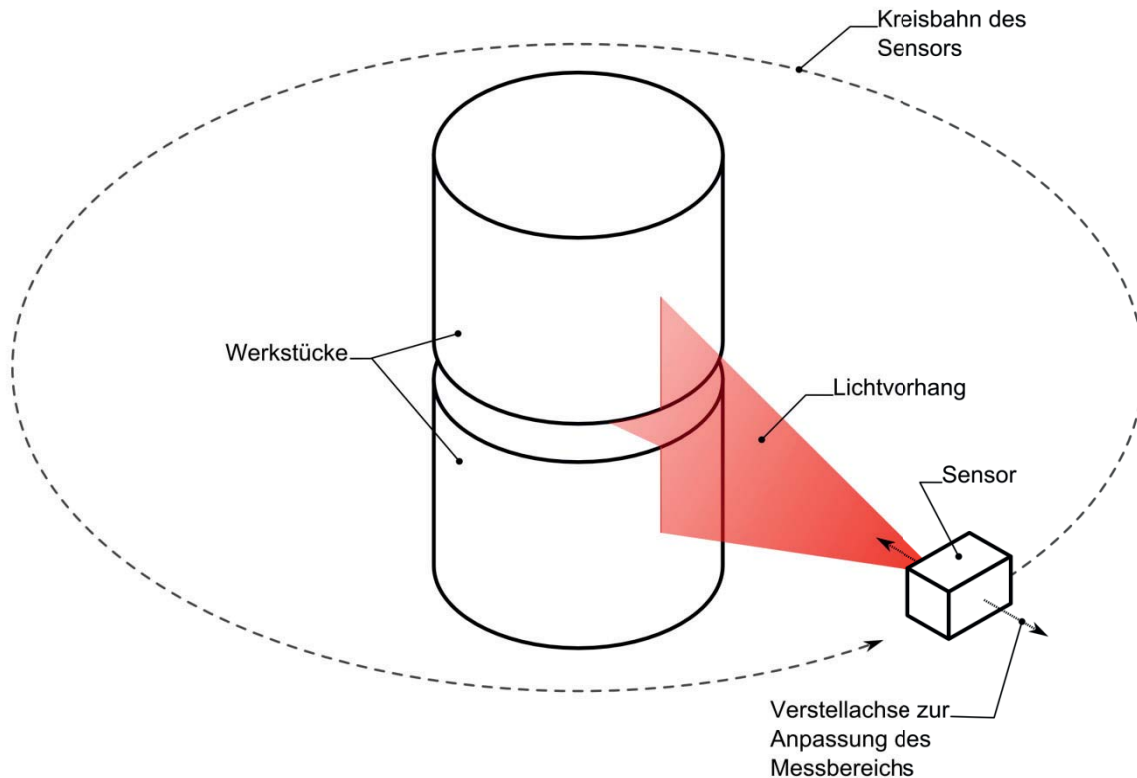
Abbildung 15: Prinzipieller Aufbau des Messsystems

5.1 Realisierung

Die Idee zum Ermitteln einer Korrekturtransformation, die die Rohre optimal zueinander aus-richtet, ist in der Abbildung 16 dargestellt. Die Lagen der Casings werden mit dem Messsys-tem dreidimensional erfasst. Anschließend wird die Transformation T_{Stell} berechnet, die das bewegliche, in der Plattform eingespannte Rohr (rot, durchgezogen, oben), auf das unbe-wegliche, im unteren Spannsystem fixierte Rohr (oben, durchgezogen, blau), optimal zuei-nander ausrichtet. Zur Ermittlung der Transformation, werden im ersten Schritt zwei Punkte-wolken erstellt, die die Referenz-Geometrien der Werkstücke im Raum repräsentieren (Im Bild gestrichelt rechts dargestellt). Diese Referenzen bilden die theoretisch perfekte Lage beider Rohre im Raum für den Fügeprozess ab.
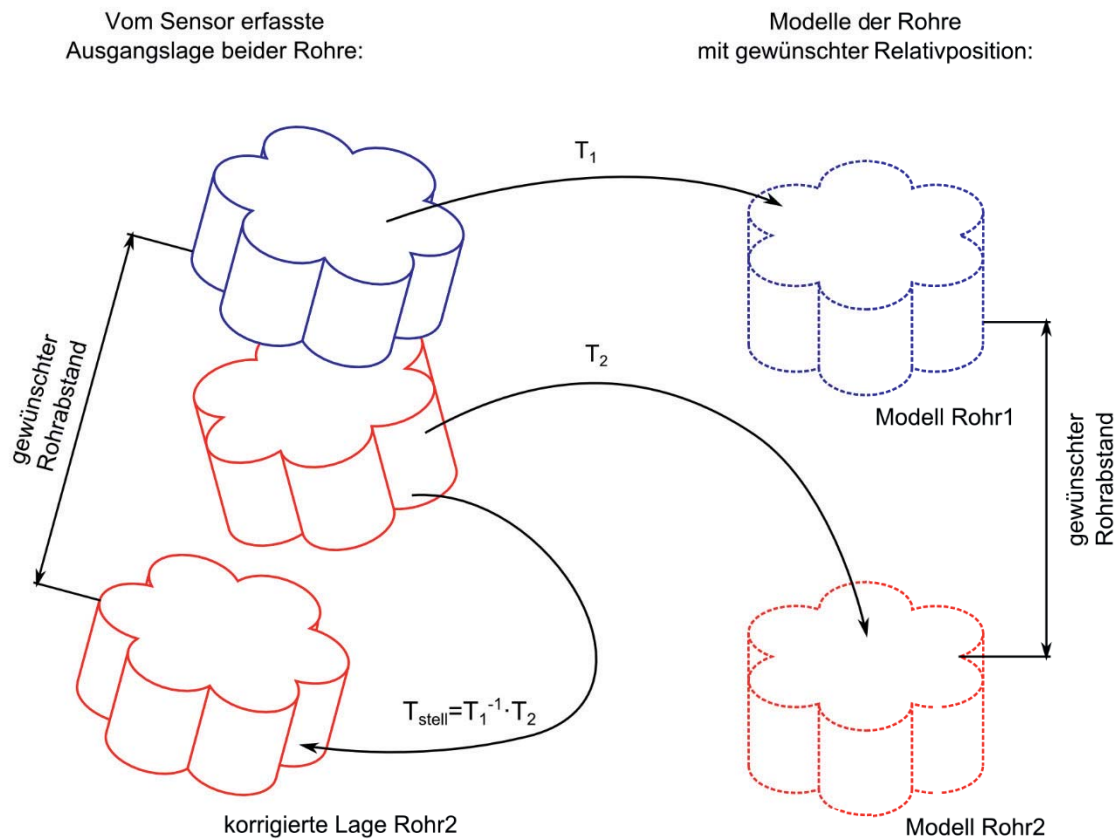
Abbildung 16: Prinzip der Korrekturvektorberechnung

Im zweiten Schritt werden die Transformationen T_1 und T_2 berechnet, die die Messpunkte beider Rohre optimal auf die jeweilige Referenz abbilden. Die Stelltransformation wird dann aus der Verknüpfung der Einzeltransformationen ermittelt. Es müssen demnach Transformation berechnet werden, mit denen durch Punktewolken dargestellte Werkstücke mit hoher Genauigkeit aufeinander abbildet werden. Diese Problemstellung wird als Registrierung bezeichnet. Als numerisches Standardverfahren werden dazu ICP-Algorithmen verwendet (Iterative Closest Point) [BESL92]. Hierbei wird die Übereinstimmung zweier Punktwolken als Gütekriterium formuliert und optimiert (meist minimiert) [JÄHN07, BESL92]. Im Rahmen des Projekts wird ein von Kjer und Wilm entwickeltes ICP-Verfahren verwendet. Das Verfahren ist unter [KJER13] frei verfügbar und dokumentiert. Aus der mit dem ICP-Verfahren berechneten Transformation wird ein sechs-dimensionaler Korrekturvektor berechnet.

Der verwendete Sensor ist der MICRO-EPSILON LLT2810-25 (vgl. Abbildung 17). Die Energieversorgung und die Kommunikation werden mit einem externen Controller realisiert. Der Sensor ist durch eine Auflösungen von 10 µm in der Tiefe (z-Achse) und 1024 Punkte in der Breite (x-Achse) gekennzeichnet. Die maximale Messdatenrate beträgt 256.000 Punkte pro Sekunde. Der Messbereich des Sensors wird in der Abbildung 17 rechts dargestellt.

Sensor	Messbereich

[Bilder: µ-Epsilon]

Bro\64535©IFW
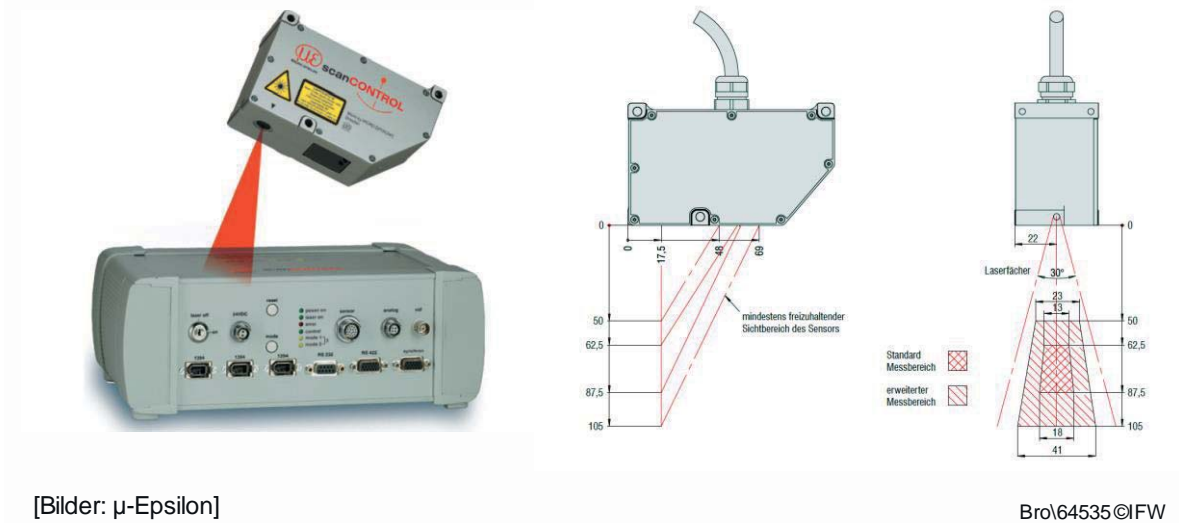
Abbildung 17: Verwendeter Sensor

Um die Hauptfunktion des beschriebenen Prinzips zu realisieren, müssen Lösungen für die wesentlichen weiteren Teilfunktionen entwickelt werden. Die Teilfunktionen sind:

- Führung des Sensors auf einer Kreisbahn
- Motor zur Bewegungserzeugung
- Übertragung (von Leistungen)
- Winkelmessung

Führung:

Der Sensor wird auf einer definierten Bahn in einem Freiheitsgrad bewegt. Zu diesem Zweck eignen sich Rundführungen. Genutzt werden können große Gleitlager, deren Innendurchmesser größer ist als der geforderte Freiraum für die Rohre (280 mm) oder auch große Wälzlager. Große Wälzlager sind erhältlich als hochsteife und sehr genaue Ausführungen in Stahl oder als deutlich kostengünstigere Ausführungen aus Aluminium und Polymer. Die auf das Lager wirkenden Kräfte und Momente beim Drehen des Sensors während des Messvorgangs sind klein. Daher kann die Tragfähigkeit der Lage vernachlässigt werden. Zum Einsatz kommt daher ein Polymer Rundtischlager.

Antrieb:

Die für die Sensorbewegung erforderliche Leistung des Antriebs ist gering. Für vergleichsweise kleine Stellleistungen sind Schrittmotoren eine geeignete kostengünstige Alternative zu Servoantrieben. Zum Einsatz kommt ein geregelter, zweiphasiger Hybridschrittmotor der Firma Nanotec®.

Übertragung (von Leistungen):

Zur Übertragung der Drehbewegung mit gleichbleibender Übersetzung des Schrittmotors auf den geführten Schlitten eignen sich z.B. Zahnradgetriebe, Reibkörpergetriebe sowie Zugmittelgetriebe. Insbesondere geeignet ist in dem vorliegenden Fall die Verwendung eines Zugmittelgetriebes, da das Rundtischlager optional mit einem verzahnten Außenring beschafft werden kann.

Winkelmessung:

Für die Determinierung des Drehwinkels eignen sich direkt messende Sensoren am Lager oder ein Sensor zur Erfassung des Drehwinkels am Motor. Die Integration eines direkten Messsystems am Rundtischlager ist vergleichsweise teuer. Die Integration eines indirekt messenden Winkelmesssystems ist deutlich wirtschaftlicher. Der Schrittmotor kann optional mi einem vormontierten Drehgeber am hinteren Wellenende beschafft werden. Dieser Drehgeber arbeitet inkrementell messend.

Die Realisierung des Systems wird in Abbildung 18 dargestellt. Das Rundtischlager ist an einem Grundkörper aus Aluminium montiert. Auf diesem ist ein Schlitten montiert, der auf einer Schwalbenschwanzführung befestigt ist. Auf der Führung ist der Sensor auf einer Adapterplatte gelagert. Der Einsatz der Führung ermöglicht es, den radialen Abstand des Sensors einzustellen. Damit können Rohre mit einem Durchmesser von 50 mm bis 300 mm vermessen werden. Mit einem Klemmhebel wird der Schlitten, auf dem sich der Sensor befindet, nach dem Einstellen an der Führung geklemmt. Das Antriebsmoment wird mit dem Zahnriemen über die Außenverzahnung des Rundtischlagers übertragen. Der Motor ist mit einem Halter an dem Grundkörper montiert. Die Vorspannkraft des Riementriebs kann manuell eingestellt werden.

Die Realisierung des Messsystems ist damit abgeschlossen. Im Folgenden können Methoden zur Berechnung der räumlichen Lagen der Casings im Raum entwickelt werden.
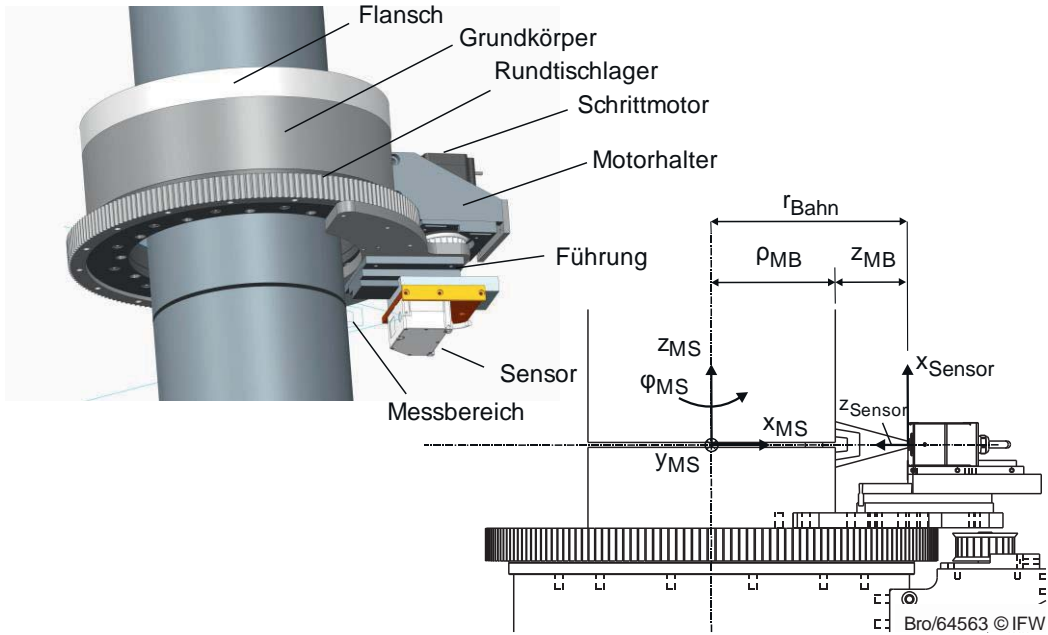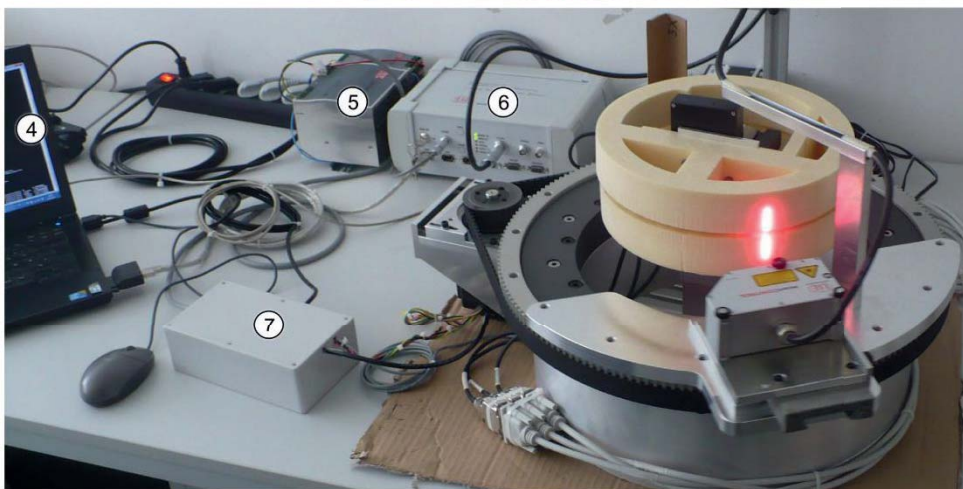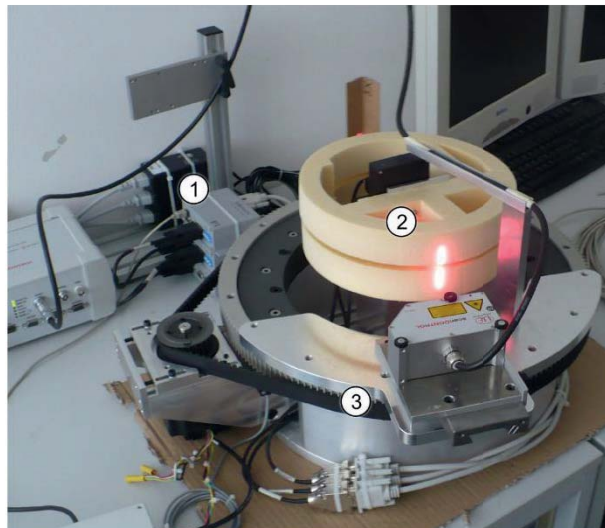
Abbildung 18: Konstruktive Realisierung

5.2 Korrekturvektorberechnung

Währen des Umlaufs des Laserscanners werden die Oberflächenpunkte der Messobjekte im Koordinatensystem des Sensors aufgenommen und gemeinsam mit den Istwerten des Drehwinkels gespeichert. Das Koordinatensystem wird von den beiden Koordinatenachsen x_{Sensor} und z_{Sensor} gebildet. Dieses bewegt sich auf der Bahn mit dem Radius r_{Bahn} um die Drehachse der Konstruktion. Um eine kartesische Repräsentation der Messpunkte im Koordinatensystem zu erhalten, wird das Messsystemkoordinatensystem (x_{MS}, y_{MS}, z_{MS}) definiert. Um im Koordinatensystem des Sensors aufgenommenen Daten in diesem Koordinatensystem darzustellen, werden diese in Zylinderkoordinaten überführt. Hierzu werden die Koordinaten ϱ_{MB}, φ_{MB} und z_{MB} verwendet. Dabei stellt ϱ_{MB} den Abstand der gemessenen Oberflächenpunkte des Werkstücks zur Drehachse dar. Die Koordinate φ_{MB} ist der Drehwinkel des Sensors. Die Transformation der importierten Punktdaten in das Zylinderkoordinatensystem wird mit Hilfe der gemessenen Abstände (z_{Sensor}) und des bekannten Umlaufradius (r_{Bahn}) realisiert (vgl. Abbildung 18):

$$\varrho = r_{Bahn} - z_{Sensor} \qquad (5\text{-}1)$$

Um die Anteile der Messpunkte den korrespondierenden Werkstücken zuzuordnen, muss die gesamte Punktewolke in der Mitte des Messbereiches geteilt werden. Die Ebene der Teilung entspricht der XY-Ebene des Messsystemkoordinatensystems. Um die Auswertung zu beschleunigen, muss der Berechnungsaufwand klein gehalten werden. Daher werden nicht alle Datenpunkte verwendet. Von besonderer Wichtigkeit sind die Daten der Rohrkanten, da dieser Bereich für den MIAB-Schweißprozess wesentlich ist. Zu diesem Zweck werden die Kanten der Werkstücke identifiziert.

Die Genauigkeit und Geschwindigkeit, die mit dem ICP-Algorithmus erreicht wird, hängen stark von der Güte einer ersten Schätzung der räumlichen Lagen der Werktücke ab. Daher wird ein Verfahren zur Vorausrichtung umgesetzt, das aus zwei Schritten besteht. Im ersten Schritt wird eine Ebene in die entsprechenden separierten Rohrkanten gefittet. Dann werden die Normalenvektoren der Ebenen berechnet. Anschließend werden die Rotationsmatrizen aus den Normalenvektoren ermittelt, die die Normalenvektoren auf die z-Achse des Messsystemkoordinatensystems transformieren. Die mit den Matrizen transformierten Rohrkanten liegen in sehr guter Näherung parallel zu den -Rohrkanten.

Im letzten Schritt der Vorausrichtung werden die Schwerpunkte von den gemessen Rohrkanten und der Referenzen berechnet. Diese Schwerpunkte werden dann auf die korrespondierenden Referenzen verschoben. Im nächsten Schritt wird der ICP-Algorithmus von Kjer und Wilm [KJER13] verwendet. Als Ergebnis liegen die Rotationsmatrizen und die Translations-

vektoren vor, die die beiden vorausgerichteten Punktewolken der Rohrkanten optimal auf die korrespondierenden Referenzen transformieren. Daraus ergeben sich homogene Transformationsmatrizen T_1 und T_2, die aus der Vorausrichtung berechnet wurden und die homogenen Transformationsmatrizen aus der Feinausrichtung vor. Die Gesamttransformation ist das Produkt der homogenen Transformationen von Vorausrichtung und ICP-Algorithmus:

$$T_1 = T_{1,\text{ICP}} T_{1,\text{vor}} \qquad (\ 5\text{-}2\ )$$

$$T_2 = T_{2,\text{ICP}} T_{2,\text{vor}} \qquad (\ 5\text{-}3\ )$$

Die Transformation zur gewünschten Positionierung des beweglichen Rohres wird anschließend berechnet mit:

$$T_{\text{stell}} = T_1^{-1} T_2 \qquad (\ 5\text{-}4\ )$$

$$T_{\text{stell}} = \left(T_{1,\text{ICP}} T_{\text{vor}} \right)^{-1} T_{2,\text{ICP}} T_{2,\text{vor}} \qquad (\ 5\text{-}5\ )$$

Ein Vektor mit Stellinformationen für alle sechs Freiheitsgrade, dessen rotatorische Freiheitsgrade in Kardankonvention vorliegen hat die Form:

$$\vec{X}_{\text{stell}} = \begin{bmatrix} x_{\text{stell}} \\ y_{\text{stell}} \\ z_{\text{stell}} \\ \alpha_{\text{stell}} \\ \beta_{\text{stell}} \\ \gamma_{\text{stell}} \end{bmatrix} \qquad (\ 5\text{-}6\ )$$

Die homogene Transformationsmatrix T_{stell} beinhaltet die Drehmatrix und den Translationsvektor. Diese hat die folgende Form:

$$T_{\text{stell}} = \begin{bmatrix} & & & x_{\text{stell}} \\ & R & & y_{\text{stell}} \\ & & & z_{\text{stell}} \\ 0 & 0 & 0 & 1 \end{bmatrix} \qquad (\ 5\text{-}7\ )$$

Die ersten drei Einträge des Stellvektors $\vec{X}_{stell}$ für die translatorischen Freiheitsgrade werden direkt aus der Matrix T_{stell} abgelesen. Die Rotationsfreiheitsgrade werden aus der Rotationsmatrix R berechnet. Die Rotationsmatrix in Kardanwinkelkonvention steht in Gleichung (5-8). ($\cos\beta$ und $\sin\gamma$ werden in dieser Darstellung durch c_β und s_γ abgekürzt [ORTM11]).

$$R = R_x(\alpha) R_y(\beta) R_z(\gamma) = \begin{bmatrix} c_\beta c_\gamma & -c_\beta s_\gamma & s_\beta \\ c_\alpha s_\gamma + s_\alpha s_\beta c_\gamma & c_\alpha c_\gamma - s_\alpha s_\beta s_\gamma & -s_\alpha c_\beta \\ s_\alpha s_\gamma - c_\alpha s_\beta c_\gamma & s_\alpha c_\gamma + c_\alpha s_\beta s_\gamma & c_\alpha c_\beta \end{bmatrix} \qquad (\ 5\text{-}8\ )$$

Durch Kombination der Einträge Kardan-Rotationsmatrix werden die Winkel berechnet:

$$\frac{-r_{2,3}}{r_{3,3}} = \frac{s_\alpha c_\beta}{c_\alpha c_\beta} = \tan\alpha \longrightarrow \alpha = \arctan\frac{-r_{2,3}}{r_{3,3}} \qquad (5\text{-}9)$$

$$\gamma = \arctan\frac{-r_{1,2}}{r_{1,1}} \qquad (5\text{-}10)$$

$$\beta = \arctan\left(\frac{r_{1,3}}{r_{1,1}c_\gamma - r_{1,2}s_\gamma}\right) \qquad (5\text{-}11)$$

Durch Einsetzen der entsprechenden Elemente der Matrix T_{stell} anstelle der $r_{m,n}$ können dann die drei fehlenden Einträge des Stellvektors ermittelt werden.

5.3 Versuchsdurchführung und Vorstellung der Ergebnisse

Für das Einstellen von Fehllagen werden hochpräzise Mikrostellantriebe verwendet. Bei der Versuchsdurchführung werden 23 Messungen (verschiedene Rohrabweichungen) durchgeführt. Die Differenzen zwischen den gemessenen und den modellbasierten Kardanvektoren werden in einem Boxplot-Diagramm (siehe Abbildung 19) dargestellt. Jede Box entspricht dem Bereich, in dem die mittleren 50% der Daten liegen und ist demnach durch das obere und untere Quartil begrenzt. Der Querstrich repräsentiert den Medianwert. Die „Fühler" an beiden Enden der Box markieren mit ihren Enden den oberen und unteren Extremwert.
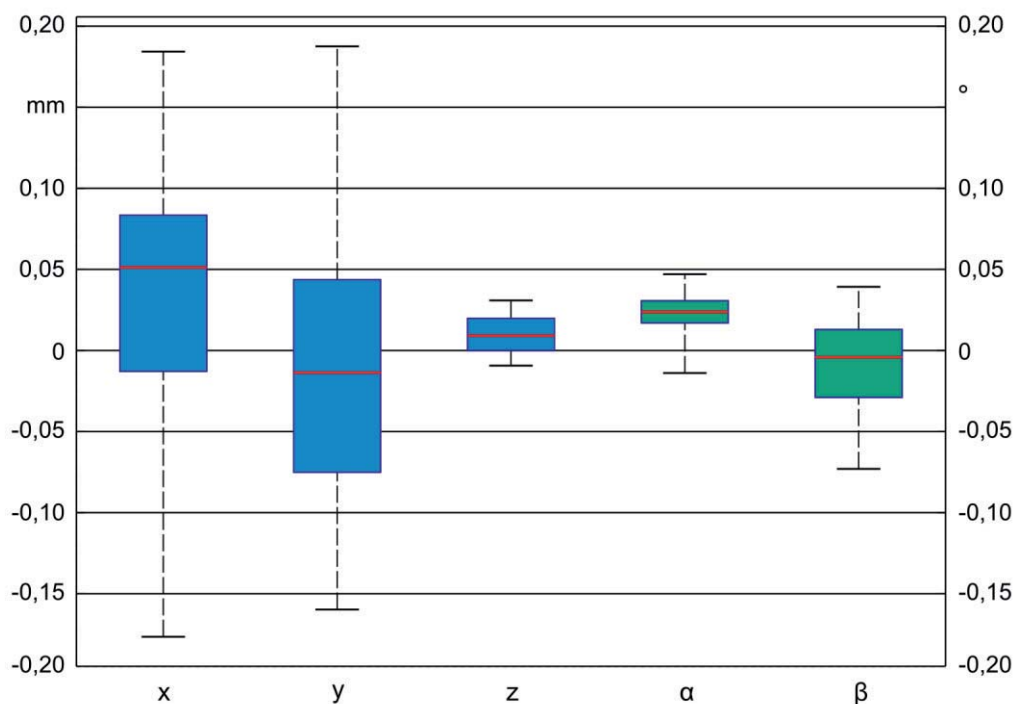
Abbildung 19: Boxplot-Darstellung der Abweichungen zwischen den gemessenen und den eingestellten Kardanvektoren.

Im Diagramm swerden von links nach rechts die Abweichungen in Richtung der x-, y- und z-Achse des Messsystemkoordinatensystems dargestellt. Für sie gilt die mm-Skala auf der

387

linken Diagrammseite. Anschließend folgen die Winkelabweichungen in α (Drehung um die x-Achse) und β (Drehung um die y-Achse). Hierfür ist die Grad-Skala auf der rechten Seite vorgesehen. Auf die Darstellung der Winkelabweichungen um die z-Achse wurde verzichtet, da diese aufgrund der Rotationssymmetrie der verwendeten Rohrproben bezogen auf die z-Achse keinerlei Aussagekraft haben.

Die translatorischen maximalen Abweichungen sind 0,2 mm in x, y und z sowie 0,1° in α und β. Auffällig ist, dass die Streuungen in x- und y-Richtung gegenüber der z-Richtung vergleichsweise groß sind. Die Streuungen der Winkelabweichungen sind gering. Der Grund hierfür ist das angewendete zweistufige Registrierungsverfahren. Für diese Verfahren werden nur die Ränder der Rohre verwendet. Diese sind annähernd ebene Punktwolken. Das Vorausrichtungsverfahren verschiebt im ersten Schritt den jeweiligen Rand in die Ebene der Referenzpunktwolke. Durch die schon sehr gute Vorausrichtung in den Ebenen und durch die Ebenheit der beiden Punktwolken an sich, wird auch das Endergebnis der Registrierung sehr genau in der Referenzebene liegen. Hieraus folgen sehr geringe Registrierungsfehler in z, α und β. Die radiale Ausrichtung der beiden kreisförmigen Punktwolken in der Referenzebene ist dagegen fehleranfälliger. Es ist vorstellbar, dass es dabei häufiger zur Konvergenz des ICP-Algorithmus in einem lokalen Minimum kommt und dass die Streuung der Abweichungen daher in der x- und y-Richtung deutlich größer sind. Weiterhin ist Anzumerken, dass das Rohr bei weitem nicht ideal rund ist. Die Genauigkeit ist allerdings in allen Freiheitsgraden für Anwendungen in Bohranlagen hinreichend.

5.4   Fazit

Zu Beginn dieses Abschnitts werden eine Methode zur Erfassung der Rohrlagen und eine Methode zum Ausrichten des beweglichen Casings auf das fest eingespannte entwickelt. Für die Geometrieerfassung der Casings wurde dann ein Messsystem realisiert. Das Kernelement des Messsystems ist ein Laserlinienscanner. Dieser lagert auf einer Rundführung und wird durch einen Schrittmotor bewegt. Durch die Anordnung wird die Geometrie beider Rohre in einem Messgang räumlich erfasst. Anschließend wurde eine zweistufige Methode zur Berechnung von Korrekturvektoren realisiert. Im ersten Schritt der Berechnungsmethode wird eine Vorausrichtung durchgeführt. In der zweiten Stufe wird die Feinausrichtung mit einem ICP-Algorithmus ausgeführt. Das System ist durch eine ausreichende Genauigkeit gekennzeichnet und ist geeignet, um in Schweißautomaten von Bohranlagen integriert werden zu können.

6 Literatur

[ASE06]   Schutzrecht WO 2006/103464 (2006)

[BESL92] Besl, P. J.; McKay, N. D.: "A Method for Registration of 3-D Shapes". IEEE Transactions on Pattern Analysis and Machine Intelligence 14 (1992) 2, S. 239–256.

[BJS05]   Sach, M.: Recent key developments and -implementations in Coiled Tubing technology - ensuring cost efficient operations in the future. Vortrag der BJ Service AS am 20.04.2005 in Grieghallen, Bergen.

[BJS09]   Schutzrecht US 7 562 909 B2 (2009)

[BMU07]   Bundesministerium für Umwelt, Naturschutz und Reaktorsicherheit, Institut für Energetik und Umwelt gGmbH: Tiefe Geothermie in Deutschland, Bonifatius GmbH, Paderborn, September 2007.

[BMU09]   Bundesministerium für Umwelt, Naturschutz und Reaktorsicherheit: Pressemitteilung zum Beschluss des Bundeskabinetts am 13.05.09. „Gabriel: Erdwärme kann wichtigen Beitrag zu Klimaschutz und Energieversorgung leisten", Stand 15.07.09. Verfügbar unter: http://www.bmu.de/pressemitteilungen/aktueller_newsletter/pm/44002.php.

[DUD02]   Schutzrecht US 6 347 664 B1 (2002)

[DYK99]   Van Dyke, K.: Rotary Drilling Series: The Auxiliaries, Unit I Lesson 9, Petroleum Extension Service & International Association of Drilling Contractors, Texas, 1999. ISBN: 0-88698-184-0

[KJER10] Kjer, H. M.; Wilm, J.: "Evaluation of surface registration algorithms for PET motion correction". Bachelor thesis, Technical University of Denmark, 2010

[MOT06]   Homepage der Firma Halliburton. Stand 06/2010. Verfügbar unter: www.halliburton.com/public/cps/contents/papers_and_articles/web/0606HEP_TubeTech_REPRINT.pdf

[GEB10]   Nobileau, Vortrag zum GeBo Jour fixe im April 2010

[JÄHN07] Jähning, A.: "Matching und Registrierung von 3D-Scans". Großer Beleg, Technische Universität Dresden, 2007.

[ORTM11] Ortmaier, T.; Kotlarski, J.: "Skript zur Vorlesung Robotik 1". Fakultät für Maschinenbau der Gottfried Wilhelm Leibniz Universität Hannover, 2011.

[OSH09] UNITED STATES DEPARTEMENT OF LABOR, OCCUPATIONAL SAFETY AND HEALTH ADMINISTRATION: Oil and Gas Well Drilling and Servicing eTool, Drilling Rig Components, Illustrated Glossary, Stand 08/2009, Verfügbar unter: http://www.osha.gov/SLTC/etools/oilandgas/illustrated_glossary.html

[PAH04] Pahl Gerhard.: Konstruktionslehre, Heidelberg, Springer, 2004

[PRE01] Schutzrecht WO 2001/57355 (2001)

[REI04] REICH, M.: Die faszinierende Welt der Bohrtechnik, Booklet, Baker Hughes, Celle 2004

[REI07] REICH, M.: Spezialbohrverfahren: Coiled Tubing Drilling. Freiberg: TU Bergakademie Freiberg. 2007

[REI09] REICH, M.: Auf Jagd im Untergrund. Bad Salzdetfurth: Add-Books, 2009.

[SCH10] SCHLUMBERGER: Homepage der Firma Schlumberger. Stand 06/2010. Verfügbar unter: www.glossary.oilfield.slb.com/Display.cfm?Term=Liner

[TEO09] TEODORIU, C.: Tiefbohrtechnik 1. Clausthal. TU Clausthal Abteilung Erdöl-, Erdgasgewinnung und Erdgasversorgung, Vorlesungsskript

[TEO10] TEODORIU, C.: Vortrag „Bohrtechnik" zum Jour fixe im August 2010

[WIN09] WINTERSHALL: Homepage der Firma Wintershall, Stand 08/2009, Verfügbar unter:
http://www.wintershall.com/erdoel_erdgas.html?&L=1

[WRA09] WRAY, B. ET AL.: Case studies: High-density elastic cements applied to solve HPHT challenges in South Texas. Beitrag im Drilling Contractor. Stand 08/2010. Verfügbar unter:
http://drillingcontractor.org/case-studies-high-density-elastic-cements-applied-to-solve-hpht-challenges-in-south-texas-2569

[XTR10]   XTREME COIL DRILLING CORP.: Homepage der Firma Xtreme Coil Drilling Corp.,
          Stand 08/2010, Verfügbar unter:
          http://www.xtremecoildrilling.com/rigs/xtc200stPhotos.html

Collaborative Research Program
"Geothermal Energy and High-Performance Drilling" (gebo)

Niedersachsen

Drilling Technology Project B4:
Geo-parameters from well logging and their uses

Final Report

Authors: Xuan Luo[1], Esther Vogt[2], Michael Z. Hou[1], Thomas Wonik[2]

Institutions: [1] Institute of Petroleum Engineering (ITE),

Clausthal University of Technology

[2] Leibniz Institute for Applied Geophysics (LIAG), Hannover

Date: 27.02.2015

B4: Geo-parameter from well logging and their uses

1 Project Overview

Project Nr.	Title	Subject of research	Project leader, institution, location
B4	Geo-parameter from well logging and their uses	geomechanics, drilling, mining, geotechniques, geophysics, petrophysics	Prof. Dr. M. Z. Hou, ITE, Clausthal University of Technology Dr. T. Wonik, Leibniz Institute for Applied Geophysics

Participating institutes and institutions of the universities and external institutions:

- Institute of Petroleum Engineering (ITE), Clausthal University of Technology
- Leibniz Institute for Applied Geophysics (LIAG)
- Baker Hughes contact: Dipl.-Ing. Thomas Dahl

List of participating scientists and engineers:

Name	Subject area	University institute or non-university institution	Position is financed by gebo funds (indicate by X)
M.Sc. X. Luo	geomechanics and geotechniques	Clausthal University of Technology	X (01.09.2011 - 31.08.2013)
Dipl.-Geophys. E. Vogt	borehole geophysics and petrophysics	Leibniz Institute for Applied Geophysics	X (01.01.2010 - 31.12.2014)
Dr. L. Zhou	geomechanics and geotechniques	Clausthal University of Technology	X (01.01.2010 - 31.08.2011)
Prof. Dr. M.Z. Hou	geomechanics, drilling, mining and geotechniques	Clausthal University of Technology	
Dr. T. Wonik	borehole geophysics and petrophysics	Leibniz Institute for Applied Geophysics	

2 Research Program

2.1 Summary

The B4 project deals with the development of correlation algorithms and a computer program for the determination of the optimal mud window using LWD (Logging While Drilling) data in real time. Four boundary conditions (Figure 1) determine a suitable mud window. The upper boundaries are Minimum Horizontal Stress (σ_h), Fracture Gradient (FG), while the lower boundaries are Pore Pressure Gradient (PPG) and Shear Failure Gradient (SFG). These four boundaries should be updated while drilling in real time considering HM (hydro-mechanical) and THM (thermo-hydro-mechanical) coupled effects.
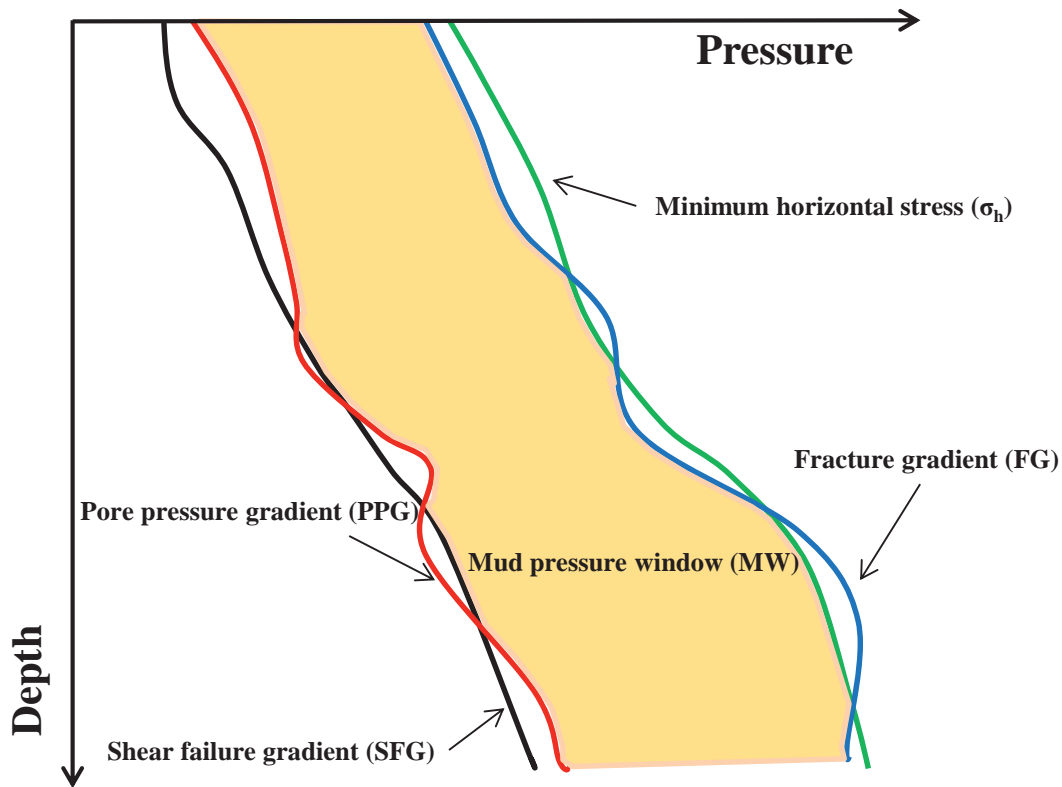
Figure 1: Lower and upper boundaries to determine a suitable mud window.

Therefore, the project B4 makes an important contribution to the total gebo project which includes the efficient and safe drilling of deep boreholes in the North German Basin for geo-thermal applications. The computer program incorporates the thermal, hydraulic, and mechanical conditions associated with drilling deep boreholes. The measurements used to calculate the mud window, as well as the results obtained by the calculation process are of great interest for the other project partners.

2.2 Relationship of the B4 project to the overall research context and networking with other projects

B4 is linked to the two gebo research fields 'geosystems' G and 'drilling technology' B: At first, borehole logs are essential to evaluate the geothermal potential of a formation. Secondly, drilling safety and efficiency is to be enhanced by the borehole stability model developed from the borehole logs.

Within the context of the other gebo projects, B4 is particularly close related to the following groups: B2 (Drilling Simulator), G3 (Mechanical properties of rock samples), G5 (Modeling of the stress field), G8 (Benchmark Models), G9 (Chemical properties of pore fluids), B9 (Innovative drilling concepts for geothermal energy exploitation). Consequently, the members of the B4 project took part in the meetings of the B and the G group.

2.3 Work packages executed relative to (original) plan and results achieved

WP 1 (ITE): Critical analysis of the evaluation models for borehole stability

There exist already a few evaluation models for borehole stability for different rock types. The aim of this work package is to critically analyze the most common evaluation models and then to find the most suitable evaluation models for drilling deep wells in the North German Basin.

Because σ_h and PPG are input parameters, they should not be calculated using borehole stability models. The borehole stability evaluation models are concerned with calculating the boundaries FG and SFG. To determine FG and SFG (Figure 2) the stress distributions around a wellbore must be calculated at first. The borehole stability evaluation criteria are chosen based on downhole conditions. The FG and SFG are determined by comparing loading and strength.
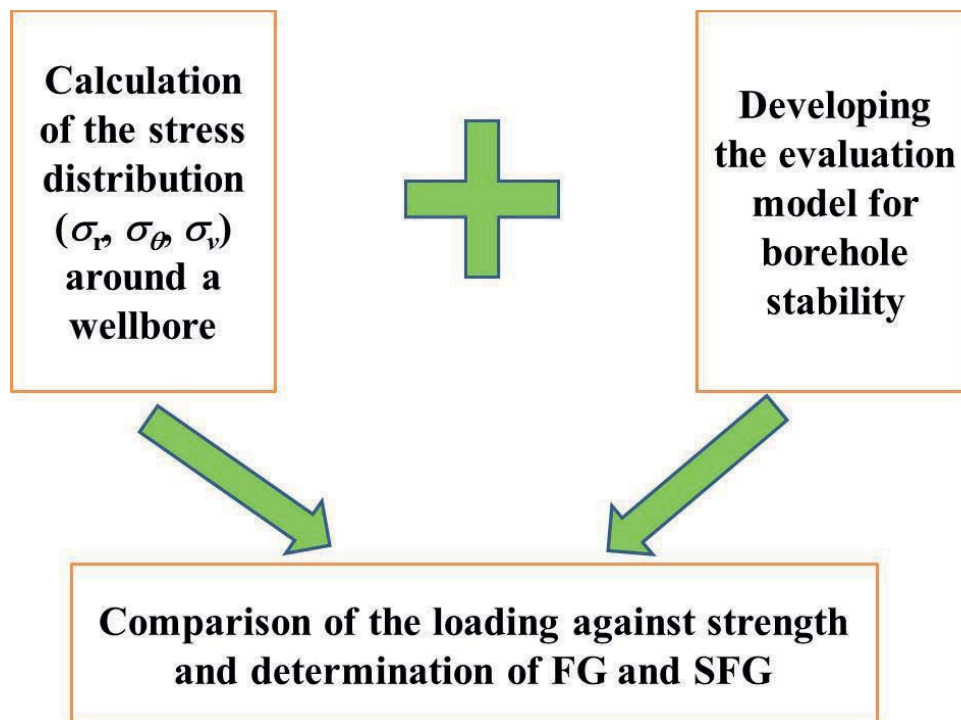
Figure 2: Principle to determine fracture and shear failure gradient (FG and SFG).

Two theories how to calculate the stress distributions around boreholes are investigated, which are linear or non-linear elasticity. These two theories are compared considering the required parameters, accuracy, and practicability.

Based on the linear elastic theory, the well-known Kirsch equations (1898) were derived to calculate stress distributions in the near field of boreholes under dry conditions (Eq. 1 to Eq. 3).

$$\sigma_r = p_i \cdot \frac{r_0^2}{r^2} + \frac{\sigma_{30} + \sigma_{10}}{2} \cdot \left(1 - \frac{r_0^2}{r^2}\right) - \frac{\sigma_{10} - \sigma_{30}}{2} \cdot \left(1 - \frac{4r_0^2}{r^2} + \frac{3r_0^4}{r^4}\right) \cdot \cos 2\theta \qquad \text{Eq. 1}$$

$$\sigma_\theta = -p_i \cdot \frac{r_0^2}{r^2} + \frac{\sigma_{30}+\sigma_{10}}{2} \cdot \left(1 + \frac{r_0^2}{r^2}\right) + \frac{\sigma_{10}-\sigma_{30}}{2} \cdot \left(1 + \frac{3r_0^4}{r^4}\right) \cdot \cos 2\theta \qquad \text{Eq. 2}$$

$$\tau_{r\theta} = \frac{\sigma_{30}-\sigma_{10}}{2} \cdot \left(1 + \frac{2r_0^2}{r^2} - \frac{3r_0^4}{r^4}\right) \cdot \sin 2\theta \qquad \text{Eq. 3}$$

where p_i = mud pressure, MPa; r_0 = borehole radius; r = distance to borehole center; σ_{10}, σ_{30} = bigger and smaller primary stress around a wellbore; σ_r = radial stress; σ_θ = tangential stress; and τ = shear stress. According to the nonlinear elastic theory, the elastic module E depends on the loading $E(\sigma)$. The relation between the elastic module and the loading was investigated by many experts. One relation after Santarelli & Brown (1986) is shown in Eq. 4.

$$E(\sigma_3) = (a\sigma_3 + b)^m \qquad \text{Eq. 4}$$

where a, b, and m are parameters, which should be determined in laboratory.

Therefore, the tangential stress depends on the radial stresses and can be calculated using Eq. 5 (Santarelli & Brown, 1986):

$$\sigma_\theta = \frac{v}{1-v}\sigma_r - \frac{E(\sigma_r)}{1-v}\int \frac{1}{E(\sigma_r)}d\sigma_r \qquad \text{Eq. 5}$$

where the radial stress σ_r can hardly be calculated analytically.

Brown et al. (1989) calculated the radial stress numerically and found out that the radial stress in nonlinear elastic rocks was similar to the radial stress in linear elastic rocks. Assuming that the radial stresses in linear and nonlinear elastic rocks are identical, Eq. 6 to calculate tangential stress in nonlinear elastic rocks was developed by Santarelli & Brown (1986):

$$\sigma_\theta = \frac{v}{1-v}\sigma_r - \frac{E^{\frac{1}{m}}-EE_2^{\frac{1}{m}-1}}{(1-v)(1-m)a} - \left\{\frac{v}{1-v}p_G - p_G\right\}\frac{E}{E_2}; \quad E_2 = (a_E p_G + b_E)^m \qquad \text{Eq. 6}$$

Figure 3 compares the radial and tangential stress distributions calculated using the linear and nonlinear elastic theory. The required parameters are listed in Table 1. The horizontal stress state is isotropic, which means that the stress distributions in the near field of the borehole are also isotropic. Figure 3 shows that the tangential stress near the wellbore wall, calculated using nonlinear elastic theory, is much smaller than that calculated using the linear elastic theory. Therefore, the minimum mud pressure gradient calculated based on the nonlinear elastic theory should be smaller than that based on the linear elastic theory. Using the minimum mud pressure gradient calculated based on the nonlinear elastic theory, the borehole wall will more likely show shear failure. For conservation reasons, the nonlinear elastic theory should not be used to determine the stress distributions.

Moreover, the number of required parameters to calculate stress distributions based on the nonlinear elastic theory is higher than those based on the linear elastic theory. Therefore and

for simplification reasons, the linear elasticity is used to derive the stress distribution around boreholes.

The linear elastic theory is also widely used in dry or non-porous rock formations. Based on the linear poro-elasticity, the stress distribution around boreholes in wet porous rock formations under drained (Eq. 7 - 9) and undrained (Eq. 11 - 13) conditions was derived by Luo (2010 a):
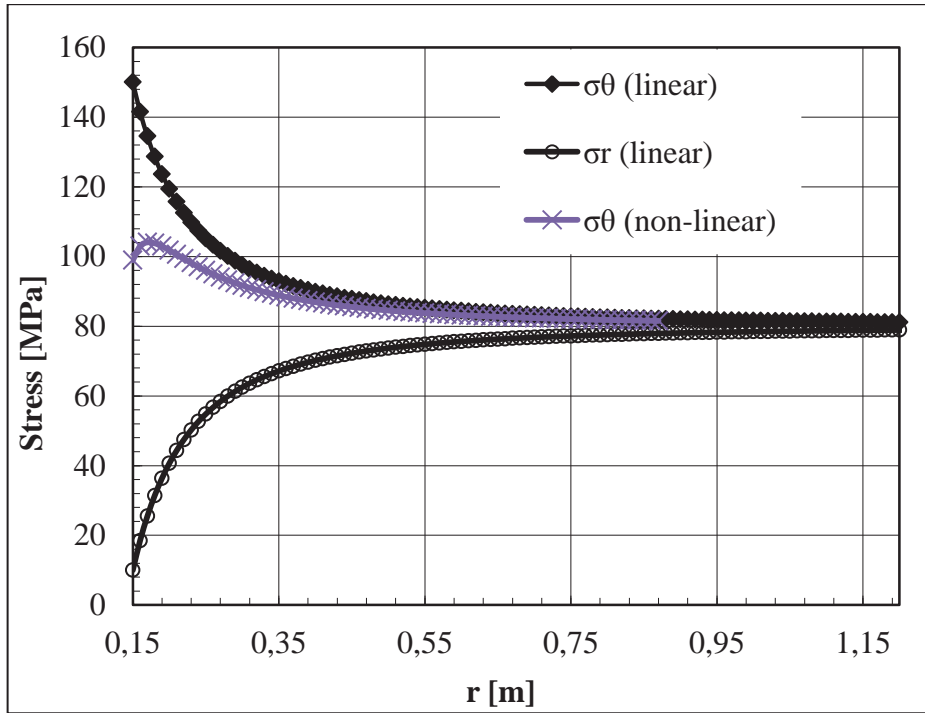
Figure 3: Stress distributions in the near field of a borehole calculated using the linear and nonlinear elastic theory.

Table 1: Parameters to calculate the stress distribution using the linear and nonlinear elastic theory

P_i [MPa]	σ_H [MPa]	σ_h [MPa]	a [-]	b [-]	m [-]	v [-]
10	80	80	2.67×10^9	3.33×10^{10}	0.0403	0.2

$$\sigma_r = p_i \cdot \frac{r_0^2}{r^2} + \frac{\sigma_{10}+\sigma_{30}}{2} \cdot \left(1 - \frac{r_0^2}{r^2}\right) - \frac{\sigma_{10}-\sigma_{30}}{2} \cdot \left(1 - \frac{4r_0^2}{r^2} + \frac{3r_0^4}{r^4}\right) \cdot cos2\theta - \alpha \cdot (p_R - p_i) \cdot \frac{r_a^2}{r^2} \cdot \frac{r^2-r_0^2}{2(r_a^2-r_0^2)} \cdot$$
$$\frac{1-2v}{1-v} \cdot \frac{\alpha \cdot (p_R - p_i)}{2(lnr_a - lnr_i)} \cdot (lnr - lnr_0) \qquad \text{Eq. 7}$$

$$\sigma_\theta = -p_i \cdot \frac{r_0^2}{r^2} + \frac{\sigma_{10}+\sigma_{30}}{2} \cdot \left(1 + \frac{r_0^2}{r^2}\right) + \frac{\sigma_{10}-\sigma_{30}}{2} \cdot \left(1 + \frac{3r_0^4}{r^4}\right) \cdot cos2\theta - \alpha \cdot (p_R - p_i) \cdot \frac{r_a^2}{r^2} \cdot \frac{r^2-r_0^2}{2(r_a^2-r_0^2)} \cdot \frac{1-2v}{1-v} \cdot$$

$$\frac{\alpha \cdot (p_R-p_i)}{2(lnr_a-lnr_i)} \cdot (lnr - lnr_0 + 1) \tag{Eq. 8}$$

$$\tau = \frac{\sigma_1-\sigma_3}{2} \cdot (1 - \frac{2r_0^2}{r^2} - \frac{3r_0^4}{r^4}) \cdot sin2\theta \tag{Eq. 9}$$

where α = Biot's coefficient, -; p_R = Formation pore pressure, MPa.

$$\sigma_r = p_i \cdot \frac{r_0^2}{r^2} + \frac{\sigma_{30}+\sigma_{10}}{2} \cdot \left(1 - \frac{r_0^2}{r^2}\right) - \frac{\sigma_{10}-\sigma_{30}}{2} \cdot \left(1 - \frac{4r_0^2}{r^2} + \frac{3r_0^4}{r^4}\right) \cdot cos\,2\theta) \tag{Eq. 10}$$

$$\sigma_\theta = -p_i \cdot \frac{r_0^2}{r^2} + \frac{\sigma_{30}+\sigma_{10}}{2} \cdot \left(1 + \frac{r_0^2}{r^2}\right) + \frac{\sigma_{10}-\sigma_{30}}{2} \cdot (1 + \frac{3r_0^4}{r^4}) \cdot cos\,2\theta \tag{Eq. 11}$$

$$\tau_{r\theta} = \frac{\sigma_{30}-\sigma_{10}}{2} \cdot \left(1 + \frac{2r_0^2}{r^2} - \frac{3r_0^4}{r^4}\right) \cdot sin\,2\theta \tag{Eq. 12}$$

$$p(r) = p_R + \frac{2B \cdot (1+v_u)}{3} \cdot \frac{r_0^2}{r^2} \cdot (\sigma_{10} - \sigma_{30}) \cdot cos2\theta \tag{Eq. 13}$$

where p(r) = radial pore pressure distribution, MPa; and v_u = Poisson's coefficient for undrained state and B = Skempton's coefficient,-.The borehole stability evaluation criteria depend on failure types and rock properties. There are two borehole failure types, i.e. tensile and compressive shear failure. For tensile failure, the widely used criterion is that the minimal stress around the borehole should not be lower than the tensile strength σ_t of the rocks around the borehole.

However, compressive shear failure shows only few types and depends on material properties and loads as well. For brittle rocks (e.g., sandstone, shale, granite etc.) there are Mohr-Coulomb (Eq. 15), Drucker-Prager (Eq. 16), modified Lade shear failure criteria, etc. Two types of Drucker-Prager shear failure criteria were investigated, which were the circumscribed Drucker-Prager and the inscribed Drucker-Prager shear failure criteria. These four failure criteria were compared considering the required parameters and the calculated results. The gebo benchmark model developed within gebo project G8 was used to calculate SFG by using different shear failure criteria.

Table 2 lists the parameters from the gebo benchmark model in different rock layers. The unknown UCS in quaternary and tertiary layers was assumed to be identical with the UCS of upper cretaceous layers. The Internal Friction Angle (IFA) was unknown and assumed to be equal to 40°. The cohesion was calculated by using Eq. 14. The horizontal stress ratios K_h and K_H were assumed to be 0.7 and 0.8, respectively. K_h is the ratio of the minimum horizontal stress divided by the vertical effective stress, while K_H is the ratio of maximum horizontal stress divided by the vertical effective stress.

$$C = (\frac{UCS}{2sin\,\varphi} - \frac{UCS}{2}) \cdot tan\,\varphi \tag{Eq. 14}$$

Table 2: Parameters from the gebo benchmark model

Depth [m]	Formation	ρ [g/cm^3]	ϕ [%]	$E^{(d)}$ [GPa]	ν [-]	UCS [MPa]
225	Quartär	1.9	-	15	0.25	-
1025	Tertiär	2.2	-	15	0.25	-
1750	Oberkreide	2.48	-	26^L	0.25	40
2000	Unterkreide	2.2	-	26	0.26^L	76
2100	JM*	2.66	1.2	33^L	0.28^L	117
2500	JL+JD*	2.63	-	33	0.28	25
2900	Keuper	2.3	-	48^L	0.26^L	45
3300	Muschelkalk	2.51	1.2	67^L	0.3^L	115
3600	OB*	2.45	-	67	0.22^L	10
4200	MB+UB*	2.23	-	59^L	0.22	98^M

*JM = Jurassic (Malm);JL+JD = Jurassic (Lias and Dogger); OB = Upper Buntsandstein;
*MB+UB = Middle and Lower Buntsandstein
$^{(d)}$= Dynamic Young's Module
^{Z1}According to Zimmer (2000)
^{L} According to Löhken & Schellschmidt (2010)
^{Z2}According to Zimmer (1993)
^{P} According to Pfeifle et al. (1983)
^{M} According to Müller (2009)
^{K} According to Korte (2004).

The Mohr-Coulomb shear failure criterion is described by Eq. 15:

$$\sigma_{1f} = N_\varphi \cdot \sigma_r + 2c \cdot \sqrt{N_\varphi}; \; N_\varphi = \frac{1+sin\varphi}{1-sin\varphi} \qquad \text{Eq. 15}$$

where the strength σ_{1f} is depending on the radial stress, internal friction angle and cohesion. The Drucker-Prager shear failure criterion is described by Eq. 16:

$$\sigma_{1f} = \sqrt{J_2} - fI_1 - g = 0 \qquad \text{Eq. 16}$$

where I_1 and J_1 can be calculated using Eq. 17 and Eq. 18.

$$I_1 = \sigma_1 + \sigma_2 + \sigma_3 \qquad \text{Eq. 17}$$

$$J_2 = -\left(s_x s_y + s_y s_z + s_z s_x\right) + s_{xy}^2 + s_{yz}^2 + s_{zx}^2 \qquad \text{Eq. 18}$$

The coefficient f and g in Eq. 16 are calculated according to two criteria: the circumscribed Drucker-Prager (Eq. 19 and Zhou, 1994) and the inscribed Drucker-Prager criteria (Eq. 20 & Veeken et al., 1989). The deviator stress s_{ij} can be calculated using Eq. 21.

$$f = \frac{2\cdot\sin\varphi}{\sqrt{3}\cdot(3-\sin\varphi)}; \; g = \frac{6\cdot C\cdot\cos\varphi}{\sqrt{3}(3-\sin\varphi)} \qquad \text{Eq. 19}$$

$$f = \frac{2\cdot\sin\varphi}{\sqrt{3}\cdot(3+\sin\varphi)}; \; g = \frac{6\cdot C\cdot\cos\varphi}{\sqrt{3}(3+\sin\varphi)} \qquad \text{Eq. 20}$$

$$s_{ij} = \sigma_{ij} - \sigma_m \delta_{ij}; \sigma_m = \frac{\sigma_1 + \sigma_2 + \sigma_3}{3}$$

<div align="right">Eq. 21</div>

The modified lade shear failure (Ewy, 1999) is described by Eq. 22.

$$\frac{I'^3}{I''} = 27 + \eta$$

<div align="right">Eq. 22</div>

where I' and I'' can be calculated using Eq. 23; η can be calculated using Eq. 24.

$$I' = (\sigma_1 + S_1) + (\sigma_2 + S_1) + (\sigma_3 + S_1) \qquad I'' = (\sigma_1 + S_1)(\sigma_2 + S_1)(\sigma_3 + S_1)$$

<div align="right">Eq. 23</div>

$$\eta = 4\mu^2 \cdot \frac{9\sqrt{\mu^2+1} - 7\mu}{\sqrt{\mu^2+1} - \mu}$$

<div align="right">Eq. 24</div>

where S_1 and μ can be calculated using

$$S_1 = \frac{c}{\mu}; \ \mu = \tan\varphi$$

<div align="right">Eq. 25</div>

The analytical solution for SFG using the inscribed Drucker-Prager, the circumscribed Drucker-Prager and the modified Lade criteria was hard to be derived, especially under drained and undrained conditions. Only the analytical solution for SFG under dry conditions using inscribed the Drucker-Prager, the circumscribed Drucker-Prager and the modified Lade criteria were derived. For comparison, the SFG under dry conditions were calculated based on the Mohr-Coulomb, the modified Lade, the inscribed Drucker-Prager and the circumscribed Drucker-Prager shear failure criteria.

Figure 4 compares the calculated SFG for brittle rocks using different shear failure criteria from 200 m to 4,200 m. For comparison, σ_h is also shown in Figure 4 with a green line. The SFG, calculated based on the circumscribed Drucker-Prager, was negative and decreased with depth, which is not logical and hence should not be used. The SFG, calculated using the modified Lade failure criterion, was mostly bigger than the minimal horizontal stress, which means that the tensile failure will be induced if the mud pressure is equal to this SFG. Therefore, the modified Lade failure criterion should not be used. The SFG, calculated using the Mohr-Coulomb and the inscribed Drucker-Prager failure criteria, is similar, which increased with depth and remains always smaller than the minimum horizontal stress. However, the analytical solution for SFG using the inscribed Drucker-Prager shear failure criterion was hard to be derived compared to the Mohr-Coulomb shear failure criterion. Till now, only the analytical solution for SFG under dry conditions using the inscribed Drucker-Prager shear failure criterion was derived. Moreover, to obtain the SFG a quadratic equation must be solved, which mainly has two solutions. These two solutions should be analyzed and the best one should be chosen. The chosen process is also a challenge for programming. Moreover, the SFG calculated using the Mohr-Coulomb shear failure criterion needs less input parameters than the use of the inscribed Drucker-Prager shear failure criterion. In conclusion the

Mohr-Coulomb shear failure criterion was chosen for linear-elastic and linear-poroelastic rock formations. It is widely used, and most of the rocks seem to follow this rule in at least a portion of their shear failure envelope.
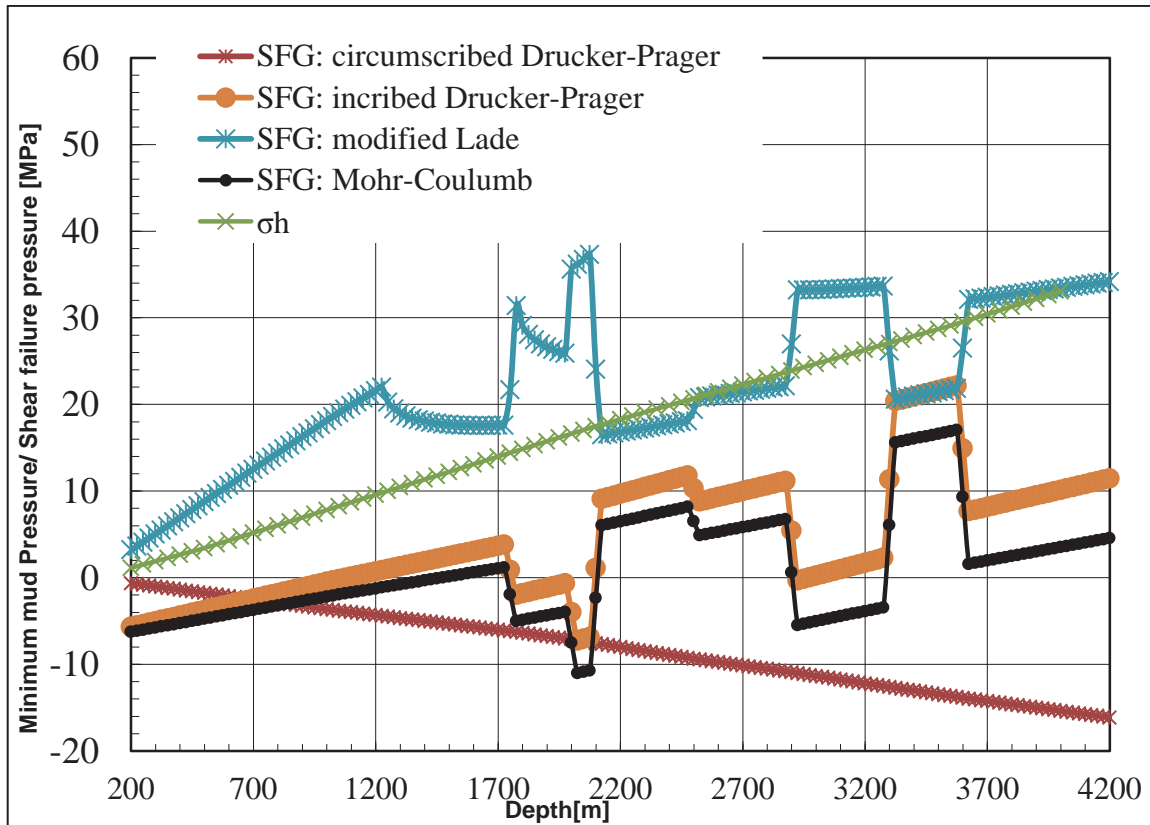
Figure 4: SFG for a vertical borehole during drilling in dry brittle rocks.

In soft rocks, the SFG is determined by limiting the Normalized Yield Zone Ratio (NYZR) value. According to Mclellan & Hawkes (2001) the NYZR can be calculated with Eq. 26

$$NYZR = \frac{\pi \cdot a^Y \cdot b^Y}{\pi \cdot r_0^2}$$
Eq. 26

where a^Y and b^Y are the radii of the elliptical plastic zone (Figure 5), r_0 is the original wellbore radius.
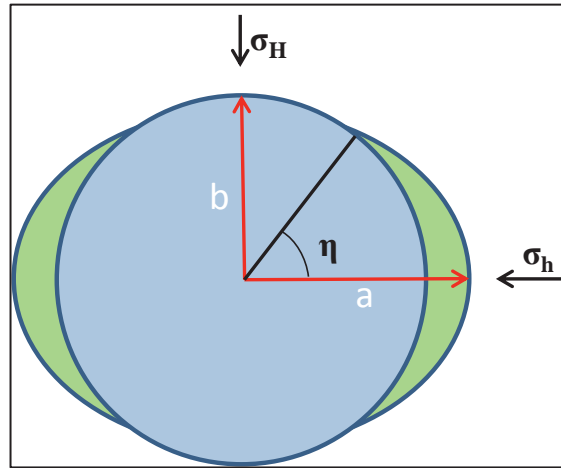
Figure 5: Yield zone around a borehole.

After the above analysis, the linear elastic theory was chosen to calculate the stress distributions in the near field of a borehole. The borehole evaluation criteria for different rock types are shown using the decision tree in Figure 6.
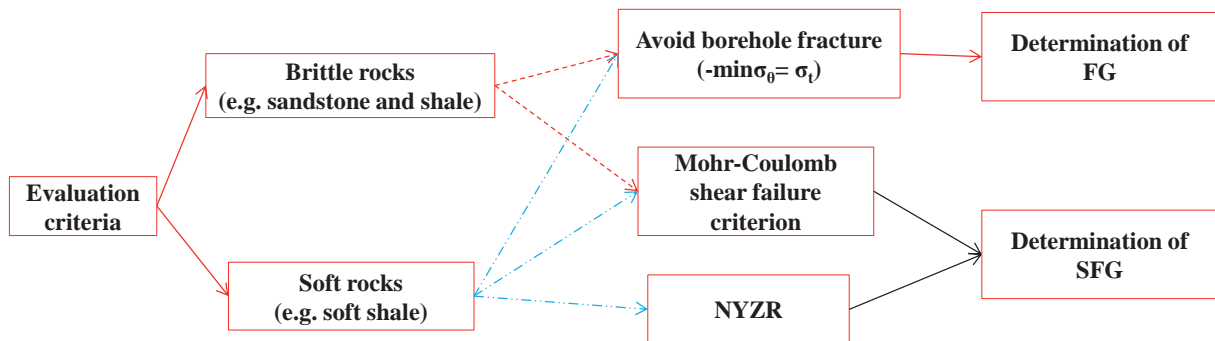
Figure 6: Evaluation criteria for different rock types.

WP 2 (LIAG): Analysis of borehole measurement methods

Some of the required input parameters for the computer program can be measured while drilling. Others can be modeled or calculated from different measurable quantities, and a few can only be estimated from published values based on the lithology. The following lists the most important parameters:

Measurable Quantities

Temperature: The temperature and the temperature gradient can be fairly easy measured in the borehole using wireline tools. Logging while Drilling (LWD) data require additional interpretation because no direct conclusions can be drawn concerning the temperature in the surrounding rock: the LWD temperature is strongly affected by the drilling process and the drilling mud. The temperature equilibrium between the borehole and the surrounding rock at the end of drilling requires waiting for a period at least as long as the net drilling time – reliable temperatures can then be measured.

Density: The density can be determined from LWD measurements. Note, however, that this requires the use of radioactive sources with today's standard technologies, and their utilization requires prior approval.

Resistivity: Logging the resistivity is a standard LWD method and is of high relevance to pore pressure determination. With the use of reference values, this can ideally be used to deduce the necessary chemical properties, which are also input parameters for the stability program.

Caliper: The diameter of the borehole can indicate caved zones in the wall of the borehole and can be measured with logging tools, both, wireline and LWD. In case of LWD measurements, the results are less accurate.

Gamma-ray: Gamma-ray logging is technically viable and requires proven environmental corrections for e.g. the borehole diameter. The logs can be used to differentiate sandstone from claystone beds. The interpretation of other lithologies is more complex.

Acoustic: LWD logs measure compression as well as shear wave velocities while drilling and are of high relevance to pore pressure determination.

However, information is only available on the formations penetrated by the drilling system as it is for all feasible measurements. Although this can be used in combination with other measurements to assess the stability of the borehole drilled so far, no information is provided by acoustic or other logs on the rock formations ahead of the bit. By using the measured velocities the Poisson's ratio can be calculated and using the density the modulus of elasticity is determined.

Deducible parameters

Porosity: Porosity can be calculated from density, resistivity, acoustic, and neutron porosity measurements.

Permeability: The measuring technique correlating with permeability is NMR (nuclear magnetic resonance). Furthermore, correlations with porosity are known, but they are empirical and only valid for rock types in a certain environment.

Stress: The vertical stress is derived from the integration of the density log and is often looked at as overburden pressure (OBG). Caliper measurements, density, gamma-ray, resistivity images, and acoustic televiewer or micro formation scanner logs have to be interpreted to determine the horizontal main normal stress by looking at borehole deformations, tensile induced fractures or breakout zones. This information reveals the direction of the main normal stress but not its magnitude. This cannot be measured in the borehole while drilling unless borehole integrity tests such as "formation integrity tests" or "leak-off tests" are conducted to evaluate the creation of tensile fractures which provide some mean of the magnitude of formation stresses. Furthermore, empirical studies exist looking at the relationship between the magnitude of the stress and the size of the caved zones.

Pore pressure: Although pore pressure (Bruce & Bowers, 2002) cannot be measured directly while drilling in non or little permeable formations, deductions about the pore pressure can be made by inputting acoustic, density or resistivity log data into suitable models. The drilling exponent can also be used to estimate pore pressure. However, some drilling parameters need to be known to calculate the drilling exponent. The biggest problem, however, is that no suitable model exists for the North German Basin. The standard models, e.g. those of Eaton (1975) or Bowers (2001) were derived empirically for younger sedimentary basins and do not work in conditions existing in the North German Basin.

Activity of mud, activity of pore fluid: Both parameters are used to determine the osmotic pressure which is also possible from concentration of ions in the pore fluid and in the mud. The concentration can be derived from resistivity measurements, if the composition of ions is known.

Fracture gradient: The fracture gradient is calculated form mechanical properties of the formation and pore pressure. It cannot be measured while drilling. Only a leak-off test after a section is cemented can provide information about the fracture gradient.

Parameters from laboratory or literature

Skempton-coefficient, Biot-coefficient, internal friction angle, cohesion, and tensile strength:
These are required mechanical parameters which can only be determined in laboratory by triaxial or shear tests. For known lithologies values from literature can be used. Triaxial tests were carried out by project G3, so data are available.

Thermal capacity, thermal expansion coefficient, and the thermal conductivity cannot be measured in the borehole – only from core analysis carried out in a laboratory. If no core material is available, values should be extrapolated from comparable formations.

Membrane efficiency: This parameter can only be measured in laboratory and determines the efficiency of the clay to hold back ions.

Based on the analysis of available borehole measurements, parameters that need further consideration are reviewed. In WP 3 correlations are evaluated to derive the parameters which cannot be measured directly.

WP 3 (LIAG): Evaluation of the correlations

The correlations between the input parameters (for the program to be developed in WP 6) and the parameters which can be logged in the borehole are only available to a certain degree. Therefore, it will be necessary to further develop the existing models and correlations which have not proven their liability in Northern Germany, or to develop new models and correlations.

Pore pressure

The pore pressure is a particularly important parameter for borehole stability and therefore also of importance for some other gebo projects. In a first stage, two models for young sedimentary basins (Eaton (1975) and Bowers (2001)) which are commonly used in the industry were applied for data from the North German Basin to investigate any potential extrapolability. No viable results were produced by either the simulations using the Eaton method, which only takes under-compaction into consideration as the cause of the raised pore pressure (the inclusion of fluids trapped by rapid sedimentation which experiences raised pressures during subsequent subsidence); or the Bowers method which also takes "unloading" into consideration as a possible cause (the release of vertical stress on the rock matrix e.g. by volume expansion from rising temperature). Because the North German Basin is an older tectonically affected basin, it will be necessary developing a new model to also take the influence of tectonics on the pore pressure into consideration. Furthermore, chemical processes and mineral transformation need to be considered.

Osmotic pressure

Since the osmotic pressure (Atkins, 1988) cannot be logged during drilling, it has to be derived from other parameters. It is significant because it indicates the direction of flow of pore fluids into the borehole or of mud into the formation – which in turn influence the stability of the borehole. Because osmotic pressure is dependent on the differences in concentration of dissolved substances in the pore fluids and in the drilling mud, a method is required which can determine the concentrations. Only argillaceous beds need to be considered here because these satisfy the conditions required for the presence of a semi-permeable membrane which can give rise to osmotic pressure. Resistivity is a parameter which can be easily measured while drilling and which is associated with the concentration. Although it depends on the concentration of the dissolved substances, it is also influenced by temperature and type of dissolved ions.

The typical composition of pore fluids of different lithologies is analyzed by the project G9 (Bozau, 2010) and taken as basis for the B4 calculations. So far backwards or inverse modeling are applied by calculating conductivities from known temperature and pore fluid composition with two different methods (Fig. 7): Firstly, the program PHREEQC by the USGS was used, which does not work for temperatures exceeding 100 °C but shows otherwise good results. Secondly, the Schlumberger chart Gen-9 was taken, which gives the empiric correlation between temperature, resistivity and concentration. It works for temperatures up to 200 °C.
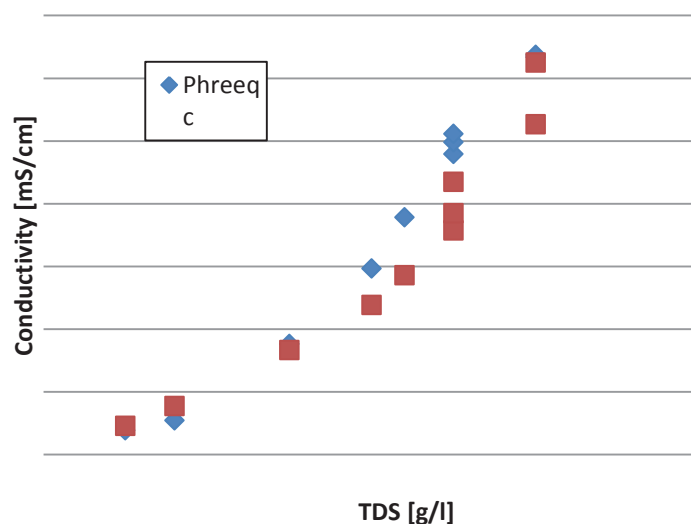
Figure 7: Comparison of calculated pore fluid conductivity from PHREEQC and Schlumberger chart Gen-9. Temperature increment between data points is 17.5 °C. TDS: Total Dissolved Solids.

Density and vertical stress

The vertical stress easily can be deduced by integrating the density over depth. So the parameter that needs to be deduced is the density over the whole length of the well.

$$\sigma_V = \int_0^z \rho(z) g \, dz \qquad \text{Eq. 27}$$

Nevertheless a correlation of the density, respectively the vertical stress, to other parameters is desirable since the density is sensitive to borehole breakouts and is not always measured. Therefore, a possible correlation between the density and compressional velocity is investigated. Some correlations for different types of lithologies can be found (Gardner et al., 1974; Bellotti & Giacca, 1978), e.g.:

$$density = 2.85 - \left(2.11 \cdot \frac{\left(DTCO - DT_{Matrix} \right)}{\left(DTCO + 200 \right)} \right) \qquad \text{Eq. 28}$$

with density in g/cm^3, DTCO is the sonic (P-wave) travel time in μs/ft, DT$_{Matrix}$: P-wave travel time in μs/ft within the matrix. The application of these equations shows, that especially the Bellotti & Giacca equation works well for formations up to 1,700 m. Below this depth the occurring shale behaves differently and requires a specific factor in the equation to match the results gained from measurements. Also in salt formations the density cannot be gained by the use of given equations. Hence the factor in the Bellotti & Giacca equation is also replaced for these formations. The results do not need to give exact numbers, but a value within 20% of the real density is good enough for the estimation of σ$_V$ according to the demands of the software presented in WP 6. Therefore, the density calculation is carried out with the adapted Bellotti & Giacca equation.

Minimum Horizontal Stress (σ$_h$)

The direction of σ$_h$ can be found out by the investigation of borehole breakouts. A caliper log, resistivity images, and acoustic televiewer or micro formation scanner logs, if available, are used for that purpose. The direction may vary with depth and location. In the Groß Buchholz Gt-1 well for example the orientation changes with depth. To determine its magnitude tests like a leak-off test (LOT) or a formation integrity test (FIT) or, as carried out in this well, a mini frac experiment need to be done.

Maximum Horizontal Stress (σH)

The orientation of σ$_H$ can be determined by the direction of induced tensile fractures, visible in UBI (Ultrasonic Borehole Imager) or FMI (formation microimager) or optical logs. Its

magnitude is not determined from these measurements. Some approaches use the width of breakouts to derive the magnitude of σ_H.

Unconfined compressive strength (UCS)

The UCS is one of the parameters the software (see WP 6) is highly sensitive to. Hence existing equations and new equations determined from laboratory measurements of gebo project G3 (Reyer & Philipp, 2014) are compared. A paper with the evaluation of the different known equations and the newly determined ones is in preparation by Vogt et al.. So far the GMI-Literature E equation (Eq. 29), provided with the GMI ModelBuilder software, produces good results and so does the NGB vp equation (Reyer & Philipp, 2014). The advantage of the NGB vp equation is that the input does not need vs and density as the calculation of the Young's modulus.

$$UCS = 6695 \cdot \exp(1.86 \cdot 10^{-7} \cdot E)$$ Eq. 29

Eq. 29 is the GMI-Literature E for sandstone with E: static Young's modulus in psi. For other lithologies other factors are used. Even though the static Young's modulus is supposed to be used as input parameter, it works well if the dynamic modulus is used. The results do not improve in case a correction is applied.

$$UCS = 4 \cdot 10^{-6} v_p^2 + 0.009\, v_p + 11.5$$ Eq. 30

Equation 30 is the NGB vp for sandstone with v_p in m/s.

Internal friction angle (*IFA) and* Biot's coefficient (α)

These mechanical properties are not deduced from logging data. It is necessary to use known numbers related to the different lithologies which are known from logging and drilling operations.

Poisson ratio (v) and Skempton coefficient

The poisson ratio can easily be determined, if compressional and shear velocity v_p and v_s are known:

$$\nu = \frac{\left(\frac{v_p}{v_s}\right)^2 - 2}{2\left(\left(\frac{v_p}{v_s}\right)^2 - 1\right)}$$ Eq. 31

Acoustic measurements need to be done for many different parameters so no further investigation is required. The Skempton coefficient has to be taken from triaxial tests of similar rock samples. Since the North German Basin is investigated well, samples to carry out such tests or measurement data should be available for the different formations.

WP 4 (LIAG + ITE): Selection of logging methods to determine the relevant parameters

According to the correlations found, the absolutely necessary logging methods are: gamma-ray, caliper, and v_p. Nevertheless, density and v_s are essential enough to make it worth measuring them. To obtain more information about stress directions tools with higher resolution like FMI or UBI are desirable. Also leak-off tests or formation integrity tests should be carried out to gain knowledge about stress magnitudes. Pore pressure prediction with known equations is impossible, but since the North German Basin is well explored, data from neighboring wells could be available. In new fields also pore pressure measurements sometimes are available.

WP 5 (LIAG + ITE): Algorithms to evaluate the data quality

Algorithms to evaluate the data quality could not be developed in this project, because enough data from different wells are not available. Instead, a sensitivity analysis was performed to categorize the input parameters based on their effects on the calculated mud window. The input parameters were categorized into three groups: must-have, low-sensitive and high-sensitive. The input parameters categorized in the "must-have" group should be measured with full accuracy. The other parameters which have relatively higher effects (i.e. in the high-sensitive group) should be measured with relatively high accuracy, while parameters which have relatively low effects (i.e. those for the low-sensitive group) can be estimated or obtained from neighboring boreholes. The sensitivity analysis was performed on three layers of the gebo benchmark model (G8) under dry, drained and undrained conditions. These three conditions cover almost all cases, which are met during drilling.

Figure 1 shows the lower and upper boundaries necessary to determine a suitable mud window. FG and σ_h (perpendicular to wellbore) build the two upper boundaries. PPG and SFG build the two lower boundaries. Because PPG and σ_h are used to build the two boundaries determining the mud pressure window, they are therefore categorized in the "must-have" group and will not be investigated. Similarly, as the minimal horizontal stress belongs to in-situ stresses, the in-situ stresses are categorized as a "must-have". The input parameters to determine FG and SFG were investigated in this work package.

To perform the sensitivity analysis, a basic case for the investigated input parameters should be defined first. Every investigated input parameter, except Poisson's ratio, varies from 20% to 180% from the basic case. The goal is to have all parameters constant and equal to the basis case. Because Poisson's ratio cannot be higher than 0.5, its variation should meet this precondition. Parameter variation is normalized by using Eq. 32 and called *NIPV*.

$$NIPV = \frac{Par - Par^{basic}}{Par^{basic}} \qquad \text{Eq. 32}$$

where *Par* = varied parameter and *Par^{basic}* = parameter in basic case. The result variation is normalized using Eq. 29 (normalized results variation = *NRV*).

$$NRV = \frac{|Re - Re^{basic}|}{|Re^{basic}|}$$

Eq. 33

where *Re* = the calculated results with varied input parameters and *Re^{basic}* = calculated results with basic input parameters. The sensitivity index S_i is calculated by using Eq. 30, which is used to indicate the effects of input parameters on the calculated result. The bigger the sensitivity index, the higher the effects of the input parameters:

$$S_i = \left| \frac{NRV}{NIPV} \right|$$

Eq. 34

Three interesting strata of the gebo benchmark model from the Northern German Basin were chosen for the sensitivity analysis. Table 3 lists the useful parameters used in the sensitivity analysis of the gebo benchmark model.

Table 3: Parameters from gebo benchmark model (G8)

Depth [m]	Formation	ρ [g/cm³]	UCS [MPa]	v [m]
2900	Keuper	2.3	45	0.26[L]
3300	Muschelkalk	2.51	115	0.3[L]
4200	MB+UB[*]	2.23	98[M]	0.22

[*]MB+UB = Middle and Lower Buntsandstein

[L] According to Löhken & Schellschmidt (2010); [M] According to Müller (2009)

Nevertheless, the parameters listed in Table 3 are insufficient to carry out the sensitivity analysis. The horizontal stress ratios K_h and K_H are assumed to be 0.7 and 0.8, respectively. The cohesion *C* was calculated using *UCS* and the internal friction angle (*IFA* or φ) according to Eq. 14, which describes the geometric relation between *UCS*, *IFA,* and cohesion. The rest of the input parameters are listed in Table 4.

Table 4: Assumed and derived parameters for sensitivity analysis ([as] data are assumed)

Depth [m]	φ [°][as]	α [-][as]	B [-][as]	σ_v [MPa]	σ_H [MPa]	σ_h [MPa]	C [MPa]
2900	40	0.5	0.5	67.7	54.16	47.39	10.5
3300	40	0.5	0.5	77.78	62.22	54.45	26.8
4200	40	0.5	0.5	98.5	78.8	68.95	22.8

Table 5 lists the input parameters for calculating FG and SFG, which were analyzed under different conditions. However, no parameters are needed for the analysis of FG under dry conditions. Because under dry conditions FG is only affected by in-situ stresses that belong to the "must-have" group. For boundary SFG the calculated sensitivity indices under dry, drained and undrained conditions for the three strata are shown in Figures 8 - 16. For the boundary FG the calculated sensitivity indices under drained and undrained conditions for the three layers are shown in Figures 17 - 22. The results are shown in pairs and separately for each condition and test layer. In each figure, the diagram on the left shows how the sensitivity index S_i varies with increasing *NIPV* from 20% to 100%, while the right diagram shows how S_i varies with decreasing *NIPV* from 100% to 20%.

Table 5: List of investigated input parameters under different conditions

Boundary	Dry	Drained	Undrained
FG	-	*α, v*	*α, v, B*
SFG	*IFA, UCS*	*IFA, UCS, α, v*	*IFA, UCS, α, v, B*
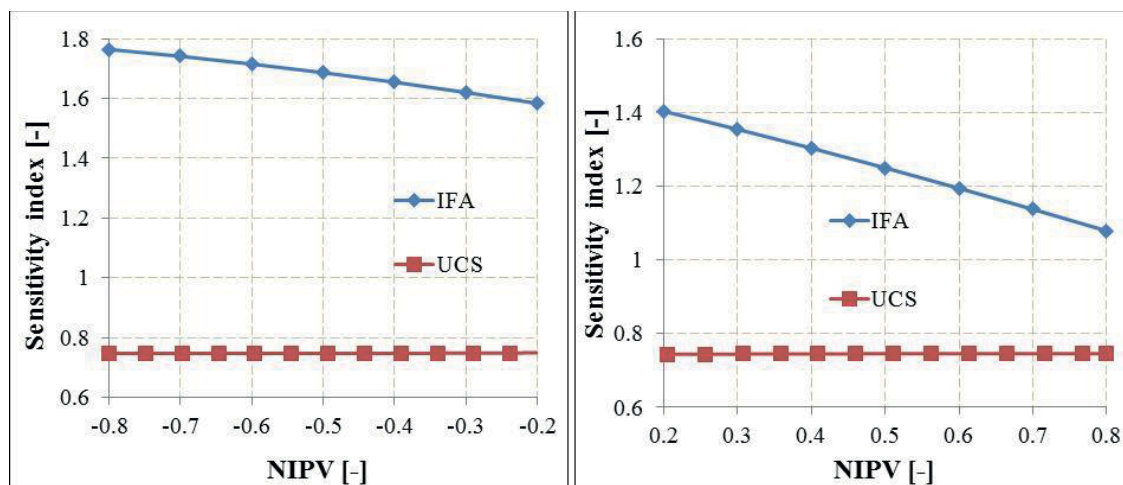
Figure 8: Variation of sensitivity index S_i with *NIPV* for SFG under dry conditions at **2,900 m**, using two input parameters, IFA and UCS.
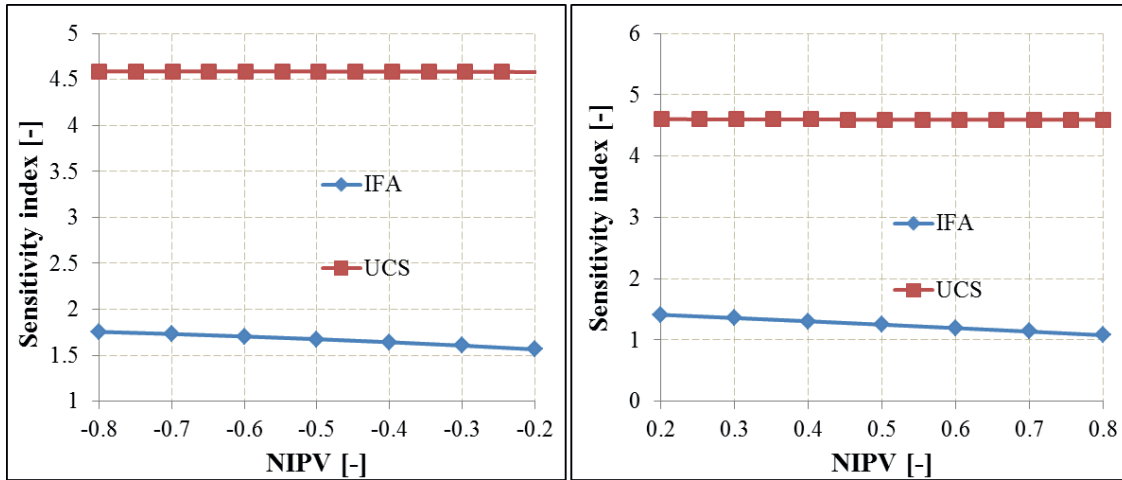
Figure 9: Variation of sensitivity index S_i with *NIPV* for SFG under dry conditions at **3,300 m**, using two input parameters, IFA and UCS.
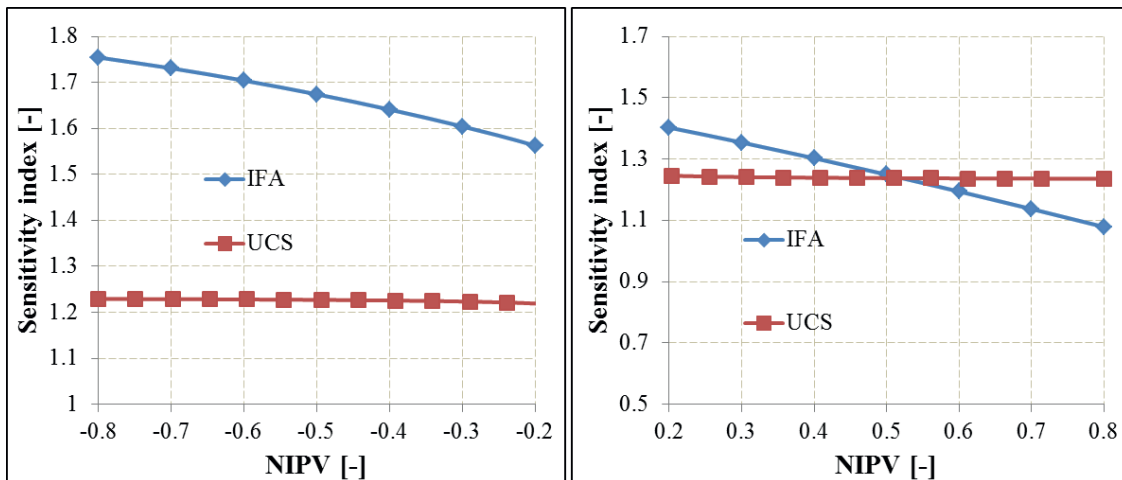
Figure 10: Variation of sensitivity index S_i with *NIPV* for SFG under dry conditions at **4,200 m**, using two input parameters, IFA and UCS.
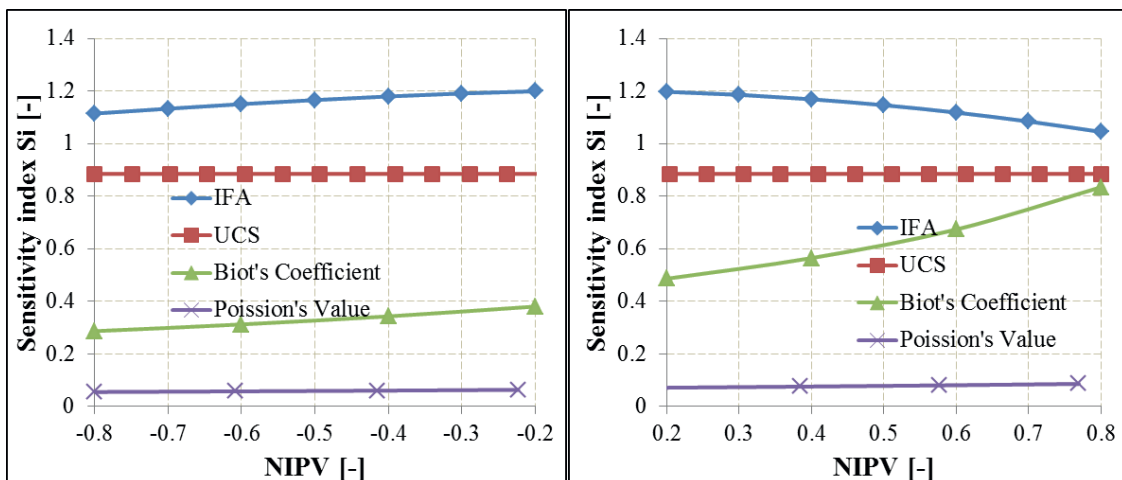
Figure 11: Variation of sensitivity index S_i with *NIPV* for SFG under drained conditions at **2,900 m**, using four input parameters, IFA, UCS, Biot's coefficient and Poission's ratio.

413
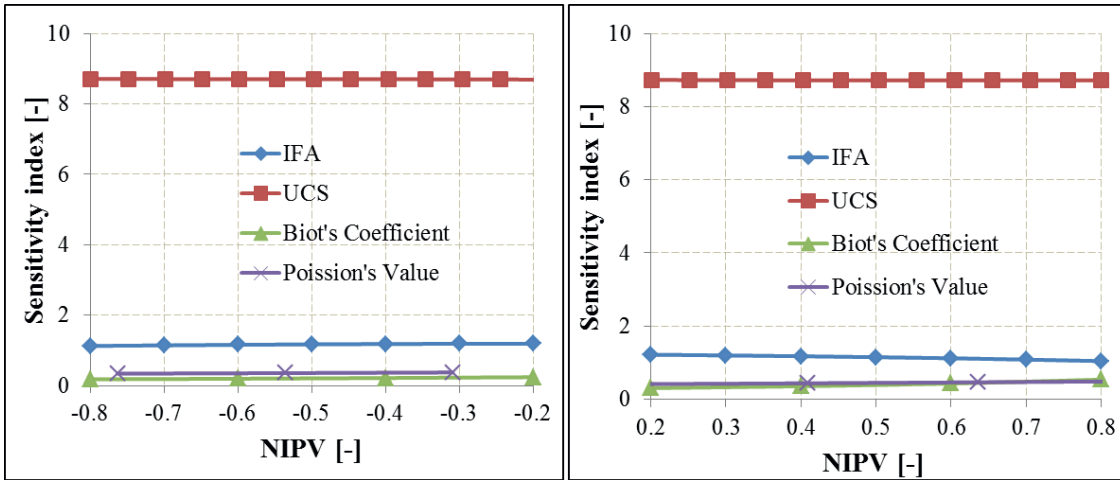
Figure 12: Variation of sensitivity index S_i with *NIPV* for SFG under drained conditions at **3,300 m**, using four input parameters, IFA, UCS, Biot's coefficient and Poission's ratio.
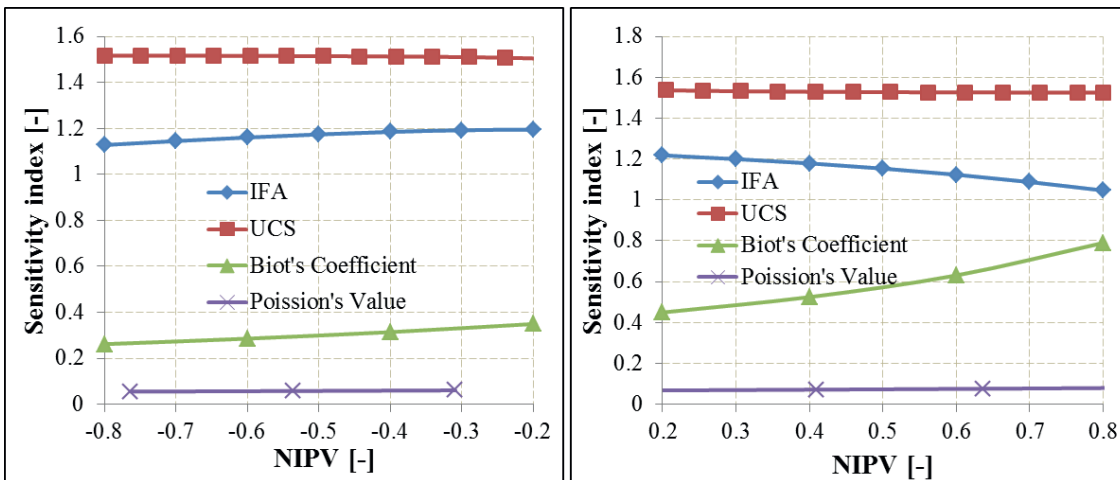
Figure 13: Variation of sensitivity index S_i with *NIPV* for SFG under drained conditions at **4,200 m**, using four input parameters, IFA, UCS, Biot's coefficient and Poission's ratio.
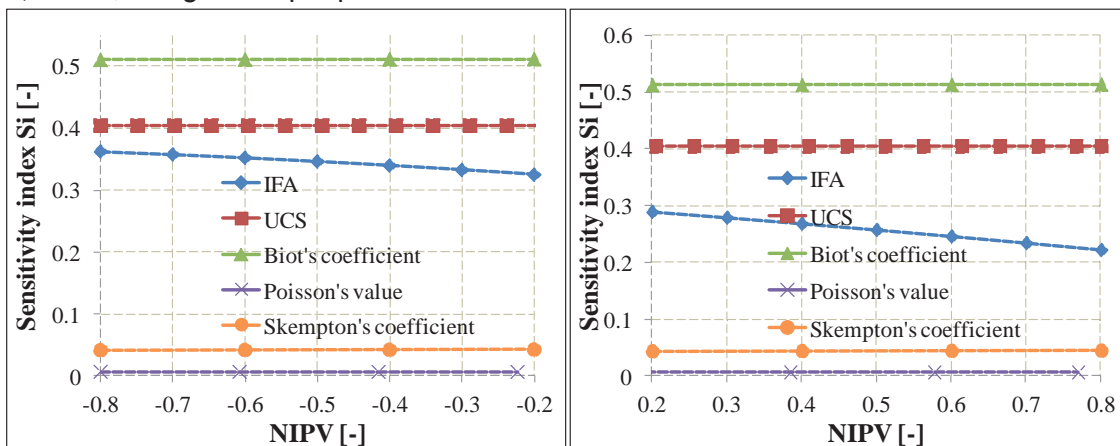
Figure 14: Variation of sensitivity index S_i with *NIPV* for SFG under undrained conditions at **2,900 m**, using four input parameters, IFA, UCS, Biot's coefficient, Poission's ratio and Skempton's coefficient.
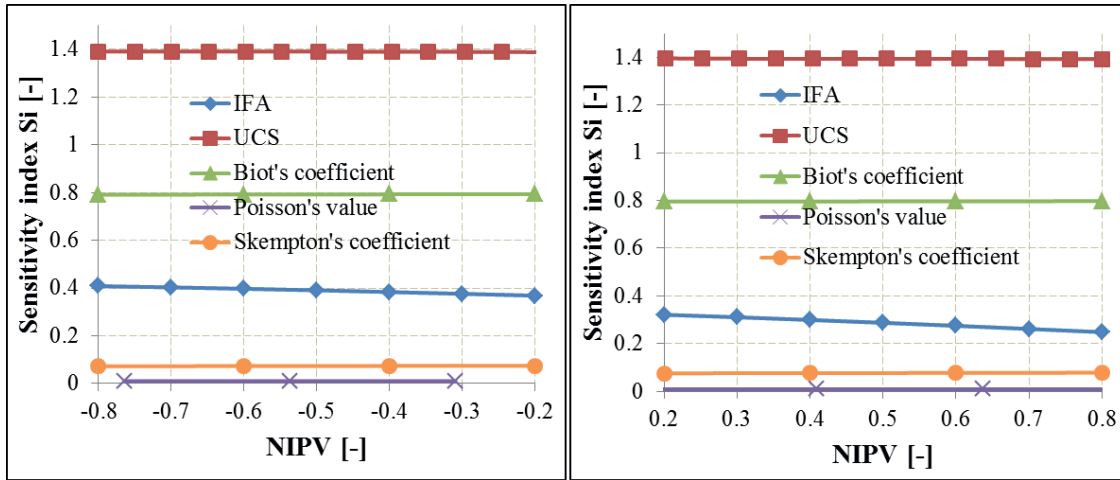
Figure 15: Variation of sensitivity index S_i with *NIPV* for SFG under undrained conditions at **3,300 m**, using four input parameters, IFA, UCS, Biot's coefficient, Poission's ratio and Skempton's coefficient.
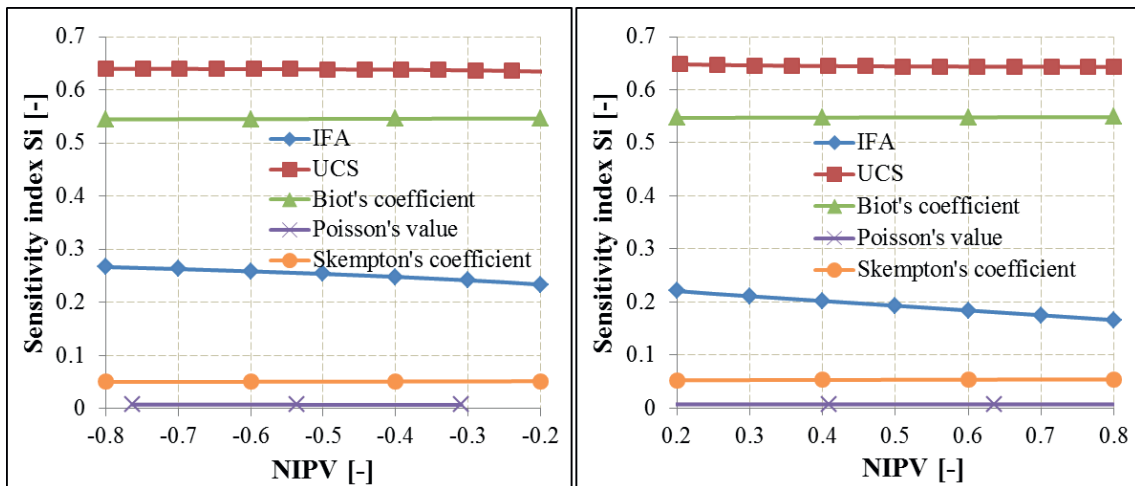
Figure 16: Variation of sensitivity index S_i with *NIPV* for SFG under undrained conditions at **4,200 m**, using four input parameters, IFA, UCS, Biot's coefficient, Poission's ratio and Skempton's coefficient.
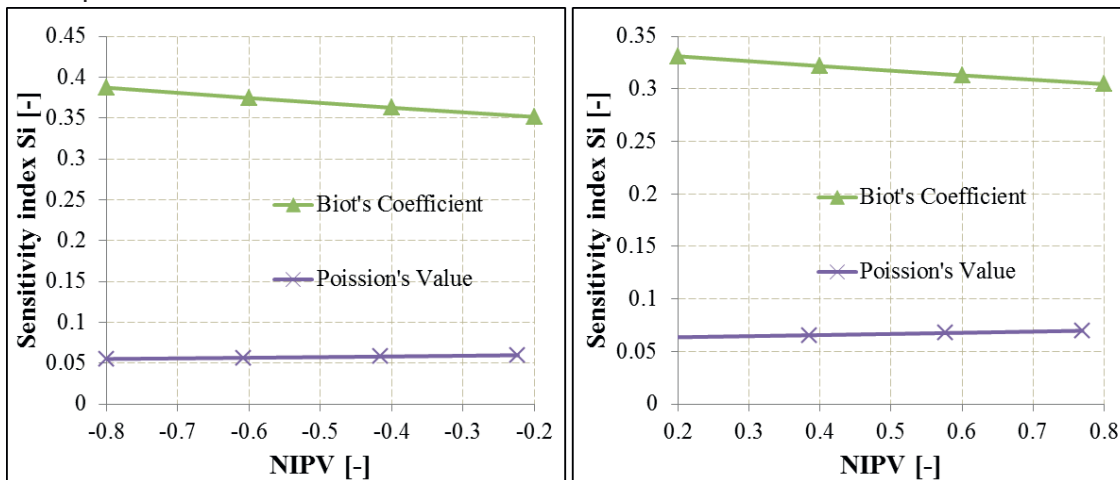
Figure 17: Variation of sensitivity index S_i with *NIPV* for FG under drained conditions at **2,900 m**, using two input parameters, IFA and UCS.

415
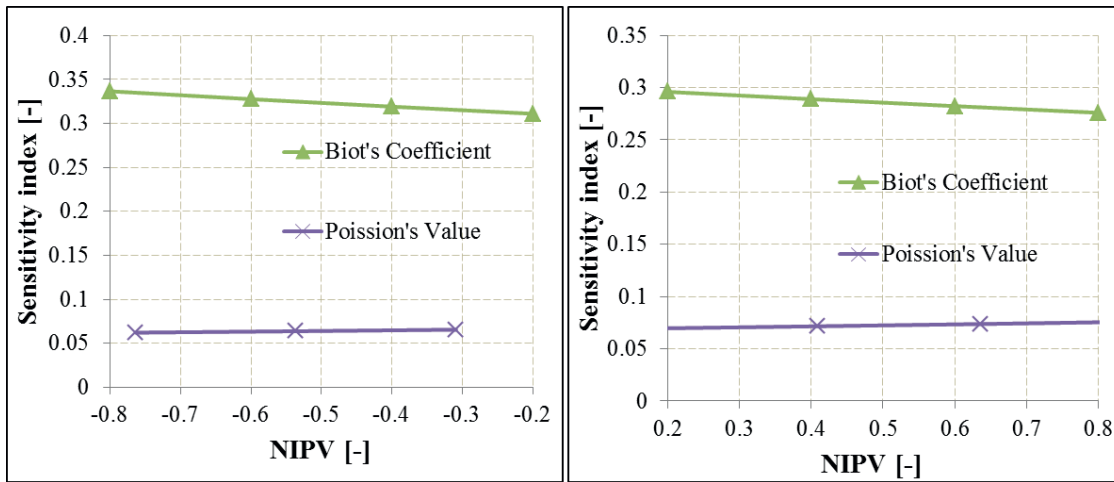
Figure 18: Variation of sensitivity index S_i with *NIPV* for FG under drained conditions at **3,300 m**, using two input parameters, IFA and UCS.
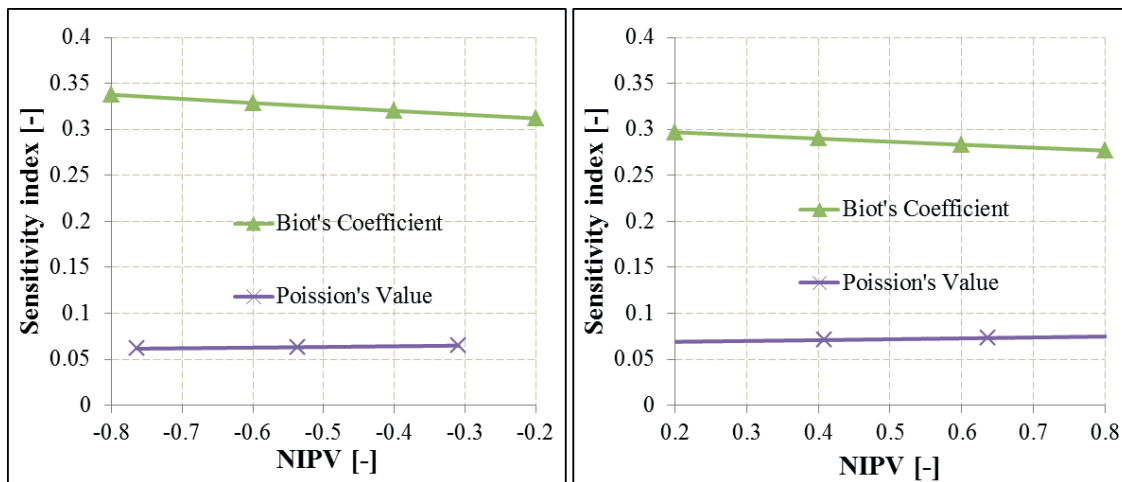
Figure 19: Variation of sensitivity index S_i with *NIPV* for FG under drained conditions at **4,200 m**, using two input parameters, IFA and UCS.
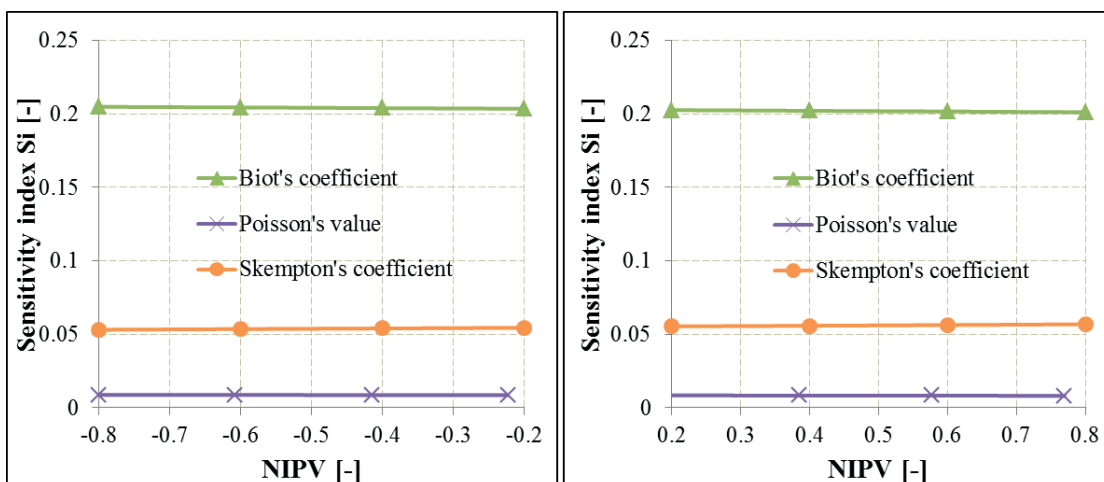
Figure 20: Variation of sensitivity index S_i with *NIPV* for FG under undrained conditions at **2,900 m**, using four input parameters: Biot's coefficient, Poission's ratio and Skempton's coefficient.
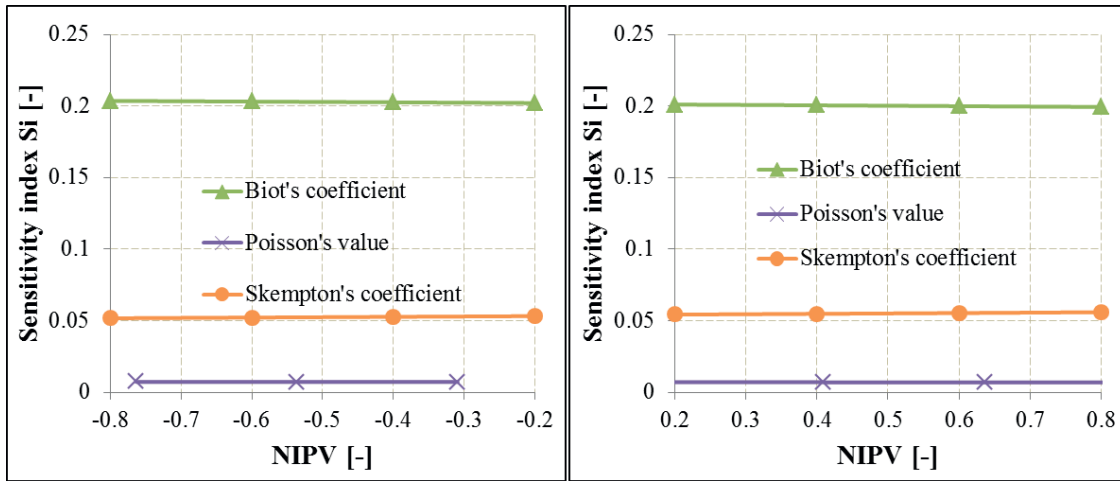
Figure 21: Variation of sensitivity index S_i with *NIPV* for FG under undrained conditions at **3,300 m**, using four input parameters: Biot's coefficient, Poission's ratio and Skempton's coefficient.
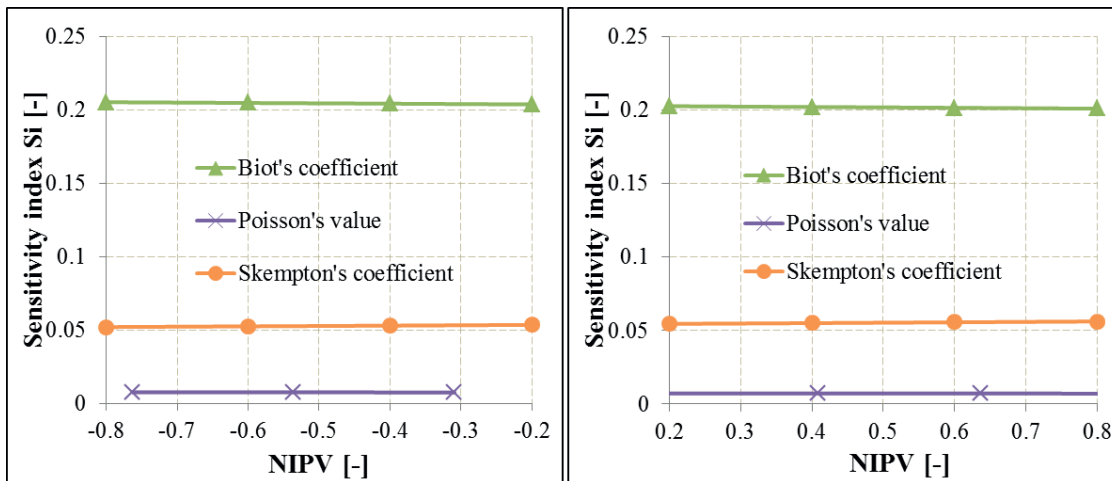
Figure 22: Variation of sensitivity index S_i with *NIPV* for FG under undrained conditions at **4,200 m**, using four input parameters: Biot's coefficient, Poission's ratio and Skempton's coefficient.

PPG and in-situ stress should be categorized as a "must-have" since PPG and σ_h build two of the four boundaries. Moreover the in-situ stresses, especially the K_h/K_H ratio, significantly affect borehole stability. For example, in the parameters listed in Table 6, FG and SFG under undrained state are 5.16 kPa/m and 8.05 kPa/m, respectively. That means FG is even smaller than SFG. The reason is that the K_h/K_H ratio is so small that there is not enough support in the σ_h direction (Figure 23). The fracture will be more likely to build in the σ_H direction. Therefore, the K_h and K_H values are most significant for the borehole stability, which is another reason why the in-situ stress should be categorized in the "must-have" group.

417

Table 6: Parameters for calculating FG and SFG

σ_v [MPa]	σ_H [MPa]	σ_h [MPa]	α [-]	B [-]	v [-]	P_R [MPa]
67.7	54.16	27.07	0.5	0.5	0.26	29
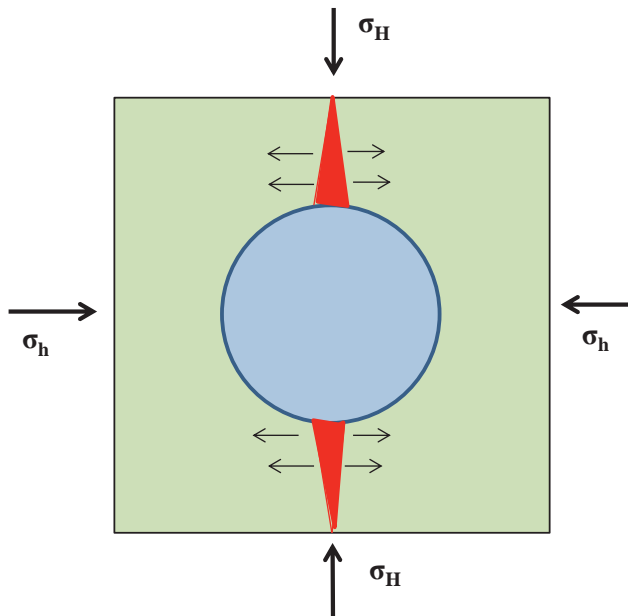
Figure 23: Illustration of tensile failure appearing in σ_H direction only since there is not enough support in σ_h direction.

IFA and UCS affect SFG under dry, drained and undrained conditions. As shown in Figures 8 - 16 the IFA and UCS sensitivity indices for SFG are always relatively higher at all three strata under dry, drained and undrained conditions. In addition to IFA and UCS, the Biot's coefficient also affects both FG and SFG under drained and undrained conditions. For FG the Biot's sensitivity indices are the largest under both undrained and drained conditions in all the three strata. For SFG Biot's sensitivity indices are also relatively high under drained and undrained conditions in all the three strata. There is however one anomaly under drained conditions at 3,300 m. In this case, the Biot's and Poisson's sensitivity indices are close to each other. The Biot's sensitivity indices are especially high under undrained conditions, which represent also the most hazardous phases during drilling (Hou et al., 2004). Therefore, IFA, UCS and Biot's coefficient are categorized in the "high-sensitive" group.

As shown in Figures 8 - 22, it is clear that the Poisson's ratio has the lowest sensitivity index under both drained and undrained conditions in the three strata for FG as well as SFG. The Skempton's coefficient is only validated under undrained conditions, and its sensitivity index is close to 0.05 in the three strata for FG as well as SFG. The Skempton's sensitivity index is

a little higher than the Poisson's sensitivity index. Therefore, Skempton's coefficient and Poisson's ratio are categorized to the "low-sensitive" group. The three groups are categorized and listed in Table 7.

Table 7: Category of input parameters according to sensitive analysis

Group	Input parameters
must-have	σ_h, σ_H, σ_v, P_R
high-sensitive	IFA, UCS, α
low-sensitive	v, B

WP 6 (ITE): Further development of the THM coupled evaluation model

The stress distribution around a wellbore is depending on the drilling conditions. In shallow drilling there are three extreme conditions, which are dry, undrained and drained conditions. The undrained state is only valid during the drilling and immediately after the drilling, especially for the low permeable rock formations, while the drained state dominates almost the total drilling phase. In deep drilling, besides the three conditions, thermal effects must be considered.

As shown in Figure 6, the FG is identical for different rocks. To avoid borehole fracture minimum σ_θ must be bigger than or equal to minus tensile strength $-\sigma_t$. Otherwise a vertical fracture would appear. Normally, the tensile strength is equal to zero. During shallow drilling thermal effects can be ignored, the FG under dry, drained and undrained conditions is therefore described by Eq. 35 – 37 (derivation refers to Luo, 2010 a).

$$FG = \frac{1}{De} \cdot (3\sigma_{30} - \sigma_{10} + \sigma_t) \qquad \text{Eq. 35}$$

$$FG = \frac{1}{De} \cdot \frac{3\sigma_{30} - \sigma_{10} - \alpha \cdot p_R \cdot \frac{1-2v}{1-v} + \sigma_t}{1 + \alpha - \alpha \cdot \frac{1-2v}{1-v}} \qquad \text{Eq. 36}$$

$$FG = \frac{1}{De} \cdot \left[3\sigma_{30} - \sigma_{10} - \alpha \cdot \left(p_R + \frac{2B \cdot (1+v_u)}{3} \cdot (\sigma_{30} - \sigma_{10}) \right) + \sigma_t \right] \qquad \text{Eq. 37}$$

During deep drilling thermal effects must be considered. Because the thermal radial stress is equal to zero at the borehole wall (Hou & Luo, 2011), only the tangential thermal stress influence affects the FG. Therefore, the FG under dry, drained and undrained conditions during deep drilling can be expressed by Eq. 38 to Eq. 40 (derivation refers to Luo, 2010 b).

$$FG = \frac{1}{De} \cdot (3\sigma_{30} - \sigma_{10} + \sigma_t + \sigma_\theta^T) \qquad \text{Eq. 38}$$

$$FG = \frac{1}{De} \cdot \frac{3\sigma_{30} - \sigma_{10} - \alpha \cdot p_R \cdot \frac{1-2v}{1-v} + \sigma_t + \sigma_\theta^T}{1 + \alpha - \alpha \cdot \frac{1-2v}{1-v}} \qquad \text{Eq. 39}$$

$$FG = \frac{1}{De} \cdot \left[3\sigma_{30} - \sigma_{10} - \alpha \cdot \left(p_R + \frac{2B \cdot (1+v_u)}{3} \cdot (\sigma_{30} - \sigma_{10}) \right) + \sigma_\theta^T + \sigma_t \right] \qquad \text{Eq. 40}$$

In brittle and soft rocks the SFG is determined with different criteria. The Mohr-Coulomb's failure criterion is employed to determine the SFG in brittle rocks, which means that the maximum effective stress should not exceed the shear strength σ_{if}. Usually the tangential stress σ_θ is the biggest stress component at the borehole wall, which should be compared to the rock shear strength to determine the minimum mud pressure. During shallow drilling thermal effects can be ignored, the SFG under dry, drained and undrained conditions can be described by Eq. 41 to Eq. 43 (derivation refers to Luo, 2010 a):

$$SFG = \frac{1}{De} \cdot \frac{(3\sigma_{10} - \sigma_{30}) - 2c \cdot \sqrt{N_\varphi}}{1 + N_\varphi} \qquad \text{Eq. 41}$$

$$SFG = \frac{1}{De} \cdot \frac{3\sigma_{10} - \sigma_{30} - 2c \cdot \sqrt{N_\varphi} - \alpha \cdot p_R \cdot \frac{1-2v}{1-v}}{2 + (1-\alpha) \cdot (N_\varphi - 1) - \alpha \cdot \frac{1-2v}{1-v}} \qquad \text{Eq. 42}$$

$$SFG = \frac{1}{De} \cdot \left\{ \frac{(3\sigma_{10} - \sigma_{30}) - 2c \cdot \sqrt{N_\varphi}}{N_\varphi + 1} + \alpha \cdot \sin\varphi \left[p_R + (\sigma_{10} - \sigma_{30}) \cdot \frac{2B \cdot (1+v_u)}{3} \right] \right\} \qquad \text{Eq. 43}$$

During deep drilling thermal effects must be considered. At the borehole wall the radial thermal stress is zero while tangential thermal stress varies is not equal to zero and constant at the borehole wall (Hou & Luo, 2011). The tangential thermal stress is therefore the only influence factor affecting the SFG for brittle rocks. Therefore, the SFG under dry, drained and undrained conditions during deep drilling can be described by Eq. 44 to Eq. 46 (derivation refers to Luo, 2010 b).

$$SFG = \frac{1}{De} \cdot \frac{(3\sigma_{10} - \sigma_{30}) - 2c \cdot \sqrt{N_\varphi} + \sigma_\theta^T}{1 + N_\varphi} \qquad \text{Eq. 44}$$

$$SFG = \frac{1}{De} \cdot \frac{3\sigma_{10} - \sigma_{30} - 2c \cdot \sqrt{N_\varphi} - \alpha \cdot p_R \cdot \frac{1-2v}{1-v} + \sigma_\theta^T}{2 + (1-\alpha) \cdot (N_\varphi - 1) - \alpha \cdot \frac{1-2v}{1-v}} \qquad \text{Eq. 45}$$

$$SFG = \frac{1}{De} \cdot \left\{ \frac{(3\sigma_{10} - \sigma_{30}) - 2c \cdot \sqrt{N_\varphi} + \sigma_\theta^T}{N_\varphi + 1} + \alpha \cdot \sin\varphi \left[p_R + (\sigma_{10} - \sigma_{30}) \cdot \frac{2B \cdot (1+v_u)}{3} \right] \right\} \qquad \text{Eq. 46}$$

To calculate the NYZR, the stress distribution in the near field should be computed first. Then the yield zone can be determined according to different shear failure criteria. If the allowable NYZR is defined, the SFG for soft rocks can be determined. As an example, Figure 24 shows the calculated NYZR as a function of the mud pressure gradient (MudPreG). The defined allowable NYZR is shown by the red line in Figure 24 (NYZR = 1.17), the cross point should be SFG (0.64 kPa/m).
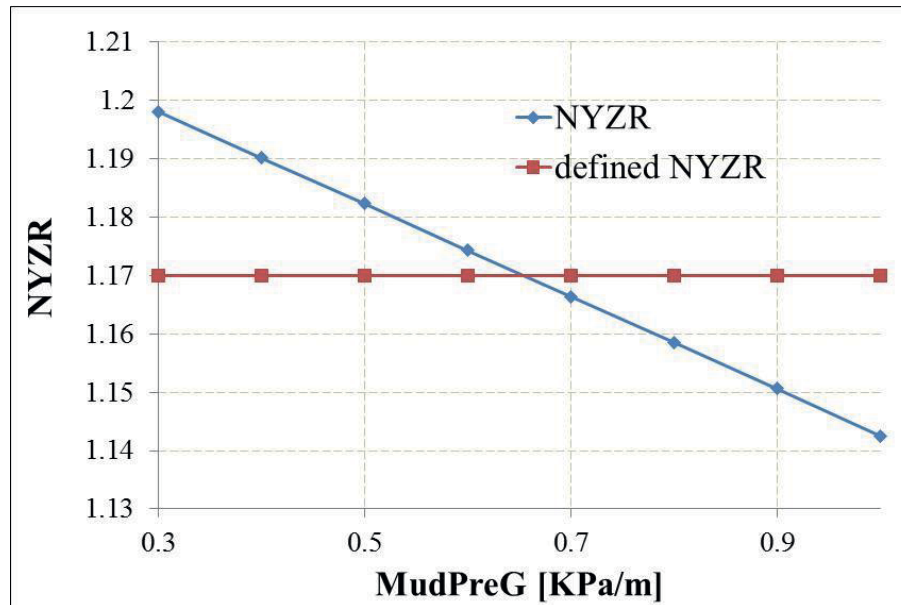
Figure 24: NYZR variation under different mud pressure gradients.

The thermal effects govern the rock hydro-mechanical response during deep drilling. The depth-dependent mud temperature inside the tubing and the annulus as well as the rock formation temperature (called temperature profile) are significant to determine the influence of thermal effects. Therefore, knowledge of accurate temperature profiles inside the annulus, tubing and rock formation along the borehole during drilling is significant for analyzing the borehole stability. Until now no physical method was engineered to measure the temperature profile inside the borehole or surrounding rock formations during the mud circulation. Existing numerical and analytical methods must assume a constant wellbore temperature (Yu et al., 2009) or constant formation temperature (Tang & Luo, 1998). Therefore, the development of a new calculation method to obtain the temperature profile in annulus, tubing and rock is significant for the borehole stability evaluation.

A semi-numerical method is developed (Luo, 2015). Using this method, the temperature in annulus, tubing and formation can be predicted at different states of circulation. Moreover, the thermal stress is obtained based on the simulated formation temperature distribution. An example well (Ex-well) was used to illustrate the results calculated using the new developed semi-numerical method. Table 8 and Table 9 characterize the Ex-well and its surrounding rocks. Figure 25 compares the tubing and annulus temperature profile at 0.9, 1.2, and 5.7 days. The red line is the nature Earth temperature. The initial mud temperature was 25 °C. In total, the mud in tubing and annulus was heated up during circulation. The mud flowing via the tubing down to the bottom hole was cooled in a shallow area and then heated up in the

deep part of the well. When the mud flowed back via the annulus, it was heated up at first and then cooled down.

Table 8: Parameters characterizing the wellbore (Ex-Well)

Parameter	Ex-Well
Radius	0.1 m
Depth	3080 m
Average thermal gradient	0.0344 °C/m
Surface temperature	25 °C

Table 9: Geothermal parameters of rock layers

Formation	interval [m]	λ [J/(m·°C·s)]	ρ [kg/m^3]	C_b [J/(kg·°C)]
Quaternary	0- 200	1.76	2089	1101
T.OSM	200-1200	2.825	2554	900
TM.OMM	1200-1550	3.06	2620	878
T.USM	1550-3080	3.05	2706	850

Table 10: Parameters for thermal stresses' calculation

Parameter	Value
Rock thermal expansion coefficient [1/°C]	$3E^{-5}$
Poisson's ratio [-]	0.2
Young's Modul [MPa]	20600
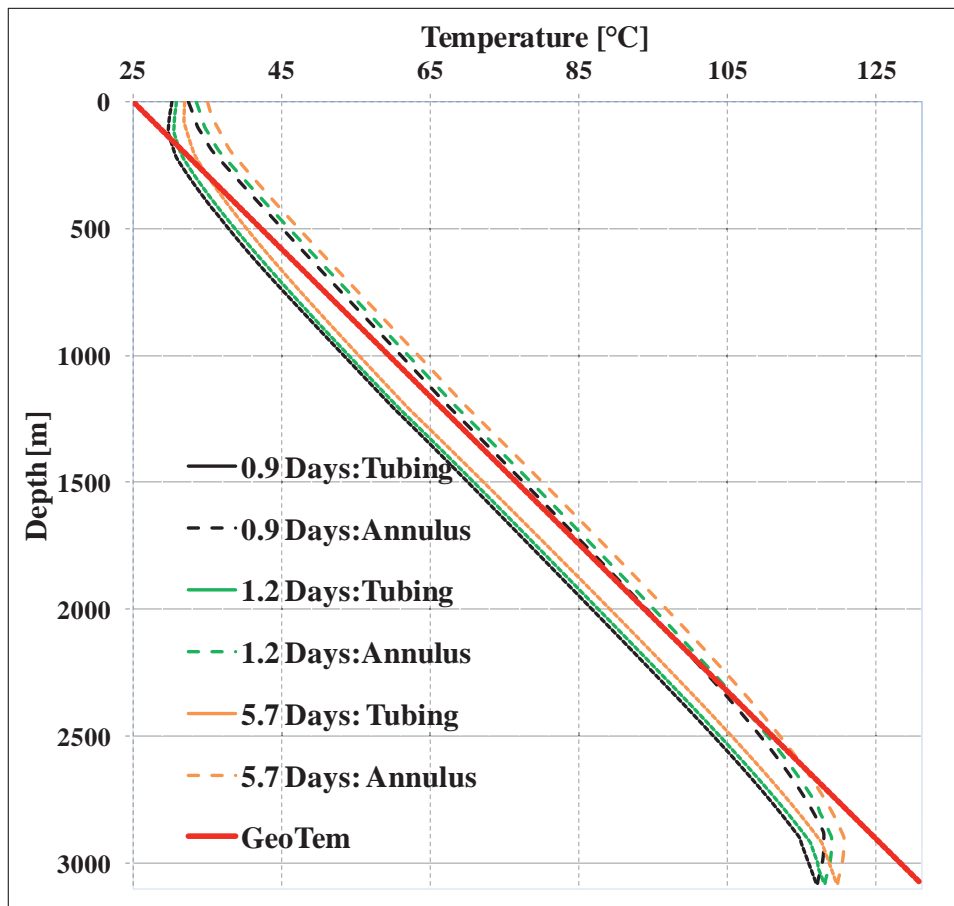
Figure 25: Tubing and annulus temperature profiles after different phases of circulation.

The thermal stresses were calculated after the temperature simulation. Figure 18 shows the formation temperature profiles in deeper rocks (2,780 – 3,080 m) at different radial positions. The left diagram shows the results after 8 hours of circulation, while the diagram on the right side presents the results after 1.7 days of circulation. Based on the temperature profile shown in Figure 26, the radial and tangential thermal stresses were calculated and shown in Figures 27 and 28, respectively. The used parameters are listed in Table 10. At the borehole wall the radial thermal stress was equal to zero, because the rock at the borehole wall can deform freely in radial direction because of the boundary conditions. Therefore, the radial thermal profile at the borehole wall was not shown in Figure 27. The tangential and radial thermal stress profiles were relatively unstable by case after 8 hours of circulation (left diagrams in Figures 27 and 28). Because after 8 hours of circulation, the annulus was still not fully filled with mud, the heat exchange between mud and formation is relatively intense if the mud firstly comes into contact with the formation. With continual circulation, the thermal stress profiles were stable (right diagrams in Figures 27 and 28).
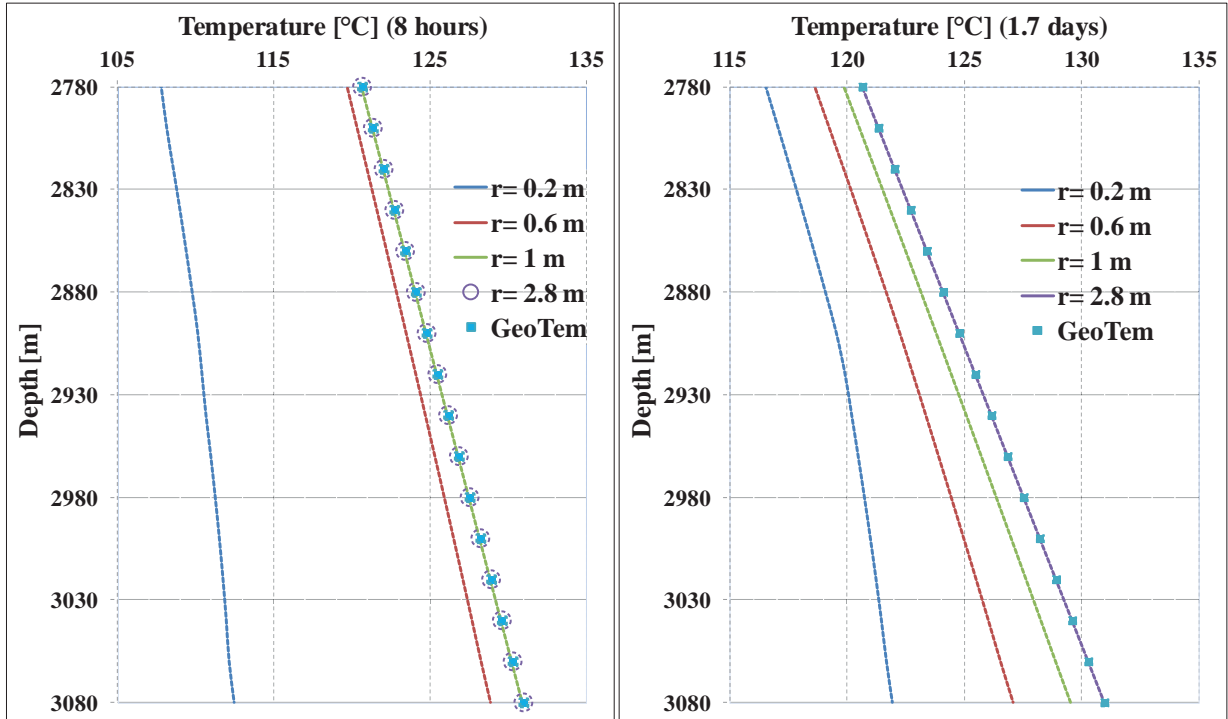
Figure 26: Formation temperature profile in depth range between 2,780 m and 3,080 m.
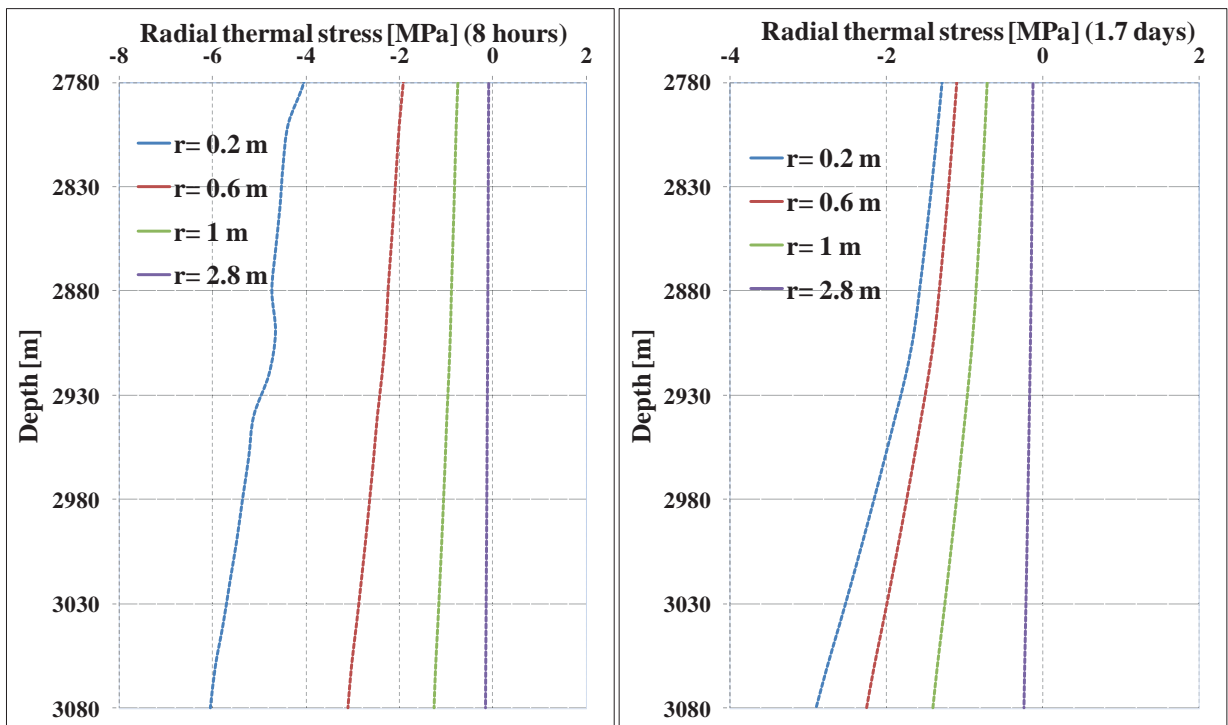
Figure 27: Radial thermal stress profiles at different radial positions between 2,780 m and 3,080 m.
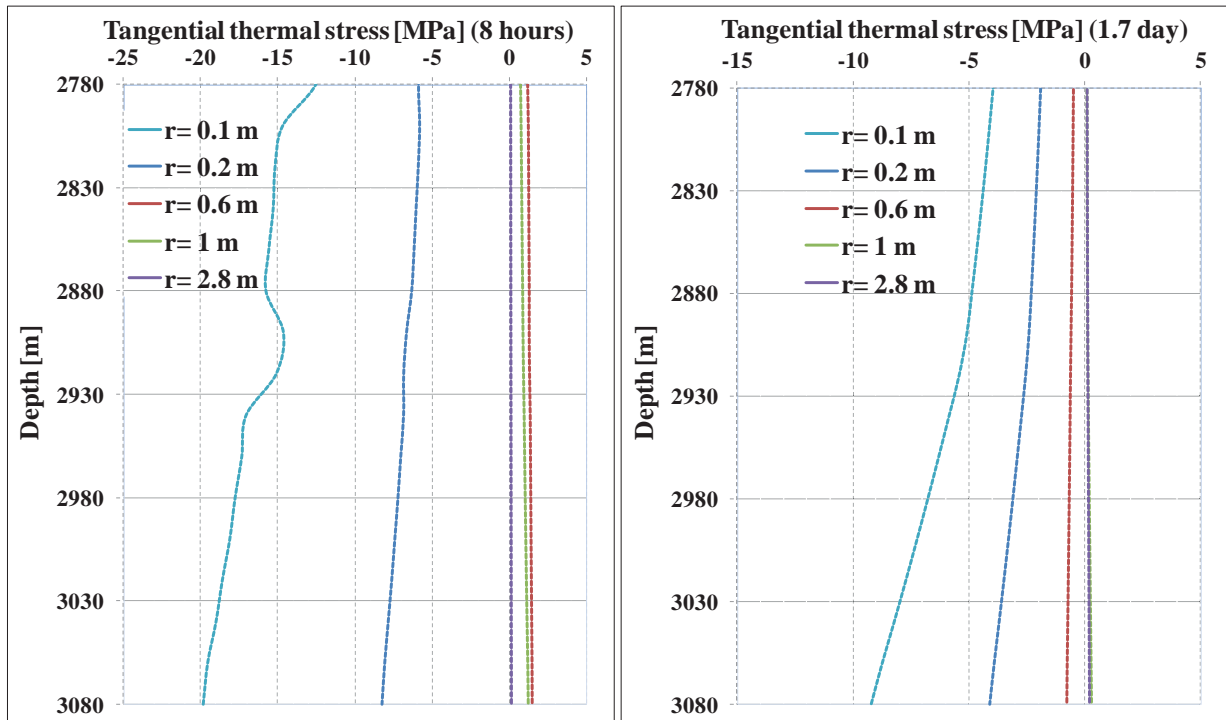
Figure 28: Tangential thermal stress profiles at different radial positions between 2,780 m and 3,080 m.

WP 7 (ITE + LIAG): Validation of the developed evaluation models and correlations

Validation of the established model to calculate SFG in brittle rocks

The software FLAC3D was employed to verify the established model to calculate SFG in brittle rocks. The SFP was calculated by using FLAC3D and established borehole stability evaluation models. Then the calculated results were compared in order to check whether the model is correct or not. This comparison is explained by Luo (2010 b).

The loading to strength ratio in the critical position were calculated under various mud pressures. Considering the Mohr-Coulomb shear failure criterion, the loading to strength ratio can be calculated using Eq. 47:

$$R_{L/S} = \frac{\sigma_{max}}{\sigma_{1f}}$$
Eq. 47

where $R_{L/S}$ is loading to strength ratio, -; σ_{max} = Maximum stress in critical position, MPa; σ_{1f} shear strength according to Mohr-Coulomb shear failure criterion (Eq. 15). If the loading and stress ratio equals to one, the adopted mud pressure is the shear failure pressure.

Figure 29 shows the stress to strength ratio distributions with different mud pressures under dry conditions. It shows that the loading to strength ratio was equal to one at the borehole

425

wall, if the mud pressure was 13.9 MPa. Therefore, the shear failure pressure determined by FLAC3D was 13.9 MPa. By using 47 the shear failure pressure was calculated and equals to 14.1 MPa.
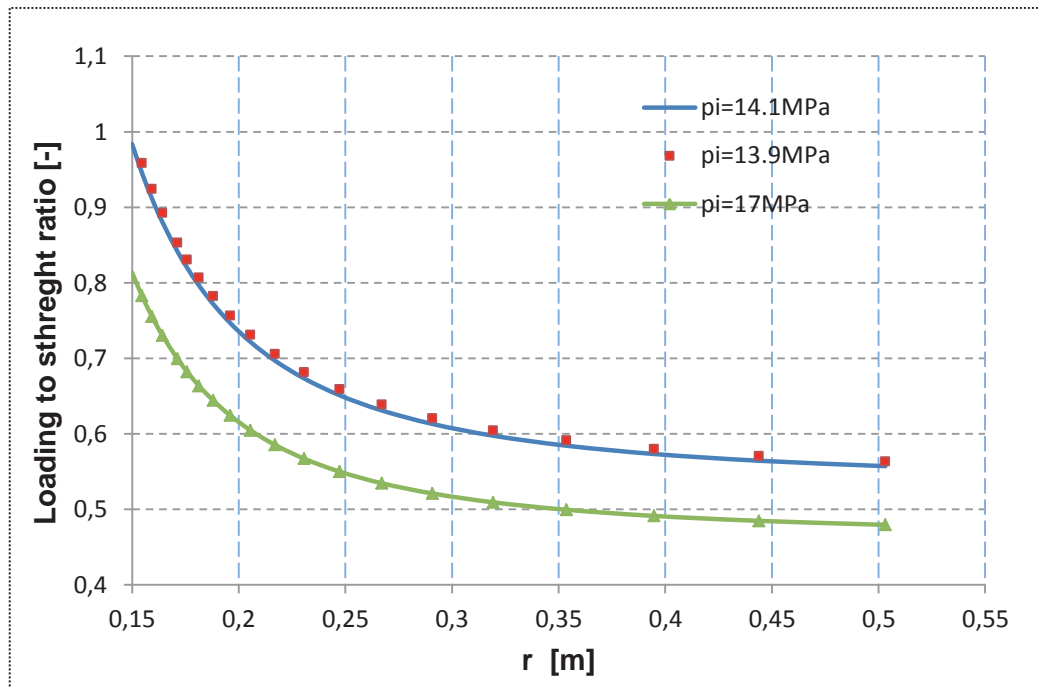
Figure 29: Loading to strength ratio distributions in the near field of a borehole during drilling with different mud pressures under dry state.

Figure 30 shows the loading to strength ratio distributions under drained conditions with different mud pressures. It shows that if the mud pressure equals 27 MPa, the loading to strength is equal to 1. Therefore, the shear failure pressure was 27 MPa determined using FLAC3D. The analytic solution under drained state was 28.1 MPa.

Figure 31 shows the loading to strength ratio distributions under undrained conditions with different mud pressures. It shows that, if the mud pressure is equal to 18.8 MPa, the loading to strength is equal to 1. Therefore, SFP is 18.8 MPa determined by using FLAC3D. The analytic solution under the drained state was 18.4 MPa. Table 11 compares the shear failure pressure calculated using FLAC3D to the models developed in the cause of the project. The results calculated using the models developed in the cause of the project models show good agreement with results determined using FLAC3D.
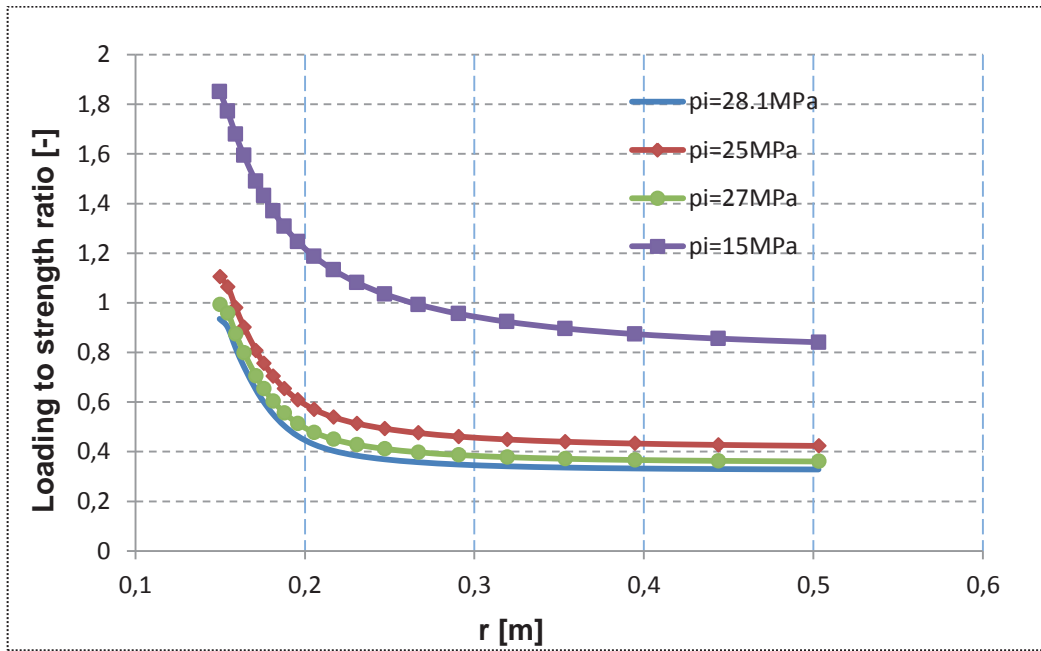
Figure 30: Stress to strength ratio distributions in the near field of a borehole during drilling with different mud pressures under drained state.
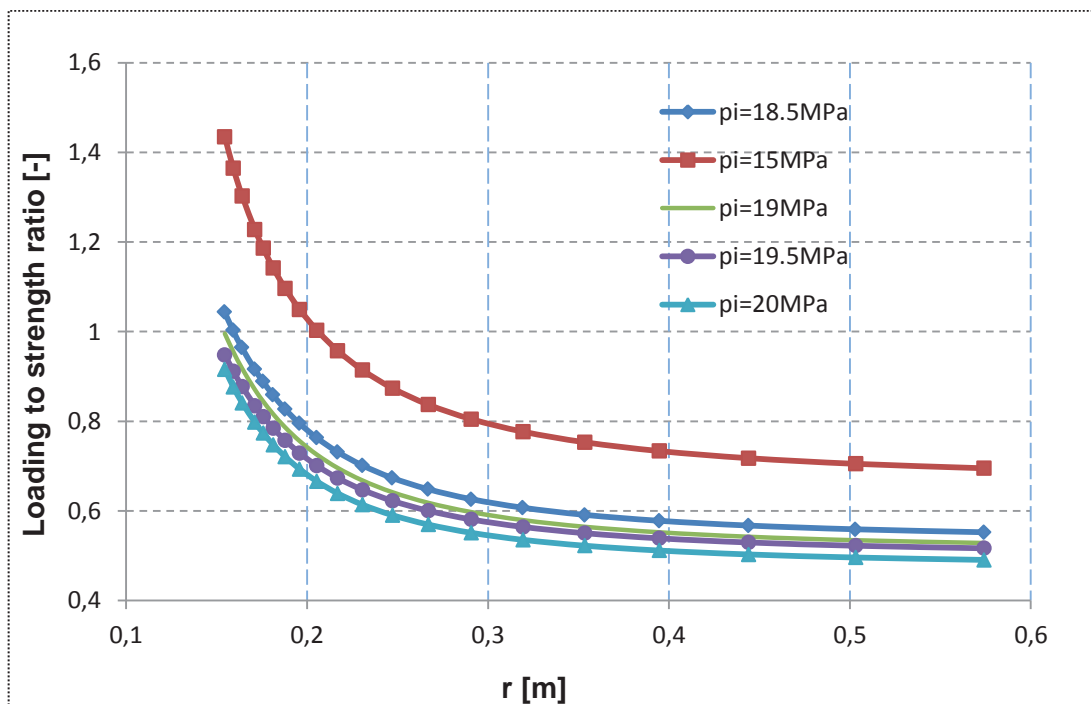
Figure 31: Stress to strength ratio distributions in the near field of a borehole during drilling with different mud pressures under undrained state.

Table 11: Shear failure pressure calculated using FLAC3D and the models developed in the cause of the project.

Method	Dry	Drained	Undrained
FLAC3D	SFP =13.9 MPa	SFP = 27.0 MPa	SFP = 18.8 MPa
models developed in the cause of the project	SFP =14.1 MPa	SFP = 28.1 MPa	SFP = 18.8 MPa

Validation of the thermal stress calculation model

The thermal stresses were calculated by using FLAC3D and compared to model developed in the cause of the project. This comparison is explained in detail by Luo (2010 b). The Figures 32 and 33 show the tangential and radial thermal stresses computed using the model developed in the cause of the project and FLAC3D. The heat flux was under conduction conditions. The conduction time was 860 s. The thermal stresses calculated using FLAC3D and the own model show good agreement to each other.
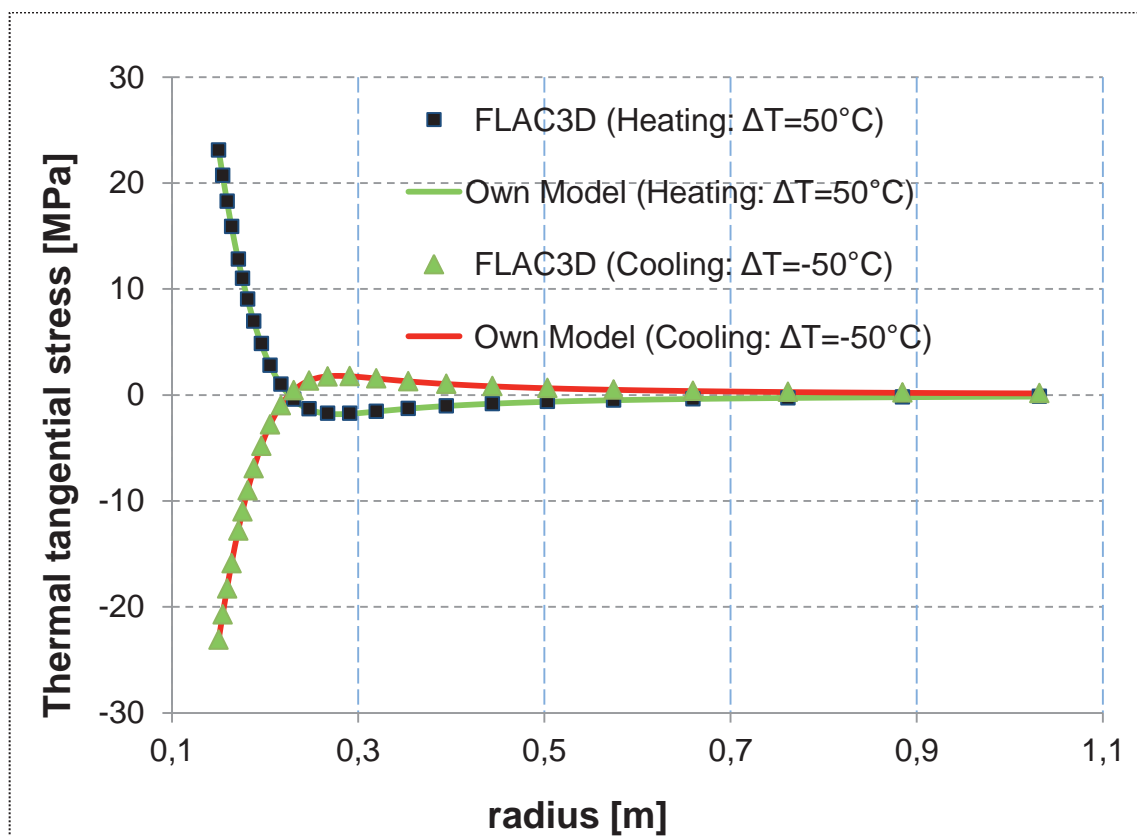
Figure 32: Thermal tangential stress distributions in the near field of a borehole at 860 s calculated with FLAC3D and own model (thermal conduction condition).
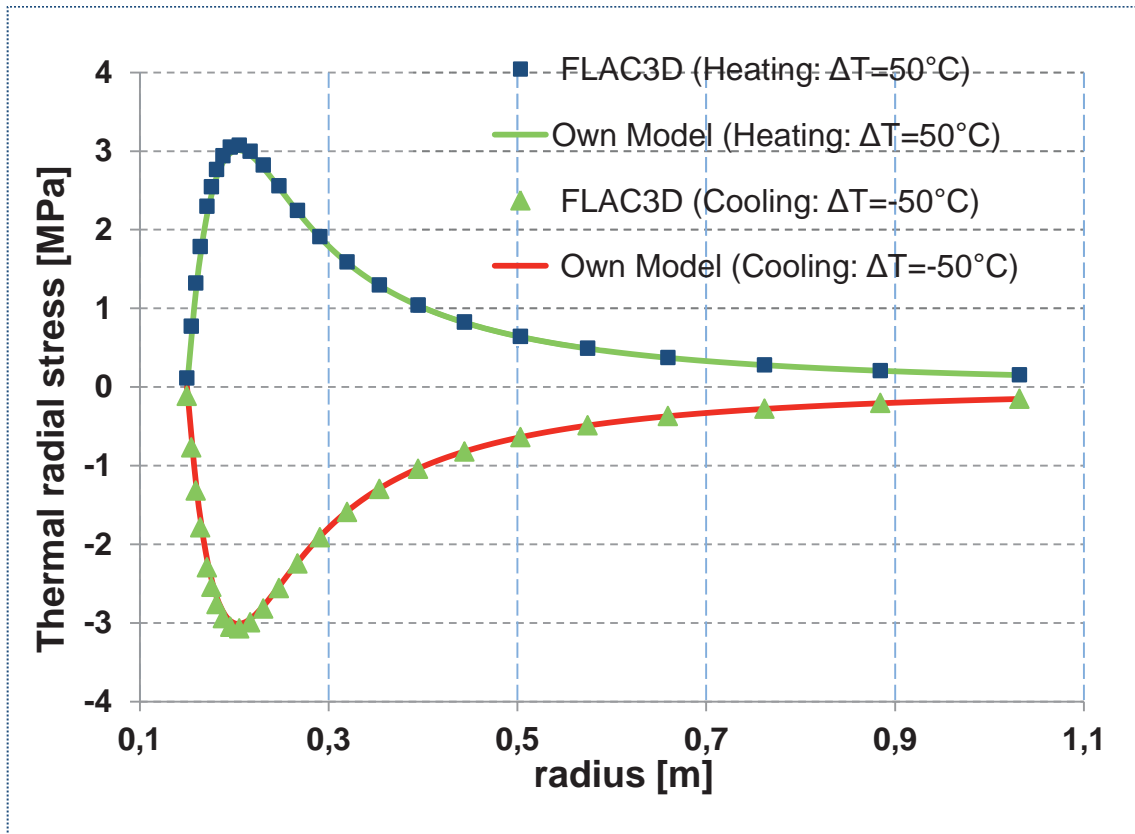
Figure 33: Thermal radial stress distributions in the near field of a borehole at 860 s calculated with FLAC3D and own mode (thermal conduction condition).

Under conduction-advection conditions, the fluid flow influences the temperature distributions. Figures 34 and 35 compare the tangential to the radial thermal stresses calculated using FLAC3D and the models developed in the cause of the project under conduction-advection conditions. The conduction-advection time was one day. The thermal stresses differences between own model and FLAC3D were relatively higher than those under conduction conditions. However, thermal stresses calculated using FLAC3D and the models developed in the cause of the project also show good agreement with each other.
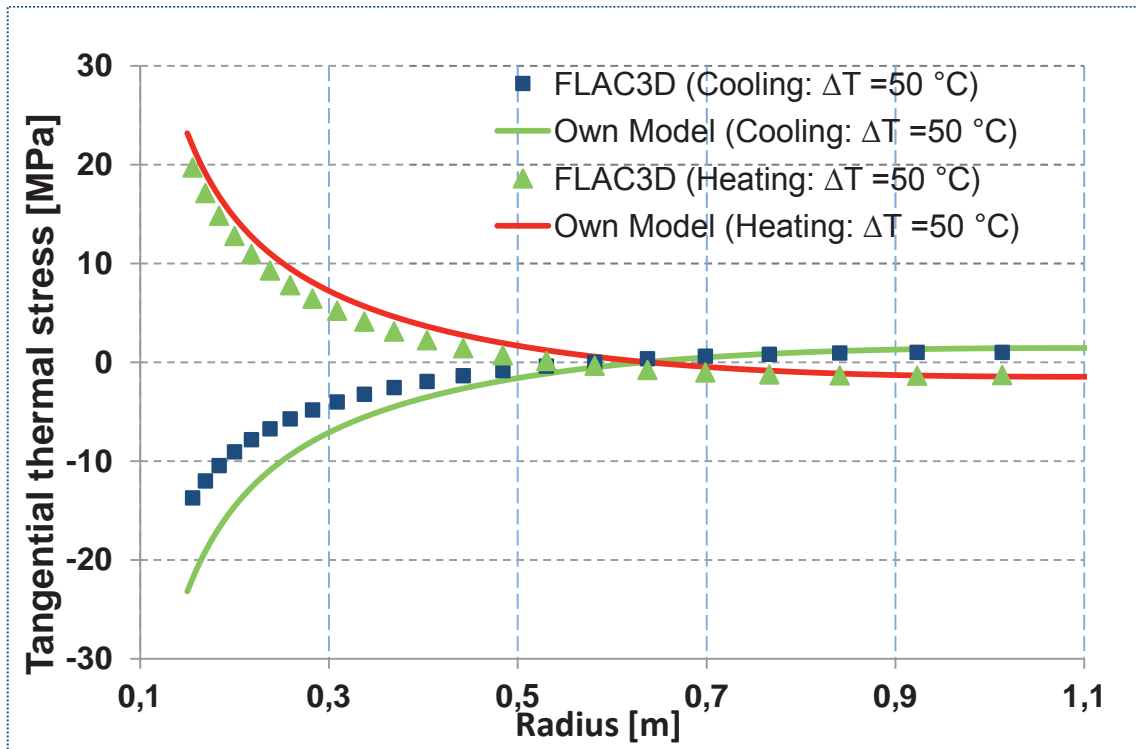
Figure 34: Thermal tangential stress distributions in the near field of a borehole calculated for one day with FLAC3D and own model (thermal conduction-advection condition).
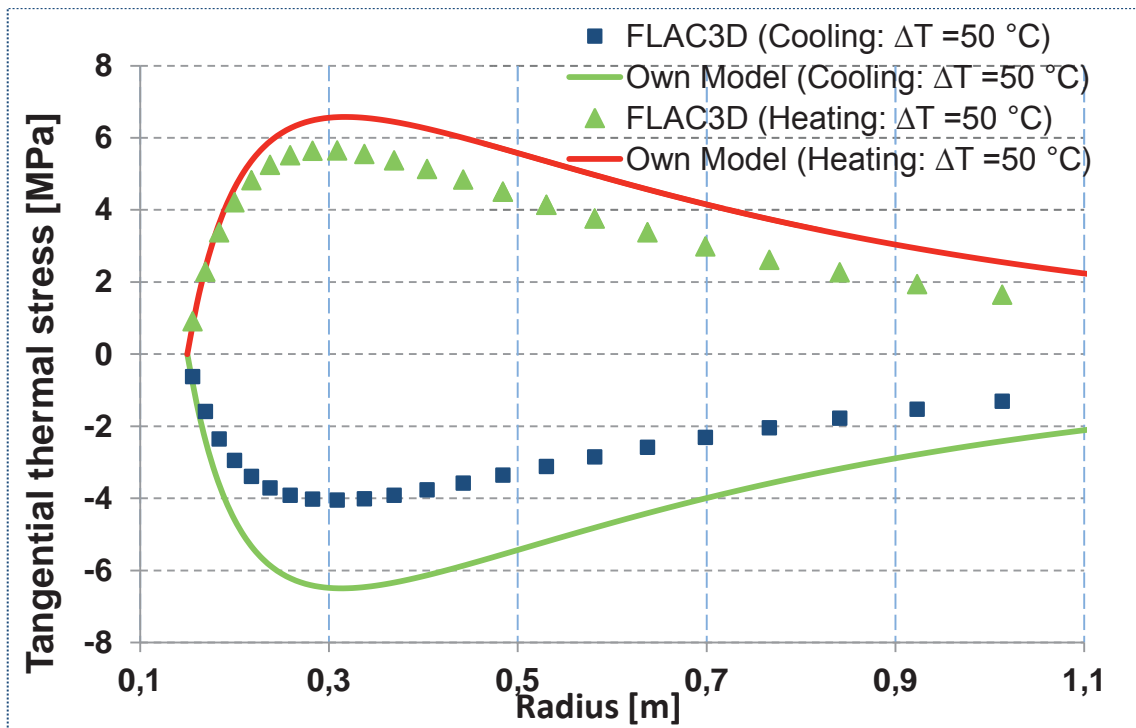
Figure 35: Thermal radial stress distributions in the near field of a borehole calculated for one day with FLAC3D and own model (thermal conduction-advection condition).

Validation of the semi-numeric method to calculate the temperature profile in tubing, annulus and formation

The verification of the own semi-numerical method is difficult, because measuring the mud temperature profile is almost impossible. Therefore, it is also difficult to verify the new developed method by comparison of the calculated mud temperature to the mud temperature profile during circulation. However, the semi-numeric method can be validated by comparing the measured wellbore outlet water temperature to the simulated outlet water temperature. Luo (2015) simulated the production process of a geothermal project with the semi-numerical method and compared to the production data to verify the newly developed method.

The temperature at the top of the Malm was determined based on different temperature logs and measurements of temperature behaviors. 121.7 °C were measured at a true vertical depth (TVD) of 3,002.4 m at the top of the Malm in the Uha GT-1a well on 19.10.2006, and 124.5 °C at 2,977 m TVD on 21.03.2007. The two cases were simulated separately for 20 days.

Figure 36 shows the simulated as well as the measured outlet temperatures from 01.01.2008 to 20.01.2008 for the two cases. Results show an increase in the outlet temperatures over the production time but at a decreasing rate. After 20 days' simulation, the outlet temperatures were nearly constant. Therefore, it could quasi be seen as having attained an equilibrium. The measured outlet temperatures mainly ranged between those of the two field cases. The simulation, reconstructing the real production process, verified the accuracy of the model due to it achieving the original outlet temperature.

Correlation evaluation

Due to missing data an evaluation of the developed correlation by using data from other wells than the Groß Buchholz Gt-1 was impossible.
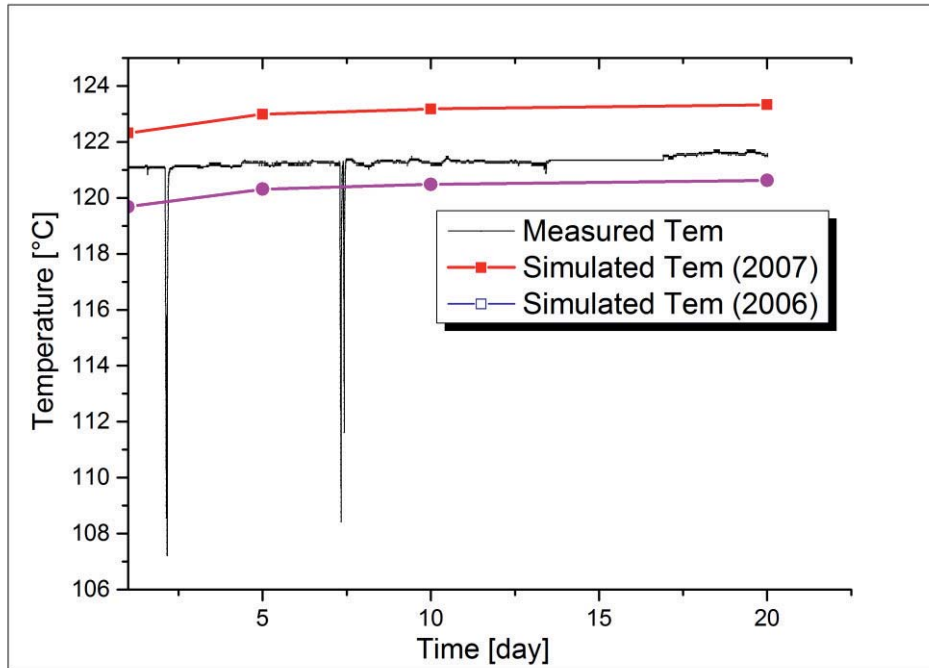
Figure 36: Time dependent simulation of outlet temperature during production process (the year 2006 and 2007 mean the simulation results based on the temperature measured in 2006 and 2007, respectively; Tem: temperature).

2.3 Project Plan

Work packages and milestones	2009	2010	2011	2012	2013	2014
WP1: critical analysis of the evaluation models for borehole stability						
WP2: Analysis of borehole measurement methods						
WP3: Evaluation of the correlations						
WP4: Evaluation of the measuring techniques to determine the parameters						
WP5: Algorithms to evaluate the data quality						
WP6: Further development of the THM coupled evaluation model						
WP7: Validation of the developed evaluation methods and correlations						

Grey: original plan.

Blue: actual plan.

The delay of three months in the project plan was due to the later start of the project.

3   Delineation of the project from other funded projects

No projects are currently being implemented by the Institute of Petroleum Engineering or the Institute for Geophysics at TUC which have any analogies with geothermal energy and/or high performance drilling technology with the content described here. The same applies to LIAG. In addition, no other projects looking at the same issues are known to exist outside of the aforementioned institutes.

4   References

Atkins, P. (1988): *Physikalische Chemie*, VCH.

Belloti, P. & Giacca, D. (1978): *Seismic data can detect overpressures in deep drilling*. Oil and Gas Journal 76, 47-52.

Bowers, G. (2001): *Determining an appropriate pore-pressure estimation strategy*. Annual Offshore Technology Conference 2001.

Bozau, E. (2010): *Bericht G9 - AP-1: Spannbreite geogener hydrogeochemischer Milieus.*

Brown, E.T., Bray, J.W. & Santarelli, F.J. (1989*): Influence of Stress-Dependent Elastic Moduli on Stress and Strains Around Axisymmetric Boreholes.* Rock Mechanics and Rock Engineering 22, 189-203.

Bruce, B. & Bowers, G. (2002): *Pore pressure terminology*. The Leading Edge, Febr., 170-173.

Eaton, B. (1975): *The Equation for Geopressure Prediction from Well Logs*. SPE 5544, 1-5.

Ewy, R.T. (1999): *Wellbore-stability prediction by use of a modified lade criterion*. SPE Drill. & Completion, 14, 2, SPE 56862.

Gardner, G.H.F., Gardner, L.W. & Gregory A.R. (1974): *Formation velocity and density – the diagnostic basics for stratigraphic traps.*

Hou, Z., Pusch, G., Somerville, J. & Hutcheon, R. (2004): *Hydro-mechanical and chemo-mechanical effects on wellbore stability in shale*. Proc. DGMK Conference, Celle, 29-30 April 2004. Hamburg.

Hou, M.Z. & Luo, X. (2011): *Investigation of thermal effect on stability of deep wellbores in low and high permeable formations*. 12th international congress on rock mechanics, Beijing, China, 18-21 Oct. 2011,Taylor & Francis Group, London, 2011-978-0-415-80444-8-1375-1319.

Kirsch, G. (1898): *Die Theorie der Elastizität und die Bedürfnisse der Festigkeitslehre.* Zeitschrift des Vereines deutscher Ingenieure 42, 797–807.

Korte, T., (2004): *Konstruktion einer Fräsvorrichtung zur Bearbeitung von Gesteinsprüfkörpern*. IMW Institutsmitteilungen 29, 21-26, Clausthal.

Luo, X. (2010 a): *Optimization of the Equivalent Drilling Fluid Density in Consideration of Hydro-Mechanical and Chemo-Mechanical Coupling Effects as well as Program Development.* Project thesis at Clausthal University of Technology, May 2010.

Luo, X. (2010 b): *Investigation of Thermal and Chemical Effects on the Wellbore Stability and Development of an Online Program "Real-Time Optimization of the Mud Window".* Master thesis at Clausthal University of Technology, Dec. 2010.

Luo, X. (2015): *Determination of a suitable mud window under HM- and THM-coupled conditions in real-time.* PhD thesis at Clausthal University of Technology, in preparation for June 2015.

Löhken, J. & Schellschmidt, R. (2010): *Forschungsverbund gebo - Geothermie und Hochleistungsbohrtechnik: Projekt G5: Hydromechanisches Verhalten geothermischer Reservoire*, interim report AP1 + AP 2.

Mclellan, P. & Hawkes, C. (2001): *Borehole Stability Analysis for Underbalanced drilling*. J. Canadian Petroleum Technology, 4, No. 5.

Müller, C. (2009): *Charakterisierung des hydromechanischen Verhaltens der Gesteine des Mittleren Buntsandsteins im Hinblick auf eine geothermische Nutzung: Strukturgeologische Geländeaufnahmen, gesteinsmechanische Untersuchungen und numerische Modellierungen*. Dissertation, 143 S., Göttingen.

Pfeifle, T.W., Mellegard, K.D. & Senseny, P.E. (1983): *Preliminary Constitutive Properties for Salt and on salt Rocks from four potential repository sites*, Technical Report, Office of Nuclear Waste Isolation Battelle Memorial Institute, Columbus, OH 43201, ONWI-450.

Reyer D. & Philipp, S.L. (2014): *Empirical relations of rock properties of outcrop and core samples from the Northwest German Basin for geothermal drilling*. Geothermal Energy Science, 2.

Santarelli, F.J. & Brown E.T. (1986): *Analysis of Borehole Stresses Using Pressure-Dependent Linear Elasticity.* Rock Mech. Sci. & Geomech. Abstr. 23, 445-449.

Tang, L. & Luo, P. (1998): *The Effect of the Thermal Stress on Wellbore Stability*. SPE 39505, SPE India Oil and Gas Conference and Exhibition, New Delhi, India, 17-19 Feb., 1998.

Veeken, C.A.M., Walters, J.V., Kenter, C.J. & Davis, D.R. (1989): *Use of plasticity models for predicting borehole stability*. ISRM International Symposium, 30 August - 2 September, Pau, France.

Yu, Y., Lin, T., Xie, H., Guan, Y. & Li, K. (2009): *Prediction of Wellbore Temperature Profiles During Heavy Oil Production Assisted with Light Oil*. SPE 119526, SPE Production and Operations Symposium, Oklahoma City, USA, 4-8 April 2009.

Zhou, S. (1994): *A program to model the initial shape and extent of borehole breakout*. Computers & Geosciences, 20, 7/8, 1143-1160.

Zimmer, U., (1993): *In-situ-Bestimmung der Dämpfung seismischer Wellen in Salzgestein*. Diplomarbeit, TU Clausthal.

Zimmer, U. (2000): *Quantitative Untersuchung zur Mikrorissigkeit aus akustischen Gesteins-eigenschaften am Beispiel von Steinsalz und Anhydrit*. Dissertation, 189 S., Berlin.

5   Publications, reports and presentations of B4 project

Chen, Y. (2010): *Analytische und empirische Modelle zur Ermittlung und Bewertung der Bohrgeschwindigkeit*. Bachelor-Arbeit, Institut für Erdöl- und Erdgastechnik an der TU Clausthal.

Hou, M.Z. & Luo, X. (2011): *Investigation of thermal effect on stability of deep wellbores in low and high permeable formations*. 12th international congress on rock mechanics, Beijing, China, 18-21 Oct. 2011,Taylor & Francis Group, London, 2011-978-0-415-80444-8-1375-1319.

Hou, M.,Z., Wonik, T., Luo, X. & Vogt, E. (2011): *Investigation of thermal effect on stability of deep wellbores with parameters from borehole logs*. Presented at GeoEnergy/gebo Conference Celle Drilling 2011 in Celle, Niedersachsen, Germany, September 12-13, 2011.

Luo, X. (2010 a): *Optimization of the Equivalent Drilling Fluid Density in Consideration of Hydro-Mechanical and Chemo-Mechanical Coupling Effects as well as Program Development*. Project Thesis, Institute of Petroleum Engineering at TU Clausthal.

Luo, X. (2010 b): *Investigation of Thermal and Chemical Effects on the Wellbore Stability and Development of an Online Program "Real-Time Optimization of the Mud Window"*. Master Thesis at Clausthal University of Technology, Dec. 2010.

Luo, X., Vogt, E., Hou, Z., Wonik, T. & Zhou, Lei (2014): *Real-time calculation of suitable mud window using the logging data while drilling.* Presented at Celle Drilling 2014 in Celle, Niedersachsen, Germany, September 15-16, 2014.

Luo, X. (2015): *Determination of a suitable mud window under HM- and THM-coupled conditions in real-time.* PhD thesis at Clausthal University of Technology, in preparation for June 2015.

Mustafayev, N. (2010): *Analytical and Empirical Models to Calculate and Evaluate the Rate of Penetration and its Influence Parameters.* Advanced Drilling & Production Topics, Institute of Petroleum Engineering at TU Clausthal.

Vogt, E. & Wonik, T. (2011): *Der Porendruck – ein bedeutender Parameter für die Bohrloch-stabilität und die Schwierigkeiten seiner Bestimmung im Norddeutschen Becken*, Jahrestagung der DGG 21.02.-24.02.2011, Köln.

Vogt, E. & Wonik, T. (2011): *Application of Geo-Parameters for Borehole Stability Modeling from LWD-Measurements in the North German Basin,* EGPD 01.03.-04.03.2011, Reykjavik, Iceland.

Vogt, E., Reyer, D., Schulze, K.C., Bartetzko, A. & Wonik, T. (2012): Modeling of geo-mechanical parameters required for safe drilling of geothermal wells in the North German Basin, Celle Drilling, 17.-18.09.2012.

B5: Assurance of efficient drill cuttings transport

1. Overview of the project

Speaker and lead university or research institution

Pro-ject-nr.	Project Title	Subject of research	Project Leader, institution
B5	Assurance of efficient drill cuttings transport	Drilling technique, Mechanics	Prof. Dr.-Ing. habil. Gunther Brenner, TUC (ITM) Prof. Dr.-Ing. Kurt M. Reinicke TUC (ITE)

Participating institutes and institutions of the University and external institutions in:

- Institut für Erdöl-/Erdgasgewinnung und Erdgasversorgung (ITE), TU Clausthal
- Institut für Technische Mechanik (ITM), TU Clausthal
- Baker Hughes Contact, Celle, Dipl. Ing. R. May

List all participating scientists:

Name	Subject area	Institution or non-university institution	Financing with funds provided for the applica-tion? (X)
Prof. Dr.-Ing. K. M. Reinicke	Petroleum Engineering	ITE	
Prof. Dr.-Ing. habil. G. Brenner	Mechanical Engineering	ITM	
Dr. Dr.-Ing. C. Teodoriu	Petroleum Engineering	ITE	
Dipl.-Ing. T. Dahl	Petroleum Engineering	BHI	
Dipl.-Ing. R. May	Petroleum Engineering	BHI	
Dipl.-Ing. R. Aragall	Mechanical Engineering	ITM	X
Dr. rer. nat. M. J. Weichmann	Petroleum Engineering, Geology	ITE	X

1.2. Research Program

1.2.1. Summary & content classification of the project in the overall project and networking

The economic and technological evaluation and optimization of the drilling process (Projects B1 and B2) needs reliable models for the description of the entire system including the drill string, drill bit and drill fluid, in order to quantify the potential of process variations and operating procedures. This is the background of the present project, where the focus is on the analysis of the hydrodynamics of the entire drilling system and the efficient and reliable drill cuttings transport. This requires an improvement of the description of multiphase flow phenomena during the drilling process. Furthermore, precise definitions of the relevant parameters, constraints and objective functions have to be formulated, which allow the quantification of the cuttings transport.

437

The work in the present project (B5) is based on interactions with other projects in GEBO as follows: Geometric and operational parameters of the system are obtained in the projects B1. External parameters for the characterization of the confining rock (temperature, porosity) are considered in B4. For a detailed characterization of the dispersed phase (cuttings) transport, input from project B6 is required. As a result of the present study, the influence of drilling fluid on the damping of vibrations of the drill string (B7) shall be quantified. Finally, the results of the present study will enter into the drilling simulator developed in B2.

1.2.2. Work packages executed relative to (original) plan and results achieved

Because of the close cooperation between the two institutes in this project, we decide not to split this report in two independent packages. Instead we presented the work flow according to the original work packages.

AP 1 - Hydrodynamic characterization

<u>Fluid flow phenomena</u>

In AP 1, the various hydrodynamic phenomena found in the well bore during drilling are defined. Cuttings transport takes place in the annular space between the drill string and the wellbore wall. This space may be concentric or eccentric. Drill cuttings transportation is an area of multiphase fluid engineering accompanying solid particles and a liquid fluid. A remarkable characteristic of such multiphase flows is the ability to form different flow patterns which cannot be represented in a closed analytical model. Thus, specific solutions for the various flow patterns are usually considered. In the present problem gravity plays a major role and therefore, the flow patterns are classified based on the inclination of the well bore. For high angles (60°-90°) or horizontal wells, transport of the particles is dominated by a rolling mechanism; at intermediate angles (30°-60°), transport takes place via a lifting mechanism and in near-vertical wells (0°-30°), particle settling determines transport. [Aragall et al., 2010a].

For the vertical case, a reliable model is required to describe the cuttings superficial velocity (cuttings volumetric flux) or, more generally, the magnitude of the interaction force on each particle due by the fluid as a function of physical parameters such as cutting properties (size, density, shape, degree of hydrophobicity and wettability) of the particle surface (contact angle, Θ), cuttings volume fraction, fluid properties (density, viscosity), fluid volumetric flux or "superficial velocity", annular geometry and drill string rotation. Unfortunately, at the present time such a general theory is restricted to extreme hydrodynamic conditions (such as low Reynolds numbers and low solid concentrations) of limited practical interest; instead a variety of empirical or semi-empirical models have been suggested which, in the majority of cases, adapt the existing theories for limiting or simpler situations to more general use with help of some empirical corrections [Di Felice, 1995].

Efficiency and cost evaluation

Due to the different phenomena originated by gravity, also efficiency parameters need to be divided between those used for vertical well bores and those for deviated and horizontal wellbores. In the case of vertical wellbores, a widely used indicator to evaluate the carrying capacity of the drilling fluid is the cuttings transport ratio

$$F_T = 1 - \frac{v_s}{v_f},$$

1.1

where v_s is the settling velocity of the cuttings and v_f is the average fluid velocity. The settling velocity is difficult to define because of various unknowns such as the shear rate distribution around the particle, particle shape and size distribution, particle concentration etc. With reference to deviated and horizontal wellbores the previous parameter is not representative and according to Luo [Luo, 1988] a critical circulating rate to avoid the formation of a cuttings bed is recommended. Furthermore, previous investigators have defined the most relevant variables and divided them as follows:

1. Controllable variables: annular fluid velocity, fluid flow regimes, rheological properties and densities of drilling fluids, hole angles, drill pipe rotary speed, penetration rate (cuttings mass rate) and the annular size.

2. Uncontrollable variables: cuttings sizes, shapes and densities, sometimes the annular size and annular geometry.

Dimensional analysis suggests the following non dimensional groups:

$$\Pi_1 = \frac{d_{hole}}{d_{string}}$$

1.2.

$$\Pi_2 = \frac{d_{hole}}{(d_{hole} - d_{string})}$$

1.3.

$$\Pi_3 = \frac{U(d_{hole} - d_{string})\rho_f}{\mu} = \mathrm{Re}$$

1.4.

$$\Pi_4 = \frac{u_p}{U}$$

1.5.

$$\Pi_5 = \frac{\rho_s - \rho_f}{\rho_f}$$

1.6.

$$\Pi_6 = \frac{(d_{hole} - d_{string})^3 \rho^2 g}{\mu^2} = Ga$$

1.7.

d_{hole} = openhole diameter	d_{string} = diameter of the string
U = average mixture velocity	ρ_f = density of the fluid
ρ_s = density of the solid	μ = viscosity
u_p = settling velocity of solid particles	g = gravity
Re = Reynolds number	Ga = Galileo number

In the following table, approximate values of the most important variables representative for the GEBO well-bores are shown:

Table 1: Field parameters for gebo

Parameter	Field Conditions
d_{hole} (mm)	220 - 300
d_{string} (mm)	115 - 150
d_{string} / d_{hole}	0.41 – 0.50 – 0.52 – 0.63
$(d_{hole} - d_{string})/ d_{hole}$	0.36 – 0.47 – 0.49 – 0.58
α (°)	0 - 90
Q (m^3/h)	24 – 150
U (m/s)	0.3 – 0.8
ρ_f (kg/l)	1 – 1.14
ρ_s (kg/l)	~ 2.5 (variable)
dp (mm)	1 – 10
C (% by volume)	0.8 – 5
μ	water and bentonite
$\dot{\gamma}$ = $12U/(d_{hole}-d_{string})$ (s^{-1})	20 – 120

α = wellbore angle Q = flow rate

d_p = particle diameter C = cuttings concentration

$\dot{\gamma}$ = shear rate

In general it is observed, that sufficiently high flow rates will always transport the generated cuttings out of the well bore. However, technically this flow rate is limited by the pumps used in the field because of the pressure losses along the well bore. Particularly at the bit jet nozzles, which help to clean the workface of the well bore and allow higher rates of penetration, the pressure losses may reach unacceptable values and jeopardize an efficient cuttings transport. Therefore, the flow rate and the rate of penetration should be used as the main parameters for optimization.

1. Optimization parameters:
   - Minimal velocities and critical points in relation to hole cleaning.
   - ROP – Bit performance
2. Boundary conditions:
   - Pressure – ECD – Pore pressure – Fracture pressure
   - Pressure loss
   - Maximal flow rate
   - Maximal pump pressure

Models

Currently used models:

1. The pressure loss models are based on standard pressure loss equations, with some enhancements. The results produced by the models are within about 15-20 % of those

440

obtained from field tests. The models use either PV (plastic viscosity), YP (yield point) and 10 s gel strength or the full Fann rheology data set as rheological input.

2. Cuttings transport models → the theoretical grounds of the models is the BBO (Basset-Boussinesq-Oseen) equation, which considers all the forces acting on a particle. Two different models are used in BHI in order to calculate the minimal transport velocity.

- Mechanistic models: the models are based on the mechanistic models from Clark and Bickham [Clark and Bickham, 1994]. These models were derived to predict the minimum flow rate required to remove all the cuttings. The models differentiate three important phenomena, which are basically influenced by the well bore angle and the flow rate.

- Empirical models: the models are based on the work from Luo [Luo, 1988]

- Difficulties:
  a) The drag force needs to be well defined.
  b) Velocity profiles are difficult to find for complicated geometries and cases (e.g. eccentric drill pipe rotation).
  c) Determination of transitions between models.
  d) Plastic force in order to describe fluids with gel properties.
  e) Contact angle of the particles → granular technology
  f) The models are only able to forecast the beginning of the movement.
  g) There are no publications on lift coefficients for none spherical particles.
  h) There are no drag coefficients for particles in non-Newtonian moving fluids.
  i) Hydraulic diameter is not always a good parameter to classify cases.

Further information on these models can be found in the first *Milestone Report* [Aragall et al., 2010b]. The output of the currently used models and further implementations from BHI is the following:

1. Total System pressure loss.
2. Maximum and minimum allowable flow rates for the given hole and drill string configurations.
3. Annular velocities.
4. Hydraulic power and specific impact force at the bit.
5. Equivalent circulating density (ECD).
6. Flow rate required for hole cleaning.
7. Mud temperature profile while circulating.
8. Mud density and rheology as a function of pressure and temperature.
9. Total cuttings concentration [%] (cuttings transported + cuttings not moving).
10. Transported cuttings [%] (cuttings flow rate / (cuttings flow rate + liquid flow rate)).

11. Flow area [%]

12. Bed Height [%].

Necessary improvements:

1. Current cuttings transport models are based on a steady-state approximation. Models able to consider the transient nature of the cuttings transport problem, including the effects of the thermal gradient and time on the rheological properties of the drilling fluid, should be developed.

2. For vertical drilling, the cuttings concentrations are still considered as uniformly distributed. Analyses of the concentrations as a function of wellbore geometry, mud properties, cuttings properties and operating conditions are necessary.

3. For vertical drilling, only settling velocities for quiescent non-Newtonian fluids are known. It is recommended to investigate the settling velocities for non-Newtonian shear flows.

4. For horizontal drilling, a mechanistic relationship including both rotation and inclination has not yet been published.

5. Clark and Bickham need to be validated with experimental data in relation to drag and lift coefficients for particles in non-Newtonian fluids.

6. Calculation of velocity profile and pressure drop for non-Newtonian models need to be validated with experimental data.

7. Turbulence transition is crucial for selecting the appropriate pressure loss correlations. The effect of eccentricity and rotation on the turbulent transition of non-Newtonian fluids requires further investigation.

AP 2 - Rheological characterization

Drilling muds

Water based muds are considered as an environmental friendly option. For this reason they are considered for the GEBO project. Moreover, water base muds present lower costs and relatively well known capabilities and properties. According to project B1 it has been decided to use the standard drilling method for the vertical part of the wellbore and coil tubing for the horizontal part.

1. Standard drilling;
   - An important difference between both drilling methods is related to stops during operation. Standard drilling methods needs to stop every time a new stack (pipe section) is introduced. Hence, drilling fluids with gel properties are necessary. In order to fulfill this requirement bentonite is normally used. In addition, bentonite offers good capabilities for the cleaning of the wellbore.

2. Coil tubing:
   - None or slow rotating drilling pipe complicates horizontal cuttings transport.

- Higher pressure losses inside the drill pipe due to smaller diameters.
- Less stops and therefore gelling properties are not necessary.

The selection of a drilling fluid is dependent on several parameters: (1) cuttings density, size and shape, (2) well bore inclination, (3) maximal flow rate and (4) temperature profile. Such parameters can only be defined when detailed design of the well and accurate knowledge of the geologic formation are available. The envisaged time period to carry out this *work package* was the last quarter of 2009 and the first quarter of 2010. At that time, the required information to propose the drilling fluid was still under investigation and was the result of project B1 [ITE, 2013a and 2013b] in 2013. Therefore, data from water based drilling fluids employed in the drilling of previous deep HP-HT geothermal wells was used to characterize the rheology. On Figure 1 the shear viscosity vs. shear rate and shear stress vs. shear rate measurements for a Geothermal Drilling Mud are shown. On Table 2 and Table 3 the fitted parameters for the Power-Law and Herschel-Bulkley rheological models are respectively shown for the fluid.

Table 2: Power-Law parameters for exemplary Geothermal Drilling Mud

Sample	Consistency index K (Pa·s^n)	Power law exponent n	r	Temperature (°C)
Stirred 30'	0.633	0.633	0.996	48.8
Aged 16hr	0.686	0.535	1.000	48.8

Table 3: Herschel-Bulkley parameters for exemplary Geothermal Drilling Mud

Sample	Yield Stress (Pa)	Consistency index K (Pa·s^n)	Power law exponent n	r	Temperature (°C)
Stirred 30'	3.24	0.278	0.745	0.999	48.8
Aged 16hr	3.80	0.110	0.785	0.998	48.8

Additional data for different samples of a drilling fluid used under high temperature conditions are shown in Table 4. In this case only the fitted parameters for the Bingham rheological model were directly available, whereas no field readings were obtained.

Table 4: Bingham parameters for high temperature drilling fluid

Sample	Yield Stress (Pa)	Plastic Viscosity (Pa·s)	Temperature (°C)
HTDF1	9.55	0.020	48.8
HTDF2	8.11	0.017	48.8
HTDF2	9.07	0.019	48.8
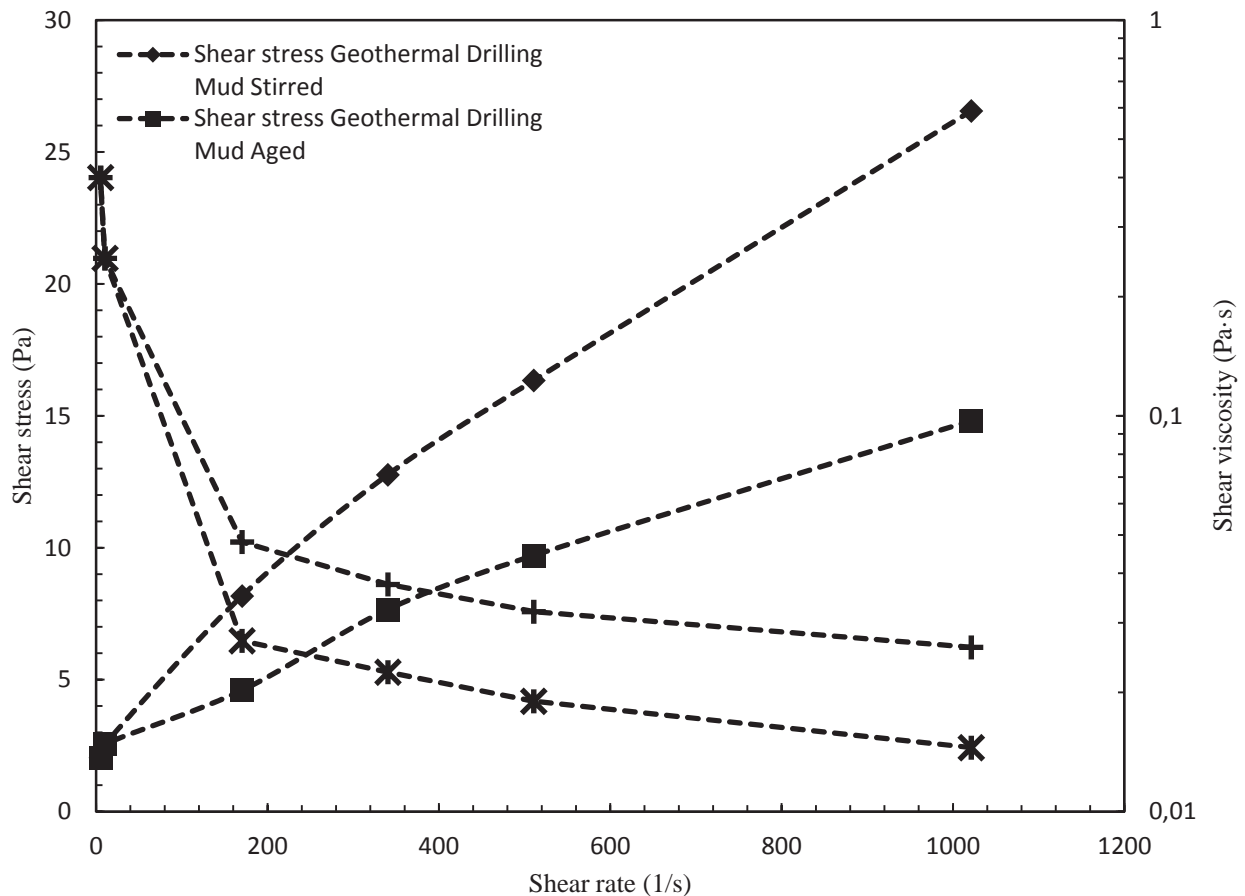
Figure 1: Shear viscosity vs. shear rate and shear stress vs. shear rate measurements for an exemplary Geothermal Drilling Mud: Stirred 30' on Multimixer + rolled 16 hr at 65 °C and Aged 16 hr at 260 °C

Cuttings

During cuttings characterization a major difficulty was the finding of cuttings generated at wellbores located in the North German region. Samples of cuttings were found for a wellbore named Breitenreiter. The same came from depths between 3260 and 3914 meters. Particle size analysis was performed at the Institute of Particle Technology of the TU Clausthal. Figure 2 to Figure 5 show the particle size distributions (PSD) data obtained for cuttings at several depths. The modes, medians and means of the PSD are shown in Table 5. In general, wide monomodal particle distributions with mean particle size around 2000 µm were obtained. The passage peak observed at particle size 0 µm belongs to cuttings smaller than the 250 µm sieve,

444

which was the smallest used in the experiments. Therefore, is not considered as a second mode. The maximum particle size measured was around 3500 µm. Furthermore, it was observed how the particle shapes are far from being spherical. The way to characterize this deviation from sphericity needs to be adapted to its definitions in the available settling velocity correlations. Finally, it was also observed that coarse particles were sometimes formed by agglomerated fine particles.

Additionally, a report on cuttings generated at hard-rock formations in well-bores constructed in USA was used to characterize the cuttings [TerraTek, 2008]. The report gives information on the cutting sizes found at several locations where deep drilling through hard-rock formations with diamond drill bits was performed. Rock types drilled were Crab Orchard sandstone, Carthage marble and Mancos shale. Drill bits investigated were M333-7-blade PDC, 737-tungsten carbide insert roller cone, M841-diamond impregnated, M121-four –bladed PDC and M233-four-bladed PDC. Percentiles D10, D50, D90 were given to characterize the particle size distributions. Percentile D50 shows values between 2.8 and 12.5 mm, whereas these are dependent on the rock types and the drill bits used. Maximum particle sizes up to 26 mm diameter were also reported.
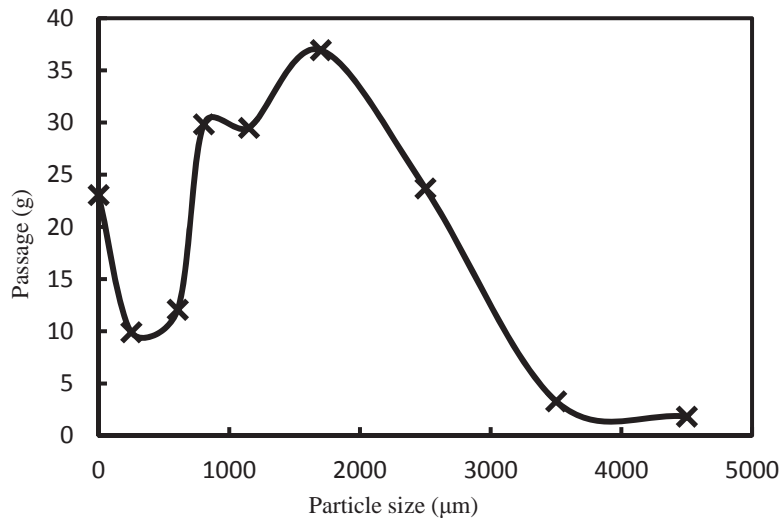
Figure 2: Breitenreiter cuttings at 3260 meters

445
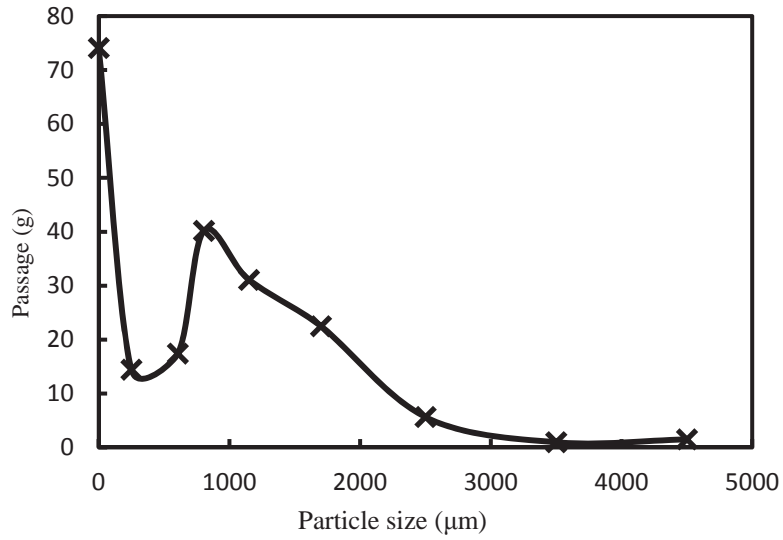
Figure 3: Breitenreiter cuttings at 3890 meters
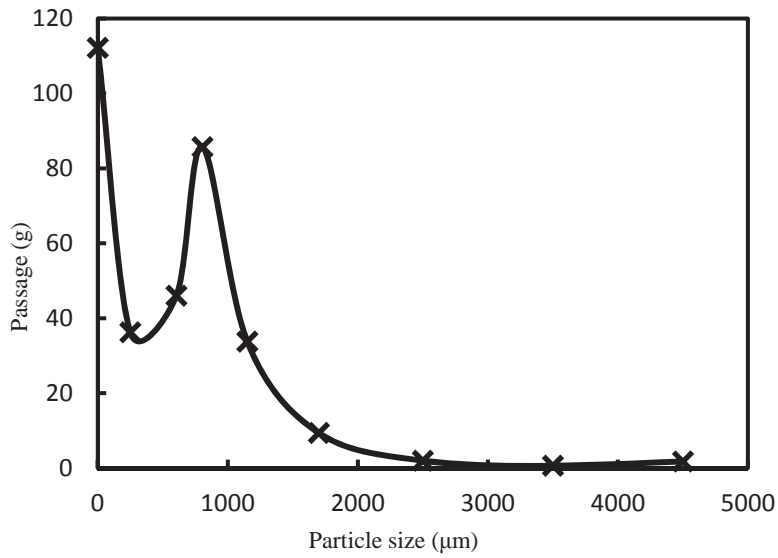
Figure 4: Breitenreiter cuttings at 3905 meters

446
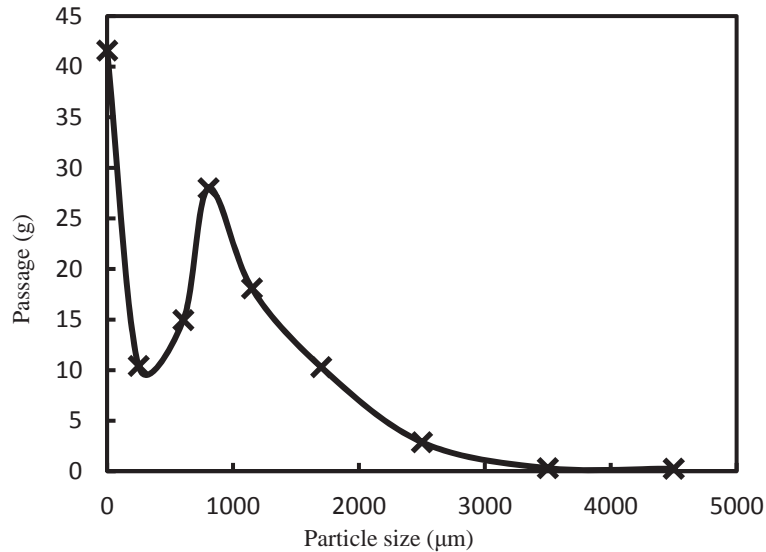
Figure 5: Breitenreiter cuttings at 3914 meters

Table 5: Statistical parameters of the cuttings from Breitenreiter

Depth (m)	Mode (µm)	Median-D50 (µm)	Mean (µm)
3260	1700	1050	2330
3890	805	700	2074
3905	805	600	1840
3914	805	680	1700

Conclusions

One of the conclusions of this *work package* was the difficulty in characterizing the rheology for geothermal wellbores without knowing the exact location of the well and the construction design. This information is crucial because very changing conditions may be found in wells close to each other and significantly different rheologies are needed to deal with different geologic conditions, as well as operating conditions as inclination or rotation. Consequently, it is recommended to precisely characterize the geologic formation and the well bore plan in order to select the drilling fluid compositions. Such information was supplied by project B1, but was not available before 2013, much later than the previewed period of time envisaged for this *work package*. For this reason, it was decided to characterize the rheology approximately by taking drilling fluids pumped in the drilling of geothermal wells. With respect to cuttings, only one sample was found for the North German region, which proved the difficulty in having access to data directly coming from the well. Information from this sample and from a report on drilled hard-rock formations in USA revealed the coarse nature of the cuttings found in hard-rock formations with mean particle diameters between 2 and 5 mm. Furthermore, the particle size distributions

447

showed monomodal character with rather wide size variations. In addition, maximal particle sizes reached values up to 26 mm.

AP 3 - Adaptation and test of the measuring technique

<u>Flow loop characteristics</u>

Multiphase-Simulation is applied in order to test mud techniques by exercising exemplary testing of circulation processes in two-phase flow of a fluid-solid-mixture. The objective is to simulate the flow simulation at low temperatures and low pressures in order to validate models derived from B5 itself and e.g. the associated project B6. The design of the Multiphase-Simulator refers to the analysis of liquid, solids and gas flows. The investigations can be performed at ambient temperature under atmospheric (i.e. up to 5 bar) pressure conditions. The unit is about 6.5 m in length and can be used in vertical, horizontal or any intermediate position. The flow loop shown in Figure 6 was designed, installed and operated by ITE.

The functional principle (Figure 7) can be divided into three main parts:

- <u>Supply Loop</u> with feed-in of fluid, solids and gas, test section, gas-slurry mixer and return flow driven by a pump (power: 11 KW, 2900 U/min, flow rate: 6-24 m³/h)

- <u>Supply and Test Range</u>: pre-test and test section with flow control (pressure measurement in entry section, test section and outflow section, differential pressure measurement in front of and inside test section) and high speed image capturing

- <u>Data Recording</u>: data acquisition section
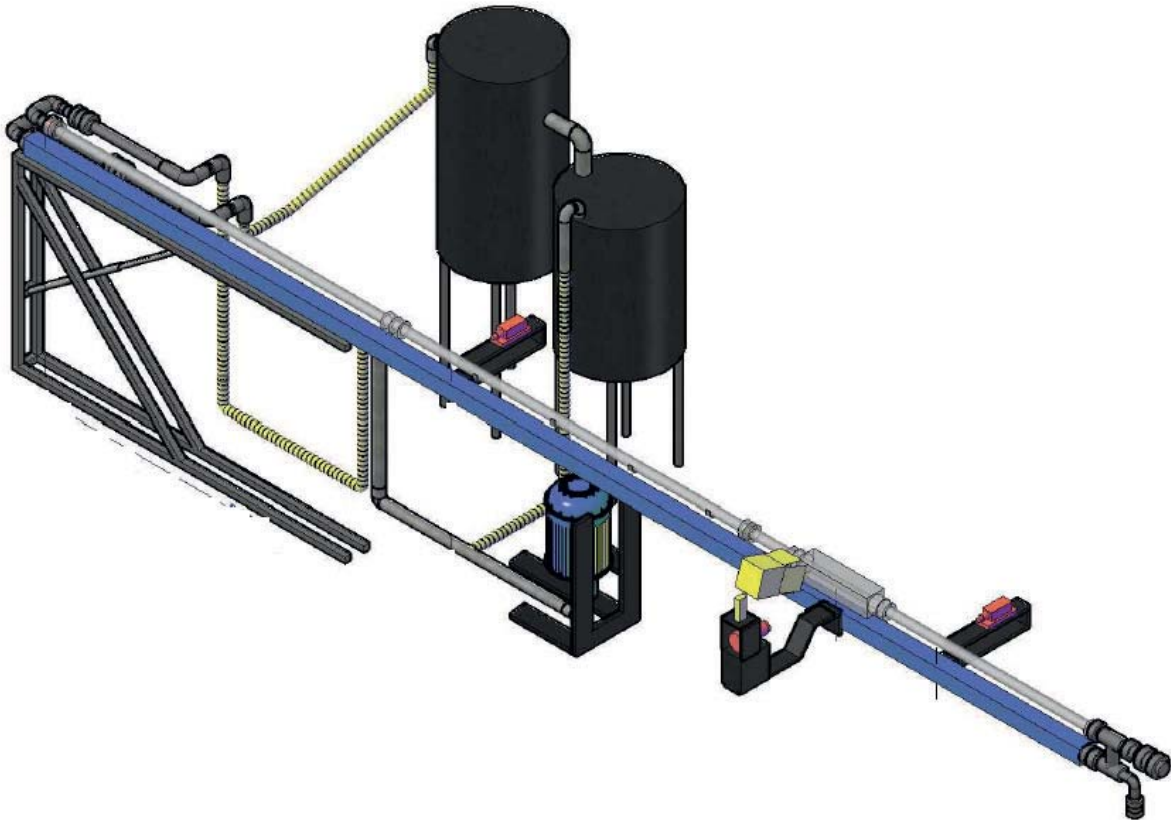
Figure 6: Flow loop at ITE
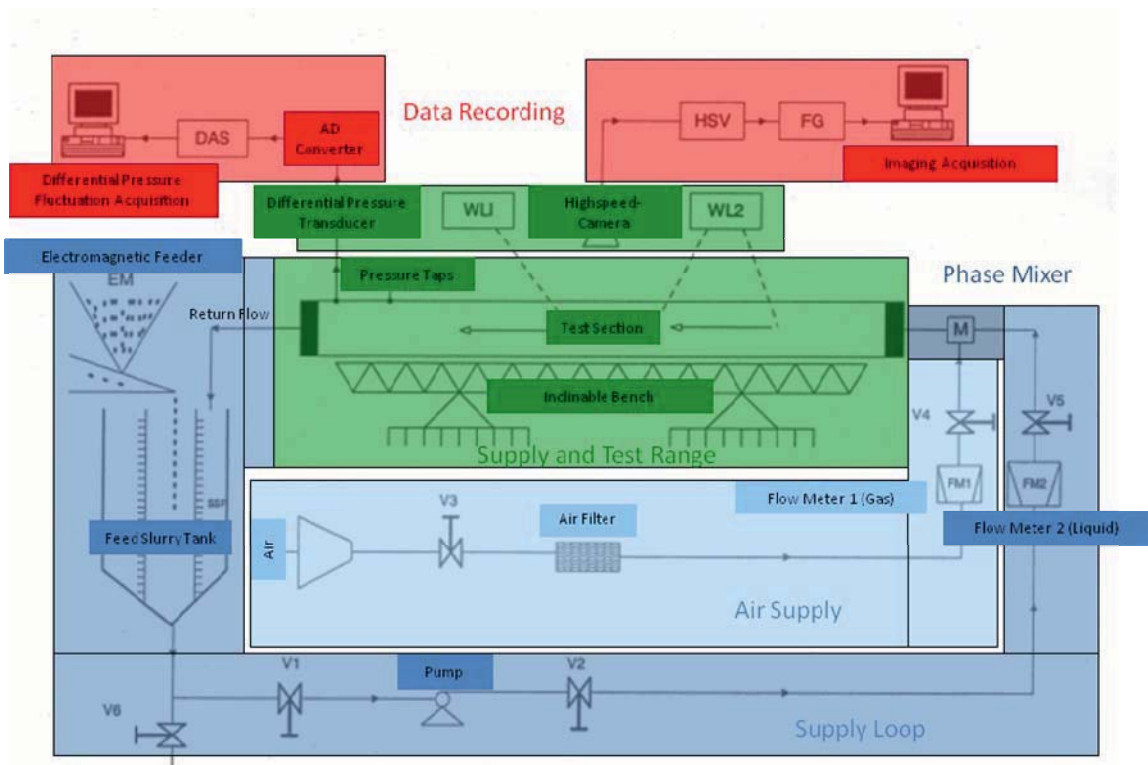
Figure 7: Functional principle of the Multiphase-Simulator (Legend: SSF: Sand Screen Filter; V1/2: Slurry Valve 1/2; V3/4/5: Gas Valve 1/2/3; V6: Discharge Valve; M: Phase Mixer = Gas-Slurry Mixer; WL1/2: White Light Il-lumination 1/2; DAS: Data Acquisition System; HSV: High Speed Video System; FG: Frame Grabber)

449

Water, respectively another fluid phase, is inserted into the system through a gas-liquid-solid separator which is supplied with the fluid by the centrifugal slurry pump from a 0.4 m^3 stainless steel slurry tank. The flow proceeds through a 25 mm ID (inner diameter) pipe of stainless steel. The flow rate is measured by means of an electromagnetic induction flow meter and controlled by the rotational speed of the centrifugal pump.

The actual test section consists of a transparent straight Plexiglas-pipe, constructed of an accurately flanged, 2-m long, interchangeable section with a length to diameter ratio of 150 and an internal diameter of 0.04 m. It is mounted by precision supports on the inclinable bench, consisting of a carbon steel beam, which is supported by a pivoting foot and a stationary foot that incorporates a hydraulic screw-jack.

The storage hopper of the solid phase is connected directly to the Loop: the particles are inserted into the tank by an electromagnetic solid feeder and thereafter in combination with the fluid supplied to the test section by the centrifugal pump. The particle loading is controlled by the vibration frequency of the electromagnetic feeder.

Pressure control of the liquid-solid flow is performed by using pressure taps at 3 meters from the entrance into the test section. A pressure transducer with an averaged resolution of 1 Pa is used to measure the local pressure losses between the pressure taps. All measurements are performed before, during and after the flow of the solid-liquid mixture. After having passed the test section the liquid-solid mixture flows into a three-phase separator where solids are separated to the solid tank using a sand screen while the fluid flows back into the system for cycling utilization through a return flow line. Bed height, average volume fraction and characteristic flow regime are measured using a high speed CCD camera. The camera is used to record the video of each experiment during 5 seconds. The pump is stopped when all solid particles have reached the separating container. The transported cuttings are removed from the receiving container by using a sieve and put to dry. Finally, the same are weighted and recycled for later experiments.

PIV measuring Technique

A flow loop was designed and installed at the Institute of Applied Mechanics at the TU-Clausthal, see [Burkhart, 2010]. This setup was designed in order to test and qualify the PIV and visualization technique for multiphase flows under laboratory conditions. In a later stage of the project, the equipment should have been installed at the multi-phase simulator at ITE. In the experiments, water was used as the continuous phase and particles of aluminum oxide where used as the dispersed phase.

The results showed, that the technique allows determining the fluid and particle velocity in a cylindrical tube separately. It also showed that further developments were necessary to improve the accuracy and robustness of the method. Subsequently, a method was employed to measure velocity profiles of the particles and of the fluid that are recorded in the same image pair. This

450

method is based on developments of Lindken and Merzkirch [Lindken and Merzkirch, 2002] and it is a combination of the three most commonly used PIV techniques for monitoring of multi-phase flows: fluorescent tracer particles, shadowgraphy and the digital phase separation by means of masking techniques. The phase separation is based on image processing in order to create appropriate masks to be applied later on the original images. Thereafter, the PIV algorithm is capable to determine the fluid velocities at the positions which are not occupied by the particles. Later, the same masks are used in conjunction with a particle tracking velocimetry (PTV) algorithm and thus provide the discrete particle velocities. The final superposition of both velocity fields supplies the multi-phase velocity field. The whole process was realized using the software "edpiv" (by Gui [Gui, 1997, Lindken, 1998, 1999]).

Problems occurred due to light reflections on the pipe walls, which led to over-exposure close to those zones. This suggested focusing more on a better matching of refractive indexes of the fluid and the confining enclosures. It was therefore intended to work with liquids that had a similar refractive index as the material used for the pipes. Since the refractive index of glass and Plexiglas is fixed (n=1.49), a matching had to be realized by employing special liquids with similar refractive index as glass. At the same time, these fluids should have rheological properties similar to the ones found in drilling fluids. In the frame of the *Master Thesis* by Kumar [Kumar, 2011] between 01.09.2010 and 31.05.2011 medicinal white oil (Ondina 927) was tested as a fluid with very similar refractive index properties (n=1.47 at 20 °C) in a newly developed vertical flow loop at ITM shown in Figure 8. Although this fluid shows Newtonian rheology, it was intended to use it as a base and thereafter mix additives to obtain rheological properties similar to those of the drilling fluids. These tests were very successful in the sense that virtually no reflections were created at the walls and fluid parabolic velocity profiles were completely acquired. First validation of the measuring technique is shown in Figure 9 where a very good agreement can be seen.

Tests with Ondina 927 and glass particles demonstrated the suitability of using such suspensions for the study of multiphase flows. The good optical properties of the borosilicate glass particles, coming from its refractive index (n=1.49), would allow the study volumetric concentrations close to those found in the drilling operations (5%). Since the combination of the physical properties of Ondina 927 and glass supplied similar settling velocities and shear rates to the ones found in drilling, it was decided to start a parallel measuring campaign concentrated on the generation of vertical transport experimental data for comparison with numerical models. These experiments were performed in the flow loop developed at ITM, where the conditions of the laboratory allowed an uncomplicated operation of the laser light source necessary for the PIV measurements, and are shown in section AP4 of this report.
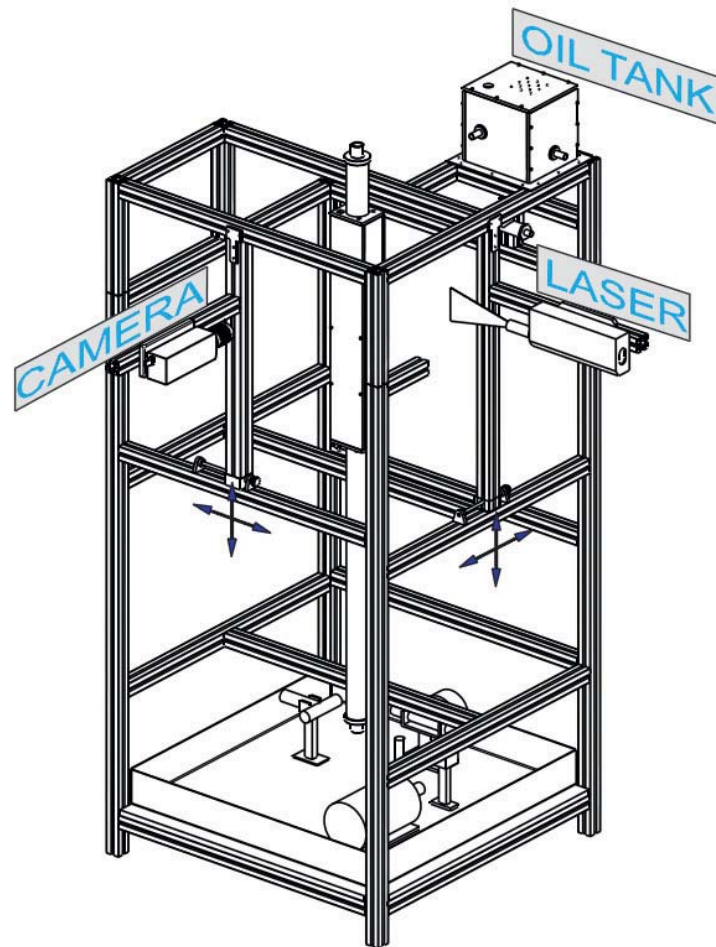
Figure 8: Flow loop at ITM
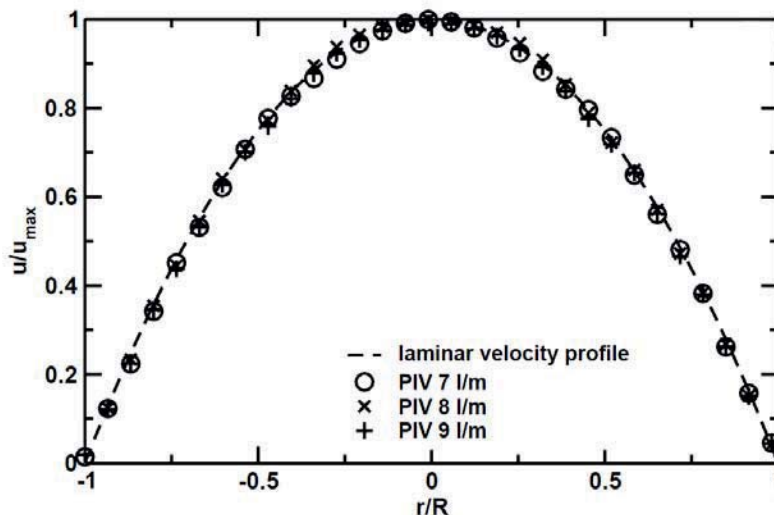
Figure 9: Comparison of measurements with analytic solutions

In the frame of the *Master Thesis* by Mäder [Mäder, 2012] between 01.05.2011 and 30.03.2012 medicinal white oil (Ondina 927) was mixed with a polymer with the commercial name of Kraton. Rheological measurements are found in the work by Mäder [Mäder, 2012]. Shear viscosity vs. shear rate and shear stress vs. shear rate diagrams for Ondina 927 + Kraton solutions are shown in Figure 10. The conclusions of this work were that pseudoplastic rheological properties

can be obtained. However, the mixtures became very viscous in comparison to the accomplished pseudoplastic behavior. Furthermore, very time and energy intensive processing was necessary. Therefore, it was decided not to use this mixture in the experimental campaign at ITE.
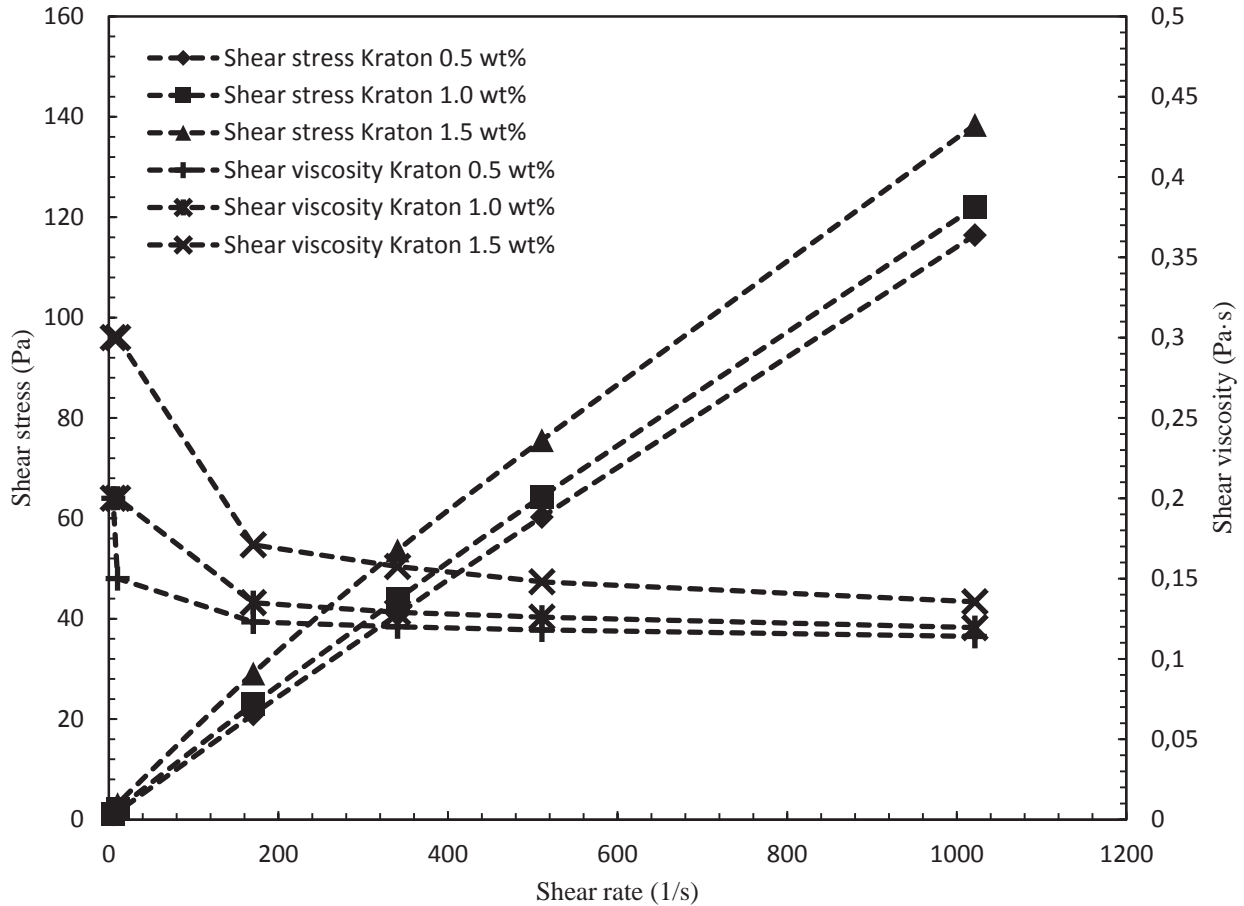
Figure 10: Shear viscosity vs. shear rate and shear stress vs. shear rate measurements for Ondina 927 + Kraton mixtures 0.5 wt%, 1.5 wt% and 1.5 wt% solutions

Table 6: Power-Law parameters for Kraton + Ondina 927 solution

Sample	Concentration (wt%)	Consistency index K (Pa·s^n)	Power law exponent n	r	Temperature (°C)
Kraton 0.5	0.5	0.157	0.953	1,000	21.6
Kraton 1.0	1.0	0.196	0.928	1,000	24.5
Kraton 1.5	1.5	0.382	0,850	1,000	25.6

Due to the difficulties in obtaining a fluid showing appropriate optical properties and pseudoplastic character simultaneously, it was decided to sacrifice optimal optical properties and select transparent fluids showing closer resemblance to the drilling fluid. The first test was performed with Polyacrylamide solutions. Rheological measurements were performed in the

frame of the *Master Thesis* by Mulchandani [Mulchandani, 2013b]. Shear viscosity vs. shear rate and shear stress vs. shear rate diagrams for polyacrylamide solutions are shown in Figure 11. On Table 7 the fitted parameters for the Power-Law model are shown for the different concentrations. It was concluded that polyacrylamide solutions showed rheological properties in agreement with those found in the drilling technique. Furthermore, the mixing process was relatively straightforward. One important inconvenience, considering the large volumetric capacity of the ITE flow loop was the high price of polyacrylamide, of 600 € per kilogram. Therefore, it was decided to search for more economical options.
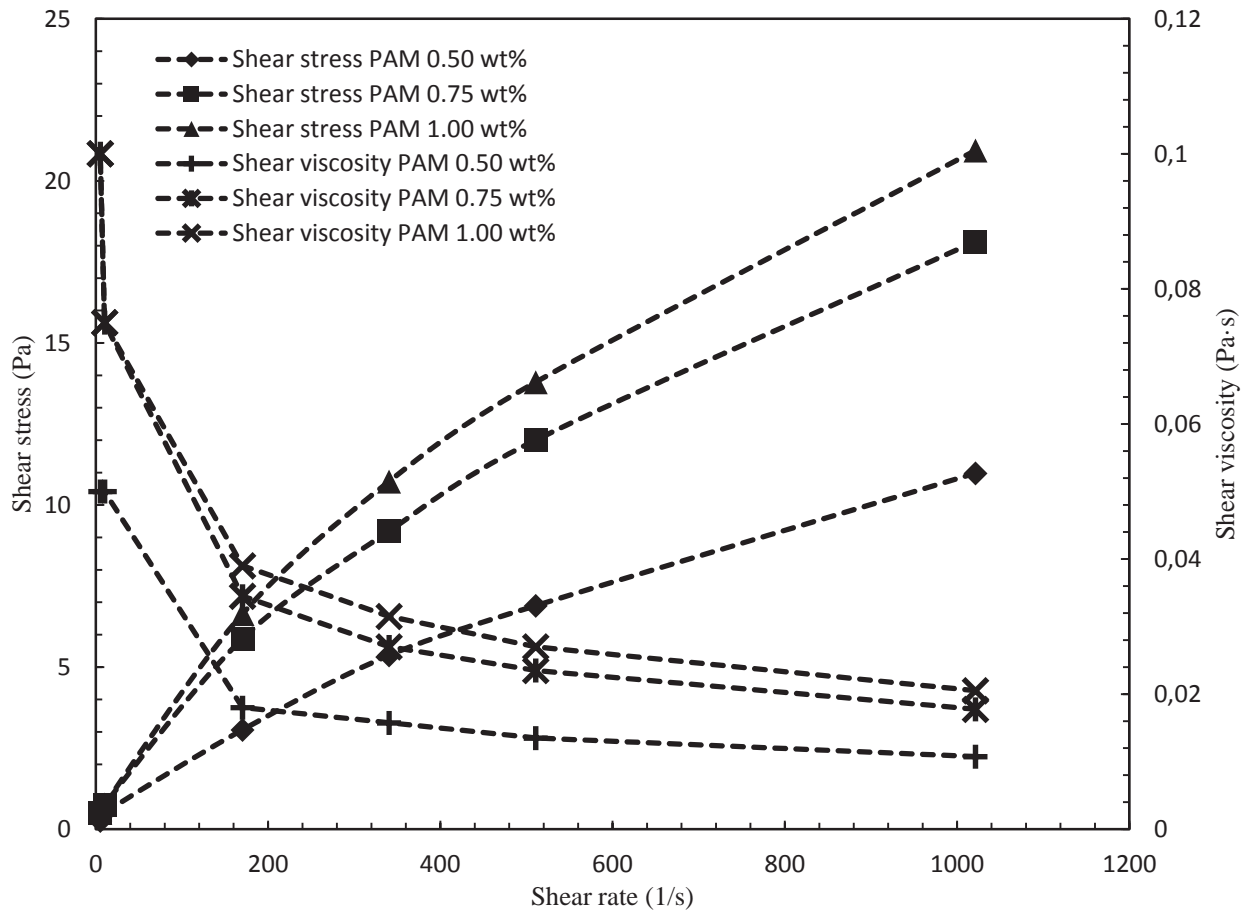
Figure 11: Shear viscosity vs. shear rate and shear stress vs. shear rate measurements for Polyacrylamide 0.50 wt%, 0.75 wt% and 1.00 wt% solutions

Table 7: Power-Law parameters for Polyacrylamide solutions

Sample	Concentration (wt%)	Consistency index K (Pa·s^n)	Power law exponent n	r	Temperature (°C)
PAM 0.50	0.50	0.097	0.682	0.999	25.6
PAM 0.75	0.75	0.234	0.628	0.999	25.6
PAM 1.00	1.00	0.259	0.634	0.999	25.6

Finally, in the frame of this project solutions of Carbopol 690 were tested. The rheological measurements were performed in the frame of the *Master Thesis* of Haider [Haider, 2014]. Solutions of Carbopol demonstrated a strong pseudoplastic character and, at high enough concentrations (> 0.075 wt%), also a finite yield stress. Shear viscosity vs. shear rate and shear stress vs. shear rate diagrams for Carbopol 690 solutions are shown in Figure 12. On Table 8 the fitted parameters for the Herschel-Bulkley model are shown for the different concentrations. The preparation of the mixtures was slightly more laborious due to the necessity to control the pH during mixing. This is necessary to obtain the desired rheology. Instructions on the preparation of Carbopol 690 solutions may be found in the *Master Thesis* by Haider [Haider, 2014]. In relation to the economical costs of Carbopol, these were comparatively lower than those of poly-acrylamide. Being 57 € per kilogram at the present date. After the previous considerations, Carbopol 690 solutions resulted in the final choice for conducting experiments at the ITE flow loop.
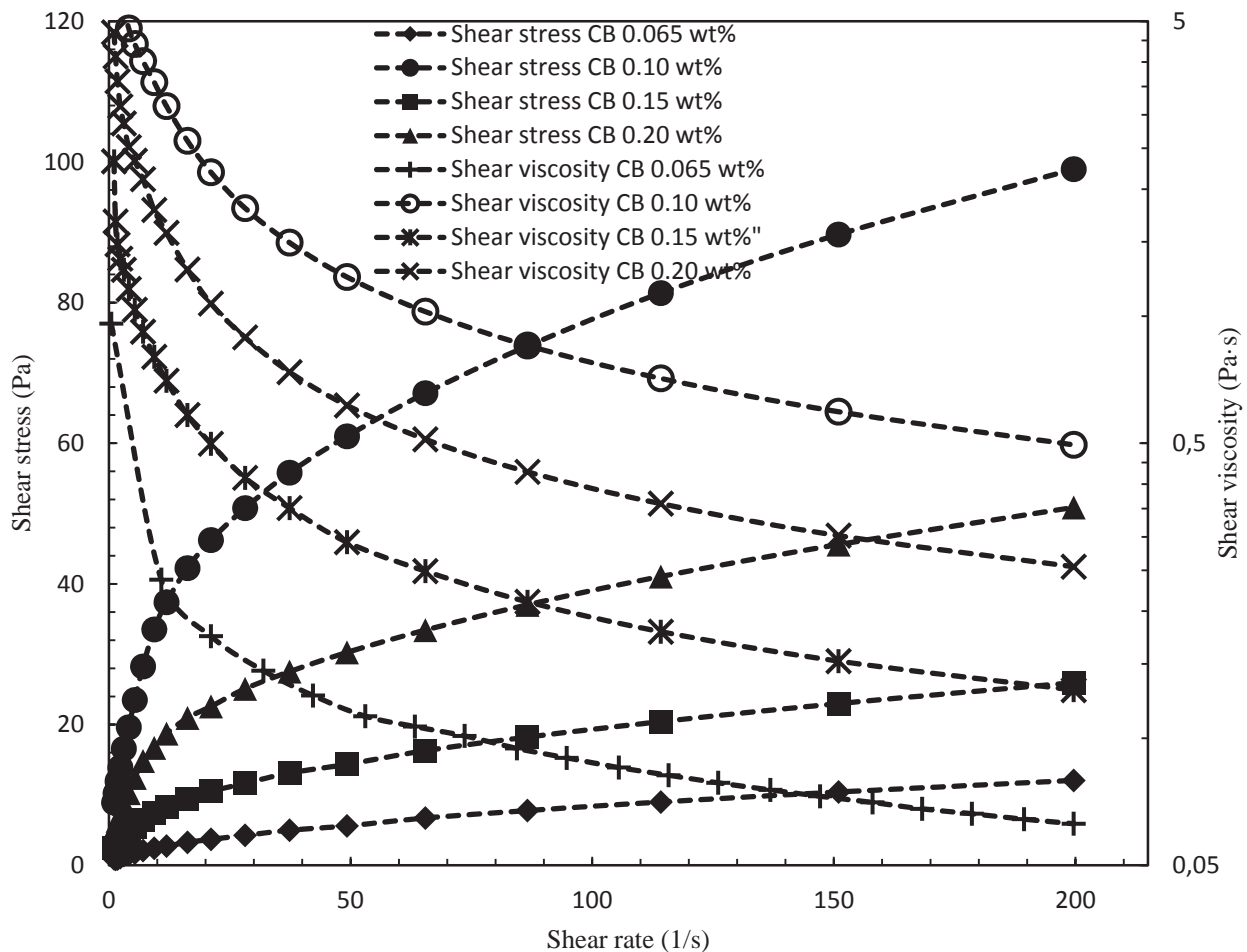
Figure 12: Shear viscosity vs. shear rate and shear stress vs. shear rate measurements for Carbopol 690: 0.065 wt%, 0.10 wt%, 0.15 wt% and 0.20 wt% solutions

455

Table 8: NV Sensor System - Herschel-Bulkley parameters for Carbopol 690 solutions

Sample	Con-cen-tration (wt%)	PH	Yield Stress (Pa)	Herschel Bulkley Con-sistency index k (Pa·s^n)	Power expo-nent in Her-schel Bulkey relation n	r	Temper-ature (°C)
CB 0,065	0,065	6,84	0,34	0,83	0,51	0,999	22
CB 0,10	0,10	-	2,65	1,79	0,48	0,999	22
CB 0,15	0,15	7,5	6,87	4,04	0,40	1	22
CB 0,20	0,20	7,1	12,37	9,71	0,40	1	22

Also, during this phase of the work, the implementation of the laser system on the ITE flow loop was regarded. Due to safety reasons, it was mandatory to cover the region where optical measurements were to be performed. This was necessary to protect personal working in the ITE workshops during the experiments. Furthermore, the cooling of the laser system has an umbilical cord length of 2.4 m, which complicated the operation of the adjustable inclination flow loop at ITE. In addition, the laser system is sensitive equipment not devised for working under harsh conditions. At that time, it was resolved that the installation of the PIV system with its laser light source in the ITE workshop was unfavorable and a research to find alternative light sources was started. The result of this research pointed out the possibility to use a LED light source. A preliminary test was performed in collaboration with DLR Göttingen. Nevertheless, the test was not successful because the device was still in the developing phase. Up to this report date, a further developed LED device on the basis of the one tested has been commercialized by the company ILA GmbH (shown in Figure 13). Its implementation should be further investigated. Following these tests, the installation of the PIV system consisting of the laser light source in the ITE workshop was deemed as not appropriate and an alternative option was proposed. This one consisted in the installation of a high speed camera, which would be able to record the flow regimes and the necessary images to perform Particle Tracking Velocimetry (PTV). A HCC-1000BGE high speed camera with a maximal acquisition rate of 1825 frames per second was installed on the ITE flow loop on March 2011.

Figure 13: LED light source by ILA GmbH

The main requirements on the solid phase to be used for the simulation of cuttings transport mechanisms are chemical and physical resistance, visibility, transport features dependent on the particle shape and density. Chemical and physical stability of the particles have to be granted in order to ensure the undisturbed function of the flow loop. To guaranty the correct feasibility of the PIV-measurements good visibility of the particles in regard to color and particle size is the main premise.

M 1 - The adaptation and testing of the measurement technique and the closure of the hydrodynamic and rheological characterization is the first milestone.

AP 4 - Experimental data collection

The content of AP4 includes the investigation of Newtonian and non-Newtonian fluids under laminar and turbulent regimes. The same should be investigated in a specifically developed facility considering concentric and eccentric annular geometries and taking into account the rotation of the inner pipe. The study should determine pressure losses and particle transport for the validation of numerical models (used in AP5) and simulations performed in project B6.

Types of experiments with multiphase flow loops

Two types of experiments may be conducted in multiphase flow loops:

- Experiment *Type 1* includes experiments used for measuring relevant physical and transport properties and supply empirical correlations.

  These experiments are usually conducted not with model validation as the objective; their main objective is to generate engineering data, which may be used directly on the field.

  For full simulation of field conditions, we should have not only geometric similarity (i.e., similar values for $do/(do\text{-}di)$) but also dynamic similarity (i.e., similar values for velocity

ratio, the Reynolds number, Re, and the properties (Galileo number, Ga)) [Kelessidis, 2004].

Multiphase flows often do not scale up in a predictable fashion [U.S.DOE, 2006]. Scale-up relationships from down-scale flow loops can only be used in a limited fashion. Thus, full scale flow loops need to be built to provide reliable parameters and operational confidences. This increases the cost of the experimental installations and its operation.

- Experiment *Type 2* includes experiments specifically designed to test different aspects of theory. For example, well-defined single particle experiments may provide insight into modeling multi-particle systems.

  This type of experiment is not commonly conducted and is very much needed. These experiments may be physical as well as computational (e.g., DEM or DNS). There is a need to define relevant material properties for different flow regimes, to develop efficient ways to represent properties in models, and to establish standards for materials.

When appropriate material systems are not available for model experiments, accurate simulation of the working conditions of an industrial plant on a laboratory- or bench-scale may not be possible. Under such conditions, experiments on differently sized equipment are customarily performed before extrapolation of the results to the full-scale operation. Sometimes this expensive and basically unreliable procedure can be replaced by a well-planned experimental strategy. Namely, the process in question can be either divided into parts which are then investigated separately or certain similarity criteria can be deliberately abandoned and then their effect on the entire process checked [Zlokarnik, 2002].

Computational fluid dynamics simulations may bridge the scale-up gap between down-scale flow loops and the field conditions. Nevertheless, constitutive equations necessary to model the multiphase phenomena need to be carefully developed. This requires, at the same time, validation of such constitutive equations with experimental data coming from the second type of experiments.

Experiments at ITM

The goal of the experiments performed at ITM was the adaptation of the particle image velocimetry (PIV) technique for the experimental flow loop at ITE. However, during the tests it was realized that detailed experimental tests for model validation (experiment *Type 2*) may also be performed. Specifically, these tests were done to investigate lift forces in multiple particle systems, particle distributions and momentum transfer in bidisperse suspension systems and settling of particles in dynamic non-Newtonian fluids. The same may be used to perform validation of highly resolved numerical models as the ones investigated in project B6.

The flow loop at ITM was developed in the frame of the *Master Thesis* by Kumar [Kumar, 2011] between 01.09.2010 and 31.05.2011. A diagram of the setup is shown in Figure 14 and the detailed geometry in **Fehler! Verweisquelle konnte nicht gefunden werden.**. An important point

was the design and construction of the particle injector (shown in Figure 15). This component of the flow loop allowed the inclusion of solid particles within the flow without flowing through the pump. With this it was possible to reduce the particle attrition and increase the control on the suspension characteristics.
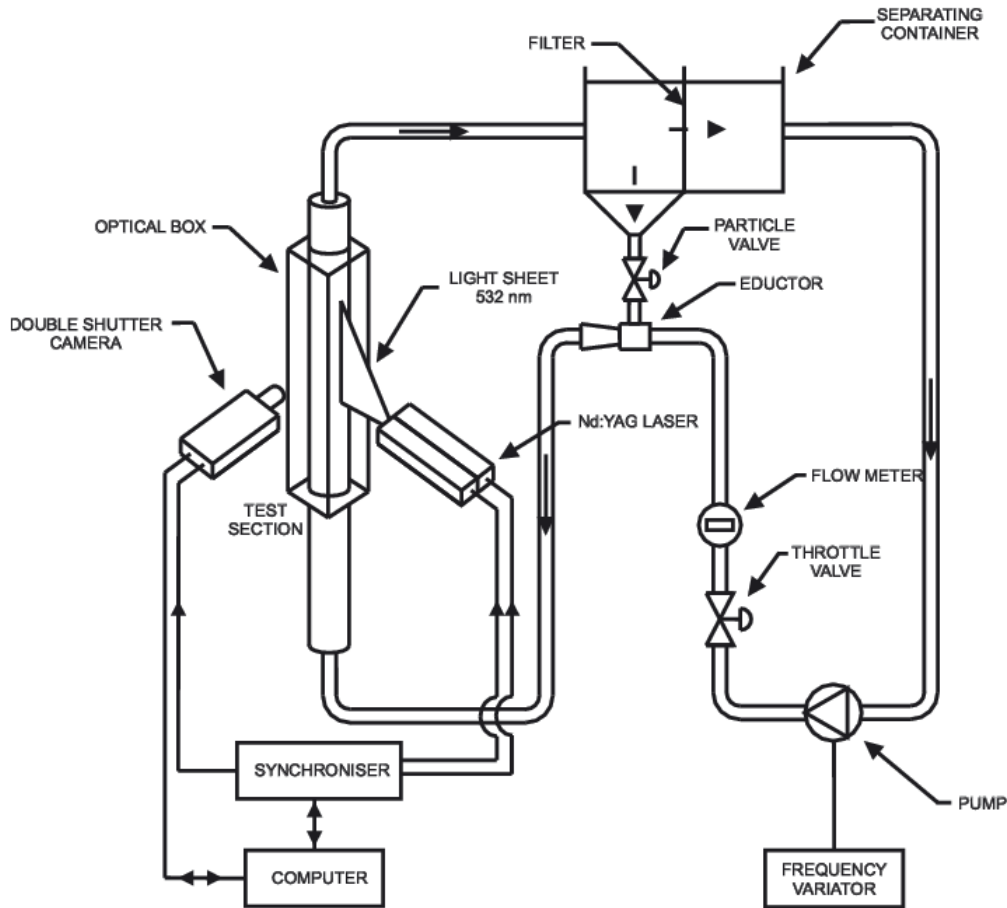
Figure 14: Vertical Multiphase Flow Loop

Figure 15: Eductor

459

a) Experiments with Newtonian liquids

The first multiphase measurement campaign was performed in the frame of the *Diplomarbeit* by Mäder [Mäder, 2012] between 01.05.2011 and 30.03.2012. This campaign allowed the validation of the adaptation of the PIV and PTV measurement methods and obtaining experimental data for monodisperse solid-liquid flow. The measurements were done with soda-lime glass particles with diameters between 1 and 5 mm at very dilute concentrations. Along with the data collection a MATLAB script based on the Hough transform was adapted to locate particles falling exactly in the plane of the laser light sheet. A first conclusion was the necessity to perform the experiments with particles offering a refractive index close to that of the working liquid and the material pipe. This would allow working with higher concentrations than the ones used until that time. Soda lime particles showed good behavior, but they absorbed too much light, as may be observed in Figure 16. For such reason, borosilicate glass particles were ordered.

The results by Mäder [Mäder, 2012] were the determination of velocity profiles for both phases and the determination of particle position distributions. With it, it was possible to determine average slip velocities. Comparison of these velocities with those predicted by state-of-the-art correlations indicated slight deviation of around 15%. To clarify this deviation particle size analysis with the method QICPIC by the Sympatec GmbH were performed. The results of the same are shown in Figure 17 and listed in Table 9. The measurements showed slight deviations of the average particle size in front of the ones indicated by the glass particles supplying company (SiLi beads). After modification of the average particle size, correlations predicted the same velocities as the ones measured with the optical technique (within a 2% error) and the same was considered applicable for further multiphase experiments.
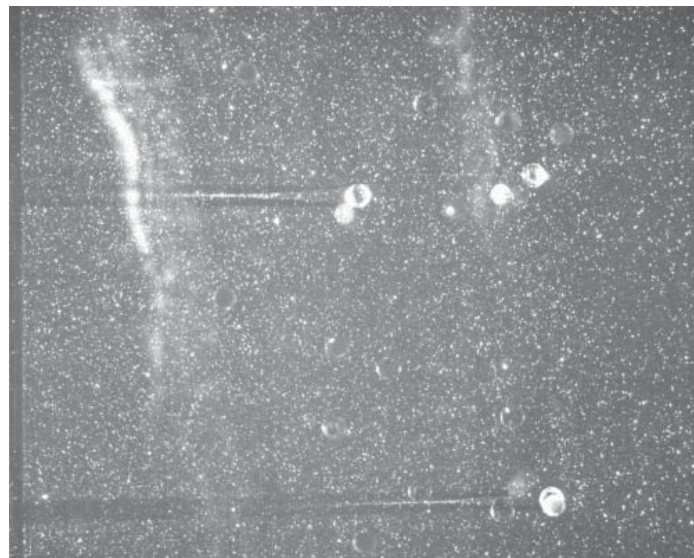
Figure 16: Exemplary image with soda-lime glass particles
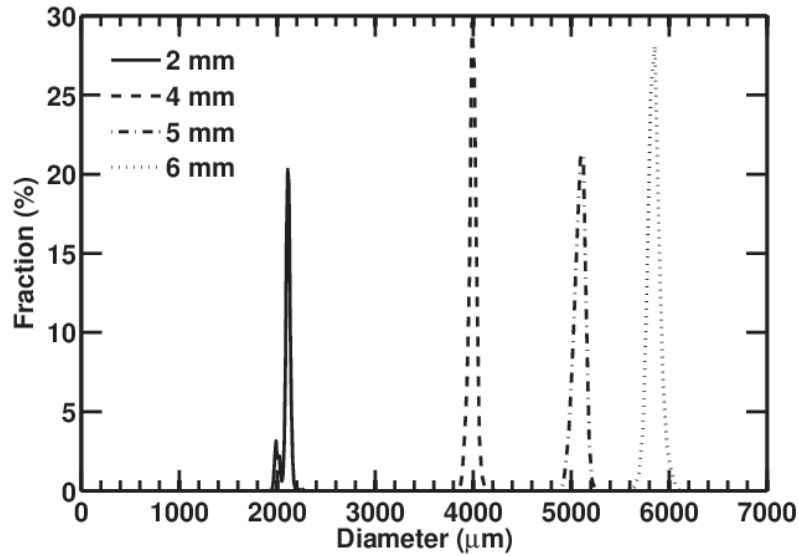
Figure 17: Particle size distributions for the used particles

Table 9: Fluid and particle properties

Light liquid paraffin
$\eta_f = -2.15T + 114.30$ mPa·s
$\rho_f = 865/(1 + 7.64 \times 10^{-4}(T-15))$ kg m^{-3}
$n_D = 1.473$ at $20°C$
Borosilicate beads
$d_{p4} = 4000 \pm 100$ μm, $d_{p5} = 5050 \pm 100$ μm and $d_{p4} = 5900 \pm 200$ μm
$\rho_p = 2230$ kg m^{-3}
$n_D = 1.464$
Soda Lime beads
$d_{p2} = 2050 \pm 100$ μm
$\rho_p = 2580$ kg m^{-3}
$n_D = 1.464$

Following the experiments of Mäder [Mäder, 2012], experiments with higher concentrations (up to 1.2% volume concentration) and bidisperse suspensions were performed with borosilicate glass particles. An image of these experiments is shown in Figure 18, where it can be seen how only the edges of the particles absorb laser light. The results were presented in the *13th Workshop on Two-Phase Flo w Prediction s in Halle, Germany, 17.-20. Septe mber 2012* [Aragall et al., 2012]. The outcomes of the experiments were velocity profiles of the liquid and dispersed particle phases and distribution histograms of the particles. An example of the same is shown in Figure 19. Particularly, the bidisperse experiments presented a particle migration effect not previously described in the literature. This effect was deemed as very interesting for the validation of momentum transfer models, especially those concentrated on the lift force acting on multiple particle systems. A further analysis of this data allowed derivation of momentum transfer for bidisperse suspensions. This analysis indicated a certain momentum transfer between species of different sizes. However, to confirm the last statement more experiments and larger particle

size ratios were deemed as necessary. Altogether, these results offered the first complete set of data for validation of highly resolved numerical models, as the ones used in project B6.
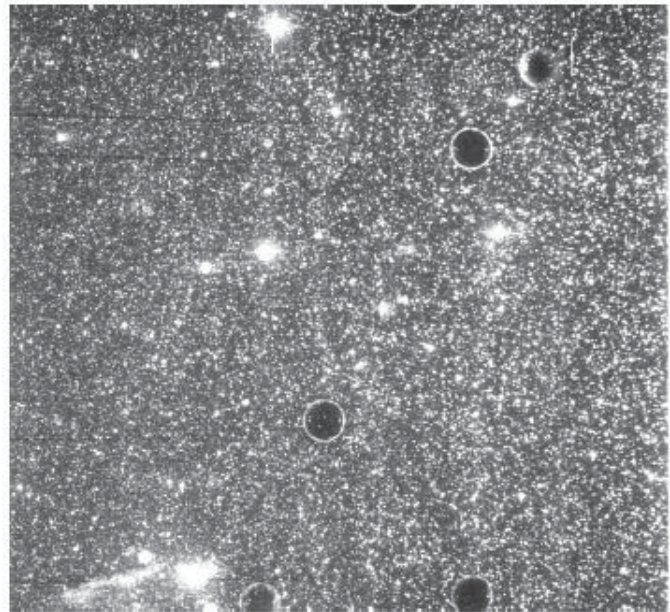
Figure 18: Exemplary image with borosilicate glass particles

Experiments with higher concentrations (up to 4% volume concentration) and larger particle sizes (6 mm diameter), were performed in the frame of the *Master thesis* by Mulchandani [Mulchandani, 2013b] between 01.09.2012 and 26.07.2014 . In those experiments an extension of the data set to further investigate the particle migration phenomena observed in the previous campaign and to confirm the momentum transfer between species was acquired. Analysis of the data corroborated the previous findings and was processed to prepare a paper [Aragall, 2015a] submitted to the *International Journal of Multiphase Flow* in December 2013. These data and the corresponding analysis formed the second complete set of data for validation of particle scale resolving numerical models.
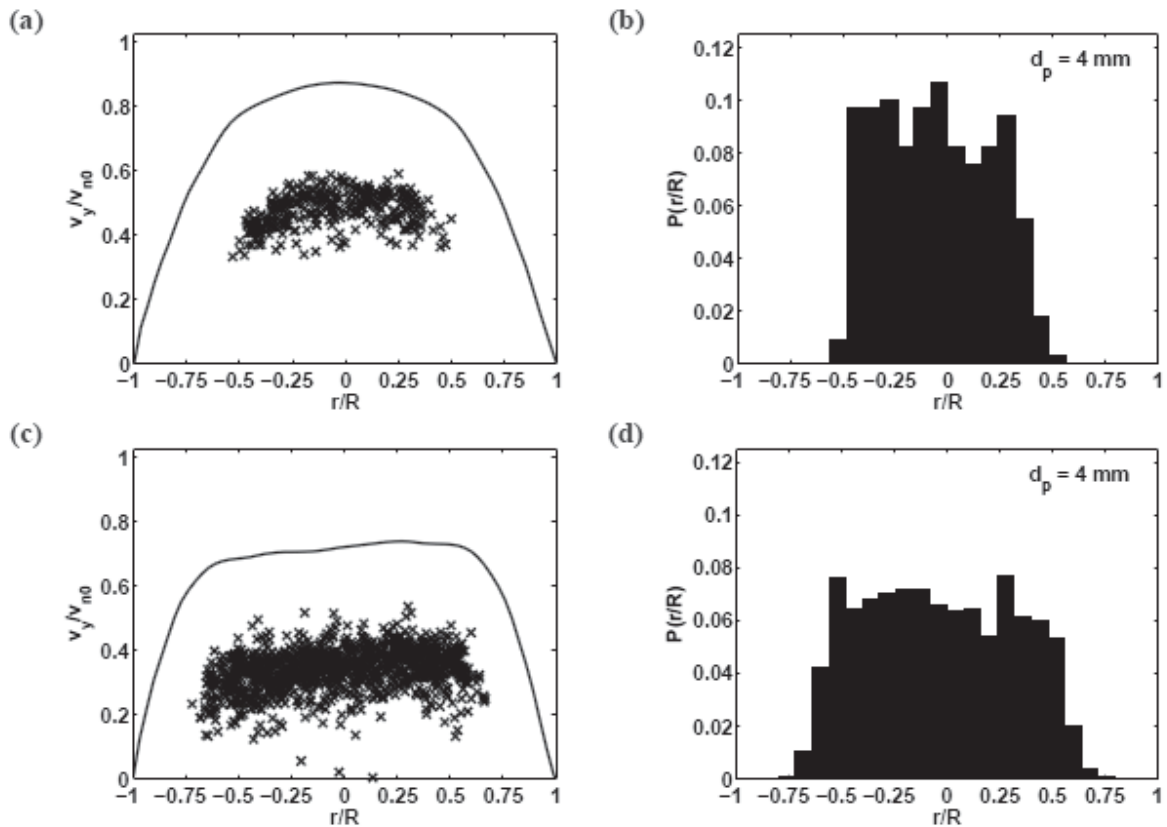
Figure 19: Vertical velocities of the 4 mm particles and normalized histograms of the particle positions for varying concentrations and constant pump velocity. ×, vertical velocities of the 4 mm particles, —, locally averaged fluid velocity profile: (a and b) exp. 7, φ4= 0.12%, (c and d) exp. 10, φ4= 0.50%.

b) Experiments with non-Newtonian liquids

As a result of the work performed in *work package* AP3, two polymers, polyacrylamide and Carbopol 690, were selected for the experiments executed with non-Newtonian carrying liquids. Experiments with polyacrylamide water solutions were performed in the frame of the *Master thesis* by Mulchandani [Mulchandani, 2013b]. The objective of the measurement using non-Newtonian fluids was to determine the particle settling in static and dynamic fluids. This was motivated by the existing discrepancies in the research community about the effect of dynamic fluid on the settling velocities of particles in shear-thinning liquids. For this reason, two state-of-the-art correlations were compared with results measured experimentally for static and dynamic fluid conditions. This comparison is shown in Table 10 and the main conclusions were the under-predicting behavior of the correlation by Luo [Luo, 1988] and the much better predicting capacity of the correlation by Ceylan [Ceylan et al.,1999]. Furthermore, for dynamic fluids larger settling velocities were measured than with static fluids, which supports statements of other authors, who have observed similar effects.

Table 10: Comparison between measured and predicted settling velocities for a fluid with $K = 0.15$ $Pa \cdot s^n$; $n = 0.7$

Particle Diameter $\varnothing_p$ (mm)	Particle Density ρ_f (kg/m^3)	Particle Reynolds Number Re_P	Pipe Reynolds Number Re	Static Fluid (correlated after Luo, 1988) (m/s)	Static Fluid (correlated after Ceylan, 1999) (m/s)	Static Fluid (experimental) (m/s)	Dynamic Fluid (experimental)
2	2580	1.69	104.73	0.048	0.057	0.083	0.086
3	2580	5.04	112.36	0.090	0.131	0.133	0.146
4	2230	7.91	108.53	0.109	0.166	0.150	0.172
5	2230	14.45	139.98	0.154	0.238	0.208	0.252

Experiments at ITE

A dimensional analysis included in the second progress report of project B5 [Aragall et al., 2014a] was performed to search for a working fluid and cuttings combination able to supply data for empirical correlations, defined as experiments of *Type 1*. Due to the conclusions of the dimensional analysis and the difficulties during the set up commented in *work package* AP3, it was necessary to reconsider the experiments performed at ITE. It was decided to use the flow loop to supply model data validation, defined as experiments of *Type 2*. In it, the possibility to incline the flow loop should offer the capacity to investigate the validity of the two-fluid and the Euler-Lagrange numerical models to predict transport of dispersed solids in inclined conducts. Furthermore, Carbopol 690 should also be used to supply data considering non-Newtonian rheology.

Initially it was intended to convert the flow loop into an annular flow loop, where the effects of eccentricity and rotation may be investigated. The initial plan was revised because difficulties in the modification of the flow loop and because the located models (two-fluid and Euler-Lagrange models) still require to be validated with the initial circular geometry. Therefore, it was decided to leave the flow loop as a circular geometry and generate experimental data considering the effects of inclination and non-Newtonian rheology on monodisperse particle transport. Furthermore, experiments at ITE suffered from the modifications in the measuring technique following the results of *work package* AP3. Instead of the PIV system, a high speed camera was implemented to measure flow regimes, bed heights and particles velocities through particle tracking velocimetry (PTV). To determine the pressure, a transducer able to acquire pressure gradients with 1 Pa resolution was firstly tested at the ITM flow loop and later implemented in the ITE flow loop.

Experiments were performed in the frame of the *Master thesis* by Haider [Haider, 2014]. The objective of the experiments was to supply measurements of the holdup, pressure losses and capture flow regimes of controlled yield power-law fluids transporting particles of 2 mm diameter

size through deviated pipes. These should supply adequate high-quality data for the purpose of assessing the accuracy of model predictions.

Data collected during the test included the applied flow rates as well as initial conditions and boundary conditions that changed throughout the test. In addition, all prescribed input, test conditions, and measurements were fully documented. In Figure 20 an example of the measurements carried out with water at 0° inclination is shown. The diagram shows pressure fluctuations with respect to time and flow rate variation with respect to time during the transport of a specified amount of cuttings. In the diagram it may be observed how the pressure losses fluctuate around a lower set pressure gradient and start increasing seconds after the cuttings are introduced in the system. The lower set correspond to the single phase pressure losses and were compared with available pressure loss correlations for verification. The higher pressure gradients have larger fluctuations during the transport of the cuttings in the test section and when these come out, pressure losses recover initial values. It can also be observed how the inclusion of cuttings in the system produces fluctuations in the flow rates supplied by the pump. This fact needs to be considered when defining boundary conditions in the simulations.
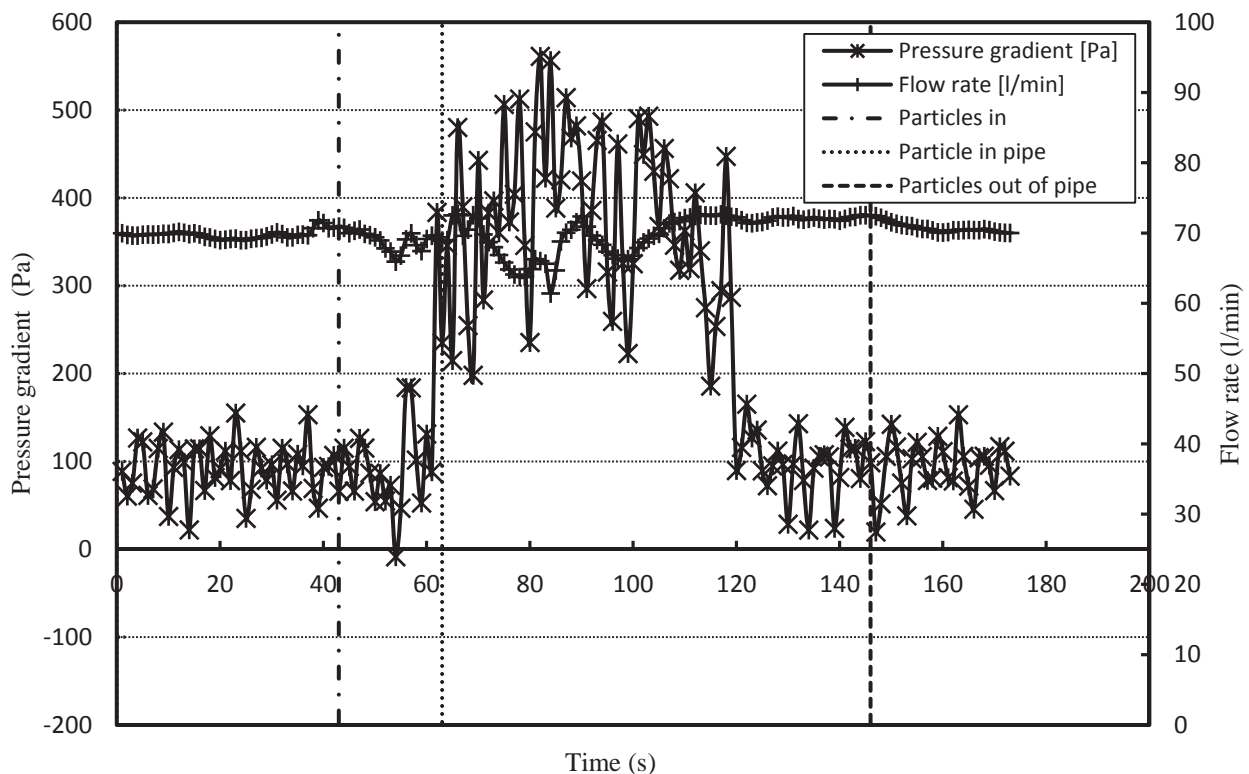
Figure 20: Pressure and flow rate progress for a cuttings transport experiment at 70 l/min and 0° inclination with water.

In Figure 21 the comparison of cuttings transport with water for increasing flow rates is shown. Single phase pressure losses for 70, 90 and 110 l/min were predicted with pressure loss correlations and are 73, 113 and 162 Pa respectively. In the diagram it can be observed how the duration of the transport, quantified through the time at which pressure losses show higher values,

465

is larger for the 70 l/min flow rates. Furthermore, it can also be observed that pressure losses for 70 l/min become higher when particles are introduced in the test pipe than with 90 and 110 l/min. This can be explained by the larger bed heights produced at lower flow rates, which reduce the area open to flow. In Table 11 the bed height occupation respect to pipe diameter for varying flow rates and inclinations is shown. As a consequence, the fluid reaches higher velocities in the free cross- sectional area and the shear stresses increase producing larger pressure gradients.
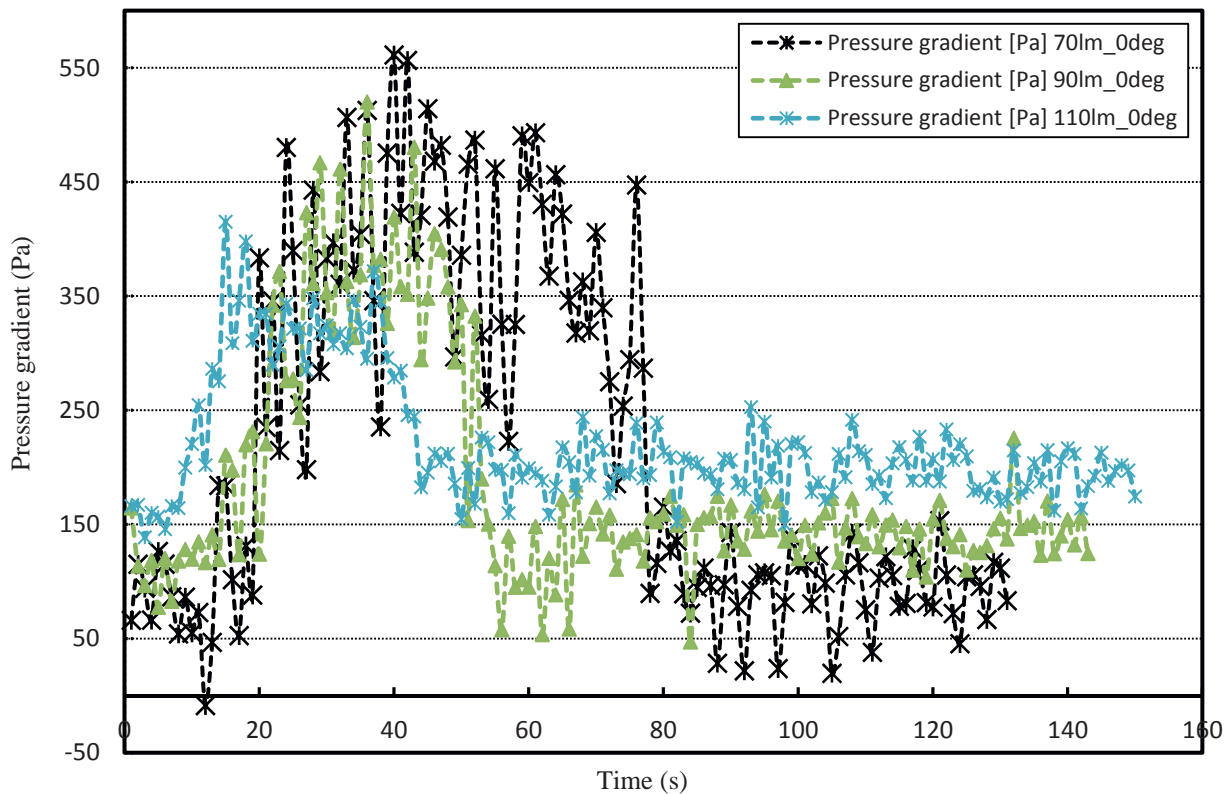
Figure 21: Flow rate variation at 0° inclination for water

Table 11: Bed height ocupation respect to pipe diameter for varying flow rates and inclinations for water

Flow rate (l/min)	0°	5°	10°	15°	25°
70	46 %	44 %	45 %	43 %	42 %
90	40 %	40 %	43 %	41 %	41 %
110	38 %	35 %	35 %	35 %	39 %

In Figure 22 the comparison of cuttings transport with water at 70 l/min for different inclinations is shown. It may be observed how the increasing angles translate in higher pressure gradients, but also in faster transport. This is probably caused by the generation of higher bed heights at higher angles. However, these bed heights take place during a short period of time and eventually reach similar heights to the ones obtained for horizontal inclination.

In Figure 23 the comparison of cuttings transport with Carbopol 690 0.065 wt% at 45° inclination and varying flow rates is shown. Larger pressure losses, compared to water, in single phase flow are due to the larger viscosities of the Carbopol solution. In contrast to the water experiments, larger flow rates with cuttings transport also translate in higher pressure losses. This is thought to be caused by the lower difference in the bed heights produced at 45 ° inclination.
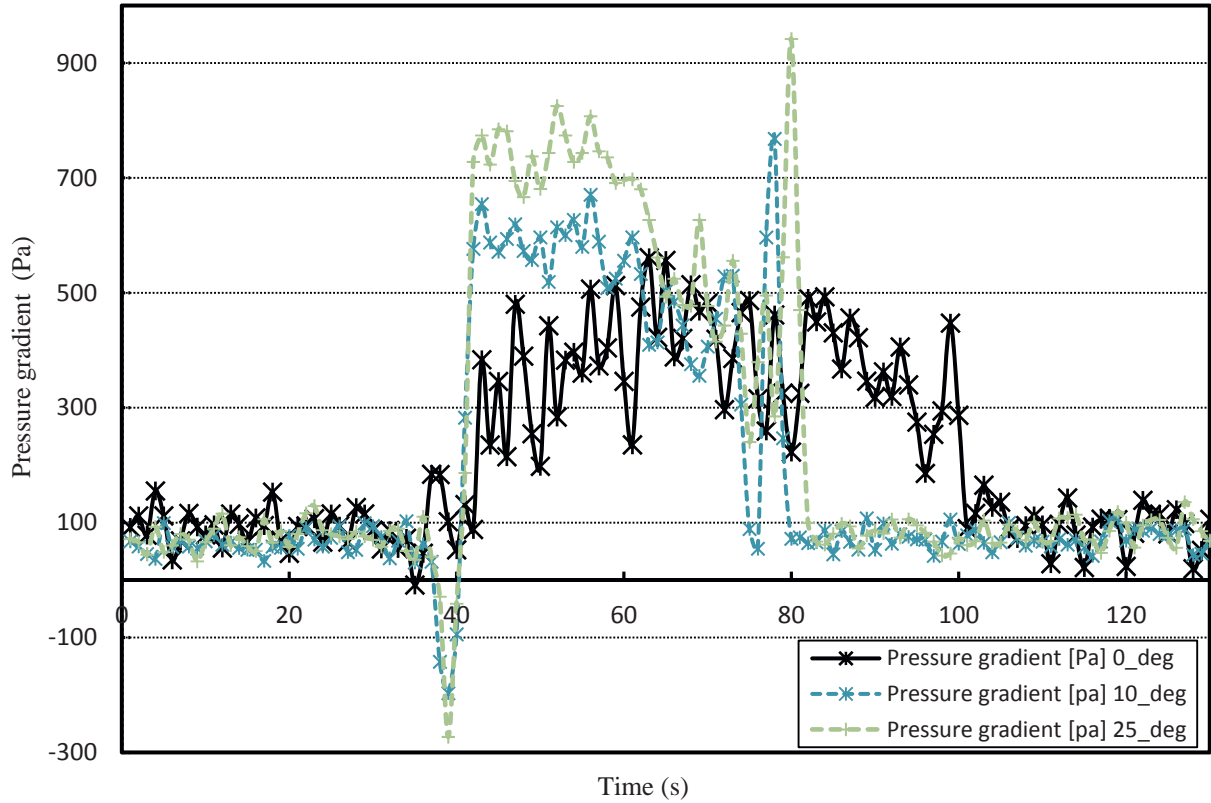
Figure 22: Inclination variation at 70 l/min for water

Table 12: Bed height occupation respect to pipe diameter for varying flow rates and inclinations for Carbopol 690 0.065 wt%

Flow rate (l/min)	0°	5°	10°	15°	25°
70	46 %	44 %	45 %	43 %	42 %
90	40 %	40 %	43 %	41 %	41 %
110	38 %	35 %	35 %	35 %	39 %

467
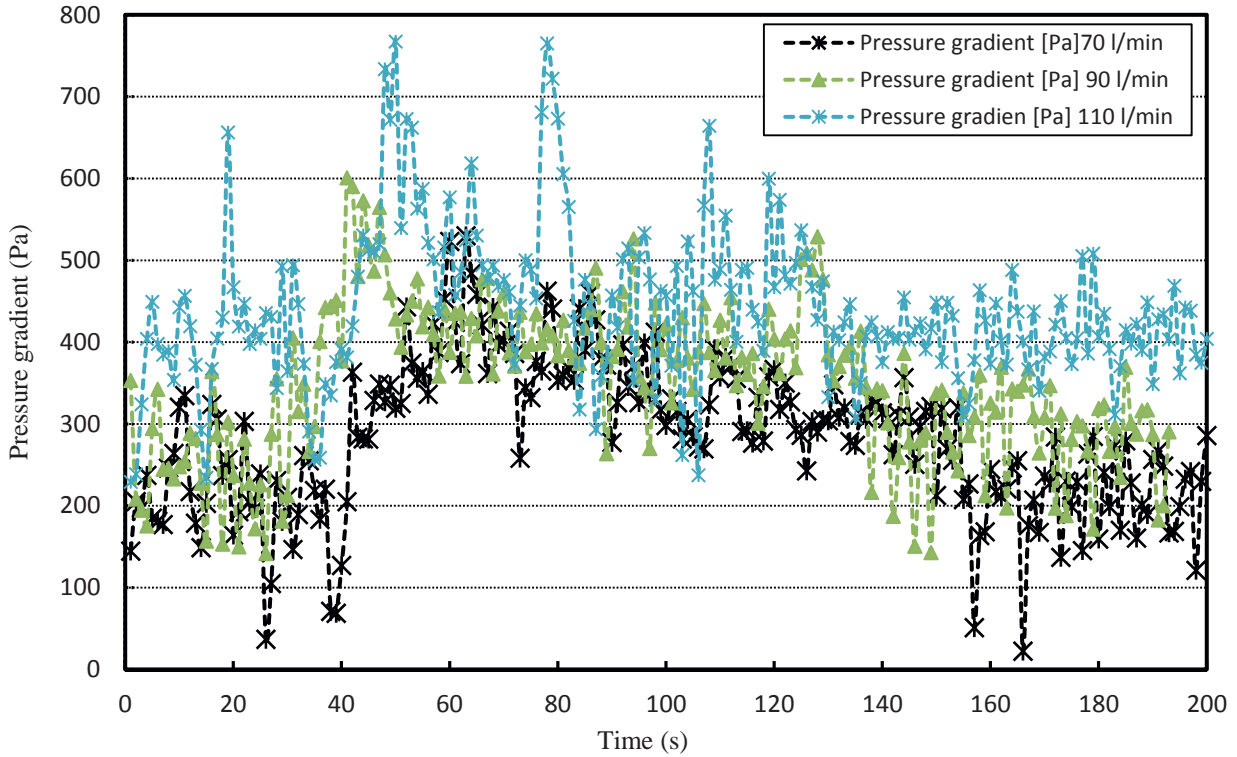
Figure 23: Flow rate variation at 45° inclination for Carbopol 690 0.065 wt%
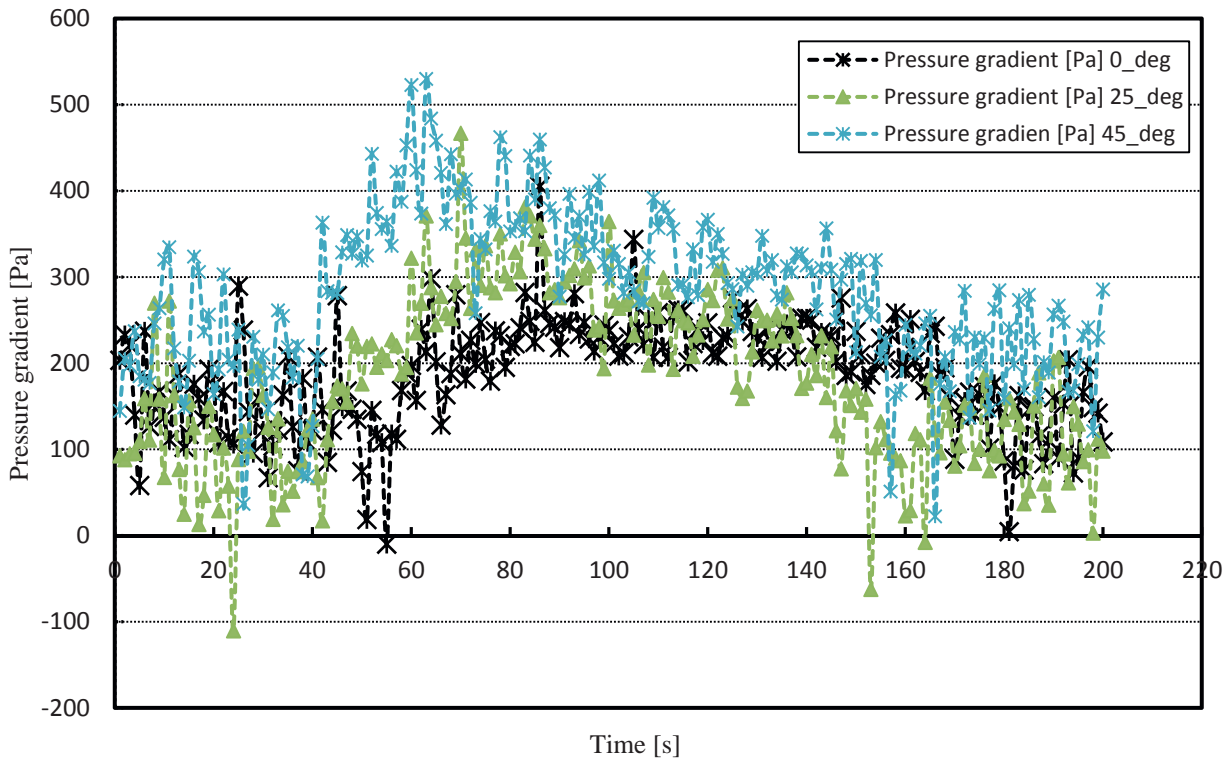
Figure 24: Inclination variation at 70 l/min for Carbopol 690 0.065 wt%

Conclusions

AP4 has supplied data sets for high resolution numerical models. These have been acquired in the ITM flow loop, which was originally constructed to test the optical measuring equipment. The

experiments were conducted with Newtonian and non-Newtonian fluids. The tests using Newtonian fluids considered mono- and bidisperse semi-dilute concentrations similar to those found in real drilling plants. The results consist of velocity profiles of the liquid and the dispersed particles, particle distribution histograms and momentum transfer evaluation. These results have been extensively documented in several publications Maeder (2012), Aragall (2012), Mulchandani (2013) and Aragall (2013). For non-Newtonian fluids the influence of fluid dynamics on the settling velocities of particles in shear-thinning fluids have been investigated. The results have been documented in the Master thesis by Mulchandani (2013). Furthermore, several test have been conducted in the ITE flow loop. Due to difficulties in the implementation of the PIV technique, a high speed camera was chosen as a substitute. Also due to difficulties in the installation of an inner pipe, the experiments were redirected to investigate specific scenarios found in cuttings transport. These scenarios include deviation of the conduct and non-Newtonian rheology transport, which are still subjects of active research.

AP 5 - Wellbore scenarios simulation

The content of AP5 includes numerical calculation of multiphase flows in annular geometries. These simulations are based on existing methods (CFD) and intend to provide an evaluation of the effects of drill string rotation, eccentricity, inclination, tool joint geometry and flow rate on the turbulent flow field and the particle transport in Newtonian and non-Newtonian drilling fluids. Findings obtained in project B6 in relation to modeling of the fluid/particle interaction should be integrated in the previously described simulations. Contrary to the model tests in multiphase simulator, HP-HT conditions may be simulated after the relevant material properties are defined in AP2 and the boundary conditions are defined in Project B4.

Modeling approaches

The work in AP5 is based on the multi-scale approach applied to drilling hydraulics as presented in the *Celle Drilling Conference 2013, Germany, 9.-10. Septe mber 2013*. A shortened version of the presentation was published in the *OIL GAS European Magazine* [Aragall et al., 2014a]. The approach consists of the utilization of different methods depending on the scale to be simulated. In Figure 1 several phenomena of interest in drilling hydraulic transport are presented. The idea of this approach is to combine information acquired at different scales to obtain a description of the whole problem as close to reality as possible. In this way, at the largest scale transient one-dimensional models are used. These models are the subject of interest in *work packa ge* AP6. However, they relay very much on closure relations describing integral properties as a function of the operating variables. Integral properties have been traditionally correlated with the use of analytic solutions or physical experiments. When analytic solutions are impossible and experimental solutions are cumbersome, numerical simulation of detailed fluid problems become a good candidate to supply the necessary information. The integral

properties investigated within this *work package* include pressure losses in annular cross sections with bed heights considering non-Newtonian rheology, drag and lift forces on particles within non-Newtonian media, solid particle holdup in sudden expansions, solid particle holdup in eccentric annular geometries and solid particle transport in deviated conducts through non-Newtonian carrying media. The methods implemented to simulate the drilling scenarios include single phase CFD simulations, two-fluid simulations and CFD-DEM simulations.

Mathematical modeling can be exercised by the use of spherical particles; meanwhile it is not possible to perform rigorous modeling on the wide spectrum of real cuttings particle shapes. However, settling velocity is strongly influenced by the particle shapes. Concerning composition and related characteristics the particles should be as realistic as possible: the main particle requirement must then be a comparable density to the expected cuttings in the well, because flow and transport behavior depend directly on this property.
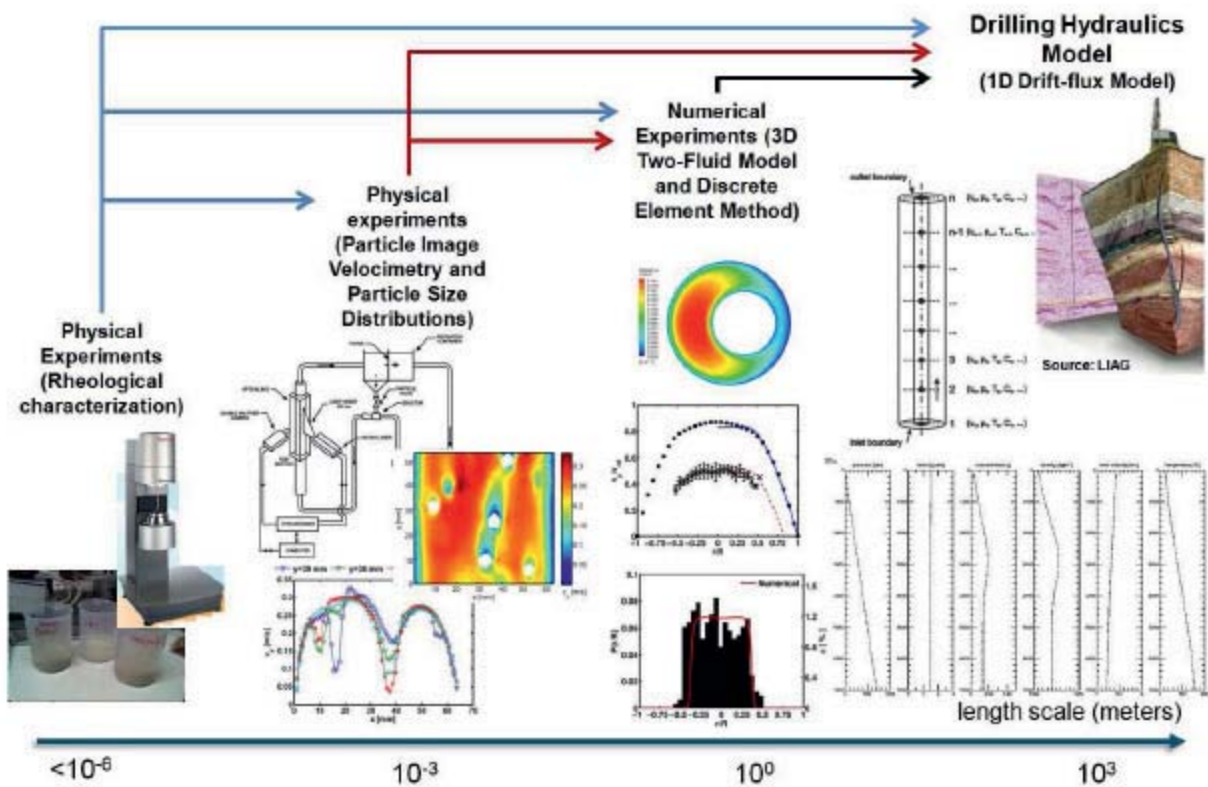
Figure 25: Different objects of interest in the drilling hydraulics problem.

Single phase CFD simulations

Single phase approaches were applied to those problems where the assumption of homogenous fluid is justified. Such assumption can be made when solid particles are uniformly distributed throughout the carrier liquid. In drilling hydraulics with water-based muds, this is found in the mixture of water with bentonite, baryte or several other additives. Furthermore, this may be the case when the size of the drilled cuttings is very small (<40 μm). Such simulations are based on the solution of the continuity and momentum equations as typically done in CFD simu-

470

lations. However, these include constitutive equations considering the non-Newtonian shear stress relation with shear rates caused by the presence of the solid particles. In this *work package*, this approach was used to simulate annular cross sections with bed heights defined by the geometry of the computational grid and a static particle immersed within several sheared non-Newtonian fluids.

a) Annular cross sections with bed heights

Simulation of annular cross sections with bed heights considering variation of the power-law index in pseudoplastic fluids was performed in the frame of a collaboration with Khan as a student assistant between 15.01.2011 and 31.08.2011. The results are condensed in a *Progress Report* [Khan, 2011]. Moreover, further simulations were done and a paper for the *19th Middle East Oil & Gas Show and Conference* was submitted on the 12.04.2014. These simulations had the objective to investigate the effect of eccentricity on the pressure losses and the stresses originated on cuttings beds.

Simulations were implemented through a two-dimensional approach, offering the cross- sectional flow field as shown in Figure 26. A momentum source was necessary to produce the flow rate. Furthermore, periodic boundary conditions were used. Multiple simulations were performed, where an important task of the work was the generation of different grids considering the several degrees of eccentricity and bed height. Once this was done, simulations with variation of the the pseudoplastic power-law index, eccentricity, diameter ratio and bed height were performed. These supplied friction factors for the different configurations. Main conclusions were the negative effect of eccentricity on pressure losses. Furthermore, a new factor was developed consisting of the ratio of the fraction of the pressure gradient acting on the cuttings bed and the total pressure gradient. This factor quantifies the shear stress concentrated on the cuttings bed surface from the total ones acting on the wetted surfaces. The results showed how eccentricities in the direction of the wellbore lower wall result in lower shear stresses on the cuttings bed, while eccentricities towards the wellbore upper wall result in larger flow rates just above the bed and therefore larger shear stresses concentrated on that region. This indicates, that placing the drill string closer to the upper wall in horizontal drilling leads to larger shear stresses above cutting beds forming on the lower wall. A diagram showing such behavior can be seen in Figure 26, where τ, alternatively tau, stands for the shear stresses acting on the cuttings bed surface. The situation of the drill string in that position could be achieved through mechanical devices. However, it would be a subject requiring an extensive design development. Moreover, this condition may be achieved temporally in case of drill string rotation. This gives an explanation for the better transport conditions found in deviated drilling when rotary drilling is applied.
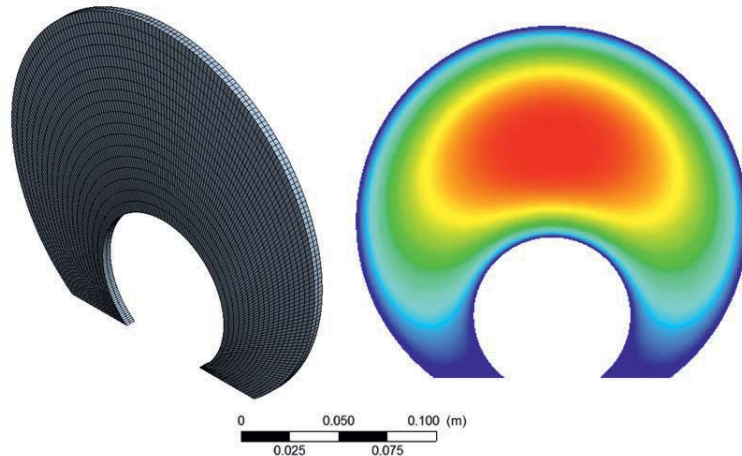
Figure 26: Flow through a horizontal, eccentric annular cross section with prescribed non-dimensional bed height of 0.05. Grid structure and velocity contour plot in a cross section.
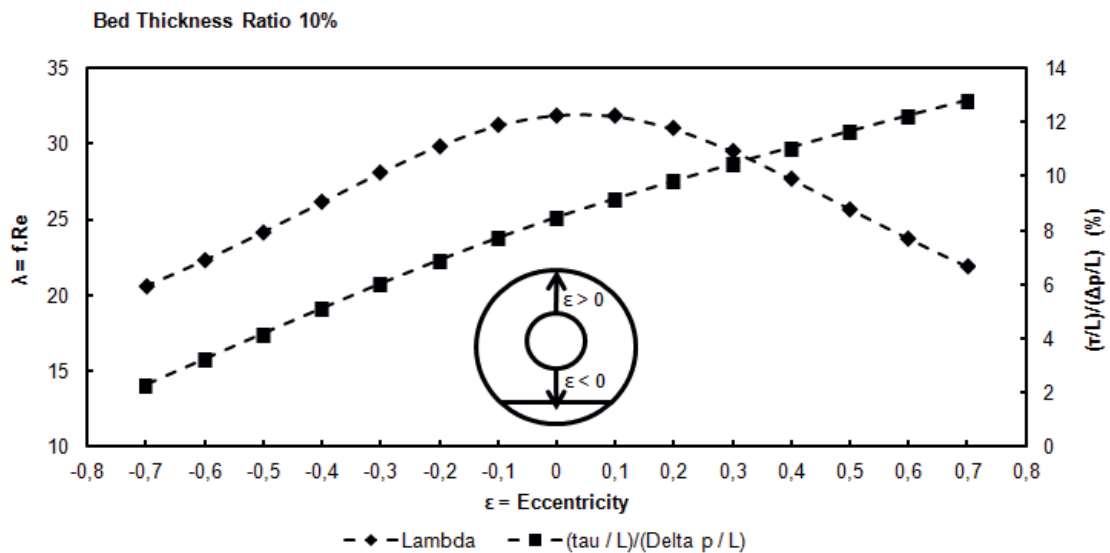
Figure 27: Diagram of the friction factor and the fraction corresponding to shear stresses on the cuttings bed in front of eccentricity for K = 0.1, n = 0.5 and Diameter ratio = 0.5.

b) Non-Newtonian particle drag and lift forces

Simulations of a static particle in Newtonian media were performed in the frame of the *Studienarbeit* by Li [Li, 2012] between 16.01.2012 and 20.04.2012. Subsequently, the simulations were extended to consider non-Newtonian media. These simulations had the objective to supply drag and lift correlations of particles immersed in Newtonian and non-Newtonian media. Therefore, these simulations may be considered as small scale simulations focused on the particle scale, that is 1 to 10 mm. Drag forces acting on spheres in Newtonian media are currently well described. However, lift forces acting on a particle due to shear flows are still subject of active research. This is due to the fact that this force is much more subtle than drag and therefore it is sometimes neglected. In any case, such forces are significant in the cuttings transport problem. Specifically, because of its importance in the distribution of particles across the cross-sections in vertical transport and in the erosion of cuttings beds in horizontal transport.

The simulations by Li were performed with the software ANSYS-CFX version 11. The study concentrated on the preparation of grid independent simulations through validation against state-of-the-art correlations, as the Schiller & Naumann [Schiller, 1935] correlation for drag, and the Saffman-Mei [Mei, 1992] correlation for lift. As known from previous studies, it was important to use grids where the external boundaries would not affect the flow fields developing around the static sphere. This resulted in simulations where the inlet surface was 20 diameters away from the center of the sphere, the outlet surface 30 diameters away and the top and bottom surfaces 15 diameters away. The study resulted in a grid with a total number of 145000 nodes which could be solved in 5 minutes on a 2x3 GHz Processors computer. The structure of the final grid is shown in Figure 28.
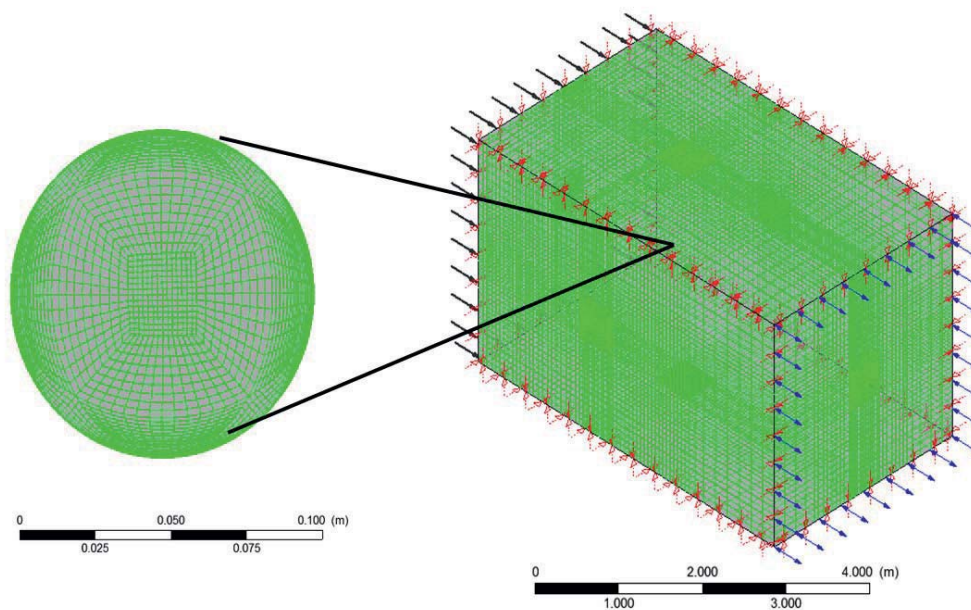
Figure 28: Discretized geometry used in the static sphere numerical experiments.

The results of the simulations supplied the velocity and pressure fields around the particle as shown in figure Figure 29. Integration of shear stresses and pressure on the surface of the sphere provided drag and lift forces. While the drag forces match perfectly state-of-the-art correlations, this was not the case for lift forces. The first correlation compared for lift forces was the one developed by Mei [Mei, 1992] on the basis of numerical experiments by Dandy & Dwyer [Dandy, 1990] and the theoretical analysis by Saffman [Saffman, 1965]. This correlation was found in the model library of ANSYS-CFX Release 12.1 [ANSYS, 2009] and it is there used for simulations of dispersed multiphase flow problems. Later on, it was found that correlations by McLaughlin [McLaughlin, 1991] offer better matching. One possible cause was pointed out by Takemura & Magnaudet [Takemura, 2009], who considered the computational domain of Dandy & Dwyer [Dandy, 1990] to be too small. In any case, the modeling approach used was considered as validated after finding the work of McLaughlin [McLaughlin, 1991]. In spite of that, con-

473

sidering the extended use of the Saffman-Mei model [Mei, 1992] there is room for further research in this direction.
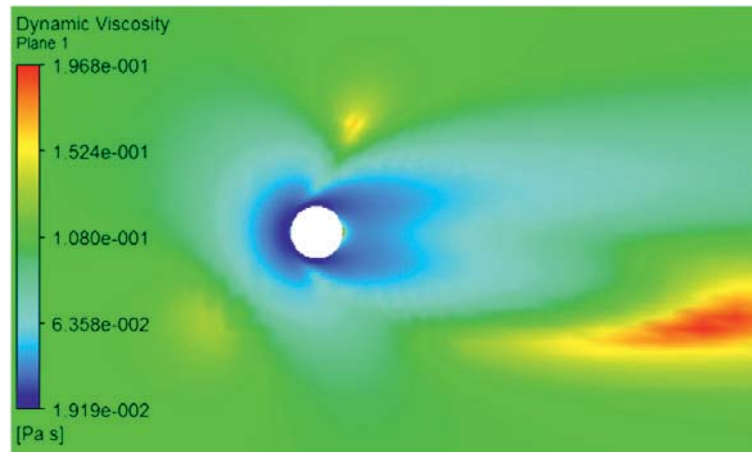
Figure 29: Viscosity field of a particle immersed in sheared non-Newtonian media.
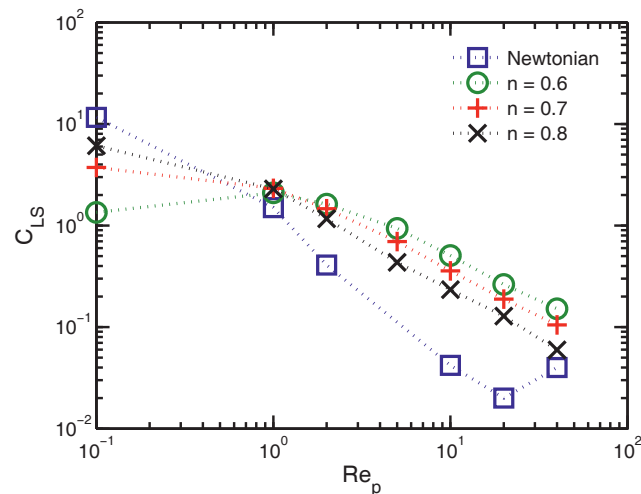
Figure 30: Lift coefficients for power-law index and particle Reynolds number, Re_p variation.

Two-fluid method

a) Validation

In the *Projektarbeit* of Zhang and Wang [Wang, 2012] the experimental results of Mäder [Mäder, 2012] were first compared with numerical simulations based on the Eulerian-Eulerian approach, also known as the two-fluid method. The simulations had the objective to analyze the capacity of this method to simulate dispersed flows with properties similar to the ones found in the cuttings transport problem. Two different implementations of the method were used: (1) the one offered by ANSYS-CFX Release 13.0 and (2) the one offered by OpenFOAM Version 2.0.0. Both codes offered matching results between them. Furthermore, comparisons with experimental results show the necessity to model the lift coefficient. Simulations using constant lift coefficients, showed poor matching with experimental results. In the case of the ANSYS implementation the Saffman-Mei model [Mei, 1992] was used. This is the option recommended by ANSYS for dispersed solid particles. In the case of the OpenFOAM implementation, no lift model was availa-

ble for Version 2.0.0. Therefore, first tests with lift models were performed with the ANSYS implementation. The same offered better matching with experimental results and it was decided to develop and include the Saffman-Mei model in the OpenFOAM implementation. Due to its higher flexibility in terms of model development, the use of the OpenFOAM library was favored for further numerical experiments. Results obtained with this implementation are compared for monodisperse experiments in Figure 31 and Figure 32 where good matching is observed. Details on the implementation are found in a paper submitted to the *International Journal of Multiphase Flow* [Aragall, 2015a].
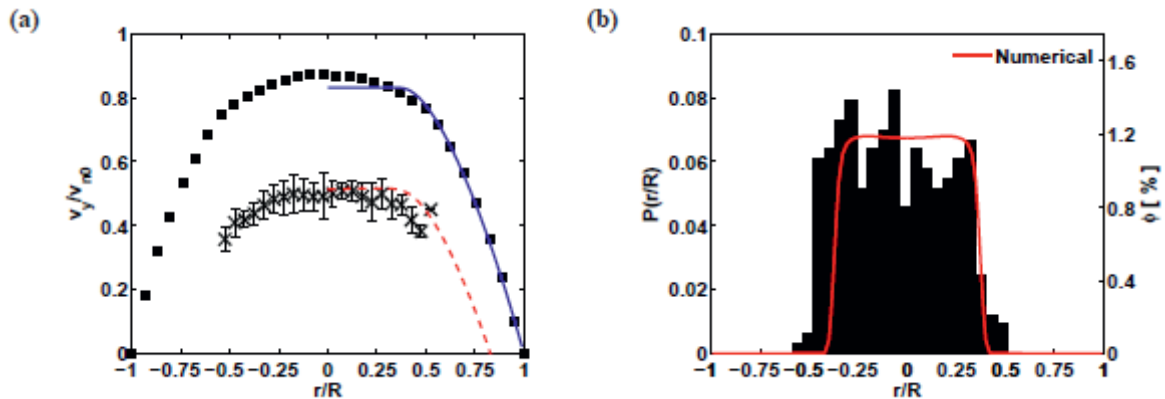
Figure 31: Exp. 7, $\phi_4 = 0.12\%$: (a) fluid and particle velocities at 1.6 meters from the entrance and (b) particle distributions and concentrations at the same position.
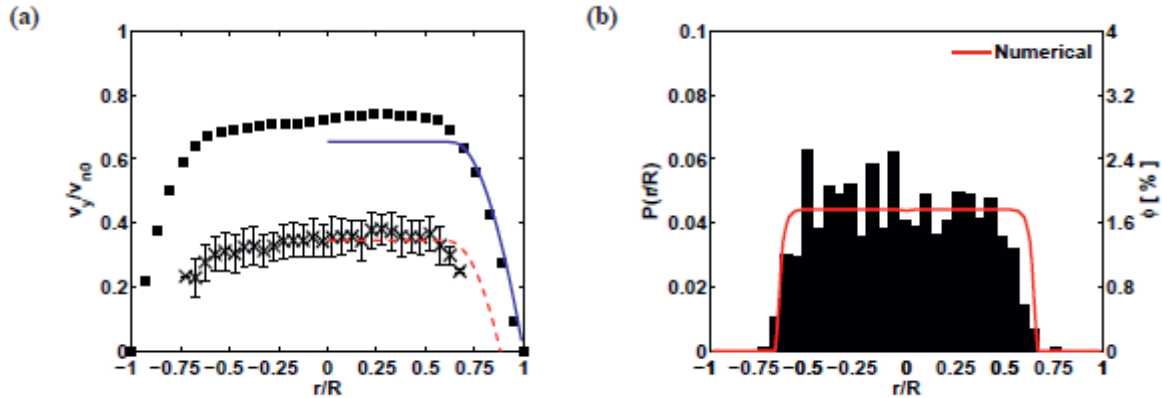
Figure 32: Exp. 10, $\phi_4 = 0.50\%$: (a) fluid and particle velocities at 1.6 meters from the entrance and (b) particle distributions and concentrations at the same position.

b) Sudden-expansion analysis

Results obtained with this implementation offered insight on the velocity and concentration development along the sudden expansion pipe used during the physical experiments. Such results may be observed in Figure 33. This simulation offers an example of a scenario, which takes place in conventional drilling when the drilling fluid transporting cuttings flows from a small casing towards a larger casing. The simulations indicate a large increase of the concentrations just in front of the expansion. This could produce clogging of the casing section. Further simulations with filed geometries should be conducted here to evaluate the relevance of this phenomena. A

475

more detailed analysis is found in a paper submitted to the *International Journal of Multiphase Flow* [Aragall, 2015a].
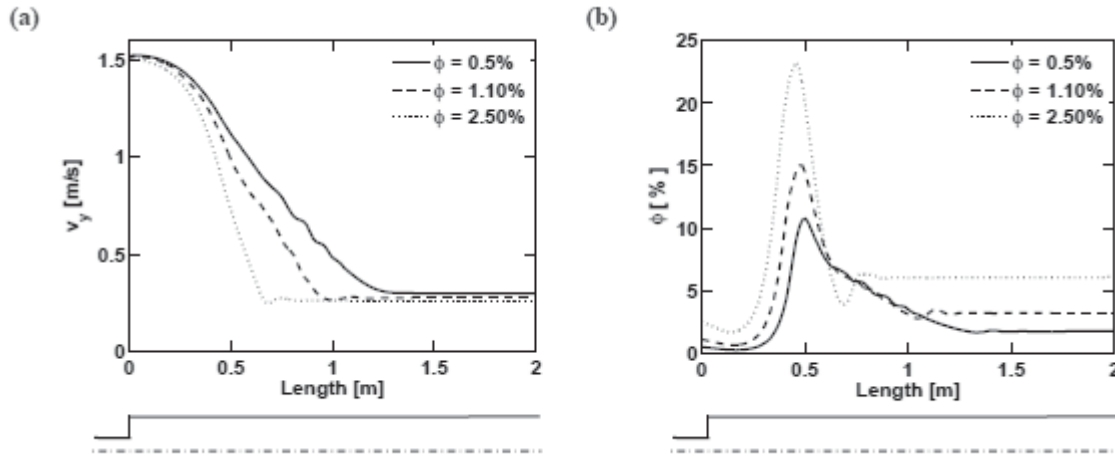
Figure 33: Numerical results of the concentration and fluid velocities along the axis for d_p = 4 mm particles and Re_c = 285: (a) fluid velocities along the axis and (b) particle concentrations along the axis.

CFD-DEM method

One of the limitations of the two-fluid model is the necessity to include rheological models for polydisperse systems. This is a very complex issue subject of active research in the multiphase flow modeling community. One alternative is the Eulerian-Lagrangian approach. This is based on the solution of the liquid phase through an Eulerian specification, where velocity and pressure fields are solved at fixed positions through the continuity and momentum equations 1.8, and solution of the solid dispersed phase through a Lagrangian specification, where the equation of motion 1.9 of the particles is solved following individual or groups of particles. Such approach drops the averaging of the particle equations of motion and reduces the necessity for closures to account for particle-particle interactions. This feature motivated the investigation of the capacity of the CFD coupling with the DEM method to simulate the experiments conducted in the ITM flow loop. The reason to select a DEM approach was due to the necessity to find modeling approaches also valid for horizontal transport problems, where wide distributions of concentrations are found. In this way, while in the upper layer semi-dilute concentrations are found, which can be modeled through two-way coupling, in the lower layer close packing requires a method able to consider contact between particles. This requires a method able to consider all the possible interactions. To perform the simulations the CFDEM implementation was selected. This is a coupling of two open source codes: (1) OpenFOAM for the Eulerian or CFD part and (2) LIGGGHTS for the DEM part.

$$
\begin{cases}
\dfrac{\partial}{\partial t}(\rho_f \alpha_f) + \nabla \cdot (\rho_f \alpha_f u_f) = 0 \\
\dfrac{\partial}{\partial t}(\rho_f \alpha_f) + \nabla \cdot (\rho_f \alpha_f u_f) u_f = -\alpha_i \nabla p + \rho_f \alpha_f g + \nabla \cdot \tau_i + n f_i
\end{cases}
\qquad 1.8.
$$

476

$$\begin{cases} m_i \dfrac{dv_i}{dt} = f_{pf,i} + \sum_{j=1}^{k_c} \left(f_{c,ij} + f_{d,ij} \right) + m_i g \\ I_i \dfrac{d\omega_i}{dt} = \sum_{j=1}^{k_c} \left(M_{t,ij} + M_{r,ij} \right) \end{cases} \qquad \text{1.9.}$$

The first step in the modeling using the CFD-DEM approach was the validation through comparison with the data acquired in the physical experiments. The validated simulations provided the basis for numerical investigations concentrated on determining the effect of eccentricity and inclination on the transport of polydisperse cuttings.

a) Validation

First validations of the model were performed through comparison with the experimental data obtained at the ITM flow loop. In contrast to the two-fluid model validation, in this case also bidisperse particle flows were considered. The same was performed within the frame of the *Master thesis* by Yu [Yu, 2014] started on 01.08.2013. As in the two-fluid model case it concentrated on the comparison of particle distributions and particle and fluid velocities at the experimental measuring position. In Figure 34 an example of the simulations performed for validation is shown.
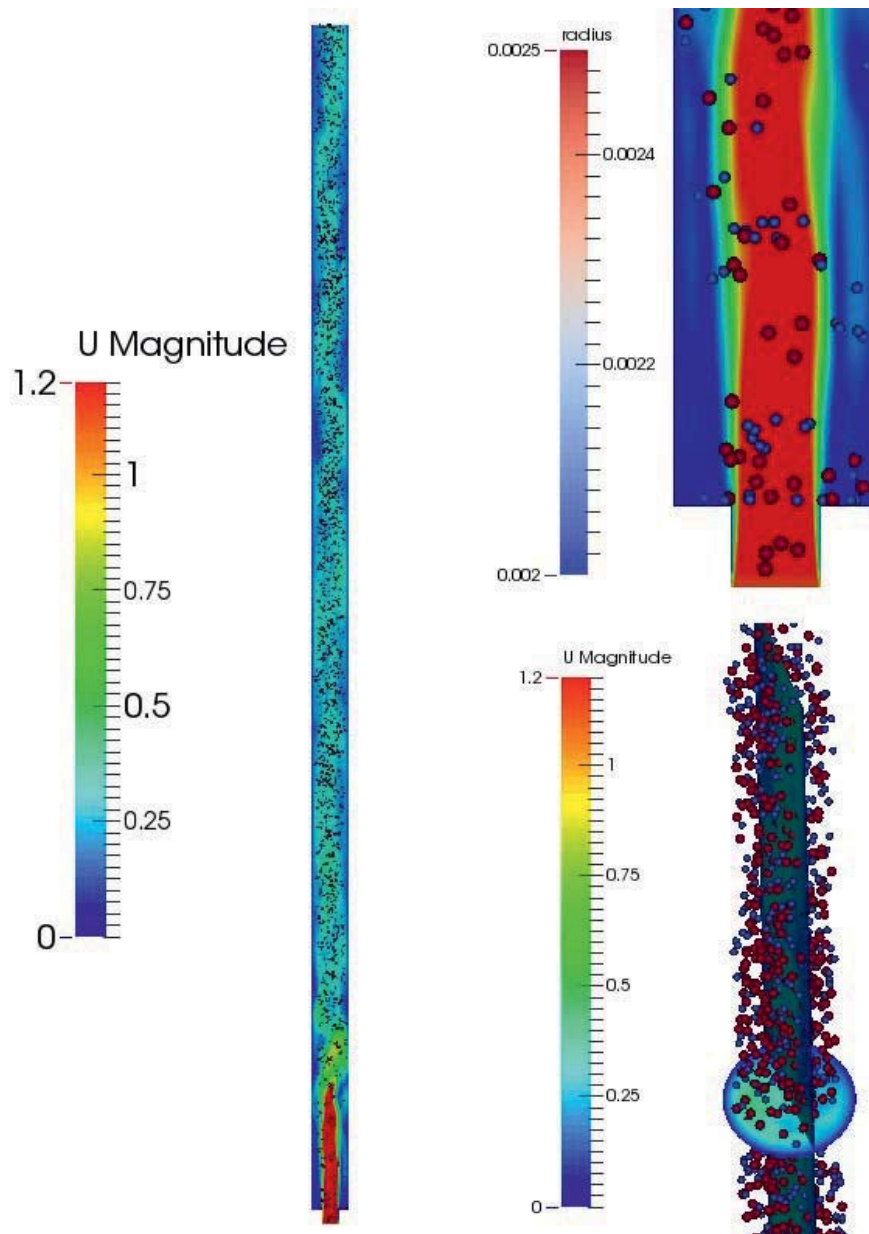
Figure 34: Views of experiment 21 [6] simulation through the CFDEM implementation.

In Figure 35 a comparison between experiment 10 [Aragall, 2015a] and a numerical simulation performed with CFDEM is shown. Comparison of figures Figure 35 (a) and (c) reveals a general good agreement. The most relevant differences are: (1) the symmetric velocity profile of the numerical simulations, whereas the physical experiments show a slightly unsymmetric profile caused by the experimental setup, and (2) the lower distribution of particle vertical velocities observed in the simulation. This is thought to be caused by the averaging of the liquid phase solution. Furthermore, in Figure 35 (b) and (d) it may be observed how the positions of the particles remain within the central core in both cases. This core matches with the region where the momentum transfer between phases induces flattening of the velocity profile. This suggests a proper modeling of the lift forces through the Saffman-Mei model [Mei, 1992].
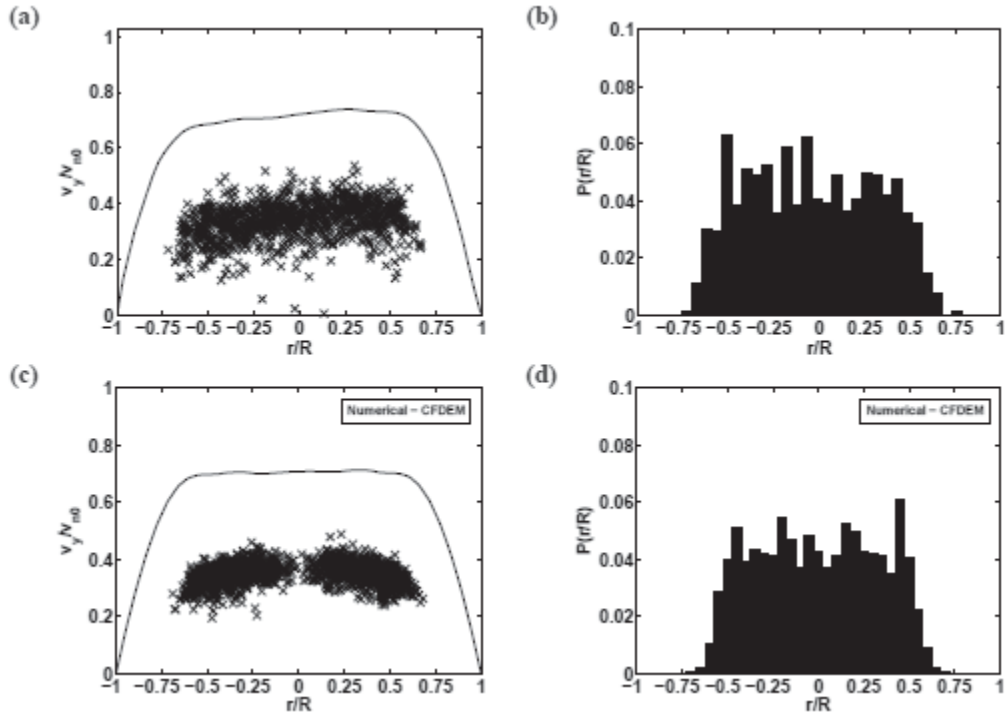
Figure 35: Vertical velocities of the 4 mm particles and normalized histograms of the particle positions for experiment 10 [Aragall, 2013], $\phi_4 = 0.12\%$. x, vertical velocities of the 4 mm particles, ---, locally averaged fluid velocity profile: (a and b) physical experiment and (c and d) numerical simulation with CFDEM.

In comparison to the experiments with monodisperse systems, bidisperse systems offer a less satisfying matching. This may be observed in Figure 36 (a and b). There it is observed how the simulations under predict the amount of momentum transfer between liquid and dispersed phases. While in the experiments the velocity profile is flattened in the inner core region and present peaks at the edges, in the simulations the inner core is narrower and no peaks are observed. The peaks on the edges are caused by the lower local concentrations at those regions, which translate in lower apparent viscosity. Thus, producing velocity profiles resembling those found in flows through packed beds, where wall channeling is observed. Furthermore, the larger velocities predicted in the simulations cause larger velocities of both dispersed species. The reasons why the simulations are not able to capture the previous behavior need to be further investigated. A possible cause is the non inclusion of the virtual mass force in the simulations.
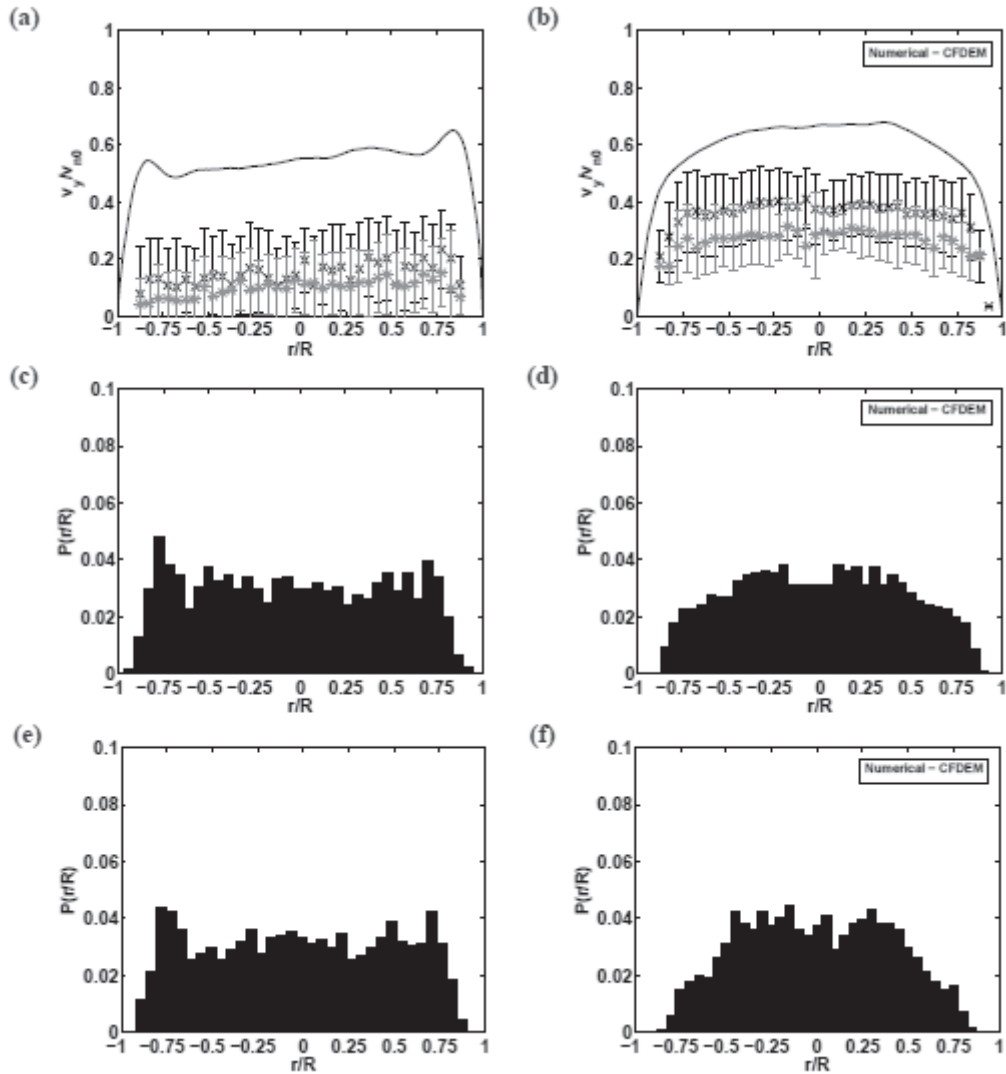
Figure 36: Fluid and particle velocity profiles and particle distributions for bidisperse system experiment 37 [Aragall, 2013], ϕ_4 = 1.50%, ϕ_5 = 1.50%. x, average vertical velocities of the 4 mm particles, I, standard deviation for particles velocity, *, average vertical velocities of the 5 mm particles, I, standard deviation for 5 mm particles, ---, locally averaged fluid velocity profile: (a) Physical experiment velocity profiles, (b) simulation velocity profiles, (c) physical experiment 4 mm particles distribution, (d) simulation 4 mm particles distribution, (e) physical experiment 5 mm particles distribution and (f) simulation 5 mm particles distribution.

Considering the previous results, it was decided to continue the numerical experiments with CFD-DEM coupling regarding only monodisperse systems, while bidisperse systems should be further analyzed. These experiments had the objective to understand the effect of eccentricity in vertical transport and inclination and horizontal transport.

b) Cuttings transport through eccentric annuli analysis

The analysis of eccentricity on cuttings vertical transport was performed within the frame of a *Bachelor Thesis* by Dai [Dai, 2014] between 01.09.2013 and 31.06.2014. The main idea was to conduct a sensitivity analysis centered on the eccentricity parameter, but also considering variation of complementary parameters present in the wellbore (particle diameter, flow rate, dynamic

viscosity and particle volume fraction). To quantify such effects, distribution, C_0, and drift-flux velocity, v_{sj} coefficients were generated through numerical simulations. These coefficients may be generated when the flow field and volume fraction on a particular cross-section are precisely described. The same are defined in equations 1.10 and 1.11, where ε is the local solid volume fraction, j_M is the mixture local volumetric flux, E_s is the solid cross-sectional average *in situ* fraction, V_M the mixture average velocity and v_{sj} is the local solid drift velocity. Precise definition of the previous parameters may be found in the *Bachelor Thesis* by Dai [Dai, 2014]. As may be observed in figure Figure 37 (a), C_0=1 indicates homogeneous distribution of the concentration, (b) C_0<1 indicates concentration at the walls exceeding that at the center and (c) C_0>1 indicates concentration at the center exceeding that at the wall. C_0 values larger than one are preferable, since these translate in faster cuttings transport out from the well. On the other hand, the drift flux velocity coefficient v_{sj} may be seen as a more complex version of the settling velocity, since this is able to include the effects of local concentrations and fluid velocities. In the case C_0=1, the drift flux velocity is equal to the settling velocity $v_{sj} = v_{sett}$.

$$C_0 = \frac{\varepsilon_s j_M}{E_s V_M}$$

1.10.

$$v_{sj} = \frac{\varepsilon_s v_{sj}}{E_s}$$

1.11.

(c)
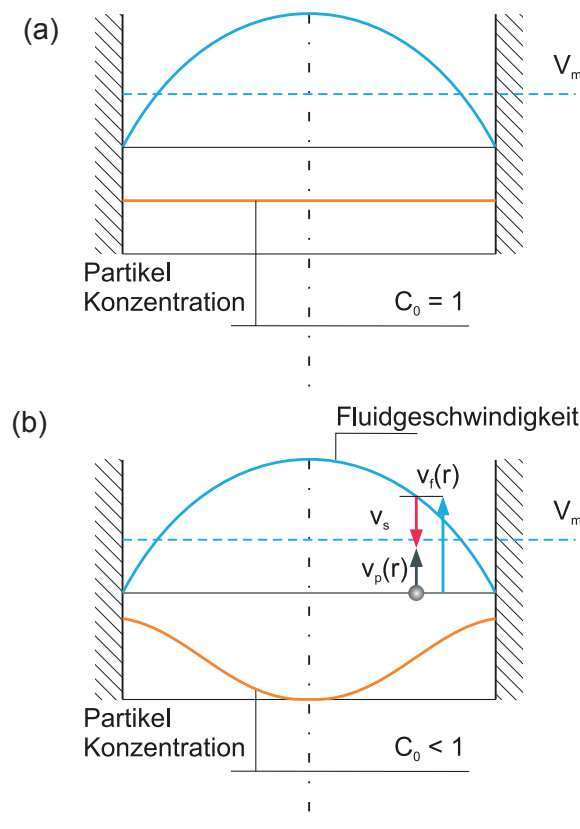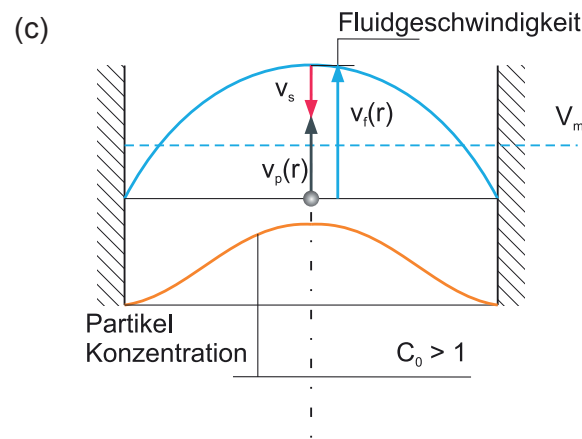
Figure 37: Graphical representation of the distribution coefficient C_0.

The simulations settings were based on findings generated in the *Master thesis* by Yu [Yu, 2014]. Furthermore, the simulations were conducted in a 1 meter long annular conduct, where periodic boundary conditions were implemented at the boundary cross sections. In Figure 38 an example of the discretized geometries is shown. In order to reduce the amount of simulations performed, an Optimal Space-Filling Design (OSF) of experiments was conducted. This one generated 9 basic experiments with variation of the complementary parameters, which should be investigated under variation of the eccentricity parameter, namely concentric and 25%, 50% and 80% eccentricity. Table 13 shows the values of the 9 basic experiments.
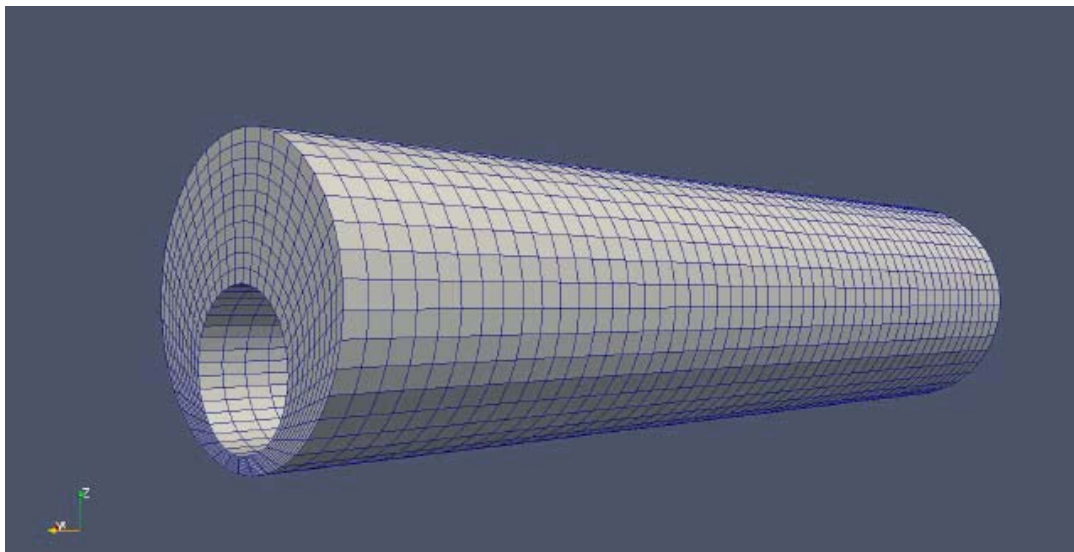
Figure 38: Discretized geometry of a 1 meter long annular conduct with 80% eccentricity.
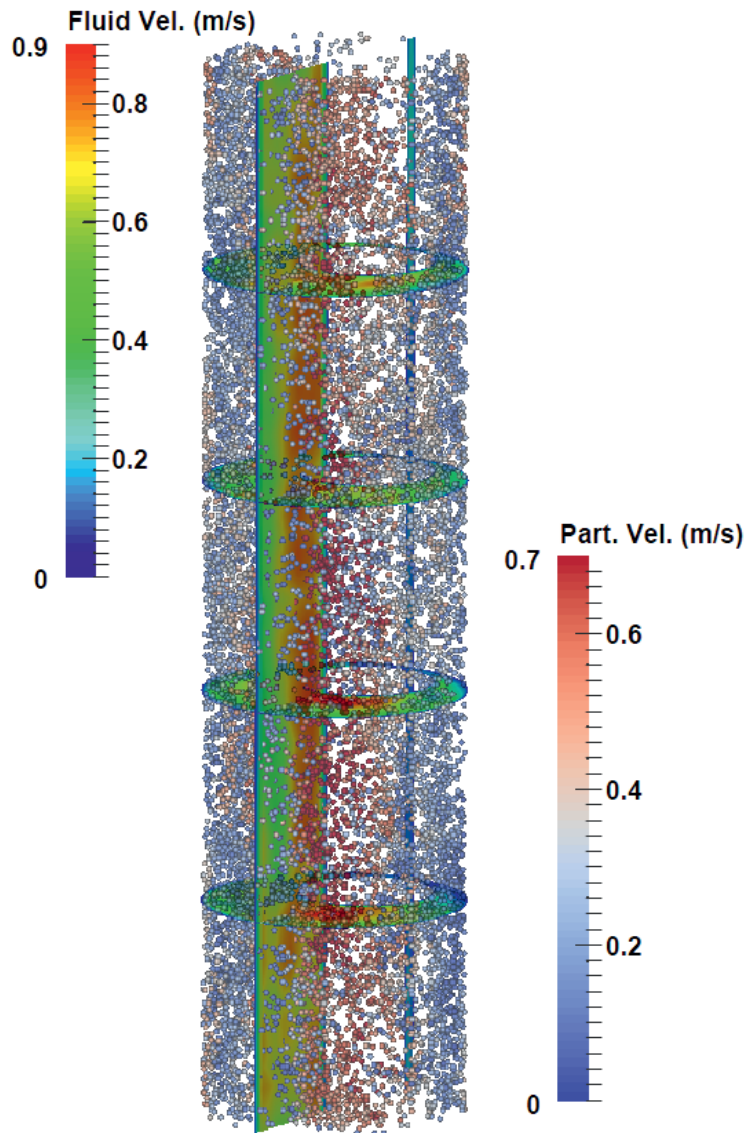
Figure 39: Contours of instantaneous fluid velocity and particle velocities in an 80% eccentric annulus corresponding to experiment #6 (16,276 particles simulated).

Table 13: Complementary parameters for the basic experiments.

Basic Experiment	Particle diameter dp (mm)	Fluid average velocity uf (m/s)	Dynamic viscosity η (Pa·s)	Particle volume fraction ε (%)
1	5	0.6	0.075	5
2	4	0.7	0.05	5
3	6	0.5	0.03	2.5
4	4	0.6	0.075	1
5	5	0.7	0.05	2.5
6	6	0.5	0.03	5
7	4	0.6	0.075	2.5
8	6	0.7	0.05	1
9	5	0.5	0.03	1

In order to guarantee the statistical convergence of the numerical results, test simulations were conducted to determine simulation time necessary to reach stability of the average fluid velocity. In this way, it was determined that the simulations should be run 80 seconds (simulation time) before results are saved. Once this time was reached, results were saved during the 10 following seconds (simulation time).

In Figure 40 the results for the distribution coefficient, C_0 are shown for the whole study. The comparison between experiments allows identification of a general trend, which is the larger value of the distribution coefficient C_0 in concentric geometries. This agrees with observations made in the field and in previous studies. This being said, it is also observed that eccentricity is not the predominant parameter affecting the particle distribution. In experiments 4, 8 and 9 the largest C_0 values are obtained. These correspond to experiments performed at the lowest concentration (1%). This trend is confirmed by the more uniform distributions observed in experiments 1, 2 and 6 where the largest concentration (5%) was simulated. Furthermore, higher viscosity seems to concentrate the particle at the center as observed in experiments from 1 to 6. This is not the case in experiments from 7 to 9, where the lowest concentration of experiments 8 and 9 exceed the effect of viscosity. Finally, both particle diameters and average velocities generate more homogeneous concentrations and therefore C_0 close to one for lower values. However, their effect is not as significant as that one of concentration in the range investigated.
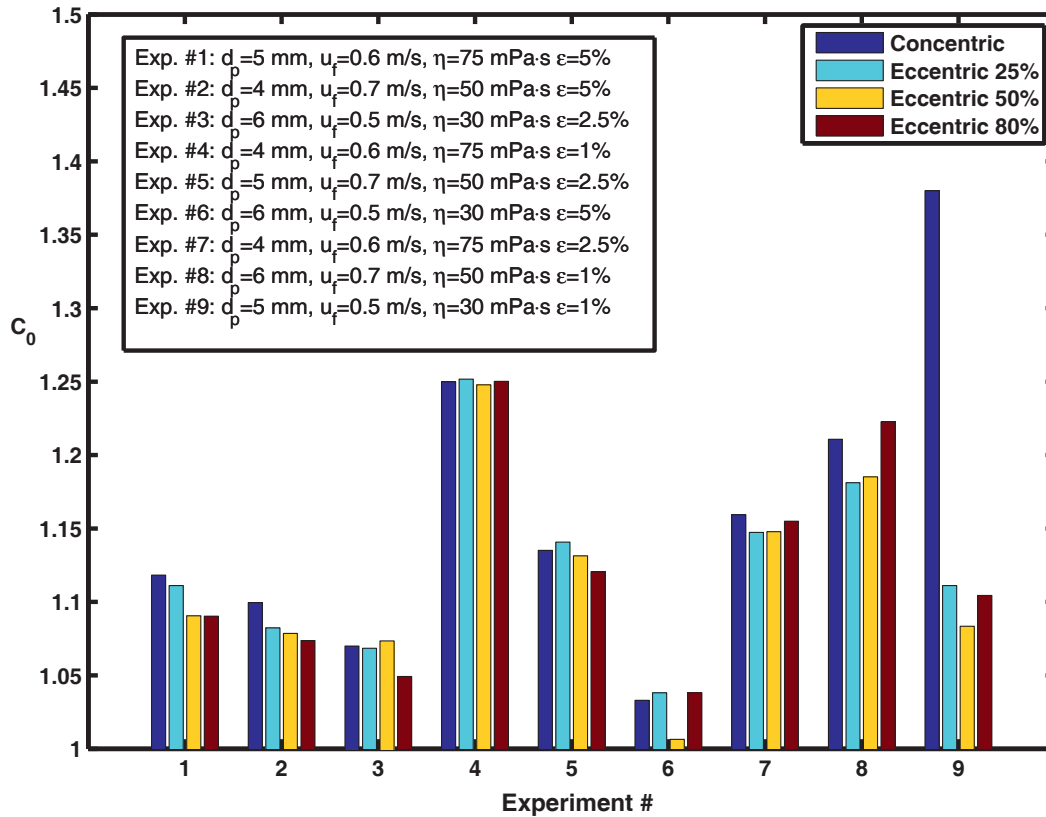
Figure 40: Bar diagram of the distribution parameter, C_0,
for the 9 basic experiments and different eccentricities.

Figure 41 shows the drift flux velocities of the solid particles v_{sj} for the whole study. For this co-efficient the effect of eccentricity is less prominent. In fact, only experiments 4 and 9 show relevant differences as a function of eccentricity. Furthermore, concentration is again here an important parameter. It is observed how larger concentrations result in slower drift flux velocities v_{sj}. This agrees with correlations considering the volume fraction for settling velocities, as that one by Richardson & Zaki [Richardson, 1954]. Contrary to the distribution coefficient case, particle diameters play a more important role for the drift flux velocity. This is also the case for viscosity. Average fluid velocities do not seem to influence this coefficient significantly.
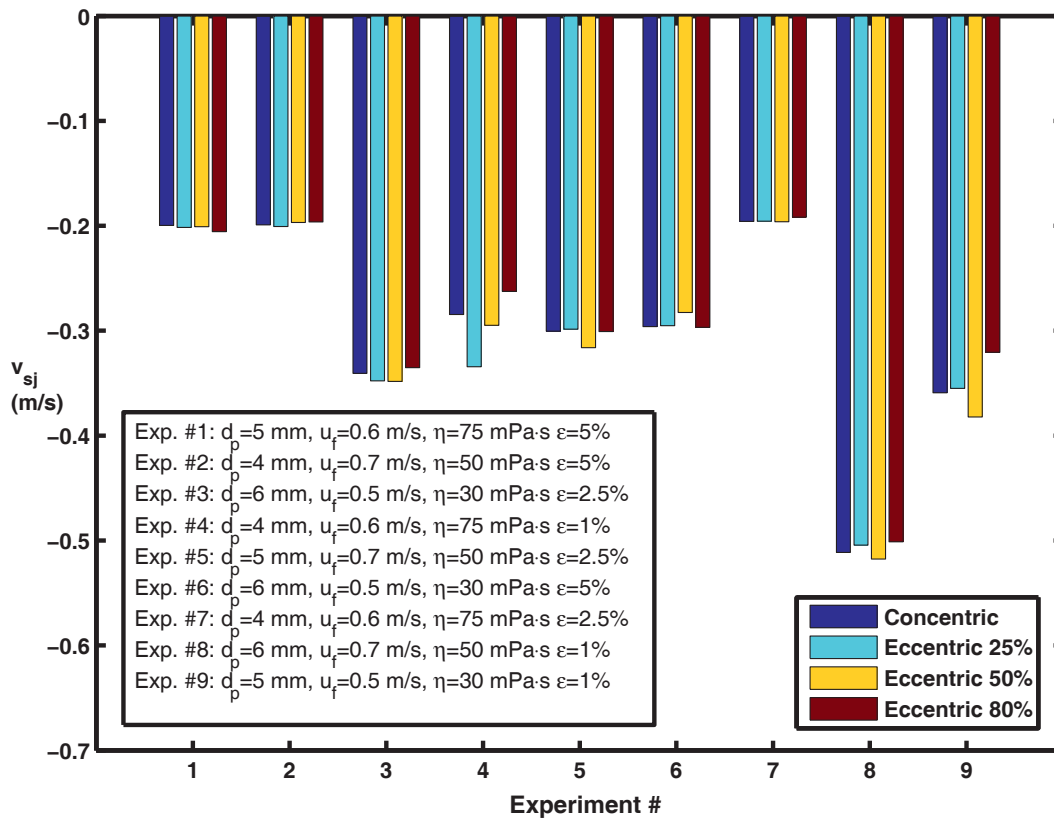
Figure 41: Bar diagram of the dirft flux velocity, v_{sj}, for the 9 basic experiments and different eccentricities.
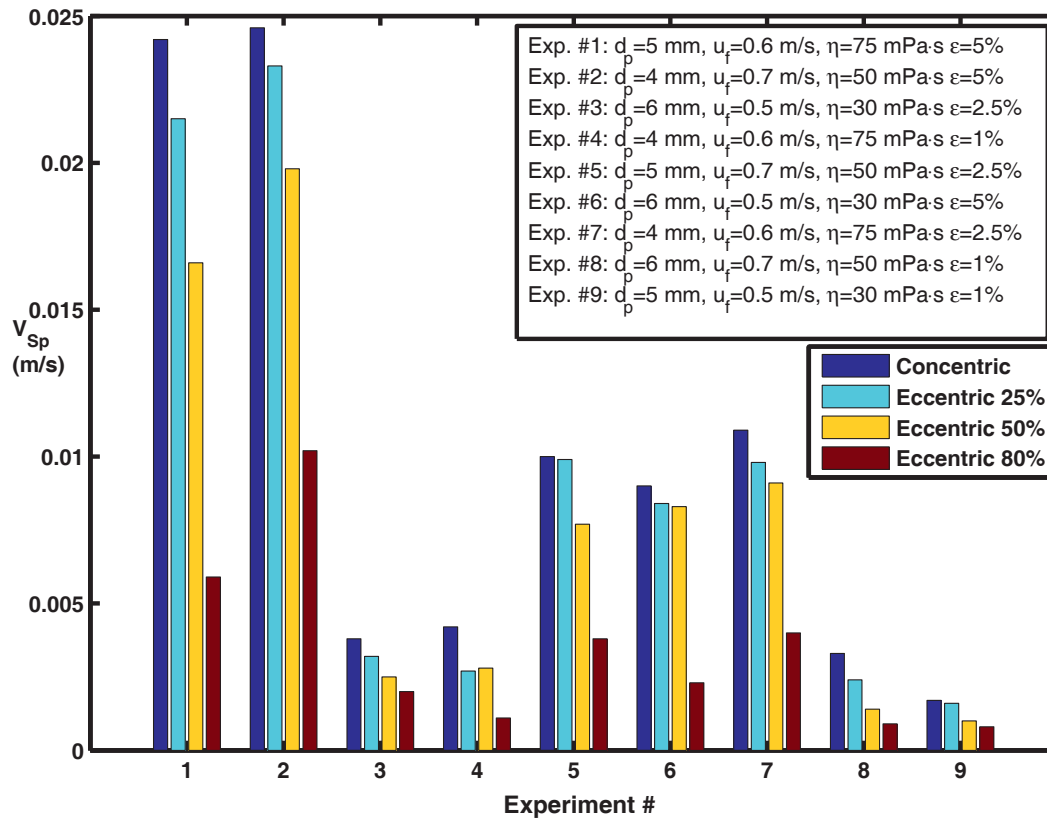
Figure 42: Effect of eccentricity on cuttings superficial velocity, V_{Sp}.

Conclusions

AP5 has supplied several data sets concentrated on different length scales. These had the objective to generate constitutive equations for models considering the complete well bore length in AP6. Several methods were used to prepare the simulations depending on assumptions taken. Single phase simulations were used to analyze the effect of eccentricity and bed heights on pressure losses in horizontal cuttings transport. Furthermore, the shear stresses on the cuttings beds were investigated. It was found that higher eccentricities towards the upper wall of the well bore could favor a better erosion of the cutting beds already formed. The way to accomplish these eccentricities should be further investigated, since the natural tendency of the drill string is to settle on the lower wall of the well bore, when not on top of the cuttings beds. Drag and lift coefficients for a static particle in a shear non-Newtonian flow were also investigated using single phase flow simulations. Significant differences compared to the Newtonian fluids were encountered. It is necessary to develop models considering these effects and include them in the modeling approaches focused on macroscopic phenomena. However, multiphase modeling approaches considering non-Newtonian rheology are still under development and subject of active research. Such multiphase modeling approaches, as the two fluid-model and the CFD-DEM coupling were investigated through comparison with the experimental data generated at ITM. It was possible to validate the Saffman-Mei [Mei, 1992] lift model for monodisperse suspensions

in Newtonian fluids. However, bidisperse suspensions required a more demanding approach such as CFD-DEM. Investigations with this method were also conducted showing good agreement for monodisperse suspensions. Bidisperse suspensions require further work. Once validation was completed, simulations analyzing the effect of a sudden expansion on the dispersed solid transport were conducted with the two-fluid model. These showed large concentration increases just in front of the expansion. This could cause blockage problems if they are not carefully considered. On the other hand, the CFD-DEM coupling was used to investigate the effects of eccentricity on dispersed solids transport. While the distribution coefficient C_0 was notably affected, other parameters were found to have a bigger influence. Models quantifying such influences should be developed. In the case of the drift flux velocity v_{sj}, the parameters affecting the settling velocity are the most relevant ones. Therefore, it is recommended to focus on the modeling of the distribution coefficient C_0 and predict the drift flux velocity v_{sj} through available settling velocity correlation models.

M 2 - Work in the AP4 and AP5 was completed after reaching the second Milestone. With it, information related to the behavior of coarse suspensions in annular ducts was gained. The same offered a better understanding of the process, which was used to find convenient modeling approaches.

AP 6 - Preparation of the parameter model

The content of AP6 includes the development of a parameter model able to consider multiple process variations to optimize the drilling progress. The model should reliably represent the relevant physical phenomena found in cuttings transport. Moreover, it should integrate findings from AP 4 and AP 5, as well as Project B6. As a further result, data for the modeling of drill string oscillations (damping through fluid) should be provided to Project B7.

<u>Modeling approach</u>

The model developed for the whole trajectory of the well needs to fulfill the requirements of speed and robustness. As commented in AP 5 this demands relatively simple and coarse models not able to resolve phenomena taking place at lower scales. Such information needs to be supplemented through constitutive equations or calibration parameters. Furthermore, the model should consider the transport of two phases, which requires the use of multiphase approaches. It is also relevant to include the effects of the heat transferred from the geologic formation to the drilling fluid because rheology and density are strongly dependent on temperature. The multiphase nature and the thermal dependency of the transport convert the problem into highly transient. Therefore, the model should also consider the time dependency in its predictions. The following input parameters need to be considered in the model:

1. Wellbore length and diameter
2. Drilling fluid flow rate
3. Fluid rheology and density
4. Rate of Penetration (ROP)
5. Cuttings size and density
6. Eccentricity
7. Rotation
8. Heat transfer relevant parameters

The parameter model is based on the drift-flux model, whereas it incorporates the effects of heat transfer from geologic formation through the energy conservation equation. The utilization of the drift-flux model is justified when the relative motion between cuttings and fluid is governed by an external force such as gravity and, as a good approximation, the magnitude of the external forces acting on the cuttings is a simple function of the magnitude of gravity, g, of the volume fraction, α, and the physical properties of the cuttings and the drilling fluid (densities, ρ_c and ρ_f, and drilling fluid viscosity, η_f) [Brennen, 2005]. Furthermore, operational parameters such as flow rate, eccentricity and rotation, may be integrated in the development of the function describing the magnitude of this force, which determines the velocity of the dispersed phase. The drift-flux model considers one momentum and one continuity equation for the description of the mixture transport (equations 1.12. and 1.13.) and one continuity equation for the description of the cuttings transport (equation 1.14.).

$$\frac{\partial A\rho_m}{\partial t} + \frac{\partial A\rho_m V_m}{\partial s} = 0 \tag{1.12.}$$

$$\frac{\partial A\rho_m V_m}{\partial t} + \frac{\partial A\rho_m V_m^{\,2}}{\partial s} = -A\frac{\partial p}{\partial s} + A\rho_m\, g\cos\phi - A\Delta p_v \tag{1.13.}$$

$$\frac{\partial \rho_d \alpha_d}{\partial t} + \frac{\partial \rho_d \alpha_d V_d}{\partial s} = 0 \tag{1.14.}$$

Furthermore, it is necessary to provide the relation between both phases

$$\alpha_d + \alpha_f = 1 \tag{1.15.}$$

The coupling with the mixture equations is done through the mixture velocity, V_m, and two calibration parameters shown in equation 1.16. and introduced in *work pa ckage* AP 5, which are the distribution coefficient, C_0, and drift-flux velocity, v_{sj}. Development of functions for the calibration parameters need to be generated through physical or numerical experiments considering the variation of the parameters affecting the relative motion between phases, as already commented in AP 4.

$$V_d = C_0 V_m + v_{sj} \tag{1.16.}$$

$$\frac{\partial \rho_d \alpha_d}{\partial t} + \frac{\partial \rho_d \alpha_d V_m C_0}{\partial s} = -\frac{\alpha_d \rho_d v_{sj}}{\partial s} \tag{1.17.}$$

Constitutive equations

Information about two particular subjects needs to be supplied through constitutive equations or closure relations. These are frictional pressure losses and cuttings velocity. All of them are very sensitive to viscosity and density. Therefore, before calculation of the transport parameters, fluid properties need to be determined according to the temperature and pressure found at the particular location and instant in time. Once this is done, they can be used as inputs in the constitutive equations. This requires the generation of an extensive data base considering the physical properties of any fluid eventually used in the simulations.

Pressure loss correlations need to consider the possible non-Newtonian nature of the drilling fluid, the cross-sectional geometries along the well-bore length and the rotation of the drill-string. All these factors together with the flow rate are used to determine the regime (laminar, transient or turbulent), which plays a crucial role in the selection of proper pressure loss correlations. Several correlations have been put forward in order to include these factors. The one initially used in the implementation by Hahn [Hahn, 2013] was taken from a paper by Naganawa [Naganawa, 2006]. In spite of that, the code was implemented in such a way, that new pressure correlations and turbulence transition criteria are easily modified. The final version of the code should include several options according to the drilling fluid used or the conditions found. This is the subject of many of the research performed in relation to drilling hydraulics and it still poses several open questions.

The second parameter, which needs to be supplemented, is the cuttings velocity. This parameter is dependent on the fluid properties, cuttings properties and operating conditions. A one-dimensional homogenous approximation assumes the settling velocity as the only parameter affecting the cuttings velocity. However, when the velocity and concentration profiles are independent of each other this is not always the case. Such profiles are the result of effects not resolved with one-dimensional models. Therefore, it is necessary to supply this information through other mechanisms. In the drift-flux model this is done through two empirical parameters: (a) the distribution coefficient and (b) the drift flux velocity, which need to be investigated for every possible condition. The distribution coefficient supplies information in relation to the distribution of the phases. Distribution coefficients greater than one indicates location of the dispersed phase at locations where the velocity of the mixture is higher. On the other hand, distribution coefficients lower than one indicates location of the dispersed phase there where velocities are lower. The drift flux velocity supplies information in relation to the local difference of velocities between phases, which may be affected by concentration or thermal gradients. The one-dimensional homogenous approximation is a particular case of the drift-flux model, where the distribution coefficient is equal to one and the drift-flux velocity is equal to the predicted settling velocity. This case was used to perform the first verification of the implemented model.

Discretization

The discretization and solving algorithm implementation was performed within the framework of the *Bachelor Thesis* by Hahn [Hahn, 2013] between 31.06.2013 and 31.12.2013. The method selected for the discretization of the drift-flux model was the finite-volume-method. This one is a direct extension of the control volume analysis and offers a clear procedure for deriving the necessary algebraic equations. The discretization of the complete length of the well is performed using a uniform mesh and time is discretized with fixed time steps. In the frame of the *Bachelor Thesis* by Hahn [Hahn, 2013], the *2nd order upwind* differencing scheme was selected. This discretization scheme ensures stability with a reduced complexity during the discretization process. However, this is paid at the cost of having numerical diffusion. Such diffusion may be counteracted by increasing the number of computational cells. An important question to answer is then how many cells are necessary to keep numerical diffusion at a required limit and how does it translate into computing time considering computational resources available at different stages of the model utilization.

Solution algorithm

The system of equations generated through discretization of the governing equations is solved through the transient SIMPLE-Algorithm (Semi-implicit Method for Pressure Linked Equations). This one is an iterative procedure, which starts by guessing a pressure field to solve the momentum equation. The obtained solution is then used to determine a new pressure field calculated through proper manipulations of the continuity equation. When a certain tolerance is reached in relation to the velocity and pressure fields variation, additional equations considering the transport of cuttings and heat are solved. Afterwards, the next time step is initially calculated by using the previous pressure field or, if the final time step is reached, the solution procedure is stopped.

Output of the model

The output of the model consists of six variables solved along the length of the well-bore with respect to time: (1) pressure, (2) velocity, (3) concentration, (4) density, (5) sink velocity and (6) temperature. In Figure 43, six diagrams are depicted, where the horizontal axes correspond to these variables and the vertical axis corresponds to depth. In this particular example, the results correspond to a simulation with conditions listed in Table 14 after 2 hours, 12 minutes and 55 seconds from the start of drilling operations. The ROP and flow rate during the first 72 minutes were respectively 18 m/h and 152 m³/h. After that moment, the ROP was increased to 36 m/h and 12 minutes later the flow rate was increased up to 286 m³/h. The diagrams show a pressure diagram almost linearly increasing, whereas the velocity is at this specific moment equal to 1.5 m/s. Concentration and density diagrams show variations caused by the varying ROP and flow rates. Both last variables show very similar trends, since these are directly related. On the right

491

side of Figure 43, sink velocity and temperature are shown. Temperature increases with depth due to transfer of heat from the formation. Similarly, sink velocity increases because of the influence of temperature on the viscosity of the transporting liquid.
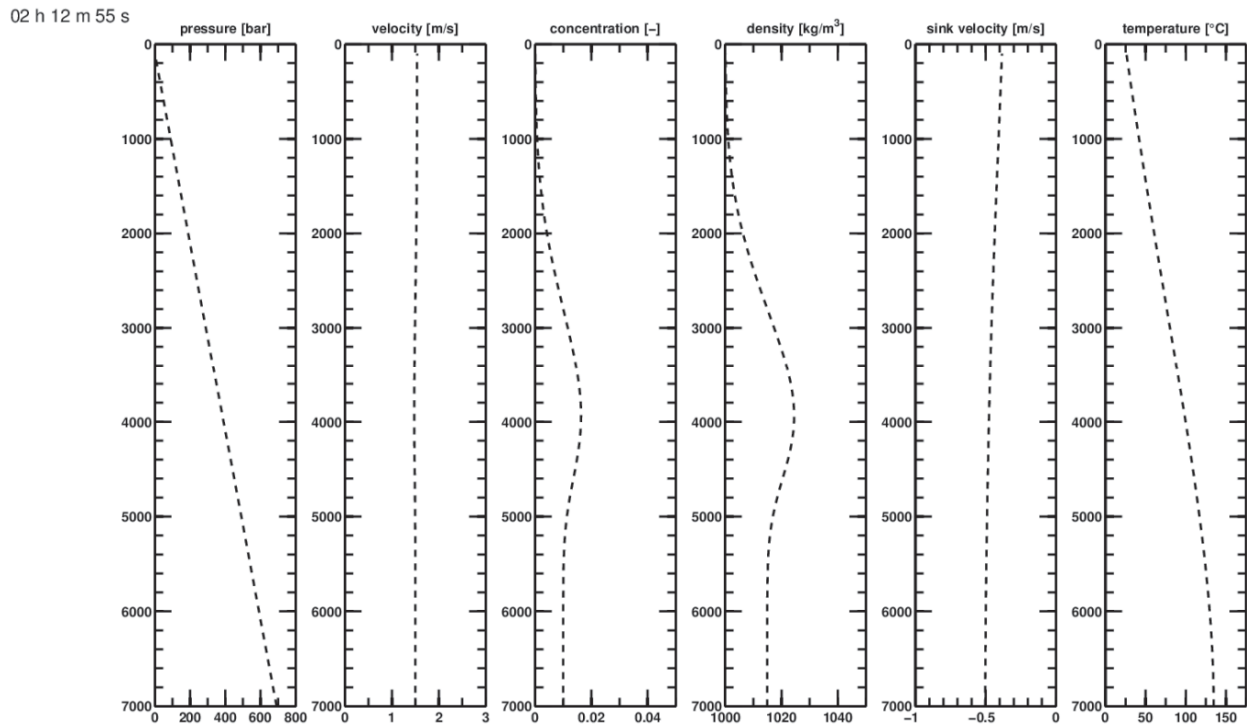
Figure 43: Output of the implemented Drift-Flux model

Table 14: Simulation input conditions

Parameter	Value
Well-bore depth (m)	7,000
d_{hole} (mm)	300
d_{string} (mm)	150
ROP (m/h)	(1) 18 / (2) 36
Q (m³/h)	(1) 152 / (2) 286
ρ_f (kg/l)	1
μ (mPa·s)	Water
dp (mm)	3
ρ_s (kg/l)	2.5

Conclusions

A model has been proposed and implemented to consider transient cuttings transport. The model is able to consider vertical sections and it can be extended to deviated and horizontal sections by coupling it with a two-layer or three-layer model. The model is able to consider the effects of temperature on the physical properties of the drilling fluid by using the energy conservation equation. However, a reliable data base is necessary to perform the coupling. It was foreseen to supply this data through the tasks performed in work package AP2. As already explained in the corresponding section, the selection of candidate drilling fluids requires a detailed

drilling program. Therefore, once this definition is obtained, the selection of the indicated drilling fluid should be performed and in case no already available data exists, an extensive analysis shall be conducted. The data or analysis should supply values of density, rheology, heat capacity and heat conductivity as a function of pressure and temperature.

A possible improvement of the model could be the transport of distribution functions, instead of scalars as it is currently done through the transport of a particular cuttings size. This could be performed through implementation of the method-of-moments. However, it requires a previous extensive and exigent analysis.

M 3 - With Milestone 3 the formulation of the model parameters is carried out and t he relevant information is delivered to the partners in Project B1 and B2.

The reformulation of project B2 requires a deeper consideration of the requirements of the cuttings transport model. Therefore, the following of recommendations by BHI on the development of transient models was favored.

AP 7 - Model verification and evaluation of wellbore scenarios

<u>Verification</u>

Two parameters were used to confirm the model was correctly implemented: (a) holdup and (b) pressure. The holdup effect is caused by the density difference of the drilling fluid and the cuttings. The same translates in a velocity difference between both phases, which causes the average in-situ fraction of the cuttings to be different from the cuttings fraction supplied into the system. Govier and Aziz [Govier, 1972] give an account of relations between average in situ fraction of a dispersed phase (in this case the cuttings) (equation 1.18.) with mixture velocity, average slip velocity and the fraction of cuttings supplied into the well-bore defined respectively in equations 1.19., 1.20. and 1.21.

$$E_c = \left(\frac{V_M + S}{2S}\right) - \left[\left(\frac{V_M + S}{2S}\right)^2 - \frac{V_M C_c}{S}\right]^{1/2} \qquad 1.18.$$

$$V_M = V_{Sc} + V_{Sf} = \frac{Q_c + Q_f}{A} \qquad 1.19.$$

$$S = V_f - V_c \qquad 1.20.$$

$$C_c = \frac{Q_c}{Q_c + Q_f} \qquad 1.21.$$

In order to perform the verification, mixture velocities, V_M, supplied cuttings fractions, C_c, and slip-velocities, S, similar to those possibly found during the drilling of a well-bore were selected. The comparison, shown in the *Bachelor Thesis* by Hahn [Hahn, 2013] showed perfect matching with in-situ concentrations calculated through the implemented drift-flux model. Furthermore, the total pressure drop composed by the hydraulic column and the pressure losses due to friction

along the annular section of the well-bore was compared with correlations of one single-phase fluid flowing through an annular section. These ones also offered perfect matching with the pressure drops offered by the implemented model.

Numerical diffusion

After verification, an analysis of the numerical diffusion due to the discretization of the model with the *2nd order upwind* scheme was performed. Ideally, the concentration progress of the cuttings should appear as a step function with a sharp edge. In this case, the degree of numerical diffusion may be quantified through the length between the concentrations in the wellbore before starting the process, i.e. null, and steady holdup reached for conditions specified in Table 15. Conditions listed in Table 15 are selected considering characterization of the gebo wellbores in *work package* AP1. As already commented, the numerical diffusion may be reduced by increasing the number of cells used to discretize the geometry. However, this increases the number of algebraic equations to be solved and consequently the computational time. In Table 16 the number of cells is put in relation with the numerical diffusion obtained and with the necessary time to compute a time step on a PC with 2 processors at 3 GHz. Likewise, Figure 44 shows the concentration development for two simulations with identical input conditions, but different number of cells. The time step is dependent on the number of cells because of the Courant Friedrichs-Lewy (CFL) condition, which limits time steps size in order to enforce convergence of the solution. In Table 16 it may be observed how 1400 cells would correspond to a real-time computation. Lower number of cells obtain faster results, but with significant numerical diffusion.

Table 15: Simulation input conditions

Parameter	Value
Well-bore depth (m)	7,000
d_{hole} (mm)	300
d_{string} (mm)	150
ROP (m/h)	18
Q (m³/h)	150
ρ_f (kg/l)	1
μ (mPa·s)	1
dp (mm)	4
ρ_s (kg/l)	2.5

Table 16: Analysis of the necessary computing time and the numerical diffusion

Number of cells	Time step (s)	Time step CPU time (s)	Numerical diffusion (m)
175	25	0.09	1000
350	12.5	0.17	720
700	7	0.85	640
1400	3	10	215
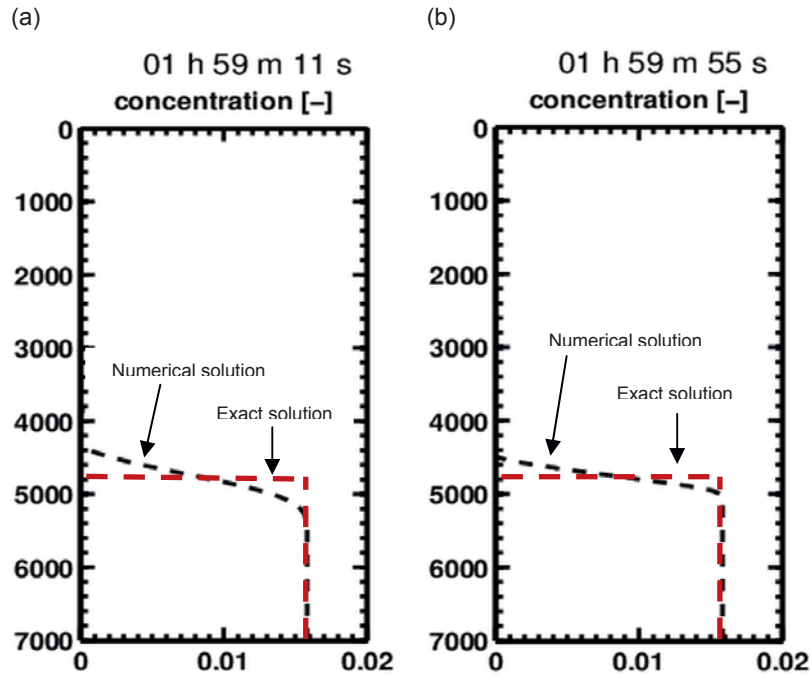
Figure 44: Comparison of the concentration development for simulation input conditions listed in Table 15 1 hour after drilling start (a) 175 cells and (b) 1400 cells

Sensitivity analysis

A sensitivity analysis considering the distribution coefficient and dimensions of the simulated well-bore following the characterization in *work package* AP1 is shown in this section. The simulation input conditions are listed in Table 17. The viscosity-temperature correlation is taken from a Newtonian fluid with slightly higher average viscosities than the ones obtained in drilling fluids mixtures located in AP2. The analysis investigates the effect of the distribution coefficient on the transport of the cuttings. As already commented in *work package* AP5, distribution coefficients greater than one indicates distribution of the cuttings concentrated on the region where higher velocities are found. On the contrary, distribution coefficients smaller than one indicates cuttings located at lower fluid velocity positions. In the case of the vertical transport of cuttings, this means that distribution coefficients lower than one are those where the particles are close to the walls. Considering that lift forces caused by shear rates will send the cuttings to more centered positions, such scenario can only take place when an additional force higher than the lift force

and in the opposite direction is present. Such force can be produced during rotary drilling, which originates centrifugal forces acting on the cuttings. The analysis done here limits itself to investigate the sensitivity of this parameter. Therefore, a more detailed analysis applying the models developed in *work package* AP5 should be performed. During the time span of the gebo project this was not possible. However, this is seen as a very interesting topic for future research.

Table 17: Simulation input conditions

Parameter	Value
Well-bore depth (m)	7,000
d_{hole} (mm)	300
d_{string} (mm)	150
ROP (m/h)	18
Q (m^3/h)	190
ρ_f (kg/l)	1
μ (mPa·s)	= 16.266 x T$^{-1.783}$
dp (mm)	6
ρ_s (kg/l)	2.5
Grid spacing (m)	10
Number of grids	700

The analysis was performed considering a 7000 meters deep wellbore where the maximum temperature reached at the bottom of the well is 150 °C. The simulation considers 5 hours of one scenario where during the first three hours of the drilling operation the ROP is of 18 m/h. The flow rate at the start is 110 m^3/h and it is increased up to 125 m^3/h after 1 hour and 15 minutes. The circulation is maintained at this flow rate until the end of the simulation. The resulting pressure, velocity, concentration, density, settling velocity and temperature distributions along the wellbore for C_0 = 1 are shown in **Figure 45**. Likewise, on Figure 46 the concentration distribution of the cuttings along the wellbore after 5 hours for three different distribution coefficients (C_0 = 0.8, 1 and 1.2) and the exact same boundary conditions are shown. Figure 46 (a) corresponds to C_0 = 0.8, which simulates a situation with high rotational speed of the drill string, Figure 46 (b) corresponds to C_0 = 1, which simulates a situation considering the current state-of-the-art assumptions of homogeneous particle distribution across the annular cross section and Figure 46 (c) corresponds to C_0 = 1.2, which simulates a situation where the lift forces maintain the cuttings at positions of maximum local velocities. Comparison of the three diagrams allows identification of two clear trends: (a) lower concentrations along the wellbore and (b) higher positions of the cuttings after 5 hours for the larger distribution coefficients. This would have large impact on the clogging potential and the time necessary to get the cuttings out of the well, translating in higher operating costs. Moreover, peaks of concentration are observed at the end of the cuttings distributions. These are caused by the larger settling velocities found at deeper po-

sitions, as shown in Figure xxx, and originated by the temperature gradient of the fluid. While these show a small overshot for C_0 = 1 and C_0 = 1.2, the situation for C_0 = 0.8 is more critical. Due to previous careful selection of the flow rates, in this scenario concentrations do not go above the limiting concentration 5% prescribed by Pigott [Pigott, 1942]. However, in real field
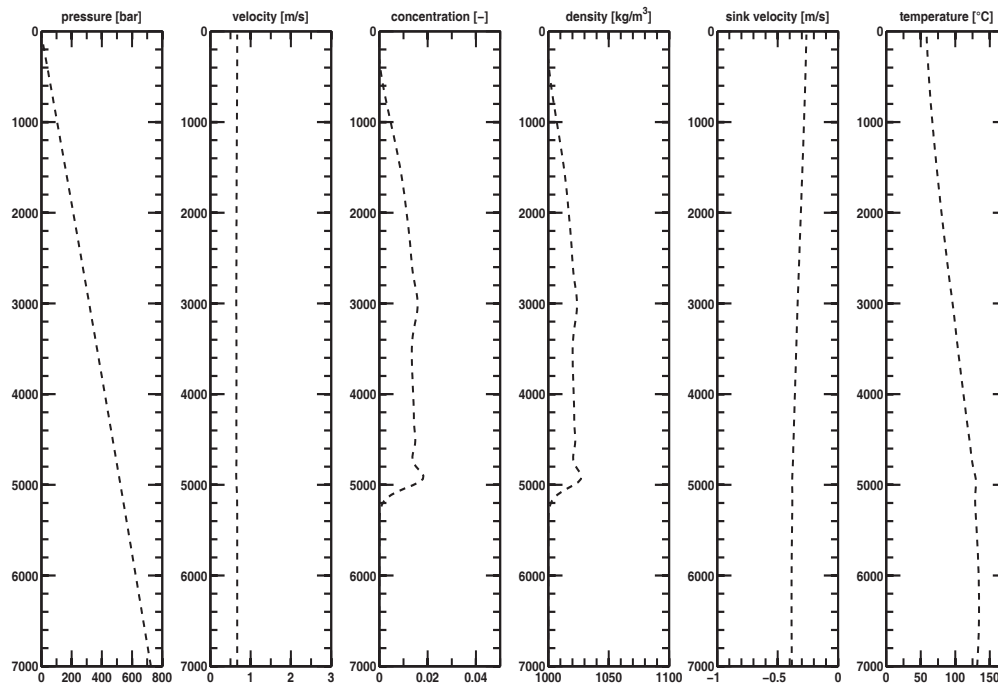
Figure 45: Pressure, velocity, concentration, density, settling velocity and temperature distribution along the wellbore for the simulation input conditions and the scenario described in the distribution coefficient sensitivity analysis after 5 hours for C_0 = 1.2.
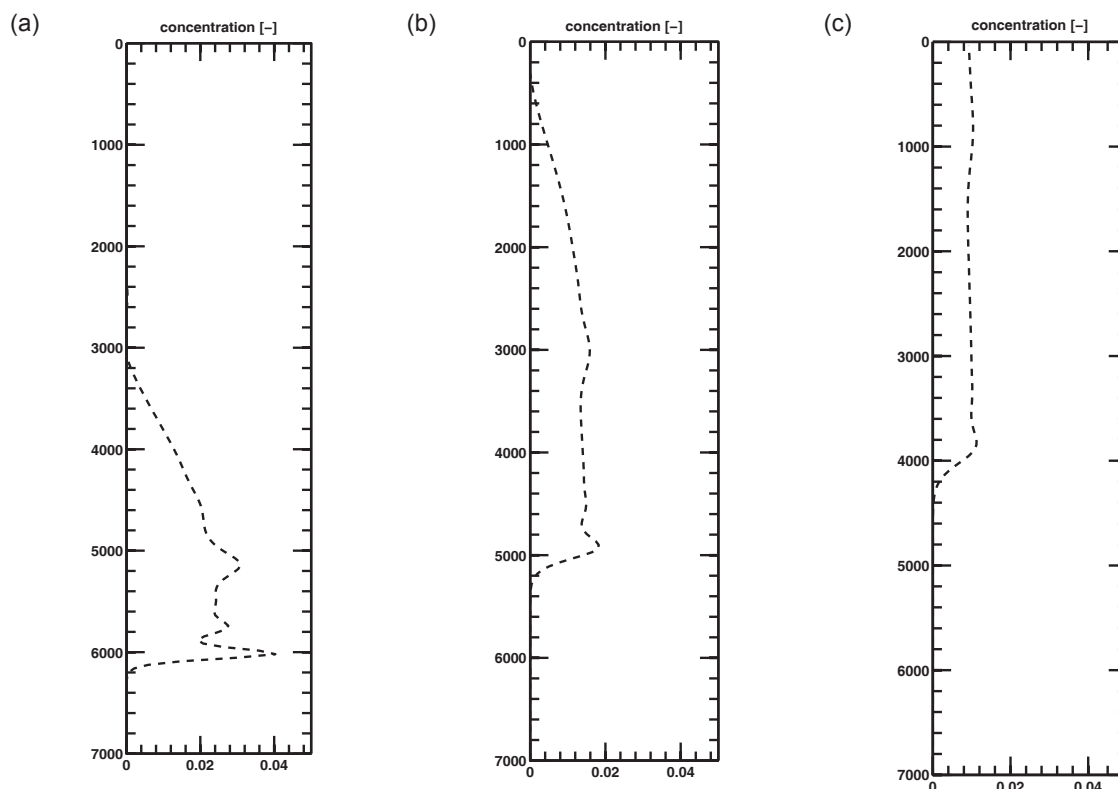
Figure 46: Cuttings distribution along the wellbore for the simulation input conditions and the scenario described in the distribution coefficient sensitivity analysis after 5 hours: (a) $C_0 = 0.8$, (b) $C_0 = 1$ and (c) $C_0 = 1.2$.

operations, where the control of the flow rate is performed on real-time and according to surface indicators, these could possibly translate in clogging problems.

1.1.2.3. Future research work and plans

Based on the findings of the present project, the following research topics should be further investigated, either experimentally or computationally.

During the project is was found, that the experimental investigation of the particle transport in a core annulus with rotating inner cylinder as a model for the rotating drill string is not possible with the present configuration. However, the effect of drill string rotation is expected to be very important with regard to the particle transport in both, vertical and deviated well bores. Here, computational experiments based on the CFD-DEM approach are economically more appropriate. Based on the present work, validated models with predictive capabilities are available for Newtonian liquids and monodisperse particles. Thus, it is proposed to focus on the investigation of the particle transport in non-Newtonian liquids and considering particle ensembles with a wider size distribution and for particles with non-spherical shape. Such computations are intended to enhance the understanding of the physical phenomena in the well bore.

On the other side, computational models are required which are able to describe the relevant phenomena on a large scale, i.e. in the entire well bore, and which are highly effective, eventually real-time capable. For this purpose, in the present work a drift-flux models was realized

which is able to describe the transport of mono-modal particles. Here, a potentially more accurate model is the method-of-moments approach, which is a well established technique in process engineering and which may be used as base for an enhanced drift-flux approach. Experimentally, the transition to turbulence in non-Newtonian liquids in a core annulus with rotating inner cylinder should be further investigated since this has a significant impact on prediction of the pressure losses in the system. Presently, it is possible to evaluate pressure losses in laminar or turbulent flows, but it is not possible to decide where (under drilling conditions, i.e. non-Newtonian liquids, with drill string rotation and eccentricity) the flow starts to become turbulent.

1.1.2.4. Project plan

The following table gives an overview of the actual workflow in the present project compared to the original plan. Some delays in the beginning are due to the late start of the project. Considerably more time was spent in AP3 for the adaptation and test of the measuring technique for technical reasons and subsequently, for the experimental data collection. After 2012, additional work was performed for the further dissemination of results which led to a number of additional publications.

Action points (work packages)	2009	2010	2011	2012	2013	2014
AP1: Hydrodynamic characterization						
AP2: Rheological characterization						
AP3: Adaptation and test of the measuring technique						
AP4: Experimental data collection						
AP5: Well bore scenarios simulation						
AP6: Preparation of own parameter model						
AP7: Model verification and well bore scenarios evaluation						

Grey, original plan

Blue, actual or current plan, respectively

For details, see Gantt chart in the Appendix.

The delay is due to later start of the project.

1.3. Delineation of the project from other funded projects

No projects are currently being implemented by the Institut für Technische Mechanik or the Institut für Erdöl- und Erdgastechnik which have any analogies with geothermy and/or high performance drilling technology with the content described here.

499

1.4. Executive summary

Project B5 was separated in seven different work packages, whereas three main tasks were defined: (1) characterization of the problem, (2) physical experiments and (3) models development.

In the characterization of the problem, a review and evaluation of the state-of-the-art models used to describe cuttings transport and hole cleaning was carried on. This one offered an overview of the research already performed and pointed out questions still open in the field. Furthermore, representative rheological properties of water-based drilling fluids circulated in geothermal and HP-HT wellbores were obtained. These offered a reference for the search of appropriate experimental fluids. Information about characteristics of the cuttings found in hard-rock formations was also gathered during this part of the project and guided the selection of the particles used during the experiments and numerical simulations.

The physical experiments part started with the construction of a small vertical flow-loop installed at ITM, where the PIV technique was adapted to the measuring of solid-liquid suspensions. Several fluids offering rheological properties similar to those of the drilling-fluids and optical properties required for the operation of the PIV technique were also evaluated during this period. At ITE works were performed to adapt the multiphase flow loop to experiments centered on the collection of data considering the transport of cuttings through deviated sections with water and Carbopol mixtures. Experiments performed at ITM and ITE supplied detailed sets of data for the validation of numerical models.

The modeling of wellbore scenarios started with the location of approaches adapted to multiphase flow problems. Following a multi-scale approach, several methods were selected to link relevant information about the physical phenomena taking place at different scales found along the wellbore. After implementation, the models were validated with data generated during the physical experiments. Effects of operating conditions as eccentricity, inclination and rotation were finally assessed.

Major findings of the project were: (1) the necessity to implement transient models able to describe the complex processes taking place during cuttings transport, (2) the acquisition of experimental data centered on the validation of specific physical phenomena occurring along the wellbore and (3) generation of information at different scales through different computational approaches and integration on a large scale model able to consider the complete length of the wellbore.

The work in the present project was accomplished by two scientific employees funded by the project and a total number of eleven (11) student co-workers and bachelor/master students. The outcome of the work is published in three (3) peer reviewed journals, six (6) workshops and ten (10) student theses.

Changes of the scheduling of the workflow have been closely discussed and approved by the coordinators and BHI.

1.5. References

Di Felice R. (1995): Hydrodynamics of liquid fluidization. Chemical Engineering Science, Vol. 50, No 8, pp 1213-1245, 1995.

Luo G. (1988): Non-Newtonian annular flow and cuttings transport through drilling annuli at various angles, PhD Thesis, Heriot-Watt University Edinburgh, 1988.

Clark R. and Bickham K. (1994): A mechanistic model for cuttings transport. *SPE Annual Technical Conference and Exhibition*, (SPE 28306), 1994.

ITE (2013a): Economic Drilling of Deep Geothermal Wells (Geothermal Energy & Gas Recovery Project), Group Project 2013 - Gebo I, Institute of Petroleum Engineering, Clausthal University of Technology.

ITE (2013b): Economic Drilling of Deep Geothermal Wells Group Project 2013 – Gebo II, Institute of Petroleum Engineering, Clausthal University of Technology.

TerraTek (2008): Deeptrek Phase 1 and 2 – Improving deep drilling performance. Technical Report, DOE Award Number – DE-FC26-02NT41657, 2008.

Lindken R. and Merzkirch W. (2002): A novel PIV technique for measurements in multiphase flows and in application to two-phase bubbly flows. *Experiments in Fluids* , 33:814-825, 2002.

Gui L. and Merzkirch W. (1997): Phase-separation of PIV measurements in two-phase flow by applying a digital mask technique. *ERCOFTAC Bulletin*, 30, 1997.

Lindken R., Gui L. and Merzkirch W. (1998): Geschwindigkeitmessungen in Mehrphasenströmungen mit Hilfe der Particle Image Velocimetry. *Chemie Ingenieur Technik*, pages 856-860, 1998.

Lindken R., Gui L. and Merzkirch W. (1999): Velocity measurements in multiphase flow by means of particle image velocimetry. *Chem. Eng. Technol, 1999.*

Kelessidis V. and Bandelis G. (2004): Flow patterns and minimum suspension velocity for efficient cuttings transport in horizontal and deviated wells in coiled-tubing drilling. SPE Drilling & Completion, Volume 19, pp 213-217, 2004.

U.S. DOE (various authors) 2006: Report on workshop on multiphase flow. U. S. Department of Energy, Office of Fossil Energy and National Energy Technology Laboratory, June 6-7, 2006.

Zlokarnik M. (2002): Scale-Up in Chemical Engineering. Wiley-VCH Verlag GmbH & Co., 1 edition, 2002.

Ceylan K., Hardem S., and Abbasov T. (1999): A theoretical model for estimation of drag force in the flow of non-newtonian fluids around solid particles. Powder Technology, 103, 1999.

Schiller L. and Naumann Z. (1935): A drag coefficient correlation. V.D.I. Zeitung 77, 318, 1935.

Mei R. (1992): An approximate expression for the shear lift force on a spherical particle at finite Reynolds number. *International Journal of Multiphase Flow*, Vol. 18, pp 145-147, 1992.

Dandy D. and Dwyer H. (1990): A sphere in shear flow at finite Reynolds number: effect of shear on particle lift, drag, and heat transfer. *Journal of Fluid Mechanics*, Vol. 216, pp 381-410, 1990.

Saffman P. (1965): The lift on a small sphere in a slow shear flow. *Journal of Fluid Mechanics*, Vol. 22, pp 385-400, 1965.

ANSYS (2009): CFX-Solver Theory Guide Release 12.1, 2009.

McLaughlin J. (1991): Inertial migration of small sphere in linear shear flows. *Journal of Fluid Mechanics*, Vol. 384, pp 183-206, 1991.

Takemura F. and Magnaudet J. (2009): Lateral migration of a small spherical buoyant particle in a wall-bounded linear shear flow. *Physics of Fluids*, Vol. 21, 2009.

Richardson J. and Zaki W. (1954): The sedimentation of a suspension of uniform spheres under conditions of viscous flow. *Chemical Engineering Science*, Vol. 3, pp 65-73, 1954.

Brennen C. (2005): Fundamentals of multiphase flow. *Cambridge University Press*, 2005.

Naganawa S. and Nomura T. (2006): Simulating transient behavior of cuttings transport over whole trajectory of extended reach well. Paper presented at IADC/SPE Asia Pacific Drilling Technology Conference and Exhibition, 2006.

Govier G. and Aziz K. (1972): The flow of complex mixtures in *pipes. Robert E. Krieger Publishing Company*, New York, 1972.

Pigott R. (1942): Mud Flow in Drilling. *Drill. and Prod. Pract.*, API 91-108, 1942.

1.6. *Publications, reports and presentations of Project*

Aragall R., Brenner G. and Teodoriu C. (2010a): Hydrodynamic characterization of drilling fluids for geothermal drilling operations. Technical Report, Institut für Technische Mechanik & Institut für Erdöl- und Erdgastechnik, TU Clausthal 2010.

Burkhart S. (2010): Bewertung der PIV-Methode zur Quantifizierung der Bohrkleingeschwindigkeit bei geothermischen Tiefbohrungen. Bachelor Thesis, TU Clausthal, 2010.

Aragall R., Brenner G., Teodoriu C. and Weichmann M. J. (2010b): Meilensteinbericht 1: Gewährleistung des effizienten Bohrkleinaustrag. Technical Report, Institut für Technische Mechanik & Institut für Erdöl- und Erdgastechnik, TU Clausthal, 2010.

Kumar P. (2011): Implementation of PIV techniques in the analysis of Hold-up phenomena of Drill Cuttings Transportation. Master Thesis, TU Clausthal, June 2011.

Aragall R., Kumar P. and Brenner G. (2011): Simultaneous measurements of solid particle and fluid velocity in two-phase pipe flows using combined PIV/PTV techniques. Paper presented

at 19. Fachtagung zu Lasermethoden in der Strömungsmesstechnik, Ilmenau, Germany, 6-8 September 2011.

Khan N. (2011): Frictional pressure drop in concentric and eccentric wellbores with bed height. ITM internal report, TU Clausthal, 2011.

Mäder C. (2012): Experimentelle Untersuchung der Bewegung von Partiklen in laminaren Rohrströmungen. Master Thesis, TU Clausthal, March 2012.

Li Y. (2012): Numerische Untersuchung von hydrodynamischen Kräften an Partikeln in Newtonscher Scherströmung mit Hilfe von CFX. Bachelor Thesis, TU Clausthal, April 2012.

Aragall R. and Brenner G. (2012): Detailed quantification of dispersed particles transport through PIV and PTV measuring technique. Paper presented at 13th Workshop on Two-Phase Flow Predictions, Halle, Germany, September 17-20, 2012.

Wang C. and Zhang Y. (2012): Untersuchungen der Zwei-Fluid-Modell für Inertialsuspensionen. Project Thesis, TU Clausthal, July 2012.

Aragall R., Mulchandani V. and Brenner G. (2013): Experimental analysis on bidispersed particle transport in laminar pipe flow. Presented at Jahrestreffen der ProcessNet Fachgruppen Agglomerations- und Schüttguttechnik und Computational Fluid Dynamics, Weimar, March 4-6, 2013.

Mulchandani V., Aragall R. and Brenner G. (2013a): Experimental analysis on bidispersed cuttings transport in laminar pipe flow. Paper presented at 11th Offshore Mediterranean Conference and Exhibition, Ravena, Italy, March 20-22, 2013. Price Winner of the European SPE Student Paper Contest 2013. 2013 SPE Annual Technical Conference and Exhibition, International SPE Student Paper Contest, New Orleans, USA, September 30-October 2, 2013.

Mulchandani V. (2013b): Experimental Analysis on Polydisperse Cuttings Transport in Newtonian and non-Newtonian Fluids. Master Thesis. TU Clausthal, July 2013.

Hahn S. (2013): Implementierung eines ein-dimensionalen, transienten Modells auf Basis des Drift-Flux-Modells mittels eines finite-Volumen-Verfahrens in MATLAB. Bachelor Thesis, September 2013.

Aragall R., Mulchandani V. and Brenner G. (2013a): Analyse von plötzlichen axialsymmetrischen Erweiterungen von bidispersen Suspensionen in laminaren Strömungen (Analysis of bidisperse suspension laminar flows in axisymmetric sudden expansions), presented at Jahrestreffen der ProcessNet Fachgruppen Fluiddynamik und Trenntechnik, Würzburg, Germany, September 25-26, 2013. Paper published at Chemie Ingenieur Technik, Number 9, Pages 1433-1434, September 2013.

Aragall R., Hahn S., Mulchandani V. and Brenner G. (2013b): Multiscale Approach for Drilling Hydraulics Modeling. Paper presented at Celle Drilling 2013, Celle, Germany, September 9-10, 2013. Published at OIL GAS European Magazine, March 2014.

Dai J. (2014): Simulation partikelbeladener Strömungen durch Ringspalt-Kanäle mittels eines CFD-DEM Ansatzes (Simulation of suspension flows through vertical annular ducts through a CFD-DEM approach). Bachelor Thesis, Mai 2014.

Yu F. (2014): Numerical simulation of the transport of bidisperse suspensions through a CFD-DEM approach. Master Thesis, April 2014.

Aragall R., Brenner G. and Teodoriu C. (2014a): Progress Report on work packages AP4 and AP5. Technical Report, Institut für Technische Mechanik & Institut für Erdöl- und Erdgas-technik, TU Clausthal, June 2014.

Aragall R., Hahn S., Mulchandani V., Brenner G. (2014b): Multiscale Approach for Drilling Hydraulics Modeling II. Paper presented at 2nd International Symposium on Multiscale Multiphase Process Engineering, Hamburg, September 24-27, 2014.

Haider H. (2014): Experimental study of cuttings transport through yield-pseudoplastic liquids in horizontal and deviated sections. Master Thesis, December 2014.

Aragall R., Mulchandani V., Brenner G. (2015a): Optical measurement and numerical analysis of mono- and bidisperse coarse suspensions in vertical axisymmetric sudden-expansion. International Journal of Multiphase Flow, Volume 69, Pages 63-80, March 2015.

Aragall R., Yu F., Dai J., Brenner G. (2015b): Closure of Drift-Flux Models for Cuttings Transport Prediction. Paper presented at Celle Drilling 2014, Celle, Germany, September 16-16, 2014. Published at OIL GAS European Magazine, March 2015.

B6: Numerical simulation of thermal non-Newtonian Fluid Dynamics

1.1 Project Overview

Speaker and lead university or research institution

Project Nr.	Title	Subject of research	Project leader, institution, location
B6	Numerical simulation of thermal non-newtonian fluid dynamics	Fluid mechanics, computational mode-ling	Prof. Dr.-Ing. habil. M. Krafczyk, iRMB Braunschweig

Participating institutes and institutions of the University and external institutions in:

- Institute for Computational Modelling in Civil Engineering (iRMB), TU Braunschweig

- Baker Hughes Contact, Celle, Dipl. Ing. T. Dahl, Dipl. Ing. R. May

List of participating scientists and engineers:

Name Subject	area	University institute or non-university institution	Position is financed by gebo funds (indicate with X)
Prof. Dr.-Ing. habil. M. Krafczyk	fluid mechanics	iRMB	
Dr. Martin Geier	fluid mechanics	iRMB	
Dr. Sebastian Geller	fluid mechanics	iRMB	X

1.2 Research   Program

1.2.1 Su   mmary

For the optimization of the drilling process, the influence of the drill cuttings on the transport features of the drilling fluid will be studied from a computational fluid mechanics point of view. The drilling fluid shows non-Newtonian fluid behavior. Detailed simulations of the drilling process are conducted to show the influence of the fluid-structure interaction on the drilling fluid dynamics. The rigid particle dynamics are modeled with the Physics Engine [12] - a rigid body motion solver, which is integrated into the fluid solver. The fluid simulation is based on a Large-Eddy (LES) turbulence model [11].

1.2.2 Relationship of the project to the overall research context and networking with other projects

The key point of the whole project is the optimization of the drilling process including an efficient energy transport through the soil. Corresponding analysis and optimization approaches should be supported by computational fluid flow simulations.

The need for reasonable input parameters for the fluid and cutting features, the bore hole geometry and the drill string motions results in strong cross-links to other projects. Experimental data is used for the validation of the material laws and transport simulations. The resulting shear stresses and pressures on the drill string are being used for the dynamic modelling of the drill string. For details, see the Gantt chart in the Appendix.

1.2.3 Work packages executed relative to (original) plan and results achieved

The goal of this work is the prediction of pressure loss and drill cutting transport properties of non-Newtonian fluids during the drilling process. A section of the bore hole is simulated in a complex three dimensional, transient simulation. The fluid is solved with the in-house code VirtualFluids [6,7,8,9], which is based on a Lattice Boltzmann approach and adaptive hierarchical isotropic Eulerian grids. The geometric information can be specified by STL files, standard geometry objects or tomographic data.

WP1, WP2: The ability of the Lattice Boltzmann approach of a coupled rigid body simulation is the basis for the developed fluid solver. The particles are considered in a Langrangian formulation und are coupled with the Eulerian fluid simulation approach. The particles are simulated as spheres with a flexible size distribution. The Newtonian motion as well as the collision of the particles is solved with the rigid body dynamics engine pe-PhysicsEngine (PE) [12]. The pe solver is a sophisticated C++ framework optimized for highly parallel simulations of rigid bodies. For the friction based rigid body collisions the PE provides several algorithms, e.g. the projected Gauss-Seidel (PGS) algorithm, a conjugate projected gradient (CPG) algorithm, a damped Newton approach and an algebraic multigrid solver.

For the coupling of this parallel structural solver with the parallel version of VirtualFluids a bidirectional coupling approach was implemented [2,8]. Forces exerted from fluid to the particles are computed with the momentum exchange method [1]. The structural solver computes the resulting rigid body motions. The new positions and velocities are updated in the fluid solver.
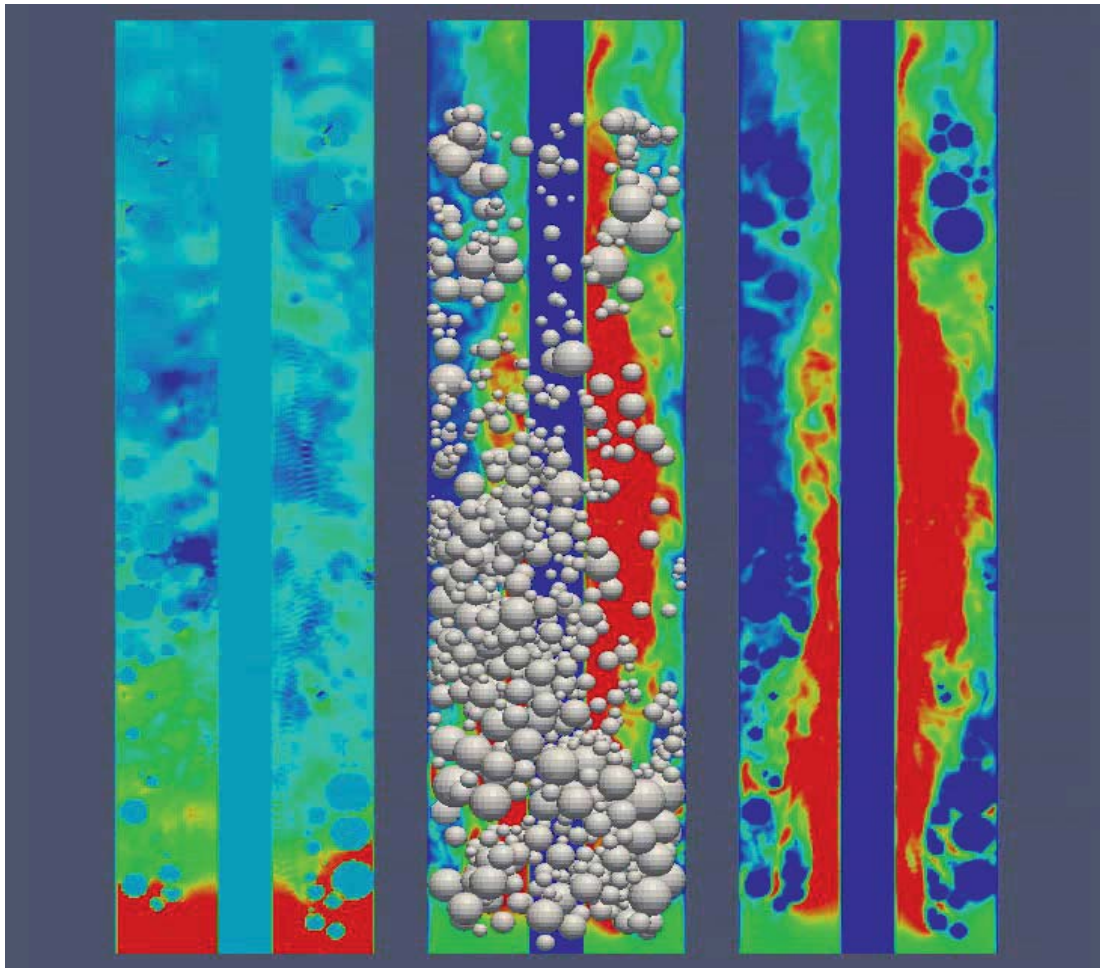
figure 1: Preliminary simulation results of the coupled rigid body – fluid simulation inside the well (pressure, velocity with drill cuttings, velocity)

The first validation test case for the coupling is the simulation of a single sinking sphere. The numerical results agree very well with analytical reference solutions. More complex cases with a elastic rectangular plate [10] are studied for different Reynolds numbers resulting in monotonously increasing deformations of the plate. The results have been compared to a commercial CFD-code (Ansys Multiphysics).

For the simulation of the turbulent flow a Large Eddy model (LES) [11] was implemented for non-uniform grids.

Initial simulations with the PE and VirtualFluids show the applicability of the coupled approach. Instabilities caused by the simulation of very small particles are solved via introducing suitable stabilization techniques for the particle dynamics.

To reduce the uncertainty with respect to the exact parameterization of in- and outflow boundary conditions, periodic boundaries for the fluid as well as the structural solver have been implemented. Thus in the simulations the fluid is driven by a body force, which is adjusted to obtain the desired average flow of velocity.

WP3: The material law for the description of the shear thinning drill fluid is the Herschel-Bulkley model which is an extension of the standard power law model describing stationary non-Newtonian fluid properties. Other models are the Carreau-Yasuda, Casson, Cross and K-L model. The Power Law, Casson and K-L [3,4] model was implemented and successfully validated with channel flow setups.

WP4: Comparison with experimental studies is in progress.

WP5: An important aspect is the influence of the drill fluid on the drill string vibrations. Therefore, a geometric model to describe a part (1-5m) of the oscillating drill string was developed and implemented for the parallel fluid solver. For different positions of the drill string, the fluid forces will be calculated and stored in a lookup table for the structural dynamics solver of project B7. A bidirectional coupling due to the MPI interface with the need of a triangulated surface mesh is possible [20]. On the nodes of the triangulated mesh the forces and stresses are evaluated and transmitted to the solver.

The resolution of the details of the small scale flow structures results in time consuming computations. Work on algorithmic improvements of the MPI [13] based parallel solver have been successfully conducted resulting in a speed-up of 250%.
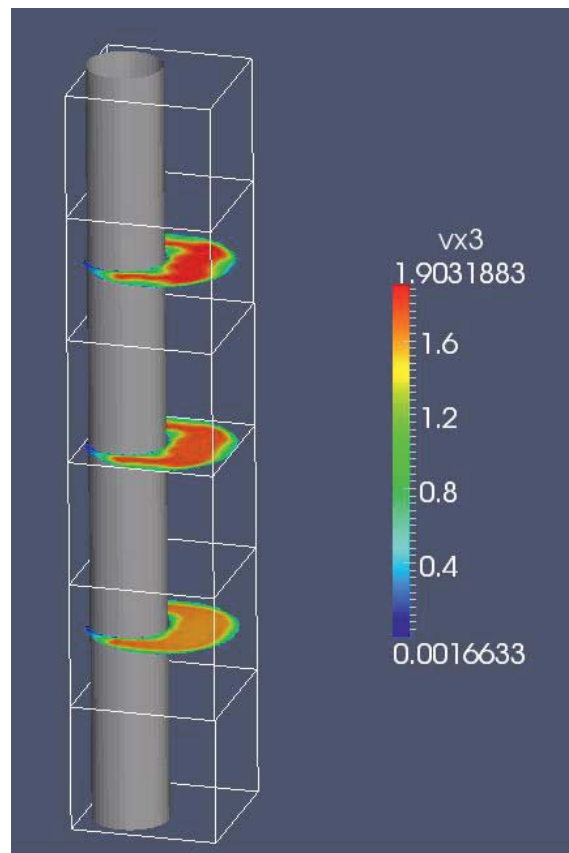
Figure 2: coupled drill string fluid simulation

1.2.4 Future research work and plans

Very small particles below grid resolution can be represented by a particle concentration variable. Hence, a further working point to address is the additional solution of an advection-diffusion-equation [17] for the drill cutting concentration. Sedimentation and erosion processes as well as the adaptation of the no slip boundary condition of the fluid will be modelled with a modified Marching Cubes [15] algorithm known from computer graphics for the construction of iso-surfaces.

As an additional aspect the influence of the rough walls on the drilling string's boundary layer is recommended. Here the fast meshing capabilities due to complex geometry are an advantage of using the Lattice Boltzmann method [16].

The high computational cost of the numerical simulations can be reduced developing specific parallel graphics hardware code based on NVIDIAs software development library CUDA [14].

Although the potential gain in performance is well beyond one order of magnitude, the corresponding LB-algorithms and data structures would have to be adapted which is probably not feasible within the first period of the project.

1.2.5 Project   Plan

Work packages and milestones	2009		2010		2011		2012		2013		2014	
WP1: coupling with rigid body dynamics engine												
WP2: transport model for particle flows												
WP3: turbulence modeling, non-newtonian fluid												
WP4: validation of experimental data												
WP5: analysis for drill string oscillations												

Grey, original plan

Blue, actual or current plan, respectively

For details, see the Gantt chart in the Appendix.

The delay for WP 5 results from additional investigation in algorithmic and conceptual improvements of the parallel flow solver. The solvers were optimized to run in acceptable runtimes. Furthermore, high diameter ratios of spheres and very small spheres caused several stability problems in the simulation process of the coupled approach. Finally, some simulation and setup parameters could only be obtained with some delay from the project partners.

1.3 Demarcation of the project from other funded projects

No projects in the context of geothermic and high end drill technique are presently funded at iRMB

1.4 Conclusions

Project B6 has succeeded to finalize some of the original work packages. A three-dimensional and parallelized Large Eddy CFD code to conduct LES-Simulations including Fluid-Structure-Interaction with solid particles a several non-Newtonian flow models has been developed and simulation results have been transferred to project partners. As project funding was terminated November 2011, the last month after the review meeting on Sept. 29th 2011 was used to consolidate the documentation of the code and bug fixes in the post-processing interface. The validation of the simulation data by experiments could not be completed due to lack of experimental data by other subprojects. The original plan to integrate the solver into a GEBO simulation framework could not be accomplished as the implementation of this framework has not been accomplished by the time subproject B6 was terminated.

Financial accounting of the project has been finalized by the end of 2011.

1.5 References

[1] M. Bouzidi, M. Firdaouss, P. Lallemand: Momentum transfer of a Boltzmann-Lattice fluid with boundaries, Physics of Fluids,vol.13, 11,p.3452-3459, 2001.

[2] N.-Q. Nguyen, A. J. C Ladd: Sedimentation of hard-sphere suspensions at low Reynolds number.Journal of Fluid Mechanics, 525, 2004

[3] S. Gabbanelli, G. Drazer, J. Koplik: Lattice Boltzmann Method for Non-Newtonian Fluid Flows, arXiv:cond-mat/0506768v1 [cond-mat.soft], 2005

[4] J. Boyd, J. Buick, S. Green: A second-order accurate lattice Boltzmann non-Newonian flow model. Journal of Physics A: Math. Gen 39, 2006.

[5] M. Krafczyk: Gitter-Boltzmann-Methoden: Von der Theorie zur Anwendung. Postdoctoral thesis, TU Munich, 2001.

[6] S. Geller, M. Krafczyk, J. Tölke, S. Turek, J. Hron: Benchmark computations based on Lattice-Boltzmann, Finite Element and Finite Volume Methods for laminar Flows, C&F,35, 2006

[7] S. Freudiger, A. Gessner, S. Geller: VirtualFluids: Ein komponentenbasiertes Framework für parallele Lattice Boltzmann Simulationen auf hierarchischen Blockgittern, Forum Bauinformatik, Graz, 2007

[8] S. Geller, J. Tölke, M. Krafczyk: Lattice-Boltzmann Method on quadtree type grids for Fluid-Structure-Interaction. In H.-J. Bungartz and M. Schäfer, editors, Fluid-Structure Interaction: Modelling, Simulation, Optimisation, Springer Verlag, 2006

[9] S. Freudiger: Entwicklung eines parallelen, adaptiven, komponentenbasierten Strömungs-kerns für hierarchische Gitter auf Basis des Lattice Boltzmann Verfahrens. dissertation, TU Braunschweig, 2009

[10] K.J. Bathe,.G. Ledezma: Benchmark problems for incompressible fluid flows with structural interactions. Computers&Structures, 85(11-14), 2007.

[11] J. Smagorinsky: General circulation experiments with the primitive equations–I the basic experiment. Monthly Weather Review, 91,1963

[12] K. Iglberger, U. Rüde: Massively parallel rigid body dynamics simulations. Computer Science – Research and Development, 23, 2009

[13] Forum M.P.I.: MPI: A Message-Passing Interface Standard, International Journal of Super-computer Applications,1994.

[14] Nvidia CUDA: Nvidia CUDA Programming Guide 3.1, 2010.

[15] W. E. Lorensen, H.E. Cline: Marching cubes: A high resolution 3D surface construction algorithm. In:SIGGRAPH'87: Proceedings of the 14th annual conference on Computer graphics and interactive techniques, Bd.21, S.163–169, 1987

[16] B. Ahrenholz: Massively parallel simulations of multiphase- and multicomponent flows using lattice Boltzmann methods, Dissertation, *Technische Universität Braunschweig*, 2009

[17] S. Geller, S. Giangreco, M. Krafczyk: Numerical simulation of erosion and deposition pro-cesses with the Lattice Boltzmann method, journal publication, in preparation

[18] S. Geller, S. Kollmannsberger, M. El Bettah, M. Krafczyk, D. Scholz, A. Düster, E. Rank: An explicit model for three-dimensional fluid-structure interaction using LBM and p-FEM, In H.-J. Bungartz, M. Mehl and M. Schäfer, editors, Fluid-Structure Interaction II: Modelling, Simulation, Optimisation, Springer Verlag, 2010

[19] S. Kollmannsberger, A. Düster, E. Rank, S. Geller, M. Krafczyk: Modelling fluid-structure interaction with high order solids and lattice Boltzmann, CST2010, The Tenth International Conference on Computational Structures Technology, Valencia, Spain, 2010

[20] E. Goraki, E. Shirani, S. Geller: Fluid structure interaction with using of lattice Boltzmann method, 13th. Annual International Conference fluid dynamic conference, Shiraz, Iran, 2010

[21] S. Geller: Ein explizites Modell für die Fluid-Struktur-Interaktion basierend auf LBM und p-FEM, Dissertation, TU-Braunschweig, 2010

[22] S. Geller, C. Janssen, M. Krafczyk: Three dimensional fluid-structure interaction using the Lattice Boltzmann method - Rigid body motion on fixed Eulerian grids, journal publication, in preparation

[23] M. Stiebler, M. Krafczyk, S. Freudiger, M. Geier: Lattice-Boltzmann large eddy simulation of subcritical flows around a sphere on non-uniform grids, accepted for publication in *Computers and Mathematics with Applications*, 2011

[24] J. Tölke, M. Krafczyk, Second order interpolation of the flow field in the lattice Boltzmann method, Computers & Mathematics with Applications, Volume 58, Issue 5, Mesoscopic Methods in Engineering and Science, Pages 898-902, ISSN 0898-1221, 2009

[25] C. Janßen, M. Krafczyk, A lattice Boltzmann approach for free-surface-flow simulations on non-uniform block-structured grids, Computers and Mathematics with Applications 59 2215-2235, 2010

[26] S. Kollmannsberger, S. Geller, A. Düster, J. Tölke, C. Sorger, M. Krafczyk, E. Rank: Fixed-grid Fluid-Structure interaction in two dimensions based on a partitioned Lattice Boltzmann and p-FEM approach, Int. J. Numer. Meth. Engng., Vol. 79, Issue 7, pp. 817 – 845, 2009

[27] S. Chen, J. Tölke, M.Krafczyk, Simulation of buoyancy-driven flows in a vertical cylinder using a simple lattice Boltzmann model, Physical Review E 79, 016704, 2009

[28] M. Krafczyk, J. Tölke, B. Ahrenholz, S. Bindick, S. Freudiger, S. Geller, C., Janßen and B. Nachtwey, Kinetic Modeling and Simulation of Environmental and Civil Engineering Flow Problems, in E. Hirschel, E. Krause (Eds.), 100 Volumes of 'Notes on Numerical Fluid Mechanics', Springer, ISBN: 978-3-540-70804-9, pp. 341 – 350, 2009

1.6 Publications, reports and presentations of Project

[1]   S. Geller, M. Krafczyk, Zwischenbericht B6: Meilenstein 1 und 2, Juli 2010

In addition, the publications [17-28] mentioned in the last section have emerged during the first period of the project. As the PIs were not aware that the publications should have been evaluated by the steering committee prior to publication, we do not list them here as official GEBO-publications.

B7: Drill String Dynamics and Modeling

1.1 Project Overview

Project Nr.	Title	Subject of research	Project leader, institution
B7	Drill String Dynamics and Modeling	Mechanical Engineering – Dynamics and Vibrations	Prof. Dr.-Ing. habil. G.P. Ostermeyer, TUBS (IDS)

Participating institutes and institutions of the universities and external institutions:

- Institute of Dynamics and Vibrations (IDS), TU Braunschweig

List of participating scientists and engineers:

Name	Subject area	University institute or non-university institution	Position is financed by gebo funds (indicate by X)
Prof. Dr.-Ing.habil. G.P.Ostermeyer	Mechanical Engineering	IDS	
Dr.-Ing. M. Müller	Mechanical Engineering	IDS	
Dr.-Ing. F. Schiefer	Mechanical Engineering	IDS	X
M.Sc. M. Shi	Mechanical Engineering	IDS	X

1.2 Research Program

1.2.1 Summary

Wells for the exploitation of geological resources are becoming more and more challenging. In particular, geothermal wells of enhanced geothermal systems, as planned in gebo, will be drilled into greater depths, under hot hard rock conditions and with complex profiles, if necessary. While the principle of (rotary) drilling is relatively simple, the understanding, prediction and analyses of the drill string dynamics are highly complex but essential for the improvement of the drilling process itself [OST14a]. This fact is also essential for the overall gebo drilling objective of minimizing the drilling cost. The individual components of a drill string are in permanent interdependence with each other. Thereby, their dynamics is continuously influenced by the drilling process, the borehole geometry and the geological conditions. In order to be able to identify and quantify different influences on drill string vibrations, new models for single components are being developed. Together with an enhancement of already existing models, these will be synthesized into an overall model for the complete system. The aim is to investigate the system's complex dynamics with the help of problem adapted modeling depths. This should be accomplished by means of a flexible and modular model structure, which allows short computing times. In particular, vibration phenomena in the range of short-term dynamics will be simulated and analyzed, such as stick-slip, whirl or bit bounce.

1.2.2 Relationship of the project to the overall research context and networking with other projects

The costs of the drilling process are the major reason for the relatively low cost-effectiveness of geothermal energy. In order to be able to reduce these costs, and in particular to make them calculable, research on the dynamic mechanisms that lead to underground damage of the drill string is essential. With its models and simulations, project B7 opens new possibilities towards a prediction and quantification of the loads, a drill string is subject to during the drilling process. The models under development will not only be able to describe single phenomena at specific locations, but will moreover allow investigations of the whole system's dynamic behavior. These results are the prerequisite for other projects and partners for statements concerning the durability of their systems, components or materials. The models of this project are adaptable and expandable, if needed, for investigations of the long-term dynamics, as carried out in project W7, in order to generate durability and fatigue relevant synthetic load spectra. With the input on drilling principles and borehole geometries, specific drill string dynamics will be considered for the application to geothermal drilling. The cross-linking with the other gebo projects is in particular given by the research field *drilling technology*, but also by the three additional research fields *geosystem*, *materials* and *technical system*. B7 generates data on drill string dynamics for the research field *drilling technology*, but also basics and models for project W7. This project, in turn, generates durability relevant load spectra by simulations of the long-term dynamics, which are the input for the research fields *materials* and *technical system*. In cooperation with B6, the interaction between drill string and drilling mud should be investigated. At the same time, B7 requires input data from the other research fields, e.g. rock and environmental parameters, as well as wellbore profiles or borehole geometries and drill string characteristics, up to material data.

1.2.3 Work packages and results

Complete model's concept & interfaces to sub-models (WP1): Based on own preliminary work and corresponding literature research, up to now state-of-the-art models for the description of drill string dynamics have been contrasted with existing simulation methods for drill string vibrations. Additionally, their suitability for further studies was evaluated. In principle, we can distinguish between hardware models and mathematical models as well as between full models and sub-models. The consideration of the real system reveals that the drill string is a one-dimensional continuum with a very small diameter compared to its length.

One short example: Let's assume a drill string with a diameter of 5'' and a length of 5000m. The relation of diameter to length is about 1 to 40000. If we compare this string to a human hair with a diameter of one-tenth millimeter, this hair has a length of 4m, hangs on a hook and will be

rotated to drill a target well. That is one main challenge of modeling and simulation the drill string dynamics. But, this is also an indicator that hardware models are always scaled geometrically. Taking into account the relationships of similarity mechanics, sub-models of drill string parts can be set up. However, the problem is that the drilling process can not be scaled. In this respect, for studies and analyses of the complex dynamics of a full drill string corresponding complex mathematical models are required. In addition to this, the model purpose determines substantially the model selection. It is a difference whether you only want to investigate a particular vibration behavior of a single drill string component or additionally also the load distribution along the entire drill string.
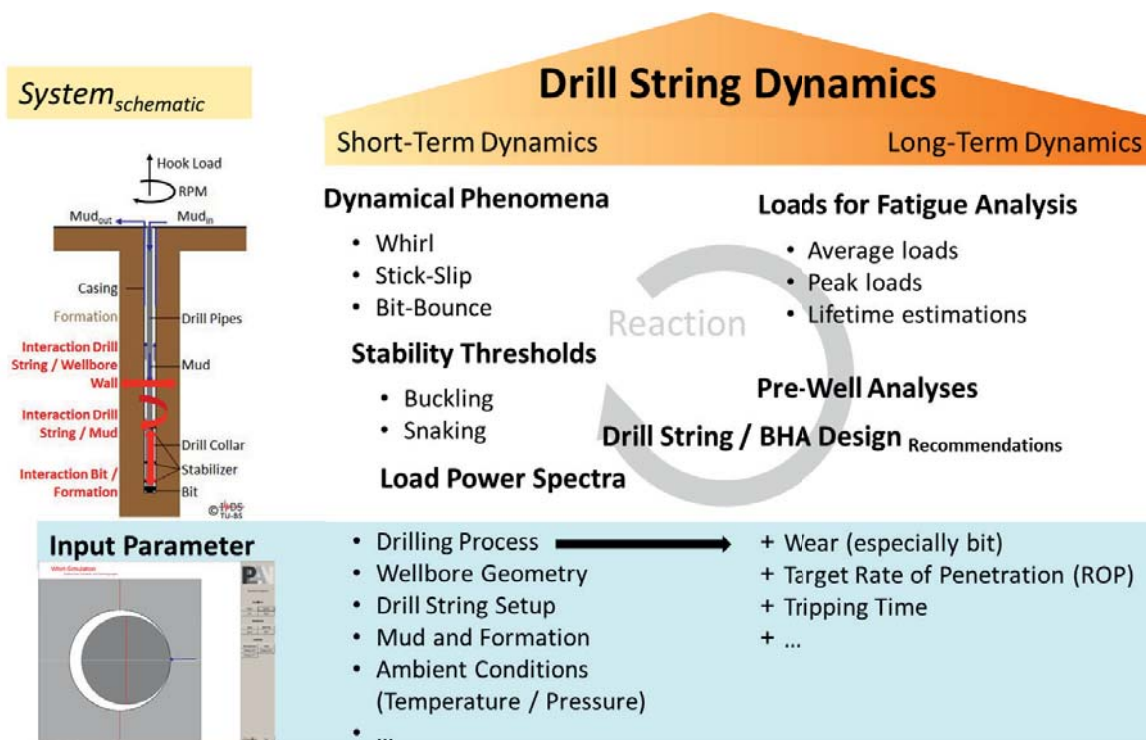
Figure 1: Modeling and drill string dynamics – model purpose

On the left side of Figure 1 is shown a schematic simplified view of the coupled system drill string / borehole with the essential interactions and the main vibration modes which are directly connected the known downhole phenomena whirl or stick-slip for instance. We divide the drill string dynamics into a short-term range and a long-term range with respect to the corresponding input parameters, shown in Figure 1. The main task of project B7 is the accurate describtion of the short-term dynamics – dynamical phenomena, stability thresholds and load spectra – with a minimum amount of computing time. In addition, project W7 has been analyzed the long-term dynamics, especially the loads for fatigue analysis [OST14b].

With the focus on simplicity, at the beginning of the project the model studies concentrate on a hybrid model of FEM (Finite Element Method) and MBS (Multibody System). A first model is depicted schematically with the respective coordinate systems in Figure 2. For each single rigid body, all six degrees of freedom, relative to the center of the borehole, are considered. The rigid bodies are connected with massless beam elements. As the project continues complex beam elements with an integrated borehole curvature parameter [OST89, HEI93] and corotational beam elements [CRI90, CRI91, JAN93] were used or developed and integrated into the simulation tools. For an efficient describtion of complex drill string dynamics in spatially curved wellbores local borehole-fixed coordinate systems were introduced at the end of the1980s [OST89]. In these coordinates the external forces, especially the nonlinear contact forces between the string and the wellbore, can be described suitable and efficient. The drill string's equations of motion have the following structure:

$$\underline{\underline{M}}\,\ddot{\underline{u}} = \underline{F}(u, \dot{u}, t)$$

Therein, the column matrix $\underline{F}$ summarizes all forces and torques. Besides elastic forces, non-linear elastic restoring forces from the borehole geometry, damping and dissipation forces, the gravity and the outer normal force at the hook, $\underline{F}$ also includes the forces from the modular sub-models for the torque on the bit, the downhole motor, impact and friction forces at the wellbore wall and additional dissipative elements.
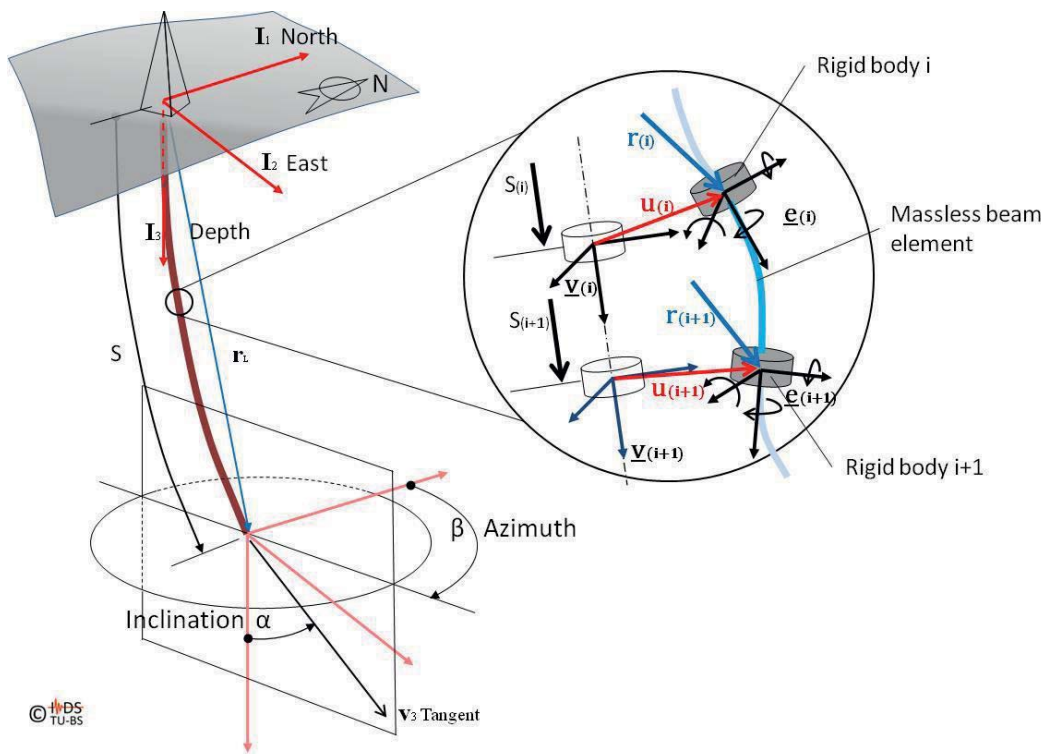
Figure 2: Coordinate systems and section of the model (schematically)

This model uses the following technique: A FEM code is utilized, which is, with respect to the masses, modeled with a lumped-mass method. This allows the use of explicit integrators for the non-linear FE modeling world. Generally, a numerical integration of pure FE models with non-linear terms must be carried out by means of multiple iterations of algebraic equations. Notably, this is very time-consuming when highly dynamic processes, such as friction, impact situations or short-time contacts, must be calculated. A numerical integration with highly optimized Runge-Kutta-Fehlberg procedures of higher order gives the opportunity to describe even rather stiff mathematical systems [OST04]. The additional algorithms required, e.g. for the inclusion of unilateral constraints or friction forces, have been developed in various other projects of the institute in the past. In this modeling world, adaptive variations of the model complexity are also possible, e.g. a variable length of the drill string or variable time transformations for the simulation of impacts. Therewith, the concept study and the first work package are finished.

Complete system's modeling (WP2): For a holistic approach that allows studies of the interactions of individual drill string components, a model has been developed, which enables a modular integration of the sub-models from work packages (WP3-6). Therewith, the aforementioned model structure is expandable and merges models of individual components into an entire model. This gives the opportunity to generate data on the dynamics of drill strings in spatially curved boreholes with very low computing time. Continuatively, the complex long-term dynamics of full drill string assemblies is being studied, considering the respective borehole trajectory and its analysis in project W7. Based on fundamental preliminary studies [OST89, HEI93, NEU97] and recent work at the institute [MEY10,11a,11b, OST13, KUE14], new and future sub-models of the individual tools can also be integrated into the existing FE models. As a first milestone (M1), first vibration simulations of the drill string and their validation on the basis of measurements are done. With the developed and fully parameterized drill string model [OST10,11,11a,SHI11], which already uses sub-models for the bit, the drill string/borehole contact and initial approaches of mud modeling, first simulations of the drill string dynamics have been done. Due to lack of measurement data, these preliminary simulations used a reasonably defined reference system. This assumes an ideal, straight and vertical borehole trajectory, drilled by a rotary drilling process. The aim at first is to simulate known phenomena, such as stick-slip and whirl, which are more dominant in straight and vertical trajectories, rather than in deviated and curved or even horizontal boreholes. The drill string dynamics is simulated for a vertical depth of the assembly of 1.000m, a borehole and bit diameter of 10 5/8", a BHA outer diameter of 8 ¼" and 5" of drill pipes. One reason for this choice of reference system and parameters is the fact that in January 2011, Baker Hughes has provided later on measurement data of a test rig (BETA) that operates up to a vertical depth of 1.000m. These are supplemented by respective simulation data, computed with BHASYSPro.

The results are shown in WP7. All simulations that were done within the scope of this project are based on the in-house simulation software PLAN [OST04], which was developed at the institute. The program environment is based on the object-oriented programming language C++ and allows a fast and simple implementation of dynamic systems into complex simulations under various operating systems. The top-down programming technique offers a variety of comprehensive mathematical and graphical functions, as well as an easy to use graphical user interface. With respect to dynamic systems or, more precisely, their mathematical models (such as the drill string in this case), extensive simulations and analyses can be realized with the help of the numerous already implemented functions. The output of simulation results can be done in various ways, e.g. by plotting them into graphics. A particularly demonstrative alternative is to convert them into online animations. The numerical calculation of the developed drill string models, which have the form of non-linear ordinary differential equations, a highly optimized Runge-Kutta-Fehlberg algorithm of the order 7/8 is generally used.
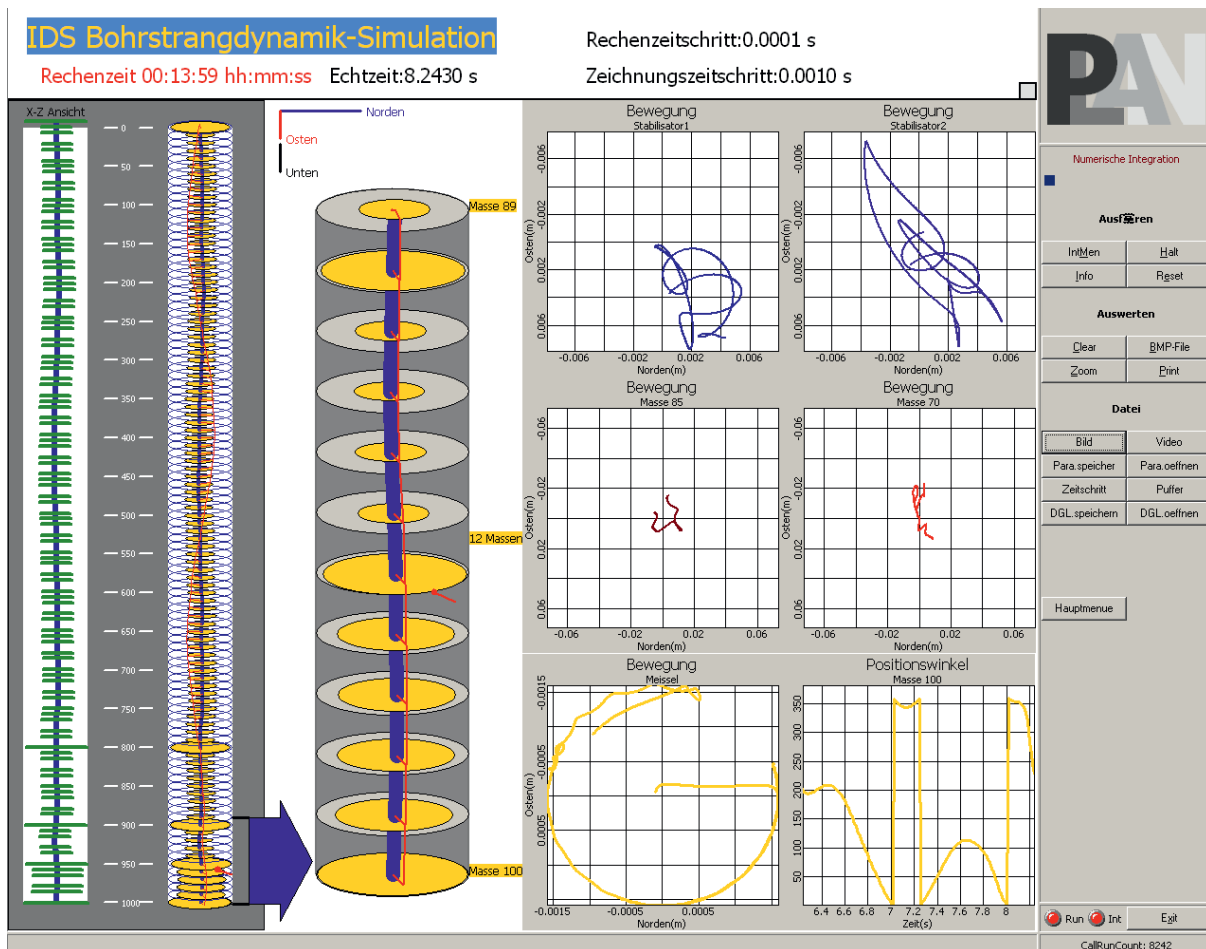
Figure 3: User interface of the simulation tool

Figure 3 shows a first sample screenshot of the user interface (PLAN simulation window) for internal use. The screen is modular, thus, it can be adjusted and expanded according to user inputs. On the left-hand side, online animations of the whole system are shown in 2D and 3D,

as well as a zoomed fraction of the drill string assembly. Towards the right, different plot graphics can be displayed that visualize motions, forces or torques. The right-hand side shows a panel of control buttons that allow the user to navigate through the program or to interact with the simulation.

With the aforementioned model, vibration simulations can be realized to test the model's functionality with respect to the simulation of dynamics phenomena. Some sample results are shown in the following. As a function of selected parameters and boundary conditions, which represent different drilling scenarios, known dynamic phenomena in deep drilling technology can be simulated, such as stick-slip and whirl. Figure 4 shows stick-slip effects on the bit at a rotational speed of 100rpm at the top drive. The stick phases, as depicted in the upper graph, are clearly visible and influence the torque on the bit accordingly, as given in the lower graph. For an increase in rotational speed at the top drive, in this study from 100 to 160rpm, stick-slip disappears. As a consequence, the torque on the bit remains constant and the rotational oscillations decay, according to the low damping implemented here.
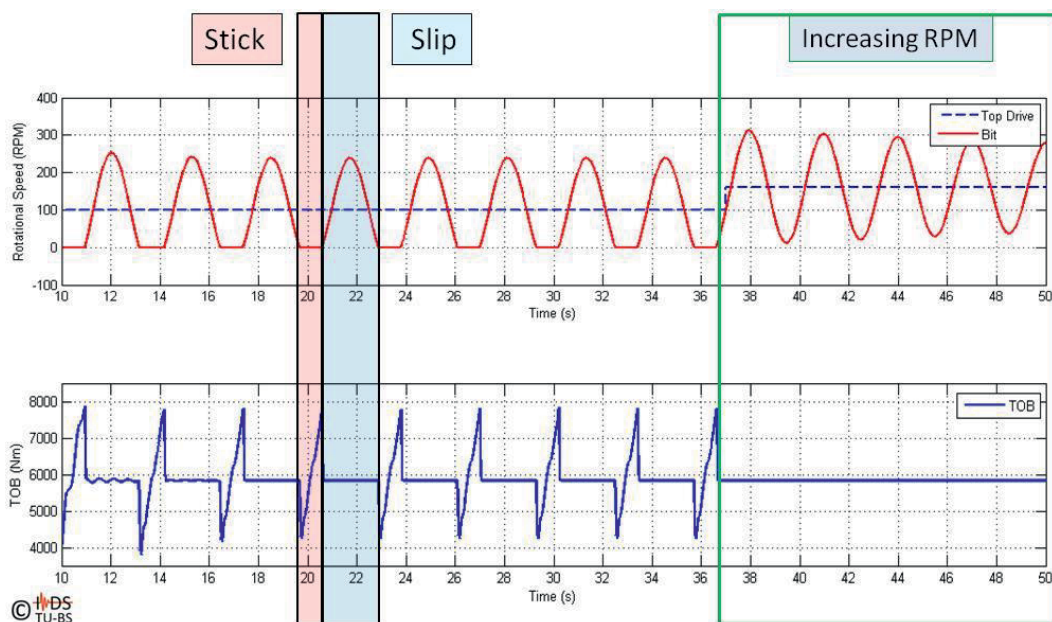
Figure 4: Stick-Slip effects on the bit

519
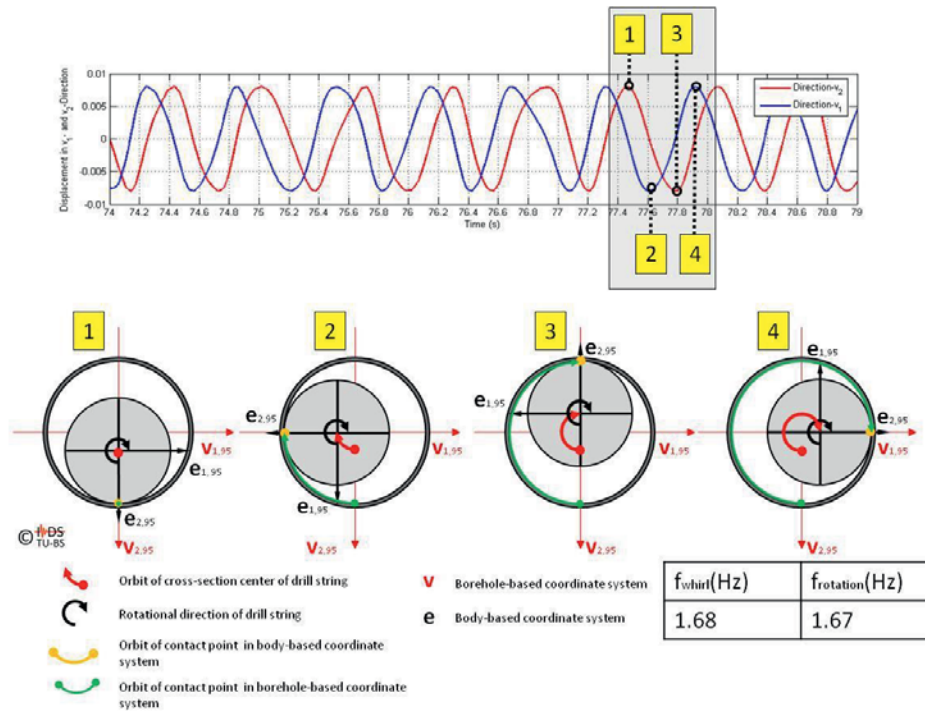
Figure 5: Forward whirl in the upper range of the BHA

Figure 5 shows forward whirl oscillations in the model at a frequency of f = 1.67Hz. These occur at a stabilizer in the range of the upper part of the bottom hole assembly (BHA). Besides the lateral deflections v_1 and v_2 (in the reference frame fixed to the borehole), a cross section is given that shows the motion of the drill string during one period of the forward whirl oscillation in four discrete steps.
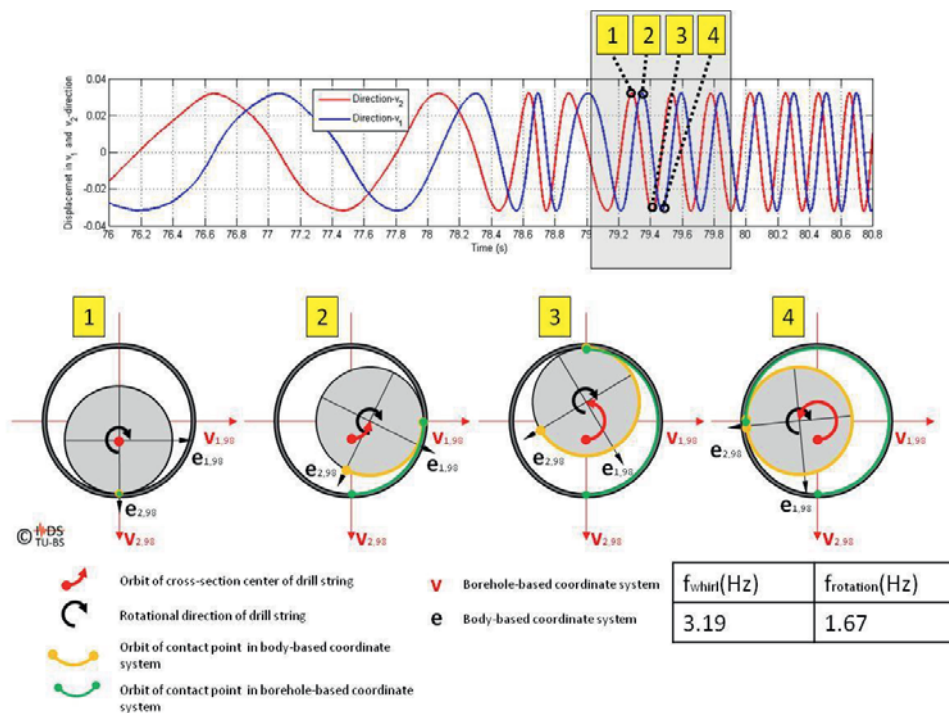
Figure 6: Backward whirl in the lower range of the BHA

Backward whirl oscillations in the model are visible in Figure 6, which occur in the middle of the BHA. The frequency of f=3.19Hz corresponds to a factor of 1.9 relative to the angular frequency, as given by the rotational speed. In addition to the lateral deflections v_1 and v_2 (again given in the reference frame fixed to the borehole), Figure 6 also shows a cross section of the drill string's motion for one period of the backward whirl oscillation, similar to Figure 5 in four discrete steps. These simulations were carried out on a standard desktop PC type "Dell Optiplex 755MT", equipped with an "Intel Pentium Dual Core" processor (2,2GHz, 800MHz, 1MB RAM) and 2GB RAM (800MHz DDRII). For a 1km drill string with 100 elements and a standard bit model, and without any optimization concerning the numerics or the algorithm efficiency, the simulation software reaches a ratio of approximately 100:1 for computing time relative to real time. Therewith, the first milestone (M1) with respect to first vibration simulations of the drill string is accomplished. Due to a lack of measurement data, a validation could only be done qualitatively by means of the simulated dynamic phenomena. The second milestone (M2) "Complete drill string model and interface to the single tools", which finalizes the concept study of WP 1, is accomplished, as well.

For further model optimization in terms of improving the computational speed while maintaining the accuracy, additional FE beam element formulations were investigated. In addition to complex beam elements already in use [OST89, HEI93] we have implemented and tested successfully corotational formulations. For running fundamental studies and principle simulations a self-chosen synthetic wellbore was considered as shown in Figure 7.
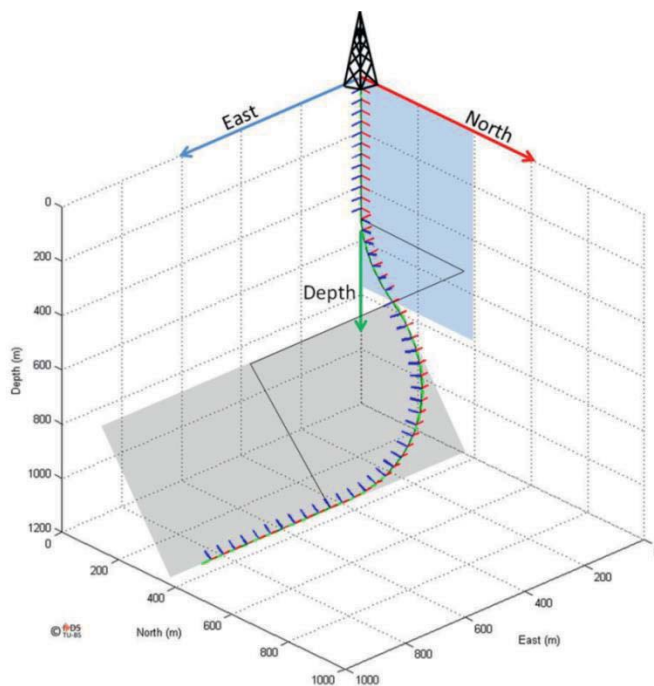
Figure 7: Synthetic wellbore for principle investigation

For the first time corotational beam formulations have been used to describe the drill string dynamics in the 1990s [JAN93]. In contrast, in our model only the corotational beam elements are described in the inertial coordinates. The external forces – especially the highly nonlinear contact forces – are still described in local borehole-fixed coordinates. The choice of suitable coordinate systems simplifies the mathematical description and optimizes clearly the numerical calculation. The corotational beam lement is an effiecient formulation due to large displacements and rotations but small local deformations that reflects exactly the conditions of the drill string behavoir. Further advantages are: Simulation of a continuous rate of penetration, the simple implementation of geometric imperfections and the independence from the wellbore profile. Thus, in addition to straight and circular sections arbitrary profiles (e.g., catenary well profiles) can be described. Figure 8 shows the current status of the user interface of the simulation tool. On the right-hand side is the panel to use and control the online simulations similar to Figure 3. On the left-hand side is shown the formation profile, the wellbore trajectory and the drill string. The color coding shows various mechanical output data (in this case the axial force). Furthermore, significant drilling parameter will be calculated and shown in text form.
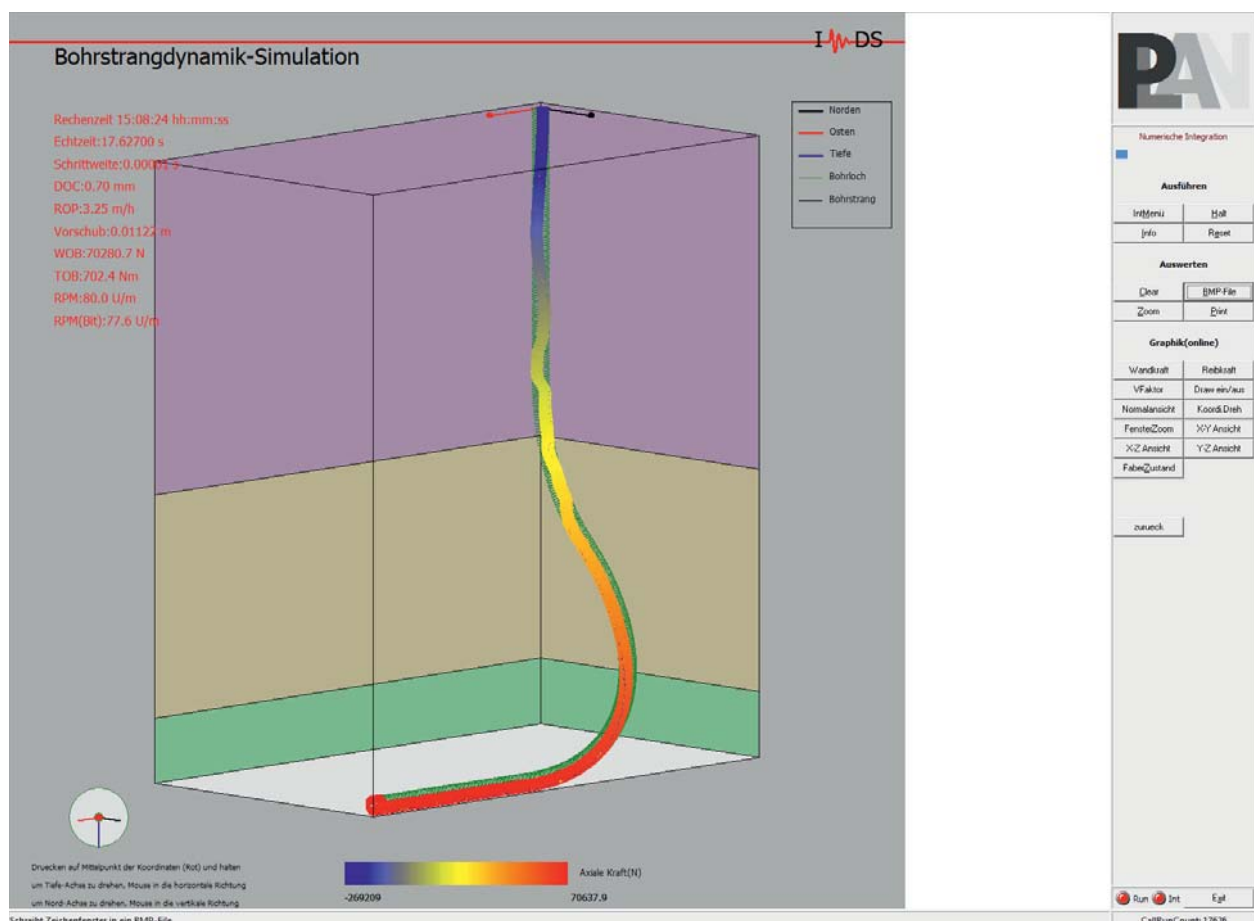
Figure 8: Current status of the user interface of the simulation tool

Of course, the simulation results ca also be written into files (e.g., load spectra, see project W7) and used for further processing. An interface to the open source visualization program ParaView has been developed in order to obtain a post processing with better graphical capabilities. Figure 9 documents simulations results using the postprocessing mode. For example, a) illustrates the dynamics of the BHA / near to the BHA and b) buckling as a result of dynamic stability studies.

a)   b)
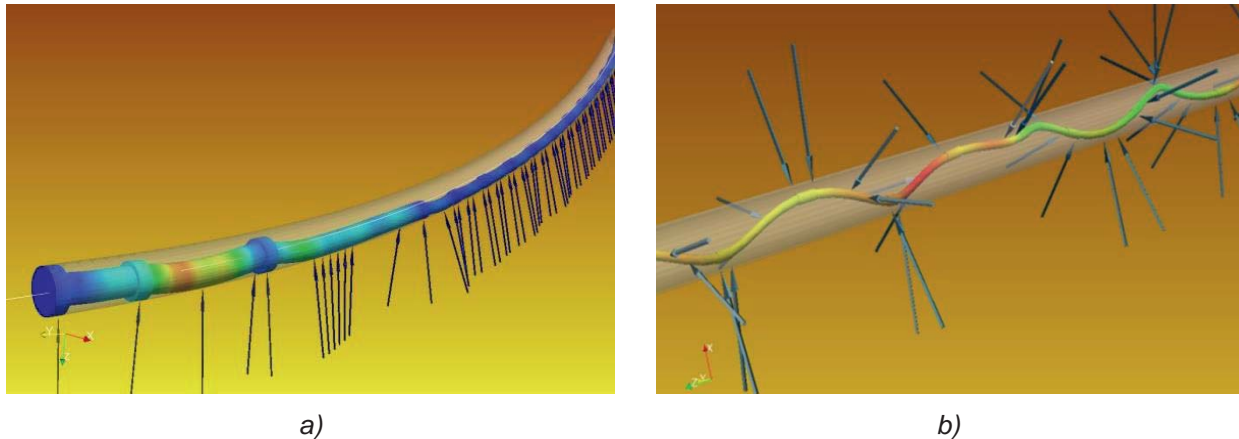
Figure 9: Simulations results using the postprocessing mode, a) BHA dynamics, b) Buckling

According to the project plan, the model of the complete system is expanded by new sub-models for single components. In parallel, existing sub-models are updated, adapted and optimized. In addition, sensitivity analyses with respect to the quality of simulation results relative to the computing time are done, under consideration of the validation in WP 7, see further below. Model parameters that need to be varied during this study are the borehole geometry, the lengths and stiffness of the elements, as well as the sub-models parameters for bit, downhole motor, interactions between drill string and borehole and interactions between drill string and fluid. The overall goal is the implementation of model complexities that vary with space and time [OST97], in order to get maximum accuracy in a minimum amount of time. This claim implies variable model elements that need to be coupleable with each other. In addition, strategies for data handling are required, in order to synthesize model specific data from a structured data pool. This structured data pool is represented by an intelligent data capsule, which includes an object-oriented realization of data collection, data conditioning and data visualization. In this sense, the data capsule is not only the basis for a comfortable visualization tool (see [OST89] for a simple version), but, moreover, an important step towards an adaptive modeling world. Investigations concerning the drilling fluid and the borehole geometry can be performed, as well, since dissipation by means of fluid flow, friction and impact on the wellbore walls significantly influence the short-term and long-term dynamics. The hereby modified dynamics can be of significant durability and fatigue relevance. Therewith, it influences the synthetic load spectra in W7 that are gained by investigations of the long-term dynamics

[OST14b]. Measurement data can also be integrated in such a data capsule. The full model constitutes the third milestone (M3), in the form of simulations of the overall system including all tools and their sub-models.

Sub-models of the components (WP 3-6):

The highest forces and torques, which act upon the drill string, are transmitted during the process of rock cutting at the bit (WP 3). Modeling of the cutting is done with a model that describes the torque on the bit as a function of its aggressiveness and the normal force on the bit. Existing models at IDS concerning the dynamic evolution of friction, heat and wear are being implemented into this model, successively [OST02]. Therein, the bit-rock interaction is modeled as a unilateral constraint, whose stiffness is a function of bit aggressiveness, bit geometry and bit efficiency, as well as the unified compressive strength of the formation [MEY10]. Different drilling techniques, such as rotary drilling processes or coiled tubing, will have different requirements on the simulation technique. In the context of gebo, there was given only practical input to rotary drilling and the used bits for this purpose. In different studies we investigate the aforementioned model [MEY10]. Thereby, the sensitivities of the falling friction characteristics (bit agressiveness) were tested substantially with respect to the self-excitation mechanism and the corresponding vibration behavior. In additon to this, a simulation tool for bit/rock-investigations with enhanced models was developed as shown in Figure 10.
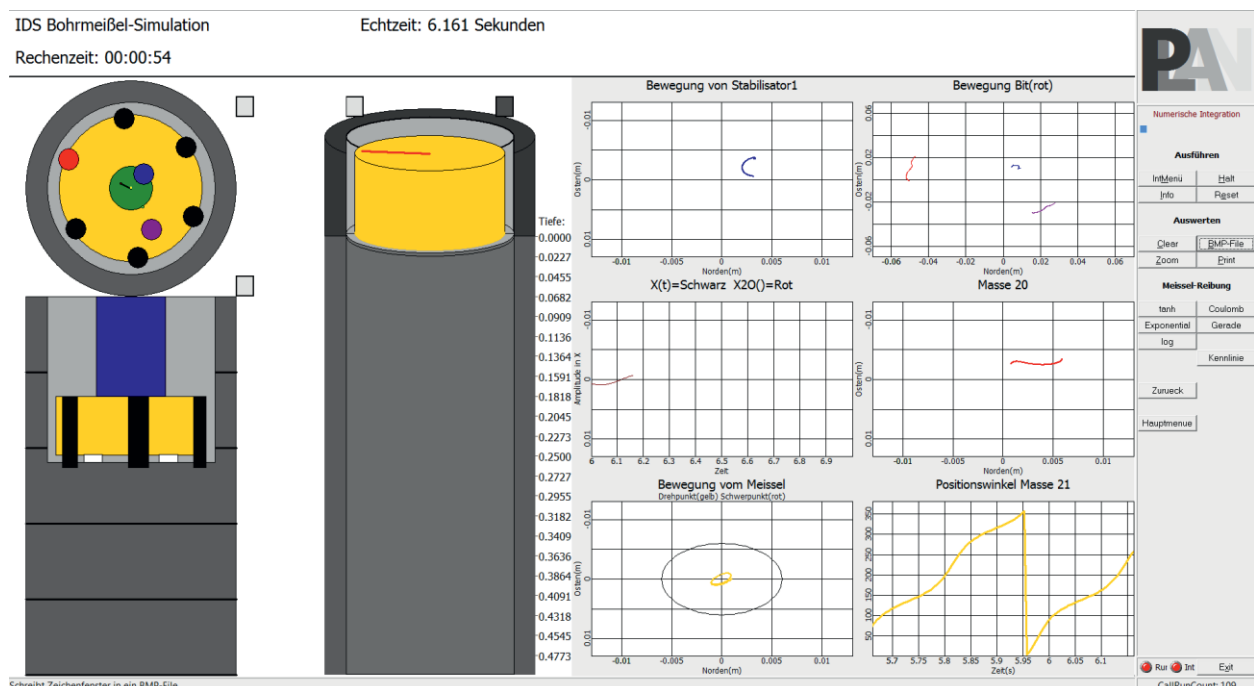
Figure 10: Inferface of simulation tool for bit/rock-investigations [BAE13]

Thus, several boundary conditions and parameters for contact forces, torques and friction characteristics can be investigate systematically. However, these bit models for complex drill string models are approximations as well as the cutting process itself.

Thus, the implementation of *downhole motors (WP 4)* is one essential prerequisite in order to be able to adapt models and simulations to different drilling techniques. Downhole motors that are actuated by the drilling fluid have eccentric rotors, whose rotational speed is given by the flow rate and the gear ratio. When actuated, the center of gravity of the motor's rotor moves in opposite direction and on a circle of constant radius around the stator's center of gravity. Due to the kinematics and the rotor's mass, centrifugal forces act on the stator. In the sub-model of the downhole motor, the additionally generated rotational speed is implemented at first, together with the centrifugal forces mentioned above. The geometric parameters and the process parameters of the downhole motor can be set in the simulation tool. Thus, the system stiffness, the unbalance forces and rotational speed changes with respect to the chosen motor configuration. The motor torque is mounted by the upper string. Model analyzes show the impact of the increasing rpm on the drilling process. The resulting vibrations affect rather slightly the drilling process. However, higher vibrations may occur at the BHA that have negative effects on BHA tools.

Because of the drill string's length and its contact with the wellbore wall, *dissipative contacts between the drill string and the wellbore wall (WP 5)* have a major influence on the propagation of vibrations in longitudinal direction of the drill string. As a first step, the contact was modeled as a unilateral constraint with Hertzian stress (linear, Kelvin, Hertzian damped contact models were also tested), which describes the impact and, at the same time, the generated friction force in tangential direction with according non-linear characteristics. For a better approximation, existing contact models are being adapted to this specific situation in the future. To determine the friction forces, different friction characteristics (Coulomb, Stribeck or dynamic friction laws [OST02]) were taken into account and were investigated in parameter studies. In the simulation tool different contact models and friction characteristics can be selected. The relevant parameters are adjustable. Usually, the wellbore cross section is assumed to be circular in simulation models. As shown in Figure 11, this assumption does not meet reality. Due to the major influence of the contact modeling on the dynamic phenomena, we focus the simulation tool development also on the integration on geometrical imperfections.

525
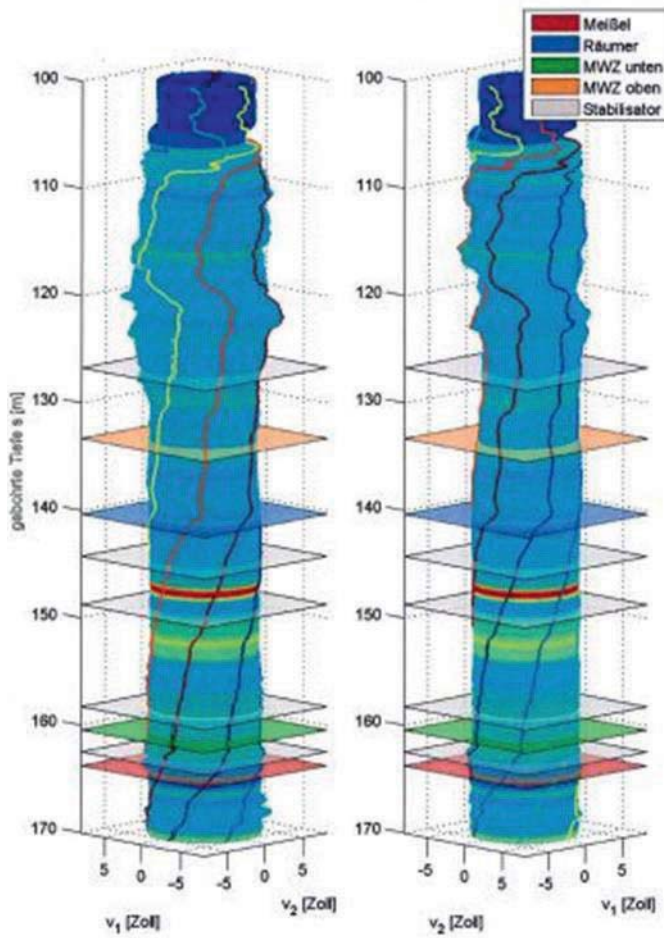
Figure 11: Measured wellbore profiles [MEY11b]

Corresponding simulations, first of all with minimal models, have shown the significant influence of even small imperfections on the dynamic phenomena [OST14a]. The simulation result of Figure 12 shows a total change in the dynamics. On the left-hand side we see a foreward whirl motion of the drill string.
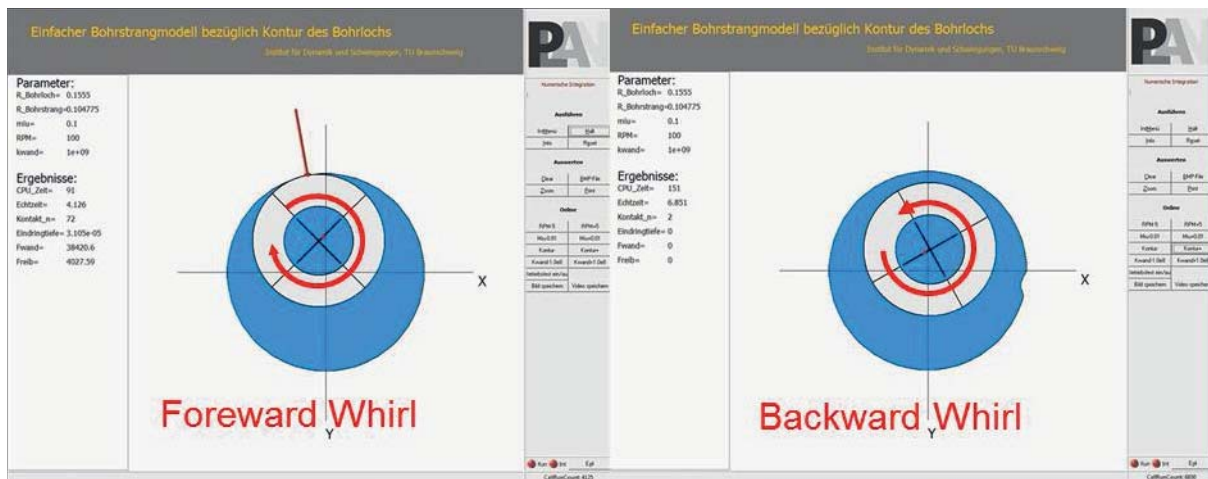
Figure 12: Dynamic phenomena with respect to geometrical imperfections of the wellbore

After contacting the even small geometrical imperfection (implemented in the time domain simulation), the motion switches into a backward whirl, shown on the right-hand side of Figure 12. Furthermore, the developed simulation tool has the ability to implement wellbore profiles with microturtuosity, see Figure 13. This research will be continued in the context of an ongoing PhD thesis. Using the developed tools, new potentials are given to analyse friction induced vibration in drilling engineering.
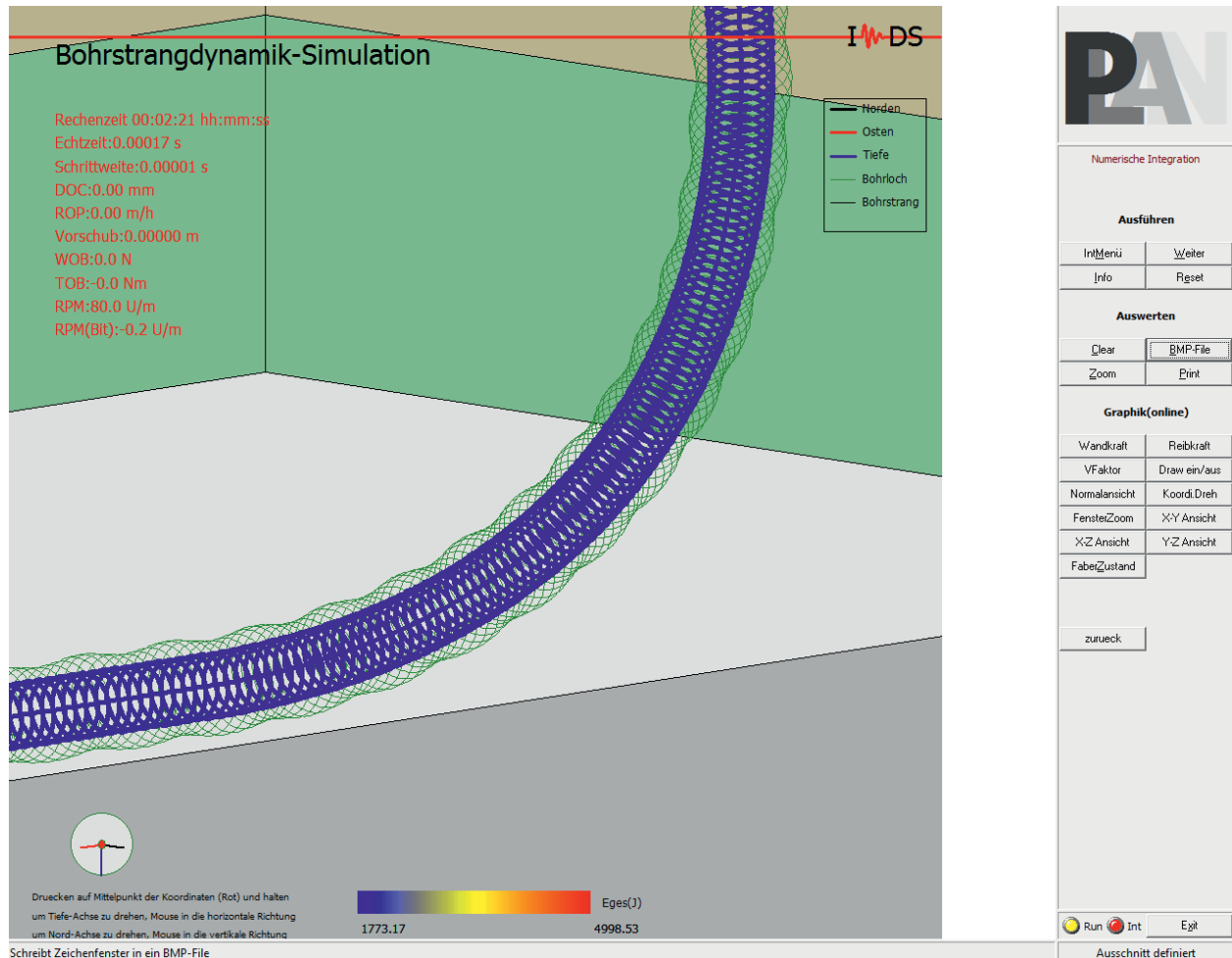
Figure 13: Simulation tool with mircotortuosity of the wellbore profile

Moreover, we have been looked for possibilities to optimize computational effort of the full model simulations with respect to the contact modeling. One option is to introduce Gaussian points in order to reduce the number of elements while maintaining model accuracy [SHI13].

The density of the *drilling fluid (WP 6)* has an influence on the moving masses, when lateral motions of the drill strings are significant. In addition, it causes a lifting effect of the string that is already implemented in the current model, and a damping of vibrations in the annulus. For the sake of simplicity, this dissipation is in the first step described by purely viscous damping. As the project continues, macroscopic damping laws for a more detailed approximation of the

527

fluid's properties should be developed in cooperation with project B6. Due to the fact that project B6 ends in midyear 2012, the collaboration was brought forward to the fourth quarter of 2010 (see project plan). Unfortunately, no lateral dynamics of the drill string was implemented in the simulation tool of project B6. Thus, a derivation of marcoscopic damping laws was not possible. However, in a simulation example restoring forces were determined with respect to a rotating drill string and its lateral position within the wellbore [OST11c]. These results were included in further analyses [REC12]. In this study, the commonly used approach for increased material damping was compared to an approach by Morrison [MOR50] with velocity-dependent and acceleration-dependent terms with respect to the vertical depth. The investigations indicate that the damping effect decreases with the vertical depth. Based on a simple 5-mass-model the damping effect of different approaches was investigated with respect to specified motion states.
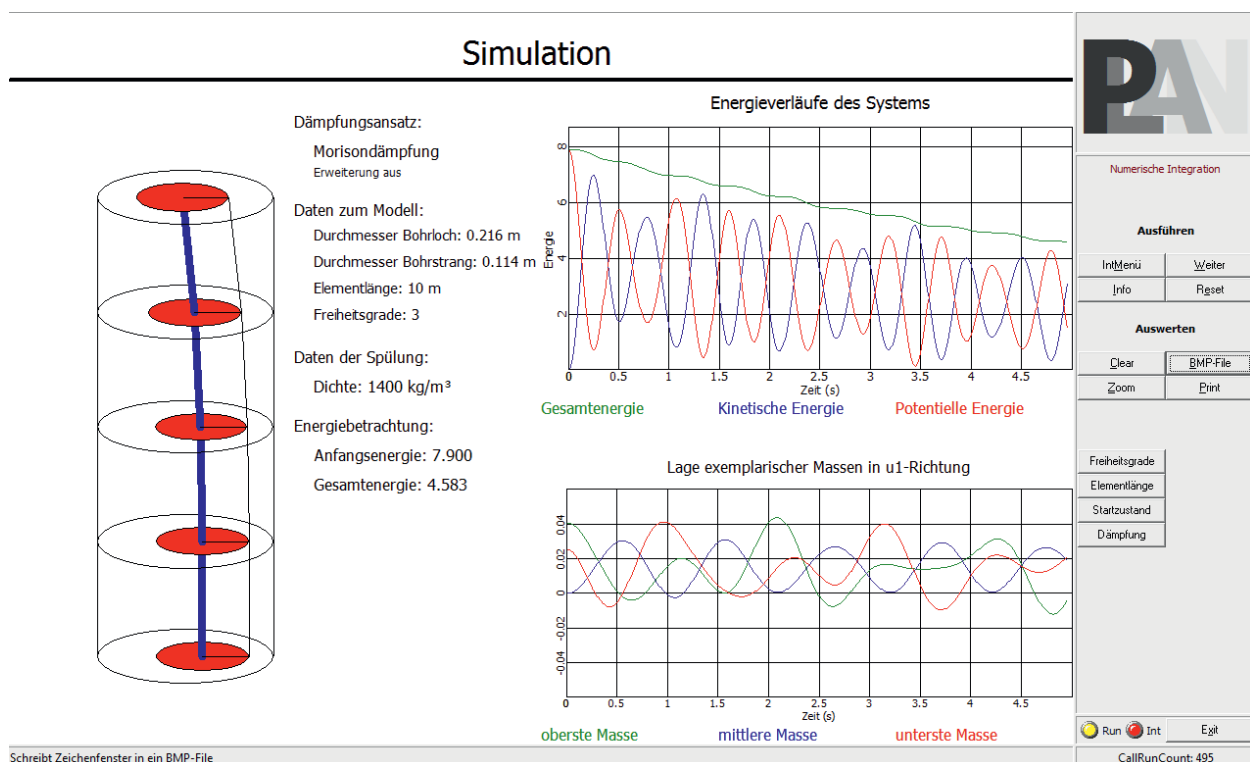
Figure 14: Simulation tool for principle investigations of damping influences [REC12]

From the gained results an enhanced approach is formulated. In principle, the lack of comparison data (from fluid-structure simulations or measurements) is the main problem to develop more suitable macroscopic damping characteristics.

Simulations and model validation (WP 7): For the prediction of vibration phenomena in the drill string, complex simulations of component models and the overall model are performed. On the basis of measurement data provided by Baker Hughes, results of the model are checked and parameters are adjusted. Baker Hughes provides data of a test rig (BETA), together with

corresponding simulation data generated with BHASYSPro [BHI98]. Here BHA_Run9_1998-10-05 is evaluated. It is a vertical wellbore (except small deviations) with a drilled depth of 809m. After filling the data capsule with the BETA input data (drill string set up, wellbore profil an geometry, formation data) we perform first of all different simulation runs for parameter fitting. In particular, we have varied the parameter for the bit-rock interaction and the contact between drill string and wellbore wall and run sensibility studies. Some selected results are shown in the next figures. Figure 15 documents as the screenshot of a post-processing movie the rotation of the drill string and the contact forces.
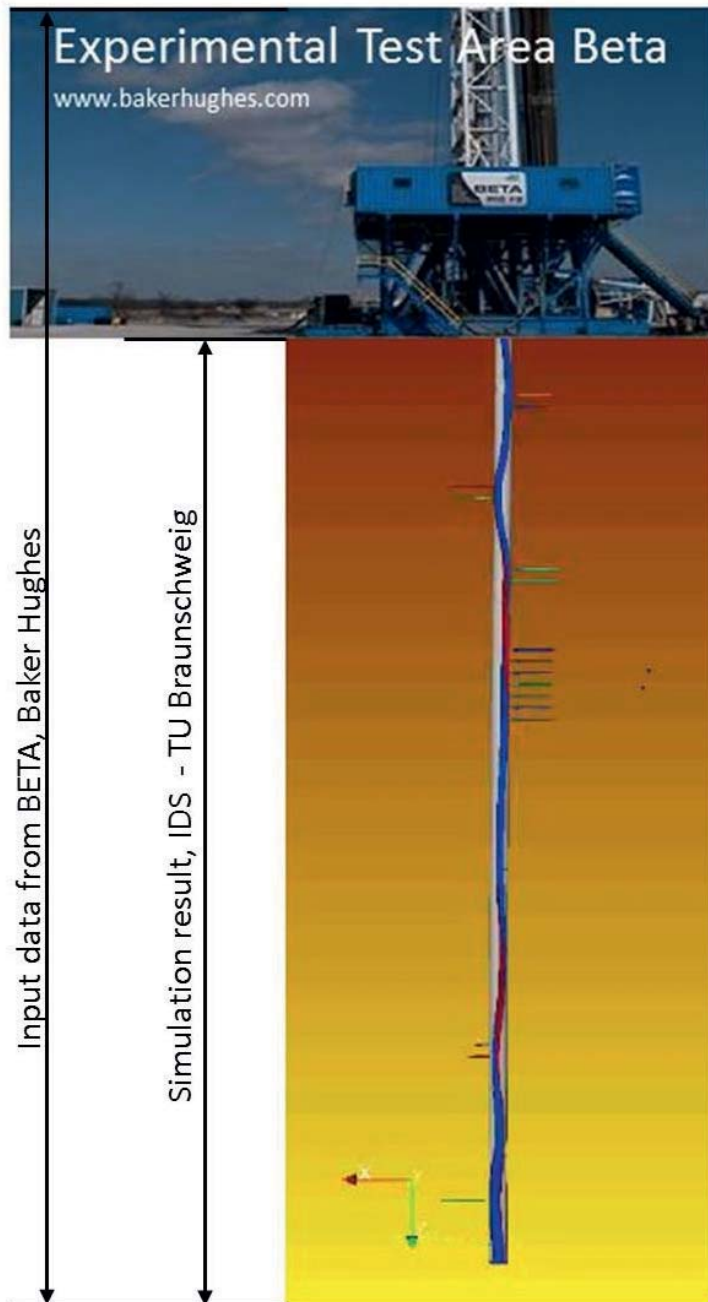
Figure 15: Validation results for vertical section of BETA
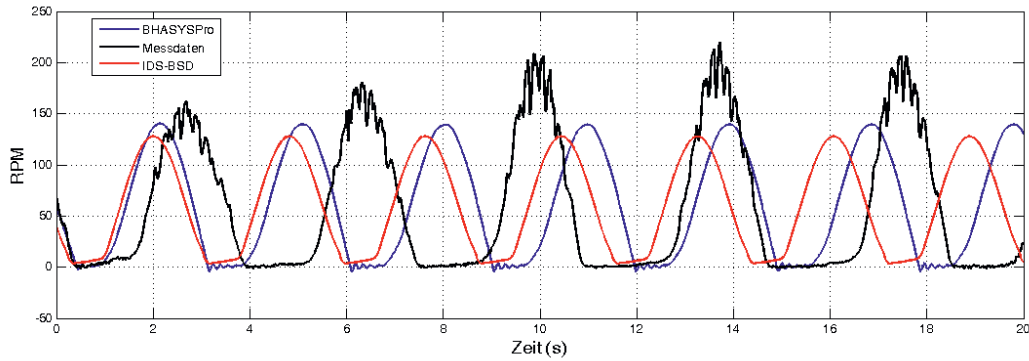
Figure 16: BETA downhole rpm measurement at BHA vs. simulation results of BHASYSPro and the IDS model

In Figure 16 the plot shows a comparison between the measured downhole rpm at BETA and the simulation results. It is found on average a relatively good correlation due the amplitudes and the stick-slip frequency. Of course, such a stick-slip behavior at the BHA can also be simulated with much simpler models (as frequently used in drilling engineering), but simple models are not able to provide results (forces, moments, displacements, velocities, accelerations, energy measures,….) along the total drill string as we can do using our model or BHASYSPro for instance. In Figure 17 we see the appropriate bending moments at the lower drill strill and together with corresponding time data we can observe the lateral dynamics.
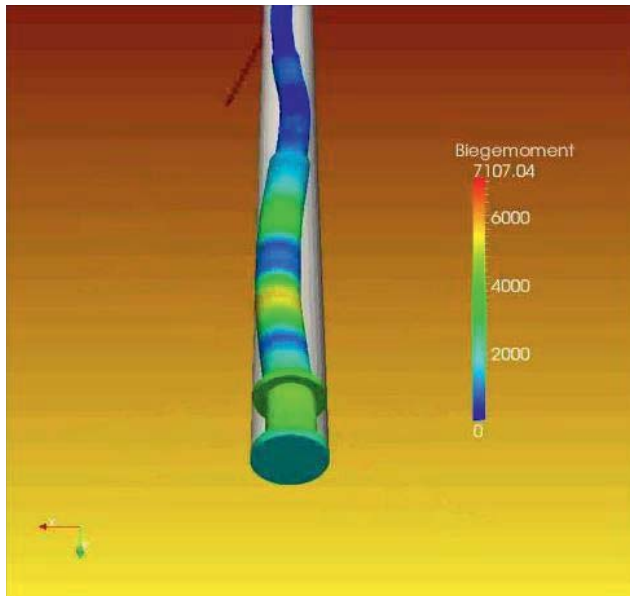
Figure 17: Simulated bending moments at BHA, drill collars and lower drill pipes
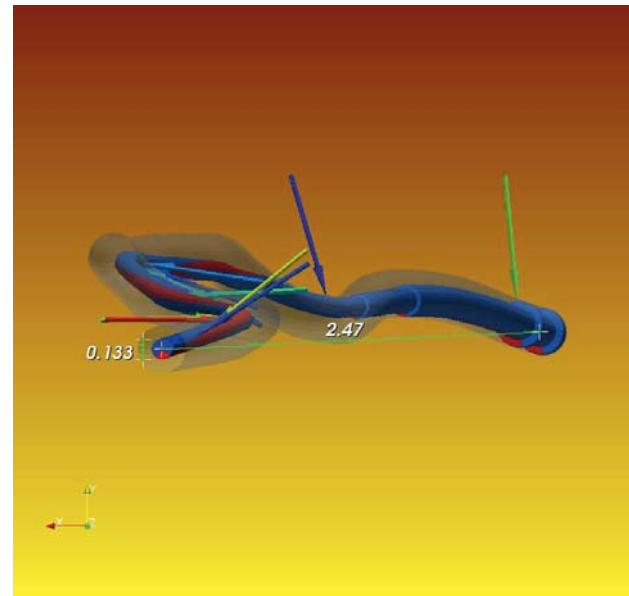
Figure 18: BETA run top view

Figure 18 shows as a top view the small horizontal deviations up to 2.47m by a length of 809m. A comparsion of Figure 15 and Figure 18 shows that the simulated contact forces corresponds

with the measured well profile. Whereever the well profile deviates to the vertical direction, contact forces are resulted. Of course, this is equivalent to the expected mechanical behavior but also a further indicator for the model quality. Additional mearsurement evaluation, results and simulations with BHASYSPro are summarized in [OST11b].

Unfortunately, there are no measurement data available for the validation of the dynamics along the string. In most cases only measurement data at one or two locations at the BHA exist. In future, "along string measurements" using wired pipe systems should be available to overcome this problem. It can be expected that the performance of complex drill string models and simulations will be significantly improved and their impact on drilling engineering will further increase.

1.2.4 Project Plan

Work packages and milestones	2009	2010	2011	2012	2013	2014
WP1: Complete model's concept & interfaces to sub-models						
WP2: Complete system's modeling						
WP3: Rock cutting at bit						
WP4: Downhole motor						
WP5: Contact drill string / borehole						
WP6: Drilling fluid						
WP7: Simulations and Model validation						

Grey, original plan. Blue, actual or current plan, respectively.

For details, see Gantt chart in the Appendix.

1.3 Delineation of the project from other funded projects

An overlapping with other public funded projects does not exist.

1.4 References

[MOR50] Morison, J. R., O'Brien, M. P., Johnson, J. W., Schaaf, S. A.: The force exerted by surface waves on piles, Petroleum Transactions (American Institute of Mining Engineers) 189: 149–154, 1950

[OST89] Ostermeyer, G.-P., Brommundt, E.: Theorie-Manual zum Programm OSPLAC – Optimal Stabilizer Placement, Institut für Dynamik und Schwingungen (ehemals Institut für Technische Mechank), TU Braunschweig, 1989

[CRI90]   Crisfield, M.A.: Consistent Co-rotational Formulation for Nonlinear Threedimaensional Beam Elements, Computer Metods in Applied Mechanics and Engineering, Vol. 81, S. 131-150, 1990

[CRI90]   Crisfield, M.A.: Non-linear Finite Element Analysis of Solids and Structures, Vol. 1, WILEY, Chichester, 1991

[HEI93]   Heisig, G.: Zum statischen und dynamischen Verhalten von Tiefbohrsträngen in räumlich gekrümmten Bohrlöchern, Dissertation, Braunschweiger Schriften zur Mechanik Vol. 13, Braunschweig/Celle, 1993

[Jan93]   Jansen, J.D.: Nonlinear Dynamics of Oilwell Drill String, 1993, Dissertation

[NEU97]   Neubert, M.: Richtungsregelung beim Tiefbohren, Dissertation, Braunschweiger Schriften zur Mechanik Vol. 32, Braunschweig/Celle, 1997

[OST97]   Ostermeyer, G.-P.: Frequenzbeschränkung der Lösung: Konsequenzen für gekoppelte MKS- und FEM-Systeme, in: Richter, G.: Verbindung von MKS und FEM-Modellen, Haus der Technik e.V., Essen, Tagung Nr. E-30-206-056-7, 1997

[BHI98]   Baker Hughes, BETA-Daten, 1998

[OST02]   Ostermeyer, G.-P.: On the dynamics of the friction coefficient, 280. WE-Haereus Seminar, Ilmenau 2002, Wear 254 (2003) 852-858

[OST04]   Ostermeyer, G.-P.: *Simulation mechatronischer Systeme*, Vorlesungsskript Institut für Dynamik und Schwingungen, TU Braunschweig, Braunschweig, 2004

[OST13]   G.-P. Ostermeyer, A. Kück: Modeling of the dynamic phenomena "stick-slip" and "whirl" of a drill string demonstrator PAMM Volume 13, Issue 1, December 2013, pages 29–30, DOI: 10.1002

[MEY10]   Meyer-Heye B., Reckmann H. and Ostermeyer G.-P.: Weight Distribution in Reaming While Drilling BHAs. Paper IADC/SPE 127094 presented at the IADC/SPE Drilling Conference 2010, New Orleans, Louisiana, 2-4 February, 2010.

[MEY11]   Meyer-Heye, B., Bubser, F., Ostermeyer, G.-P.: Der OSTrator - Dynamik von Tiefbohrsträngen erleben. DGMK Frühjahrstagung 2011

[MEY11a] Meyer-Heye, B., Reckmann, H., Ostermeyer, G.P.: Underreamer Dynamics, IADC/SPE – 139893, Amsterdam 2011

[MEY11b] Zum Einfluss von Räumwerkzeugen auf die Dynamik von Tiefbohrsträngen, Dissertation Schriftenreihe Institut für Dynamik und Schwingungen, TU Braunschweig, ISBN 978-3-8322-9897-5, 2011

[KUE14]   Kück, A., Recke, B., Ostermeyer, G.-P.: Reduction of non-linear drill string models using proper orthogonal decomposition, PAMM Volume 14, Issue 1, pages 205–206, December 2014, DOI: 10.1002/pamm.201410090

[WEC09] Weckend, Carsten: Konzeption, Aufbau und Inbetriebnahme eines Demonstartors für Bohrstrangschwingungen, Studienarbeit am Institut für Dynamik und Schwingungen, TU Braunschweig, 2009

[KEI10] Keisenberg, T.: Pendelmodell zur Beschreibung der Bohrstrangdynamik, Diplomarbeit am Institut für Dynamik und Schwingungen, TU Braunschweig, 2010

[MAU10] Mau, Fabian: Aufrüstung eines Schwingungsdemonstrators mit Steuerungs- und Messtechnik, Studienarbeit am Institut für Dynamik und Schwingungen, TU Braunschweig, 2010

[REC12] Recke, Bastian: Untersuchung des Einflusses der Spülflüssigkeit beim Tiefbohren, Studienarbeit am Institut für Dynamik und Schwingungen, TU Braunschweig, 2012

[VOE12] Voelpel, Aaron: Analyse dynamischer Bohrstrangeffekte anhand von Minimalmodellen, Bachelorarbeit am Institut für Dynamik und Schwingungen, TU Braunschweig, 2012

[BAE13] Baeck, Michael: Modellierung und Simulation eines Polycrystalline Diamond Compact(PDC)-Bohrmeißels, Studienarbeit am Institut für Dynamik und Schwingungen, TU Braunschweig, 2013

[ZHA13] Zhang, Li: Vergleichsstudie zu Modellen in der Bohrstrangdynamik unter Anwendung der FE-Software Abaqus, Masterarbeit am Institut für Dynamik und Schwingungen, TU Braunschweig, 2013

[GUI13] Gui, Yan: Prinzip Studie von Key-Seating-Phänomena und 3D-Visualisierung der Bohrstrangdynamik-Simulation unter ParaView, Masterarbeit am Institut für Dynamik und Schwingungen, TU Braunschweig, 2013 [LIA13] Liang, Jinghu: Modellierung und Simulation für reibbehafteten Kontakt Bohrstrang/Bohrloch, Studienarbeit am Institut für Dynamik und Schwingungen, TU Braunschweig, 2013

[WIE14] Wiese, Mats: "Untersuchung von Parameterübertragung zwischen Bohrstrang-modellen", Bachelorarbeit am Institut für Dynamik und Schwingungen, TU Braunschweig, 2014

[DOB14] Dobrowolski, Thomas: Untersuchung des Zusammenhangs von Gesteins-eigenschaften und Prozessdynamik beim Tiefbohren, Studienarbeit am Institut für Dynamik und Schwingungen, TU Braunschweig, 2014

[FRE14] Freckmann, Karsten: Detektion dynamischer Effekte eines Bohrstrangsimulators, Studienarbeit am Institut für Dynamik und Schwingungen, TU Braunschweig, 2014

1.5 Publications, reports and presentations of Project

[OST10] Ostermeyer, G.-P., Schiefer, F.,Shi, M.: Erste Schwingungssimulationen zum Bohrstrangmodell, Interner gebo-Meilensteinbericht – IDS-Bericht 2010-15

[OST11] Ostermeyer, G.-P., Schiefer, F.,Shi, M.: Modellbildung des Gesamtbohrstranges, Interner gebo-Meilensteinbericht – IDS-Bericht 2011-02

[OST11a] Ostermeyer, G.-P., Schiefer, Shi, M.: Complex Drill String Simulation, Celle Drilling 2011

[OST11b] Ostermeyer, G.-P., Guo, Y., Shi, M., Schiefer, F.: Vergleich der simulierten Ergebnisse von BHAsysPro mit Messdaten von BETA, Interner Bericht, Institut für Dynamik und Schwingungen, TU Braunschweig 2011

[OST11c] Ostermeyer, G.-P., Schiefer, F., Krafczyk, M., Geller, S.: Bohrstrangschwingungen und Fluidkräfte auf Bohrstrang, Interner Informationsaustausch im Forschungsverbund gebo, TU Braunschweig – Institut für Dynamik und Schwingungen, Institut für rechnergestützte Modellierung im Bauingenieurwesen, 2011

[OST12] Ostermeyer, G.-P., Schiefer, Shi, M., Srisupattarawanit, T.: Drill String Dynamics and Modeling, Status-Presentation on gebo Jour Fixe Research Area Drilling, 10.02.2012

[OST13a] Ostermeyer, G.-P., Schiefer, Shi, M., Srisupattarawanit, T.: Drill String Dynamics and Modeling, Status-Presentation on gebo Jour Fixe Research Area Drilling, 08.11.2013

[OST14] Ostermeyer, G.-P., Schiefer, Shi, M., Srisupattarawanit, T.: Drill String Dynamics and Modeling, Status-Presentation on gebo Jour Fixe Research Area Drilling, 07.02.2014

[OST14a] Ostermeyer, G.-P., Schiefer, F., Shi,M.: Reflections on Modeling and Simulation of Drill String Dynamics within gebo, OIL GAS European Magazine 2014 and presentation on Celle Drilling 2013

[OST14b] Ostermeyer, G.-P., Esderts, A., Schiefer, F., Runge, S., Shi, M., Srisupattarawanit, T.: gebo final report W7 "Design of Fatigue Resistant Mechanical Componets for Drill String Applications", 2014

[SHI11] Shi, M., Schiefer, F., Ostermeyer, G.-P.: A contribution to efficient calculation of complex drill string dynamics for deep hole drilling, to be published in PAMM 2011

[SHI13] Shi, M., Srisupattarawanit, T., Schiefer, F., Ostermeyer, G.-P.: On the wellbore contact of drill string in a Finite Element Model, Proc. 84th GAMM, Novi Sad, Serbia, 2013

B8: Monitoring und Regelung von Bohrstrang-Beanspruchungen

1.1 Project   Overview

Speaker and lead university or research institution

Project Nr.	Title	Subject of research	Project leader, institution, location
B8	**Monitoring und Regelung von Bohr-strang-Beanspruchungen**	Erdöl-/Erdgastechnik (ITE) – Bohrtechnik	Dr. Dr-Ing. Catalin Teodoriu, TUC (ITE)

Participating institutes and institutions of the University and external institutions in:

- Institute of Petroleum Engineering (ITE), TU Clausthal

- Baker Hughes, Celle, Dipl. Ing. D. Dashevski

List of participating scientists and engineers:

Name Subject	area	University institute or non-university institution	Position is financed by gebo funds (indicate with X)
Dr. Dr-Ing. Catalin Teodoriu	Erdöl-/Erdgastechnik – Bohrtechnik	ITE, TU Clausthal	
M.Sc. Parimal Patil	Erdöl-/Erdgastechnik – Bohrtechnik	ITE, TU Clausthal	
-	-	-	-

1.2 Research   Program

1.2.1 Su   mmary

The aim of the project is to optimize the rate of penetration with ensuring less damage to the downhole drilling tools by developing methods and techniques for compensating the severe vibrations generated while drilling.

1.2.2   Relationship of the pro ject to the o verall re search conte xt and networking with oth er projects

The important aspect of the whole joint project is to optimize the overall rate of penetration and the subsequent drilling process using an automatic monitoring system. The downhole data will be used as a feed to the surface controlling system which will act as a monitoring and control-ling unit configured to provide optimal changes in weight on bit, and rotational speed of the drillstring and this will be carried out in B8. The project will need inputs such as vibration model from B7, rate of penetration model from B4, and formation rock properties, drilling efficiency in particular environment, etc. from G3. The output of this project which is the laboratory setup will help to validate the models developed in B7.

1.2.3 Work packages executed relative to (original) plan and results achieved

Following are the work packages

AP 1: Understanding downhole forces, critical loads, critical rotary speeds, integrating newly developed technology with drilling system, static and dynamic modeling of a drillstring with the formation modeling together will result in significant improvement in overall drilling performance of the complete system. The state of the art of monitoring and controlling of drillstring vibrations was reviewed using published data. The search was carried out based on the laboratory models developed so far for analyzing the downhole vibration in the laboratory. Basically, there exist three main types of vibrations: axial, lateral and torsional. Bit bounce is the cause of axial vibrations which results in bit damage. Lateral vibrations are even more destructive as it can create large shocks as the BHA impacts the wellbore wall. This always results in mass imbalance condition leading to backward or forward whirl condition. Torsional vibrations can lead to irregular downhole bit rotation. This condition always referred as stick-slip condition which is one of the severe forms of vibrations in which bit at certain point of time stops rotating and then starts spinning with the maximum rotational acceleration. This torsional fluctuation fatigue drill collars, connections, damage bit and may also result in high stresses resulting in catastrophic failure. Bit induced stick-slip and that of due to drillstring are often separated as they require different actions to mitigate. In order to study these phenomena separately, an experimental study is needed to understand this torsional mode of vibration and different controlling actions need to be defined. The setup will allow us to re-generate the realistic condition in the laboratory. Both the bit and the drillstring will be excited to induce stick-slip in the setup and allowing us to study parameters which have greater influence on stick-slip. These include: rotary speed, axial load, mechanical properties of drillstring and bottom-hole-assembly viz.: length, stiffness, and inertia, also wellbore geometry, fluid forces and interaction with wellbore. Friction characteristics will be analyzed between bit and formation as well as between drillstring and formation. Experiments will be reproducible on the test setup.

Lithology identification from the monitored data could be of significant use for recognizing the lithology being encountered at the bit in real time. The dynamic drilling parameters measured may be used to determine a type of lithology, since different lithologies have different physical and mechanical properties. By correlating the dynamic drilling data to the value associated with certain types of lithology, the lithology encountered at the bit can be determined approximately while drilling. The method of defining the lithology using log will always result in time lag as the measurements are acquired some distance behind the bit. Operating drilling parameters can be used as input to determine drilling response, rock shear strength, and mechanical specific energy. Seismic while drilling or vertical seismic profile can also be used to determine lithology sequence below the bit. With the help of software solution like artificial

neural network, prediction of lithology can be achieved in real time. But in order to train the complex neural network large range of input data is required.

Unfortunately at this time not sufficient data was found in order to be able to perform further investigations on the relationship between lithology and bit vibrations.

The literature part of this work package has been completed. Several concepts for the laboratory setup have been proposed. These concepts have been also evaluated to have no conflict within NTH (Niedersachsische Technische Hochschule) similar developments.

AP 2: Approach to mitigate the downhole stick-slip vibrations starts with regeneration of the phenomena in the laboratory which must be repeatable. Following schematic shows the complete system in which input parameters are rotation per min, torque and axial weight resulting rate of penetration and vibrations as output. The main objective is to suppress the torsional vibrations (stick-slip). Changing either the excitation or the dynamic characteristics of the structure will change the vibrating response in the drillstring. Excitation forces from the formation cannot be controlled but the amplitude and the frequency of excitation can be changed by monitoring and controlling the operational parameters.
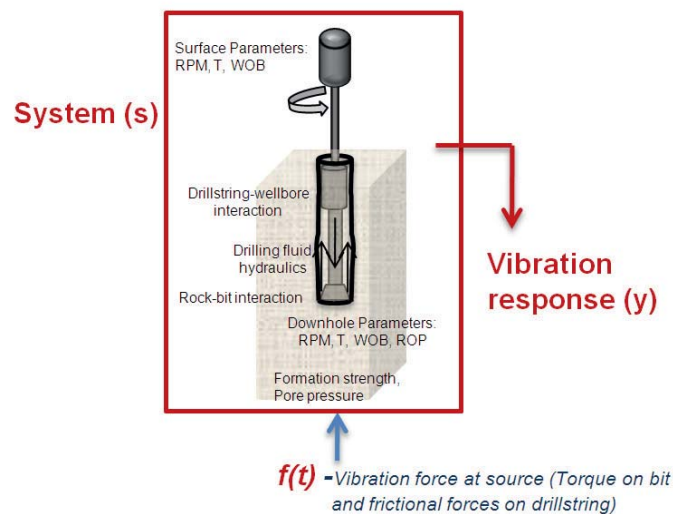
Figure 1 Drilling system representing the input and output forces

Based on the extensive literature review done in the first working package the following laboratory setup was designed, as shown in figure 2. It consists of 6 m long stainless steel pipe placed in the Plexiglas tube. Diameter of the glass tube varies from 6 – 12 mm. Stabilizers will be placed along the steel pipe and the fluid inside the tube and the annulus.

Using law of similitude, which is described in the later part of this section, the outer and inner diameter of the steel pipe is determined and comes to as 4 mm and 2 mm respectively. At the bottom of the string, disc representing a bit is attached. Axial shaker will be placed at the bottom to induce vibrations in axial directions. Magnetic tension brakes will provide side forces on the

bit. Fine magnetic power will help induce some friction at the bit. Various sensors will be placed along the system in order to record the vibration data. At this stage we consider LASER measurement as a reliable data acquisition concept. This data will be used to analyze the influencing parameters to induce stick-slip at the bit as well as drillstring. Friction along the steel pipe as well as at the bit will be studied.
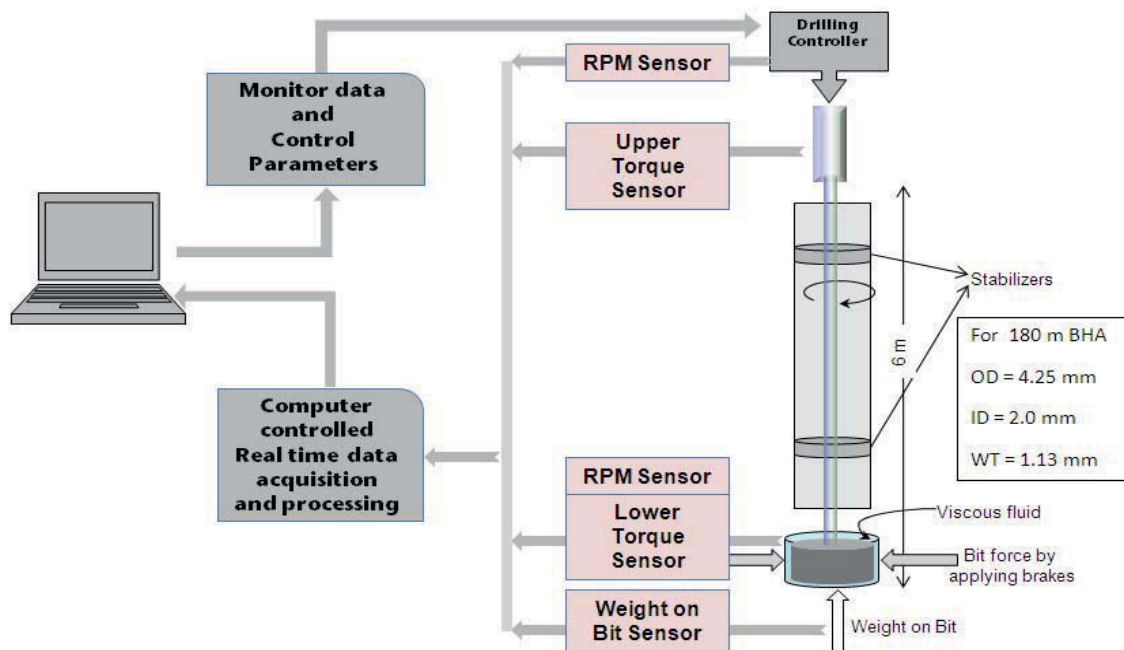
Figure 2 Proposed laboratory set up

The laboratory setup was designed based on the application of the law of similitude.

For drilling a well up to 5000 m to 7000 m, the bottom-hole assembly of length 180 m is generally required to put the axial weight on bit. Scaling down of 6000 m of drillstring for 6 m lab setup gives us at the end outer diameter of a pipe as 0.09 mm and inner diameter as 0.07 mm with 0.01 mm of wall thickness. The resulting downscaled sizes are not feasible to carry out experiments in the laboratory, hence, only a part of complete drillstring can be scaled in order to physically study it in the laboratory. For example 180 m of the drill string section is scaled down to 6 m. Following Table 1 gives the dimensions and the operating limits of the schematic, shown in Fig 16, to be built at ITE, TU Clausthal. A second model will be used for the BHA downscaling. Following are the representations for different parameters in the real as well as model:

L	denoted the length,	g	acceleration due to gravity,
OD	outer dimater,	ID	inner diameter,
V	linear velocity,	α	angular velocity,
T	time interval,	F	forces,
T	motor torque,	T_{bit}	torque at bit,

| T_{pipe} | pipe torque | | K | stiffness, |
| RPM | rev per minute | | WOB | weight on bit |

Table 1 Dimensions and the operating parameters for real and model set up

Variables Real		Model	Units
Length	180	6 (1:30)	m
OD	127 (5")	4.25	mm
ID	57 (2 ¼")	2	mm
Pipe thickness	35 (1.375")	1.13	mm
Wt. per unit length	83.328 (56 lb/ft)		Kg/m [1 lb/ft = 1.488 kg/m]
Steel density	7850 (490 lb/ft^3)	7850 (490 lb/ft^3)	Kg/m^3 [1 Kg/m^3 = 16.01 lb/ft^3]
Weight on bit	0 – 134 (0 – 30)	To be calculated	kN (klbf)
Torque on bit	0 – 10 (0 – 7)	To be calculated	kNm (klbf-ft)
Rotations per min	0 – 200 (0 – 21)	To be calculated	rev/min (rad/sec)

The acceleration (g) in the model cannot be reduced. Below in the text, subscript attached to the above parameters denotes the parameter for real and model setup. The model was built at a scale of 1:30. Table 2 summarizes all all downscaled parameters.

:

Table 2 Dimensional scaling

Parameter	Scaled term
Length	$L = 30 \times l$
Area	$Area_{real} = n^2 \times Area_{lab}$
Volume	$Volume_{real} = n^3 \times Volume_{lab}$
Velocity	$V_{real} = \sqrt{n} \times V_{lab}$
Force	$Force_{real} = n^3 \times Force_{lab}$
Torque	$Torque_{real} = n^4 \times Torque_{lab}$
Stiffness	$K_{real} = n^2 \times K_{lab}$

Table 3 Parameter scaling

Operating parameter	Scaled value
RPM$_{lab}$	0 – 1095 rev/min
WOB$_{lab}$	0 – 0.5 kg
Torque-on-bit$_{lab}$	0 – 12.345 mNm

M 1: Based on the literature search and the past laboratory models collaborating them with the objectives of this project, the above explained laboratory setup has been designed.

The actual construction of the experimental setup should be done so that no duplication of the existing facilities within NTH will be done. One, more complex, dynamic simulator was in 2010 at the University of Hannover under development, therefore we had to postpone our construction until both concepts have been compared and analyzed. This is the reason why the experimental setup was not built in 2010. The actual concept in gebo is complementary to the Hannover simulator. As of today, we know that there is a substantial difference between our facility which is design to proper support the gebo research activity and the existing testing rigs within NTH.

The lithology related work requires large amount of data for validating of any theoretical approach. Finding public domain data proof to be very difficult. Several possible sources have been proposed lately by our Board Committee and we will try to access any available data.

AP 2: The experimental setup was built and the mathematical models for stick-slip interaction of the drillstring and the bit were developed (for more details see PhD Thesis of Mr. Parimal Patil, Appendix A). The models were validated using the built laboratory facility. The developed setup was calibrated so that it should represent the downhole dynamic condition in the wellbore. Testing within the facility shows good repeatability of the results under the same operating conditions. The facility was primarily used to study stick-slip influencing parameters. For example, the influence of operating parameters such as the axial weight and the rotational speed will be studied. The effect of length of the string, its stiffness and the inertia on the dynamics of the string was analyzed. Figure 3 shows a detailed view of the built experimental setup.

AP 3: Based on the results in the AP2 we conclude that the development of an adaptive control mechanism in order to suppress the stick-slip vibrations in the drillstring requires sensors at the bit in order to identify the vibration phenomena. A concept of controller was proposed as a solution, see Figure 4.

M 2: The progress of the setup development and the models describing the interactions between drillstring/formation and bit/formation was done see Appendix A.

M 3: Some field testing data were used to compare the simulation results as shown in the Appendix A. However, due to limited amount of data and time, a full validation of the models with field testing was not possible. The simulations results however show a promising method to model and later control downhole vibrations.

Figure 3. Scheme of the experimental setup to study drill string vibrations
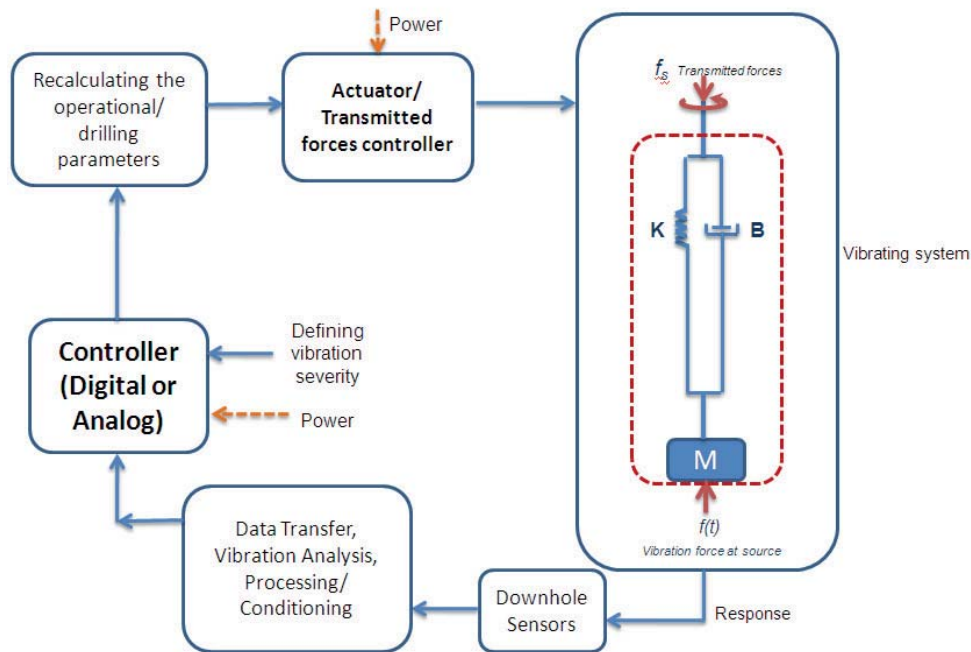
Figure 3. Scheme for automatic monitoring and controlling of drillstring vibrations

Overall the following achievements of the project can be noted:

- Modeling of torsional drillstring in order to reproduce stick–slip with integration of bit–rock interaction model and the rate of penetration model.
- Investigating parametrically the stick–slip influencing parameters.
- Effects of drilling parameters on torsional vibrations.
- Effects of drillstring properties on torsional vibrations.
- Analyzed the effect of friction coefficient on bit speed.
- Built experimental facility called 'torsional simulator' to reproduce torsional vibrations in the laboratory.
- Matlab/Simulink model for analyzing torsional vibrations under the influence of different drilling parameters, ad rock strength.

Mathematical modeling for torsional drillstring has been performed in order to reproduce stick–slip phenomenon. The effect of different surface WOB on downhole TOB has been analyzed. The friction factor at rock–bit interaction has been considered as decaying with increasing bit speed which is realistic instead of considering a constant value. The simulation result of TOB vs WOB were compared with the field data and show the similar trend. The effects of surface drilling parameters and the drillstring properties on TOB have been presented. Rock cutting mechanism using PDC bit is model based on simple mechanics. The WOB and TOB has been resolved for the components associated with the frictional process and with the cutting process. Use models suggested by Detournay & Defourny (1992) for the cutting components of TOB and

542

WOB, also friction components of TOB and WOB, the effects wear flat length of the PDC cutter on their resolved components of TOB and WOB have been studied. As the wear flat length on the PDC cutter increases, the profile of the PDC providing required depth of cut will reduce resulting in lower rate of penetration. This study could provide a basis for optimizing drilling operations for higher rate of penetration.

1.2.4 Project   Plan

Work packages and milestones	2009	2010	2011	2012	2013	2014
AP1: Literature and patent search, Selection / design of mechanical models, Planning of laboratory tests						
AP2: Development and application of models for the dynamics of the BHA and Validation of the models						
AP3: Validation of models with simulations and field testing						

Grey, original plan

Blue, actual or current plan, respectively

For details, see Gantt chart in the Appendix.

The project started with 4 Months delay, therefore the delay in the project evolution.

1.2.5   Future research work and plans

Based on the Black box model of the bit rock interaction a fully integrated controlling system can be built. This will require however the knowledge of downhole vibrations in real time, and with the existing drillstring model is limited to stick-slip phenomena.

1.3   Delineation of the project from other funded projects

There are no projects currently being carried out at ITE, TU Clausthal on the above mentioned work other than Geothermal Energy and High Performance Drilling Research Program (GEBO).

Literature

Parimal Patil, Catalin Teodoriu, Kurt M. Reinicke: "A Comprehensive Review of Drillstring Vibrations, Modelling and Experimentation", 'East Meets West' SPE Student Conference - Poland Section, April 8 - 9, 2010, Krakow, Poland.

Parimal Patil, Catalin Teodoriu, Kurt M. Reinicke: "Monitoring and Controlling of drillstring vibrations", First European Geothermal PhD day, Feb 12, 2010 in GFZ Potsdam, Germany.

Patil, P. A., & Teodoriu, C. (2013, March). Model development of torsional drillstring and investigating parametrically the stick-slips influencing factors. ASME's Journal of Energy Resources Technology, Vol. 135 , pp. 0131031 - 0131037.

544

B9: Innovative drilling concepts for geothermal energy exploitation

1.1 Project Overview

Project Nr.	Title	Subject of research	Project leader, institution
B9	Simulation for power production with terrestrial heat on basis of cellular automata with back coupling to the process of the drilling schedule	Drilling Engineering, Petroleum Engineering (ITE) Mechanical Engineering – Dynamics and Vibrations (IDS)	Dr. Dr.-Ing. Catalin Teodoriu, TUC (ITE) Prof. Dr.-Ing. habil. G.-P. Ostermeyer, TUBS (IDS)

Participating institutes and institutions of the universityies and external institutions:

- Institute of Dynamics and Vibrations (IDS), TU Braunschweig

- Institute of Petroleum Engineering (ITE), TU Clausthal

List of participating scientists and engineers:

Name	Subject area	University institute or non-university institution	Position is financed by gebo funds (indicate by X)
Dr. Dr.-Ing. Catalin Teodoriu	Petroleum Engineering	ITE	
Dipl.-Ing. Iska Gedzius	Petroleum Engineering	ITE	X
Prof. Dr.-Ing. habil. G.P. Ostermeyer	Mechanical Engineering	IDS	
Dr.-Ing. M. Müller	Mechanical Engineering	IDS	
Dr.-Ing. F. Schiefer	Mechanical Engineering	IDS	X
Dr.-Ing. Srisupattarawanit	Mechanical Engineering	IDS	X

1.2 Research Program

1.2.1 Summary

Reducing the costs of geothermal energy harvesting in Niedersachsen has to take into account optimization in many directions. Within gebo new techniques of drilling processes are in the focus as well as new designs of geothermal exchangers. In B9 we use a close collaboration of experts on drilling techniques and experts on new computational methods in order to highly reduce the computation times for reservoir dynamics and well path optimization. This allows varying geothermal energy harvester properties in a wide range by wellbore and crack geometry as well as by dynamic fluid and thermal properties on short and long time scales.

1.2.2 Relationship of the project to the overall research context and networking with other projects

The project B9 interacts with other projects by virtue of the necessary information to define the geothermal reservoir as input data and the optimized well path as output data. Necessary are for example input parameters from B4, G3, G7, G6 and G9. The optimized well path will be used in B1 for drill string design and well planning.

1.2.3 Work packages executed relative to (original) plan and results achieved

Description of the innovative geothermal well concepts WP 1, (ITE):

An economic recovery of energy from the deep subsurface of Niedersachsen requires innovative concepts. Geothermal projects should be

- low cost (preferably single well concepts)
- of high yield (for example achieved by multiple stimulation)
- sustainable (i.e. "mining" a large volume of the subsurface heat with controlled corrosion and scaling)

The published field cases for deep geothermal energy production typically use 2 or 3 wells for production and injection. The "Horstberg" and "GeneSys" projects of BGR in the Munster and Hannover area, respectively, are first attempts of single well enhanced geothermal systems (EGS). The published single well projects in Northern Germany demonstrate technical viability, but are uneconomic.

Against this background, several concepts are presented and evaluated to determine the heat recovered over time. A comparison of the presented concepts is shown in Table 1.

One-Well-Concept - Open System

In an open system, the carrier fluid for the geothermal energy is in contact with the rock of the geothermal reservoir and any fluid that the rock may contain. Contact is established either as the fluid flows through the permeable reservoir and/or as it flows through fractures. Petrothermal systems require fractures. They may be either naturally present or artificially created.

An open geothermal system, independent of the permeability of the geothermal reservoir, can be generated by drilling two or more horizontal laterals of sufficient length out of a large diameter, vertical well and to connect the laterals by fractures to form an enhanced geothermal system. A large diameter vertical section is needed to minimize the outflow resistance and ensure high flow rates. The laterals may be either above each other or next to each other. According to B1 these laterals are drilled after the geothermal reservoir have been proven by a vertical "pilot hole".
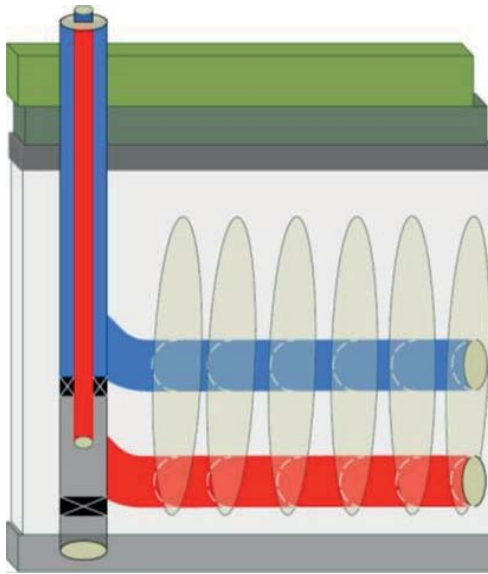
Figure 1:

Innovative one-well-concept with a horizontal section. Blue is the injector and red the producer, they are connected with fracs

The vertical section through the target horizon is necessary in order to record the geology, measure the rock properties and the stress distribution at the level of the geothermal reservoir. This information is important for the planning and execution of the horizontal well sections and hydraulic fractures. Fractures will open in a direction perpendicular to the least principal stress.

Under normal conditions this is a horizontal stress, which is typically dependent on direction, usually as a result of tectonic stresses. To be able to create a fracture perpendicular to the direction of the horizontal section of a well, the direction of the well path must coincide with the direction of the least principle stress. [ECO89]

Figure 1 shows the concept with two horizontal laterals connected by artificially created fractures serving as heat exchangers. In operation, cold water (in blue) is injected down the well through the tubing-casing-annulus into the upper lateral, passes through the fractures, and is produced as hot water (in red) through the lower lateral and produced back to the surface via the tubing.

The fractures are created by hydraulic fracturing treatments. During the treatment a fracturing fluid is pumped down the well. Pumping rates higher than what the formation can absorb result in increasing pressures. If the pressure exceeds the fracturing pressure, the formation will crack open. As injection is continued, the fracture continues to grow. [ECO89]

Fractures are executed as propped fractures or as unpropped fractures. For a propped fracture, the created fracture is filled with proppants during the treatment. The proppant fill prevents a closure of the fracture once the pumps are stopped. For a water frac treatment, one relies on the existence of shear stresses causing the fracture faces to be displaced against each other while the fracture is open. Because of the irregular surface of the fractures faces any displacement would prevent a perfect closure of the fracture leaving some channels open for flow. To be successful, shear stresses must be present, the fracture must be long enough and rock has to be hard enough to prevent a healing of the fracture.

Multiple fractures from horizontal wells at large depths have been carried in Germany in a few tight gas wells. For these wells, with a horizontal section of approx. 1.000 m, the horizontal section was cased and cemented and then section-wise perforated, fraced, sanded up starting from the end. This process takes several weeks to carry out.
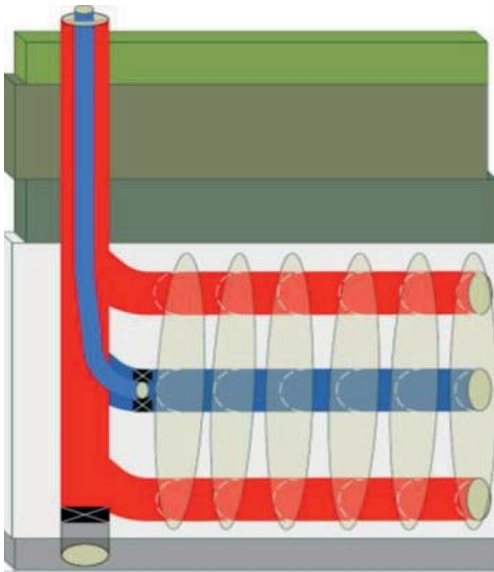
Figure 2:

One-well-concept with one injector (in blue) and two producers (in red) again from the blue into the red well.

In a first approximation symmetrical fractures [ECO89] with respect to the injection well will be created in the fracturing process resulting in an inefficient use of the heat exchanger areas, if only two laterals are employed as in Figure 1. Simulations and economic evaluations are being carried out to evaluate the benefit of a third lateral penetrating the fractures close to the top. In the three-lateral well configuration shown in Figure 2, cold fluid would be injected into the middle lateral and produced through the upper and lower laterals. The uniform distribution of the injected cold fluid across the created fractures requires special attention to avoid a short circuit of the injected cold water through the fractures offering the least resistance to flow.

Under favorable conditions geophones may be installed to monitor the fractures as they grow. The heat exchange between annulus and the tubing must be considered in order to reduce the temperature loss from the target to the surface.

One-Well-Concept - Closed System

The one well closed system discussed next, does not require any fracturing operations. For all practical purposes closed systems are an extension of geothermal heat probes. Because the system is "closed" the thermal fluid is not in contact with the rock of the geothermal reservoir, but flows inside a cased hole. Closed systems avoid the risks resulting from the hot and highly mineralized reservoir brines but have a significantly lower heat exchanger area. In addition, concepts like the one evaluated will require complex drilling operations and hence directional drilling systems which work in high temperature environment.
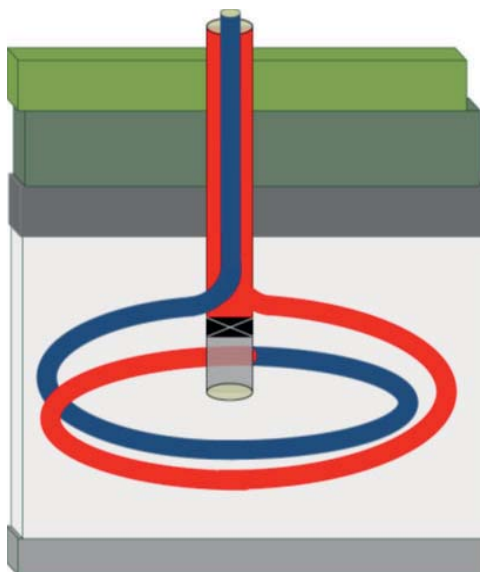
Figure 3:

Innovative closed system. The fluid is injected by the smaller diameter (blue) and produced by the annulus (red). Thermal water has no contact to the rock

548

A possible concept for a closed system with recovery efficiencies better than achieved with a normal geothermal probe is shown in Figure 3. For this concept, a well - having reached the target geothermal reservoirs – is deviated (from a position above the total depth of the vertical well) out of the vertical and steered in a spiral ending at the bottom of the vertical well again. To avoid excessive loading of the tubular, deviation radii should not lead to excessive loading levels for the tubulars employed. In operation, cold fluid would be pumped down the tubing into the spirally-wound well, and produced back to the surface through the annulus. In this concept it is also necessary to estimate the heat loss in annulus and tubing.

Two-Well-Concepts – Open Systems

Two well or even three well open systems are the standard for hydrothermal energy production. A two well system proposed for petrothermal energy production has been proposed by *ENRO Geothermie GmbH* in 2008. Two well systems pose less technical risk for drilling and operation and require smaller borehole diameters. Due to the modern drilling technology innovative two-well-concepts do not cause any problems in providing the boreholes. But – as the name implies – two well systems require the drilling of two well, which increases the economic risk of such systems. However the special attention is on economy of the 70% of the capital investments that belongs to the drilling. [BMU07]. The two well concept proposed by *ENRO Geothermie GmbH*, also described in [NEU09], is introduced.
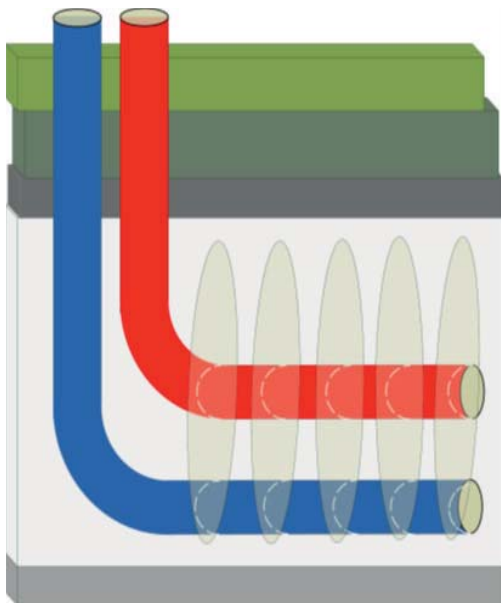
Figure 4:

Two-well-concept, blue well is the injector, red the producer

In order to make a point about the economy of an innovative two well concept, an already known well path is described briefly [NEU09]. The system consists of two horizontal wells with the horizontal sections drilled parallel to each other in the direction of the least principle stress (Figure 4). The advantage is that only one well site must be approved and constructed. Having completed the well to be fractured, preferably with an uncemented liner equipped with external packers, the fracture treatments are carried to connect to the second well, completed open hole or with a screen.

Challenges of one-well-concepts include (ITE):

- Drilling larger diameter wells because of the counter-current flow all the way down to the reservoir,
- Complex completion to accommodate counter-current flow
- Providing insulation between the counter-current flow of cold fluid in the tubing and hot fluid in the annulus

for closed systems

- Complex steering at high temperature

and for open systems

- Generation of sustainable heat exchanger,
- Controlling the distribution of fluids into the fracture systems,
- Knowing the state of stress in the formations to be fraced.

Table 1: Advantages and disadvantages for one-well and two-well concepts

	Advantages	*Disadvantages*
One-Well-Concepts – Open System	- only one vertical well drilled - large heat exchanger area - reduced drill time for the vertical section - lower costs than Two-Well-Concept	- vertical well drilled with a bigger diameter - and/or lower flow rate than Two-Well-Concept or Multilateral Concept - tubing insulation to minimize heat exchange between annulus & tubing - complex completion - contact to saline brines - complex thermal stresses
One-Well-Concepts – Closed System	- only one vertical well drilled - reduced drill time for the vertical section - lower costs than Two-Well-Concept - no frac jobs needed - no contact with saline brines - possibility to use fluids other than water	- small heat exchange area - vertical well drilled with a bigger diameter - and/or lower flow rate to Two-Well-Concept - tubing insulation to minimize heat exchange between annulus & tubing - complex drilling operations - complex completion - complex thermal stresses
Two-Well-Concept	- higher flow rates - large heat exchanger area - simple completion	- high drilling costs - longer drill time than One-Well-Concept - contact to saline brines

Model's concept and interfaces to single models (WP 1), IDS:

Simulation tools for geothermal reservoirs are available in both - academic and commercial software packages. Most of them are not explicitly developed to evaluate geothermal reservoirs, such as THOUGH2, whose purpose is to consider problems from geology and geological physics. It was developed by Earth Science Division, Lawrence Berkley National Laboratory in 1999 primarily to predict underground water flow and heat transfer. In 2003, C. Clauser presented the software package SHEMAT for heat transfer and fluid flow. Commercial software packages are for instance SVHeat, from SoilVision System, and ECLIPSE and INTERSECT from Schlumberger. Also COMSOL, the multiphysics software package, can be used to simulate heat transfer. Although some academic and industrial research projects used the tools listed above to simulate geothermal reservoirs, the complexity of the investigated systems was limited due to the high respective computational effort, when transient processes are investigated.

Recently, the method of Cellular Automata (CA) gained more importance in the field of applied natural sciences. Generally speaking, its philosophy correlates with a simplified mathematical structure which allows fast computations with still high accuracy. It has been implemented for many complex problems in physics, chemistry, biology and engineering. The CA is a discrete modeling technique where the domain will be initially discretized into a lattice of cells. A set of states or inner variables is assigned to the cells; the physical processes can be obtained via the interaction of a cell and its concerned neighbors. This method is also very appropriate to describe multi scale phenomena as occurring in geothermal reservoirs. The following figures show the different length scales of geothermal reservoirs and the time scales of essential physical processes.
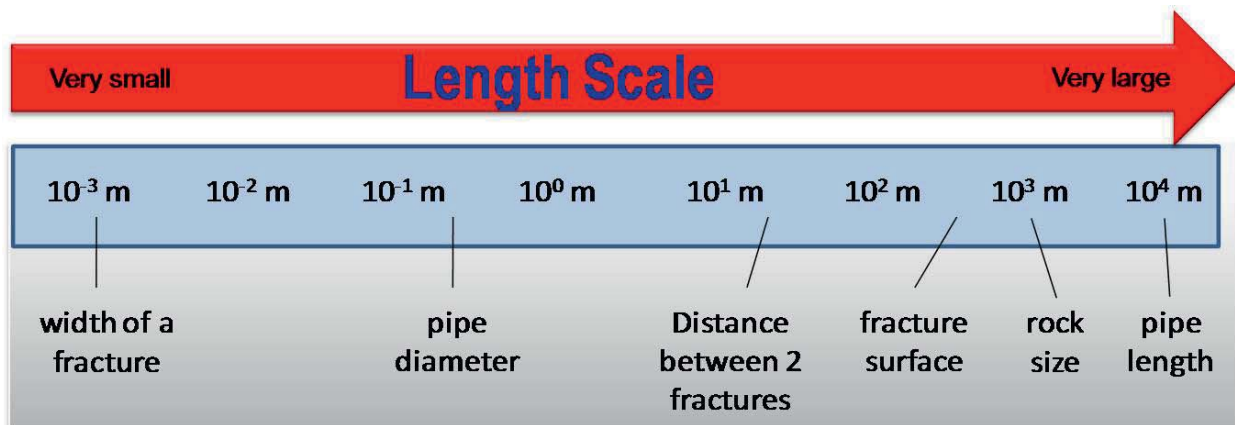
Figure 5: Length scale of geothermal reservoirs
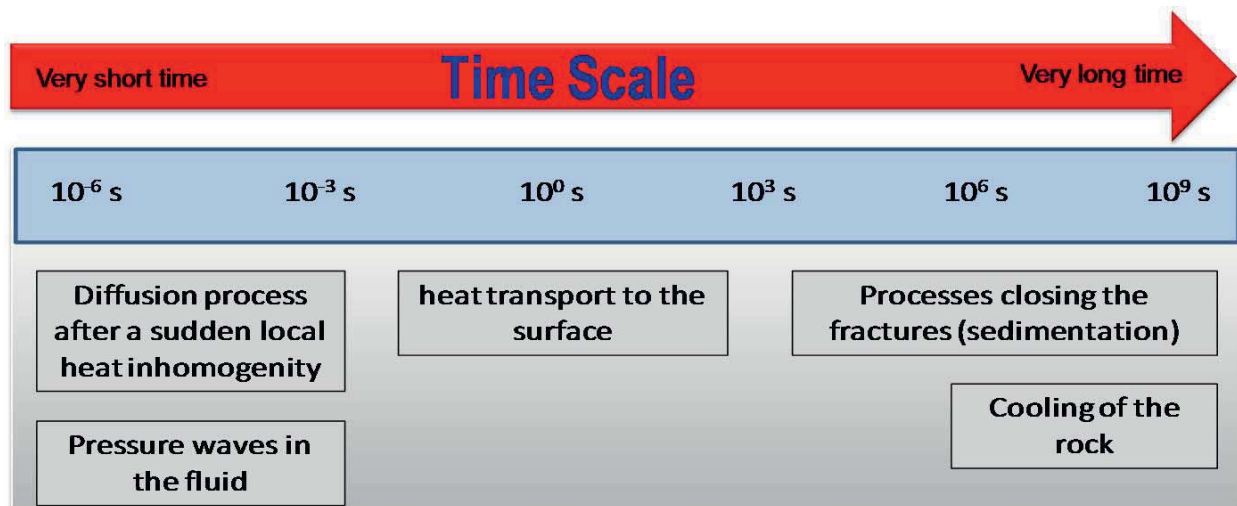
Figure 6: Time scale of geothermal reservoirs

On basis of our project work and appropriate searches at the ITE various options of the drilling production and the stimulation are analyzed and presented. The IDS methods for the simulation of geothermal reservoirs are compared and evaluated for instance in cooperation with gebo-project G7.

Modeling of the system (WP 2), IDS:

With respect to the evaluation of a geothermal reservoir, the CA method is in principle able to describe the interdependencies of fluid velocity, pressure and temperature within arbitrary geological formations. The way how these processes can be approached is demonstrated in the following. In order to evaluate the geothermal energy of a reservoir, the fundamental processes to be considered are:

- The fluid flow through the pipes, the fracs and the porous rock
- The heat transfer within the rock and within the fluid
- The interactions between the rock and the fluid (pressure gradients, convection phenomena).

Generally, a Cellular Automaton model is governed by the 4 fundamental issues "spatial discretization", "set of inner (state) variables", "neighborhood definition" and "transition function" [WOL02]. Their realization with respect to the questions to be answered here is pointed out in the following.

Spatial Discretization

The first model for general investigations discretizes the geological formation with a 2-dimensional equidistant quadratic mesh. It consists of roughly 200 x 300 cells.
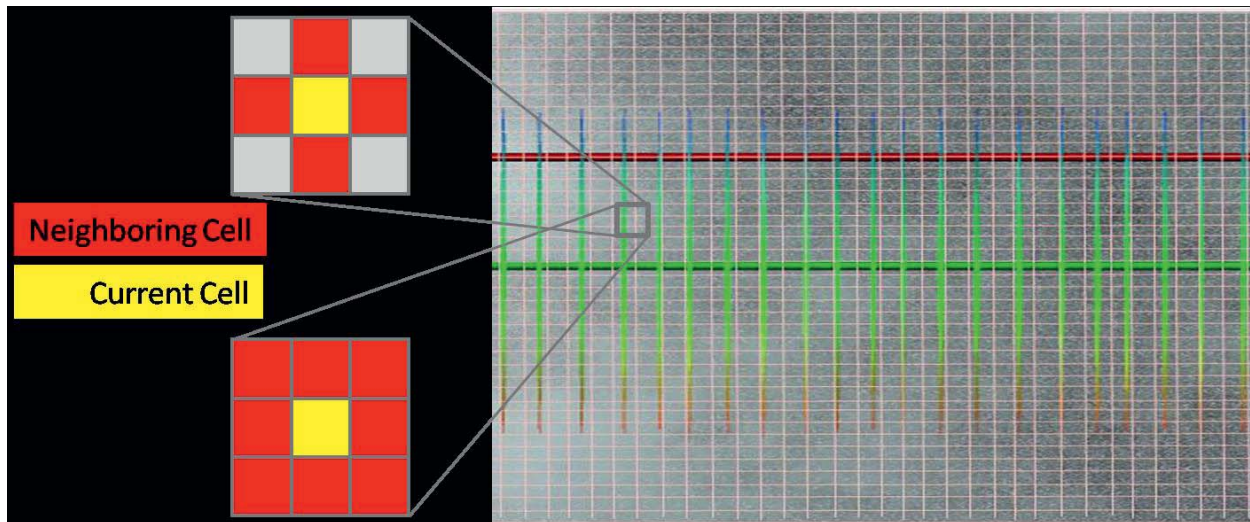
*Figure 7: Spatial discretization and neighborhood definition with Neumann type (top)
and Moore type (bottom)*

Neighborhood

In this model two cells are defined to be neighbors when they share a common edge in the 2-dimensional mesh.

Set of inner variables

Each cell contains the variables "constitution" (fluid or rock (type of rock, permeability), "pressure", "temperature" and the "velocities of the fluid" at the boundary between neighbored cells. The pressure and temperature are scalar values and the fluid has two velocity components. All variables are stored for each cell.

Transition function

Actually, the transition function represents the time evolution of the system. Usually one total update step corresponds to a certain time increment. The IDS model consists of a set of 6 basic rules (see Figure 8). These are explicated below.
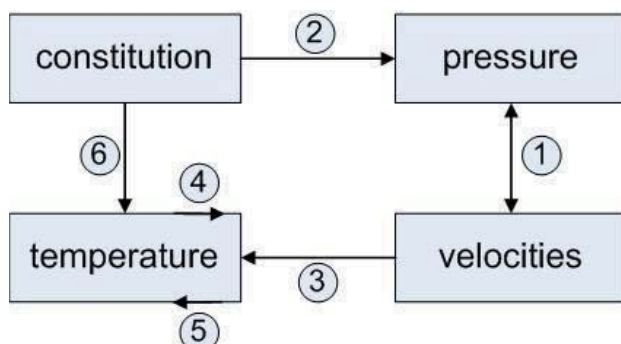
Figure 8:

  Set of rules within the IDS model

553

Rule 1: The fluid flow in the pipes

According to the 2-dimensional Navier-Stokes equations [BAT00] in a Cartesian coordinate system x-y

$$\frac{\partial v_x}{\partial t} = \frac{1}{\rho}\left\{-\frac{\partial p}{\partial x} + \mu\left(\frac{\partial^2 v_x}{\partial x^2} + \frac{\partial^2 v_x}{\partial y^2}\right)\right\} + g_x - \left\{v_x\frac{\partial v_x}{\partial x} + v_y\frac{\partial v_x}{\partial y}\right\}$$

$$\frac{\partial v_y}{\partial t} = \frac{1}{\rho}\left\{-\frac{\partial p}{\partial y} + \mu\left(\frac{\partial^2 v_y}{\partial x^2} + \frac{\partial^2 v_y}{\partial y^2}\right)\right\} + g_y - \left\{v_x\frac{\partial v_y}{\partial x} + v_y\frac{\partial v_y}{\partial y}\right\}$$

in combination with the law for water compression using "penalty pressures"

$$K = -V \cdot \frac{dp}{dV}$$

the inner variables "pressure" and "velocities" interact with each other. Herein p is the pressure, v_x and v_y the fluid velocity components in x- and y-direction, ρ the fluid's density, μ the fluid's dynamical viscosity, g_x and g_y the body forces in x- and y-direction, K the bulk modulus and V the respective volume. The horizontal direction is x (positive to the right), the vertical direction is y (positive to the bottom). So g_y considers the gravitation, g_x is zero. Density and viscosity depend on temperature, as well as K is generally temperature- and pressure-dependent. All this is taken into account.

Rule 2: The pressure at the interface between fluid and porous medium

In the case that a cell of type "fluid" has a neighbor of type "porous rock", the fluid flow is governed by an additional resistance, which can be expressed by Darcy's law

$$\vec{q} = -C\vec{\nabla}h$$

($\vec{q}$: flow, C: hydraulic conductivity, h: gauge level). The simulation regards this phenomenon by modifying the pressure of the related cells.

Rule 3: Heat convection by the fluid flow

The velocity of the fluid is in a range where the heat transport due to the flow is of significant importance. For each cell an energetic balance equation according to the first law of thermodynamics

$$\dot{Q} = \frac{d}{dt}(c \cdot \rho \cdot V \cdot T)$$

is formulated, $\dot{Q}$ is the heat flux and c the fluid's thermal capacity. The implemented rule therefore refers to the velocity and temperature gradients at the cell (and therefore the difference between inflow and outflow) leading to a change of the thermal energy amount (and thus temperature) in the cell.

Rule 4: Heat conduction

Within the porous medium the heat transport by conduction is of high relevance, especially for the evaluation of the reservoir. In order to describe this process Fourier's law

$$\frac{\partial T}{\partial t} = a \left(\frac{\partial^2 T}{\partial x^2} + \frac{\partial^2 T}{\partial y^2} \right)$$

is applied (a is the thermal conductivity). The heat flux is realized by the energy exchange of neighbored cells going along with this law [OST07].

Rule 5: Heat convection at the interface between porous medium and fluid

Caused by the high temperature of the rock, convection of the fluid will occur near the rock. This is included by a modification of the energy exchange rate in Rule 4 between two neighbored fluid cells near the porous medium.

Rule 6: Heat transfer from the porous medium to the fluid

The amount of energy which is transferred by the formation into the fluid is the core of the question to be answered. The physical law for this phenomenon is

$$\vec{q} = \alpha \vec{\nabla} T$$

with the heat transfer coefficient α. Similar to Rule 5 this effect is taken into account by a modified energy exchange rate, in this case between a cell of constitution "porous medium" and a cell of constitution "fluid".

Boundary conditions

The cells explained so far can be interpreted as "natural cells" since their task is to describe the physical processes inside of the Automaton. For the implementation of boundary conditions, it is helpful to define additional "technical cells" which are actively steering the inflow and outflow of the fluid. In this simulation pressure-dependent velocities at in- and outflow have been implemented.

With the help of the 6 rules and the boundary conditions special numerical algorithms have been applied in order to receive quickly the unsteady and steady state solution of the problem. The simulations run fast. The Figures 9-12 show the results of the simulation. The complex situation in the fluid flow in particular near geometrically distinctive features such as edges and curvatures can be seen in Figure 9. The belonging pressure distribution in the porous medium and the fluid can be taken out of Figure 10.
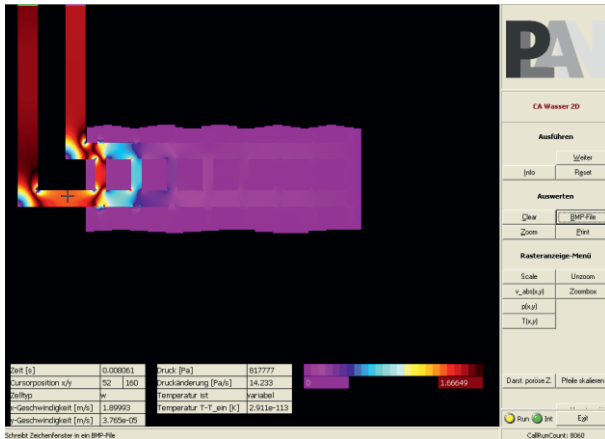
Figure 9: Simulated field of velocity magnitude
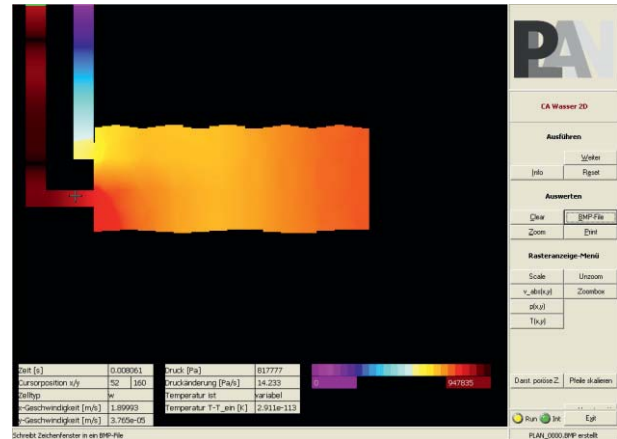
Figure 10: Simulated pressure distribution
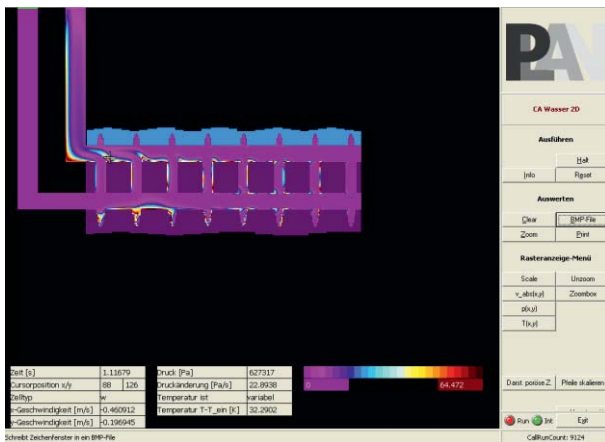
Figure 11: Simulated temperature field
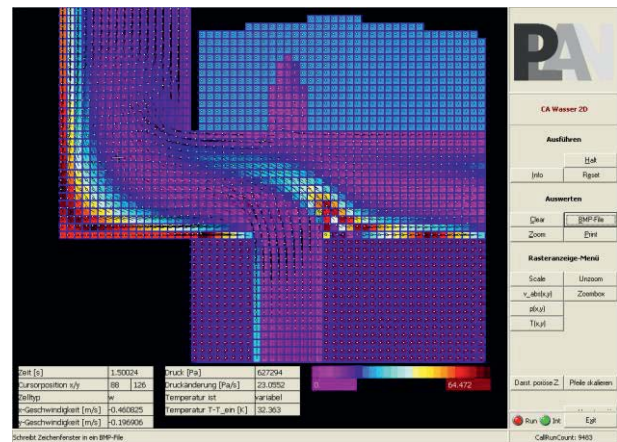
Figure 12: Temperature field and velocity components (arrows), zoomed area

In Figure 11 the heat flow can be identified. The moving fluid hereby has a lower temperature than the fluid areas which are not moving (e.g. in the corners). This effect conforms to the fluid flow convection and its physical fundamentals. Figure 12 shows a zoomed section of Figure 11. It also contains the velocity components (illustrated by the direction and magnitude of the arrows). In order to check the physics of fluid flow and heat transfer some numerical examples are run in the following.

(i)   Physics of Fluid Flow in Complex Geometry

This numerical example deals with fluid flow through complex geometry according to the short time dynamics, see in Figure 13. The fluid flows into the domain from the inflow side (left) and to the outflow side (right) with respect to given boundary conditions, e.g., pressure or velocities. The fluid interacts to the structure (modeled as rigid body and completely fixed (no movement and deformation)) during the flow process.

Water density	1000 kg/m^3
Dynamics viscosity	0.001 Ns/m^2
Bulk modulus	2.08e9 N/m^2
time step	1.0E-6 sec.
cell size	0.1 m.
atm. Pressure	101325.0 N/m^2

Descriptions	L1	L2	L3	L4	L5	L6	L7
Magnitude	150*DS	30 *DS	50 *DS	30* DS	41 *DS	69 *DS	97* DS
Descriptions	H1	H2	H3	H4	H5	H6	H7
Magnitude	90* DS	40* DS	5 *DS	30*DS	19* DS	14* DS	9* DS
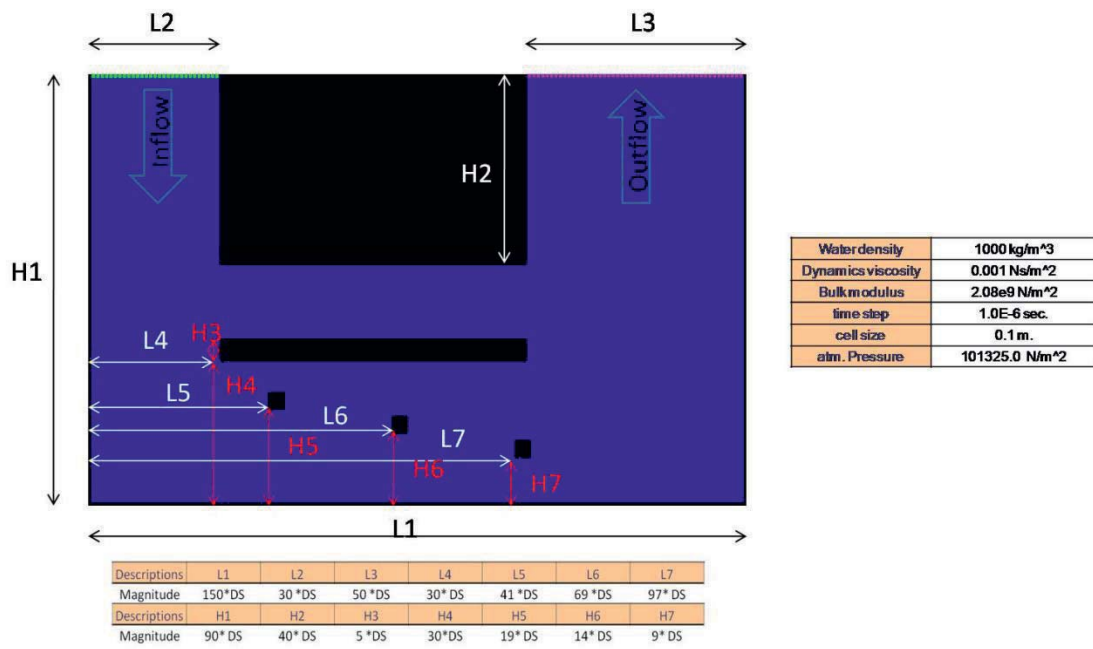
Figure 13: Domain of problem for fluid flow in complex geometry

The simulation begins by setting the boundary conditions: inflow at the source cell and outflow boundary at the drain cell.
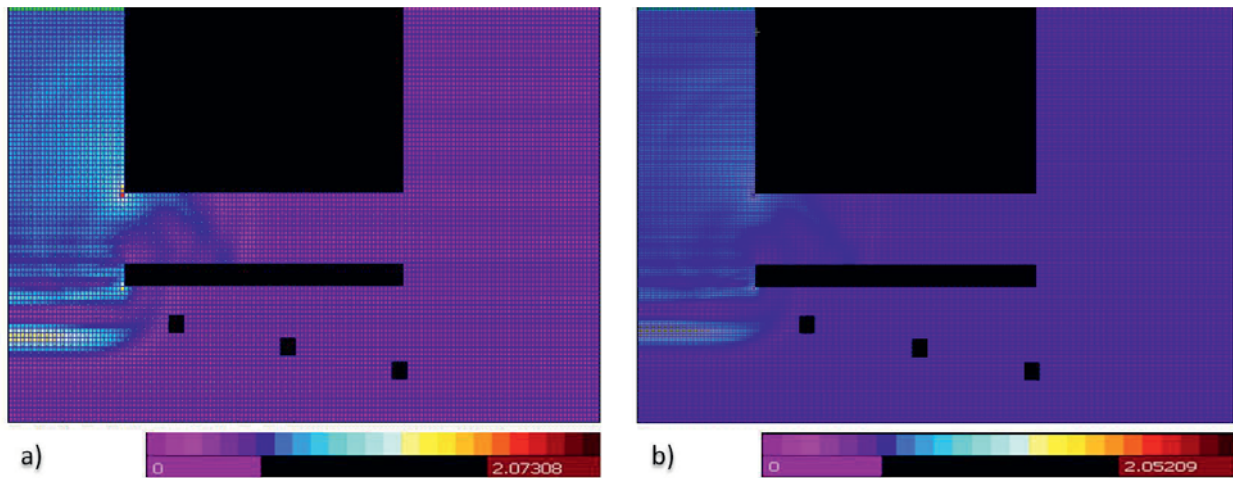
Figure 14: Results of velocity a) initial cell; b) refinement cell.

The results show impressively that the fluid continuously flow from source cell to water cell. The energy is transferred forward from one cell to the neighbor's cell. During the updated time, velocity and pressure are computed. The simulation can be run until 100,000 time steps without any numerical problems or instability. The physics of the fluid flow can be clearly presented in the results, such as reflection of velocity wave, wave deformation. In addition an adaptive cell refinement and time adaptive refinement have been done as shown in Figure 14. Smooth results can be found in the case of small cell. Also the fluctuation can be performed in small cell.

(ii)   Physics of Fluid Flow in Porous Medium

The simulations were continued with the fluid interaction to porous media. The inflow at the source cells is in vertical direction and the fluid flow through three different kinds of porous media to the outflow at drain cells. The domain of the problem is shown in Figure 15.

Water density	1000 kg/m^3
Dynamics viscosity	0.001 Ns/m^2
Bulk modulus	2.08e9 N/m^2
time step	1.0E-6 sec.
cell size	0.1 m.
atm. Pressure	101325.0 N/m^2
Resistance flow for P1	0.2*atm.Pressure
Resistance flow for P2	1.0*atm.Pressure
Resistance flow for P3	2.0*atm.Pressure

Descriptions	L1	L2	L3	L4
Magnitude	28* DS	12* DS	2* DS	14* DS
Descriptions	H1	H2		
Magnitude	28* DS	20* DS		
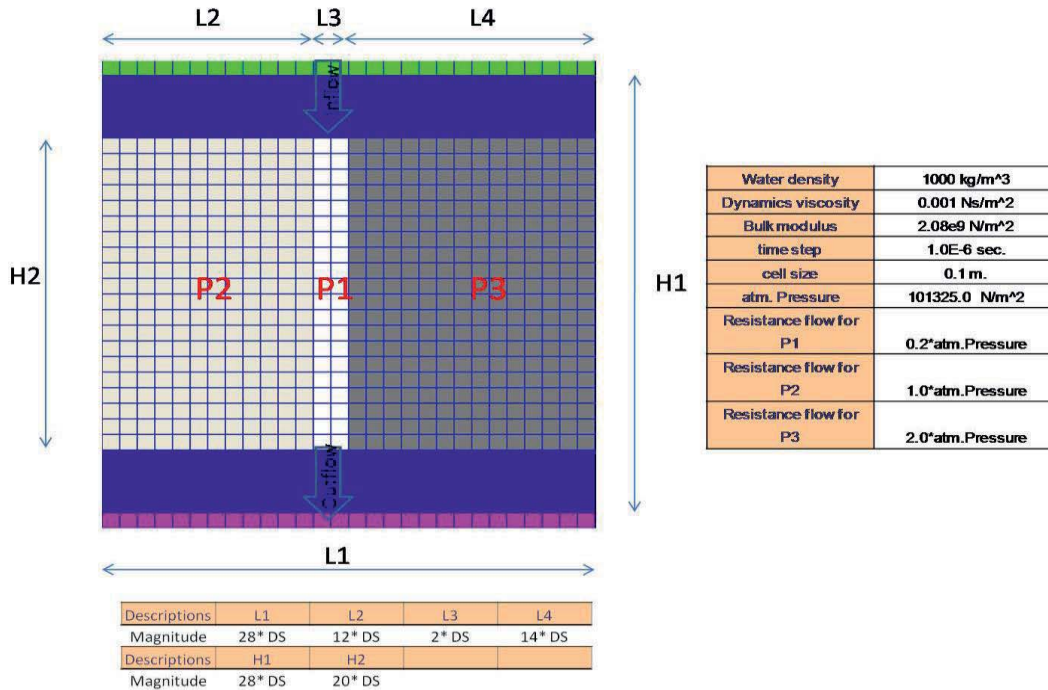
Figure 15: Domain of problem for fluid flow in porous media

The fluid flow is very fluctuately at the beginning of simulation. This fluctuation is reduced during the updated time steps. The stationary state is obtained at 6,000 time steps.
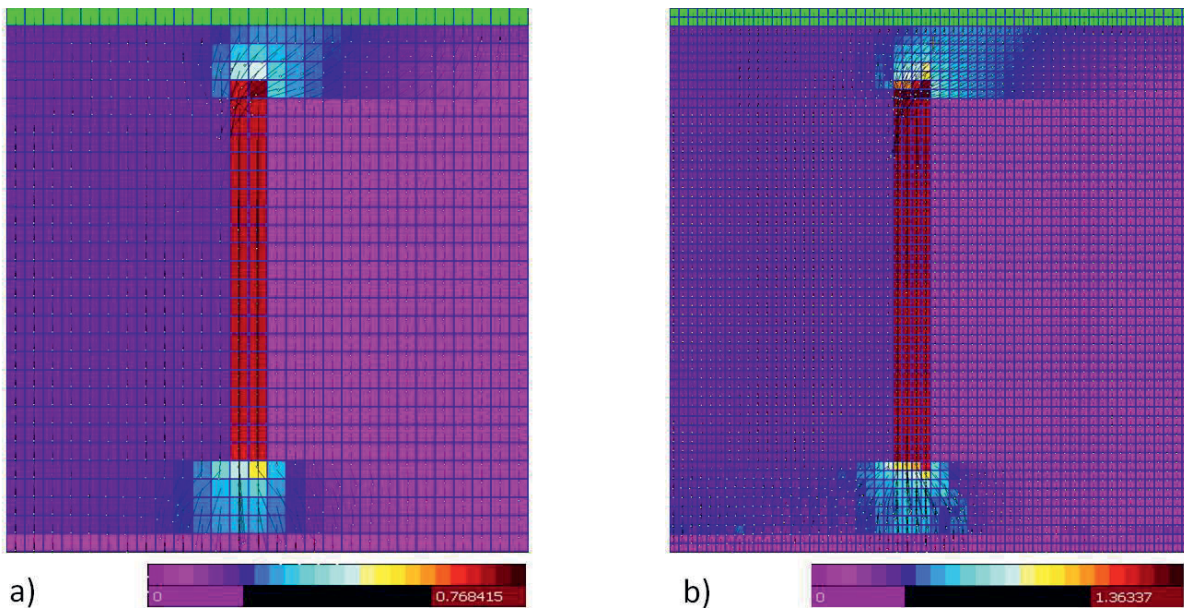
Figure 16: Results of velocity in porous media a) initial cell; b) refinement cell.

Similar to the previous example an adaptive refinement is implemented. The results show very clearly a better quality using adaptive refinement. In Figure 16, we can observed the flow at the critical part of the domain (outflow) with higher velocities. While flowing along the porous media, the pressure is reduced due to the properties of the porous material. This model can be used for modeling flow through porous media and gives acceptable results as discussed before. Therefore, this model is adequate for model extension and simulation of more complex problems.

(iii)   Physics of Fluid Flow and Heat Transfer in Deep Geothermal Reservoir

This example is investigated for a first simulation testing of complex geothermal reservoirs using the CA model. The overview of the problem is shown in Figure 17. The reservoir is located approximately 5,000-7,000 m downhole.
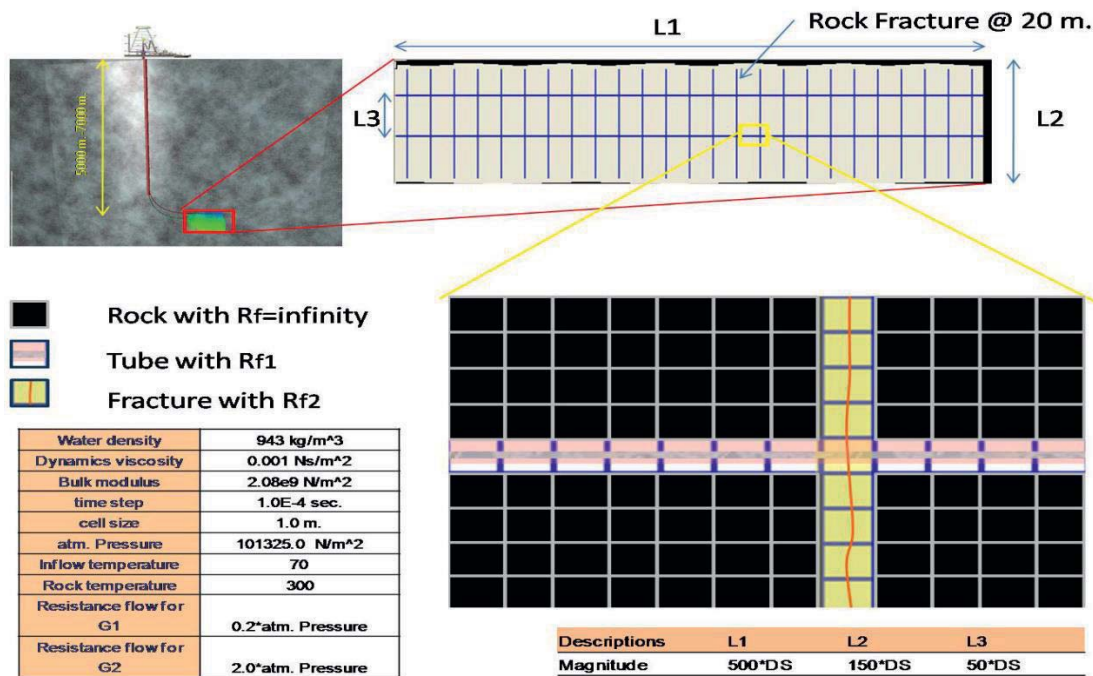
Figure 17: Domain of the problem of a geothermal reservoir

The dynamics of the fluid flow is simulated until stationary flow state is arrived. Then the dynamics of heat transfer is calculated with the stationary solution of the fluid flow. Figure 18 shows the results of temperature, which is lower at nearby the inflow cells. Far away from the inflow cells the temperature are getting higher with respect to the the flow through the rock fracture cells and the effect of heat convection.
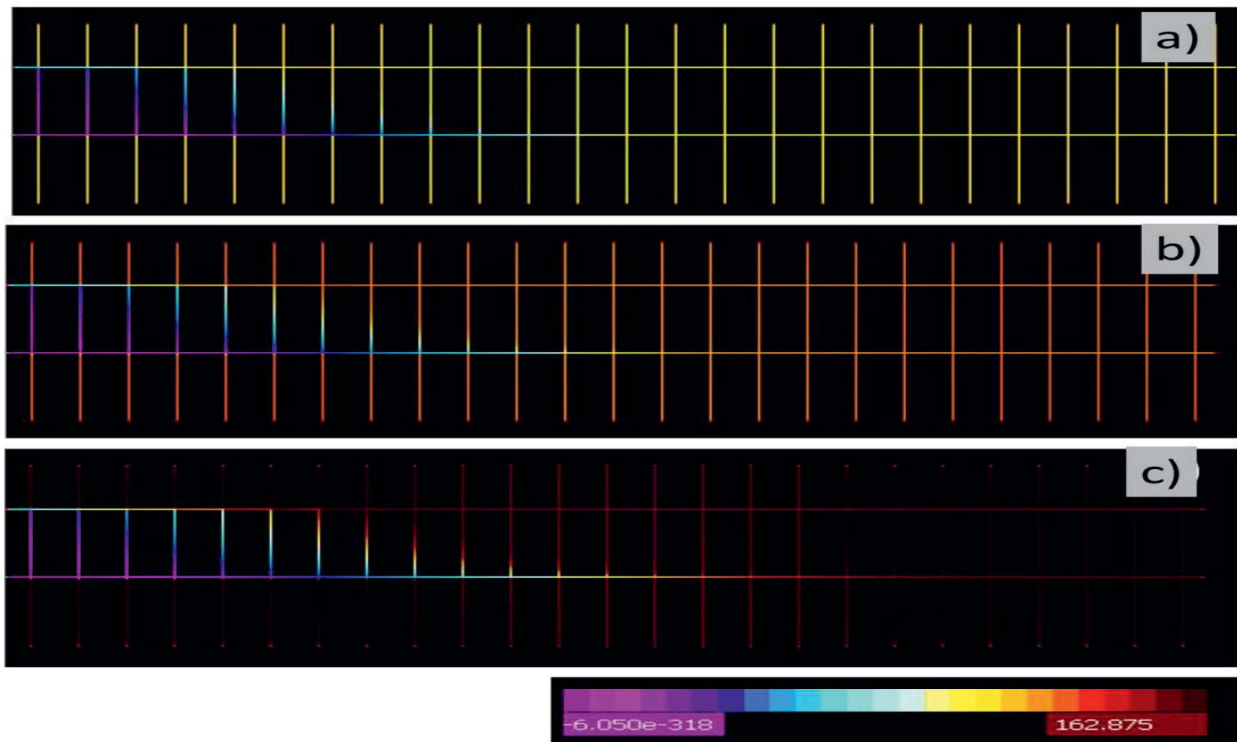
Figure 18: Temperature (°C) in the multifracs, a) start of simulation, b) flow state instationary, c) flow state stationary

Evaluation und concept optimization (WP 3), IDS:

The energy amount which can be transported from the formation via the fluid to the earth's surface mainly depends on the total energy amount of the formation itself, the velocity field of the fluid and the pressure situation. So far the model shown here is able to compute these interactions properly as shown exemplarily in the numericals simulations before. Hence, the model's functionality is proven and this is the starting point for further detailed investigations.

Until the end of the project there was the possibility to look in more detail in the basics of fluid flow distribution of complex geothermal reservoirs and the belonging heat transfer in single fracs as well as in multi-frac reservoirs.

(i)   Physics of Fluid Flow and Heat Transfer in Geothermal Reservoir with respect to different Flow Resistance

This model case is investigated in order to test the effect of flow resistance as shown in Figure 19. The CA model is used for geothermal system as described before. Up to now, the simulations were investigated geothermal reservoirs without controlling the flow resistance.

560

Descriptions	L1	L2	L3	L4	L5	L6	H1	H2	H3
Magnitude	400*DS	330*DS	300*DS	22*DS	16*DS	30*DS	53*DS	84*DS	150*DS
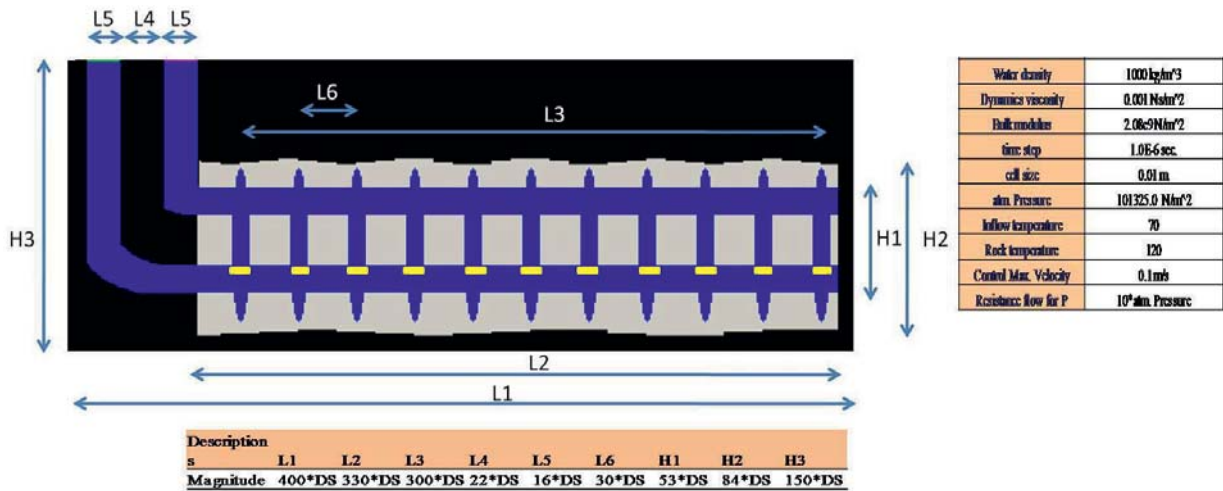
Figure 19: Domain of the problem of Geothermal Reservoir

In basic simulation cases, the flow resistance can be controlled by new developed technical cells for the CA-model. The simulation process is as before. The simulation run for the solving dynamics of fluid flow and dynamics of heat transfer until the stationary fluid flows is arrived (at 9000 time step approximately). After that, the simulation uses the stationary fluid flow and solves the dynamics of heat transfer. This approach makes the simulations significantly faster. The results show the smooth characteristic of fluid flow. The velocity, the pressure and the temperature can be obtained and the simulations continue without numerical instability.
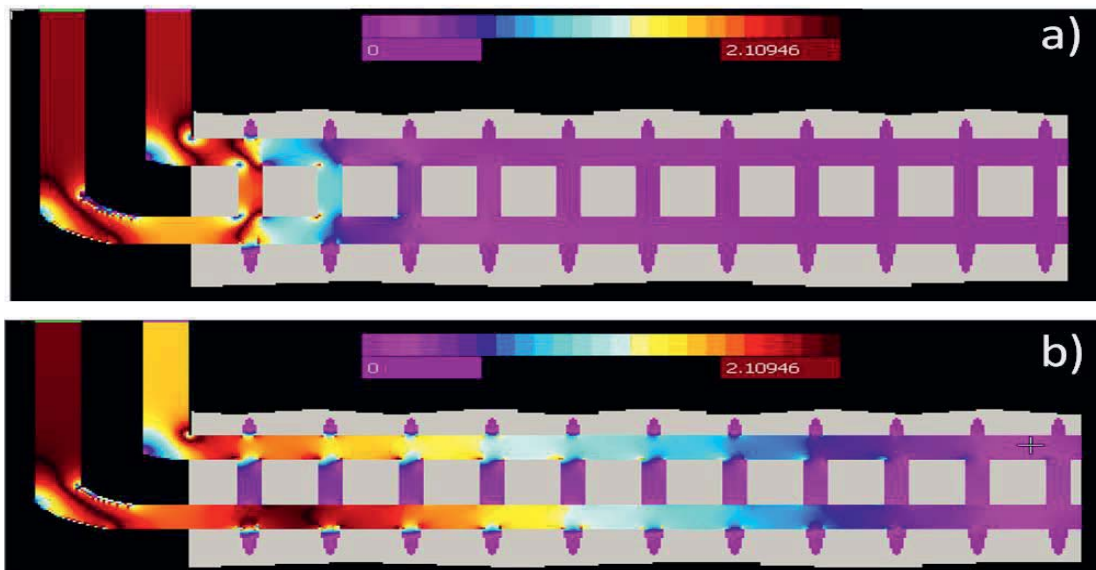
Figure 20: Result of comparison velocity field: a) with no flow resistance control, b) with flow resistance control

Due to the fluid velocity, the effect of controlling the flow resistance yields to significantly difference result as shown in Figure 20. The "controlling case" (Figure 20a) show the equal flow

561

in each fracture, while "non-controlling case" (Figure 20b) show that the flow are active only in the first fractures close to the inflow point. The simulation example shown in Figure 20b might represent a hydraulic breakthrough which is unacceptable for the geothermal energy projects.

Using the implemented technical cells we are able to control the fluid flow. As a result of this part we can obtain a reservoir evaluation and optimization with respect to fluid flow. It does not matter whether the resistance to flow is set by natural parameters or controlled by technical solutions.

(ii)   Simulations to the Energy Production of Geothermal Reservoirs

Before calculating the total system of an exemplary geothermal reservoir, we initially test our CA modeling in terms of accuracy of result and computational time. The first example deals with circular geometry of the rock fracture with the injection point location at center of rock fracture.
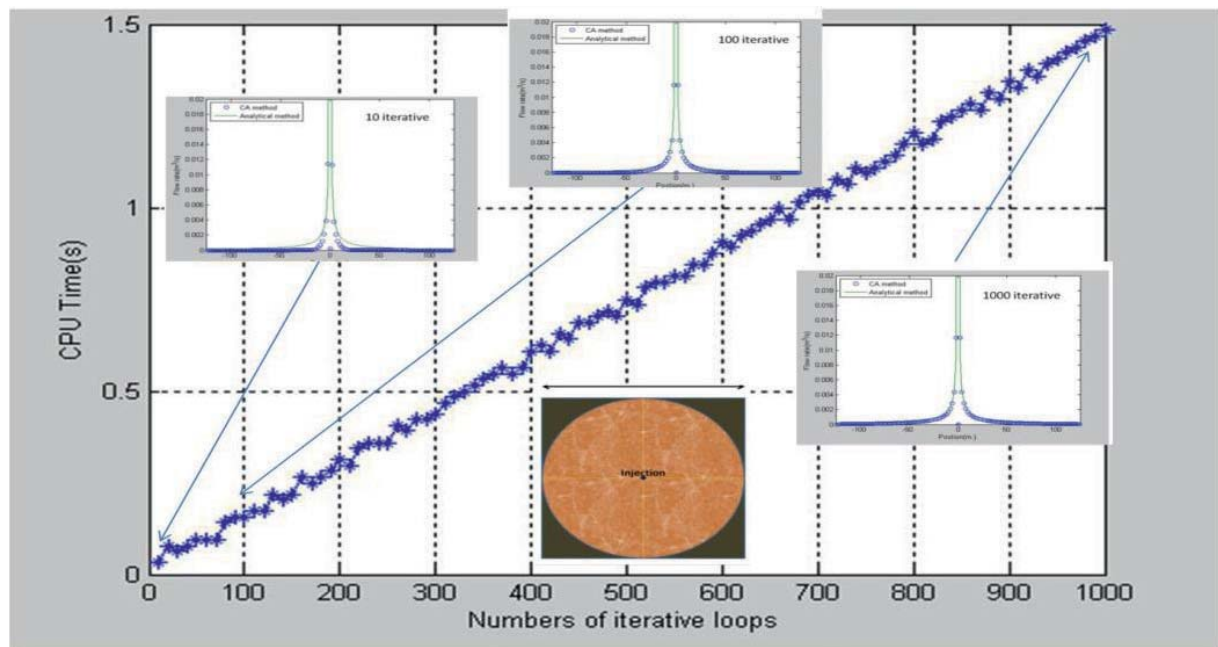
Figure 21: CPU Time of comparison CA model with analytical solution

The results show the functionality of the CA model. The numerical solution converges after about 100 loops with sufficient accuracy to the analytical solution.

After comparing the CA solution and with the analytical solution of a known example we analyses with the CA an arbitrary geometry of rock fracture.Three different types of fracture geometries and tube locations are selected, see Figure 22.
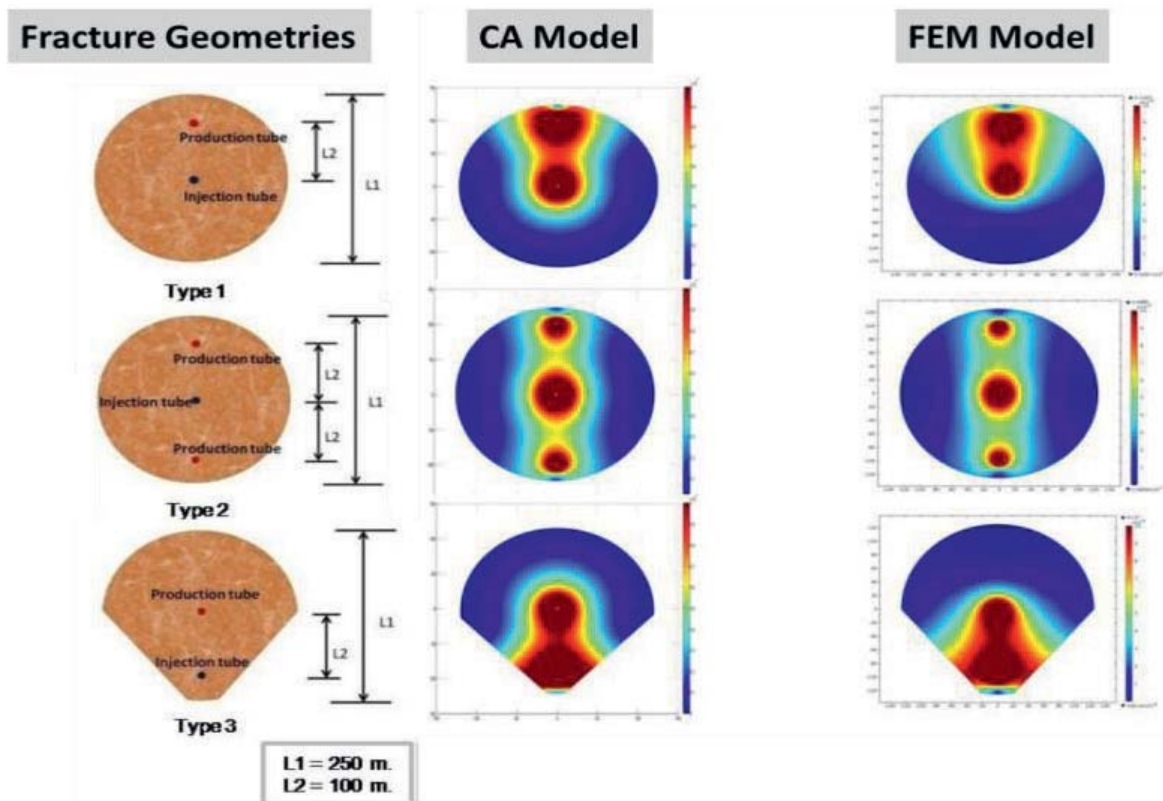
Figure 22: Results of absolute velocity: (Left) type of fracture geometries, (Middle) CA model, (Right) FEM Model (simulated in Project G7)

The results of CA model show a reasonable flow in rock fracture, e.g. for type1. The flow velocity is very high at injection and production tube and is gradually reduced until the boundary line. Also shown is the effect of finite domain at the boundary. In order to validate our CA model, we also compare the results of velocity fields with a conventional finite element method. The in Project G7 produced results are similar and show the same physical characteristic of the flow inside rock fracture.

Next example deals with the simulation of a geothermal reservoir with 50 fractures as shown in Figure 23. The CA model performed the fluid flow and heat transfer in multi-fractures.

Descriptions	L1	L2	L3	Wf
Magnitude	1,000 m.	250 m.	100 m.	2.0E-2 m.
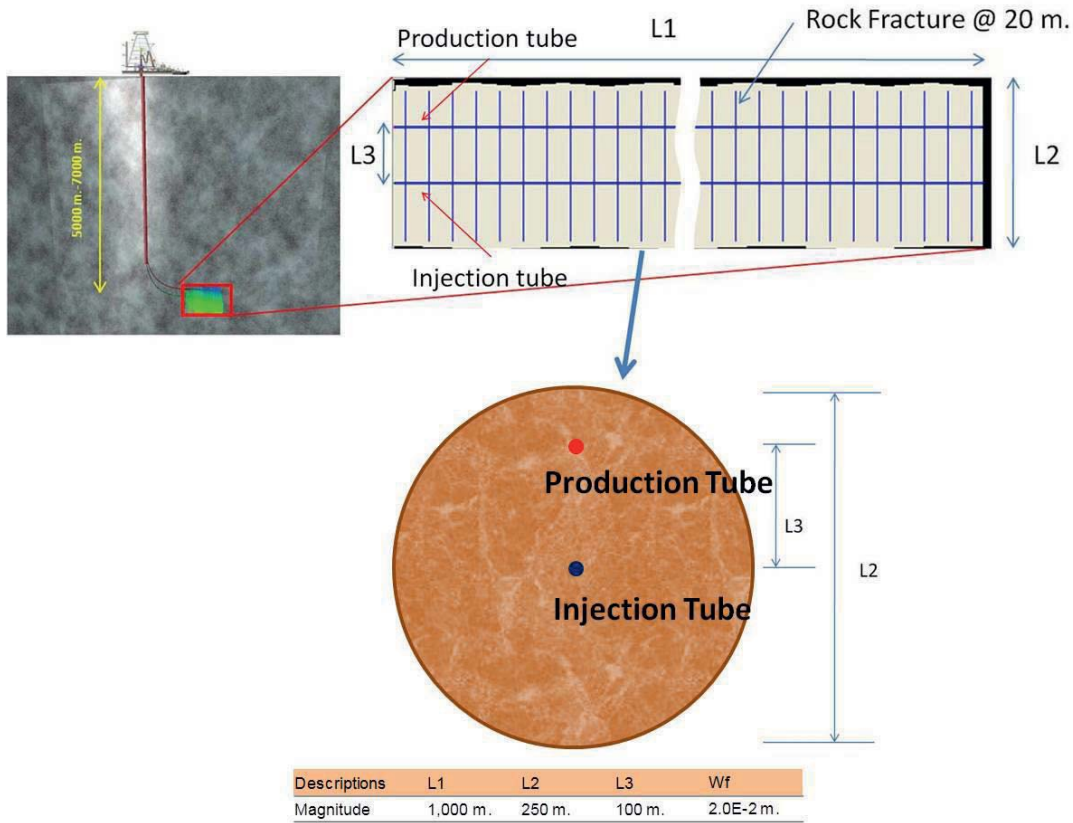
Figure 23: Domain problem of multifractures of geothermal reservoir

Firstly we show the results of the flow inside the multi-fractures with a variable flow resistance in the fracture (af) and in the pipe (ar). Figure 24 documents the results a wide parameter range of the flow resistances.
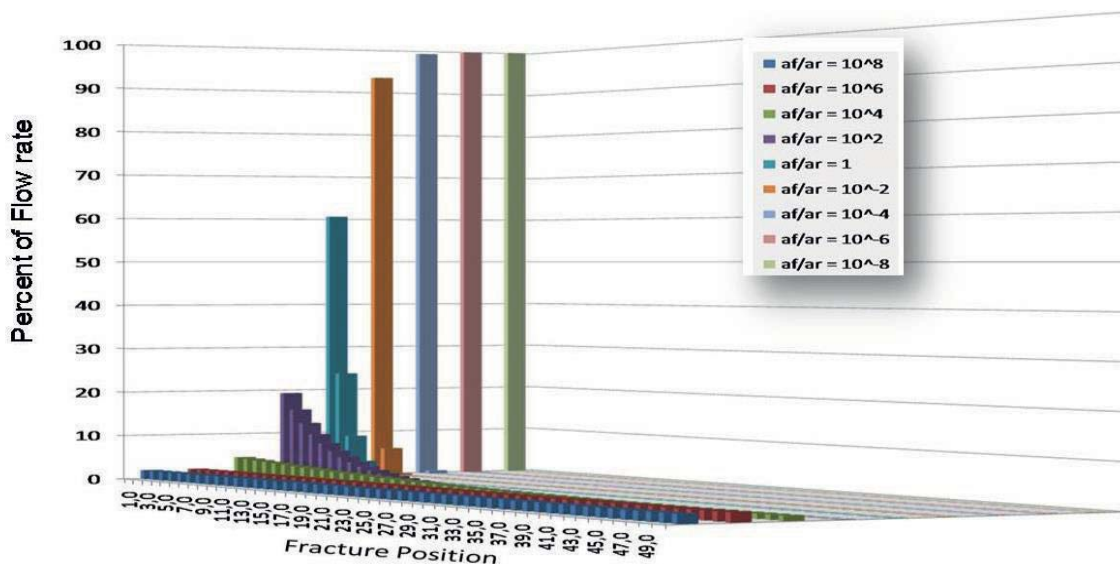
Figure 24: Flow rate in multifractures with respect to flow resistant

In Figure 25 the velocity inside each fracture for the case af = ar is exemplarily shown. It can be can observed that in this case only the first five fracture are active (10% of the total fracture number).
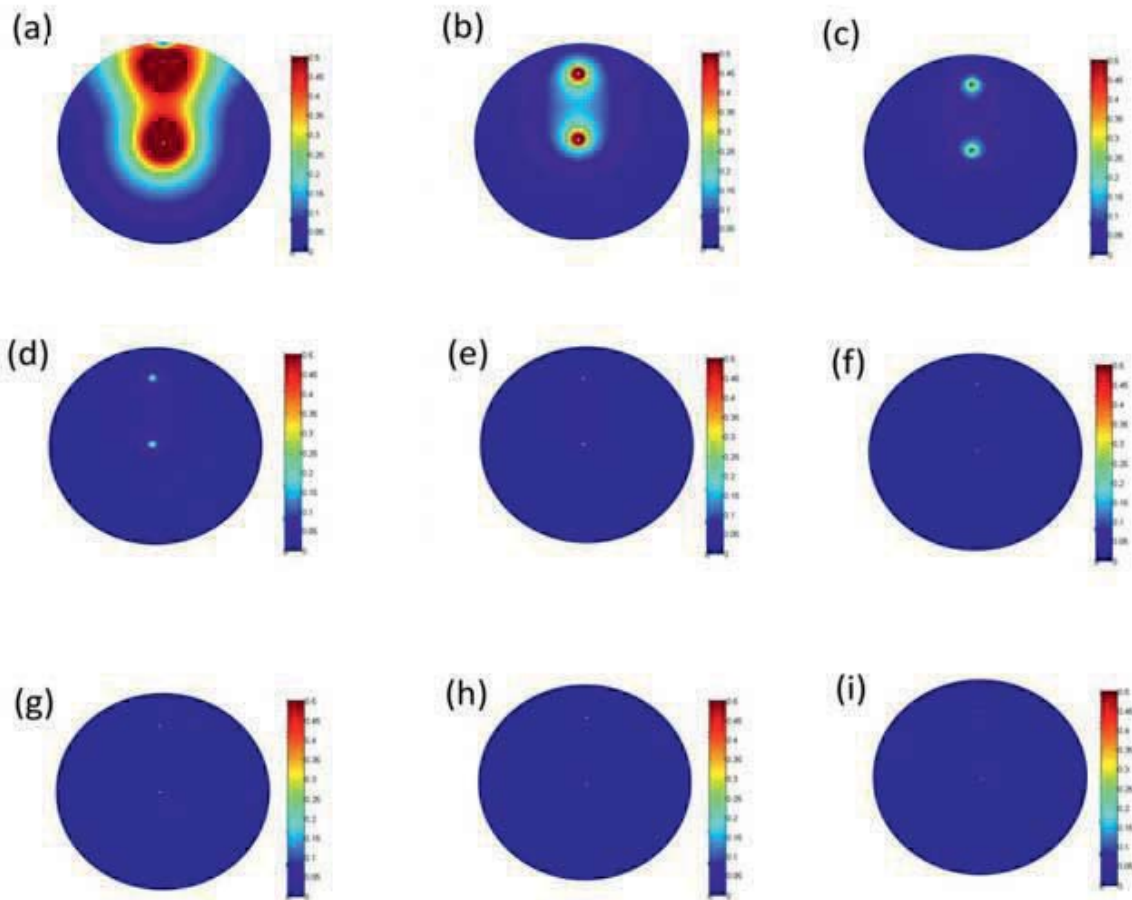
Figure 25: Flow rate in first 9th fractures

Usually, the parameter range of enhanced geothermal systems EGS is about af/ar = 10^4–10^6 with respect to the achievable permeabilities of fractures. The presented CA model is able to simulate complex geothermal reservoirs under variable states of fluid flow regimes. Thus, it is in principle possible to investigate the functionality of complex geothermal reservoirs in which individual fracs are not effective or the fluid flow is technically controlled. For example, in the simulation a geothermal reservoir can be optimized in which different hydraulic fracs are activated alternately in order to optimize the long-term energy harvesting.

The main objectives in the near future are the optimization of short-term and long-term calculations of the dynamics and the enhancement of the multiphysics performance in order to describe correctly gas or other geological reservoirs. A further important aspect is the usability of the modular simulation toolbox, in order to tailor its tools for general ease of use.

WP2: Modelling of the minimum wellbore construction size (ITE):

Parameterization of the proposed concepts was completed. The parameters shown in Table 1 have been identified to achieve a gross output of 7 MW (5 MW net).

Tabelle 1: Calculated flowrates to guarantee the 5 MW net output power (efficiency in the brakets is refering to the ORC equipment based on the actual reported values)

Depth $\diagdown$ ΔT	Temperate BK	$\dot{V}_{min} \left[\dfrac{l}{s}\right] (\eta = 10\%)$	$\dot{V}_{max} \left[\dfrac{l}{s}\right] (\eta = 17\%)$
5000 m $\diagdown$ **$\Delta T=30°C$**	130°C	$\dot{V}_1$ = 307,25	$\dot{V}_1$ = 180,84
	150°C	$\dot{V}_2$ = 235,74	$\dot{V}_2$ = 138,75
	170°C	$\dot{V}_3$ = 196,30	$\dot{V}_3$ = 115,53
6000 m $\diagdown$ **$\Delta T=40°C$**	150°C	$\dot{V}_4$ = 241,81	$\dot{V}_4$ = 142,32
	180°C	$\dot{V}_5$ = 241,81	$\dot{V}_5$ = 99,23
	210°C	$\dot{V}_6$ = 149,53	$\dot{V}_6$ = 88,01
7000 m $\diagdown$ **$\Delta T=50°C$**	220°C	$\dot{V}_7$ = 199,14	$\dot{V}_7$ = 117,21
	250°C	$\dot{V}_8$ = 161,10	$\dot{V}_8$ = 94,78
	280°C	$\dot{V}_9$ = 139,31	$\dot{V}_9$ = 82,00

Table 2 shows the flow velocity as a function of casing diameter. It can be seen that only few configurations allow velocities below 3 m/s which is considered a limit for liquid flow. As a result we consider that the casing size must be larger than 9 5/8", while maximum flow rate will be limited to 120 l/s. Such high flowrates has never been achievd in existing EGS projects, however they are common in hydrotermal applications.

For a lower flowrate, the 8 5/8" casing can offer a low pressure drop and can be a good candidate only if the reservoir Temperature is higher than normal gradient. From the well construction point of view (costs vs. heat output) the 9 5/8" is the first option, especially when reservoir temperature is less than expected gradient temperature at that particular depth.

The generated parameter (see appendix A) has been used by IDS for their flow through fractures and reservoir simulation.

Table2. Calculated flow velocities for different casing sizes

Depth	$\dot{V}_{max}\left[\frac{l}{s}\right]$ $(\eta = 17\%)$	u [m/s] (7 in)	u [m/s] (8 5/8 in)	u [m/s] (9 5/8 in)	u [m/s] (10 3/4 in)	u [m/s] (11 3/4 in)	u [m/s] (13 3/4 in)
5000 m	$\dot{V}_1 = 180{,}84$	14,69	9,90	7,77	6,25	5,12	3,87
	$\dot{V}_2 = 138{,}75$	11,48	7,59	5,96	4,79	3,93	2,97
	$\dot{V}_3 = 115{,}53$	9,56	6,32	4,96	3,99	3,27	2,47
6000 m	$\dot{V}_4 = 142{,}32$	11,78	7,79	6,11	4,92	4,03	3,05
	$\dot{V}_5 = 99{,}23$	8,89	5,88	4,62	3,71	3,04	2,30
	$\dot{V}_6 = 88{,}01$	7,28	4,82	3,78	3,04	2,49	1,88
7000 m	$\dot{V}_7 = 117{,}21$	5,71	3,78	2,96	2,38	1,95	1,48
	$\dot{V}_8 = 94{,}78$	4,62	3,05	2,40	1,93	1,58	1,19
	$\dot{V}_9 = 82{,}00$	3,99	2,64	2,07	1,67	1,37	1,03

WP 3 Optimization (ITE)

One additional one well concept will be defined. The multilateral one-well-concept has been implemented to develop a shale gas reservoir in the Bakken formation (USA), see Figure 5. Five multilaterals were drilled 200 m apart from each other. Formation depth was approx. 1.000 m. The length of the horizontal sections was around 5.000 ft (ca. 1.500 m). Each lateral was fractured 10 times. Fractures were about 100 m apart and of a design half length of 300 – 500 m. Figure 26 shows the microseismicity recorded during the fracturing treatments. For the treatments a novel fracturing technology was applied which allows multiple fracturing treatments to be carried out in one day. For its application a liner with external packer is introduced into the horizontal section, but the liner is not cemented. The concept will be considered to recover geothermal energy and evaluated for viability and economics in geothermal wells at large depths and high temperatures.
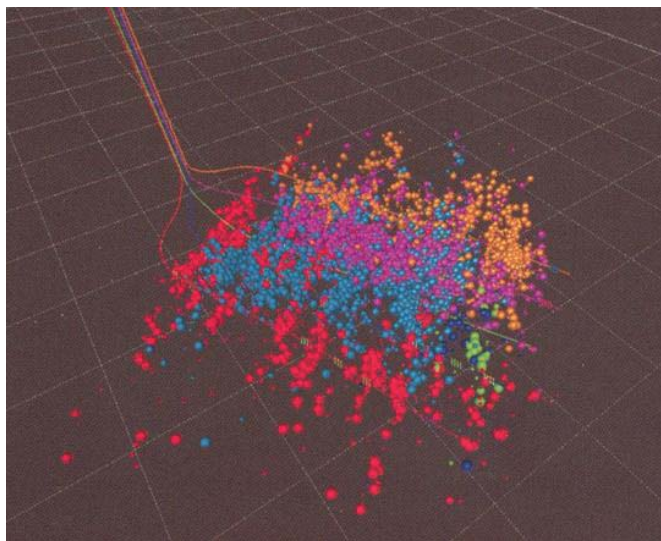
Figure 26:
MicroSeismic Houston, Multi Frac Bohrungen in der Bakken Formation (between Saskatchewan, Montana, North Dakota) [BAK10]

After the first step of the parameterization of the different concepts it is mandatory to look at optimization opportunities will be . Important issues are the hydraulic resistance and the heat output. Hydraulic resistance is very important for the fluid flow and as well as for the heat

exchange. Knowing the hydraulic resistance is the key to optimizing the system. Assuming that each frac has the same hydraulic resistance, a short circuit is possible. Whereby the heel of the well of the underground heat exchanger cools down and at the toe there is no circulation.

Another issue to be looked at is the creation of shear fracs by pumping signifigantly higher volumes of liquid into the subsurface as in the first European geothermal project (Soultz-sous-Forêts in France).

Within WP3 the following aspects for the one-well-concepts were also investigated:

- Hydraulic resistances inside the fractures (see IDS WP2)
- Lifetime of the underground heat exchanger (see IDS WP2)
- Fracture propagation and shape.

An intensive study of fracture propagation in deep reservoir have been performed. The study have shown that the Fracture have a natural tendency to move upwards until a fracturing resistant formation (i.e. salt) will stop it. Figure 27 shows such a fracture simulation, but more then 40 scenarios have been investigated.The results show that it is possible to place only two paralel wells, one at the bottom, from which also the fractures are genertated and a second at a distance no longer that 200 m from the exsting one.
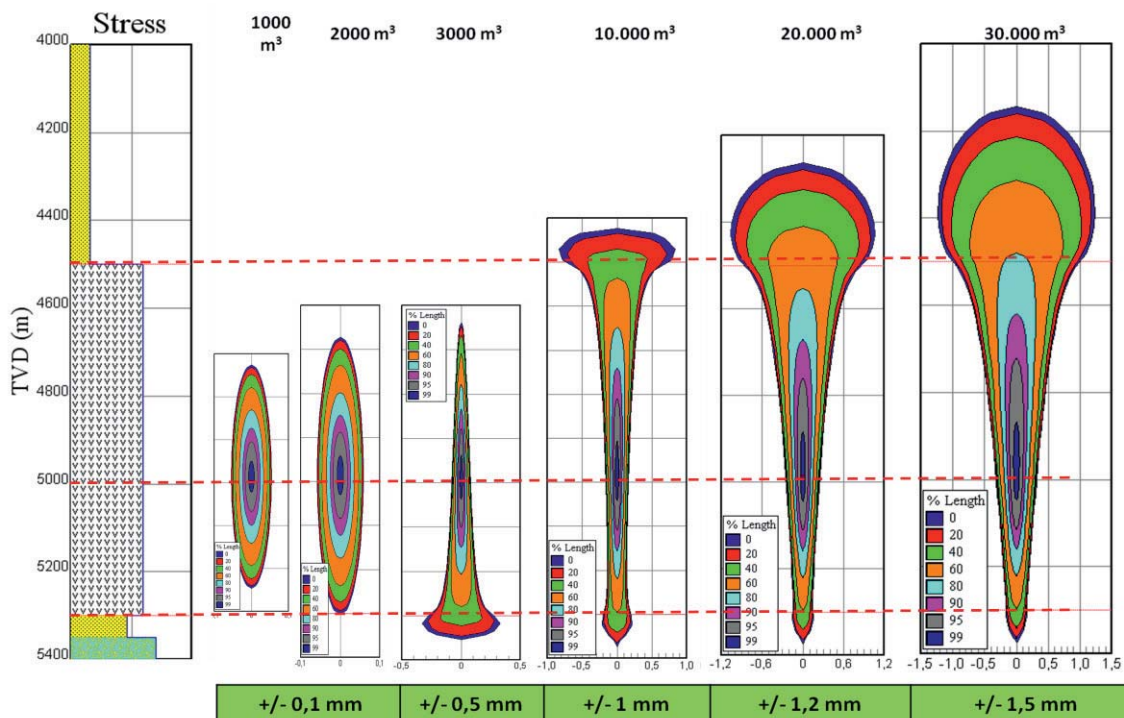
Figure 27. Fracture propagation as a function of injected volume, for the 5000 m case scenario.

Another study performed togetehr with B1 have investigated the optimum placement of wells to optimum extract the heat. Figure 28 shows the patern used for the study. For simetrical

fractures the beste well placement is three paralel wells, whereas the injector is located in the center, and the producers ooutside.

Figure 27. Estimated fracture efficiency as a function of well placement. [TEO13]

1.2.4   Project Plan

Work packages and milestones	2009	2010	2011	2012	2013	2014
WP1: Model's concept and interfaces to single models						
WP2: System's modeling						
WP3: Evaluation und concept optimization						

Grey, original plan

Blue, actual or current plan, respectively

For details, see Gantt chart in the Appendix.

1.3   Delineation of the project from other funded projects

An overlapping with other funded projects does not exist.

1.4 References

[BAT00]   G. K. Batchelor: „An introduction to fluid mechanics", Cambridge University Press, 2000

[BAK10]   Private Communication; SPE ATCE Conference 2010, Florence

[BMU07]   Bundesministerium für Umwelt, Naturschutz und Reaktorsicherheit (BMU); Institut für Energetik und Umwelt GmbH; Druck: Bonifatius GmbH, Paderborn; 2007

[ECO89]   Economides, Nolte, Reservoir Stimulation-Second Edition, Wiley, 1989

[EVA09]   K. Evans, B. Valley, M. Häring, R. J. Hopkirk, C. Baujard, T. Kohl, T. Megel: Studies and support for the EGS reservoirs at Soultz-sous-Forêts, Edited by Sandrine Portier and François-D. Vuataz, Centre for Geothemal Research - CREGE, c/o CHYN, University of Neuchâtel, Switzerland

[NEU09]   T. Neu, I. Gedzius: Bohr- und Sprengtechnik für die Gewinnung tiefer Erdwärme; Glückauf - Zeitschrift für Rohstoff, Bergbau und Energie, Januar 2009

[OST07]   G.-P. Ostermeyer, M. Müller: "New Insights into the tribology of brake systems", Proceedings of the Institution of Mechanical Engineers, Part D: Journal of Automobile Engineering, IMechE, Vol. 222 (2008), 1167-1200

[WOL02]   S. Wolfram: "A new kind of science", Wolfram Media Inc., Champaign IL, USA, 2002

1.5 Publications, reports and presentations of Project

[GED10]   Gedzius, Optimum geothermal well constructions to maximize the heat output and minimize cost, European Geothermal PhD-Day, 12.2.2010, Potsdam

[OST11]   Ostermeyer, G.-P., Srisupattarawanit, T., Müller, M.: Modellkonzept zur Bewertung geothermaler Energiereservoire, Interner gebo-Meilensteinbericht – IDS-Bericht 2011-04

[OST11]   Ostermeyer, G.-P., Müller, M., Srisupattarawanit, T.: Time-efficient Calculation of Complex Geothermal Reservoirs Using Cellular Automata, Celle Drilling 2011

[SRI11]   Srisupattarawanit, T., Ostermeyer, G.-P.: Cellular Automata (CA) for Simulations of Complex Geothermal Reservoirs, PAMM 2011

[GED11]   Gedzius, Optimum geothermal well constructions to maximize the heat output and minimize cost, European Geothermal PhD-Day, 2.3.2011, Reykjavik

[TEO13]   Teodoriu, Haggemann, Krebs, A discussion about fracture efficiency with application to geothermal energy, Celle Drilling 2013

Appendix A

Parameterfestlegung

Lagerstätte Vulkanit			
Gestein	Basalt		
Dichte (Basalt) [g/cm^3]	3		
Wärmeleitfähigkeit (Basalt) [W/mK]	1,3 - 2,3		
Spezifische Wärmekapazität (Basalt) [MJ/m^{3}K]	2,3 - 2,6		
Mächtigkeit [m]	200 -400	200 -400	200 -400
Teufe [m]	5000	6000	7000
Temperatur der Zielformation [°C]	200	250	280
effective Porosität [%]	< 1%		
Permeabilität [μD]	< 10 microdarcy, 10^{-17} m^2 = < 1 microdarcy, 1^{-18} m^2		

Fracs Vulkanit	
Permeabilität [μD]	0,1 darcy
Risslänge [m]	120 - 150 m
Rissabstände [m]	20 m
Rissbreite	< 2 mm
Proppant/Stützkorn	X

Futterrohre – Fall „cased hole" (egal ob Futterrohr oder Faltrohr verwendet wird)

Material	N 80							
Wärmeleitfähigkeit [W/mK]	15							
Produktionsrohr OD Durchmesser [inch]	8 5/8		9 5/8		10 3/4			
ID Durchmesser [m]	0,19988		0,2244		0,2502			
OD Durchmesser [m]	0,2191		0,2445		0,2730			
relative Wandrauhigkeit ε/d [mm/mm]	0,002 53		0,001 985		0,0015 97			
Bohrlochdurchmesser/Meißeldurchmesser	10 5/8		12 1/4		14 1/2			

Injektionsrohr OD Durchmesser [inch]	6 5/8	7	7	7 5/8	7 5/8	8 5/8		
Produktionsrohr OD [m]	0,1683	0,1778	0,1778	0,1937	0,1937	0,2191		
Produktionsrohr ID [m]	0,1504	0,1617	0,1617	0,177	0,177	0,1985		

Injektionsringraum zwischen:	(8,625 & 6 5/8) oder (8,625 & 7)			(9,625 & 7) oder (9,625 & 7 5/8)			(10,75 & 7 5/8) oder (10,75 & 8 5/8)		
Teufe [m]	5000	6000	7000	5000	6000	7000	5000	6000	7000
Temperatur [°C] Bohrlochkopf	170	210	240	170	210	240	170	210	240
Volumenstrom Injektionsrohr/Ringraum [m³/s]	0,1155	0,088	0,082	0,1155	0,088	0,082	0,1155	0,088	0,082
Kick-Off-Point Produktionsbohrung (Beginn der Ablenkung)	4900 m / 4351,36 m			5900 m / 5351,36 m			6900 m / 6351,36 m		

Kick-Off-Point Injektionsbohrung (Beginn der Ablenkung)	5000 m	6000 m	7000 m
	4451,36 m	5451,36 m	6451,36 m
Packer Setting Depth [m]	4400	5400	6400
Ablenkung	5°/100 ft		
Länge der abgelenkten Strecke (von Vertikal - Horizontal) [m]	862		
Länge der Horizontalstrecke [m]	500 - 800		
Abstand der Horizontalbohrungen [m]	100		

Zementation

Zement	Class G								
Wärmeleitfähigkeit [W/mK]	< 1,3								
≈	8 5/8´´			9 5/8´´			10 3/4´´		
Zementvolumen [m³] (hinter dem Injektionsrohr)	5 km	6 km	7 km	5 km	6 km	7 km	5 km	6 km	7 km
	785,39	942,48	1099,56	1099,55	1319,47	1539,38	1570,79	1884,95	2199,11
Zementdicke [m]	0,0509			0,0655			0,097		

Formationswasser

	170°C	210°C	240°C
Dichte [kg/m³]	5 km	6 km	7 km
	852,57	799,36	750,75
(dynamische) Viskosität [Pa*s]	$2,77 \cdot 10^{-4}$	$1,9 \cdot 10^{-4}$	$1,47 \cdot 10^{-4}$
Spezifische Wärmekapazität [J/kgK]	4183		

Schriftenreihe des Energie-Forschungszentrums Niedersachsen (EFZN)

Band 30-3

Das EFZN ist eine wissenschaftliche
Einrichtung der

TU Clausthal

in Kooperation mit den Universitäten

Technische
Universität
Braunschweig

GEORG-AUGUST-UNIVERSITÄT
GÖTTINGEN

Leibniz
Universität
Hannover

CARL
VON
OSSIETZKY
universität OLDENBURG

Final Report

of

Geothermal Energy and High-Performance Drilling Collaborative Research Program (gebo)

Niedersachsen

Partners:

Technische Universität Braunschweig (TUBS)

Technische Universität Clausthal (TUC)

Gottfried Wilhelm Leibniz Universität Hannover (LUH)

Georg-August-Universität Göttingen (UGOE)

Leibniz-Institut für Angewandte Geophysik (LIAG)

Bundesanstalt für Geowissenschaften und Rohstoffe (BGR)

Energie-Forschungszentrum Niedersachsen (EFZN)

Speaker:
Kurt M. Reinicke;
Georg-Peter Ostermeyer

Goslar, July 2015

Contents

W1: Life Cycle of Coated High-Performance Materials

1 Project Overview

Speaker and lead university or research institution

Project Nr.	Title	Subject of research	Project leader, institution, location
W1	Life cycle of coated high-capacity materials under influence of corrosion and multiaxial high temperature fatigue load	Mechanical Engineering/ Materials	Prof. Dr. Joachim Rösler/ Institute for Materials, Technische Universität Braunschweig

Participating institutes and institutions of the University and external institutions in:

- Institute for Materials (IfW), Technische Universität Braunschweig

- Baker Hughes, Dr. H. John

List of participating scientists and engineers:

Name	Subject area	University institute or non-university institution	Position is financed by gebo funds (indicate with X)
Prof. Dr. Joachim Rösler	Mechanical Engineering/ Materials	IfW	
Dr. Ing. Tatiana Fedorova	Mechanical Engineering/ Materials	X	X

2 Research Program

2.1 Summary

The materials used in the high-capacity drilling techniques are exposed to complex mechanical demands, where high temperatures, cyclic loadings and multiaxial stress conditions play a decisive role.

The objective of the W1 project is to develop a multiaxial stress condition test environment. The influence of temperature, pressure, tension and torsion should be evaluated specifically on life cycle of coated high performance materials. Another significant aspect is to do research on the influence of corrosion under high temperature (from 40°C to 110°C) and fatigue loading. This knowledge is to be applied in the context of geothermal subsurface constructions, specifically for materials used in casing-structures, whose proposed life cycle may exceed 50 years.

2.2 Relationship of the project to the overall research context and networking with other projects

A focus of the Gebo research association lies on the evaluation of realistic work environments and the development of high-strength and temperature-resistant materials and coatings. Significant requirement for the W1 project is the construction of a suitable test environment, allowing for the analysis of materials for the high-capacity drilling technology under the action of multiaxial fatigue loading, elevated temperatures and corrosive environments. The input necessary for the project (newly developed material systems and load spectra) and its output (material specifications and explanations of functional failure mechanisms) build the basis for the networking with other projects.

2.3 Results

The first objective of this project was to develop a test stand which allows research on the mechanical behavior of materials under the simultaneous influence of temperature and cyclical-multiaxial load. Because of the complexity of the test environment it was necessary to use non-contacting 3D measurement techniques and thermography.

The construction of a torsion system was arranged on the Schenck 160 kN hydraulic system (see Fig.1a). The torsion system was developed by the Institute for Materials. For these tests, the geometry of a standard specimen was changed due to the necessity to use a newly developed cooling equipment for high temperatures (see Fig. 1b, 2).

Besides the development of a new specimen geometry, control of the inside surface quality was an extremely important parameter. For example, decreasing the roughness of specimens inside surface from 4.5 μm (GEBO6ZD250) to 2.0 μm (GEBO7ZD250) increased the life time strongly from $1.58*10^5$ cycles to $1.6*10^6$ cycles. Consequently, a roughness of 2.0 μm was ensured for all following specimens.

The projected highest temperature of experiments was 350°C. On that account, it was essential to develop a new cooling equipment (Fig. 3) which allows protecting the hydraulic system from overheating.

The heating of the specimen could be facilitated by using a HF heating system. The temperature control was realized with brazing of a thermocouple element and two pyrometers. The thermocouple element was a reason for early failure of the specimen because of local surface damage. On that account, the fixation of the thermocouple element on the specimen was changed and realized with Teflon insert which presses the thermocouple element on the specimen surface (see Fig. 4). The basic schematic of the test environment with complex specimen layout can be seen in Fig. 5.
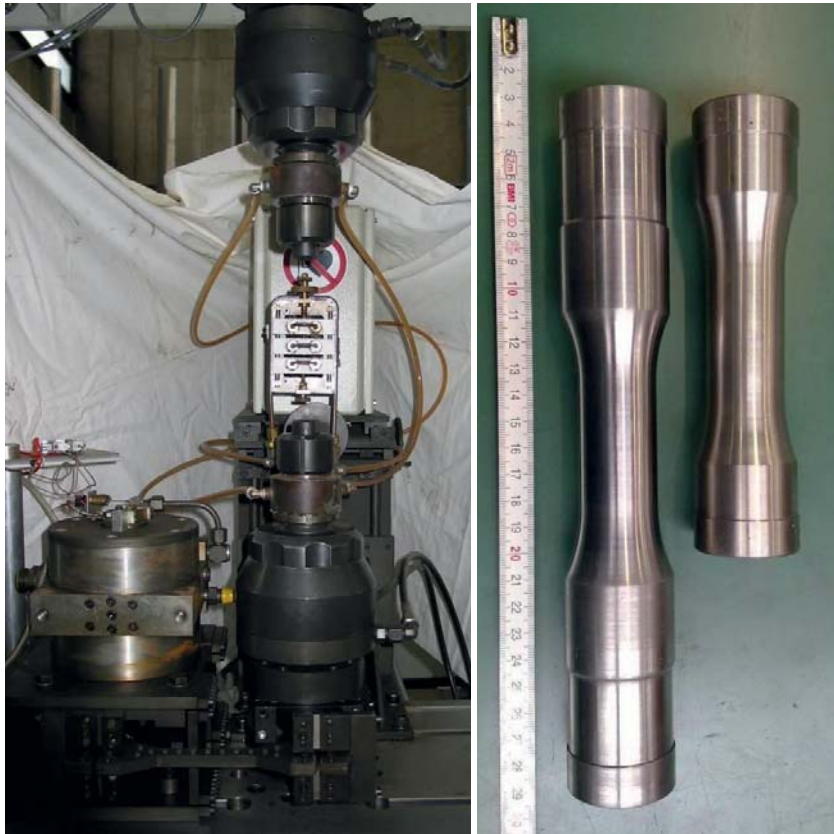
Fig. 1.: a) Servohydraulic testing machine with integrated torsion system (on the left side); b) Comparison between a standard specimen (right) and newly developed specimen (left).
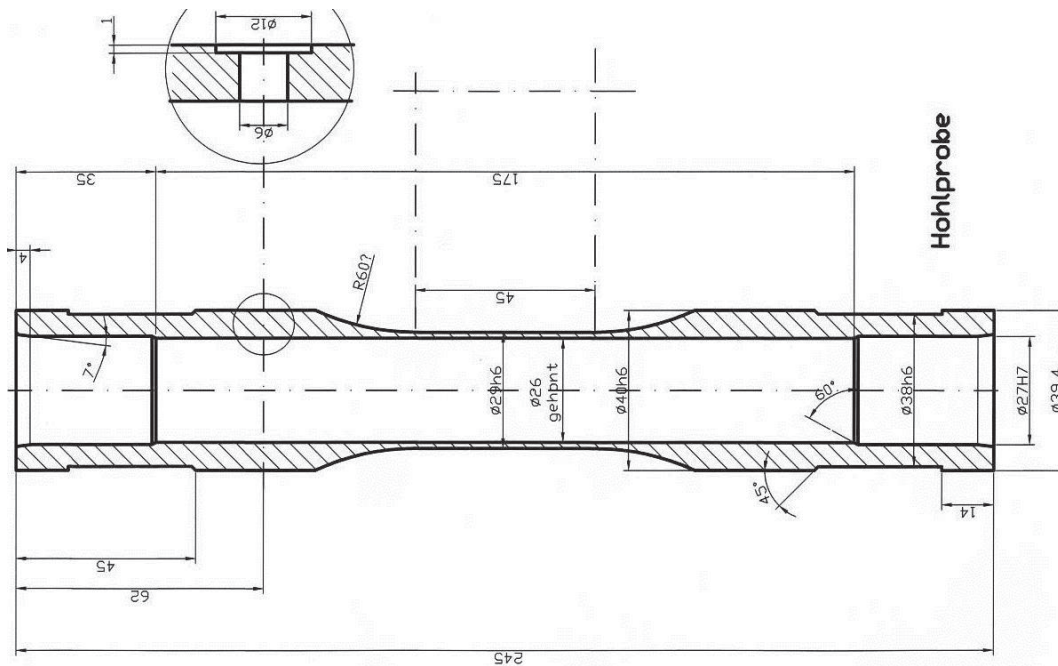
Fig. 2.: The drawing of the newly developed test specimen.

.
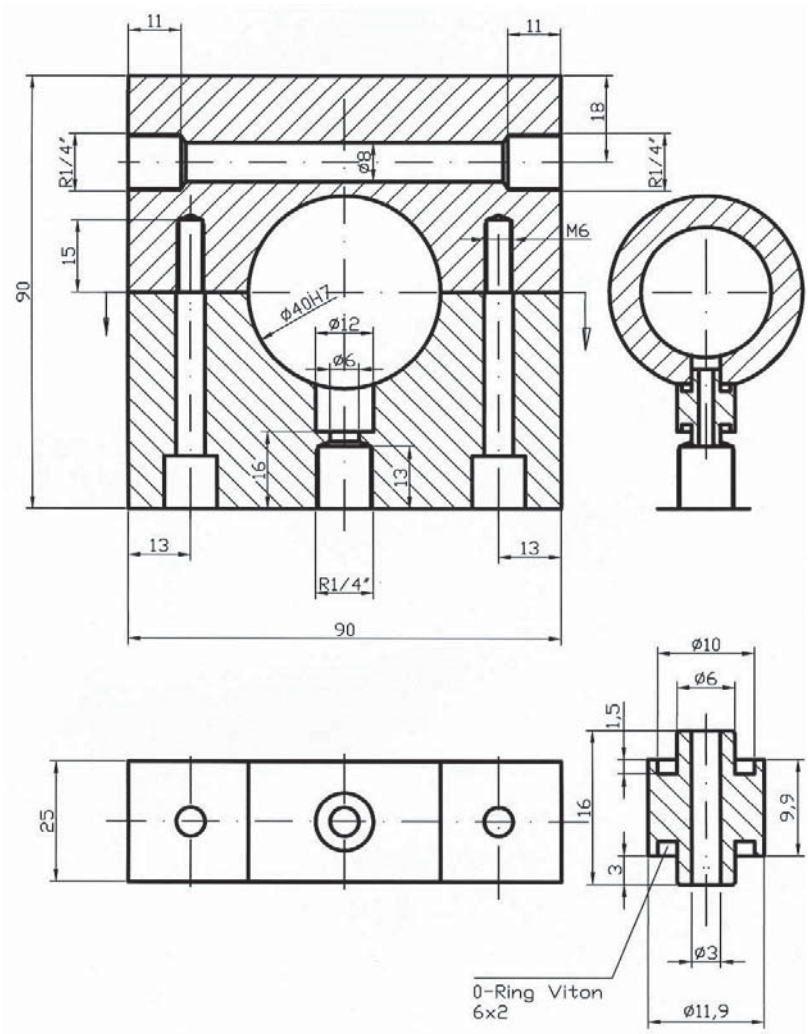
Fig. 3.: The newly developed cooling equipment.
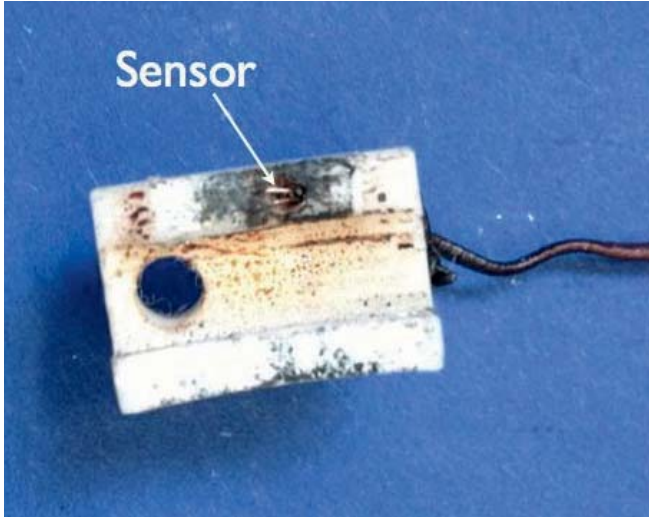
Fig. 4.: The newly developed thermocouple element.
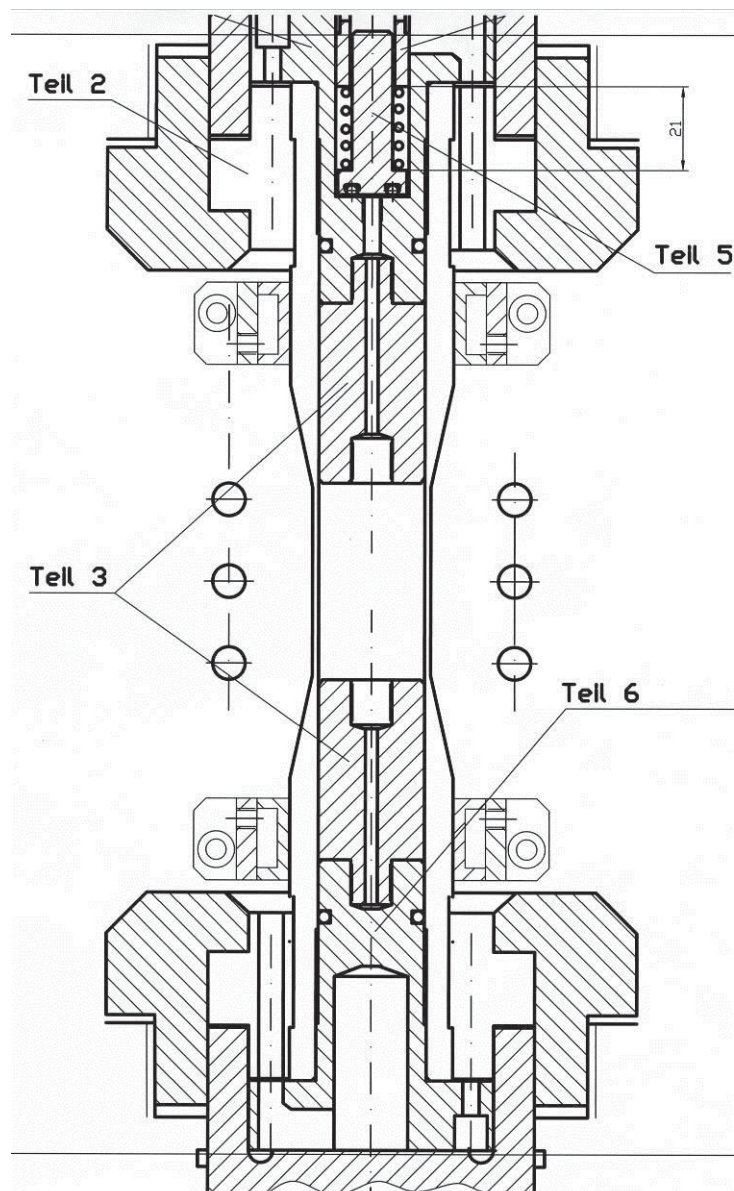
Fig. 4.: Specimen layout with HF heating system ("Teil 5" – pressure control valve; "Teil 3" – spacer, defining the volume for the corrosion media; "Teil 6" – place for layout of pressure sensor).

Another significant aspect of this project was the development of a new set-up for fatigue testing under a corrosive environment. In contrast to standard corrosion tests, the corrosion medium was taken inside the specimen.

Two different corrosion media were used during this project. The first one is a saline solution with 18% salt and was used at a temperature of 80°C. The second one is damp salt (10.5 cm^3 salt and 4 cm^3 water) for tests at temperatures up to 120°C. A special Teflon core was applied in order to reduce the volume of the corrosion medium for tests at 120°C due to safety reason

(Fig. 5a). Besides, a pressure sensor was used in all tests with corrosion medium. It allows a better control of the tests because temperature and pressure must be adjusted precisely during the experiment. If the pressure or the temperature increase in an uncontrolled manner and if either one exceeds a defined value, the equipment is immediately stopped by the pressure sensor. The pressure control valve is used as a passive safety system and opens at 6 bars. In addition, all tests with corrosion media are done with permanent overpressure between 2.7 and 8 bars. This device can be seen in Fig. 5b.

Teflon core

a)   b)
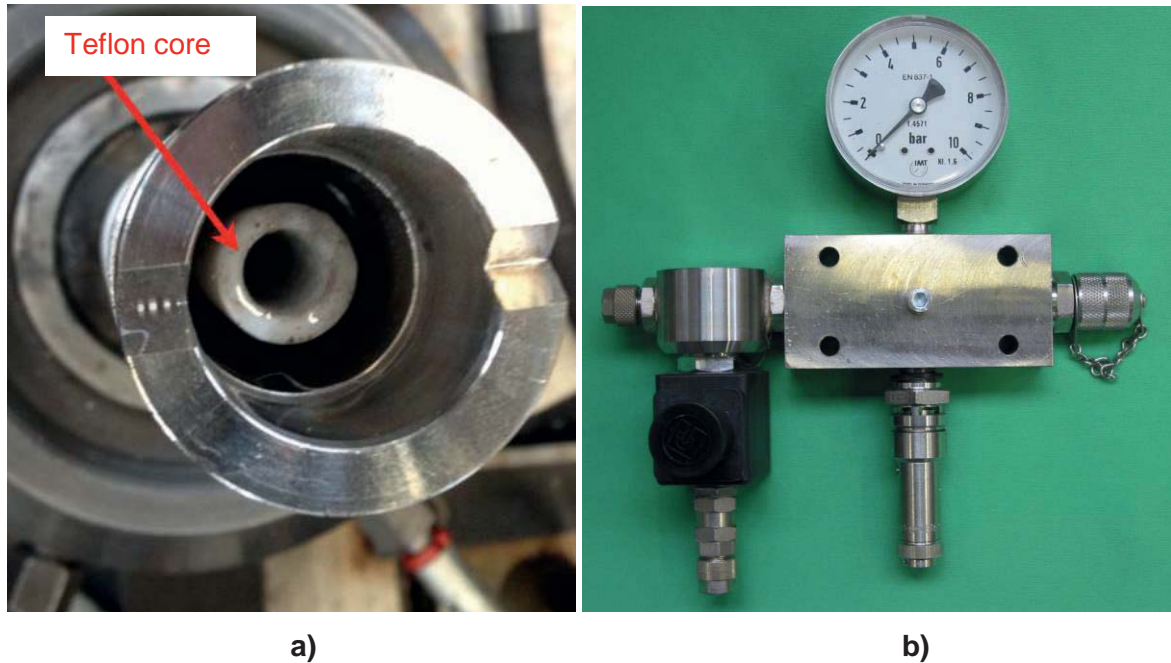
Fig. 5.: a) Teflon core installed into specimen; b) The device for pressure control during corrosion tests.

The investigation of mechanisms of functional failure of newly developed coating systems should be studied after development of the multiaxial stress condition test environment. However, as coating process development took longer than anticipated the main focus of this research was switched in agreement with Baker Hughes to the investigation of functional failure under multiaxial high temperature fatigue loading and corrosion of alloy P550 and alloy 718. Both alloys are used in the high-capacity drilling techniques. The chemical compositions of the two alloys are given in Tables 1 and 2. Alloy P550 is an austenitic corrosion resistant steel and alloy 718 is a nickel based superalloy.

Table1: Chemical composition of P550.

	Fe	Mn	Cr	Ni	N	Mo	Si	C	P
wt.%	Basis	21,26	18,46	1,67	0,67	0,54	0,15	0,044	0,022

Table2: Chemical composition of Alloy 718.

	Ni	Fe	Cr	Nb	Mo	Ti	Al	C	P
wt.%	52,14	19,00	18,65	5,06	3,00	0,94	0,52	0,021	0,007

The thermodynamic simulations with ThermoCalc (Version 4.1) were carried out for both alloys (see Fig. 6). The brittle phases such SIGMA or HCP_A3 are thermodynamically stable in alloy P550 at room temperature. The homogenous microstructure and high strength can be achieved during production process and cold work hardening. It limits a maximal application temperature of this alloy at 400°C.
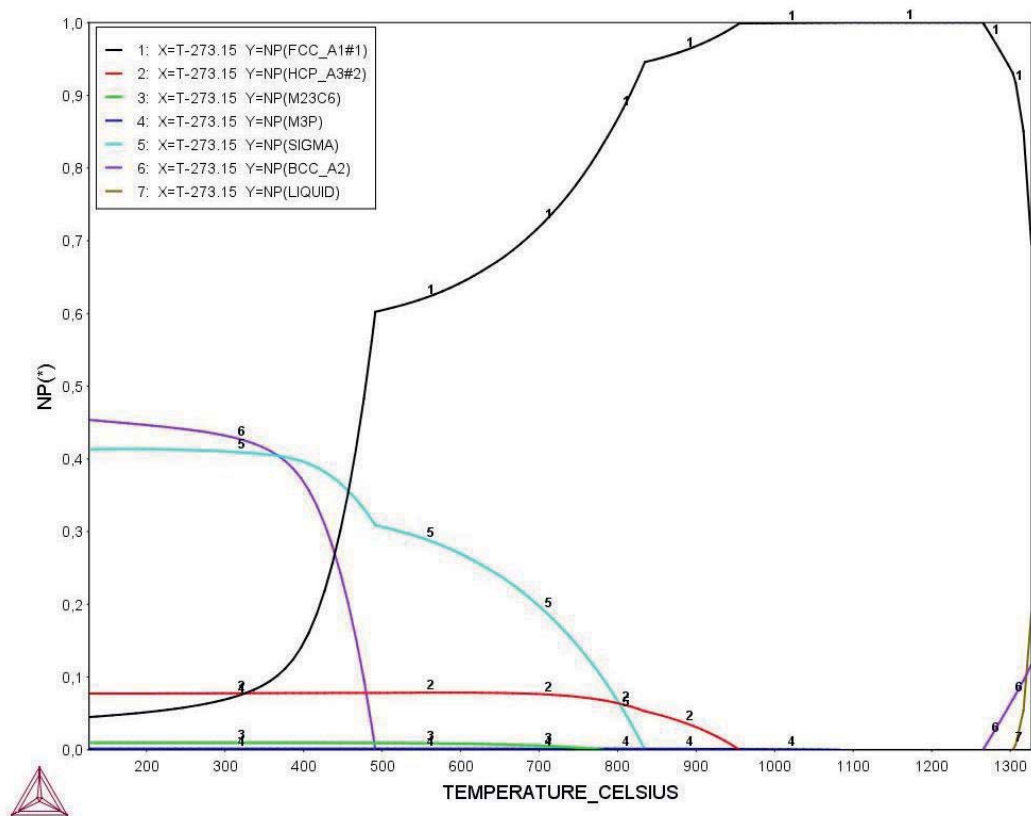
a) **Alloy P550**
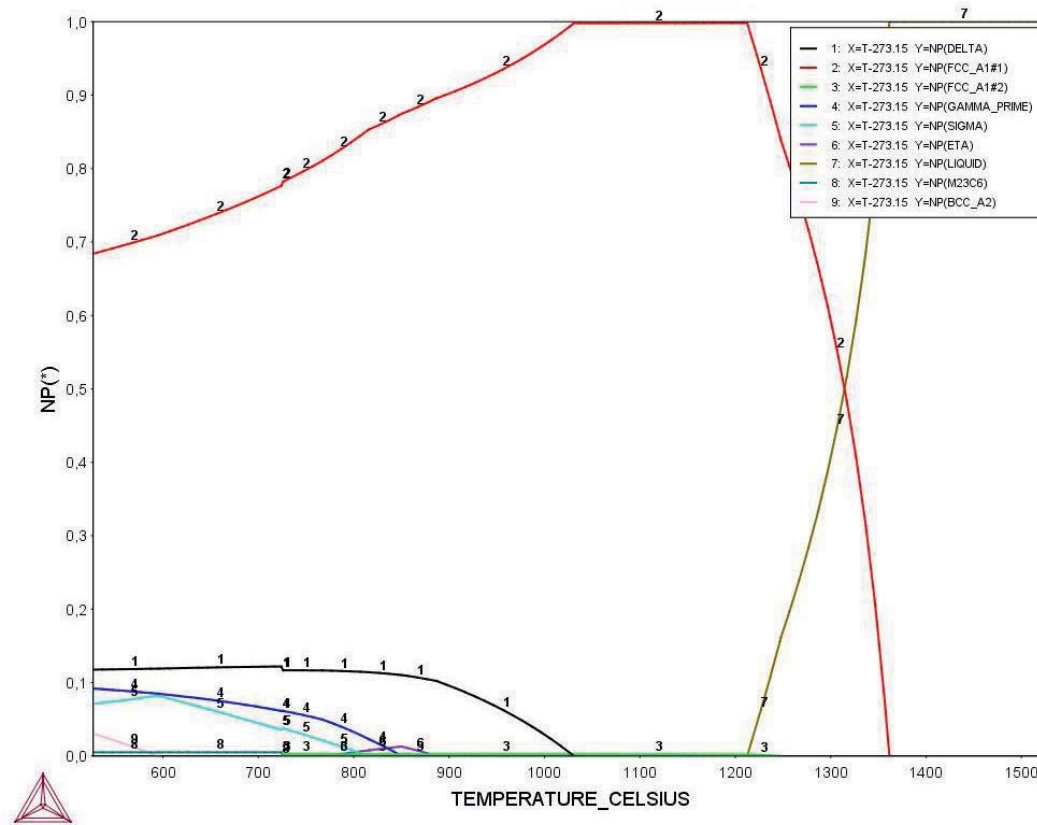
b) Alloy 718

Fig. 6.: ThermoCalc calculation: a) Alloy P550; b) Alloy 718.

Fig. 7 shows the microstructure (by scanning electron microscopy SEM) of alloy P550 as delivered (a) and after heat treatment at 800°C (b). The degradation of microstructure can be clearly seen. The precipitations agglomerate on grain boundaries, explaining the limited application temperature of alloy P550.

The thermodynamic simulation of Alloy 718 shows that, as in alloy P550, some brittle phases such as DELTA or ETA are thermodynamically stable at application temperature. Both phases are not allowed if this alloy is used in high-capacity drilling because they reduce corrosion resistance. For this reason, both phases must be absent in light optical images at a magnification of 500x. A homogenous microstructure and high strength can be achieved during production process and forging process. The maximum application temperature of Alloy 718 is about 650°C.
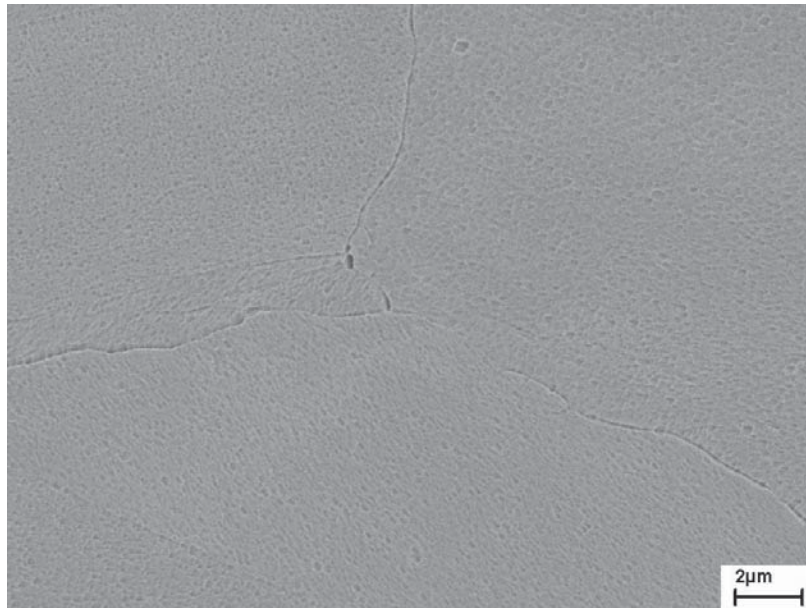
a)
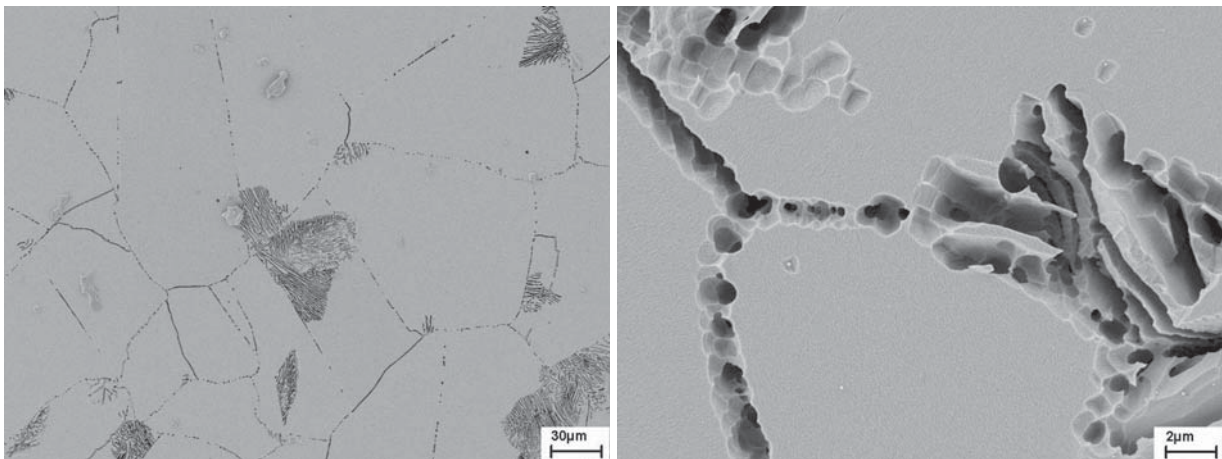
b) **c)**

Fig. 7.: Microstructure of alloy P550; a) as delivered; b) and c) after heat treatment at 800°C, showing agglomeration of precipitates on the grain boundaries.

Fig. 8 shows the typical microstructure (SEM) of Alloy 718 for application in the high-capacity drilling techniques. Very small precipitations of the DELTA phase can be seen on triple points of grain boundaries and near carbides.

583
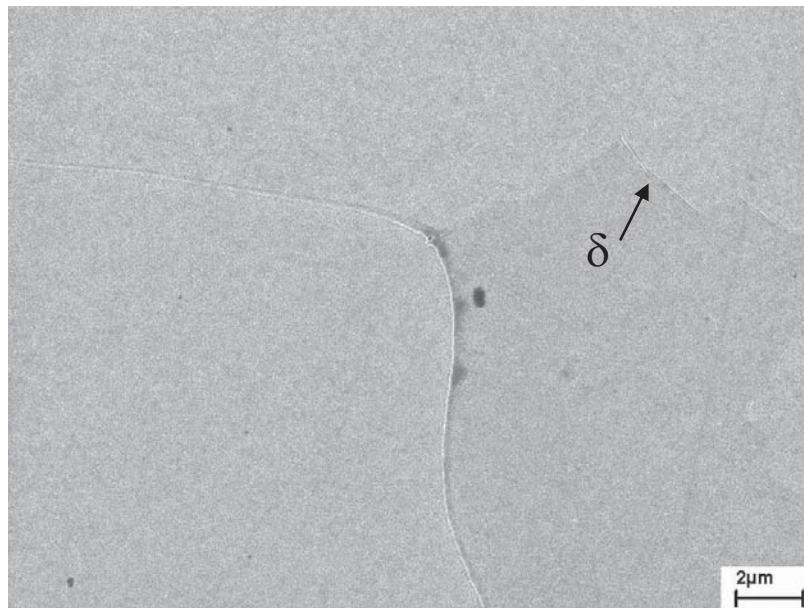
a)
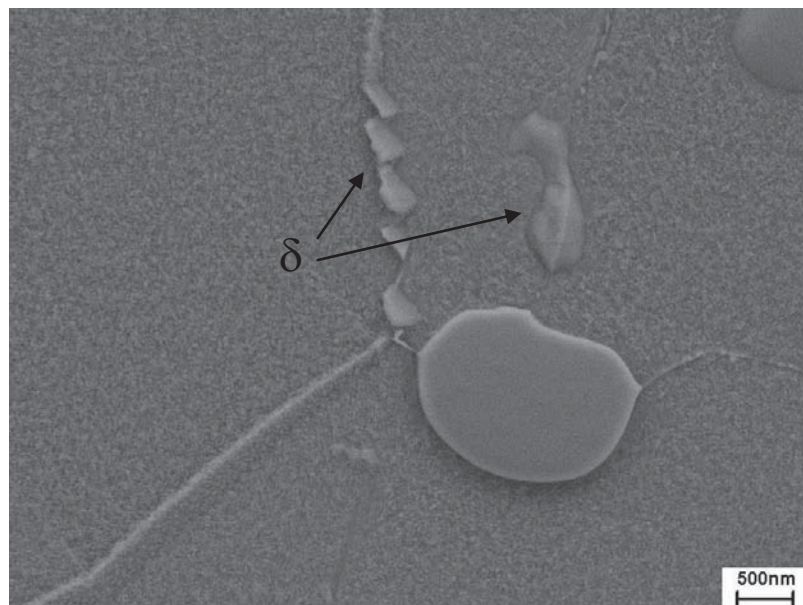
b)

Fig. 8.: Microstructure of alloy 718; a) grain boundaries with small precipitations of DELTA phase; b) DELTA phase precipitations near carbides (see arrows).

In the beginning, it was decided to check the mechanical behavior of alloy P550 under uniaxial fatigue loading (compression and tensile) at 350°C. In accordance with the data of Baker Hughes, the first experiment was conducted under a stress amplitude of σ_a=600MPa, R-value of -1 and a frequency of 3Hz. The temperature profile was controlled by means of three thermo-couple elements (on the top, center and bottom each) and regulated to 350°C ± 3°C. Upon

commencing the experiment, the temperature in the center of specimen increased up to 400-410°C, yet the temperature on the top and bottom remained constant (350°C). The specimen failed after 1892 cycles. The fractured specimen can be seen in Fig. 9. The characteristic colors (see Fig. 10) near the fractured surface (under the HF ring) show the temperature to be higher near the fractured surface. Obviously, the stress amplitude of 600MPa at 350°C is too high for this material. In order to prevent an increasing specimen temperature during the tests, it was decided to decrease the stress amplitude to 300 MPa. The highest test temperature was decreased to 250°C as agreed with Baker Hughes.

Further, mechanical properties of alloy P550 were also examined. Hardness measurements as well as tensile tests at room temperature (RT), 100°C and 350°C were done. The specimens for notched impact testing were removed perpendicular and parallel to the direction of deformation, leading to impact energies of 44J and > 210J, respectively. The results of the tensile tests are summarized in Table 3.

Table 3: Mechanical properties of P550.

	E, [GPa]	$R_{p0.2}$, [MPa]	R_m, [MPa]	A, [%]
RT	196	1135	1200	17,5
100°C	176	990	1011	18,1
350°C	162	744	839	20,2

Fig.9: Fractured specimen of alloy P550.
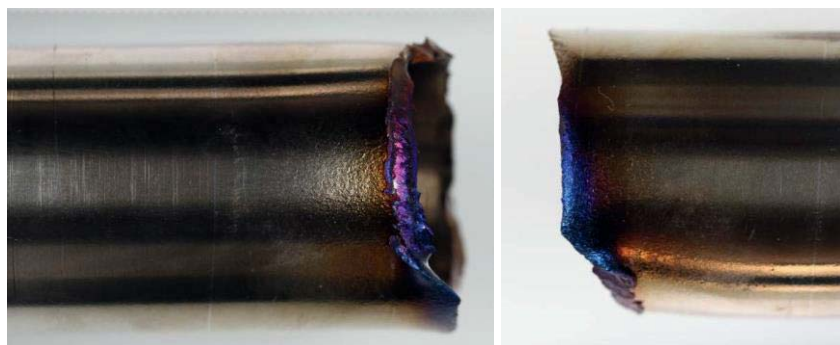
Fig.10: Characteristic colors of fractured specimen of alloy P550.

The behavior of P550 under multiaxial high temperature fatigue loading was also studied. In Table 4 the test conditions are summarized. Test nomenclature GEBO**X**ZDT(**T°C**)K refers to test number (**X**), normal stress (**Z**), torsion (**T**), temperature (**T°C**) and corrosion (**K**). Corrosion **K1** refers to tests with saline solution. Corrosion **K2** refers to tests with damp salt.

Table 4: Mechanical properties of alloy P550.

Test	Temperature, °C	σ_a, MPa	τ, MPa	f, Hz	Life cycles, N_f
GEBO1ZD350	350	600	/	3	$1.89*10^3$
GEBO2ZD250	250	600	/	3	$1.03*10^3$
GEBO3ZDRT	RT	600	/	3	$5.99*10^4$
GEBO4ZDRT	RT	600	/	0,3	$>6.00*10^3$
GEBO4ZD100	100	600	/	0,3	$3.96*10^3$
GEBO5ZD250	250	300	/	1	$1.28*10^5$
GEBO6ZD250	250	300	/	3	$1.58*10^5$
GEBO7ZD250	250	300	/	3	$1.60*10^6$
GEBO8ZDT250	250	327	150	3	$4.39*10^5$
GEBO9ZDT250	250	300	150	3	$>2.05*10^6$
GEBO10ZDT250	250	400	200	3	$7.73*10^4$
GEBO11ZDT250	250	350	175	3	$2.32*10^5$
GEBO12ZT250	250	400	200	3	$4.03*10^5$
GEBO13ZDT80	80	300	150	3	$>1.70*10^6$
GEBO14ZDT80K1	80	300	150	3	$>4.60*10^5$
GEBO18ZDT80K1	80	300	150	3	$1.10*10^6$
GEBO19ZDT80	80	300	150	3	$4.72*10^5$
GEBO20ZDT80	80	300	150	3	$6.26*10^5$
GEBO21ZDT250	250	300	150	3	$6.19*10^5$
GEBO22ZDT250	250	300	150	3	$1.50*10^6$
GEBO23ZDT80	80	300	150	3	$6.68*10^5$
GEBO24ZDT120K2	120	300	150	3	$3.63*10^5$
GEBO25ZDT120K2	120	300	150	3	$3.17*10^5$
GEBO26ZDT80K2	80	300	150	3	$1.36*10^5$

Increasing the test temperature from 80°C to 250°C at constant mechanical load has no significant effect on the cyclic life of alloy P550. While the average cyclic life of the alloy at 80°C is $N_f \approx$ $9.0*10^5$ (see Table 4, specimen 13, 19, 20, 23), it is about $1.4*10^6$ (specimen 9, 21, 22) at 250°C. But, an increasing mechanical load at constant temperature of 250°C decreases the cyclic life around 80% to about $2.37*10^5$ cycles (see Table 4, specimen 10, 11, 12).

The influence of corrosion on cyclic life of alloy P550 was studied at 80°C and 120°C. Using a saline solution at 80°C has no significant effect on the cycles to failure (see Table 4, specimen 14, 18). In contrast to the saline solution, the damp salt reduced the cyclic life dramatically. This can be seen in Table 4 inspecting the results for specimens 24, 25 and 26. Pitting corrosion and salt accumulation were frequently detected on the inside surface of the specimens. The specimen GEBO25ZDT120K was tested at 120°C with damp salt and is presented in this report as an example. The inside surface with crack and damaged oxide film can be seen In Fig. 11.
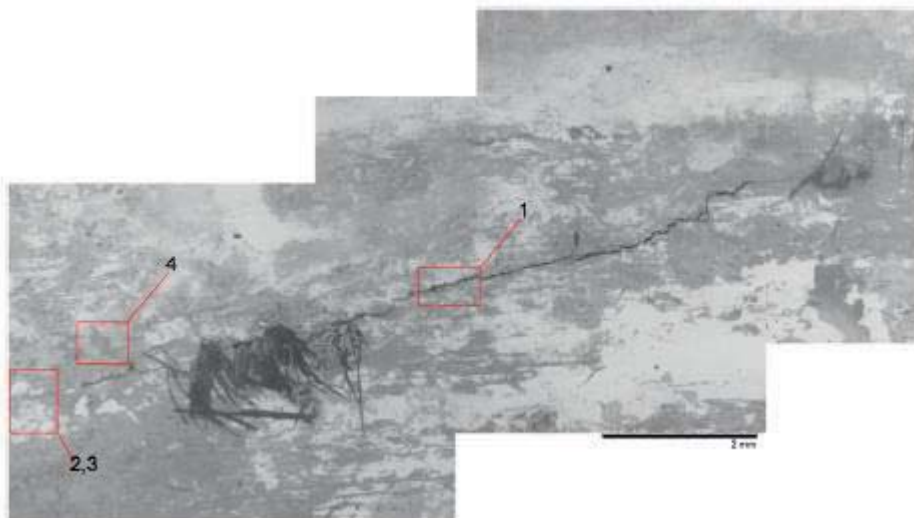
a)
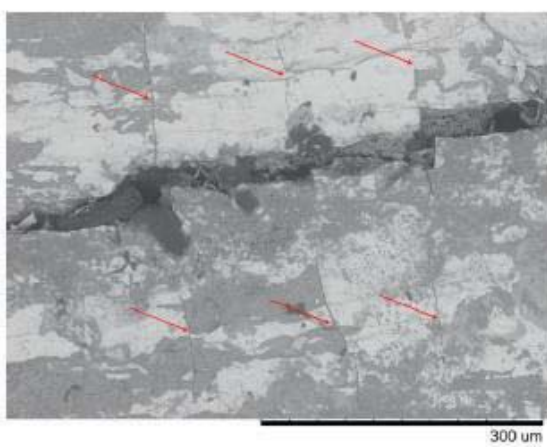
b) Position 1   c) Position 4

d) Position 2   e) Position 3
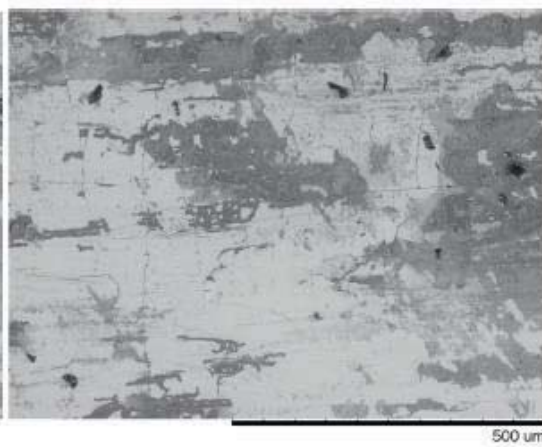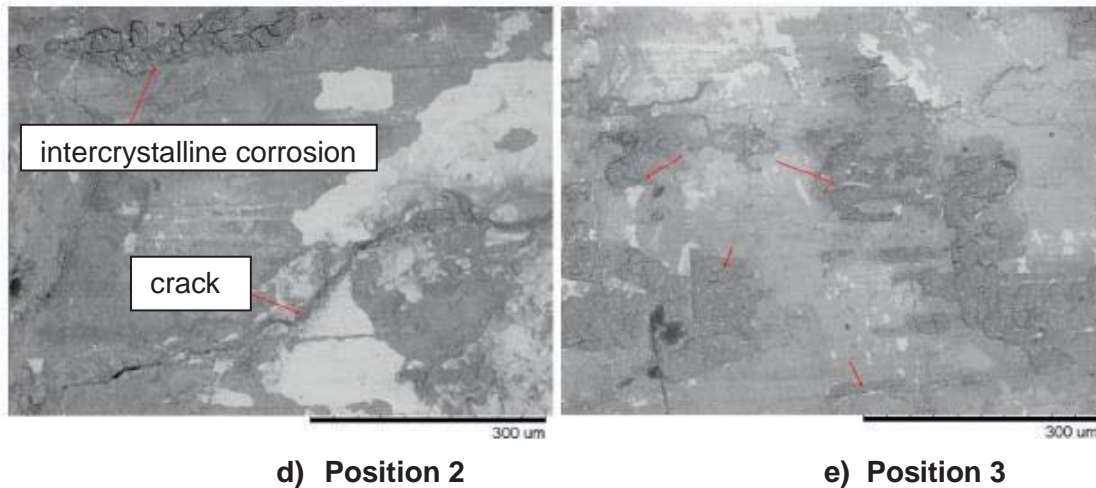
Fig. 11.: GEBO25ZDT120K2; a) macro crack; b) and c) the surface near the macro crack; d) and e) intercrystalline corrosion.

The surface of alloy P550 after tests with corrosion media shows also intercrystalline corrosion (Fig. 11d). The increasing of temperature and Cl^- concentration increases the corrosion effect.

The next step of investigations was a study of the mechanical behavior of alloy 718 under multi-axial high temperature fatigue loading. In order to get better comparable results two specimens (718_3 and 718_4) were tested at 120°C under multiaxial fatigue load without corrosion environment. Table 5 summarizes the details of this study. As in alloy P550, using the saline solution at a temperature of 80°C has no significant effect on the cyclic life of alloy 718. In contrast to the saline solution, applying damp salt decreases the cyclic life of this nickel based superalloy dramatically. Specimens 718_1, 718_2, 718_5 and 718_6 were tested with damp salt at different temperatures.

Table 5: Mechanical properties of alloy 718.

Test	Temperature, °C	σ_a, MPa	τ, MPa	f, Hz	Life cycles, N_f
GEBO718_1ZDT120K2	120	300	150	3	$2.81*10^5$
GEBO718_2ZDT120K2	120	300	150	3	$1.89*10^5$
GEBO718_3ZDT120	120	300	150	3	$1.68*10^6$
GEBO718_4ZDT120	120	300	150	3	$1.16*10^6$
GEBO718_5ZDT80K2	80	300	150	3	$3.31*10^5$
GEBO718_6ZDT80K2	80	300	150	3	$5.19*10^5$
GEBO718_7ZDT80K1	80	300	150	3	$1.18*10^6$

As example, the macro crack on specimen GEBO718_4ZDT120 can be seen in Fig. 12. This specimen was tested at 120°C without corrosion medium. The macro crack can be seen in Fig. 12a also after white – red investigation. In addition, micro cracks, slip lines und broken carbide precipitates can be identified.
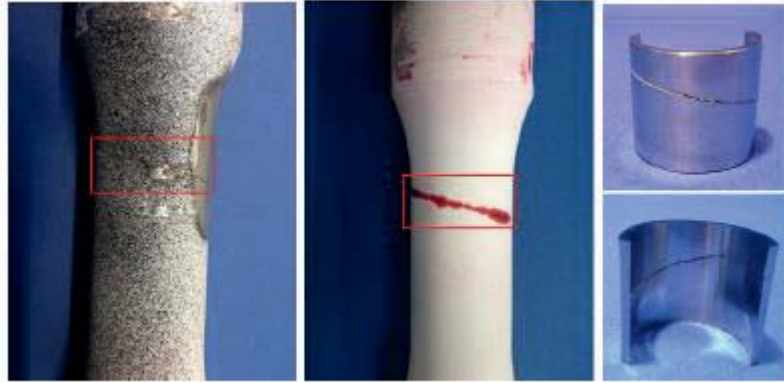
a)
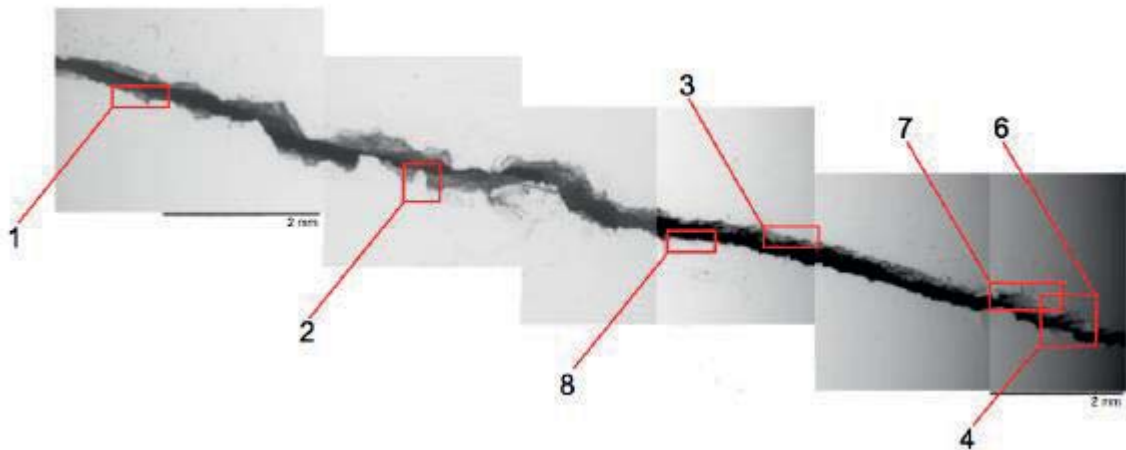
b)

c) Position 1

d) Position 2

e) Position 3
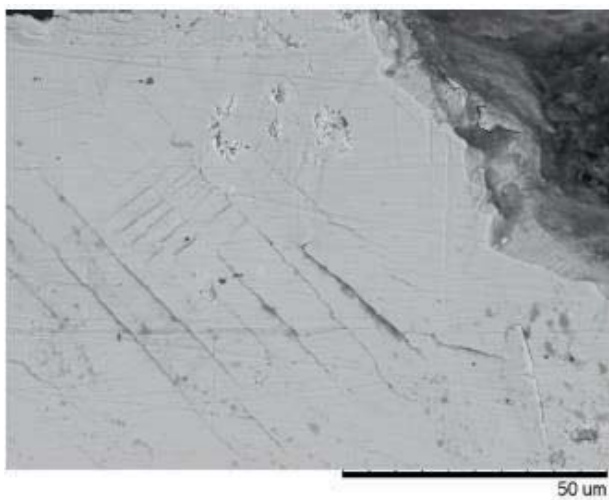
f) Position 4
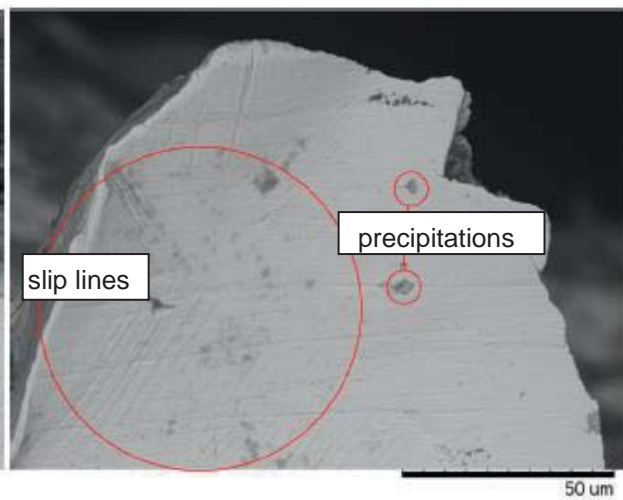
g) Position 5

h) Position 6
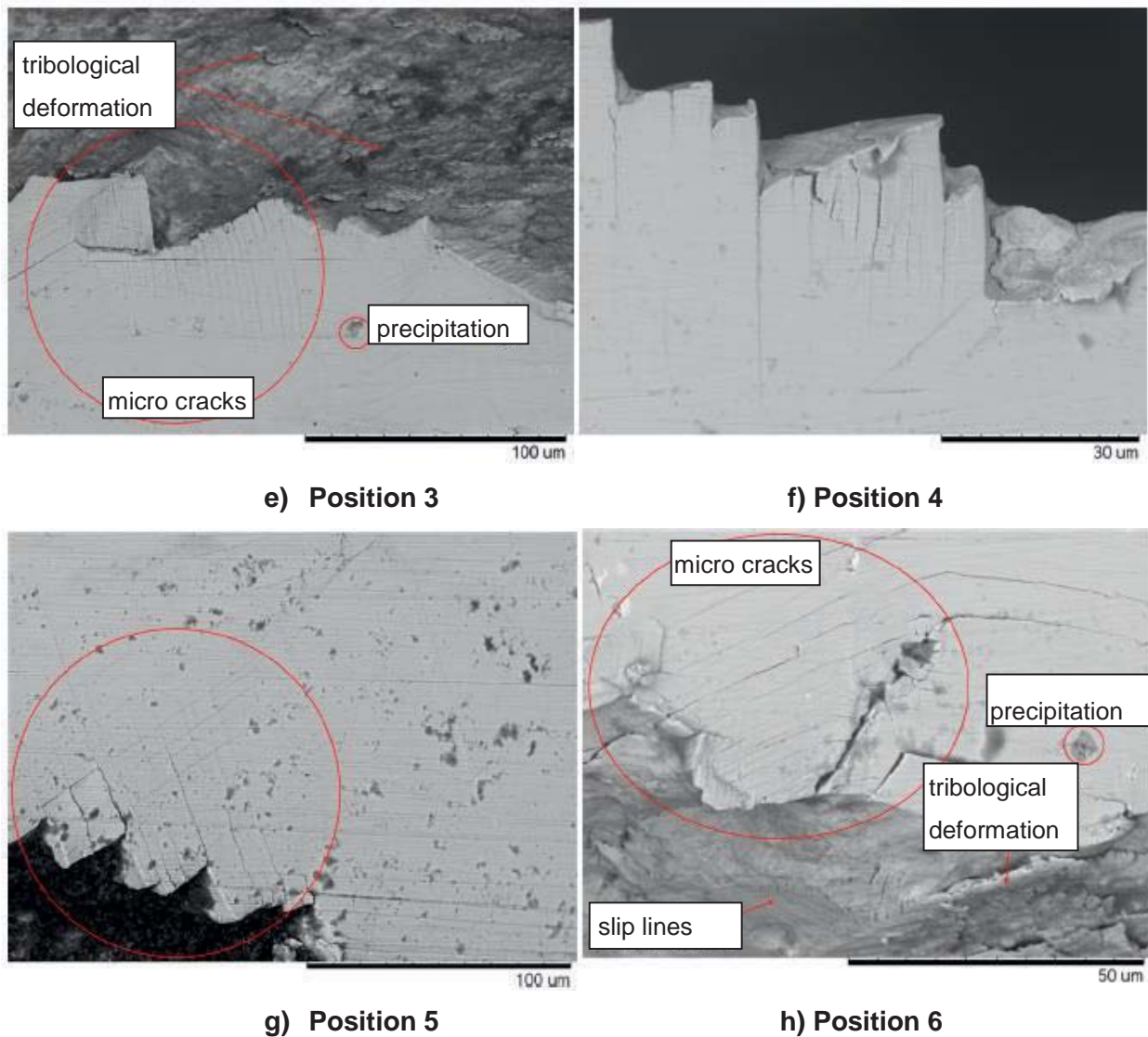
Fig. 12.: GEBO718_4ZDT120; a) and b) macro crack; c) and d) micro cracks and slip lines; e), d), g) and h) micro cracks, precipitations and tribological deformation.

The increasing of Cl$^-$ concentration and/or temperature decreases the cyclic life of alloy 718 strongly. The pitting corrosion areas extend and can be frequently detected on the specimen surface. As example, the specimen GEBO718_5ZDT80K is presented in Fig. 13.

a)

b)

c) Position 2 and 4

d) Position 3

e) Position 5
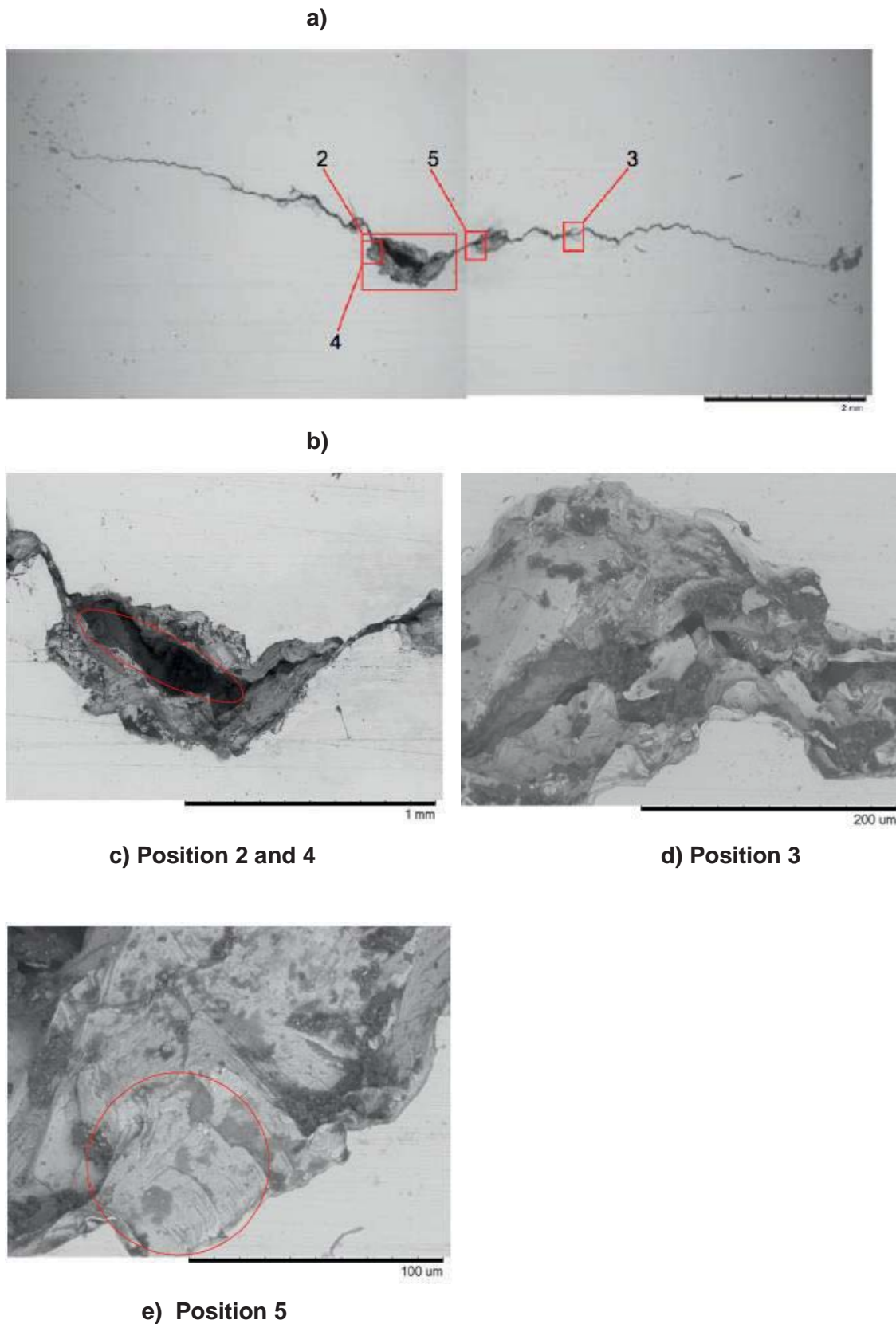
Fig. 13.: GEBO718_5ZDT120; a) and b) macro crack; c) and d) pitting corrosion; e) striations.

The multiaxial stress condition test environment was developed during this project which allows investigating the influence of temperature, pressure, tension, torsion and corrosion on the cyclic life of high performance materials. The corrosion influence and fatigue loading could be studied under high temperature between 80°C and 120°C.

This knowledge can be applied in the context of geothermal subsurface constructions, specifically for materials used in casing-structure, whose proposed life cycle may exceed 50 years.

W3: Materials and surfaces for application under extreme conditions

Sven Hartwig, Claus-Peter Klages*

Institut für Oberflächentechnik, Technische Universität Braunschweig,

Bienroder Weg 54E, D38108, Germany, *e-mail: claus-peter.klages@ist.fraunhofer.de

One of the main aims of the gebo network is the development of new drilling concepts and the optimization of the drilling process for geothermal energy generation. In the material orientated part of gebo the work was focused on the challenge of increasing demands of abrasion and corrosion with increasing drilling depth. The project W3 investigated electrochemically deposited nanocomposite layers consisting of a nickel matrix and embedded multi-walled carbon nanotubes (MWCNT) with regard to their possible use as wear and corrosion protection layers for applications in drilling technologies. The possibility of strengthening the abrasion resistance of electrochemically deposited protection layers by nanotechnology was investigated. The layers developed in this project were in the first instance prototypically aimed at an application in hydraulic drilling motors and would thus potentially contribute to the optimization of the drilling process due to a higher reliability of the system.

1 Introduction to the scope of the project

Electrodeposited nickel is commonly used as a decorative or corrosion protection layer for a variety of applications [1]. Nickel protection layers have unique properties like high hardness and high corrosion resistance. Tribological characteristics of nickel layers can be improved by codeposition with other metals such as tungsten or cobalt (NiW, NiCo). Furthermore, the metal layer performance can be improved by the incorporation of dispersed particles, especially nanoparticles, to build a composite layer. Recently the application of carbon nanotubes (CNT) as dispersoids in polymer, ceramic or metal-matrix composites has been reported, in which the extraordinary structural and mechanical properties of CNTs are utilized [2]. One of the most challenging tasks to accomplish electrodeposition of Ni-MWCNT composite layers is the creation and stabilization of MWCNT dispersions in the plating electrolyte. Stabilizing a nanotube dispersion in the presence of high salt concentrations and during electroplating turned out to be the first and most important barrier to be overcome in the project. The evaluation of a suitable dispersion technique is described in chapter 4.20.2. Furthermore, the influence of the dispersion technique on the deposits and the dispersion quality in the plating process is investigated. An

unexpected discovery of a self-ordering phenomenon of nanopores in a nickel deposit is describes in the chapter 4.20.3. The chapter 4.20.4 covers the plating process itself. The process parameters were tested concerning the characteristics of the resulting layers. The layer morphologies, inner structure and CNT distribution through the deposit were characterized.

The third part of this report (4.20.5) addresses the characterization of the Ni-MWCNT layers with regard to wear and corrosion resistance properties. The wear resistance of the layers was tested by Taber™ and Calo™ tests. The corrosion characteristics of the deposits were tested electrochemically by current density/potential measurements. The scope of this report is limited to a presentation of basic results achieved in W3.

2 MWCNT dispersions in nickel electrolytes

The generation of CNT dispersions in liquids is normally achieved by sonication or application of strong shearing forces. The hydrophobic character of CNTs, their special shape and high specific surface normally lead to rapid back-formation of agglomerates. Therefore a suitable stabilization of the dispersions is generally required, either using electrostatically or sterically working additives, or by utilization of properly chemically modified CNTs. Another challenge for the dispersion quality is the high ionic strength of the plating electrolyte and the plating process itself, due to the frequently observed phenomenon of electrocoagulation.

Before the MWCNTs were dispersed they had to be pretreated by milling and filtering. The first step of creating the dispersion of MWCNTs on a laboratory scale was then done by a high-energetic ultrasonic field generated by a sonotrode with a tip diameter of 3 mm, operating at 400 W and 24 kHz. This high-energetic ultrasound field is needed to break up the agglomeration between singular tubes. The amount of MWCNTs which can be dispersed in a solution is limited by the viscosity increase with the concentration of dispersed MWCNT, making the circulation and further sonication of the liquid impossible beyond a certain point. The MWCNT amount which was used in experiments described below ranged between 0.01 and 10 g/l. The required duration of ultrasound treatment depends on the sonicated volume and is about one minute per 3 ml.

A way to stabilize dispersions is by modifying the MWCNTs surface chemically or by plasma like as described in the literature [3]. These methods proved to be reliable for a stable high-concentration dispersion of MWCNT in pure water. Addition of salts, however, generally led to a collapse of these dispersions, which raised the need to apply surfactants to stabilize MWCNT dispersions in nickel electrolytes instead of chemical modifying the surface. Various cationic, anionic and zwitterionic tensides, and polyelectrolytes were tested. It was found that only a few additives among those investigated could guarantee a

long-term stability of the dispersions in nickel electrolytes, such as sodium dodecyl sulfate (SDS), dodecyltrimethylammonium bromide (DTAB) and polydiallyldimethylammonium chloride (PDADMAC). These surfactants were also tested in combination with different nickel plating baths: Watts nickel, Wesley nickel, nickel sulfamate and alkaline nickel baths. The stability of the MWCNT dispersions of all possible combinations was tested visually by microscopy of thin dispersion films and by dynamic light scattering measurements (DLS). The only dispersion breakdown was seen after 20 h with SDS in an alkaline nickel bath whereas all other dispersions were stable for longer than 10 weeks. In the plating process, however, these dispersions behaved differently: The maximum lifetime of a dispersion was achieved with PDADMAC in a Watts nickel bath for 30 min. The decreased stability can in principle be caused by temperature changes while plating, local pH changes, and by the phenomenon of electrocoagulation. Using these dispersions it was possible to deposit thin, relatively rough Ni-MWCNT dispersion layers with thicknesses up to 6 μm.

To achieve higher dispersions stability in the plating process in order to deposit thicker layers and to run a plating bath more effectively, new dispersants had to be investigated. The best solution to this challenge was the use of a new water soluble, partially charged polymer which additionally stabilizes the dispersions sterically. This polymer was synthesized by radical copolymerization of (meth)acrylic acid, styrene, and a polyethylene glycol (PEG) prepolymer, using azobisisobutyronitrile as an initiator. Acrylic or methacrylic acid was used to create polar/charged groups in the polymer backbone. Styrene was used as part of the backbone and as an aromatic and hydrophobic group to interact with MWCNT and attach the polymer backbone to the nanotube surface.
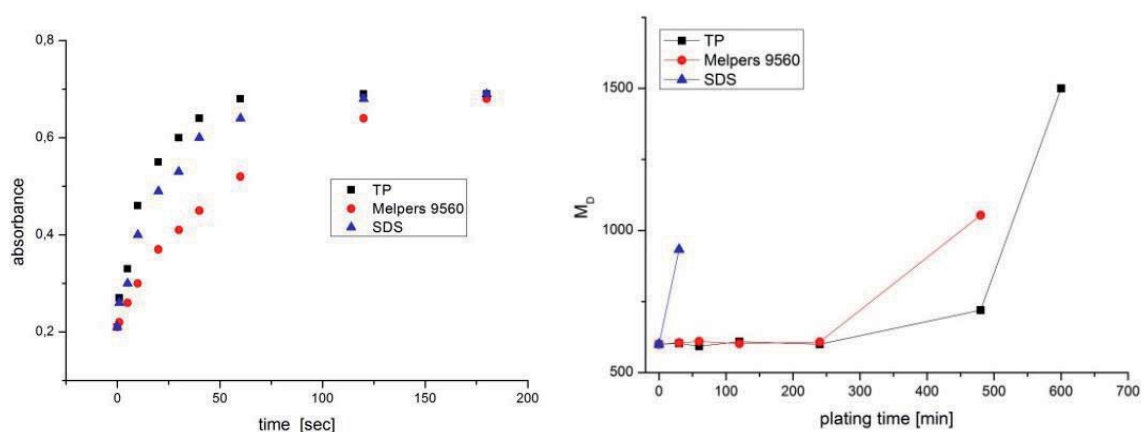
Figure 4.20.2.1: Absorbance measurements at 350 nm of centrifuged 10 ml samples of MWCNT in nickelsulfamate electrolyte 200 g/l (left); dynamic light scattering measurements of the average diameter, sample taken from 1 l nickel sulfamate plating bath at 4 A/dm^2 for 40 cm^2 substrate area, direct current (right)

The PEG prepolymer was PEG methyl ether acrylate (PEGma) or PEG methyl ether methacrylate (PEGmma) which acts as sterically hindering side chains. Tests showed that a mixture of acrylic acid, styrene, and PEGma 1000 g/mol with a molar ratio 1 : 7 : 3 creates the terpolymer (TP) with the highest potential to disperse MWCNT stably in acidic nickel electrolytes. Figure 4.20.2.1 shows the results of UV absorbance and dynamic light scattering measurements to compare the ability of dispersing MWCNT in nickel sulfamate electrolytes. The synthesized TP is compared with SDS and with Melpers 9560, a commercial surfactant (BASF) and structurally related with the TP. The absorbance measurement shows that the TP can stabilize MWCNT dispersions faster than Melpers 9560 and the test under application stress shows a very long and constant dispersion quality. SDS stabilized dispersions agglomerated after 30 min of plating in the test. The stabilization of carbon nanoparticle dispersions by surfactants which combine sterically demanding and electrically charged functional groups like the synthesized TP were protected by filing a patent application (application number US20120446218).

In summary the dispersion quality and stability plays the main role for an effective plating of Ni-MWCNT layers. The developed amphiphilic terpolymer ensures high stability of the MWCNT dispersion in acidic nickel electrolytes even under demanding plating conditions. In addition a commercial surfactant was found which has the ability to stabilize MWCNT dispersions for plating and thereby simplifying an upscaling of the plating dimensions.

3 Ordered nanoporous nickel layers

A new self-organization phenomenon was observed during pulse current electrodeposition of nickel layers without MWCNT in order to investigate the effect of the new developed surfactants to the deposition process. The formation of hexagonal arrays of 1D nanopores during nickel growth from electrolytes containing Melpers 9560 was discovered.
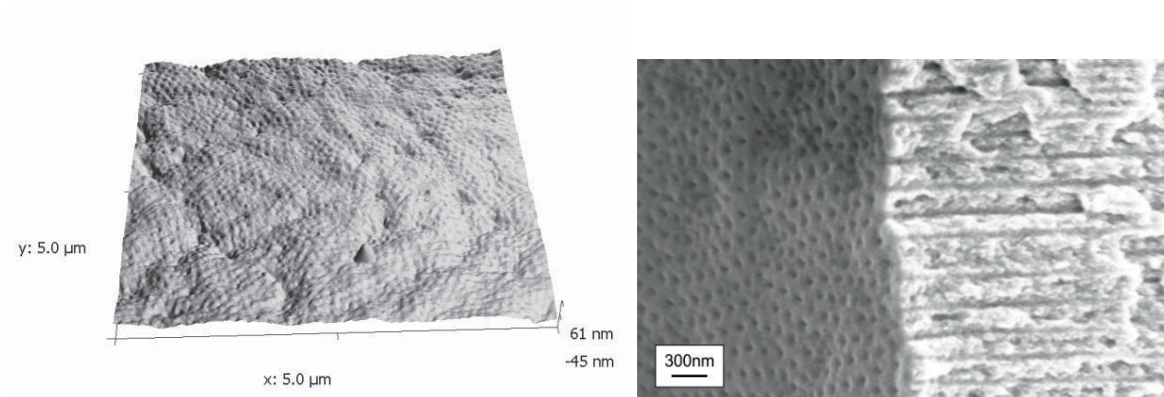
Figure 3.1: Atomic force microscopy 3D image of 5 x 5 μm ^{2} of the nickel NPA surface (left); SEM image of nickel NPA cross section (right)

Scanning electron microscopy (SEM) analysis of cross sections (Figure 3.1 right) revealed that the pores are channels of ca. 40 nm diameter extending virtually through the whole layer, parallel to the growth direction. The hexagonal order extends in domains of about 1 µm size. The maximal deposited nickel nanopore array area (NPA) was 10 cm^2. To trigger the self-organization phenomenon only a narrow process parameter window can be applied. The electrodeposition was done at room temperature from a nickel electrolyte containing 100 g/l nickel sulfamate hexahydrate, 7 g/l nickel chloride hexahydrate, 12 g/l boric acid and 500 mg/l Melpers 9560. In addition the pulse plating parameters are important, minor changes lead to a loss of the hexagonal ordered nanopore structure.
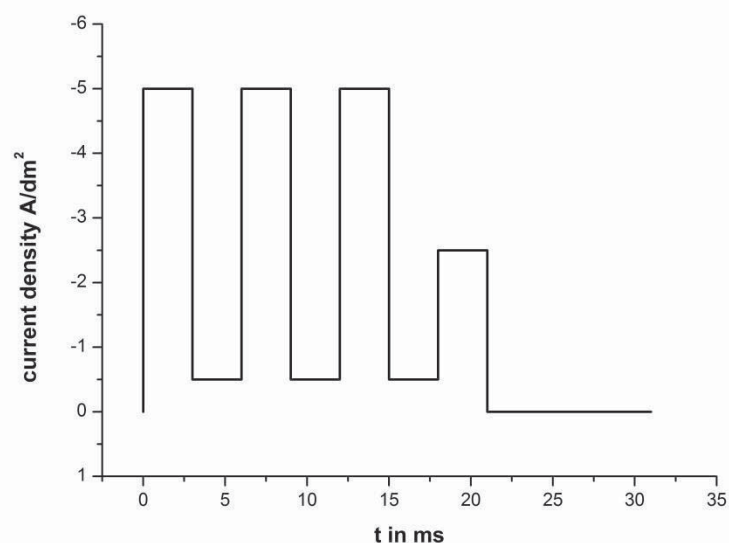
Figure 3.2:   Diagram of the repeat unit of the pulse current pattern for the generation of nickel NPAs

The current pattern in Figure 3.2 is a 21 ms comb pulse with a current density drop to nearly zero and a pulse pause of 10 ms. Besides the pulse plating parameters the surfactant Melpers 9560 is essential. Melpers 9560 is an amphiphilic polymer and may thereby stabilize nanobubbles in the plating process due to its hydrophobic styrene groups. The mechanism responsible for the self-organization can hypothetically be attributed to an array of hydrogen nanobubbles acting as templates. Together with Baker Hughes, Inc., a patent application was filed for this discovery (publication number US 2013/0029170 A1) The invention is expected to have a huge application potential in separation, battery and sensor technology, but the investigation and development of nanoporous layers was beyond the scope of the present project.

4 Ni-MWCNT composite layer deposition

The focus of interest lies on nickel as a matrix metal for composite layers. Nickel is distinguished for its corrosion resistance and it is known to form composite layers with nanoparticles [4]. MWCNTs are a material with impressive physical properties, such as high tensile strength and E modulus, and are therefore predestinated to be used for composite materials. Two types of MWCNTs were obtained from Bayer MaterialScience / Germany (B) and Nanocyl S.A. / Belgium (N). They differed in length (B: 1-10 µm, N: 1.5 µm), diameter (B: 13-16 nm, N: 9.5 nm) and form of delivery (B: granulate, N: powder). In order to deposit Ni-MWCNT layers electrochemically MWCNTs must be dispersed stably in a nickel electrolyte plating solution. For cost reduction regarding an application of Ni-MWCNT in industrial scale the commercial dispersant Melpers 9560 was used to stabilize MWCNT dispersions in the following plating experiments. Electroplating of nickel was done in two ways, namely the standard DC plating and pulse plating. DC plating gives only the possibility of setting the current density as most important parameter. Organic additives are then frequently used to control the coating properties auch as hardness, crystallite size, and leveling. In first experiments Ni-MWCNT was electrodeposited with direct current densities between 1 and 40 A/dm^2 and with or without brightening additives. Because of the conductivity of a part of the MWCNTs and their filament-like shape direct current plating leads to very rough layers owing to the growth of spherical grains. Figure 4.1 shows an SEM image of such layers. The primarily incorporated MWCNTs protruding from the surface can provide new starting points for nickel deposition. These growing grains develop into spherically shaped deposits, which then can incorporate MWCNTs in a repeating cycle. This growth mechanism is much faster than the layer growth itself, hence no dense and abrasion resistant layer can be deposited in this way.
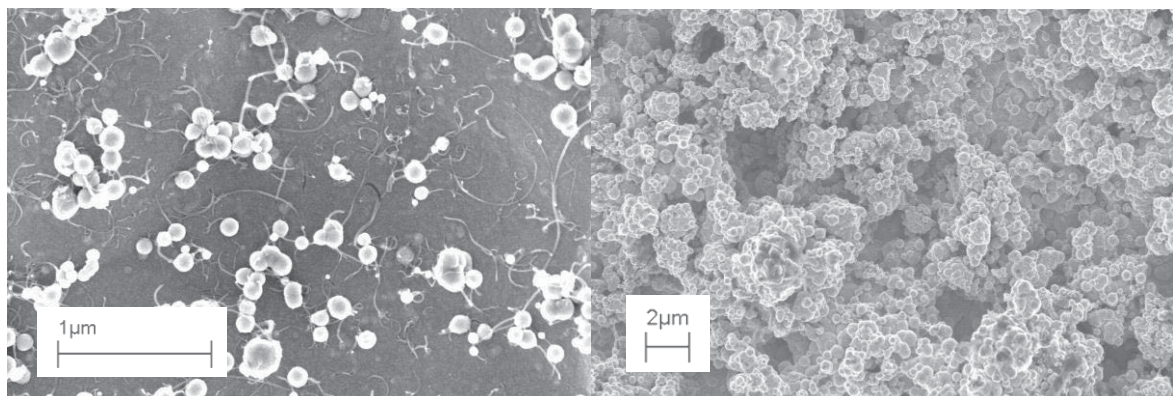
Figure 4.1: SEM images of the spherical Ni-MWCNT layer growth by DC plating; initital spheres on incorporated MWNCT (left), rough surface of a Ni-MWCNT surface plated with 4 A/dm^2 DC and 0,1 g/l MWCNT in the electrolyte (right)

Experiments with brightening and leveling additives did not lead to an improvement of the surface morphology and a densification of the coatings. Therefore, to prevent the spherical growth and promote the layer growth pulse reverse plating was applied. Pulse plating enables control of the nickel layer growth properties without organic additives. By using reverse, anodic pulses growing spheres can be dissolved again. Other advantages of pulse plating are that pulse pattern can be adjusted to get a higher integration of MWCNTs and a higher overvoltage can be applied, compared to DC plating, enabling the deposition of nickel alloys such as NiW with higher tungsten contents. Pulse plating uses pulse pauses and pulse durations in the range of milliseconds. Two pulse designs developed in the project are shown in Figure 4.2.
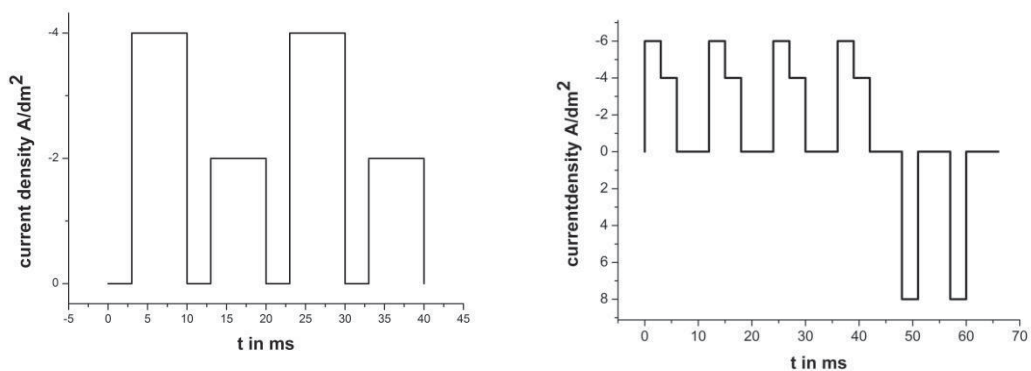
Figure 4.20.4.2: Pulse design without reverse pulses and with low current density for a very fine crystallite growth and growth of few spherical deposits (left); pulse design with high current density reverse pulses and without spherical growth (right)

The left diagram shows a pulse design used for semi-bright and hard nickel-MWCNT dispersion layers without reverse pulses. The pulse pattern is described by alternating 4 and 2 A/dm^2 deposition pulses of 7 ms duration with a 3 ms pulse pause. The pulse pause is needed to restore the nickel ion concentration close to the surface by diffusion in order to enhance the layer growth in comparison to the growth of spherical deposits. Reverse plating pulses can be applied to minimize the spherical growth even more. Figure 4.2 (right) shows the optimized pulse pattern used to completely avoid spherical particle growth. The optimization was done for pulse pattern, pulse current density, pulse and pulse pause duration and the number of cathodic and anodic pulses, led by an analysis of SEM images of the correspondingly deposited Ni-MWCNT layers. The resulting pulse plating pattern consists of four deposition pulses of 6 ms duration (3 ms at 6 A/dm^2 and 3 ms at 4 A/dm^2) with 6 ms pulse pause, and two anodic pulses of 3 ms duration with 6 ms pause. Another effect of the reverse pulses are less incorporated MWCNT in the layers since the anodic dissolution can remove slightly attached MWCNTs. The SEM images of the Ni-MWCNT layers corresponding to the diagrams in Figure 4.2 are

shown in Figure 4.3. The left SEM image shows a surface with high content of incorporated MWCNTs and - compared to SEM image 4.1 (right) - only relatively few spheres. The right SEM image shows no spheres on the surface but a smooth surface with fine grains and incorporated MWCNTs. Experiments run with the described pulse plating parameters were also used to characterize wear and corrosion properties of the Ni-MWCNT layers.
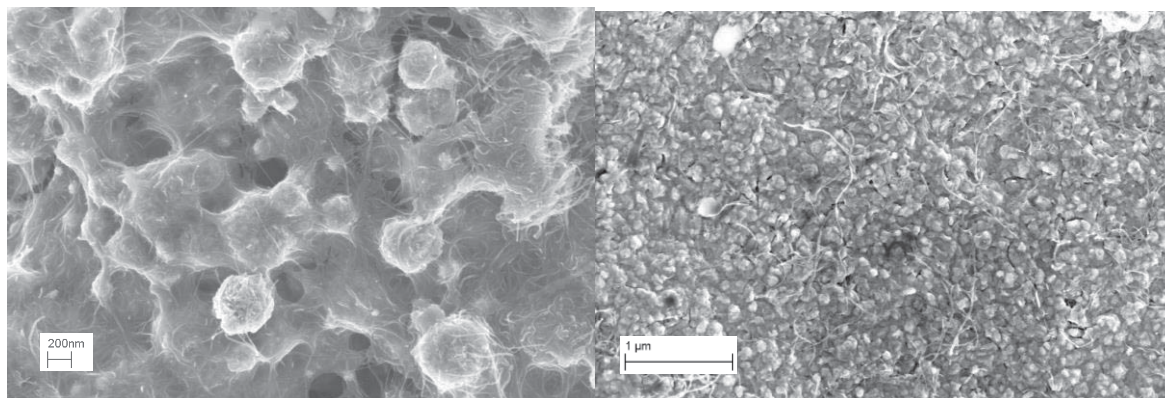
Figure 4.3: SEM image of layers plated with a pulse pattern with low current density for a very fine crystallite growth and a high integration of MWCNTs (left), Pulse pattern with high current density reverse pulses and a low integration of MWCNTs (right)

5 Ni-MWCNT composite layer characterization

The amount of MWCNTs in the nickel layers was determined using two different methods, either (i) by gravimetric analysis after dissolving the metal in a suitable acid or (ii) by glow discharge optical emission spectroscopy (GDOES). Because the analyzed sample is continuously sputtered by a glow discharge, GDOES allows to measure the depth profile of elemental composition of a material. Results of the gravimetric analyses were correlated with the GDOES measurement results in order to check if the latter method, which is especially simple and fast, could be a way to measure CNT concentrations in metal-matrix composites routinely. A good agreement of the methods or at least a linear correlation is not self-evident because Ni-MWCNT layers are much more heterogeneous then multi-component samples which are normally measured by GDOES. Figure 5.1 shows the correlation between gravimetric and GDOES analyses. Although the GDOES results are generally significantly smaller - for potential reasons which cannot be discussed here, the correlation of the results is reasonable and could form the basis for calibrating GDOES measurements. In this way the MWCNT content in a layer and in addition the distribution through the layer can be determined very fast.
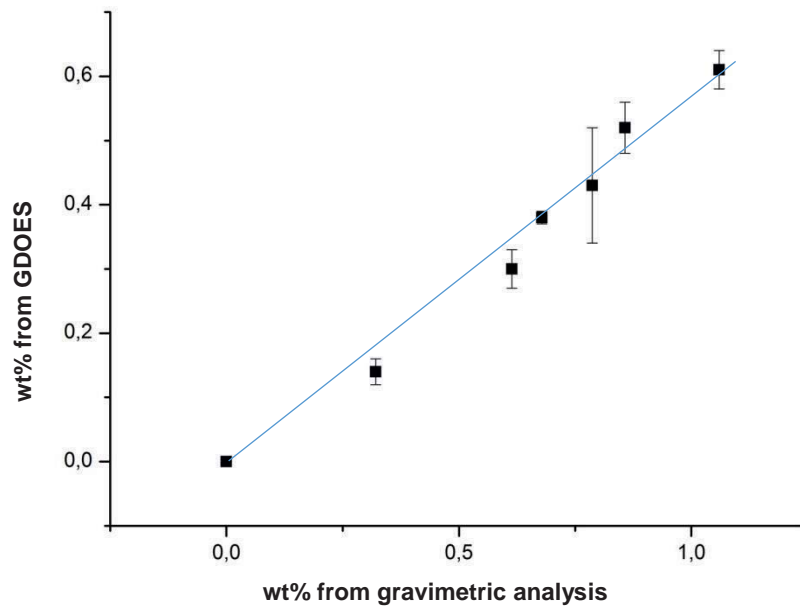
Figure 5.1: Correlation of gravimetric and GDOES analyses of the MWCNT content of different Ni-MWCNT layers

Based on the pulse pattern of Figure 4.2 (right) and GDOES measurements the influence of the MWCNT amount in the electrolyte dispersions and the amount of MWCNT incorporated in the nickel matrix was studied. The limiting factors of these experiments were the viscosity of the dispersions and the roughness of the deposited nickel layers.
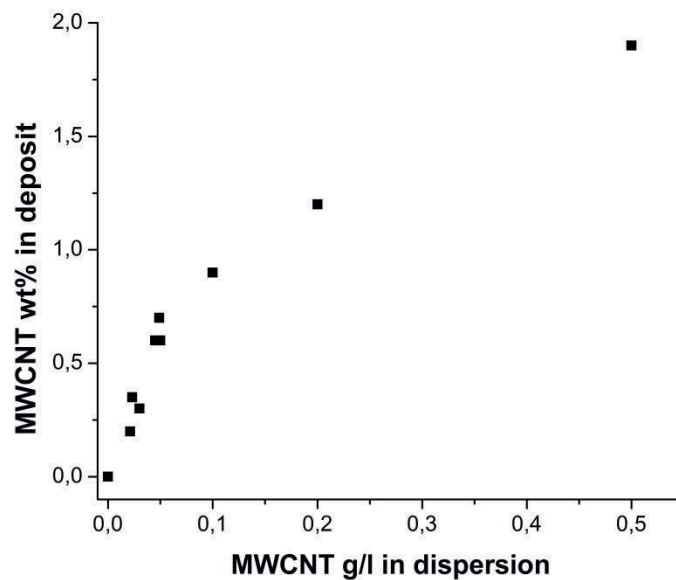
Figure 5.2: Results of GDOES measurements of Ni-MWCNT layers deposited from nickel electrolytes with different amounts of MWCNT in the dispersion

Rising contents of MWCNTs dispersed in solution resulted in increasing incorporation and a spherical layer growth occurred again with high amounts of MWCNTs despite the developed pulse reverse plating. Figure 5.2 shows the dependency of the amount in the MWCNT dispersions in the nickel electrolyte and in the deposit. At and above 0.8 g/l the deposited layers were too rough to be measured by GDOES without further preparation by grinding. Above 0.1 g/l in the dispersion the slope of the curve relating concentrations of MWCNT in the solid and in the electrolyte is significantly lowered.

In order to investigate the wear and corrosion resistance of Ni-MWCNT layers and to optimize the plating parameters towards best layer properties the deposits were characterized by Taber™ and Calo™ test and current density/potential corrosion measurements. Furthermore the plated Ni-MWCNT layers were characterized with respect to their hardness using a Fischerscope HM2000 tester. Figure 5.3 shows abrasive wear properties of Ni-MWCNT layers measured by Taber™ test in dependency of their amount of incorporated MWCNTs measured by GDOES. It can be seen that a minimum occurs at 0.3 wt% of MWCNT in the nickel layers.
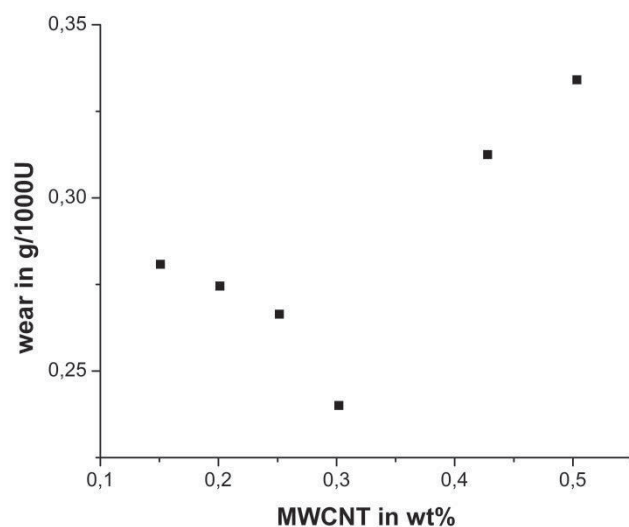
Figure 5.3: Results of Taber™ test wear measurements with an H10 wheel under 1 kg duty of Ni-MWCNT layers with different MWCNT content

As seen in earlier studies the roughness is increasing with a higher amount of MWCNTs in the deposits, because of the spherical growth mechanism. A possible reason for the increasing abrasive wear with increasing amount of MWCNTs are the spherically grown regions, which can break out of the nickel matrix as a whole. The best reproducible achieved results for wear resistance and hardness are shown in Table 5.1. The Calo™ test showed a minimum of wear resistance at a higher amount of incorporated MWCNTs compared to the Taber™ test. As the tested area in the Calo™ test were only

some 100 µm^2 small regions of spherical growth are not detected thereby the minimum is at higher MWCNT amounts.

Table 5.1: Material data from developed Ni-MWCNT layers

Layer	Hardness [HV]	Wear [m^{3}m^{-1}N^{-1}10^{-15}] Calo test™	Wear [g/1000rot.] Taber test (H10)
Ni (pulse plating)	400	20	0.4
NiW	600	15	-
Ni-MWCNT (0.5 wt% MWCNT)	600	9	0.35
Ni-MWCNT (0.3 wt% MWCNT)	900	13	0.22
NiW-MWCNT	800	6	0.18
Steel (bulk)	1000	30	-
Hard chromium	1200	10	-

The corrosion properties of the Ni-MWCNT layers were investigated electrochemically by current density/potential measurements. Figure 5.4 shows polarization curves of nickel deposited by pulse plating and Ni-MWCNT composite layers, respectively, from Table 5.1. The nickel reference was also deposited by pulse plating to achieve nano-crystalline nickel layers with a high corrosion resistance and to avoid wrong interpretation by process effects.
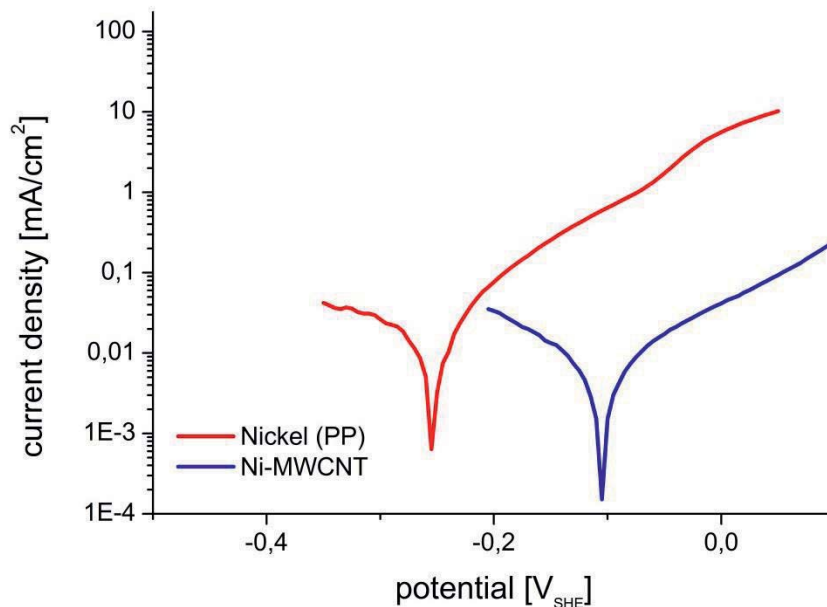
Figure 5.4: Polarization curves of different Ni-MWCNT systems

The corrosion potential of Ni-MWCNT layers, in comparison to pure nickel layers from pulse plating, is shifted positively to 0.1 V. Furthermore, the Tafel plot for the corrosion

603

current density leads to 0.03 mA/cm^2 for pure nickel and 0.01 mA/cm^2 for Ni-MWCNT which is in the same order and a little bit smaller. The corrosion resistance of Ni-MWCNT is not significantly different from the resistance of nanocrystalline nickel layers.

6 Upscaling of Ni-MWCNT composite layer deposition

Upscaling effects of the Ni-MWCNT layers electrodeposition were investigated by increasing the nickel electrolyte volume from 0.5 to 5 l at a constant cathode surface to electrolyte volume of 4 cm^2/l. It was found that the layer roughness increases and wear resistance decreases. SEM inspections of the layers showed no spherical growth but incorporated agglomerates. In addition light scattering measurements approved the poor quality of the MWCNT dispersion in the nickel electrolyte. The challenge was that the same ultrasonic energy per volume is needed to disperse the MWCNT uniformly in the electrolyte. To solve this problem in an industrial scale process sonication flow-through cell batteries would assure the ultrasonic energy per volume which is needed. In the experiment this problem was solved by stepwise sonication of 20 ml dispersion. Another precondition is that for a coating of a drilling motor rotor (5 m length) a pulse reverse power source of 13 kA pulse current power and a self-induction secure cabling is needed. This is not standard equipment in coating companies and is an investment of 160 k€.

7 Summary

In the gebo project W3 "Materials and surfaces for applications under extreme conditions" the electrodeposition of Ni-MWCNT composite layers was investigated. The development of such layer systems was focused on two topics, a long-time stable dispersion of MWCNTs in nickel electrolytes and the development of the plating process parameters. In the first part of the work a new surfactant for high quality and long-time stable dispersions was developed and a commercial product with nearly the same potential for MWCNT dispersions was found. In the second part the electrodeposition was changed from DC plating to pulse reverse plating and the coating morphology from rough deposits dominated by a spherical growth mechanism to hard and dense layers. A fast method to determine the amount of MWCNTs embedded in the nickel composite layers with high accuracy was developed by the combination of gravimetric and GDOES analysis. The characterization of the Ni-MWCNT wear and corrosion resistance of Ni-MWCNT layers showed that the wear resistance and hardness are improved, compared to nickel layers deposited by pulse plating, while the corrosion resistance was not changed significantly. The NiW-MWCNT layers showed a further increased wear resistance but lack in corrosion resistance. Studies for an up scaling of the plating process showed the importance of the dispersion quality for the electrodeposition of Ni-MWCNT

layers in large scale plating bathes. Sonication flow-through cell batteries would assure such a quality of the dispersions but have to be tested in larger scales than 5 l. In summary a layer system for application as protection layer on small drilling tools was optimized and may be applicable on large drilling tools for applications under extreme conditions.

8 Literature

[1] G. A. DiBari, Metal Finishing (**2002**) 34-49.

[2] S. R. Bakshi, D. Lahiri, A. Agarwal, International Materials Reviews 55 (**2010**) 41-64.

[3] S. Arai, M. Endo, N. Kaneko, Carbon 42 (**2004**) 641-644.

[4] B. Wielage, T. Lampke, M. Zacher, D. Dietrich, Key Eng. Mat. 384 (**2008**) 283-309.

606

Geothermal Energy and High Performance-Drilling
Collaborative Research Program

Research Report project W4:

Coatings with high electrical conductivity and abrasion resistance

Project leader: Prof. Dr.-Ing. habil. Dr.-Ing. E.h. Dr. h.c. Friedrich-Wilhelm Bach
Institut für Werkstoffkunde (Materials Science), Leibniz
Universität Hannover, Germany

Garbsen, November 25th, 2014

Prof. Dr.-Ing. H. J. Maier
Institutsdirektor

W4: Coatings with high electrical conductivity and abrasion resistance

Project Overview

Project No.	Title	Subject of research	Project leader, institution, location
W4	Coatings with high electrical conductivity and abrasion resistance	Mechanical Engineering, Material Science	Prof. Dr. Fr.-W. Bach, Institut für Werkstoff-kunde, LU Hannover

Participating Institutes and institutions of the universities and external institutions:

- Institut für Werkstoffkunde (Materials Science), Leibniz Universität Hannover, Germany

- Baker Hughes Contact: Dr. Bartscherer

List of participating scientists and engineers:

Name	Subject area	University or non-academic institution	Position is financed by gebo funds (indicated by X)
Prof. Dr.-Ing. habil. Dr.-Ing. E.h. Dr. h.c. Friedrich-Wilhelm Bach*	Mechanical Engineering	IW	
Prof. Dr.-Ing. Hans Jürgen Maier**	Mechanical Engineering	IW	
Dr.-Ing. habil. Kai Möhwald	Mechanical Engineering	IW	
Dr. rer. nat. Markus Neumann	Mechanical Engineering	IW	X (1th period)
Dr. rer. nat. Ulrich Holländer	Mechanical Engineering	IW	X (2th period)

* deceased in August 18th 1014
**director of the institute and successor of Prof. Bach

Research Program

Summary

The objective of the GEBO research project W4 was the development of new coating materials and appropriate coating processes applicable for the wear and corrosion protection of steel components in drilling engineering. The project W4 focused on two topics.

The first one was the development of coatings with a high electric conductivity and concomitant wear resistance, suitable for a certain application in the field of sensors techniques for the analysis of rock formation in the bore hole. Appropriate materials properties have been expected from particle enhanced copper based coating systems. Thus, different kind of coating tests (brazing, electroplating and thermal spraying) were performed and basic copper coating properties analysed, see intermediate report. The main finding was that an HVOF (high velocity oxygen fuel spraying) process could be successfully employed to apply hard metal enhanced copper coatings resulting in electric conductivities of the copper matrix of up to 30 MS/m. In the following parameter studies were performed in order

to find the optimum process parameters for the application of copper - tungsten carbide composite coatings with a hard metal fraction of 50 wt.%. In addition, the coating properties were improved by a heat treatment of the coated specimens, and coatings with good adhesive and cohesive bonding were obtained.

The hybrid process, i.e. thermal spraying and additional heat treatment, developed for the application of copper-hard metal composite coatings is suitable for all materials that can tolerate a thermal treatment at temperatures up to 1050 °C. A combination of the coat tempering process with an annealing process of appropriate substrate (precipitation hardening steels) is possible.

The research activities in the second half of the project period, were governed by the development of cost-efficient coating solutions, in order to substitute conventionally used expensive high-alloyed steel qualities by coated low cost steel in the future. Application examples in drilling engineering are high volume components like drill pipes and tubing or casing components.

For this purpose a powdery iron-based coating material from the system Fe-Cr-Al-B-Si was developed, which is suitable for thermal coating processes like thermal spraying or braze coating. In the specified alloy system the elements aluminium, boron and silicon where chosen in order to depress the melting point of the alloy and to get hard intermetallic precipitations, whereas the alloying element chromium mainly enhances the corrosion resistance of the material. By means of thermodynamic modelling of the alloy system and thermochemical investigations of the melting behaviour of selected alloy compositions an optimized system with the composition Fe-19Cr-7Al-7Si-2B (in wt.%) with a melting range of 1125-1180 °C was obtained.

Application tests of the developed coating material on steel components were performed using atmospheric plasma spraying (APS) and high velocity oxygen fuel spraying (HVOF) combined with vacuum furnace sintering processes, in order to minimize coating porosity, to improve the coating adhesion and to generate hard precipitations in the coating structure.

Coated specimens were characterized by metallographic investigations and scanning electron microscopy. These investigations confirmed that the chosen parameters for the heat treatment of the thermal sprayed coatings yield dense coatings with a good metallurgical bonding to the substrate. In addition, intermetallic precipitations - mainly iron and chromium aluminides and borides - were formed during heat treatment. This fact is mirrored by the measured hardness of the coatings. The space resolved Vickers hardness yield mean values of about 600HV0.3 of the coating itself and continuously decreasing values towards the unaffected steel substrate. The overall Rockwell hardness of the coating was about 57 HRC using optimized heating parameters.

Furthermore electrochemical corrosion tests based on current density-potential-measurements using aqueous chloride solutions were performed. The data, which were compared with measurements done with a commercial nickel based reference coating (Ni-19Cr-10Si), showed a similar corrosion behaviour like the nickel-based system.

In summary, the iron-based coating system developed seems to be a promising alternative to the commercially available nickel-based coating systems. The fact that the material costs of the iron alloy is only 1/3 of the nickel-based alloys makes this coating system particularly interesting for large-volume applications like drill pipes. The necessary heat treatment might be coupled with annealing processes for the pipe material itself, when appropriate pipe steel qualities are chosen. However, additional application-oriented investigations, which cover the specific requirements concerning wear and corrosion resistance under the actual service load of the component to be coated should be performed.

Relationship of the project to the overall research context and networking with other projects

An essential aspect of the collaborative project is to optimize both the drilling process as well as the subsequent transport of geothermal energy up through the earth's crust. In order to achieve these objectives, various drill-string and bore holes components, must be coated in a suitable manner and adapted to the respective requirements. Thus, specific coating systems had to be developed in project W4. A coating with high electric conductivity and good wear resistance had to be developed for the so-called Transient Transmitter, the tool that is employed to measure the rock formation's conductivity. In addition, an economical coating system for the protection of high-volume components is needed, in order to minimize the costs for exploration and use of geothermal energy sources. Networking within the project is derived from both the input, which is necessary for the project, (material data and damage mechanisms, assessment of the developed coating system's fatigue life, and the simulations of the surfaces behaviour) as well as its output (e. g coated materials and coating characterization).

Work packages executed relative to (original) plan and results achieved

Copper-based coating system

The objective was to develop a coating that exhibits the maximum possible value of electrical conductivity. Since copper, with $\sigma = 59.1$ MS/m, exhibits the second highest conductivity to silver ($\sigma = 61.35$ MS/m), it was employed as the base material for the coating to be developed. Eddy current measurements of the effective conductivity of the deposited copper coatings using different coating processes (see intermediate project report) had shown that thermally sprayed copper coating using HVOF still have an electric conductivity of about 30

MS/m, which seemed to be sufficient for the application envisaged. However, copper itself is extremely soft, and thus, has poor wear resistance. An enhancement of the wear resistance without a significant reduction of the electric conductivity can be achieved only by implementing hard particles (hard metals like tungsten carbide) in the copper coating or covering the coating with a wear resistant top coat (again tungsten carbide for example). Both solutions were tested using HVOF coating processes.

A composite coating with a uniform distribution of WC-particles was realised by spraying powder mixtures of Cu and WC/Co with maximum WC/Co contents of 50 wt. % (equal to 40 vol. %) using spraying parameters that allow for an simultaneous deposition of both components, see figure 1. The analysis of the coating structure confirmed the desired composition.

In figure 2, left picture, linear precipitations in the copper phases of the coating are observed, which are due to a partial oxidation of the copper particles during the spray process. This oxide phases vanished by a heat treatment of the coated specimen in a vacuum furnace at 1030 °C.

In order to realise a wear resistant top coating on copper coats, coating tests were performed using two powder feeders, one for the copper and one for the hard metal. The tests had shown that an adhesive deposition of WC/Co on pure copper was not possible, since the soft copper surface could not bind to the impacting WC/Co particles. This problem could be avoided by the application of a graded coating structure, starting with pure copper and then successively feeding more and more WC/Co to the spray gun such that pure hard metal was deposited only at the end of the process, see figure 3.

Conclusion and outlook

An application of hard metal enforced copper coatings is possible by means of high velocity oxygen fuel spraying. With respect to the electric conductivity of these coatings a thermal treatment of the coated components at temperatures of about 1030 °C in a vacuum ore protective gas furnace is recommended, since an elimination of oxidic precipitations in the copper matrix and an enhancement of the adhesive and cohesive bonding strengths take place then. For the use of these coatings substrate materials are required that tolerate such a heat treatment without loss of the desired mechanical properties. However, the heat treatment might be coupled with annealing processes for the substrate itself, when hardenable steel qualities are chosen.

Digital image analysis		
coating fraction	as sprayed	heat-treated
copper	balance	balance
WC/Co	37.1%	39.8%
pores	4.7%	5.1%
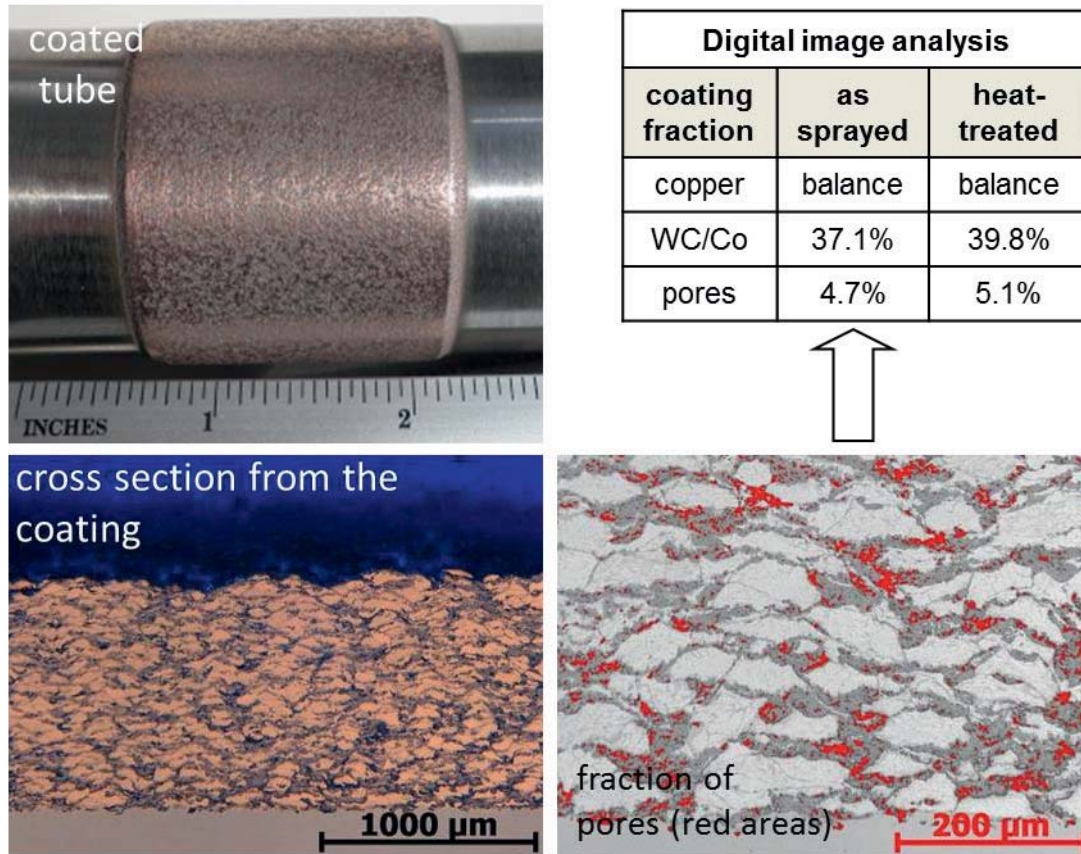
figure 1: thermally sprayed composite coating constituted of copper and hard metal (WC/Co)
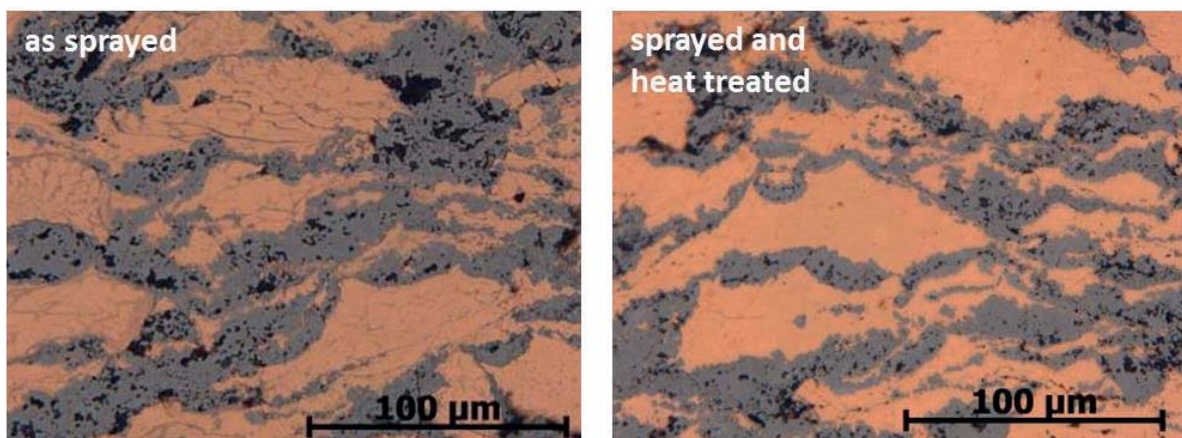
figure 2: coating microstructure before and after heat treatment at 1030°C
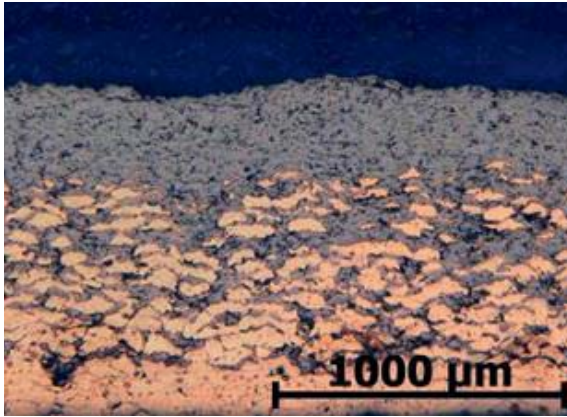
figure 3: composit coating with gradual transition between copper and hard metal

Iron-based coating system

The idea of using resistant coatings –also in drilling engineering- is not entirely new. For instance, so called self-fluxing alloys are already widely used. These alloys are applied by thermal spraying and then the coating is remelted by heating up the coated component up to the liquidus temperature of the coating material. The heat treatment generates a metallurgical bonding to the substrate and enhances the adhesion und cohesion of the coating.

Commercially available self-fluxing coating powders are always nickel or nickel-cobalt-based with additional elements like chromium, boron and silicon. From an economical view point this is a great disadvantage. Material costs of at least 200 € per coated square meter, resulting from the high nickel and cobalt prices, may be excepted for rather small coated high performance tool of a drill set. Thus, the coating of high-volume components, like pipes, tubes or casings, with nickel or cobalt-based, self-fluxing alloys cannot be realised economically.

Given this scenario, there is a great interest for cost-efficient alternatives, i.e. the development of iron-based coating alloys without any nickel or cobalt. A promising iron-based material was found based on the five-element system iron-chromium-aluminium silicon-boron, which could achieve the requirements for a self-fluxing alloy.

The selected alloy elements have different functions: Chromium and aluminium shall ensure a good corrosion resistance. In addition, aluminium as well as the additional elements boron and silicon lower the liquidus temperature of the alloy down to attractive values for a remelting process of the coating. With respect to the wear resistance, it is important to get hard precipitations in the alloy's microstructure. Boron, silicon and aluminium do react with iron and chromium and can form very hard intermetallic compounds.

The chosen iron-based system was analysed by means of thermodynamic modelling and thermochemical measurements using a variety of compositions.

The outcome of these investigations was an alloy composition with 19% chromium 7% aluminium 7% silicon, and 2% boron (in wt.-%). The melting range of this alloy is 1124 to 1180 degree Celsius, cf. table 1.

table 1: iron-based coating alloy

chemical composition in wt.%					melting range in °C
Fe	Cr	Al	Si	B	
balance	19	7	7	2	1124-1180

The thermal spraying processes APS and HVOF were employed in order to process the iron-based coating material developed. Coating tests were done on plane steel surfaces as well as on steel tubes. The substrate was in both cases an unalloyed steel, cf. figure 4.

In addition, coated specimens using a commercial Ni-based coating system, were manufactured. These specimens were used as reference system especially for the corrosion experiments. For this purpose, the ternary system Ni19Cr11Si was chosen. The melting range of this system (1080-1135 °C) is close to the iron-based system. This reference alloy has a good corrosion resistance in different corrosive media, and thus, is a good bench mark for the evaluation of the corrosion behavior of the test system.
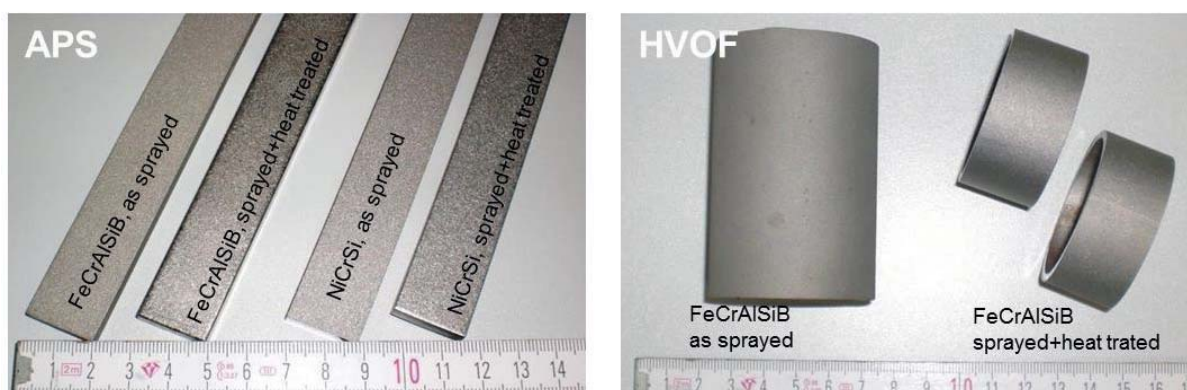
figure 3: coated steel specimen (unalloyed steel)

table 2: parameters of heat treatment

no.	coating	T-t-regime
WB 1	Fe-based	1150 °C/5min
WB 2	Ni-based	1105 °C/5min
WB 3	Fe-based	1170 °C/2min +1130 °C/30min
WB 4	Ni-based	1120 °C/2min +1090 °C/30min

The coated specimen were heated using two different parameter sets for each coating system as summarized in table 2. According to the chosen parameters, the maximum temperatures were set within the particular melting ranges of the alloys in all cases, and basically a higher temperature with a shorter treatment time and vice versa were chosen.

In figure 5, scanning electron microscope images of the coatings in cross section are shown. The pictures on the left side illustrate the coating structure of the sprayed coating before the heat treatment. In the condition "as-sprayed" the substrate and the coating differ clearly in their appearances, and a sharp interface between the materials is visible. In the coating, single spray particles can be identified, which are deformed to stacked pan cakes. The surface of the coating is rather rough.

After the heat treatment the structure of the coating is entirely different, cf. right pictures in figure 5. The coating now features a very smooth surface. The borders between the particles have vanished and the coating appears like uniform solid. At the same time, the sharp interface between the coating and substrate has disappeared too. In fact, a continuous transition with a distinctive diffusion zone in the parent material has been formed during the heat treatment.
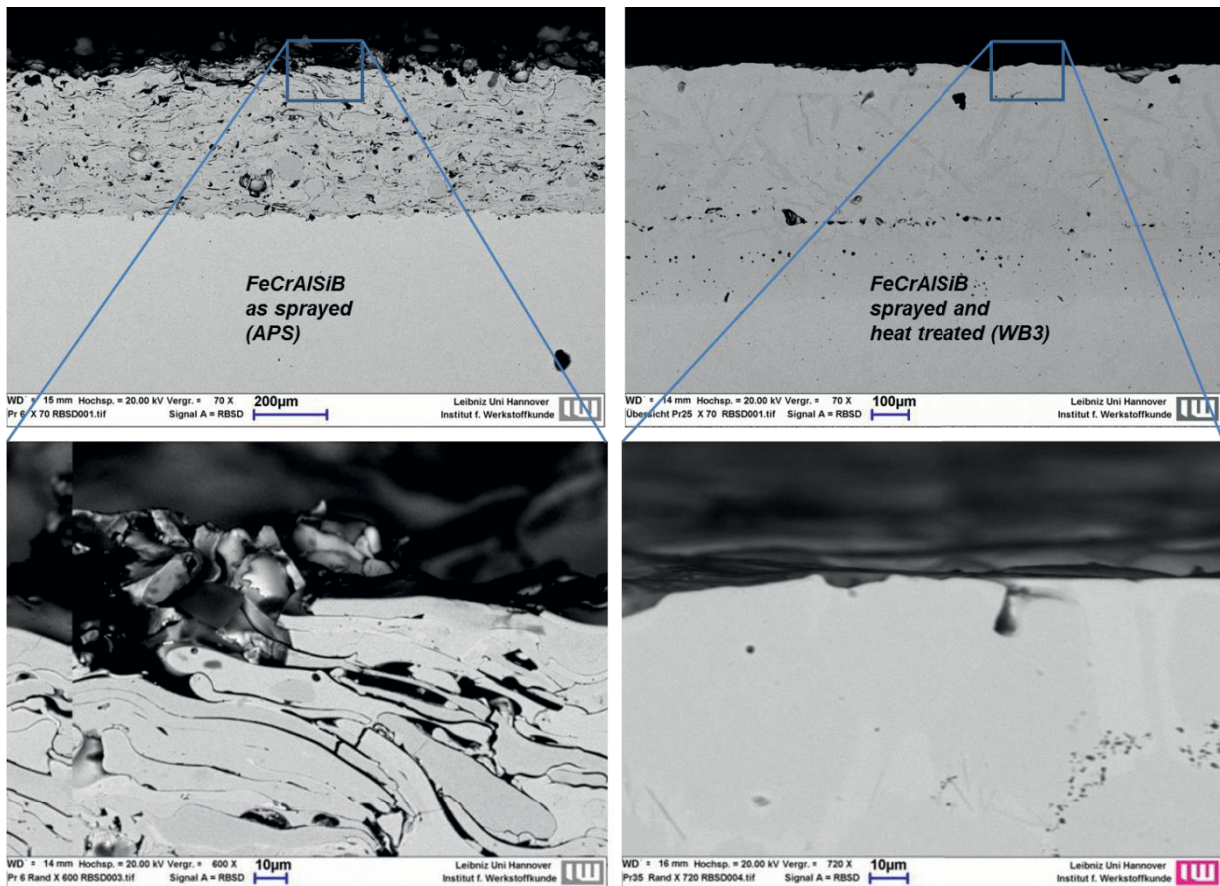
figure 5: SEM-images from FeCrAlSiB-coatings before and after heat treatment

A more detailed look into the coating's microstructure is given in figure 6. The coloured pictures on the right are mappings of the relevant elements in the coating and the adjacent

parent material. These mappings give a qualitative impression of the elemental distribution in the materials.

While iron is, of cause, detected in both materials, the elements chromium, silicon and aluminium are mainly concentrated in the coating and in the adjacent diffusion zone of the steel. In addition, distinct areas in the coating were found, where the chromium is enriched, while the concentrations of the other elements are low. These areas depict the positions of intermetallic precipitations in the coating, see dark gray arears in the lower left image of figure 6. These precipitations are sharp edged polygonal crystals with typical dimensions of the order of some ten microns. Spot analysis of these crystals show that they contain chromium and iron with approximately the same weight fractions. Although the light element boron, which is also an alloying element of the coating material, cannot be readily detected by EDX-analysis, these precipitations are in fact mixed chromium-iron-borides.

The pale grey matrix around these borides is iron rich and contains the elements aluminium, silicon and chromium with about 5 weight percent for each.

	C	Al	Si	Cr	Mn	Fe
EDX 1	0.79	0.21	0.11	42.41	0.12	56.36
EDX 2	1.29	4.56	5.49	4.78	0.10	83.78

values in wt%
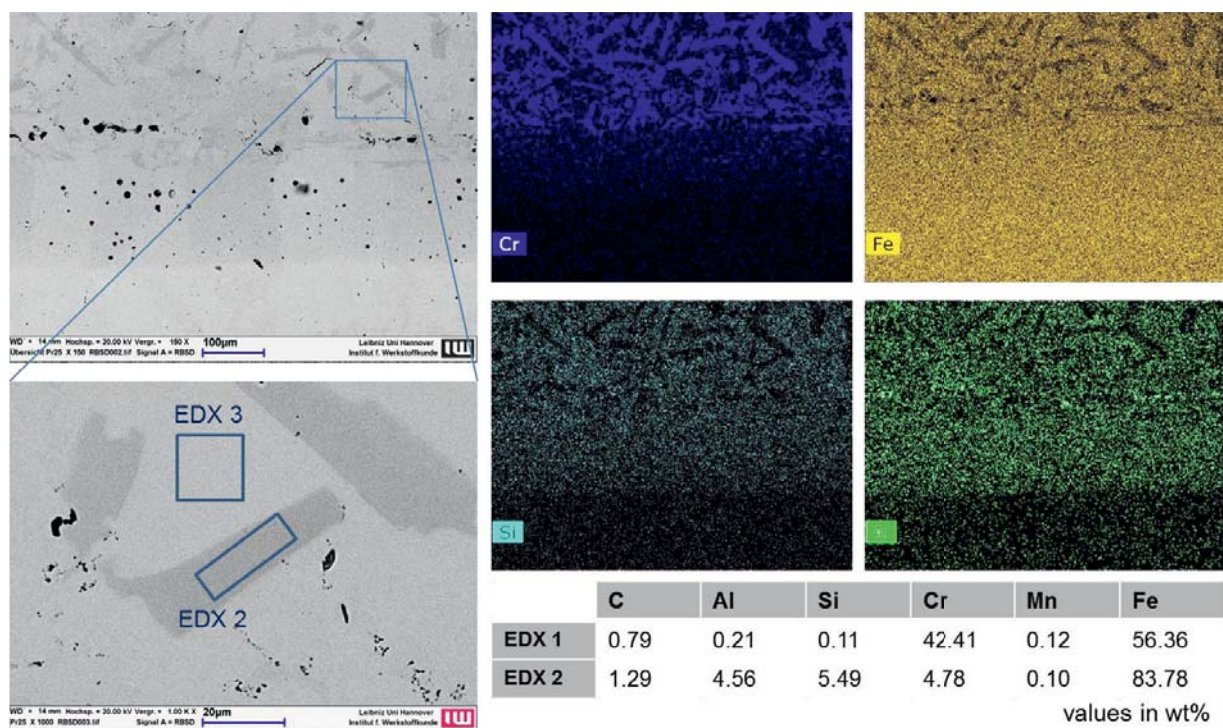
figure 6: EDX-analysis of FeCrAlSiB-coating after heat treatment

This was confirmed by a line scan, where the distribution of the elements were measured starting in the coating and finishing in the unaffected steel substrate, see figure 7. Apart from the scattering of the data due to crossing the chromium enriched intermetallic precipitations, the chromium, silicon and aluminium concentration remains at about 5 weight percent within the coating, followed by an almost linear decrease of these values, when crossing the diffusion zone. Corresponding to this is the course of the iron concentration. In the coating a

constant upper limit of about 85 % was found, which then rises linearly in the diffusion zone until a maximum value near 100 % is reached in the substrate.
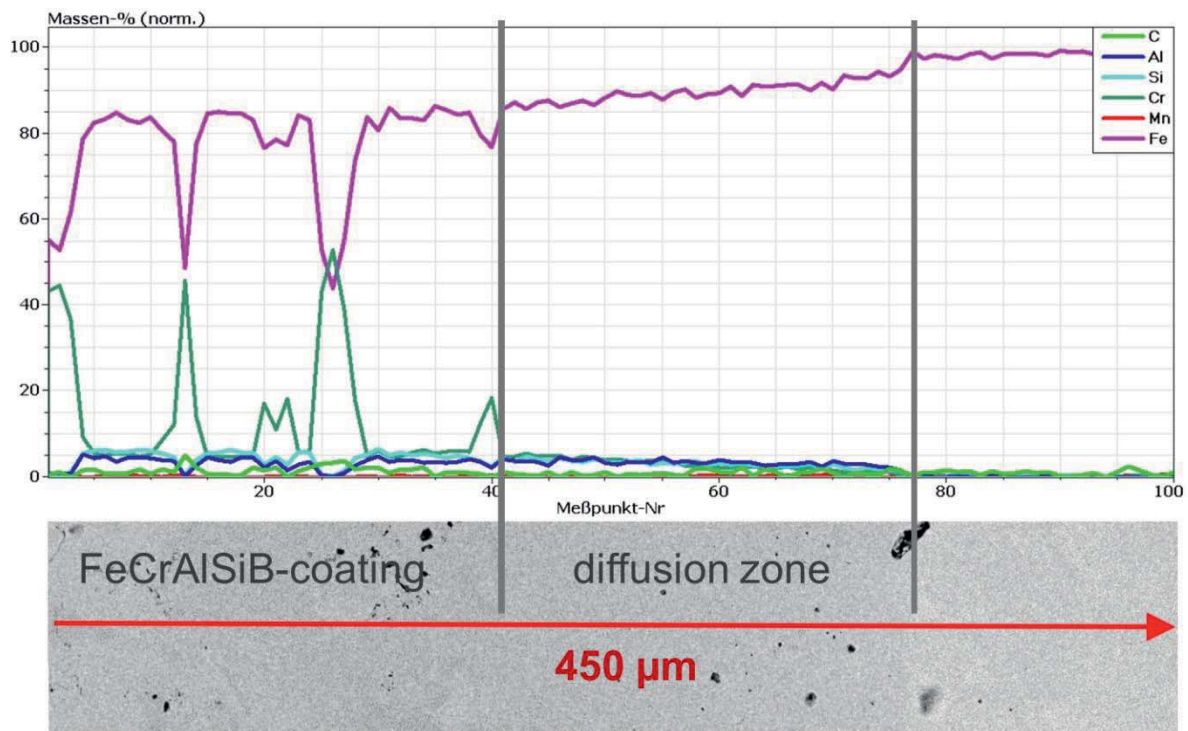
figure 7: line-scan (EDX) from FeCrAlSiB-coating and adjacent parent steel material

In addition to the analysis of the chemical and metallurgical properties of the iron-based coating, further aspects, which are important for resistant coatings, were investigated.

A key issue concerning the wear resistance of a coating is its hardness. Different standardized test procedures for measuring it are known. An appropriate method to determine the course of hardness along a microscopic distance is the measurement of Vickers hardness with small indentation forces, done with a pyramidal diamond tip.

The result of such a measurement is plotted in the diagram of figure 8. Accordingly the average coating hardness is ≈ 650 HV, while the substantial scatter of the values in the coating are due to the hard precipitations.

Within the diffusion zone a strong gradual reduction of the hardness to final values of about 120 HV is observed. The lengthover which this happens, correlates with the observed diffusion depth of the elements present in the coating alloy.
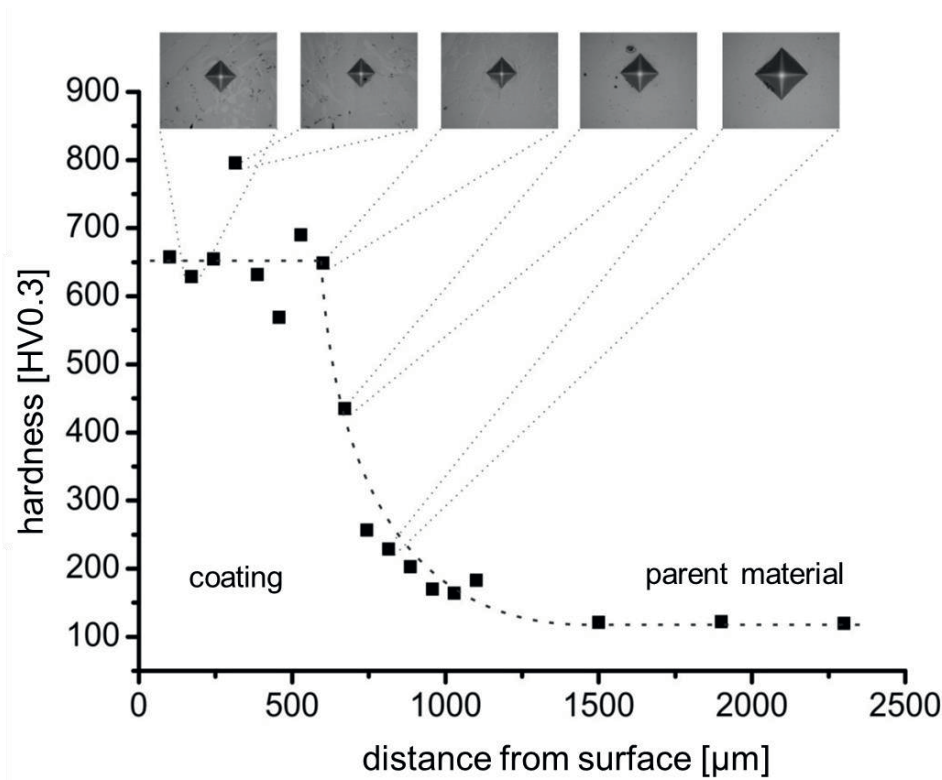
figure 8: Vickers hardness as function of distance to surface

table 3: Rockwell hardness ofFeCrAlSiB-coatings

condition	hardness HRC
as sprayed	36.4 ± 0,9
heat treated WB1	56.6 ± 2,2
heat treated WB3	52.6 ± 0,8

A more practical quantity for the evaluation of wear resistance is given by the Rockwell hardness. The indentations, done by a hard sphere on the coated surface, are much greater and give therefore an overall measure of the coating hardness. As listed in the table 3, the Rockwell hardness of the sprayed coating is – before heat treatment – 36 HRC. The value rises up to 57 HRC in the case of the WB1-parameters after the heat treatment. The Rockwell hardness resulting after heat treatment is therefore equal to values that are typical for self-fluxing Ni-based coatings. Thus, a similar wear resistance of the iron-based coating is expected.

table 4: conditions for electrochemical measurements (current density-potential-curves)

electrolyte	5 wt.-% NaCl solution
reference electrode	Ag/AgCl
counter electrode	Platinum
temperature	RT, 80 °C
scan rate	2 mV/s

Another important aspect is the corrosion behaviour of the coatings. A means to estimate the corrosion resistance are current density-potential-curves, which were recorded using aqueous chlorine solutions at different temperatures, see table 4 and the diagrams in figure 9.

618

Characteristic indicators for the corrosion behaviour are the inflection points of the current-density, which yield the so called „free corrosion potential" E_{cor} , and the magnitude of the anodic passivation current density i_{pass} in the flattened part of the curves. With further anodic polarisation a drastic increase in dissolution rate of the coating take place above E_{trans}.

Independent of the temperature and the type of heat treatment, the free corrosion potentials of both coating systems are very close to each other, cf. Figure 9 and table 5.. The passivation current densities of the iron based coatings at room temperature are even lower than for the nickel-based coating; however the current density in passive regime is smaller in case of the iron-based coatings.

At 80 °C this passivation areas are significantly smaller for all materials with similar values of the current densities and the onset for a drastic corrosive reaction is now nearly identical for all systems.

Thus, a similar corrosion resistance of the coatings can be expected for the conditions tested. This is supported by metallographic analysis of the specimen after anodic polarization at 80 °C, see figure 10. Both materials show localized corrosion defects on the surface with a similar depth of corrosion attack.
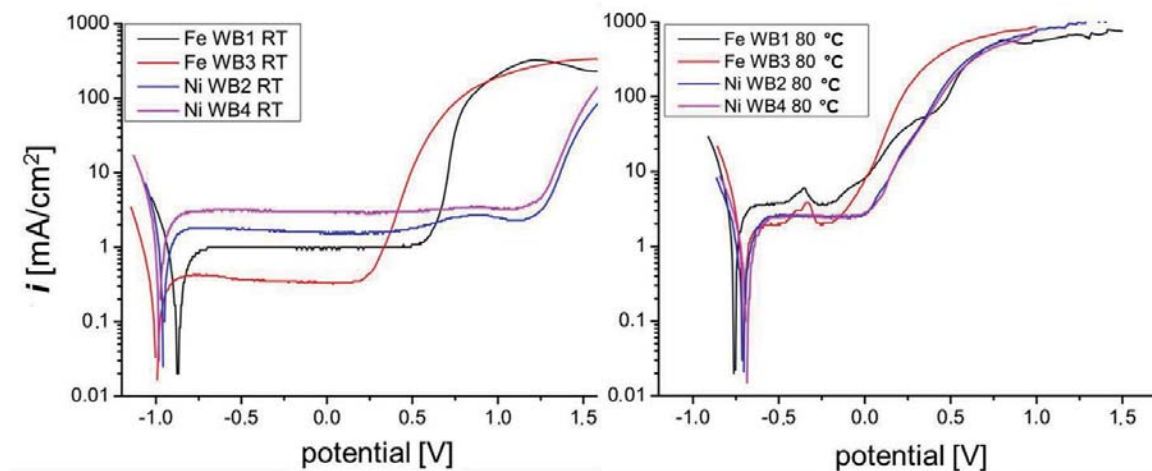
figure 9: current density-potential-curves

table 5: characteristic electrochemical values* of tested coatings from the plotted diagrams in figure 9

Coating	WB	E_{kor}/mV vs. Ag/AgCl	i_{passiv}/mA cm-2	E_{trans}/mV vs. Ag/AgCl
FeCrAlSiB	1	-872/-762	1.0/3.8	+625/-185
FeCrAlSiB	3	-997/-709	0.4/2.1	+327/-152
NiCrSi	2	-958/-714	1.6/2.5	+1316/+11
NiCrSi	4	-983/-695	3.0/2.6	+1292/+11

*black values at room temperature (RT), red values at 80 °C
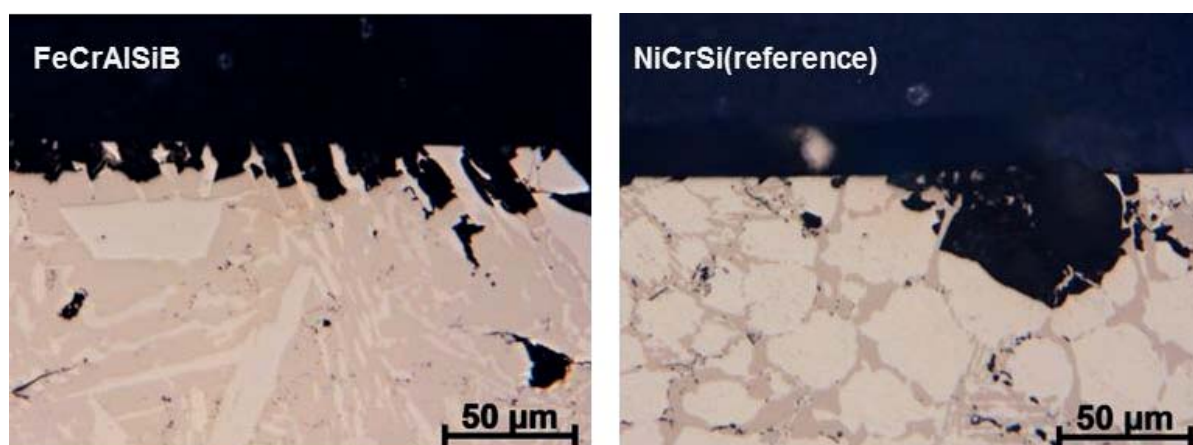
figure 10: optical images of coatings after anodic polarization at 80 °C in 5 wt.% chloride solution

Conclusion and outlook

The objective of the study was the development of a cost-efficient alternative to nickel-based, so-called "self-fluxing" alloys that can be used as a wear resistant coating material. A promising alloy was discovered in the iron-chromium-aluminium-silicon-boron system with a composition of 19%Cr, 7% aluminium, 7% silicon and 2% boron.

Coating tests using atmospheric plasma spraying and high velocity oxygen fuel spraying were performed and appropriate process parameters for a reliable deposition of the material by these spray processes could be identified.

The sprayed coatings could be sintered successfully at temperatures of 1150 °C, yielding dense coatings with a strong metallurgical bonding to the substrate and a distinct diffusion zone between coat and parent material.

With respect to the hardness of the coating a gradual transition of the values in this diffusion zones was detected, and the coating itself has an overall Rockwell Hardness of about 57 when using an optimal heat treatment.

The electrochemical corrosion measurements show that the heat treated coatings achieve a corrosion resistance similar to nickel-based coating systems in aqueous chloride solutions.

Due to the use of only cheap constituents, the material costs of the developed coating alloy is only one third that of the commercially available nickel-based material.

With respect to large components a heat treatment in a furnace is probably not the best approach. For coated tubes or pipes, for example, an induction heating for the remelting of the coating material might be better, and future research should address this point..

Furthermore, for the envisaged components practical corrosion and wear tests have to be performed, which take into account the actual service loads.

Finally, more economical coating processes than HVOF and APS do exist, which are worth to be tested for the iron-based system. For example, arc spraying using appropriate filler wires of the alloy or a braze coating process, where the coating material is deposited by means of pastes or suspensions and then brazed are promising alternatives.

Project Plan

Work packages and milestones	2009	2010	2011	2012	2013	2014
WP1: Development of coating systems						
WP2: Qualification of the materials for the various processes						
WP3: Characterisation of the coating systems						
WP4: Application field testing, evaluation of results						

Grey, original plan

Blue, actual plan

Publication of the project results

U. Holländer, J. Frank, K. Möhwald, F. W. Bach; Development of iron-based wear and corrosion resistant coatings for drilling engineering applications, Celle drilling 2014, 15/16.09.2014, Celle, Germany

622

W5: Material, welding- and conditioning technology at the deep drilling

1 Project Overview

Project Nr.	Title	Subject of research	Project leader, institution, location
W5	Material, welding- and conditioning technology at the deep drilling	Material-, joining-, automation- and conditioning technology	Prof. Dr.-Ing. habil. Dr.-Ing. E. h. Dr. h. c. Fr.-W. Bach, Prof. Dr.-Ing. H. J. Maier LUH (IW) Prof. Dr.-Ing. B. Denkena, LUH (IFW)

Participating institutes and institutions of the universities and external institutions:

- Institute of Materials Science (IW), Leibniz Universität Hannover

- Institute of Production Engineering and Machine Tools (IFW), Leibniz Universität Hannover

List of participating scientists and engineers:

Name	Subject area	University institute or non-university institution	Position is financed by gebo funds (indicate by X)
Prof. Dr.-Ing. habil. Dr.-Ing. E.h. Dr. h.c. Fr.-W. Bach	Material science	IW	
Prof. Dr.-Ing. H. J. Maier	Material science	IW	
Dr.-Ing. Th. Hassel	Material science / welding technology	IW	
Dipl.-Ing. A. Varahram	Material science / welding technology	IW	X
Prof. Dr.-Ing. B. Denkena	Production engineering and machine tools	IFW	
Dipl.-Ing. Leif Behrens Dipl.-Ing. Stephan Woiwode	Production engineering and machine tools	IFW	X

2 Research Program

2.1 Summary

Aim of the project is the simplification of the tubularhandling at the well, where at the common applied tool jointsfor the elongation shall be replaced with the electric arc welding. With this method especially the application of endless coiled tubes shall be realized. Main research points are the implementation of the weldseam-preparation, the development of the welding techniques as well as the removal machining of the joint patch and the cutting of the drill pipe at the deconstruction.

2.2 Relationship of the project to the overall research context and networking with other projects

One goal of the whole joint research project is to reduce the drilling costs under "hot-hard-rock" conditions. In the project W5 technologies, which simplify the tube handling, shall be investigated. These technologies were applied to replace the threaded connections for the elongation by electric arc welding. The relationship of the project to the overall research context and networking with other project results of the necessary input (requirements of the drill techniques and automation, geohydraulic parameters, characteristics of the well and drill pipe load profile) as well as its output (feasibility of the coiled-tubing by welding connections, characteristics of the drillstring and processdata within the component assembly).

2.3 Work packages executed relative to plan and results achieved

WP1: IW: Conception

Target of gebo sub-project W5 is the substitutionof threaded connections by fast connecting with less production time for drillpipes. MIAB welding distinguishes itself by short cycle times and easy automation which lead to an expected reduction of drilling costs and drilling times respectively [4, 5].

Task of working package 1 is the determination of welding parameter fields to configure further construction assemblies of a MIAB test system. After a detailed literature research on MIAB welding processes welding parameters like required arc deflecting force and coil design could be calculated. These values are used for further configurations of the test rig.

Calculation of the force acting on the magnetic arc

In the first instance the required force to deflect the magnetic arc on the atmosphere is calculated. It is assumed that the arc can be treated as a cylindrical current-carrying conductor. The magnetic field strength H_L is defined as [1]:

$$H_L = \frac{F_L}{l}; [H_L] = \frac{A}{m} \tag{1}$$

Entering the magnetomotive force $F_L = I_L n_L$and the circumference of the conductor respectively the arc $l = 2\pi r$ into equation 1, H_L is:

$$H_L = \frac{I_L n_L}{2\pi r} \tag{2}$$

The arc radius r is assumed to be 0.75 mm. The current I_L = 500 A and the number of turns of the arc $n_L = 1$. The magnetic field strengthH_L is:

$$H_L = \frac{500\,A*1}{2\pi*0.0075\,m} = \mathbf{10610.33}\ \frac{A}{m} \tag{3}$$

With the magnetic field strength H_L the magnetic flux density B_L can be determined to:

$$B_L = \mu H_L; \quad [B_L] = \frac{Vs}{m^2} = T \tag{4}$$

With $\mu = \mu_0 * \mu_r$, $\mu_r = 1$, $\mu_0 = 4\pi * 10^{-7} \frac{Vs}{Am}$ it is:

$$B_L = 4\pi * 10^{-7} \frac{Vs}{Am} * 10610.33 \frac{A}{m} = 0.0133 \frac{Vs}{m^2} = \mathbf{0.0133\ T} \tag{5}$$

With the help of the magnetic flux density B_L from equation (5) the required force for the arc deflection F_L can be evaluated:

$$F_L = B_L I_L l; \quad [F_L] = N \tag{6}$$

For an arc length of $l = 0.005\ m$ the deflecting force F_L on the atmosphere is:

$$F_L = 0.0133\ T * 500\ A * 0.005\ m = \mathbf{0.033\ N} \tag{7}$$

Inert or forming gas is used to improve the control of the arc during the welding process. Benefits are advanced ignition behavior and electric conductivity, stabilization and relighting of the arc, short circuit resolution and protection of the welding zone. In order to calculate possible variances of the force F_L under realistic weld conditions the force F_L was determined for argon, helium and carbon dioxide as gases. Because only the susceptibility χ_M of argon is known, the permeability μ_r can be determined with:

$$\chi_{m,Ar} = \mu_R - 1 \tag{8}$$

For argon with $\chi_{m,Ar} = -19.7 * 10^{-6}$ the permeability is

$$\mu_r = -19.7 * 10^{-6} + 1 = \mathbf{999980.3 * 10^{-6}} \tag{9}$$

and the magnetic flux density results to

$$B_L = 4\pi * 10^{-7} \frac{Vs}{Am} * 10610.33 \frac{A}{m} * 999980.3 * \mathbf{10^{-6}} = \mathbf{13.334 * 10^{-3}\ T.} \tag{10}$$

The force F_L results to:

$$F_L = 13.334 * 10^{-3}\ T * 500\ A * 0.005\ m = \mathbf{0.033\ N} \tag{11}$$

As seen in these calculations, the effect of the permeability μ_r of the respective gases on the force F_L is very small or even not existing. Equivalently the permeabilities of helium and carbon dioxide are calculated as following:

$$\mu_{r,He} = -1.9 * 10^{-6} + 1 = \mathbf{999998.1 * 10^{-6}} \tag{12}$$

$$\mu_{r,CO_2,} = -1.2 * 10^{-8} + 1 = \mathbf{999999.9 * 10^{-6}} \tag{13}$$

According to only minimal variations of permeability μ_R, the magnetic flux density B_L and force F_L are:

$$B_{L,He} = 4\pi * 10^{-7}\, \frac{Vs}{Am} * 10610.33\, \frac{A}{m} * 999998.1 * 10^{-6} = \mathbf{13.333 * 10^{-3}\, T} \qquad (14)$$

$$B_{L,CO_2} = 4\pi * 10^{-7}\, \frac{Vs}{Am} * 10610.33\, \frac{A}{m} * 999999.9 * 10^{-6} = \mathbf{13.333 * 10^{-3}\, T} \qquad (15)$$

$$F_L = 13.333 * 10^{-3}\, T * 500\, A * 0.005\, m = \mathbf{0.033\, N} \qquad (16)$$

It is noticeable that tube geometry has no influence on the force. Factors of influence are tube distance, diameter of the arc and welding current. The arc diameter cannot be operated directly and is assumed to be 1.5 mm. This assumption has to be identified experimentally in the next project run.

The tube distance is assumed to be constant at 5 mm for further examinations. At closer distances short circuits occur by drop formation of the welding material. Deductively the only variable in calculations of the force F_L is the welding current.

In figure 1 the force F_L is represented in dependency of the welding current.
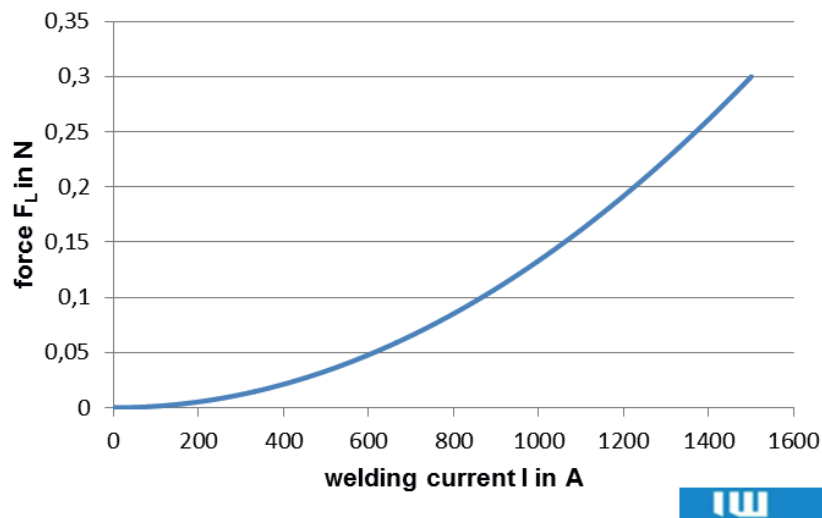
Fig. 1: Force F_L as a function of welding current I

Calculation of the magnetic coil

Preliminary considerations proved the coaxial arrangement of the coil elements as the most promising version. It guarantees a homogeneous magnetic field on the tube circumference (Fig. 2).
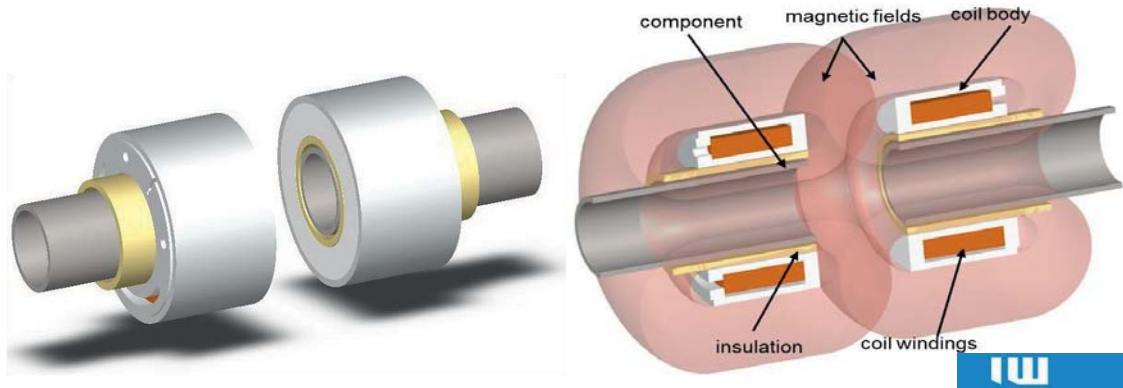
Fig. 2: Design of the magnetic coils (left) and sectional view

This implies that the magnetic field produced by the coils spreads as shown in fig. 2. The coils are inversely poled. As a result the magnetic flux lines coming from both sides and meeting in the weld gap getconcentratedat this point and do not overlap. As a consequence the magnetic field density rises and the flux lines escape to the outside rotation-symmetrically and return around the respective coil. The preliminary calculation of the magnetic coils took place analytically to define the dimension of the coils and to produce a magnetic field that is strong and stable enough. Therefore it is crucial to be able to describethe interactions of welding current, material, applied magnetic field, force on the arc and its course of movement as accurately as possible.

To deflect the arc, the magnetic field has to feature an ideal size and orientation. The generation of the magnetic field is realized with coils. The force acting on the arc has to be larger than F_L.

$$F_L = \mathbf{0.033\ N} \tag{17}$$

Due to the fact that magnetic fields can only be calculated accurately inside of a coil, the induced force F_S is multiplied by a coefficient of safety $S = 3$ and called $F_{S,min.}$:

$$F_{S,min.} = F_S * S = 0.033\ N * 3 = 0.099\ N \tag{18}$$

With $F_{S,min.}$ and equations 3/ 5/ 7, the number of windings n_S can be determined through:

$$n_S = \frac{F_{S,min.} * 2\pi r}{\mu_0 * \mu_r * I_S^2 * l_S} \tag{19}$$

The coil current I_S is assumed to be 3 A, the length of the coil body (winding length) is $l_S = 40\ mm$ and the radius r of the coil conductor is 0.4 mm.

$$n_S = \frac{0.099 \text{ N} * 2\pi * 0.0004 \text{ m}}{4\pi * 10\text{-}7 \frac{Vs}{Am} * (3 \text{ A})^2 * 0.04 \text{ m}} = 550$$

With values as given above the number of coil turns has to be 550 to generate a deflecting force of 0.099 N.

If a security of $S = 3$ does not suffice to actuate the arc in a controlled way, an adaption with adjustable coil current is possible.

Calculation of the coil voltage

From the calculation of coil windings the number of windings $n_{S,min} = 550$ and coil current $I_S = 3 \text{ A}$ are already known. For a body length of 40 mm and a diameter of the coil wire of $d_D = 0.87 \text{ mm}$ (with protective coating), 43 windings per layer can be produced. Every layer has an increasing coil diameter of $2*d_D$. Applying a commercial copper wire of 100 m length 16 layers can be achieved.

The conductor length l_D results from:

$$l_D = \sum_{n=1}^{16} 43 * 2\pi * (r_0 + [n-1] * d_D) = 99.77 \text{ m} \tag{20}$$

With a conductor length of $l_D = 99.77 \text{ m}$ and the specific resistance of the copper conductor $\rho_{cu} = 17.3 * 10^{-3} \frac{\Omega mm^2}{m}$ the coil resistance can be calculated to:

$$R_S = \rho_{cu} * \frac{l}{A} = \rho_{cu} * \frac{l}{\pi * r_D^2} = 17.3 * 10^{-3} \frac{\Omega mm^2}{m} * \frac{99.77 \text{ m}}{\pi * (0.4 \text{ mm})^2} = 3.43 \ \Omega \tag{21}$$

With the coil resistance and coil current, the coil voltage can be calculated by Ohm's law:

$$U_S = R_S * I_S = 3.43 \ \Omega * 3 \text{ A} = 10.3 \text{ V}. \tag{22}$$

The calculations are based on acceptances, idealized considerations (magnetic field, coil voltage) and basic formulas. They are designed for one distinct geometry (coil body, coil conductor). However, these are irreplaceable for a fundamental determination of parameter fields. Therefore, components for expanded application parameters (e.g. higher coil voltage) are selected or adapted additionally.

Distribution of the magnetic fields

Inside of a coil there is a homogeneous magnetic field. Accurate statements about the magnetic field are possible only for this area. In fig. 3 it can be seen that the magnetic field

within the coil is homogeneous and inhomogeneous outside of the coil. This has to be determined in further experiments.
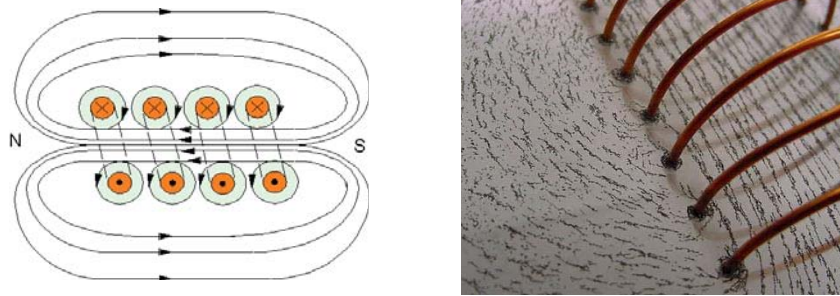
Fig. 3: Example of coil magnetic field lines [2, 3]

Weldability of the drill pipe

The drill pipe materials are construction steels (low-alloyed steels), lightly modified in their chemical composition. The weldability of structural steels first of all depends on the carbon percentage in the material. This is safe up to a carbon concentration of C≤0.22%. The carbon percentage of Coiled-Tubing materials is at most 0.15% C. Therefore, the weldability is to be classified as unproblematic. For the first welding tests a structural steel P235GH and for the following experiments, a API J55 drill pipe material are available.

WP 1: IFW: Study of the Process

For the connection of drilling tubulars by welding, a plane surface of the contact area has to be provided. For this purpose the tubulars have to be machined. Thus, experimental examinations for the identification of suitable machining strategies have been conducted. Aim of the experimental examinations is the conceptual comparison of the material removal processes applied on drilling tubulars. Therefore, technological cutting experiments on a laboratory scale have been carried out to evaluate the required energy, the resulting cutting forces and the chip shape of the applied machining processes. Milling and turning have been selected as machining processes for the preparation and finishing of the welding seam (Fig. 4) in agreement with the project partner. Axis parallel turn-milling and orthogonal turn-milling are investigated in detail.

At the beginning of the machining experiments, the tube material QT-800 was characterized analytically in terms of its mechanical and chemical properties. Based on similar physical properties to the mild steel C45, comparable cutting process parameters have been selected for the machining of QT-800 with coated (AlTiN) carbide cutting tools. For machining C45 AlTiN is a typical tool coating.
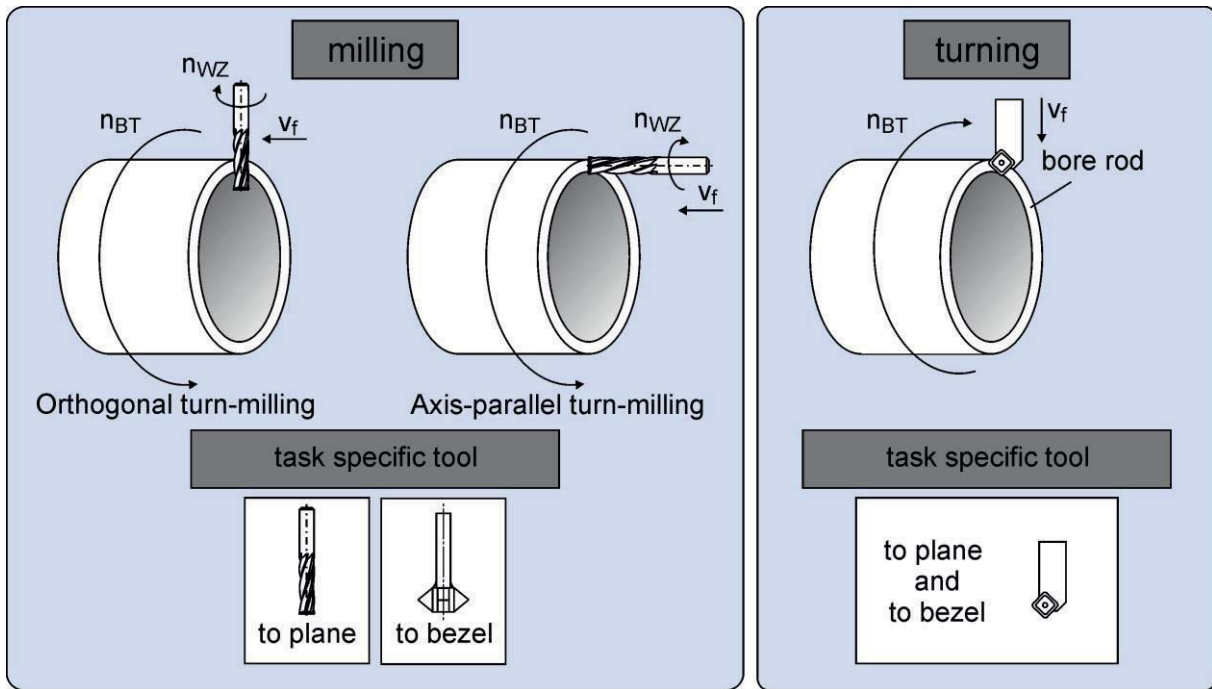
Beh/59828 © IFW

Fig. 4: Selected cutting processes for the machining of tubulars

Axis-parallel turn-milling

Within the examinations the axis-parallel turn-milling was initially examined to identify technological process limits for the concept of the machining device. A 4-axis milling machine Heller MCi 16 was used. All experiments are carried out without cooling lubricant. The feed motion of the cutting tool is generated by the machine table on which the drilling tubulars were clamped. The cutting forces were measured with a Kistler 9123CQ05 dynamometer. The used solid carbide milling tool with TiAlN coating has a diameter of $D_{WZ} = 8$ mm and a number of teeth of $z = 6$. The geometrical cutting parameters, depth of cut a_p and cutting witdh a_e were chosen according to the manufacturer's recommendations for mild steel ($a_p = 1$ mm, $a_e = 4$ mm). The cutting speed v_c was set to 120 m/min. The feed rate per tooth was $f_z = 0.36$ mm. These parameters are the initial values for the technological examinations. In the following examinations the cutting speed was varied in the range of $v_c = 100 - 130$ m/min. The feed rate per tooth remains constant at $f_z = 0.36$ mm.

For the examined process parameters, process forces at a reasonable level (100 - 250 N) result. Here a steady state of the machining process is resulting. To determine the required energy, the cutting power P_c was calculated. The cutting power results from the cutting force and cutting speed according to Eq. 23. Figure 5 presents the progress of the cutting force F_c and the calculated cutting power P_c.

$$P_c = F_c \cdot v_c \tag{23}$$

Thereby, a typical progress of the cutting forces for machining of steel appears. With increasing cutting speed the cutting forces decrease. Consequently the cutting power P_c

decreases as well. This can be attributed to increasing temperatures in the cutting zone, due to the changing cutting speed, which promote the chip formation.
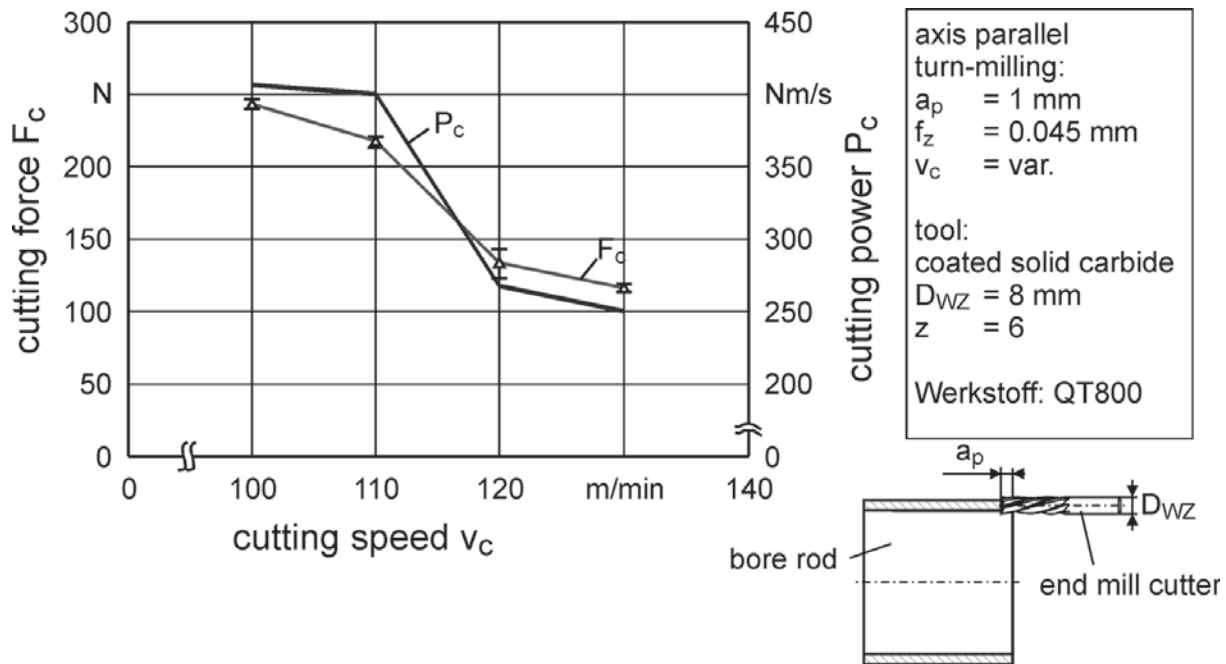
Fig. 5: Process forces and cutting power for axis-parallel turn-milling

The generated surface roughness was measured by a Mahr Perthometer PGK with tactile stylus method. The axis parallel turn-milling process generates low values of the average maximum height of roughness with $Rz \leq 10$ µm. The measured distance of the groove was close to the value of the feed per tooth with $f_z = 0.36$ mm. The achieved surface quality enables the melting of two tubulars. The results can not be transferred directly for turning or axis-ortogonal turn-milling. Therefore further examinations were conducted.

The chip geometry was also analyzed for the machining process. For each parameter combination very short discontinuous chips were generated. The short discontinuous chips can easily be taken away by the cooling lubricant and can be rated as uncritical for the machining process. This fact should be taken into account for the construction of the machining device.

In order to rate the process forces for cutting steel QT-800 and to give a forecast for future machining operations, they are calculated by the Kienzle method for steel C45E. The same process parameters were chosen and were compared to the experimentally determined cutting forces of QT-800. Therefore, the medium chip thickness h_m for the axis-parallel process has to be calculated. The chip thickness for milling depends on the operation direction angle φ and is consequently not constant ($h=f(\varphi)$, Fig. 6).
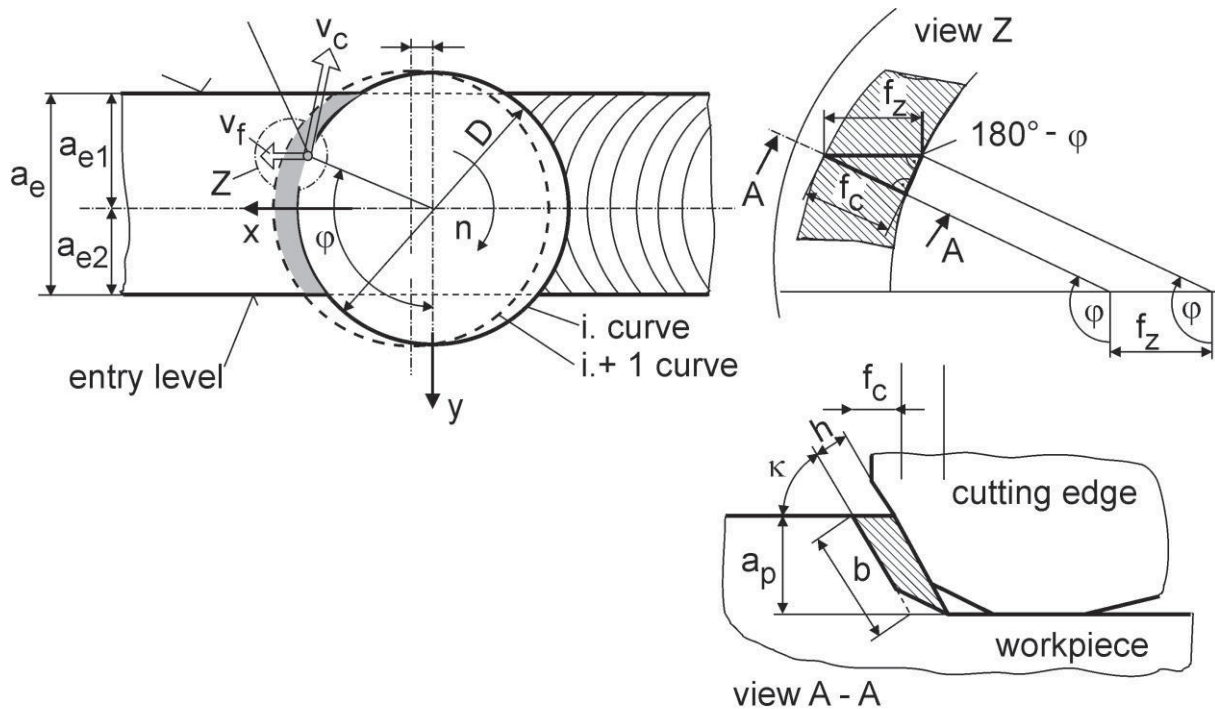
Fig. 6: Cutting conditions for milling

For the determination of the resulting forces and the cutting power a medium chip thickness is assumed, which can be calculated by Eq. 24.

$$h_m \approx \frac{360°}{\pi \cdot \Delta\varphi} \cdot \frac{a_e}{D} \cdot f_z \cdot \sin\kappa \tag{24}$$

However, not all teeth of the milling tool are in contact at the same time, therefore an average cutting force for each tooth has to be calculated (Eq. 25). This can be referred to the teeth in contact by the usage of the angle $\Delta\varphi$.

$$F_{cm} = F_{cm,z} \cdot z_e = F_{cm,z} \cdot \frac{\Delta\varphi}{360°} z \tag{25}$$

For the calculation of the average cutting force the calculation method of Kienzle (Eq. 26) was used.

$$F_{cm,z} = k_{c1,1} \cdot b \cdot h_m^{1-m_c} \tag{26}$$

The material constants $k_{c1,1}$ and m_c are the principal values of the specific cutting force k_c. For the material C45E it can be calculated according to Eq. 27. The comparison of the measured cutting forces with the predicted forces, which were calculated by means of the Kienzle-method, shows that the process cutting forces at the cutting speed $v_c = 120$ m/min are slightly smaller than the predicted ones (Fig. 7).

632

$$k_{c1,1} = 1475 \frac{N}{mm^2} \; und \; m_c = 0,2119 \qquad\qquad (27)$$
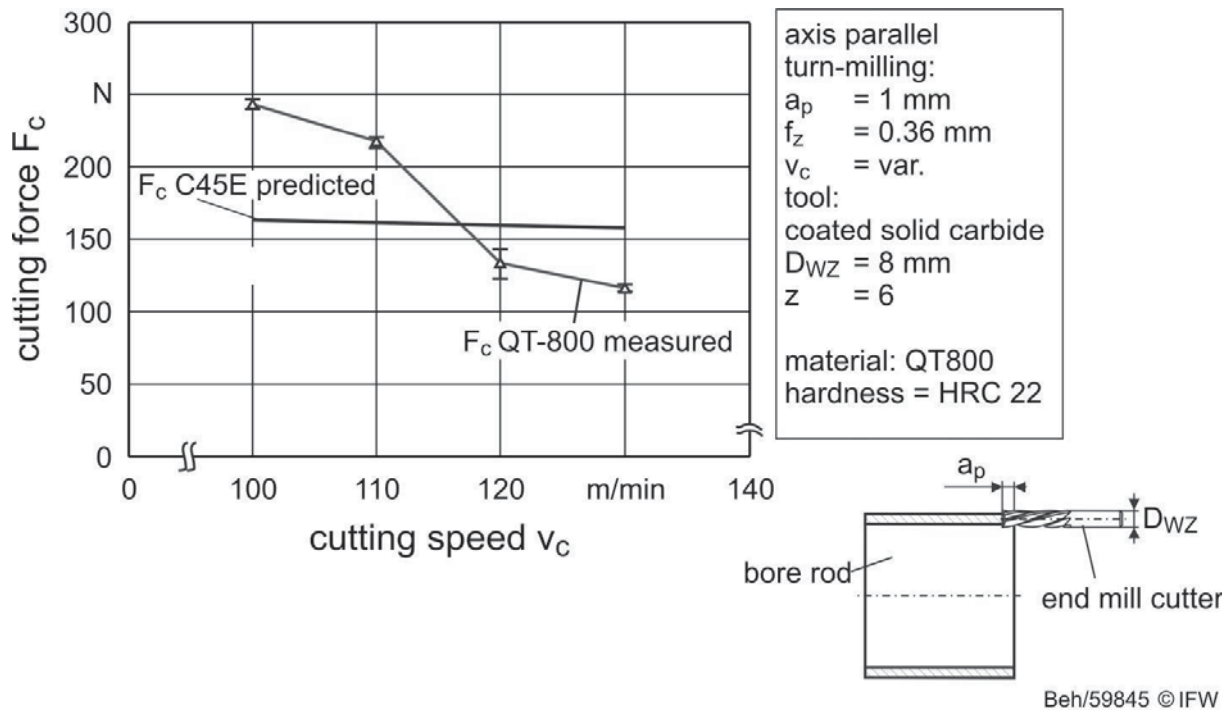
Fig. 7: Comparison of predicted and measured cutting forces

Kienzle´s calculation method and the usage of the specific values for steel C45E enable the forecast of the cutting forces, which can be applied to other cutting processes. For the axis-parallel turn-milling good machinability regarding chip formation and surface quality was reached.

This reveals, that for the machining of the QT-800 the recommended process parameters ($v_c \geq 120$ m/s) and the cutting force prediction with the Kienzle-method can be applied. Here, an overestimation of the process force is resulting, which is non-critical for the machining process.The Kienzle-method is also applicable for the turning and orthogonal turn-milling. Thus, adequate process parameters for the other selected manufacturing processes can be derived. Furthermore, the predicted cutting forces and rates can be used for the design and conception of the cutting system. This indicates an adequate machinability for the QT-800 in order to prepare and finish the joint of the coiled tubes.

Turning

The influence of the process parameters on the resulting surface quality of the machined tubulars was examined accordingly in experimental turning investigations. Thereby, detailed experiments were carried out to identify process parameters that guarantee a stable and productive machining process. In this context the specific cutting force k_c for QT-800 was

calculated for turning to determine cutting forces and power. For the experimental investigations a cutting insert made of KC9125 was used. With this tool, the machining of mild steel in a roughing and finishing operation is possible. The pivotable fixing of the rectangular shaped tool enables the external machining, as well as face machining and chamfering. Turning is also suitable for maching with interrupted cut, such as the machining of tubulars with welding joint. A chip breaker geometry supports the chip formation.

The experiments were taken out based on a fully fractional designed experimental plan. The cutting speed was varied in six steps between $v_c = 50 - 500$ m/min (50, 100, 150, 200, 300. 500). The feed rate was set to f = 0.1 mm/U and f = 0.25 mm/U. The depth of cut was $a_p = 2$ mm. This experimental design was used for face machining and chamfering. The chamfer is realised with an angle of 40°. All experiments are carried out without cooling lubricant.The cutting force, the force in feed direction and the passive force as well as the chip formation and the surface roughness are used for process evaluation. During machining, the cutting forces are measured and will be used for the calculation of torque and power. The resulting force progression is illustrated in figure 8. With increasing cutting speed v_c a reduction of the cutting force appears. From a value of $v_c = 200$ m/min the cutting forces approximate a limiting value. This progress can be explained by increasing process temperatures, which influence the chip formation positively. The cutting force F_c has the highest values and the passive force F_p the lowest values. Increasing the feed rate raises the force level.
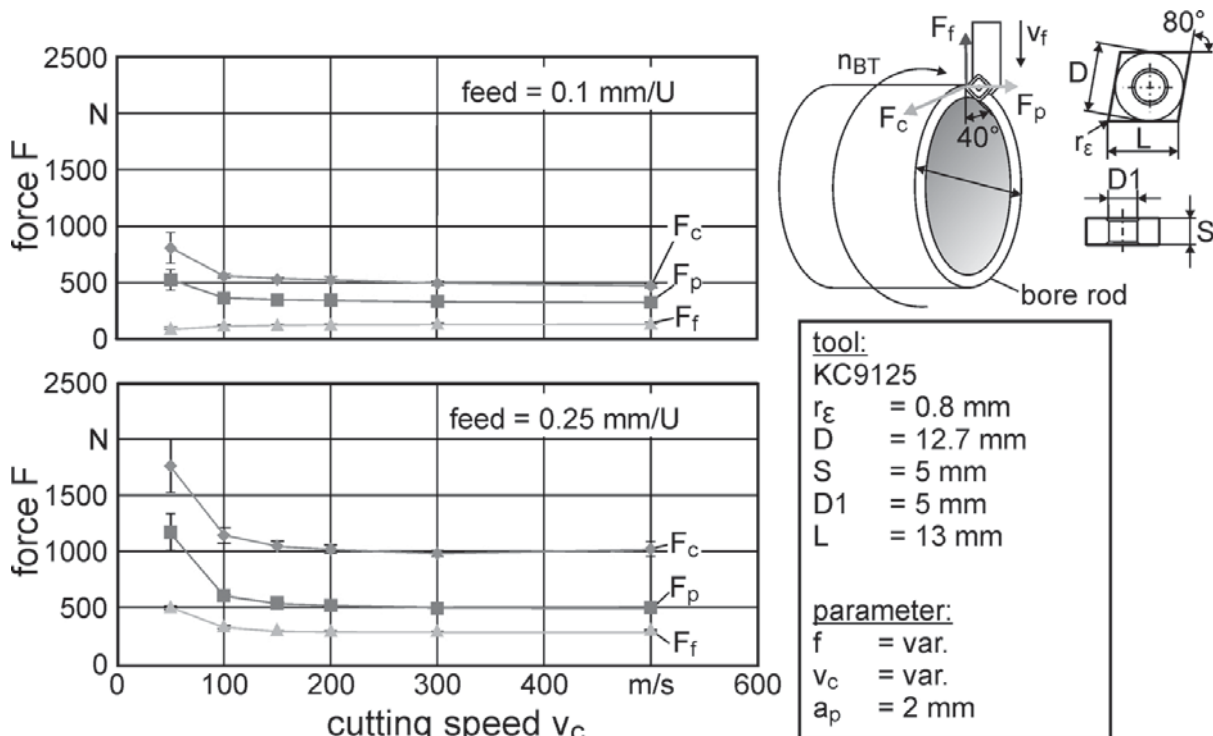
Beh/62943 © IFW

Fig. 8: Process forces for face turning

The generated chips of the face cutting operation are illustrated in figure 9 for both feed values. For the feed f = 0.1 mm cylindrical-helical chips result for the cutting speed v_c = 100 m/min, which fade to ribbon chips (v_c = 500 m/min). This chip geometry is classified as unfavourable for turning, because the chips can wrap around the workpiece. For a feed of f = 0.25 m/min cylindrical-helical chips are generated up to a cutting speed of v_c = 300 m/min which can be rated as suitable for the machining process.
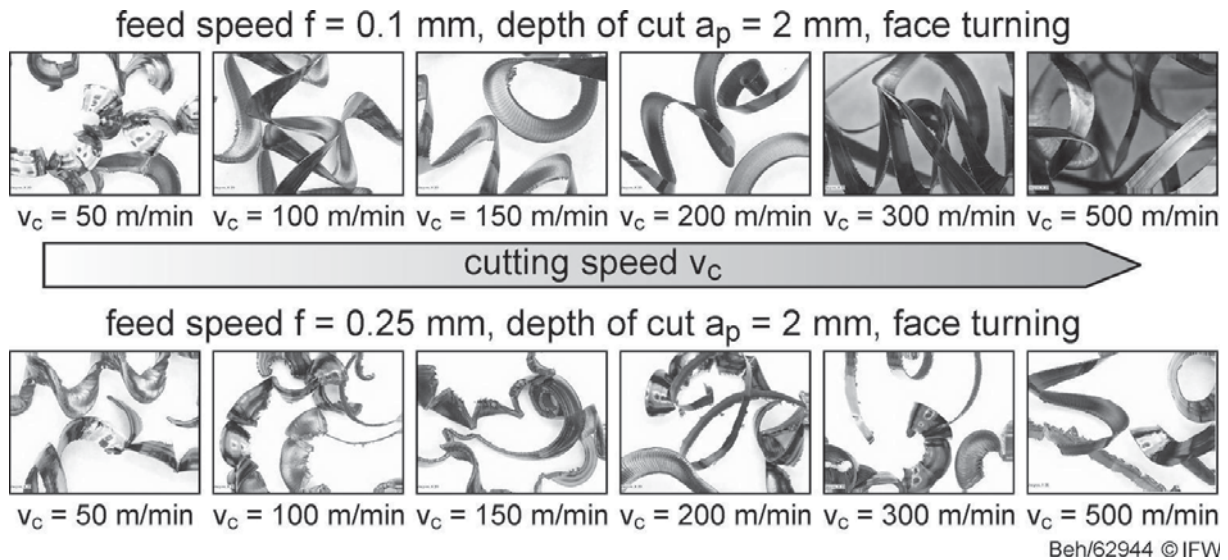
Fig. 9: Chip formation for turning

The measured surface roughness values increase when raising the feed. The measured maximum height of roughness values for the feed f = 0.1 mm as well f = 0.25 mm are lower than Rz = 10 µm. For a feed of 0.5 mm a maximum height of roughness values geater than Rz = 50 µm was measured. Furthermore, the measured maximum height of roughness Rz correlates with the calculated theoretical roughness Rth. The theoretical roughness Rth can be calculated by the usage of the variables corner radius r_ε and the feed f.

Experiments for chamfer turning were conducted and reveal the same process behavior as for face turning. The process forces show the same characteristic progression as the forces for face turning (fig. 10). In a direct comparison to face turning, they are on a lower level.

For a feed of f = 0.1 mm and a cutting speed of v_c = 300 m/min unfavourable long cylindrical-helical chips result. When exceeding the value f = 0.25 mm at any cutting speed, unfavourable chip geometries result. These chips range from long cylindrical-helical chips (v_c = 50 m/min) to ribbon chips (v_c = 500 m/min). A consideration of the surface roughness is not needed, because the chamfers are not a contact area for welding.
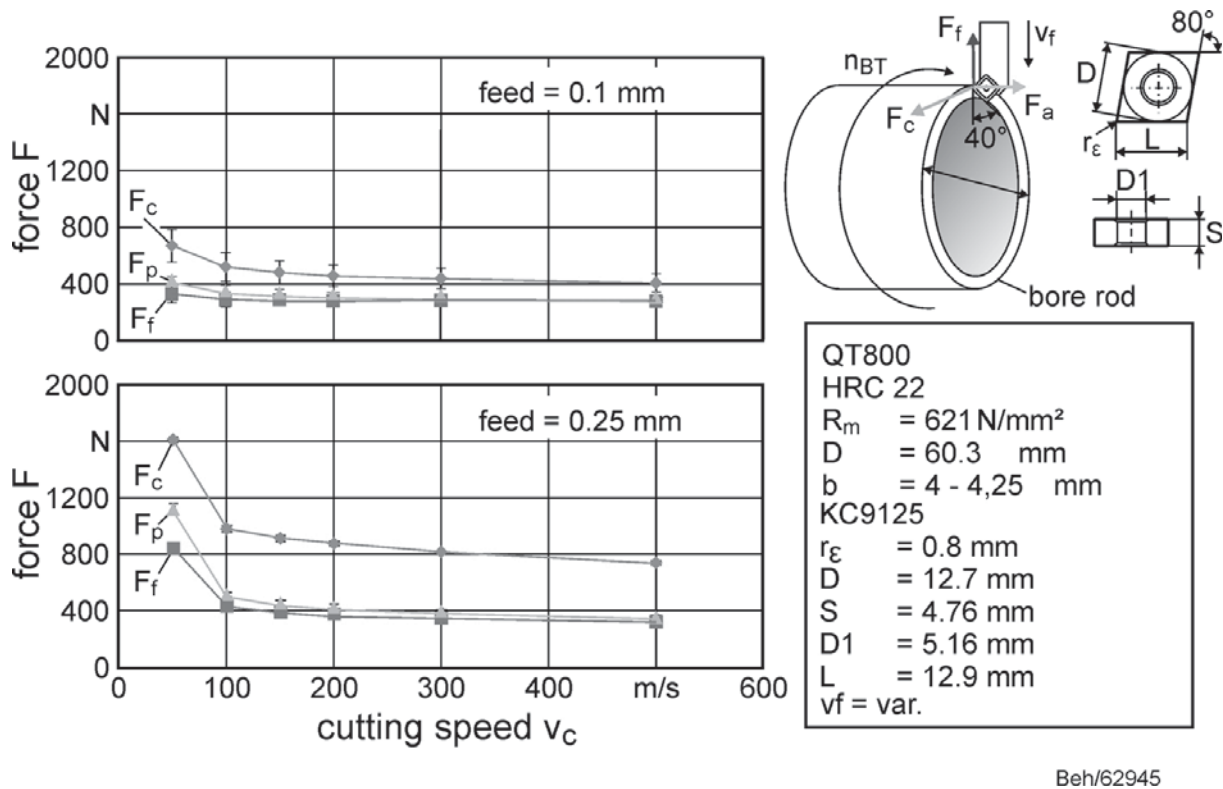
Fig. 10: Process forces for chamfer turning

For a fast preparation of the tubulars welding area, the cutting speed v_c and the feed f are the main influential variables. The higher these variables are chosen, the faster the machining operation is completed. Limits of the process are the chip formation and the generated surface roughness of the welding spot. For the surface roughness the feed rate of f = 0.25 mm/min is the limiting boundry. At higher feed rates, roughness values greater than Rz = 10 µm result. For the chip formation during face turning a cutting speed of v_c = 200 m/min and a feed rate of f = 0.25 mm are suitable. For turning of chamfers a cutting speed of v_c = 200 m/min and a feed rate of f = 0.1 mm/min are acceptable.

Axis-orthogonal turn-milling

For examinations of the axis-orthogonal turn-milling process the feed per tooth was increased to a maximum of feed per tooth f_z = 0.12. The tool cutting speed was constant (v_c = 120 m/min). In case of increasing the feed f_z, a linear rise of the process forces was measured. The calculated specific force F_{cmz} is nearly identical with the cutting force F_c (**fig. 11**). The progression of the generated suface roughness values is not linear like the progression of the measured process forces (**fig. 12**). Up to a feed per tooth of f_z = 0.8 mm a nearly linear progression appears up to Rz = 5.6 µm. For a further increase of the feed per tooth to f_z = 1.0 mm, the progression of the measured roughness values flattens and reaches a maximum of Rz = 5.7 µm. Another increase to f_z = 0.12 mm results in a lowering of the

rougness values to Rz = 4.7 µm. The calculation of the theoretical roughness Rth deviates noticeably from the machined surface roughness.
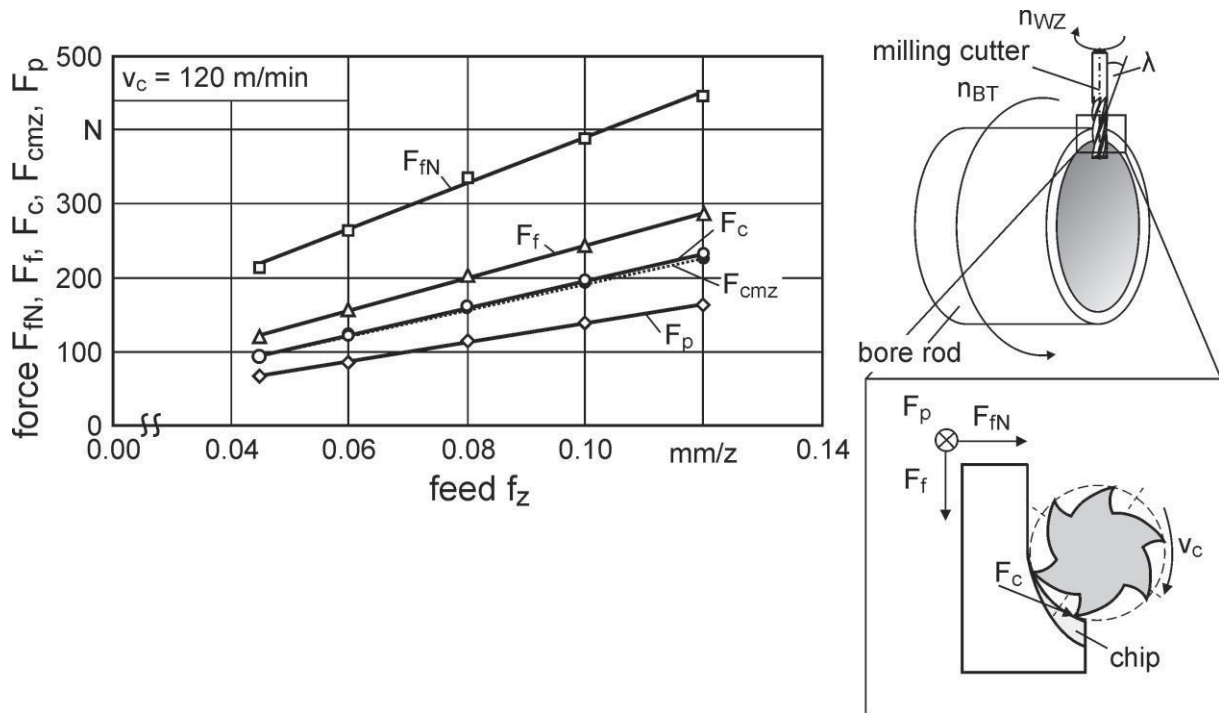
Fig. 11: Process forces for axis-orthogonal turn-milling
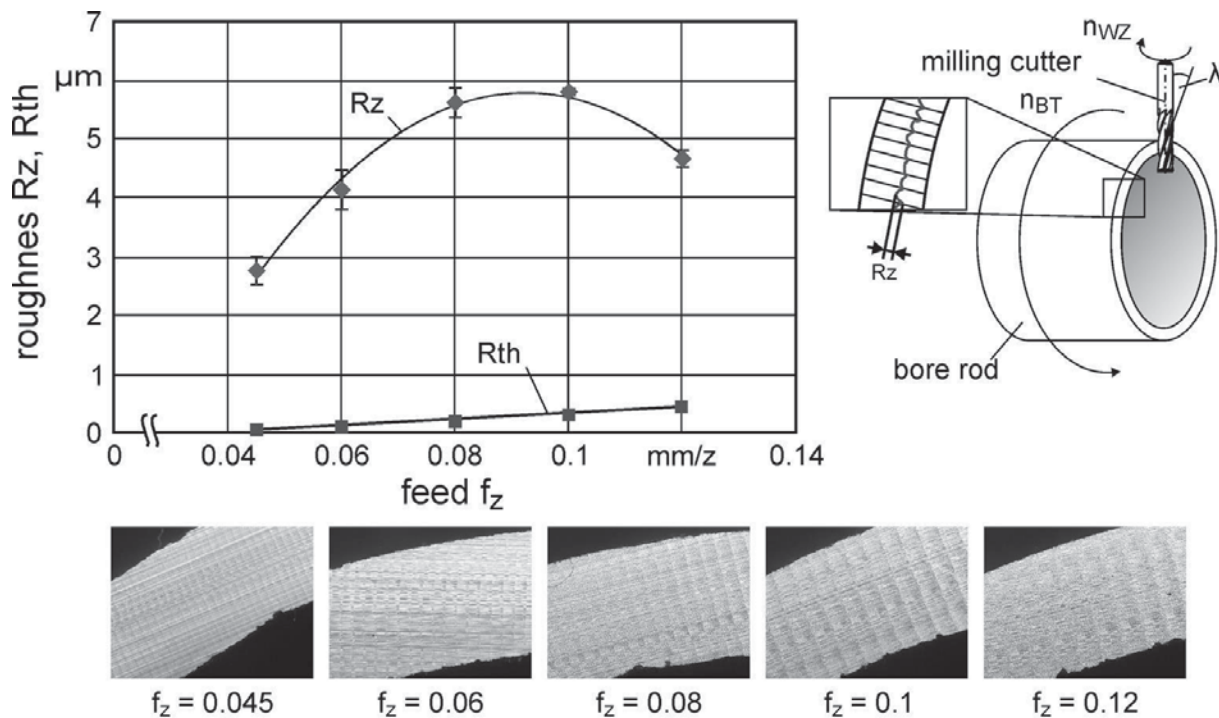
Fig. 12: Surface roughness for axis-orthogonal turn-milling

The process load is significantly smaller than for turning but higher than for axis-parallel turn-milling. The generated surface roughness of the welding spot (< Rz = 6 µm) is consistently better than after turning. Furthermore, axis-orthogonal turn-milling offers advantages to compensate tool wear by shifting. Also axial positioning inaccuracy can be compensated in the same way. The chip geometry can be rated as uncritical, similar to the axis-parallel turn-milling process, because only short chips were generated. The limits of the axis-orthogonal turn-milling are currently not reached for the used tool concerning topography, chip geometry and process forces.

WP2/3 IW- Construction, assembling and startup of a MIAB welding test rig / Determining and optimization of material characteristics:

WP2.1: The individual assembly groups were designed and the MIAB test rig was constructed based on calculations in WP1.

The FEA simulationsoftware ANSYS^{TM}

In parallel to the production part, magnetic field simulations of the coil system have taken place using the ANSYS^{TM} software. The simulation minimizes the development effort and supports it. The qualification of the results took place basing on measurements with a magnetometer on real component parts.

For the exact coil design, an analytical calculation is not sufficient, since statements are only possible in the homogeneous field region. The field orientation and field strength can only be studied and visualized sufficiently with a magnetic field simulation based on the finite element analysis (FEA). The FEA is a widely used, numerical calculation method that is used to describe and check physical phenomena mathematically. At the Institute of Materials Science ANSYS is already successfully used for the simulation of steel quenching behaviour. It is a so-called general-purpose program that covers a wide range of applications. Its applicability is to be investigated. The results from the magnetic field simulation contain the visual representation of the orientation and the field strength of the coils.
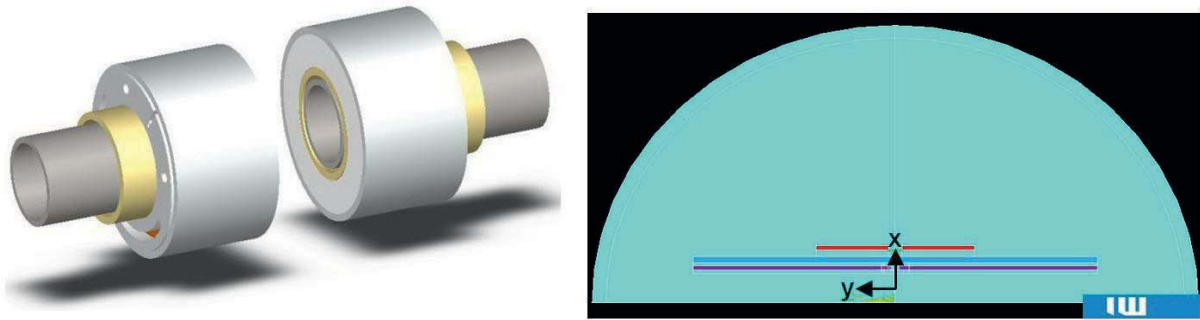
Fig.13:Basic coil design (left) and FEA simulation model (right)
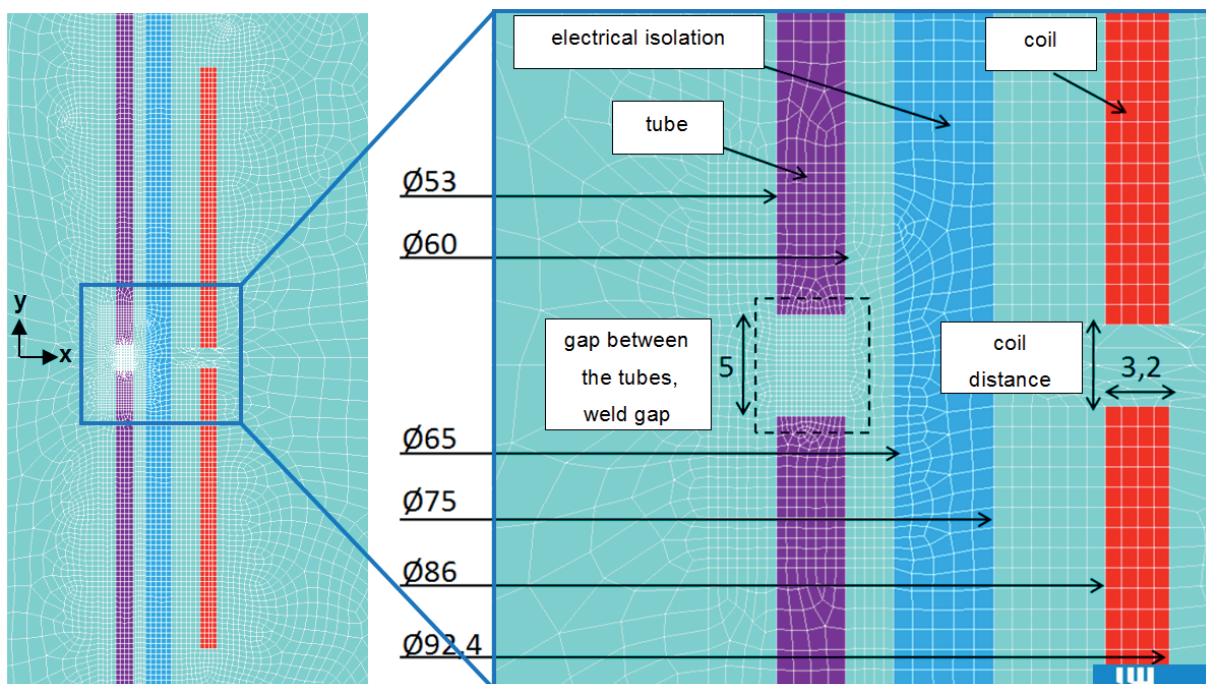
Fig. 14: FEA model and geometry of the components in mm

Figure 4 shows the concept's realization with the preprocessor. It was modeled only one half of the geometry. The y-axis represents the axis of rotation of the axial symmetry modeled elements. All results presented in this chapter are to reflect on this axis to visualize a complete structure section. Fig. 14 shows an enlarged detail of the model with already meshed elements.

The coils poled inversely. This serves to concentrate the magnetic field between the pipe-joint surfaces and to increase the magnetic flux density. The model has been rotated by 90°. This is of great importance for the solver. For a correct calculation of the results, the vertical axis (y-axis) must be defined as a rotation axis when using axisymmetric element properties in a 2D analysis with ANSYS. To rotate the 2D model around the symmetry axis, and thus to simulate a real 3D geometry, it was thus possible to generate only half of the 2D model. For

this purpose all related elements were modeled with axially symmetric properties. In table 1, the output parameters are displayed, which were used for the model generation.

Parameter /Variable	Value	Abbreviation
arc length	$5\ mm$	l_L
coil windings	70	n_S
coil current	$10\ A$	I_S
current density per coil	$3{,}24\ \dfrac{A}{mm^2}$	j_S
coil distance	$10\ mm$	d_S
cross-link density of the elements	0,001	meshfakt

Tab. 1: FEA model parameters

Magnetic flux lines and magnetic vector potential

Figure 6 shows the model's arrangement of magnetic flux lines, and an enlarged detail in the region of interest between the tube and coil end faces.

Inside the tubes, the low resolution can be seen. However, already here the course of the magnetic flux lines can be detected. They are attracted and absorbed by the tubes acting like coil coresand pass inside the tubes densely crowded towards the center, leaving the end surfaces again. Symmetrically to the reflection axis between the two coils, the magnetic fields repel in opposite directions. Then they extend outdoors around the coils and return back to the tube's rear sides again. Inside thetubular components area, the concentration of the vector potential is negligible. This is due to the coil cores effect of the tubes with high magnetic permeability which absorb the magnetic field.
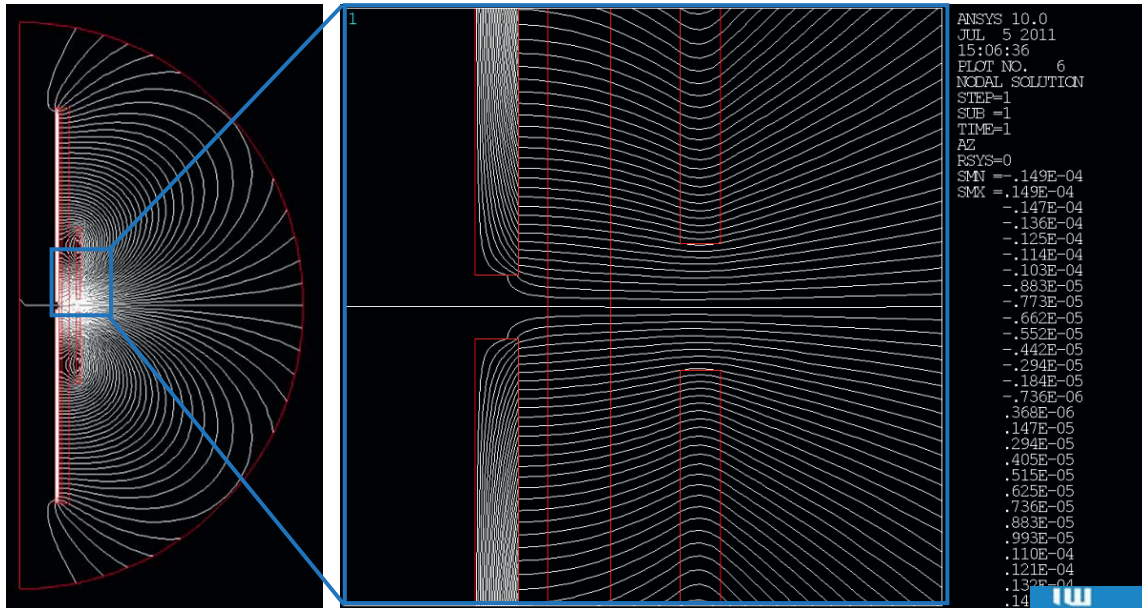
Fig. 15: Flux lines of the FEA model
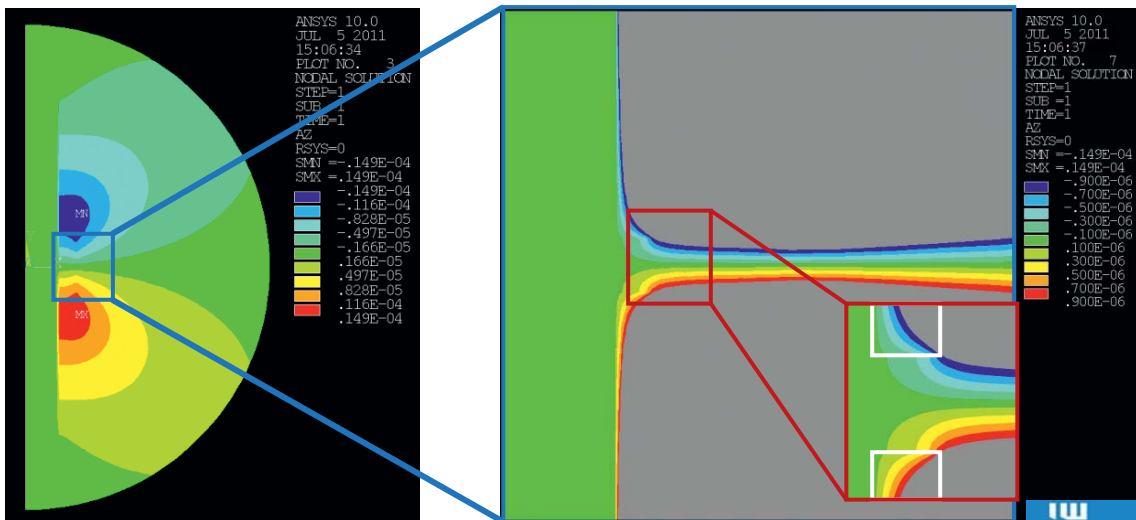
Fig. 16: Magnetic potential of the complete model

The graph on the right side of fig. 16 is shown in an adapted resolution and shows a greatly enlarged section of the arc area. In the zoomed view the components to be welded are shown as white frames. One can clearly see the exit of the flux lines from the tubular end faces and recognize the change in direction and the straight-line path to the outside.

Magnetic flux density

The distribution of the magnetic flux density was calculated for this concept too. The vector course in fig. 17 can be seen for the overall model.

641
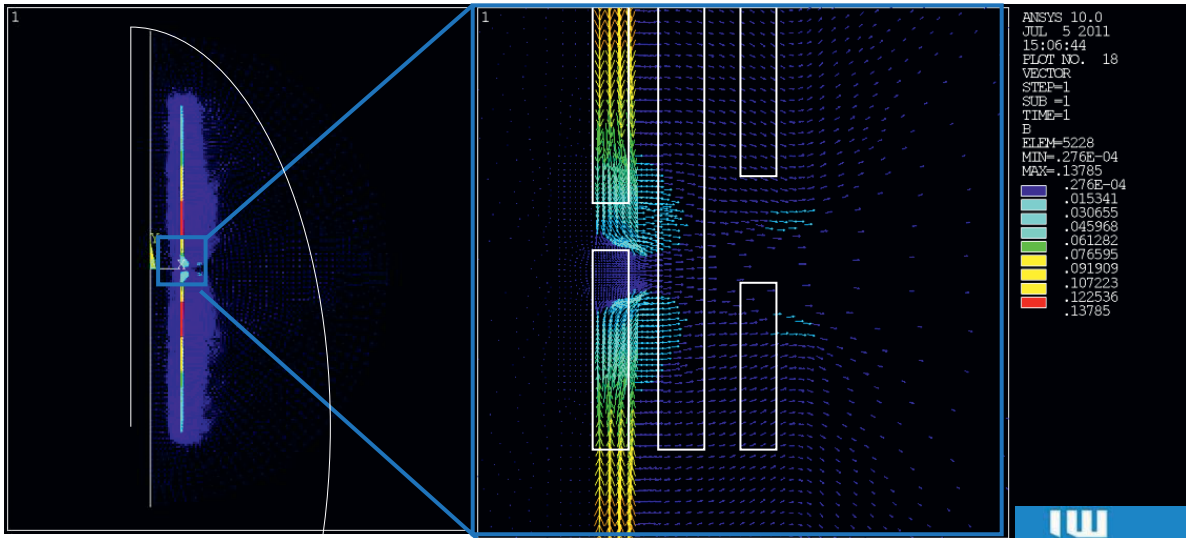
Fig. 17: Vectors of theflux densityin the entirerange of values

It is clearly visible that the magnetic flux density amount increases within the components and decreases after emerging the air space. The area in the arc region is enlarged in fig. 18.
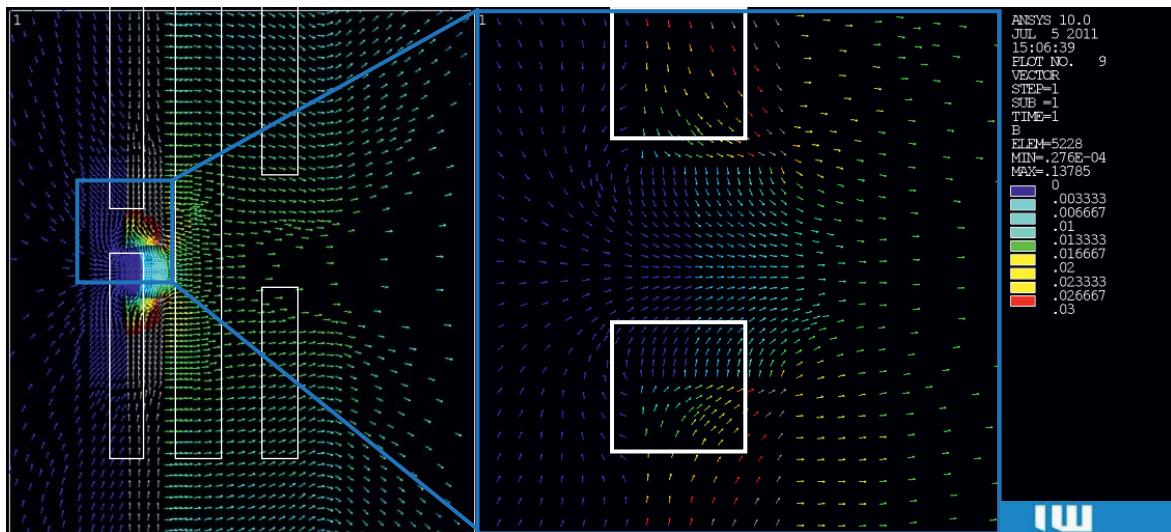
Fig. 18: Vectors of theflux density(0T bis 0,03T)

It clearly shows the desired course of the magnetic field vectors straightly crossing the arc from inside out. The emerging vectors exiting perpendicularly out of the pipe ends get deflected at 90° already within a distance of about 1 mm. The orientation of the magnetic vectors in the arc region can be calculated from fig. 18. For presenting the relations in the arc region more accurately, the magnetic flux density amounts have been evaluated overall and in radial direction according to the arrangements shown in fig. 19.

642
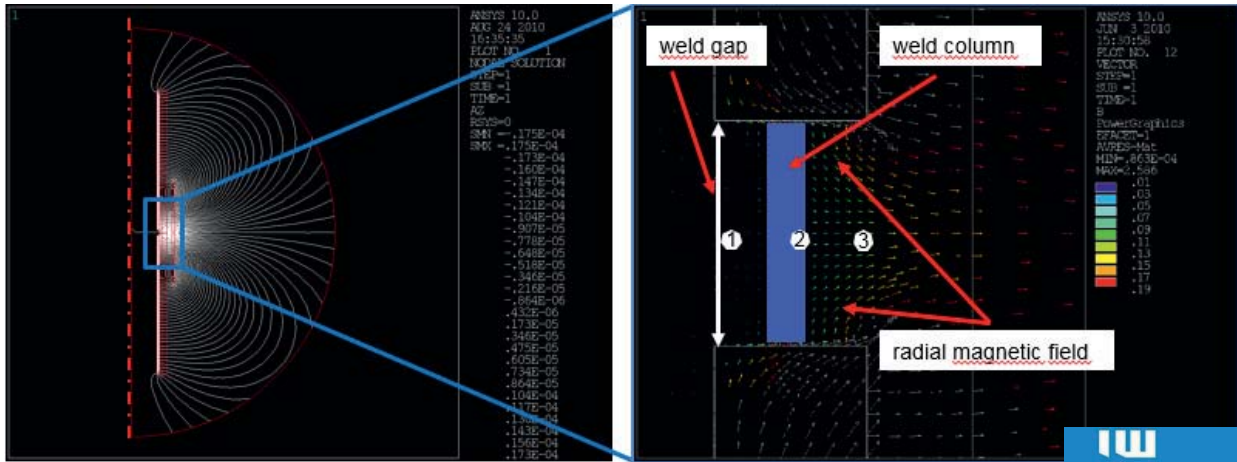
Fig. 19: Symmetrical base model of magnetic field lines and orientation in the weld gap

Three virtual measurement points have been moved in the welding gap (fig. 19). The values of magnetic flux density in sum (B_{SUM}) and in radial direction (B_X) were applied over the path (fig.20). Using the analytical calculations (WP1) and the FEA-calculations of inhomogeneous magnetic fields based on ANSYS it was possible to develop the required magnetic field formers for the MIAB welding process.
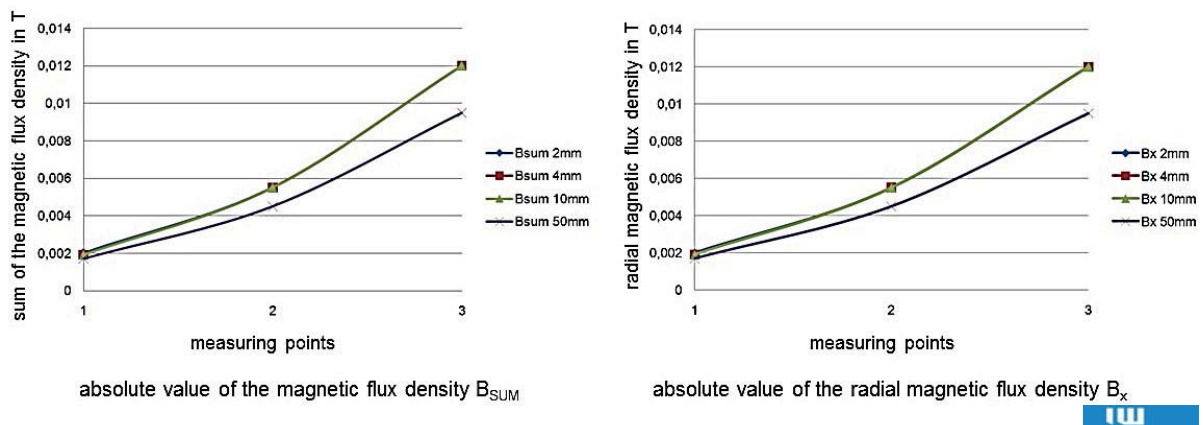
Fig. 20: Analysis of the magnetic flux density in the welding gap

The fundamental construction of the machine consists of the coil system, the work holding device, the hydraulic moving unit, the welding current source and the measuring and regulating systems. Furthermore the electric connections and hydraulic pipes were adapted and it was made sure that the assembly groups are isolated thermally and electrically from each other. The test rig is shown in figure 21.
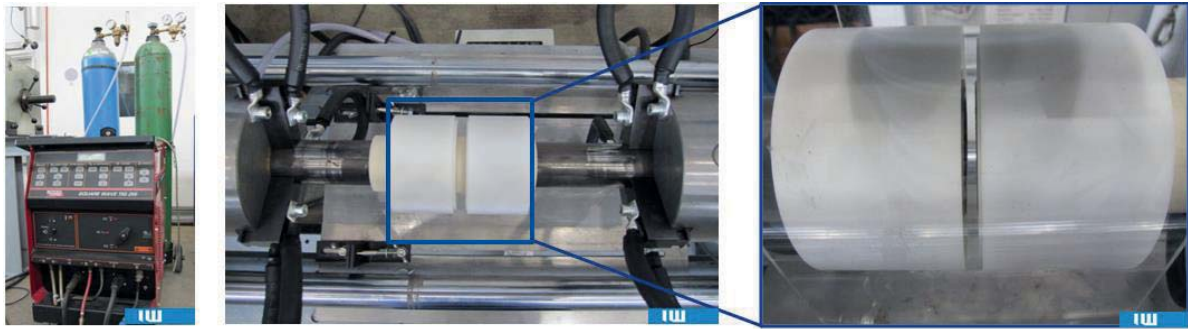
Fig. 21: Test rig Version 1
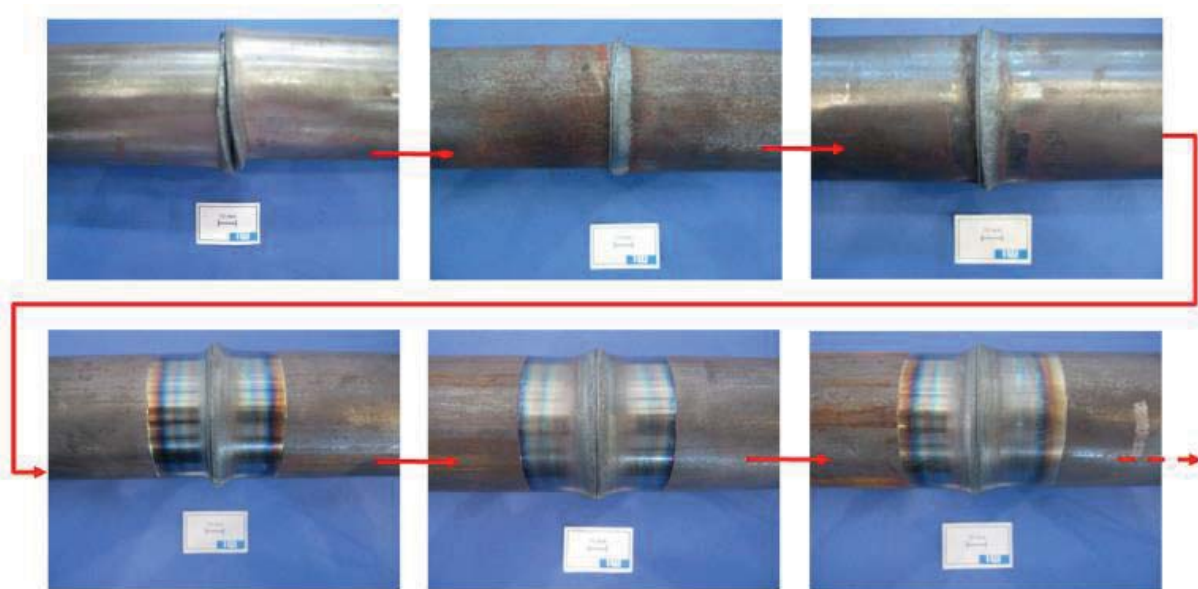
Fig. 22: Results ofthe first welding tests, material P235GH

WP3.1: The welding tests of the first MIAB rig version (WP2.1) showed significant displacement and lack of fusion in the weld (fig. 23).

Figure 23 illustrates typical microstructure composition of the welded joints. The welding seam has a martensitic structure with shares of bainite. The heat affected zone and the base material are ferritic / perlitic.An H_2-analysis of the weld has been performed to exclude possible hydrogen embrittlement by the shielding gas. The results of the studies show no indicating values for possible embrittlement. The measured values of the base material even exceed that of the welds (tab. 2).
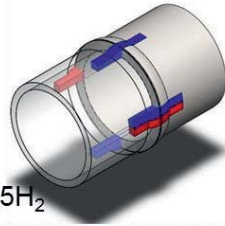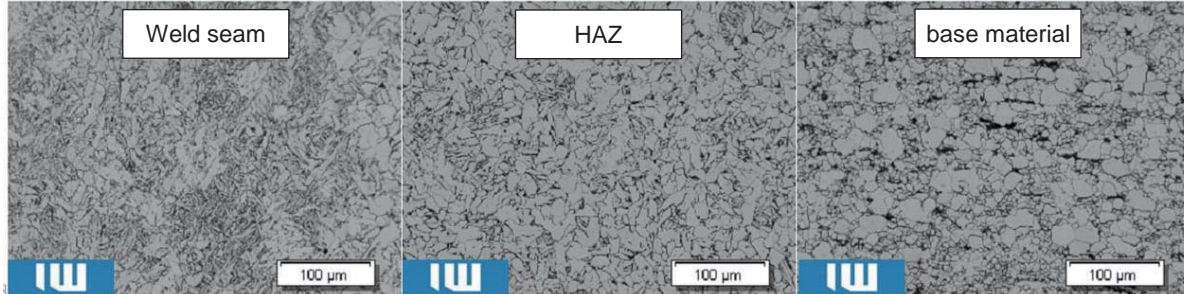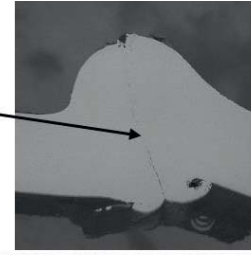
Fig. 23: Welding parameters and cross-section structure image of the weld seam

	base material	weld seam			
		specimen 1	specimen 2	specimen 3	specimen 4
hydrogen in ppm	8,87	3,66	3,83	2,45	5,00

Tab. 2: H_2-analyse of base material and weld seam, material P235GH

WP2.2: Based on the results of WP3.1, a development of the experimental test rig in WP2.2 was carried out. Focuses were on the optimization of the clamping system (offset minimization), removing the oxide layer or lack of fusion in the weld zone through specific formation of the shielding gas, increasing the compression rate and improving the operability. Figure 24 shows the components of the test rig after implementing the design. In tests, an offset of the welded connection between the tubes was observed. Therefore, an additional clamping at the respective pipe ends with fixed and floating bearing was installed to the existing fixture.

For further investigations, a welding chamber that encapsulates the weld zone is used. This allows an inert gas atmosphere during the welding process.
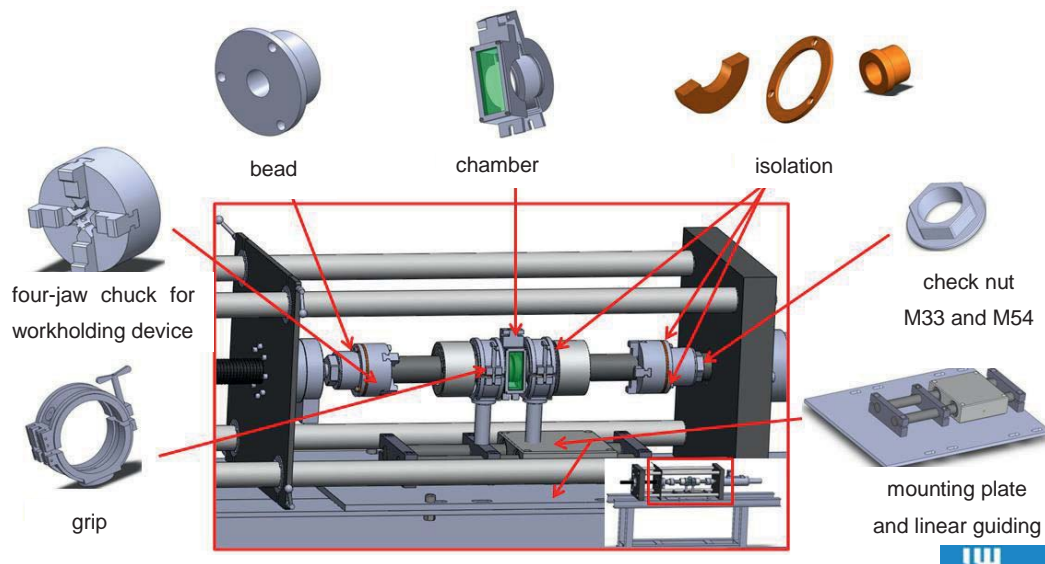
Fig. 24:   Assembly parts in focus of optimization efforts

The installation of a pressure accumulator to the hydraulic valve block and the re-regulation of the control system allowed the enhancement of the compression rate by a factor of eight. For optimum control of the hydraulic system, the controller of the company Doli GmbH was adapted. This can be controlled by programmable flow software.

A more efficient welding power source with up to 1000 A welding current and the time control of different welding currents could be realized by adapting a programmable welding power source from EWM,Tetrix. The system provides the ability to deposit developed programs for the welding job (tube geometry and material) and retrieve.
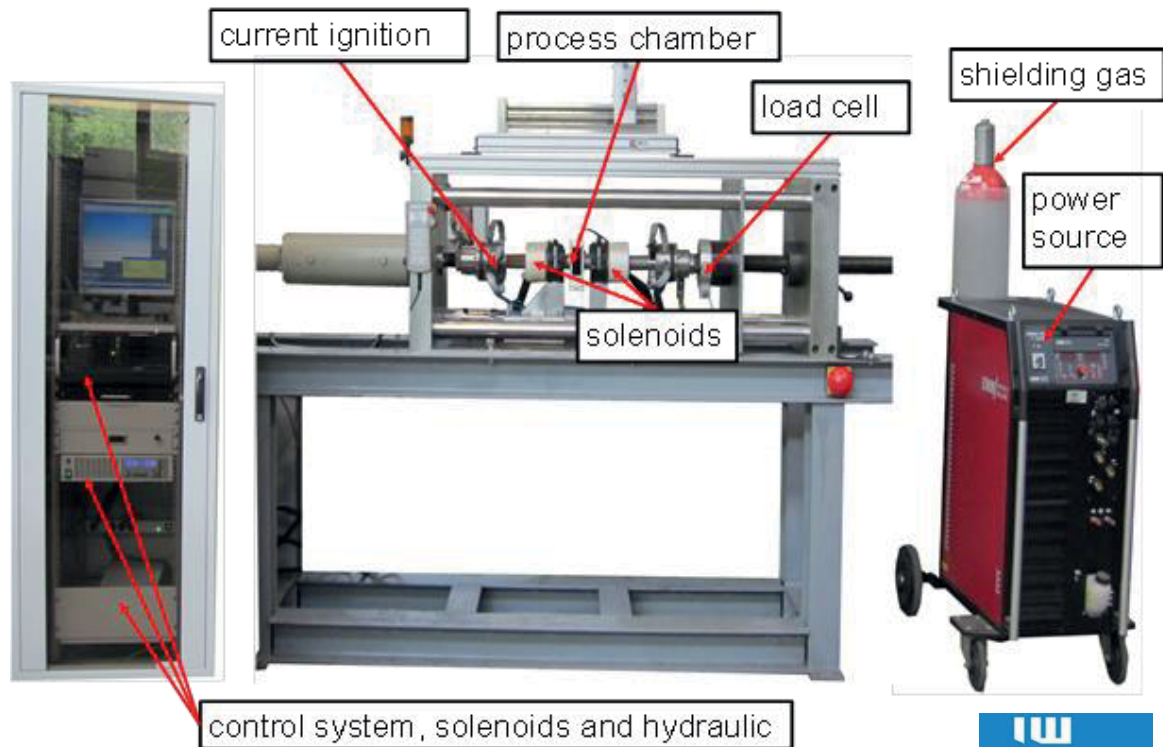
Fig. 25: Assembly parts in focus of optimization efforts

WP3.2: In this work package the investigation of the implemented design changes in WP 2.2 have been made. Another point is a suitable formation of preventing scalings and notches in the connection. For the formation a gas ring or a welding chamber was used.
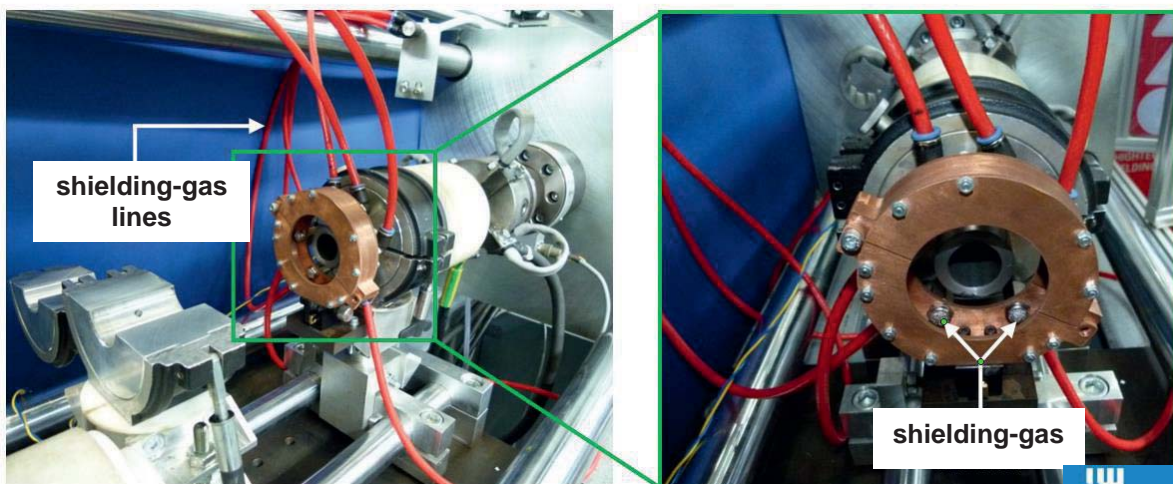
Fig. 26: Formation with shielding-gas ring
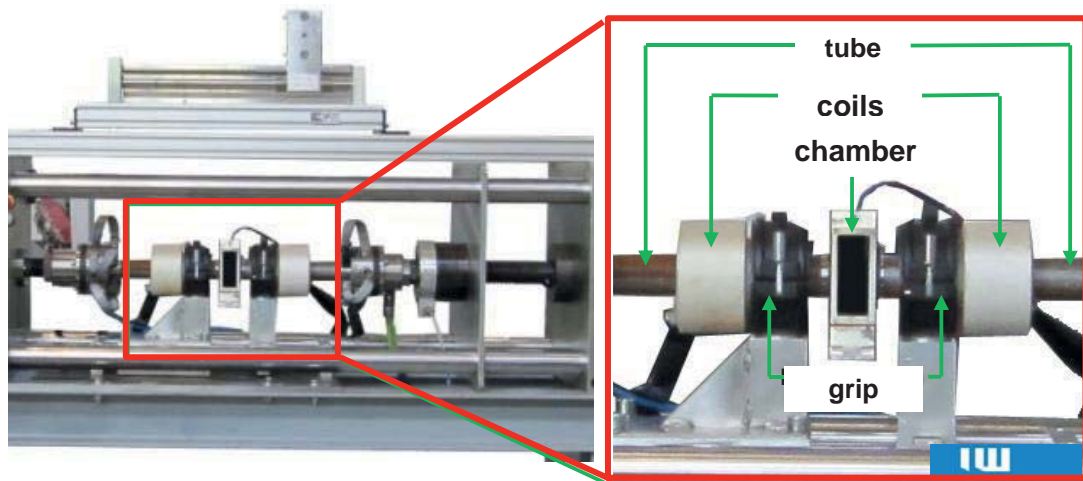
Figure 27: Shielding-gas formation with a chamber

The shielding gas was initiated from outside or inside. The results of the welds are shown in fig. 28 – 30.Here welding with welding chamber and inner formation have achieved best results.Itprevents scaling on the surface and ensures a smooth arc rotation. Other advantages of this shielding gas formation show the macrosection images in unetched condition (fig. 30). It becomes clear that welding with process chamber prevents oxides in the joint zone and possible notch effect can be minimized by an unfavorable weld shape.
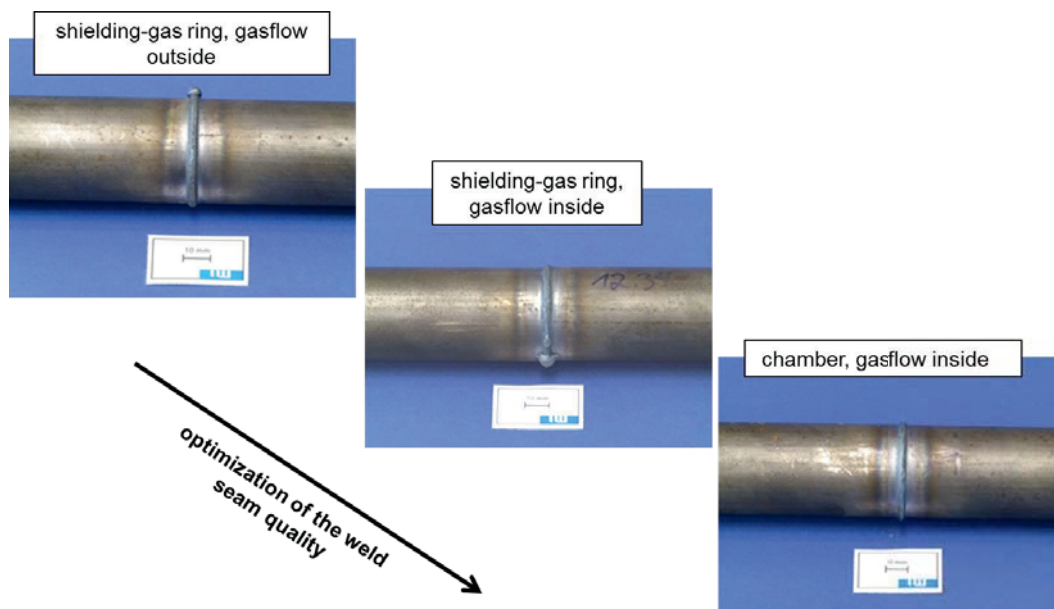
Fig. 28: Results of the welding tests, material J55
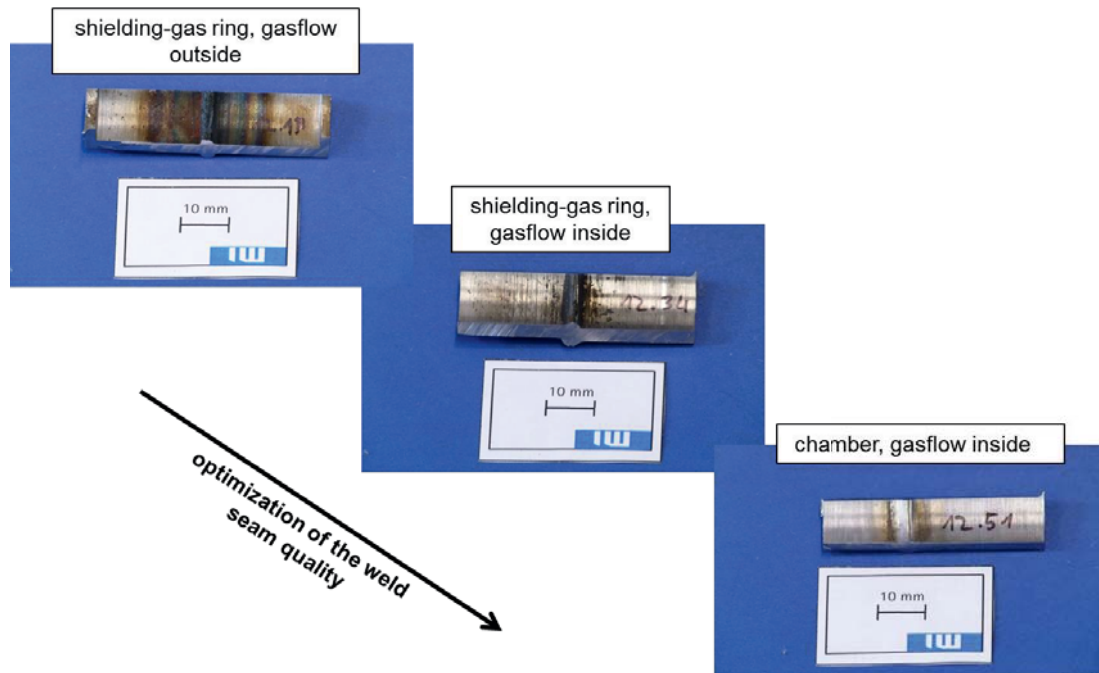
Fig. 29: Results of the welding tests, inside view, material J55
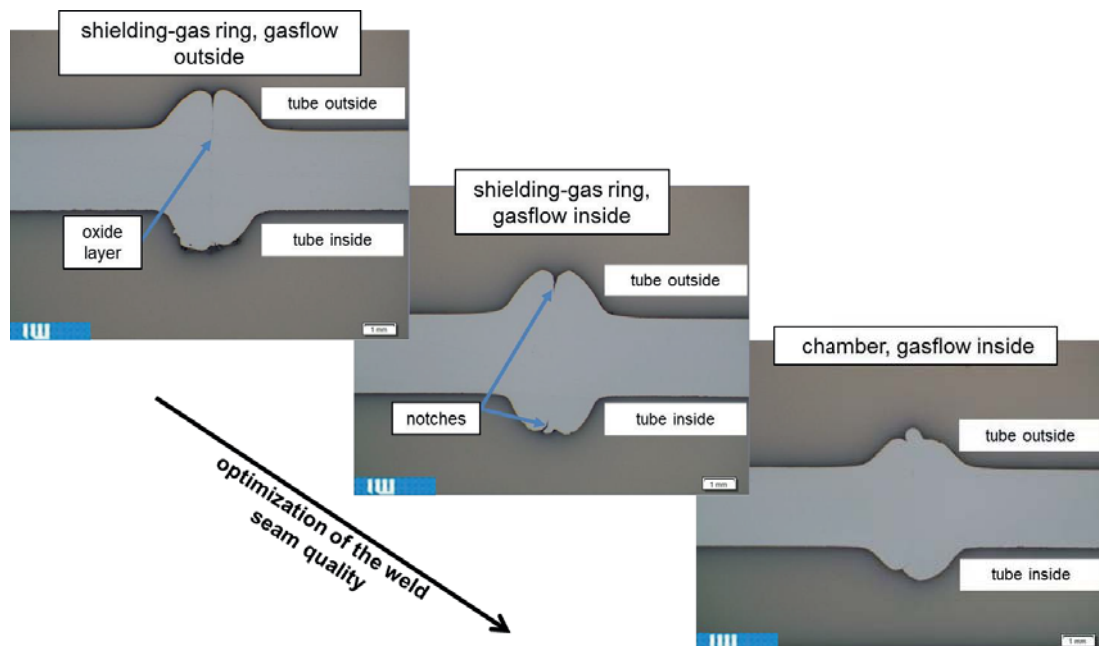
Fig. 30: Makrosection image of the weld seams, unetched, material J55

Metallographic examinations of the weld also show a weld without fusion defects and inclusions (fig. 31). The heat affected zone has a ferritic-pearlitic structure.The weld has a mixed microstructure of ferritic-pearlitic and bainite-martensite structure. The weld bead is primarily martensitic.

649
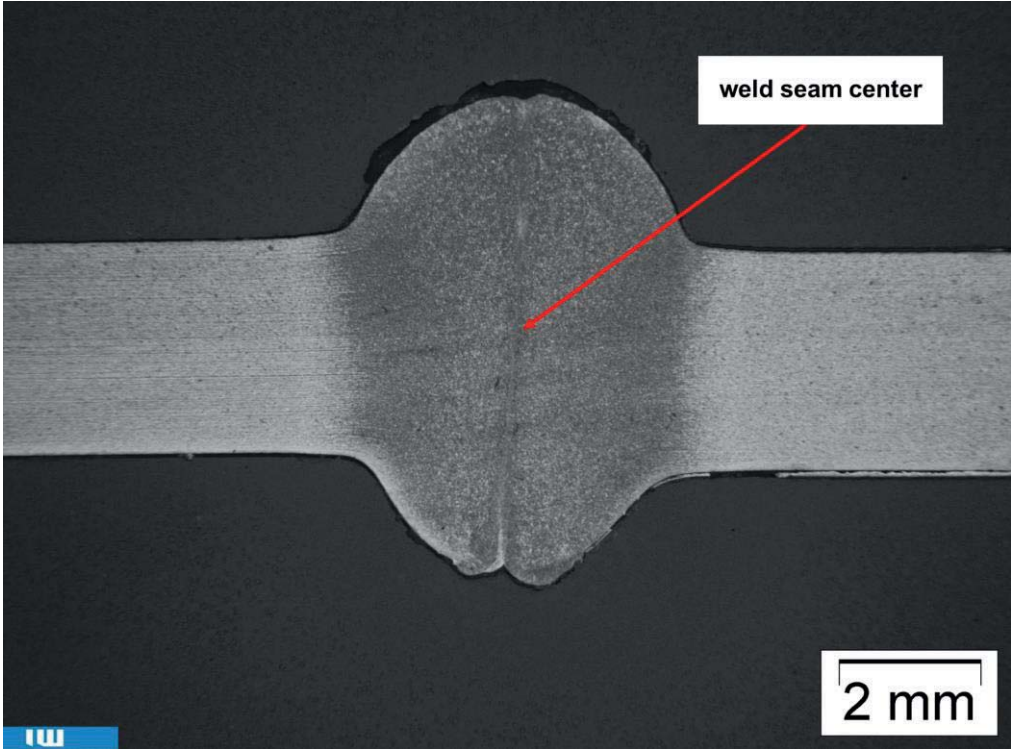
Fig. 31: Structional image of the weld seam, etched with 2% HNO_3, material J55
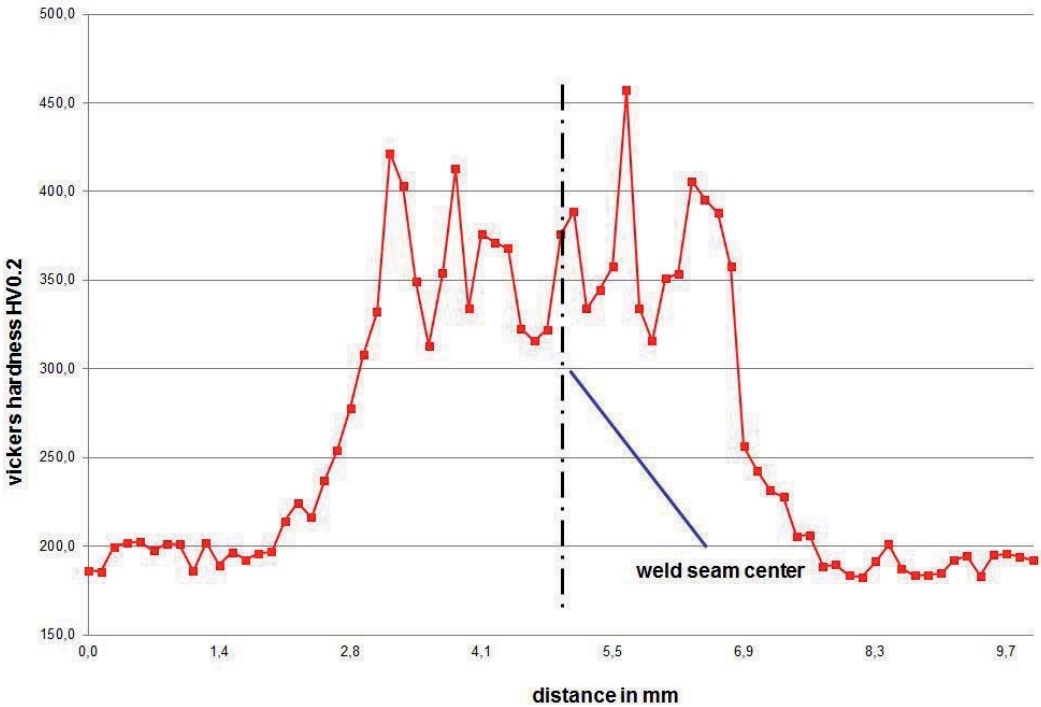
Fig. 32: Microhardness test of the weld seam, Vickers HV0,2, material J55

The micro-hardness tests (Vickers) of welded joints show a basic hardness of 190HV0,2. The hardness of the weld in arithmetic average is at about 380HV0,2. The hardness values

650

scatter strongly and confirm the mixed structure already shown in the metallographic investigations in the weld.

For further experiments an automation of the welding process is planned. This ensures the reproducibility of results and transfer to the industrial application.

WP 2/3: IFW: Process selection an designing/ Qualification of the removal process and designing of a machine tool

Process selection

Based on the experimental investigations for turning and milling of the tubulars, a comparative matrix for possible maching processes was created. Closely followed by turning, the axis-orthogonal turn-milling was qualified for the machining of the welding zone. However, during turning the cutting speed is generated by the rotation of the workpiece. Therefore a standard turning process can not be applied to tubulars at the drilling location. For the examinations the cutting tool was rotated around the tubular. The axis-orthogonal turn-milling offers the highest fault tolerance for the positioning of the tool. This applies to the feed direction movement of the tool in axial directon as well as for the movement in radial direction. Both processes enable the machining of a plane surface, necessary for the welding of the tubulars. Nevertheless the generated surface roughness after turning was only slightly better than after milling. The examined machining processes according to DIN 8580 for the machining of the welding zone are rated by the most important criteria (**table 3**).

Tab. 3 evaluation matrix

	turning	Milling Axis-parallel	Milling Axis-orthogonal
time	*short*	*mean*	*mean*
accuracy	*high*	*high*	*high*
costs	*average*	*average*	*average*
material	*tool dependant*	*tool dependant*	*tool dependant*
wear	*average*	*average*	*average*
reliability	*average*	*average*	*high*
chip foramtion	*long, parameter dependant*	*short*	*short*
fault tolerance	*average*	*average*	*high*

Axis-orthogonal turn milling - Tool wear and process limitations

As already shown, the process limits of the axis-orthogonal turn-millig have not been reached. In order to verify the tested process parameter for several cuts, wear test with 25

cuts with an unused tool were conducted. The firtst 20 cuts were assumed for an average drill hole depth of 5000 m, whereby 10 tubulars with a length of 500 m were machined on both sides. Additional 5 cuts were performed for overrun. Here tools of different providers were tested to guarantee a robust process. A low priced tool (milling cutter 1) and a tool of the upper price segment (milling cutter 2) were used. At the beginning the maximum process parameters of the process study were used. In the following the feed was increased up to $f_z = 0.2$ mm. The used milling tool ($z = 6$) showed a stable process behavior up to $f_z = 0.16$ mm. For $f_z = 0.2$ high prozess forces appeared as well as an instable process run. The process forces for the feed rate f_z up to 0.16 mm were at a constant level at every cut. Figure 33 presents the progression of the measured process forces. For each parameter setting an unused tool was used.
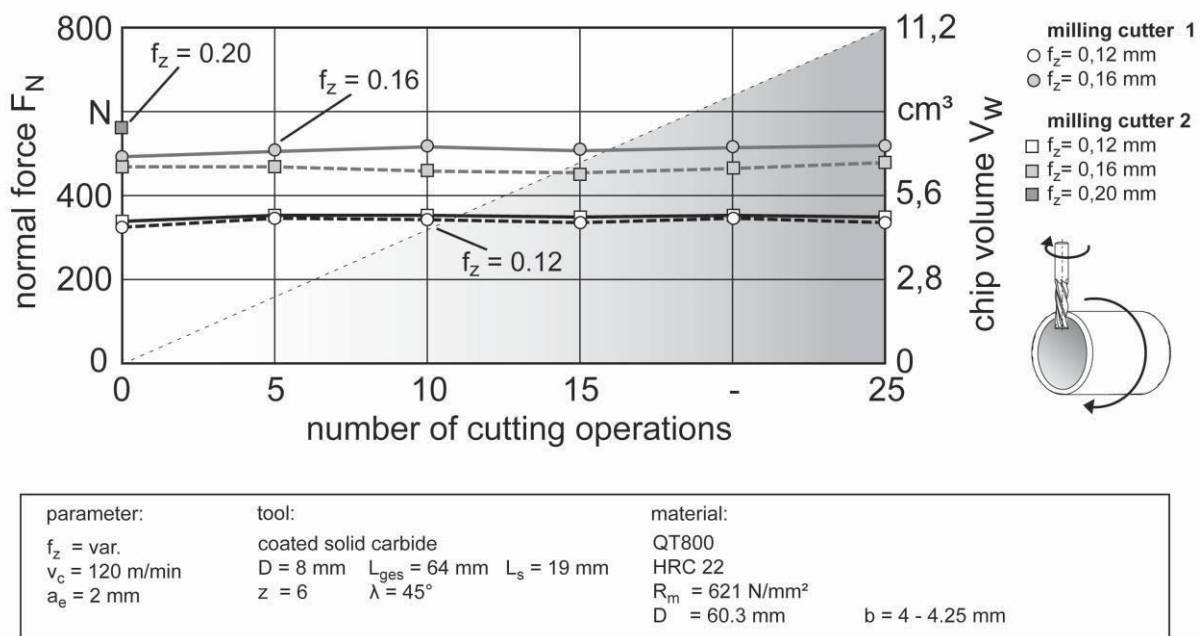
Fig.33 *process force progression for 25 cuts*

For a feed per tooth of $f_z = 0.12$ mm the curve progression of the normal forces F_N for booth tools were on a comparable level of 350 N. By increasing the feed per tooth to $f_z = 0.16$ mm a small deviation of 20 N appeared. With regard to to the process load both tools are suitable. Subsequent to the 25 cuts, the cutting tool wear was examined. Hereby no wear marks were located. A further increase of the feed per tooth to $f_z = 0.2$ mm resulted in higher forces. For this feed the process forces increased in average above 1050 N for machining the welding seam (**fig. 32**). An unstable process behavior appears. Further investigations were carried out with cutting tools with $z = 5$ cutting edges. The feed per tooth $f_z = 0.16$ mm and $f_z = 0.2$

mm were examined as well. The process and wear behaviour is comparable to the results with the cutting tool with z = 6 cutting edges.
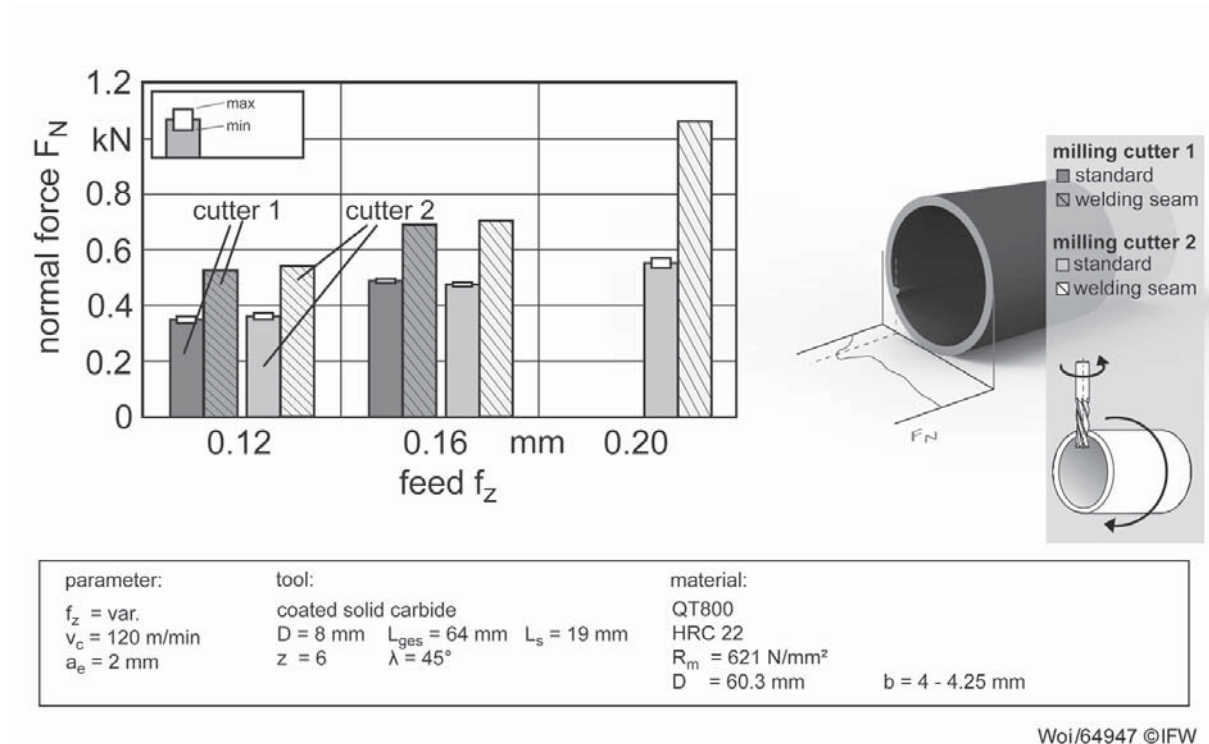
Fig. 32 Normal forces relating to the wall thickness

To identify the influence of the wall thickness of the tubulars, tubulars with b = 3 mm and b = 4 mm wall thickness were machined. For a feed rate of f_z = 0.12 the normal process force is Fn = 380 N for b = 4 mm and for b = 3 mm the process force in average is Fn = 300 N. Increasing the feed per tooth to f_z = 0.16 mm causes a normal process force of Fn = 500 N for b = 4 mm and a process force of Fn = 450 N for b = 3 mm.

The examination of the generated chip geometry reveals a change from short and uniform chips for f_z = 0.12 mm to a short and irregular chip geometrie with various chip thickness for f_z = 0.16 mm. This behavior also indicates a process limit. Metallographic examinations of the machined area show no significant structural change caused by the machining process.

So the used cutting tool is suitable for a feed up to f_z =0.16 mm.

Design of a machine concept

Three concepts for milling machines have been designed by using methodical design. The first concept is shown in Fig. 33. The machine can be assembled to a handling device e.g. an "iron roughneck". The machine clamps at the coil and is decoupled from the handling device. The feed axis moves the tool to the workpiece. With means of the rotational device, the machine moves around the coil while milling it. With changeable tools it is possible to cut the coil and to machine the chamfer for the weld preparation and to remove the joint patch after welding. With changeable powered tools, either the axis parallel turn-milling (use of a changeable tool with right-angled drive) or orthogonal turn-milling can be conducted.
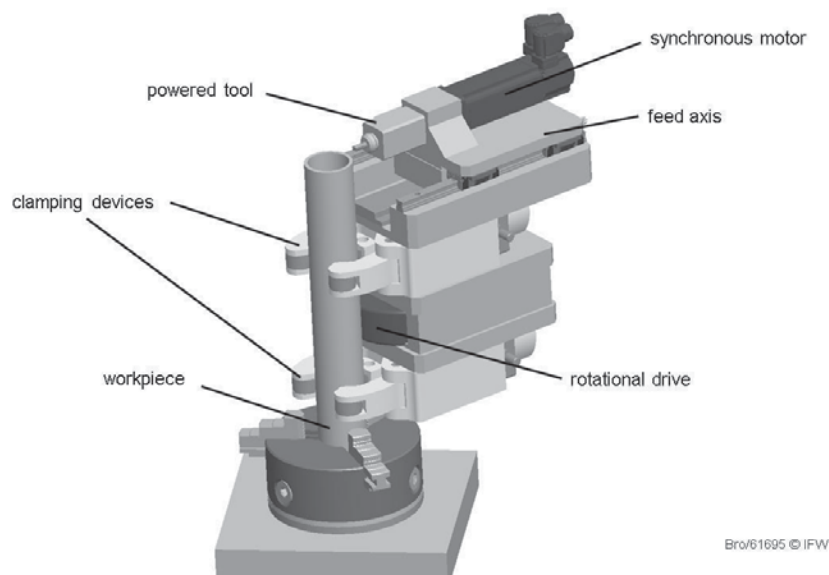
Fig. 33 First machine-concept

In the second machine-concept, which is shown in Fig. 34 a separable welding machine is integrated into the z-axis of the stationary milling machine. The milling machine is able to perform axis-parallel milling for weld preparation as described above. To increase the productivity an additional b-axis was integrated to allow the pivoting of the milling tool. Therefore, only one spindle is needed and the two coils can be machined in one clamping. With this machine kinematic, cutting of the coil cannot be executed because the turning of the coil is not possible. To still enable the cutting of coiled tubing, a circular saw was integrated. This machine allows a very fast cutting of the coil if needed. After the weld preparation of the ends of the work-pieces with the milling tool, the welding tool is positioned between the ends of the coils and the new delivered coil is stationed for welding. The welding process is accomplished as described previously in this report. After welding, the hydraulic cylinders apply the necessary force for the completion of the magnetic arc welding-process. Afterwards, the welding tool is opened and positioned in its home position.
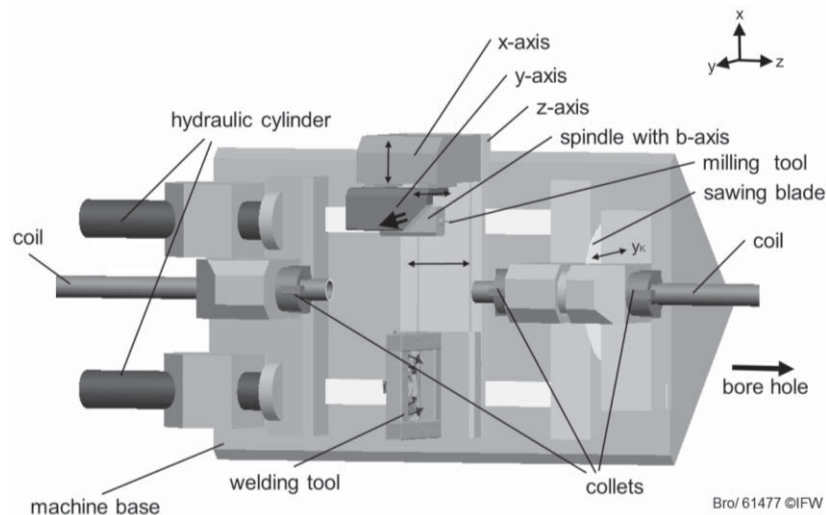
Figure 34 Second machine-concept

The third concept is shown in Fig. 35. In this concept, turrets with multiple powered tools are used. Each turret is moved by means of three linear axes and one rotation axis to position and orientate the tool to the workpiece. With different tools, cutting, removing the joint patch after welding and machining of the chamfers for weld preparation is possible. The figure shows the variant with four turrets whereby a synchronous machining of both ends of the coil is possible.
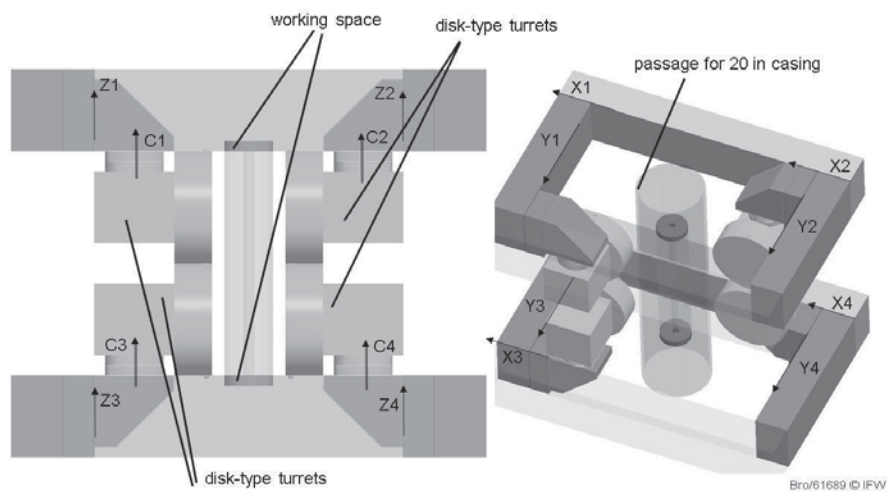
Fig. 35: Third machine-concept

WP 4 *IW* – Processsoptimization and prototype production:

The results of WP2 and WP3 will be implemented into the test rig. This can be used for a requirement profile of the prototype welding-rig.

655

The MIAB system consists of four main control components:

- Hydraulic unit (press force),
- Coil control (magnetic field),
- Welding parameters (welding current power source) and
- Inert gas control.

At timing of system components is required for the later application. This made possible by a master PLC control and programming of sequential control as well as signal processing. For the implementation a Siemens S7-200 controller was used. Programming of signal processing and the user interface were performed at the Institute of Materials Science. The operation of the touch panels consists of four sequential consecutive steps:

1. Task selection (single review of the components / welding test)
2. Entering the magnetic field shaper parameters,
3. Selection of welding program including an arc start monitoring,
4. Control of all launch conditions and release of welding (fig. 36).

Fig. 36: Primary PLC control system

With the implemented control it is possible to weld positive results of WP3.2 reproducible and ensure consistent quality (fig. 37).

Fig. 27: Automated welding process, results of the welding test

WP 5 IW – Validation and conceptual industrial realization:

In this workpakage the results of the previous workpackage will be investigated critically. Critical elements of the machine for the industrial application are determined and approaches for further optimization are developed.

Based on WP2 and WP3, the influence of main parameters could be identified and the weld quality can be optimized.In particular pressing speed, regulations of the gas composition and inert gas flow rates as well as temporal coordination of the four main system components (WP4) are important. The industrial classification of the different materials which are approved by API, further research is necessary. Here mechanical tests such as pressure / burst tests and torsion tests of the welded joint under temperature influence are required. The points above recommended to be developed with industry or in a research project after the projekt's ending.

An encapsulation of the weld zone is furthermore required, due to explosion risk on the rig. At IW the design of a welding process chamber was developed (fig. 38). This allows a transfer into industrial applications.
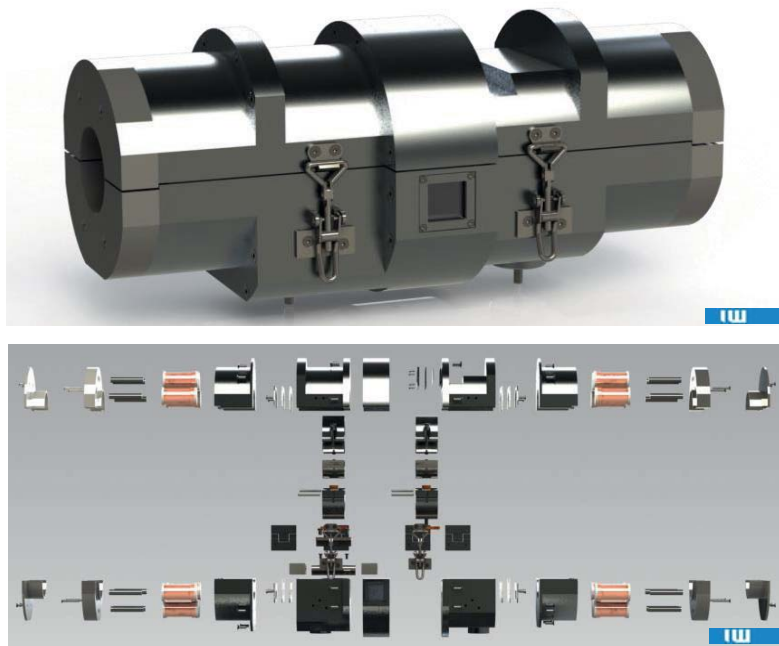
Fig. 38: Design of the welding process-chamber

2.4   Project Plan

Work packages and milestones		2009		2010		2011		2012		2013		2014	
WP1	Conception	▬											
	Study of the process	▬											
WP2	Assembling and machining of welded pipe connections		▬	▬									
	Process selection and designing			▬	▬								
WP3	Determining and optimization of material characteristics				▬	▬	▬						
	Qualification of the removal process and designing of a machine tool					▬	▬	▬					
WP4	Processoptimization and prototype production						▬	▬	▬				
	Prototype realization								▬				
WP5	Validation and conceptual industrial implementation										▬		

3 Delineation of the project from other funded projects

At present at the Institute of Materials Science and at the Institute for Production Engineering and Machine Tools of the LUH no projects are executed which are connected with high performance drilling technology. The applied project is not affected by any planned or running projects.

4 References

[1]   Hagmann, Gert: *Grundlagen der Elektrotechnik*, 11. Auflage, AulaVerlag, Wiebelsheim, 2005

[2]   N.N.: *http://www.brinkmann-du.de/physik/sek1/ph09_04a.htm*, 2009

[3]   N.N.: *http://www.lmtm.de/PhysiXTM/elehre/bilder/ms4.jpg*, 2009

5 Publications, reports and presentations of Project W5

[4]   Rosen, S., Varahram, A., Möhring, H.-Ch., Hassel, T., Denkena, B., Bach, Fr.-W: Der Forschungsverbund Geothermie und Hochleistungsbohrtechnik, Teilprojekte B3, W5 und W6, Journal: Geothermische Energie, 2010

[5]   Varahram, A., Hassel, T., Bach, Fr.-W.: Schweißparameterfelderfür Coiled-Tubing Werkstoffe, Report: Milestone I, 2010

[6]   Denkena, B., Behrens, L.: *Projekt W5 – Werkstoff, Schweiß- und Bearbeitungstechnik beim Tiefbohren.* Meilensteinbericht M1, 2010

[7]   Varahram, A.: *MBL-Versuchsstand zum Verschweißen von rotationssymmetrischen Bauteilen,* Jour-Fixe, Celle, November 2010

[8]   Bach, Fr.-W., Denkena, B., Behrens, L.: *Werkstoff, Schweiß- und Bearbeitungstechnik beim Tiefbohren. Prozessauslegung und Kraftmodellierung beim Drehen,* Jour fixe Werkstoffe, Projekt gebo W5, Celle, 2010

[9]   Bierbaum, M.; Varahram, A.; Hassel, T.: *Computerised analysis and optimisation of the MIAB-Welding process with the ANALYSATOR HANNOVER*, Joint Intermediate Meeting of IIW Comm.IV, XII and SG212. International Institute of Welding, IIW. Bundesanstalt für Materialprüfung, B. A.M. Berlin, 19.04.2012.

W6: Design of Folded Tubulars for Casing Applications

1 Project Overview

Speaker and lead university or research institution

Project Nr.	Title	Subject of research	Project leader, institution, location
W6	Design of Folded Tubulars for Casing Applications	Material-, joining-, automation- and conditioning technology	Prof. Dr.-Ing. habil. Dr.-Ing. E. h. Dr. h. c. Fr.-W. Bach, Prof. Dr.-Ing. H. J. Maier LUH (IW) Prof. Dr.-Ing. B. Denkena, LUH (IFW)

Participating institutes and institutions of the University and external institutions in:

- Institute of Materials Science (IW), Leibniz Universität Hannover
- Institute of Production Engineering and Machine Tools (IFW), Leibniz Universität Hannover

List of participating scientists and engineers:

Name	Subject area	University institute or non-university institution	Position is financed by gebo funds (indicate with X)
IW: Prof. Dr.-Ing. habil. Dr.-Ing. E. h. Dr. h. c. Fr.-W. Bach	Materials science	IW	
IW: Prof. Dr.-Ing. H. J. Maier	Materials science	IW	
IW: Dr.-Ing. Th. Hassel	Materials science/ welding technology	IW	
IW: Dipl.-Ing. A. Varahram	Materials science/ welding technology	IW	X
IFW: Prof. Dr.-Ing. B. Denkena, LUH (IFW)	Production engineering and machine tools	IFW	
IFW: Dipl.-Ing. S. Rosen	Production engineering and machine tools	IFW	X
IFW: Dr rer. nat. habil. B. Breidenstein	Production engineering and machine tools	IFW	

2 Research Program

2.1 Su mmary

Aim of this project is the development of geometries for the production of folded steel tubes for casing applications, which will be unfolded on-site without damage by expansion. Thus a gas proof lining of the wellbore and a stabilization of its wall result. The production of longitudinally welded folding geometries, which allow a multiplication of the external diameter, and their expansion by isostatic pressure inside, a plastic deformation into a tube cross section takes place. The resulting cross section corresponds to the wellbore diameter, so that the lining can be fixed in the well. The development of highly ductile materials, such with strains between 30% and 50%, provides the potential for the application as such linings. Additionally these materials possess high strengths, by what the geothermal circumstances, like the well cavity pressure in case of tectonic destruction, remain within the functional profile. The unfolding concepts, which are to be developed within this project, also possess a high potential for the insertion of the lining in coiled state, in order to obtain longer gas proof sections.

2.2 Relationship of the pro ject to the o verall re search conte xt and networking with oth er projects

A basic aspect of this joint research project is the optimization of the drilling and completion process as well as of the future energy transport through the soil. Adequate analysis and optimization approaches are supported by computer based simulations from project W7.

2.3 Work packages executed relative to plan and results achieved

WP1: IW-Development of geometry and material choice:

During the production of deep wells it is necessary to protect the well against a collapse after drilling a defined section. This is achieved by using steel tubes, called casings and liners, which are lined with cement behind. According to conventional techniques, the well diameter decreases telescope-like with increasing depth, because the new tube has to be fed through the previously introduced casing string. A casing always runs from the surface to the final depth. In contrast, liners are mounted and sealed at the end of the already built-in casing string.

The gebo monobore well is a borehole with a constant diameter along its complete length with the exception of the conductor and surface casing as shown in figure 1. To produce such a well, tubes have to be developed, which can be expanded to a defined diameter after they have been descended into the well. The contoured tubes have the same circumference as the casing set before. Due to the structure they have a smaller diameter than the final expanded size. These

folded tubes are expanded in the well in a two-stage process. First, the tube is hydraulically expanded with an internal pressure and then calibrated with a cone to the final diameter, as demonstrated in figure 1. This procedure allows the realization of a constant diameter from surface casing to the target depth.

Using this method large drilling diameters in the upper area of the well can be avoided. This leads to an increase of drilling speed and less completion work. In producing smaller diameter wells, cheaper drilling rigs and power units can be used. A monobore well construction also eliminates the necessity for the respective drilling equipment of the diverse-sized well diameters.
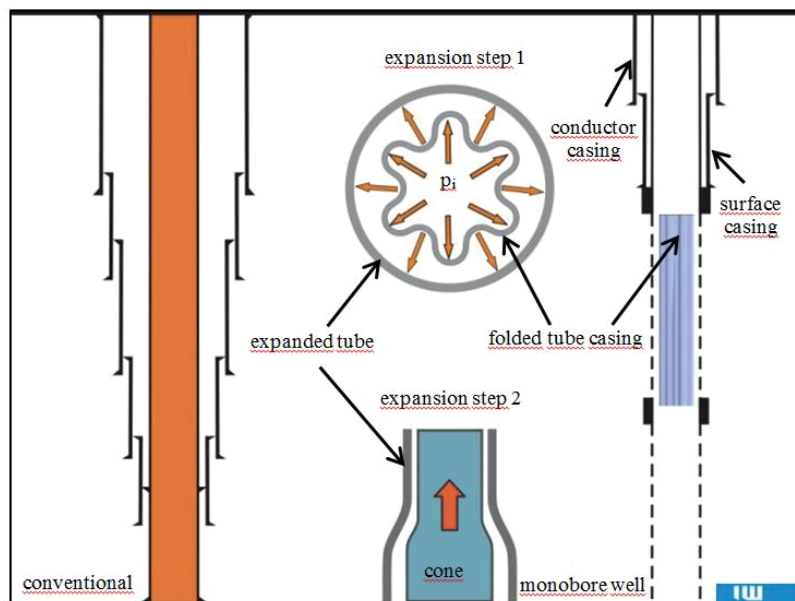
Fig. 1:   Conventional and mono borehole casing design

The first working package includes the development of different tube geometries and the choice or adaptation of materials as well as the examination of their production possibilities. The design of the device for the manufacturing of folded tubes should allow a simple adaption to different geometries. The roll forming to shape offers the best possibility for the production of profiled steel tubes. Another alternative is the production of partially segmented tubes by profiling or hydraulic forming and subsequent longitudinal sealing. Figure 2 shows a first draft representation of a truing-tool. The form of the rolls and the infeed can vary arbitrarily. The deformation applied to the tubes is realized by integration of the device into a tensile–testing machine. Seamless tubes as well as longitudinally seam welded tubes are suitable as base geometry.

663
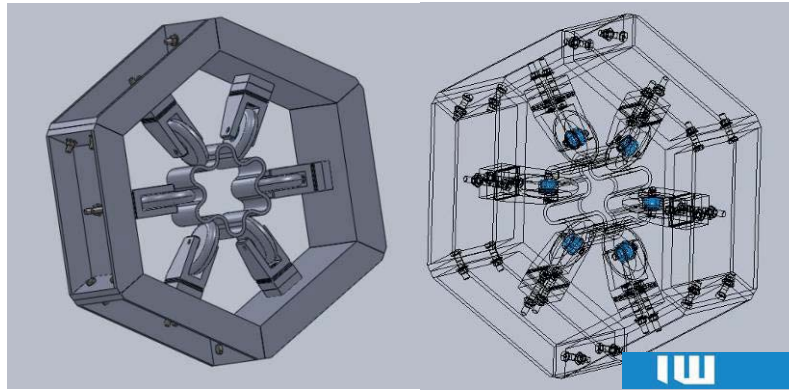
Fig. 2:   Conceptual draft of a truing-tool

Several simple as well as more complex geometries were constructed which were designed to fulfill the purpose of a folded casing. With the help of FE-expansion-simulations a first rating of the form and the material is possible. Based on these findings optimization attempts are executed in further steps. Three geometries have been selected for the first iteration loop (Fig. 3). Here, it was a matter of gaining initial scientific insights from the observation of the expansion or of the developing routine performance. In figure 4 the stress-strain relation of the material properties applied in the simulation is displayed.

The simulations show that the relation of the initial diameter to final diameter after the expansion is too large and the elongations are too small. In a second iteration loop the diameter ratios have been balanced. In the expanded condition the geometries show an outer diameter of D=165 mm. The wall thickness in each case is 6 mm (Fig. 5). These and new material data from highest-strength and -ductile materials were provided for expansion-simulations. The second simulation loop showed locally limited load peaks. A compensation can be made by increasing the wall thickness. The geometries shown in figure 4 are maintained in the third iteration loop.
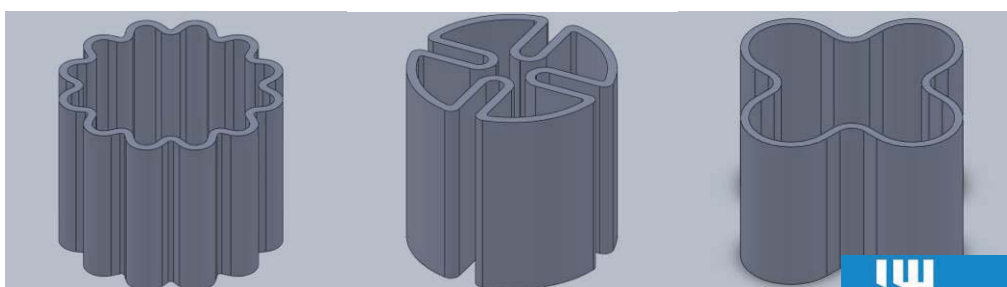
Fig. 3:   First iteration loop: bend geometries
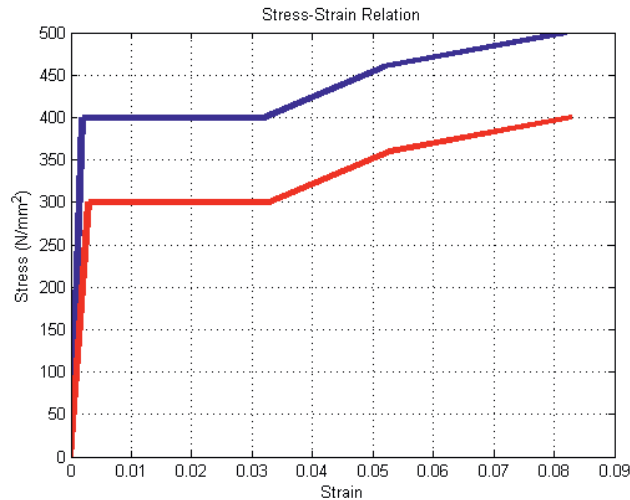
Fig. 4: First iteration loop: Material selection [1]
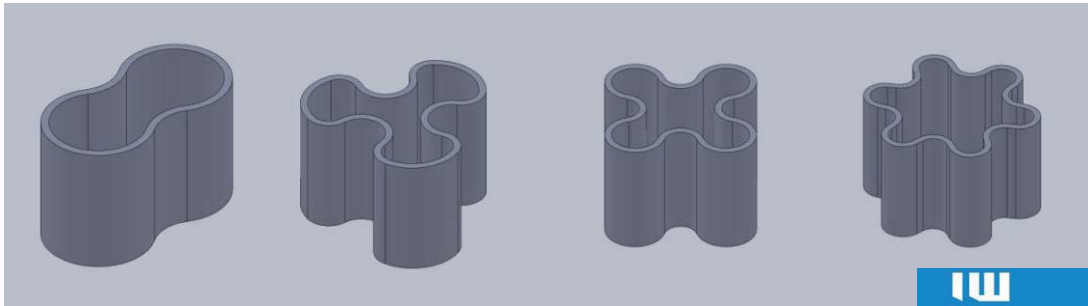
Fig. 5: Second iteration loop: Bend geometries

In the gebo group a new and innovative mono-borehole concept is aimed for. To realize this, foldable casing structures are necessary which can be expanded in the borehole. The first work package of sub-project W6 focuses on geometry development and material selection as well as suitable production processes.

The work for W6 is supported by expansion simulations conducted by IDS-TU Braunschweig. Based on the simulation results it was possible to gain valuable insights and make geometry optimizations as well as material adaptations. A flexible concept for the production of the particular geometries has been developed in compliance with the FE simulations. In the next iteration loop the wall thickness of the tubes will be adapted to the load peaks and other materials will be considered.

665
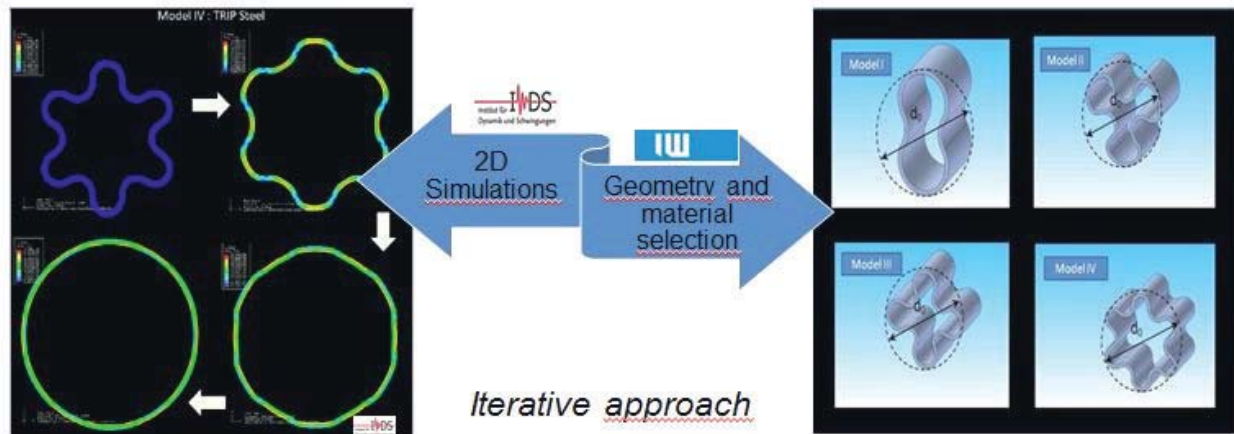
Fig. 6: FE Simulation, IDS Braunschweig

WP2: IW-Construction, assem bly and startup of a test ri   g for the production of folded basic geometries: After the selection of the geometries suitable production methods must be evaluated. The focus of these investigations lies on draw-bending and roll-forming using only separate rolls instead of roller pairs. In figure 7 the possible profiles, the truing tool and a total view are presented including the testing unit.
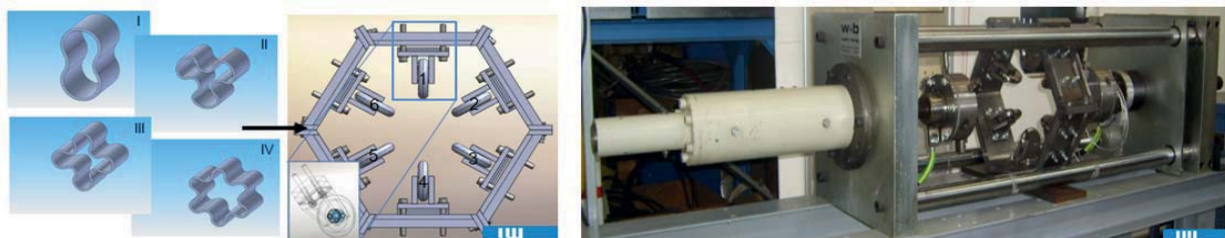
Fig. 7: Basic geometries, truing tool and test rig

The truing rolls are made of cold work steel 1.2379. This material features high wear resistance, ductility and dimensional stability. The source material is delivered in soft-annealed condition. For reaching the desired mechanical qualities of the rolls a heat treatment (tempering) took place. The roll holder consists of three individual parts that are joined by welding.

The production process of the folded tubes is a multi-level forming process. Shims are used for feeding the truing rolls. These are inserted between frame and roll holder. The frame is made up of six partial segments which consist of a baseplate, two side plates and two reinforcing braces. A forming force is required to profile the tubes in axial direction. As drive unit a servo-controlled hydraulic tensile testing machine is used (fig. 8).
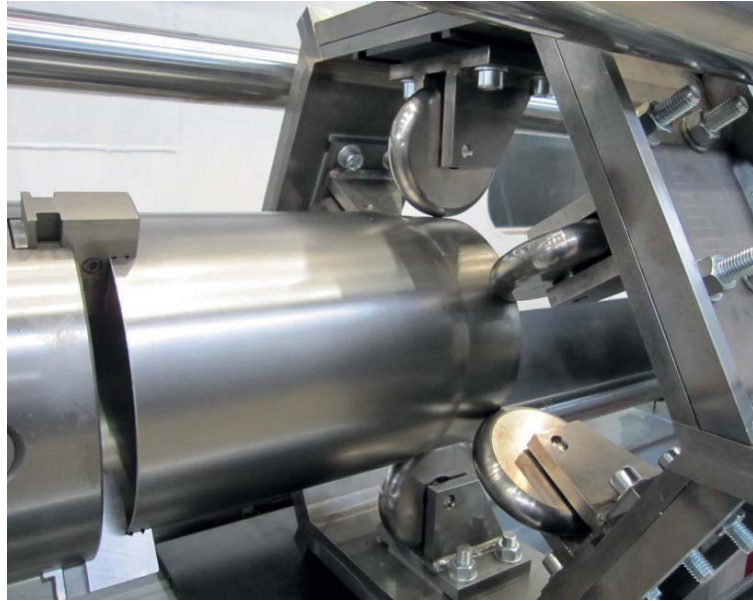
Fig. 8:   Forming process, IW
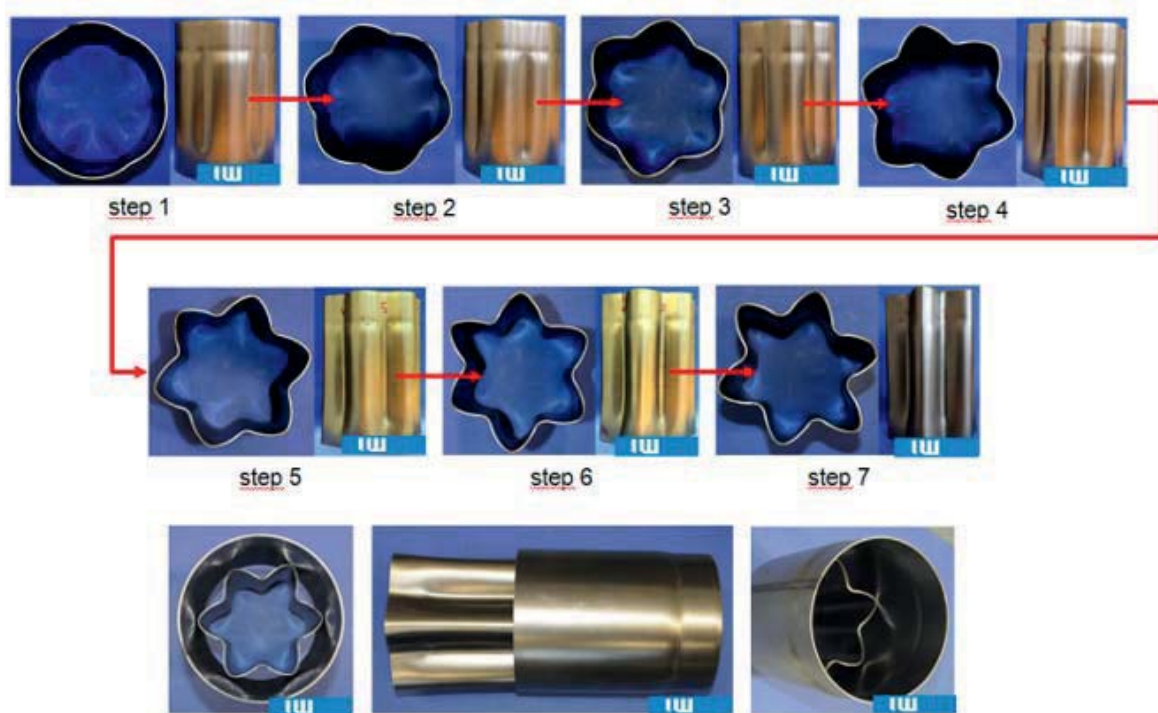
Fig. 9:   Folded tubes

The qualification of the truing tool was realized with thin-walled tubes. For the first folding test tubes with an inside diameter $d_i = 180$ mm were used. The length amounts to 250 mm with a wall thickness of 2 mm. The test tubes consist of structural steel, are longitudinally welded and not heat treated later on. After each profiling step the tube is turned around a roller track in a clockwise direction. The rotation is initiated to compensate possible layout irregularities of the truing rolls. The test results are presented in figure 9. After the tests the truing tool showed no delay or wear effects. Inserting the folding tubes in the initial cross-section was realized after the seventh step with 4 mm of backlash. Form tolerance variations of the folding tubes are due to the tubes themselves (welded longitudinally and not heat treated). The tubes feature an inhomogeneous material behavior and locally different basic stress conditions which are not crucial yet for the qualification of the test rig.

WP3 /IW - Development and assembly of the folding mechanism

For the first investigations a stainless steel, which matches the requirements was selected. This standard steel X2CrNiMoN22-5-3 (1.4462) has a high yield strength of $R_{p0.2} \geq 480$ N/mm^2, an ultimate tensile strength of more than 680 N/mm^2 and an elongation of $A \geq 25\%$ in solution-annealed condition. This material is a high chromium-nickel-molybdenum alloyed steel and is corrosion resistant, especially against pitting, crevice corrosion and stress corrosion cracking. The results show deviations compared to model four. These occur because of the clamping support of the test rig and the alignment of the forming tool.
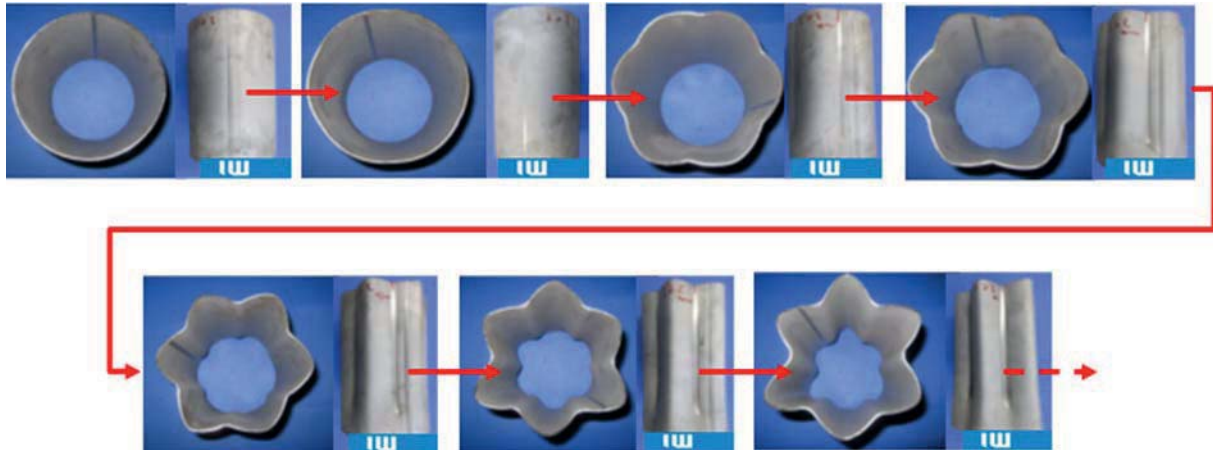
Fig. 10: Folded tubes of model 4, material 1.4462 and wall thickness 2.7 mm

The production of folded tubes by roll forming showed up as a suitable and efficient production method. The folded structures were used for further residual stress analysis of the segments. Manufacturing of folding structures with a larger diameter and wall thickness could not be performed, due to the test rig limitation and project resources.

WPs 1-3 IFW: Residual stress measurements

The first three of these work packages are concerned with enabling existing residual stress measurement techniques to determine stresses at folded and unfolded tubes, as well as during the forming processes.

Residual stresses can shorten or even end lifetime of a compound, especially if tensile residual stresses are existent. In order to avoid tensile residual stresses that endanger the folded and unfolded tubes, it is necessary to know the residual stress state of the tube material at every step of the process chain from the basic material to the unfolded tube.

The chosen method of stress determination is the $\sin^2\psi$ method, realized on an X-ray diffractometer. The chosen equipment (GE XRD 3003 TT) possesses a theta/theta goniometer, so that the investigated specimen does not have to be moved during measurement. The extra large specimen table allows stress measurement also on big samples (Fig. 11).

technical data:

detector type:	position sensitive detector 12°, 4096 channels
goniometer:	
measuring range 2θ:	0 - 165°
min. stepsize:	0.0005°
radius:	170 - 300 mm, variable
generator power:	
high voltage:	2 - 60 kV
current:	2 - 80 mA
max. power:	3.5 kW
res. stress accuracy:	± 10 MPa
max. : specimen size	600 x 600 x 150 mm³
max. specimen weight:	50 kg
measuring range:	
lateral	100 x 100 mm²
vertical	150 mm
positioning accuracy:	
lateral	1 µm
vertical	1 µm

source: GESensing and Inspection Technologies

My/48671 ©IFW

Fig. 11: X-ray diffractometer for residual stress determination

In preparation for bending tests, sheet strips of the grades DC05, DP600 and TRIP700 with a size of 200 x 80 x 1.5 mm³ have been prepared. Before determining the residual stresses, a spot of about 1 cm² in the centre of the sheet surface, where the stress is measured, has been dezincified by electrolytical polishing (Fig. 12). All three grades proved to be residual stress free before bending.

Fig. 12: Specimen for bending tests with dezincified spot in the center

In order to determine the residual stress of the tubes after folding, simplified bending and un-bending experiments are performed with different materials that come into consideration. A typical specimen for this is shown in Fig. 12. The bending is performed parallel to the vertical line. It is achieved by a simple assembly consisting of a prism and a cylinder of 35 mm diameter. A force F works on both ends of the specimen (Fig. 13).

The grade of bending is determined by measurement of the bending angle 2α after load relieving of the specimen. Bending is performed in several steps between $2\alpha = 0°$ and $2\alpha = 90°$, unbending between $2\alpha = 90°$ and $2\alpha = 0°$. After each step the residual stress σ_l is determined transverse to the bending axis. The results of these bending experiments are presented and discussed in the following.

In the initial state the material DC05 is residual stress free. By bending between $2\alpha = 0°$ and $2\alpha = 90°$ a compressive residual stress arises after load relieving as a result of springback (Fig. 14, top). It reaches its maximum of about -80 MPa at $2\alpha = 20°$ and remains constant until $2\alpha = 90°$. During unbending residual stress turns into the tensile range, where at about $2\alpha = 70°$ it settles down at a value of about 80 MPa. This value remains constant until the end of the experiment. Thus, a residual stress hysteresis between -80 MPa and 80 MPa appears. The elastic limit of the material (DC05) is at $R_{p0,2} = 140 - 180$ MPa, so that the danger for a serious damage is not given, yet.
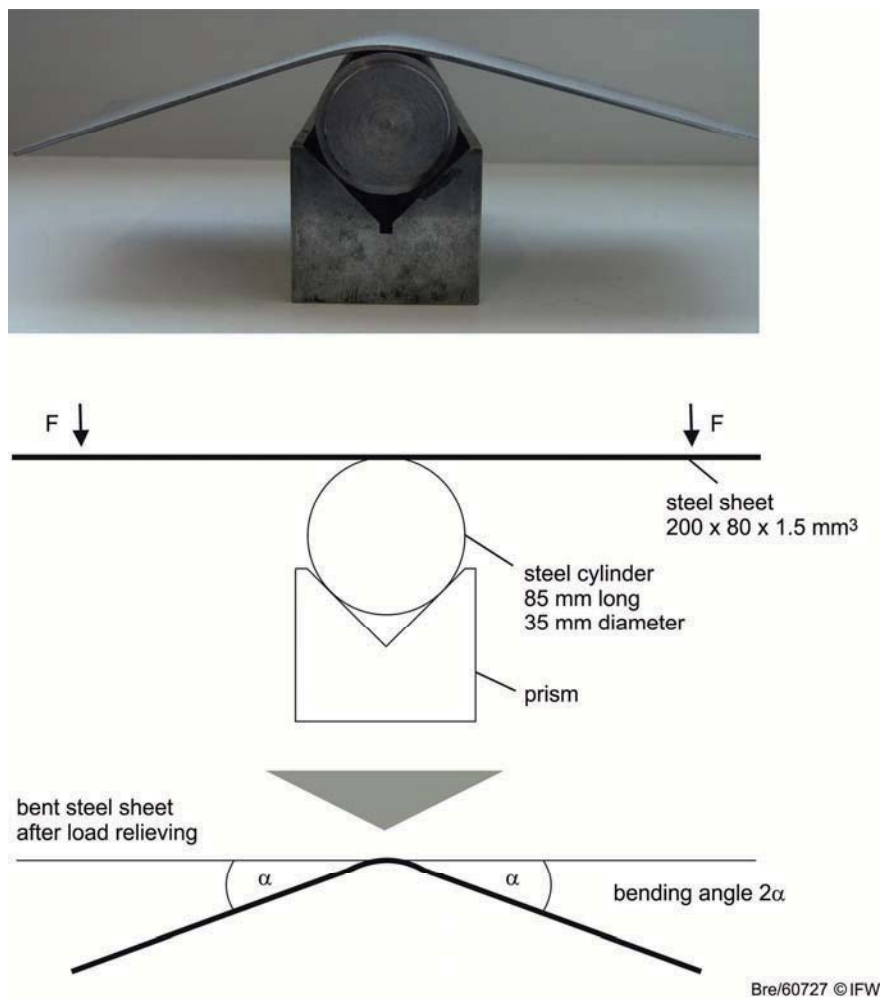
Fig. 13: Simple mechanism for bending and unbending experiments

For the higher strength material DP600 the hysteresis is running between -210 MPa and 170 MPa (Fig. 14, center). With an elastic limit of $R_{p0.2}$ = 300 – 470 MPa there is also no danger for material damage by residual stress.

The same is observed for the third investigated material TRIP700. The hysteresis here exists in the range -230 MPa to 180 MPa. The elastic limit of this material is $R_{p0.2}$ = 420 - 560 MPa (Fig. 14, bottom).

The full width at half maximum (FWHM) of the X-ray peaks contains information on micro stress, which as a result of dislocation density allows conclusions on hardness changes. An enlarged FWHM may thus stand for a greater hardness of the material.

All three materials show an increase of FWHM at the beginning and versus the end of the bending experiments (Fig. 15). A hardness determination HV0.05 confirmed the rise of the hardness during bending (Fig. 16). Depending on the material, hardness increases are +6.2% (DC05), +11.2% (DP600) and +18.4% (TRIP700).
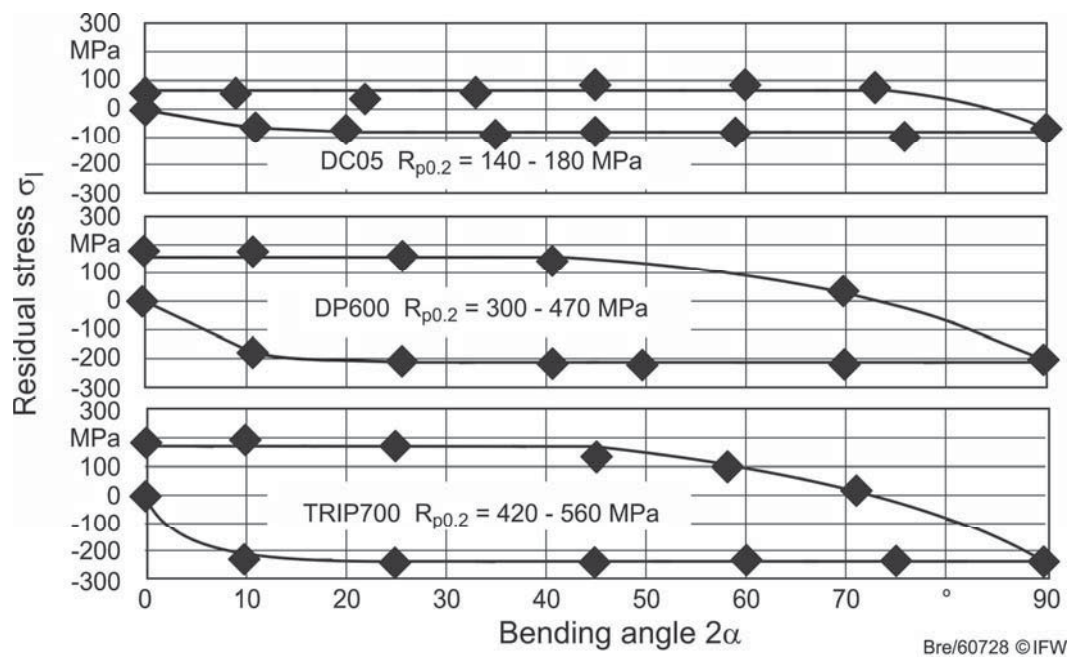
Fig. 14: Residual stress hystereses for DC05, DP600 and TRIP700 as a result of bending and unbending

672
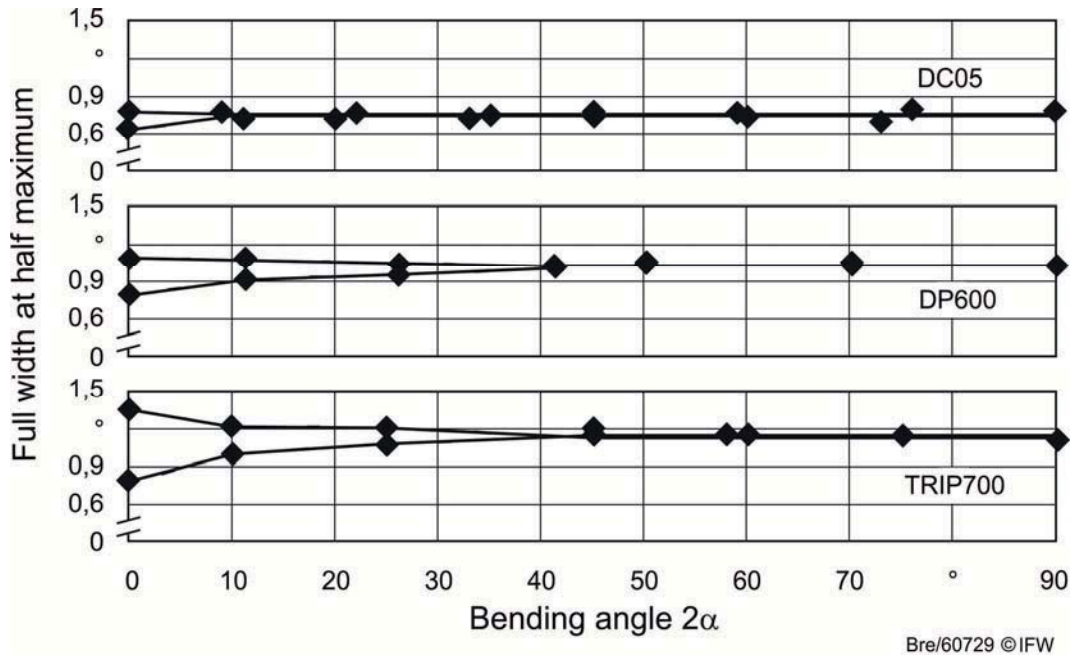
Fig. 15: X-ray peak full width at half maximum during bending and unbending

As the tubes which will be folded and unfolded are welded, analogous specimens with a longitudinal welding seam have been prepared, and the bending and unbending experiments have been performed. The results are presented here from the example material DC05. The specimens have been bent at right angle to the welding seam, and residual stress has been determined in the marked dots 1 to 11 (Fig. 17) after load relieving parallel and lateral to the seam.
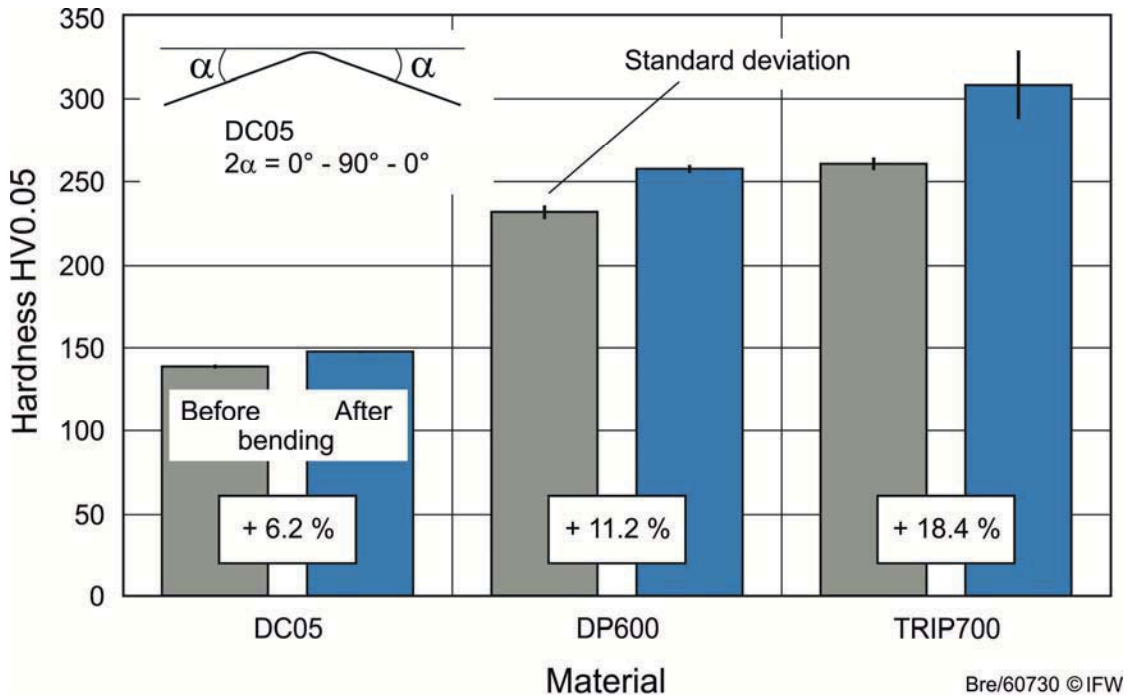
Fig. 16: Hardness increase by bending

673
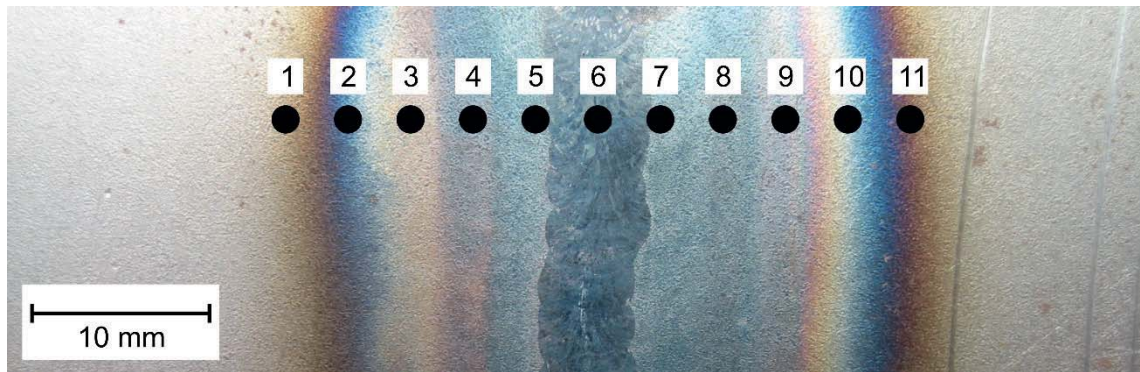
Fig. 17: Welding seam and positions for residual stress determination

The residual stress distributions depending on bending angle 2α and measurement position are shown in Fig. 18 and Fig. 19. Parallel to the seam the stress values along the seam itself show the extrema: strongest compressive stress after bending, strongest tensile stress after unbending. The maximum tensile stress of about 200 MPa exceeds the elastic limit of the basic material, so that damages like micro cracks may already appear after one single bending and unbending operation. The residual stresses in lateral direction do not bear this danger. SEM micrographs from the seam confirm the assumption (Fig. 20), as cracking of the material can be shown here.

In order to determine the load stresses *during* bending and unbending, a simple device has been constructed (Fig. 21), which can be mounted into the diffractometer (Fig. 22).
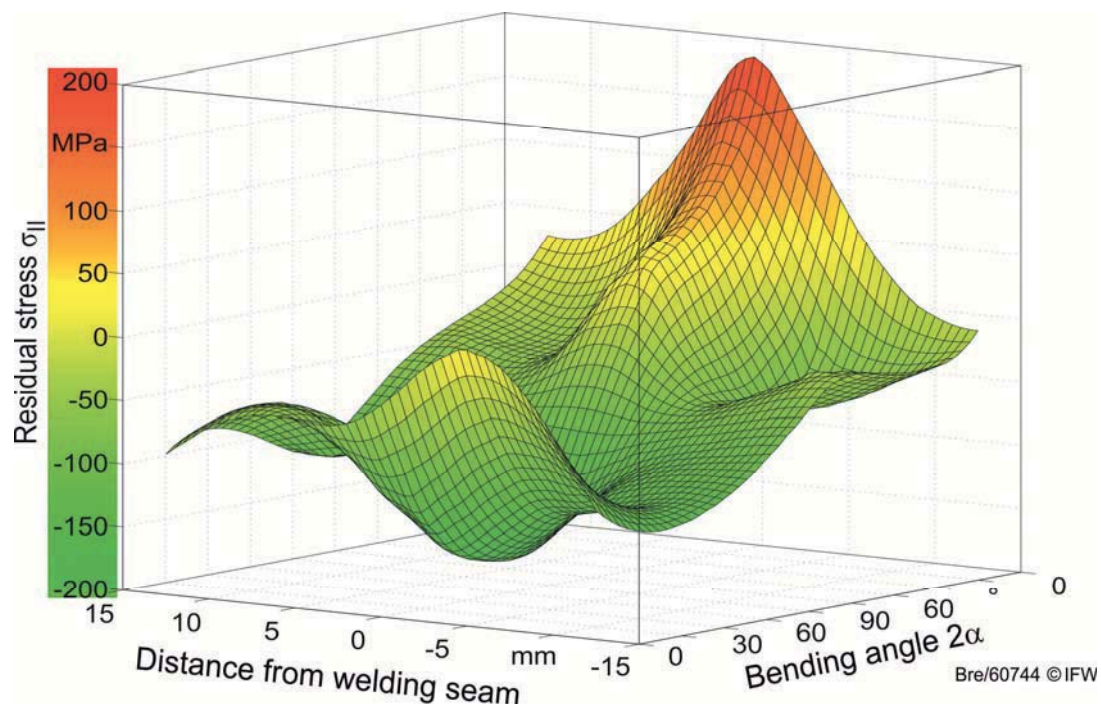
Fig. 18: Parallel residual stresses in welding seam and heat affection zone of DC05 after bending and unbending
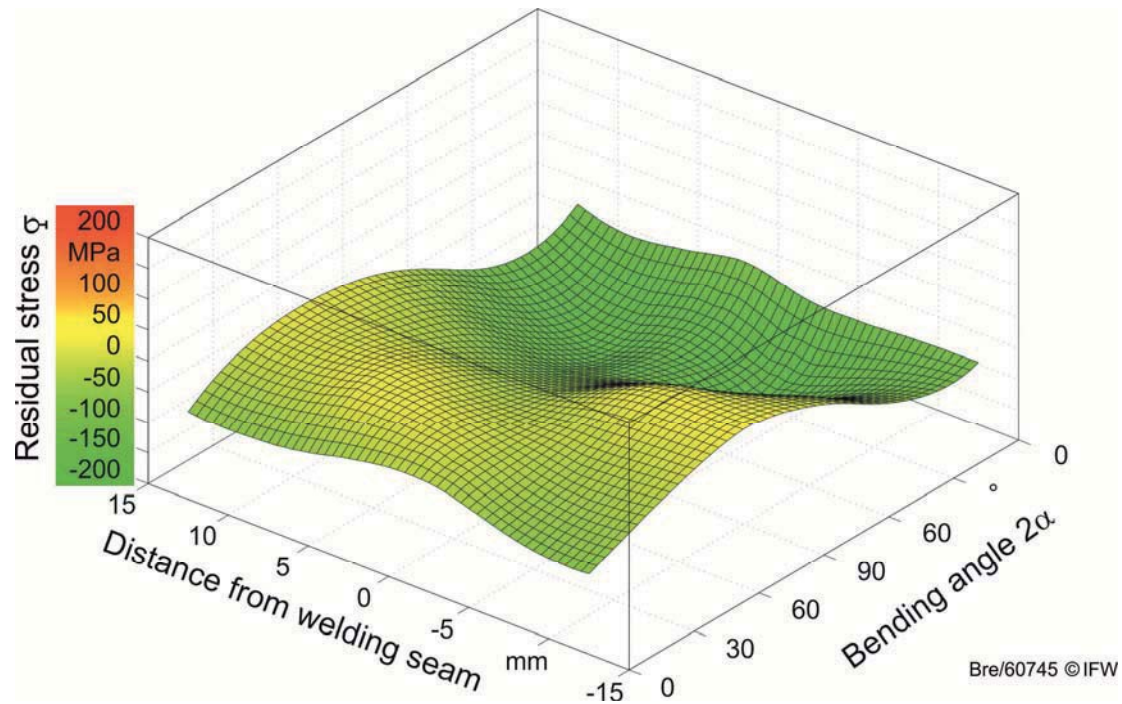
Fig. 19: Lateral residual stresses in welding seam and heat affection zone of DC05 after bending and unbending

The load induced stresses during bending and unbending form their strongest values in the welding seam. As in this experimental arrangement the effect of springback is prevented, during bending tensile load stress is existing and during unbending compressive load stress (Fig. 23). For the investigation of residual stresses before and after tube folding a simple device has been constructed, which allows for shadow-free residual stress determination of tube segments with suppressed springback (Fig. 24).
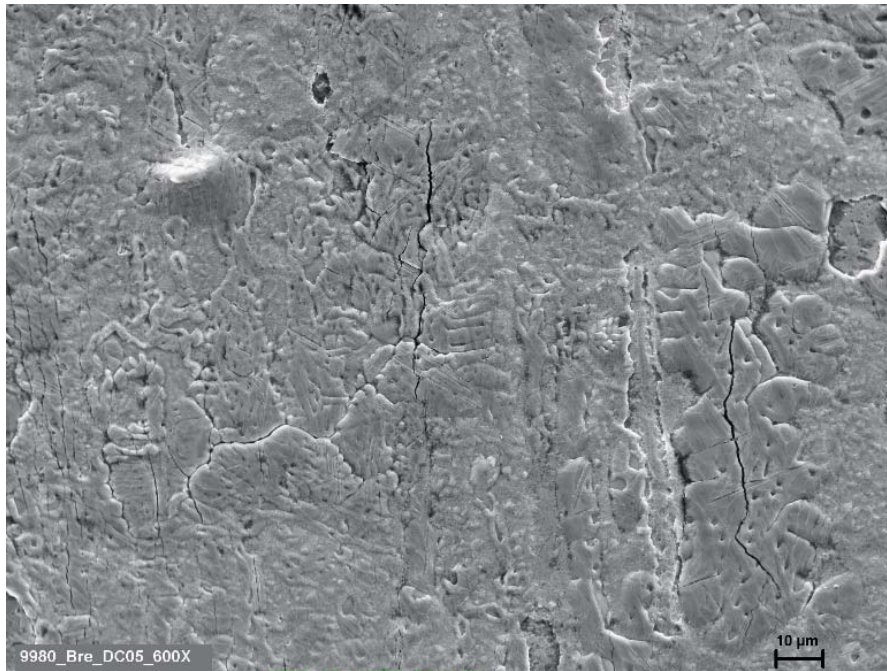
Fig. 20: Micro cracks near welding seam in DC05 after bending and unbending
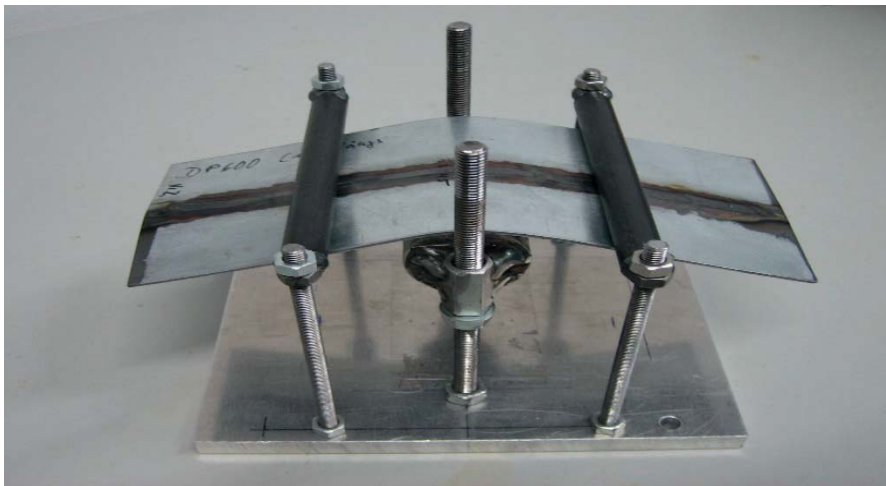
Fig. 21: Device for applying load stresses

Residual stresses in both, parallel and transversal direction to the seam, have been determined at different positions in and near the welding seam before and after forming. The maximum tensile residual stresses are not in the welding seam but at the lowest position of the profile. For the material 1.4462 (ASTM A182F51) with the highest measured tensile stress of $\sigma \approx 350$ MPa, the elastic limit of $R_{P0.2} = 460$ MPa is not reached. Examples for the parallel residual stresses, i. e. the circumferential direction of the bending cylinder, before and after bending are given in Figs. 25 and 26.

Fig. 22: Device for measuring load stresses during bending and unbending mounted to the Diffractometer
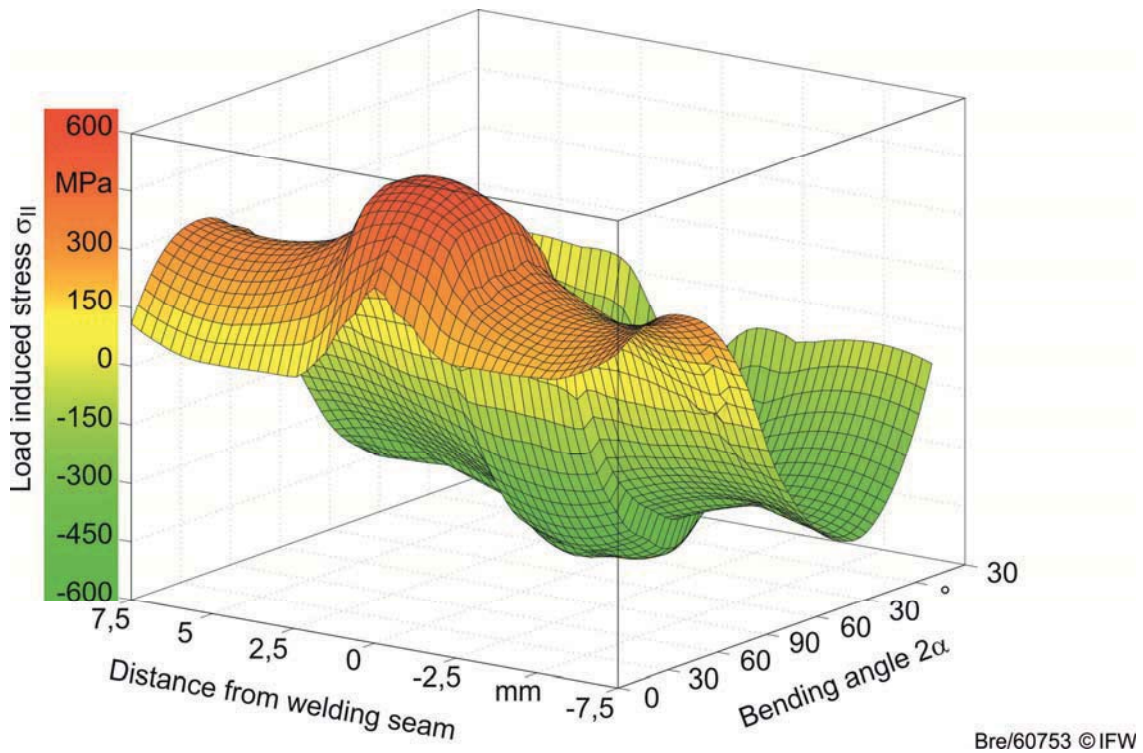
Fig. 23: Load induced stress $\sigma_{\parallel}$ in TRIP700 during bending and unbending

677

Fig. 24: Device for measuring residual stress at tube segments with suppressed springback
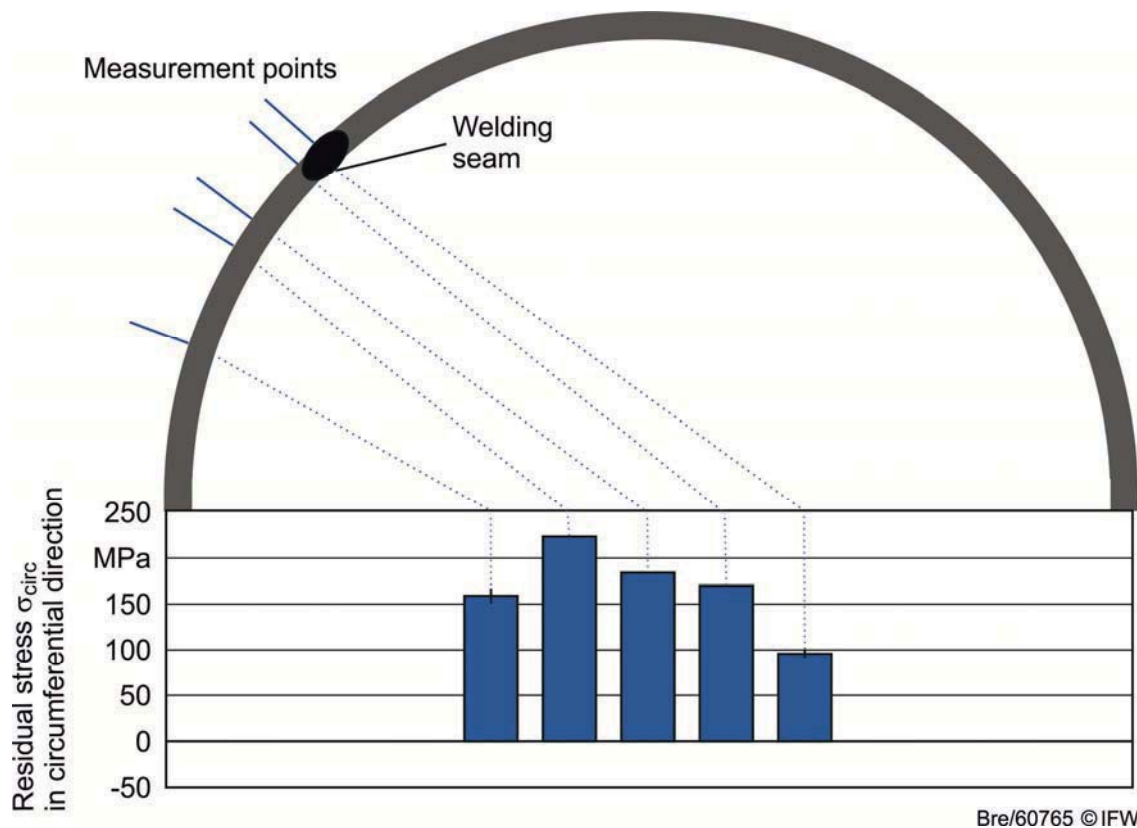
Fig. 25: Residual stresses in circumferential direction before folding
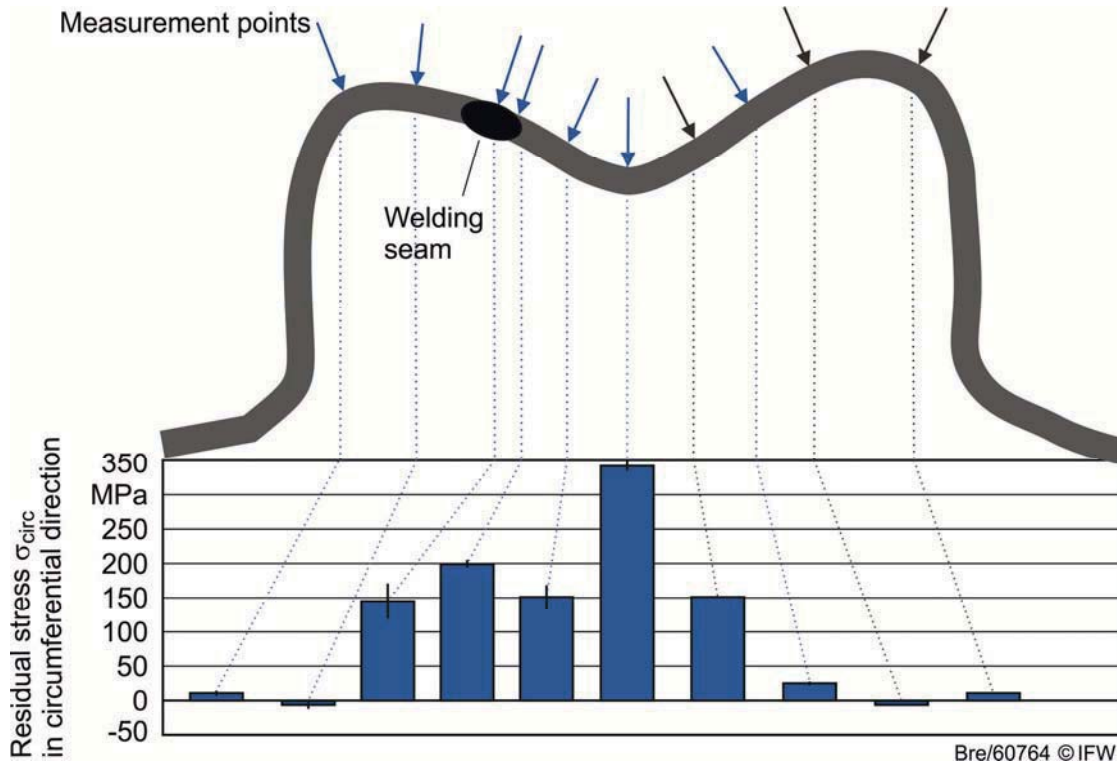
Fig. 26: Residual stresses in circumferential direction after folding

After the residual stress determinations in folded state the segment has been flattened in a press. The flat state is regarded as the unfolded state, as a device for unfolding has not been developed. Both, internal and external surfaces show residual stresses between -300 and 250 MPa after unfolding, where the welding seam does not exhibit a specially endangered region for cracking (Figs. 27 and 28).
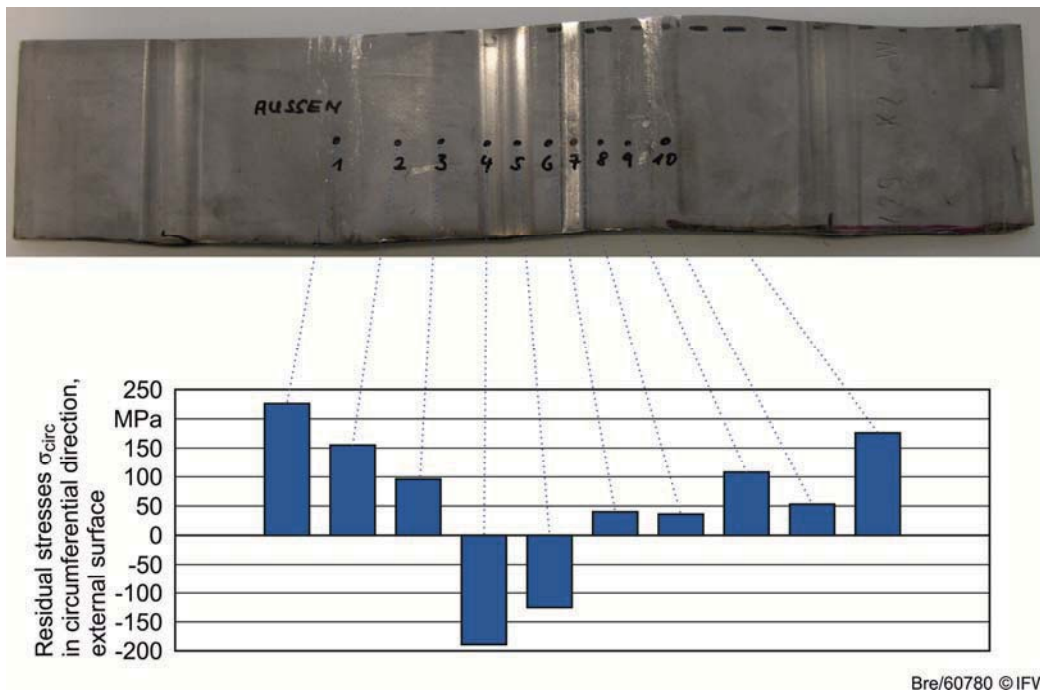
Fig. 27: Residual stresses in circumferential direction after unfolding, external surface

679
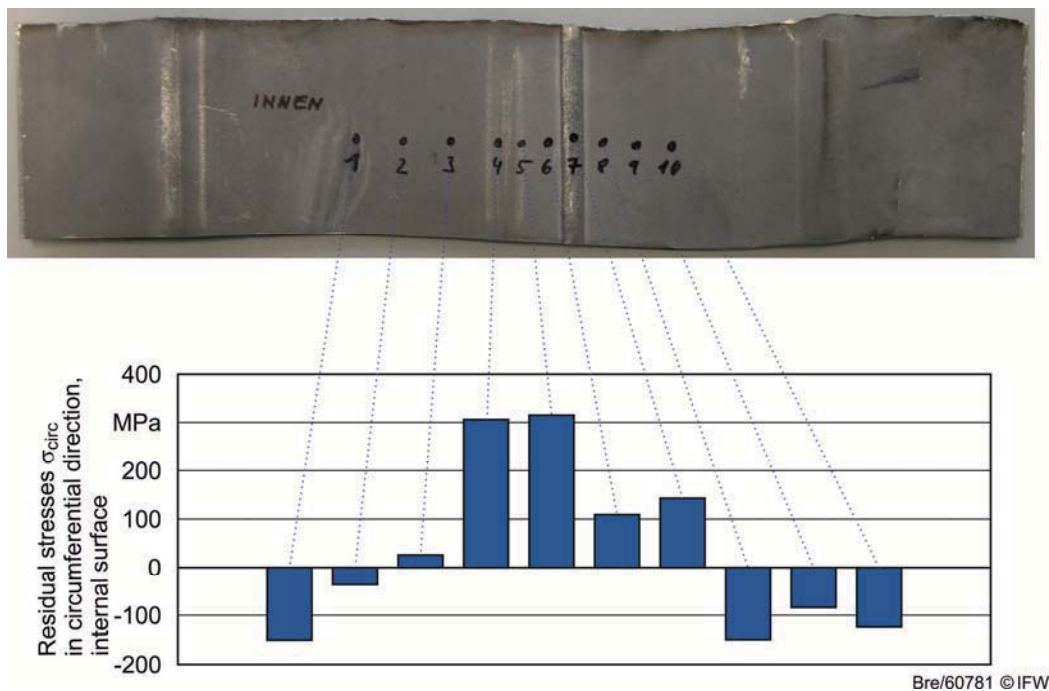
Fig. 28: Residual stresses in circumferential direction after unfolding, internal surface

Conclusions for work packages 1 to 3: By construction of relatively simple devices it is possible to investigate residual stresses and their generation during tube folding by means of the X-ray $\sin^2\psi$ method. During folding residual stresses develop with their maximum values in the welding seam. Already after the first folding critical values for crack initiation may be reached. This can be avoided by a skilled positioning of the welding seam concerning true strain during folding. Then the seam is no longer the most endangered range of folded and unfolded tubes. However, the hardness increase due to repeated forming has to be considered, as the material becomes more brittle.

WP4 /IW –Process optimization and prototype production

To minimize the geometric deviation, a constructive change of the forming tool has been performed, focusing was on the tool clampings. Based on the testing machines a clamping device was developed, which was installed on the machine columns of the test rig. Thus, proper positioning of the tool is ensured.
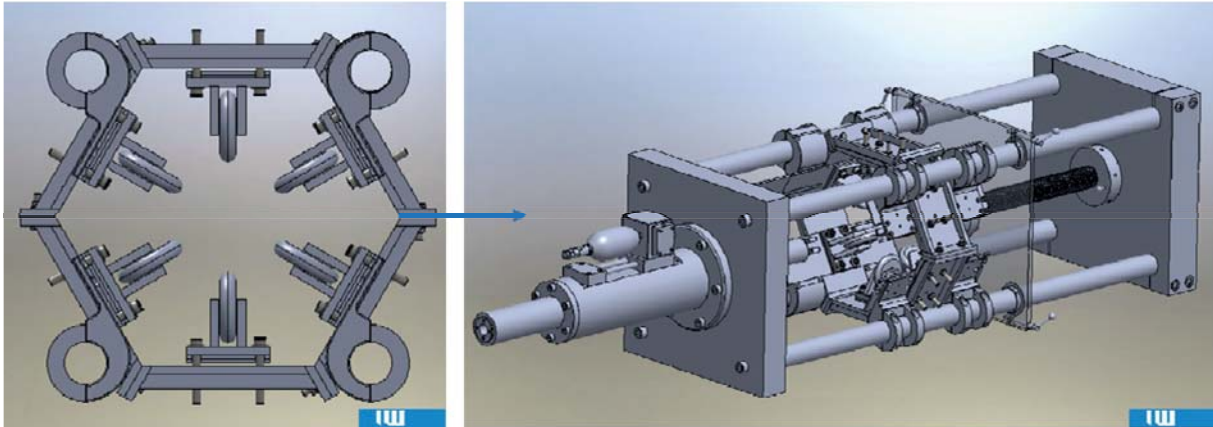
Fig. 29: Optimization of the test rig by centering device

To ensure the reproducibility of the results and industrial operation of the rig an automation of the forming process was made using a PLC control system and the programming equivalent to the project W5 - WP4 was made.

WP 4: Activatable folding constructions

Primarily it had been contemplated to investigate the snap dome effect for possible applications in the field of tube folding. This means that by application of force or temperature the tube is forced into a metastable (folded) state. When force or temperature are relieved, the tube would click back into its stable (unfolded) state. After material, folding geometry and tube wall thickness had been fixed, this intention was regarded as not practicable.

Alternatively it was investigated whether a correlation between the applied forming force and the resulting residual stress can be found. The aim of this work package is to find out, whether it is possible to predict the expected residual stresses, if the forming forces are known. For the experiments two materials with different properties have been chosen: 1.7225 (AISI 4140) and 1.1730 (AISI 1045).

From these materials disks with a diameter of d = 100 mm and a thickness of t = 30 mm were prepared. The disks have been stress relieved by annealing. Two disks of the same material have been mounted to a press, together with an intercalated cylindrical carbide forming tool with a diameter of d = 20 mm and a height of t = 10 mm, and a chamfer on both sides (Fig. 30).
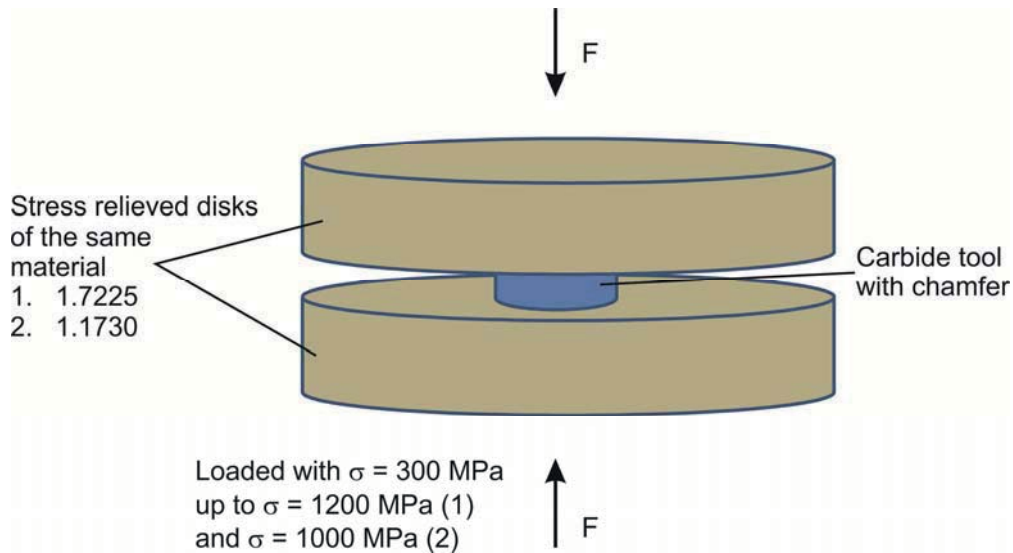
Fig. 30: Experimental arrangement for pressure investigations

This arrangement has been charged with a force of F = 83.72 kN, corresponding to σ = 300 MPa. After relief, the disks are replaced by new ones and the force is increased in steps of 100 MPa up to 1000 MPa (1.1730) and 1200 MPa (1.7225), respectively. For each load new disks are taken. The resulting residual stresses are arranged concentrical around the tool imprint. For the characterization of their distribution, residual surface stresses have been determined along the specimen radius in three azimuthal directions (Fig. 31).
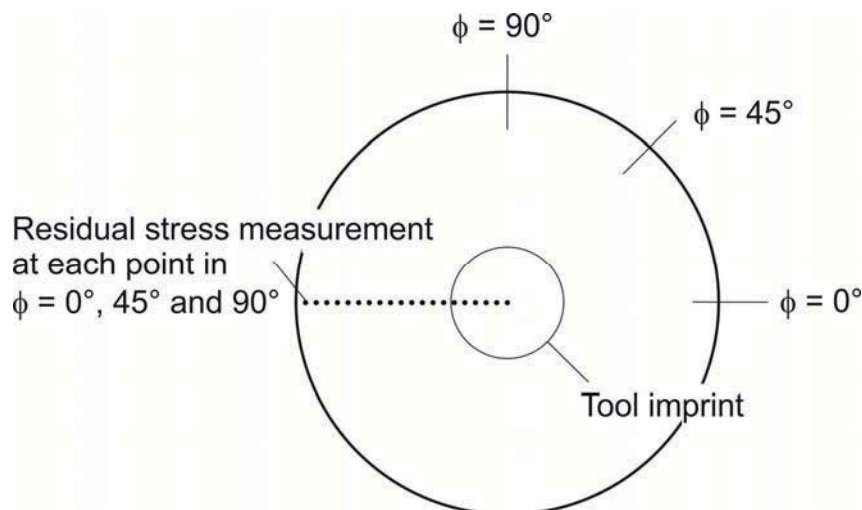
Fig. 31: Residual stress measurement positions at charged disks

A typical residual stress distribution after load and relief is shown in Fig. 32 for the example of 1.1730 after a load of 700 MPa and the principle stress σ_{22}.
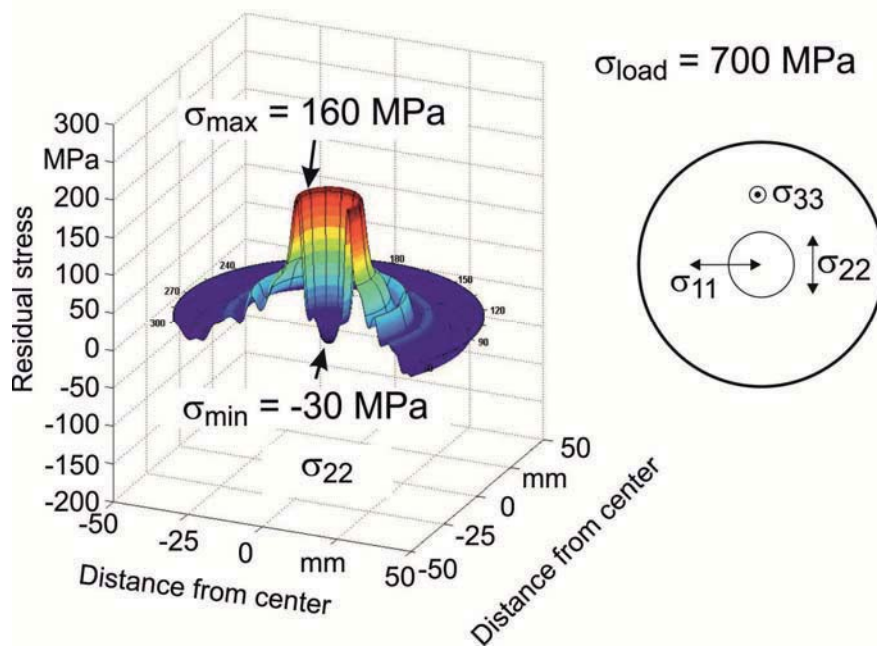
Fig. 32: Principle stress σ_{22} in 1.1730 after load of 700 MPa

In the tool center area slight compressive stress is observed, while in the outer tool edge area the highest tensile residual stress has formed. In order to get a comparable quantity for the total stress as a result of specimen loading the von Mises effective stresses were computed for every measured point. Finally the sum of all von Mises stresses over one specimen diameter was taken and plotted over the specimen load (Fig. 33).
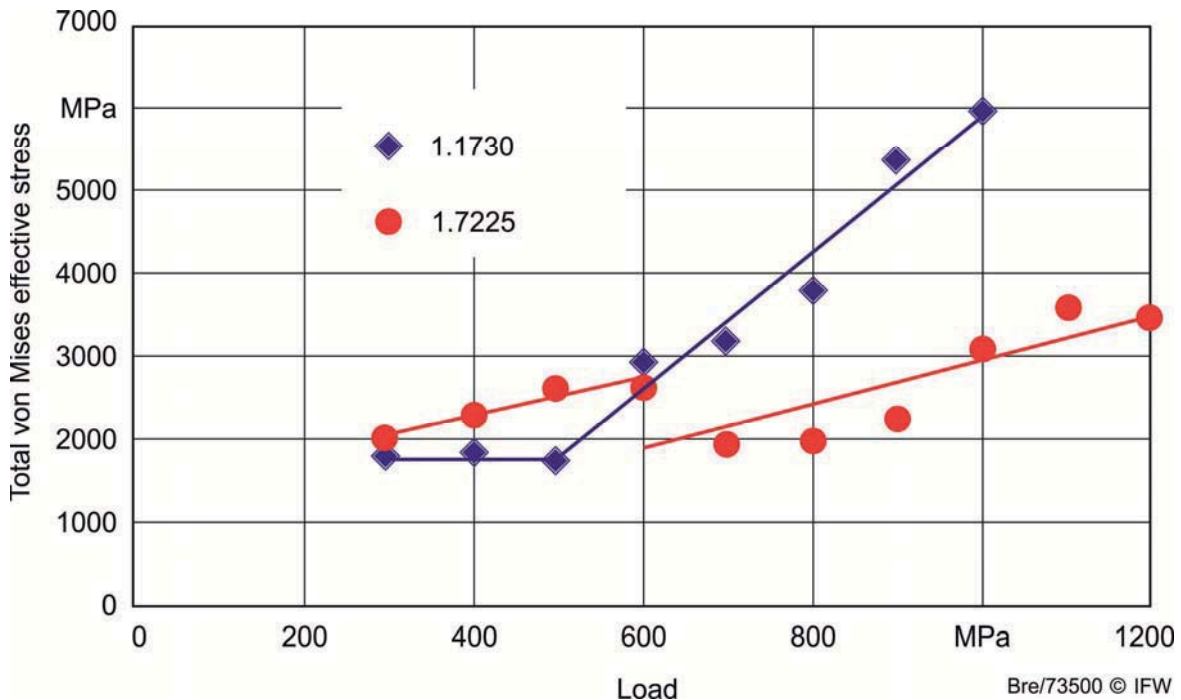
Fig. 33: Total von Mises effective stresses depending on material and load
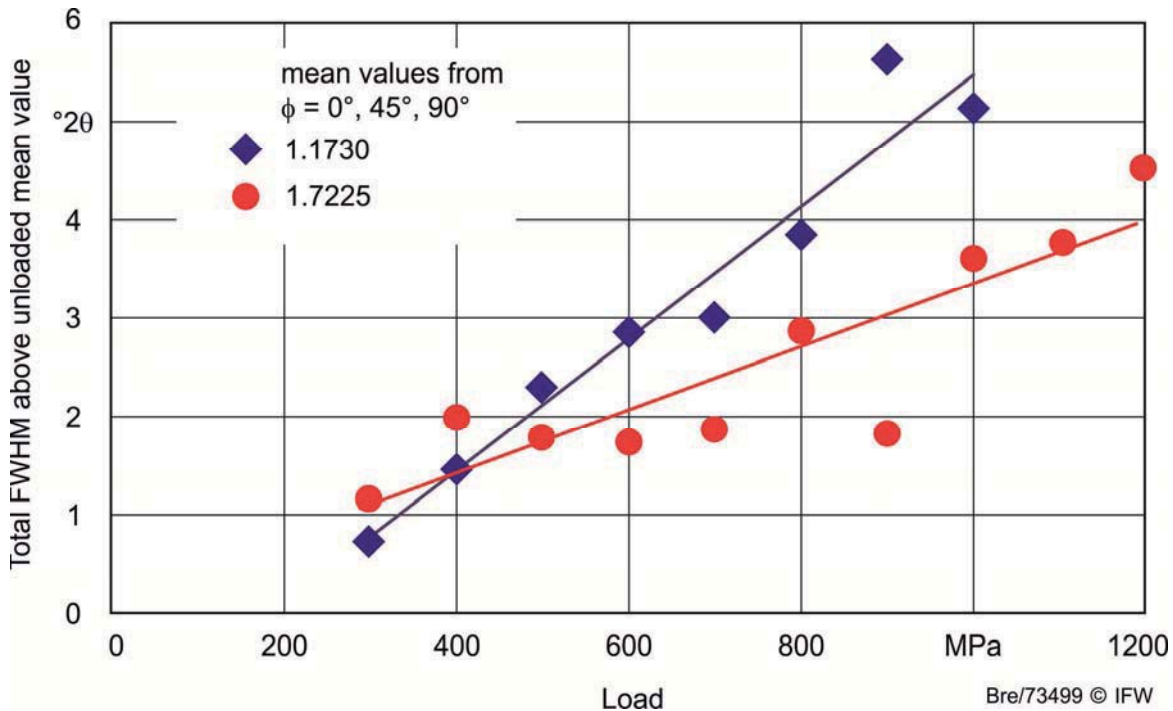
Fig. 34: Total peak half widths FWHM depending on material and load

Above a certain material specific load a linear increase of the total von Mises effective stress is observed. The ratio of the reciprocal values of the slopes of these lines is $m_{1.7225}/m_{1.1730}$ = 1.98 ≈

2. Very similar results are found if the X-ray peak half widths (FWHM) are taken as a comparable measure for micro stresses (Fig. 34). The ratio of the reciprocal slopes in this case is $m_{1.7225}/m_{1.1730}$ = 2.09 ≈ 2. This value can be attached quite well to a mechanical material property, which has been determined experimentally during these investigations: the compression strength σ_D. The ratio of the compression strengths of the two investigated materials is $\sigma_{D\ 1.7225}/\sigma_{D\ 1.1730}$ = 2.16 ≈ 2.

Conclusions for work package 4: The sum of the induced surface near residual stresses is depending on the compression strength of the material, as could be shown by extensive investigations. The local distribution of the stresses, however, is strongly depending on the applied process, tools and parameters. The prediction of the local stress distribution has to be investigated process specifically. The complexity of this research exceeds the here reported project so that new investigations will be applied for in future projects.

WP5 IW/IFW -Transmission of the results as well as conceptual construction is to be realized in contact with the industry.

The production of folded tubes in 1:1 scale and standardized API qualification procedure is recommended for operation release.

2.4 Project Plan

Work Packages (WP)		2009				2010				2011				2012				2013			
WP1	IW / Development of geometry and material choice																				
	IFW / Residual stress analyses of basic material																				
WP2	IW / Creation of segments and assembly of parts																				
	IFW / Configuration of a measuring unit																				
WP3	IW / Development of a folding mechanism																				
	IFW / Residual stress analyses during tube unfolding																				
WP4	IW / Process optimization and prototype production																				
	IFW / Switchable folded constructions																				
WP5	IW / IFW / Validation and industrial realization																				

3 Delineation of the project from other funded projects

At present in the Institute of Materials Science and in the Institute for Production Engineering and Machine Tools of the LUH no projects are executed which stand in connection with high performance drilling technology. The applied project is affected by no planned or running projects.

4 References

[1]   Srisupattarawanit, Tarin: *Numerical Analysis of Metal Forming Expansion Processes with Elasto-Plasticity Model,* IDS Braunschweig sub-projekt W7, Braunschweig, 2009

[2]   Teodoriu, Catalan: *Bohrlochkonstruktion, Beispielbohrung, Bohrstrang und Futterrohr,* gebo B1 Milestone I, Institut für Erdöl und Erdgastechnik, TU Clausthal, 2010

[3]   Macherauch, E.; Müller, P.: *Das sin²ψ-Verfahren der röntgenographischen Spannungsmessung.* Zeitschrift für angewandte Physik, 13, 7, 305-312,1961

5 Publications, reports and presentations of Project

[4] Rosen, S., Varahram, A., Möhring, H.-Ch., Hassel, T., Denkena, B., Bach, Fr.-W: *Der Forschungsver bund Geotherm ie und Hochleistun gsbohrtechnik*, sub-projekts B3, W5 und W6, Journal: Geothermische Energie, 2010

[5] Varahram, A., Hassel, T., Bach, Fr.-W.: Faltgeometrie und Materialauswahl, Report: W6 - Milestone I, 2010

[6] Varahram, A.; Srisupattarawanit, T.; Breidenstein, B.; Hassel, T.; Schiefer, F.; Bach, Fr.-W.; Ostermeyer, G.-P.; Denkena, B.: *Konstruktion gefaltete und aufweitbare Rohre zur Bohrlochauskleidung*, 3. Nano und Material Symposium Niedersachsen, Celle, 2010

[7] Varahram, A.: *Konstruktion gefaltet e und aufweitbare Rohre zur Bohrl ochauskleidung,* Jour-Fixe, Celle, 2010

[8] Breidenstein, B.: *Konstruktionen g efalteter Rohre zur Bohrlochauskleidung* , Jour fixe Werkstoffe, Celle, 2010-11-05

[9] Breidenstein, B.; Denkena, B.: *Eigenspannungen*, Report: W6 - Milestone I, 2010

[10] Varahram, A.; Srisupattarawanit, T.; Breidenstein, B.; Hassel, Th.; Schiefer, F.; Denkena, B.; Ostermeyer, G.-P.; Bach, Fr.-W. : *Design of Folded Tubulars fo r Expandable Casing Applications,* Celle Drilling 2011, Celle, 2011

[11] Varahram, A.; Bär, F.; Hassel, Th.; Overmeyer, L.; Bach, Fr.-W. : *Design of Folded Tub ulars for Expandable Casing Applications* , Proceedings of the 16th Annual International Conference on Industrial Engineering Theory, Applications and Practice. IJIE Stuttgart, 2011

[12] Bär, F.; Varahram, A.; Hassel, Th.; Overmeyer, L.; Bach, Fr.-W.: *Cost-efficient Monobore Well Constr uction for Geotherm al Energy,* Proceedings of the 16th Annual International Conference on Industrial Engineering Theory, Applications and Practice., IJIE Stuttgart, 2011

[13] Aret Varahram, Bernd Breidenstein, Friedrich-Wilhelm Bach, Hans Jürgen Maier, Thomas Hassel: *New Desi gn and Construction of Expandable Casing Tubes* , 10th Plastic deformation of metals, Dnepropetrovsk UA, 2014

[14] Thomas Hassel, Aret Varahram, Bernd Breidenstein, T. Srisupattarawanit, G.-P. Ostermeyer, Hans Jürgen Maier: *New Design and Constr uction of Expanda-ble Casing Tubes,* Celle Drilling 2014, Celle

[15] A. Varahram, B. Breidenstein, T. Hassel, F.-W. Bach, H. J. Maier: *New design and construction of expandable casing tubes,* Forschung im Ingenieurwesen 78 (3-4), S. 145-149, 2014

W7: Design of Fatigue Resistant Mechanical Components for Drill String Applications

1 Project Overview

Project Nr.	Title	Subject of research	Project leader, institution, location
W7	Design of Mechanical Components for Fatigue Strength Under Variable Amplitude Based on Load Distributions and Computation of Folded Tubular	Mechanical Engineering	Prof. Dr.-Ing. A. Esderts (IMAB) Prof. Dr.-Ing. habil. G.P. Ostermeyer (IDS)

Participating institutes and institutions of the universities and external institutions:

- Institute for Plant Engineering and Fatigue Analysis, TU Clausthal

- Institute of Dynamics and Vibrations (IDS), TU Braunschweig

List of participating scientists and engineers:

Name	Subject area	University institute or non-university institution	Position is financed by gebo funds (indicate by X)
Prof. Dr.-Ing. A. Esderts	Mechanical Engineering	IMAB	
Dipl.-Ing. S. Runge	Mechanical Engineering	IMAB	X
Prof. Dr.-Ing. habil. G.P. Ostermeyer	Mechanical Engineering	IDS	
Dr.-Ing. F. Schiefer	Mechanical Engineering	IDS	X
Dr.-Ing. T. Srisupattarawanit	Mechanical Engineering	IDS	X

2 Research Program

2.1 Summary

Dynamic load spectra of components of drill strings under fatigue stress and resulting fatigue life times are to be assessed by combining measured stresses and results of simulations. Therefore, the complex dynamics of complete drill strings will be analysed in long-term studies based on measured data and also based on long-term simulations with respect to particular borehole trajectory. Next to environmental influences like temperature and corrosive media, the position of the respective component in the drill string and the local drilling course are also taken into account in the assessment. Stress-dependant designs can be realized based on the load spectrums, enabling life time monitoring to ensure a trouble-free operation.
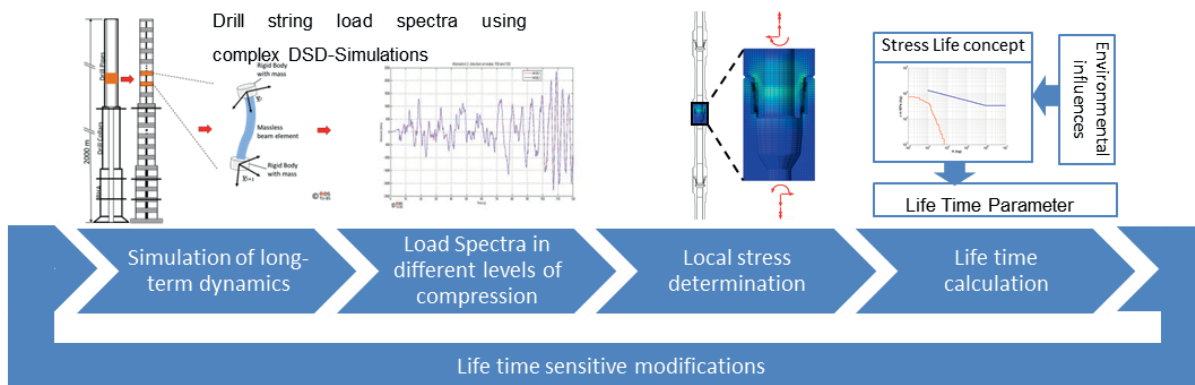
Figure 1: Project overview

2.2 Relationship of the project to the overall research context and networking with other projects

In the context of the research cluster numerous new tools, materials and material systems are to be developed. The central aim is to increase the life time of components employed downhole to minimize time and costs of geothermal drillings. The knowledge of the loads to be expected on the employed components is of decisive importance for the design and planning of service intervals. By using methods specially adapted to the expected load spectra of geothermal drilling, it will be possible to utilize the fatigue strength of single components under variable amplitude optimally and to simultaneously minimize failure rates. Monitoring makes it possible to react to the occurrence of unexpected overloads and to adapt service intervals dynamically accordingly.

Component-related load spectra will be assessed based on simulations, measured stresses from test drillings, test stands of other projects – e.g. project B8 – and experiences of the research partners. In addition to the modeling and simulation techniques developed in project B7 "Drill String Dynamics and Modeling" the complex long-term dynamic of complete drill strings will be analyzed with respect to given borehole trajectories. The belonging simulation results will be interpreted and prepared for life time calculations. The gathered knowledge about the specific downhole loads will be made available as input for future designs and process planning.

The numerical analysis of the unfolding and expansion mechanisms is undertaken in close cooperation with the W6 project. W6 designs the tube cross sections and sets material parameters, which are then analysed in this project to assess their suitability. The simulation results assist the W6 project in optimizing folded tubular geometries and materials.

2.3   Work packages and results

Long-term dynamics of drill strings and load spectra

Measured data collection (WP 1):

The previous course of the gebo-project has shown the problems by collecting significant measured data to generate load spectra. At present measured data of deep drillings or geothermal drillings do not exist within the gebo research project. Baker Hughes had provided a few measurement data set of their test rig (BETA) that operates up to a vertical depth of 1000m. At this stage the existing data set is not adequate for detailed investigations.

Load spectra of measured data (WP2):

On the basis of measured data provided by Baker Hughes (data of the test rig BETA), fundamental techniques to generate load spectra conditions are developed.

However, the provided data do not allow reliable statements on the long-term dynamics with respect to the process time and the amounts of data. But in principle it is possible to isolate single load spectra due to known system's states. The aim is to obtain characteristic dynamic load spectra in a typical dimension. Furthermore, methods for a load spectra reduction, e.g. rain-flow counting method, can be applied. As mentioned above further measured data of deep drilling or geothermal drilling, provided by gebo or external projects, were not available, but the techniques or the developed concept to generate such characteristic load spectra can be used. Nonstandard events will be considered in WP 5.

In close cooperation with project B7 models have been developed that enable to integrate measurement data at discrete points as external excitations (*Combination measured data and simulation data (WP4)*). Typically, such measurement data are only available at individual and very few locations on the drill string. The simulations of the IDS models provide the extrapolation of those measured data along the entire drill string.

Load spectra of simulation data (WP 3):

To enable a first life time calculation in WP1 dynamic load spectra are computed within a new developed reference system, see Figure 4. The drill string dynamic is highly non-linear, if the wellbore wall, the friction and dissipation are taken into account. Therefore, a new finite element tool has been developed. Classical FEM programs were not suitable because of the facts that the nonlinearities either been ignored or the numerical cost was too extensive. The FEM programs developed here used firstly elastic multibody dynamics with lumped masses coupled by massless Timoshenko beam elements. Afterwards, we use a full FE-formulation with corotational beam elements. This technique is excellent to run fast and accurate analyses with respect to arbitrary wellbore trajectories. Initially, for the following studies

assumptions were done which are listed here: borehole and bit diameter of 10 5/8", BHA with a length of 50m and an outer diameter of 8 ¼", drill collars with a length of 150m and an outer diameter of 5" and drill pipes with a length of 1800m and an outer diameter of 5". Afterwards, more complex models were calculated, see Figure 32.
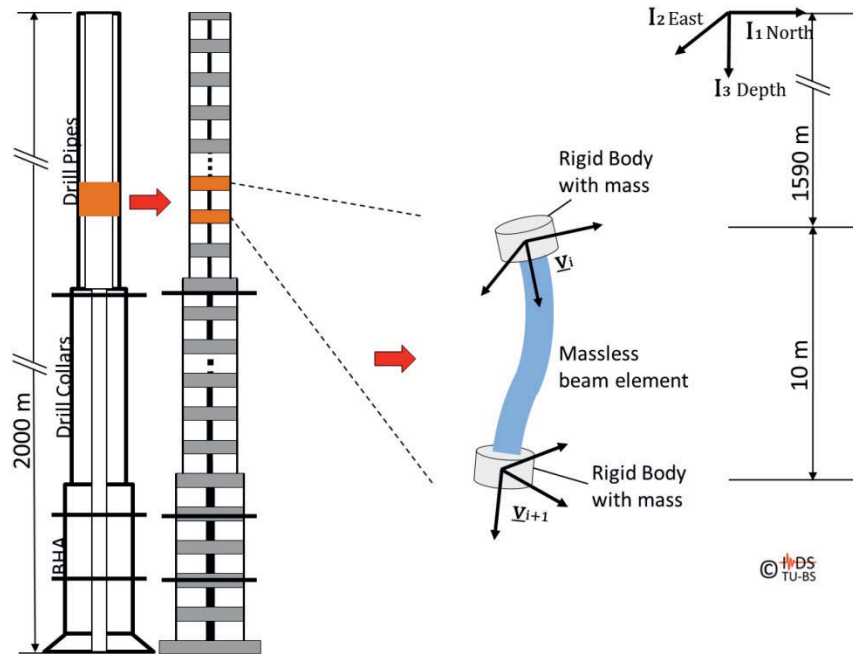
Figure 2: First reference-system for dynamic load spectra

First of all an ideal-straight vertical borehole was assumed as required by the gebo research field *Drilling Technology*. The drill string dynamics was exemplarily analyzed at a vertical depth of 2000m. Enlarging the modeling and simulation techniques developed in project B7 first of all the complex drill string dynamic of the chosen drill strings was analyzed in a time period of 120 seconds.

a)   b)
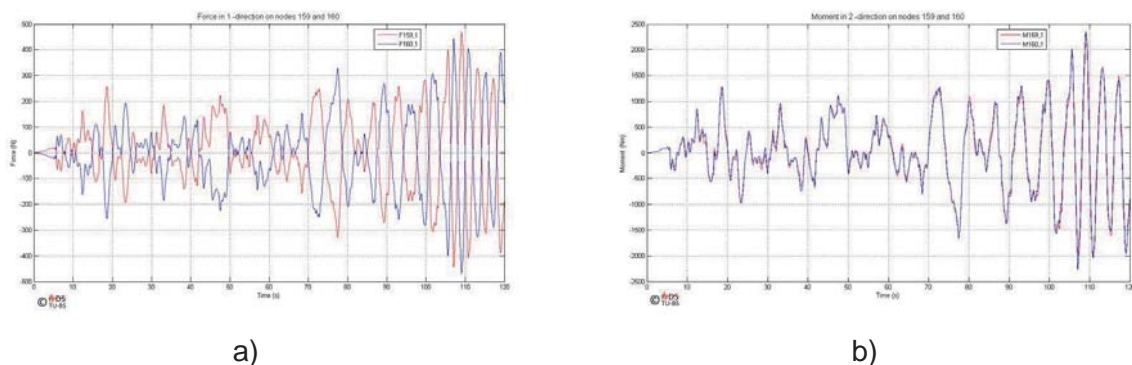
Figure 3: Dynamic load spectra with the model in Figure 2 as

a) force-time-diagram b) Dynamic load spectra as bending moment-time-diagram

In Figure 3 two exemplary dynamic load spectra are shown. Due to the fact that the life time calculation in WP1 had to be done for a NC 50 connection of drill pipes, the reference model

690

was analyzed in a deep drill pipe section (1590m vertical depth). These load spectra from simulations have been made available to the project partners for start of lifetime calculations of threaded connections.

Measured data usually cover only short time intervals and only very few nonstandard events at special points of the drill string, see explanations above. These measured data are used to validate complex simulation runs. So, the virtual environment for long term simulations and nonstandard events are used and data compression methods as rainflow-counting are coupled to these simulations to create realistic data for lifetime computation, interpolating the short time pictures of a few measurement sensors on the string with respect to time and geometry. With respect to different drilling scenarios the data capsule in its current state, which is be developed at IDS in the B7 project, enables a convenient description of the drill string dynamics. Using realistic long-term dynamic analyses load spectra can be prepared position-severed and event-severed (*Nonstandard events (WP5))*. In particular, event-severed investigations consider drilling scenarios with distinctive impact loads, stick-slip, whirl and bit bounce. This can be also compared with belonging measured data. Within the research collaboration gebo a reference well from project B1 was only available for the last half year, see part gebo reference well. Due to these time constraints, we did not run analyses with respect to nonstandard events for the gebo reference well.

As a result of the project work follows that currently load spectra for the long-term dynamics are to be generated by suitable simulations, not by measurement data as originally planned. The necessary fundamentals for a suitable simulation tool have been developed in Project B7. With regard to the short-term dynamics the models and simulations have been validated with some external available measurement data. In the Project W7 this tool has been enhanced to meet the requirements for long-term simulations.

Strategy to run long-term simulation

For running fundamental studies a synthetic wellbore was considered, similar to Project B7. This synthetic wellbore is shown in Figure 4. It consists of a vertical section, two curved sections with different dog leg severities and finally a horizontal section. The basic strategy is to run time domain simulation in discrete intervals followed by an interpolation between the intervals. This is one of many strategies to calculate the drill string dynamics on long-time scales.

691
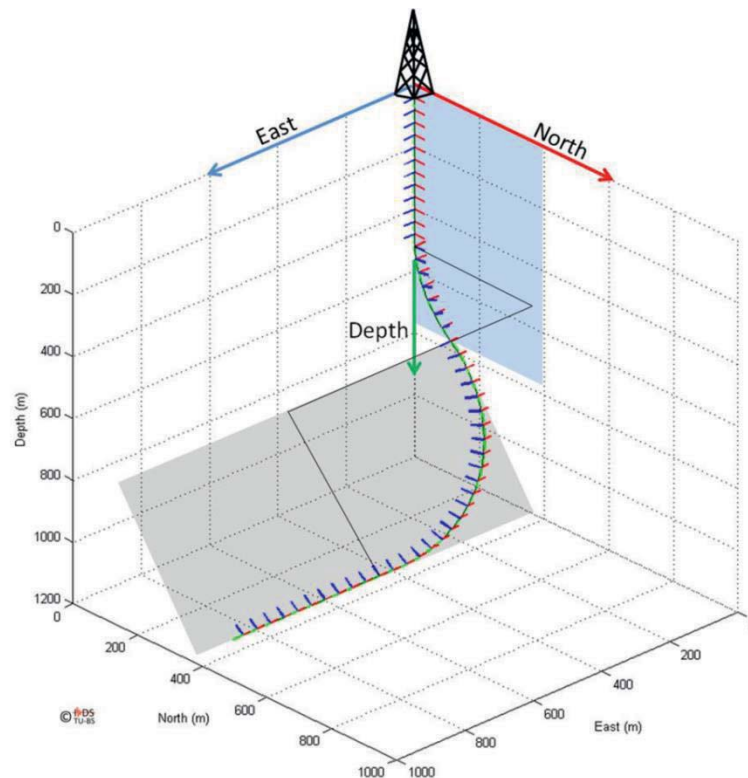
Figure 4: Synthetic wellbore for principle investigation

To achieve practicable time for analyses the long-term dynamics main challenges are the model accuracy and the computing time which is studied and analysed fundamentally in Project B7. The overall goal here is the generation of fatigue relevant load spectra by suitable simulations in discrete intervals. For this purpose it is necessary that these intervals are representative for the considered drilling sections. Representative in this context means that all significant dynamic effects have been taken into account. These dynamic effects depend on the drilling process, the borehole trajectory and geometry, the formation and environmental influences (e.g., temperature and pressure) as well as nonstandard events (e.g., impacts between the drill string and the borehole, extreme vibrations due to backward whirl phenomenon or other dynamic phenomena). The models developed by IDS are able to investigate and analyze these dynamics effects and phenomena.

In order to validate the models and the corresponding simulation results with respect to the aforementioned influencing factors, a large number of appropriate data is necessary.

692
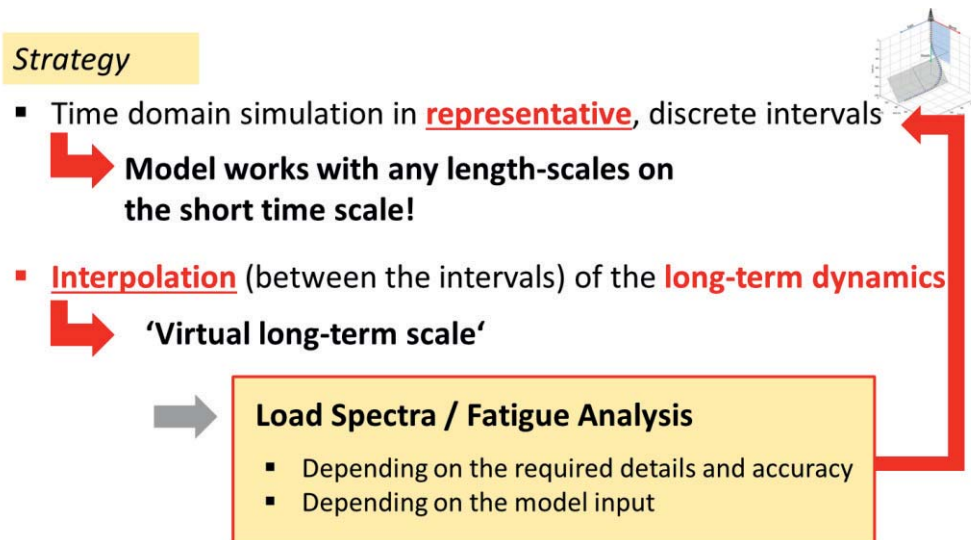
Figure 5: Strategy of long-term investigations

Assuming that an appropriate validation and analysis of the short-term dynamics is done and the representative interval is identified, the strategy is to interpolate the long-term dynamics between the representative intervals. Figure 5 shows schematically this strategy. Hence, the model works with any length-scale on the short time scale and the interpolation generates a virtual long-term scale. The obtained load spectra depend on the requirements of the fatigue analysis (e.g., location, accuracy) and also depend highly on the model input. This provides again requirements for the representative, discrete intervals. This strategy is a quasi-closed loop formulation to interpolate the long-term drill string dynamics and to generate fatigue-relevant load spectra in an iterative process.

In the last months of the project W7 a first model input was given by the group project "Economic drilling of deep Geothermal wells" of the Technical University of Clausthal /THE 13/. It is a concept study without corresponding measured data for further model validation. The final work on this topic is documented in the section gebo reference wellbore.

Until these investigations on the gebo reference wellbore the principle studies and test of the strategy for long-term dynamics were done using the drilling of the synthetic wellbore shown in Figure 6 /OST 13/. From this work, a simulation tool has been created that simulates the drilling of any spatially curved boreholes while recording the dynamic load spectra.

Thereby, different input data can be set using the developed data capsule. Such input data are drilling process data (hook load, rpm, downhole motor parameter,…), formation data (ucs, young modulus,…), wellbore data (inclination, azimuth, dogleg severity, diameter and length of wellbore sections,…) and drill string data (geometry, material, BHA setup,…). The simulations provide output data as results of the numerical calculation.
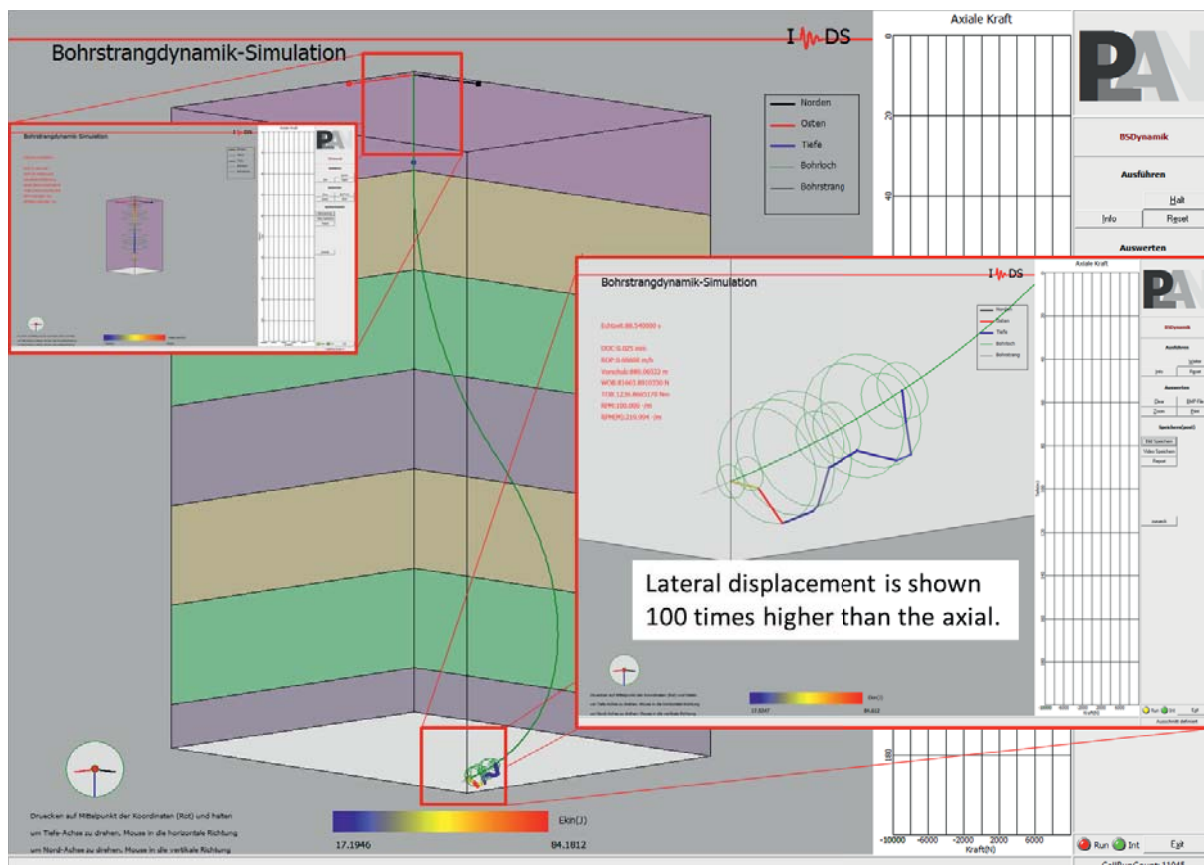
Figure 6: Simulation of drill string dynamics: 50m-BHA is drilling a given wellbore trajectory using corotational beam elements

The essential output data in this project are the dynamic loads and load spectra which can be used as raw data or in prepared form (e.g. with rain-flow counting method) for life time calculations. The simulations provide also well known drilling process parameter as the rate of penetration (ROP), the downhole rpm, torque on bit (TOB) and weight on bit (WOB).

With the feedback and integration of life time relevant component parameters life time sensitive modifications of the long-term simulation could be performed as planned, see Figure 1 and Figure 5.

To study drill strings in any spatially curved wells on arbitrary time scales all the developed techniques allow the development of new mesoscopic lifetime concepts. Thus, the IDS developed locally resolved energetic evaluation measures for instance. In addition, local effect variables, as the time integrated amount of energy flow and concepts of technical pain /OST 05, SCH 08/, will be introduced for logging of component related reliabilities.

For future research work this will move to a close cooperation with the work packages and achieved results of project W8.

Life time concept

Numerous variables determine the fatigue behavior of metallic components. Starting from mechanical properties ascertained on fatigue specimen under laboratory conditions a prediction for mechanical components underlies effects like:

- local stress concentration and stress distribution,
- multiaxial loading,
- production process,
- temperature,
- corrosion and
- surface conditions etc.

that need to be considered by a lifetime concept. For drilling applications state of the art is represented by the nominal stress concept provided by the API guideline /API 95/. The concept was developed for drilling into severe doglegs and takes into account the bending stresses occurring in bent drilling courses. Insufficiencies in the load assumption of the appearing bending stresses were identified through analytical examinations in /GRO 91/. The strength characteristics of the drill pipes in form of stress cycle diagrams were determined experimentally. The experiments did not consider the weight of the drill string and the resulting static tensile forces superimposed on the dynamic loads. The mathematical concept therefore includes a mean stress correction to allow for the overlaid static stress. The concept is classified as a rough design formula because the local stresses, relevant for the fatigue due to the geometry are not taken into account by the API guideline. The standard DS 1 /DS1 04/ uses the fracture mechanics concept according to Forman under application of the same load assumption provided by API. This concept also does not take into account the local stresses. The standard DS-1 supplementarily uses a strain life concept for the evaluation of e.g. geometric notches like "slip cuts" (mechanical damages to the drill pipe).

The IDS simulations yield complex load data which describe multiaxial stresses of various drill string elements. Using a local fatigue life calculation concept the geometry of the component can be taken into account for the calculation of local and multiaxial stresses. Stress-cycle (s/n) diagrams do not have to be determined experimentally for each component, as opposed to the nominal stress concept. In contrast to this, only material specific stress-cycle curves need to be determined. A local stress concept is chosen for the calculation of the drill string components within gebo research program, Figure 7.
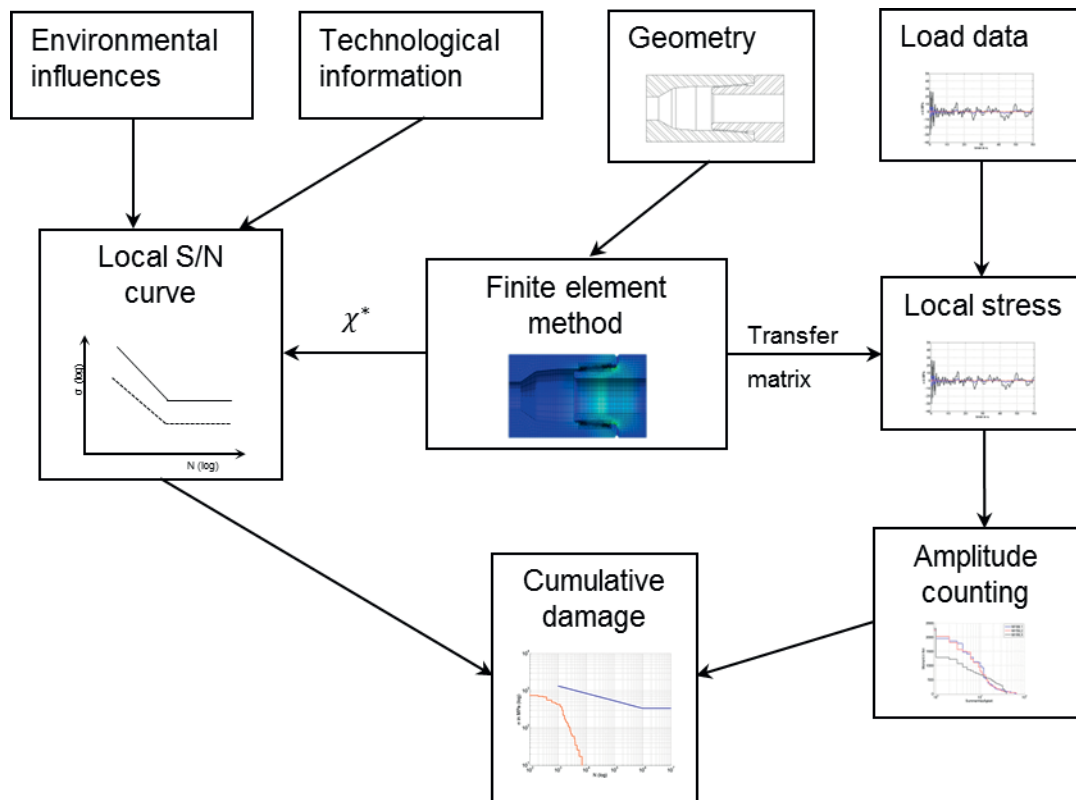
Figure 7: Life time assessment based on local stresses and stress gradients

To facilitate consideration of arbitrary geometries, the finite element simulation is engaged to determine local stress properties. As this numerical method can be complex and time consuming, it will be performed as a pre-analysis. Saving geometry - dependent properties to a database, lifetime assessment can be realized with high computational velocity.

The lifetime calculation concept is based on FKM guideline with local stresses, /FKM 03/. The guideline is an established concept for general machinery. Therefore various relevant effects on fatigue mechanisms are being covered. Whereas in dependency on material group influences are being assessed, corrosion effects are not being taken into account within the proposed guideline. An approach to take corrosive influences into account is being additionally integrated into the concept.

Temperature influence

In general metals show a decay of fatigue strength with increasing temperature. For steel alloys, fatigue strength properties can be assessed over a temperature range up to 500°C. For aluminum alloys a limit temperature of 200 °C is being defined. The FKM guideline provides a multiinear approach in dependency on material groups, Figure 8.

Stainless steels are being excluded from this empirical model because of an insufficient database.

696
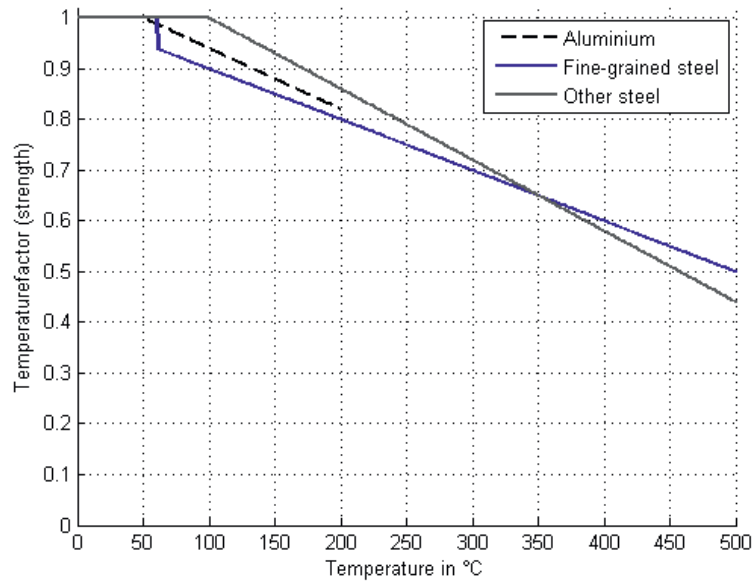
Figure 8: Temperature dependency of fatigue strength after /FKM 03/

Corrosion Fatigue

Corrosion fatigue mechanisms mainly depend on presence of a passive layer. As chromium- and nickel-chromium steels show passivated surfaces, corrosion effects occur locally and result in pitting- or intergranular corrosion. In fracture analysis particular intergranular fatigue corrosion cracks can hardly be distinguished from pure fatigue cracks. In contrast, non-passivated steels e.g. non- or low-alloyed steels underly large-area corrosion and transcrystalline cracking, /WEN 98/. The presence of corrosion decreases strength properties in general and annihilates the fatigue limit, Figure 9.
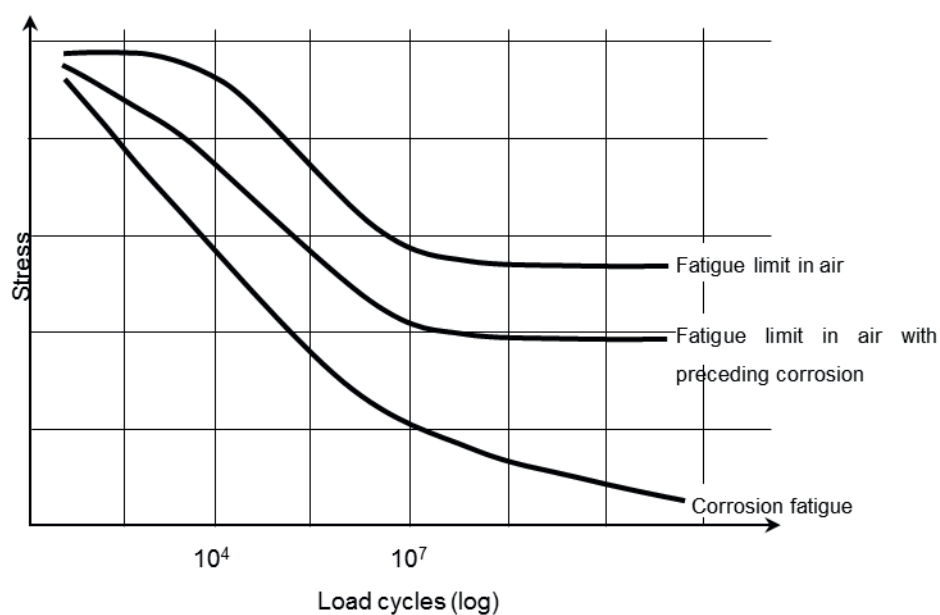
Figure 9:Schematic s/n curves under corrosion and in air, /WEN 98/

Calculation concepts to evaluate corrosion fatigue effects exist for pressure tank or power plant components. As these concepts provide only information for specialized application with respect to material and corrosive environment it may not be transferred to drilling application.

In /BER 09/ a general concept to evaluate corrosion fatigue based on cumulative damage is proposed. This concept is based on a database of experimental fatigue tests on various steel alloys in environments with water, NaCl solutions and acids in an temperature range up to 200 °C. Corrosion fatigue is herein assessed on the main influencing factors: corrosive-medium, temperature, pH-value, oxygen content, tensile strength, chromium content and molybdenum content. This concept estimates an appropriate s/n curve by factorizing an s/n curve for non-corrosive conditions. Additionally the loss of fatigue limit is taken into account and the effect that severely notched components show less sensitivity to corrosion.

Fatigue tests conducted by Hughes Tool Co. on full scale drill pipe show expected properties, Figure 10.
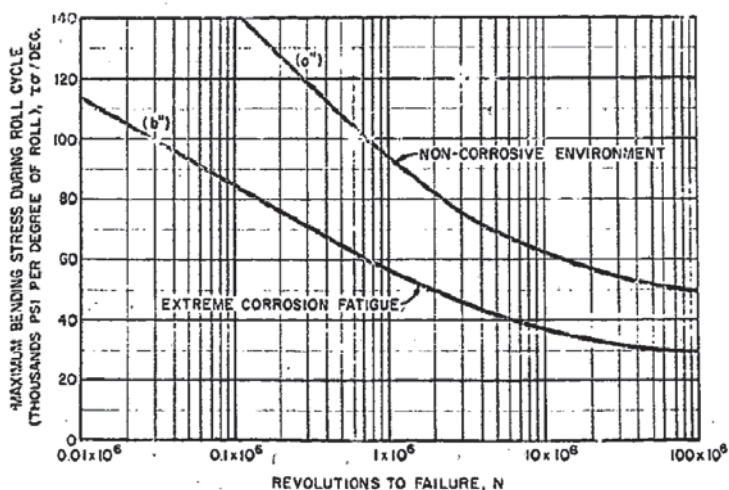
Figure 10: Full-size fatigue tests under corrosive- and non-corrosive environment, /HAN 63/

Extreme corrosive conditions herein lead to a factorial decrease of fatigue strength to 60 % with respect to tests in non-corrosive environment. As the lower curve is said to be non-conservative for small amplitudes, therefore a fatigue limit is not being present either. Further test conditions are unknown.

For the purpose of general lifetime assessment within gebo a factorial concept is being used. As operating conditions are being roughly known as well as specific alloy characterization under corrosion is still an object of research this is seen as appropriate method. For a more specific consideration it is recommended to conduct fatigue tests under working conditions.

A suggestion for corrosion strength factors based on /BER 09/ is made in Table 1.

Table 1: Proposal for corrosion strength factors

	Mild corrosive environment	Moderate corrosive environment	Harsh corrosive environment
None- and low-alloyed steel	0,74	0,61	0,61
Chromium steel	0,64	0,54	0,34
Nickel-chromium steel	0,68	0,53	0,44

Classification of corrosive environments depends on sensitivity of each steel group towards certain influences, based on /BER 09/. None- and low- alloyed steel underlies harsher corrosion effects with growing acidic strength. Corrosion effects become milder with higher chromium content, higher tensile strength and higher temperature (lower oxygen saturation).

Chromium steels are more sensitive to corrosion with growing NaCl – content and are less subjected to corrosion with growing chromium content.

Nickel-chromium steels underly harsher corrosion with sulfuric acid strength (until ~ 20%), higher temperature and lower pH-value.

Local stress determination

The dynamic loading of a mechanical component causes an internal stress distribution which is dependent on geometry and material properties. As material properties can be assumed to be homogenous and isotropic, the stress distribution is defined by geometry presupposing that locations where loads are introduced can be determined. An assumed mechanical system is shown in Figure 11.
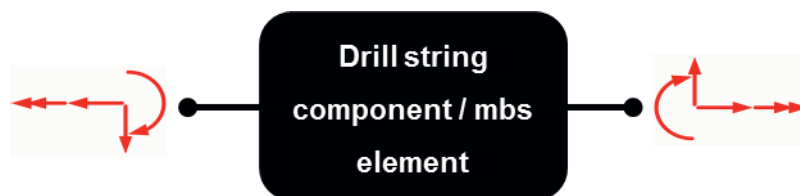
Figure 11: Mechanical system

As the number of load introducing locations is two, subsequently only interactions with the upper and lower located components within a drillstring are being considered. Therefore it must be assumed that all interactions with the borehole walls occur outside of each component or in existing load introducing locations.

These assumptions require a sufficiently fine discretization in multi-body simulation. For stress determination purpose, multi-body discretization should not exceed more than one (considered) drill string component.

To allow assessment of randomly complex geometries finite element method is involved to determine local stress properties. While transient analysis of finite element models expense extremely high numeric effort, especially with high number of degrees of freedom or nonlinearities, the calculation of local stresses must be simplified to allow an efficient computation.

Following assumptions are made:
- A drill string component is a linear system that can be described by a transfer matrix.
- Damping forces within a drill string component can be neglected.
- Inertia forces within a drill string component can be neglected.

These assumptions allow further simplification of the mechanical model, Figure 12
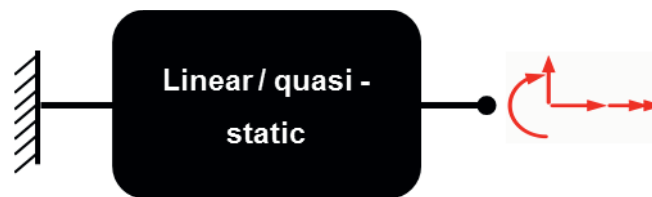
Figure 12: Linear and quasi-static mechanical system

The finite element model may now be setup as a static analysis. Loads are being applied in single loadsteps in an arbitrary load introducing position while all degrees of freedom of the other load introducing locations are locked. Load introducing locations in finite element and multi body simulation shall be coincident. For each loadcase, e.g. bending or longitudinal force, a loadstep is generated where a defined portion of load is applied, e.g. 1 Nm torque or 1 N force. As a model is not fully linear due to e.g. nonlinear contacts, uniform loads may be chosen in the dimension of operational loads.

A transfer matrix is then created by the quotient for each observed location and loadcase:

$$transfer\ matrix(loadcase, location) = \frac{stress\ tensor(loadcase, location)}{unitary\ load(loadcase)} \qquad Equation\ 1$$

Herein the local stress tensor describes all stress components in a body/component related coordinate system.

The total stress tensor describing the time-stress curve for a specific location on a component for a specific location in the drill string (mbs-element) is being computed after Equation 2 with a superposition of stresses deriving from different loadcases.

$$stress\ tensor(time, location, mbs\_element) =$$
$$\sum_{n=1}^{nloadcase} load(n, mbselement) \cdot transfermatrix(n, location) \qquad \text{Equation 2}$$

A threaded connection in a tool joint is a special case that makes it necessary to consider static stresses due to the pretension within the component. The transfer matrix therefore is determined

$$transfer\ matrix\_preload(loadcase, location) =$$
$$\frac{stress\ tensor(loadcase, location) - stresstensor\_preload(location)}{unitary\ load(loadcase)} \qquad \textit{Equation 3}$$

Calculating the total stress tensor the stress tensor that describes stresses deriving from outer loads is superimposed with the preload stress tensor describing inner loads.

$$stress\ tensor\_preload(time, location, mbs\_element) =$$
$$stress\ tensor(time, location, mbs\_element) + transfer\ matrix\_preload(loadcase, location)$$
$$\text{Equation 4}$$

The proposed method allows a fast calculation of the local stresses after a preceding finite element analysis. As the transfer matrices are only geometry-dependent a database for drill string components can be set up.

The simplifying assumptions lead to a defective result from mathematical point of view. Indeed the errors are expected to be small. As the frequency spectrum of downhole vibrations is lowfrequent neither high inertia loads nor do relevant structural damping loads occur. To minimize this error, multi-body-simulation discretization should not be too rough and the assessed location within a component should not be too far from load introduction location. A growing error in this estimation will cause a shorter (calculated) lifetime of a component and is thereby on the "safe" side.

Stress gradient determination

The stress gradient describes the stress decay behind a notch within the material volume. Generally a stress gradient is dependant on geometry, the type of load and the position of the load introduction into a component. For simple geometries with ordinary load conditions analytical formula can be found to determine stress gradients. As complex geometries or complex load conditions require numerical methods, finite element method is generally used to determine stress gradients.

The stress gradient is defined as the maximum gradient of stress within a component volume in the direction perpendicular to the stress direction, Figure 13.

$$\chi^* = \frac{1}{\sigma_{max}} \left(\frac{d\sigma}{dx} \right) \Bigg|_{x=0}$$
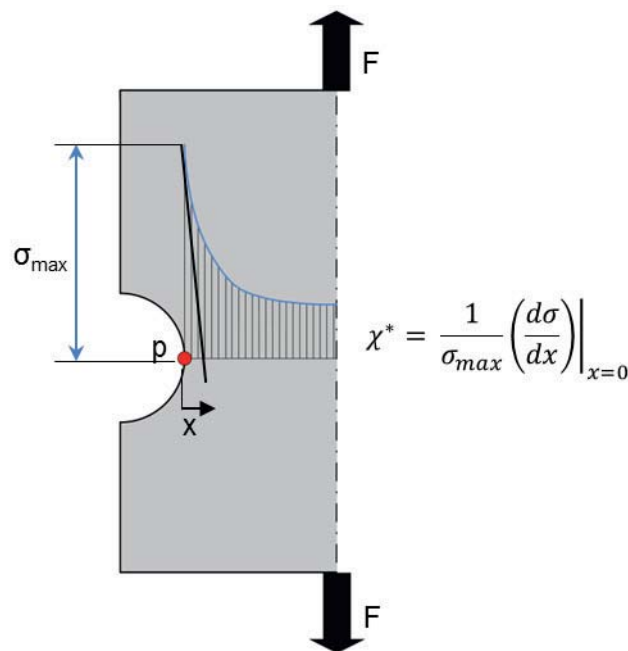
Figure 13: Stress gradient in a notched tensile rod

Typical fatigue calculations consider surfaces and the assessed positions underly two-dimensional stress states. It is assumed that no surface loads are applied e.g. contact pressure. Therefore two independent stress gradients can be obtained - one for each non-zero principal stress.

As numerical results are present in discrete points (nodal positions), stress gradient determination requires result interpolation within the finite element mesh. Whereas life time assessment is performed for surface nodes, stress data within the volume and along a specific path needs to be evaluated by interpolation, at least in one further position.

For an example model with a coarse discretization (for demonstration purpose) the determined path vectors for stress gradient determination are shown, Figure 14. For visualization the vectors are inverted.

Each path vector is determined as a surface orthogonal vector, directed towards the inner volume. Hence the path vectors are geometrically determined on finite element mesh data.
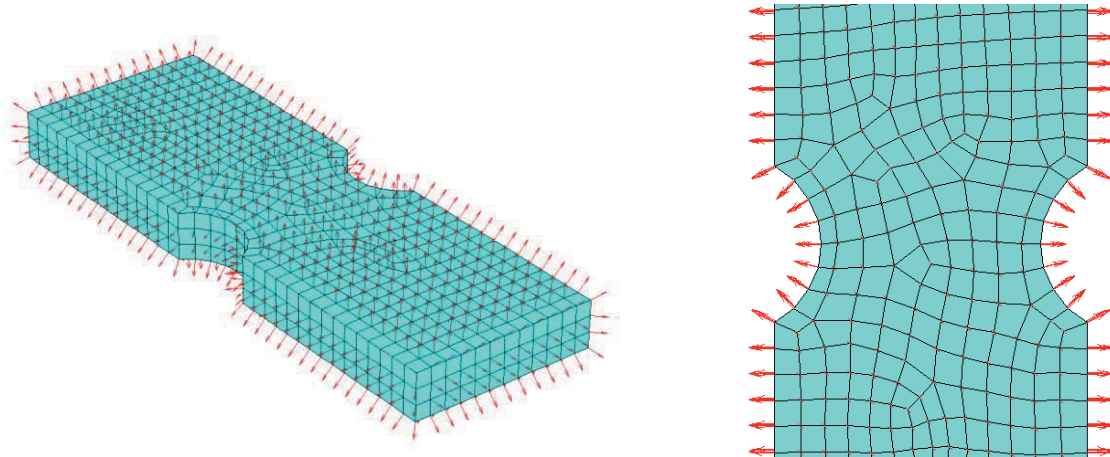
Figure 14: Orthogonal path vectors

For an exact interpolation of stress results along the path vector native finite element shape functions are being used. However, this approach requires determination of local finite element coordinates of the interpolation points (inverse mapping) with the non-trivial demand on numerical solving.

The procedure of interpolation can be described by three main steps:

1. Determination of the enclosing element of the considered interpolation point coordinate
2. Transformation of interpolation point coordinates into element coordinates.
3. Evaluation of differentiated shape functions for stress results.

In the first step the inverse mapping algorithm may already indicate if the enclosing element has been determined, but as this is numerically to expensive efficient search algorithms are combined. The introduction of a virtual net allows reducing the element search list drastically, Figure 15.

703
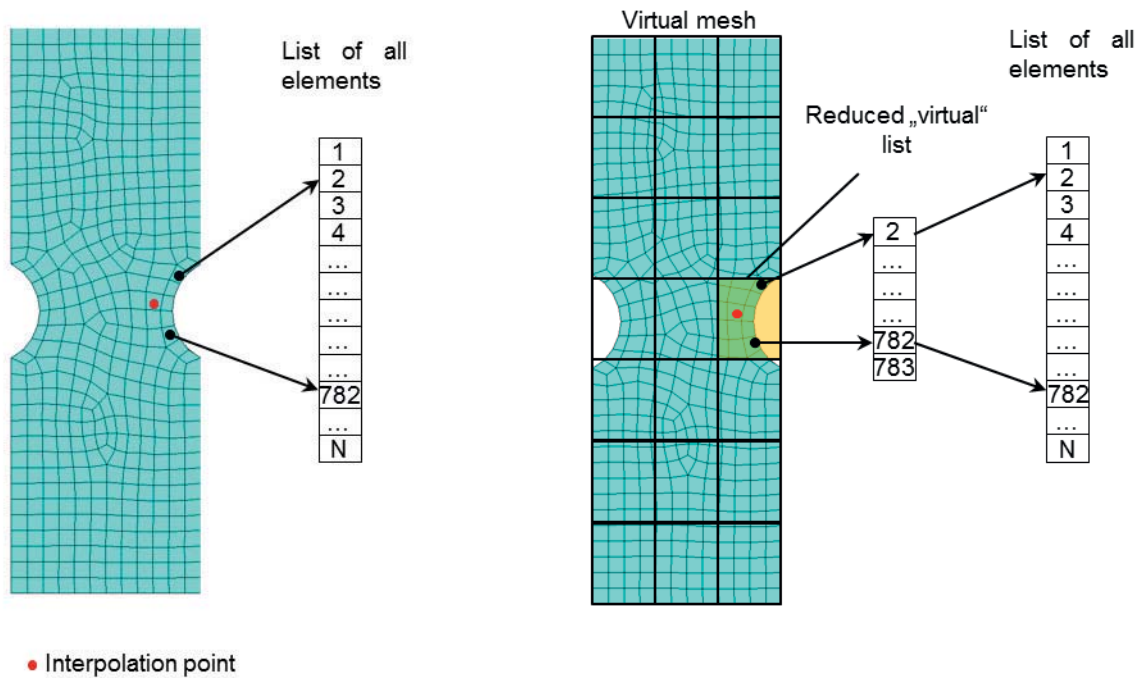
Figure 15: Virtual meshing

In order to transform physical coordinates to element coordinates the element types needs to be detected. For this application a shape-checking algorithm has been implemented to recognize most of Ansys structural elements by checking the nodal configuration of each element. Thereby each element is being linked with its appropriate shape function. Element coordinates then can be derived using Newton-Raphson method. Element coordinates also reveal if the interpolation point lies within an element.

The stress distribution now is being delivered by first order derivation of the shape function. To avoid numerical differentiation, the derivations of each shape functions are implemented for a direct solution. For this purpose averaged nodal results are being used to avoid discontinuous stress curves. This estimation error may be tolerated as it can be controlled by finite element model discretization.

For quadratic shape functions a linear stress distribution results. Therefor a stress gradient can only be constant within quadratic elements. The distance from the surface to the first interpolation point should be sufficiently small that the interpolation point lies always within the surface-attached-element. Thereby path discretization length may be adapted to the net discretization.

Interpolation results for the demonstration model are shown in Figure 16.
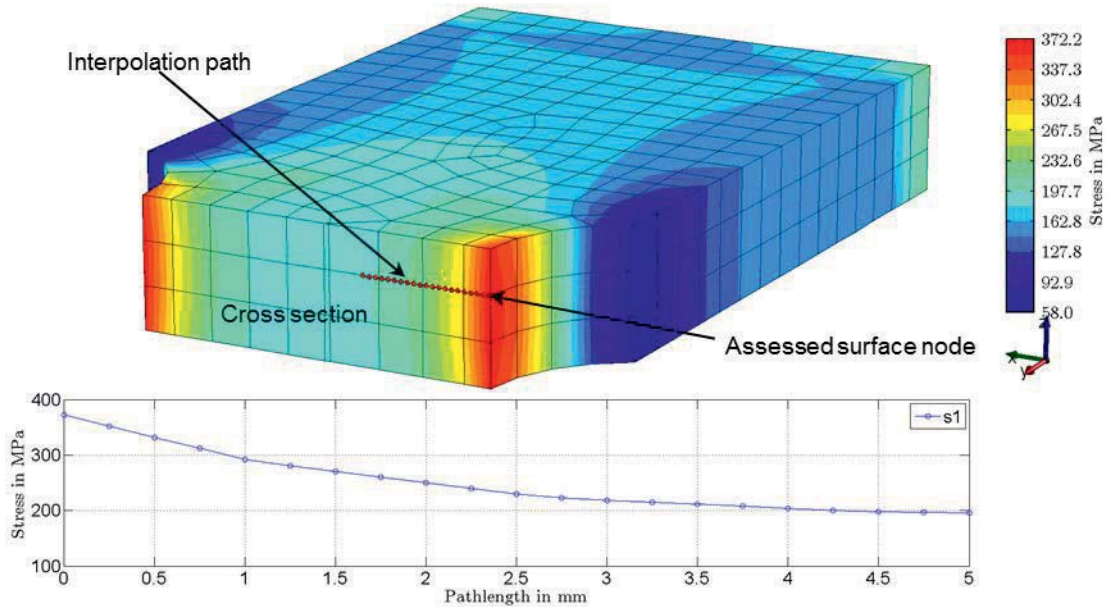
Figure 16: Stress interpolation result, example

In this example a path of 5 mm with a discretization step of 0.25 mm is used. The path starts at the investigation node on the surface where stress results already known. For straight analysis of stress gradients it is sufficient to determine one interpolation point e.g. at 0.25 mm depth. In this example we can see the piecewise linear stress decay curve resulting from quadratic shape functions.

Generally all three components of principal stresses are being evaluated. The analysis of all surface nodes leads to a stress gradient distribution shown in Figure 17 to Figure 19. Again this coarse mesh is not appropriate to determine stress gradients and is solely used for demonstration.
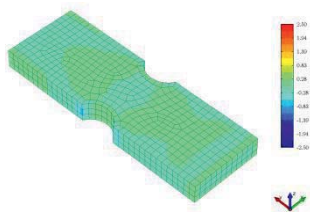
Figure 17: Stress gradient S1
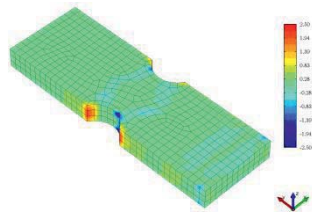
Figure 18: Stress gradient S2
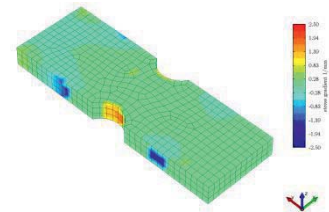
Figure 19: Stress gradient S3

705

As computational costs are expensive, uncritical nodes may be filtered and excluded from further evaluation. The result of surface node filtering at 60 % of maximum von Mises stress is shown in Figure 20 to Figure 22.
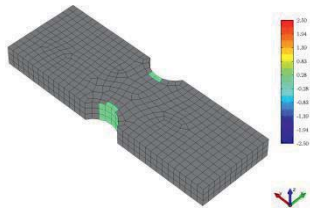
Figure 20: Filtered results of S1
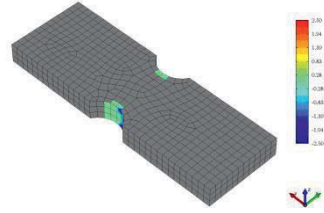
Figure 21 Filtered results of S2
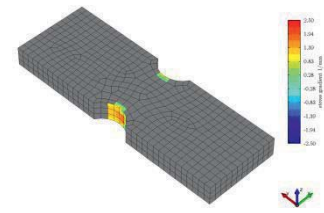
Figure 22 Filtered results of S3

Software application

The described cumulative damage concept has been programmatically implemented in MATLAB with object oriented programming approach. This application is command-line based and does not have a graphical user interface. The software is divided into three parts:

1. Preprocessor,
2. Damageprocessor and
3. Postprocessor

The calculation sequence is shown in Figure 23.
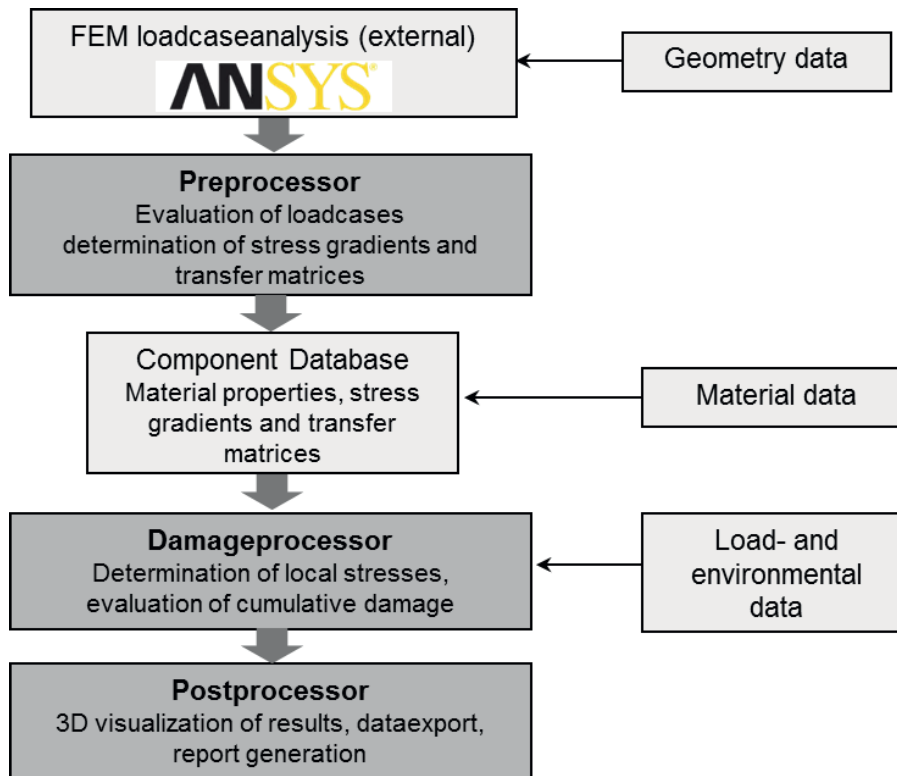
Figure 23: Processing Sequence

The preprocessor includes an interface for the data import from the preceding finite element analysis. Information about nodal positions, -numbers and results as well as element numbers and nodal association to the elements is being transferred and can be seen as minimum requirement. An unlimited number of independent load step results can be imported. For each loadstep-dataset stress gradients and transfer matrices are being assessed. As the number of assessed nodes should not exceed the number of relevant nodes, a selection of nodes for further calculation can be defined either directly by node number or by filtering e.g. on high von Mises stresses. In contrast to stress gradient determination, in fatigue calculation only surface nodes are being assessed.

Various methods for three-dimensional visualization e.g. with specific stress results are being implemented for example: Figure 24 and Figure 25.
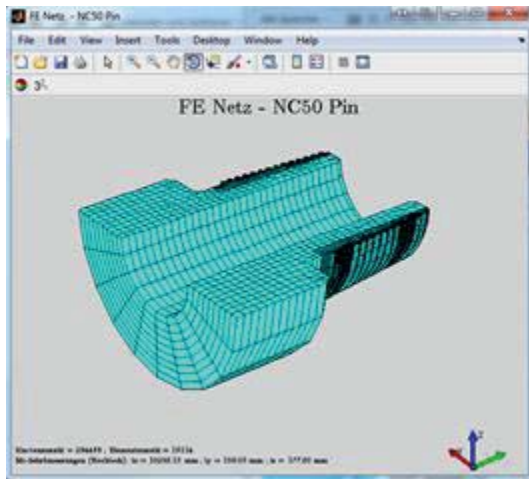
Figure 24: Graphics of finite element mesh
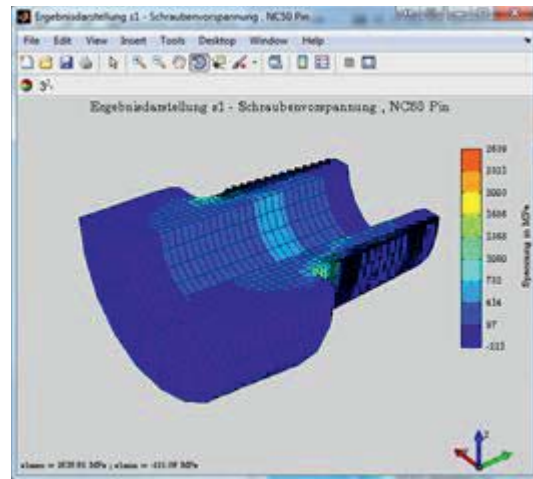
Figure 25: Result graphics of 1 . principal stress of prestress loadcase

The damageprocessor includes the lifetime calculation concept itself and the determination of local stress spectra based on outer loads from mbs simulation or e.g. analytical bending loads. Optional extrapolation of loads is performed based on load spectra as it is most efficient in terms of numerical effort.

The postprocessor contains methods for evaluation of life time assessment results. Three-dimensional visualization based on cumulative damage, load factors or predicted lifetime cycles are available. For more detailed information about the lifetime assessment procedure particular calculation variables and calculation references are outlined in a report. Report generation is done within damageprocessing. The latex based document is finally compiled to a portable document file (pdf).

Two example pages of a report are shown in Figure 26. The report is based on the chapters of the fkm guideline and includes input- and calculated- variables as well as calculation references.

"Continuous" life time assessment with reporting would generate massive quantities of reports. Therefore the reporting function should be used for investigation on a small number of investigated nodes. Thus reporting may be used for detailed analysis and verification of the calculation.
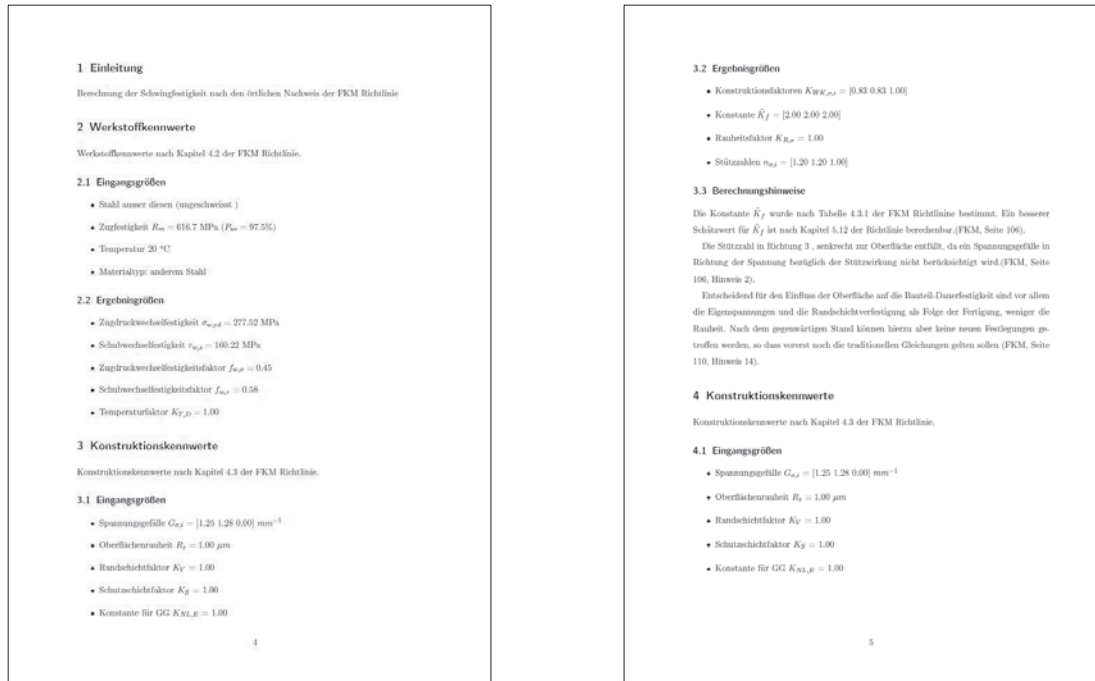
Figure 26: Example pages of reporting

Furthermore an export method allows transferring results of life time assessment for further applications e.g. animation of drilling processes or technical systems reliability of downhole components.

Fatigue animation

For visualization of fatigue simulation results an animation tool has been developed. Cumulative fatigue damage is visualized on an animated drillstring by colouring each drillpipe element while drilling process. A bar graph is also used to visualize the progress of fatigue damage, Figure 27.

Trajectories of gebo wellbore proposals are being parametrically predefined. Based on analytic bending moment calculation according to /API 95/, cumulative damage can be calculated while animation.

709
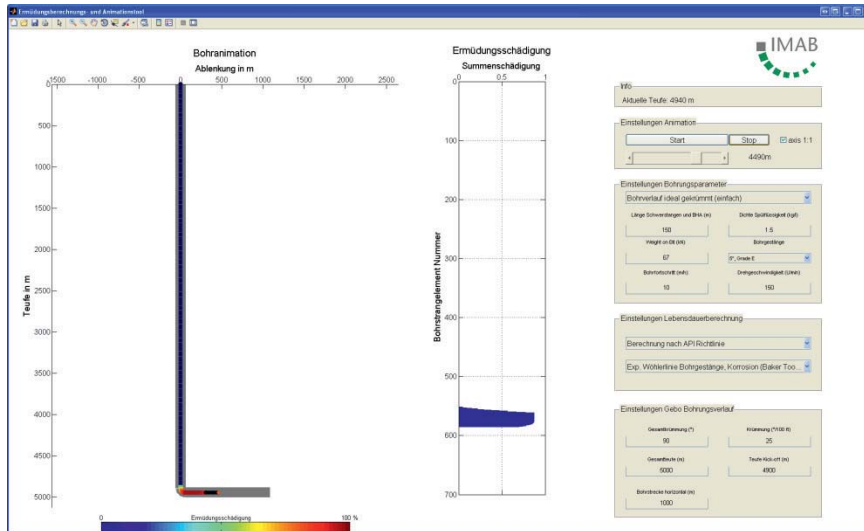
Figure 27: Graphical interface of animation tool

Furthermore arbitrary trajectories can be modeled e.g. based on measurement data. For example curvature measurement data of continental scientific drilling program in Windischeschenbach has been published and was implemented into the fatigue animation tool. With simplified assumptions for drilling conditions and with bending loads from analytic bending moment calculation a fatigue distribution with two focal regions is being calculated. Relevant problems while drilling were identified within logbook and compared to simulation results which already show a rough correlation with simulation results, Figure 28.
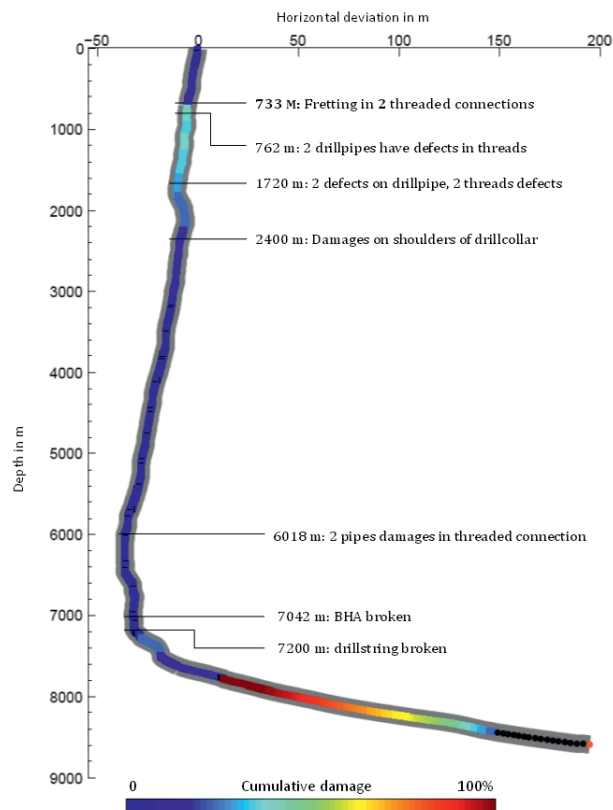
Figure 28: Windischeschenbach damage correlation in the field

Gebo reference wellbore

A case study on geothermal deep drilling wells has been made by the Institute of Petroleum Engineering of Technical University of Clausthal in 2013 /THE 13/. The Projects W7 and W8 chose the injector well 2, located in Salzwedel, as their reference well. The aim was to define a common basis for further investigations. As already described, the fatigue evaluation should be done exemplarily for threaded connections (request of Baker Hughes as the client with professional background). Therefore, IDS provides load spectra of the drill string dynamics for certain locations of the threaded connections with respect to selected sections of drilling the reference wellbore. IMAB uses these load spectra for fatigue analysis of the threaded connection NC 50.

Dynamic load spectra

Due to the remaining project period of 6 month after getting the data, we divided the reference wellbore into 6 investigated sections, see Figure 29. For each section the belonging dynamic load spectra was generated by simulation according to the paragraph "Long-term dynamics of drill strings and load spectra".
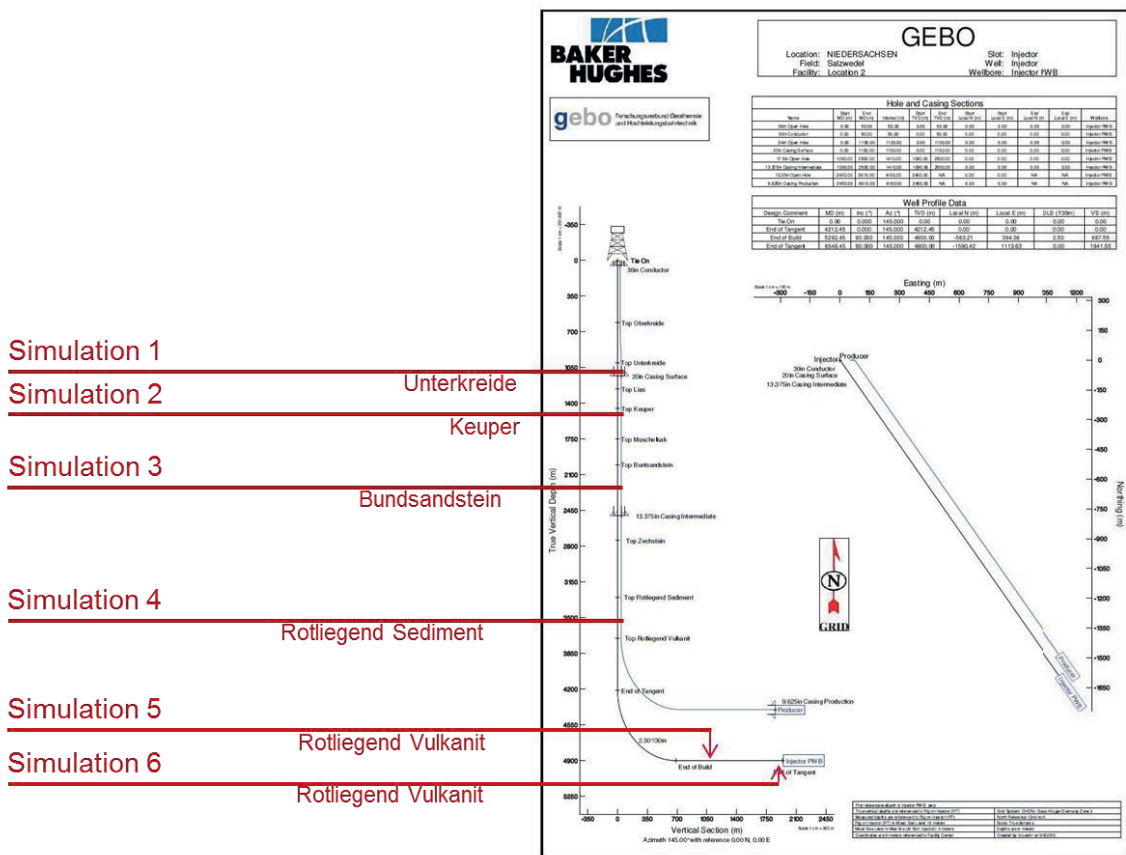
Figure 29: Reference wellbore, formation (/THE 13/) and simulation intervals

Essential formation parameters are listed in Table 2. The value are given by the work group geosystem of gebo (/GEO 11/). From these data, reasonable averages for the long-term simulations were assumed due to the given formation zones, see /THE 13/.

	Formation	Depth (m)	Youngmodulus (GPa)	UCS (MPa)
1	Sandstein	610	26	40
2	Oberkreide	1000	26	40
3	Unterkreide	1260	25	70
4	Lias	1450	33	25
5	Keuper	1750	48	45
6	Muschelkalk	2000	67	115
7	Buntsandstein	2740	59	98
8	Zechstein	3300	36	25
9	Rotliegend Sediment	3700	36	25
10	Rotliegend Vulkanit	5000	50	150

Table 2: Formation parameter
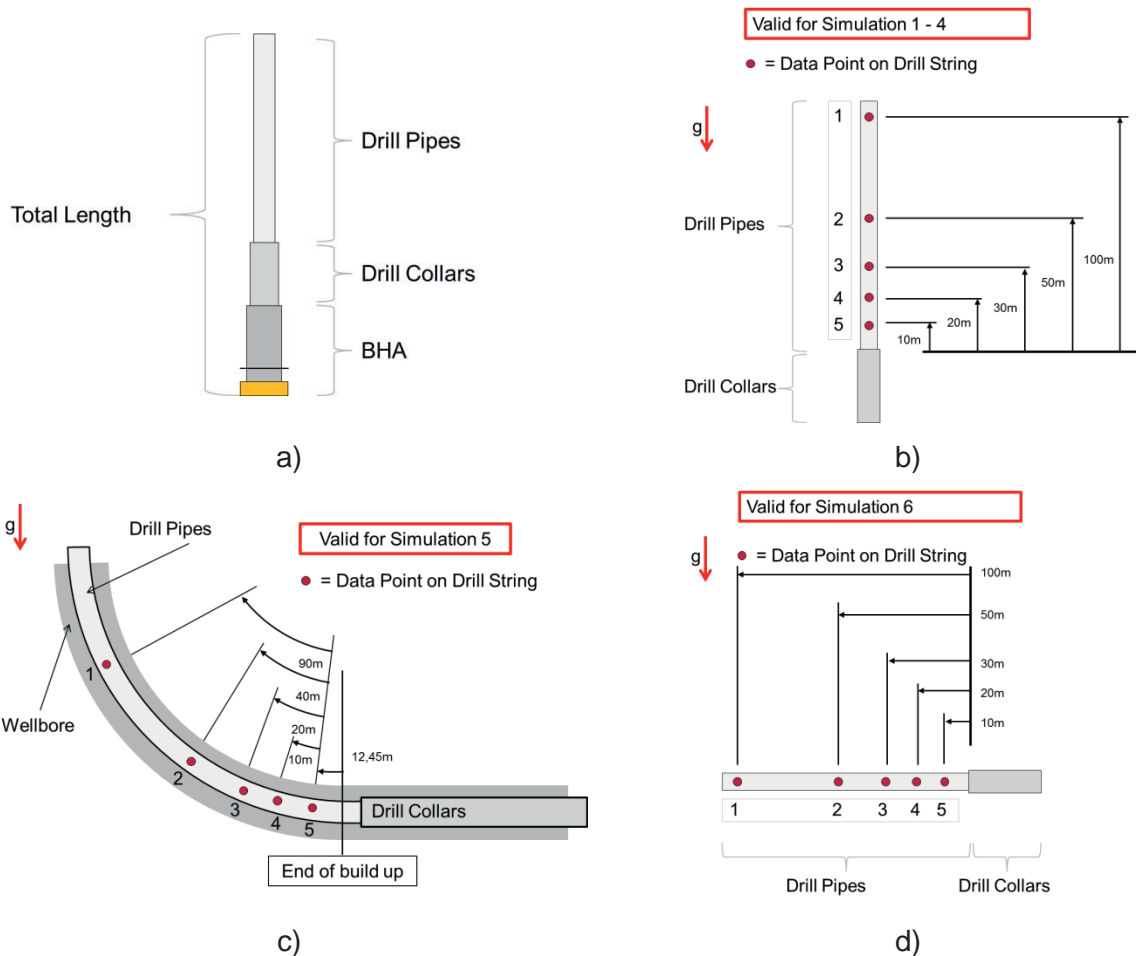
Figure 30: Schematic Setup of Drill String(a), Data Point on Drill String (b-d)

As a start, drilling the reference wellbore is divided into six simulation intervals as shown in Figure 30. The drill string setup is shown schematically in Figure 30a). In detail, the setup to each simulation interval is documented in /THE 13/. For the lifetime calculations of the threaded connections five exemplary data points have been chosen. Figure 30 shows the dimensioning in the vertical section (b) simulation 1 - 4), the curved section (c) simulation 5) and the horizontal section (d) simulation 6).

The first task was to parameterize the IDS model of the coupled system drill string and wellbore with the given input data (geometry, material and drilling process data) and to check the simulations accuracy and stability. The next step was to run time domain simulations in a time period of 30 seconds. According to the aforementioned basics of long-term simulation and simulated load spectra we updated the data exchange (shown in Figure 31) using 30-seconds simulation data. The computed displacement, internal forces and moments are described in wellbore-fixed coordinates, see /OST 14-2/.
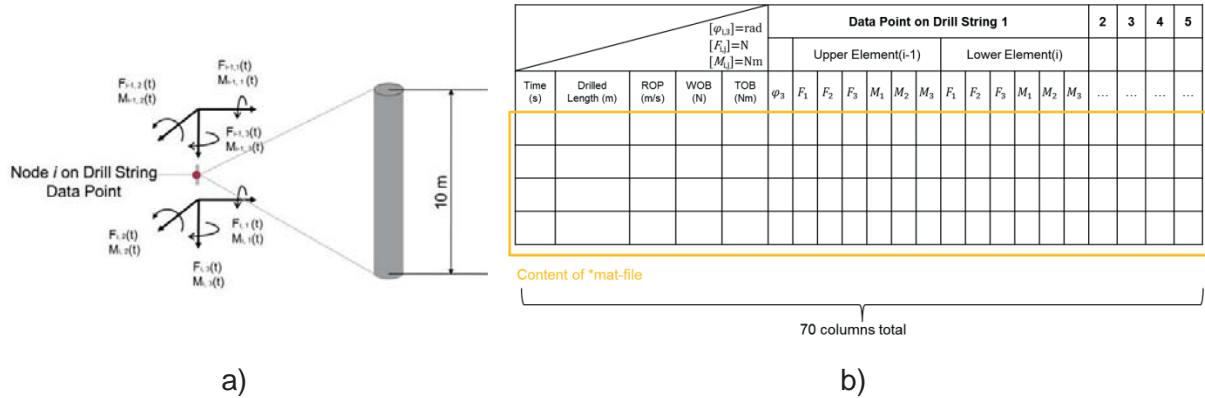
Figure 31: Schematic Setup of Drill String(a), Data Point on Drill String (b-d)

With respect to the remaining project time these simulated load spectra are assumed to be characteristic for the extrapolation of the drilling sections.

The simulated dynamic load spectra of the six investigated reference wellbore sections are documented in exchange matlab files, see /OST 13-1/. To get an impression of the generated simulation and the corresponding load spectra, the simulation results for the simulation 5 and the related load spectra for the data points are shown exemplarily in the following. In Figure 32 the simulations interface show the initial position of the drill string for simulation 5.
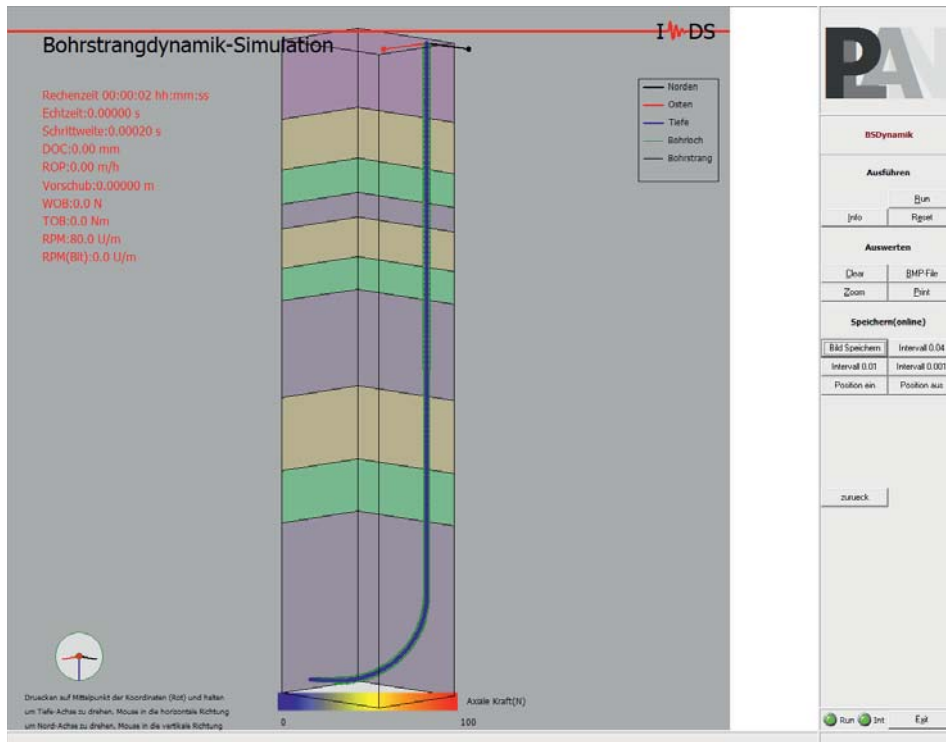
Figure 32: Simulation interface, 3D-view on simulation 5

Figure 33 shows the bending moment M_2 with an amount of the maximum amplitude less than 300Nm at the five data points. In comparison, the amount of the maximum amplitude of the bending moment M_1 is up to 7500Nm as shown in Figure 34. Thus, M_1 is by more than one order of magnitude higher than M_2. In both bending moments, the dynamics of the drilling process are diagramed. In addition, the curvature of the wellbore determines significantly the bending moment M_1 due to the resulting quasi-static bending.
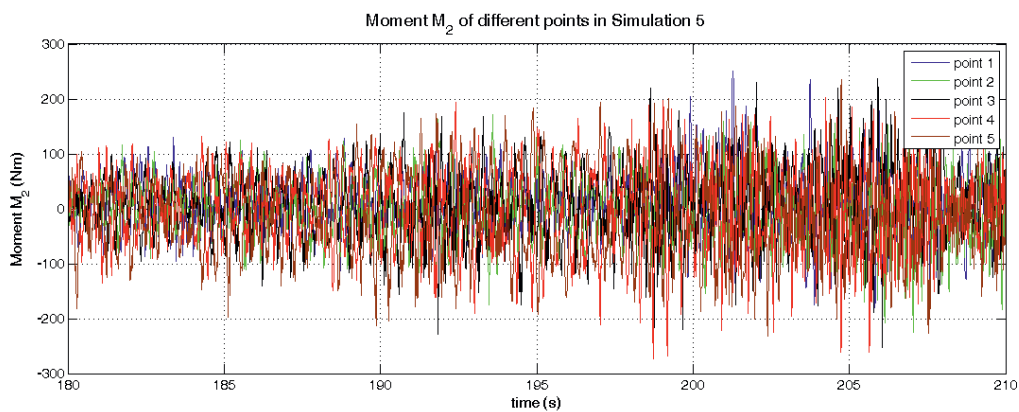
Figure 33: Moment M_2 of Simulation 5 over 30 seconds, data points 1-5
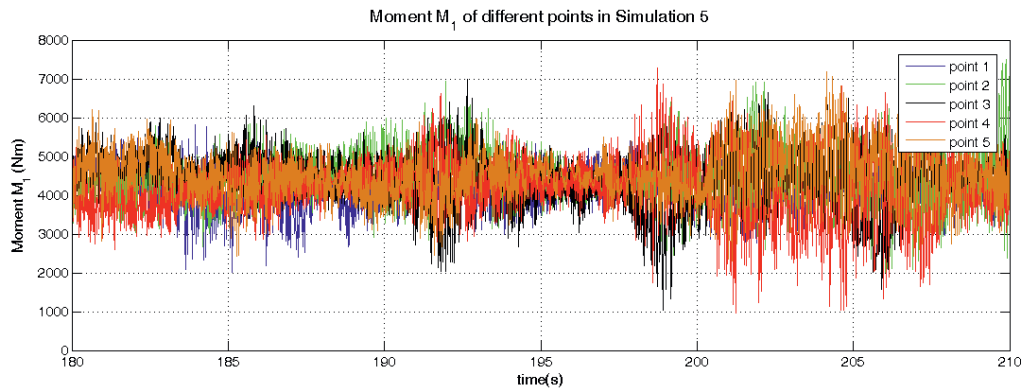
Figure 34: Moment M_1 of Simulation 5 over 30 seconds, data points 1-5

For a better overview, the bending moment M_1 over time is shown only for the data point 2 in Figure 35. In the plot above, the data are shown in time frames of 30 seconds and 5 seconds. Frequency analysis results yield to frequencies in the range of the drill string's rpm and to higher-frequency parts.
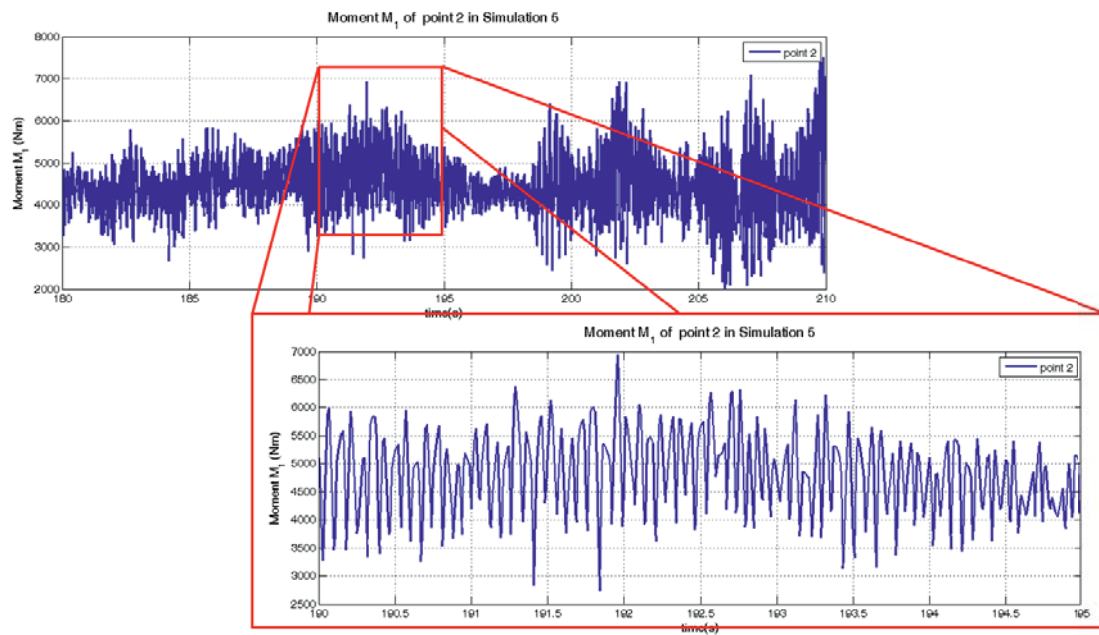
Figure 35: Moment M_1 of Simulation 5, data point 2

Using these load spectra it is possible to run lifetime calculation of threaded connections in six different drilling sections of the gebo reference wellbore.

715

Investigated mechanical parts: Threaded connection NC50

Tool joint NC50 has been chosen to examine fatigue effects in the connection of two consecutive drill pipe elements. Operating experiences of drilling processes exhibit that threaded connections frequently show fatigue damages. Fatigue cracks occur dominantly in first and last engaged threads. Threaded connections are generally identified as most sensitive component to fatigue damage in a rotary drillstring assembly.

NC50 connection geometry is being defined by API specification 7 /API 95/.
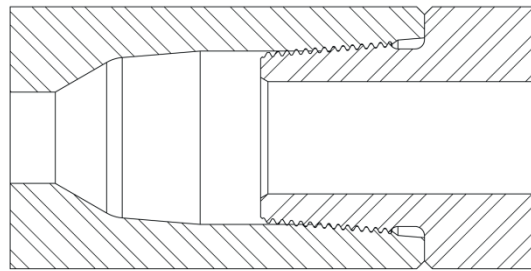
Figure 36: Geometry of NC50 connection

Commonly tool joints are being made of forged steel. Drill pipe and tool joints are buildup by a welding process e.g. frictional welding, inertia welding or flashwelding, /GRO 91/. Due to this production process drill pipe and tool joint may have different materials and therefore different material properties that need to be distinguished in a fatigue assessment.

Load transfer factors are being determined with a finite element model, Figure 37: Finite element modell of NC50 connection, Figure 37. Due to three dimensional stress effects (caused by torsional loading) the finite element model must be three dimensional. Thread pitch is being neglected, so the model is axisymmetric. The linear elastic material model is parameterized with modulus of elasticity ($2.1 \cdot 10^5$) and poisson ratio (0.3). All contacts between pin and box (thread and shoulder) are assumed to be frictional, with a friction coefficient of 0.08.
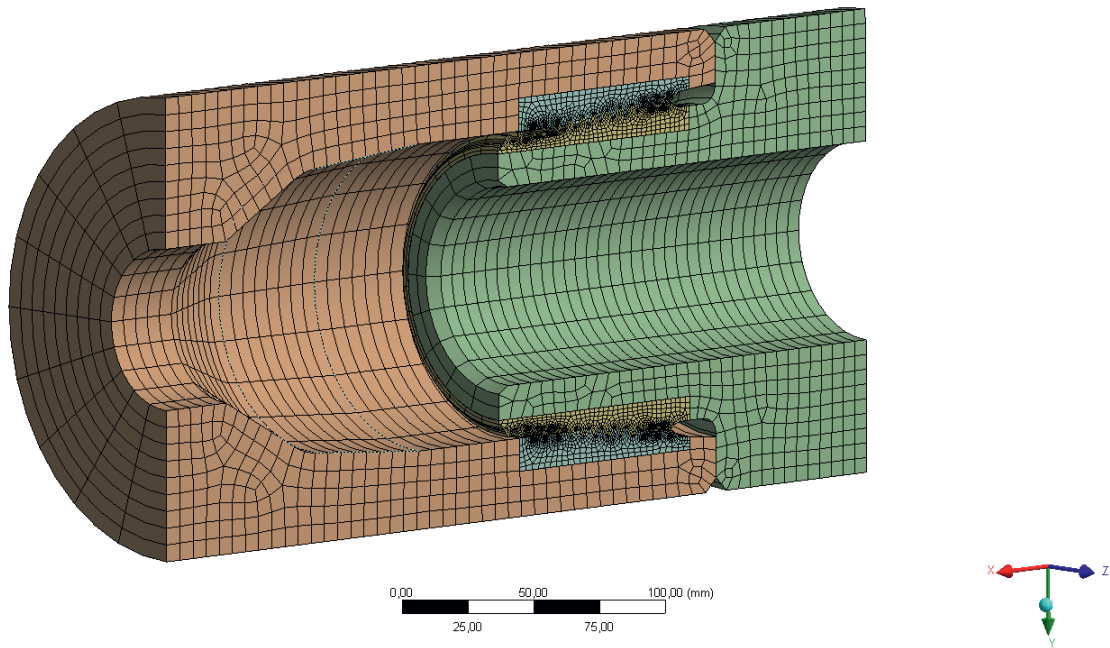
Figure 37: Finite element modell of NC50 connection

Pretension of the connection is modeled by a pretension force element. The pretension force is analytically determined with /API 95/. A make-up-torque of 44 kNm results in a pretension force of 3450 kN, /ESD 10/. Application of unitary loads occurs in the preloaded model.

Investigated mechanical parts: Drill String with "slip cuts"

To evaluate the influence of mechanical damages of the drill pipe caused by the interaction with rock while drilling a general geometric model has been set up. Herein a failure-geometry of a semicircle on the outer side of a 6 5/8" drill pipe is being assumed, Figure 38.
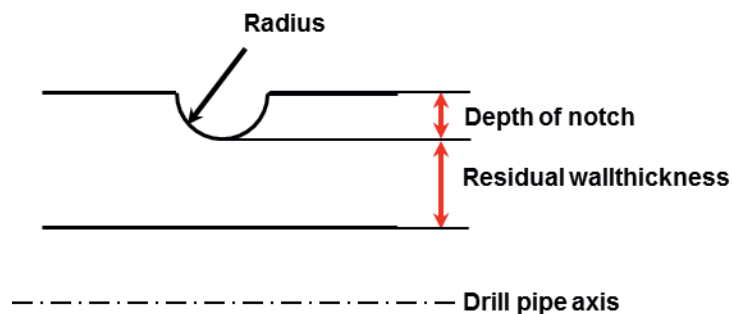
Figure 38: Slip cut model

717

Table 3: Properties of "slip cut" model

Outer Diameter	168.28 mm (6 5/8")
Inner Diameter	149.86 mm (5.9")
Quality	S-135 Premium

Different levels of severeness are being modelled by varying the depth of the notch. Figure 39 shows the slip cut model with different damages in the range from unnotched until a reduction of wall thickness about 25 %.
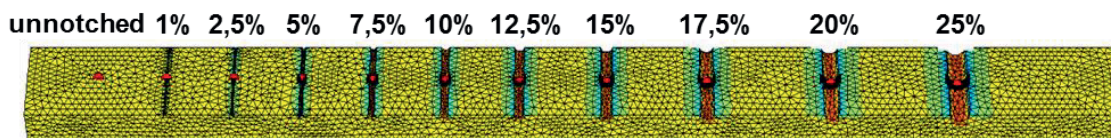
Figure 39: Slip cut Finite Element Model

The evaluated points are marked with a red dot and are positioned in the lowest point of the notches. All notches are modelled with a fine discretization finite element mesh around the evaluated points, Figure 40.
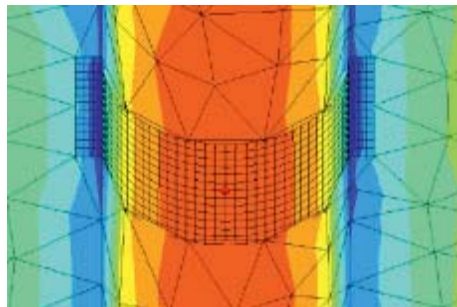
Figure 40: Detail of finite element mesh in "slip cut" notch

Extrapolation of load spectra

In order to receive characteristic and continuous load spectra for the entire drilling process the simulated load data is being extrapolated. For the Salzwedel reference borehole six load spectra can be calculated. These load spectra are assumed to be characteristic for the extrapolation regions. The proposed extrapolation regions are shown in the multicolored well trajectory, Figure 41. Each coloured region indicates the start and end points based on the position of the drillbit, whereas gathered simulation data along the drillstring is represented by a red cross.
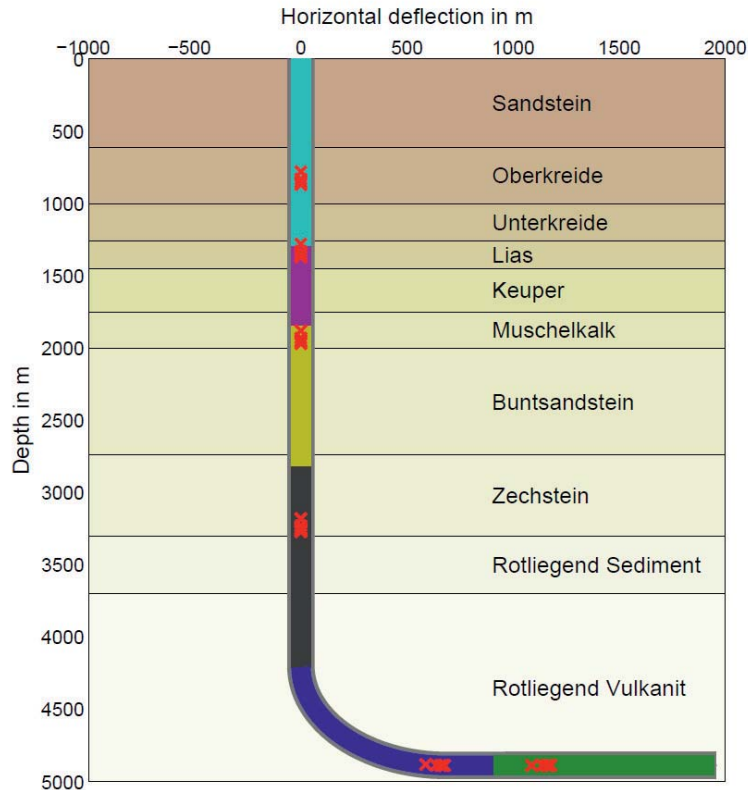
Figure 41: Extrapolation regions of reference wellbore

The number of underlying characteristic load spectra should be sufficiently high to take all operating conditions and thus the different load conditions into account. The extrapolation regions may be chosen for those regions where operating conditions are expected to be similar.

Based on the expected rate-of-penetration the load spectra are being linearly extrapolated. The life time concept allows the extrapolation based on rainflow matrices, which is more efficient in means of computation time and memory requirements.

The simulation data can obviously be extrapolated in time domain under certain assumptions. Whereas the distribution of loads along the drillstring cannot be extrapolated and shall directly delivered by the simulation model or measurement. Evaluation of multiple points along the drillstring may allow a load data interpolation of characteristic load spectra for a quasi-continuous load distribution.

Thus the combination of load spectra extrapolation (time domain) and load spectra interpolation (position domain) allows surveying or assessing life time properties at every position during the whole drilling process. Like time-domain, all position states can be seen as one-dimensional along drillstring.

Environmental influences

Reasonable discretization allows considering environmental influences to be constant within each extrapolation region. The temperature in each region (mean temperature) is being assessed based on a temperature gradient (e.g. 30 °C/km). Comparative analysis with corrosive environments is also taken into account by an intermediate corrosion strength factor of 0.6.

Cumulative Damage Results: Slip Cuts

The severeness of wall thickness reduction and notches lowers fatigue resistance of drill pipe. The complete drilling process of reference wellbore Salzwedel causes only small fatigue damage to a drill pipe when a non-corrosive environment is assumed. Even with a wall thickness reduction of 25 %, cumulative fatigue is expected to be below 20 % after well completion, Figure 42.

A moderate corrosive environment drastically increases cumulative fatigue damage. Whereas unnotched drill pipe is still uncritical, wall thickness reduction above 17.5% is expected to reveal fatigue failures while drilling process, Figure 43.
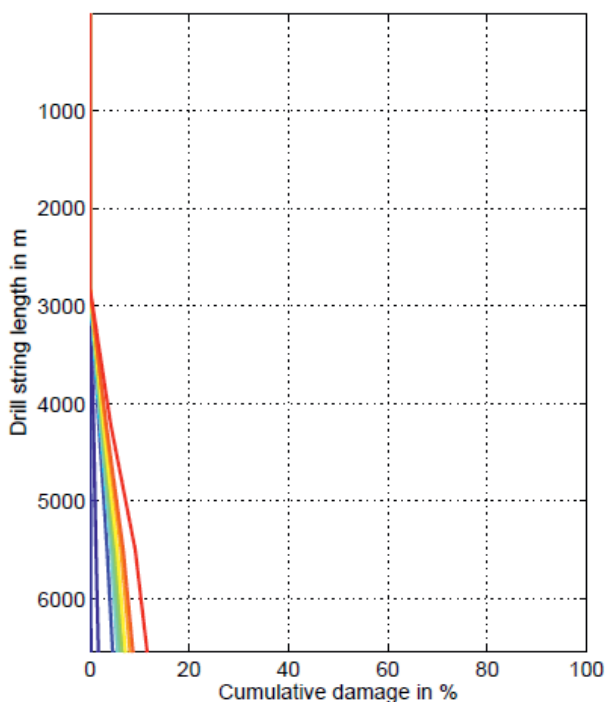
Figure 42: Damage of drill string element 5 without corrosion
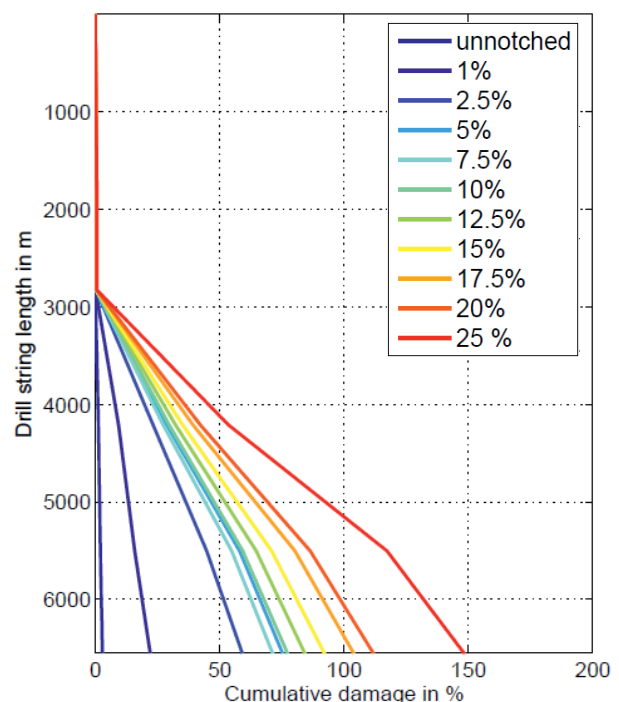
Figure 43: Damage of drill string element 5 under (moderate) corrosion

Composition of load factors is independent on effect of corrosion. Figure 44 and Figure 45 show that torsional and bending loads dominantly lead to fatigue damage whereas axial- and radial force components show negligible influence.
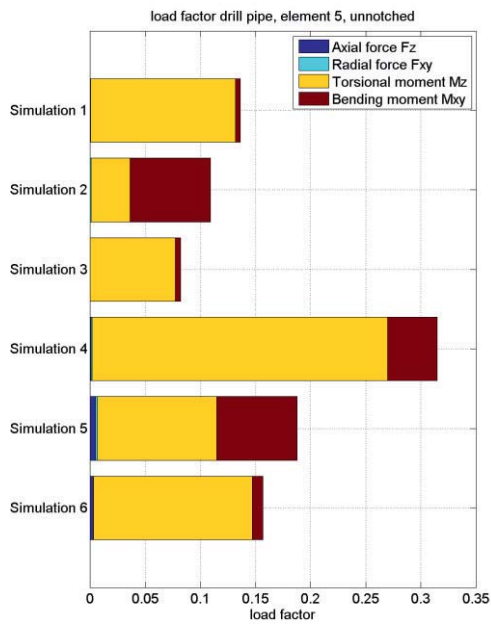
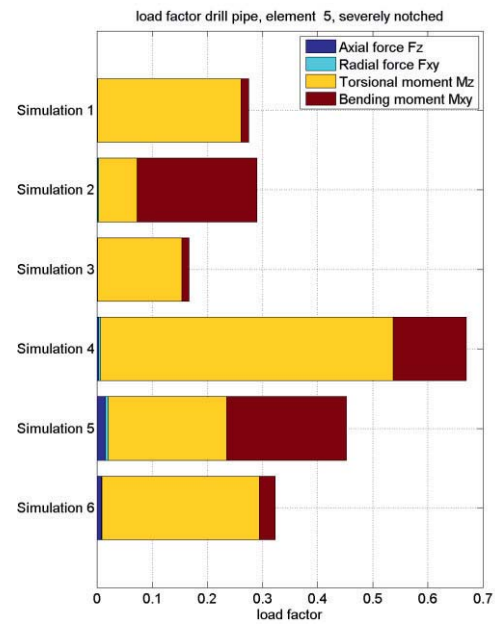*Figure 44: Load factor composition for unnotched drill pipe 6 5/8"*

Figure 45: Load factor composition for severly notched (25 %) drill pipe 6 5/8"

Cumulative Damage Results: NC50

The cumulative damage for the NC50 connection is negligible low for all locations on pin and box. As expected the presence of corrosion in the threaded connection has a negative effect on lifetime but creates also negligible damage.

The analysis of the load factor reveals a low degree of utilization. The load factors of the four different load components give information about the dominating load components.

In gebo milestone report /ESD 10/ it could be shown that the first engaged thread of the pin (thread number 1) and the last thread of the box (thread number 12) are most critical, Figure 55 and Figure 56. Field experiences match this result, e.g. /MAC 06/.

Load factor composition of NC50 pin reveals the fatigue-sensitivity of the first thread in comparison to the last engaged thread, Figure 46 and Figure 47. Whereas in the first thread the highest fractions of damage result from torsional and lateral loads, the last thread is more sensitive to bending loads.
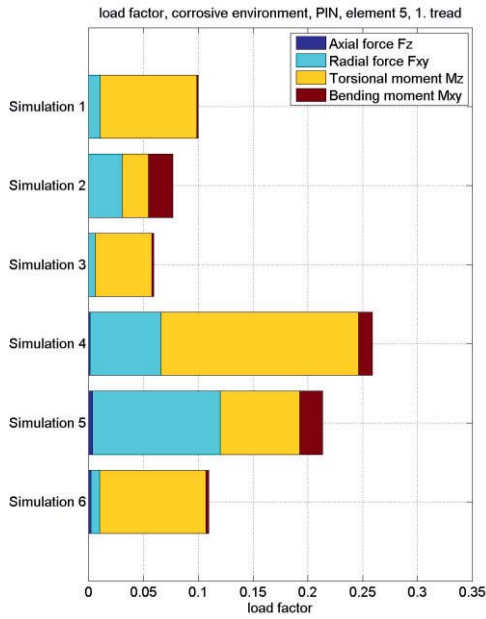
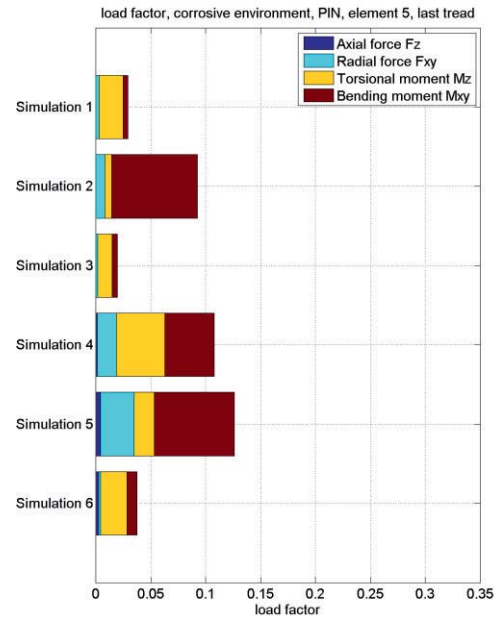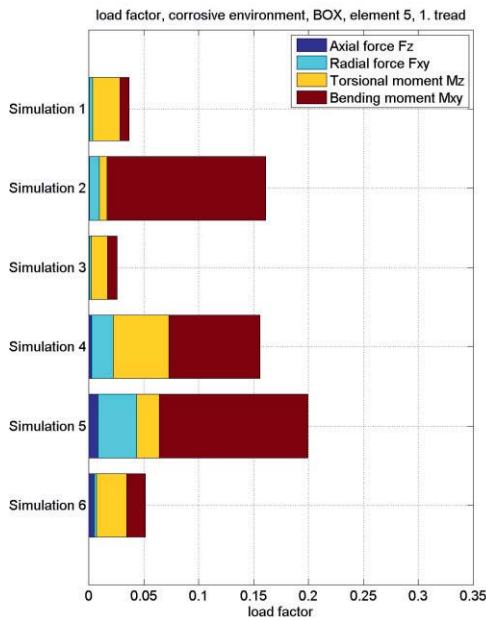*Figure 46: Load factor composition for first thread of NC50 pin*

Figure 47: Load factor composition for last (12.) thread of NC50 pin

Load factor composition of NC50 box exhibits inverse distribution of load factors compared with the pin. The first engaged thread from the viewpoint of the box is thread number 12. Therefore it is plausible that the highest load factors can be found on thread number 12 and results are pairwise similar between pin and box. The sensitivity to load-components is also similar to those of the pin.

Figure 48: Load factor composition for first thread of NC50 box
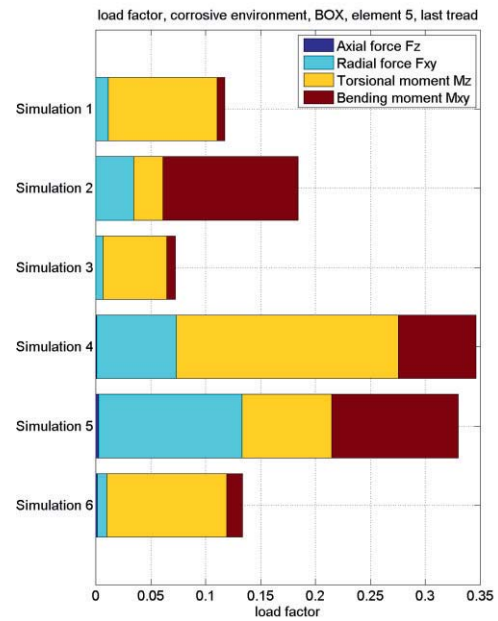
Figure 49: Load factor composition for last (12.) thread of NC50 box

Analysis of unfolding and expansion mechanism (WP 7), IDS:

At the beginning of the gebo project one project leader (project W2) started a new position at a different university outside of lower Saxony. However, the project results were necessary for project W6. Therefore, the IDS adopted the necessary tasks without additional funding as described in the following in addition to the above documented research work of project W7. In these investigations commercial FEM programs were used in contrast to the IDS in-house FEM developments (special developed FEM programs) during the other research work of the gebo project.

In this additional work package the expansion mechanism of folded tubular for casing applications are analyzed by using FEM simulations. A folded tubular can be expanded for example by internal pressure or a cone expander. The geometries have been developed by *IW, LUH* in the project W6. Our objective is the investigation of the expansion mechanism with different geometries and material properties given by W6. In an iterative manner it is possible to improve and optimize the geometries and used materials with respect to the casing applications, which are required by the drilling process of project B1. For the accurate description of this expansion process an elasto-plasticity-model is needed because of the high nonlinear effects in geometry and material behavior. Therefore, a nonlinear finite element method (FEM) was used /OST10/, combined with necessary numerical algorithms.

Geometry of the folded tubular and material properties

The investigated geometries, which was developed in project W6, are shown in Figure 50Figure 1. The ratio of initial diameter to wall thickness is 28.
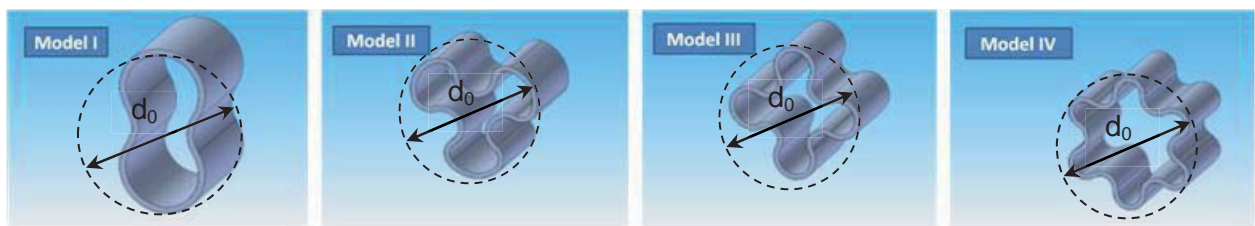

Figure 50: Geometries of the folded tubular

The geometries were analyzed with three different types of materials: normal mild steel, TRIP steel and TWIP steel. The belonging stress strain curves are shown in Figure 51.
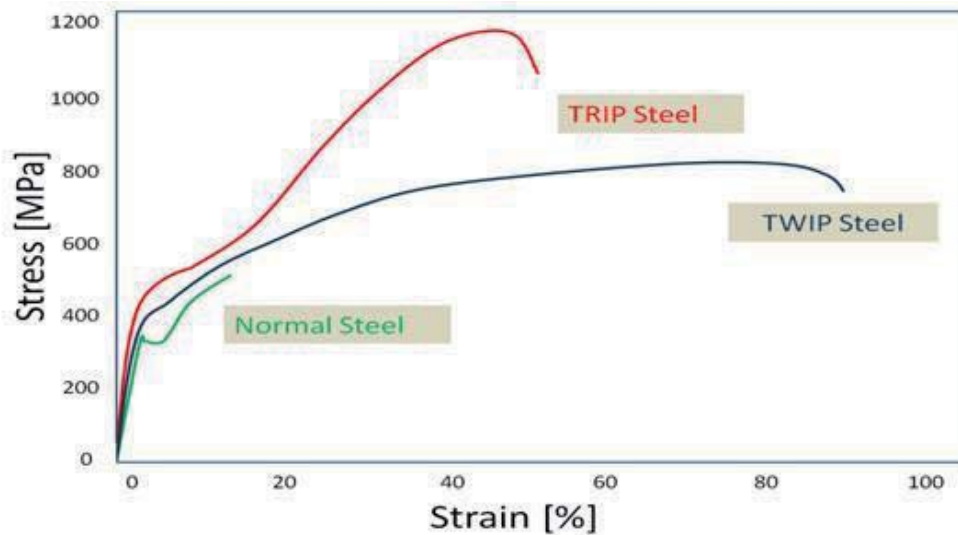
Figure 51: Stress-strain curves of normal steel, TRIP steel and TWIP steel

The normal mild steel was used for representing steel, whose strain is less than 20 %. While TRIP steel was used for representing high strength steel. The strength is higher than 1000 N/mm^2 and the rupture strain is about 50 % approximately. A plastic flow process occurs in TRIP steel with phase transformation from Austenite to Martensite lattice. The atoms build up a new crystal structure during the deformation process; this is the reason why TRIP's strength can be increased significantly. The strain can be increased corresponding to the new bonding of crystal structure. TWIP steel was used for representing high deformation steel, whose strain is about 90 % at rupture point. In the plastic flow process for TWIP steel, the strength can be increased with lower magnitude compare to TRIP steel. The strain can be increased significantly due to the so-called Twinning effect.

Numerical calculation and results

The elasto-plasticity models have to be solved numerically. To obtain reasonable solutions with acceptable accuracy, high requirements towards the modeling technique and the numerical treatment are necessary. The nonlinearity in this computation includes geometrical nonlinearity due to the large deformations and the material nonlinearity which describes the nonlinearity of the material laws. The element meshes are implemented with quadratic element type for increased accuracy. The iterative Newton method is used to obtain the nonlinear solution, while the system equation solver is the direct method. The time increment is automatically adapted in the computation process /OST10/.

For the following simulations, the unfolding and expansion process was generated by using rotationally symmetric internal pressure increasing linearly in time up to a maximum of 15 N/mm² (normal steel) or 30 N/mm² (TRIP steel, TWIP steel). If the model's structure fails during this process because of exceeding the rupture stress, the calculation is interrupted.

After all, the model's expansion ratio is determined with respect to the chosen parameter. The percentage expansion ratio is $\eta = \left(\frac{d_1 - d_0}{d_0}\right) \cdot 100\%$, wherein the initial diameter is d_0 and the final diameter after the expansion is d_1.

Table 4: Numerical results of the expansion process

Descriptions	Material	Expansion rate (N/mm^2 s)	Max. Stress (N/mm^2)	Pressure (N/mm^2)	Evaluation	Expansion Ratio %
Model 1 Set # I	normal steel	1,50E+01	5,00E+02	5,71E+00	*failure*	-
Model 1 Set # II	TRIP steel	3,00E+01	6,05E+02	3,00E+01	*Ok.*	-1,41E+01
Model 1 Set # III	TWIP steel	3,00E+01	5,89E+02	3,00E+01	*Ok.*	-1,41E+01
Model 2 Set # I	normal steel	1,50E+01	5,00E+02	8,16E+00	*failure*	-
Model 2 Set # II	TRIP steel	3,00E+01	7,23E+02	2,98E+01	*Ok.*	2,01E+01
Model 2 Set # III	TWIP steel	3,00E+01	6,18E+02	3,00E+01	*Ok.*	1,96E+01
Model 3 Set # I	normal steel	1,50E+01	5,00E+02	6,61E+00	*failure*	-
Model 3 Set # II	TRIP steel	3,00E+01	8,46E+02	3,00E+01	*Ok.*	2,15E+01
Model 3 Set # III	TWIP steel	3,00E+01	6,28E+02	3,00E+01	*Ok.*	2,06E+01
Model 4 Set # I	normal steel	1,50E+01	5,00E+02	4,33E+00	*failure*	-
Model 4 Set # II	TRIP steel	3,00E+01	7,46E+02	3,00E+01	*Ok.*	2,27E+01
Model 4 Set # III	TWIP steel	3,00E+01	6,30E+02	3,00E+01	*Ok.*	2,29E+01

The results of the expansion process with different geometries and different materials are presented in Table 4: Numerical results of the expansion process. For all geometries, normal steel fails before a round geometry could be formed. In contrast, TRIP and TWIP steel can be formed until a round geometry is reached without damages. Concerning again the maximum stress, the TRIP steel has higher magnitudes compared to TWIP steel at the same internal pressure, because of the material's nonlinearity. TRIP steel is harder and TWIP steel can be reformed easier than TRIP steel. The expansion mechanisms can be found in Figure 52 and in Figure 53, where the critical part of the structure in the expansion process is shown. The gray color presents the critical part of the tubular structure, where the strain reached the rupture point.
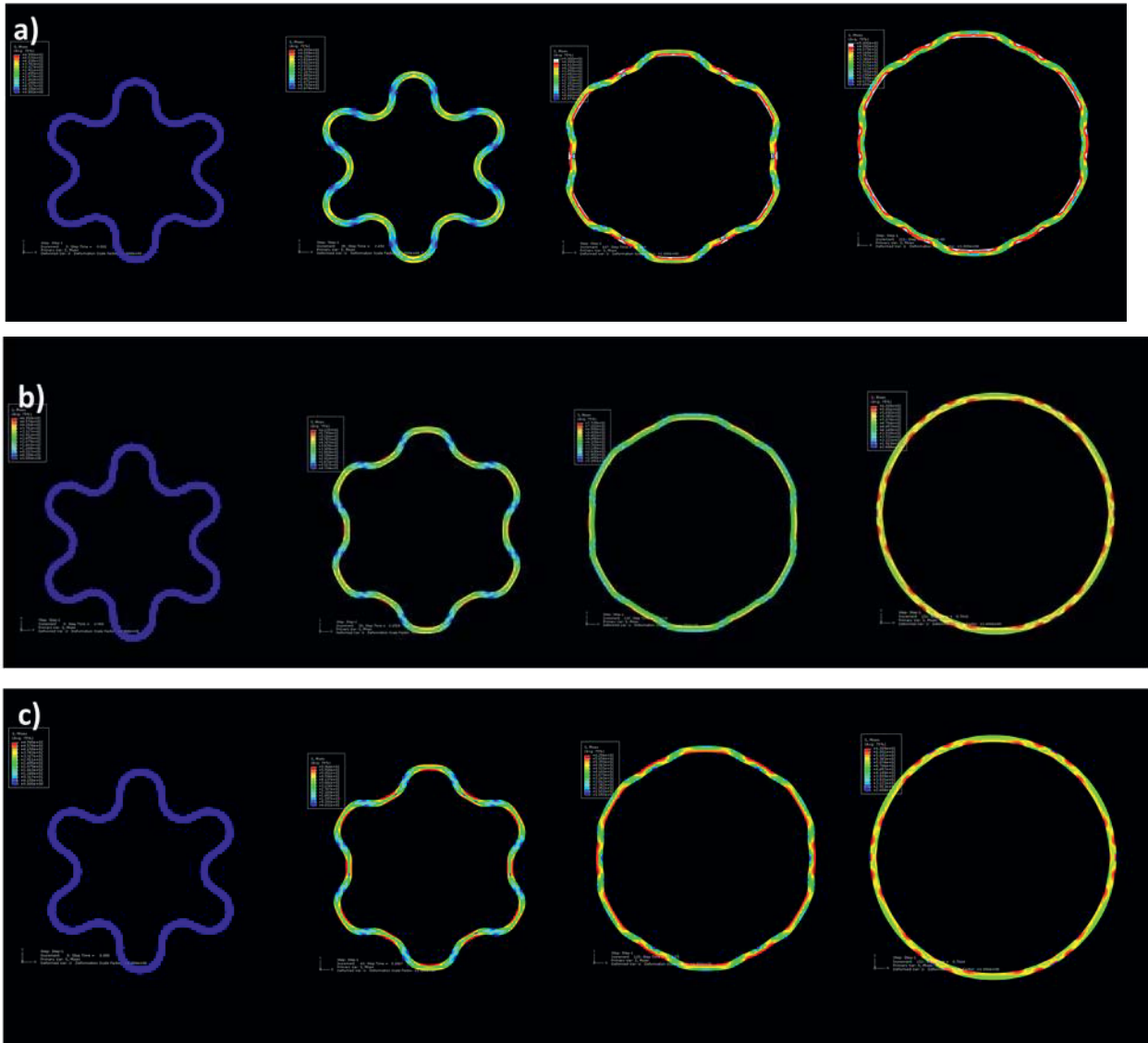
Figure 52: Expansion process for model IV; a) normal steel, b) TRIP steel, c) TWIP steel

Concerning numerical results of the internal pressure expansion process, the plastic strain occurred after the pressure was increased. At some pressure the tubular were reformed. Theoretically, if materials do not arrive at the rupture point when increasing the internal pressure, they should be reformed until the round geometry occurs. If they arrive at the rupture point, they will be damaged before the round geometries have formed.
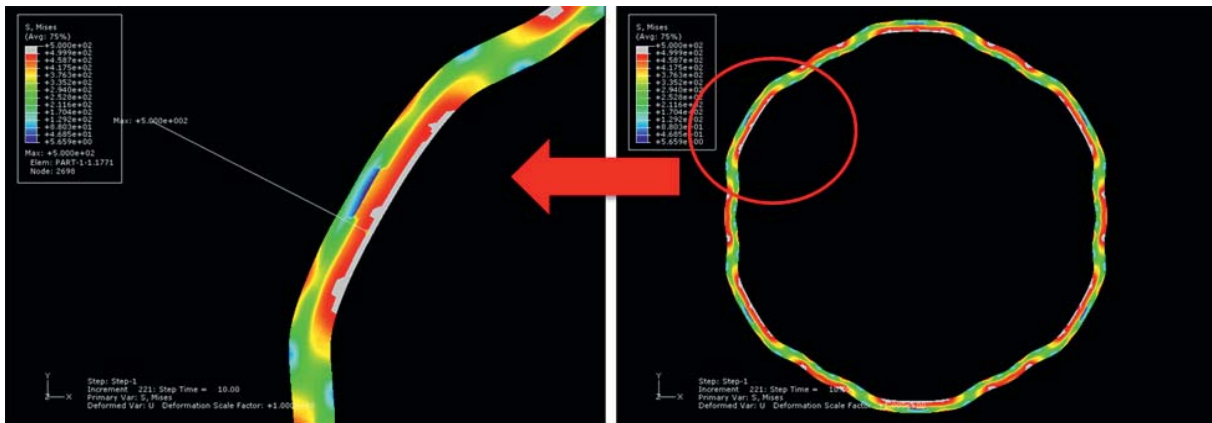
Figure 53: Expansion process at critical part of structure for model IV

The additional milestone M1 „Modeling and Simulation of Expansion Mechanism of Given Tubular Geometries" is reached.

We also carried out simulations to the case of three dimensions with driving cone expander, see Figure 54. The tubular were expanded by driving a cone structure through them. The expansion shape of the cone will automatically expand the tubular corresponding to plasticity, friction behavior and contact mechanism. The different materials (normal mild steel, TRIP steel and TWIP steel) were used again, similar to the case of internal pressure expansion.
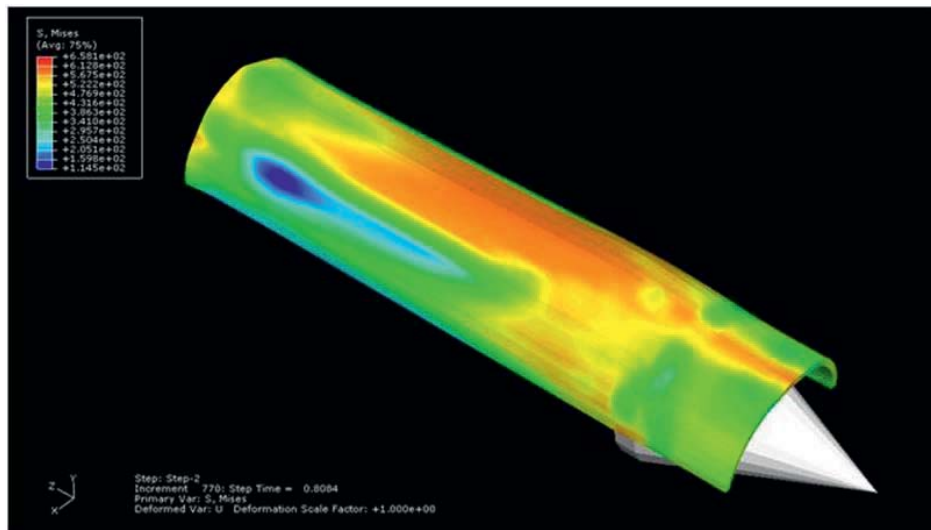
Figure 54: Mechanism of expansion process with driving cone expander (TWIP)

The simulations qualitatively obtain similar results related to the investigated materials. In the case of normal mild steel, plastic strain has already arrived the rupture point before the expansion process has been completed. The cases of TRIP and TWIP steel were different, the tubular can be completely expanded by the cone expander without any macroscopic damages.

727

3 References

/API 95/   Recommended Practice for Drillstem Design and Operating Limits, API Recommended Practice Bulletin RP7G, 15th edition, Washington D.C., 1995

/BER 09/   C. Berger, Korrosionsbedingte Maschinenbauteilfestigkeit II, Vorhaben Nr.278, Forschungskuratorium Maschinenbau, Heft 303, Frankfurt am Main, 2009

/DS1 04/   Tom H. Hill, P.E., Standard DS-1, Drill String Design and Operation, third edition, volume 2, T H Hill Associates, Hillmont, 2004

/FKM 03/   B. Hänel, FKM guideline, Analytical Strength Assessment , 5th edition, VDMA publishing house, Frankfurt am Main, 2003

/GEO 11/   gebo Geosystem: Benchmarkmodelle Interne Plattform gebo, Datei: benchmark_horstberg_loehken_nov2010_update20110712.xls, 2011

/GRO 91/   G.Y. Grondin, G.L. Kulak; Fatigue of Drill Pipe, Structural Engineering Report No. 171, Department of Civil Engineering, Edmonton, 1991

/HAN 63/   J. Hansford, A. Lubinski, Effects of drilling vessel picht or roll on kelly and drill pipe fatigue, Journal of petroleum technology, 1964

/MAC 06/   K.A. Macdonald, J.V. Bjune, Failure analysis of drillstrings, pp. 1641-1666, Engineering failure analysis, edition 14, 2007

/OST 05/   Ostermeyer, G.-P.: Mesoscopic Particles. MKS-Tool for multidisciplinary applications with different length and time scales, erschienen in: J.M. Goicolea, J.Cuadrado, J.C.García Orden (eds.), Multibody Dynamics 2005 (ECCOMAS 2005)

/SCH 08/   Schiefer, F., Ostermeyer, G.-P.: Technical Pain Sensor - Concept and Application. Proceedings of the MOVIC 2008, München (2008), Paper 1152

/SIL 07/   G.H.C. Silva et. al, Exact and efficient interpolation using finite elements shape functions, Ecole nationale superieure des mines de Saint-Etienne, France, 2007

/THE 13/   C. Theodoriu, et.al., Economic drilling of deep Geothermal wells, group project, draft version, Technical University of Clausthal, 2013

/WEN 98/   E. Wendler-Kalsch, H. Gräfen, Korrosionsschadenkunde, Springer Verlag, Berlin, 1998

4 Publications, reports and presentations of Project W7

/ESD 10/   Esderts, A., Runge, S., Lebensdauer einzelner Bauteile, Interner gebo-Bericht,

Meilensteinbericht, 2010

| /OST 10/	Ostermeyer, G.-P., Srisupattarawanit, T., Schiefer, F.: Berechnung und Simulation von Entfaltungsmechanismen gefalteter Rohrstrukturen, Interner gebo-Bericht – IDS-Zwischenbericht 2010-11
/OST 11/	Ostermeyer, G.-P., Schiefer, F.: Erste synthetische Lastkollektive aus Simulationen, Interner gebo-Bericht – IDS-Meilenbericht 2011-03
/OST 11-2/	Ostermeyer, G.-P. Srisupattarawanit, T., Schiefer, F., Esderts, A., Runge, S., Interim report of gebo, 2011
/OST 11-3/	Ostermeyer, G.-P., Schiefer, Shi, M.: Complex Drill String Simulation, Celle Drilling 2011
/OST 13/	Ostermeyer, G.-P., Schiefer, Shi, M.: Reflections on Modeling and Simulation of Drill String Dynamics within gebo, Celle Drilling 2013
/OST 13-2/	Ostermeyer, G.-P., Schiefer, Shi, M.: Datenaustausch W7: Dynamische Lastkollektive aus Bohrstrangdynamiksimulationen, Institut für Dynamik und Schwingungen TU Braunschweig, 11.11.2013
/OST 13-3/	Ostermeyer, G.-P., Schiefer, Shi, M.: Long-term Dynamics of Drill Strings and Dynamical Load Spectra, Status-Presentation on gebo Jour Fixe Research Area Drilling, 06.12.2013
/OST 14/	Ostermeyer, G.-P., Schiefer, F., Shi,M.: Reflections on Modeling and Simulation of Drill String Dynamics within gebo, OIL GAS European Magazine 2014
/OST 14-2/	Ostermeyer, G.-P., Schiefer, F., Shi,M.: gebo final report project B7, 2014
/SHI 11/	Shi, M., Schiefer, F., Ostermeyer, G.-P.: A contribution to efficient calculation of complex drill string dynamics for deep hole drilling, PAMM 2011
/SHI 13/	Shi, M., Srisupattarawanit, T., Schiefer, F., Ostermeyer, G.-P.: On the wellbore contact of drill string in a Finite Element Model, Proc. 84th GAMM, Novi Sad, Serbia, 2013
/SRI 11/	Srisupattarawanit, T., Ostermeyer, G.-P.: On Standard Predictions of Reformability and Collapse Resistance for Expandable Tubular based on Elasto-Plasticity Model, submitted to COMPLAS XI, Barcelona 2011

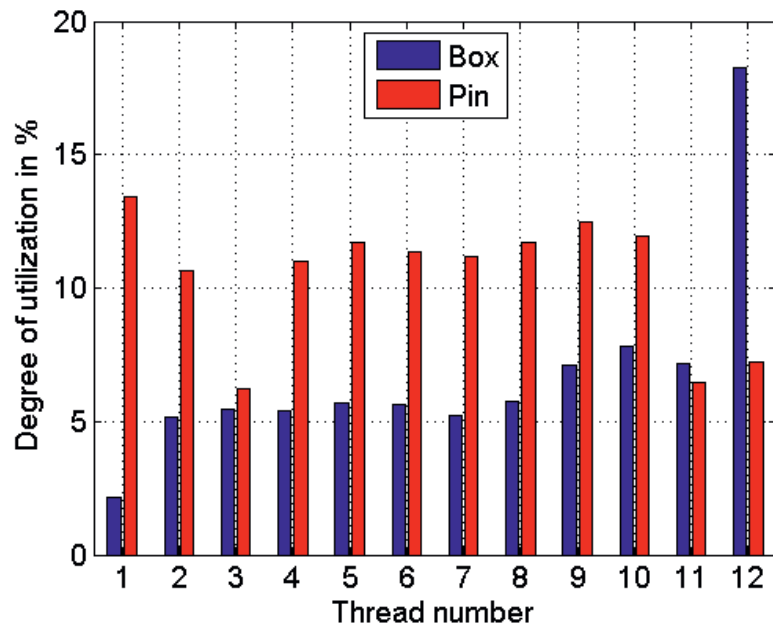## 5 Appendix
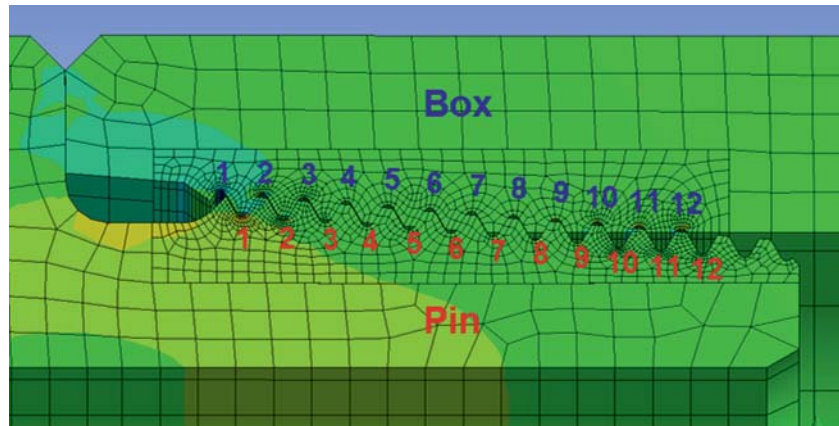
Figure 55: Thread enumeration, NC50 connection

Figure 56: Fatigue analysis of NC50 threads, milestone report /ESD 10/

gebo

Final report

Project W8:

Technical Systems Reliability
of Downhole Components

February 2015

TU Clausthal, Institut für Elektrische Energietechnik

Prof. Dr.-Ing. H.-P. Beck

TU Clausthal, Institut für Maschinelle Anlagentechnik und

Betriebsfestigkeit

Prof. Dr.-Ing. A. Esderts

Authors: Anne Friedrichs, Hilmar Darrelmann

Content

1 Project Overview

Project Start: 01.04.2009

Project End: 30.06.2014 (after cost-neutral extension)

Speaker and lead university or research institution

Project Nr.	Title	Subject of research	Project leader, institution, location
W8	Technical Systems Reliability of Downhole Components	Electrical Engineering, Mechanical Engineering	Prof. Dr. H.-P. Beck, TUC (IEE), Prof. Dr. A. Esderts, TUC (IMAB)

Participating institutes and institutions of the University and external institutions in:

- Institute for Electrical Power Engineering (IEE), TU Clausthal (TUC)

- Institute of Plant Engineering and Fatigue Analysis (IMAB), TU Clausthal (TUC)

Actual Baker Hughes contact: Dr. E. Bartscherer, J. Lehr

Former Baker Hughes contact: Dr. H. John, J. Stevens

List of participating scientists and engineers:

Name	Subject area	University institute or non-university institution	Position is financed by gebo funds (indicate with X)
Prof. Dr.-Ing. Hans-Peter Beck	Electrical Engineering	IEE	
Prof. Dr.-Ing. Alfons Esderts	Mechanical Engineering	IMAB	
Dipl.-Ing. Hilmar Darrelmann	Electrical Engineering	IEE	
Dipl.-Wirtschaftsing. Anne Friedrichs	Mechanical Engineering	IMAB	X (partial)

2   Introduction

2.1   Abstract

Reliability of technical systems has been initially studied in the area of aviation and aerospace for safety reasons. Subsequent the view was widened to many other technical systems as well as mass production for either safety or economical reason within the last 80 years.

In order to drill geothermal wells at great depths economically, the consideration of the reliability is of crucial importance. Just as unplanned outages and thus costly downtime can be reduced.

Reliability characteristics and statistics are known from analyses of wells in gas and oil area to a depth down to 4000 meters and a temperature of about 150 °C. These include the ambient conditions such as oscillations and vibrations. In addition to this feedback there are simulations on operations during the drilling process, which are considered in the drilling planning as well as fatigue tests on components and assemblies. A further consideration in the direction of systematic reliability studies is seen rarely though.

In deep geothermal drilling projects in hot hard rock formations with a depth of up to 6000 meters, drill string lengths up to 8000 meters and temperatures up to 220 °C exist an increased uncertainty in the reliability assessment. One of the reasons is the unknown behavior of most electronic components at that temperature range. Another one is the lifetime of the drill string components under particular stress in hard rock formation.

The aim of this reliability calculation is to determine the probability of failure-free operation over the entire drilling action, including electrical, electronic and mechanical components, as well as the drilling process. As part of the research project gebo the subproject W8 deals with the reliability of downhole systems employed under deep geothermal conditions.

The project deals with the reliability of components and their interaction in the deep drilling technology. In consideration of the failure rate of novel parts and devices, of the availability of the total system and of potential redundancies and maintenances, questions concerning plant safety and reliability are addressed.

Thereby W8 provides an important and meaningful input to the complete research network gebo.

First, a fundamental model that is based on a Failure Mode and Effects Analysis (FMEA) is created, which contains the important components for the determination of the system reliability. This should be extended, if necessary, and afterwards validated with the help of field data from real drilling projects.

2.2 Project goal and motivation

As one of the main objectives, the gebo project intends to increase the cost-effectiveness of geothermal drilling projects, especially in the North German Basin. For this purpose, the cost of maintenance, for the drilling process itself and in particular those which are caused by random failures are to be minimized.

As part of the subproject W8, critical components of the drill string should be identified and then their reliability and security should be assessed. Via feedback of these results to the appropriate sub-projects, it is possible to optimize the components, so that failure rates and maintenance intervals could be lowered. This also limits the portion of costs (maintenance and random failures), which contributes significantly to the achievement of the entire project goal, reduction of the overall costs.

Therefore, the most important element of the project W8 is the calculation of reliability of the newly to be developed components and assemblies. This means, that the knowledge of possible redundancies is necessary, as well as the fact, that maintenance intervals may not be ignored.

The principal aim of W8 is the reduction of drilling costs. A quite determining factor in this case is the number of unplanned failures or drilling stops, which isn't predictable during the drilling planning. However, maintenances or drilling stops which are caused by e.g. bit changes are projectable.

To have a tool which can predict exactly these unplanned failures with a certain probability, drilling stops appeared in the past have to be analyzed and to be numbered with a failure rate.

The aim is the development of a program for reliability calculation, in which all downhole components find consideration.

When a downhole failure appears, a whole roundtrip is necessary that, with increasing deep, costs time and therefore is also more cost extensive.

A consideration of upper hole system elements is not done in this project.

3 Basics in reliability

3.1 Basic concepts

„Reliability is the probability that a consideration unit processes a demanded function under given terms of employment during an agreed duration without any failure". The word probability includes the possibility that the unit fails during the demanded duration.

The probability of a failure is expressed by the reliability function R (t). Different distribution functions are based for the reliability function for technical components and equipment, depending on character of the failures appearing by chance. Typical distribution functions are the Exponential and Weibull distribution for electrical and electronically components and the normal or log-normal distribution (so called logarithmic-normal distribution) for mechanical stressed components.

The reliability function is defined by the failure rate λ, i.e. by the number of failures per time unit. In case of an exponential distribution, the failure rate represents the special case of a constant over time.

Generally the interdependence between failure rate and reliability function can be expressed as follows:

$$R(t) = e^{-\int_0^t \lambda(x)dx}$$
(3.1.1)

As an example, the reliability function is represented with an exponential distribution in the following **Figure 1**.

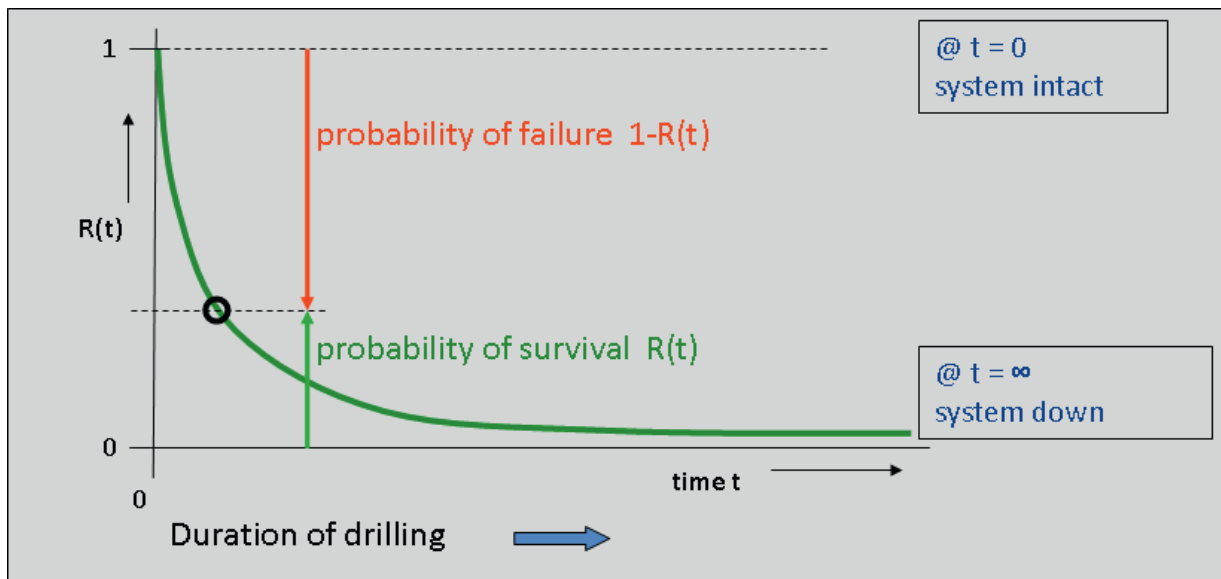**Figure 1:** **Course of the exponential reliability function**

At the time t = 0, the system runs and the intact probability R (t) = 1. The reliability curve falls according to an e-function over the time. At t = ∞, the system fails for certain with R (t) =0.

The failure rate follows the curve represented in **Figure 2** for many technical types of equipment. Higher failures per time unit can be recorded in an early phase. The real operation, and therefore the relevant time domain for the reliability calculation, starts after a burn-in phase with a low and constant λ over lifetime. The component or the system finally has to be exchanged by rising values due to wear, assuming a constant failure rate λ, the reliability function appears as follows:

$$R(t) = e^{-\lambda t}$$

(3.1.2)

For components which experience wear or fatigue during operation time, the failure rate isn't constant. Normally it rises over time. The same is valid if the environmental conditions of the component change. Particularly the temperature and mechanical influences are effective here. In case of an operation in different drilling depth with variable formation and increasing temperatures, it is to start out from a non-constant failure rate. Different distributions can be chosen for components suffering of wear. As a generalization of the exponential distribution with an additional parameter β, the Weibull distribution is the most frequent used in the technique. Then the reliability function looks like the following:

$$R(t) = e^{-(\lambda t)^{\beta}}.$$

(3.1.3)

If β > 1 the failure rate increases over time, which represents wear. If β = 1, one gets the exponential function. If there exist measuring rows about failures distributed statistically, it's often tempted to nearer the measurements into a suitable Weibull distribution (β). The advantage is, that it can be calculated further with a closed solution for R (t) and that conclusions on causes of the failures can already be derived from the course of the distribution.

As presented below, such an approximation could be done only insufficiently for the present situation of a changing failure rate over the drilling process. Hence, it was reverted to the general correlation of equation 3.1.1 and the course from λ was inserted in the numerical process as a discrete row.
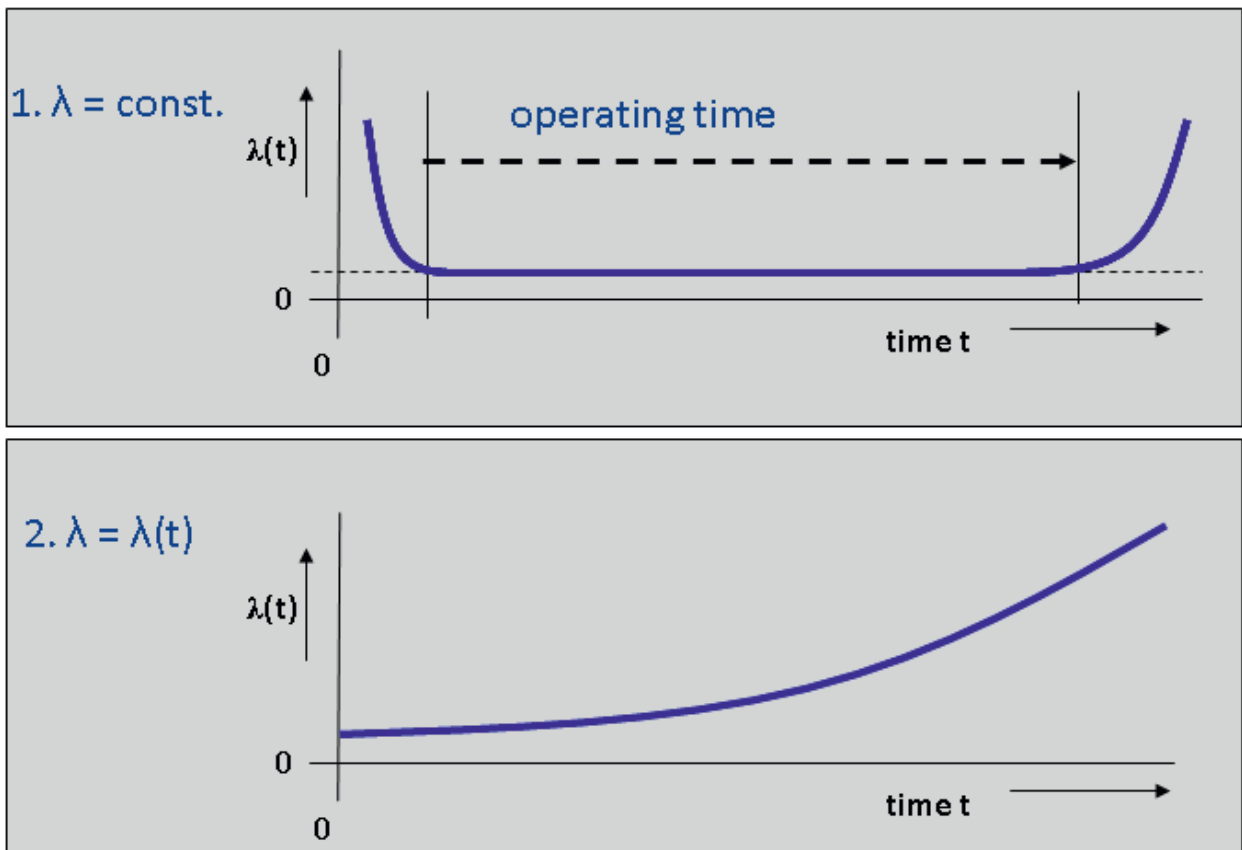

Figure 2: Course of the failure rates over time (1. steady value in the consideration period; 2. rising value due to ageing or changes in the environment)

The failure rates have to be calculated for all components.

If the consideration unit is extended to several components, the failure rates of the individual components have to be added up.

The total failure rate or its reciprocal value determines as a statistical size at which time, from the beginning of consideration time, a failure could appear. For some elements or also for the complete system, this mean time until failure, MTTF (mean times to failure), can be considerably longer than the effective operating time of the system which doesn't mean that the system cannot fail during the operating time since it is a statistical mean average value.

3.2 Failure Mode and Effects Analysis (FMEA)

In the course of the drilling with active drilling activity, with Roundtrips due to tool changes and finally Casing, unexpected disturbances which can be assigned to either the used material or the process appear with a certain probability.

The reliability model takes the failure probability of the components considering the operating conditions according to classic calculation basics from the literature into account.

The failure probability also is calculated during the single process steps.

The failures with the random distribution of her appearance require one certain time quota each for the fault removal and resumption of the drilling business to which a statistical size can be assigned.

The combination of failure rates of the components and processes with each other and with their effect on the drilling course is carried out with the help of the Failure Mode and Effect analysis (FMEA). The failure rates only depend on the components and the environment factors. They are assumed as independent of statistical events, which appear at other components. A real redundant operation isn't looked at.

In such a case, the failure of a component wouldn't have any effect on the drilling process since the redundant component takes over the task. This procedure isn't possible at faults in the drill string. On the other hand, failures, that allow a restricted further process like restricted data acquisition are taken into account correspondingly in the FMEA, but, at the moment, do not flow in onto the reliability model.

Starting out from this status Quo the failure rates of the individual components can be changed if other, particularly new components are used. The same applies to changed process flows which can come along with the use of new components. Statistical failure data for new components for the input into the calculation model have to be taken on the basis of known calculation methods of material technology or out of table plants.

The model takes only into account the unexpected, coincidental failures distributed statistically in the process of drilling which lead to an unplanned interruption. Planned interruptions in the drilling course due to bit changes or other reasons downhole which are already taken into account in the drilling planning don't receive attention in the reliability calculation. All processes up-hole and the components used there are left aside as well (as e. g. the Preventer).

3.3 Basic Failure rates of electrical components

The bottom hole assembly (BHA) of the drill string contains a variety of complex electronic assemblies which record data of the environment in the drill hole. Temperature, acceleration, torque, magnetic field and Georadar are included. Additionally there are assemblies for Pulser, electricity generation and power supplies. Known failure mechanisms of these assemblies find their way through in the area of the insulating material of the components, at soldering points, plugs and screwed connections, as well as due to faults by over-load out of voltage or current and thus faster aging. These failures at single components then lead to a function failure of the assembly appearing suddenly and by chance.

Many electrical and electronic components show a constant failure rate during their operating time as long as the surroundings and working conditions don't change. Different sources, particularly the military U. S. norm MIL 217f., offer an extensive data collection to failure rates of electrical, electronic and electromechanical components. The tables are available in a digital format. The data collections are based on observation values on an extensive statistical base each over many years so that these sources can be used with a high level of confidence.

The database for the individual components is so extensive that a sub-structure can be carried out according to execution, load and further business modes. The failure rate of a component therefore exists of a basic value λ_B and a chain of different

complication factors π. As essential factors have to be named here: operation environment π_E (mechanical influences), load π_L (exploitation), quality level π_Q and temperature π_T. The product of the individual factors yields the failure rate of the component.

$$\lambda_{component} = \lambda_B \cdot \pi_E \cdot \pi_L \cdot \pi_Q \cdot \pi_T \qquad (3.3.1)$$

The operation environment is subdivided into typical application cases of laboratory surroundings over the mobile area up to the use in weapon systems in the military norms. To gain the correct factors in this case for the use of the components in the BHA, the mechanical load to be expected has to be compared or coordinated during the drilling process with the use cases indicated in the tables. As represented below, vibration loads which have an effect on the drill string or the BHA during the course of the drilling are consulted to this.

The temperature factor is found out by the environmental temperature along the depth. If necessary a difference to the component temperature inside the BHA must be taken into account. For some components the link between temperature and complication factor in the sources is given as an equation which then can be taken into the calculation program.

The data or equations are often no longer usable for temperatures above 125° due to a missing data base, i. e. a special extrapolation of the failure rate becomes necessary above this temperature level. It also can mean that the component cannot be used in the questioned temperature range.

The following **Figure 3** shows the temperature course of the drilling at, "gebo2", and an exemplary course of the complication factors for environment and load in dependence of different formations which reflect different mechanical loads (vibrations). The stairs correspond to the different drilled formations.
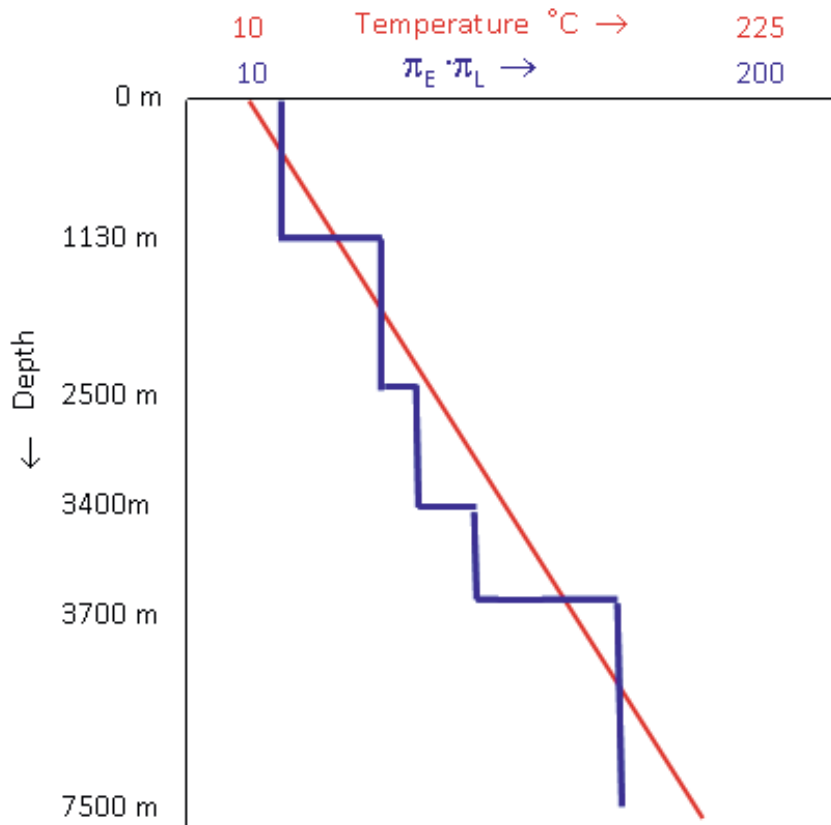
Figure 3: **Temperature course and environmental factors along the drilling process**

3.4 Basic failure rates of mechanical components

In the calculation program the following mechanical components which aren't different in their failure relevance are taken into account. If one of these components fails, this leads to the complete interruption of the total drilling process. Additionally, a roundtrip is necessary to replace the damaged component.

- Drill String

The drill string is one of the most essential elements for the process of drilling since it connects the rotating bit on the sole of the drill hole with the drilling rig. It therefore functions as a spin axis to transfer required torque at the tool. Furthermore it shall give the necessary load to the bit and it shall make possible that the mud can be transferred. The string consists mainly of the components explained briefly in the following:

- Drill Pipe, DP

Single Drill Pipes are screwed or welded together to so-called "pipe tours". Besides, in the standard case three pipes are connected to one tour. Especially the thread and

743

the weld connections are defeated by raised wear and, hence, need separate attention in the reliability consideration.
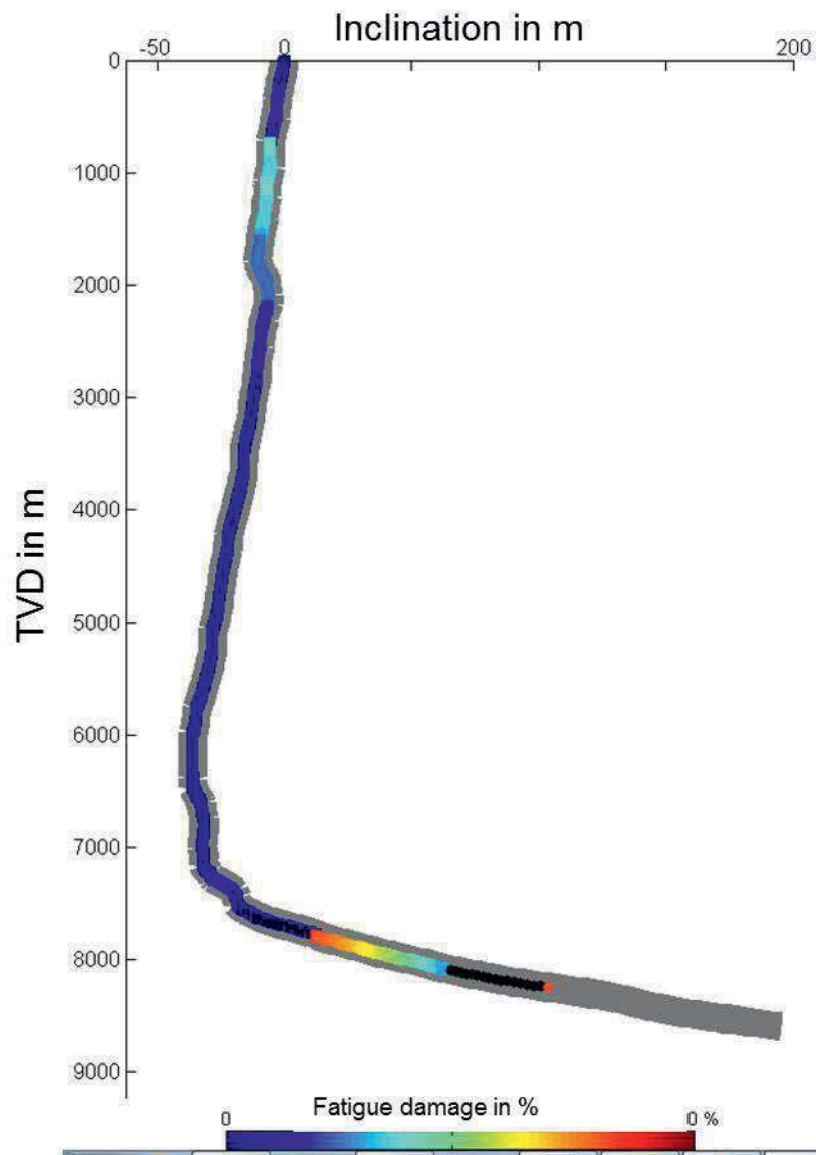

Figure 4: **Drilling Course with color marked fatigue damage of the thread connections**

Figure 4 shows an extract from the fatigue damage course along a drill pipe during an exemplary drilling process. This simulation has been developed and made available by the project W7.

Besides, a red color categorizes a very high damage whereas blue shown areas represent low to no damage. Underneath the bending area of the pipe, a raised damage, which is strongly at the outage border, is clearly to be recognized. Alike

behaves the upper part of the string which gets a theoretical fatigue damage of about 50% due to the raised tensile stress when the string becomes longer.

Frequent failure mechanisms finding consideration in the program are as follows:

-   Thread damages:

The thread ways are often (partly totally) destroyed by burr and seizing. In addition, the formation of scoring is observable.

-   Corrosion

-   Demolition of the string

-   Instabilities of the hole:

    Especially in deeper segments of a drilling process these properties are increasing.

•   Drilling motor

The drilling motor is numbered with a failure rate during reliability analysis and isn't submitted to any further consideration because it doesn't rank among the failure-critical components.

i. Bottom Hole Assembly (BHA)

Due to many components, but also due to the geometry, the drill string in total represents a failure-critical element.

During the drilling process, the string suffers from different, partly dynamic, loads, which, in some cases, overlap each other and which thereby form a complicated load profile (bending-tension-compression-strain).

-   Chemical stress due to mud (corrosion)

-   Thermal stress

-   Other influences, which arise by the used drilling technology, by the different formations (abrasion of the drilled formation) and by other properties

-   Axial and torsion oscillations, which are caused by the tools and the gear downhole

-   Radial oscillations caused by the gear downhole

- Rotary straightening at bended areas of the hole by rotation of the string at strain

Already at a bend of 5°/100m bending stresses of more than 100 MPa can appear. This requires a consideration when estimating the fatigue strength for finite life characteristics, as well as it is simulated in project W7.

1.1.1. Mud

In the drilling process the mud serves as a release medium for drilled rock material and for the fluids and gases entered in the hole during drilling. Its other duties are manifold and different according to the drilling-technical situation.

1.1.2. Pipe Handling

By the construction the following stresses are to be considered:

- Axial stress (tension/compression) due to tare weight

- Thermally induced length changes

- Burst

- Collapse

3.5 Comparative data of the drilling technology

The aim of reliability calculation is the prediction of failure events which appear in statistically distributed time. The exactness of the prediction, not the exact time, but those of the average time which passes up to the next failure grow with the number of information that is available for calculation. Without knowing the failure scenarios, operating modalities and already known failure rates of components, only a very inexact behavior can be calculated.

An important point in this case is the consideration of statistical failure data from the immediate application of the considered components. The more detailed and more extensively these data can be determined and evaluated, the more exactly is the prediction result. For the present project, it means to search data from the area of drilling technology with failure statistics from real drilling operations. On this occasion, drilling plans, which ran off under similar conditions as the intended geothermal drillings, are from special interest.

The first helpful source by searching for data from real drilling projects was the Continental Deep Drilling Program (KTB). This is a publicly promoted drilling project form the 90s with the aim to investigate the earth's crust in depths down to approx. 9000 meters. Beside the fact that the KTB drillings due to its big depth and hard rock fit to the planned gebo drillings, it is advantageous that all data of this project are described in detail and are freely accessible on the internet.

As other possible sources more than 30 drilling plans of geothermal wells in Germany from the past 15 years, which are listed in **Table 1** were identified. As these plans were promoted mostly publicly, it seemed reasonable to get and to process moreover drilling technical data. However, for different reasons of organizational and juridical kind only few of these projects were accessible for data research. Also in geothermal projects the drilling works are awarded to professional companies that often classify their recorded data as confidential, so that the operators aren't allowed to transmit this to third party.

Finally, Baker Hughes signaled support with data from geothermal drilling projects in the USA, as well as with failure statistics of general worldwide drilling plans which were collected during the last 10 years.

Standort	Bundesland	Betreiber	Aktuelle Entwicklung	Inbetriebnahme
Aachen, Super C	NRW	RWTH Aachen		Voraussichtlich 2010/11
Aschheim, Feldkirchen	Bayern	AFK GmbH	In Betrieb	
Aying Dürrnhaar	Bayern	SGG GmbH		
Bernried	Bayern	BE Geothermal GmbH	In Planung	
Biberach	BW		In Betrieb	
Bruchsal	BW	Ewb GmbH		2009
Erding I + II	Bayern	Evonik	In Betrieb	
Groß Schönebeck	BB	GFZ Potsdam	Dauertest	Ende 2010
Grünwald	Bayern	Erdwärme Grünwald GmbH	Bohrung am 04.12.2009	2011/2012
Hannover	NDS	BGR	Bohrung seit 22.06.2009	2012
Insheim	RLP	Pfalzwerke AG	2. Bohrung Mitte 2009	Ende 2010
Kirchstockach	Bayern	SGG GmbH	Bohrung abgeschlossen	2011
Landau	RLP	Geo-x GmbH	In Betrieb	2007
München-Riem	Bayern	SWM GmbH	In Betrieb	2004
Neubrandenburg	MV	Neubrandenburger Stadtwerke GmbH	In Betrieb	1987
Neuried	BW	Hybridkraftwerk Neuried	2009 erneute geologische Untersuchungen	
Neuruppin	BB	S.I.N. GmbH	In Betrieb	2007
Neustadt Glewe	MV	Erdwärme-Kraft GbR	In Betrieb	2004
Poing	Bayern	E.ON Bayern	In Bau	
Prenzlau	BB	Stadtwerke Prenzlau	In Betrieb	1994

Pullach	Bayern	IEP	In Betrieb	2005
Riedstadt	Hessen	HotRock	Abschluss seismologischer Untersuchungen 2009	
Rülzheim	RLP	HotRock	In Bau	
Sauerlach	Bayern	SWM GmbH	In Bau	2010/11
Simbach/Braunau	Bayern	GSB GmbH	In Betrieb	2001
Straubing	Bayern	Stadtwerke Straubing GmbH	In Betrieb	1999
Unterföhring	Bayern	GEOVOL Unterföhring GmbH	In Betrieb	2009
Unterhaching	Bayern	Geothermie Unterhaching GmbH&Co KG	In Betrieb	2009
Unterschleißheim	Bayern	GTU	In Betrieb	2003
Utting	Bayern	GEOenergie Bayern GmbH	Bau	
Waren	MV	Stadtwerke Waren GmbH	In Betrieb	1984
Weinheim	BW		Probebetrieb	
Wolfratshausen	Bayern	Enex Power Germany GmbH	Beginn Bohrung Juni 2010	

Table 1: **Drilling plans of geothermal wells in Germany since 1984**

All together, the extent in accessible and usable data for the present project is relatively small. However, failure frequencies could be recognized and differentiated after typical component failures from the areas of Mechanics (drill string) and electronics (BHA). Partially, it was possible to assign also surrounding terms, like depth, formation and temperature directly to the failure, so that the differentiation rises.

4 The gebo drilling model

4.1 Geology and drilling course
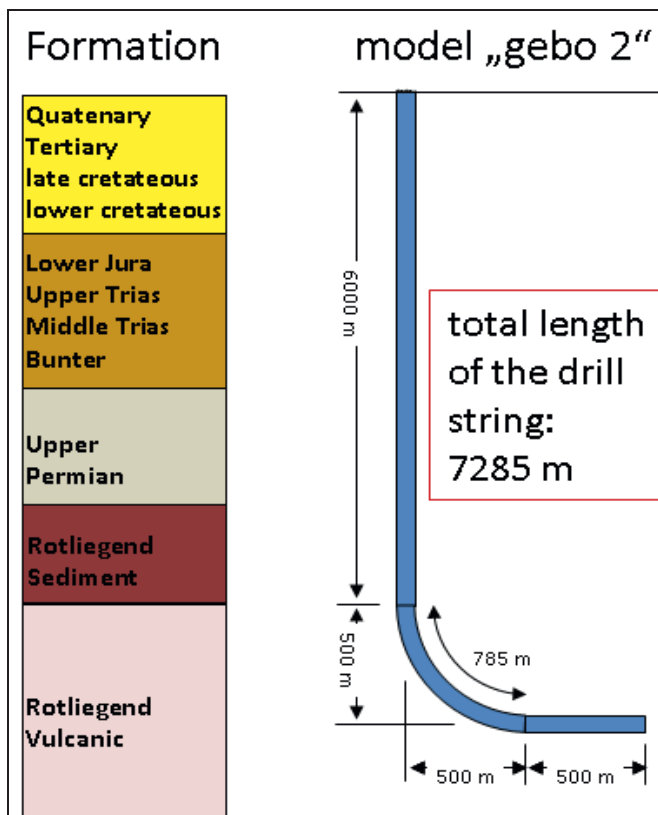
Figure 5:   Suggested reference drilling model with drilling course and formation

The project called "gebo 2" was an exercise for the students of the Institute of Petroleum Engineering of the Clausthal University of Technology. Besides, aim was to draft with the help of five differently given drilling locations the suitable drilling planning for the injection as well as for the production hole plus to analyze the realization possibilities. As geologic suitably and realizable to gebo turned out the injection drilling of location 2, cf. **Figure 5**. The corresponding drilling planning in kind of the time-depth diagram is shown in **Figure 6**. This drilling plan altogether with its formation was taken over in the program.

For the calculation of the failure type, the roundtrip first is only considered as a temporal delay of the drilling progress, while the change of temperature isn't valued due to the catching up and the re-putting down of the drill string. For the time of a roundtrip, the load of the components is supposed to zero.
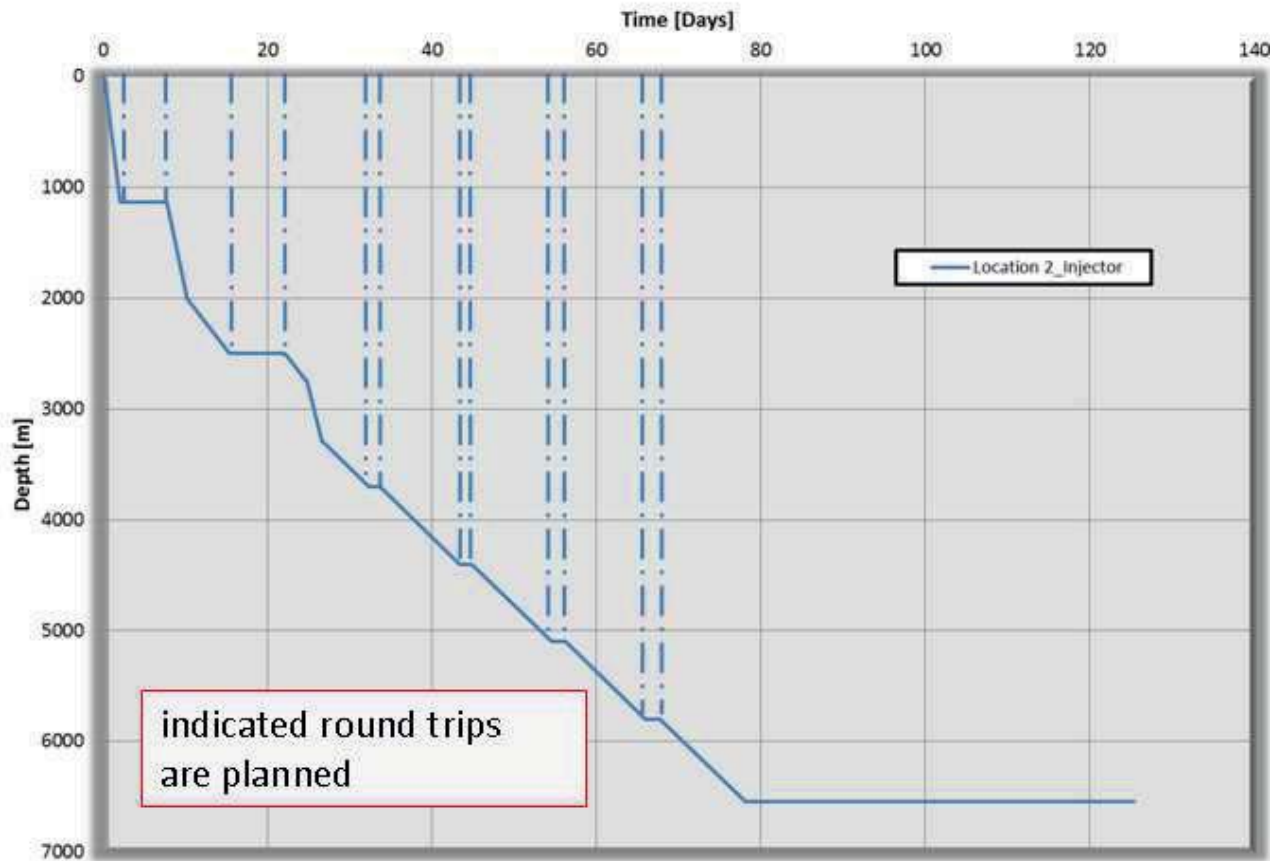
Figure 6: **Time-Depth diagram with planned roundtrips**

4.2 Equipment and processes

The drilling tools presumed for this model are also taken from the student project gebo 2. These are listed in the following

Table 2 and in **Figure 7**.

Component	Dimension	Quantity
Bit	24"	1
Bit	17 ½"	1
Bit	12 ¼"	1
Bit	8 ½"	1
Navigation Tool	9 ½"	3
Navigation Tool	8 ¼"	1
Stop Sub	9 ½"	3
Stabilizer	23 ¾"	1
Stabilizer	17 3/8"	2
Stabilizer	8 3/8"	2

Pulser	8 ¼"	1
MWD	8 ¼"	1
Filter	9 ½"	3
Filter	8"	1
Circulation Sub	9 ½"	3
Float Sub	9 ½"	3
Float Sub	8"	1
Drill Collar	9 ½"	27
Drill Collar	8"	9
Reamer	12 ¼"	1
Jar	9 ½"	3
Jar	8"	1
Accelerator	9 ½"	3
Accelerator	8"	1
XO Sub	9 ½"	3
XO Sub	8"	1
HWDP	6 5/8"	21
Drill Pipe	6 5/8"	4

Table 2:   Structure of the planned drill string and the BHA
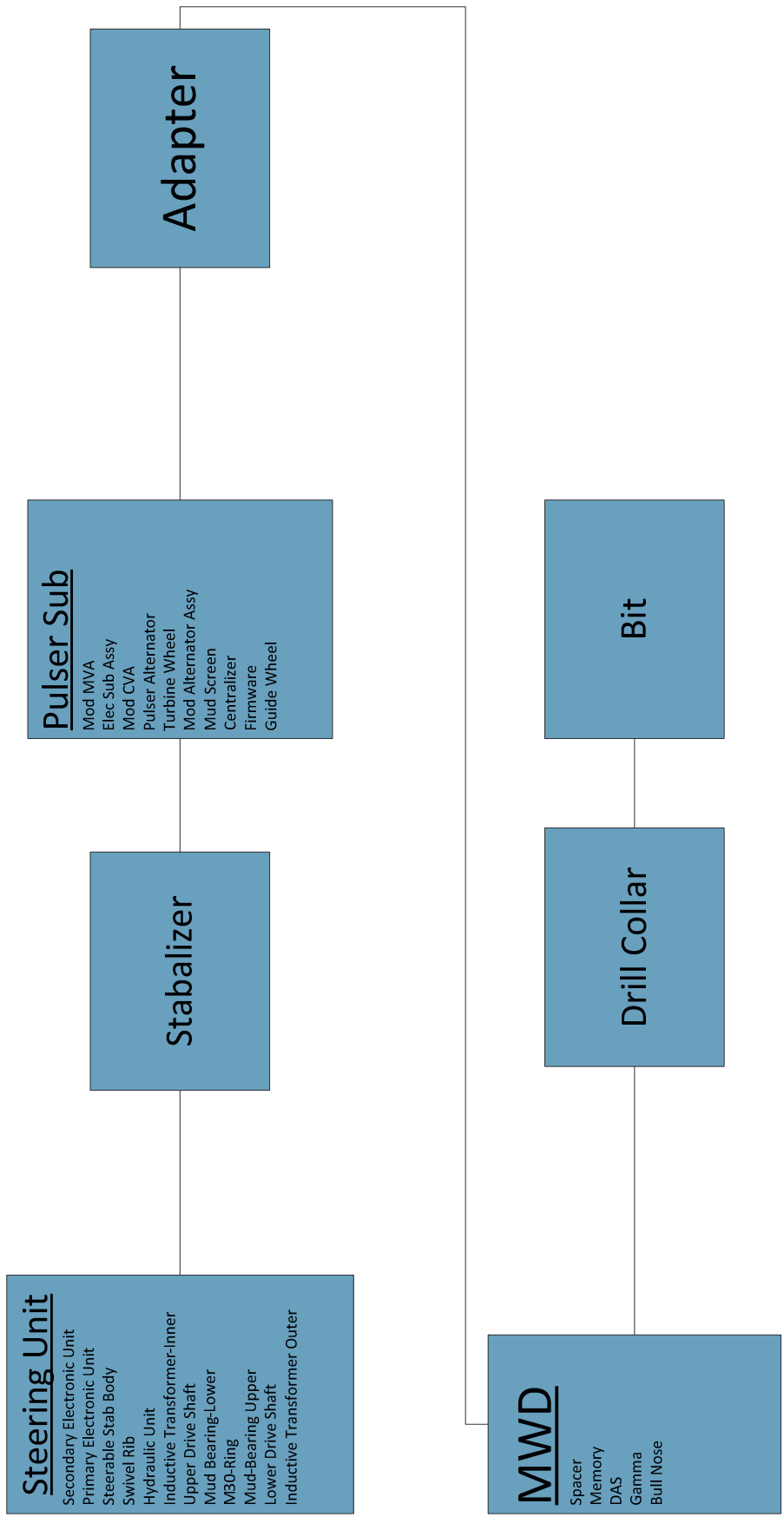
Figure 7: Arrangement of the BHA components

5 The reliability model

5.1 Practice of reliability calculation

The reliability model used here considers all for the determination of the total failure rate of the downhole system relevant processes and components, including every failure possibilities having regard to the environmental conditions. The failure rates ascertained for the single points are tied together in suitable manner and therewith the total probability of the appearance of a failure is calculated for the duration of the drilling process.

As a result of the failure analysis, at first all electric and mechanical components are looked at. It is supposed that all available components are needed in functioning state. This leads to the conclusion that it doesn't exist any redundancy within the components and that therewith all failure rates can be added. If components are used whose failure not necessarily leads to a shutdown of the drilling process, but which allows a limited further operation without time delay, then these components are not further considered in the reliability calculation.

To simulate operating conditions for the components very close to reality, the drilling process is represented completely. ROP and the direction of drilling have been discretized in steps of 10 meters. In addition, the formation is considered, as well as the temperature course with a steady gradient rate which is typed in in each case discretely in the grid. The intended roundtrips may also flow in as changing surrounding conditions.

Electric, electronic and electromechanical components:

As described in segment 3.3., the table of the American MIL 217 serves as a starting basis for electric and electronic components. The basic values of the failure rates are taken over directly into the model and, if necessary, components can be summarized to begin to groups. From the data of the drilling process other factors, as a function of time or depth, are won.

According to the geological formation which is drilled through in each case, the measured oscillation values from field data are assigned to and then flow in by comparison of the environmental factors from the table with the difficulty factor. If no

data are given for single areas, a mean value from π = 35, which corresponds to an environmental factor for the mobile area, is suggested.

In the MIL 217, tables as well as formulas are given concerning the dependence of temperature of the failure rates for the respective electric or electronic components. It is to be noted that the dependences are only valid for a restricted temperature range and cannot be integrated readily into the model. For higher operating temperatures, the failure rates must be extrapolated in suitable manner. Thus, mechanical connection elements and switch connections are practically steady in their failure rate in the regarded temperature range, while ceramic elements show a linear dependence. The components which contain insulating material on plastic base, and in particular semiconductor, show a very exponential dependence. For this two different procedures are integrated into the model for extrapolation and can be activated alternatively. On the one hand the exponential extrapolation from the MIL 217 with adapted factors is taken over for the higher temperature area, on the other hand dependence according to Arrhenius is determined, which has proven its validity for the life time of certain elements. The temperature dependence of the life time according to Arrhenius is derived from the reaction velocity of chemical processes which have a negative influence on their life time in the case of electronic parts. Besides, semiconductor components, like transistors, processors, memories and sensors have a dependence of its functional ability on the operating temperature. At last, the failure rate for the respective component or the assembly suitable dependent on the temperature has to be ascertained or confirmed by validation. Further details are to be found in the chapters 6.1 and 6.2.

Mechanical components:

To the inquiry of the failure rates of the mechanical components no standards or table works exist like the MIL standard for the electronic components. To determine the basic failure rates here, from preserved field data a failure rate for every component (HWDP, stabilizers, Kelly, bit) is generated. The drill string has the special property that here, beside the material, also the thread connections are defeated by raised loads. The screw connection process itself, as well as the stresses in the later drilling process have a negative effect to the life time. In these connections the most frequent rope demolitions occur. These also show the reports of drilling projects. To be able to illustrate the behavior of the life time of threaded

connections, the project W7 has intensely dealt with the damage mechanisms in thread connections in drill strings. Resultant from that, the program uses an Excel table, which has been created in this project by computational simulation, for the calculation of the failure rates of the drill string.

As the loads on the string increase with progressive drilling process, one of the essential factors is the depth of the drilling. The reliability program can extract the suitable failure rate in desired depth from the Excel table for every pipe number and uses this for further calculations. Besides, it is supposed that the order of the used drill pipes does not change during the whole drilling course. The first pipe receives the number 1, the second one the number 2, etc., cf. **Figure 8**.
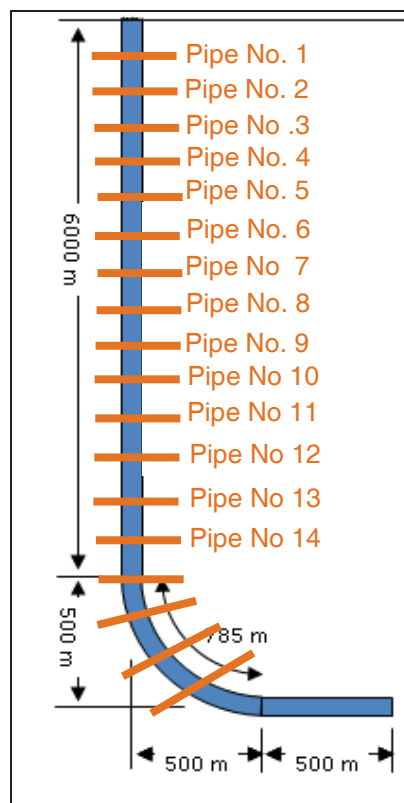
Figure 8:   **Drill string with pipe numbers**

In the reliability program, this failure rate is multiplied (cf. Chapter. 5. 2.) with difficulty factors (environment and roundtrip) according to the settings in order to receive the complete failure rate.

5.2   Determination of failure rates

The basic failure rates for the different components are determined from different sources, then compared with each other and finally processed for the use case. On

the one hand, real data of single components from the field exist, on the other hand data can be derived from drilling reports of real geothermal drilling projects (e. g., KTB). The last mentioned are difficult to receive in sufficient numbers mainly for mechanical components, because these are sensitive and often confidential customer data. Furthermore, one can also refer to the lab tests which were carried out with the same or similar components under comparable conditions. The life time calculation was applied for mechanical components in the present project by FEM due to the high effort for random check. Therefore, a drilling simulation was programmed with the help of Mat Lab. This happened in the gebo project W7 and was made available to the project W8 as a result file.

For the electronic components the definition of the basic failure rates occurred with the help of the MIL standard. Up to operating temperatures of 125°C a temperature dependence of the failure rates is given there, moreover, it must be extrapolated in suitable manner.

MIL STD 217

As mentioned above, the MIL 217 for different electric components offers failure rates in dependence on the operating temperature. For passive parts, like resistors, capacitors and inductances there is the following basic relation:

$$\lambda_b = a \cdot \exp(c \cdot (\tfrac{T+273}{d})^b) \qquad (5.2.1)$$

The value for d is chosen in that way, that the quotient becomes one by reaching the reference temperature (mostly 125°C). The exponent varies with the type of component between 5 and 18. The values for a and c represent basic values of the suitable components and are taken from appropriate tables. For active parts, like diodes and transistors, the following dependence is given:

$$\lambda_b = a \cdot S \cdot \exp(c \cdot (\tfrac{1}{T+273} - \tfrac{1}{d})) \quad (5.2.2)$$

Here, d is chosen in that way, that the expression in the bracket becomes zero at the reference temperature of 25 °C. The values for a, S and c represent basic values again. Because of the rising temperature dependence from λ, c must be assigned in the exponent a negative value.

The indicated temperature dependence from the MIL standard cannot be verified in detail for single components, because a suitable database is not available. For single

assemblies or systems from known assembly's failure statistics are available and have been taken for a comparison, as described below.

Arrhenius

As an alternative to the basis of the temperature dependence which is won from the MIL standard, one could chose the temperature dependence of life time expectations, or the deductive failure rates from it according to Arrhenius. According to the law of Arrhenius, the speed of a chemical reaction depends on the temperature as shown in the following equation:

$$v = v_0 \cdot \exp(-\tfrac{E_a}{kT})$$ (5.2.3)

with E_a as an activation energy, K as a Boltzmann-constant and T as the temperature in Kelvin.

Out of this an acceleration factor can be derived, dependent on temperature which corresponds to the increase of the failure rate. Besides, the value of E_a will be found around 0.5 Ev / K.

$$\lambda_2 = \lambda_1 \cdot \exp(\tfrac{E_a}{k}(\tfrac{1}{T1} - \tfrac{1}{T2}))$$ (5.2.4)

The course of the failure rate is also recordable more simple with the help of the following exponential connection:

$$\lambda_T = \lambda_{T,20} \cdot 2^{(T-20)\cdot\frac{1}{40}}$$ (5.2.5)

The expectation is based on a basic value at a temperature of 20°C. The quotient in the exponent determines the increase. With lead acid batteries one assumes, for example, that a rise of the operating temperature by 10 degrees in each case results a halving of the life time, what was confirmed from many lab tests and feedbacks by users. Accordingly one can expect that for this case the failure rate rises in each case around the factor 2. Then for this, a value of 10 would be to be used in the denominator of the quotient. Nevertheless, for electronic components this value delivers a too strong dependence of the failure rate on the temperature, so that a more suitable value must be found to receive a correspondence with data from real drilling plans.

Course of the failure rate about the temperature – comparison with field data

At the time of setting up the program no detailed information about the components which are used in the assemblies of the BHA was given. Hence, beside single components the program offers at this point the possibility to give entire assemblies also. Then the failure rates for these assemblies aren't derived from the MIL manual, but are to be taken from other sources. From a data source, based on classical oil and gas drillings to 3000 m a failure rate has been determined for a period of 2 years by 8E-4 h^-1 as a mean value of electronic assemblies in the BHA. Besides, the components saw temperatures of from 0 to 90 °C. The average drilling duration per drilling plan is attached in this source with 360 hours. The course of a rising failure rate, dependent on the temperature of all regarded assemblies in the statistics, is shown in the following **Figure 9**. The relations mentioned in the formulas above is the basis to these curves. The environmental factor is assumed to be constant at first with a value of 35. The average of the failure rates (0,0008) over the entire period corresponds again to the value taken from the statistics of the field data.
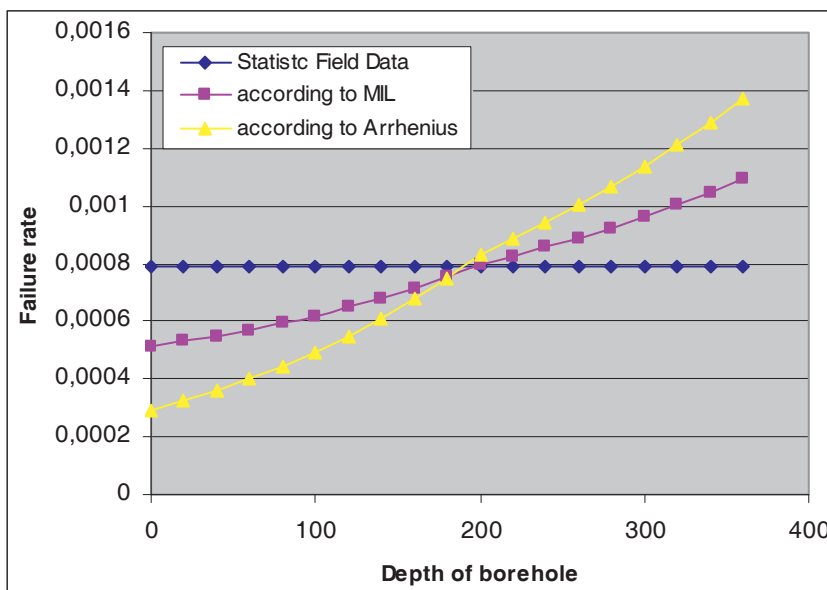
Figure 9: **Course of the failure rate for the drilling duration taking the temperature from field data into account**

The unsteadiness in the course at 200 h coheres with a change of the drilling speed ROP of 10 m/h on 6 m/h which means a slower temperature rise over the time. The mean values of the ROP are taken from the data of the regarded drilling plans. The calculation of the reliability function from the failure rates with Mat Lab is shown in the segment 6. 1.

Extrapolation of the failure rate above 125°C

Aim is the extrapolation of the failure rates dependent on temperature up to 200 °C with the same parameters which were determined from the field data. The following **Figure 10** shows this, in each case for the failure rates and for the reliability function. Now the time scale extends to almost 1400h which corresponds to a depth of 6000 meters.
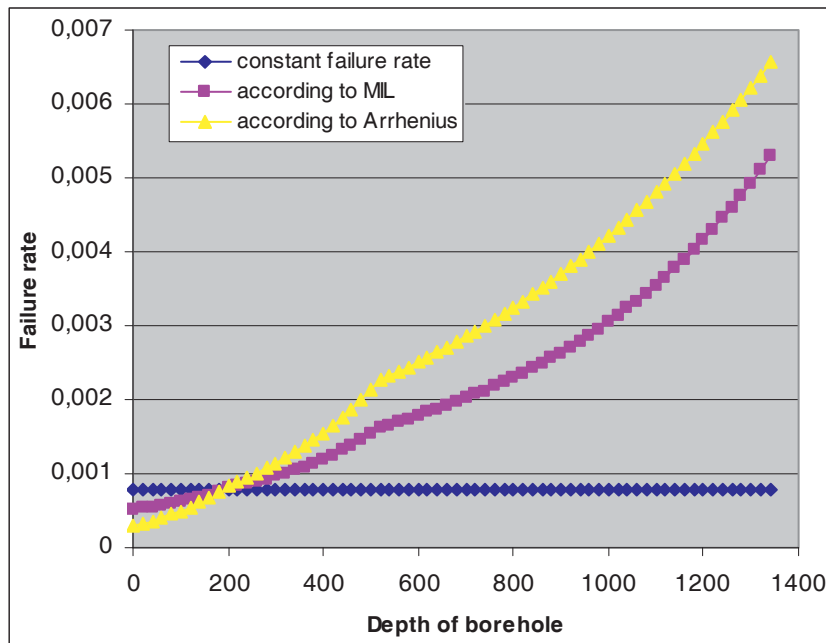

Figure 10: **Extrapolated course of the failure rate for the drilling duration taking the temperature into account**

The point of unsteadiness at 500h is again caused by a change of the drilling speed ROP from 6 m/h to 2.5 m/h.

Adoption of the parameters into the calculation program

The evaluation of the field data, as well as a preselection of the parameters for the failure rates, temperature and environmental factors with comparison to the field data has been carried out upfront with the help of Excel tables. Then the ascertained parameters have been adopted into the reliability calculation program in which then the entire calculation was carried out.

5.3   Structure of the calculation program

The reliability model described in chapter 5.1 is realized as a calculation program with the help of Mat Lab. The process of this program corresponds to the patterns shown in **Figure 11**.
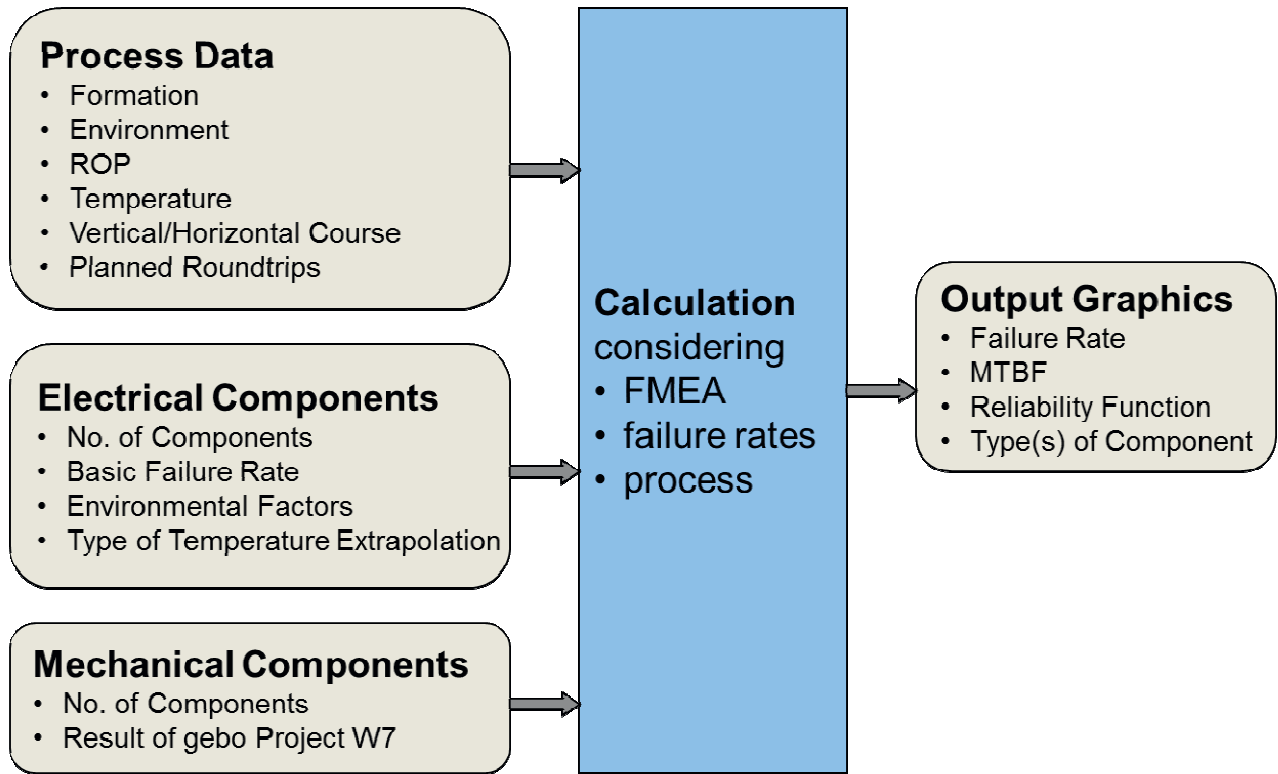
Figure 11:   Structure of the reliability calculation

The following description shows the functional structure with the help of the program handling with all input and output possibilities. By this, the parameters changeable by the interface as well as the program sequence are explained. The following **Figure 12** shows the mask after starting the program. Essentially, a central output area and different areas around the plot which allow the parameter input can be identified.
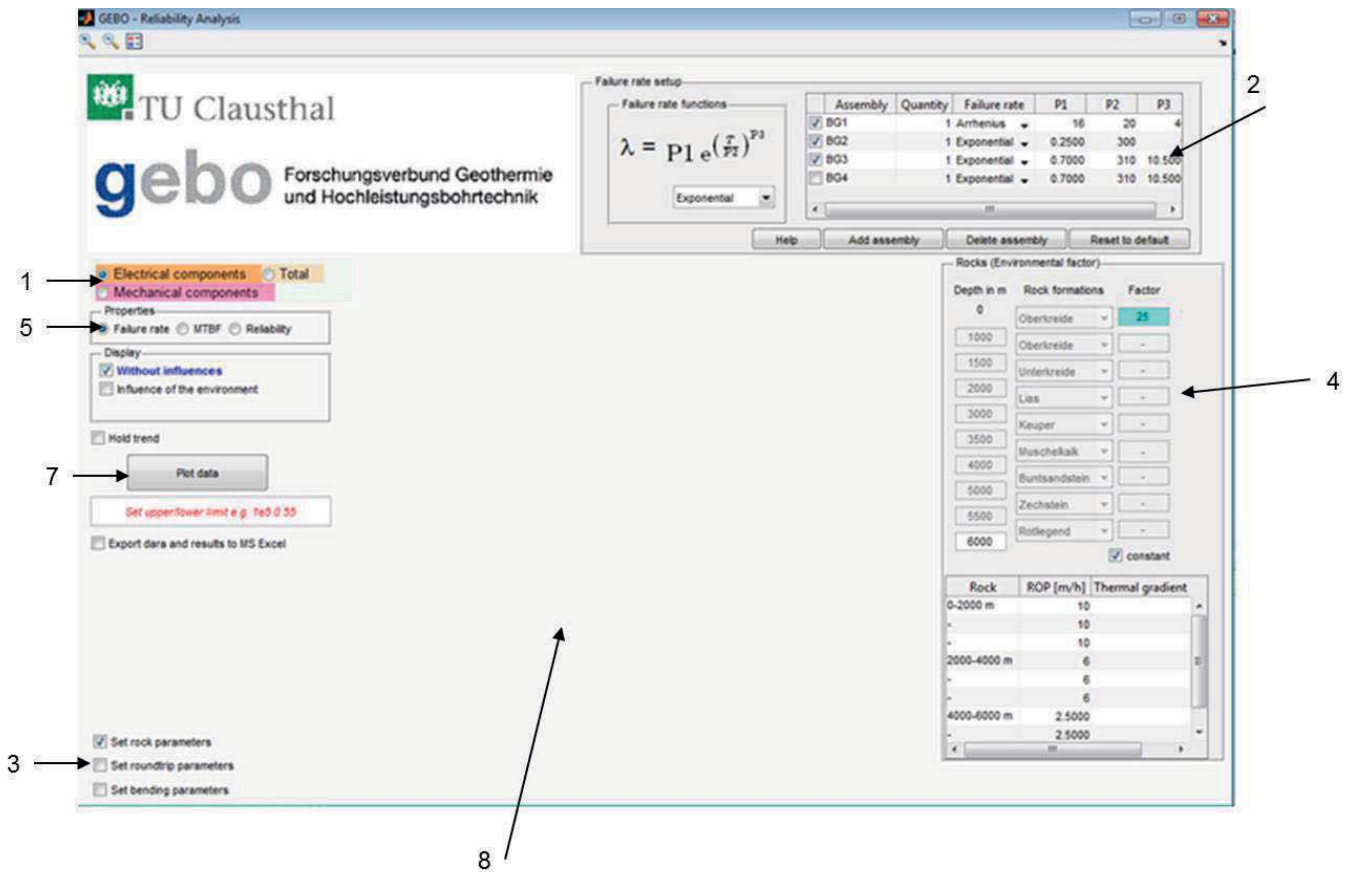
Figure 12:   Program mask after starting
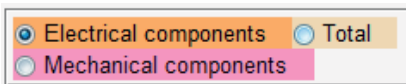
Figure 13: Choice area No. 1

The choice area No. 1, shown in **Figure 13**, allows first the parameter input for the electric or mechanical components and fixes which components should be considered in the calculation. There is the possibility to determine the reliability only for electric or only for mechanical components or for both together. According to the choice, field 2 of the input masks changes. If electric components are selected, one receives the following input mask in field 2, cf. **Figure 14**.
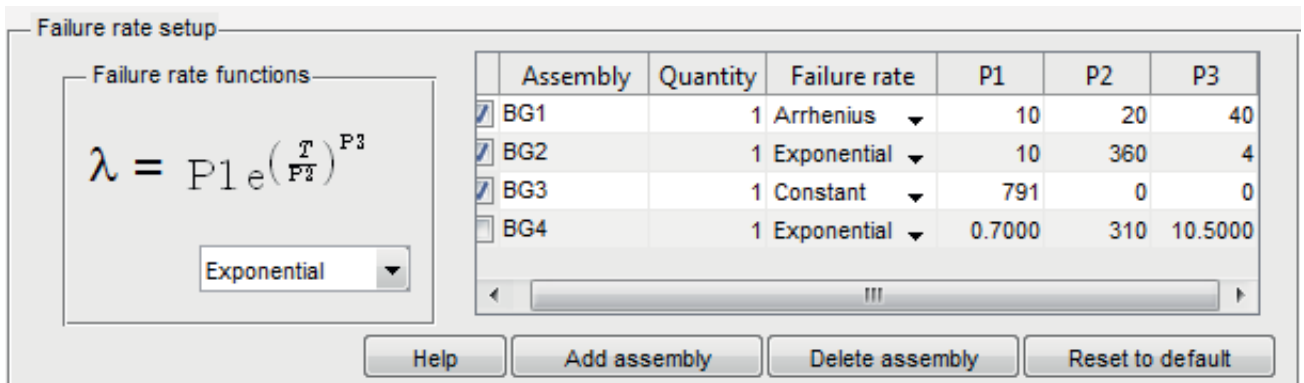
Figure 14: Input mask of field 2 for electric components

Any number of components can be listed here and can be taken up in the calculation by putting of the hook. For every assembly parameters of the failure rates are either steady or are to be set after two firmly deposited formulas (Arrhenius or Exponential). On the left side the chosen formula can be looked at for better illustration. If mechanical components are selected the input mask, cf. **Figure 15** appears in field 2. Here, single components can be selected in their quantity. The underlying basic failure rates are generated from the Excel file from project W7 and not changeable.
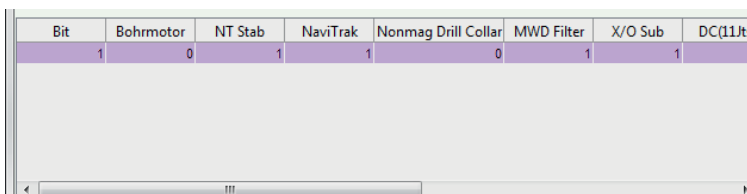
Figure 15: Input mask of field 2 for mechanical components

Figure 16: Input mask of field 3 for parameters

Field 3 (cf. **Figure 16**) allows the selection of different fields for the setting of other characteristics of the drilling. These are the rock parameters, the roundtrip parameters and the bend properties in case of a not purely vertical drilling. The fields appear in field 4. For the setting of the rock parameters **Figure 17** appears in field 4.

763

Figure 17: Input mask of field 4 for rock parameters

Here the formations over the depth can be set according to the desired drilling course. In addition, under the option "Factor" the difficulty factor during the drilling of this formation can be adapted individually or consistently (box "constant"). In addition, the ROP and the temperature gradient can be set per formation. As a default setting a temperature gradient of 3.5°C /100 m is assumed. The calculation occurs in discreet steps of 10 m (MVD). All the other parametres (time, temperature, TVD) are converted into these discreet steps.

For the change of the bending parameters of the drilling course the window of **Figure 18** opens in field 4.

Figure 18: Input mask of field 4 for bending parameters

Here the bend degree is to be set in degree per depth (MVD). In addition, the length of the horizontal drilling is to be given in metres.

With the lower check box one can allow to mark in the later graphic issue the point of the bend beginning and ending.

Figure 19:   Input mask of field 5 for properties

Field 5, 6, 7 and 8 serve for the control and the graphic output of the results. With field 5 in **Figure 19** it is selectable whether it should be shown failure rate, the MTBF or the reliability.

Figure 20:   Input mask of field 6 for display

Further, with the option Display from field 6 in **Figure 20** can be fixed whether the graph should be shown with influence of the environment, so accordingly of the environmental   factors   set   before,   or   without   other   influences.

Figure 21:   Input mask of field 7 for data plotting

The calculation as well as the graphical presentation of the result occurs with the button "plot data" from field 7 in **Figure 21**. Besides, lower or upper borders can be still put to scale of the abscissa. Additionally, an output of the numerical results is possible in an Excel table.
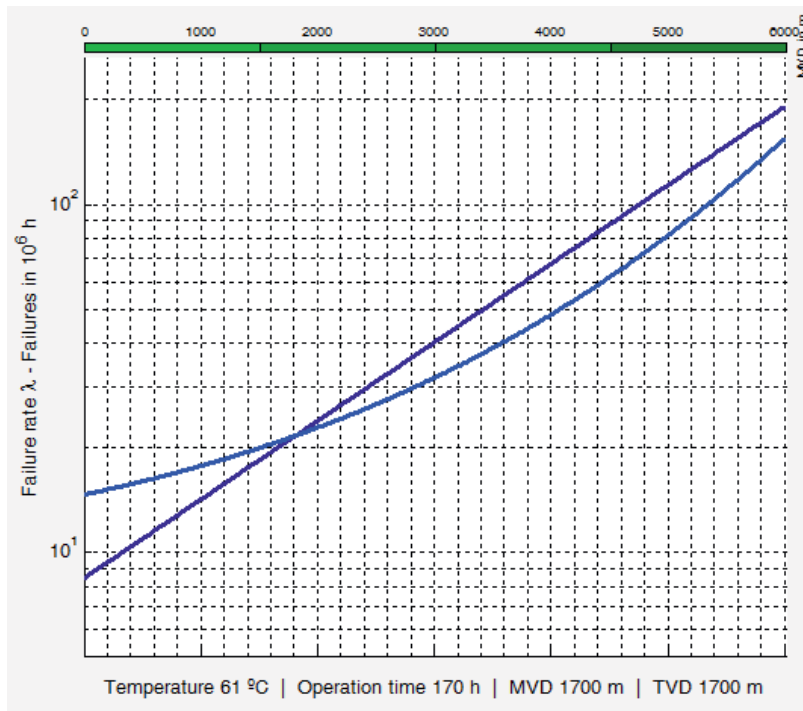
Figure 22: **Example for result**

Field 8 in **Figure 22**. in the center of the surface shows the results graphically. Depending on which property was selected in field 5, the abscissa shows the failure rate, the MTBF or the reliability function.

The ordinate gives MVD, TVD, drilling time and temperature in dependence of the position of the cursor.

6   Results

6.1   Validation to 3000 m

For the validation of the calculation results normally no failure rates ascertained in practice are available for single components, so that a validation only can be carried out with the help of total assemblies or several assemblies in a common group. In particular, the validation is important because of the higher application temperature, as mentioned, the extrapolation is not covered with data up to more than 125 °C. As the following picture shows, a comparison of the calculated reliability function with the result of the failure statistics is adducted for a time after a mean drilling duration of 360 hours for validation. The moment corresponds to a depth of 3000 meters.
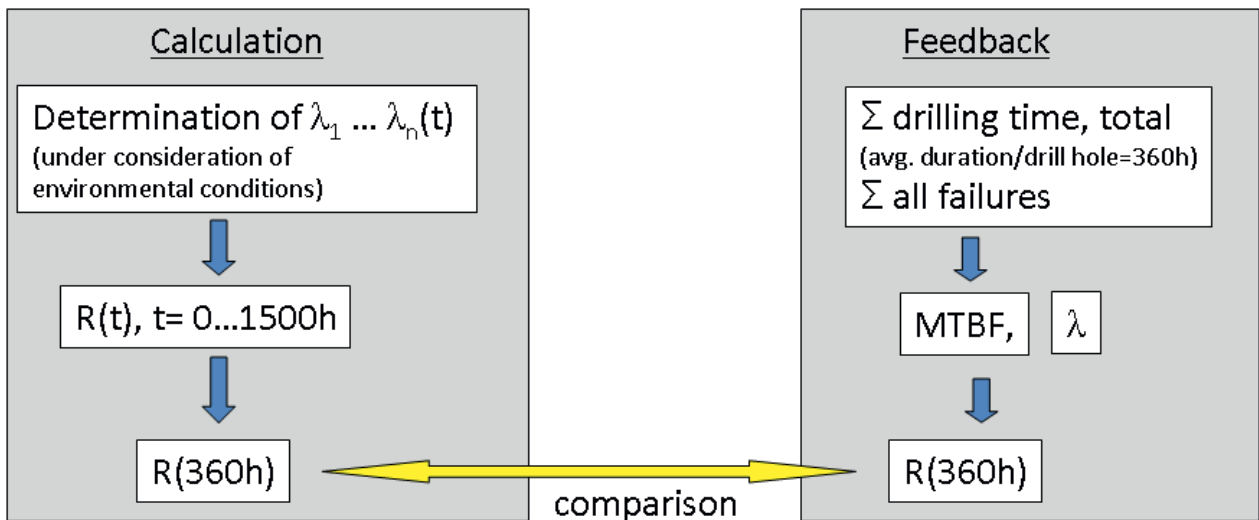

Figure 23:   Validation of the calculated Reliability Function at t = 360 hrs.

Hence, first there is no calculation with single components, but at assembly level. Therewith, a direct comparison with field data is possible. For the temperature dependence of the failure rates for single components the following common approach is based for the assemblies, see **Figure 23**:

$$\pi_T = e^{(\frac{T+273}{360})^4} \qquad (6.1.1)$$

according to exponential function and

$$\pi_T = \pi_{T,20} \cdot 2^{(T-20) \cdot \frac{1}{40}}$$ (6.1.2)
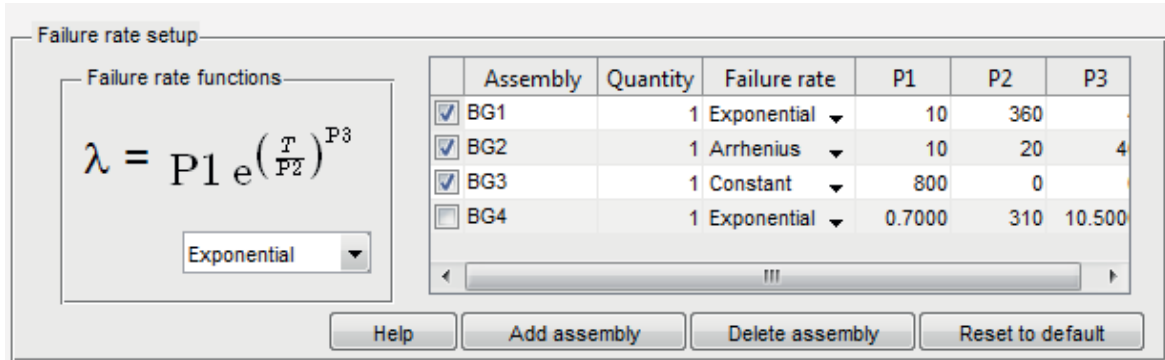
according to Arrhenius.

Figure 24:   Input data according to the equations above

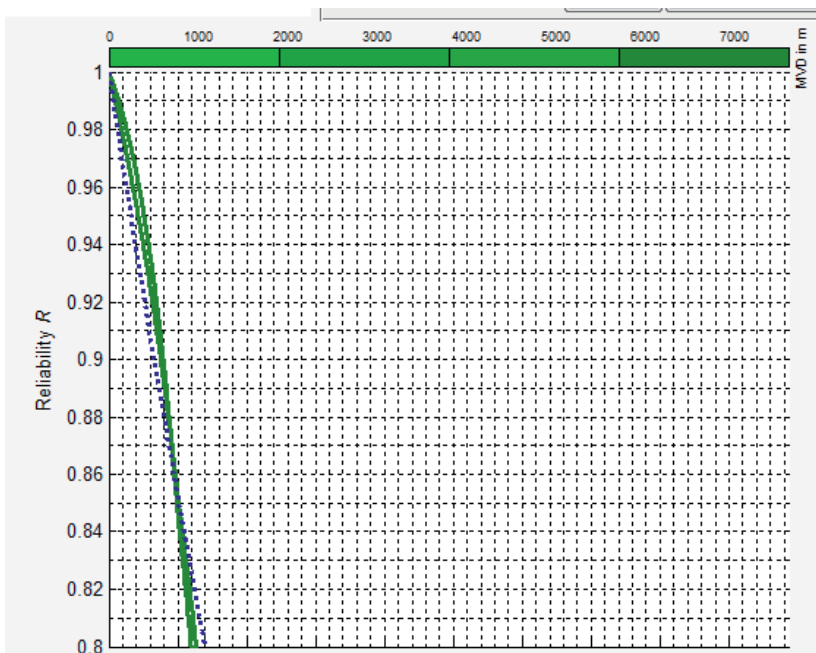For comparison both calculated courses are shown in the result plot in **Figure 25**.

Figure 25:   Course of the reliability function for the drilling duration taking into account the temperature from field data

The course with steady λ from the field data corresponds to the simplified exponential function, while the courses with rising λ on the origin function are based on equation 3. 1. 1. At the end of the drilling project the courses must meet by definition. Due to the fact that in the first part of the drilling the temperature is lower and therewith the failure rate, the survival probability (not failure probability) is at first higher if considering the temperature.

As mentioned above for electronic assemblies, exist a failure static from drilling projects up to a depth of on average 3000 m (90 °C) which was made available by Baker Hughes. The data are received from the years 2005 to 2008. Altogether, it consists of 1.7 million application hours with approx. 800 appeared failures, by the way, with falling failure rate over the years.

The input values of the reliability calculation are orientated by these data up to a depth of 3000 meters, so that the arithmetic results agree on average with these data. In the recordings of the predrilling KTB and main drillings, as well as the evaluated geothermal drillings aren't found any indications to the non productive times which are caused by failure in the electrical system or electronics. Hence, the validation of the electric area cannot be expanded on these drilling plans.

For the area of mechanical components the following course of the reliability function with the database from the project W7 is calculated (see **Figure 26**).

Figure 26:   Course of the reliability function for mechanical components

By comparison of the arithmetic result to the unplanned stops received from the field data, a good correspondence is found.

The following **Figure 27** summarizes the evaluations of the KTB and the present geothermal drillings. It shows the number of unplanned failures per km of drilling activity over the achieved depth of the respective project. With drilling projects to

3000-m depth one determines 30 events per km, so a total of 90 events. With projects reaching up to 8000 m (KTB), one receives 50 stops per km, i. e. a total of 400 events.
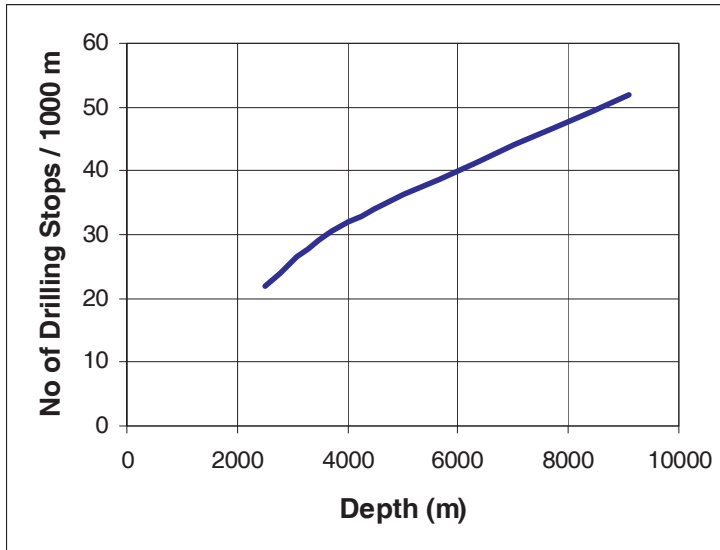

Figure 27: **No. Of drilling stops per 1000m related to Depth**

6.2 Extrapolation on the drilling model

The following ff shows the extrapolated course of the reliability function for the whole drilling process down to 7000 m. The blue curve is based on the field data with constant failure rate without influence of temperature. The green curves are the exponential and the Arrhenius functions as indicated in the diagram.
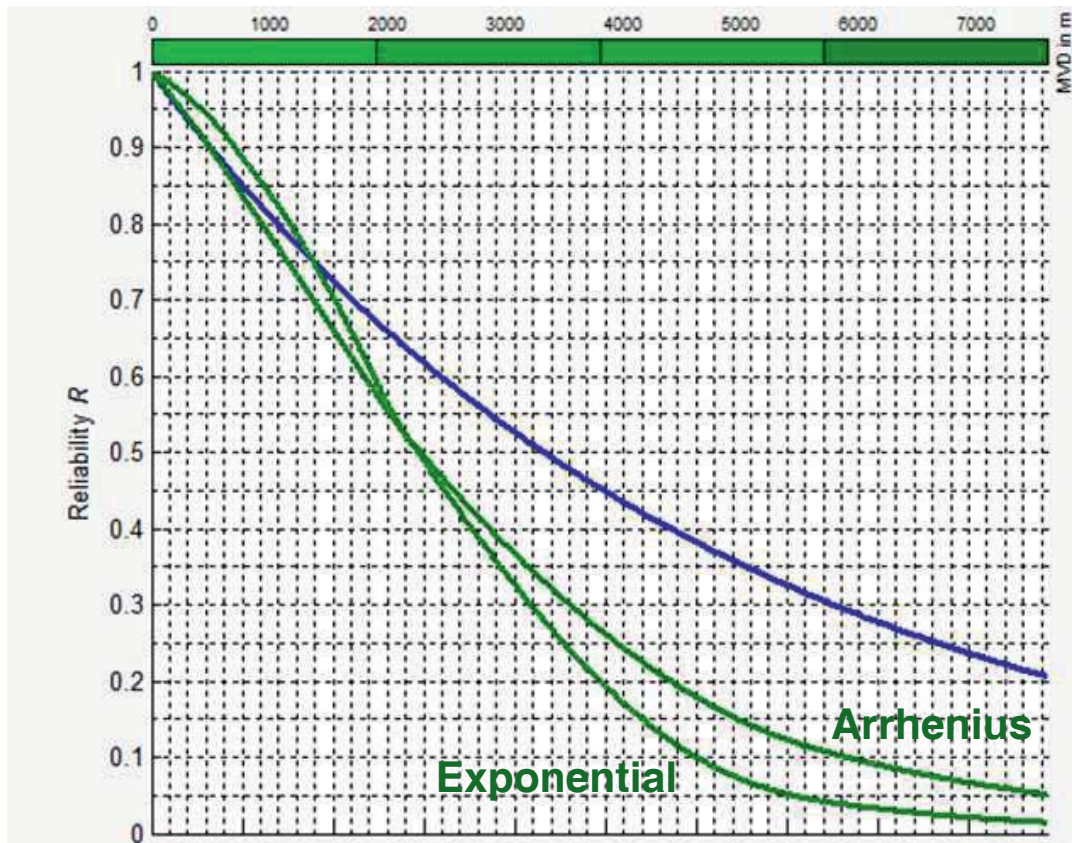

Figure 28: **Extrapolated course of the reliability function for the drilling duration taking into account the temperature**

At the end of the drilling project a very high failure probability (1-R (t)) of more than 90% appears due to the higher temperature. Related to a mean failure rate of approx. 0,0025h^-1, it means that a MTBF value of 400 h or approx. 3,5 failures per drilling projects due to failures in these assemblies of the BHA.

The following screenshots (**Figure 29, Figure 30, Figure 31**) show the reliability, MTBF and the failure rate including both, mechanical as well as electrical components.

Figure 29: Course of the reliability function for electrical and mechanical components

Figure 30: Course of the MTBF function for electrical and mechanical components

Figure 31:   Course of the failure rate for electrical and mechanical components

The curves for MTBF and failure rate experience a change in the gradient at 6000 meters due to the beginning of the horizontal part of the drilling.

6.3   Outlook

Within the scope of the project gebo W8 a calculation program has been created, that permits a many-sided and adaptable use by the assessment of the reliability of drilling projects. Although the productions of components and processes downhole were focused, the draught is not limited to it, but can be extended on other subsystems.

In the future, the program should be applied for the assessment of the whole reliability of a complete drilling system. New developments of components for higher temperature ranges or other drilling processes (e. g. , Coiled Tubing) should have an influence and their influence on the overall system should be valued.

Furthermore, it is necessary and possible at any time for the improving of the results to add other field data or test results to the assemblies.

Besides, the program can be optimized and developed further with the aim to create a sort of online monitoring system with that statements can be met to the reliability of the active components already during the drilling process. In this manner expensive failures can be avoided.

774

7 Course of the project W8

7.1 Linking within the gebo project

As already mentioned in chapter 5.2, a narrow cooperation with the part project W7 exists from which result files for the further processing have been made available.

In addition the part project G9 helped by understanding of the suitable geologic conditions.

To get a lot of insight and understanding for the area of the drilling technology, the narrow cooperation with the part projects of the area B was of essential meaning. In addition, this area led the student working group „gebo 2" from which the geology and the drill string construction for the present drilling model has been originated.

On industrial side, the cooperation and support of Baker Hughes turned out to be very helpful.

7.2 Data research

The calculation of the reliability of a system assumes the knowledge of the functional connections of the system which are lighted up in the FMEA and are examined for possible failures to be expected. Moreover, real drilling courses with their used components are to be studied. To execute the FMEA, a smaller number of drilling courses is enough. This job could be finished substantially by the data of the KTB drillings.
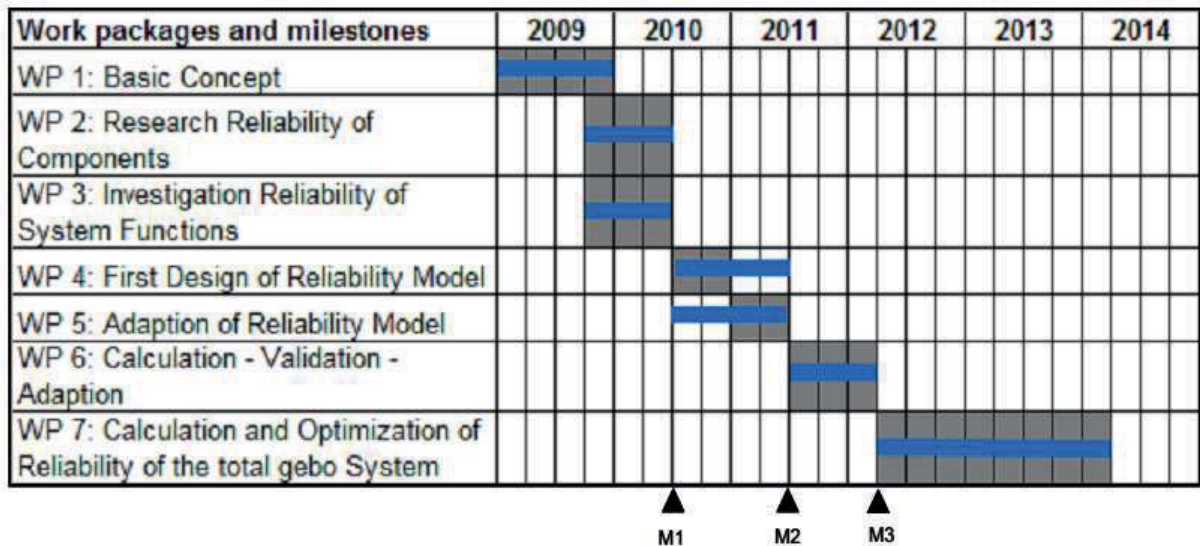
The second important point for the calculation of the reliability for the used components is the determination of failure rates close to reality. As it concerns statistical dimensions, the exactness of the prediction of the reliability depends on the size of the database. To get an expressive amount of failure rates, the data search was an essential as well as very time consuming part of the whole project.

The experiences of the data accessibility of the KTB project tempted first into the acceptance to receive drilling data relatively simply. Nevertheless, the readiness to the revelation of the partly sensitive data with projects which were financed from private sides was low. Hence, the search concentrated on the publicly promoted drilling projects at which the accessibility of the data is a little easier.

In addition, Baker Hughes made an anonymous database from which failure rates of various components or assemblies arise available.

7.3 Aim reaching (target performance comparison)

Work packages and milestones	2009	2010	2011	2012	2013	2014
WP 1: Basic Concept						
WP 2: Research Reliability of Components						
WP 3: Investigation Reliability of System Functions						
WP 4: First Design of Reliability Model						
WP 5: Adaption of Reliability Model						
WP 6: Calculation - Validation - Adaption						
WP 7: Calculation and Optimization of Reliability of the total gebo System						

M1: Data-recall of Reliability Key Figures

M2: Method Selection and first Reliability Analysis

M3: Results of State of the Art

The working packages up to WP6 were done in planned manner, but, however, have taken up partly clearly more time. Causes for this are, above all, the already mentioned delays and the additional expenditure with the collection and evaluation of field data.

The milestone M1 was compiled in time and a report was provided. The milestone 2 was reached at the same time with the interim report within the scope of the interim evaluation. Because of that no separate report occurred. Milestone 3 was reached just at the project end, so that the suitable report is incorporated in this final report.

Beside the reports, the respective state of the project has been presented on common project events as well as at the CelleDrilling 2014 conference.

8 Appendix

8.1 Acknowledgement

All partners in the project thank the ministry of science and culture of Lower Saxony and the company Baker Hughes Inteq for the financial support without the project could not have been realized. Special thanks go to Baker Hughes for the technical support in many talks, as well as for the supply of data material as a basis executed calculations.

8.2 Nomenclature

BHI   Baker Hughes Inteq

MWK   Ministry of science and culture of Lower Saxony

                Niedersächsisches Ministerium für Wissenschaft und Kultur

FMEA   Failure Mode and Effects Analysis

MIL HDBK   United States Military Standards, Military Handbook

IEE   Institute for Electrical Power Engineering, TU Clausthal

IMAB   Institute of Plant Engineering and Fatigue Analysis, TU Clausthal

MTTF   mean time to (first) failure

MTBF   mean time between failures (repairable system), uptime

MTTR   mean time to repair, downtime

BHA   bottom hole assembly

KTB   continental deep drilling project, Kontinentales Tiefbohrprogramm,

ROP   rate of penetration

MWD   measuring while drilling

MVD   Length of drill string

TVD   vertical depth of borehole

8.2   List of literature

Drilling Technology and Geothermal Energy

1. Belohlavek, Kai-Uwe (2006): Untersuchungen zum Zusammenhang zwischen Gesteinsfestigkeits-eigenschaften und Kenngrößen der Gesteinszerstörung durch einzelne Bohrzähne zur Beschreibung des Bohrens mit Rollenbohrwerkzeugen. Dissertation. TU Bergakademie Freiberg, Freiberg.

2. BINE Informationsdienst (Hg.) (2003): Geothermische Stromerzeugung in Neustadt-Glewe. Projektinfo 09/03. Bonn.

3. BINE Informationsdienst (Hg.) (2007): Geothermische Stromerzeugung in Landau. Projektinfo 14/07. Bonn.

4. BINE Informationsdienst (Hg.) (2009): Geothermische Stromerzeugung im Verbund mit Wärmenetz. Projektinfo 10/09. Bonn.

5. BINE Informationsdienst (Hg.) (2009): Geothermische Stromerzeugung in Soultz-sous-Forets. Projektinfo 04/09. Bonn.

6. BINE Informationsdienst (Hg.) (2010): Geothermische Energie aus Sedimentgesteinen. Projektinfo 05/10. Bonn.

7. BINE Informationsdienst (Hg.) (2004): Geothermie. basis Energie 8. Bonn.

8. Bundes-Umweltministerium (Hg.): Tiefe Geothermie in Deutschland. Broschüre. Berlin.

9. Bundesverband Geothermie (2010): Tiefe Geothermieprojekte in Deutschland. Berlin.

10. Emmermann, R. (1992): KTB Hauptbohrung, KTB-Report 92-2.

11. Engeser, B (1996): Das kontinentale Tiefbohrprogramm der Bundesrepublik Deutschland KTB. Bohrtechnische Dokumentation ; mit 256 Tabellen. Hannover: Niedersächsisches Landesamt für Bodenforschung (KTB-Report, 95-3).

12. Hatzsch, Peter (1991): Tiefbohrtechnik. Stuttgart: Enke.

13. Reich, Matthias (2003): Untersuchung komplexer Bohrgarnituren mit integriertem, schaltbarem Erweiterungswerkzeug. Dissertation. TU Bergakademie Freiberg, Freiberg.

14. H. Reckmann, M. Jenkins, F. Schuberth, C. Linke, C. Herbig (2010 Verständnisgewinn und Erhöhung der Zuverlässigkeit bei Tiefbohrprozessen): durch Visualisierung der Systemdynamik, DGMK/ÖGEW-Frühjahrstagung 2010, DGMK-Tagungsbericht 2010-1, ISBN 978-3-941721-05-0

15. Hanno Reckmann, Pushkar Jogi, Franck Kpetehoto, Sridharan Chandrasekaran, John Macpherson : MWD Failure Rates Due to Drilling Dynamics, IADC/SPE 127413

16. A. Ovolabi et. al, Economic Drilling of Deep Geothermal Wells, Group project gebo II, TU-Clausthal 2013

17. D. Vicente, Entwicklung eines Berechnungsprogramms zur Zuverlässigkeitsanalyse eines geothermischen Tiefbohrsystems unter Verwendung von MatLab, Studienarbeit 2012

18. A. Friedrichs, H. Darrelmann, Reliability Aspects in Deep Drilling Projects, CelleDrilling Conference 2014

Reliability

19. Bertsche, Bernd (2004): Zuverlässigkeit in Maschinenbau und Fahrzeugtechnik. Ermittlung von Bauteil- und System-Zuverlässigkeiten. 3., überarb. Berlin: Springer.

20. Birolini, Alessandro (1997): Zuverlässigkeit von Geräten und Systemen. Mit 50 Tabellen. 4. Aufl. Berlin: Springer.

21. Eberhardt, Otto (2008): Gefährdungsanalyse mit FMEA. Die Fehler-Möglichkeits- und Einfluss-Analyse gemäß VDA-Richtlinie ; mit Anwendungsbeispiel "Gefährdung von Maschinen". 2. Aufl. Renningen: expert-Verl. (Edition expertsoft, 63).

22. Gaede, Karl-Walter (1977): Zuverlässigkeit, mathematische Modelle. München ;Wien: Hanser.

23. Härtler, G. (1983): Statistische Methoden für die Zuverlässigkeitsanalyse. Lehrbuch. 1. Aufl. Berlin: VEB Verlag Technik.

24. Heinhold, Josef; Gaede, Karl-Walter (1979): Ingenieur-Statistik. 4., verb. u. wesentl. erw. München ;, Wien: Oldenbourg.

25. Höfle-Isphording, Ute (1978): Zuverlässigkeitsrechnung. Einführung in ihre Methoden. Berlin: Springer.

26. Kreyszig, Erwin (1977): Statistische Methoden und ihre Anwendungen. Mit zahlreichen Tabellen. 6. Aufl. Göttingen: Vandenhoeck & Ruprecht.

27. Ludwig, Bjørn (1995): Methoden zur Modellbildung in der Technikbewertung. Dissertation. TU Clausthal, Clausthal-Zellerfeld.

28. Ludwig, Bjørn (2000): Management komplexer Systeme. Habilitation. TU Clausthal, Clausthal-Zellerfeld.

29. Storm, Regina (1995): Wahrscheinlichkeitsrechnung, mathematische Statistik und statistische Qualitätskontrolle. 10. Aufl. Leipzig: Fachbuchverl.

30. Tilman, W. (2001): Optimierung der Instandhaltung und Zuverlässigkeitsstruktur von Kraftwerksanlagen. Entwicklung einer Lösungsmethodik und Untersuchungen an einem Heizkraftwerk mit Druckwirbelschichtfeuerung sowie einer Gasturbinen-Baureihe. Dissertation. TU, Dresden.

31. Robert B. Abernethy (1994), The New Weibull Handbook, Gulf Publishing Co

Standards and Norms

32. DIN EN 50126, 03/2000: Bahnanwendungen - Spezifikation und Nachweis der Zuverlässigkeit, Verfügbarkeit, Instandhaltbarkeit, Sicherheit (RAMS).

33. DIN EN 61709, 01/1999: Bauelemente der Elektronik - Zuverlässigkeit - Referenzbedingungen für Ausfallraten und Beanspruchungsmodelle zur Umrechnung.

34. DIN EN 60812, 11/2006: Analysetechniken für die Funktionsfähigkeit von Systemen - Verfahren für die Fehlzustandsart- und -auswirkungsanalyse (FMEA).

35. DIN EN 61025, 08/2007: Fehlzustandsbaumanalyse.

36. DIN EN 61703, 09/2002: Mathematische Ausdrücke für Begriffe der Funktionsfähigkeit, Verfügbarkeit, Instandhaltbarkeit und Instandhaltungsbereitschaft.

37. DIN EN 61078, 10/2006: Techniken für die Analyse der Zuverlässigkeit - Zuverlässigkeitsblockdiagramm und Boole'sche Verfahren.

38. DIN EN 61165, 02/2007: Anwendung des Markoff-Verfahrens.

39. MIL-HDBK-472_1966, 1966: Maintainability Prediction.

40. MIL-STD-217F_1991, 1991: Reliability Prediction of Electronic Equipment.

41. MIL-STD-882D_2000, 2000: Practice for System Safety.

Schriftenreihe des Energie-Forschungszentrums Niedersachsen (EFZN)

Band 30-4

Das EFZN ist eine wissenschaftliche
Einrichtung der

TU Clausthal

in Kooperation mit den Universitäten

Technische
Universität
Braunschweig

GEORG-AUGUST-UNIVERSITÄT
GÖTTINGEN

Leibniz
Universität
Hannover

CARL
VON
OSSIETZKY
universität OLDENBURG

Final Report

of

Geothermal Energy and High-Performance Drilling Collaborative Research Program (gebo)

Niedersachsen

Partners:

Technische Universität Braunschweig (TUBS)

Technische Universität Clausthal (TUC)

Gottfried Wilhelm Leibniz Universität Hannover (LUH)

Georg-August-Universität Göttingen (UGOE)

Leibniz-Institut für Angewandte Geophysik (LIAG)

Bundesanstalt für Geowissenschaften und Rohstoffe (BGR)

Energie-Forschungszentrum Niedersachsen (EFZN)

Speaker:
Kurt M. Reinicke;
Georg-Peter Ostermeyer

Goslar, July 2015

Contents

T1: High temperature electronics

1 Overview of the project

Speaker and lead university or research institution

Project Nr.	Title	Subject of research	Project Leader, institution, location
T1	High temperature electronics	Microelectronics	Prof. Dr.-Ing. Holger Blume, LUH (IMS), Hannover

Participating institutes and institutions of the university and external institutions in:

- Institute of Microelectronic Systems, Leibniz Universität Hannover

- Baker Hughes Contact, Dr. Thomas Kruspe and Dr. Sascha Schwarze

List of participating scientists and engineers:

Name	Subject area	Institution or non-university institution	Position is financed by gebo funds (indicate with X)
Prof. Dr.-Ing. Holger Blume	Microelectronics	IMS	
Prof. Dr.-Ing. Erich Barke	Microelectronics	IMS	
Dr.-Ing. Markus Olbrich	Microelectronics	IMS	
Dipl.-Ing. Rochus Nowosielski	Microelectronics	IMS	X
Dipl.-Ing. Oliver Scharf	Microelectronics	IMS	X

2 Research Program

2.a Summary

The gebo research project has the aim to research and survey new concepts for geothermal energy generation in deep geological formations. To ensure the profitability of this regenerative energy source high efficiency and effectiveness as well as low geological and technical risks are required.

The efficiency of geothermal energy generation is heavily affected by the temperature of the geological formation. Within the gebo project a temperature of 250°C is assumed for profitable geothermal applications. This high temperature is considered to be problematic in drilling technology. Common drilling tools can only be used for temperatures up to 200°C. As there are no integrated electronic components for this temperature available on the market, the applicability of Silicon-On-Insulator (SOI) technologies for the use in integrated mixed signal circuit is researched in this project.

781

The Institute of Microelectronic Systems takes part in the gebo research project within the research field "technical systems" by researching verification methods for integrated analog components under high temperature conditions and concepts for a reliable digital architecture for an optimized signal processing of algorithms used in drilling technology.

Especially the analog components of the sensor interface need a high accuracy which has to be guaranteed over the whole temperature range. To estimate the properties of the circuit design techniques like Corner Case or Monte Carlo simulations are commonly used. These methods need a large amount of simulation runs and therefore computation time. Nevertheless, these methods do not guarantee that the worst or the best case of the circuit property under investigation is included by the simulation results. To eliminate this uncertainty one goal of the project is to research verification methods which guarantee the inclusion under all possible combinations and for large temperature ranges. Therefore, an existing simulation method is enhanced and adapted to SOI technology.

Currently available high temperature SOI technologies have a minimal structure size of 0.8 or 1.0 µm, respectively. This heavily limits the achievable complexity of digital circuits. Furthermore, the maximal clock frequency decreases significantly with increasing temperature. Thus, another goal of the project T1 is to develop a concept for an MWD (measurement while drilling) ASIC which is able to perform the measurement, control and communication tasks in the drilling head at an environmental temperature of 250°C. This requires an optimization of the signal processing algorithms considering memory efficiency and performance, as well as to ensure the operational reliability.

2.b Relationship of the project to the overall research context and networking with other projects

The gebo project's currently aspired drilling concept for a geothermal power plant requires the drilling of several deflected holes of a true vertical depth of 6 kilometers with a target ambient temperature of 250 °C. In order to build up the down-hole heat exchanger without short circuits the drilling path needs to follow the drilling plan with high accuracy. For such purposes MWD tools are used in deep drilling applications today. Without the support of such a tool the concepts of the gebo project cannot be realized. The MWD tools use large scale integrated electronic circuits for control and measurement tasks. Currently such electronic components are not available commercially for the expected ambient temperatures. That fact prevents the availability of MWD tools for geothermal deep drilling applications. Thus, the contribution of T1 for the gebo project is to investigate the possibilities for a realization of MWD-electronics, to identify best-suited processor architecture designs for high temperature applications and to increase the reliability of an MWD-ASIC implementation during design time. Besides the

technological challenges the work of the T1 project is driven by the goal to minimize operating costs. The efficient processor architecture makes a single-chip MWD realization possible, which reduces costs per MWD application to a minimum. Beside the directional measurements an MWD tool also measures mechanical stress of the Bottom Hole Assembly (BHA) and the drill string. That information helps to control the drilling process and to reduce the wear of the bit. Increasing the reliability of the MWD electronic reduces the possibility of a tool malfunction and a costly replacement of the BHA.

In order to realize the MWD functionality, external sensors for measurements under high ambient temperature are needed and are developed in the projects T2, T5 and T6. In combination with the results of T3 and T4 drilling at even higher temperatures could become possible. The implementation of the geo-radar in project T7 will require many arithmetic calculations in the BHA. The results of T1 are valuable for a realization of such a radar system under high temperature conditions.

2.c   Work packages executed relative to (original) plan and results achieved

AP 1:

Standard bulk-CMOS processes cannot be use for operating temperatures above 150 °C. In a standard bulk wafer only the upper few micrometers are processed during the fabrication and are significant for the function of the IC. All transistors are connected to each other via the subtrate, so they can influence each other. Especially, at higher temperatures, an effect called latch-up can occur. PMOS and NMOS transistors placed next to each other build up a parasitic PNPN structure which behavior is equivalent to that of a thyristor. Once this thyristor is triggered, it conducts until the power supply is turned off. In the worst case the parasitic thyristor shorts the power rails. It may be triggered by the temperature-dependent leakage currents in the pn-junctions. By using a Silicon-On-Insulator (SOI) process the latch-up effect can be avoided. The isolator (often SiO_2) separates the transistors from the substrate so they are independent from each other.

In AP1 it was investigated which SOI processes are commercially available. A summary is given in Table 1. In co-operation with Baker-Hughes the process H10 of the Fraunhofer Institute for Microelectronic Circuits and Systems (FhG-IMS) was selected. It is suitable for operation temperatures up to 250 °C and offers libraries for digital components. Its structure size of 1 µm limits the possible clock rate so it is necessary to perform architecture optimizations to achieve the performance requirements. The provided Process Design Kit (PDK) of the H10 process was installed and tested with small analog and digital circuits.

Manufacturer	Minimal size	Maximal operation temperature	Number of metal layers	Availability of design support
Honeywell	0.8 µm	225 °C	3	No
X-Fab	1 µm	225 °C	3	No
Telefunken	0.8 µm	225 °C	3	No
FhG-IMS	1 µm	250 °C	3	Yes

Table 1: Overview of available high temperature SOI processes

AP2:

The behavior of integrated analog circuits is affected heavily by transistor parameters like the threshold voltage or the oxide thickness. Due to the fabrication process these values are not constant but may vary. Another parameter with a huge influence on the circuit behavior is the temperature. Circuits for geothermal use, like in the gebo project, need to function in a large temperature range from 0 to 250°C To ensure the reliability of the circuit under these varying conditions it is necessary to consider these effects during circuit design.

To simulate such variations point arithmetic methods, for example Monte Carlo or Corner Case Analysis, are commonly used. Both methods are based on simulations with nominal parameter values. They differ from each other in the way the samples are selected. During the Corner Case Analysis all varying parameters are simulated with their minimal and maximal values. A complete simulation of n varying parameters takes 2^n simulation runs. By comparison, the Monte Carlo Analysis uses random samples to perform nominal simulations. The more samples are used the more significant is the result. Both methods need a lot of simulation runs, but cannot guarantee that a circuit property (for example an output voltage) lies within a given range. The worst or the best case may be missed by these techniques in certain conditions. The Monte Carlo Analysis may not cover them due to its statistical nature. The Corner Case Analysis only includes them if the functions are monotonic. For a non-monotonic function, which may be as simple as a parabola, the extremum is missed if it is located in between the corner points.

An alternative to point arithmetics are range arithmetics such as the affine arithmetic [1]. Each varying parameter is not represented by a fixed nominal value, but by a sum of a central value and several deviation symbols. This so called affine form is given in Equation 1. The deviation symbols are valid globally so linear correlations are kept during the calculation. The result of an affine simulation is a range which can be simplified to an interval. The output variable is

guaranteed to lie within this interval under all regarded parameter variations. The worst and the best case are always included.

$$\hat{x} = x_0 + \sum_{i \in \mathbb{N}_{\tilde{x}}} x_i \, \epsilon_i \qquad \epsilon_i \in [-1,1]$$

Equation 1

The MOSFETs of the selected process H10 are described using BSIMSOI models [2]. This is an extension of the BSIM3 models (3) to cover SOI specific effects. To verify circuits built with this process using our affine simulator AMV, we implemented a special affine BSIMSOI model in this project. As the BSIMSOI model is a very general model, it covers a broad range of effects. Not all effects are used to describe the H10 process. The possibilities to model impact ionization, selfheating, additional gate or bulk resistances and gate tunnel currents are not used. Furthermore, adoptions are needed to minimize the overestimation. Terms which only have a small influence on the result for this process were neglected. To estimate the influence of the simplifications, the implemented affine model was compared to the complete implementation in the commercial simulator Cadence Spectre. A good match was observed at all temperatures. A comparison of the output characteristics for 27 °C and 250 °C is given in Figure 1.
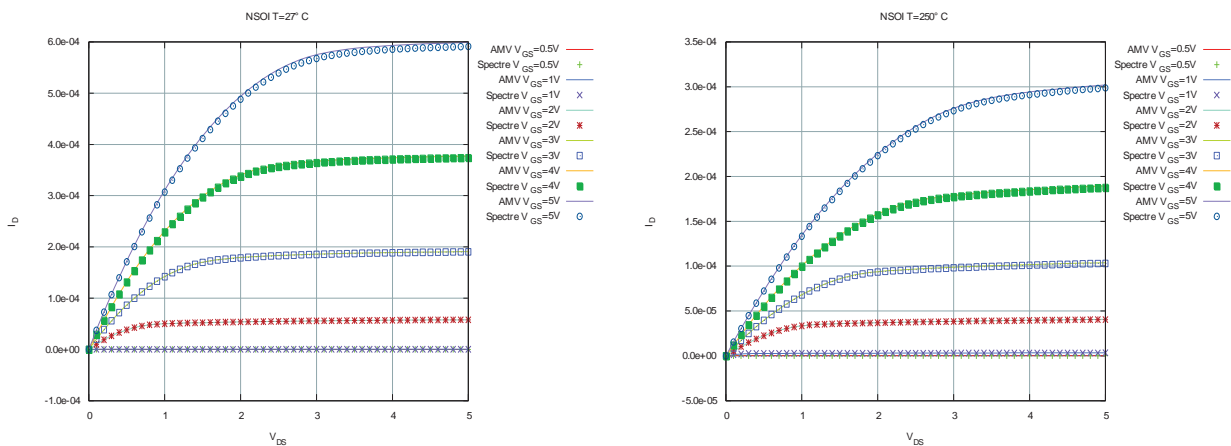
Figure 1: Comparison of output characteristics simulated with Cadence Spectre and the affine simulator AMV

The suitability of the affine simulation method was shown by the simulation of some example circuits. One of these was the active lowpass filter given in Figure 2 . The opamp of the filter consists of eight transistors modeled using the affine BSIMSOI model. The affine simulation result is shown in Figure 3 along with some Monte Carlo samples. The inclusion of the Monte Carlo results by the affine results can be observed at any time.

Figure 2: Circuit of lowpass filter

Figure 3: Simulated output voltage V_{out}

■ Affine

■ Monte Carlo

AP 3:

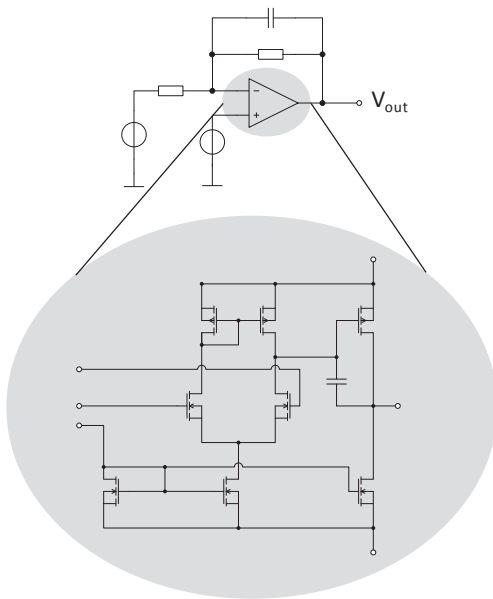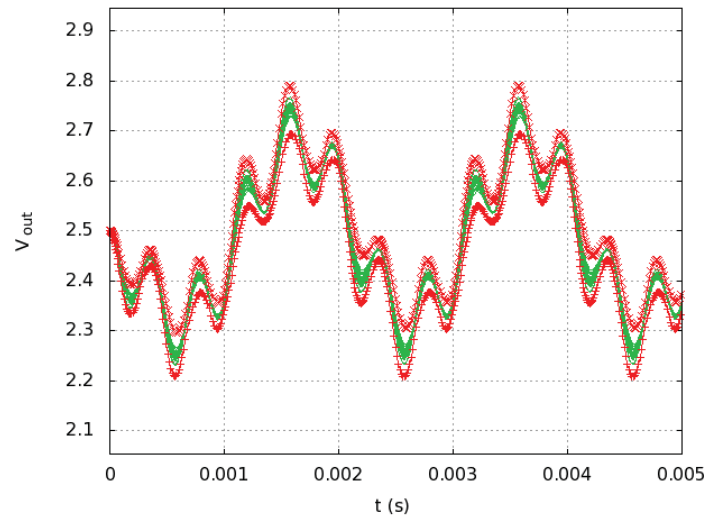With the existing implementation of the affine simulator it was not possible to simulate more complex circuits. The overapproximation grow too large to allow the solving algorithm to converge. So further measures to reduced the overapproximation were needed in addition to the optimization of the BSIMSOI model equations for affine arithmetic performed in AP2.

One measure is the use of special approximations for composite functions. As derivatives of most elementary functions are monotone, it is sufficient to consider the values at their borders. In general, derivatives of composite function are nonmontone so a search for the extrema is needed. Special approximations for composite functions which are common in the BSIMSOI model were implemented. One example is the function

$$f(x) = e^{1+\ln(x)}.$$

By introducing the affine function $\mathrm{lnexp(x)}$, which performs this operations in one step the overapproximation can be reduced.

Another measure to reduce overapproximation is to use an improved calculation of the minimum and maximum of quadratic affine forms. They are an extension of affine forms with quadratic deviation symbols to achieve a better approximation of nonlinear functions.

$$\hat{x} = x_0 + \sum_{i\in\mathbb{N}_{\tilde{x}}} x_i \epsilon_i + \sum_{i\in\mathbb{N}_{\tilde{x}}} \sum_{j\in\mathbb{N}_{\tilde{x}}}^{j\geq i} x_{ij}\epsilon_{ij}$$

In the previously existing implementation the minimum and maximum of a quadratic form were calculated by neglecting the correlation between linear and quadratic symbols. This leads to overapproximation. It can be reduced by considering the extrema of the describing equation for every deviation symbol ε_i:

$$f(\varepsilon_i) = a\varepsilon_i^2 + b\varepsilon_i + c$$

The extrema's position depends on the the quadratic term and can lie inside or outside the considered interval $-1 < \varepsilon_i < 1$. If

$$\left|\frac{-b}{2a}\right| < 1$$

holds, the extremum lies inside the interval and has to be considered in the calculation. Extrema which lie outside the interval do not have to be considered and can be replaced by the values at the corners $f(1)$ or $f(-1)$, respectively. The minimum and maximum can be described as

$$\min(\tilde{x}) = x_0 - \min_{i\in\mathbb{N}_{\tilde{x}}}(f(\varepsilon_i))$$
$$\max\ (\tilde{x}) = x_0 + \max_{i\in\mathbb{N}_{\tilde{x}}}(f(\varepsilon_i)).$$

These equations respect the correlation between i and ii according to

$$\varepsilon_{ij} \in \begin{cases} [-1,1] & \forall(i \neq j) \\ [0,1] & \forall(i = j) \end{cases}$$

The correlation between j and ji is neglected for performance reasons as this would require root finding for a function with n dimensions. With these improved calculation of the minimum and maxmium the overapproximation can be reduced.

Furthermore, an operational amplifier (Opamp) was designed in AP3 in coordination with Baker's high temperature electronics group. It consists of eight MOSFETs in the high temperature H10 technology selected in AP1. Its circuit is shown in Figure 4. This Opamp was analysed in several basic circuits, for example the inverting amplifier in Figure 5 and the non inverting amplifier in Figure 6. We assummed the parameter uncertainities in Table 2 for simulation. The results are shown in Figure 7 and Figure 8. Comparision with the given results

787

of Monte Carlo simulations show that the inclusion of the results is always maintained. The runtime of the affine simulation compared to 1000 Monte Carlo simulation performed with the moninal part of our simulator is significantly reduced. The runtime for the affine simulation of the non-inverting amplifier is 58,7%, for the inverting amplifiet 23,2% of the time needed for the Monte Carlo simulations.
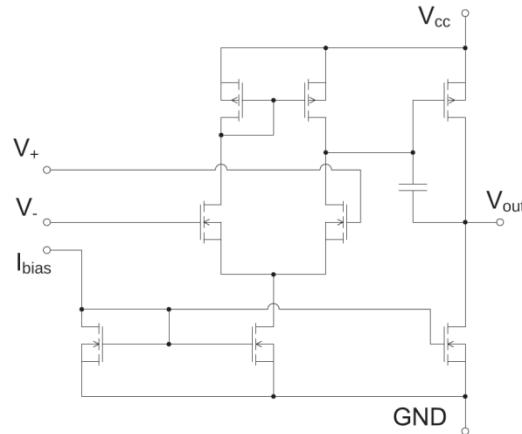
Figure 4: Operational amplifier in H10 technology
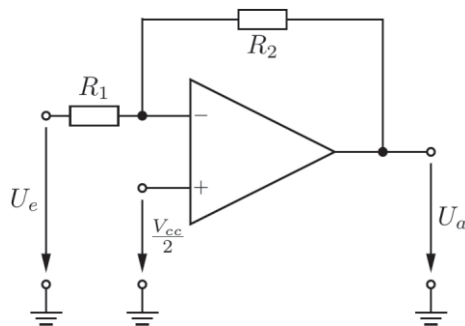
Figure 5: Inverting amplifier
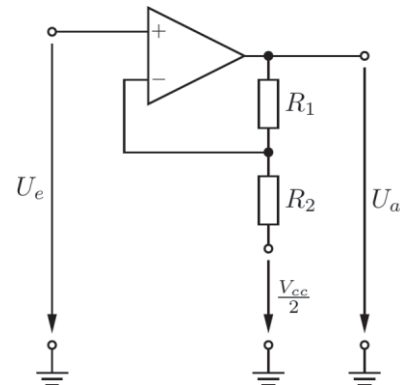
Figure 6: Non inverting amplifier

Parameter	Nominal value	Deviation
R_1	200kΩ	±8kΩ
R_2	400kΩ	±12kΩ
V_{th0}	1,116V	±0,02V
T	27°C	3°C

Table 2: Parameters of the inverting and non inverting amplifier

The temperature range which can be covered with range arithmetic simulation is limited, because temperature effects are strongly nonlinear and have an influence on many equations of

the model. This leads to overapproximation and the simulation algorithm does not converge. To cover larger temperature ranges it is nessecary to perform multiple simulation runs with the affine simulation approach as well. The summarized results of AP1 to AP3 were published on the Analog conference [3]. It was shown that the affine simulation can be used to verify circuits with the BSIMSOI model containing parameter uncertainties. It offers shorter simulation run times and a formal verification of the circuit behaviour.

Figure 7: Simulation result for inverting amplifier

Figure 8: Simulation result for non inverting amplifier

AP4:

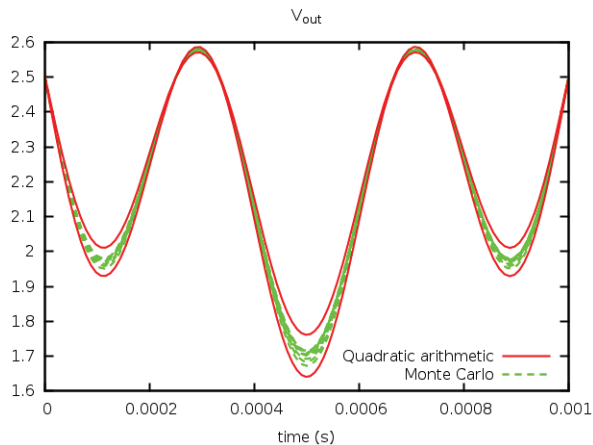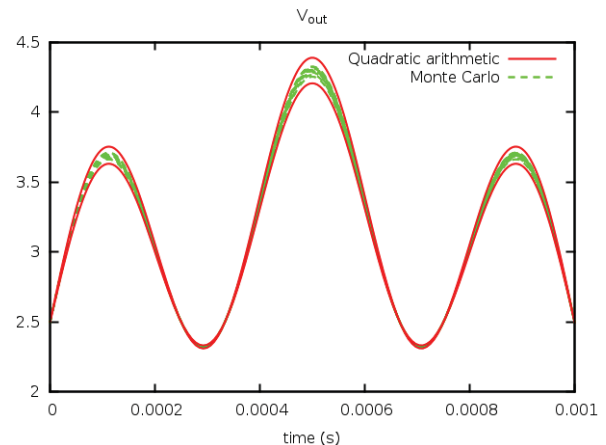The goal of AP4 was to investigate the needs for digital signal processing down hole, evaluate the used algorithms and identify the requirements for an application specific implementation in hardware considering the limitations introduced by the chosen high temperature technology from AP1.

A typical MWD application uses magnetic flux and acceleration sensors in order to compute the geometric orientation of the BHA by azimuth and inclination. Since the sensors and analogous sensor amplifiers have temperature induced non-linear characteristics, a thermo transducer as third sensor type is mandatory to correct the effects inferred by temperature changes. Beside the position calculation, information about the mechanical wear can be derived from the sensor data mentioned above. All information has to be transmitted to the control station at the surface. The process of sending data up hole is called telemetry and solved in several ways. One promising, but expensive solution is to integrate optical fibers inside the wall of drill pipes enabling a high throughput communication link. One of the main goals of the gebo project is to lower the costs for drilling, thus the less expensive mud pulse telemetry is more reasonable.

As starting point for the application analysis and profiling a prototype for a high temperature MWD system of Baker Hughes was selected. In that prototype down hole digital signal

processing is performed by a multiprocessor based acquisition and processing system for operations up to 175 °C. Based on the analysis of that prototype, a concept for realization of an MWD system has been identified and is shown in Figure 9.
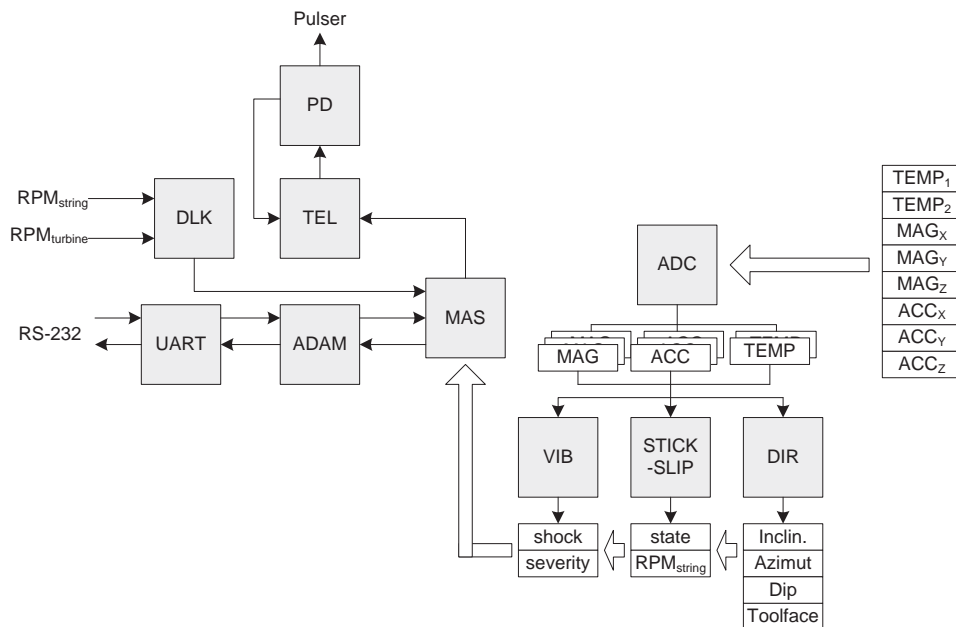

Figure 9: Proposed System architecture for the gebo HT-MWD as result of AP4.

The system shown can be split into three parts by the kind of data flow.

The first part is called here measurement data acquisition and processing and is composed of the modules ADC, DIR, VIB and S-S. The ADC module controls the analog to digital converter and stores the sampled sensor data from the accelerometers (ACC), magnetic flux sensors (MAG) and thermo transducers (TEMP) for later processing. Each of the following modules has its own requirements for sampling rate and resolution. The directional module DIR calculates the azimuth, inclination, toolface and the magnetic dip angle as main parameters, as also the magnetic and gravitational vectors. The VIB module measures the lateral and axial vibrations while the S-S module computes the stick-slip severity. Both modules implement proprietary algorithms by Baker Hughes.

The second part is called here communication system and is composed of the modules TEL, DLK and PD. This system's part manages the communication with the control station at the surface. The TEL module receives MWD data for transmission and encodes it with an encoding scheme used by Baker Hughes, called Advantage Combinatorial. This scheme uses a variant of a pulse position encoding to express a data word with as less pulses as possible during a given time period. After encoding the data is passed to the pulser driver module (PD), which drives a signal for the pulser driver according to the required timing. Incoming commands from the drilling operator are called Downlink and are decoded in the DLK module.

The third part of the system is called here the master system. This part coordinates the data flow from the acquisition system to the communication system, checks for system health and provides an interface to other drilling tools of the BHA. For that the proprietary protocol ADAM II of Baker Hughes is used. The corresponding protocol handling is done by the ADAM module. The interface to Baker Hughes modules is optionally and not in the main focus.

The requirements for precision of parameter calculation in the directional module are taken from the Baker Hughes NaviTrak specification and are shown in Table 3.

	Range	Resolution	Accuracy (±)
inclination	0° – 180°	0,1	0,2
azimuth[1,2]	0° – 360°	0,35	1
tool tace (mag.) [1]	0° – 360°	1,4	1,5
tool tace (grav.)[2]	0° – 360°	1,4	1,5
temperature	0 °C – 150 °C	2	3
total magnetic field	0 – 70000 ga	100	200
dip angle[1]	-90° – 90°	0,1	0,3
gravity magnitude	0 – 1100 mg	1	2
[1] Assuming typical magnetic field strength at a latitude of 30°			
[2] Valid for an inclination greater than 5°			
[3] Switch MFT ←→ GFT at 5° inclination			

Table 3: Precision Requirements for directional measurements in the BHI NaviTrak tool.

To determine the requirements for implementation of an MWD application in the chosen high temperature SOI technology the above mentioned HT-MWD tool prototype of Baker Hughes was profiled during AP4. Details of that profiling are confidential and are part of a separate 150 pages report written for the High Temperature Electronics Group at Baker Hughes, Celle.
The intended use of the H10 technology mentioned in AP1 implies significant performance reduction for integrated digital circuits. Figure 10 shows exemplary area-time results after place&route for an 8-bit multiplier. The minimum achievable clock period, the maximum clock frequency, respectively, degrades by a factor of nearly 5 during an ambient temperature shift from 100 °C to 250 °C. In comparison, today's microcontrollers are manufactured with much smaller feature sizes like 130 nm and below. Thus, Figure 10 also shows the performance degradation by a factor of 15 resulting from using the much coarser 1.0 µm H10 technology for 100 °C ambient temperature and an increased area need by two orders of magnitude opposed to a 130 nm technology.
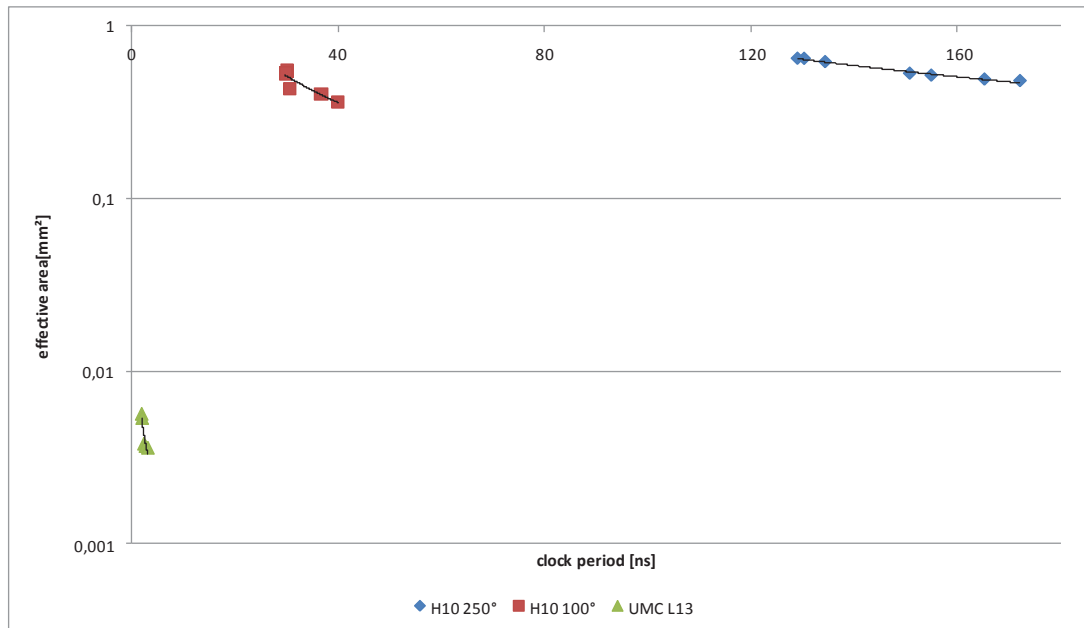
Figure 10: Area-Time diagram for an 8-bit Braun multiplier in 1.0 μm technology at different temperatures compared to a 130 nm technology at typical temperature after place&route.

In summery the computational requirements for data acquisition and processing exceed the expected performance of a 68HC11 compatible microcontroller in the chosen SOI technology by a factor of at least 10, neglecting further demands of computational resources for the communication and the master system. The significantly increased area need is a main constraint, which has to be considered in AP5.

Beside the main focus of AP4, evaluation of architectural variants of potential arithmetic units started as outlook for AP5. Figure 11 shows the area-time results for a Braun and a Booth multiplier in H10 technology after place&route. A systematic evaluation of arithmetic unit variants for use with the H10 technology is one topic of AP5.

Figure 11: Area-Time diagram after place&route of two 8-bit multiplier variants in the targeted H10 technology.

AP 5:

The use of modern drilling tools makes it necessary to determine the location and the operating status of the tool as precisely as possible and to send this information to the ground station. Th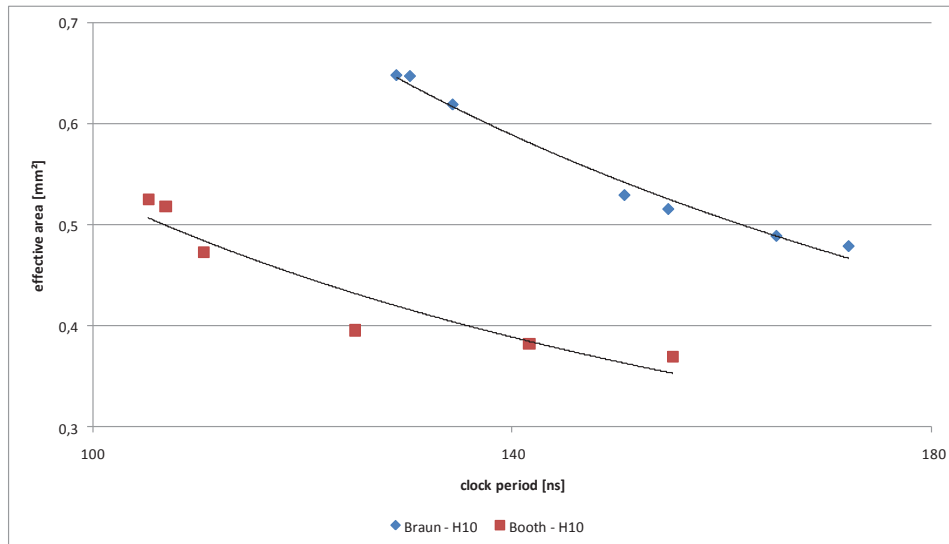is basic functionality is grouped under the term Measurement While Drilling (MWD). Implementation of MWD functionality for the high temperature range up to 250 °C allows drilling of geothermal wells and supports the implementation of various drilling concepts. Once the requirements have been presented in AP4, in AP5 an architectural concept was deducted, which can provide the MWD functionality at 250 °C.

As a result of the strong limitations on today's high-temperature technologies preferably processor systems with a narrow bus are suitable for the implementation of programmable architectures, because of minimized wiring and chip area demands for the placement of the circuit logic. For the selection of the processor two architectures were compared: an Atmel AVR8 compatible 8-bit processor as a RISC variant and a Motorola M68HC11 compatible 8-bit processor as CISC variant [4]. The particular processor architecture is shown in Figures 12 and 13.

The synthesis of both architectures in the high-temperature SOI technology FhG-H10 showed an average area of about 4 mm² for both cores. However, each AVR8 instruction is 16-bits wide, while the HC11 instruction length can be 8-bit or 16-bit long. As a result, the instruction memory occupied in the CISC processor is smaller (see Figure 14).
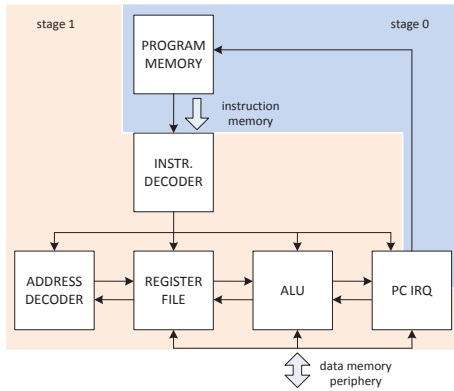
Figure 12: Block diagram of 8-bit AVR8-RISC processor
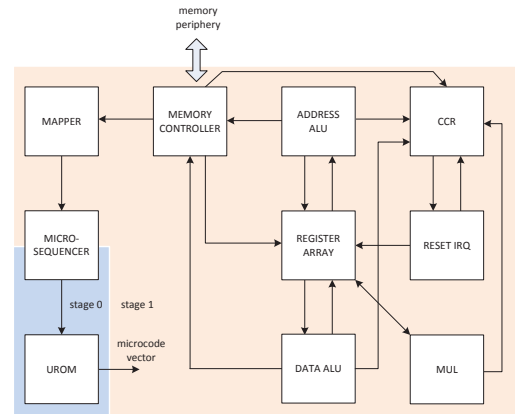
Figure 13: Block diagram of 8-bit HC11 CISC processor

	Dhrystone	FFT 128	FP ADD	FP MUL
cycles	23%	23%	36%	29%
memory	99%	89%	112%	126%
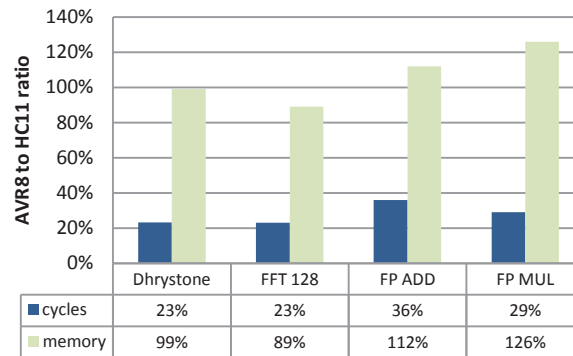
Figure 14: Comparison of the required clock cycles und program memory size for the evaluated processor architectures. The values are normalized to the HC11 architecture. (FP - Floating Point)

This in turn leads to a smaller memory size and a correspondingly reduced on-chip area. On the other hand, the processing speed of the RISC processor is more efficient, with fewer cycles required for the processing of an algorithm. However, the speed advantage of factor four shown in Figure 14 is diminished by the longer data paths in the RISC core. This has a direct impact on the maximum clock frequency of the design, as shown in Figure 15. The maximum clock frequency of the CISC design is about twice higher than that of the RISC design. Thus, the AVR8 processor can process data twice as fast as the HC11 processor, but also requires up to 20% more chip area for the instruction memory.
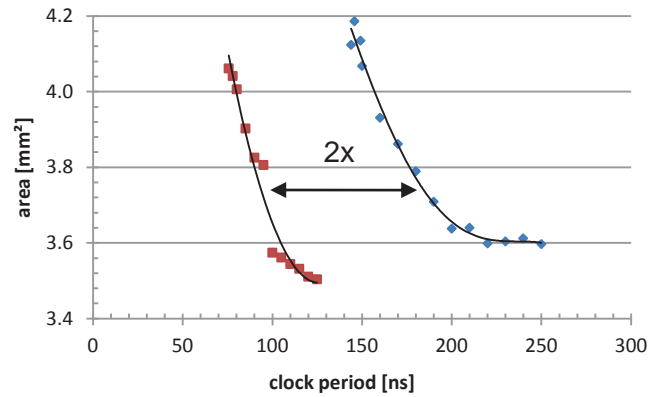
Figure 15: Synthesis results in terms of clock period over chip area. Technology: FhG H10

Taking into account the results and after consultation with the industry partner Baker Hughes the architectural concept for the MWD ASIC was further evaluated on the basis of the HC11 processor. As identified in AP4 the demands on throughput cannot be met by the HC11 processor exclusivly. Thus, additional hardware modules are proposed which take computing load off the processor core and process data in parallel. The proposed approach is shown in Figure 12. Next to the HC11 processor additional modules are connected to the on-chip bus. The POLY-module is a programmable multiply-add unit for calculating polynomials. It supports calibration computations of the recorded sensor data. The CORDIC-module is an implementation of a conventional algorithm for iterative calculation of trigonometric functions in computer systems. The Telemetry encoder implements a proprietary encoding scheme for the mud pulse telemetry. The SPI module implements a synchronous serial interface. The timer module is a programmable timer which can interrupt the sequential program processing in the processor and can signal the processing of an alternative program code. This is particularly relevant for the periodic acquisition of sensors samples. The light-gray shaded blocks represent analog components and thus are not part of AP5.

Figure 16: Proposed architecture concept for a high temperature MWD ASIC

795

The large number of mathematical operations per second, as it was identified in AP4, makes a direct calculation using the HC11 processor not possible within the specified time. In part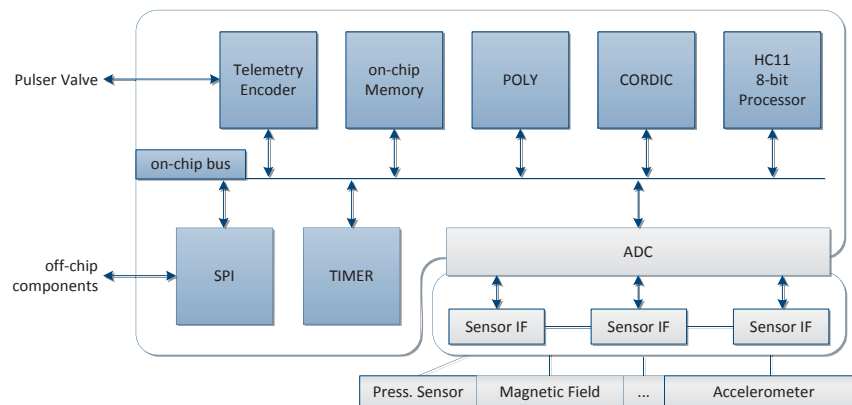icular, the dynamic vibration measurements require a lot of computing time. For example, the calculation of the square root performed in floating point format using the HC11 floating-point library requires 16354 clock cycles. However, for the calculation of the square root function only 180 clock cycles are available, if the processor is clocked at 2 MHz.

The required acceleration of the processing of mathematical operations is achieved by means of the CORDIC method. CORDIC is an acronym for "Coordinate Rotation Digital Computer." The algorithm was introduced in 1959 by J. E. Volder [5] and extended in 1971 by J. S. Walther [6]. The idea of CORDIC is based on an iterative rotation of a vector by known partial angles. These rotations can be formulated as a 2-dimensional rotation matrix. With the help of addition theorems, there are three iterative equations:

$$X_{i+1} = X_i - m d_i 2^{-i} Y_i$$
$$Y_{i+1} = Y_i + d_i 2^{-i} X_i$$
$$Z_{i+1} = Z_i - d_i \alpha_i$$

By choosing the starting values for X, Y, Z and m, the following expressions can be calculated directly:

m	$d_n = \operatorname{sign} z_n$ (*Rotation Mode*)	$d_n = -\operatorname{sign} y_n$ (*Vectoring Mode*)
1	$x_n \to K(x_0 \cos z_0 - y_0 \sin z_0)$	$x_n \to K(\sqrt{x_0^2 + y_0^2})$
	$y_n \to K(y_0 \cos z_0 + x_0 \sin z_0)$	$y_n \to 0$
	$z_n \to 0$	$z_n \to z_0 + \arctan \frac{y_0}{x_0}$
0	$x_n \to x_0$	$x_n \to x_0$
	$y_n \to y_0 + x_0 z_0$	$y_n \to 0$
	$z_n \to 0$	$z_n \to z_0 + \frac{y_0}{x_0}$
-1	$x_n \to K(x_0 \cosh z_0 + y_0 \sinh z_0)$	$x_n \to K(\sqrt{x_0^2 - y_0^2})$
	$y_n \to K(x_0 \cosh z_0 + y_0 \sinh z_0)$	$y_n \to 0$
	$z_n \to 0$	$z_n \to z_0 + \operatorname{artanh} \frac{y_0}{x_0}$

Table 4: CORDIC modes and corresponding mathematical functions

In addition, it is also possible to compute even more elementary functions by repeated applications of CORDIC or by a combination of partial results:

$$\tan z = \sin z / \cos z \qquad\qquad \tanh z = \sinh z / \cosh z$$

$$\arcsin w = \arctan(w / \sqrt{1 - w^2}) \qquad \arccos w = \arctan(\sqrt{1 - w^2} / w)$$

$$\text{arsinh}\, w = \ln(w + \sqrt{1 + w^2}) \qquad \text{arcosh}\, w = \ln(w + \sqrt{1 - w^2})$$

$$e^z = \sinh z + \cosh z \qquad\qquad \ln w = 2\,\text{artanh}((w - 1)/(w + 1))$$

$$\sqrt{w} = \sqrt{(w + 1/4)^2 - (w - 1/4)^2}$$

The CORDIC algorithm is particularly well suited for a hardware implementation, as long as the computations can be carried out in a fixed-point format. This has already been investigated in AP4. Figure 17 shows a general drawing of the CORDIC data path for hardware implementation.
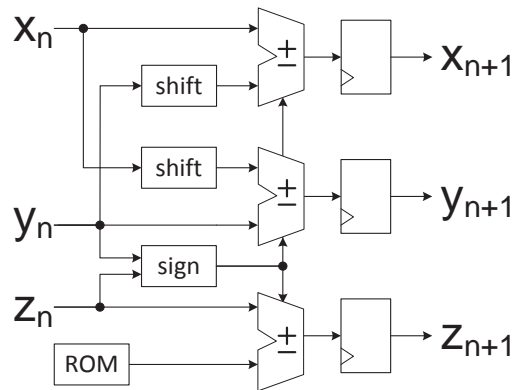
Figure 17: Block diagram for a hardware implementation of the CORDIC module

The blocks labeled *shift* correspond to a binary shift operation, and thus to the term 2^{-i}, the sign block controls the adder and corresponds to the symbol d_i. The ROM contains the partial angle α_i. The CORDIC functions can be used directly to calculate the necessary equations for MWD navigation. Figure 18 shows an example of the H-field computation with the aid of the CORDIC module.
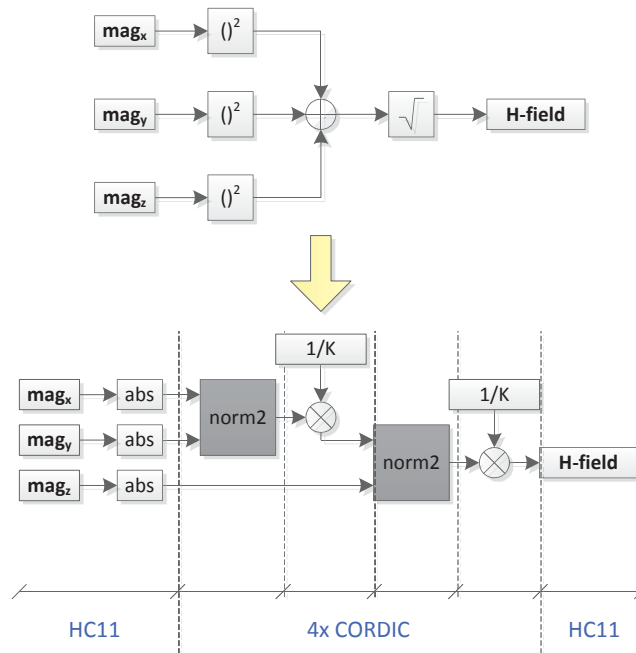
Figure 18: Example for H field computation with the CORDIC module

The norm2 operation corresponds to the normalization operation $x_n \rightarrow K(\sqrt{x_0^2 + y_0^2})$.

By twice application of the norm2 operation and the multiplication $y_n \rightarrow y_0 + x_0 z_0$ with the constant $1/\mathrm{K}$, the H field is calculated from the three magnetic field components.

Table 5 lists the achievable accuracy of the CORDIC module.

function	cycles	worst case error
ATAN2	71	2^{-12}
DIV	71	2^{-15}
MUL	61	2^{-14}
NORM2	70+61	2^{-12}
SQRT	70+61	2^{-12}

Table 5: Required cycles and worst case error for selected CORDIC functions

An internal evaluation of the computation speed showed that a mathematical operation on average requires less than 180 cycles at a 2 MHz clock for execution. This is achievable with the CORDIC module.

The POLY module implements Horner's method

$$f(x) = \big((a_n x + a_{n-1})x + \cdots + a_1\big)x + a_0$$

for computation of polynomials. Computation of polynomials is required in order to compensate the non-linearity of analog components and sensors. The POLY-module contains a combination of multipliers and adders to perform the compensation, without processor assistance. For this purpose, the module reads the sensor value x and the coefficients automatically from dedicated registers and performs the correction polynomial. This way the evaluation of e.g. a third-order compensation polynomial is performed in parallel in three cycles only.

For estimation of the required chip area, the CORDIC module and the POLY-module were synthesized in both the H10 FHG technology (SOI 250 °C) and in the XI10 XFAB technology (SOI 225 °C). The required area and the achievable clock frequency for different word lengths are shown in Figure 19 and 20.
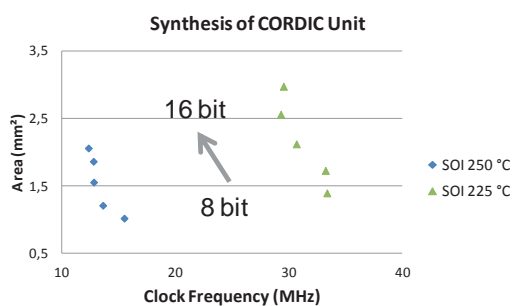
Figure 19: Synthesis results for the CORDIC module for different data path width
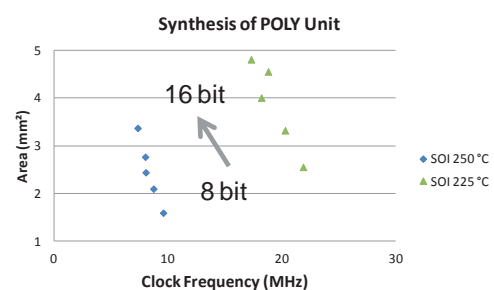
Figure 20: Synthesis results for the POLY module for different data path width

Before a digital ASIC can be fabricated, it is mandatory to verify the whole system. This can be achieved by emulation. In that case the emaulation is carried out in configurable hardware blocks, which are called field programmable gate array (FPGA). The emulation of the designed MWD architecture has been performed on the Altera DE2-Developmentboard shown in Figure 21.
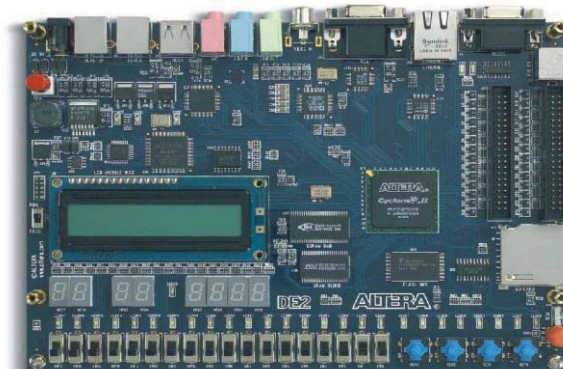
Figure 21: Altera-DE2 development board used for emulation of the design

Figure 22 depicts the mapped emulation platform. The host PC is connected via an RS-232 interface to the FPGA board. On the FPGA the proposed architecture is mapped. Beside this, an ADC module is emulated also. This way synthetic sensor data can be provided to the processor system. Via the host PC interface both the memory of the processor and the ADC module may be read and written, as well as the processor can be stopped and the current state can be queried. This allows emulation of a sensor node, as well as testing the soft- and hardware design.
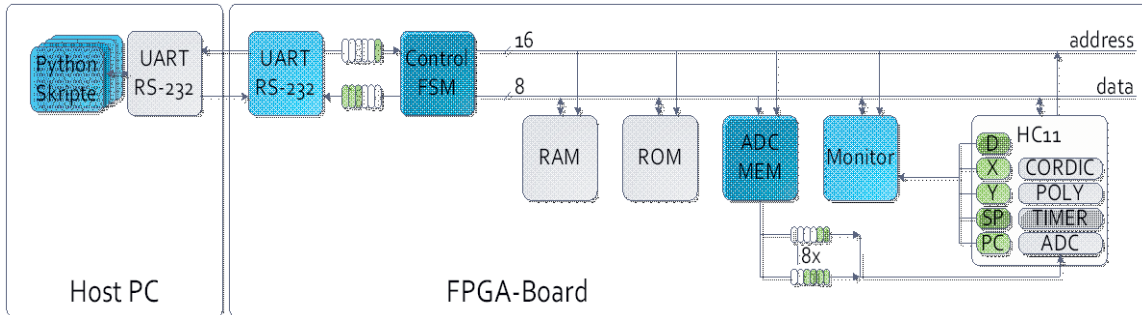
Figure 22: Block diagram of the emulation system

The generation of synthetic data is performed using a sensor simulator created additionally during the course of T1 AP5. This piece of software simulates the drilling operation, which depends on the position of the bore hole on the earth ellipsoid. Then, the rotation of the drill bit can be specified with any number of points along a path, as shown in Figure 23.
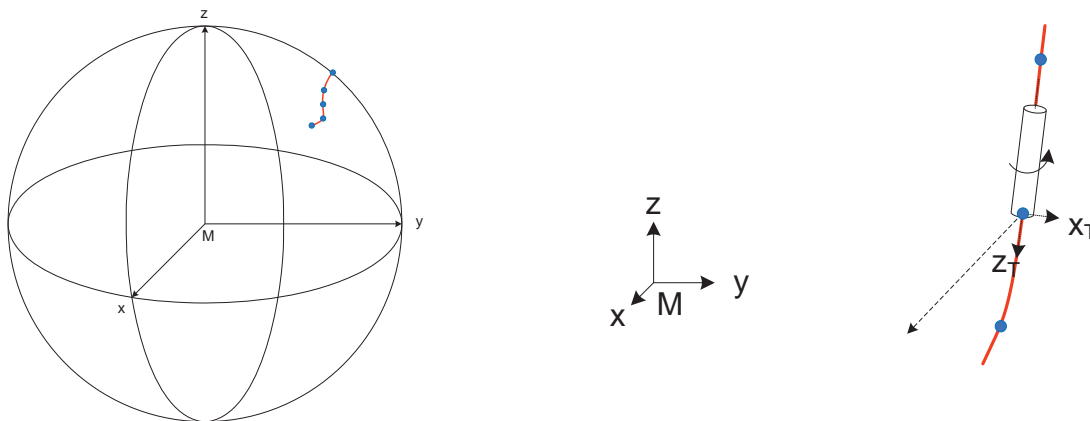
Figure 23: Coordinate systems and drilling path used with the sensor simulator

As a simulation result, the gravitational component, which is directed toward the center of the earth, is projected on three mutually orthogonal tool axes, with the z-axis oriented along the tool's axis. For the simulation of the geomagnetic field, the model of the National Geophysical Data Center [7] is used. Here again the magnetic field component is projected on the three mutually orthogonal sensor axes.

The contribution of AP5 has shown that an ASIC implementation of the MWD functionality for geothermal applications can be realized. The presented architecture concept is based on an 8-bit processor core and additional functional units. In particular, the CORDIC module allows accelerated mathematical calculations more than 100 times faster than corresponding floating point operations in hardware. The total area of the processor logic can be estimated to 12.4 mm² chip area. However, the estimate does not include additional chip area required for memory and the pad ring.

As a overall result of AP4 and AP5, the proposed architecture concept and the presence of the emulation platform are a good basis for implementing a high-temperature ASICs as MWD prototype for geothermal drilling applications.

2.d   Project Plan

Work packages and milestones	2009			2010			2011			2012			2013			2014		
AP1: Design flow for suitable SOI technology	███																	
AP2: Circuit Design Methods for Analog Components				███														
AP3: Verification of analog components							████											
AP4: Evaluation of selected signal processing algorithms	████																	
AP5:Research of detailed architecture concepts							███											

Grey, original plan

Blue, actual or current plan, respectively

For details, see Gantt chart in Appendix.

3   Delineation of the project from other funded projects

Currently there are no other projects at the Institute for Microelectronic Systems concerning geothermal energy or high-performance drilling.

4   Bibliography

4.a   Cited Bibliography

[1] D. Grabowski, M. Olbrich and E. Barke, "Analog circuit simulation using range arithmetics," in *Proceedings of the 2008 Asia and South Pacific Design Automation Conference*, Los Alamitos, 2008.

[2] BSIM Group, *BSIMSOI 4.2 MOSFET MODEL Users' Manual,* 2009.

[3] O. Scharf, M. Olbrich and E. Barke, "Anwendung der affinen Arithmetik auf das BSIMSOI-Modell zur Simulation von Parameterschwankungen," *Analog '11, Entwicklung von Analogschaltung mit CAE-Methoden,* 2011.

[4] R. Nowosielski, T. Zirkelbach and H. Blume, "Evaluation of the RISC-CISC Trade-off for ASIC Implementation in a 250 °C SOI-Technology," in *ICT.OPEN 2012 Conference*, 2012.

[5] J. E. Volder, "The CORDIC Trigonometric Computing Technique," in *Electronic Computers, IRE Transactions on*, 1959.

[6] J. S. Walther, "A Unified Algorithm for Elementary Functions," in *Spring Joint Computer Conference, Proceedings of*, 1971.

[7] National Geophysical Data Center, [Online]. Available: http://www.ngdc.noaa.gov/. [Accessed 2011].

[8] W. L. X. J. e. a. Xuemei Xi, *BSIM3v3.3 MOSFET Model Users Manual,* 2005.

4.b Presentations

- *High Temperature – challenge 250.* **Blume, Holger.** Celle: Gebo Jour Fixe, October 2010. PhD Seminar, High-Temperature Electronics

- *Approximation of Elementary Functions for MWD applications.* **Nowosielski, Rochus.** Celle: Gebo Jour Fixe, October 2010. PhD Seminar, High-Temperature Electronics

- *Simulation of Analog Circuits with Affine Arithmetic.* **Scharf, Oliver.** Celle: Gebo Jour Fixe, October 2010. PhD Seminar, High-Temperature Electronics

4.c Theses

- *Analysis and Implementation of Approximation Methods for Calculation of elementary Mathematical Funcitons.* **Deng, Di.** Master Thesis, August 2010. Institute for Microelectronic Systems, LUH.

- *Analysis and Implementation of Dedicated Mathematical Functional Units for extending a microcontroller architecture.* **Wang, Yuqin.** Master Thesis, October 2010. Institute for Microelectronic Systems, LUH.

4.d Reports

- *Evaluation of the HT-MWD Master Controller.* **Nowosielski, Rochus.** BHI Internal Report, August 2010. Baker Hughes Inc., Celle.

T2: Technique for high-temperature electronics (pressure sintering)

1   Project Overview

Speaker and lead university or research institution

Project Nr.	Title	Subject of research	Project leader, institution, location
T2	Joining technique for high-temperature electronic devices (pressure sintering)	Electrical engineering/Institute of Semiconductor Technology	Waag, Andreas, Prof. Dr. habil, IHT (project leader) Peiner, Erwin, PD Dr. habil., IHT (deputy project leader)

Participating institutes and institutions of the University and external institutions in:

- Institute of Semiconductor Technology (IHT), TU Braunschweig (TU-BS)

- Baker Hughes INTEQ (BHI): Dr. Sascha Schwarze, Dr.-Ing. Thomas Kruspe, Dr. Sebastian Jung, Dr. Rüdiger Hild, Dr. Karsten Moldenhauer, Dipl.-Ing. Christian Schnöing, Dipl.-Ing. Antje Steller, Dipl.-Ing. Gerald Hinrichs und Dr. Sunil Kumar

List of participating scientists and engineers:

Name	Subject area	University institute or non-university institution	Position is financed by gebo funds (indicate with X)
Waag, Andreas, Prof. Dr. habil.	Electrical engineering	IHT, TU-BS	
Peiner, Erwin, PD Dr. habil.	Electrical engineering	IHT, TU-BS	
Kähler, Julian, Dr.-Ing., E13	Electrical engineering	IHT, TU-BS	X, 05/2009 - 03/2013
Stranz, Andrej, Dr.-Ing., E13	Electrical engineering	IHT, TU-BS	X, 03/2014 – 11/2014

2   Research Program

2.1   Summary

A high-temperature (HT) resistant die attach has been developed for electronic devices and sensors to be used for data logging (measurement while drilling: MWD) during deep drilling of wells for enhanced geothermal systems (EGS). Furthermore, a novel HT-resistant micro electro mechanical system (MEMS) sensor has been realized for vibration monitoring of the drill string and the bottom-hole assembly (BHA).

2.2   Relationship of the project to the overall research context and networking with other projects

An important aspect of the entire collaborative project was to optimize the drilling process and the subsequent energy transport through hot rocks. Modern drilling systems are equipped with

803

electronic modules for electric power supply, communication and sensor technologies. Within the frame of the collaborative project "gebo", a future exploitation of EGSs in depths of about 4000-6000 m was considered. Corresponding drilling process are expected to place more heavy demands on MWD components and assembly, which will face over weeks or months downhole temperatures up to 250°C to 300°C as well as vibration and shock loads up to 40 *g* rms and 160 *g*, respectively [Flo12, Wal09]. For a trouble-free operation of electronic devices and sensors underground, a reliable joining technique is required. Meanwhile, the necessity of an appropriate packaging technology for downhole sensors, e. g. autonomous MEMS-based inertial units for MWD, has found recognition [Wan13]. The project T2 has developed a HT-resistant packaging technology for electronics, optoelectronics and sensor systems for MWD and provided it to the project partners. For this reason the joining technique of this project was an important cross-cutting technology. Through the design of a MEMS sensor, the IHT also made an important contribution to the development of non-available bare chips of HT-resistant sensors suitable for vibration monitoring during the drilling process.

2.3   Work packages executed relative to (original) plan and results achieved

WP 1: "Testing and evaluation of the pressure sintering process":

The pressure-sintering technology should be tested and evaluated for die attach of HT ICs and components which are used for MWD. The findings regarding the basic process control should deliver important inputs for the circuit designs of HT electronics (project T1) as well as the projects T5 and T6.

For the pressure sintering process, devices and substrates need oxide-free noble metal closures in order to achieve good adhesion between chip and substrate. Thus, having a temperature-stable metallization system was the basis of all further investigations. Unfortunately, commercial LEDs and photodiodes (PD) used in project T5 were delivered with gold-alloy-contacts, which are not suitable for silver sintering and, furthermore, are not high-temperature resistant. Hence, the joining partners had to be coated prior to the joining process. Within this project package-dependent metallization systems produced by reactive sputtering and electron beam evaporation were tested under long-term temperature loading by measuring the change of sheet resistance over time and on the basis of optical investigation. For the expected operation temperatures of 250 °C and above, a diffusion barrier between the adhesive and the contact layer was necessary to prevent the formation of inter-metallic phases, which led to a reduction of the overall system reliability. Best results were found with titanium (Ti) as undercoating, palladium (Pd) or titanium nitride (TiN) as diffusion barrier and gold (Au) as contact layer. The results of the measurements led to the conclusion that the layer systems Ti/Pd/Au and Ti/TiN/Au can withstand temperatures of 260 °C for at least 40 and 4000 hours, respectively. Consequently, these metallizations are "BHI-suitable" for short-time and long-term evaluation of die-

attaches, respectively. Besides, they were used in WP2 for coating and structuring of Al_2O_3-ceramic-substrates, which are required for the assembly of the optical-pressure sensor in project T5.

The objective of this work package was to demonstrate that the scope of applications of silver sintering could be expanded to the assembly of hybrid circuits within the gebo project. In doing so, silicon test dice of dimensions of optoelectronic devices used in T5 were produced and attached to suitable substrates. Afterwards, some of the samples were long-term annealed at 300 °C. On the basis of shear tests at room temperature (RT), the adhesive strength of the compounds was analyzed. It was shown that the pressure sintering process is generally suitable for the chip-substrate contact, i. e. high bond strengths were achieved on different substrates. In addition, commercial photodiodes (EPC 440-0.9, manufactured by Epigap) provided by project T5 were metalized and bonded on Al_2O_3-ceramic-substrates. The functioning of these devices was tested successfully. However, the test showed that the large 50-tons press, which was used for achieving the necessary contact pressure for die attach, was associated with elaborate handling and poor positioning accuracy of the bare die. As a very promising novel approach we modified a Pick & Place Bonder providing high placement accuracy (work was continued in WP2). Further results were described in detail in a Baker Hughes intermediate test report [Schn10a].

WP 1 was successfully completed. Its results showed that the pressure-sintering process can meet the basic project requirements (high-temperature stable die attach up to 350 °C and above of specific devices used for BHI, T5 and T6). The findings were important inputs for the circuit design of HT-electronics (project T1) and the projects T5 and T6.

WP 2: "Pressure sintering for TU-BS and LUH":

The work package WP2 included the development of a pressure sintering process for HT-electronics and optoelectronics. Agreements were made with BHI and the projects T5, T6 with respect to the delivery of bare dice, substrates and circuit boards to the IHT. The objective of this WP was to provide pressure sintered test samples to BHI. Besides, LEDs and PDs had to be bonded on substrates for project T5.

A new challenge for the pressure sintering technique as mentioned in WP1 was the bonding of small devices with high positioning accuracy. In order to meet the project requirements, a novel joining technique was developed in work package WP2. Here, a modified Flip-Chip Bonder (Fineplacer), a standard tool for micro assembly which provides high placement accuracy (2 µm), is used for precise die-attach. The general process flow is the following (see **Fig. 1**): First, the electronic component (coated with silver paste) is picked up by a special handling device with an intake for vacuum suction, which was designed in stainless steel and manufactured at the IHT. After that, the devices are positioned with the help of an optical microscope

and an *x-y*-positioning table. Simultaneously, the joining partners can be observed via a vision alignment system. Then the chip and the substrate (heated by a heating plate to process temperature) are bonded by a manual bonding force module, which allows a variation of the applied contact force between the joining partners.
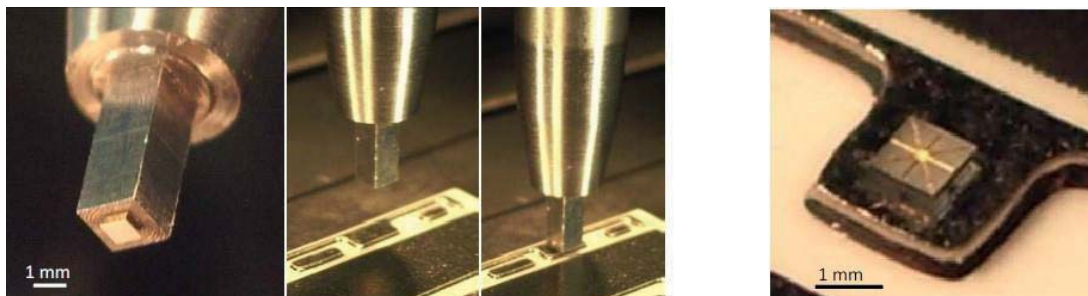

Fig. 1   Process sequence of the Pick & Place Pressure Sintering (P&PPS) technique
a) Handling device and LED (coated with silver powder), b) Positioning and
bonding of the device, c) Bonded LED on DCB substrate (Ni/Au-metallization)

Within this work package extensive investigations were carried out regarding process optimization. It was found that it is very important that the pressure is applied uniformly on the device; otherwise the surface was damaged. Therefore, the Fineplacer setup was improved arriving at an angle between chip and substrate which is now significantly smaller than 1°. Besides, the silver paste used for die attach was optimized. The novel mixture comprises particles of micrometer and nanometer sizes. For safe and easy handling the micro-nano-particle mixture is dissolved in a paste. With this paste it was possible to reduce the necessary process pressure from 40 MPa to 3 MPa while meeting the adhesion criteria of the American military standard for chip-substrate contacts (MIL-STD-883H), which is a requirement of BHI (input from Dipl.-Ing. Christian Schnöing, BHI). Moreover the handling device made of stainless steel was replaced by a much softer one made of high-performance plastic (Polyetheretherketon, PEEK). This way, damage of highly pressure-sensitive devices was avoided (important input for T5 and T6). In addition, a low-temperature process was developed, which ensures compatibility with conventional adhesive die-attach (input from BHI, meeting 12/08/10, Braunschweig). The process temperature was successfully reduced within the WP2 from 250°C to 200°C by adding Ag-nano-particles to the standard paste. The results were verified by shear tests at RT of bonded GaN-LEDs. In comparison to actual competing approaches (e.g. [Lei10]: $T = 275°C$; $t = 20$ min; $p = 0 - 5$MPa,) our novel process offers low pressure at lower temperature and shorter process time.

Thermal FEM-simulations were performed and verified by a thermal imaging camera (Vario-CAM hr Inspect) to analyze the temperature at the joining layer. The camera was kindly provided by Dipl.-Phys. P. Milde (TU-BS, EMG, T4). It was found, that for a setup with a stamp made of stainless steel the temperature of the heating plate must be higher by 10°C than the desired

temperature at the joining layer due to heat losses. We found a reduced temperature loss using a handling device made of PEEK.

With the help of the joining technique developed in WP2 various test samples (see **Fig. 2**) were realized. For example, commercial InGaN LEDs (Cree) were bonded on Direct-Copper-Bonded (DCB)-substrates and annealed for 500 h at 250 °C, which are typical conditions for MWD-applications. In addition, functioning tests of bonded GaP-PD (Epigap) were performed up to 250 °C. The results confirmed that the joining technique has no negative impact on the functionality of the device and can be used to at least 250 °C. Finally, different optoelectronic modules were assembled for T5 (layout: Dr.-Ing. Alexander Leis, LUH, IMR, T5). The substrates were structured and metalized (TI/Pd/Au) at the IHT in a photolithographic Lift-off process. For it, different emulsion masks had to be designed. In agreement with T5, the top-side contacts of the optical pressure sensor were not carried out within the WP2. The pressure sintering technique was also used to realize a sandwich structure for connecting HT-stable fluxgate sensors (project T6). All tasks within WP2 were discussed in detail with the project partners from T4, T5 and T6 at the quarterly meeting of the T-projects and during the monthly jour-fixe events in Celle.

Fig. 2   Realization of specimen for T5 and Baker Hughes:
Optoelectronic module consisting of two PDs and LEDs bonded on Al₂O₃-substrate (left) and bonded BC817/Fairchild and SIGC15T60/Infineon on Al₂O₃-substrate for testing at BHI (right).

In agreement with Baker Hughes, specimens were assembled consisting of transistors (BC817/Fairchild, SIGC15T60/Infineon) and Au- thick-film-substrates. The tests were performed at BHI. The results were discussed in detail with representatives of BHI at project meetings. We found a significant influence of Ar-plasma cleaning on the adhesion, which was further investigated in WP3. For details we refer to the respective Baker Hughes final test report [Schn10b]. Based on the findings of WP1 and the intermediate test report [Schn10a] additional specimens were assembled with a new parameter set. This test series showed very promising shear strengths of the bonded components.

The work package WP 2 was completed successfully and the first milestone M 1 "Pressure sintering for LUH (IMR)/T5 and TU BS (EMG)/T6" was reached within this work package.

<u>WP 3: "Pressure sintering for BHI":</u>

The objective of this WP was to provide a qualified module according to specifications to BHI. For this purpose, ceramic substrates and passive components in metal casings obtained from BHI were investigated. Inputs for the work package are heat dissipation concepts from the projects T3, T4.

Based on the findings from the previous work packages WP1 and WP2, further investigations were planned with Baker Hughes. First, the effect of Ar-plasma cleaning before die attach was analyzed. While Ar-plasma cleaning is a standard process in packaging for MWD, the objective of these investigations was to ensure compatibility with conventional adhesive for die-attach. The effect of plasma cleaning was analyzed by measuring the contact angle of the surface. The results of shear tests at RT indicated a negative influence of the Ar plasma cleaning on the adhesion of the die. However, the effect of the plasma cleaning tended to decrease subsequently. As a result, a settling time of one hour was observed to be necessary to achieve good adhesion when combining plasma cleaning with pressure sintering. The intermediate test report from Baker Hughes showed very promising results regarding shear strength and reduction of surface damages of bonded devices [Schn10c]. As an alternative to the one-hour settling time, which may not be acceptable for high throughput, an additional two-minutes drying step of the sinter paste above the evaporation temperature of the solvents (> 100°C) was successfully tested. We concluded that the plasma-induced high surface energy of the substrate metallization impedes this evaporation process and thus the sintering process.

As mentioned before, one objective of T2 was to provide a qualified multi-chip module (MCM) according to specifications of BHI. In order to achieve this goal, further investigations regarding process optimization of the Pick & Place Pressure Sintering (P&PPS) technique [Käh11a] were carried out. For example, the standard deviation of the shear strength of bonded devices had to be reduced (input from WP2). Besides, it should be made possible to bond large-area dice (e.g. SIGC15T60, Infineon, 4 ×4 mm^2) by reducing necessary process pressure and testing of other materials for the handling tool. Using silicone we found an improvement of the process capability of P&PPS by a factor of two [Käh11b]. The softer material compensates surface irregularities leading to a more uniform pressure application to the chip during P&PPS. This way, the SIGC15T60 could be tightly attached, i. e. the requirements of the US military standard MIL-STD-883H were fulfilled [Käh11c].

Subsequently, stability under long-term annealing and temperature cycling had to be tested with die-attaches based on different silver pastes, which was done at BHI. A disadvantage of sintered Ag as joining layer with respect to stress accommodation is its high Young`s modulus, which was found at low porosity. Sintered Ag of low porosity has a relatively low capability to relieve thermal stress induced by temperature cycling between chip and substrate, which is caused by different coefficients of thermal expansion of both. Therefore, tests were performed

at BHI to investigate the potentially resulting negative consequences for the long-term reliability of die attaches. These tests which are based on the expected environmental conditions during deep drilling comprised initial shear testing, shear testing at 225°C, shear testing after annealing at 250°C for 100 h, and 50-times temperature cycling between -40°C and 200°C [Schn10d]. Before, further optimization of the Ag pastes was done with respect the effect of Ag nanoparticles on the performance of the die-attach (shear strength, electrical and thermal resistivity) [Käh11c]. Since P&PPS requires oxid-free noble metal finish of chip- and substrate metallizations, which are not standard for some dies to be used in the BHA, different metallization systems (Ti/Pd/Au, Ti/Pt/Au, Ti/TiN/Au) were investigated to be deposited additionally on top [Käh11d]. Based on these results in WP 4 MCMs of a BHA were assembled and qualified according specifications from BHI. A further improvement of the thermal conductivity of the sinter layer using diamond powder as additives was investigated by appointment with BHI in WP 4.

As the most important result of this WP the milestone M 2: "Providing first pressure sintered samples according specifications to BHI" was reached in 09/2011. The work package WP 3 was successfully completed.

WP 4: "Investigation of the production capability, transfer":

Based on the results in WP 3, two Pulser-Driver (PD) MCMs of a BHA were assembled using P&PPS. Selected components (20 dies, sizes between 0.38×0.38 mm^2 and 3.9×3.9 mm^2) of two samples of a standard PD of a BHA were attached using P&PPS at 250°C, 10 N/mm^2, and 2 min on a LTCC (low-temperature cofired ceramic) substrate (**Fig. 3**). Before, passive components, μC, etc. were already assembled at BHI using standard adhesive die-attach. Some of the dies lacked a noble metal closure and had thus to be metallized prior to P&PPS according to WP 3. The completely assembled PD MCM was then transferred to BHI for a comprehensive qualification. To simulate downhole conditions, temperature loading at 200°C (continuous, 500 h) and from -20°C to 200°C (cyclic, 100 times) followed by shock loading (750 *g*, 0.5 ms half sine, 6 directions, 25 shocks each direction) was performed with both assembled MCMs [Schn13]. Only few of the large ICs detached from the LTCC during cyclic temperature loading, namely in the early stages of testing. As already stated in WP 3, we found that careful surface treatment to deactivate the metallization surface prior to P&PPS was critical for stable MCM assembly. This interpretation was confirmed by the fact that the sintered die-attaches, which survived the temperature treatment, did not detached after subsequent shock loading. These tests show that also some of the components failed, which were adhesively attached at BHI. Elemental analyses of the surfaces of the detached components did not unambiguously reveal the reason for this effect [Schn12].
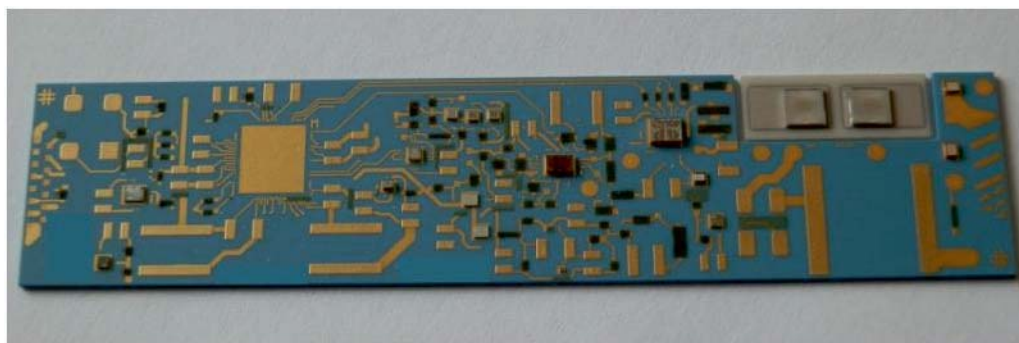
Fig. 3   **PD with diodes, transistors, and ICs attached using P&PPS. Passive components, µC, etc. were mounted using a standard adhesive process prior to P&PPS.**

The second main objective of this WP was the integration of electronic components on a test substrate using pressure sintering in combination with alternative die-attach processes suitable for production such as Flip-Chip (FC). For it, quad comparators (e.g. LM139A, 1×1 mm^2) stud-bumped (Au) at BHI were investigated. FC die-attach means that unhoused devices are directly, i. e. without further electrically connecting wires like gold wire bonds, mounted face-down to a circuit board. FC has the advantage with respect to the conventional back-side die-attach that it is space-saving. The integration density on a hybrid circuit, e.g. on a MCM, is thus considerably higher [Fre01].

The challenges with a P&PPS-FC process were on one hand in the deposition of sinter paste on the bumps for electrical connection. On the other hand very high precision was necessary during the positioning of the chip to the substrate. Au stud bumps were fabricated on the 14 Al contact pads using a wire bonder. A ceramic circuit board, on which the bumped chip had to be attached, was patterned using photolithography followed by a lift-off step at IHT. Subsequently, either the bumps or the pads on the circuit board had to be covered by Ag sinter paste. Both approaches were tested using the transfer method [Pal06]. First we tried to stamp the dried paste from the carrier foil onto the bumps (#1: $p = 13$ N/mm^2; $T = 230$°C, $t = 2$ min). Here we had to make sure, that no excessive paste remains between the bumps leading to a shortcut. Three paste thicknesses on the carrier foil (35 µm, 8 µm, 5 µm) were tested. In the case of the large thickness, which corresponds to the bump height of 30 ± 3 µm, the cohesive force in the layer were too high with respect to the adhesion of the paste to the bumps. Better results were obtained with 8 µm and 5 µm. Shortcuts between the bumps could be avoided. In a second approach we deposited the paste on the ceramic circuit board. At a paste layer thickness of 8 µm we were able to remove the excessive material between the pads entirely. This way, line of 110 µm in width and a distance of 40 µm were covered with Ag paste. With increased paste layer thickness (20 µm) we failed to remove the excessive material between the lines. In this case we had to work over the board under a microscope using micro manipulators and needles. After paste coating we then performed the P&PPS-FC process with the following parameters

(#2: p = 13 N/mm^2; T = 230°C, t = 2 min). A positioning accuracy of few 10 μm was achieved. The electrical function of the completed test samples were successfully tested according to the data sheet of the LM139A.

For a final evaluation of the P&PPS-FC process shear strength measurements were performed at room temperature. We observed a shear force of 2.8 N and 4.5 N for the test samples assembled using the approaches #1 and #2, respectively. Taking into account the small contact areas of the 14 bumps with diameters of 70 μm to 90 μm we calculated a shear strength of 31 N/mm^2 to 52 N/mm^2 (#1) and 50 N/mm^2 to 83 N/mm^2 (#2), which is by far sufficient for downhole applications. In both cases, the weak link was between the Au stud bumps and the Al contact pads of the chips, i. e. the adhesion of the sinter layer to the bumps was higher. In **Fig. 4** both approaches of the novel P&PPS-FC process are shown.
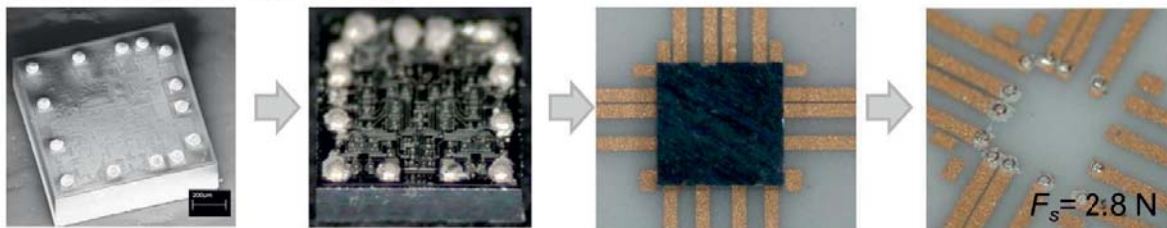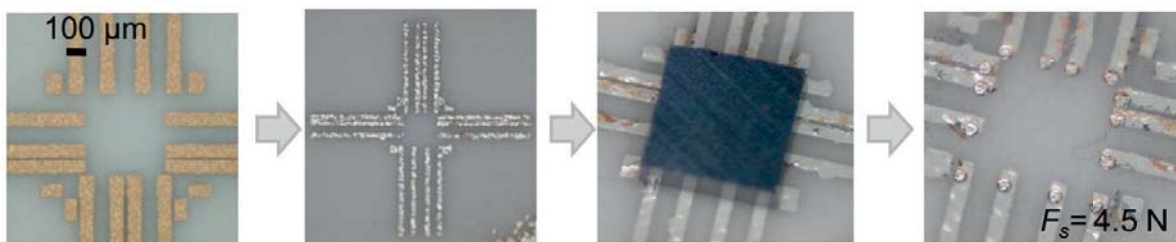

Fig. 4 **P&PPS-FC processes: deposition of paste on bumps (#1, upper row) and on the ceramic circuit board (#2 lower row).**

Another objective was the assembly of 3D-modules (e.g. an optoelectronic chip bonded on a Peltier cooler). Such thermoelectric (TE) coolers are attractive for downhole applications, e. g. spot cooling of single chips of a MCM, since they are compact and do not need moving parts. However, commercially available TE coolers are restricted to ≤ 200°C which is attributed to the interconnects rather than to the active material [Käh13]. Therefore, we employed P&PPS to assemble the TE material, i. e. very brittle bismuth telluride legs to a metal bridge carrier. We did the process at 5.5 N/mm^2 and 250-270°C to ensure that the bismuth telluride pellets were not damaged while yielding a low contact resistivity comparable to lead-free solder. Subsequently, we operated the realized cooler device up to ambient temperatures of nearly 300°C while maintaining a temperature difference of more than 40 K, i.e. the temperature limit of commercial coolers was considerably outperformed. The internal resistance of the TE cooler was stable

within 1.3 % after 850 cycles between 100°C and 250°C. A schematic of the device and a photograph of the cooler operated under normal ambient conditions in shown in **Fig. 5**. Both top-side and bottom-side contact were realized using P&PPS.
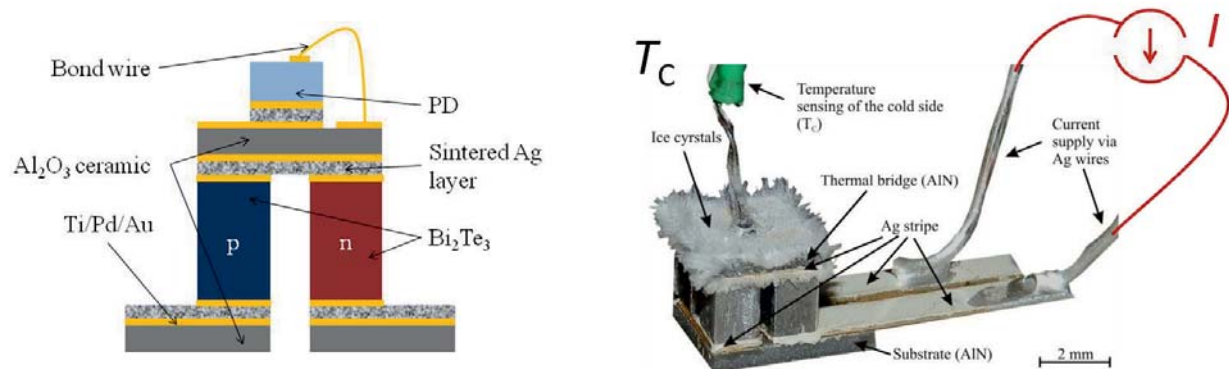

Fig. 5 **Peltier chip cooler fabricated using P&PPS: schematic (left) and photograph of device operated with a current *I* (right).**

Finally, with the help of the P&PPS, vibration sensors, which were developed in WP 6, were bonded on substrates (**Fig. 6**). Here, the tiny spring-mass structure of the MEMS (micro-electro-mechanical system) with a spring thickness of only 6.2 μm has to be protected from loading by the stamp. Therefore, in this case a silicon stamp with a central recess was developed, by which the pressure is applied only to the frame of the spring-mass element. Furthermore, the sintering pressure was reduced to 4 N/mm^2. Nevertheless, the process led to very reproducible adhesion, i. e. a shear strength of 13.0 ± 1.4 N/mm^2 at room temperature, which did not deteriorate at 250°C (12.4 ± 1.9 N/mm^2).
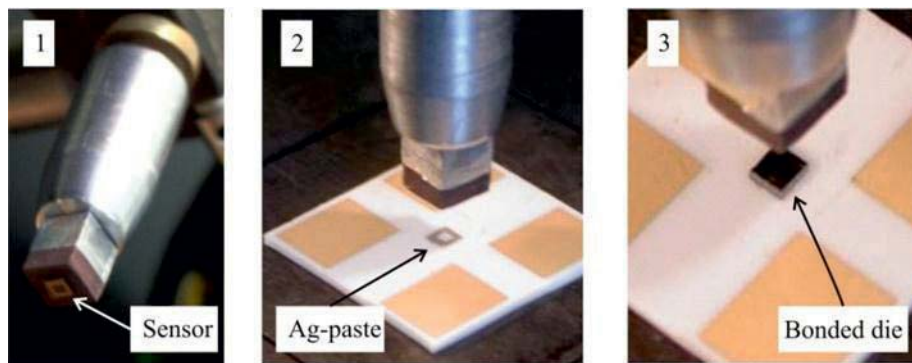
Fig. 6 **MEMS vibration sensor picked using a stamp with a recess for the delicate spring-mass element (1), a ceramic circuit board with Ag paste transferred to it from a carrier foil (2) and board after P&PPS of the MEMS die (3).**

As an alternative to the costly Ag, P&PPS using copper was investigated. Successful die-attach was observed at p = 40 N/mm^2, T = 350°C, and t = 2 min under normal ambient conditions. A diffusion barrier was necessary and oxide had to be removed by pre-annealing of the paste under oxygen-free conditions. With layer thickness of 100 μm we obtained a porosity of 39 %,

an electrical conductivity of 12.9 MS/m, a thermal conductivity of 94 W/m/K, and a shear strength of 9 N/mm^2.

In **Tab. 1** the die types and sizes, the sintering process parameters (temperature, pressure, time), and the recommended stamps are given. The sizes of the investigated dies vary from 0.6 mm^2 to 15 mm^2, the temperatures from 200°C to 270°C, and the pressures from 4 N/mm^2 to 20 N/mm^2. For the small robust chips (LEDs, PDs) a stainless steel stamp was selected which has a narrow suction port (200 µm in diameter) to pick the tiny chips. For the silicon dies the stainless steel stamp caused damage on the surface. Therefore, in this case we developed and used a softer PEEK stamp. For the larger IC dies, misalignment of pressure application was a more severe issue, which we were able to alleviate using a silicone stamp. Here, the best reproducibility was found with silicone at 250°C and 3 N/mm^2.

Table 1 Dies selected for module fabrication and process parameters of P&PPS.

Die	Area (mm^2)	Temperature (°C)	Pressure (N/mm^2)	Time (min)	Stamp
Fairchild; BC817	0.79 × 0.79	200 - 250	10 - 20	2	PEEK
Nat. Semicond.; LM139A	1.0 × 1.0	250	15	2	PEEK
Infineon; SIGC15T60	3.9 × 3.9	250	5	2	silicone
Cree; InGaN-LED	1.0 × 1.0	250	15 - 20	2	steel
Epigap; GaP-PD	0.9 × 0.9	250	15 - 20	2	steel
This group; MEMS vibration sensor	1.22 × 1.22	250	4	2	silicone
Peltron; *p*-,*n*-TE-legs	1.5 × 1.5	250 - 270	5.5	3.5	silicone

The milestone M 3: "Pressure sintering of flip-chip HT-ICs" was successfully reached in 12/2012. The work package WP 4 was successfully completed.

WP 5: "Evaluation, testing, integration of HT-vibration sensors":

Within this work package a concept for a HT-resistant MEMS vibration sensor based on silicon, SOI (silicon on insulator) and/or DLC (Diamond-like carbon) for MWD was developed. The objective was the fabrication and delivery of a specified sample to Baker Hughes.

First, for the characterization of piezoresistive Wheatstone bridges integrated into the vibration sensor for MWD a measuring setup was designed and fabricated. With it, specimens were tested under constant temperature and vibration loads (up to 250 °C and 30 *g*, respectively). Moreover, setup allowed temperature cycling tests. Before MEMS testing, the behavior of different designs of piezoresistive bridges made of *n*-silicon with *p*-doped resistors were analyzed. The

tests confirmed that diffused silicon resistors are not suitable for MWD due to a leakage-induced drop of the bridge voltage at temperatures above 125 °C. In order to expand the temperature range of piezoresistive sensors, then resistors were fabricated by doping into the top layer of *n*-Silicon-On-Insulator (*n*-SOI) material. The aim was to insulate the thin silicon well from the bulk substrate material through an oxide layer. In doing so, the temperature range could be increased up to 200 °C which not yet fulfilled the requirement. In order to expand the scope of piezoresistive sensors further, a novel approach was necessary (**Fig. 7**). Here strain gauges, resistors and interconnects were realized in the device layer of a *p*-SOI wafer and separated from each other by etching down to the oxide layer. This way, full insulation and thus leakage-current-free operation of piezoresistive bridges were achieved. The use of highest-doped resistor material was possible and with it very small temperature coefficients were achieved for the resistors which were connected to a full Wheatstone-bridge. Long-term annealing tests showed that the bridges can be used for MWD applications at temperatures of at least 250 °C. This concept is very attractive as indicated by the intense research activities of several groups working on piezoresistive SOI sensors. However so far, operation of sensor at high temperatures was not demonstrated [Kuo09] and efforts are focused on the development of pressure sensors [Zha10].
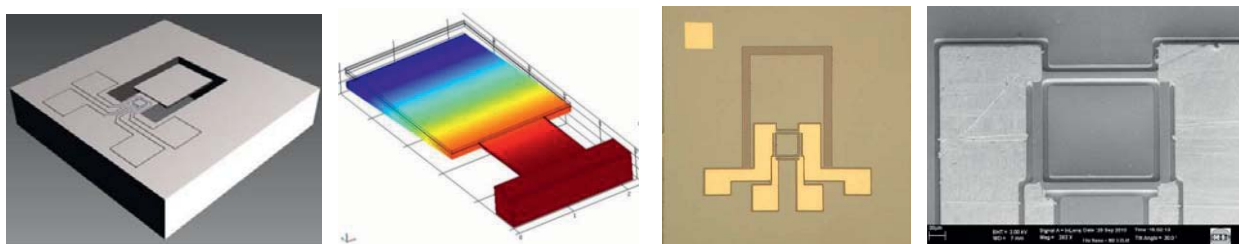

Fig. 7   **Development of high-temperature resistant Wheatstone bridges: Vibration sensor layout and modelling using AutoCad (design) and COMSOL (surface stress due to load), respectively (left and middle left) and top view of *p*-SOI piezoresistive Wheatstone bridge using optical microscopy and SEM picture (middle right and right).**

As a the main result in WP 5, the development and characterization of HT-stable piezoresistive bridges made of *p*-SOI of low temperature coefficient, has been completed successfully. Furthermore, the parameters for a total production of HT-vibration sensors with integrated Wheatstone bridges were determined as an input data for the work package WP 6. The progress of the projects was presented on a meeting with BHI and a quarterly meeting of the T-projects in Garbsen. A US patent application on the novel approach of combining silver sintering and sensor technology for MWD applications was submitted [Käh12a].

The work package WP5 was successfully completed.

<u>WP 6: "Modification of HT-vibration sensors according to project specific requirements":</u>

The concept for the vibration sensor, which was developed in WP 5, was modified according to project specific requirements (bandwidth, resonance frequency...) and further improved. A challenge was, for example, the inductive-coupled plasma (ICP) deep etching of silicon-on-insulator (SOI) material, which was needed for the realization of a spring-mass resonator (Input from WP 5). Another input from WP 5 was, that the offset-voltage of the Wheatstone bridges had to be decreased to enable high-resolution noise measurements. In order to improve the accuracy of implemented geometries, the sensor fabrication process was modified. The challenging objective was to use chromium masks for the photolithography instead of formerly employed emulsion masks. Important inputs from project W7 were synthetic life relevant load spectra and thus a realistic description of the vibration while drilling.

Piezoresistive MEMS vibration sensors based on SOI wafers benefit from an insulation of the strain gauge from the substrate by the oxide layer, which enabled both very low offset and temperature dependence of offset as described in WP 5. To meet the project specific requirements by BHI we then used so-called double-layer (DL) SOI instead of standard SOI. Here, the spring constant and thus the resonance frequency were accurately defined by additional function and sacrificial layers. We realized a delicate spring-mass element with a defined spring thickness of 6.2 µm on a chip size of only 1.5 × 1.5 mm^2. As described in WP 4 the tiny spring-mass element had to be protected during P&PPS. For this purpose a silicone stamp with a center recess was used and the sintering pressure was reduced to 4 N/mm^2. A realized sample of this prototype is shown in **Fig. 8**.
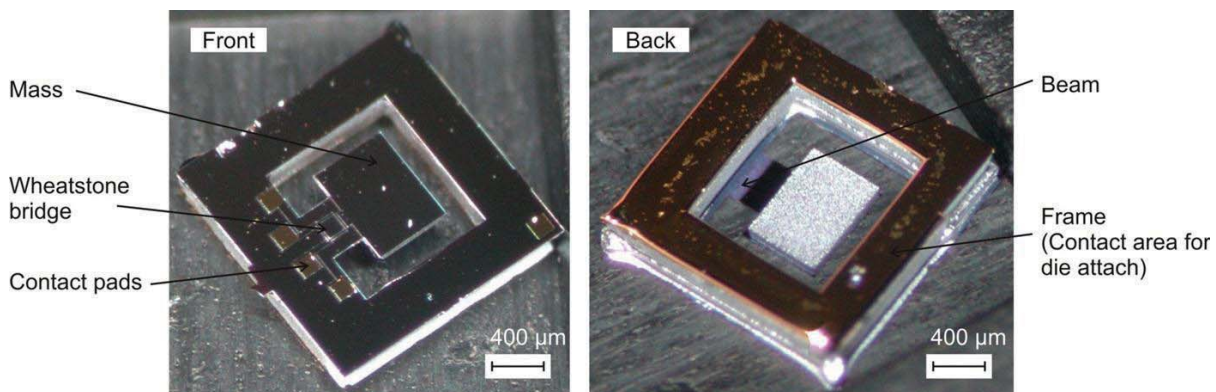
Fig. 8   DL-SOI piezoresistive MEMS vibration sensor: top view (left) and backside view (right).

Completed sensors were characterized in a range of temperatures showing an offset drift of less than 1 % after 400 temperature cycles between 110 °C and 250 °C and an offset temperature coefficient of *TCO* = 16 µV/V/K. On the temperature-controlled vibration table the sensitivity was measured within ± 30 *g* revealing values of 2 µV/V/*g* and 3 µV/V/*g* at room temperature and 250°C, respectively (**Fig. 9**). Very low drift was found for the sensor signal at ± 10 *g* after tem-

perature cycling over a total time of 75 h. Resolution amounted to 50 mg in a bandwidth of 5 kHz.

Fig. 9 **Development of high-temperature resistant Wheatstone bridges:**
Vibration sensor layout and modelling using AutoCad (design) and COMSOL (surface stress due to load), respectively (left and middle left) and top view of p-SOI piezoresistive Wheatstone bridge using optical microscopy and SEM picture (middle right and right).
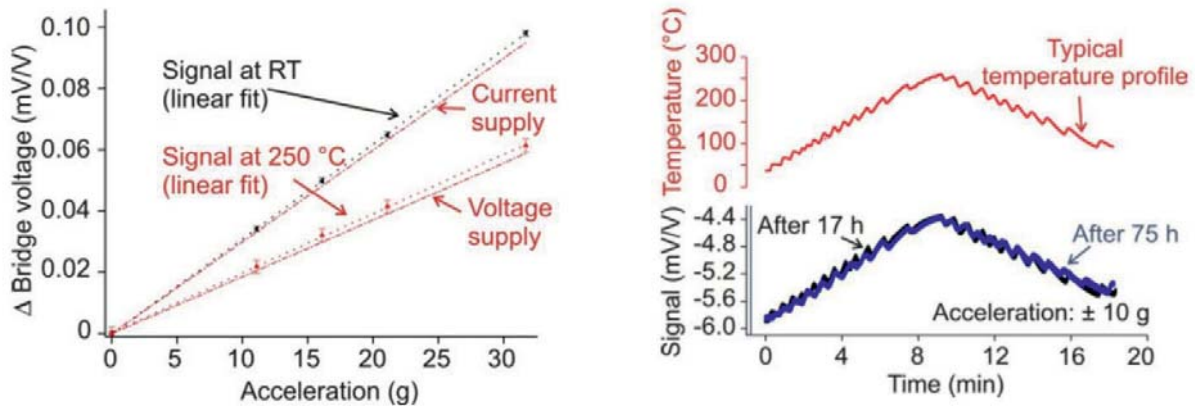
Sensor performance data were collected in **Table 2** in comparison with the specifications required by BHI. We find that almost all requirements were fulfilled. Range and Overloading capability were not yet fully checked due to the limitations of the temperature-controlled shaker setup developed at IHT. Taking the beneficial fracture properties of micromachined silicon into account we can expect that these features are provided by the realized MEMS device.

Table 2 Required and measured specifications of MEMS vibration sensor.

Parameter	required	measured
Shear strength	> 6.1 N/mm^2	13.0 $\pm$ 1.4 N/mm^2 (RT) 12.4 $\pm$ 1.9 N/mm^2 (250°C)
Range	$\pm$ 50 g	$\pm$ 30 g
Overload limit	> 750 g	-
Spectral noise density	< 1 mg/√Hz	0.65 mg/√Hz (RT … 250 °C)*
Bandwidth	0 … 2 kHz	0 … 1.6 kHz

Future work will concentrate on the integration of two further axes of vibration sensing on one chip to provide full 3D functionality. To save chip area, the electronics for signal processing will have to be integrated monolithically as well. A HT-stable CMOS technology (cf. T1) will be necessary in this case, e. g. based on thin-film SOI. First modelling work showed that three spring-mass elements, one out-of-plane sensor as above and two in-plane sensors rotated by 90° to

each other might be integrated on a chip of 7.5×5 mm^2. As the next step this analytical study has to supported by finite element modelling.

The work package WP 6 was successfully completed.

2.4 Project Plan

Work packages and milestones	2009	2010	2011	2012	2013	2014
WP1: "Testing and evaluation of the pressure sintering process"						
WP2: "Pressure sintering for TU-BS and LUH"						
WP3: "Pressure sintering for BHI"						
WP4: "Investigation of the production capability, transfer"						
WP 5: "Evaluation, testing, integration of HT-vibration sensors"						
WP 6: "Modification of HT-vibration sensors according to project specific requirements"						

M1 ▲   M2 ▲   M3 ▲

M1: "Pressure sintering for LUH (IMR)/T5 and TU BS (EMG)/T6"

M2: "Providing first pressure sintered samples according specifications to BHI"

M3: "Pressure sintering of flip-chip HT-ICs"

Grey, original plan

Blue, actual plan

For details, see Gantt chart in the Appendix.

Research assistant Dr.-Ing. Julian Kähler started with his work not before May 2009. That was the main reason why the work packages WP 1 and WP 5 did not begin as scheduled, i.e. not until 05/2009 and consequently were completed only on 01/2010 and 11/2010, respectively. Furthermore, the tasks within WP 2 arose to be more complex than initially expected. As described above under paragraph WP 2, a novel joining technique had to be developed in order to meet the requirements for T5, T6 and BHI communicated by the project partners in the course of the work. In particular, the structuring of substrates for T5 appeared to be more time-consuming than foreseen. On 11/2010, WP 2 and the corresponding first milestone M1 were completed. After he had successfully finished his PhD thesis, Dr.-Ing. Kähler retired from gebo in March 2013. From March 2014 to November 2014, Dr.-Ing. Andrej Stranz was in charge of the project.

There has been a good fit between actual costs and the financing plan. At the end the funds were completely consumed.

817

3 Delineation of the project from other funded projects

At the Institute of Semiconductor Technology were no projects ongoing simultaneously with gebo or funded that are associated with geothermal and/or deep drilling. Within the research project "silicon-based thermoelectric nano-systems" (DFG, SiNanoTherm, PE 885/2-1, 06/2009 – 08/2012) silicon nanowires were investigated as a potential material for thermoelectrics. Pressure sintering was used to fabricate thermoelectric power generator (TEG) modules. In the DFG project "Direkte Abwärmeverstromung in thermoelektrischen Energiesystemen" (WA860/13-1) together with Prof. Beck, TU Clausthal pressure sintering was used for BiTe-based TEGs. In both cases, only TEGs were investigated which were not relevant for down applications. Vice versa, thermoelectric coolers (TECs), which were investigated in T2 of gebo for downhole chip cooling, were not addressed in the mentioned DFG projects. Both devices are different in size (two TE couples vs. ten thermocouples or nanowires) and construction (silver vs. copper interconnects), i. e. the assembly using pressure sintering required completely different parameters that had to be developed for each project separately.

4 References (State of the art)

[Flo12]   F. R. Florence and J. Burks, "New Surface and Down-Hole Sensors Needed for Oil and Gas Drilling", Proc. IEEE I2MTC (Graz, Austria, 2012), pp. 670–675.

[Fre01]   Frear, D. R., Jang, J. W., Lin, J. K., & Zhang, C.," Pb-Free solders for Flip-Chip interconnects", J. Minerals, Metals and Mat. Soc. **53** (2001) 28-33.

[Käh11a] J. Kähler, T. Kruspe, S. Jung, G. Palm, A. Stranz, A. Waag, E. Peiner, "Method and Apparatus for Joining Members for Downhole and High Temperature Applications", US 2012/0292009 A1; WO 2012/161987 A1.

[Käh11b] J. Kähler, N. Heuck, A. Stranz, A. Waag, and E. Peiner, "Pick-and-Place Silver Sintering Die Attach of Small-Area Chips", IEEE Trans. Components, Packaging and Manufacturing Technol. **2** (2012) 199-207.

[Käh11c] J. Kähler, N. Heuck, G. Palm, A. Stranz, A. Waag, E. Peiner, "Low-Pressure Sintering of Silver Micro- and Nanoparticles for a High Temperature Stable Pick & Place Die Attach", Proc. EMPC-2011, Brighton, UK, 12-15 Sept. 2011, pp. 1 – 7.

[Käh11d] J. Kähler, A. Stranz, L. Doering, S. Merzsch, N. Heuck, A. Waag, E. Peiner, "Fabrication, Packaging, and Characterization of p-SOI Wheatstone Bridges for Harsh Environments", Microsyst. Technol. **18** (2012) 869-878.

[Käh13]   J. Kähler, A. Stranz, A. Waag, E. Peiner, "Thermoelectric Coolers with Silver-Sintered Interconnects", J. Electron. Mater. **43** (2014) 2397-2404.

[Kuo09]   Kuo, H.-I. et al., "Smart-Cut™ Piezoresistive Strain Sensors for High Temperature Applications", Proc. IEEE Sensors Conf. Christchurch, New Zealand, 25.-28. Oct. 2009.

[Lei10]   Lei, T. G., "Low-Temperature Sintering of Nanoscale Silver Paste for Attaching Large-Area (>100mm2) Chips", IEEE Transactions on components and packaging technology, vol. 33, no. 1, (2010).

[Pal06]   Palm, G.,"Verfahren zur Befestigung von elektronischen Bauelementen auf einem Substrat", German Patent No. DE102004056702B3 02.03.2006.

[Schn10a] C. Schnöing, "Analysis and test with Ag sintered components", (Intermediate Internal Report, BHI, 27th August 2010).

[Schn10b] C. Schnöing, "Analysis and test with Ag sintered components", (Final Internal Report, BHI, 12th October 2010).

[Schn10c] C. Schnöing, "Test with Ag sintered components (2nd generation)", (Intermediate Internal Report, BHI, 2nd December 2010).

[Schn11] C. Schnöing, "Test with Ag sintered components (2nd generation)", (Final Internal Report, BHI, 10th January 2011).

[Schn12] C. Schnöing, "Failed Adhesive Joints at Sinter-Demo: SEM & EDX Analysis of Samples Sintered at University of Braunschweig", (Internal Report, BHI, 29th August 2012).

[Schn13] C. Schnöing, "Ag Sintering Demonstrator: Results of Manufacturing and Test", (Internal Report, BHI, 24th January 2013).

[Wal09] E. Wall, "Geothermal Technologies Program: Multi-Year Research, Development and Demonstration Plan: 2009–2015 with program activities to 2025", US Department of Energy, 2009.

[Wan13] Zhenhua Wang, Michael Poscente, Dobromir Filip, Marian Dimanchev, Martin P. Mintchev, "Rotary In-Drilling Alignment using an Autonomous MEMS-Based Inertial Measurement Unit for Measurement-While-Drilling Processes", IEEE Instrumentation & Measurement Magazine, December 2013, 26-34

[Zha10] Zhao, Y. et al., "An ultra-high pressure sensor based on SOI piezoresistive material", Journal of Mechanical Science and Technology, vol. 24, no. 8, p.1655-1660, (2010).

5 Journals, patent applications, conference proceedings, student reports, and presentations of project T2

5.1 Journals

[1] G. Palm, J. Kähler, A. Stranz, R. Neumann, N. Heuck, A. Bakin, E. Peiner, A. Waag, "Mikro-Nano-Integration unter Druck – Drucksintern als Lotersatz", PLUS **6/2010** 1376-1382.

[2] J. Kähler, N. Heuck, A. Stranz, A. Waag, and E. Peiner, "Pick-and-Place Silver Sintering Die Attach of Small-Area Chips", IEEE Trans. Components, Packaging and Manufacturing Technol. **2** (2012) 199-207, DOI: 10.1109/TCPMT.2011.2170571.

[3] J. Kähler, A. Stranz, A. Waag, and E. Peiner, "Packaging of MEMS and MOEMS for Harsh Environments", SPIE J. Micro/Nanolith. MEMS MOEMS **11** (2012) 021202, DOI:10.1117/1.JMM.11.2.021202.

[4] J. Kähler, A. Stranz, L. Doering, S. Merzsch, N. Heuck, A. Waag, E. Peiner, "Fabrication, Packaging, and Characterization of p-SOI Wheatstone Bridges for Harsh Environments", Microsyst. Technol. **18** (2012) 869 878, DOI: 10.1007/s00542-011-1396-6.

[5] J. Kähler, N. Heuck, A. Wagner, S. Stranz, E. Peiner, and A. Waag, "Sintering of Copper Particles for Die Attach", IEEE Trans. Components, Packaging and Manufacturing Technol. **2** (2012) 1587-1591, doi: 10.1109/TCPMT.2012.2201940.

[6] J. Kähler, A. Stranz, A. Waag, E. Peiner, "Thermoelectric Coolers with Silver-Sintered Interconnects", J. Electron. Mater. **43** (2014) 2397-2404; DOI: 10.1007/s11664-014-3078-5.

[7]   J. Kähler, A. Stranz, A. Waag, E. Peiner, "Pressure-Assisted Sintering Die-Attach for High-Temperature Electronics", Oil Gas Europ. Mag. (2015), submitted.

5.2 Patent applications

[1]   J. Kähler, T. Kruspe, S. Jung, G. Palm, A. Stranz, A. Waag, E. Peiner, "Method and Apparatus for Joining Members for Downhole and High Temperature Applications", US 2012/0292009 A1; WO 2012/161987 A1.

[2]   J. Kähler, T. Kruspe, S. Jung, A. Stranz, A. Waag, E. Peiner, "Thermoelectric devices using sintered bonding", US 2012/0291454 A1; WO 2012/116107 A1.

[3]   J. Kähler, E. Peiner, A. Stranz, A. Waag, "High temperature piezoresistive strain gauges made of Silicon-On-Insulator", US 2013/0068008 A1; WO 2012/141843 A3.

5.3 Conference proceedings

[1]   J. Kähler, A. Stranz, N. Heuck, G. Palm, A. Waag, E. Peiner, "Die-Attach for High-Temperature Applications using Fineplacer- Pressure- Sintering (FPS)", Proc. ESTC2010, 13.-16. Sept. Berlin, 2010, pp. 1-5; DOI: 10.1109/ESTC.2010.5642808.

[2]   J. Kähler, L. Döring, S.. Merzsch, A. Stranz, A. Waag, E. Peiner, "Design and Fabrication of Piezoresistive p-SOI Wheatstone Bridges for High-Temperature Applications", Proc. SPIE 8066, 806603 (2011); doi:10.1117/12.886855.

[3]   J. Kähler, N. Heuck, G. Palm, A. Stranz, A. Waag, E. Peiner, "Low-Pressure Sintering of Silver Micro- and Nanoparticles for a High Temperature Stable Pick & Place Die Attach", Proc. EMPC-2011, Brighton, UK, 12-15 Sept. 2011, pp. 1 - 7.

[4]   J. Kähler, A. Stranz, A. Waag, E. Peiner, S. Jung, T. Kruspe, "Sinter-Attach of Peltier Dice for Cooling of Deep-Drilling Electronics", Proc. IEEE Intern. Instrum. Meas. Technol. Conf. (I2MTC), May 13-16, 2012, Graz, pp. 658 – 663; DOI: 10.1109/I2MTC.2012.6229481.

[5]   J. Kähler, A. Stranz, E. Peiner, A. Waag, "Sinter-Attach of High-Temperature Sensors for Deep-Drilling Monitoring", Proc. ICEPT-HDP 2012, August 13-16, 2012, Guilin, China, pp. 1594 - 1599; DOI: 10.1109/ICEPT-HDP.2012.6474912.

[6]   J. Kähler, A. Stranz, A. Waag, E. Peiner, "Thermoelectric Coolers with Silver-Sintered Interconnects", 11th Europ. Conf. Thermoelectrics (ECT 2013), 18-20 November 2013, ESA/ESTEC, Noordwijk, The Netherlands.

5.4 Student reports

[1]   Julian Kähler, "Entwicklung eines Sinterverfahrens zur Chipmontage von Bauelementen und Sensoren für Hochtemperatur-Elektronik", PhD Thesis, Braunschweig, 2012 (Dr.-Hut, Munich, Germany, 2012).

[2]   Jörg Kludt, "Platziertes Drucksintern für den Aufbau hochtemperaturfester Hybridschaltungen", Diploma Thesis, IHT, October 2010. (Input for WP2/WP3)

[3]   Likang Zhou, "Hochtemperatur-Charakterisierung von Vibrationssensoren unter Verwendung eines neuerstellten Messplatzes", Diploma Thesis, IHT, September 2010. (Input for WP5)

[4]   Tillmann Ludwig, "Charakterisierung und Fertigung hochtemperaturfester, piezoresistiver Wheatstone-Messbrücken aus SOI", Student Research Project, IHT, February 2011. (Input for WP6)

[5] Lars Holzberger, "Optimierung und Erprobung hochtemperaturfester piezoresistiver Vibrationssensoren", Student Research Project, IHT, September 2011. (Input for WP6)

[6] Felix Grosser, "Untersuchung und Bewertung der Eigenschaften druckgesinterter Verbindungsschichten", Bachelor Thesis, IHT, September 2011. (Input for WP5)

[7] Jiang Li, „Evaluierung des Sinterverfahrens zum Aufbau von Bi2Te3-basierten Peltier-Modulen", Master Thesis, IHT, May 2012. (Input for WP5)

[8] Melanie Nothdurft, „Aufbau und Charakterisierung von Peltier-Modulen für Hochtemperatur-Anwendungen", Student Research Project, IOT (Inst. f. Oberfächentechnik, TU-BS), January 2013. (Input for WP5)

5.5 Presentations

[1] J. Kähler, A. Waag, E. Peiner, "Sensors for data logging during deep drilling", SPIE Newsroom (2011), doi: 10.1117/2.1201105.003695.

[2] E. Peiner, "Die Attach using Pressure-Assisted Sintering for High-Temperature Applications", Presentation during the opening ceremony of the Elsold GmbH & Co. KG at their new premises in Ilsenburg, Germany, 27. Juni 2013;
http://www.elsold.de/fileadmin/englisch/Presse_Downloads/VortragPeiner_ChipAssembling_130627.pdf

[3] J. Kähler, A. Stranz, A. Waag, E. Peiner, "Pressure-Assisted Sintering Die-Attach for High-Temperature Electronics", International Conference for Advanced Drilling Technology, 15 - 16 September 2014, Congress Union Celle (Celle Drilling 2014).

Abschlussbericht

T3: Technik für Hochtemperatur-Elektronik (Substrate, Entwärmung)

Inhalt

1 Ziel des Teilprojekts

In diesem Teilprojekt wurde ein aktiv gekühltes Platinensystem entwickelt, das die Wärmeabfuhr für elektronische Komponenten ermöglicht.

Die Elektronik wird in der Bohrgarnitur eingesetzt und ist dort Temperaturen bis zu 250°C ausgesetzt. Ziel war es, die Elektronik unter einer Temperatur von maximal 170°C zu halten. Des Weiteren sind geringere Temperaturen wünschenswert.

Schwerpunkt des Teilprojekts T3 war die Entwicklung einer aktiv gekühlten Elektronik. Zusätzlich ist es jedoch nötig, die Elektronik effektiv und platzsparend gegen die Umgebung zu isolieren. Der zur Verfügung stehende Bauraum ist durch die Bauform der Bohrgarnitur begrenzt. Zur Isolation wurden verschiedene Möglichkeiten untersucht und prototypisch aufgebaut.

Der benötigte Wärmetauscher war nicht Gegenstand dieses Teilprojekts.

2 Stand der Technik

Die bisher verwendete Elektronik ist ca. 25 mm breit und bis zu 300 mm lang. Die Platinen sind beidseitig bestückt und vergossen. Die Wärmeabfuhr der Elektronik geschieht derzeit über passive Wärmeleitung durch die Vergussmasse und Ableitung an die Umgebung. Die Elektronik wird in gefrästen Taschen auf der Außenseite der Bohrgarnitur verbaut und ist gegen Druck und Feuchtigkeit geschützt. Die derzeit verwendete Elektronik hält Umgebungstemperaturen in der Größenordnung um 150°C stand. Bei höheren Umgebungstemperaturen ist eine passive Wärmeabgabe an die Umgebung nicht mehr möglich.

Bei einer zweiten Variante wird Elektronik in einer vakuumisolierten Thermosflasche eingeschlossen. Hier ist ein längerer Einsatz aufgrund der inneren Aufheizung nicht möglich.

Eine Zufuhr von Kühlmittel von der Erdoberfläche ist nicht möglich, daher muss eine aktive Kühlung innerhalb der Bohrgarnitur erfolgen. Die dazu nötige Energie wird voraussichtlich dem Strom der Spülflüssigkeit entnommen und sollte möglichst gering sein. Um die Elektronik aktiv zu kühlen, ist eine Wärmesenke notwendig. Diese wird derzeit entwickelt und ist nicht Teil des Teilprojektes T3.

3 Zusammenstellung möglicher Methoden

Stand der Technik ist die Kühlung einzelner Bauelemente mit verschiedenen Methoden. In [Sch99] wurden gängige Methoden verglichen und geben eine Orientierung, welche Kühlleistung mit konventionellen Methoden erreichbar ist:

Bezeichnung	Thermischer Widerstand [K/W]	Kühlfläche [cm²]	Flächenbezogener thermischer Widerstand [K cm²/W]
Kühlkörper ICs	46	1,2	55,2
CPU Kühler ohne Lüfter	9,5	14,4	136,8
CPU Kühler mit Lüfter	2,3	14,4	33,1
Peltier-Element mit Kühlkörper	1,2	14	16,8
Heatpipe mit Kühlblechen	0,4	14	5,6
Mikrokühler nach Schiefelbein1999	0,23	0,18	0,04

Für die verwendeten Elektronikplatinen galt es, eine Methode zu finden, die nicht nur einzelne Bauelemente kühlt, sondern die Platine als Ganzes.

Als Alternativen zur bisherigen passiven Entwärmung wurden folgende Konzepte betrachtet:

- Kühlung der Elektronikplatine mittels in der Platine befindlicher Kühlkanäle
- Direkte Umspülung der Elektronik mit Kühlmittel
- Kühlung der Vergussmasse mittels Kühlmittel
- Flächige Kühlung mittels Peltier-Elemente

3.1 Kühlung der Platine mittels eingelassener Kanäle und Kühlmittel

3.1.1. Funktionsweise

Innerhalb der Platine werden Kühlkanäle eingelassen, die durch eine Flüssigkeit oder ein Gas durchströmt werden können (siehe Abbildung 1). Die Firma Ilfa verfügt bereits über entsprechende Fertigungsverfahren und einen Prototypen. Eine systematische Untersuchung der Eigenschaften und Einflussfaktoren hatte bislang nicht stattgefunden. Faktoren wie Form und Fläche der Kühlkanäle, das verwendete Kühlmittel, Anzahl der Wärmevias etc. mussten im Rahmen des Gebo-Projekts untersucht werden.
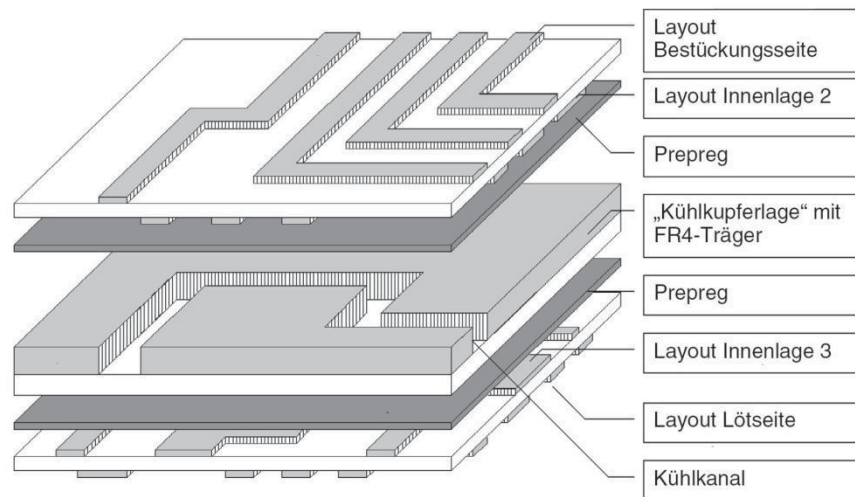
Abbildung 1: Ilfa Platinenlayout [ILFA03]

Bisher existierten nur prototypische Erfahrungen des Herstellers. So wurde nachgewiesen, dass ein Leistungstransistor mit einer Leistung von 25 W auf 70°C gekühlt werden konnte [ILFA03]. Genauere Informationen hat Ilfa bisher nicht zur Verfügung gestellt. Eine Simulation hat ergeben, dass diese Temperatur im Bereich des Möglichen liegt. Je nach Simulationsparametern lässt sich aber auch eine geringere oder höhere Temperatur erreichen. Daraus folgt, dass sich die bisher verfügbaren Daten nicht zur Validierung der Simulation eigneten.

Der Platzbedarf ist bei diesem Verfahren sehr gering. Die Platine wird durch die verwendeten Kanäle etwas dicker. Je nach Art der Kühlkanäle liegt dies im Bereich von 1 bis 2 mm. Zusätzlich sind Zuleitungen notwendig. Am meisten Platz nehmen hier die Anschlussstutzen ein, um die Schläuche an der Platine zu befestigen.

Der begrenzende Faktor für die Kühlleistung ist die Leistung des Wärmetauschers innerhalb der Platine. Die Kühlleistung ist abhängig vom Kanallayout, dem verwendeten Fluid und der Leistungsfähigkeit der Pumpe.

Es handelt sich hierbei um ein geschlossenes System, d.h. die Auswirkungen auf die Elektronik sind gering. Die Verlegung der Kühlkanäle in der Platine stellt allerdings Anforderungen an das Layout der Platine und der Elektronik.

Zu beachten: Ilfa verfügt über ein Patent zum Einbau von Kühlkanälen in die Platine.

3.2 Umspülung der Elektronik mit Kühlmittel

Alternativ zur innenliegenden Kühlung ist eine Umspülung der Elektronik durch ein Kühlmittel denkbar. Der größte Vorteil dieses Verfahrens ist, dass bisherige Platinen weiter verwendet werden können und keine Neuentwicklung elektronischer Komponenten notwendig ist.

Die technischen Schwierigkeiten des Verfahrens sind erheblich. Es stellt sich die Frage nach der Verträglichkeit des verwendeten Kühlmittels mit der Elektronik, ins-

827

besondere bei hohen Temperaturen. Diese ist möglicherweise dadurch zu gewähr-leisten, dass die Elektronik vor dem Einbau mit einer Schutzschicht überzogen wird. Im Projekt durchgeführte Simulationen einer isolierten Elektronik haben darüber hin-aus gezeigt, dass ein wesentlicher Teil der abzuführenden Wärmemenge von außen aus der Umgebung eingetragen wird. Eine Umspülung der Elektronik mit Kühlmittel führt zwangsläufig zu einer erheblichen Verringerung der Isolationsdicke. Hieraus resultiert wiederum ein stark erhöhter Leistungsbedarf an die Wärmesenke, die oh-nehin ein kritisches Element darstellt. Aufgrund der dargestellten Schwierigkeiten wurde dieser Ansatz im Projekt nicht verfolgt, wenngleich eine erfolgreiche Umset-zung nicht ausgeschlossen ist.

3.3 Kühlung der Vergussmasse mittels Kühlmittel

Ein weiterer Ansatz ist die Kühlung der Vergussmasse bzw. des Isolationsstoffes der Platine, indem dieser mit einem Kühlmittel durchströmt wird. Zusätzlich zu den zuvor genannten Schwierigkeiten, treten hierbei weitere Fragestellungen auf. Als vielver-sprechendster Isolationsstoff hat sich ein Keramikpulver herausgestellt, dass aller-dings nicht in Kontakt mit Flüssigkeiten kommen darf. Dieser Ansatz wurde im Pro-jekt folglich nicht weiter verfolgt.

3.4 Kühlung mit Peltier-Element

Die Kühlung von Elektronik mittels Peltier-Elemente ist möglich. Allerdings haben diese nur einen Temperaturbereich von bis zu 170°C. Zusätzlich erzeugen die Ele-mente selbst eine nicht zu vernachlässigende Wärmemenge, die abtransportiert werden muss.

Zur Kühlung der gesamten Elektronik ist dieses Verfahren nicht geeignet. In speziel-len Fällen mag die Kühlung einzelner Bauelemente sinnvoll sein.

3.5 Auswahl zu erprobender Kühlmethoden

	Passive Ent-wärmung	Kühlung durch Peltier-Element	Umspülung der Elektronik	Kühlung der Vergussmasse	Kühlung der Platine
Platzbedarf	gering	gering	?	gering	gering
Sicherheit	Kein Risiko		Abhängig vom Kühlmittel		
Mechanische Robustheit	Sehr hoch	?	?	?	Hoch
Technisch Um-setzbar	Nicht bei 250°C		wahrscheinlich	fraglich	Prototyp existiert
Kühlleistung der Elektronik	Gering	Hoch	Hoch	Gering	Hoch
Auswirkung auf	Keine	Keine	Ioneneintrag,	Keine	Layout

Elektronik			Verunreini-gung und Kor-rosion		Anpas-sungen
Wartbarkeit	Nicht nötig	?	?	?	?
Schutz der Elektronik vor Wärmeeintrag	Nein	Nur das je-weils gekühlte Element	Gut	Gut	Mäßig

Die direkte Kühlung der Platine durch innenliegende Kühlkanäle wurde als vielver-sprechendster Ansatz ausgewählt.

4 Lösungskonzept

4.1 Ausgewählte Kühlmethode

Es wurden verschiedene Möglichkeiten der aktiven Entwärmung untersucht. Der An-satz mit dem höchsten Potenzial ist die Kühlung der Platine durch integrierte, flüssig-keitsdurchströmte Kühlkanäle.

Das Einfügen von Kühlkanälen in die Platine bietet einen platzsparenden und effizi-enten Weg der Entwärmung. Die Platine wird großflächig gekühlt. Durch eine Ver-dichtung der Kühlkanäle an kritischen Stellen kann die Kühlleistung lokal erhöht wer-den.

Neben der Platine müssen auch die Zuleitungen der Kühlflüssigkeit zur Platine iso-liert werden, um ein vorzeitiges Erwärmen der Flüssigkeit zu verhindern. Die Platine wird zum Schutz der Elektronik vor Vibrationen weiterhin vergossen bzw. in ein Isola-tionsmaterial eingebettet. Abbildung 2 zeigt den schematischen Gesamtaufbau. Die Zuleitungen führen zu einem Wärmetauscher, der allerdings nicht Teil von T3 ist.
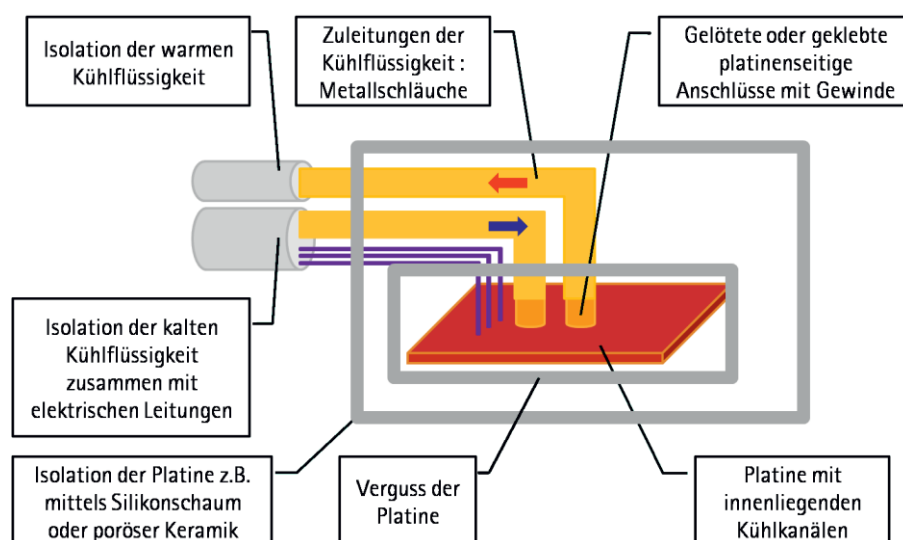

Abbildung 2: Skizze des Gesamtaufbaus

Als Zuleitungen kommen Metallwellschläuche oder Teflonschläuche in Frage. Beide halten den geforderten Belastungen stand. Für den elektrischen Anschluss existieren hochtemperaturfeste Leitungen, deren Belastbarkeit deutlich über dem geforderten Temperaturbereich liegt.

Der Arbeitsbereich des verwendeten Kühlmittels liegt über 100°C. Hier kommen Transformator- und Thermoöle in Frage. Am Markt existiert eine große Auswahl solcher Öle, darunter auch Öle mit niedriger Viskosität und guter Umweltverträglichkeit. Simulationen haben gezeigt, dass der Druckabfall bei benötigter Strömungsgeschwindigkeit unter 1 bar liegt, was auch mit kleinen Pumpen erzeugbar ist.

Die folgende Liste zeigt eine Übersicht, welche Materialeigenschaften und Konstruktionscharakteristika einen Einfluss auf die Eigenschaften des Kühlsystems haben.

- Kühlmittel
  - Viskosität
  - Wärmekapazität
  - Wärmeleitfähigkeit
  - Umweltverträglichkeit
  - Temperaturbereich
  - Haltbarkeit
- Kühlkanäle
  - Form und damit verbundene Oberfläche zum Kupfer
  - Strömungseigenschaften, Querschnitt, Form, Länge
  - Position und Weg der Kanäle in der Platine
  - Geschwindigkeit der Kühlflüssigkeit im Kanal
- Platinenaufbau
  - Anzahl der Layer
  - Entfernung des gekühlten Kupfers vom „heißen Layer", d.h. Wärmedurchgangswert
  - Verbindung des Bauteils zur Platine
- Dämmung nach außen
  - Dicke und Wärmeleitwert
  - Vibrationsfestigkeit der Isolation
  - Empfindlichkeit gegen Feuchtigkeit
  - Temperaturbeständigkeit der Isolation
- Layout der Elektronik
  - Anzahl und Position wärmeleitender Vias
  - Position besonders wärmeintensiver Bauteile (Anfang, Mitte, Ende der Kühlschleife)
- Leistungsfähigkeit des Wärmetauschers
- Leistungsfähigkeit der Pumpe (Druck, Volumenstrom)

4.2 Bewertung der Kühlleistung

Der Wärmedurchgangswert vom Bauteil bis zum Kühlmittel setzt sich aus mehreren kritischen Faktoren zusammen. Die Wärme muss vom Bauteil auf die Platinenoberfläche übertragen und von dort aus weiter auf die gekühlte Kupferschicht abgeleitet werden. Dort geht die Wärme auf die Kühlflüssigkeit über.

Der Übergang vom Bauteil auf die Platinenoberfläche findet über die Lötkontakte der Elektronik oder Kühlflächen am Bauteil statt, die mit der Platine verbunden werden. Der Übergang von der Platinenoberfläche zur gekühlten Kupferlage kann über Thermovias effizient erfolgen. Allerdings bedingt dies, dass alle mit Thermovias verbundenen Flächen auf dem gleichen Potenzial liegen (vgl. Abbildung 3).
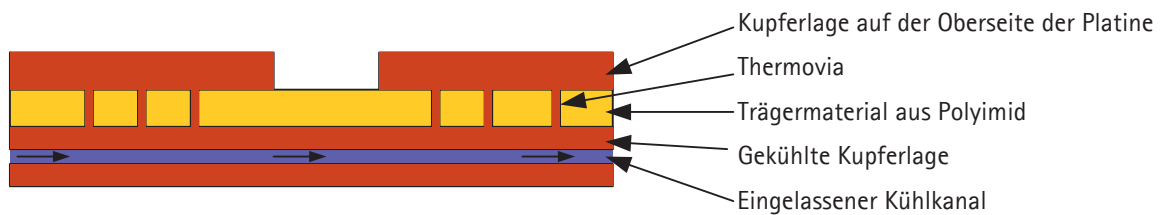

Abbildung 3: Thermovias verbinden thermisch und elektrisch

Kupferflächen, die nicht auf dem gleichen Potenzial liegen, können nicht mit Thermovias verbunden werden. Daraus folgt eine vergleichsweise schlechte Wärmeleitung von der Platinenoberfläche zur gekühlten Lage. Bei Multilayerplatinen verschärft sich dieses Problem durch die große Anzahl dazwischenliegender Schichten. Um dem entgegenzuwirken, kann auf beiden Seiten der Platine eine gekühlte Schicht integriert werden. Abbildung 4 zeigt einen beispielhaften Aufbau einer Platine mit 8 Kupferlagen und zwei zusätzlichen gekühlten Schichten.
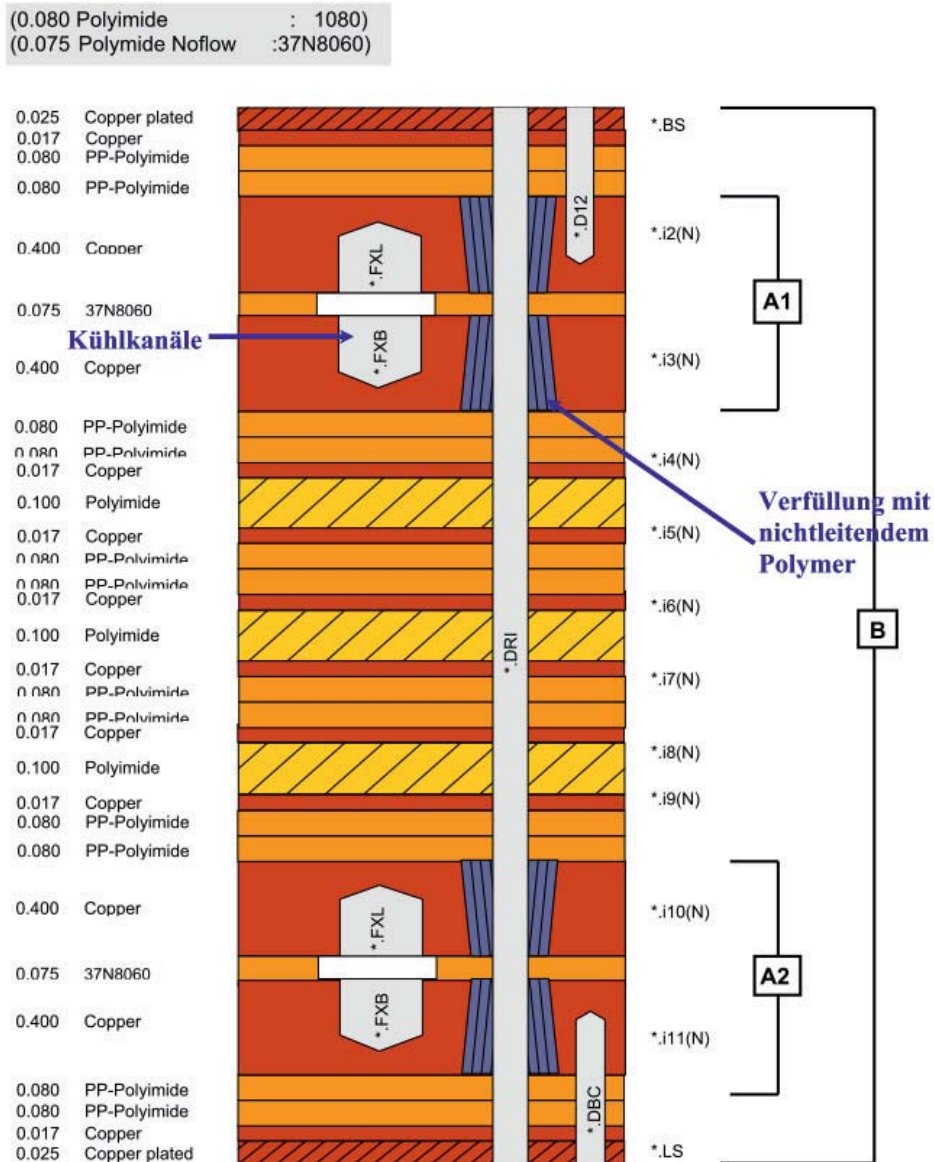
831

Abbildung 4: Multilayeraufbau einer Platine mit innenliegenden Kühlkanälen

Zur Untersuchung der Wirksamkeit der Kühlmethode wurden erste Simulationen durchgeführt. Hierbei wurde untersucht, wie der Kühlkanal beschaffen sein muss, um den Wärmeübergang vom Kupfer auf die Flüssigkeit zu optimieren und wie sich dabei der nötige Druck zur Erzeugung des Kühlmittelstroms verhält. Abbildung 5 zeigt die Abhängigkeit der durchschnittlichen Platinentemperatur einer Platine der Größe 25 mm x 100 mm und einer Wärmeleistung von 10 W. Die Wärmeleistung wird gleichmäßig auf die Platine aufgebracht. Das Kühlmittel hat eine Eingangstemperatur von 100°C. Der Kühlkanal hat einen Querschnitt von 1 mm x 0,6 mm.

Die verschiedenen Kurven ergeben sich aus einer Vielzahl simulierter Aufbauten, die hier nicht im Detail beschrieben werden sollen. Die mit „min" bezeichnete Kurve stellt dabei den minimal zu erreichenden Temperaturdurchschnitt dar. Es ist zu sehen, dass bei geeignetem Aufbau der Wärmeübergang nahe am möglichen Maximum liegt. Kritische Faktoren sind hier die Kontaktfläche zwischen Kupfer und Kühlmittel

und die Ausbildung von Turbulenzen im Kühlmittel. Je mehr Turbulenzen erzeugt werden, desto besser funktioniert der Wärmeübergang.

Durch die Erzeugung von Turbulenzen steigt allerdings auch der benötigte Druck. Abbildung 6 zeigt die auftretenden Drücke am Eingang des Kühlkanals bei gegebener Strömungsgeschwindigkeit. Wie sich zeigt, sind die benötigten Drücke bei den verwendeten Aufbauten relativ gering.
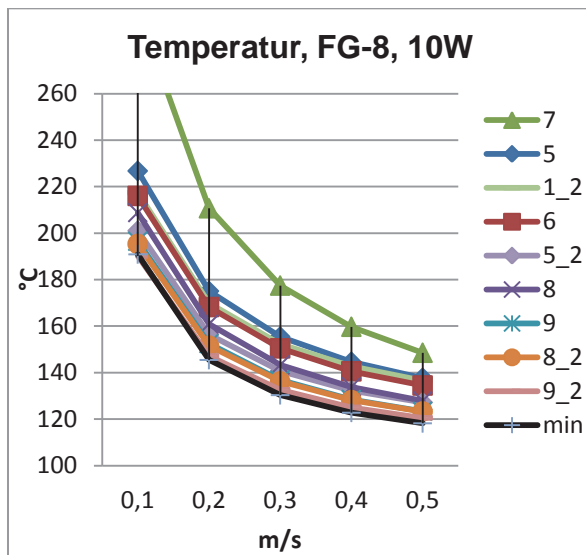

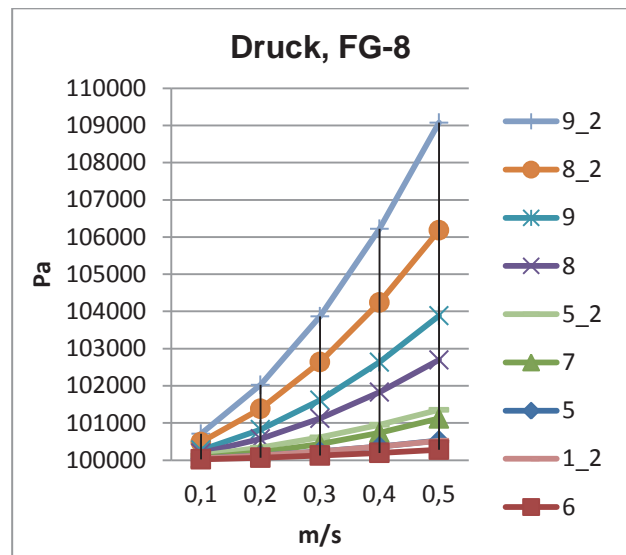Abbildung 5: Abhängigkeit der Temperatur von der Strömungsgeschwindigkeit

Abbildung 6: Abhängigkeit des Drucks von der Strömungsgeschwindigkeit

5 Isolation

Neben der Kühlung der Platine ist die Isolation gegen die Umgebung ein kritischer Faktor. Die Kühlleistung des benötigten Wärmetauschers ist noch nicht bekannt, aber sicher begrenzt. Voraussichtlich liegt die Wärmeleistung durch das Eindringen der Wärme durch die Isolation über der der Elektronik.

Als Isolation kommt eine Vakuumisolation oder eine Isolation mittels Silikonschaum oder mikroporöser Keramik in Frage. Es wurden verschiedene Aufbauten hinsichtlich ihrer Haltbarkeit und Isolationswirkung untersucht. Eine Vakuumisolation in Form einer runden Thermosflasche ist Stand der Technik und bereits erprobt. Alternativ dazu kann ein gestütztes Vakuum in beliebigen Gehäuseformen aufgebaut werden. Hierdurch wäre auch die Integration der Elektronik in die Seitenwandung der Bohrgarnitur möglich, da ein flacher Aufbau mit dünner Seitenwandung möglich wird.

Silikonschaum ist einfach zu verarbeiten und ebenfalls unter den gegebenen Bedingungen einsetzbar. Allerdings liegt die Isolationswirkung deutlich unter der Vakuumisolation oder der porösen Keramik (vgl. Tabelle 1).

Mikroporöse Keramiken haben eine gute Isolationswirkung. In verpresster Form zeigte sich das Keramikpulver außerdem resistent gegen Vibrationen.

Stoff	Wärmeleitfähigkeit [W/mK]
Polyimid (37N)	0,3
Silikon	0,19
Silikonschaum	0,06
poröse Keramik Silcapor High	0,02
Vakuumdämmplatte	0,006

Tabelle 1: Wärmeleitfähigkeiten verschiedener Stoffe

Erste Simulationen des Wärmeeindrangs von außen zeigen, dass die abzuführende Wärmeleistung bei einer Platine der Größe 25 mm x 100 mm und einer Isolationsstärke von 10 mm poröser Keramik im Bereich von 2,5 W liegt. Da Platinen mit einer Länge von bis zu 300 mm verwendet werden, ist die Wärmeleistung entsprechend deutlich höher.

5.1.1. Silikonschaum
Silikonschaum wird in Platten geliefert und ist temperaturstabil bis mindestens 230°C. Bis 250°C verfärbt sich dieser, bleibt aber intakt, solange er nicht mechanisch stark belastet wird.

5.1.2. Poröse Keramiken
Mikroporöse Keramiken werden vorwiegend für Hochtemperaturanwendungen im Bereich von 1000 °C und höher verwendet. Typische Anwendungsgebiete sind Isolationen von Hochöfen oder Schmelzen. Dazu wird Keramikpulver unter hohem Druck in eine Form gepresst. Wird die Form entfernt, behält das gepresste Pulver seine Form, ist aber nur begrenzt mechanisch belastbar.
Die fertig gepressten Teile sind sehr empfindlich gegen Vibrationen. Bei Herstellern wie beispielsweise Silca ist es allerdings möglich, das Keramikpulver direkt zu beschaffen. In Versuchen wurde das Pulver in die Kammer gefüllt, in die später die Elektronik eingefügt werden soll. Dazu wurde zuerst eine Schicht Pulver, dann die Elektronik und wieder eine Lage Pulver übereinandergeschichtet und anschließend verpresst. Der Druck lag dabei im Bereich von 10 N/cm² und somit deutlich unter dem Druck, der zur Herstellung fester Keramikstrukturen verwendet wird. Der Druck reichte aus, um das Material leicht zu verfestigen.

Durch das Montieren eines Deckels wird nun verhindert, dass sich das Volumen des gepressten Blockes wieder vergrößern kann. Hierdurch wird dieser resistent gegen Vibrationen. Mikroporöse Keramiken zeigen folglich ein hohes Potential als Isolationsmaterial für die eingebaute Elektronik.

5.1.3. Thermosflasche

Thermosflaschen sind in der Regel rund ausgeführt. Durch das Vakuum zwischen zwei Wänden bzw. das Vakuum zwischen Außenwand und Elektronik findet keine Wärmeleitung statt. Einzig die Wärmestrahlung führt zum Eindringen von Wärmeenergie. Wegen der runden Bauform wird im Falle der betrachteten Elektronik vergleichsweise viel Platz verschwendet. Für Spezialanfertigungen ist eine Mindestdicke des Vakuums von 5 mm üblich. Hinzu kommen die Wandungen. [KGV]

Eine Alternative stellen vakuumisolierte Gefäße mit gestütztem Vakuum dar [Ker]. Wird das Vakuum mit einem Pulver gefüllt, stützt dieses die Wände gegeneinander ab. Des Weiteren reduziert das Pulver erheblich die freie Weglänge der im Vakuum verbliebenen Gasmoleküle und reduziert die Rest-Wärmeleitfähigkeit. Abbildung 7 zeigt die Verwendung von Keramikpulver oder einer Faserplatte als Stützmaterial im Vergleich.
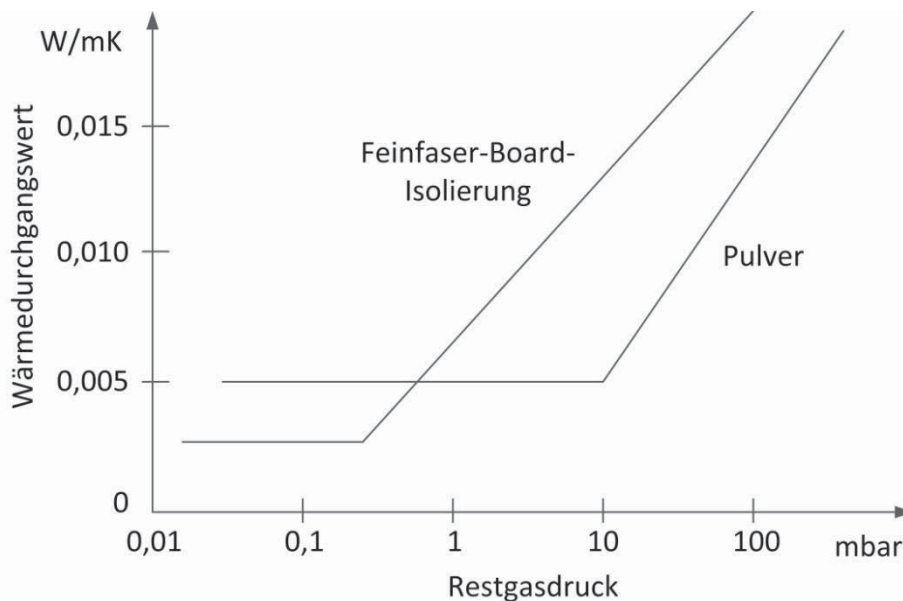

Abbildung 7: Isolationswert Vakuum [Ker].

Wird der Vakuumbehälter zweiwandig ausgeführt, dringt Wärme entlang der Wandung aus Richtung des Deckels in das Gefäß ein. Abbildung 8 stellt dies schematisch dar. Wird beispielsweise angenommen, dass die vergossene Elektronik eine Kantenlänge von 30 x 30 mm hat, das Gehäuse aus Stahl (50 W/mK) besteht und 1 mm Wanddicke hat, ergibt sich eine Querschnittsfläche von $4 * 0,03m * 0,001m = 0,00012m^2$. Bei einer Wärmeleitfähigkeit von 50 W/mK, einer Länge von 0,1 m und einer Temperaturdifferenz von 100K ergibt sich

$$\frac{50\frac{W}{mK} * 0,00012m^2 * 100K}{0,1m} = 6W$$

als Wärmeeintrag.

Bei einem hochlegierten Stahl mit 20 W/mK ergibt sich entsprechend ein Eintrag von 2,4 W. Um dies zu verhindern, kann das Gefäß einwandig ausgeführt werden, allerdings ist der technische Aufwand hierfür hoch.
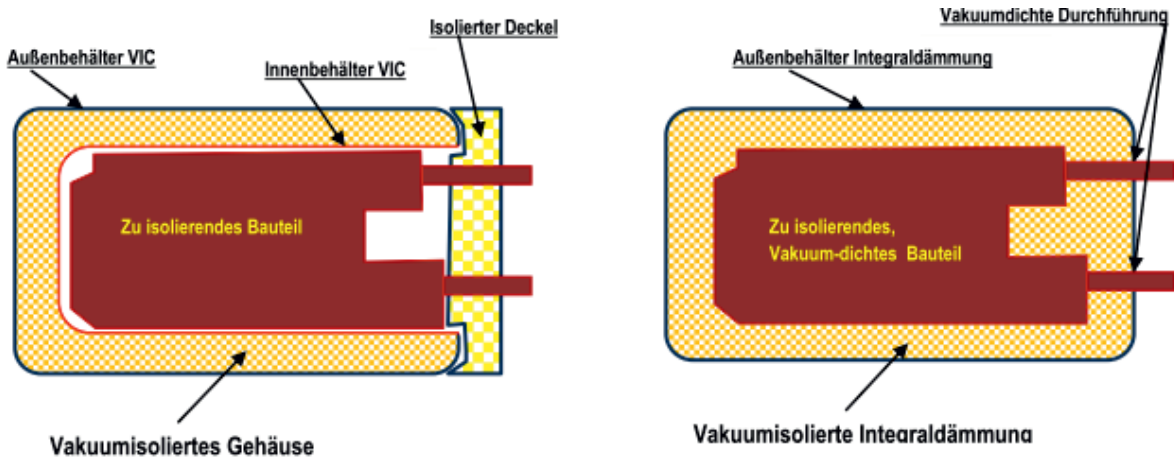

Abbildung 8: Vakuumisolation von Kerspe [Ker]

Abbildung 9 zeigt einen alternativen Aufbau. Die Elektronik ist in einem Innenbehälter eingeschlossen. Dieser wird gasdicht mit dem Außenbehälter verbunden. Diese Durchführung muss nun so gestaltet werden, dass der Wärmeeintrag möglichst gering ist.
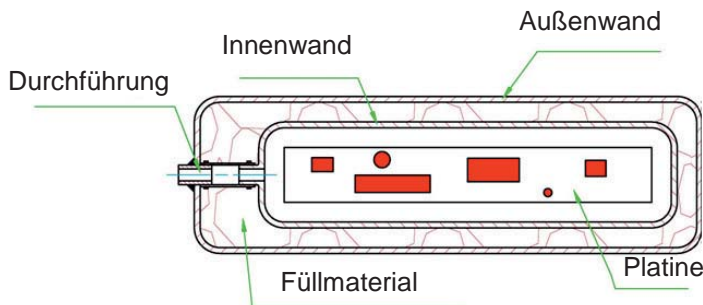
Abbildung 9: Aufbau Vakuumisolation ITA

Als Durchführung kann beispielsweise ein Metallwellschlauch verwendet werden. Dieser ist kommerziell verfügbar. Abbildung 10 zeigt den Aufbau eines solchen Schlauches. Aufgrund der Wellen beträgt das Verhältnis zwischen der Länge des Schlauches und der Pfadlänge entlang des Materials ungefähr 3. Ein 10 mm langer Schlauch entspricht ausgezogen also ca. 30 mm Metallrohr. Die Wandstärke beträgt in der Regel unter 0,2 mm, im recherchierten Beispiel 0,18 mm bei einem Durchmesser von 28 mm. Die Querschnittsfläche des Rohres beträgt dann

$$0,0144^2 * Pi - 0,01422^2 * Pi = 1,6 * 10^{-5}\ m^2$$

und der resultierende Wärmeeintrag

$$\frac{50\frac{W}{mK} * 0,000016 m^2 * 100 K}{0,3 m} = 0,27 W.$$

Abbildung 10: Aufbau eines Metallwellschlauches
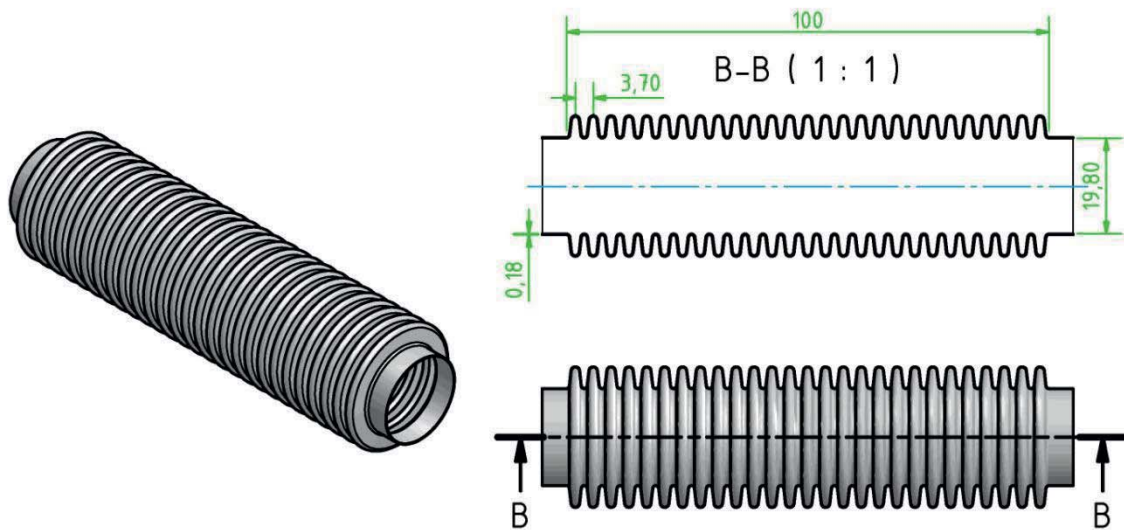
6 Analytische Berechnung der Kühlleistung

Um die Einflüsse verschiedener Material- und Konstruktionsparameter abzuschätzen, wurden diese zunächst analytisch untersucht.

6.1 Verwendete Formelzeichen

$\dot{Q}$ Wärmestrom in W

c Wärmekapazität in $\frac{kJ}{kg*K}$

$\dot{m}$ Massenstrom in kg/s

u   Geschwindigkeit in m/s

ρ Dichte in kg/m³

A   Fläche in m²

ΔT Temperaturdifferenz

α Wärmeleitzahl W/mK

v kinematische Viskosität m²/s

η dynamische Viskosität kg/ms oder Ns/m²

l Länge des Kühlkanals

T_W Temperatur der Kanalwand

T_1 Temperatur der Flüssigkeit am Kanalausgang (x=1)

T_0 Temperatur der Flüssigkeit am Kanaleingang

$\overline{T_F}$ Durchschnittstemperatur der Kühlflüssigkeit

6.2 Kenngrößen

Die charakteristische Länge d ist geometrieabhängig. Bei einem runden Rohr ist sie gleich dem Durchmesser des Rohres. Für einfache Geometrien wie beispielsweise einen quadratischen Rohrquerschnitt sind Tabellenwerke erhältlich. Je weiter sich die Form des Querschnitts allerdings von einem runden Rohr entfernt, desto ungenauer werden die verwendeten Werte. Bei Geometrien wie sehr flachen Rechtecken muss der Wert experimentell ermittelt werden.

Die **Reynoldszahl** gibt an, ob in einem Kanal eine laminare oder turbulente Strömung vorliegt:

$$Re_d = \frac{c * d}{v} = \frac{c * d * \rho}{\eta} \tag{1}$$

Für die verwendeten Öle ergibt sich hier eine Reynoldszahl für z.B. 35 für Midel bei 0,2m/s und einer charakteristischen Länge von 1 mm. Eine Reynoldszahl kleiner 2300 bedeutet, dass die Strömung laminar und nicht turbulent ist. Für unsere Anwendung liegt die Reynoldszahl deutlich unter dieser Grenze.

Die **Nußeltzahl** ist das Verhältnis der für die Strömung charakteristischen Länge d und der Dicke der Temperaturgrenzschicht δ. α ist die Wärmeübergangszahl.

$$Nu_d = \frac{d}{\delta_\vartheta} = \frac{\alpha * d}{\lambda} \tag{2}$$

$$\alpha = \frac{Nu * \lambda}{d} \tag{3}$$

Für ein rundes Rohr, das hinreichend lang ist, ergibt sich bei laminarer Strömung die Nußeltzahl 3,66. Bei kürzeren Rohren ergibt sich eine höhere Nußeltzahl, verursacht durch die anfänglich nicht vorhandene Strömungsgrenzschicht. Für kurze Rohre, in denen die Grenzschicht nicht voll ausgebildet ist, gilt:

$$Nu_{d,lam} = 0,644 * \sqrt[3]{Pr} * \sqrt{Re_d * d/l} \tag{4}$$

Für den Übergang gilt:

$$Nu_{d,lam} = \sqrt[3]{3,66^3 * 0,644^3 * Pr * (Re_d * \frac{d}{l})^{3/2}} \tag{5}$$

Für die Länge des Kühlkanals ist die Länge anzunehmen, die die Flüssigkeit in einem geraden Rohr strömen kann. An scharfen Kurven ist dieses ggf. zu Ende und ein neues Rohr beginnt.

Mit der **Wärmeleitzahl**, Fläche und Temperaturdifferenz lässt sich der Wärmestrom bestimmen.

$$\dot{Q} = \alpha * A * \Delta T \tag{6}$$

$$\Delta T = \frac{\dot{Q}}{\alpha * A} = \frac{\dot{Q} * d}{Nu * \lambda * A} \tag{7}$$

Der Zusammenhang der Temperatur mit der abgeführten Leistung ergibt sich aus:

$$\dot{Q} = c * \dot{m} * \Delta T \tag{8}$$

$$\dot{m} = u * \rho * A \tag{9}$$

$$\Delta T = \frac{\dot{Q}}{c * \dot{m}} = \frac{\dot{Q}}{c * u * \rho * A} \tag{10}$$

Hiermit lässt sich im stationären Zustand mit der Eingangstemperatur der Flüssigkeit die Ausgangstemperatur bestimmen. Diese ist unabhängig von der Verteilung der Temperatur auf der Platine.

Beispielsweise ergibt sich für das Thermoöl Midel bei einer Leistung von 10 W und einer Strömungsgeschwindigkeit von 0,2 m/s und einem Querschnitt von 0,6 mm² eine Temperaturdifferenz von 44 K.
Die Frage ist nun, wie hoch die Temperatur des Kühlkörpers ist, durch den die Wärme abgeführt wird. Im einfachsten Fall wird die Temperatur im Kühlkörper als homogen angenommen.
Im Gesamtsystem interessiert zusätzlich noch die durchschnittliche Abweichung der Durchschnittstemperatur des Kühlkörpers von der Flüssigkeit.

6.3 Temperaturverteilung der Flüssigkeit

Es ist schwierig, die Temperaturverteilung der Flüssigkeit zu berechnen. Hierzu ist es entweder nötig, für jeden Ort den Wärmestrom zu kennen oder die Temperatur der Kanalwand muss bekannt sein.

Die folgende Grafik zeigt den Temperaturverlauf zwischen Ein- und Ausfluss abhängig von der (konstanten) Wandtemperatur. (Beispiel Midel, 10 W, 0,2m/s, Querschnitt 0,6 mm², Eintrittstemperatur 100°C, Ausgangstemperatur errechnet 144°C)
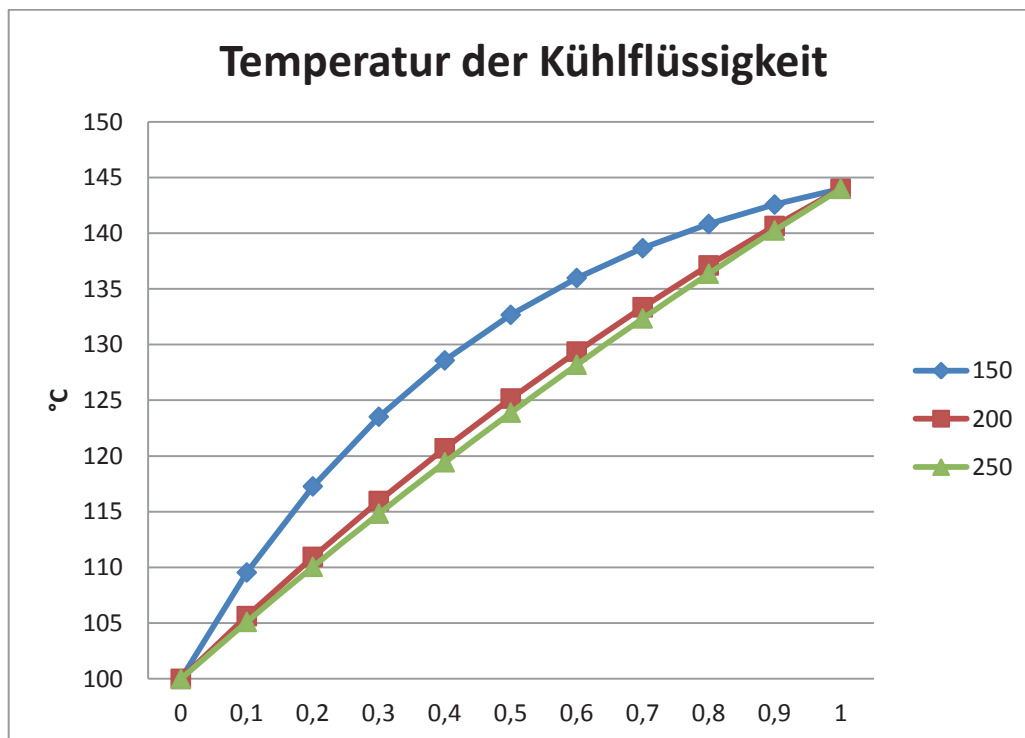
Abbildung 11: Temperatur der Kühlflüssigkeit entlang des Kühlkanals, normiert auf die Länge des Kanals

Errechnen lässt sich die Verteilung wie folgt. Die Temperatur der Flüssigkeit ergibt sich zu

$$f(x) = T_W - (T_W - T_0)e^{-ax} \tag{11}$$

Nun wird definiert, dass x in Einheiten der Kanallänge gemessen wird, d.h. $x \in [0; 1]$. Bekannt sind f(0) und f(1). Aus f(1) = T_1 ergibt sich:

$$T_1 = T_W - (T_W - T_0)e^{-a} \tag{12}$$

$$-a = ln \frac{T_W - T_1}{T_W - T_0} \tag{13}$$

$$f(x) = T_W - (T_W - T_0)e^{ln\left(\frac{T_W - T_1}{T_W - T_0}\right)x} \tag{14}$$

$$f(x) = T_W - (T_W - T_0)\left(\frac{T_W - T_1}{T_W - T_0}\right)^x \tag{15}$$

Mit der Stammfunktion

$$F(x) = T_W * x - (T_W - T_0)\left(\frac{T_W - T_1}{T_W - T_0}\right)^x * \frac{1}{ln\left(\frac{T_W - T_1}{T_W - T_0}\right)} + C \tag{16}$$

C wird hier so gewählt, dass gilt: $F(0) = 0$, woraus folgt

$$F(x) = T_W * x - (T_W - T_0)\left(\frac{T_W - T_1}{T_W - T_0}\right)^x * \frac{1}{ln\left(\frac{T_W - T_1}{T_W - T_0}\right)} \tag{17}$$
$$+ \frac{(T_W - T_0)}{ln\left(\frac{T_W - T_1}{T_W - T_0}\right)}$$

6.4 Temperatur der Platine

Der Wärmestrom ergibt sich zu

$$\dot{Q} = \int_0^A \alpha * \Delta T \, dA \tag{18}$$

Nimmt man an, dass α und der Umfang konstant sind und die Temperatur der Kanalwand in einem beliebigen Querschnitt in Fließrichtung gleich ist, dann folgt

$$\dot{Q} = \int_0^1 \alpha * \Delta T * U \, dx \tag{19}$$

$$\dot{Q} = \int_0^1 \alpha * f(x) * U \, dx \tag{20}$$

$$\dot{Q} = \alpha * U * \int_0^1 f(x) \, dx \tag{21}$$

Aufgrund der Integration von 0 nach 1 ergibt sich, dass das Integral genau der Durchschnittswert der Temperatur der Kühlflüssigkeit entspricht.

Die Stammfunktion selbst ist allerdings abhängig von der Wandtemperatur des Kühlkanals. Für hinreichend große Temperaturdifferenzen zwischen Kanalwand und Kühlflüssigkeit ergibt sich allerdings, dass die Näherung $\overline{T_F} \approx (T_1 + T_0)/2$ verwendet werden kann. Damit lässt sich theoretisch die durchschnittliche Wandtemperatur bestimmen:

$$\overline{T_W} = \overline{T_F} + \frac{\dot{Q} * d}{Nu * \lambda * A} \tag{22}$$

$$\overline{T_W} = \frac{T_1 + T_0}{2} + \frac{\dot{Q} * d}{\lambda * A * \sqrt[3]{3{,}66^3 * 0{,}644^3 * Pr * \left(Re_d * \frac{d}{l}\right)^{3/2}}} \tag{23}$$

$$\overline{T_W} = T_0 + \frac{\dot{Q}}{c * u * \rho * A}$$
$$+ \frac{\dot{Q} * d}{\lambda * A * \sqrt[3]{3{,}66^3 * 0{,}644^3 * Pr * \left(\frac{c * d}{v} * \frac{d}{l}\right)^{3/2}}} \tag{24}$$

Problematisch ist die Bestimmung der Größen für d und Nu. Die Bestimmung von d ist stark abhängig von der Geometrie, d.h. d ist eigentlich ein geometrieabhängiger Proportionalitätsfaktor, der nicht von einer Geometrie auf eine andere übertragbar ist. In die Nußeltzahl geht unter anderem auch die Länge des Rohrs, die Prandtlzahl und die Reynoldszahl ein. Die Nußeltzahl ist also abhängig von den Stoffeigenschaften des Fluides und der verwendeten Geometrie.

Unbekannte sind hier d und l und beide sind nicht ohne weiteres bestimmbar. Die genannten Formeln gelten nur für ein rundes Rohr und nur so lange die Strömung laminar ist. Der Kühlkanal hat in der Realität eher einen flachen, rechteckigen Querschnitt. Durch die Geometrie der Anschlussstücke und Knicke im Kühlkanal ist die Strömung nur teilweise laminar.

Aufgrund der Komplexität der Geometrien ist die analytische Berechnung des Wärmeübergangs nicht exakt möglich. Sind die Werte für d und l empirisch ermittelt, lassen sich damit aber für die verwendete Geometrie oder ähnliche Aufbauten Vorhersagen treffen. Anhand der Formeln lässt sich lediglich der Einfluss der verschiedenen Größen erkennen.

7   Simulation des Kühlsystems

Es wurden mehrere Beispielplatinen entworfen, anhand derer der Einfluss der verschiedenen Parameter bestimmt und bewertet wurde.

Um Simulationsfehler zu minimieren, wurde auch der Einfluss verschiedener Parameter auf die Simulation getestet. Dazu gehören

- Art des Meshings, Zellenanzahl, Inflation, etc.
- Eingangsturbulenz
- Feinheit der Turbulenz-Modellierung (First Order / High Resolution)

Erste Simulationsversuche haben gezeigt, dass der Übergang vom heißen Layer zum gekühlten Layer und der Übergang von dort auf die Flüssigkeit von besonderer Bedeutung sind. Letzteres ist wiederum von der Geometrie der Kühlkanäle abhängig. Zu untersuchende Kriterien, die die Wärmedurchgangszahl beeinflussen, sind:

- Kühlkanalfläche,
- Kühlflüssigkeitsgeschwindigkeit,
- Wärmekapazität der Flüssigkeit,
- Verbindung des oberen Kupfers mit dem Kern,
- Turbulenz,
- Homogene Wärmeverteilung → Wie müssen die Kanäle aussehen, damit die Wärme auch bei ungleicher Erzeugung auf der Platine möglichst gut abgeführt werden kann?
- Empfindlichkeit gegen produktionsbedingte Abweichungen und Modellierungsfehler

7.1.1.   Ergebnisse der Vorversuche

Kritisch sind die Übergänge vom Bauteil auf das Kupfer, von dort in die innere Kupferlage und der Übergang vom Kupfer auf die Kühlflüssigkeit. Während bei den ersten beiden Punkten Lösungen existieren (Kühlflächen am Bauteil, Wärmevias), ist das Layout der Kühlkanäle noch offen.

$$R = R(Bauteil\text{-}Cu) + R(Cu\text{-}Cu_{Kern}) + R(Cu_{Kern} - Kühlmedium)$$

Für die Kontaktierung vom Bauteil zum Kupfer kommt entweder Lot oder ein wärmeleitender Kleber in Frage. Der Wärmeübergang vom oberen Kupfer in das gekühlte erfolgt durch Wärmevias. Wie später beschrieben, sind bis zu 10 % Kupferanteil im Prepreg (PP) erreichbar, was einer Wärmeleitzahl von ca. 30 W/mK entspricht.

843

Mit $\dot{Q} = \frac{\lambda}{d} A * \Delta T$ ergibt sich z.B. bei einer Fläche von 1 cm x 1 cm, einer PP-Dicke von 0,16 mm und einer Leistung von 1 W eine Temperaturdifferenz zwischen der Platinenoberseite und dem Kupferkern von

$$\Delta T = \frac{\dot{Q} * d}{\lambda * A} = \frac{1W * 0{,}00016m}{30\frac{W}{mK} * 0{,}0001m^2} \approx 0{,}05K$$

Bei einem Aufbau ohne Wärmevias ergibt sich mit einer Wärmeleitfähigkeit des PP von 0,2 W/mK analog eine Temperaturdifferenz von 8 K. Der zu erwartende Simulationswert liegt demnach zwischen diesen beiden Werten.

Beim Layout der Kühlkanäle ist auf eine möglichst große Fläche zwischen Kupfer und Kühlmedium zu achten. Noch kritischer wirkt sich die Turbulenz der Strömung aus. Eine turbulente Strömung überträgt die Wärme von der Kanalwand in das Fluid um ein Vielfaches besser als eine laminare Strömung.

Eine weitere Designaufgabe stellt das strömungstechnische Layout dar. Beispielsweise zeigte sich, dass parallele Kühlkanäle sehr ungleich durchströmt werden können, sodass die Wärmeverteilung innerhalb der Platine sehr ungleichmäßig wird.

Das Layout der Kühlkanäle stellt die schwierigste Teilaufgabe dar und wurde daher als Schwerpunkt der Simulationen ausgewählt.

7.1.2. Berechnung der Ausgangstemperatur

Anhand der Formel (10) lässt sich für gegebene Wärmeleistung und Materialeigenschaften die Ausgangstemperatur der Kühlflüssigkeit berechnen. So ergibt sich beispielsweise für Midel:
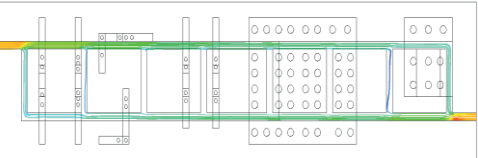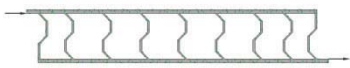
- Dichte 0,911 g/ml,
- Wärmekapazität von 1880 J/kgK,
- Kühlmittelgeschwindigkeit: 200mm/s bei
- Querschnitt von 1mm x 0,6mm,
- Volumenstrom 120mm³/s (0,12ml/s).

Bei einer Leistung von 10 W ergibt sich eine Temperaturdifferenz zwischen Eingang und Ausgang von 48,7°C, bei 12W bereits 58°C.

Für einen Versuchsaufbau, der dem Ilfa-Prototypen ähnelt, ergibt sich für Wasser als Kühlmittel eine Fluidgeschwindigkeit von 300 mm/s und bei einer Leistung von 25 W eine Temperaturdifferenz von 33,5°C. Die Größenordnung ist zwar richtig, da es sich aber um geschätzte Werte handelt, ist es nicht möglich, damit die Simulation zu validieren.

7.1.3. Kanallayouts

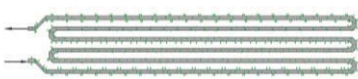|	
Abbildung 12: Kühlkanal Layout 1	Die Idee an diesem Layout ist, die Platine weitestgehend parallel zu durchströmen, um eine gleichmäßige Kühlung zu erhalten. Die Kühlung der einzelnen Bereiche in der Platine wären somit möglichst unabhängig voneinander. Parallele Strecken müssen einen kleineren Querschnitt haben als die langen Strecken, um einen Druckabfall in die richtige Richtung zu erzeugen. Anderenfalls erhält man eine stark ungleich verteilte Strömung. Ein- und Ausfluss sind an gegenüberliegenden Seiten. Dies könnte ein Nachteil bei der Konstruktion sein.
Abbildung 13: Ungleiche Verteilung der Strömung	Durch die Anzahl der Querverbindungen kann die Fläche zwischen Kupfer und Kühlmittel variiert werden.
Abbildung 14: Kühlkanal Layout 2	Nachteil bei diesem Layout: Die Flüssigkeit erwärmt sich von einer Seite zur anderen, sodass eine Platinenseite schlechter gekühlt wird als die andere.
Abbildung 15: Kühlkanal Layout 3	Wie Layout 1, allerdings erfolgt eine Erhöhung der Kühlfläche durch längere Kanäle.
Abbildung 16: Kühlkanal Layout 5	Ein- und Ausfluss sind hier auf der gleichen Seite. Bei diesem Layout und dessen Varianten kommt die erwärmte Flüssigkeit sehr nahe an die noch kalte heran. Da die gekühlte Kupferlage sehr gut Wärme leitet, wirkt sich dies aber nicht nachteilig aus. Kontaktfläche Fluid/Kupfer: 0,00120217 m²
Abbildung 17: Kühlkanal Layout 6	Wie Layout 5, nur mehr Kontaktfläche. Kontaktfläche Fluid/Kupfer: 0,00180155 m²
Abbildung 18: Kühlkanal Layout 7	Wie Layout 5, nur weniger Kontaktfläche, aber höhere Strömungsgeschwindigkeit. Kontaktfläche Fluid/Kupfer: 0,000632194 m²

 Abbildung 19: Kühlkanal Layout 8	Die Schleife ist so angeordnet, dass der komplette Kanal seriell durchflossen wird. Das größte Temperaturgefälle tritt dabei an der Schmalseite der Platine auf, sodass sich die schlechtere Wärmeaufnahme der erwärmten Flüssigkeit weniger bemerkbar macht. Kontaktfläche Fluid/Kupfer: 0,00121377 m²
 Abbildung 20: Kühlkanal Layout 9	Wie Layout 8, aber mit verlängerter Kühlschleife. Kontaktfläche Fluid/Kupfer: 0,00173675 m²
 Abbildung 21: Layout 10	Kanal wird seriell durchflossen. Wärmeverteilung evtl. gleichmäßiger, da Hin- und Rückfluss nah beieinanderliegen.

7.2 Untersuchung des Einflusses der Modellierungsparameter

Die Simulation der Wärmeverteilung innerhalb der gekühlten Platine besitzt mehrere Herausforderungen. Zum Einen ist das Seitenverhältnis des simulierten Körpers sehr ungünstig. Dadurch müssen die Zellen in einer FEM-Simulation sehr klein gewählt werden, woraus eine sehr große Anzahl von Zellen resultiert. Zum Anderen besteht die Platine aus einer großen Zahl von Körpern. Darüber hinaus verhält sich eine Wärmeflusssimulation sehr empfindlich gegenüber einer zu gering gewählten Zellenanzahl. Es war folglich zu untersuchen, welche Vereinfachungen durchgeführt werden können, um das Simulationsergebnis signifikant zu ändern.

7.2.1. Meshing

Vor der FEM-Simulation muss das Modell vernetzt werden. Die Vernetzung des Festkörpers und der Flüssigkeit unterliegen dabei unterschiedlichen Anforderungen. Es zeigte sich, dass die Zellen im Kupfer weniger kritisch sind. Sind sie zu groß gewählt, konvergiert das System nicht und gibt völlig unplausibel Ergebnisse aus, z.B. Temperaturen um den absoluten Nullpunkt. Bei Quaderzellen reicht eine Zellengröße von 1 mm aus.

Aufgrund des kleinen Kanalquerschnitts stellt sich im Fluid schnell eine laminare Strömung ein. Dies bewirkt, dass die Strömungssimulation keine hohen Ansprüche an die Zellengröße besitzt. Überraschenderweise zeigte sich, dass Zellen, die kleiner als ¼ der Kanalhöhe sind, keine weitere Verbesserung des Simulationsergebnisses bringen.

Die Anzahl der Inflation-Layer im Fluid hat dagegen einen deutlicheren Effekt. Die folgende Tabelle zeigt Beispiele für eine kleine Anzahl von Lagen.

Beispielmessung:

	4 Inflation Layer	5 Inflation Layer
Zellengröße im Kanal 1/2	165,02 °C (max. 167,78 °C)	
Zellengröße im Kanal 1/3	163,74 °C (max. 165,71 °C)	163,54 °C (max. 165,50 °C)
Zellengröße im Kanal 1/4	163,05 °C (max. 164,94 °C)	162,69 °C (max. 164,52 °C)

Die Anzahl der nötigen Lagen hängt von der Strömungsgeschwindigkeit ab, da diese die Dicke der thermischen Grenzschicht im Fluid beeinflusst. Im Bereich einer Strömungsgeschwindigkeit unter 1 m/s stellte sich aber bei einer Lagenanzahl von 15 Lagen keine weitere Verbesserung des Ergebnisses ein.

7.2.2. Modellvereinfachungen

Radien

An Kanten sind keine Radien vorgesehen. Innerhalb des Festkörpers ist keine nennenswerte Beeinflussung der Wärmeleitung zu erwarten. Innerhalb des Kühlkanals kann dies allerdings die Turbulenz der Flüssigkeit beeinflussen. In den simulierten Platinen konnte allerdings kein Effekt nachgewiesen werden.

Wärmevias

Die Wärmevias sind idealerweise als dünne Kupferrohre zu modellieren (Wanddicke 25µm, Durchmesser 0,5-1 mm). Die zu erwartende Schichtdicke und die Anzahl der zu modellierenden Einzelheiten stellt dabei aber sowohl vom Arbeitsaufwand als auch von der Rechenleistung eine Herausforderung dar.

Als Vereinfachung wird eine Via-durchsetzte Fläche als Körper simuliert, der eine zuvor berechnete Wärmeleitfähigkeit besitzt. Der Wärmewiderstand des virtuellen Materials setzt sich dann aus einer Parallelschaltung der Wärmewiderstände des Kupfers, des Kunststoffes der Zwischenschicht und ggf. dem Material im Inneren des Vias zusammen.

Für Wärmewiderstände gilt analog zum elektrischen Widerstand:

$$\frac{1}{R_{th}} = \frac{1}{R_{th1}} + \frac{1}{R_{th2}} + \frac{1}{R_{th3}} + \dots \tag{25}$$

$$R_{th} = \frac{l}{\lambda * A} \tag{26}$$

Für Durchbohrungen muss das Verhältnis zwischen Platinendicke und Bohrdurchmesser mindestens 8:1 betragen. Die Bohrung muss aufgrund der Platinendicke mindestens einen Durchmesser von 0,5 mm haben, der Abstand zwischen den Bohrungen 0,8 mm bzw. 0,3 mm Wandstärke.

Die Blind-Vias müssen mindestens den Durchmesser haben, den sie auch tief sind. Das heißt, um die gekühlte Kupferlage zu kontaktieren, muss der Bohrdurchmesser 1 mm betragen.

Werden sehr viele Vias nebeneinander gebohrt, besteht die Elementarzelle des entstehenden Gitters aus einem Sechseck. Der Anteil des Kupfers in der Platine muss dementsprechend nur für das eine Sechseck berechnet werden. Werden die Bohrungen der Wärme-Vias so angeordnet, dass die Elementarzelle des Gitters ein Quadrat ist, verschlechtert sich das Verhältnis um ca. 15%.

Die folgende Tabelle zeigt die Berechnung des Kupferanteils in der Via-Fläche für verschiedene Varianten. Variiert wird der Abstand der Vias zueinander (Dicke der Wandung), die Art der Elementarzelle (Sechseck, Rechteck) und der Bohrungsdurchmesser.

Variante	1	2	3	4
Bohrungsdurchmesser [mm]	0,5	0,5	0,5	1
Kupferauftrag [mm]	0,025	0,025	0,025	0,025
Dicke der Wandung [mm]	**0,3**	**0,5**	**0,8**	**0,5**
Abstand (2r_i) [mm]	**0,8**	**1**	**1,3**	**1,5**
Radius Sechseck r [mm]	0,462	0,577	0,751	0,866
Fläche Sechseck A [mm²]	0,554	0,866	1,464	1,949
Kantenlänge Rechteck 1 [mm]	1,000	1,000	1,000	1,000
Kantenlänge Rechteck 2 [mm]	0,800	1,000	1,300	1,500
Fläche Rechteck [mm²]	0,800	1,000	1,300	1,500
Fläche Bohrung [mm²]	0,196	0,196	0,196	0,785
Fläche Freiraum [mm²]	0,159	0,159	0,159	0,709
Fläche Kupfer [mm²]	0,037	0,037	0,037	0,077
Anteil Kupfer/Sechseck %	6,731	4,308	2,549	3,930
Anteil Kupfer/Rechteck %	4,663	3,731	2,870	5,105
Wärmeleitwert Kupfer W/mK	350,00	350,00	350,00	350,00
Wärmeleitwert Kunststoff W/mK	0,20	0,20	0,20	0,20
Wärmeleitwert Luft W/mK	0,02	0,02	0,02	0,02
Gesamtwärmeleitwert Sechseck W/mK	23,69	15,24	9,10	13,88
Gesamtwärmeleitwert Rechteck W/mK	16,48	13,22	10,22	17,97

Bei dichter Anordnung der Vias ergibt sich für das virtuelle Material eine Wärmeleitfähigkeit zwischen 9 und 24 W/mK, je nach Dichte der Vias. Berechnet man die Wärmeleitfähigkeit ohne die PP-Schicht zwischen Leiterbahn und gekühltem Layer, erhält man eine um ca. 2 % verringerte Wärmeleitfähigkeit. Für eine Anordnung von Vias in einer Reihe, z.B. entlang einer Leiterbahn, ergeben sich aufgrund der suboptimalen Anordnung geringere Werte.

Bei einer PP-Schichtdicke von 0,16 mm ergibt sich für die Wärmeleitfähigkeit von 15 W/mK eine Wärmedurchgangszahl von 93750 W/m²K oder 0,09375 W/mm²K. Als Vergleich dazu ergibt die Wärmeleitfähigkeit der PP-Schicht von 0,2 W/mK eine Wärmedurchgangszahl von 1250 W/m²K bzw. 0,00125 W/mm²K.

Rechnerisch ergibt sich für eine Via-besetzte Fläche von 100 mm² für 10 W eine Temperaturdifferenz von T = 10 W / (100 mm² * 0,09375 W/mm²K) ≈ 1,1 K.

7.3 Bewertung der Leistungsfähigkeit der Kühlkanallayouts

7.3.1. Parameter

Anhand von Simulation wurde die Leistungsfähigkeit der Kühlmethode untersucht. Eingangsparameter sind hier:

- Verwendetes Kühlmittel (Dichte, Wärmekapazität, Wärmeleitfähigkeit, Viskosität)
- Volumenstrom bzw. Strömungsgeschwindigkeit des Kühlmittels
- Kontaktfläche des Kühlmittels mit dem Kupfer
- Einfluss des Kanallayouts, hier z.B. interessant als Ergebnis die Wärmedurchgangszahl vom Kupfer auf den Kühlkanal

Als Ausgangsgrößen können dann gemessen werden:

- Druck am Zufluss
- Temperatur der Oberfläche (Min, Max, Durchschnitt)
- Temperatur der Flüssigkeit am Ausgang (auch errechenbar aus Eingangsparametern)

7.3.2. Ergebnisse

Geometrien mit einem hohen Anteil an parallelen Strömungen weisen ein mangelhaftes Kühlverhalten auf. Zum Einen lässt sich schwer kontrollieren, durch welche der parallelen Kanäle wie viel Flüssigkeit fließt. Unter Umständen kann sich das sehr ungleich verteilen. Zum Anderen folgt aus der geringen Strömungsgeschwindigkeit in parallelen Kanälen, dass sich schnell eine laminare Grenzschicht ausbildet, die einen effizienten Wärmeübergang verhindert. Eine Reduzierung des Kanalquerschnitts kann beide Schwierigkeiten mildern, da eine höhere Druckdifferenz zwischen verschiedenen Orten im Layout und eine höhere Strömungsgeschwindigkeit erreicht werden kann. Allerdings ergeben sich hierbei Schwierigkeiten bei der Produktion (Herstellbarkeit, Fertigungsschwankungen) und im Betrieb (Verstopfung). Ein un-

gleichmäßiger Strom oder die Verstopfung eines Kanals könnte fatal für die dort befindliche Elektronik sein.

Aus Sicht der Kühlung hat sich eine komplett einkanalige Führung als besser beherrschbar erwiesen. Die Strömungsgeschwindigkeit ist höher, was zu mehr Turbulenzen und einer besseren Wärmeabfuhr führt. Allerdings steigt hierdurch auch der nötige Druck am Kanaleingang an. In langen Kanälen können zusätzlich Schikanen eingebaut werden, um die Strömung turbulent zu machen. Dies hat einen erheblichen Einfluss auf die Kühlung, erhöht aber wiederum auch den Druck am Kanaleingang. Abhängig von Breite und Länge der Platine, verfügbarem Druck und Volumenstrom muss das Layout entsprechend angepasst werden.

Im Folgenden werden die Ergebnisse der Simulationen für verschiedene Geometrien, Strömungsgeschwindigkeiten und Öle erläutert. Aufgrund der technischen Schwierigkeiten bei Geometrien mit hoher Parallelisierung wird hier nur eine Beispielgeometrie betrachtet.

Temperatur

Wie sich zeigt, ist die Temperatur stark abhängig vom gewählten Layout und der gewählten Strömungsgeschwindigkeit. Vom gewählten Öl ergibt sich nur eine geringe Abhängigkeit. Letzteres ergibt sich dadurch, dass die Strömungsgeschwindigkeit trotz unterschiedlicher Viskositäten konstant gehalten wird. Hierdurch variiert im Gegenzug allerdings stark der Eingangsdruck (siehe unten).

Das Layout hat im Wesentlichen zwei Faktoren, die die Temperatur bestimmen. Zum Einen spielt die Kontaktfläche der Flüssigkeit mit dem Kupfer eine Rolle, die möglichst hoch sein muss. Der zweite Faktor ist die Wärmeübergangszahl, die stark von der Geometrie und den damit verbundenen Turbulenzen abhängt.

Wie in den Grafiken zu erkennen, sinkt die Temperatur beim Übergang von einer Geometrie auf eine ähnliche mit erhöhter Fläche (Geometrien 8 und 9 bzw. 5,6 und 7). Sehr deutlich ist auch der Effekt von Schikanen, die in den Kanal eingebaut werden (Geometrien 8 und 8_2 bzw. 9 und 9_2).

Beim Übergang von Geometrie 5 auf Geometrie 6 fällt auf, dass trotz der starken Erhöhung der Kontaktfläche die Temperatur der Platine nicht im gleichen Verhältnis abnimmt. Hier macht sich bemerkbar, dass durch die parallelen Kanäle Flüssigkeit langsamer strömt. Durch die hieraus resultierende dickere thermische Grenzschicht ergibt sich eine geringere Wärmeübergangszahl.
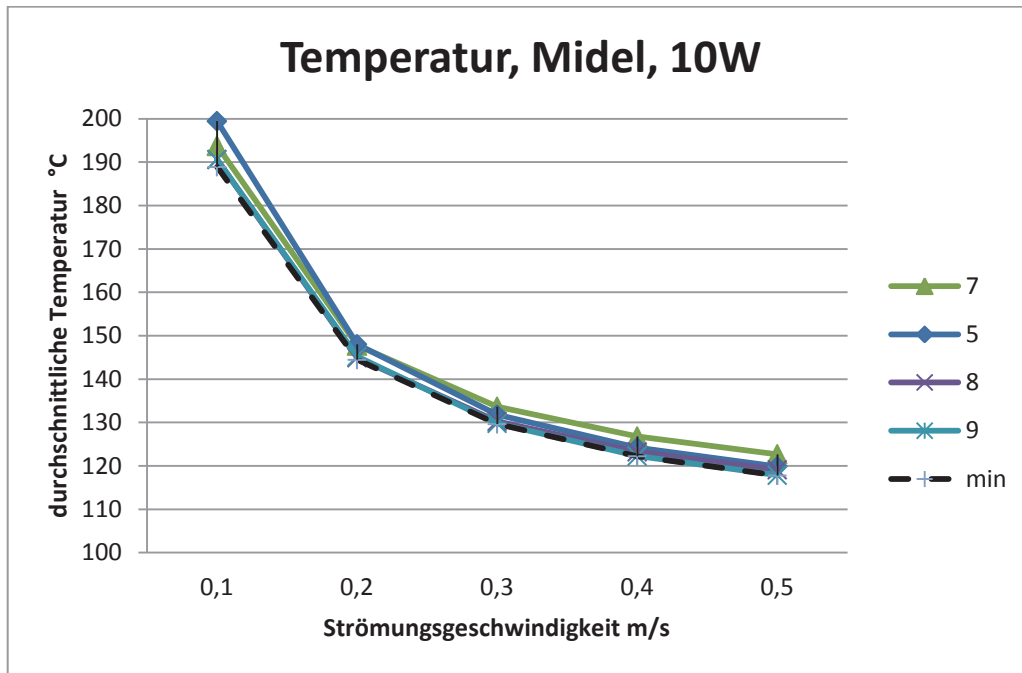
Abbildung 22: Durchschnittliche Platinentemperatur je nach Layout und Strömungsgeschwindigkeit
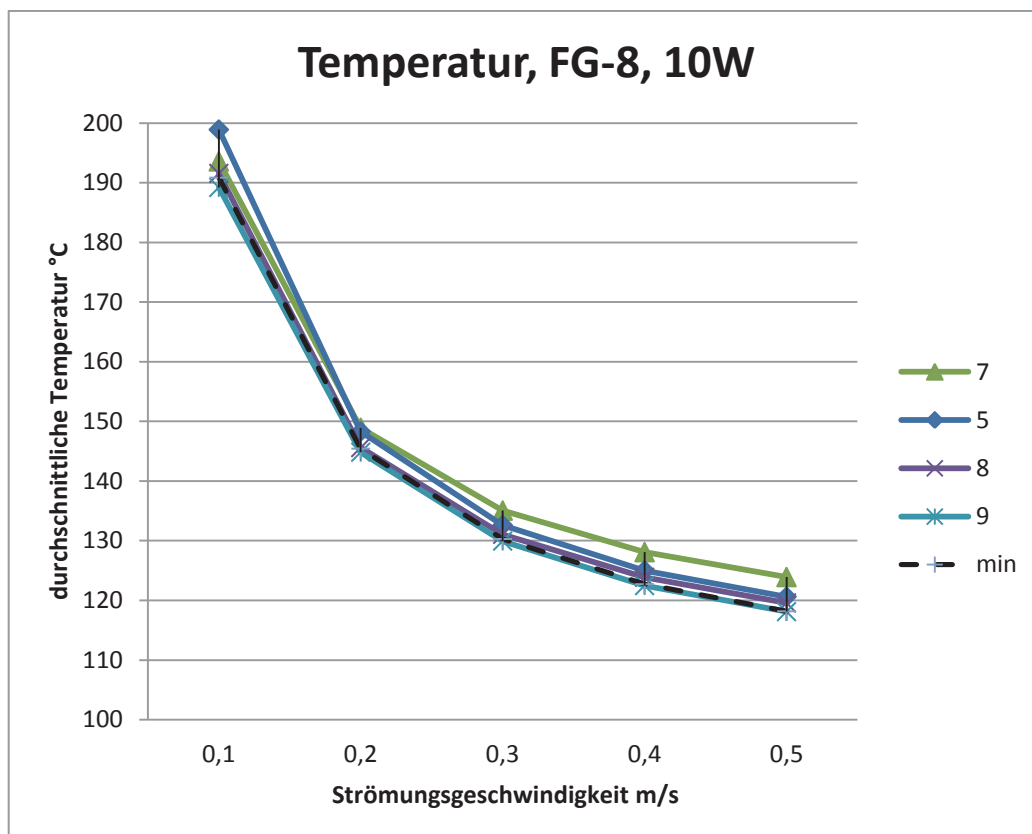
Abbildung 23: Durchschnittliche Platinentemperatur unter Verwendung eines alternativen Kühlmittels

851

Abbildung 24 verdeutlicht, dass das Kanallayout 5 mit paralleler Strömung zu einer ungleichmäßigen Oberflächentemperatur der Platine führen kann. Dies wird wie beschrieben durch eine ungleichmäßige und langsame Durchströmung der Kühlkanäle hervorgerufen. Abbildung 25 und 22 zeigen die Wärmeverteilung auf und in der Platine.
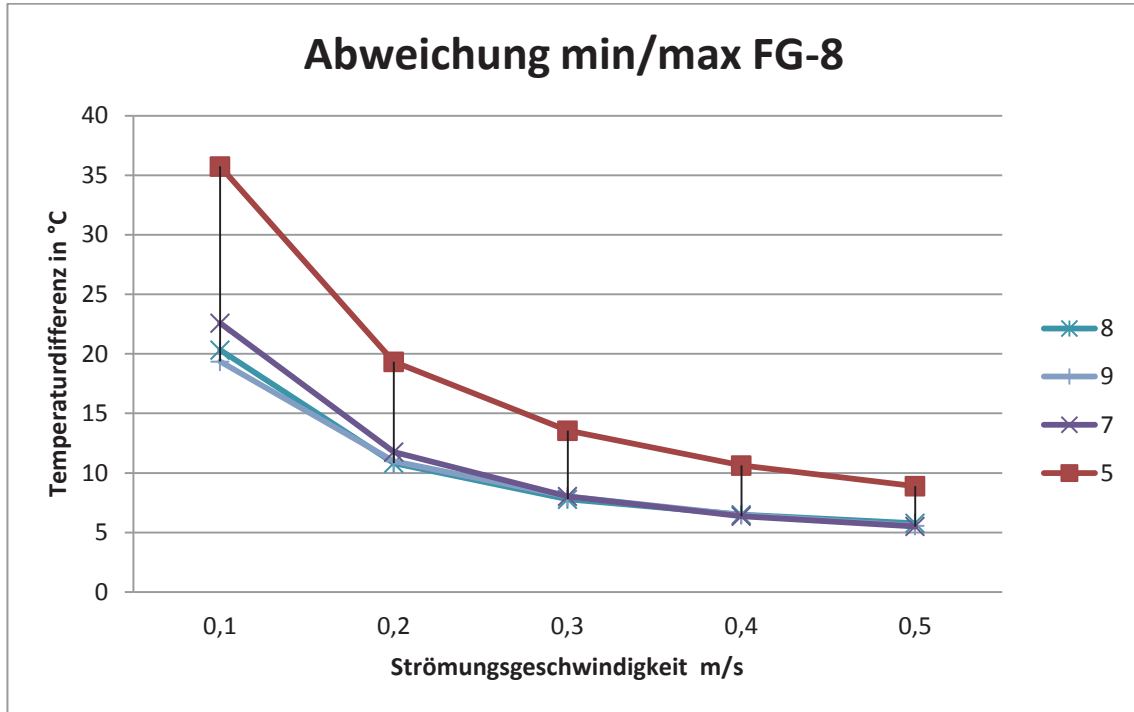
Abbildung 24: Abweichung zwischen minimal und maximal auftretender Temperatur auf der Platinenoberfläche
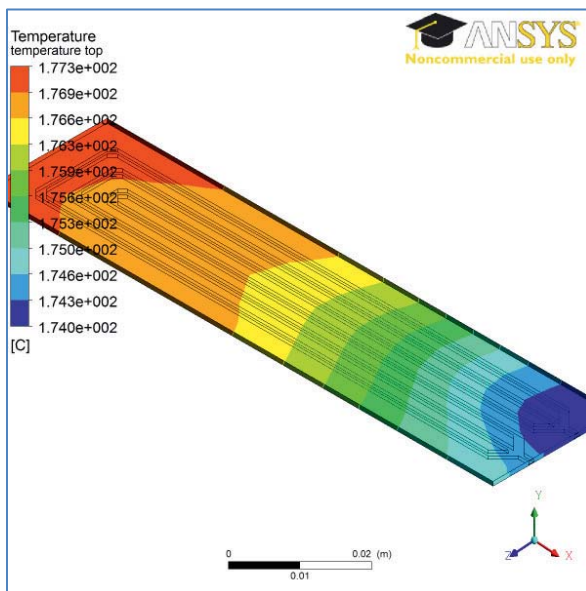
Abbildung 25: Temperatur Platine
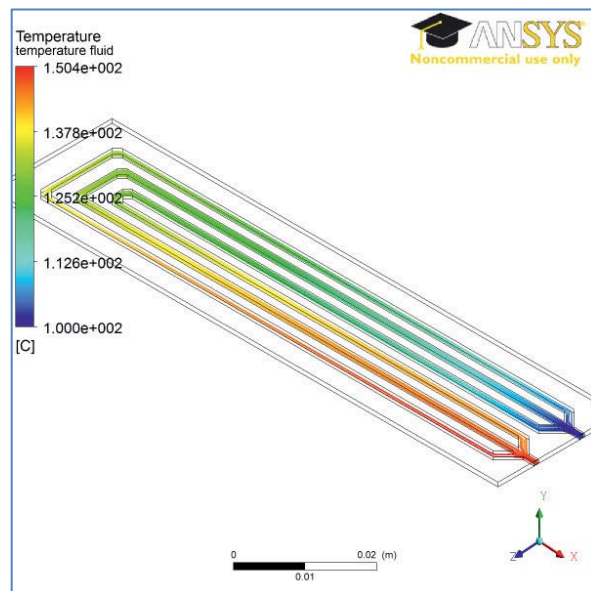
Abbildung 26: Temperatur der Kühlflüssigkeit in der Platine

Die folgenden zwei Grafiken zeigen die Wärmedurchgangszahl an der Kühlkanalwand. Es zeigt sich, dass die Platine mit nur einem seriell durchströmten Kanal den höchsten Wärmedurchgang an der Kanalwand zeigt. Die Gesamtkühlleistung ist bei den Layouts 8 und 9 allerdings besser, da die Kanalfläche wesentlich größer ist.
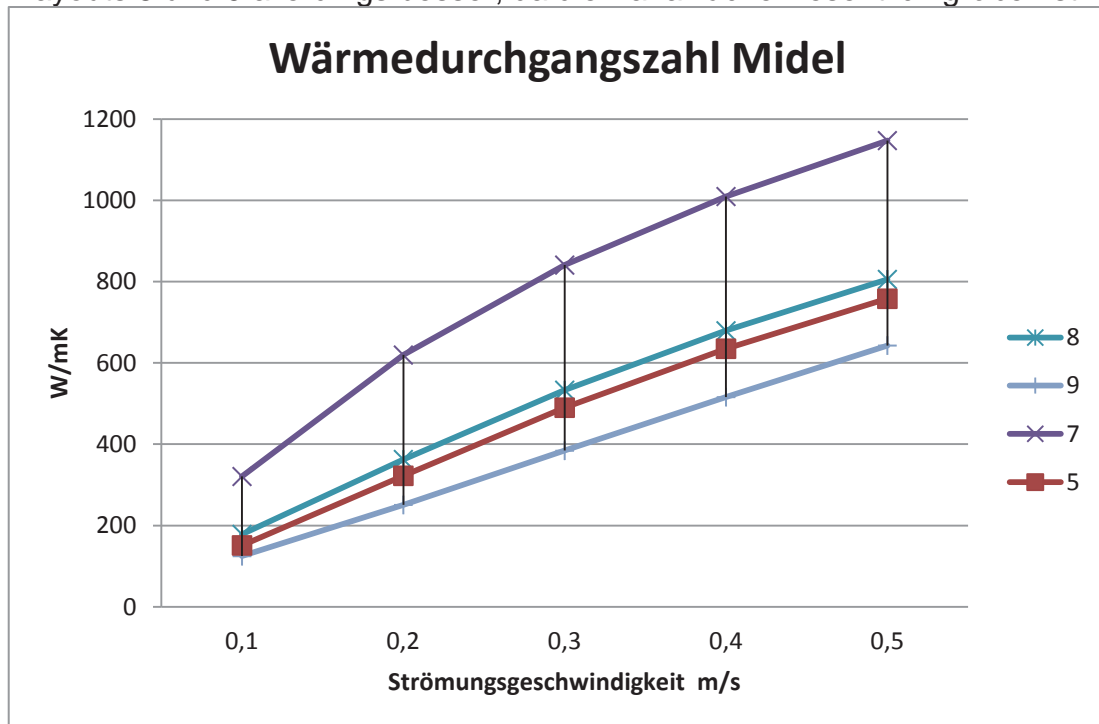
Abbildung 27: Wärmedurchgangszahl für verschiedene Kanallayouts
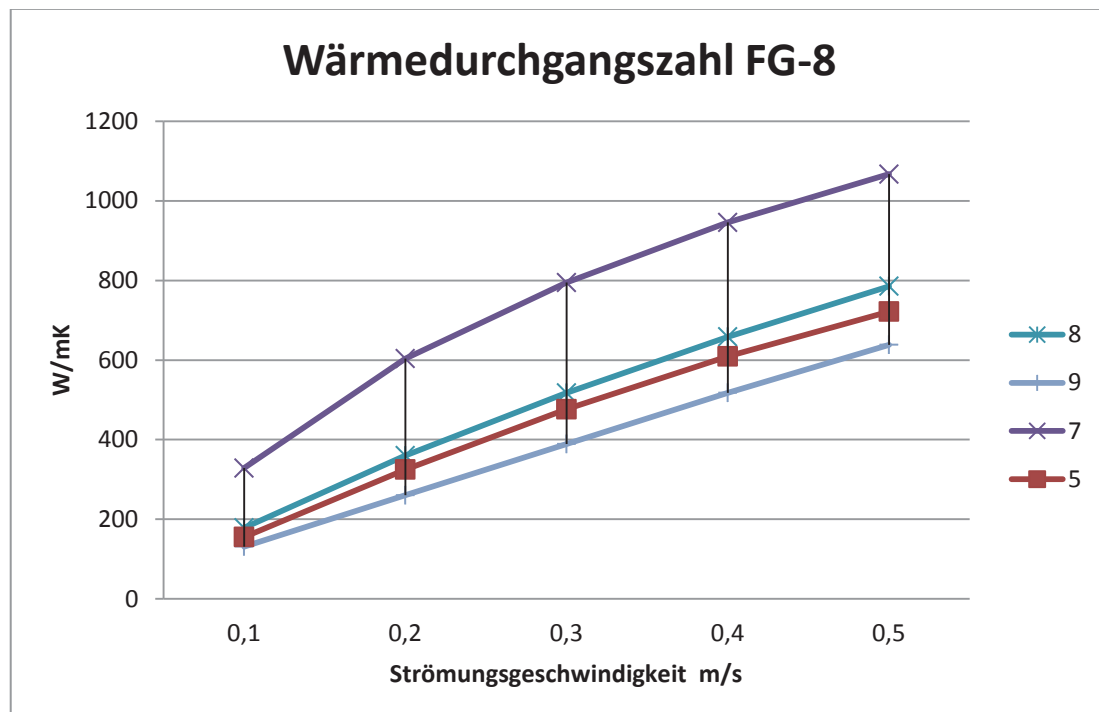
Abbildung 28: Wärmedurchgangszahl unter Verwendung eines alternativen Kühlmittels

Druck

Wie zu erwarten ist, sinkt der nötige Eingangsdruck bei zunehmender Parallelisierung des Kühlmittelstroms. Schikanen im Kanal führen hingegen zu einer starken Druckerhöhung. Die Unterschiede zwischen den Kühlmitteln FG-8 und Midel sind durch die unterschiedliche Viskosität der beiden Öle zu erklären. Bei gleicher Strömungsgeschwindigkeit der Öle ergibt sich für beide eine annähernd gleiche Kühl-leistung (Abbildung 31).
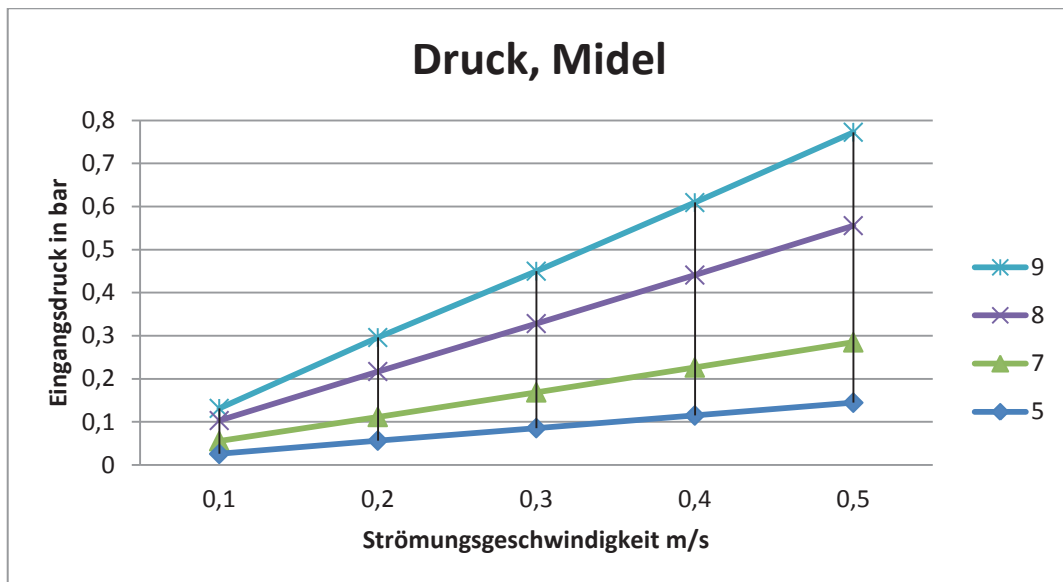
Abbildung 29: Eingangsdruck der Platinen
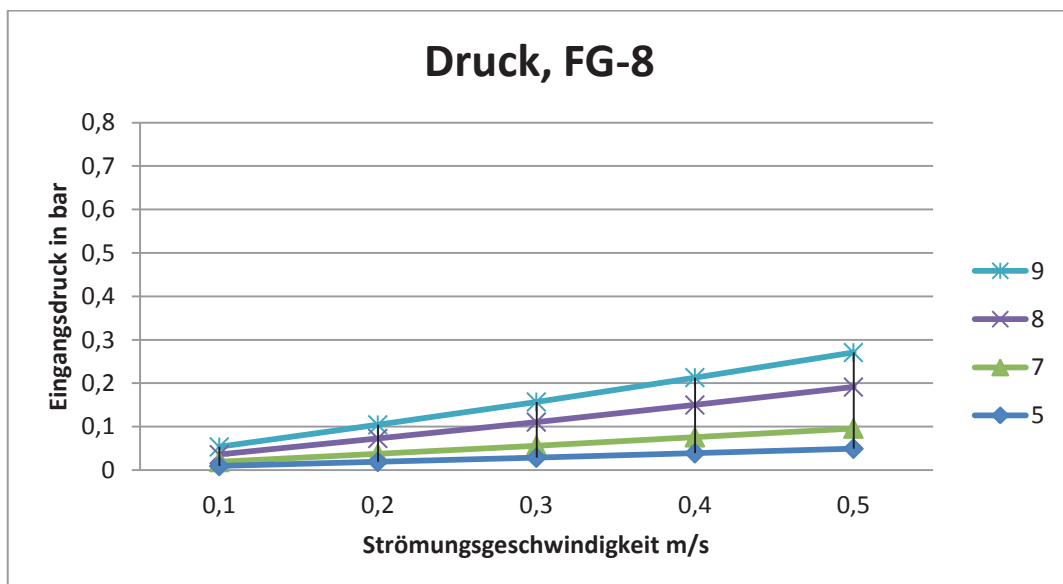
Abbildung 30: Eingangsdruck der Platinen unter Verwendung eines alternativen Kühlmittels

854
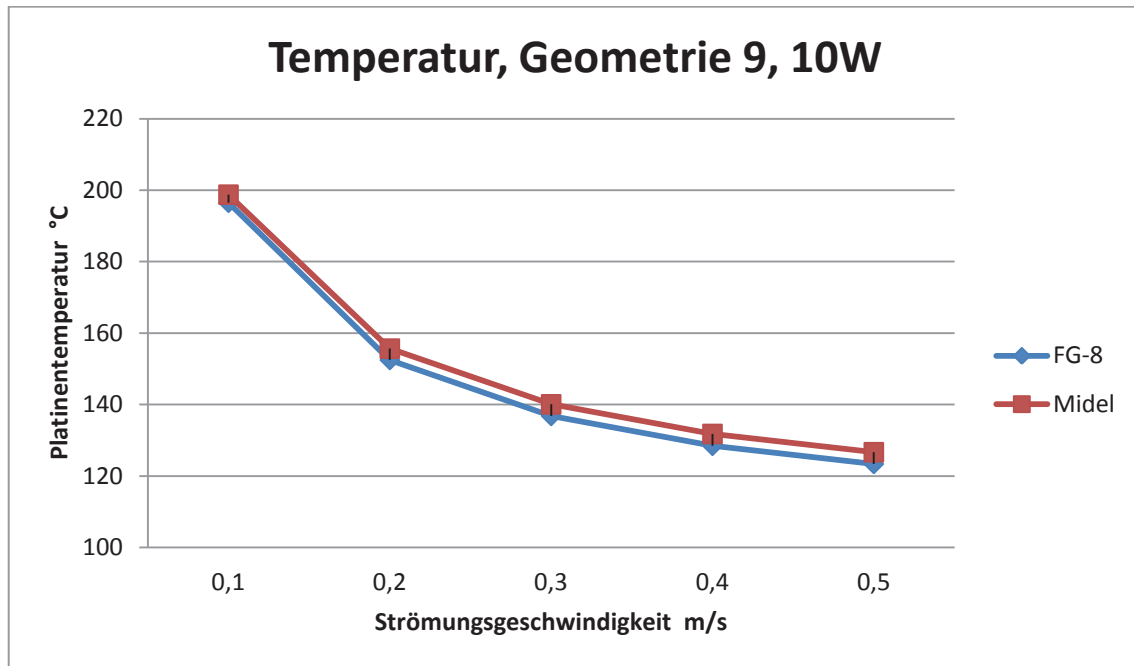
Abbildung 31: Vergleich der Platinentemperatur für verschiedene Kühlmittel

7.4 Wärmefluss von außen

Für verschiedene Isolationsarten und -dicken wurde per Simulation der Wärmedurchgang von außen bestimmt. Als ungefähre Abschätzung kann man den Wärmefluss durch die große Fläche auf der Platinen Oberseite berechnen. Mit einer Kantenlänge von 100 mm x 25 mm und einer Isolation von 10 mm mit einem Wärmeleitwert von 0,06 W/mK ergibt sich ein Wärmestrom von 2,25 W. In der Realität wird der Wärmestrom oberhalb des Wertes liegen, da die Ränder vernachlässigt wurden. Des Weiteren wird in der Realität Wärme von Ober- und Unterseite eingetragen, d.h. der berechnete Wert verdoppelt sich.

$$\dot{Q} = \lambda * \frac{A}{l} * \Delta T$$

2 * 0,06 W/mK * 0,10 m * 0,025 m * 150 K/0,01 m = 2 * 2,25 W = 4,5 W

In der Simulation wurde ein Wert von 4,97 W bei einer Temperaturdifferenz zwischen Platine und Umgebung von 115 K bestimmt. Wird der Wärmeleitwert der Isolation auf einen Wert von 0,02 W/mK gesenkt, reduziert das den Wärmeeintrag auf 2,56 W.
Um den Einfluss der Isolation abzuschätzen, wurden Vergleichssimulationen durchgeführt. Die Dicke der Gesamtisolation betrug jedes Mal 10 mm. Im ersten Fall bestand diese vollständig aus Silcapor High (0,02 W/mK), im zweiten Fall mit innen und außen jeweils einer Silikonschaumschicht (0,06 W/mK) von 1 mm Stärke und im dritten Fall mit einer Silikonschaumschicht von 2 mm Stärke. Die Folgenden Abbildung verdeutlichen die Ergebnisse:

855
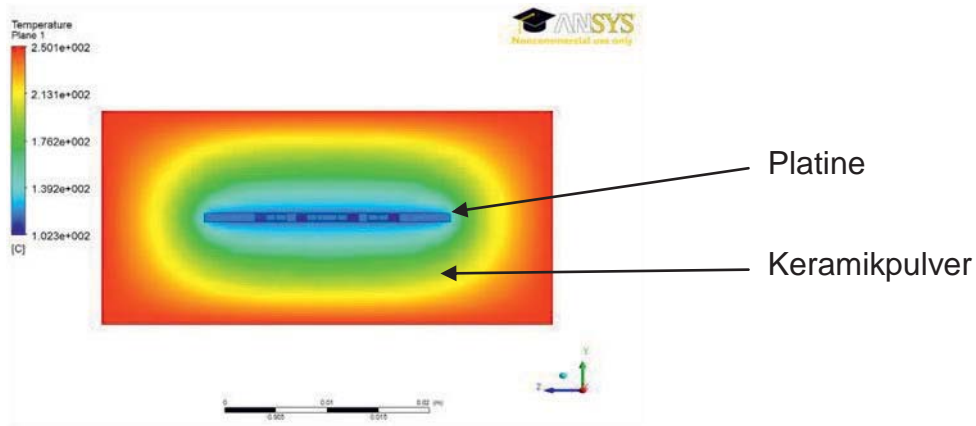
Abbildung 32: Isolation aus Keramikpulver Silcapor High,
Wärmeeintrag 2,56 W
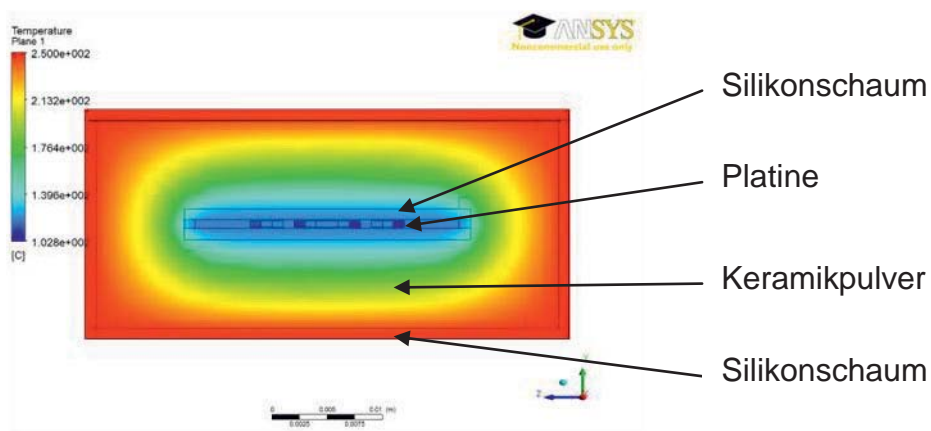
Abbildung 33: Isolation aus Keramikpulver Silcapor High und 1 mm Silikonschaum,
Wärmeeintrag 2,98 W
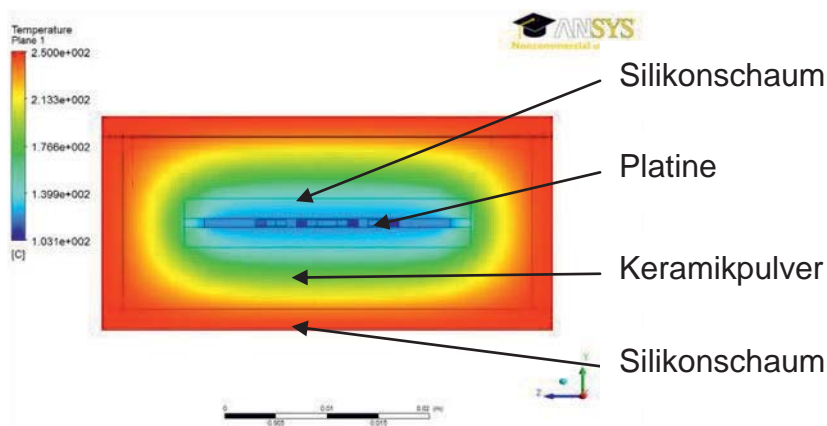
Abbildung 34: Isolation aus Keramikpulver Silcapor High und 2 mm Silikonschaum,
Wärmeeintrag 3,39W

8 Validierung der Simulation

Zur Untersuchung der Kühlleistung wurde ein Versuchsstand aufgebaut. Dieser besteht aus einer drehzahlgeregelten Pumpe, einem Ausgleichsbehälter, einem Wärmetauscher zur Kühlung oder Beheizung des Kühlmittels und Messtechnik. Der Kühlkreislauf ist bis zu einer Temperatur von 180 °C ausgelegt. Abbildung 35 und Abbildung 36 zeigen ein Foto und den schematischen Aufbau der Versuchseinrichtung.

Die Pumpleistung lässt sich im Bereich von 0,5 ml/s bis 5 ml/s einstellen. Mittels Temperatursensoren wird die Differenztemperatur zwischen Ein- und Auslass der Platine ermittelt. Aus Pumpleistung, Temperaturdifferenz und Wärmekapazität des Kühlmittels lässt sich anschließend die abgeführte Wärmemenge berechnen. Mittels eines Differenzdrucksensors wird der Druck zwischen Ein- und Auslass der Platine gemessen.

Die Steuerung des Versuchsstands und die Messdatenaufzeichnung sind mittels LabView implementiert. Neben den Daten des Kühlkreislaufs besteht die Möglichkeit, Daten von bis zu 10 Temperatursensoren auf der Platine aufzuzeichnen.

Zur Validierung bisheriger Simulationen wurden die Platinen bei Raumtemperatur mit Wärmeleistung beaufschlagt und mittels einer Wärmebildkamera beobachtet. Die Platinen sind mit 10 SMD Widerständen mit 0,25 W Nennleistung bestückt, die mit einer Wärmeleistung von 0,5 W betrieben werden. Ein zweiter Platinentyp ist mit zwei Leistungstransistoren mit interner Temperaturbegrenzung bestückt, die im Kurzschlussbetrieb betrieben werden. Anhand der angelegten Spannung und des Stroms wird die abgegebene Leistung berechnet.
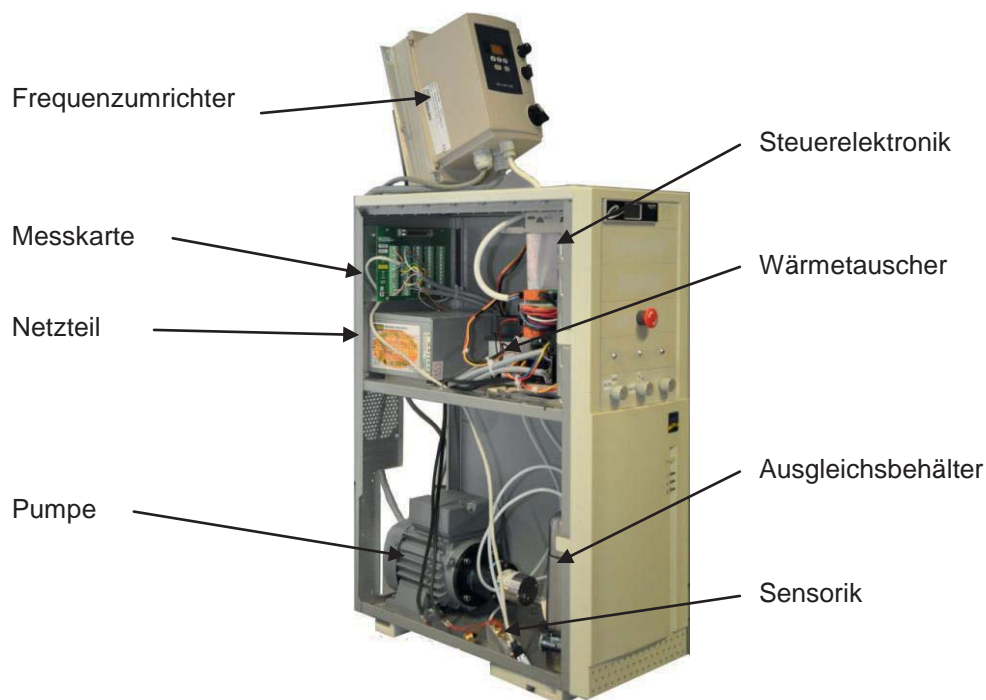
Abbildung 35: Foto des Versuchsstandes zur Platinenkühlung
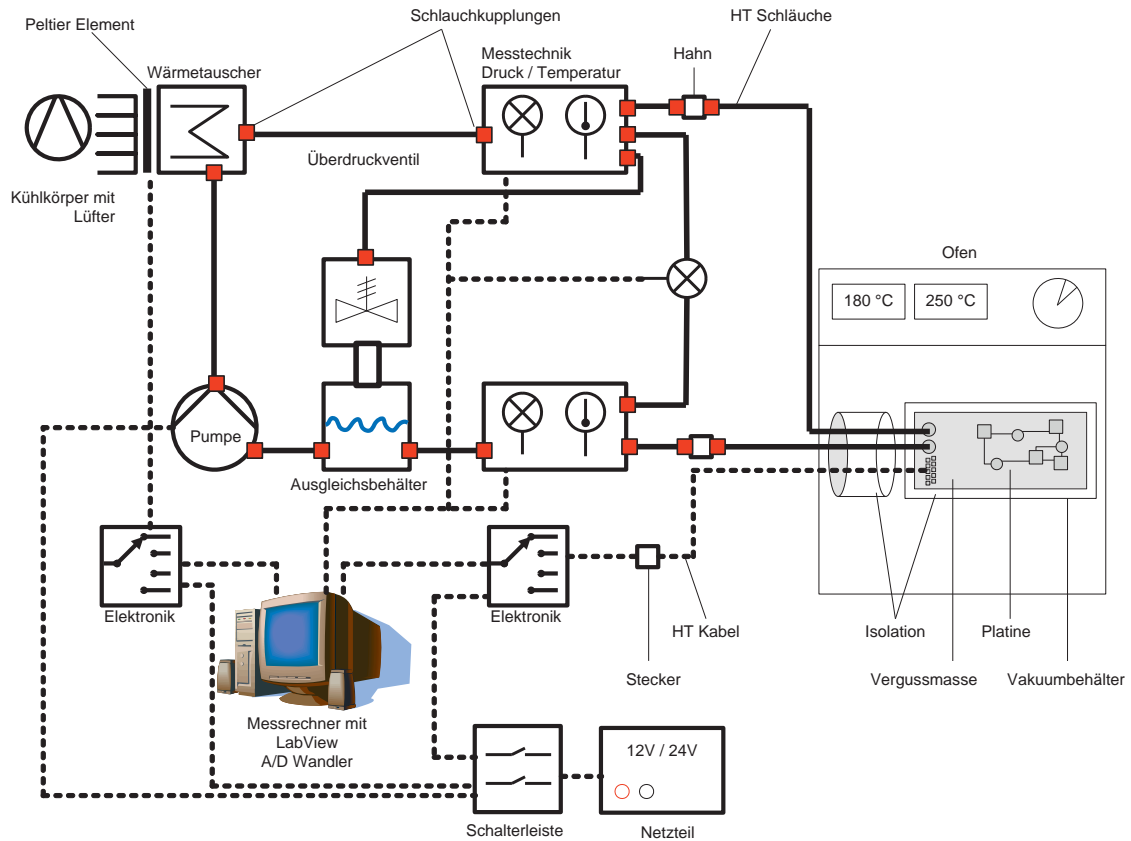
Abbildung 36: Schema des Versuchsstandes

Abbildung 37 zeigt das Wärmebild und das Simulationsergebnis einer Testplatine bei Raumtemperatur. Das Kühlmittel hat eine Temperatur von 50 °C, die Durchfluss-menge beträgt 0,5 m/s. Für die Versuche wurde aufgrund der einfachen Handhabung Wasser verwendet. Die Wärmeabgabe an die Umgebung wurde in der Simulation mitberücksichtigt. Die Werte der Simulation stimmen dabei mit den gemessenen Temperaturen überein. Gleiches gilt für die berechneten und simulierten Drücke zwischen Ein- und Auslass der Platine. Diese lagen im Bereich um 0,1 bar.
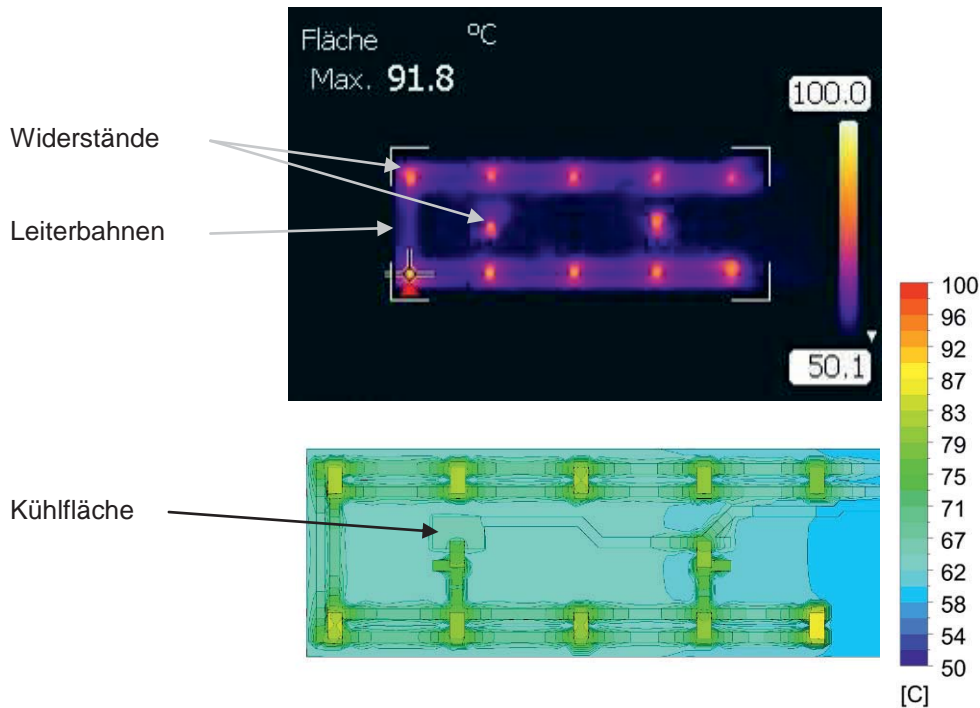
Abbildung 37: Wärmebild und Simulationsergebnis einer Testplatine

9 Schläuche

Als Schlauchverbindungen für das Kühlmittel kommen Metallwellschläuche und wärmebeständige Kunststoffschläuche in Frage.

Metallwellschläuche sind in verschiedenen, vorkonfektionierten Durchmessern, Längen und Anschlusstypen erhältlich. Der minimale Innendurchmesser beträgt in der Regel 6 mm. Aufgrund der geringen Fließgeschwindigkeit ist ein dünnerer Durchmesser wünschenswert.

PTFE (Teflon) Schläuche bleiben bis zu einer Temperatur von 260 °C stabil. Der maximale Druck wird für einem Schlauch mit 2 mm Innendurchmesser und einer Wandstärke von 1 mm mit ca. 16 bar angegeben. Bei einer Temperatur von 250 °C ergibt sich ein Minderungsfaktor von 0,28, d.h. ein Druck von 4,5 bar. Mit einer Metallumflechtung kann dieser Wert deutlich erhöht werden, allerdings müssen die Schläuche dann fertig konfektioniert geliefert werden. Da das Kühlmittel innerhalb des Schlauches ohnehin keine hohe Temperatur erreichen soll, sind diese Werte ausreichend. PTFE-Schläuche sind nicht diffusionsdicht gegen Gase, d.h. sie können nicht als Vakuumisolation eingesetzt werden. Der geringe Innendurchmesser ist notwendig, um eine hohe Fließgeschwindigkeit und somit eine geringe Aufheizung des Kühlmediums im Kreislauf zu gewährleisten.

10 Herstellung der Platinen

Wie im Meilensteinbericht 1 beschrieben, werden die innenliegenden Kühlkanäle hergestellt, indem in zwei Kupferflächen Kanäle eingebracht werden. Diese Kupferflächen werden anschließend verklebt oder mit einem Prepreg verpresst. Die Verfahren des Verklebens und des Verpressens weisen prozesstechnisch wesentliche Unterschiede auf.

Beim Verkleben wird auf eine Kupferlage ein Kleber aufgetragen. Die Fläche kann dabei eine beliebige Form aufweisen. Dieses Verfahren lässt folglich beliebige Formen für eingebrachte Kühlkanäle zu. Während das Verfahren bei Platinen mit FR4 Prepreg gut beherrschbar ist, zeigte sich bei Polyimidplatinen, dass kommerziell erhältliche Klebstoffe nicht zuverlässig funktionieren.

Für erste Prototypen wurden die Kupferlagen verklebt. Abbildung 38 zeigt den schematischen Aufbau. Im Gegensatz zum Meilensteinbericht 1 wurde nur eine gekühlte Lage verwendet, um den Einfluss des Abstandes der Platinenoberfläche zur gekühlten Kupferlage zu untersuchen. Es gelang allerdings nicht, die Dichtigkeit der Platinen zu gewährleisten. Abbildung 39 zeigt Bilder der Verklebung der Kupferlagen. Es ist zu erkennen, dass sich die verklebten Lagen voneinander abgelöst haben und die Klebefläche beschädigt ist.

Die Ablösung ist durch das Auftragen einer zu geringen Klebermenge verursacht worden. Wurde während der Herstellung allerdings die Klebemenge erhöht, drang dieser beim Verpressen weiterer Lagen in die Kühlkanäle ein. Der Grund ist die sehr geringe Viskosität des Klebstoffes bei den nötigen Prozesstemperaturen der weiteren Verpressvorgänge. Es konnten keine geeigneten Klebstoffe gefunden werden, die dieses Verhalten nicht aufweisen.

Beim Verpressen der Kupferlagen mit einem Prepreg wird die Form der Kühlkanäle im Kupfer auch im Prepreg ausgefräst. Dies bedeutet, dass für den Kanal grundsätzlich keine Formen verwendet werden können, die Teile aus dem Prepreg komplett umschießen, da diese dann vom Prepreg abgetrennt werden. Darüber hinaus können keine dünnen Stege produziert werden, da sie beim Handling der Nutzen verrutschen (Abbildung 40). Mögliche Kanallayouts werden dadurch weiter eingeschränkt.

Oberfläche mit guter Küh-

Gekühlte Kupferlage

Elektrische Isolation

Vias

Weniger gekühlte Oberflä-
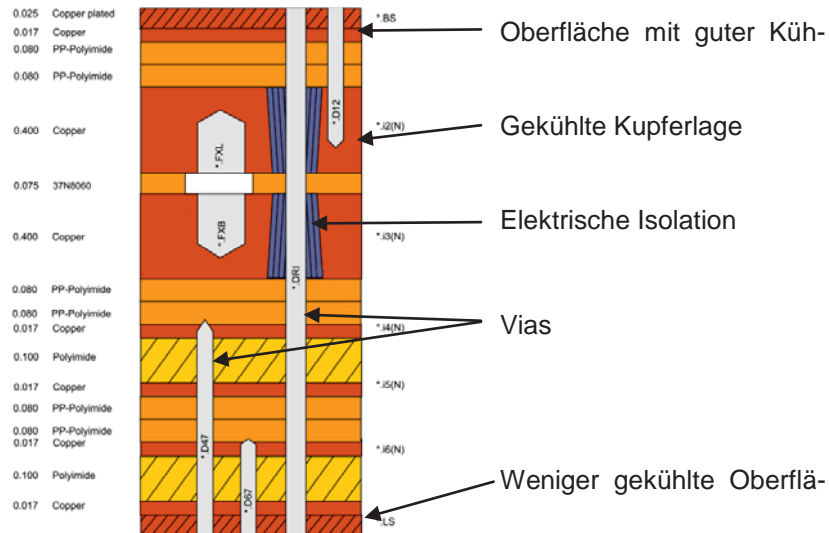
Abbildung 38: Schematischer Aufbau der Versuchsplatinen

Ablösung der Kupferlagen

Kühlkanal

Passform für Anschlüsse

Defekt im Kle-   Thermische
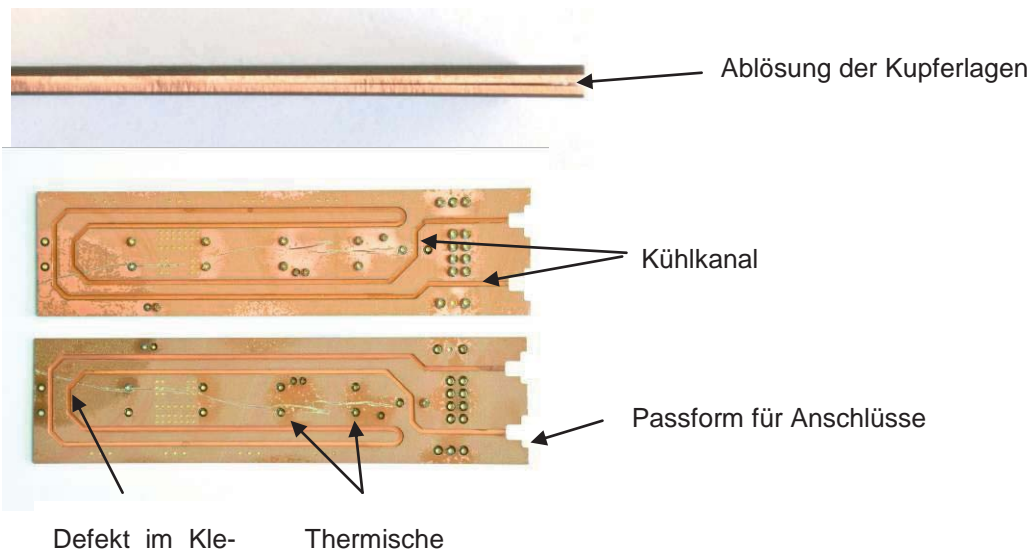
Abbildung 39: Schaden an der Verklebung der Kupferlagen

Polyimid Prepreg vor dem Verpressen verrutscht
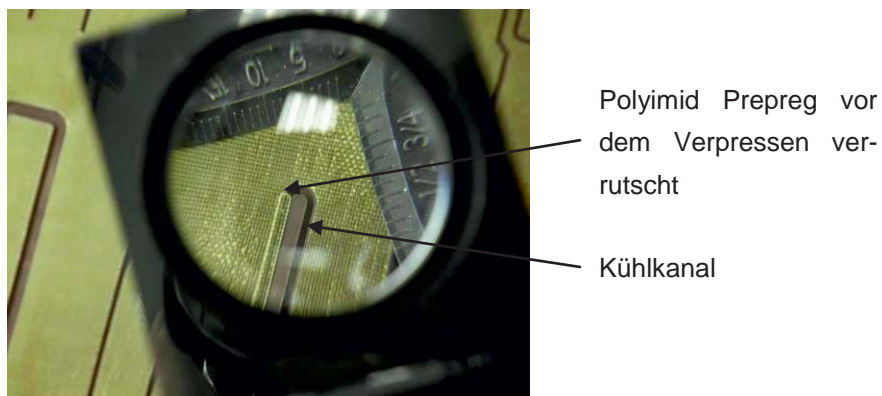
Kühlkanal

Abbildung 40: Einige Kanallayouts verursachen ein Verrutschen der Polyimidschicht

Die Produktionsanlagen von Platinenherstellern sind auf die Erzeugung sehr kleiner Strukturen optimiert. Das Fräsen breiter Kühlkanäle dauert sehr lange und ist dadurch vergleichsweise teuer. Es wurde versucht, externe Hersteller für die Erzeugung der Kühlkanäle zu qualifizieren, allerdings stellt die Einbringung 200 µm tiefer Kanäle in eine 300 µm düne Kupferfolie eine Herausforderung an die Präzision der eingesetzten Maschinen dar. Alle durchgeführten Versuche wiesen erhebliche Schäden an den Mustern auf. Abbildung 41 zeigt ein Beispiel: Beim Fräsen des Kanals wurde die 100 µm dicke Restschicht verformt, was ein anschließendes Laminieren in der Platine unmöglich macht. Weitere Schäden ergaben sich durch das Aufreißen der Kupferlage durch den Fräser. Aufgrund der höheren Prozesssicherheit wurde der Kupferkanal folglich weiterhin vom Platinenhersteller erzeugt.

Abdruck des Kupferkanals auf der Rückseite der Kupferfolie
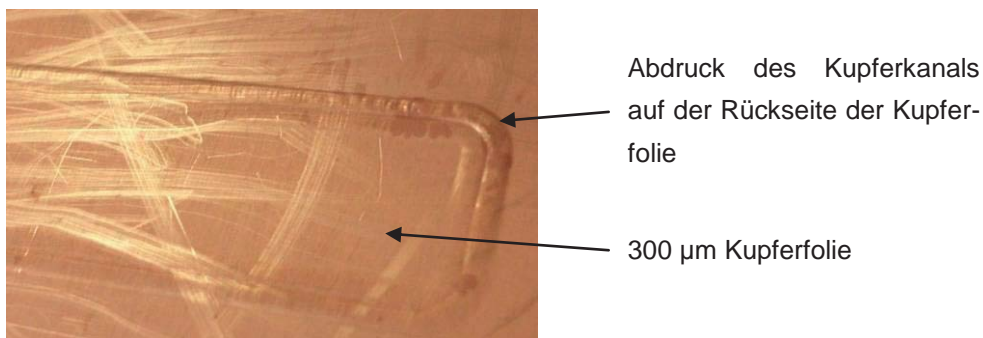
300 µm Kupferfolie

Abbildung 41: Fehlversuch beim Einbringen der Kühlkanäle in die Kupferfolie

Um das Eindringen des Prepregs in den Kühlkanal während des Verpressens zu verhindern, wurde auf der Kupferfolie ein Steg neben den Kühlkanälen erzeugt. Dieser erhöht die Prozesssicherheit und ermöglicht die Herstellung schmalerer Kanäle (Abbildung 42). Die Platinen konnten auf diese Weise erfolgreich hergestellt werden.

Kühlkanal

Steg

Abbildung 42: Ein Eindringen des Prepregs in den Kanal wird durch einen Steg verhindert

11 Kühlmittel

11.1.1. Mögliche Kühlmittel

Wasser kommt aufgrund der hohen Temperaturen nicht in Frage. Auch ein Wasser-Glykol-Gemisch entwickelt bei einer Temperatur von 250 °C einen erheblichen Dampfdruck.

Öle sind für einen weiten Temperaturbereich erhältlich, auch deutlich über 300 °C hinaus. Die Wärmekapazität ist geringer als die von Wasser und die Viskosität höher. Zusätzlich können Öle eine Gefahr für Mensch und Umwelt darstellen, allerdings sind auch weitgehend ungiftige Thermoöle verfügbar.

Um das Kühlmittel zu bewegen, ist eine Pumpe notwendig. Da der Kühlkreislauf bei einer Temperatur von 250 °C wieder anlaufen können muss, muss die verwendete Pumpe diesen Temperaturen standhalten. Auf dem Markt sind zwar Pumpenköpfe verfügbar, die dem entsprechen, allerdings keine Antriebe. Für den Bohrstrang müssten entsprechende Elektroantriebe entwickelt werden, was den in diesem Projekt leistbaren Aufwand übersteigt.

Eine weitere Alternative stellen Metalle dar, die schon bei Raumtemperatur flüssig sind. Beispiele hierfür sind Quecksilber und eutektische Legierungen wie NaK und GaInStan.

11.1.2. Quecksilber

Quecksilber ist ein giftiges Schwermetall und verdampft bereits bei Raumtemperatur. Es ist stark gesundheitsschädlich und umweltgefährdend und darf ohne besondere Sicherheitsvorkehrungen nicht verwendet oder gelagert werden. Die Verwendung ist gesetzlich stark eingeschränkt.

11.1.3. NaK-78

NaK ist ein Eutektikum aus Natrium und Kalium mit einem Schmelzpunkt von ca. -11 °C. Es wird beispielsweise zur Kühlung von Kernreaktoren eingesetzt. Es reagiert explosiv mit Wasser und Sauerstoff. Der Zündpunkt liegt bei ca. 120 °C, sofern es als Flüssigkeit vorliegt, entzündet sich aber schnell selbst in Tropfenform. Im Falle eines Brandes ist es nicht mit CO_2, Halon, Löschpulver oder Schaum löschbar. Feuerlöschdecken sind aufgrund der hohen Temperaturen nicht verwendbar. Nach Angaben verfügbarer Sicherheitsdatenblätter verursachen bereits Mengen unter 1 g (0,8 ml) möglicherweise tödliche Explosionen. Von weiteren Versuchen mit NaK wurde daher abgesehen.

11.1.4. GalInStan

GalInStan ist ein Eutektikum aus Gallium, Indium und Zinn. Der Schmelzpunkt liegt bei ca. -19 °C. Der Siedepunkt liegt bei ca. 1300 °C. Es weist mit 6,44 g/cm³ eine hohe Dichte auf. Die Wärmeleitfähigkeit liegt bei 16,5 W/mK (zum Vergleich Kupfer: 400 W/mK, Stahl: 15 W/mK).

GalInStan ist weitgehend unlöslich in Wasser und organischen Lösungsmitteln und daher ungiftig. Es neigt allerdings dazu, Oberflächen zu benetzen (auch Glas) und geht Legierungen mit anderen Metallen ein. Insbesondere lässt sich Aluminium in GalInStan exotherm auflösen.

Versuche haben gezeigt, dass es mit Messing reagiert, was nach Herstellerangaben von der verwendeten Messinglegierung abhängig ist. Gleiches gilt laut Hersteller grundsätzlich auch für Kupfer, wobei Reaktionen mit Kupfer im Allgemeinen seltener auftreten. Nach Herstellerangaben kann eine mögliche Reaktion durch das Bilden einer Kupferoxidschicht verhindert werden. Genauere Angaben waren nicht zu erhalten. In den durchgeführten Versuchen benetzte GalInStan zwar Kupfer, reagierte aber nicht damit. Abbildung 43 zeigt exemplarisch die Beispiele einer Messingmutter und eines Kupferkanals, die 48 Stunden bei 150 °C mit GalInStan benetzt wurden.
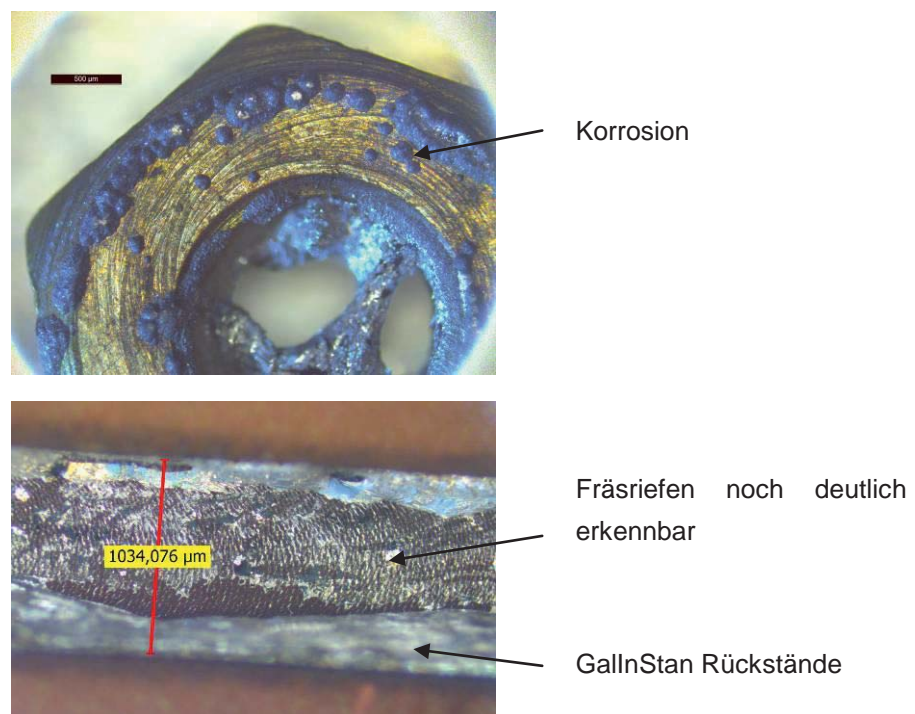
Abbildung 43: Messing reagiert mit GalInStan, das verwendete Kupfer nicht

Der Vorteil von Flüssigmetallen als Kühlmittel liegt in der Möglichkeit, eine elektromagnetische Pumpe ohne bewegliche Teile zu verwenden. Grundsätzlich gibt es dafür zwei Realisierungsvarianten.

Es existieren elektromagnetische Pumpen zum Fördern von Metallschmelzen, die ein elektrisches Wechselfeld erzeugen und nach dem Prinzip eines Kurzschlussläufermotors funktionieren. Die Regelung ist vergleichsweise aufwendig und kommerzielle Systeme sind aufgrund des genannten Anwendungsfeldes nicht zur Integration in einen Bohrstrang geeignet.

Ein weniger effizientes, aber einfaches Verfahren ist das Bewegen des Metalls mittels der Lorentzkraft. Eine Umsetzung einer Flüssigmetallkühlung für CPU-Kühler wurde 2011 von der Firma Danamics angeboten, ist aber heute nicht mehr verfügbar. Abbildung 44 zeigt ein Bild des realisierten Versuchsaufbaus. Der magnetische Kreis kann über einen Permanentmagneten oder gewickelte Spulen geschlossen werden. Der Strom senkrecht zum Magnetfeld wird über Messingschrauben angeschlossen. Senkrecht zu beiden Feldern wird das Flüssigmetall zugeführt. Zwei weitere Messingschrauben dienen der Messung des Kurzschlussstroms im Flüssigmetall, der durch die Lorentzkraft verursacht wird.

Die notwendige Stromstärke beträgt mehrere Ampere. Die Wärmeverluste sind entsprechend hoch. Die Versuche ergaben gleichzeitig eine sehr geringe Pumpleistung. Der Ansatz wurde nicht weiter verfolgt.
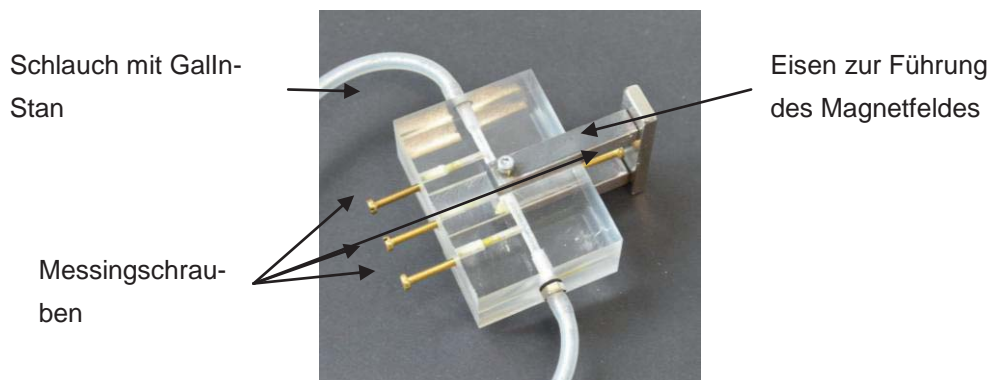
Abbildung 44: Versuchsaufbau als elektromagnetische Pumpe, zur besseren Übersichtlichkeit ohne gewickelte Spule

12 Mechanische Pumpen

12.1 Pumpkonzepte

Für die Förderung von Flüssigkeiten wird in der Regel eine Pumpe eingesetzt. Bei statisch arbeitenden Pumpen und dem Einsatz von inkompressiblen Fluiden wird auch von Verdrängerpumpen gesprochen. Diese fügen dem Fluid, zum Beispiel durch Volumenänderung des Arbeitsraumes, Energie zu. Es wird eine Vielzahl von

Bauarten mit verschiedenen Eigenschaften unterschieden. Einige relevante Bauformen sollen hier angesprochen werden.
Hierzu zählen:

- Drehkolbenpumpen
- Schraubenpumpen
- Flügelzellenpumpen
- Zahnradpumpen
- Hubkolbenpumpen
- Membranpumpen

Durch die Vorgabe einer geringen Bauteilgröße und die Förderung eines relativ geringen Volumenstromes können einige der erwähnten Pumpen ausgeschlossen werden. In Abbildung 45 ist der Aufbau einer Drehkolbenpumpe zu sehen. Die Rotoren stehen nie in Kontakt zueinander. Dadurch ergeben sich definierte Spalte, in denen Strömungsverluste auftreten. Aufgrund dieser Verluste werden Drehkolbenpumpen bevorzugt für große Volumenströme sowie höhere Viskositäten eingesetzt [Far04, S. 12]. Zudem wird neben dem eigentlichen Pumpenraum ein weiterer Raum zur Synchronisation mittels Zahnrädern benötigt.
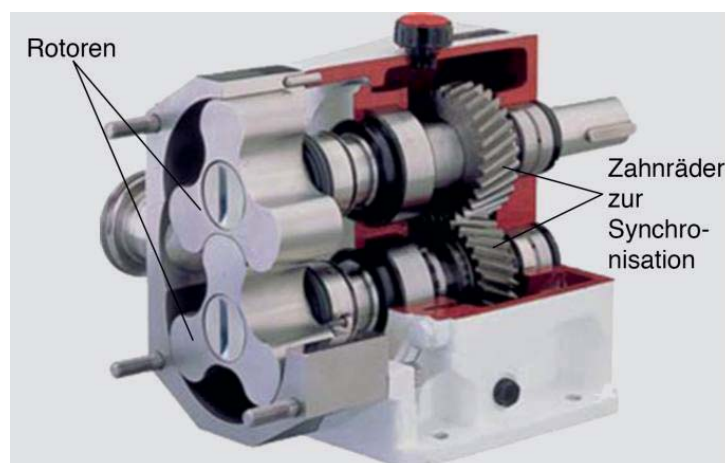
Abbildung 45: Drehkolbenpumpe, Quelle:[Dit12] leicht modifiziert

Die Schraubenpumpen fördern das Fluid ohne Änderung des Verdrängungsraumes und erzeugen somit nahezu keine Volumenstrompulsation. Jedoch ist die Fertigung relativ kostenaufwendig [Far04, S. 165]. Ein Vorteil der Flügelzellenpumpen ergibt sich durch ihren einfachen Aufbau. Zudem ist die Fertigung in kleinen Baugrößen sehr gut möglich. Wie in Abbildung 46 zu sehen, werden Schieber durch die Fliehkraft gegen die Außenwände gedrückt, wofür jedoch eine gewisse Drehgeschwindigkeit nötig ist. Deshalb werden Flügelzellenpumpen mit einer relativ hohen Drehzahl betrieben [Far04, S. 97]. Dadurch ergibt sich wiederum ein hoher Volumenstrom. Zahnradpumpen decken ein großes Arbeitsspektrum ab und überzeugen durch einen einfachen Aufbau [Ebn11, S. 4]. Dies gilt ebenso für Hubkolbenpumpen, welche für

feinste Dosieraufgaben sowie für große Volumenströme eingesetzt werden können [Som10].
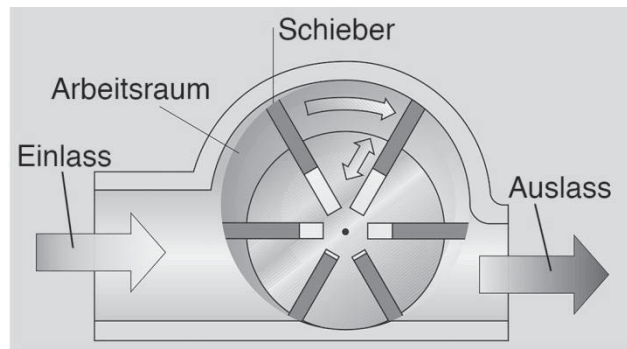
Abbildung 46: Flügelzellenpumpe, Quelle:[Sch12] leicht modifiziert

Schon nach dieser ersten Betrachtung stellt sich heraus, dass die Drehkolbenpumpe durch das relativ große Bauvolumen ungeeignet ist. Die Schraubenpumpe scheint grundsätzlich in Frage zu kommen. Aufgrund der relativ geringen Anforderungen an die Volumenstrompulsation sind jedoch kostengünstigere Bauformen vorzuziehen. Bei der Flügelzellenpumpe ist schnell ersichtlich, dass durch die hohe Drehzahl die Realisierung eines kleinen Volumenstromes problematisch ist. Für die Zahnradpumpe ist der Antrieb problematisch. Motoren mit einer möglichen Umgebungstemperatur von 250 °C sind heute nicht verfügbar. Im Folgenden wird die Hubkolbenpumpe und die Membranpumpe näher untersucht.

12.2 Hubkolbenkumpe

12.2.1. Auslegung
Die Vor- und Nachteile der Hubkolbenpumpe lauten:

- relativ einfache Fertigung
- großer Anwendungsbereich
- viele unterschiedliche Antriebskonzepte
- unkomplizierte Abdichtung durch zylindrische Fläche
- erhöhte Anfälligkeit durch viele bewegliche Bauteile (Kolben, Ventile)
- hohe Volumenstrompulsation

Auch die schmale und längliche Form kommt dem vorhandenen Bauraum positiv entgegen. Die hohe Volumenstrompulsation lässt sich durch eine doppeltwirkende Hubkolbenpumpe und größere Hubfrequenzen vermindern.

Zunächst werden einige Hauptabmessungen für den Betrieb bestimmt. Wie zuvor bereits berechnet, soll ein Volumenstrom von $6 \cdot 10^7$ m^3/s erreicht werden. Auch bei

der Hubkolbenpumpe ergeben sich Verluste im Volumenstrom, woraus ein volumetrischer Wirkungsgrad folgt. Dieser setzt sich aus mehreren Komponenten zusammen:

- Leckageströme an den Ventilen
- Leckageströme am Kolben
- Bauteilelastizität
- Kompressibilität der Förderflüssigkeit

Da es sich bei der Kolbendichtung um eine dynamische Dichtung handelt, ist eine vollständige Abdichtung nie möglich und ein Teil des Volumenstromes geht verloren. Zudem ergeben sich Dichtungsverluste an den Ventilen. All diese Faktoren werden in dem volumetrischen Wirkungsgrad zusammengefasst. Näherungsweise kann dieser berechnet werden. Ein genauer Wert kann auch hier, allerdings nur durch nachträgliche Versuche, ermittelt werden. Für die Vorauslegung wird ein Wirkungsgrad von $\eta_V = 0,9$ angenommen. Durch die guten Abdichtungsmöglichkeiten des Kolbens liegt dieser Wert bei oszillierenden Maschinen in der Regel noch etwas höher. Damit ergibt sich ebenfalls $\dot{Q}_{gth}$ zu:

$$\dot{Q}_{gth} = \frac{\dot{Q}_e}{\eta_V} = \frac{6 \cdot 10^{-7} \, \frac{m^3}{s}}{0,9} = 6,67 \cdot 10^{-7} \, \frac{m^3}{s} = 0,04 \, \frac{l}{min}$$

Mit dem Hubvolumen V_H und der Hubfrequenz n, welche die Anzahl der Arbeitsspiele pro Minute angibt, gilt:

$$\dot{Q}_{gth} = V_H \cdot n$$

Um eine möglichst robuste Bauweise zu erhalten, wird das Hubvolumen so groß gestaltet, wie es der vorhandene Bauraum erlaubt. Somit werden zur Erfüllung des geometrisch theoretischen Volumenstromes weniger Hubfrequenzen benötigt, was die Betriebsdauer der Ventile erhöht und zu weniger Verschleiß führt. Allerdings vergrößert sich mit sinkender Hubfrequenz die Volumenstrompulsation. Das Hubvolumen ergibt sich mit dem Kolbendurchmesser D und dem Kolbenhub s zu:

$$V_H = \frac{\pi}{4} \cdot D^2 \cdot s$$

Durch die Wahl eines relativ großen Durchmessers ergibt sich mehr Bauraum zur Positionierung der Ventile. Allerdings erhöht sich ebenfalls das Gewicht des Kolbens, was bei Antriebskonzepten mittels Magnetfeld nachteilig ist. Um ausreichend Platz für das Gehäuse und mögliche Antriebskonzepte zu gewährleisten, wird ein Kolbendurchmesser von 10 mm gewählt. Bei der Wahl des Kolbenhubes ist man hingegen relativ frei, exemplarisch wird dieser als 10 mm angenommen. Damit lässt sich die minimal erforderliche Hubfrequenz wie folgt berechnen:

$$V_H = \frac{\pi}{4} \cdot 0,1^2 \, dm^2 \cdot 0,1 \, dm = 7,854 \cdot 10^{-4} \, dm^3$$

$$n = \frac{\dot{Q}_{gth}}{V_H} = \frac{0,04 \, \frac{dm^3}{min}}{7,854 \cdot 10^{-4} \, dm^3} = 50,93 \, \frac{1}{min}$$

Es wird also eine Hubfrequenz von ca. 51 Druckhüben pro Minute benötigt. Nun kann die theoretische Antriebsleistung der Pumpe berechnet werden:

$$P_{th} = \dot{Q}_{gth} \cdot \Delta p_v = 6,67 \cdot 10^{-7} \, \frac{m^3}{s} \cdot 25427,39 \, Pa = 0,017 \, W$$

12.2.2. Betrachtung und Auswahl der Bauteile

Für die richtige Funktion der Pumpe sind vor allem die Ventile und die Abdichtung des Kolbens relevant. Bei der Abdichtung des Kolbens handelt es sich um eine dynamische Dichtung, welche niemals vollständig leckagefrei ist. Durch die auftretende Leckage wird allerdings auch die nötige Schmierung sichergestellt. Ihre Aufgabe besteht darin, den Kolbenraum von der Umgebung zu trennen, außerdem ermöglicht sie einen Druckaufbau des zu fördernden Mediums. Grundsätzlich wird je nach Abdichtungsart zwischen dem herkömmlichen Kolben und einem Tauchkolben unterschieden [Eif08, S. 108]. Bei einem herkömmlichen Kolben wird die Dichtung auf dem Kolben selbst befestigt. Ein Beispiel hierfür ist der Kolbenring als Dichtung, welcher besonders aus der Motorentechnik bekannt ist. Der sogenannte Tauchkolben zeichnet sich dadurch aus, dass die Dichtung nicht am Kolben selbst, sondern im Gehäuse angebracht ist. Diese Bauweise wird in der Pumpentechnik am häufigsten verwendet. Die Dichtungen im Pumpengehäuse werden grundsätzlich in Stoffbuchspackungen und Formringe unterschieden. In Abbildung 47 sind beide Typen dargestellt.

(a) *Stoffbuchspackung*   **(b)** *Formring*
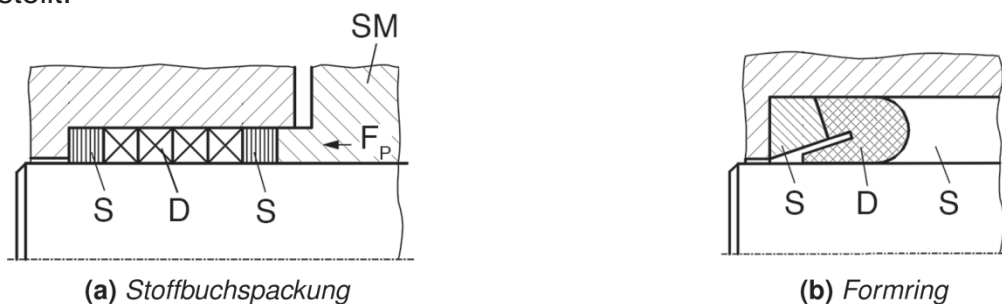
Abbildung 47: Dynamische Dichtungstypen; S=Stützringe, SM=Spannmutter, D=Dichtring, Quelle: [Eif08, S. 109], leicht modifiziert

Bei den Stoffbuchspackungen wird häufig durch eine zusätzlich aufgebrachte Spannkraft F_P, hier durch eine axiale Spannmutter, eine Vorspannung erzeugt. Durch die Pressung der einzelnen Ringe ergibt sich eine radiale Ausdehnung, welche eine

Presskraft auf den Kolben erzeugt. Dieser Anpressdruck muss nun den Druck im Arbeitsraum übersteigen. Es werden in der Regel mindestens zwei Packungen hintereinander benötigt, um auch die Stoßflächen der einzelnen Packungen abdichten zu können. Bei den Formringen hingegen ist keine extra Vorspannung nötig. Durch den Druck im Arbeitsraum wird die Dichtung an den Kolben gepresst. Daraus ergibt sich ein geringerer Druck als bei den Stoffbuchspackungen, wodurch die Reibung und der Verschleiß geringer sind. Zudem ergeben sich kürzere Wartungsintervalle, da kein manuelles Nachspannen nötig ist. Des Weiteren wird nur eine Dichtung benötigt, was zu einem geringeren Bauraum führt. Bei der Auswahl entsprechender Materialien, wie PTFE, sind Temperaturen von 250 °C ebenfalls möglich.

12.2.3. Antrieb durch Reluktanzprinzip

Die elektrische Energie wird lediglich zur Erzeugung magnetischer Kräfte genutzt, die dann ohne ein weiteres mechanisches Übertragungsglied die Bewegung des Kolbens bewirken. Dadurch ergibt sich ein relativ einfacher und kompakter Aufbau. Die erzeugte Bewegung beruht auf dem Reluktanzprinzip. Durch die Änderung des magnetischen Widerstandes, auch Reluktanz genannt, wird eine Kraft hervorgerufen, die immer so wirkt, dass sich der magnetische Widerstand verringert. Es gibt eine Vielzahl von unterschiedlichen Bauformen, die dieses Prinzip ausnutzen. In Abbildung 48 ist ein möglicher Aufbau anhand eines Topfmagneten dargestellt. Die Grundelemente sind hierbei ein verschiebbarer Anker, der Eisenrückschluss (Stator), der aus einem weichmagnetischen Werkstoff besteht, die Erregerspule und ein Luftspalt zwischen Stator und Anker.
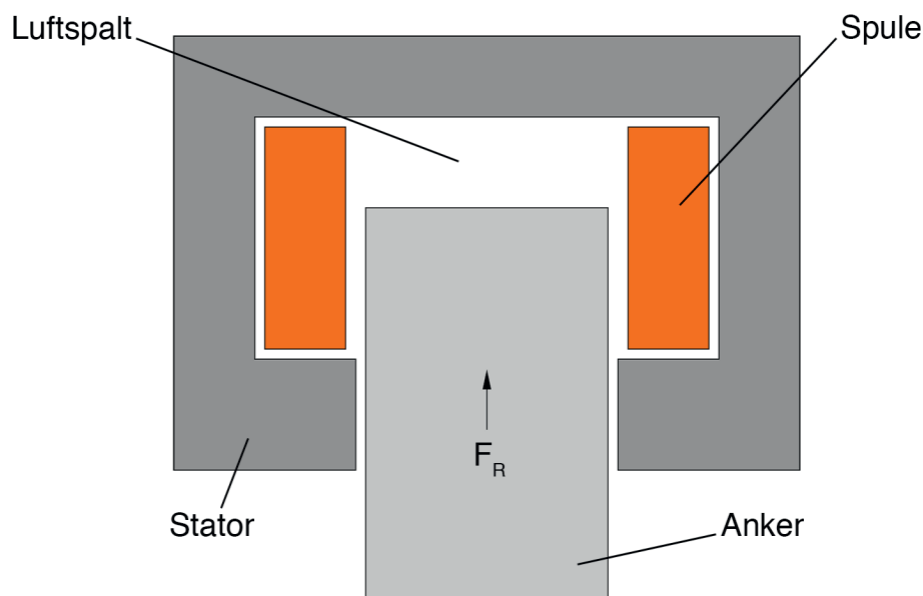
Abbildung 48: Aufbau eines Topfmagneten

Sobald die Spule mit Strom durchflossen wird, ergibt sich ein Magnetfeld im Stator und im Anker. Durch das Reluktanzprinzip wirkt nun eine Kraft auf den Anker, sodass

sich dieser so bewegt, dass der Luftspalt verringert wird, um den magnetischen Widerstand zu minimieren. Da dieses Prinzip nur in eine Richtung wirkt, muss eine Rückstellung des Ankers durch eine externe Kraft erzeugt werden. Hierzu kann im einfachsten Fall eine Feder genutzt werden. Dieser grundsätzliche Aufbau kann nun auf die Hubkolbenpumpe übertragen werden.

Über eine Spule wird die elektrische Energie in magnetische Energie umgewandelt, wodurch sich ein magnetischer Kreis bildet. In Abbildung 49 ist ein allgemeines magnetisches Ersatzschaltbild dargestellt. Hierbei ist θ die magnetische Spannungsquelle, die sich aus der Spulenwindungszahl w multipliziert mit dem Spulenstrom I zusammensetzt. Der Widerstand R_{mFe} beschreibt den Eisenkreis, der Widerstand im Arbeitsluftspalt wird durch $R_{m\delta}$ (δ) dargestellt und ist abhängig von der Position des Ankers. Zudem entsteht durch das Streufeld ein zusätzlicher konstanter Widerstand $R_{m\sigma}$.
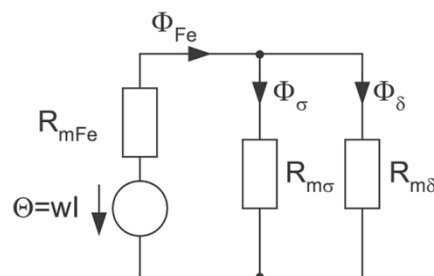
Abbildung 49: Magnetisches Ersatzschaltbild,
Quelle: [Kallenbach2012, S. 16], leicht modifiziert

Der gesamte magnetische Fluss ϕ_{Fe} teilt sich demnach auf die beiden Widerstände auf und es entsteht ein Verlust von ϕ_{σ}. Mit der Annahme, dass ein homogenes Magnetfeld im Kolben vorliegt und die magnetische Flussdichte nur eine Komponente senkrecht zum Kolbenboden besitzt, gilt für die entstehende Magnetkraft F_{magn} nach [Kal12, S. 66]:

$$F_{magn} = \frac{B_{\delta}^2 \cdot A_{magn}}{2 \cdot \mu_0} = \frac{B_{\delta}^2}{8 \cdot \mu_0} \cdot \pi \cdot D_{magn}^2$$

Die Größe der magnetischen Kraft hängt also von dem Durchmesser des Kolbens D_{magn}, der magnetischen Flussdichte B_{δ} und der Permeabilität des Vakuums ab. Die magnetische Flussdichte hängt wiederum von folgenden Faktoren ab:

• der Spule
• den elektrischen Eingangsgrößen
• der Geometrie des Magnetkreises und somit den Verlusten im Streufeld
• den verwendeten Werkstoffen

871

Die magnetische Kraft muss die nötige Energie aufbringen, um die Federkraft zu überwinden und eine vollständige Bewegung des Kolbens zum unteren Totpunkt zu gewährleisten. Die Feder muss hingegen so ausgelegt werden, dass sie bei vertikalem Einbau der Pumpe die Gewichtskraft des Kolbens überwindet und den nötigen Druck ausübt, sodass die Wärmeträgerflüssigkeit zur Druckseite ausgeschoben werden kann. Weiterhin muss immer eine gewisse Vorspannung gegeben sein, damit der Kolben durch die Vibrationen im Bohrstrang keine ungewollten Bewegungen ausführt. Im Folgenden werden die einzelnen Bauteile des magnetischen Kreises betrachtet. Wie zuvor erwähnt, ist unter anderem der Werkstoff des Ankers und des Stators für die erreichbare Energie ausschlaggebend.

Für den technischen Einsatz im Magnetismus kommen ferro- und ferrimagnetische Stoffe zum Einsatz. Für den Einsatz im Stator und Anker eignen sich weichmagnetische Stoffe. Die sich ergebenden Anforderungen sind demnach eine hohe Permeabilität und eine hohe Sättigungsflussdichte, sodass eine hohe magnetische Kraft bei möglichst geringer eingesetzter Energie erreicht wird. Mit der Sättigungsflussdichte wird der Wert der Flussdichte bezeichnet, welcher auch durch Steigerung der Feldstärke nicht mehr erhöht werden kann. Dies begrenzt wiederum die Leistungsfähigkeit des Magnetkreises. Kritisch ist, dass weichmagnetische Stoffe besonders temperaturabhängig sind und bei der sogenannten Curie-Temperatur in den paramagnetischen Zustand wechseln. Dies bedeutet, dass der Werkstoff ab dieser Temperatur als nichtmagnetisch anzusehen ist. Durch die hohe Umgebungstemperatur von bis zu 250°C und der entstehenden Wärme in der Spule muss also ein beständiger und dennoch leistungsfähiger Werkstoff gefunden werden. In Abbildung 50 ist die Sättigungspolarisation über die Temperatur für verschiedene Stoffe aufgetragen. Dabei ist ersichtlich, dass besonders Vacoflux50 auch bis 400 °C keine große Änderung der Sättigungspolarisation erfährt. Zudem ist die maximale Polarisation sehr groß. Vacoflux50 ist eine Kobalt-Eisen-Legierung mit einer hohen Curie-Temperatur von 950 °C. Dadurch ist dieses Material für den Einsatz geeignet.
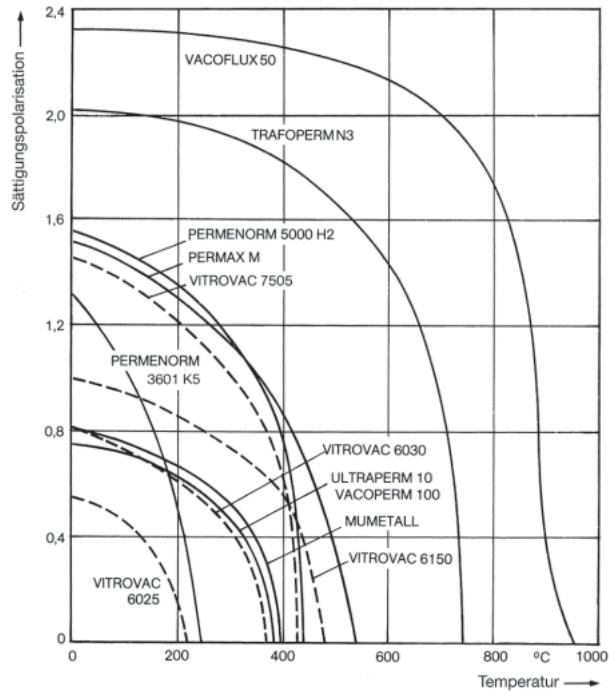
Abbildung 50: Temperaturverhalten verschiedener weichmagnetischer Stoffe, Quelle: [Vac12]

Bei der Wahl der Spule erweist sich die hohe Umgebungstemperatur als problematisch. Die Spulenwicklung muss der Außentemperatur sowie der Eigenerwärmung standhalten. Infrage kommen könnte hier eine Kupferwicklung, die mit PTFE ummantelt ist. Nachdem die wichtigsten Bestandteile des magnetischen Kreises behandelt wurden, gilt es nun, einen ersten Entwurf der Pumpe, inklusive des Antriebes, zu erstellen. In Abbildung 51 ist dieser dargestellt. Zur besseren Übersicht sind einige Bauteile farbig markiert.
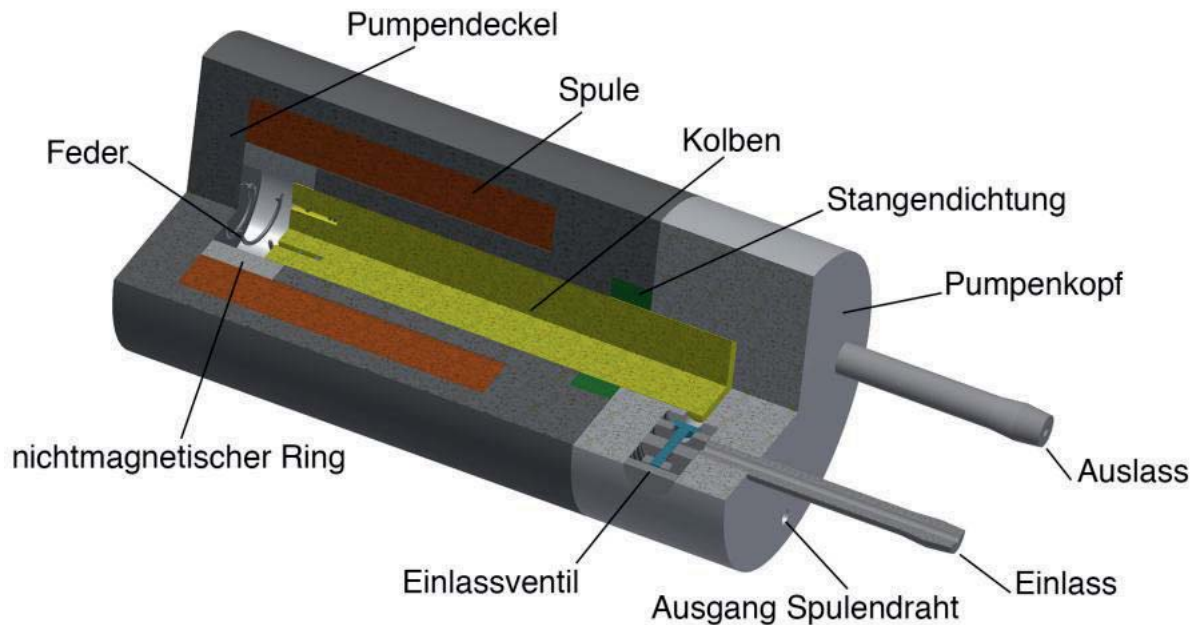
Abbildung 51: Entwurf der Hubkolbenpumpe

Der Pumpendeckel, der Stator und der Anker bestehen aus dem zuvor ausgewählten Vacoflux50. Dadurch bildet sich das magnetische Feld hauptsächlich in diesen Teilen aus. Ziel ist es, dass sich die magnetischen Feldlinien vornehmlich über den Anker im Arbeitsspalt ausbreiten und so eine möglichst hohe magnetische Kraft erzeugen. Hierzu wird der Kontakt zwischen Pumpendeckel und Stator durch einen nichtmagnetischen Ring unterbrochen. Der Pumpenkopf wird ebenfalls aus einem nichtmagnetischen Material gefertigt, sodass sich auch hier keine unnötigen Verluste bilden können. Da die entstehenden Kräfte durch das Reluktanzprinzip mit größer werdendem Arbeitsluftspalt sinken, wird der Kolbenhub nicht wie in Abschnitt 5.2.1 mit 10 mm angenommen, sondern auf 5 mm reduziert. Dadurch ergibt sich folgendes:

$$V_H = \frac{\pi}{4} \cdot 0,1^2 \, dm^2 \cdot 0,05 \, dm = 3,927 \cdot 10^{-4} \, dm^3$$

$$n = \frac{\dot{Q}_{gth}}{V_H} = \frac{0,04 \, \frac{dm^3}{min}}{3,927 \cdot 10^{-4} \, dm^3} = 101,86 \, \frac{1}{min}$$

Nach einem ersten konstruktiven Entwurf der Pumpe werden die benötigten Kräfte und Spulengrößen ermittelt. Die Gleichungen zur Auslegung des elektromagnetischen Kreises stammen aus [Kal12]. Zur Berechnung der erforderlichen Magnetkraft gilt es allerdings vorerst, die Kraft der Rückstellfeder zu betrachten. Wie zuvor berechnet, ergeben sich Druckverluste von ca. 0,25 bar in den Rohrleitungen. Die Federkraft muss diesen Gegendruck also zu jedem Zeitpunkt überwinden. Je nach Einbauposition muss die Federkraft zusätzlich die Gewichtskraft des Kolbens aufbringen. Durch die gewählten Kolbenabmessungen von D=10 mm , L=50 mm und eine

874

Dichte für den Werkstoff Vacoflux50 von ρ_V=8,91 g/cm³ ergibt sich die minimal erforderliche Federkraft zu:

$$F_{F,min} = \Delta p_{V,Ges} \cdot \frac{\pi \cdot D^2}{4} + \frac{\pi \cdot D^2}{4} \cdot L \cdot \rho_V \cdot g$$

$$= 25000\,Pa \cdot \frac{\pi \cdot 0,01^2\,m^2}{4} + \frac{\pi \cdot 0,01^2\,m^2}{4} \cdot 0,05\,m \cdot 8910\,\frac{kg}{m^3} \cdot 9,81\,\frac{m}{s^2} = 2,31\,N$$

Daraus folgt, dass die Feder zum Ende des Druckhubes noch eine Kraft von 2,31\ N aufrechterhalten muss. Somit ergibt sich wiederum, dass die Magnetkraft bei maximalem Arbeitsluftspalt noch mehr als $F_{F,min}$, abzüglich der Gewichtskraft, aufbringen muss. Die Gewichtskraft kann jedoch nur bei einem senkrechten Einbau mit oben befindlichem Pumpenkopf abgezogen werden. Es gilt also:

$$F_{magn.,min} = F_{F,min} - \frac{\pi \cdot D^2}{4} \cdot L \cdot \rho_V \cdot g = 1,97\,N$$

$$B_\delta = \sqrt{\frac{F_{magn,min} \cdot 8 \cdot \mu_0}{\pi \cdot D_{magn}^2}} = \sqrt{\frac{1,97\,N \cdot 8 \cdot 1,2566 \cdot 10^{-6}}{\pi \cdot 0,01^2\,m^2}} = 0,25\,T$$

Im Luftspalt wird also mindestens eine konstante magnetische Flussdichte von 0,25 T benötigt. Der magnetische Fluss ergibt sich also zu :

$$\Phi = \int B dA = B_\delta \cdot \frac{\pi \cdot D_{magn}^2}{4} = 0,25\,T \cdot \frac{\pi \cdot 0,01^2\,m^2}{4} = 1,96 \cdot 10^{-5}\,Wb$$

Der magnetische Fluss ist im gesamten Magnetkreis konstant. Für die weitere Berechnung soll nun ein vereinfachtes Modell der Hubkolbenpumpe herangezogen werden. Dieses ist in Abbildung 52 dargestellt.
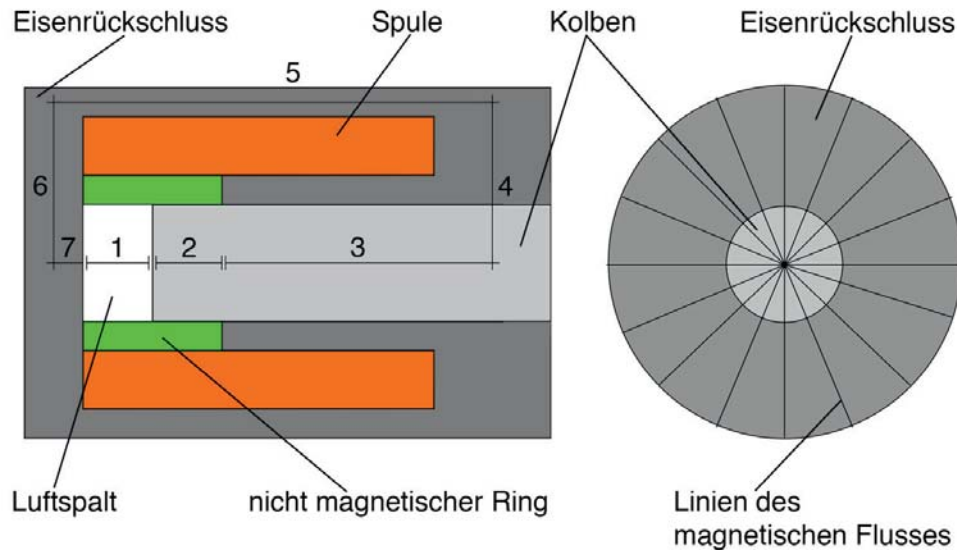
Abbildung 52: Berechnungsmodell der Hubkolbenpumpe

Bei diesem Modell wird angenommen, dass sich kein Streufluss einstellt und kein magnetischer Fluss in dem nicht magnetischen Ring vorhanden ist. Wie in der Abbildung zu erkennen, ist die Pumpe in sieben verschiedene Bereiche eingeteilt, in welchen sich die magnetische Flussdichte durch die unterschiedlichen Flächen verändert. Mithilfe der Flächen, zu denen die magnetische Flussdichte senkrecht wirkt, und dem konstanten magnetischen Fluss kann nun die jeweilige Flussdichte bestimmt werden. Die geometrischen Größen sind dem Pumpenentwurf der Abbildung 51 entnommen. Mit dieser Flussdichte wird nun aus der Hystereseschleife (Magnetisierungskurve) die entsprechende Feldstärke H_i abgelesen.

Auf die Durchführung der vollständigen Berechnung soll an dieser Stelle verzichtet werden. Die Ergebnisse sind in der folgenden Tabelle aufgelistet:

Bereich	1 bzw. (δ)	2	3	4	5	6	7
Flussdichte in T	0,25	0,25	0,11	0,21	0,09	0,3213	0,25
Feldstärke in A/cm		0,505	0,486	0,497	0,486	0,514	0,505

Da in Bereich 4 und 6 die magnetische Flussdichte senkrecht durch eine zylindrische Mantelfläche wirkt, verändert sich die Fläche kontinuierlich. Dies ist in Abbildung 52 rechts dargestellt. Wie zu sehen, steigt die Flussdichte zur Mitte hin an. In der Tabelle wurde deshalb ein mittlerer Wert angegeben. Dieser wurde durch Aufteilung des Volumens in 2750 Teileelemente berechnet. Mit den nun erhaltenen Werten kann eine erste Dimensionierung der nötigen Spulenwindungen w vorgenommen werden. Hierbei wird angenommen, dass ein Erregerstrom von I=2 A anliegt und der maximale Luftspalt δ = 6 mm beträgt.

$$\Theta = w \cdot I = \sum H_i \cdot l_i + \frac{B_\delta \cdot \delta}{\mu_0}$$

In der Gleichung gibt l_i die jeweilige mittlere Weglänge an, in welcher sich der Fluss ausbreitet. Umgestellt nach der Windungsanzahl und mit eingesetzten Werten folgt:

$$w = \frac{0,505\,\frac{A}{cm} \cdot 0,6\,cm}{2\,A} + \frac{0,486\,\frac{A}{cm} \cdot 2,25\,cm}{2\,A} + \frac{0,497\,\frac{A}{cm} \cdot 1,375\,cm}{2\,A} + \frac{0,486\,\frac{A}{cm} \cdot 3,75\,cm}{2\,A}$$

$$+ \frac{0,514\,\frac{A}{cm} \cdot 1,375\,cm}{2\,A} + \frac{0,505\,\frac{A}{cm} \cdot 0,3\,cm}{2\,A} + \frac{0,25\,T \cdot 0,006\,m}{1,2566 \cdot 10^{-6}\,\frac{N}{A^2} \cdot 2\,A} = 599,23$$

Die Spule muss also mindestens 600 Windungen aufweisen, um die nötige Kraft aufbringen zu können. Durch die idealisierte Rechnung wurden jedoch die Verluste nicht betrachtet. Hierzu wird die Windungszahl vorsorglich um 20 % erhöht. Es wird also von einer Windungszahl w=720 ausgegangen. Mit der neu festgelegten Windungszahl wird nun die resultierende Flussdichte im Luftspalt errechnet.

$$B_\delta \approx \frac{w \cdot I \cdot \mu_0}{\delta} = \frac{720 \cdot 2\,A \cdot 1,2566 \cdot 10^{-6}\,\frac{N}{A^2}}{0,006} = 0,3\,T$$

$$F_{magn.,min} = \frac{0,3^2\,T^2}{8 \cdot 1,2566 \cdot 10^{-6}\,\frac{N}{A^2}} \cdot \pi \cdot 0,01^2\,m^2 = 2,81\,N$$

Der Kraftverlauf im Luftspalt ist in Abbildung 53 dargestellt.
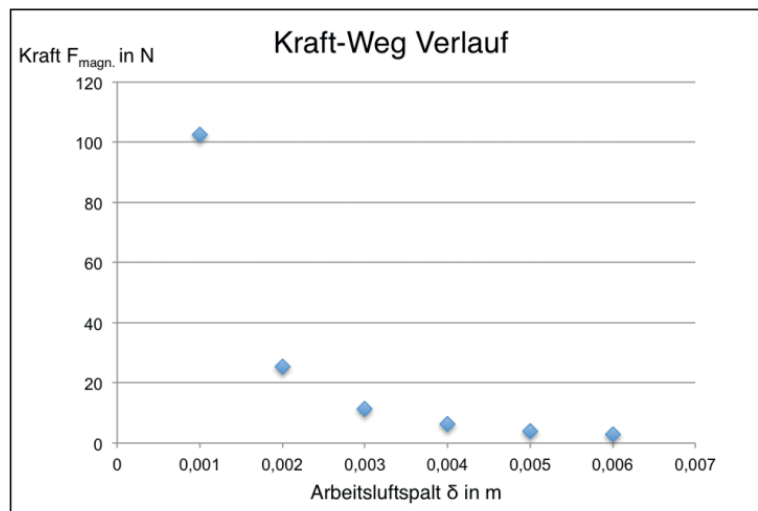
Abbildung 53: Kraft-Weg Verlauf des Kolbenhubes

Hierbei ist allerdings zu beachten, dass besonders bei sehr kleinen Luftspalten die Näherung schlechter wird. Durch den kleiner werdenden Spalt steigt die Flussdichte weiter an. Wie in der Hystereseschleife zu sehen, steigt ab einer gewissen Höhe der Flussdichte die Feldstärke ebenfalls stark an, weshalb diese nicht mehr vernachläs-

sigt werden kann. Aufgrund dessen ist abschließend zu empfehlen, durch eine Analyse nach der Finite-Elemente-Methode, die bisherige Geometrie zu optimieren, den magnetischen Kreis zu verbessern und die exakten magnetischen Kräfte zu ermitteln. Damit lässt sich dann eine genaue Auslegung der Ventile sowie der benötigten Rückstellfeder durchführen.

Abbildung 54: Prototyp der Hubkolbenpumpe

12.3 Piezoelektrische Membranpumpe

12.3.1. Anforderungen und Funktionsprinzip

Alternativ zu der bereits betrachteten und ausgeführten Hubkolbenpumpe soll an dieser Stelle ein Konzept einer in die Elektronikplatinen integrierten Membranpumpe untersucht werden. Diese muss ebenfalls den in [Marquardt2013] angesprochenen Anforderungen genügen, welche wie folgt lauten:

- Temperaturbeständigkeit bis 250 °C
- Volumenstrom von $\dot{V} = 0{,}036 \frac{1}{\min}$
- Förderdruck > 0,25 bar
- Kompakte Baugröße, insbesondere in der Tiefe gilt < 30 mm

Der grundsätzliche Aufbau einer Membranpumpe ist in Abbildung 55 dargestellt. Beim Fördern einer inkompressiblen Flüssigkeit können wie schon bei der Hubkolbenpumpe zwei Takte unterschieden werden. Im ersten Takt verformt sich die Membran so, dass der Förderraum vergrößert wird, was zu einem Unterdruck führt. Aufgrund dessen öffnet das Einlassventil und das zu fördernde Medium strömt ein. Nach dem Erreichen der maximalen Ausdehnung der Membran schließt das Einlassventil und die Membran dehnt sich in die entgegengesetzte Richtung aus. Dies führt wiederum zu einer Verkleinerung des Förderraums. Somit baut sich der Förderdruck auf, das Auslassventil öffnet und die Flüssigkeit wird ausgestoßen.
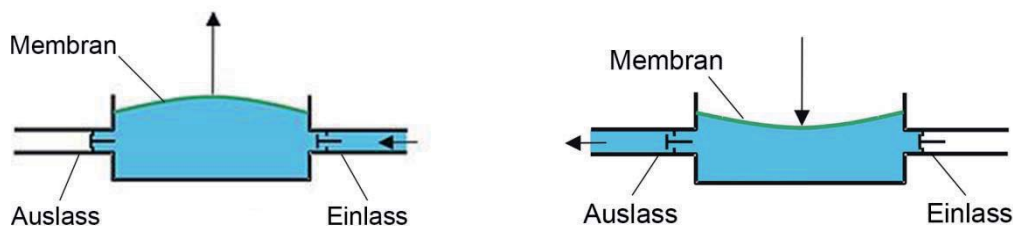
Abbildung 55: Membranpumpen

Für den Antrieb der Membran kommen verschiedene Konzepte in Frage. Einige sollen hier kurz angesprochen und für diesen Einsatzzweck bewertet werden.

12.3.2. Membranwerkstoff und Verdrängungsvolumen

In der Regel wird die elastische Membran aus Metallblech, PTFE oder Elastomeren gefertigt. Der Werkstoff spielt insbesondere bei der Temperaturbeständigkeit und der maximalen Verformung der Membran eine wichtige Rolle. Aufgrund der maximalen Betriebstemperatur von 250 °C kommt nur noch Metallblech als Werkstoff in Frage [Eif08]. Dieser ist jedoch hinsichtlich der möglichen Dehnung am schlechtesten zu bewerten. Nach [Eif08] kann als Richtwert angenommen werden, dass das Verhältnis von Hub zu Durchmesser des dehnbaren Teils der Membran nur 1,5 % beträgt. Mit der Annahme eines Membrandurchmessers von d=20 mm und dem Hub w lässt sich in einer ersten Abschätzung das maximale Verdrängungsvolumen V_h wie folgt berechnen:

$$w = 0,015 \cdot d = 0,015 \cdot 20 \, mm = 0,3 \, mm$$

$$V_h = 2 \cdot w \cdot \pi \cdot \frac{d^2}{4} \cdot 0,7 = 2 \cdot 0,3 \, mm \cdot \pi \cdot \frac{20^2 \, mm^2}{4} \cdot 0,7 = 131,95 \, mm^3$$

Durch die 2 wird berücksichtigt, dass die Membran in beide Richtungen ausgedehnt wird. Der Faktor 0,7 ist eine erste Schätzung und reduziert das Volumen, da die Membran nicht waagerecht ausgedehnt wird, sondern gewölbt ist. Ein genauer Wert kann erst ermittelt werden, wenn die Antriebsart und damit die Art der Verformung

ausgewählt ist. Mit dem vorgegebenen Volumenstrom und dem Verdrängungsvolumen ergibt sich die benötigte Hubzahl n zu:

$$n = \frac{V}{V_h} = \frac{0,036\,\frac{l}{min}}{0,00013195\,l} = 272,83\,\frac{Hübe}{min}$$

12.3.3. Bauarten

Die Bauarten der Membranpumpen können insbesondere durch die Art des Antriebes der Membran unterschieden werden. Dabei soll an dieser Stelle zunächst zwischen einer mechanisch und einer hydraulisch angetriebenen Membran unterschieden werden. In Abbildung 56 sind die beiden verschiedenen Konstruktionen dargestellt. Bei dem mechanischen Antrieb ist die Membran fest mit dem Kolben verbunden und kann durch die Bewegung des Kolbens exakt ausgelenkt werden. Diese Bauart ist jedoch nur für kleine Drücke geeignet, da die nicht vom Kolben gestützten Bereiche der Membran dem gesamten Systemdruck ausgesetzt sind. Die Bauweise mit einem hydraulischen Antrieb ist hingegen auch für hohe Systemdrücke geeignet, da die Membran ganzflächig von der Hydraulikflüssigkeit gestützt wird. Negativ ist jedoch, dass eine zusätzliche Abdichtung des Hydraulikraumes erforderlich ist. Zudem ist eine definierte Auslenkung, besonders in dem hier erforderlichen Maßstab, deutlich aufwendiger umzusetzen. Wie zu Beginn in den Anforderungen erwähnt, wird nur ein relativ geringer Förderdruck benötigt, weshalb das einfachere Konzept der mechanisch angetriebenen Membran bevorzugt wird.
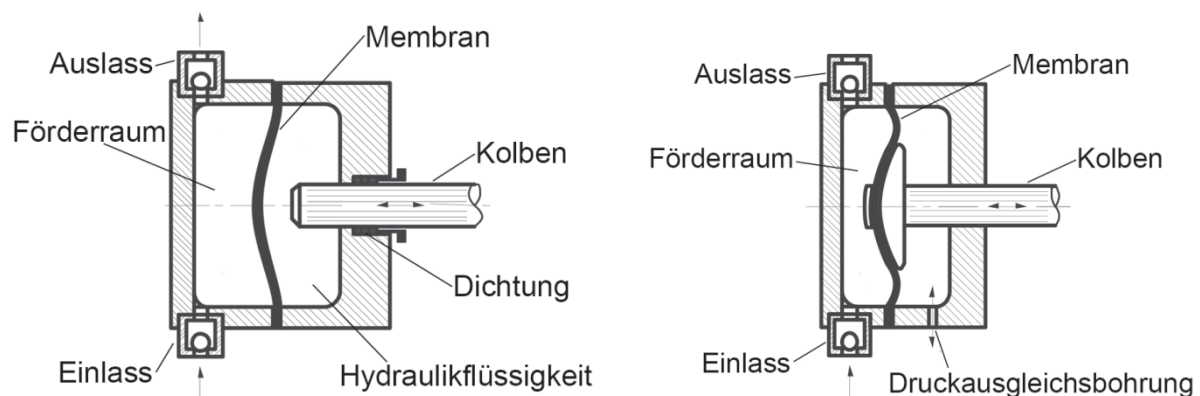
Abbildung 56: Bauarten von Membranpumpen Quelle: [Eif08]

12.3.4. Antriebskonzepte

Im nächsten Schritt muss ein geeigneter Antrieb des Kolbens gefunden werden. Herkömmliche mechanische Antriebe, wie zum Beispiel Kurbeltriebe oder Feder-

Nocken-System, kommen aufgrund des geringen Hubes von nur 0,3 mm bzw. 0,6 mm bei beidseitiger Auslenkung nicht in Frage. Als Alternative bietet sich ein elektromagnetischer Antrieb an. Im Gegensatz zu dem bei der Hubkolbenpumpe eingesetzten Antrieb ist eine Konstruktion mittels Feder durch die geringe Auslenkung nicht möglich. Dementsprechend muss ein Antrieb gewählt werden, der in beide Richtungen elektromagnetisch angesteuert wird. Eine Möglichkeit besteht in der Kombination eines Elektromagneten und eines Dauermagneten. Aufgrund der hohen Betriebstemperatur von bis zu 250 °C wird die Auswahl eines Werkstoffes für den Einsatz als Dauermagnet stark eingeschränkt. Um eine Entmagnetisierung zu verhindern, kann zum Beispiel ein gesinterter SmCo-Magnet eingesetzt werden [mag12]. Ein erster Entwurf des bereits auf der Platine integrierten Antriebs ist in Abbildung 57 zu sehen. Je nach Stromrichtung in der Spule verändert sich die Polung und der Dauermagnet wird entweder abgestoßen oder angezogen. Wenn der Dauermagnet auf der Membran befestigt wird, kann so eine Pumpbewegung hervorgerufen werden. Hierbei ist jedoch noch zu berechnen, ob die entstehenden Kräfte ausreichend groß sind, da der Bauraum und somit die Windungen der Spule begrenzt sind.
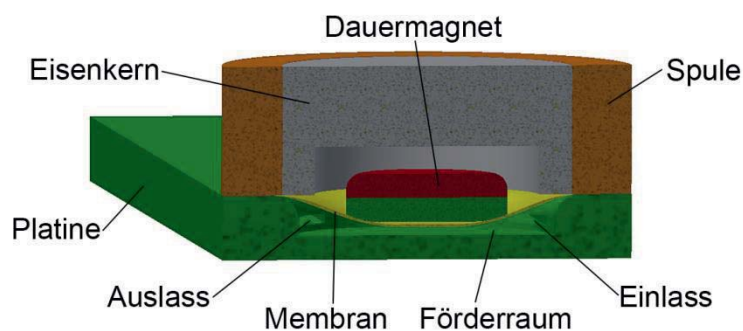
Abbildung 57: Membranpumpe mit elektromagnetischem Antrieb

Für eine erste Abschätzung der zur Verformung der Membran benötigten Kräfte wurde eine Belastungsanalyse durchgeführt. Die erforderlichen Kräfte sind dabei stark von der Geometrie der Bauteile und dem Material der Membran abhängig. Für die Simulation wurde eine Membran mit 20 mm Durchmesser und einer Dicke von 0,3 mm verwendet. Der Dauermagnet hat im unverformten Zustand eine runde Auflagefläche mit einem Durchmesser von 2 mm. In Abbildung 58 sind die Ergebnisse für eine Aluminiummembran und für eine Edelstahlmembran dargestellt. Bei der Aluminiummembran ist eine Kraft von 35 N erforderlich, um die Verformung von 0,3 mm hervorzurufen. Bei der Edelstahlmembran steigt die erforderliche Kraft auf 95 N an. Dementsprechend müssen die Abstoßungskräfte zwischen dem Elektromagneten und dem Dauermagneten diese Kräfte aufbringen. Zur Berechnung der Magnetkräfte ist eine genauere Untersuchung mit einer entsprechenden FEM-Analyse notwendig.

881

(a) Aluminiummembran   (b) Edelstahlmembran
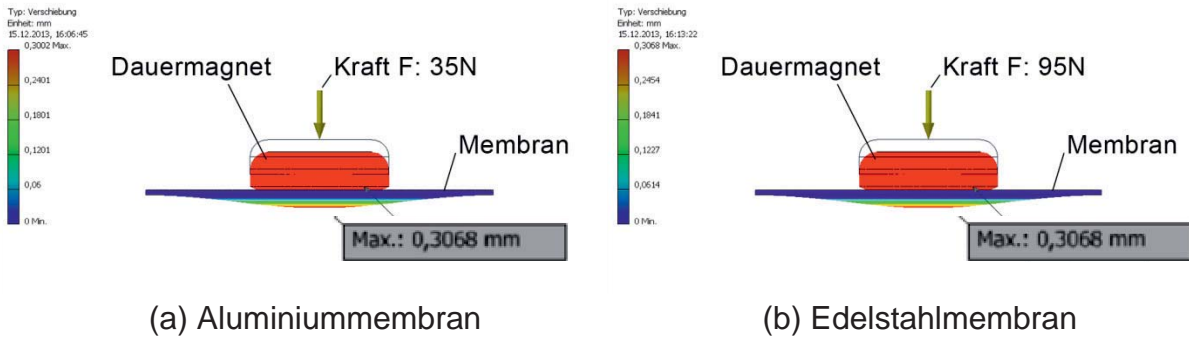
Abbildung 58: Ergebnisse der Belastungsanalyse zur Membranverformung

Eine weitere Alternative stellt ein Antrieb mittels Piezoaktor dar. Bei dem inversen Piezoeffekt wird durch das Anlegen einer elektrischen Spannung eine Verformung des Bauteils hervorgerufen, welche für die Bewegung der Membran genutzt werden kann. Die Integration des Piezoaktors kann in verschiedenen Formen erfolgen. Einerseits ist die Ausführung des Kolbens als Piezoelement denkbar, aber auch das direkte Befestigen eines Piezoelements auf der Membran [cur13], welches beim Anlegen einer Spannung zu einer Biegung führt, ist möglich. Diese beiden Integrationen sind in Abbildung 59 dargestellt. Die zuletzt genannte Bauweise zeichnet sich besonders durch die sehr kompakte Bauweise aus. Unter Umständen kann zudem vollständig auf die Membran verzichtet werden, was den Aufbau noch weiter vereinfacht. Nachteilig an dieser Konstruktion ist der hohe Entwicklungsbedarf für ein entsprechendes Piezoelement.

(a) Antrieb mit Piezoaktor als Kolben   (b) Antrieb mit an Membran gekoppeltes Piezoelement
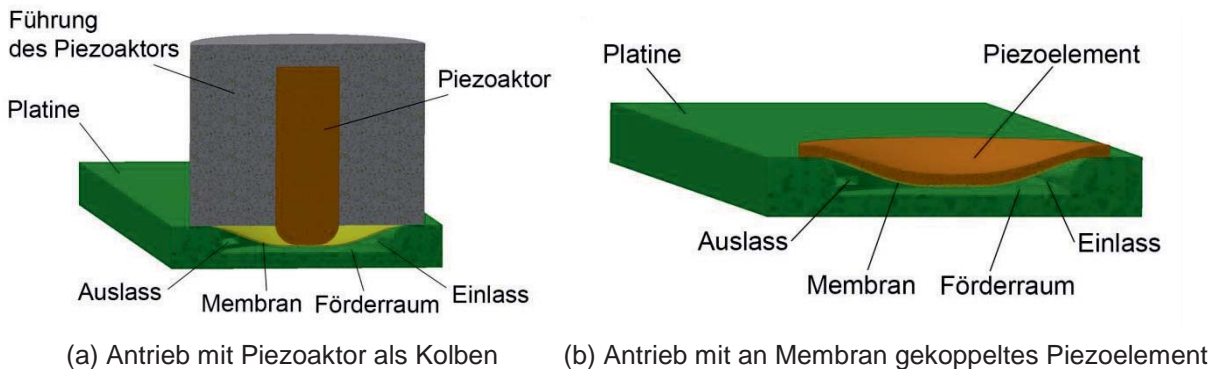
Abbildung 59: Membranpumpen mit piezoelektrischem Antrieb

Zu überwindende Probleme beim Piezoantrieb sind die Temperaturbeständigkeit der Piezokeramiken, die hohen Betriebsspannungen und die für Piezoaktoren langen Stellwege. Für den Einsatz bei Temperaturen bis 250 °C eignet sich beispielsweise der Werkstoff PIC300 von Piceramic [Pic]. Zur Vergrößerung der Stellwege für die Bauweise aus Abbildung 59a können unterschiedliche Ansätze verfolgt werden. Zum einen besteht die Möglichkeit Stapelaktoren zu verwenden, wodurch sich die Aus-

dehnungen der einzelnen Elemente addieren und zum anderen kommen verschiedene mechanische Übersetzungen in Frage. In Abbildung 60 sind zwei Konstruktionen dargestellt. Problematisch ist allerdings, dass sich die Baugröße stark vergrößert. Aufgrund dessen zeigt die Bauweise aus Abbildung 59b das größere Potenzial.

(a) Stapelaktor Quelle: [Pie]

(b) Piezoelement mit mechanischer Übersetzung Quelle: [Ced]
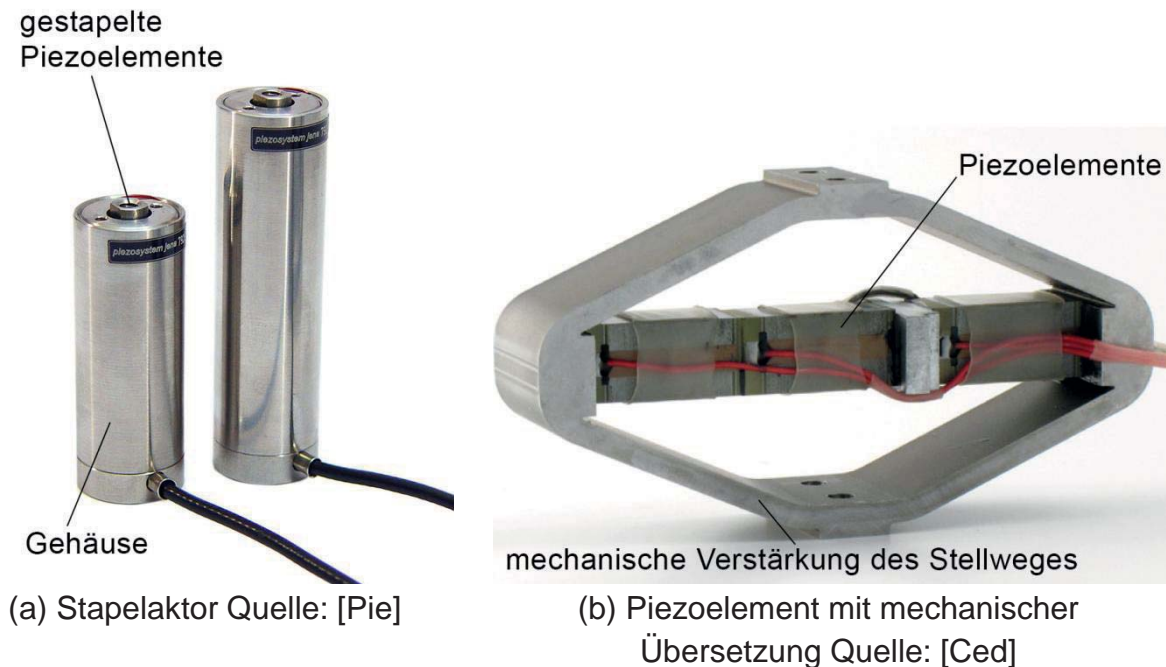
Abbildung 60: Beispiele zur Vergrößerung der Stellwege von Piezoaktoren

13 Zusammenfassung

Ziel des Projekts war die Kühlung von Elektronik innerhalb einer Bohrgarnitur. Der geplante Einbauort bedingt eine kleine Baugröße des Kühlsystems. Die Umgebungstemperaturen sind mit 250 °C vergleichsweise hoch.

Als vielversprechender Ansatz wurde die Kühlung der Elektronik mittels Kühlkanälen innerhalb der Leiterplatte ermittelt. Für die Umsetzung des Systems ist unter anderem eine Bewertung der Kühlleistung notwendig.

Im ersten Schritt wurde gezeigt, dass eine analytische Berechnung der Kühlleistung schwierig ist. Aufgrund der komplexen Wechselwirkungen und vielen Vereinfachungen kann davon ausgegangen werden, dass die Berechnung der Kühlleistung nur einen groben Anhaltspunkt für die Leistungsfähigkeit des Kühlsystems gibt.

Die Simulation der gekühlten Platine erwies sich trotz des großen Aspektverhältnisses als machbar. Da die Strömung in den Kühlkanälen laminar erfolgt, ist die Modellierung der Strömung nachrangig. Maßgeblich für das Ergebnis ist die hohe Auflösung der Simulation im Bereich der thermischen Grenzschicht. Die Elementanzahl in der durchgeführten FEM-Simulation konnte so auf ein verwendbares Maß reduziert

werden. Die Versuche ergaben eine gute Übereinstimmung zwischen der Simulation und den durchgeführten Versuchen.

Die Herstellung der Platinen erwies sich als schwierig. Der zugrundeliegende Prozess war bisher für FR4 basierte Platinen erprobt. Die Umsetzung auf Polyimid scheiterte zunächst an der Verklebung der Kupferlagen des gekühlten Layers. Nachdem der Flüssigkleber durch eine weitere gefräste Polyimidlage ersetzt wurde, konnten Platinen hergestellt werden, die sich in den durchgeführten Versuchen stabil verhielten. Die Verwendung der gefrästen Polyimidlage schränkt allerdings die zulässigen Kühlkanallayouts ein.

Als Kühlmittel wurden Öle und Flüssigmetalle untersucht. Letztere lassen sich theoretisch elektromagnetisch pumpen. In Versuchen konnte allerdings keine ausreichende Pumpleistung erreicht werden. Öle sind über einen weiteren Temperaturbereich einsetzbar und deren Verwendung weitgehend unproblematisch. Allerdings ist eine mechanische Pumpe notwendig.

Zum Pumpen des Kühlmittels wurden verschiedene Konzepte untersucht. Aufgrund des geringen Bauraums und der hohen Temperaturen sind die meisten gängigen Pumpkonzepte nicht umsetzbar. Prototypisch wurde eine Hubkolbenpumpe erfolgreich umgesetzt. Membranpumpen wurden theoretisch untersucht und erscheinen weiterhin vielversprechend, da im Gegensatz zu Hubkolbenpumpen keine bewegte Dichtung notwendig ist.

[AGK]   Isolationswerkstoffe von AGK, http://www.agk.eu/

[Ced]   Cedrat Technologies. http://www.cedrat-technologies.com/en/technologies/actuators/piezo-actuators-electronics.html, Abruf: 12.12.2013

[cur]   Curiejet. http://www.curiejet.com/en/products/list.php?pin=099861a6e97183485912f85df4e401fd&type=s, Abruf: 12.12.2013

[Dit12]   Ditec GmbH. Stand: 2012. http://www.ditecgmbh.de/pumpen/img/drehkolbenSLR.jpg, Abruf: 15.10.2012

[Ebn11]   Ebner, D.; King, T.; Scheller, C.; Willimsky, E.: Zahnradpumpen Schlüsselkomponenten für das präzise Fördern von Flüssigkeiten. Moderne Industrie, 2011

[Eif08]   Eifler, W.; Schlücker, E.; Spicher, U.; Will, G.: Küttner Kolbenmaschinen: Kolbenpumpen, Kolbenverdichter, Brennkraftmaschinen. Vieweg+Teubner Verlag, 2008

[guh]   http://www.guh-isolite.de/index.php?id=214

[Ilfa]   ILFA Feinstleitertechnik, http://www.ilfa.de/

[ILFA03]   Abschlußbericht über das BMBF-Verbundprojekt "Mikrokühlsystem für die Leistungselektronik", Teilvorhaben: "Flüssigkeitskühlsystem für elektronische Baugruppen"

[Kal12]   Kallenbach, E.; Eick, R.; Quendt, P.; Ströhla, T.; Feindt, K.; Kallenbach, M.; Radler, O.: Elektromagnete: Grundlagen, Berechnung, Entwurf und Anwendung. Vieweg+Teubner Verlag, 2012

[mag12]   magnet-world. Stand: 2012. http://www.magnet-world.de/index.php?article_id=117&clang=0, Abruf: 16.12.2013

[Mar13]   Marquardt, T.: Konzeption von Hochtemperaturpumpen für die aktive Kühlung von Elektronik in Tiefbohrköpfen / Leibniz Universität Hannover. 2013. – Forschungsbericht

[Midel]   Midel Transformatoröl, http://www.midel.com/brandsicherheit.htm

[Pic]   Piezosystem. http://www.piezosystem.de/ piezo_nanopositionieung/piezo_aktoren_nano_positioniersysteme/stapelaktoren/serie_pahl/, Abruf: 12.12.2013

[PdW]   Praxis der Wärmeübertragung: Grundlagen, Anwendungen, Übungsaufgaben, http://books.google.de/books?id=Vwi7MVVqCW8C&lpg=PA190&ots=sNg0-PAyPg&dq=rohrstr%C3%B6mung%20w%C3%A4rme%C3%BCbergang&pg=PA187#v=onepage&q=rohrstr%C3%B6mung%20w%C3%A4rme%C3%BCbergang&f=false

[Sch12]   Schmalz. Stand: 2012. http://katalog.schmalz.com/, Abruf: 15.10.2012

[Sch99]   Schiefelbein, F.; Bradish, R.: Integrierte Mikrokühlsysteme für elektroni-
             sche Bauelemente, Abschlußbericht der Siemens AG zum BMBF-
             Verbundprojekt. Berlin, 1999.

[Silca]   Silca Isolite GmbH, http://www.silca-online.de

[Som10]   Sommerfeld, A.: Antriebskonzepte für miniaturisierte Pumpen, Universität
             Rostock, Diss., 2010

[Swagelok]   Swagelog Fluid Systems GmbH, http://www.swagelok.com/

[Techtrans] Techtrans, 048V - Isolationsfolien zum Schutz vor thermischer, optischer
             und elektromagnetischer Strahlung sowie vor Gasen,
             http://www.techtrans.de/html/bereich/material/048.htm

[Telle]   Erwin Telle GmbH, Werkstoffe, Schläuche, etc, http://www.telle.de/

[vaQtec]   Vakuumisokationsplatten von va-Q-tec,
             http://www.va-q-tec.com/was_ist_ein_vip_de,181.html

[VDE]   VDE Hochtemperatur Elektronik – Stand und Herausforderungen

[Vac12]   Vacuumschmelze. Stand: 2012. http://www.vacuumschmelze.de/
             fileadmin/documents/broschueren/htbrosch/Pb-pht-0.pdf, Abruf:
             10.11.2012

[Wiki01]   Wärmeübergangskoeffizient auf Wikipedia,
             http://de.wikipedia.org/wiki/W%C3%A4rme%C3%BCbergangskoeffizient

[Wiki02]   Leiterplattenwärmemanagement auf Wikipedia,
             http://de.wikipedia.org/wiki/Leiterplatte#W.C3.A4rmemanagement

[Wiki03]   Verdampfungswärme auf Wikipedia,
             http://de.wikipedia.org/wiki/Verdampfungsw%C3%A4rme

[WTE]   wissenschaft-technik-ethik.
             http://www.wissenschaft-technik-ethik.de/wasser_dampfdruck.html

[WÜ]   Wärmeübertragung, Grundlagen und Praxis, Buch

[Porex]   Porextherm, http://www.porextherm.com/web/de/produkte/wds.htm

[KGW]   KGW Isotherm, http://www.kgw-isotherm.de/kontakt.html

[Ker]   Gestützte Vakuumisolierungen als Leichtbaukomposite
             für Automotive und Aerospace, Dr.-Ing. Jobst H. Kerspe, TEB Dr. Kerspe

T4: Thermal Management

1 Project Overview

Speaker and lead university or research institution

Project Nr.	Title	Subject of research	Project leader, institution, location
T4	Thermal Management	Electrical Engineering	Prof. Dr. Meinhard Schilling, TU BS (emg), AOR Dr. Frank Ludwig, TU BS (emg)

Participating institutes and institutions of the university and external institutions in:

- Institut für Elektrische Messtechnik und Grundlagen der Elektrotechnik, TU Braunschweig (emg)

- Baker Hughes INTEQ (BHI), Celle, Dr. Th. Kruspe, Dr. S. Jung

List all participating scientists and engineers:

Name	Subject area	University institute or non-university institution	Position is financed by gebo funds (indicate with X)
Schilling, Meinhard, Prof. Dr.	Electrical Engineering	emg	
Ludwig, Frank, Dr. rer.nat.	Electrical Engineering	emg	
Milde, Stefanie, Dipl.-Phys.	Electrical Engineering	emg	X
N.N. Hiwi	Electrical Engineering	emg	X

2 Research Program

2.1 Summary

The challenge is to investigate the application of new materials and methods of thermal management to use them for geothermal energy exploration and high performance drilling technology at working temperatures up to 250 °C. The main goal is to achieve a self-regulating sensor system and data processing while drilling even under harsh conditions (high temperature and pressure, vibrations). For this purpose, passive thermal management techniques are developed matching the specifications of drill string by the use of modeling time-dependent heat fluxes. Furthermore, material properties and other influencing factors are observed experimentally.

2.2 Relationship of the project to the overall research context and networking with other projects

An essential aspect of the entire joint research project is the optimization of drilling process as well as the subsequent energy transport through the earth. The cooperation within the project occurs by the exchange of the required input data (process parameters, geometries and measured values to validate models) and output (e.g. shear stresses and pressure close to the driller,

conductivities of different structured heat exchangers). The most important collaborations are shown in the Gantt chart (see appendix).

2.3 Work packages executed relative to (original) plan and results achieved

The project is divided in six work packages which will be explained here in three passages because of their associated content. The first section deals with the basics of phase change cooling like the mathematical background for modeling phase change and the selection criteria for a suitable material. The chosen material is characterized in the second and third section. The second part focuses on the influencing factors of inserted metal matrices and thermal stability. The experiments are supported by numerical simulations. The effect of orientation as well as a final demonstrating experiment is presented in part three.

WP 1 and WP 2: Modeling heat fluxes and development of passive cooling concept for 200 °C.

For modeling heat fluxes, temperature fields and phase transitions the finite-element-method-based software package COMSOL Multiphysics is used. The core physics are expanded by the heat transfer module as well as the LiveLink to Autodesk Inventor.

To shield the electronic system implemented in the drilling tool from heat exhaustion, one needs to be aware of the two main heat sources. On the one hand the ambient temperature increases with depth by about 3 K/100 m. For this reason, a thermal insulation is inevitable. On the other hand one has to consider Joule heating within the electronics assembly. Therefore, a cooling system is needed. Both active (T3) and passive methods (T4) can be used for this purpose.

A major amount of heat is transported via conduction through the walls inside the drilling tool. To reduce the temperature rise inside, it is essential to inhibit conduction by minimizing the thermal conductivity. The electronics could be isolated thermally by using an application similar to a thermal flask which takes advantage of the very low thermal conductivity of vacuum. By modeling different possibilities of implementation, several problems of residual heat fluxes showed up. Especially, the seal and connecting wires are the biggest sources of thermal losses. Besides improving the insulation by using convenient seals and thermally insulated wires as well as making the inner walls on the sealed side of flask narrower to reduce heat conduction, it is also possible to add a phase change material [2]. These materials have a low thermal conductivity (<1 W/mK) and store heat while melting. So, the temperature would be kept constant for as long as the material is melting. This was modeled in different setups. It showed that the insulation can be supported by phase change materials when enough material is used. In general, the thermal conductivity is too high to use a phase change material as insulating material.

The thermal conductivity may be reduced by combining the material with a ceramic matrix. This would also increase the mechanical stability and the invariance to vibrations.

Passive cooling of electronics assemblies is limited. Nevertheless, it can support active cooling and can act as a buffer in case the active cooling system fails. Passive thermal management just takes advantage of material properties and existing temperature gradients. Hence, it includes a wide field of activity beginning with materials research for the particular devices, enhancing the thermal contact using thermal interface materials, dissipating heat with heat spreader and heat pipe as well as storing heat in heat sinks or phase change materials. This project focuses on dissipating and storing heat to avoid hot spots on the PCB.

Latent heat storage gets applied for energy storing purposes or as passive cooling unit. During phase transitions, the thermal energy is employed for breaking bonds of atoms and molecules and is therefore not available for a temperature rise. Phase transitions only depend on material parameters and heat transfer conditions which is why no forces or switches need to be applied. Several phase transitions can be used for storing heat. For using it in this particular application only solid-liquid transitions are considered. Although the enthalpy is higher for liquid-vapor phase transitions, the volume would dramatically increase. Furthermore, solids are easier to handle. Solid-solid phase transitions are possible too, but less heat could be stored. For modeling phase transitions, the apparent heat capacity method is used. While melting a peak in the (apparent) heat capacity $c_{p,app} = c_{p,pc} + \delta \cdot \Delta H$ is simulated to consider the latent heat [7,8]. The phase change material melts at the temperature $T_{melt} \pm \Delta T / 2$. The apparent heat capacity method uses the melting enthalpy ΔH and δ which describes the peak with the melting temperature range ΔT as half width:

$$\delta = \frac{\exp(-(T - T_{melt})^2 / \Delta T^2)}{\Delta T \sqrt{\pi}} \tag{1}$$

The summand $c_{p,pc}$ describes the change in heat capacity caused by the phase transition. Usually the liquid phase of materials has a higher specific capacity.

$$c_{p,pc} = c_{mat} + \frac{\Delta H}{T_{melt}} H(T) \tag{2}$$

The Heaviside function $H(T)$ is smoothed depending on the melting temperature range ΔT. This also causes the width of δ peak. So, the obtained results depend on the chosen melting temperature range.

The performance of a PCM heat sink depends on material properties which should be adapted for the specific problem:

- Melting temperature: The melting temperature T_{melt} should be some degrees lower than the maximum allowed temperature, but not too low (less performance) or too close to T_{crit} because many materials melt within a temperature range ΔT.

- High specific capacity: The specific capacity c_p defines the increase in temperature before and after the melting process.

- High enthalpy and high density: The enthalpy ΔH determines the amount of heat that can be stored during phase change. As the space is limited, a specific enthalpy $\Delta h = \rho \cdot \Delta H$ should be used which is the product of enthalpy and density. The result specifies the amount of heat stored per volume (instead of per mass).

- Thermal stability: To use the PCM as often as possible, a repeatable phase transition must be present even after many melting and solidification processes. In particular, the phase separation reduces the thermal stability.

- Subcooling: Often the solidification temperature of phase change materials is lower than the melting temperature. While the solidification takes place the temperature rises again up to the melting temperature. The temperature peak is called subcooling (or super cooling) and depends on various factors.

- High thermal conductivity: A high thermal conductivity ensures that the heat is properly distributed in the PCM and quickly removed from the hot spot. Besides metals the most PCM have a very low thermal conductivity. To increase the thermal conductivity metal matrices can be inserted into the PCM.

- Volume change: The volume of material should change as little as possible. Solid-liquid transitions usually induce an increase of volume of less than 10%.

- Chemical reactions: The material should not interact with surrounding materials (e.g. corrosion).

- Ecological and economical aspects: Phase change materials should be non toxic, recyclable and available for low cost.

As phase change materials have low heat conductivity, a metal matrix shall increase the overall thermal conductivity and thus improve the performance. The metallic heat sink acts as a so called thermal conductivity enhancer (TCE). The optimal volume ratio between metal and phase change material is difficult to identify. One needs enough metallic components to increase the conductivity to a useful level, but at the same time one wants to use a large amount of phase change material to store as much heat as possible. The combination of heat sink and phase change material has been modeled to study the influence of different heat sinks. Therefore, two finned heat sinks of same volume were compared, while the number of fins and the inner surface of heat sink 1 were doubled to build heat sink 2. The combined heat sinks were placed on a component taken from the demo board provided by Baker Hughes and loaded with a Joule

heat of 50 mW. The results are displayed in figure 1. It turned out that an increase in contact area has very small effect on the temperature profile. The difference between both temperature curves is less than 0.1 K. To validate the model the phase change material (PCM 1, $dH_1 = 150$ J/g) was replaced by another one (PCM 2) with the higher specific enthalpy $dH_2 = 339.8$ J/g. This time a longer flattened temperature curve could be observed. The duration of the melting process almost got triplicated. Without any kind of heat sink mounted on the warming chip the model reached a temperature of 40 °C after 16.5 minutes. With the attachment of combined heat sink and phase change material 40 °C was reached after 47.5 min and 86.3 min, respectively. So in this case, to improve the thermal performance of heat sink combined with phase change material, it is necessary to increase the specific enthalpy and the volume of phase change material.
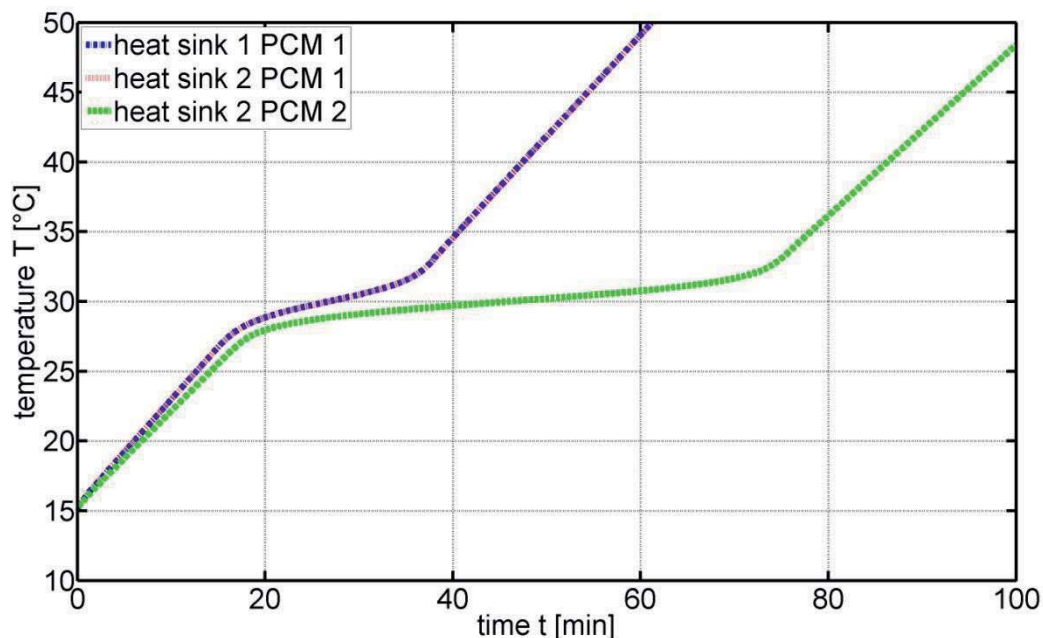
Figure 1: Comparison of the modeled temperature profiles. The temperature rise is retarded due to the use of a latent heat storage unit. The contact area between metal matrix and PCM of heat sink 1 is doubled for heat sink 2. The effect of contact area is negligible for PCM 1. The specific enthalpy of PCM 2 is higher than the enthalpy of PCM 1. The higher latent heat results in a distinctive temperature plateau.

Instead of using an off-the-shelf finned heat sink, it is also possible to use metal foam or graphite as matrix. A bachelor thesis was assigned to study and test different matrices. The experiments were planned with a phase change material with a melting temperature in the range of 150 °C to 200 °C. Different heat sinks and metal structures with varying geometrical parameters were tested to figure out which one is suitable for the requirements. Furthermore, the preparation of samples and the handling was studied. One task, for instance, was to keep the phase change material inside the heat sink while melting and afterwards.

How much thermal energy can be stored strongly depends on the volume of material. To achieve a major increase in phase change material volume, the material can be kept in a container. In this case, the heat needs to be transported into a container by heat pipes. By this means, the phase change material can act as a heat sink.

For the best possible cooling performance the phase change needs to fulfill plenty requirements. Table 1 gives an overview of some possible high temperature phase change materials.

Table 1: Overview of some chosen high temperature phase change materials [3,11,12].

material	melting temperature [°C]	specific enthalpy [MJ/m^3]	thermal conductivity [W/mK] (solid)	additional information
magnesium chloride hexahydrate	117	262.023	0.704	salt hydrate, phase can separate, may be corrosive
erythritol	120	503.20	0.733	sugar alcohol, non corrosive
mannitol	167	480.32	n.a.	sugar alcohol, non corrosive
galactitol	188	533.52	n.a.	sugar alcohol, non corrosive
UTEC 6541	133	131.67	0.4	commercial, Braskem, uhmw polyethylene
A164	164	435	n.a.	commercial, PCM Products Ltd., organic

M1: Concept for 200 °C was successfully finished.

WP 3 and WP 4: Development of demonstrator setup. Test and implementation of passive cooling concept.

For further investigations, the phase change material galactitol (also called dulcitol, CAS-Nr. 608-66-2, T_{melt} = 185-188 °C, T_{eva} = 275-280 °C, ΔH = 351 J/g, $\rho_{20°C}$ = 1470 kg/m^3 [11]) was selected. Galactitol is a so called sugar alcohol which is a reduction product of carbohydrates. Hence, it is non-toxic and environmentally safe.

Several experiments to study the influence of a metal matrix on the cooling ability of phase change materials were performed. Two different finned heat sinks and two pin heat sinks with a base of 50 mm x 50 mm were chosen as metal matrix for the investigation in a bachelor thesis [5]. The studies are performed using a simple assembly. The heat sink combined with phase change material is placed on a metal block with a base of 50 mm x 50 mm. This sample is placed on a heating plate. The complete assembly was thermally insulated against ambience by filling it with perlite. Temperatures were measured inside the perlite, inside the phase change material and between heat sink and heater with type K thermocouples.
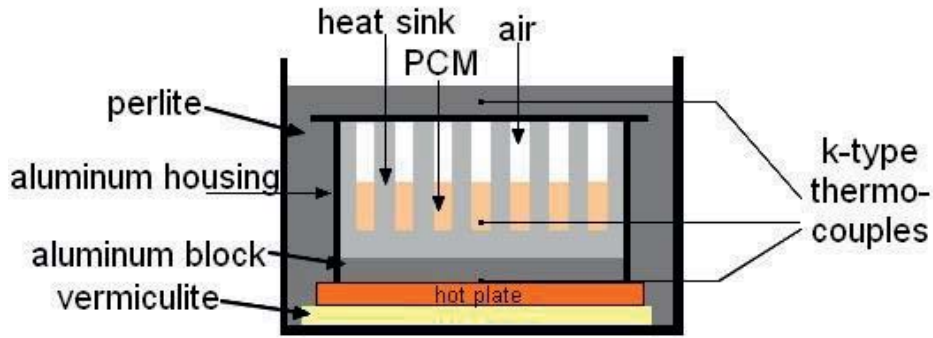
Figure 2: Measurement unit to study the influence of different metal matrices. The PCM-metal-hybrid is enclosed in an aluminum housing to prevent leakage. The whole system is placed on a hot plate. To insulate the unit thermally against ambience the complete system is put in a box of steel which is filled with perlite.

The geometric parameters of the used heat sinks are given in table 2. Heat sink 1 consists of 11 smooth fins while the surface of the 6 fins of heat sink 2 is waved. Heat sinks 3 and 4 are made of round and rectangular pins, respectively. The influence of contact area A and volume ratio $R = {V_{PCM}}/{V_M}$ is studied experimentally for different heating power. The mass of galactitol is kept constant (30 g).

Table 2: Geometric data of the used heat sinks. The contact area includes the aluminum housing.

heat sink	contact area A [m^2]	matrix volume V_M [10^{-6}m^3]	volume ratio R
heat sink 1	0.015280	44.590	0.4577
heat sink 2	0.009491	68.612	0.2974
heat sink 3	0.012424	35.374	0.5769
heat sink 4	0.011962	29.327	0.6959

The results of the experimental study are shown in figure 3. The idea was to find the optimal geometrical parameters of metal matrix (TCE) that enhances the allover thermal conductivity. The contact area affects primarily the heat transfer into the phase change material. The metal matrix affects conduction and convection processes. Particularly, natural convection influences how uniform the melting processes. In a fixed total volume it is necessary to find the best volume ratio because matrices reduce the volume of phase change material. A maximum in melting time is recognizable for the contact area as well as the volume ratio. A potential influence of thermal instabilities is not considered in this study.

893
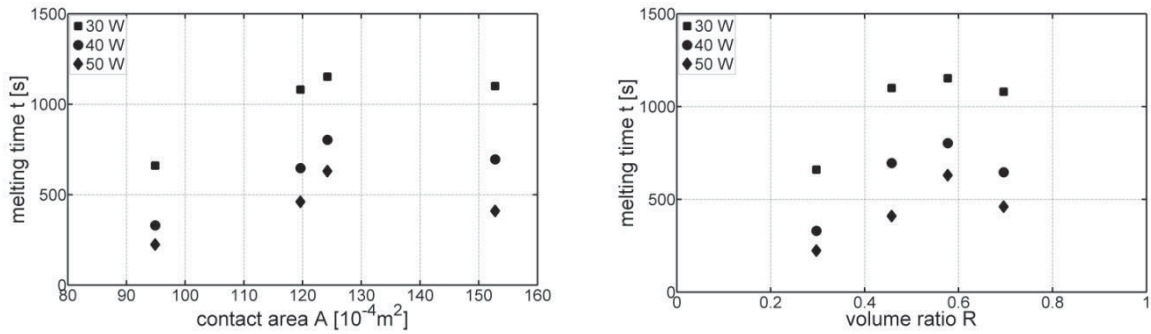
Figure 3: (a) Melting time versus contact area for different heating powers. (b) Melting time versus volume ratio for different heating powers. Both series of measurement show a maximum melting time for specific geometric parameter.

Experimentally it is quite difficult to vary just one influencing parameter. Thermal instabilities as well as the heat transfer conditions affect experiments, too. Therefore, a numerically study is performed. To vary the contact area with fixed volumes a ripped aluminum cube got designed. The cavities are filled with galactitol. Thinner and multiplied fins lead to higher surfaces (see figure 4(a)). A rising number of pins with smaller diameter cause a variable volume ratio while the contact area is constant (see figure 4(b)).
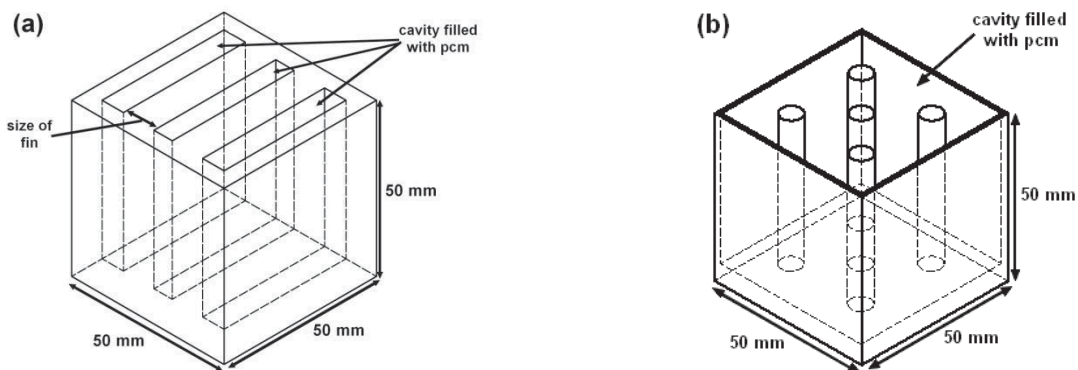
Figure 4: CAD design of metal matrices for parametric study. (a) Finned aluminum chassis with fixed PCM mass and varying contact area. (b) Aluminum housing with a different number of pins. The contact area is constant, the volume ratio varies.

Figure 5 shows the results from the parametric study. To determine the melting time, a high-grade polynomial was fitted to the temperature curve. The polynomial was differentiated to calculate the melting time from the points with the greatest curvature. Because of the constant volume of phase change material and the metal matrix, the melting times were almost equal for different contact areas. To display the influence of the contact area on phase transition, figure 5(a) shows the melting time determined by a fixed temperature interval (184 °C to 190 °C). Short times correlate with a broadened temperature plateau, while the plateau is more distinc-

tive for longer melting durations. It is noticeable that an increase of contact area changes the temperature plateau up to specific value. Afterwards, the increasing the area has no further effect. Figure 5(b) displays the influence of volume ratio $R = V_{pcm}/V_{matrix}$ on the melting times calculated from the already mentioned polynomial fit. The rising melting temperature can be explained by the higher volume of phase change material. But the influence seems to be limited, so that a further increase of pcm volume does not have a significant effect. While the experiments showed a maximum melting time for different contact areas and volume ratios, the model predicts a converging melting time. One possible cause for the differences between experiment and model (cf. figure 3) may be that the models are not affected by instabilities and heat transfer conditions. Furthermore, the model does not include convection.
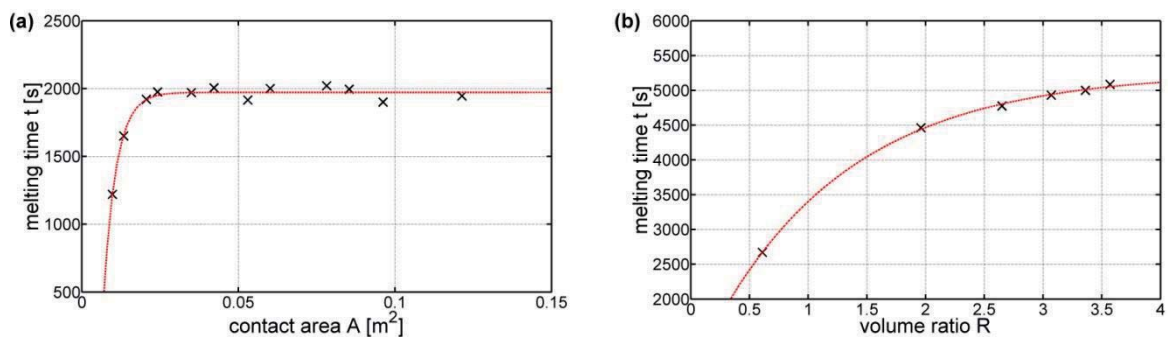
Figure 5: Numerical study to investigate the influence of contact area and volume ratio. (a) Melting time versus contact area. (b) Melting time versus volume ratio. Both figures show a rising melting time up to a limit value. So the influence of contact surface and volume ratio is limited.

Besides studying the cooling performance depending on the metal matrix, the thermal stability was observed. To study the thermal stability of the melting process four samples were prepared which take geometrical influences into account, too. The first sample is taken out of the test series made for the bachelor thesis. It is made of a commercial aluminum heat sink (heat sink 1) filled with 30 g galactitol. The mass of galactitol is fixed for all measurements. Two samples are made with copper meshes of different rod diameter. The last sample is prepared without metal matrix. The melting times were computed via the polynomial fit again. The results, shown in figure 6, exhibit a distinct drop of melting duration with a rising number of measurements. The values differ because of different geometric influences. To better distinguish the individual gradients, the results were fitted exponentially. The three metal matrices show a similar decrease in melting time. Without matrix the drop is slightly faster. Thermal degradation has multiple sources. The phase change material can posses impurities and phase separation effects. In addition to the material, the installation of the phase change material plays an important role, too. The evaporation of water can be compensated by an extra water principle [4]. An oxygen-

containing atmosphere can also drag degradation [9]. A sealed material container can prevent such consequences.
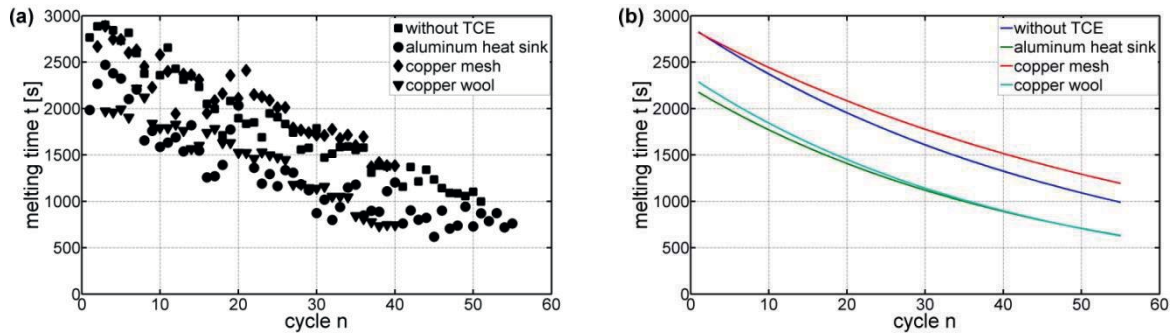
Figure 6: Melting time versus measurement cycle for different thermal conductivity enhancing techniques. For better identification the times are fitted exponentially. The melting times differ because of the varied contact area and volume ratio. Nevertheless, the thermal stability is quite similar. The duration of melting process decreases rapidly with increasing number of measurements.
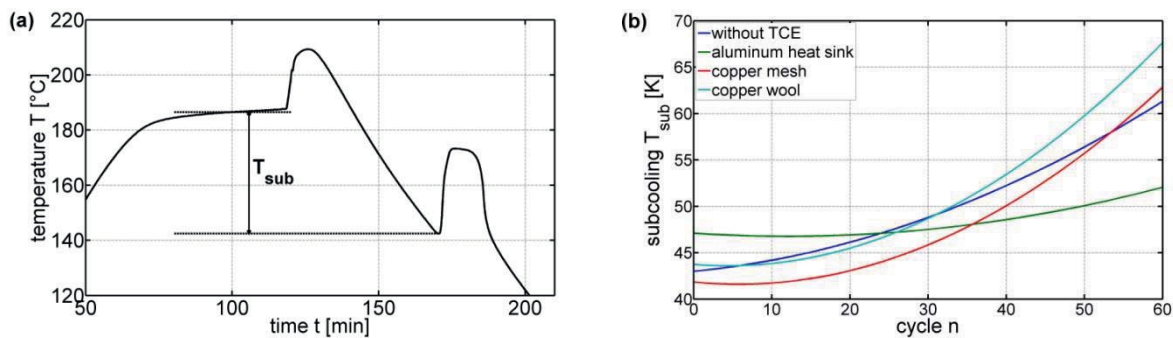
Figure 7: (a) Definition of subcooling as difference between of average melting temperature and minimum temperature peak. (b) Thermal stability of subcooling for three different matrices and one study without matrix.

The temperature of subcooling T_{sub} is defined as difference between the average melting temperature determined from the fitted temperature curve and the minimum temperature reached during solidification (see figure 7(a)). When phase change materials are used as energy storage a low subcooling is preferred so that the stored energy is available when it is necessary. For cooling purposes low subcooling is less relevant, but rather large subcooling can protect temperature sensitive components while releasing heat. According to Royon et al. [13] the width of temperature plateau during solidification depends on heat transfer conditions and is the shorter the higher the temperature difference between ambience and solidification temperature. Günther et al. [6] developed a new algorithm for studying the simulation of subcooling. They proved numerically that the temperature plateau shortens for stronger subcooling. The reduction is explained by the fact that the temperature rise to the plateau also requires heat energy. For very strong subcooling the plateau even disappears. Since the subcooling depends on the stored

896

heat, it is affected by thermal instabilities. Figure 7(b) displays this relation for an aluminum heat sink, copper mesh, and copper wool as well as without matrix. For a better identification the data were adapted with a second grade polynomial. For the copper matrices the running of the curves is quite similar with an almost constant difference between them. Both consist of a mesh which is very uniformly spreaded in the phase change material. Without any thermal conductivity enhancement technique, the subcooling is more stable against thermal cycling. The lowest change of subcooling was measured for the aluminum heat sink.

M 2: Implementation of passive cooling system for 200 °C was successfully finished.

WP 5 and WP 6: Further development of cooling concept for 250 °C and implementation.

The inserted metal matrix affects the natural convection within the galactitol while it is melting [1,14,15]. Since directional drilling causes a change of orientation it is necessary to verify whether this change has an effect on convection and melting processes. Therefore a cylindrical sample holder was constructed (see figure 8(a)).
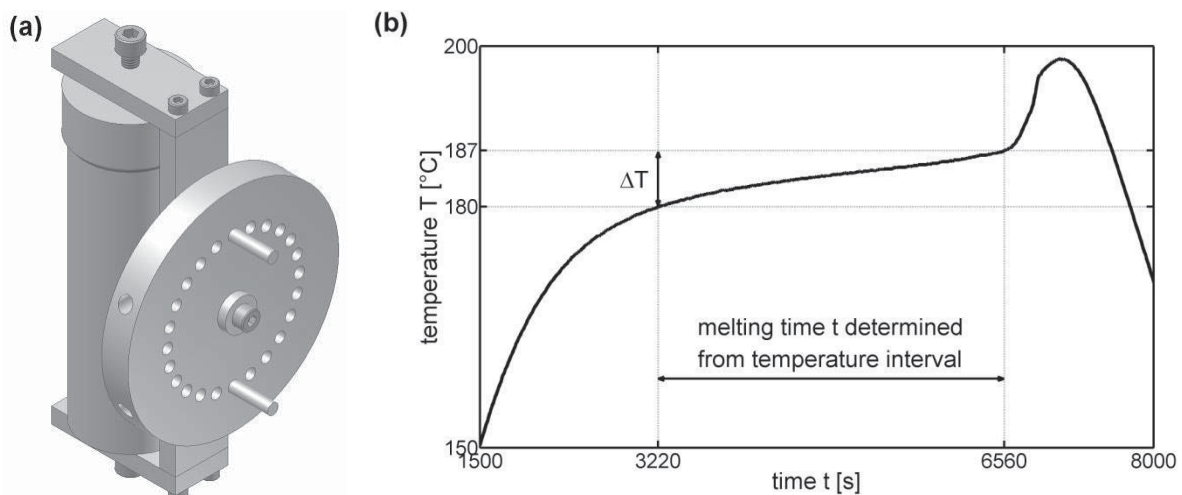
Figure 8: (a) Cylindrical sample holder mounted on a plate. The dowels fix the cylinder in a chosen position. (b) Temperature curve measured in the center of sample holder. The marked melting temperature interval is used for determining the melting time.

Two samples were prepared, one with copper mesh and one with copper wool. The cylinders contain 75 g galactitol and each 8.6 g of the copper matrices. Because of different wire cross sections, the surface of copper mesh is about 15% less than that of the copper wool. Three thermocouples were placed inside the cylinder through bore holes. The sample holder is mounted on a round plate, which enables the rotation of the cylinder at fixed angles. Start position is the vertical orientation of the cylinder and is denoted as 0°. The adjustable rotation angle

is 15° or multiples of it. The complete system is placed in an oven. To prevent that thermal instabilities affect the measurements, twenty cycles of heating (2.5 hours at 200 °C) and cooling were performed. The oven temperature was 215 °C. The melting time was determined by a defined melting temperature interval $\Delta T = 7K$ as displayed in figure 8(b).

Figure 9(a) shows the measured melting time depending on deflection angle. The difference on melting for both copper matrices results from the different contact surface between matrix and galactitol. However, the dependence of melting time on the orientation of the cylinder is similar for both matrices. The vertical position causes a maximum in melting time, while the horizontal position shows a minimum. The measurement had to be stopped because of leakage, but there are still enough data to show a relation. Subcooling seems to be not related explicitly to the deflection angle.
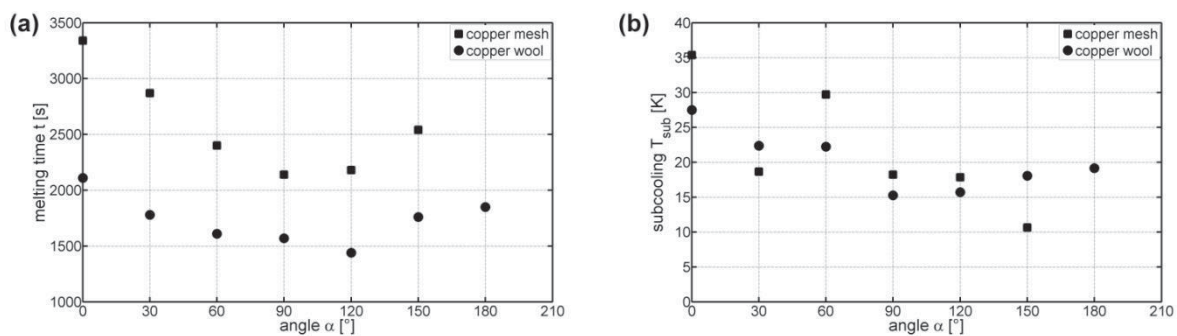
Figure 9: Effect of orientation on melting process. (a) Melting time versus angle of deflection. Both copper matrices show a minimum time span for horizontal orientation and a maximum time span for a vertical orientation. (b) Subcooling shows no concrete relation to rotation.

The achieved results were used to build a final demonstrator. A metal cylinder with inner diameter 100 mm and height 240 mm was filled with 155 g copper mesh and 2305 g galactitol. Two thermocouples were placed inside the cylinder. The complete assembly was placed in the oven and the temperature was logged. The measured oven temperature was 202.5 ± 7.5 K. Figure 10 displays the recorded temperature curve in the center of the cylinder. The determined melting time is 74 minutes. Former studies attest a shorter melting time for a horizontal position of cylindrical sample holder. This may also affect the duration of melting in this case. The much stronger distinctive temperature plateau during solidification is particularly striking. This emphasizes the influence of different heat transfer conditions on subcooling effects.
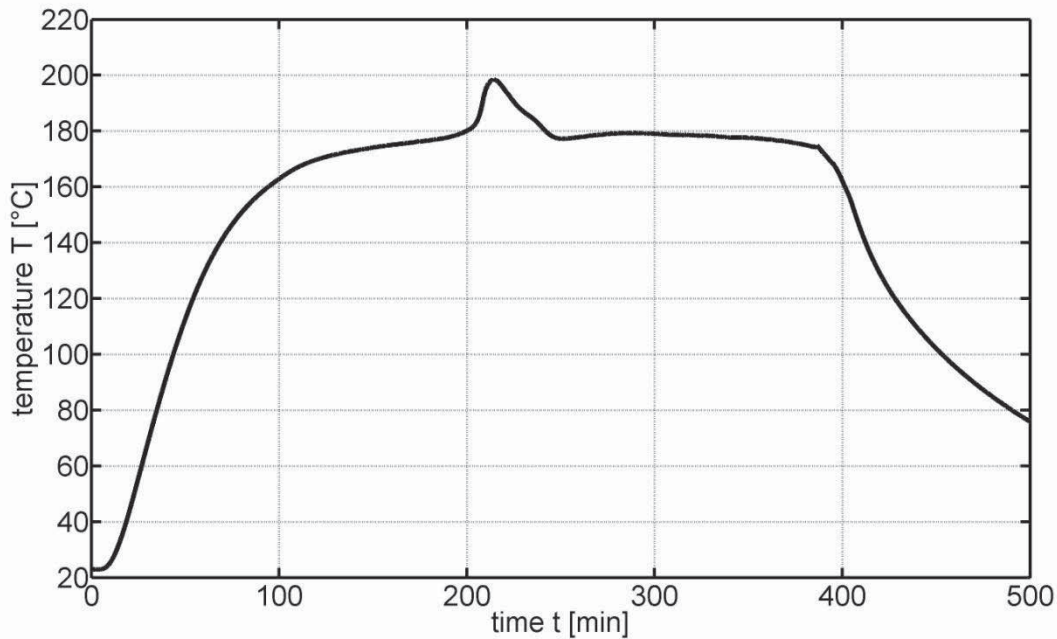
Figure 10: Recorded temperature curve for a higher volume of phase change material. The temperature rise is slowed by the melting of the pcm. At the highest measured temperature the oven was switched off and the cool down starts. Meanwhile, the phase change material solidifies.

M 3: Implementation and qualification of enhanced passive cooling system for 250 °C.

Cooperation with other projects:

- Within project T2 a diploma thesis was assigned to study the temperature distribution and heat fluxes along the plunger. The experiments have been supported by project T4 by measuring the temperatures with an infrared camera.
- Exchange of data and information with project T3.
- The high temperature fluxgate coil system developed on project T6 was modeled with Ansys to study the thermal expansion. The results showed an expansion small enough to keep the parts together. This was confirmed by the experiments.

2.4   Project Plan

Work packages and milestones	2009		2010		2011		2012		2013		2014	
WP 1: modeling heat fluxes												
WP 2: working out concept and test of materials for 200°C												
WP 3: development of passive cooling system for 200°C												
WP 4: implementing, test and system integration of passive cooling concept for 200°C												
WP 5: enhancement of cooling system for 250°C												
WP 6: implementing, test and system integration of passive cooling concept for 250°C												

Grey, original plan

Blue, actual or current plan, respectively

For details, see Gantt chart in the Appendix.

Dipl.-Phys. S. Milde was hired on 01.08.2009 to work on the project T4. This caused the delay of about six months referred to the original timetable. Since the work packages were separated into a cooling system for 200 °C and one for 250 °C, but the general considerations were focused on 250 °C from the beginning, the research on WP 5 and WP 6 will start with a larger overlap with WP 4 to compensate for the delayed start. Thus, the project was finished on time.

3   Delineation of the project from other funded projects

At the Institut für Elektrische Messtechnik und Grundlagen der Elektrotechnik no further projects besides the gebo projects were simultaneously performed which are related to geothermal energy and/or high performance drilling technology.

4   References

[1] R. Baby and C. Balaji. *Experimental investigations on thermal performance enhancement and effect of orientation on porous matrix filled PCM based heat sink*. International Communications in Heat and Mass Transfer **46**, p. 27-30 (2013)

[2] G. A. Bennett: *Thermal Protection Methods for Electronics in Hot Wells*. High-Temperature Electronics, IEEE Press, p. 111-124 (1999)

[3] Braskem. Data Sheet Ultra High Molecular Weight Polyethylene (UHMWPE). 2011

[4] A. A. El-Sebaii, S. Al-Heniti, F. Al-Agel, A. A. Al-Ghambi and F. Al-Marzouki. *One thousand thermal cycles of magnesium chloride hexahydrate as a promising PCM for indoor solar cooking*. Energy Conversion and Management **52**, p. 1771-1777 (2011)

[5] M. Grabowiec. *Einfluss eines Phasenwechselmaterials auf die Kühlleistung thermisch isolierter Kühlkörper*. Bachelor Thesis. TU Braunschweig (2011)

[6] E. Günther, H. Mehling and S. Hiebler. *Modeling of subcooling and solidification of phase change materials*. Modeling and Simulation in Materials Science and Engineering **15**, p. 879-892 (2007)

[7] H. Hu and S. A. Argyropoulos. *Mathematical modeling of solidification and melting: a review*. Modelling and Simulation in Materials Science and Engineering **4**, p. 371-396 (1996)

[8] S. R. Idelsohn, M.A. Storti and L.A. Crivelli. *Numerical methods in phase-change problems*. Archives of Computational Methods in Engineering **1**, p. 49-74 (1994)

[9] H. Kakiuchi, M. Yamazaki, M. Yabe, S. Chihara, Y. Terunuma, Y. Sakata and T. Usami. *A Study of Erythritol as Phase Change Material*. IEA Annex 10 – PCMs and Chemical Reactions for Thermal Energy Storage. Second Workshop. Sofia. 1998

[10] H. Mehling and L. F. Cabeza. *Heat and cold storage with PCM*. Springer Berlin Heidelberg (2008)

[11] Merck Millipore. Sicherheitsdatenblatt Dulcit. 2011

[12] PCM Products Limited. Product Brochure. PlusICE Phase Change Materials. 2012

[13] L. Royon and G. Guiffant. *Heat transfer in paraffin oil/water emulsion involving super-cooling phenomenon*. Energy Conversion and Management **42**, p. 2155-2161 (2001)

[14] X. Wang, A. S. Mujumdar and C. Yap. *Effect of orientation for phase change material (PCM)-based heat sinks for transient thermal management of electric components*. International Communications in Heat and Mass Transfer **34**, p. 801-808 (2007)

[15] W. Ye, D. Zhu and N. Wang*. Effect of the inclination angles on thermal energy storage in a quadrantal cavity*. Journal of Thermal Analysis and Calorimetry **110**, p. 1489-1492 (2012)

902

T5: High-Temperature Sensors – Project Overview

Speaker and lead university or research institution

Project Nr.	Title	Subject of research	Project leader, Institution, location
T5	High-Temperature Sensors	Mechanical Engineering	Prof. Dr.-Ing. Eduard Reithmeier, Leibniz Universität Hannover (imr) Prof. Dr.-Ing. Lutz Rissing Leibniz Universität Hannover (IMPT)

Participating institutes and institutions of the University and external institutions in:

- Institute of Measurement and Automatic Control (imr), Leibniz Universität Hanover

- Institute of Micro Production Technology (IMPT), Leibniz Universität Hanover

- Baker Hughes Contact: Dr.-Ing. Thomas Kruspe, Dr. Sebastian Jung

List of participating scientists and engineers:

Name	Subject area	University institute or non-university institution	Position is financed by gebo funds (indicate with X)
Prof. Dr.-Ing. Eduard Reithmeier	Mechanical Engineering	imr	
Dipl.-Phys. Alexander Leis	Mechanical Engineering	imr	X
Prof. Dr.-Ing. Lutz Rissing	Mechanical Engineering	IMPT	
Dipl.-Ing. (FH) Anja Wien-ecke	Mechanical Engineering	IMPT	X

1 Research Program

1.1 Summary

Aim of the subproject T5 is the development of two sensor systems: a pressure sensor and a magnetic field sensor to measure the Earth magnetic field. Both sensors shall be able to operate under harsh geothermal environment in the downhole. Different sensor technologies for pressure measurement and magnetic field measurement are examined for their applicability within a drilling system. Promising sensor solutions are selected, simulated and designed, fabricated and characterized with regard to the intended measurement task.

1.2 Relationship of the project to the overall research context and networking with other projects

To achieve the objectives of the subproject T5 the evaluation of drilling process parameters is necessary. For this purpose additional information from Baker Hughes INTEQ in form of a specification sheet is required. Based on this, a specific sensor package for the required geothermal

903

conditions (pressure range, temperature range, shock, vibration and so on) is developed in direct cooperation with subprojects T1 (high-temperature electronics), T2 (pressure sintering), T3 (active cooling), and T4 (passive cooling). For better understanding of the crosscollaborations the networking is presented in form of a Gantt chart (see Appendix).

The subproject T5 is divided in two separate research blocks, executed by the imr (work packages WP 1 till WP 4) and the IMPT (WP 5 till WP 8) and intended to be finally merged in the last work package (WP 9). While the imr has developed a pressure sensor, the IMPT has dealt with the development of a magnetic field sensor for high temperature environments. Both involved institutes have developed their sensor independently from each other but with regularly exchange of information.

1.2.1 First research block: Development of a pressure sensor (**imr**)

WP1: Specification of pressure sensor (specification sheet).

Within this work package the environmental conditions which take place during the drilling process were determined. A specification sheet for the pressure sensor was prepared in direct cooperation with Baker Hughes INTEQ. The requirements to the pressure sensor were:

- pressure range: 0 bar…2,000 bar;
- temperature range: -40°C…+250°C;
- maximal sensor length: 34 mm (can be longer, if required);
- maximal sensor diameter: 19 mm.

Work package WP 1 was completed successfully and on time.

WP2: Selection of appropriate pressure measurement method

Within this work package different pressure measurement methods (piezoelectric, piezoresistiv, optical [MAT09]) were compared to one another. In addition to the sensors, the measurement chains as a whole were analyzed. To the best of the authors knowledge, no commercial pressure sensor is available, which satisfies simultaneously the specified requirements for deep geothermal drilling with respect to pressure range, temperature range, shock resistance, and measurement accuracy. This makes the realization of a new pressure sensor within the gebo-project desirable.

The Table 1 summarizes the commercially available pressure sensors, whose technical characteristics almost match the specified requirements.

Table 1: Overview of commercially available pressure sensors

Manufacturer	Sensor	Measurement method	Operating temperature range (°C)	Pressure range (bar)	Length (mm); Diameter (mm)
Omega	PX1004	piezoresistiv	-50…+340	0…700	61; 25,7
Kistler	RHU50	piezoresistiv	-10…+300	0…2.000	61; 12,7
Quartzdyne	QMB115-30-200	piezoelectric	up to +200	0…2.070	192,4; 22,2
Kulite	ETMER-UHT-375(M)	piezoresistive	-55…+225	35…1.400	30; 14
STW	OEM – pressure sensor	piezoresistive	-40…+350	up to 800	33,2; 17
Paine Electronics	Pressure trans-ducer 211-50-070	no information	up to +260°C	0…3.450	50,54; 12,7
Sensonetics	Downhole Pressure Trans-ducer Series 1000	piezoresistive (silicon on sap-phire)	-55…+260	up to1.380	13; 15

Alternative to the conventional piezoresistive or piezoelectric methods, modern optical measurement methods can be used for pressure monitoring in downhole. Optical measurement techniques offer following advantages: non-contact and therefore thermally decoupled measurements, high resolution and low temperature sensitivity. Thermal stability is especially attractive in deep geothermal drilling. Following measurement schemes can be potentially used for pressure monitoring in deep geothermal drilling:

- Intensity modulation through waveguide deformation (micro bending);
- Triangulation through membrane deformation (photodiodes line);
- Triangulation through membrane deformation (one photodiode, intensity modulation);
- Chromatic aberration through membrane deformation;
- Frequency modulation through Faser-Bragg-Grating deformation;
- Intensity modulation through induced optical birefringence.

All these optical methods have been analyzed in detail. Some of them were computer simulated with specific software. The mechanical properties of sensors were simulated with finite element methods (FEM-Method, "Comsol" - software); the optical characteristics were simulated with a ray tracer (i.e. the simulation program "Zemax"). The optical methods were compared to each other on the base of the simulation results or of direct calculations. The gebo-Project struggles to operate the whole measurement system - including all optical and electronic components - downhole. All optical measurement schemes were compared to one another on this basis. The results of this comparison are presented in Table 2. The judgment criteria were based on the

requirements for deep geothermal drilling. The table is constructed as follows: "+" stays for a positive, "±" for a neutral and "-" for a negative mark. By evaluating the comparison table, it becomes obvious that the intensity modulation by means of stress-induced birefringence is the most suitable optical pressure monitoring method for the deep geothermal drilling.

Table 2: Comparison table of optical measuring methods for the deep geothermal drilling

Measuring method	Implementation	Compliance with the geothermal conditions (temperature up to 250°C)	Miniaturization potential (diameter 19 mm, length 34 mm)	Temperature sensitivity	Accuracy / resolution	Robustness
intensity modulation	Waveguide deformation (micro bending)	±	+	-	±	+
triangulation method	membrane deformation (one photodiode)	±	±	-	-	±
triangulation method	Membrane deformation (photodiodes line)	±	±	-	±	±
chromatic aberration	Distance measurement	-	+	+	+	-
frequency modulation	Faser-Bragg-Gitter (FBG)	-	+	-	+	-
intensity modulation	Stress-induced birefringence (photoelastic effect)	±	+	+	+	+

Before light intensity modulation based on stress-induced birefringence was finally selected as a pressure measuring method, an experimental study of this effect was performed to check its suitability in deep geothermal drilling.

Stress-induced birefringence arises in isotropic media through the application of mechanical stress: force or pressure. If the applied pressure acts in only one direction and is not too large, the dependence of stress-induced birefringence on the applied pressure is linear and can be expressed as: $\Delta n = n_o - n_e = k \cdot P$, where n_o is the refractive index for ordinary rays in the medium, n_e refractive index for extraordinary rays, k the stress-optical constant (in Pa^{-1}), and P the applied pressure (in Pa).

The test bench for analyzing of stress-induced birefringence consisted of a red LED as a light source (wavelength 650 nm), a polarizer with its polarization axis oriented at an angle of 45° to the force direction, an optical lens for focusing the LED's light, a fused silica prism as a sensing element, an analyzer with its polarization axis perpendicular to the polarizer's one, a photodetector, and an electronic module. Pressure was simulated using different weights (100 g, 200 g, 500 g and 1 kg). Because the contact area was smaller than 0.3 mm², the pressure in the contact area reached at least the value P = 1 kbar.

Fused silica shows no natural birefringence. That's why no light could be transmitted through the test system without pressure application. By increasing of pressure (weight) the transmitted light intensity increased. The transmitted light intensity could be expressed as $I=I_0 \cdot sin^2(\pi \cdot d \cdot k \cdot P/\lambda)$, I_0 being the intensity of the transmitted light without pressure application, d the optical path in fused silica prism through the birefringent area, and λ the light wavelength.

The measurements were performed several times to build the mean values and its deviations. The standard deviation of the measured results was relative large. This was caused by the high sensitivity of stress-induced birefringence or photoelastic effect to the stress direction. In the test bench the direction of force could not be hold constant. A free space gave the possibility for the force direction to drift. In the case of direction-independent pressure measurement (as is the case in fluids) this problem can be disregarded.

On the base of the comparison matrix (see table 2) and the experimental study we founded that intensity modulation based on stress-induced birefringence, is the most suitable optical measurement method for pressure measurement in deep geothermal drilling. Moreover, it was decided that the pressure sensor "Kistler" (see Table 1) shall be tested with respect to its applicability in deep geothermal drilling as an alternative or a reference sensor.

Work package WP 2 was completed successfully on time.

WP3: Pressure sensor prototyping

Aim of this work package is the characterization and optimization of the sensor construction. Within this work package a pressure sensor prototype based on the measuring method selected in work package WP2 was designed and manufactured.

An optical pyramid was designed (see Fig. 1) as a sensing element for the pressure sensor based on the photoelastic effect (stress-induced birefringence). The form of a pyramid was chosen because it combines two important operating functions: that of a sensing element and that of a light reflector. The beams originating from the LEDs reflect on the pyramid sides at an angle greater than the angle of total reflection. This means there is no light leakage by reflections. As a pyramid material we had the choice between very hard optical crystals such as quartz (mohs hardness 7), sapphire (mohs hardness 9) or diamond (mohs hardness 10). All these materials are suitable for downhole applications under harsh geothermal environment. For the pressure sensor prototype fused silica glass was selected as a pyramid material. Fused silica glass offers several advantages compared with other materials:

- no natural birefringence;
- a high stress-optical constant $k = 3.4 \times 10^{-12}$ Pa^{-1} (for comparison: sapphire has a stress-optical constant $k = 1.2 \times 10^{-12}$ Pa^{-1});
- a low temperature expansion coefficient: $\alpha = 0.5 \times 10^{-6}$ K^{-1} at room temperature (for comparison: constantan has $\alpha = 14.9 \times 10^{-6}$ K^{-1} at room temperature).

The main challenge in the construction of the optical sensor for downhole applications is the choice of the semiconductor optical components: the optical source and the detector. At present there are no commercial LEDs (LED: Light Emitting Diode) or PDs (PD: Photo Detector) which can operate at a temperature of 250°C. Resistance to vibration and shock while drilling is a further important issue in the search for such components. Still, various research centers and laboratories have reported about high-temperature prototypes of photodetectors based on gallium nitride (AlGaN/GaN) and silicon carbide (SiC). Such detectors are expected to operate in the UV and blue spectral range at temperatures as high as 400°C. The existence of LEDs based on silicon carbide (for example 6H-SiC) which can operate in UV spectrum at temperature as high as 350°C is also reported in the literature but these are not on the market yet. Commercially available high-temperature SiC photodetectors manufactured by firm sglux (www.sglux.de) in Berlin (Germany) can be employed at temperatures up to 170°C. However, we were recently able to obtain photodetector-chips prototypes of the same company without packaging which could resist preliminary temperature tests up to 400°C. Temperature-resistant assembling of these chips on a substrate has been carried out in direct cooperation with subproject T2 (pressure sintering).
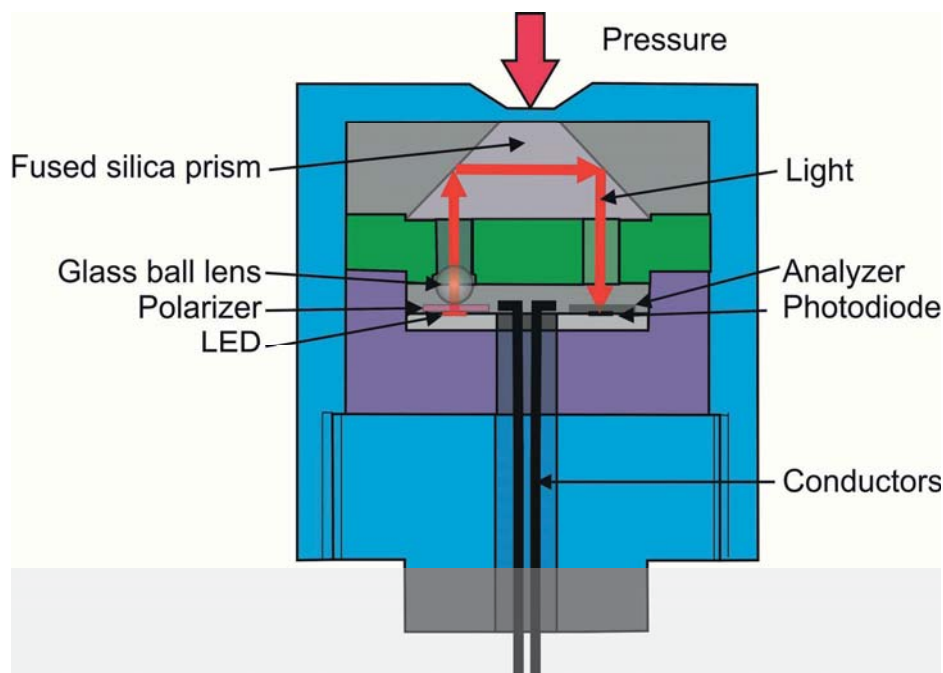

Fig. 1: Current design of pressure sensor based on the photoelastic effect

In any case, the construction of a pressure sensor based on photoelastic effect seems already nowadays feasible for downhole applications. It has however to be noted that the required optical components are still under investigation and, at present, very expensive. For this reason in constructing the first pressure sensor prototype commercially available and cheaper optical

components (LEDs and PDs) in the blue spectral ranges were used. We opted for optical components of the company "EPIGAP" for the first pressure sensor prototype. These components can operate up to a temperature of 125°C. For the final construction, high-temperature optical components will be used.

The pressure sensor construction needs to be simple, well-defined, and robust. The proposed sensor construction contains a minimal number of elements: an LED as an optical source, a fused silica pyramid as a sensing element and a photodiode as a detector (see Fig. 1). Two polarizing elements (one polarizer and one analyzer) are necessary, too.

With the help of a ray tracing optical simulation program (ZEMAX) we found that the application of one glass ball lens in front of the LED having a focusing effect on the emitted light can significantly increase the light intensity at the photodetector.

In addition to the measuring beam, a reference beam must be included in the sensor construction to compensate for temperature fluctuations. For this purpose one additional LED and one additional PD were implemented in the sensor construction. No polarizing elements are necessary for the reference beam.

The first sensor prototype was designed and manufactured in WP 3. The characterization of the prototype showed that optimization of sensor parameters was necessary:

- The distance between optical elements (LEDs and PDs) and basement of fused silica pyramid was reduced: 4 mm instead of 8 mm;
- The diameter of the drill-hole for light guidance in the pyramid holder was increased: 2 mm instead of 1 mm.
- no glass ball lens was required since it was not sufficiently efficient
- a new substrate layout with the central hole was required to optimize the power-supply line for the LEDs/PDs into the sensor cavity.

The optimized sensor construction is shown in Fig. 1. The characterization of the optimized sensor prototype confirmed that the new sensor construction is more suitable for practical application than the original one. In the new construction, enough light for the desired measurement was transmitted through the pyramid from one LED to the PD.

Work package WP 3 was completed successfully on time.

WP 4: Long-time test of pressure sensor

In this work package the behavior of both measuring systems (the reference pressure sensor RHU50 and the pressure sensor based on the photoelastic effect developed at imr) have to be studied under long-term pressure. Within this work package, a measurement chain consisting of following commercial components - OEM pressure sensor RHU50 of "Kistler" and data acquisition system MGCplus of HBM - was calibrated with the help of dead-weight tester BH2 of the company "europascal". A dead-weight tester BH2-4000 has a maximal permissible error smaller

than 1.5x10^{-4} of the measured value. This means that at a pressure of 2 kbar the maximal permissible error is smaller than 0.3 bar. First the calibration of this measuring system was performed at room temperature (20°C). We found that the stochastic error for examined system was in this case less than 0.06% of full scale (FS). The systematic error could be corrected using a third order polynomial. In this case the corrected systematic error was smaller than 0.08% FS i.e. the total error for this measuring system is smaller than 0.1% FS (compared with 1% FS in the sensor datasheet). After that the temperature test was performed with the help of a heating plate. The heating plate was contacted with the pressure sensor contact surface and simulated the hot medium. The temperature of heating plate could be controlled with an accuracy of ±0.5°C. The thermal tests of the system show that the system is very sensible to temperature changes. By the test of thermal drift of zero-point we found that at a temperature of 250°C the pressure error was greater than 10% FS. This means that for downhole applications of the system an additional temperature sensor might be needed to compensate for the temperature drift.

In addition, the long-term stability of a developed fiber optic pressure and temperature sensor was evaluated. A schematic of the fiber optic sensor is shown in Fig. 2. The sensor consists of a Single-Mode (SM) fiber comprising a Fiber Bragg Grating (FBG), a fused silica glass capillary and a 200µm outer diameter fused silica fiber. All sensor components were bonded together by using a fusion splicer. Due to its fused silica structure and hence resistance to corrosion, the fiber optic sensor is perfectly applicable for the long-term monitoring of geothermal wells. The performance of the fiber optic sensor was tested in the pressure range from 0 to 500 bar at temperature of up to 175 °C. As the sensor can determine pressure and temperature at the point of measurement, a small temperature induced pressure error during measurement was obtained even at high temperatures. Furthermore, the reflection at the outer surface of the 200µm fiber can be used to additional measure refractive index of the surrounding medium. Therefore, the fiber optic sensor can also be used to determine refractive index changes within borehole environments.
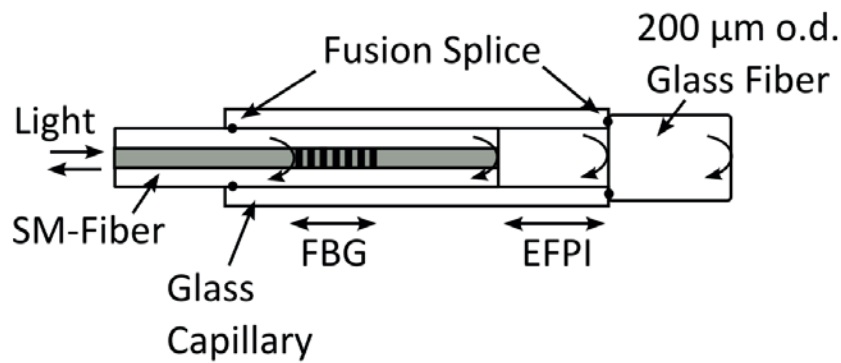
Fig. 2: Schematic of the fiber optic pressure and temperature sensor. The sensor consists of an Extrinsic Fabry Perot Cavity (EFPI) and a FBG. The reflection at the outer surface of the 200µm fiber can be used to additionally determine the refractive index of the surrounding

The first milestone (M1) to study the long-term stability and thus to qualify the pressure sensor and its measuring chain for the application under harsh geothermal environment (which was determined in WP 1) is reached.

Project plan

Work packages and milestones / imr	2009	2010	2011	2012	2013	2014
WP1: Specification of the pressure sensor (specification sheet)	▬					
WP2: Selection of an appropriate method for pressure acquisition	▬					
WP3: Pressure sensor prototype construction		▬				
WP4: Long-time test of the pressure sensor		▬				
WP9: integration in the complete system					▬	▬

Grey: original plan

Blue: actual or current plan, respectively

▲: Milestone

For details, see Gantt chart in the Appendix.

1.2.2 Second research block: Development of a magnetic field sensor (IMPT)

For the determination of the drilling head's position, a magnetic field sensor has to be developed, measuring the Earth magnetic field. These data combined with inclination measurement data and the length of the drilling string enable the subordinate system to calculate the actual position of the drilling head. The measurement is conducted during the drilling breaks when a new run of drillpipes is screwed on the drill string and the pump is not working. The magnetic

field sensor is part of the Measurement While Drilling (MWD) tool, located above the hydraulic motor.

WP 5: *Specification of magnetic field sensor (specification sheet)*

The active and passive cooling system, developed in T3 and T4, sets the measurement conditions at a temperature of about 160 °C. The developed sensor system has to work at this temperature, but it has also to withstand temporary temperatures of 250 °C during drilling breaks. Therefore one criteria of the developed sensor is that it can be applied at 250 °C for a certain time. Moreover to measure the magnetic field of the Earth, the sensor shall provide the necessary sensitivity in the field range of ±80 A/m ~ ±100 µT, forming the second important requirement of the sensor. Furthermore, its integration in the drill string makes small sensor dimensions necessary (< 1 cm^3). And last but not least, the sensor shall be simple in fabrication and feature a robust design (e. g. to withstand damage by vibrations).

To reach these demands, an appropriate measurement principle combined with an adequate material combination and sensor geometry has to be elucidated.

WP 6: *Selection of an appropriate film system of the magnetic field sensor*

Selection of measurement principle

For sensing the magnetic field, different measuring principles exist. One principle which provides the potential to withstand higher temperature and to feature the necessary sensitivity to measure the relatively small magnetic field of the Earth (40 A/m ~ 60 µT) is the Giant Magnetoresistive Effect (GMR) in its spin valve configuration. Furthermore, its fabrication by thin film technology makes small sensor size and a robust design possible.

GMR sensors work according to the principle that their resistance depends on the strength or direction of the external magnetic field. A simple GMR-spin valve layer stack comprises four layers: two ferromagnetic layers, which are separated by a non-magnetic spacer layer, and an antiferromagnetic layer. One of the ferromagnetic layers is magnetically coupled to the adjacent antiferromagnet. This coupling (exchange biasing) fixes magnetic direction of the domains in the coupled ferromagnetic layer. Therefore this layer is called pinned layer. The domains of the second ferromagnetic layer are free in their orientation and can be rotated by an external field. This layer is the free layer. The resistance is determined by the relative orientation of the magnetization direction between the pinned and the free layer. The resistance reaches its maximum, when the magnetization direction in the ferromagnetic layers is antiparallel to each other and takes a minimum in parallel orientation. The maximum GMR-effect can be calculated by equation 1.

$$GMR_{\text{max}} = \frac{dR_{\text{max}}}{R_{\text{min}}} = \frac{R_{\text{max}} - R_{\text{min}}}{R_{\text{min}}} \qquad [1]$$

with dR_{max} as the resistance change and R_{max} and R_{min} as the maximum and minimum resistance respectively.

Fig. 2 shows exemplarily the resistance characteristic of a GMR layer stack. As it can be seen, it consists of two combined hysteresis loops. The hysteresis loop located at zero field belongs to the free layer and the hysteresis loops which is shifted by the exchange bias field H_{eb} from zero field (because of the coupling to the antiferromagnet) belongs to the pinned layer. For measurements, the hysteresis loop of the free layer is the decisive one. To realize a high sensitivity, this hysteresis loop should be marked by a high resistance change occurring within a small magnetic field. Ideally the loop is centered at zero.

In this report, the GMR-effect is evaluated by the minimum resistance (R_{min}) / voltage (U_{B_min}) and the maximum change of resistance (dR_{max}) / voltage (dU_{B_max}).
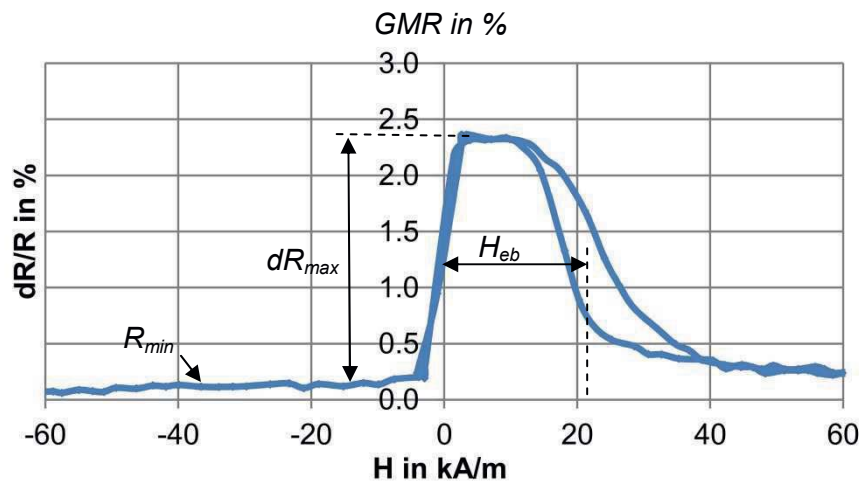
Figure 2. GMR-spin valve hysteresis loop

Adaption of GMR-layer stack: Choice of materials and their combination with regard to realize high thermal stability and high sensitivity in the required measurement range

To increase the GMR sensor's temperature stability and sensitivity, the classical stack of four layers is adapted. Ferromagnetic and antiferromagnetic materials which keep their magnetic properties also at 250 °C are selected. Here, CoFe featuring a Curie temperature[1] of more than 1,000 °C and NiMn with a Blocking temperature[2] of about 450 °C are used. Furthermore, the

---

[1] Curie temperature: temperature above which a ferromagnetic substance loses its ferromagnetic characteristics and becomes paramagnetic

[2] Blocking temperature: temperature above which the coupling between the antiferromagnet and the adjacent ferromagnet does not exist anymore

materials are chosen in that way that their miscibility with their neighboring layers is low – otherwise diffusion barriers are supplemented. Moreover a synthetic antiferromagnet is integrated to magnetically stabilize the layer stack. To realize a high sensitivity, NiFe is used as free layer. Its low coercivity combined with its low anisotropy constant provides good soft magnetic characteristics, higher than that of CoFe. The completed layer stack is shown in fig. 3 and comprises the following layers: a Ta seed layer, a free layer of NiFe, a CoFe diffusion barrier, a nonmagnetic spacer of Cu, a pinned layer with a synthetic antiferromagnet composed of CoFe/Ru/CoFe and NiMn as antiferromagnet, and Ta as capping layer. Additional optimization concerns the quality of the thin sputtered layers (0.8 nm - 52 nm), which are sensitive to their growth conditions. Here several parameter studies are conducted. The detailed results are published at the conferences EMSA 2014 [Wie14b] and MMM 2014 [Wie15a]. It was found that a correlation between a spin valve's thermal stability and its inherent exchange bias H_{eb} exists [Wie14b]. The layer stacks featuring a high exchange bias are more resistant against diffusion processes compared to those layer stacks with low coupling strength. The investigations published at MMM 2014 elucidate the sputtering parameters and layer thicknesses promoting a high exchange bias [Wie15a]. The thickness of the final layer stack is less than 100 nm.
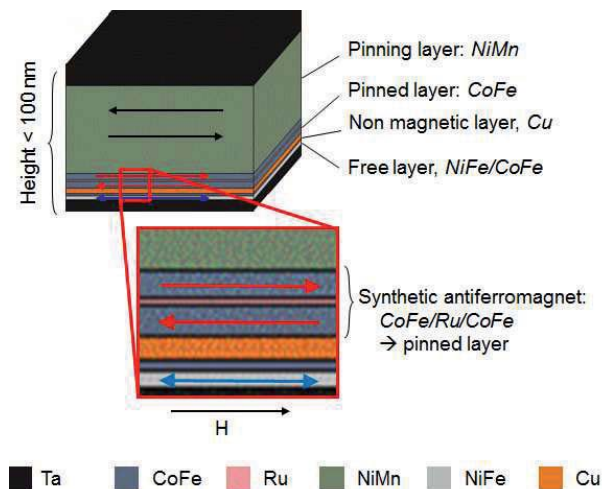
Figure 3. Adapted layer stack [WIE13]

To investigate the stability of the optimized layer stack at temperatures of 250 °C, the layer system is tested on chip level and afterwards in simple meander shape.

Thermal evaluation of the layer stack on chip and meander level to find out its thermal long term stability and the signal's dependency on temperature

To prove the layer stacks' thermal stability, the layer system is sputtered on Si-Chips of 15 x 15 mm^2 in size. After their annealing to establish the coupling of CoFe to the adjacent anti-

ferromagnet NiMn, the layer system is heated for several hours at 250 °C. In between, the resistance characteristic is determined at room temperature by four-point measurement. The data are visualized in fig 4. The diagram shows the minimum resistance R_{min} and the maximum resistance change dR_{max} (for reference see fig. 2)
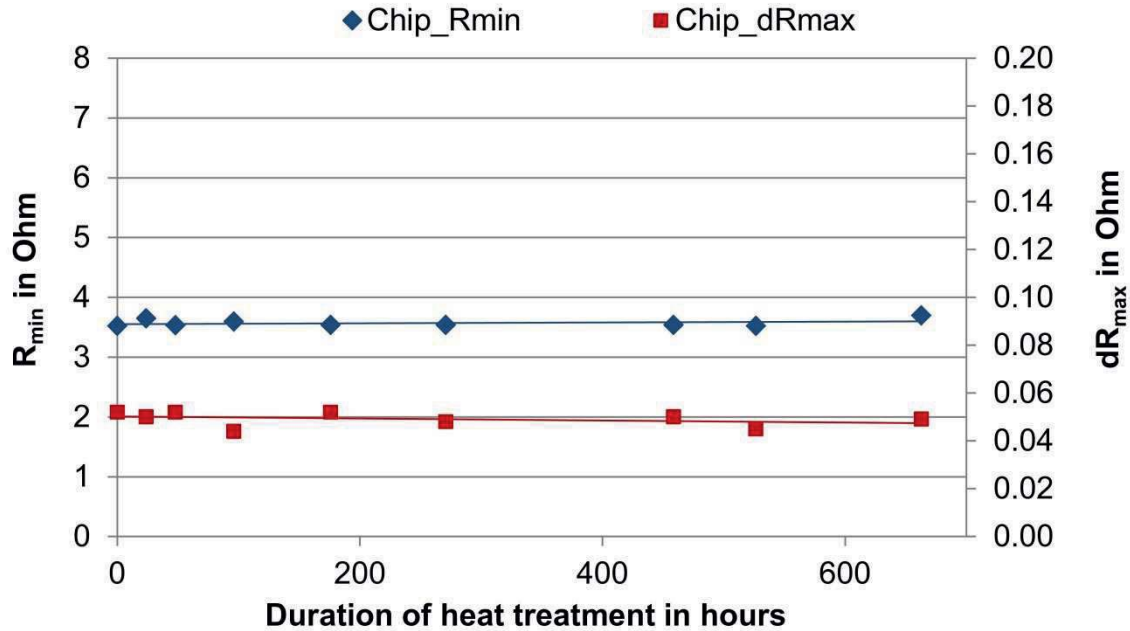

Figure 4. Minimum resistance and the maximum resistance change after thermal treatment at 250 °C for several hours – chip level [Wie15b]

As it can be seen, hardly any change took place after 660 h. Neither the resistance increase nor the maximum resistance change decreases and therefor the GMR-effect is still constant (see equation 1). The results show that no significant diffusion processes takes place and the magnetic function of the layers is not disturbed.

To investigate the influence of the shape on the signal's thermal stability, the layer stack is structured into meander shape with 130 mm length and 7 μm in width. The meander structures are also heated for several hours at 250 °C. In between, the resistance characteristic is measured at room temperature. The diagram visualized in fig. 5 shows exemplary the results of one meander.
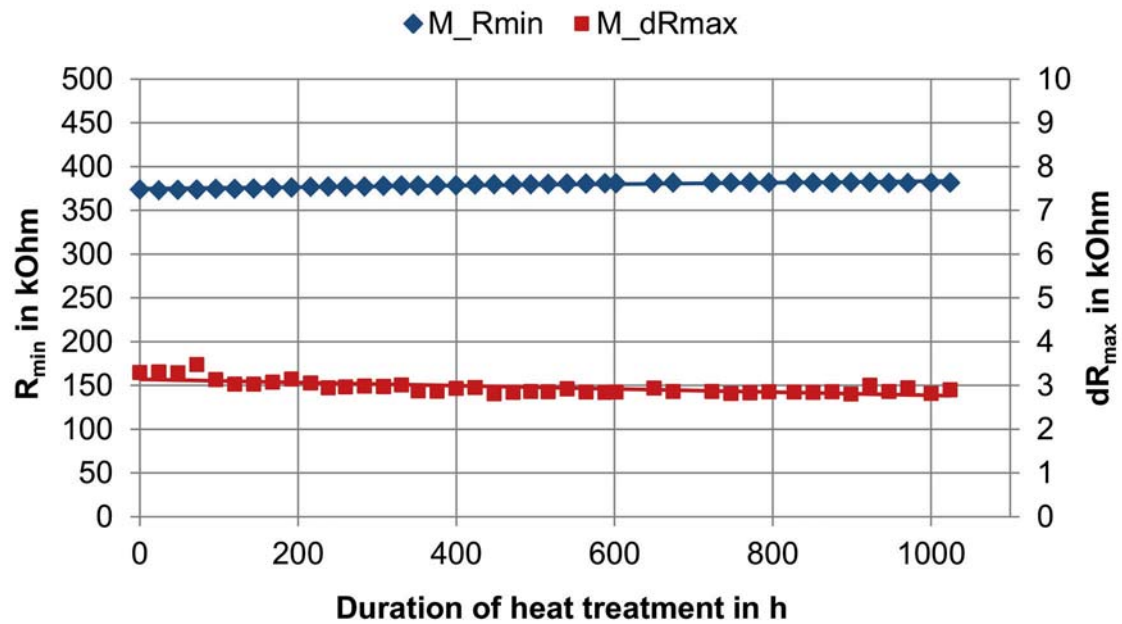
Figure 5. Minimum resistance and the resistance change after thermal treatment at 250 °C for more than 1,000 hours – meander level

As it can be seen, after 1024 h at 250 °C, the basic resistance remains nearly constant and only a small decrease of maximum resistance change can be observed. The reduction of the maximum resistance change starts after 72 h and proceeds within the next ~380 h. After 448 h at 250 °C, a constant state is reached and no further degradation of maximum resistance change can be observed for the next 576 h of thermal treatment. The signal is still ~85 % of the original value of the just annealed sample. Compared to the layer system on chip level, the shaped system on meander layer provides a greater lateral boundary surface and therefore more unfavorable diffusion paths. This might be the reason for the "initial" degradation of signal. But nevertheless a constant state is reached after nearly 450 h.

Besides the measurements after thermal treatment, the signal is characterized within a temperature range from -75 °C to 246 °C. For this, the meander structures are heated from room temperature to 246 °C and afterwards cooled down to -75 °C and finally warmed up to room temperature. The measurement results are depicted in fig. 6.
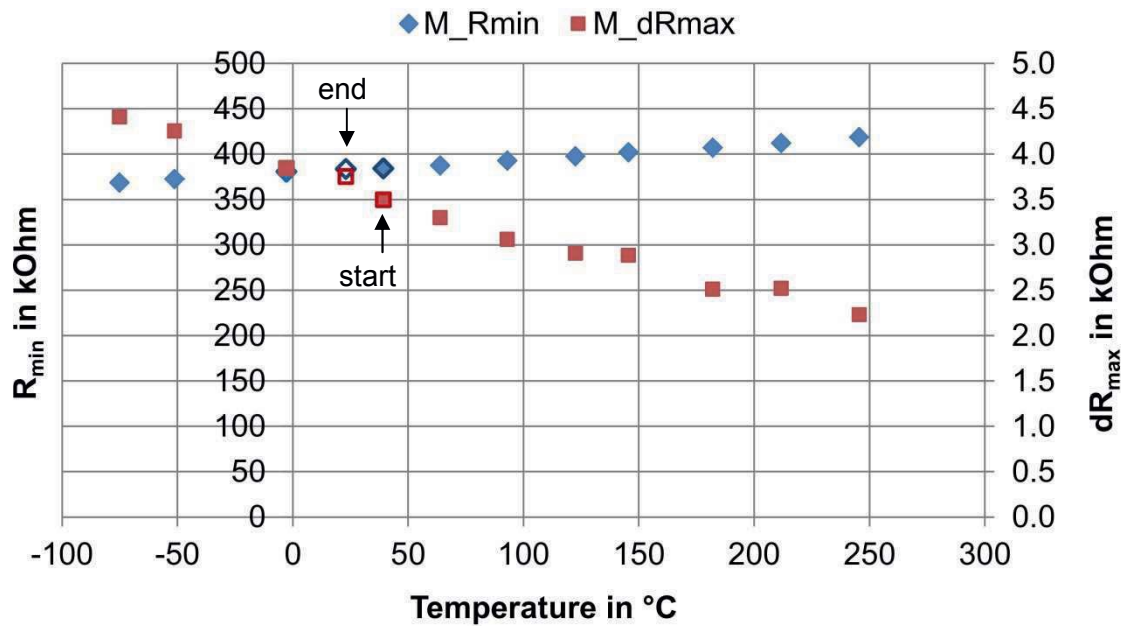
Figure 6. Minimum resistance and the resistance change at a certain temperature – meander level [Wie15b]

As might be expected, the increase in temperature leads to an increase in basic resistance, whereas the maximum resistance change decreases. The temperature dependency shows an almost linear behavior. Whereas the maximum resistance change at room temperature is 3.75 kΩ; it increases to 4.41 kΩ at -75 °C and decreases to 2.23 kΩ at 246 °C. With reference to the room temperature data of the meander structures, the signal loss is 47 % at 246 °C. These effects are reversible and the consequence of temperature dependent scattering of phonons and magnons in the layer materials. At room temperature the resistance and maximum resistance change are readjusted, which proves that the changes are reversible.

Another aspect is the sensors sensitivity, since the sensor has to be able to measure the small Earth magnetic field. The sensitivity can be calculated by equation 2.

$$Sensitivity = \frac{dR}{dH}$$
[2]

With reference to fig. 2, the loop at zero field (that one of the free layer) has to be high and steep, so that within a small magnetic field dH a high resistance change dR takes place. On chip level, the layer stacks inherent sensitivity is 8 mΩ per 100 A/m. On meander level with its 130 mm in length, the sensitivity is much higher and a resistance change of 391 Ω within 100 A/m can be reached.

WP 7: *Magnetic field sensor prototype construction*

Development of sensor design to reduce temperature dependent signal loss and to increase the sensor's sensitivity.

Besides the optimization of the GMR layer stack, another possibility to increase the sensor's thermal stability and its sensitivity can be realized by an adequate design. The description of the detailed design is published in MST proceedings 2013 [Wie13]. Fig. 7 visualizes the whole sensor design.
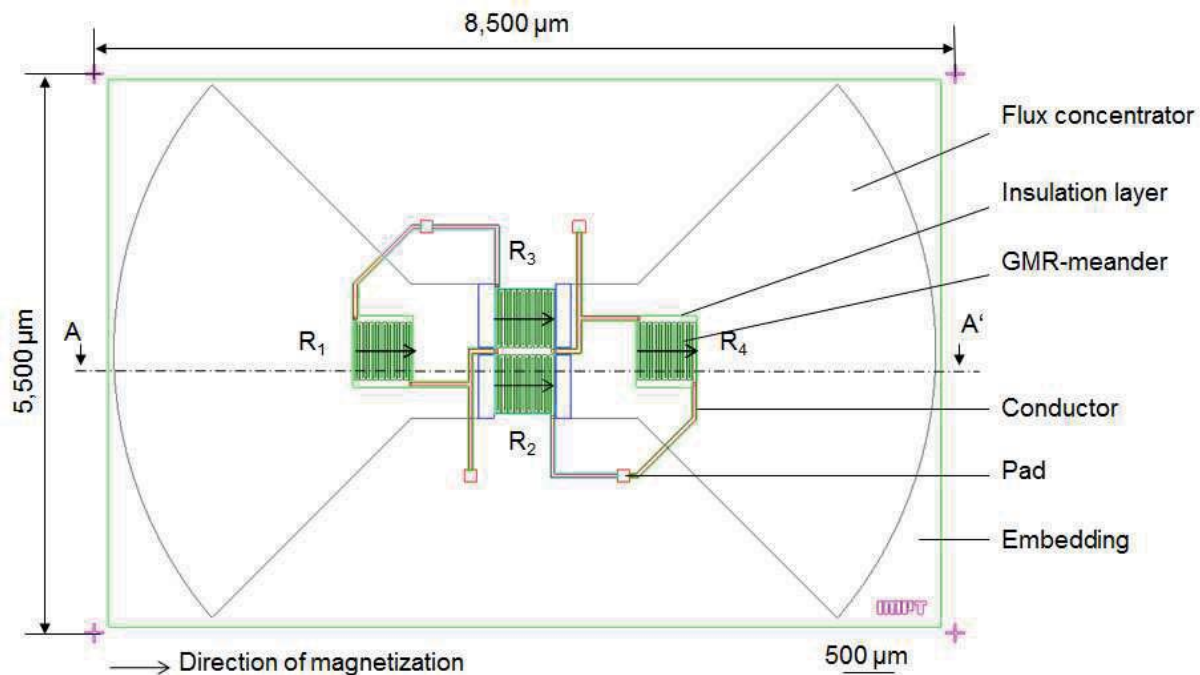

Figure 7. Sensor layout [WIE13]

The sensor consists of four meander systems each of ~ 11 mm in length connected to a Wheatstone bridge, enabling a differential signal which reduces reversible signal loss by temperature rise. Two of the meander systems (R_1, R_4) are covered by flux concentrators (FC) whereas the other two meander systems (R_2, R_3) are located in the gap between the FC. The covered meanders are shielded from the magnetic field and their resistance change is just the result of temperature change. The resistance of the meander systems in the gap is influenced by both the external magnetic field and the temperature. The differential signal makes it possible to eliminate a huge component of the temperature influence. Besides shielding, another important function of the FC is the amplification of the external magnetic field. The flux concentrators of soft magnetic material "collect" and focus the external magnetic flux into the gap, where the two unshielded meander systems are located. With the design shown in fig. 7 and $Ni_{81}Fe_{19}$ as FC material, a theoretical amplification of the external field by the factor 3.7 can be realized. The shielding and amplification function of the FC depends not only on their geometry but also on their magnetic properties. Materials with high permeability and low coercivity have to be used.

918

Besides $Ni_{81}Fe_{19}$, NiFeMo in different compositions is investigated [Wie14c], which provides even higher soft magnetic characteristics than $Ni_{81}Fe_{19}$. But also a nanocrystalline foil (VITROPERM 800, Vakkumschmelze) was taken into consideration. To integrate these materials into the sensor design further research is necessary.

With a size of 8.5 mm x 5.5 mm x <1 mm, the sensor is smaller than 1 cm^3 and therefore compatible with the restricted place in the drilling string. The cross section of the sensor is shown in fig 8. Here you can see the meander systems in the gap and those ones being covered by the flux concentrators, the contact pads, the embedding, the insulation layer as well as the alignment marks.
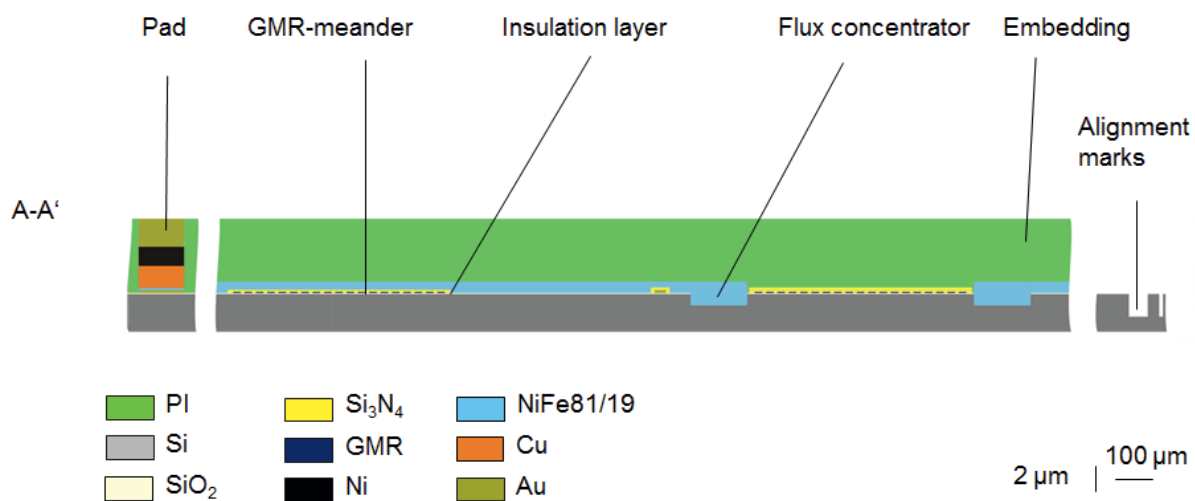
Figure 8. Cross section of the sensor (through A-A' in fig 7)

Fabrication of the magnetic field sensor.

The sensor is fabricated by thin film technology. The detailed fabrication process is described in [Wie14a]. On the basis of the appropriate film system evaluated in WP 6, the sensor structures are fabricated by a combination of photolithography, sputtering and electroplating processes.

On Si-wafers of 100 mm in diameter, 108 systems are fabricated simultaneously. The Si-wafers are covered with an insulation layer of SiO_2.

First of all, the alignment marks are etched by deep reactive ion etching. The necessary Cr masks for the photolithography processes are designed by the IMPT according to the sensor layout visualized in fig. 7 and finally fabricated by Delta Mask BV.

Subsequently to the fabrication of the alignment marks, the conductors and meander systems are sputtered and structured by lift-off technique, alternatively by ion beam etching. Afterwards, the insulation layer is deposited by plasma enhanced chemical vapor deposition and structured using deep reactive ion etching. To realize the coupling between the pinned layer and the antiferromagnet, an annealing step is conducted. For 8 h, the structures are heated at 260 °C and cooled in an external magnetic field of 40 kA/m. In preparation of the FC, cavities located close

to the meanders in the gap are etched. These cavities contribute to the vertical homogenization of the magnetic field in the gap. As illustrated in fig. 9, the meander systems in the gap are consequently centrally located in vertical direction between the FC.
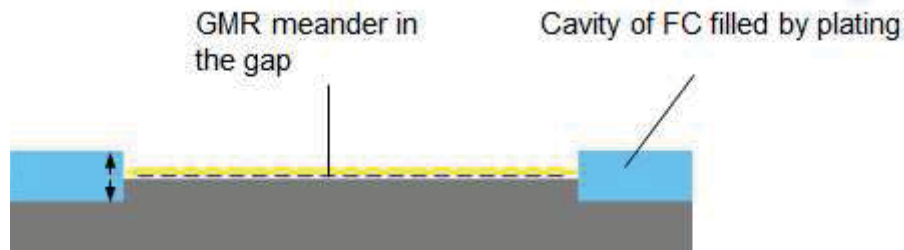

Figure 9. GMR meander centralized between the FC

The so prepared structures are subsequently covered with an electrically conductive seed layer and the FC and contact pads are electroplated. To protect the structures against humidity and abrasion, they are embedded in polyimide. The selected polyimide is applicable up to temperatures higher than 300 °C. After dicing to separate the sensor systems, each of them is bonded onto a ceramic circuit board and electrically contacted by wire bonding (fig. 10).
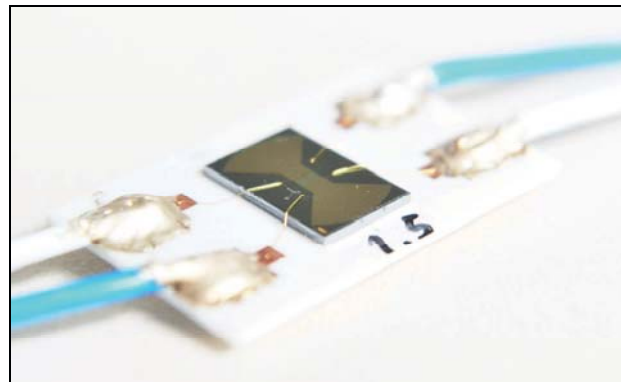
Figure 10. Bonded sensor [Wie15b]

WP 8: *Characterization and long-time test of the magnetic field sensor:* second milestone (M2).
In WP8, the sensor systems are characterized: at room temperature, within a temperature range of -75 °C to 250 °C and after thermal treatment at 250 °C for several hours.
To characterize the sensor, it is operated with a constant current of 1 mA. Fig. 11 shows exemplarily the bridge voltage characteristic of a sensor.
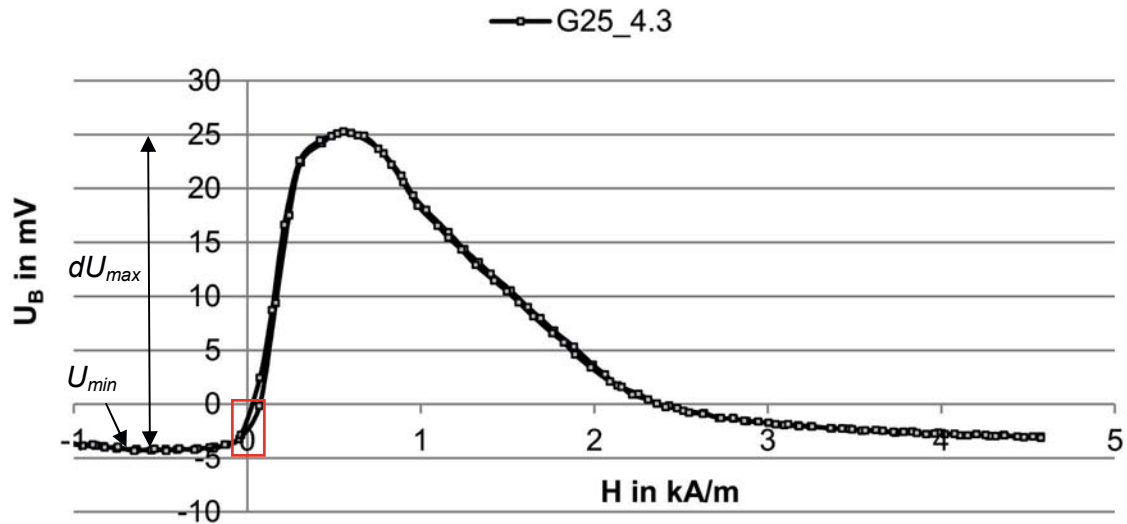
Figure 11. Magnetic field dependent change of bridge voltage of one of the investigated sensors

At room temperature the maximum voltage change is approximately 30 mV within a magnetic field of 307 A/m (sensitivity of 9.8 mV/100 A/m). But this sensitive area is shifted by 187 A/m out of zero field and shows a hysteresis loop with a coercivity of 10 A/m. Both last named features, offset field and coercivity, are disadvantageous for measuring a magnetic field smaller than 80 A/m like the Earth magnetic field. Fig. 12 visualizes the voltage change within the aspired measurement range (red square in fig. 11).
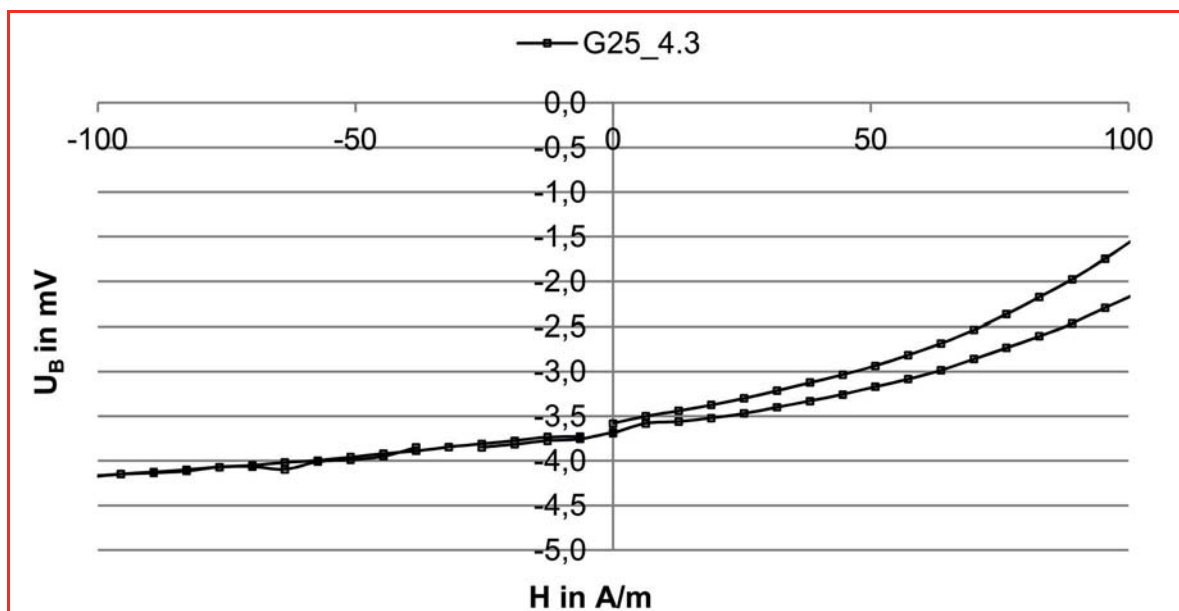
Figure 12. Magnetic field dependent change of bridge voltage within a field range of ±100 A/m

As it can be seen, the sensor's output depends on the direction of the magnetic field. Within the range from -100 to 0 A/m, the voltage change is 0.52 mV, whereas the voltage change in the

range from 0 to +100 A/m is much higher (2.0 mV). But here the sensor features a hysteresis. All in all considering small changes of the magnetic field (1-10 A/m), only voltage changes in the range of several µV can be reached. For a reliable measurement of these small magnetic field changes, a subsequent amplification is necessary.

To increase the sensor's inherent sensitivity within the targeted field area, its hysteresis loop has to be shifted with its deepest incline into zero field area (reduction of offset field). For this e. g. an additional coil or permanent magnet has to be supplemented in the sensor design.

After the characterization of the sensor at room temperature, the sensor's long term stability is investigated. For this the sensor was stored at 250 °C for several hours and its characteristic is measured in intervals. The results are visualized in fig. 13. As it can be seen, after more than 130 h of thermal treatment, no signal degradation can be observed. Neither the minimum bridge voltage (U_{B_min}) nor the maximum voltage change (dU_{B_min}) is altered.
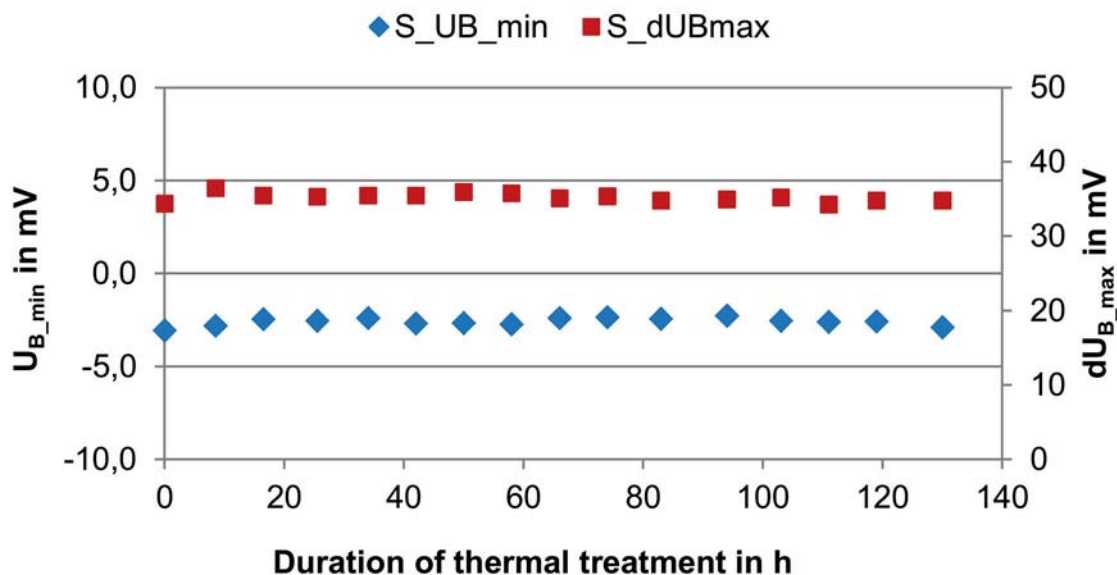

Figure 13. Minimum bridge voltage and maximum bridge voltage change after thermal treatment at 250 °C for several hours – sensor level

To investigate the sensor's signal at different temperatures, the sensor is heated or cooled respectively to different temperatures and the magnetic field dependent change of bridge voltage is recorded (as seen in fig. 11). The signal's temperature dependency is visualized in fig. 14. It can be seen, the sensor's temperature characteristic is similar to that of the single meander systems (shown in fig. 6). A temperature increase leads to an increase of the bridge voltage U_{B_min} and to a decrease of the maximum voltage change dU_{B_max}. At 250 °C the output signal is reduced to approximately 11 % of the room temperature signal. Compared to the single meander systems, the sensor's signal temperature dependency is much higher even though a differential signal is created with the bridge. It can be assumed that the magnetic properties of the

flux concentrator material are reduced with temperature increase. And with the degraded properties their shielding function is diminished. To improve the sensor's temperature stability, a magnetic material with a much higher Curie temperature has to be applied, but nevertheless providing low coercivity and high permeability.
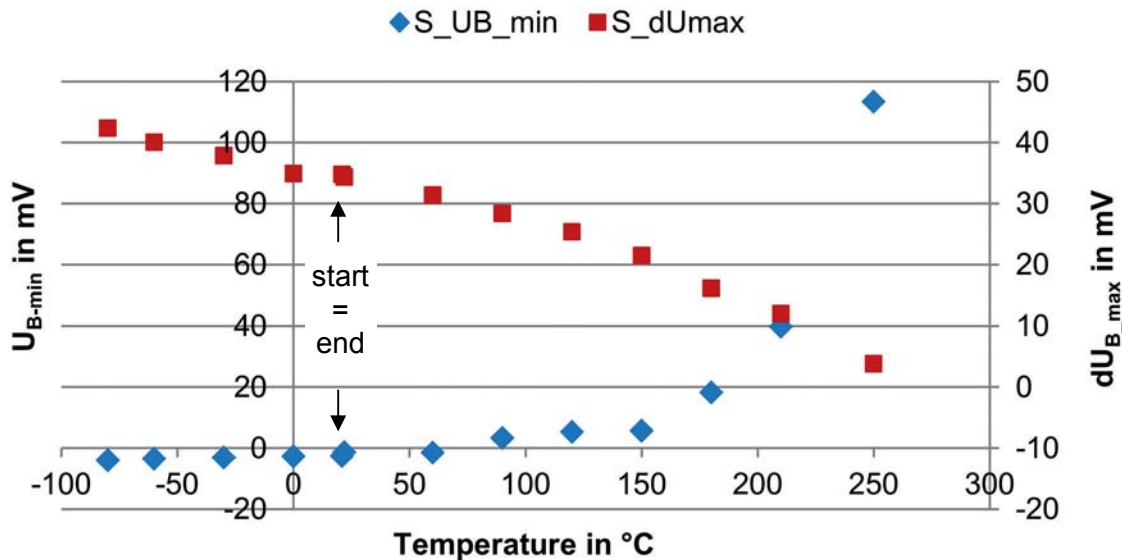

Figure 14 Minimum bridge voltage and maximum bridge voltage change measured at different temperatures – sensor level

It can be concluded that the sensor has a good long term thermal stability, but its temperature characteristic as well as its sensitivity have to be improved. One starting point is the improvement of the flux concentrator material, which should feature a higher Curie temperature and a lower coercivity. Moreover a further enhancement of the sensor's sensitivity can be realized by shifting the sensitive area of the loop into zero field. For this purpose, an additional magnetic field e. g. produced by a coil or a permanent magnet has to be supplemented.

All in all it can be concluded that the fabricated sensor has the potential to be applied in drilling equipment. Its good thermal stability combined with its robust design and its small size makes the sensor attractive for equipment applied in harsh environments with high temperatures, shocks and limited space. But nevertheless the sensor needs further improvements.

With the characterization of the sensor, the second milestone is reached.

WP 9: *Integration in the complete system*

In consultation with the project partner Baker Hughes INTEQ, the final integration of both sensors in the drilling string is not realized. Instead, the resources of this work package are used to complete the development and the characterization of the sensors (see WP 4 and WP 7+8). Therefore the third milestone cannot be reached.

1.3 Project Plan

Work packages and milestones / IMPT	2009	2010	2011	2012	2013	2014
WP5: Specification of the magnetic field sensor (specification sheet)			▓			
WP6: Selection of an appropriate film systems (magnetic field sensor)			▓	━━━	━━━	
WP7: Magnetic field sensor prototype construction				▓	━━━	━━━
WP8: Characterization and long time test of the magnetic field sensor				▓	▓ ━	━━━
WP9: Integration in the complete system					▓	
					▲ ▲	▲

Grey: original plan

Blue: actual or current plan, respectively

▲: Milestone

For details, see Gantt chart in the Appendix.

2 Publications

Patent title is "Drucksensor auf Basis vom photoelastischen Effekt". It will be filed to the Leibniz Universität Hannover in 1.Q 2011.

[WIE13]   A. Wienecke, M. C. Wurz, L. Rissing (2013): Integrierte Sensorik für Hochtempera-turumgebungen, GMM, VDI/VDE-IT (eds) Tagungsband: **MikroSystemTechnik-Kongress** 2013. Von Bauelementen zu Systemen, 14.-16. Oktober 2013 in Aachen, pp. 555–558

[WIE14a]   A. Wienecke, L. Rissing (2014): Thin film fabrication of highly sensitive earth magnetic field sensor, Tagungsband **Smart Systems Integration** 2014, 8th International Conference & Exhibition on integration issues of miniaturized systems - MEMS, NEMS, ICs and electronic components 2014, pp. 595–598

[WIE14b]   A. Wienecke, L. Rissing (2014): Relationship between thermal stability and layer-stack/structure of NiMn-based GMR systems, **EMSA** 2014 (accepted for IEEE Transactions on Magnetics)

[WIE14c]   A. Wienecke, K. Müller-Weihrich, L. Rissing (2014): Investigation of Electrodeposit-ed NiFeMo for Application as Flux Concentrator in Magnetic Field Sensors, **ECS** 2014 (accepted)

[WIE15a]   A. Wienecke, R. Kurppe, L. Rissing (2015): Influence of growth conditions on ex-change bias of NiMn-based spin valves, **MMM 2014** (accepted Journal of Applied Physics 2015)

[WIE15b]   A. Wienecke, L. Rissing (2015): Development of a magnetic field sensor for tem-peratures up to 250 °C, **European Oil and Gas Magazine** 2015 (accepted)

K. Müller-Weihrich: Vergleich mehrerer Verfahren zur Herstellung weichmagnetischer Flussfüh-rungen, Projektarbeit, 2014

3 References

[MAT09]   M. Matysek, O. Meckel, J. Rausch, A. Rettig, A. Röse, S. Sindlinger, T. A. Kern, (Hrsg.): Entwicklung Haptischer Geräte. Springer Verlag, 2009

926

T6: Fluxgate Sensors for 250°C

1   Project Overview

Speaker and lead university or research institution

Project Nr.	Title	Subject of research	Project leader, institution, location
T6	Fluxgate Sensors for 250°C	Electrical Engineering	Prof. Dr. Meinhard Schilling, TUBS (emg) AOR Dr. Frank Ludwig, TUBS (emg)

Participating institutes and institutions of the University and external institutions in:

- Institut für Elektrische Messtechnik und Grundlagen der Elektrotechnik, TU Braunschweig (emg)

- Baker Hughes INTEQ, Celle, Dr. Th. Kruspe, Dr. S. Jung

List of participating scientists and engineers:

Name	Subject area	University institute or non-university institution	Position is financed by gebo funds (indicate with X)
Prof. Dr. Meinhard Schilling	Electrical Engineering	emg	
Dr. Frank Ludwig	Electrical Engineering	emg	
Dr. Dennis Rühmer	Electrical Engineering	emg	X
Dipl.-Ing. Patrick Sebbes	Electrical Engineering	emg	
Sebastian Bögeholz, B.Sc.	Electrical Engineering	emg	

2   Research Program

2.1   Summary

The application of sensors for the navigation in the magnetic field of the earth and for the determination of the surrounding soil conductivity using magnetic field sensors at operation temperature up to 250°C is investigated. The general goal is to obtain precise information on the position of the drilling head and on the surrounding soil constitution during the drilling process even at extreme conditions and high temperatures. For this goal, magnetic field sensors – adapted to the requirements in the drilling head including the associated readout electronics – are developed. The activities include the design and the realization of sensor elements, the electronic circuit development and the selection and test of the required high temperature elec-

tronic components. A three-axis vector fluxgate sensor with corresponding readout electronics for operation temperatures up to 250 °C is demonstrated.

2.2 Relationship of the project to the overall research context and networking with other projects

An essential aspect of the whole collaborative project consists in the optimization of the drilling process and of the related thermal energy transport. The interconnectness of the collaborative project arises from the input required for the project (process parameters and geometries as well as experimental data for the validation of material models and thermal transport simulations) and from the output (e.g., shear stress and pressure in the drilling head vicinity as well as conductivities of differently structured heat exchangers). The most important cross-linkings are depicted in the Gantt diagram (cf. appendix).

2.3 Work packages executed relative to (original) plan and results achieved

AP 1: Planning of electronics circuit and fluxgate sensors for 200°C

Regarding the fluxgate sensor, a survey of materials was carried out that can be used for temperatures up to 250 °C. This concerns the bobbin, the coil wire, the core and bond materials. As coil wire Estersol 180 was found to be suited having a low intrinsic resistivity and an operational range of > 250 °C. For the bobbin, the ceramic material ALSINT 99.7 was chosen exhibiting amagnetic behavior and having a thermal expansion coefficient adapted to that of the core material. To mechanically fix the coils and to provide sufficient chemical protection, acetoxy silicone Loctite 5398 was identified to be suitable and can be applied for temperatures up to 350 °C.

The most crucial component in fabricating a high temperature fluxgate is the core. It should be soft magnetic, have a sufficiently high permeability up to 250 °C, and the magnetic fields amplitude required to drive the core into saturation should stay within reasonably achievable limits. The material VITROVAC 6025Z which has been used at the institute for the realization of highly sensitive room temperature fluxgates [1] is not suitable for high temperature operation due to its comparably low Curie temperature of 200 °C. From discussions with the Vacuumschmelze GmbH & Co. KG, VITROPERM 800R was identified as a promising candidate for the realization of a high temperature fluxgate. The basic properties and possible applications of this material can be found on the webpage of the Vacuumschmelze GmbH & Co. KG [2]. Its Curie temperature amounts to 600 °C, well above the intended operational range. In order to obtain a magnetization versus magnetic field curve which is optimized for fluxgate application, the VITROPERM

800R stripes were subject to a thermal annealing procedure after cutting them to the required length. Unfortunately, the annealed VITROPERM 800R stripes are rather brittle so that they had to be put into the desired shape before the annealing step. This also means that a Förster (double core) or Vacquier geometry is recommendable (Fig. 1).
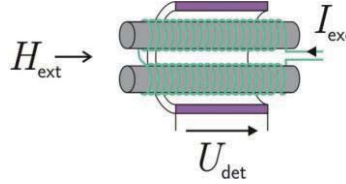

Fig. 1: Schematic setup of fluxgate sensor in Vacquier geometry.

The core material was characterized with a precision impedance analyzer. The determined temperature dependence of the effective magnetic permeability is depicted in Fig. 2. The permeability at 260 °C is only about 6 % below the room temperature value. Long-term and cycling tests did not show any detectable degradation.
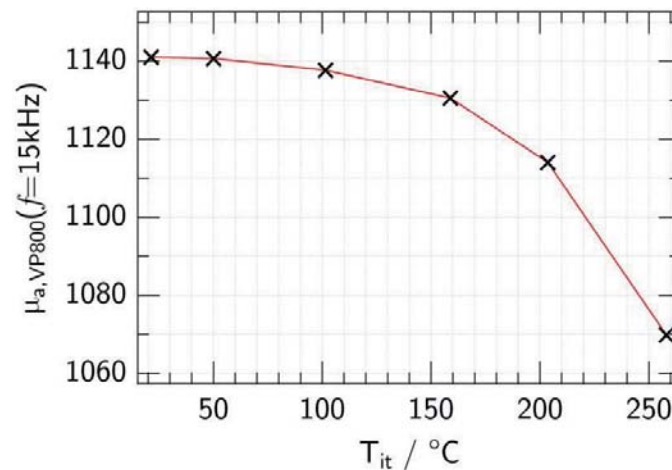
Fig. 2: Temperature dependence of effective permeability of VITROPERM 800R core material.

With regard to the readout electronics, all fluxgate sensors developed at the institute are operated with a feedback circuitry and second-harmonic detection [3]. This concept combines a large dynamic range and high sensitivity. For the room-temperature fluxgates, a separate compensation coil is utilized. For the high-temperature fluxgate it is advantageous to realize a current feedback to get rid of the compensation coil and to simplify the sensor. The basic principle of a current feedback is depicted in Fig. 3. Here the feedback signal is directly fed into the detection coil [4]. Calculating the temperature coefficient of the closed-loop sensitivity for the current feedback mode (Fig. 3) one finds

$$\alpha_{\text{FG}} = \frac{1}{U_{\text{INT}}} \frac{dU_{\text{INT}}}{dT} = \frac{1}{R_{\text{meas}} + R_{\text{sec}}} \left(\frac{dR_{\text{meas}}}{dT} + \frac{dR_{\text{sec}}}{dT} \right) - \frac{1}{k_{\text{sec}}} \frac{dk_{\text{sec}}}{dT} \quad (1)$$

with the detection (secondary) coil constant k_{sec}. Since both terms in equation (1) have opposite signs, the coefficient α_{FG} can be minimized by a proper choice of the feedback resistance R_{meas}.
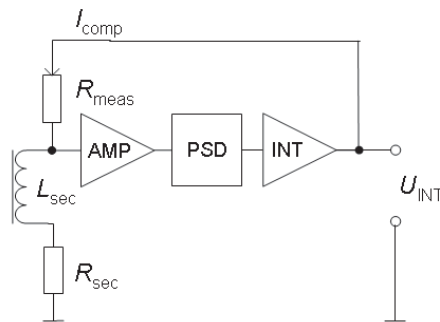

Fig. 3: Current feedback scheme.

For high temperature operation, the fluxgate readout electronics must considerably be simplified, i.e., the number of electronic components must be reduced. This also includes the search for suited high temperature components (operational amplifiers, resistors, capacitors, oscillators).

AP 2: Realization of fluxgate sensors and electronics

Using VITROPERM 800R cores with nearly identical magnetic properties, several Vacquier type fluxgate sensors were built and tested.

For the initial tests, a sensor with a core length of 45 mm was built. To mechanically protect the prototype sensor it was sealed with acetoxy silicone Loctite 5398. The sensor was operated with the institute's room temperature electronics adapted to the sensor and modified for current feedback.

At room temperature, the following sensor parameters were measured: The closed-loop sensitivity amounts to S = 130000 V/T. The linearity, measured in the range of ±50 µT, was found to be better than 40 ppm and comparable to that of the commercial room-temperature fluxgate magnetometer Mag03-IEL from Bartington Instruments, Ltd. [5]. The magnetic field noise was measured in a triple mu-metal shield and amounts to 15 pT/Hz$^{1/2}$ at 100 Hz with a 1/f corner at 10 Hz. These specifications are appropriate for the intended application within the GeBo project.

The sensor characterization at temperatures up to 200 °C was performed in the test laboratory "Magnetsrode" of the TU Braunschweig. For a value R_{meas} = 5.36 kΩ, a value of α_{FG} = 33.2·10^{-6} °C^{-1} was measured, corresponding to an increase of the closed-loop sensitivity of less than 0.6 % compared to the value of $S \approx$ 130000 V/T obtained at room temperature.

930

Assuming $dR_{meas}/dT = 0$ for the room temperature electronics, taking $R_{sec} = 55.8\ \Omega$ and using the temperature coefficient of copper for $(dR_{sec}/dT)/R_{sec}$ one obtains for the first term on the right-hand side of equation (1) $40.5 \cdot 10^{-6}\ °C^{-1}$ which is only slightly larger than the measured value given above. Thus, the temperature dependence of the closed-loop sensitivity is dominated by the temperature coefficient of the resistance of the detection coil wire. The remaining difference must be attributed to the temperature coefficient of the coil constant k_{sec} which amounts to $7.3 \cdot 10^{-6}\ °C^{-1}$. The measured temperature coefficient of the coil constant k_{sec} is most probably caused by an increase of the coil cross-sectional area due to thermal expansion of the wire. Details of the realized and tested high-temperature fluxgate are published in [6]. As pointed out before, according to equation (1) a reduction of the temperature coefficient of the closed-loop sensitivity could be obtained by further optimizing the feedback resistor R_{meas}.

Since a sensor length of 45 mm was too large to build a three-axis vector sensor that fits the geometrical specifications by Baker Hughes INTEQ, later sensors were built with 30 mm core length.

To reduce the complexity of the signal processing electronics, only a limited number of components including a small number of value variations were intended. Spice simulations were performed which yielded to an accordant electronics schematic that consists out of passive as well as commonly used active components like operational amplifiers. A market analysis of high temperature electronic components was performed. According to this study, wirewound resistors and special ceramic capacitors can operate within a wide temperature range exceeding +250 °C while maintaining a small temperature coefficient. Commercially available wirewound resistors and ceramic capacitors were obtained from Vishay and Kemet, respectively. Their performance was evaluated in a high temperature environment. The measurements showed relatively small temperature coefficients $\Delta R/R$ in the range of $10^{-7}\ °C^{-1}$ and $\Delta C/C$ in the range of $10^{-5}\ °C^{-1}$. A comparison between the temperature coefficients of standard X7R capacitors and special high temperature types is depicted in Fig 4.
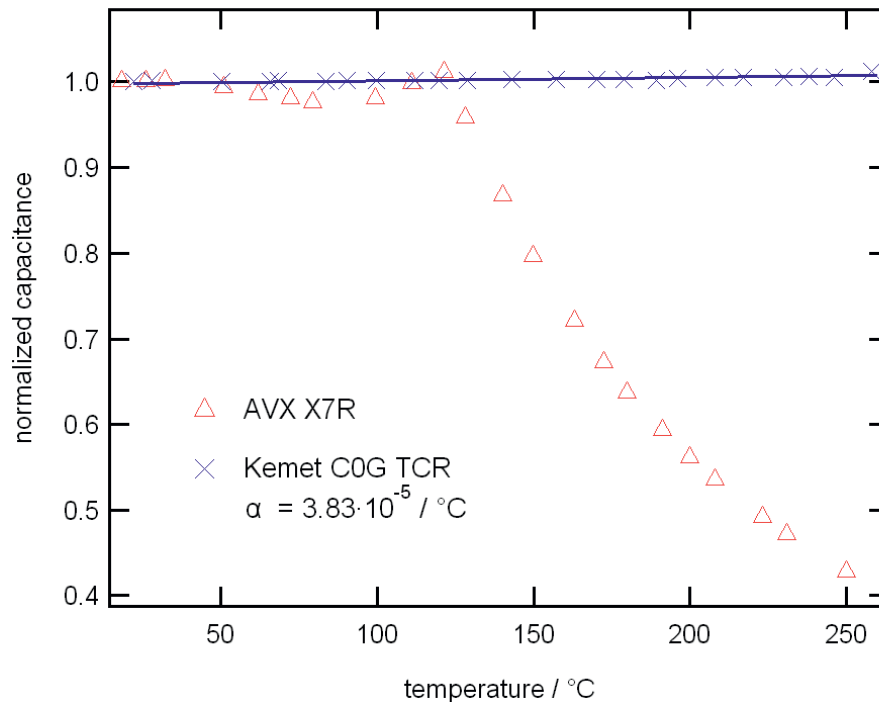
Fig. 4: Normalized capacitance as function of operating temperature of different commercially available ceramic capacitors.

Active electronic components including operational amplifiers, standard logic circuits and field-effect transistors were obtained from Cissoid and Honeywell. These components are fabricated using the silicon-on-insulator (SOI) process which leads to minimized leakage currents [7, 8]. High temperature tests were performed. These tests confirmed the qualification of the components to operate in a high temperature environment up to 250 °C for a prolonged period of time. The circuits were realized on a commercially available circuit board that consists of fiber enhanced Teflon material (obtained from Rogers Corporation). The thickness of the copper plating was increased and the material was coated with photoresist so it could be photochemically processed. The solder connections were made using a high-melting-point solder (composition Sn5Pb93.5Ag1.5) which has a melting point of approx. 300 °C and is well suited for the intended temperature range. A detail of a completed circuit board with two active components and one capacitor is shown in Fig. 5. The active SOI-processed circuits are mounted in proprietary integrated-circuit sockets manufactured at our institute.
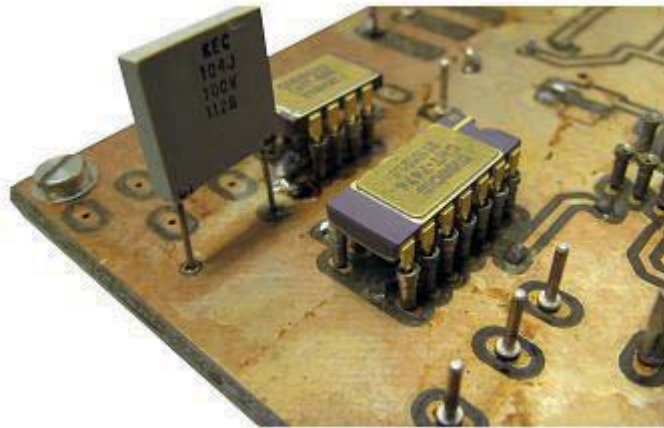
Fig. 5: Detail of the high-temperature electronics showing active components as well as a high-temperature ceramic capacitor. Despite this traditional through-hole-mounting technology, surface mounted device (SMD) technology was also applied.

The complete electronic circuit consists of different stages which were realized on discrete circuit boards. The so called excitation side is used to drive the sensors excitation coils. A logic oscillator based on the well-known NE555 component is used to generate the excitation signal. This signal is stabilized by a cascade of logic flip-flops. Afterwards, it is amplified by a chain of two field effect transistors, one p- and one n-channel MOSFET. The negative half cycle is provided by a tank circuit [9]. Although the used Vitroperm core material requires relatively large magnetic fields to be driven into saturation, the described electronic circuit generates a sufficient current amplitude without producing a critical amount of excess heat. The frequency stability of the generator as function of the temperature is depicted in Fig. 6. As can be seen, frequency variations are insignificant and correspond to a spice simulation using real values and measured temperature coefficients.
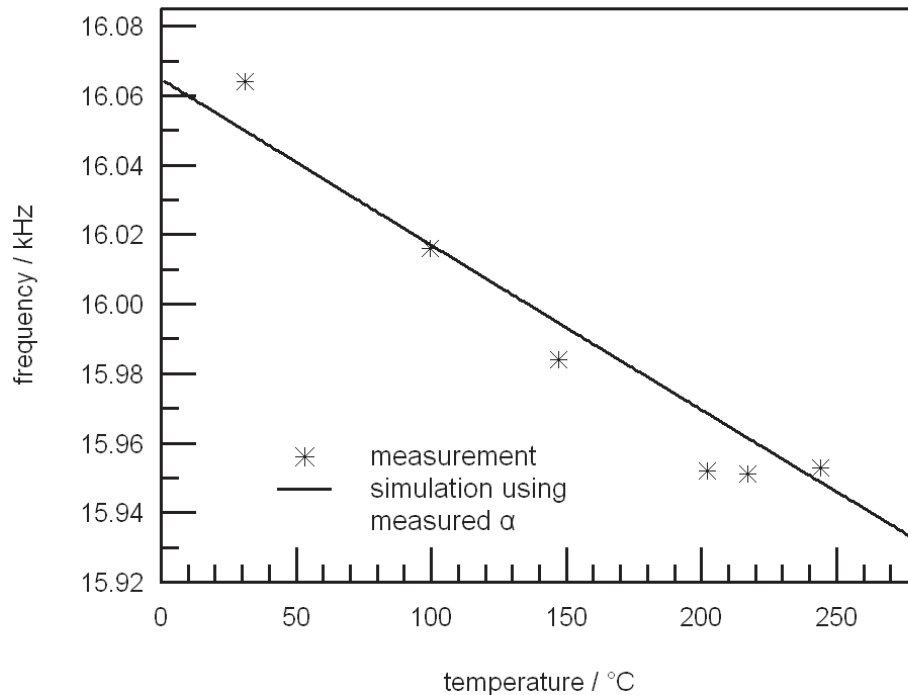
Fig. 6: Oscillator output frequency as function of the temperature. Measurement results were compared to simulation results using real values and measured temperature coefficient α.

The so called detection stage of the signal processing electronics is used to process the signal induced in the detection coil of the fluxgate sensor and to provide the compensation current. It is based on the well known method of readout of the second harmonic [3, 10]. Therefore, the electronic circuit consists of a pre-amplifier stage, a phase selective rectifier which is used as demodulator and an integrator which is used as a lowpass filter and also provides the feedback current (cf. Fig. 3). The circuit design provides adaptation and tuning to the used fluxgate sensors, e.g., the bandwidth and the closed-loop sensitivity can be adjusted.

The predescribed sensor was connected to the electronics using Teflon based coaxial cable. The interconnections between the individual electronic stages were made either using the same Teflon or high temperature resistant silicone elastomer cables.

AP 3: Operation and test at 200 °C

The initial characterization of the high temperature Vacquier fluxgate sensor described in AP 2 was performed with the institute's standard room temperature readout electronics [3]. Details are summarized in AP 2. The complete high temperature electronic circuit was successfully tested in the high temperature environment up to 200 °C using a room temperature sensor. All relevant parameters stayed within acceptable limits so the electronic circuits as well as the ref-

erence sensor design are usable in a temperature range up to 200 °C. An important factor is the temperature sensitivity of the output voltage as function of the temperature. Also, the impact of the electronic circuit has to be taken into consideration. The electronic components were placed in a high temperature environment, while the sensor stayed at room temperature. Fig. 7 shows the results. As can be seen, the temperature coefficient of the electronics amounts to $-1.5 \cdot 10^{-4}$ °C^{-1}. Hence, even at 250 °C, the electronic output voltage is minor 3 % lower than at room temperature.
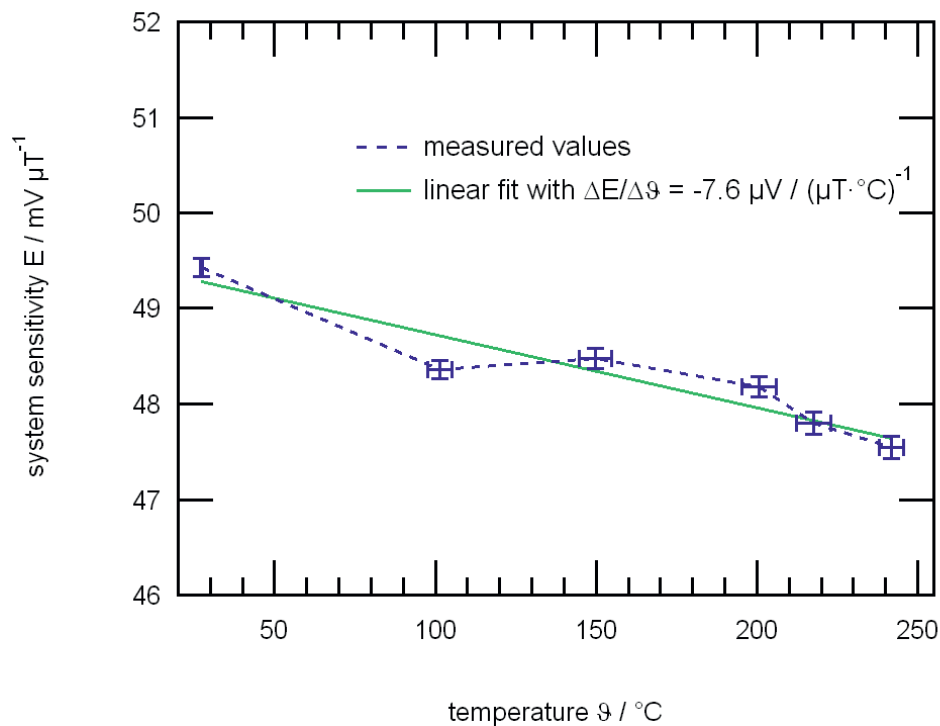
Fig. 7: System sensitivity measured while only the electronic circuits were subject to the high temperature environment.

Fig. 8 depicts a section of the actual circuit board after it was exposed to the high temperature environment. As can be seen, all solder joints stayed faultless. However, it is very important to properly clean the circuit board, as flux residue gets scorched and might lead to stealthy connection problems.
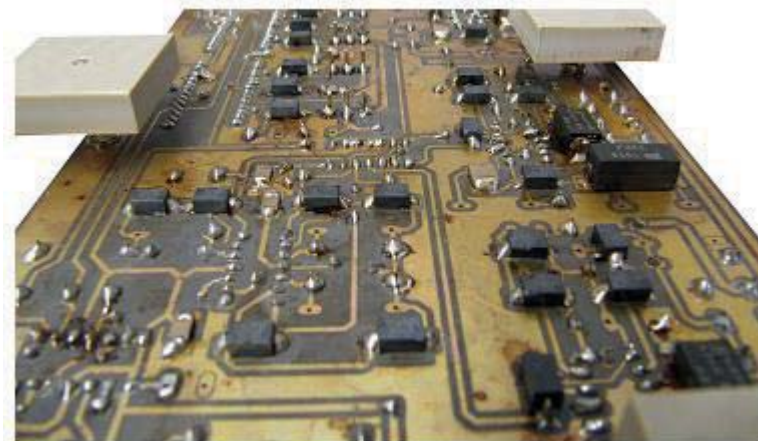
Fig. 8: Detail of an electronic circuit after prolonged exposure to the high temperature environment (250 °C). No connection problems at the solder joints were evident.

AP 4: System integration at 200 °C

No separate system integration at 200 °C, i.e., combining high temperature fluxgate sensors with the high temperature readout electronics, was carried out since the initial tests proved that both sensors and electronics – including minor modifications – are capable of being operated up to 250 °C. Therefore, system integration results are described in detail in AP 6.

AP 5: Planning for 250 °C

The selected materials used in the reference sensor were evaluated concerning their application for operating temperatures up to 250 °C. The Vitroperm core material possesses a Curie temperature of 600 °C. Hence, even an elevated operating temperature of 250 °C remains uncritical. The thermal expansion coefficients between the core material and the temperature resistant supporting Alsint ceramic rods are matched. Hence, also this material was applicable. The copper wire called "Estersol E180" which was used to wind the coils was subject to a long time high-temperature evaluation. While it can be successfully used for more than hundred hours at operating temperatures of 250 °C, a superior alternative was found. Polyimide covered copper wire offers a higher temperature stability, even at temperatures higher than 250 °C. However, a disadvantage is the need to mechanically strip the coating prior to electrical connections. A simple solder process it not applicable for its removal. The individual components of such a fluxgate sensor during the assembly process are shown in Fig. 9.

Fig. 9: Individual components of a fluxgate sensor during the assembly process. Left: Bobbin with detection coil and core with excitation coil. Right: Complete, assembled sensor.

The intended operational area of the used Teflon coaxial cables ends at approx. 250 °C. Polyimide based coaxial cables offer a greater safety margin and can be operated up to 300 °C. However, these cables do not offer the same flexibility as Teflon cables. Electrical connections were made using copper ferrules and again, mechanical support was given by high temperature resistant silicone elastomer. To capsule the sensor against environmental mechanical stress, a housing made of machinable ceramic Macor material was designed. A limited strain-relief which protects the sensor during handling and installation operations was provided by gluing the coaxial cables with the acetoxy silicone. The completed three-axis fluxgate sensor prior to the filling step is shown in Fig. 10.

Fig. 10: Completed three-axis fluxgate sensor prior to silicone filling.

Concerning the electronic circuits, the applied passive components are usable at operating temperatures exceeding 250 °C. Their casings and temperature coefficients provide stable operations in the intended temperature range. While most of the active components are specified up to 225 °C for continuous operation, their operational range can be extended to 250 °C. Allowing a shorter life span of several hundred hours, most devices even stay operational up to 300 °C. Their electrical parameters stay stable within acceptable tolerances that will not disturb the fluxgate operation and readout process. Hence, they are reasonably well suited for the intended purpose. Also the used circuit boards, the soldering technique and the connection cables allow continuous operation at 250 °C. In summary, the predescribed electronic circuits are usable for operation temperatures up to 250 °C.

AP6: Advancement, operation, test and system integration at 250 °C

Three fluxgate sensors were built using the polyimide covered copper wire and coaxial cables. They were integrated in a ceramic Macor housing and form a three-axis vector fluxgate. Due to limited installation space, the fluxgates were not mounted orthogonally. Instead, they were mounted at angles of 37° in xy- as well as in yz-plane. Orthogonal magnetic field signals can be obtained e.g. by digital signal processing of the electronics output signal. The electronic circuits were multiplied to operate three individual fluxgates. The electronic components were tuned to their respective fluxgate counterpart. A bandwidth of 1.8 kHz was adjusted to allow a full experimental evaluation including white noise measurements. However, to lower the total output noise for the intended dc magnetic field measurements, the bandwidth can be reduced accordingly, e.g. by tuning the used detection resonance circuit.

The sensor system consisting of fluxgates and corresponding electronics was characterized in a shielded room temperature environment. The sideband sensitivity which does not take the electronics into account [1] was found to be 24.5 kV/T. The closed-loop sensitivity was adjusted to be 28 kV/T which results in a dynamic range of ±175 µT that suits the intended operation. Noise values were found to be 1.48 nT/(Hz)$^{1/2}$ at 10 Hz, 740 pT/(Hz)$^{1/2}$ at 80 Hz and 43 pT/(Hz)$^{1/2}$ at 1 kHz (white noise). These values are approximately one order of magnitude higher than low noise room temperature sensors. As tests have shown, the major noise sources are the active electronic components which were not optimized for low noise operation. The sensors themselves offer much lower noise values comparable to room temperature sensors if being operated by proper low noise electronic circuits like the room temperature fluxgate electronics developed at our institute [3]: 9.8 pT/(Hz)$^{1/2}$ at 100 Hz, 4.7 pT/(Hz)$^{1/2}$ at 1kHz (white noise).

Since the environmental temperature in the evaluation laboratory "Magnetsrode" is limited to 200 °C, high temperature tests of the sensor system were performed in a commercially available convection oven, which offers limited shielding against environmental stray fields. A temperature resistant test coil provided a calibration field. The sensor system was successfully tested for approximately hundred hours at an operation temperature of 250 °C. About 25 heating and cooling cycles were successfully performed. Long term evaluation experiments are still ongoing and show promising results. The sensor system was characterized in the high temperature environment. Flux density noise spectra obtained at different operating temperatures are shown in Fig. 11. Noise values were found to decrease with increasing temperature. The noise values at 250 °C are approx. 30 % lower than room temperature values (at a frequency of 20 Hz). While Nyquist noise of the fluxgate coil resistance increases with higher temperature, the observed noise reduction originates from lowered noise values of the operational amplifiers. A

noise evaluation of these operational amplifiers showed that the noise decreases by factor 9 (frequency 100 Hz) between room temperature and 250 °C.
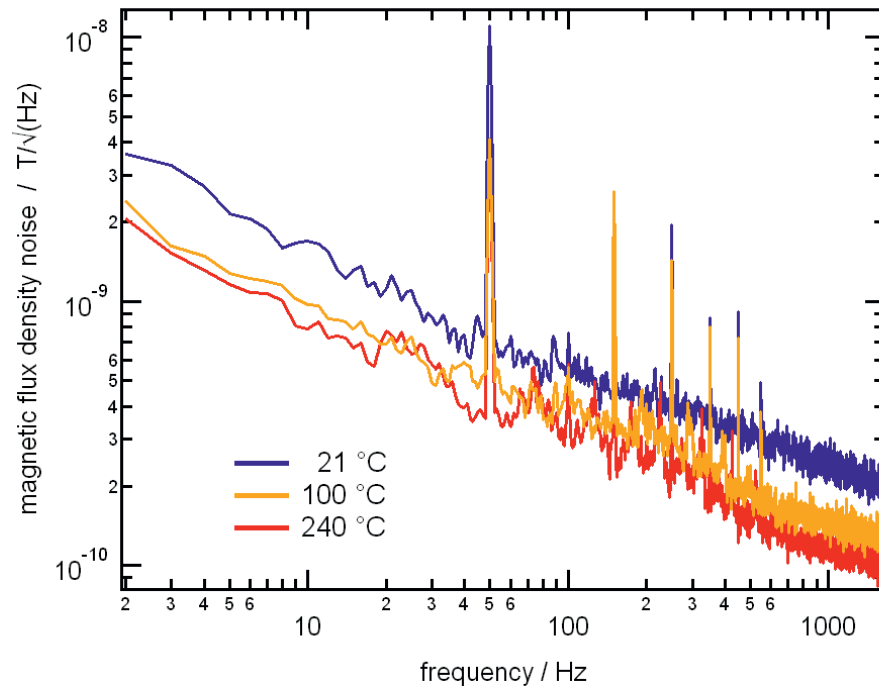

Fig. 11: Magnetic flux density noise spectra of the sensor system output obtained at different operating temperatures.

An important factor is sensor crosstalk. The compensation field of a fluxgate sensor is also present at its outside and can be detected as parasitic signal by the other sensors. In this setup, the non-orthogonal alignment of the three sensors leads to relative high crosstalk values. A calibration field B_{cal} was generated by alternately using the detection coil of one of the three fluxgates solely as field generator. This field was detected by the other sensors as B_{meas}. The reduction ratio B_{meas}/B_{cal} amounts to 6.8 % between the middle and one of the side sensors. However, if only the orthogonally aligned side sensors are considered, B_{meas}/B_{cal} amounts to significantly lower 0.7 %. Also the temperature stability of these crosstalk values was evaluated. According to experimental data, the crosstalk amplitude at 250 °C gets about 16 % lower for the combination of the side sensors. The reduction is smaller for the combination middle vs. side sensors (less than 3 %).

Since both the excitation coil resistance and the chain resistance of the FET-transistors increase with temperature and the excitation current is voltage driven, a reduction in excitation current amplitude could be observed. A graphical representation can be seen in Fig. 12. A temperature related decreasing inductance of the excitation coils counteracts this behavior. In total, at 250 °C the excitation current amplitude is about 25 % lower than at room temperature. How-

ever, deep magnetic saturation of the fluxgate core is still achieved and the fluxgate stays operational.
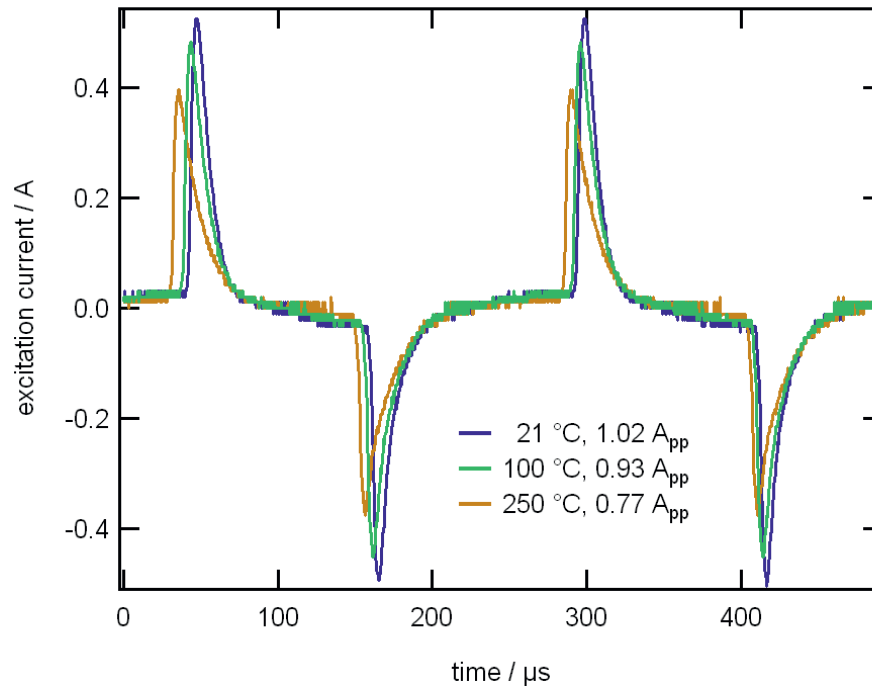

Fig. 12: Excitation current measured at different operating temperatures.

A combination of factors leads to a temperature related decrease in bandwidth. At 250 °C the system's bandwidth is approx. 50 % lower than at room temperature. This reduction arises mainly from the enlarged coil resistance of both the excitation and the detection coil. This enlargement leads to detuning of the readout resonance circuit, enlarging its Q-factor and lowering the bandwidth. Also the total feedback resistance ($R_{sec} + R_{meas}$ in eq. 1) is changed which leads to an increased system sensitivity. Due to slew rate limitations, the integrator circuit that drives the compensation current gets slower. Thus, the bandwidth is reduced. A third factor is the lowered excitation current amplitude which also has an impact on the total bandwidth. This effect is not yet fully understood and will be subject to further investigations. However, the reduction in bandwidth is not crucial for the intended DC-operation. If, on the other hand, AC-operation is required the observed reduction in bandwidth can be taken into account at the sensor set-up.

The total sensor system possesses a positive temperature coefficient α that amounts to $6.8 \cdot 10^{-4}$ °C^{-1}, as is shown in Fig. 13. Regarding eq. 1, it can be seen that the left term on the right side is dominated by the temperature dependent coil resistance dR_{sec}/dt. dR_{meas}/dt which describes the temperature coefficient of the feedback resistor can be neglected, since its value is three orders of magnitude smaller than dR_{sec}/dt. On the other hand, if a feedback resistor with

940

properly chosen temperature coefficient with opposite sign is applied, the left term on the right side of eq. 1 can be minimized. According to the previously mentioned high temperature tests with different resistors, a coal-type resistor is a promising candidate, since it possesses a negative temperature coefficient while maintaining mechanical thermal stability. Consequently, the temperature coefficient α of the sensor system can be lowered by 25 % (to a value of $5.1 \cdot 10^{-4}$ °C^{-1}) if such a resistor is applied (ref. Fig. 13).
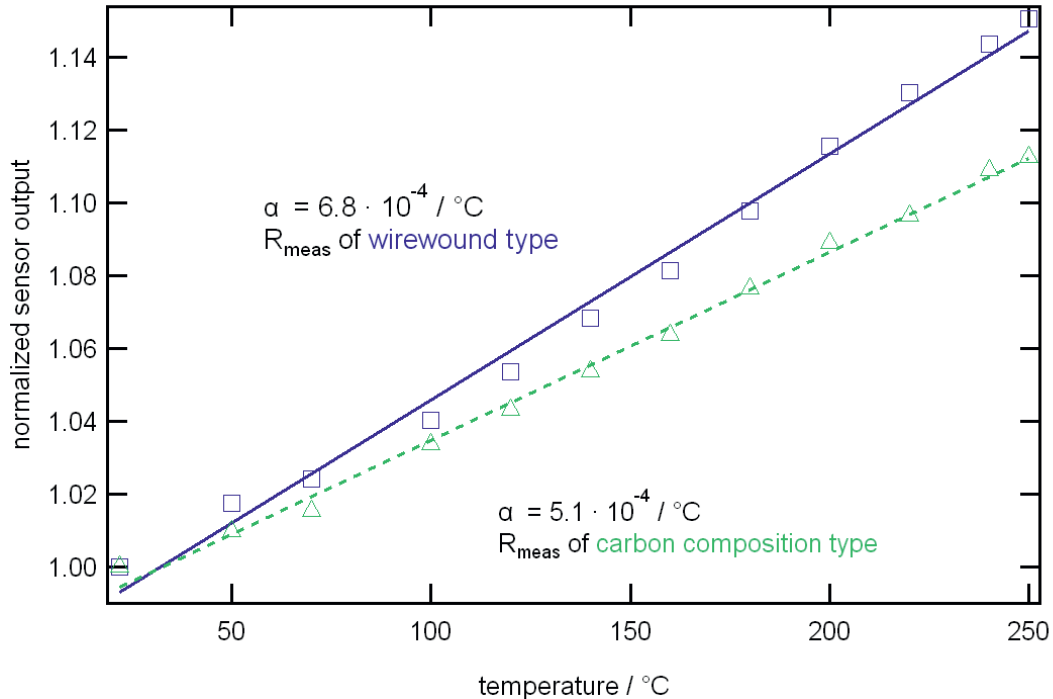
Fig. 13: Normalized sensor system output voltage as function of the temperature. Two different types of feedback resistor R_{meas} were used.

The right term of eq. 1 amounts to approx. 50 % (value of $3.38 \cdot 10^{-4}$ °C^{-1}) of the initial temperature coefficient. This value is significantly larger than the value measured with the reference sensor (cf. AP 2) and is owed to the new sensors geometry. Future works may consider changes in geometry (e.g. detection coil length and thickness) to optimize this parameter.

To summarize, all work packages and milestones were successfully finished. A three-axis vector fluxgate magnetometer including current-feedback electronics operational up to 250 °C and fulfilling the sensor specifications provided by Baker Hughes INTEQ is available.

2.4   Project Plan
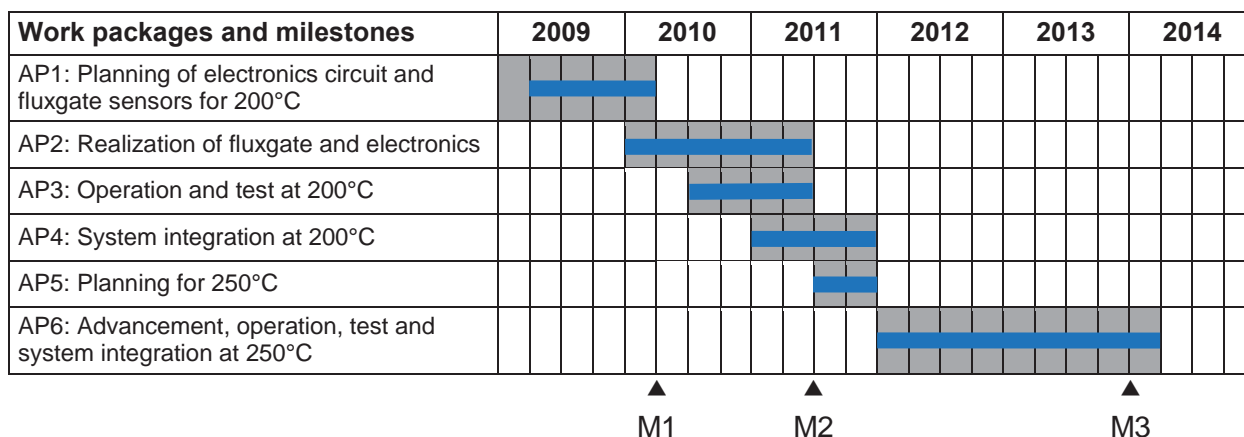
Work packages and milestones	2009	2010	2011	2012	2013	2014
AP1: Planning of electronics circuit and fluxgate sensors for 200°C	▬					
AP2: Realization of fluxgate and electronics		▬				
AP3: Operation and test at 200°C		▬				
AP4: System integration at 200°C			▬			
AP5: Planning for 250°C			▬			
AP6: Advancement, operation, test and system integration at 250°C				▬	▬	▬

<div align="center">▲ M1   ▲ M2   ▲ M3</div>

Grey, original plan

Blue, actual or current plan, respectively

For details, see Gantt chart in the Appendix.

3   Delineation of the project from other funded projects

At the Institut für Elektrische Messtechnik und Grundlagen der Elektrotechnik no further projects besides the GeBo projects are currently performed which are related to geothermia and/or high-performance drilling technics.

4   References

[1] C. Hinrichs, J. Stahl, K. Kuchenbrandt, and M. Schilling: *Dependence of sensitivity and noise of fluxgate sensors on racetrack-geometry*. IEEE Trans. Magn. **37**, 1983-1985 (2001).

[2] Vacuumschmelze GmbH & Co. KG, Hanau, Germany (www.vacuumschmelze.de).

[3] R. Piel, F. Ludwig, and M. Schilling: *Noise optimization of racetrack fluxgate sensors.* Sensor Letters **7**, 317-321 (2009).

[4] F. Primdahl: T*emperature compensation of fluxgate magnetometers*. IEEE Trans. Magn. **6**, 819-822 (1970).

[5] Bartington Instruments, Ltd., U.K. (www.bartington.com).

[6] P. Sebbes, F. Ludwig, and M. Schilling: *Fluxgate magnetometer for temperatures up to 180°C.* J. Electrical Engineering **61**, 21-23 (2010).

[7] M. A. Huque, S. K. Islam, B. J.Blalock, C. Su, R. Vijayaraghavan, L. M. Tolbert: *Silicon-on-insulator based high-temperature electronics for automotive applications.* Industrial Electronics 2008, IEEE International Symposium on (2008): 2538-2543

[8] D. Flandre: *Silicon-on-insulator technology for high temperature metal oxide semiconductor devices and circuits.* Mater. Sci. Eng., B: B **29.1** (1995): 7-12

[9] P. Ripka, W. G. Hurley: *Switching-mode fluxgate*. Transducers, Solid-State Sensors, Actuators and Microsystems, 12th International Conference on, Vol.2 (2003): 1283-1286

[10] P. Ripka: *Review of fluxgate sensors*. Sens. Actuators A **33** (1992): 129-141

5   Publications, reports and presentations of Project T6

- P. Sebbes, F. Ludwig, and M. Schilling: *Fluxgate magnetometer for temperatures up to 180°C.* Journal of Electrical Engineering **61**, 21-23 (2010) (ISSN 1335-3632).

- F. Ludwig, P. Sebbes, and M. Schilling: *Fluxgate magnetometer for temperatures up to 180°C.* Talk at the Magnetic Measurements 2010 Conference in Prague, 12.-15. September 2010.

- D. Rühmer, S. Bögeholz, F. Ludwig, and M. Schilling: *Vector fluxgate magnetometer for high operation temperatures up to 250 °C.* (submitted to Sensors and Actuators)

944

T7: Intelligent sensor equipped drilling tools

1 Project Overview

Speaker and lead university or research institution

Project Nr.	Title	Subject of research	Project leader, institution, location
T7	Intelligent sensor equipped drilling tools	Engineering	Prof. Dr.-Ing. Ludger Overmeyer, LUH (ITA)

Participating institutes and institutions of the University and external institutions:

- Institute of Transport and Automation Technology (ITA), Leibniz University Hannover

- Baker Hughes, Dr.-Ing. Thomas Kruspe

List of participating scientists and engineers:

Name	Subject area	University institute or non-university institution	Position is financed by gebo funds (indicate with X)
Prof. Dr.-Ing. Ludger Overmeyer	Engineering	ITA	
Dr. rer. nat. Andreas Stock	Engineering	ITA	
Jan-Florian Höfinghoff	Engineering	ITA	X

2 Research Program

2.1 Summary

The aim of project T7 was to investigate and evaluate sensor system concepts that can be implemented into the bottom hole assembly (BHA) of a drill string. Main objective was to design and manufacture a ground penetrating radar (GPR), in position to work in this harsh environment. Therefore, a GPR system matching the geometrical and electrical boundary conditions was developed, where mechanical protection is guaranteed. With the help of this system, the drill process can be optimized due to the detection of the position of boundary layers such as fault lines and deviating rock structures ("frac zones"). Furthermore, the achievement of the frac process itself can be investigated, whose success is essential for an efficient heat exchange in the overall geothermal project.

Ground penetrating radar is an emerging technology finding wide application e.g. in soil exploration, UXO detection, archeology and concrete inspection [1-4]. Detection of boundary layers is possible, due to the hard dry rock (HDR) formations in Lower Saxony being mainly composed of sand- and limestone. These rocks are quite transparent to radar frequencies [5]. This project investigated the detection range, spatial resolution and antenna configuration for frequencies

945

from 100 MHz to 1 GHz with the help of simulation and measurement. This frequency range offers a good tradeoff between detection range and spatial resolution [6].

Within the project T7 a dissertation entitled "Untersuchungen zu Anwendbarkeit von Georadar in der Bohrgarnitur" emerged [17].

The project T7 consists of 4 work packages (AP):

AP1: Concepts for the integration and protection of the GPR system in the BHA.

AP2: Concepts, designs and measurements for the integration of the GPR. Decisions regarding the position inside the BHA, the employed frequency and qualified antenna concepts for good and reliable detection of underground objects.

AP3: Evaluation of the GPR and measured data and optimization for an effective drilling process.

AP4: Prototype testing of the GPR-inside-BHA-concept.

2.2 Relationship of the project to the overall research context and networking with other projects

Sensor systems incorporated into the bottom hole assembly today, such as geoelectrical ones, suffer from insufficient detection range and resolution. Detection of frac zones and their growth during the frac process allows a more efficient exploration but cannot be observed with current systems in a global manner. Ground penetrating radar can overcome this problem due to its better ratio regarding detection range and resolution. It can therefore complement the contemporary systems. The goal was therefore to achieve a ground penetrating radar solution for the integration into the metallic bottom hole assembly.

The Institute of Transport and Automation Technology has wide experience in using ground penetrating radar systems in mining applications [7-10]. A remarkable example is a project in cooperation with RWE Power AG targeted to incorporate a ground penetrating radar system in the buckets of a wheel excavator used for open cast coal mining. Therefore, the ITA can provide a considerable know-how in implementation of such systems and data analysis for efficient layer detection. An overview of the benefit using ground penetrating radar in the context of geothermal energy is shown in [11].

2.3 Work packages executed relative to (original) plan and results achieved

AP1 – Integration and protection concepts

The integration of the ground penetrating radar system can be divided in two parts. The first part includes the radar electronics. Ground penetrating radar systems used today feature a small electronic device serving for signal generation, modulation and sometimes even processing, mounted into the ground penetrating radar itself or enclosed in a connection box between the radar and a personal computer. This personal computer controls the electronic device (setting the frequency, bandwidth, etc.) and displays the reflection pattern received by the antennas. State of the art electronics exist for signal modulation and processing, suitable for all kinds of tasks including drill applications. Thus, there is no need to develop a special electronic device for the gebo project. Existing ones can be adopted with the help of other gebo projects, namely T1 and T3, and easily integrated into the BHA.

The second part includes the development of the ground penetrating radar antenna serving for emitting the signal generated by the electronics. A challenge is to optimally place the antenna inside the bottom hole assembly, despite the little space available. The bottom hole assembly itself is made of metallic materials, inherently impeding the radiation of electromagnetic waves. The antenna must be shielded from the metallic mass of the bottom hole assembly to ensure good performance. The outer side of the antenna must be protected by a nonmetallic cover to guarantee free radiation, which at the same time must be able to withstand the harsh environment inside the well bore even during the drilling process.

Three concepts for antenna integration were investigated and are presented below.

Concept 1

Concept 1 elaborates the integration of the antenna into the "stabilizer", a component always present to stabilize the drill string inside the hole. It is hereby intended that the antenna is located inside a fin of a stabilizer, so that only a small amount of drilling fluid can flow between the antenna and the soil with the stabilizer almost touching the wall. In this way, high attenuation input by the drilling fluid, consequently affecting the radar signal can be vastly decreased. Furthermore, since the antenna is incorporated into the stabilizer, there exists no need for moving parts. Unfortunately, stabilizers are very short in respect to the frequencies used for ground penetrating radar. For a typical radar frequency of 100 MHz, the resulting half wave dipole antenna would be approximately 1.5 meters long, hence much bigger than common stabilizer lengths employed in the bottom hole assembly. This concept can be used only for frequencies of 1 GHz and above, where on the other hand the detection range is very small especially if fluids are present.

Concept 2

Concept 2 avoids the technical restrictions of concept 1 regarding antenna length and frequency, by directly implementing the antenna into the bottom hole assembly. In this case, the antenna is mounted on a hydraulic punching tool, a state of the art device nowadays widely used for guiding the drilling bit [12]. While in sleep mode the antenna lies inside the contour of the bottom hole assembly, therefore not obstructing the drilling process. During operation the antenna will be pressed against the well bore, hence achieving a direct contact with the surrounding rock. The main disadvantages of this solution are the moving parts of the hydraulic mechanism. Several antenna parts, such as transmission cables, are susceptible to the harsh environment and could be easily damaged. Furthermore, little rocks inside the drilling fluid can potentially incapacitate the mechanism by getting jammed between the antenna and the bottom hole assembly.

Concept 3

Finally, to overcome the technical limitations of the previously described approaches, concept 3 was chosen and used further on in project T7 as demonstrated in figure 1. The bottom hole assembly itself is designed featuring a small cavity where the antenna is integrated. This is important to ensure the cavity will not bring any crucial consequences to the mechanical stability, while providing electrical isolation and mechanical protection to the antenna lying inside the bottom hole assembly. During antenna operation, the whole bottom hole assembly is pressed onto the well bore wall to minimize the effects of the drilling fluid. The antenna length and consequently the frequency are only limited by the length of the bottom hole assembly section. It is further possible to omit the hydraulic mechanism, if the bottom hole assembly is designed in a way which minimizes the distance between the antenna and the well bore wall (uncircular diameter).

Figure 1: Antenna integration into the BHA (not to scale) [17]

Protection concept

The material used for protecting the antenna against the harsh environment must be nonmetallic to ensure electromagnetic wave propagation. Such materials must exhibit low electric and thermal conductivity while at the same time is in position to withstand high temperatures, pressures and forces. Further-

948

more, they must be insusceptible to the employed drilling fluid. Suitable cover materials include ceramics, high performance plastics such as PEEK and PAI and potential composite materials made of both.

AP2 – Concepts, designs and measurements for the integration of the GPR

The main objective in AP2 was to investigate ways for the integration of an effective and reliable ground penetrating radar system into the bottom hole assembly according to concept 3. Efforts mainly have to focused on the antenna, being the radars key component. Good radiation and detection performance has to be achieved despite the drawback factors metallic bottom hole assembly, little space, high temperatures and stresses and different soils and liquids.
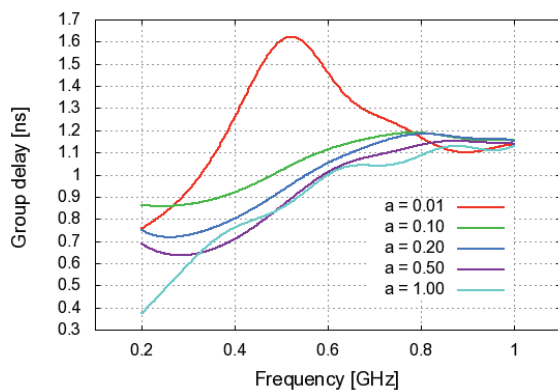
Figure 2: Group delay of a resistively loaded dipole antenna as function of the loading factor "a" [17]
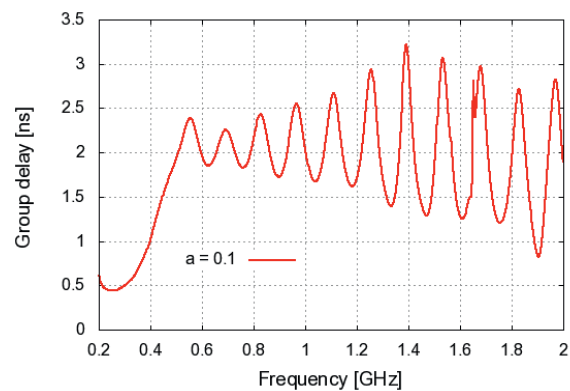
Figure 3: Group delay of the dipole antenna above a metallic reflector

To radiate short radar pulses without distorting the pulse form, the antenna needs to exhibit very broadband characteristics. Important is the group delay, the time needed for a signal of a specific frequency to propagate from one antenna to another, to be almost constant over the pulse's frequency span [13]. ground penetrating radar signals are inherently very broadband, comprising plenty of distinguished frequencies. Failing to adequately fulfill this prerequisite will lead to induced pulse distortions consequently making the detection of echoes much more difficult.

There exist different types of antennas which incorporate this broadband, constant-over-frequency group delay characteristics e.g. biconical, horn and vivaldi antennas [14]. These antennas are however geometrically large in the considered frequency band and radiating direction and will not fit into a bottom hole assembly. One solution to overcome this problem in size is using half-wave dipole antennas. On the other hand, dipole antennas, though geometrically small, do not exhibit good group delay characteristics, thus further modification is evidently needed. One well suited technique for improving the antenna pulse behavior is the resistive

949

loading [15]. A simulation model was created with the software Ansoft HFSS, to visualize the influence of resistive loading on the group delay for 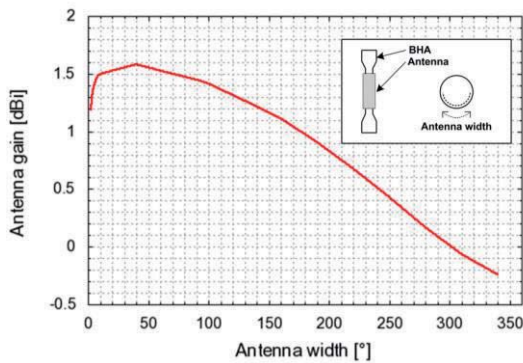a half-wave dipole antenna at 500 MHz (center of considered frequency band). The result is illustrated in figure 2, where group delay versus frequency is depicted as function of the loading factor "a". An optimum for a=0.1 is observed, where the group delay is almost the same for all frequencies. A disadvantage of resistive loading is the resulting lower antenna gain, consequently leading to reduced performance in comparison to an antenna not featuring this enhancing technique.

Figure 4: Gain of an inverted-F antenna inside the BHA as a function of antenna width

A prototype of this dipole antenna was fabricated and measured to prove the concept. Group delay for the resistively loaded antenna varies within ± 0.5 ns generating a clean shaped pulse, whereas the same antenna without resistive loading varies within ± 1.25 ns generating a pulse with reverberations not negligible.

Unfortunately, group delay deteriorates when the dipole is located above a metallic plate (i.e. the BHA) due to reflections between the antenna itself and the metallic plate. Simulated group delay versus frequency is depicted for this case in figure 3. It is clearly observed that the group delay now fluctuates between 0.5 ns and 3 ns instead of 0.85 ns and 1.2 ns without the presence of the metallic plate (figure 2, a = 0.1).

Figure 5: Simulation model of the ground penetrating radar antenna inside the bottom hole assembly [17]

Furthermore, antenna designs known for good performance over metallic ground planes were investigated. In this case, a 100 MHz inverted-F antenna (geometrically similar to the dipole, but featuring different feed) over a cylindrical metallic ground plane (BHA) was modeled in Ansoft HFSS. Due to the fact that the antenna has the largest dimensions at the lower end of the considered frequency band (100 MHz – 1GHz), this is the worst case for implementation. The radiating efficiency of dipole like antennas over a metallic
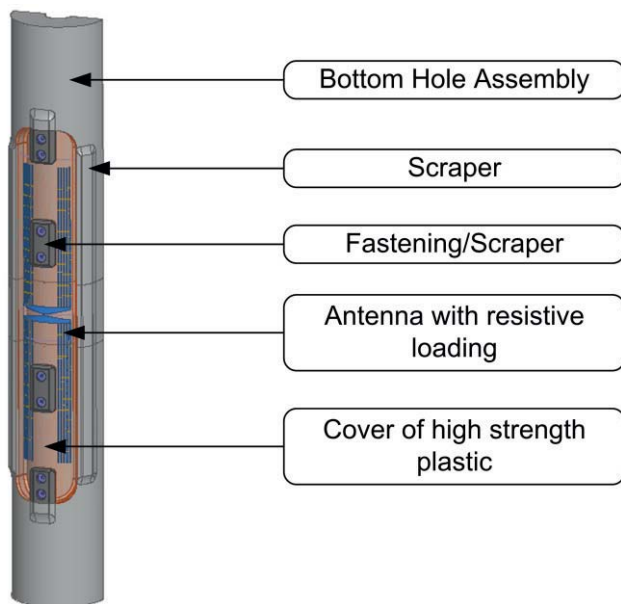
ground plane can be enhanced by flattening the antenna structure, thus increasing the width of the radiating edges. The objective was to investigate the optimum antenna width around the bottom hole assembly circumference for maximum antenna gain thereby allowing maximum
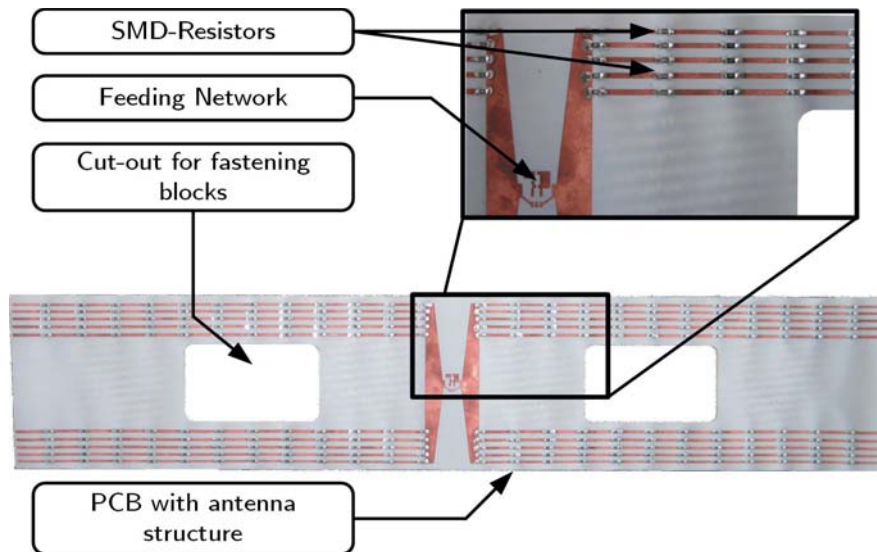

Figure 6: Realized, resistive loaded antenna for the implementation into the bottom hole assembly [17]

field radiation into the surrounding rock. Figure 4 illustrates the antenna gain versus its width in relation to the bottom hole assembly circumference, spanning 1 to 340 degrees. An optimum at approximately 45 deg is observed.

Due to these considerations efforts were mainly focused on overcoming these technical difficulties of a pulse-radiating, resistively-loaded, half-wave dipole antenna over a metallic plate. Therefore, a model was set up with the help of the software Ansoft HFSS and Autodesk Inven-
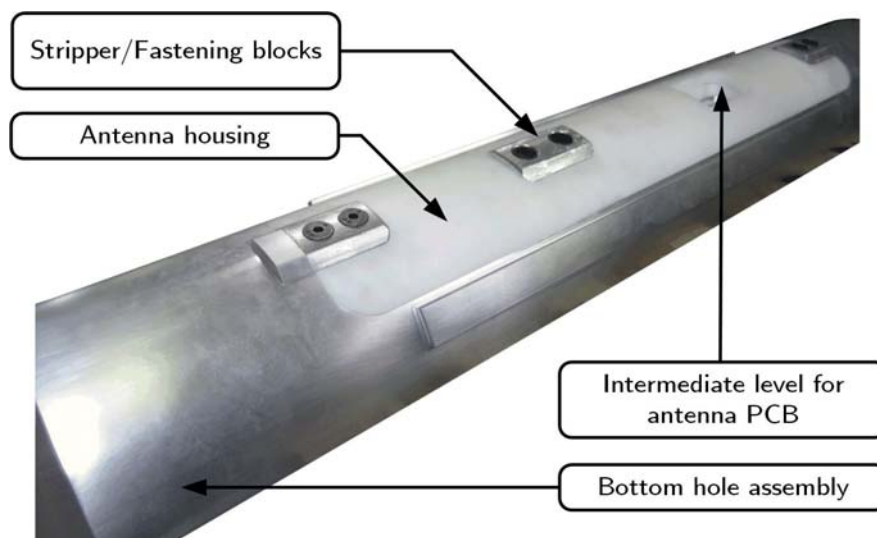

Figure 7: Developed prototype of the bottom hole assembly with integrated radar antenna [17]

951

tor to co-simulate and optimize the radiation characteristics of the antenna and the mechanic stability of the modified bottom hole assembly. Figure 5 shows the simulation model of the integrated antenna, Figure 6 the realized, resistive loaded antenna which was optimized with the help of intense parametric studies regarding the geometry and resistive loading. Figure 7 shows the developed prototype of the bottom hole assembly made of aluminum for the bottom hole assembly and polyoxymethylen (POM) for the antenna housing. Extensive information about the parametric studies, the mechanic stability investigations and the overall implementation can be found in [16] and [17].

New measurement tools

Commercial ground penetrating radar systems are proprietary solutions where the manufacturer's transceiver is only exclusively combined with the manufacturer's recommended antennas. The development and evaluation of a customized ground penetrating radar antenna designed for the bottom hole assembly requires the use of special measurement devices. The Institute of Transport and Automation Technology in cooperation with Sympuls Aachen GmbH, has developed a special TDR/Radar measurement and test device. The TDR-3000TER is configured in such way that beside the time domain reflectometry (TDR mode) functionality for the qualification of antennas, it can also produce short pulses and detect the reflected echo (GPR mode). The pulse center frequency can be selected between 50 MHz and 500 MHz so the most interesting GPR frequencies can be examined. Field tests can be carried out for diverse antennas, while a transmit/receive impulse diagram can be easily visualized with the help of a personal computer.

Investigation of rock and fluid influences

The influence of the surrounding material, especially the existing water, regarding the overall system performance has to be considered. Therefore, measurements with a commercial ground
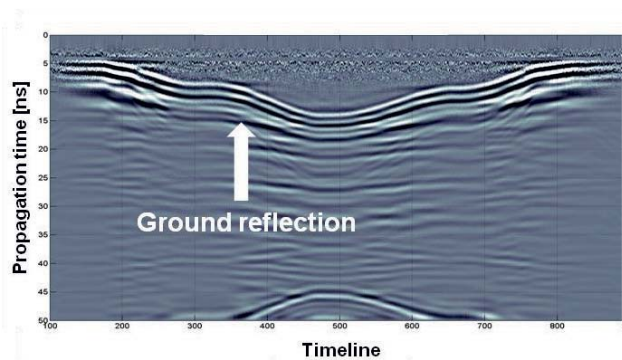

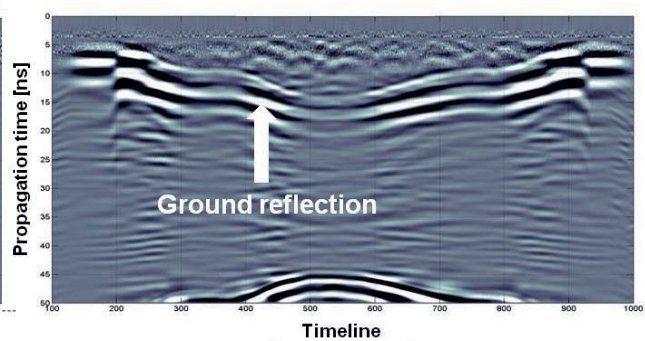**Figure 8: Radargram of ground detection through a sandstone plate saturated with salt water**

Figure 9: Radargram of ground detection through a closed salt water layer

penetrating radar system from the Italian manufacturer IDS have been done with an associated antenna at 600 MHz which is close to the center of the considered frequency band. The antenna of the system was raised from ground to approx. 80 cm, than to approx. 160 cm and back to 80 cm and ground (see figures 8, 9 – from left to right) and the detection and position of the ground layer was monitored. This was done with several specimens mounted directly in front of the antenna to observe the influence on electromagnetic wave absorption and layer detection. Figure 8 shows a processed radargram of a sandstone plate (4 cm thick) saturated with salt water (salinity 20 vol. %). Figure 9 shows the same measurement with a salt water layer (salinity 20 vol. %) of 1 cm thickness. Field attenuation was measured for these specimens resulting in -7 dB (sandstone) and -8 dB (water layer) at 600 MHz. Despite the fact that attenuation is almost equal in both cases one can see that a closed water layer produces more distortion due to the much higher permittivity of the water. Nevertheless, ground detection is possible even in the
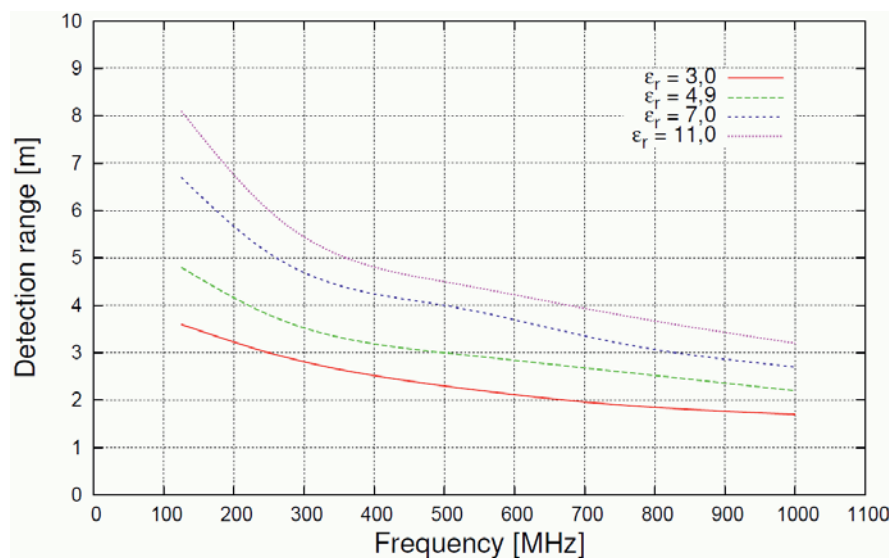

Figure 10: Anticipated detection range for different rock permittivity and frequencies for a rock conductivity of 15 mS/m [17]

presence of a closed salt water layer. Since rock porosity decreases with depth (sandstone 3 % at 4000 m), the negative influence of the water inside the rock can be neglected. Minimization of the drilling fluid influence (closed fluid layer) must be achieved by proper BHA engineering.

To investigate the detection range and resolution in bedrock (hard dry rock) simulations with the help of the software ReflexW and measurements in a quarry were done. Furthermore, information from [18] was used. Figure 10 shows the anticipated detection range for different permittivity of the surrounding rock and different frequencies. The high impact of these two values is clearly to see and has to be considered for each application regarding the use of ground penetrating radar. Additionally, the electromagnetic behavior of the ground penetrating radar system itself, such as impulse power, antenna efficiency and receiver sensitivity has to be considered

due to their significant effect on the detection range. Extensive information about these investigations can be found in [17].

AP3 – Evaluation of the GPR and measured data and optimization for an effective drilling process

The developed ground penetrating radar antenna (Fig. 6), integrated into the metallic bottom hole assembly (Fig. 7) was evaluated with the help of the above mentioned radar system TDR-
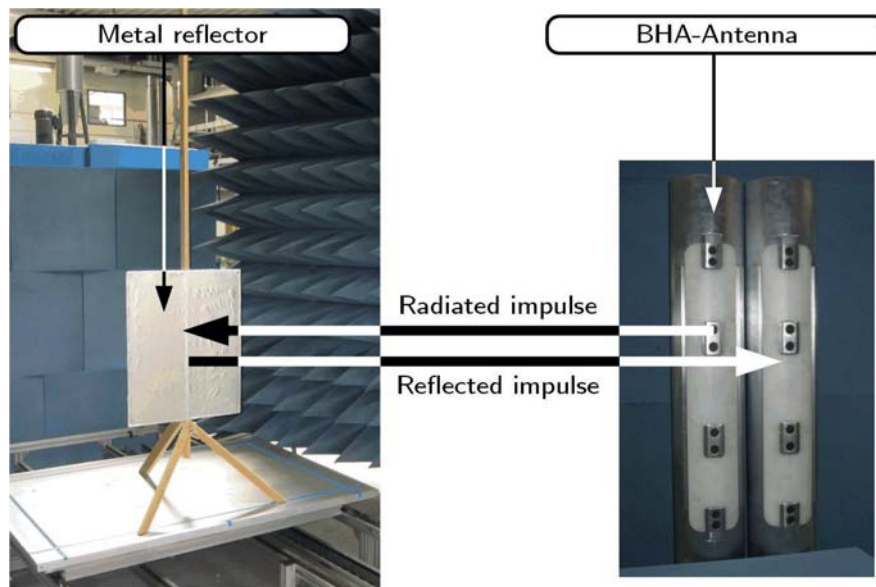

Figure 11: Measurement setup for the verification of the radar system [17]

3000TER from Sympuls Aachen and the spectrum analyzer FSH 3 from Rohde&Schwarz. Measurements were carried out at the institute's hall. Figure 11 shows a measurement setup; figure 12 the radargram of the measurement for the verification of the radar system. A metallic reflector of size 40 cm by 60 cm, positioned in front of the antennas at a distance of 1 m (11 ns), is moved with constant speed to a distance of 3.5 m (28 ns). A clear representation of the reflectors reflection can be found and shows the good functionality of the radar system. Furthermore, antenna parameters such as transmission loss and group delay were measured and compared to the simulated values. Good compliance could be found. Extensive information about these investigations can be found in [17].
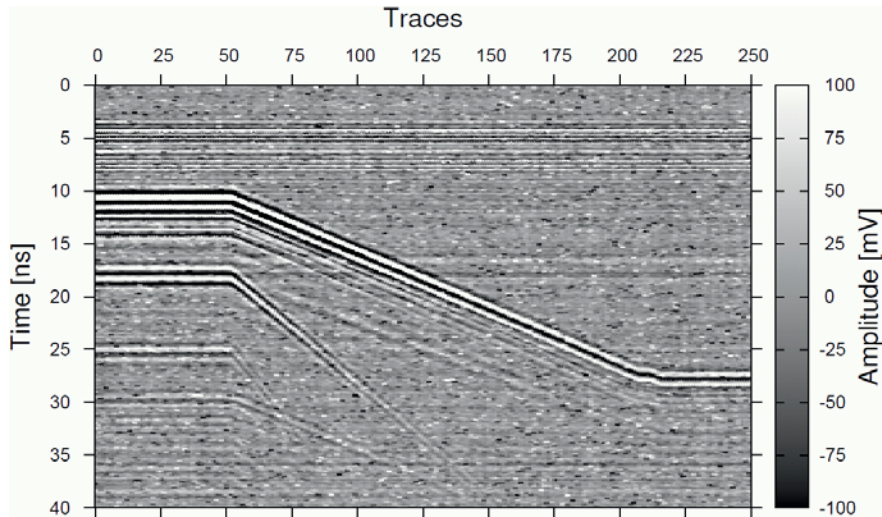
Figure 12: Radargram of the measurement for the verification of the radar system [17]

Further investigations were made regarding the data transmission to the surface. State of the art transmission technologies such as mud pulse techniques suffer from limited transfer rate of approx. 10 Mbit/s. Transmission of the raw data of the ground penetrating radar can therefore not be transmitted in an adequate time. Goal is to extract the relevant information prior it's transmission out of the raw data with proper algorithms inside the electronic of the bottom hole assembly. The investigations have shown that a data reduction of more than 90 % can be achieved. The remaining data can be transmitted via the mud pulse technique in an adequate time compared to the rate of penetration. Extensive information about this topic can be found in [19].

AP4 – Prototype testing of the GPR-inside-BHA-concept
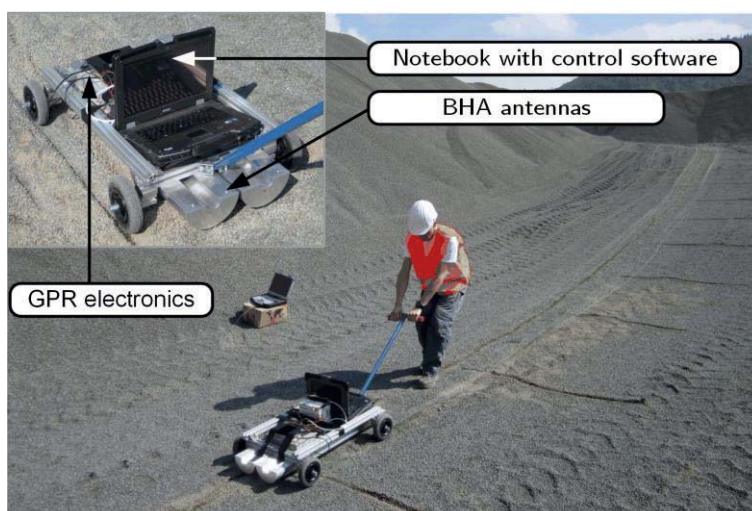
Figure 13: Field measurement in a quarry at a heap of gabbro with the bottom hole assembly ground penetrating radar system [17]

To further evaluate the demonstrated bottom hole assembly antennas, field measurements were carried out in a gabbro quarry of the company "Norddeutsche Naturstein GmbH" near the town of Bad Harzburg in Northern Germany. For comparison the commercial 600 MHz system of the Italian company IDS was used. Measurements were taken at a heap of gabbro of grain size 5

955

mm. This scenario is shown in figure 13. Along the compacted heap, radargrams were recorded, both with the commercial and the bottom hole assembly system.

Figure 14 shows the recorded radargrams for the bottom hole assembly (upper) and the commercial radar system (lower). It is seen, that the bottom hole assembly system has clearly lower reverberation and higher clarity compared to the commercial system. This leads to a clear representation of the underground reflectors. On the other hand, the penetration depth is clearly lesser compared to that of the commercial system by at least a factor of 3. This factor has to be optimized for a commercial impact. Nevertheless, the developed and investigated resistive loaded antenna for integration into the confined space of a metallic bottom hole assembly is suitable to bring forth the use of ground penetrating radar at drill string applications. Extensive information about these investigations can be found in [17].
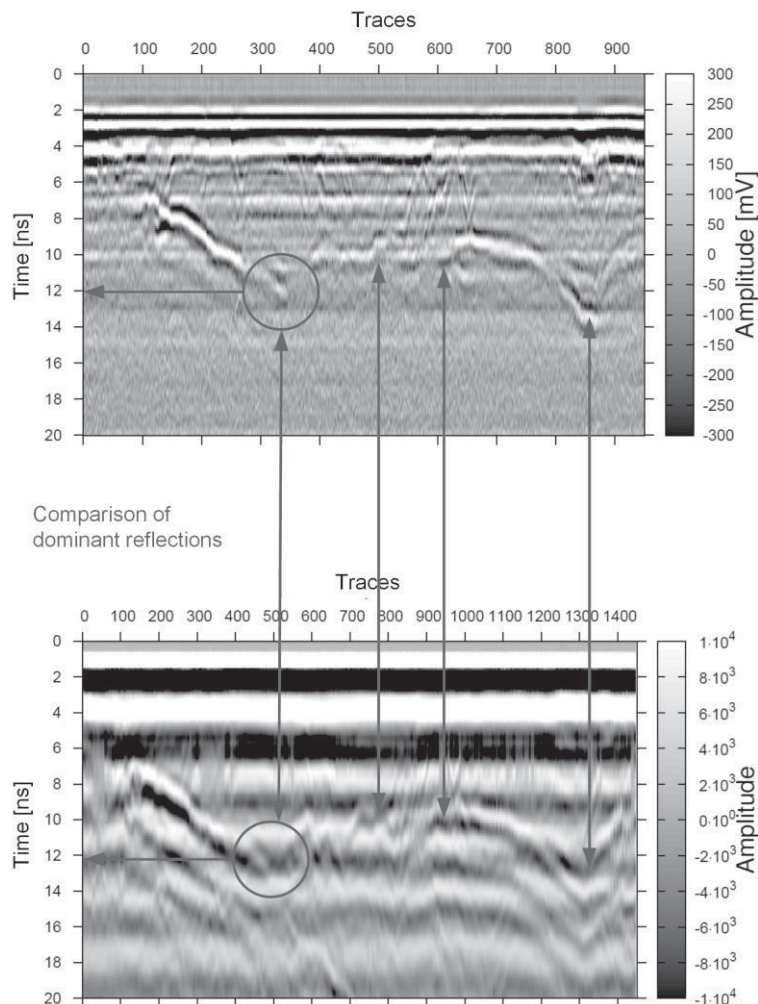

Figure 14: Comparison of major reflections, recorded with the investigated bottom hole assembly system (upper) and the commercial radar system (lower) at a heap of gabbro of grain size 5 mm [17]

2.4 Future research work and plans

2.5 Project Plan

Work packages and milestones	2009			2010			2011			2012			2013			2014		
AP1: Concept																		
AP2: Ground penetrating radar inside the bottom hole assembly																		
AP3: Data analysis of the sensor																		
AP4: Prototype																		

Grey, original plan

Blue, actual or current plan

For details, see Gantt chart in the Appendix.

3 Delineation of the project from other funded projects

The ITA is not involved in any project regarding geothermal or drilling techniques.

4 References

[1] **Knödel, K.; Krummel, H.; Lange, G.** (2005): Geophysik. Berlin: Springer (Handbuch zur Erkundung des Untergrundes von Deponien und Altlasten, / BGR, Bundesanstalt für Geowissenschaften und Rohstoffe ; Bd. 3)

[2] **Fritzsche, M.** (2001): Anwendung von Verfahren der Mustererkennung zur Detektion von Landminen mit Georadaren. Dissertation. Karlsruhe: Universität Karlsruhe, Institut für Höchstfrequenztechnik und Elektronik

[3] **Sternberg, B.; McGill, J.** (1995): Archaeology studies in southern Arizona using ground penetrating radar. In: Journal of Applied Geophysics, Vol. 33, No. 1-3, pp. 209-225.

[4] **Maierhofer, C.** (2003): Nondestructive Evaluation of Concrete Infrastructure with Ground Penetrating Radar. In: Journal of Materials in Civil Engineering, Vol. 15, No. 3, pp. 287-297

[5] **Landolt, H.; Hellwege, K.-H.; Madelung, O.** (1982): Zahlenwerte und Funktionen aus Naturwissenschaften und Technik. Gruppe 5, Band 1b. Neue Serie. Berlin: Springer.

[6] **Davis, J.; Annan, A.** (1989): Ground-Penetrating Radar for High-Resolution Mapping of Soil and Rock Stratigraphy. In: Geophysical Prospecting, Vol. 37, pp. 531-551

[7] **Overmeyer, L.; Kesting, M.** (2007): SIMT Technology – Sensor Identification of Material Type and Detection of the Interfaces. In: Bulk solids handling, Vol. 27, No. 2, pp. 112-118

[8] **Kesting, M.; Overmeyer, L.** (2008): Integration von Sensortechnologien zur Trennflächen- und Materialerkennung im Tagebau. 13. Fachtagung Schüttgutfördertechnik. S. XI 3-15

[9]   **Kesting, M.; Overmeyer, L.; Niemeyer, J.** (2008): Integration of Sensor Technologies at Bucket Wheel Excavator for Identification of Material Type and Detection of Interface Layers. In: 17th International Symposium on Mine Planning and Equipment Selection

[10]   **Kesting, M.; Niemeyer, J.; Mathiak, T.** (2009): Integration of Sensor Technologies at a Bucket Wheel Excavator for Identification of Material Type and Detection of Interface Layers. In: The Canadian Institute of Mining, Metallurgy and Petroleum, APCOM

[11]   **Höfinghoff, J.-F.** (2010): Besser sehen in 4000 Metern Tiefe: Georadar für die Tiefe Geothermie. Ingenieurspiegel: Public Verlag GmbH, pp. 57

[12]   **Reich, M.** (2003): Untersuchung komplexer Bohrgarnituren mit integriertem, schaltbarem Erweiterungswerkzeug. Dissertation. Freiberg: Technische Universität Bergakademie

[13]   **Lüke, H.** (1999): Signalübertragung. Grundlagen der digitalen und analogen Nachrichtenübertragungssysteme. Berlin: Springer

[14]   **Turk, A.; Sahinkaya, D.; Sezgin, M.; Nazli, H.** (2007): Investigation of Convenient Antenna Designs for Ultra-Wide Band GPR Systems. In: 4th International Workshop on Advanced Ground Penetrating Radar, pp. 192-196

[15]   **Lestari, A.; Yulian, D.; Liarto; Suksmono, A.; Bharata, E.; Yarovoy, A.; Ligthart, L.** (2007): Improved Bow-Tie Antenna for Pulse Radiation and its Implementation in a GPR Survey. In: 4th International Workshop on Advanced Ground Penetrating Radar, pp. 197-202.

[16]   **Höfinghoff, J.-F.; Overmeyer, L.** (2013): Resistive Loaded Antenna for Ground Penetrating Radar inside a Bottom Hole Assembly. In: IEEE Transactions on, 2013. - ISSN 0018-926X; DOI: 10.1109/TAP.2013.2283604

[17]   **Höfinghoff, J.-F.** (2013): Untersuchungen zur Anwendbarkeit von Georadar in der Bohrgarnitur. Dissertation. In: Berichte aus dem ITA, Band 4/2013. Garbsen: PZH Verlag

[18]   **Noon, D. A.; Stickley, G. F.; Longstaff, D.** (1998): A Frequency Independent Characterization of GPR Penetration and Resolution Performance. In: Journal of Applied Geophysics, Vol. 40, No. 1, pp. 127-137

[19]   **Mathiak, T.** (2013): Automatische Trennschichterkennung mittels Georadar am Schaufelradbagger. Dissertation. In: Berichte aus dem ITA, Band 1/2014. Garbsen: PZH Verlag

Links to homepages of institutes

Technische Universität Braunschweig:

Institut für Dynamik und Schwingungen	www.ids.tu-braunschweig.de
Institut für Elektrische Messtechnik und	
Grundlagen der Elektrotechnik	www.emg.tu-bs.de
Institut für Festkörpermechanik	www.tu-bs.de/fm
Institut für Geophysik und Extraterrestrische Physik	www.igep.tu-bs.de
Institut für Halbleitertechnik	www.iht.tu-bs.de
Institut für Oberflächentechnik	www.tu-bs.de/iot
Institut für rechnergestützte Modellierung im Bauingeniuerwesen	www.irmb.tu-bs.de
Institut für Werkstoffe	www.tu-bs.de/ifw

Technische Universität Clausthal:

Institut für Endlagerforschung	www.ielf.tu-clausthal.de
Institut für Elektrische Energietechnik	www.iee.tu-clausthal.de
Institut für Erdöl- und Erdgastechnik	www.ite.tu-clausthal.de
Institut für Geophysik	www.ifg.tu-clausthal.de
Institut für Maschinelle Anlagentechnik und Betriebsfestigkeit	www.imab.tu-clausthal.de
Institut für Technische Mechanik	www.itm.tu-clausthal.de

Gottfried Wilhelm Leibniz Universität Hannover:

Institut für Werkstoffkunde	www.iw.uni-hannover.de
Institut für Fertigungstechnik und Werkzeugmaschinen	www.ifw.uni-hannover.de
Institut für Transport- und Automatisierungstechnik	www.ita.uni-hannover.de
Institut für Mess- und Regelungstechnik	www.imr.uni-hannover.de
Institut für Mikroproduktionstechnik	www.impt.uni-hannover.de
Institut für Mikroelektronische Systeme	www.ims.uni-hannover.de

Georg-August-Universität Göttingen:

Geowissenschaftliches Zentrum	www.gzg.uni-goettingen.de

Leibniz-Institut für Angewandte Geophysik	www.liag-hannover.de
Bundesanstalt für Geowissenschaften und Rohstoffe	www.bgr.bund.de
Energie-Forschungszentrum Niedersachsen	www.efzn.de
Baker Hughes	www.bakerhughes.de